Downloaded from orbit.dtu.dk on: May 05, 2023

DTU Library

Foundations of Active Control - Active Noise Reduction Helmets

Elmkjær, Torsten Haaber Leth

Publication date:
2008

Document Version
Publisher's PDF, also known as Version of record

Link back to DTU Orbit

Citation (APA):
Elmkjær, T. H. L. (2008). *Foundations of Active Control - Active Noise Reduction Helmets*.

General rights
Copyright and moral rights for the publications made accessible in the public portal are retained by the authors and/or other copyright owners and it is a condition of accessing publications that users recognise and abide by the legal requirements associated with these rights.

- Users may download and print one copy of any publication from the public portal for the purpose of private study or research.
- You may not further distribute the material or use it for any profit-making activity or commercial gain
- You may freely distribute the URL identifying the publication in the public portal

If you believe that this document breaches copyright please contact us providing details, and we will remove access to the work immediately and investigate your claim.

Technical University of Denmark

Torsten H. Leth Elmkjær

Foundations of Active Control - Active Noise Reduction Helmets

PhD thesis, November 2008

DTU Electrical Engineering
Department of Electrical Engineering

Foundations of Active Control

Active Noise Reduction Helmets

Torsten H. Leth Elmkjær

Terma AS
Hovmarken 4
DK-8520 Lystrup
Denmark
`tln@terma.com/`

Ørsted, DTU
Ørsteds Plads, Acoustic Technology, Bldn. 352
DK-2800 Lyngby
Denmark

Foundations of Active Control

Active Noise Reduction Helmets

Torsten H. Leth Elmkjær

Ph.D. Dissertation

Skødstrup, November 7, 2008

Terma AS
Hovmarken 4
DK-8520 Lystrup
Denmark
`tln@terma.com/`

Ørsted, DTU
Ørsteds Plads, Acoustic Technology, Bldn. 352
DK-2800 Lyngby
Denmark

Technical University of Denmark Press

Publication Data:
Torsten H. Leth Elmkjær
Foundations of Active Control
Active Noise Reduction Helmets
ISBN 978-87-911-8485-7

Copyright © 2008 Elmkjær

This work is dedicated — *Alma, Othilie and Marianne* —

ABSTRACT

This Ph.D. thesis includes fundamental considerations about topologies, algorithms, implementations, methods etc., that can enter in the next generation of active control (AC) systems.

Specifically, a new variant of feedforward control referred to as confined feedforward active control (CFFAC) is proposed. This topology is constituted from a set of reference sensors that are positioned on a surface that completely *confines* the desired *zones of quite*. A set of performance sensors monitors the achieved noise reduction. This CFFAC topology in turn is embedded in a multiple-input and multiple-output (MIMO) system that facilitates both feedforward and feedback control. The general system is then referred to as hybrid MIMO confined-feedforward feedback (HMIMOCFFFB) active noise reduction (ANR) system. The investigation of a multi-channel ANR system with hybrid feedforward and feedback topologies is motivated by requirements of high ANR attenuation in extreme noise environments as typically experienced onboard airborne military platforms. Noise recordings acquired on such platforms reveal very high sound pressure levels often exceeding 140 dB re. 20 μPa. Moreover, these noise signals exhibit large temporal as well as spatial variations. Inherent limitations are related to the use of stand-alone feedback AC implementation commonly applied in modern ANR headset. In such systems the anti-noise signal is notoriously behind the primary disturbance in time. Accordingly, in demanding military applications requirements on more advanced and effective ANR system designs prevail.

The achievable ANR performance in a feedforward system (FFS) is to a large extent determined by the degree of *coherence* between the set of reference sensors and the set of error sensors (or performance sensors). Accordingly, this thesis includes a number of coherence analysis that are based on diffuse sound field measurements in a reverberant chamber and measurements conducted onboard a CH-47D Chinook helicopter. From these coherence analysis it can be concluded that the CFFAC system with 10 reference sensors applied to pilot helmets potentially provides approximately 25 dB noise reduction at 100 Hz decreasing to approximately 10 dB attenuation at 900 Hz. Moreover, there is no apparent sign of saturation of the noise reduction with an increasing number of reference sensors. Accordingly, by using more reference sensors the *spatial sampling rate* is increased which in turn most likely also will lead to an increased ANR bandwidth. The hybrid system is also constituted from a continuous-time feedback system (FBS) and a discrete-time FBS. The continuous-time FBS is primarily responsible for additional *broadband* noise reduction, whereas the discrete-time FBS primarily is responsible for the attenuation of periodic signals.

Owing to the requirement on causal operation of a physical AC system time delays will also to a large extent determine the achievable performance in FFS design and in particular in FBS design. A quantity referred to as the spatially-weighted-averaged acquisition lead time is introduced to represent the averaged time-advance obtained by each reference sensor relative to each performance sensor involved in the proposed CFFAC system. A problem exist when one attempts to model a physical spatially distributed system with no obvious input and output channel definition by a finite lumped-elements multi-channel system. Usually, no unique transfer function

exist as the system is not point-wise excited, but excited over an area as in the case of diffuse sound field illumination.

A new method for acoustical signal processing that is referred to as joint-channel residual spectral analysis (JCRSA) is developed. The JCRSA method is used for the extraction of joint signal information from different observation positions in space. The idea is to separate each spectrum in a *coherent spectrum* and a *residual spectrum*. The contents of the coherent spectrum can be obtained from a linear superposition of the other signals, whereas the residual spectrum bears information that is unique to each specific channel. In a specific example a system consisting of 10 reference sensors flush-mounted on a Gentex HGU-55/P helmet that in turn is mounted on a head and torso simulator (HATS), is exposed to diffuse sound field illumination. By applying the JCRSA method the spatially-weighted-averaged acquisition lead times provided by the reference sensors relative to the performance sensors are estimated to be as much as 800-900μs.

The thesis also includes a detailed description of a new idea for a computational efficient implementation of a multi-channel system in which the adaptive filters for adaptive control as well as the adaptive filters used for plant modeling are allowing to take different lengths.

A new and more general variant of the affine projection algorithm has been developed. This adaptive filter algorithm that is denoted by multiple-channel-$\alpha\gamma\Pi\epsilon$-affine projection algorithm includes parameters for both weight-driven and control-effort-driven *leakage*, *adaptive tap-weight regularization* as well as *numerical regularization*. A simplification of this algorithm leads to the MC-$\alpha\gamma\Pi\epsilon$-NLMS algorithm that is an extended variant of the NLMS algorithm.

Off-line simultaneous system identification capabilities of a complex system involving a total 4 secondary paths, 20 feedback paths and 4 control-performance paths is demonstrated. Different adaptive filters and parameterizations hereof are examined.

A novel and general *multi-rate adaptive filter* for adaptive AC has been developed. Specifically, a system involving 3 different sampling rates has been implemented and the results hereof are presented. In this multi-rate system conversion take place at highly oversampled rates in order to reduce the delays in the secondary paths. The *non-adaptive control* is performed at a somewhat lower rate. Hereby, a compromise between delays related to the generation of the anti-noise signal and the computational load involved is ensured. Finally, the *adaptive control* that might be computational intensive takes place at an even slower sampling rate hereby relaxing the requirements on a high bandwidth. It is demonstrated that computational savings as high as 40% can be achieved in a $192, 24, 3$ kHz triple-rate system as compared with a 24 kHz single-rate system without sacrificing the ANR performance.

It is common engineering practice to apply an assumption of Gaussian distributed signals. However, many phenomena encountered in daily life fall into a generalization of the normal distribution that is referred to as α-stable distributions. Noise sources encountered in the domain of AC are sometimes best fitted to the family of α-stable distributions. This thesis includes a brief technical introduction to the stable distributions and description of the adaptive filter that can be used for AC.

Large parts of the HMIMOCFFFB system including the developed methods and algorithms have been implemented in a real-time environment (RTE) that includes a signal processor. Test on the helmet system will continue and a dedicated reference test unit (RTU) for AC is currently being designed.

RESUMÉ (IN DANISH)

Denne Ph.D. afhandling omfatter fundamentale betragtninger omkring topologier, algoritmer, implementeringer, metoder etc., der kan indgå i næste generation af aktive kontrol systemer.

Specifikt foreslås der en variant af feedforward kontrol refereret til som indesluttet feedforward aktiv kontrol forkortet IFFAK. I denne topologi indgår et sæt reference sensorer, der er positioneret på en overflade, der fuldt ud indeslutter de ønskede *stille-zoner*, hvori et sæt performance sensorer monitorerer den opnåede støjreduktion. Denne indesluttet-feedforward aktiv kontrol (IFFAK) topologi er indlejret i et mange-input-mange-output (MIMO) system, der omfatter både feedforward og feedback kontrol. Det totale system er refereret til som et hybrid MIMO indesluttet-feedforward FBS (HMIMOIFFFBS).

Undersøgelsen af et komplekst multi-kanals aktiv støjreduktion (ASR) system med hybrid feedforward og feedback topologier er motiveret ud fra krav om høj aktiv støjdæmpning i ekstreme støjmiljøer, som f.eks. opleves ombord på luftbårne militære platforme. Støjoptagelser erhvervet ombord på sådanne fartøjer afslører lydtryk, der ofte overstiger 140 dB re. 20 µPa. Endvidere udviser disse støjsignaler store tidslige såvel som spatiale variationer. Naturlige begrænsninger i feedback baserede aktiv kontrol (AK) systemer som typisk anvendes i moderne ASR støjværn, hvor modstøjssignalet notorisk er forsinket i forhold til den primære forstyrrelse, sætter en øvre grænse for, hvor stor en aktiv dæmpning, der kan opnåes. Således, hersker der i krævende militære applikationer et krav om nye mere avancerede og effektive ASR løsninger.

Den opnåelige ASR i et FFS er i stor udstrækning bestemt af *kohærensen* mellem sættet af reference sensorer og sættet af fejl- eller performance sensorer. Således omfatter denne afhandling en del kohærensundersøgelser baseret på diffustfeltsmålinger i et støjkammer samt målinger, der er foretaget i en CH-47D Chinook helikopter. Fra disse kohærensanalyser kan det konkluderes, at IFFAK systemet anvendt på pilothjælme giver mulighed for ca. 25 dB støjreduktion ved 100 Hz faldende til ca. 10 dB dæmpning ved 900 Hz. Endvidere, er der ikke nogen umiddelbare tegn på en mætning med stigende antal reference sensorer. Således vil et større antal reference sensor forventeligt kunne øge den øvre ASR frekvensgrænse for systemet, der bestemmes af den rumlige samplingstæthed. I hybridsystemet indgår der både et kontinuerlig-tids FBS og et diskret-tids FBS. Disse vil bidrage med yderligere støjreduktion primært overfor bredbåndet støj henholdsvis overfor periodiske signaler.

Tidsforsinkelser udgør en anden bestemmende faktor for den opnåelige effekt i et FFS design, men specielt i et FBS design, eftersom fysiske systemer altid opererer *kausalt*. For at vurdere størrelsesordenen af det tidsforspring som hver reference sensor giver i forhold til hver fejlsensor i det foreslåede IFFAK system indføres en størrelse, der betegnes som den *spatialt-vægtet middeltidsgevinst*. Der eksisterer imidlertid et problem, når man forsøger at modellere et fysisk system med en endelig rummelig udstrækning og hvor der således ikke er nogen indlysende input-output definition med et endeligt-element multi-kanals system. Som regel eksisterer der ikke nogen unik overføringsfunktion eftersom systemet ikke bliver punktvist stimuleret, men derimod stimuleret

over et areal som for eksempel under diffustfelts belysning.

En ny akustisk signalbehandlingsmetode, der betegnes som samlet kanal residual spektral analyse (SKRSA) er udviklet. Denne metode benyttes til ekstraktion af fælles signal information fra forskellige observationspunkter i rummet. Ideen er at separere hvert spektrum i et *kohærent spektrum* og et *residual spektrum*. Indholdet i det kohærente spektrum kan opnåes som en linear kombination af spektrene fra de andre kanaler, hvorimod indholdet af det residuale spektrum er unikt for den pågældende kanal. I et specifikt eksempel, belyses et system bestående af et sæt reference sensorer monteret på en Gentex HGU-55/P hjælm, der igen er påmonteret en hoved og torso simulator med et diffust lydfelt. Under anvendelse af SKRSA metoden estimeres den spatialt-vægtet middeltidsgevinst til at være i størrelsesorden 800-900µs.

Afhandlingen omfatter også en detaljeret beskrivelse af en ny idé til en beregningsmæssig effektiv implementering af et multi-kanals system, hvor både de adaptive filtre, der indgår i den aktive kontrol såvel som de adaptive filtre, der indgår til modellering af systemoverføringsfunktionerne kan antage individuelle længder.

En ny og mere generel variant af APA algoritmen er udviklet. Denne adaptive filter algoritme inkluderer parametre for både wægt-styret og kontrol-effekt-styret *lækage*, *adaptiv tap-vægte regulering* såvel som *numerisk regulering* og betegnes MC-$\alpha\gamma\Pi\epsilon$-APA. En simplificering af denne algoritme, fører til MC-$\alpha\gamma\Pi\epsilon$-NLMS algoritmen, der er en udbygget variant af NLMS algoritmen.

Systemets evne til off-line simultant at kunne identificere et complex system bestående af ialt 28 enkelt systemgrene bliver demonstreret. Forskellig adaptive filtre samt parametering heraf bliver udforsket.

Et nyt og generelt multi-hastigheds systemkoncept for aktiv kontrol er udviklet. Specifikt implementeres og testes et system, hvor der i alt samples med tre forskellige hastigheder. På multi-hastighedsniveau 0 benyttes en meget høj samplingsfrekvens med henblik på at reducere forsinkelser i konverteringstrinene, der indgår i de sekundære grene. Den ikke adaptive kontrol udføres på det lavere multi-hastigheds niveau 1. Herved tilsikres et kompromis imellem forsinkelser til afgivelse af modstøjssignaler og krav til en endelig system båndbredde. Sluttelig foregår den *adaptive kontrol* ved det lavere multi-hastigheds niveau 2. Herved begrænses den ofte beregningsmæssige tunge adaptive filter opdatering til en så lav samplingsfrekvens som muligt.

I et specifikt eksempel demonstreres, at en beregningsmæssig besparelse på ca. 40% kan opnås under opretholdelse af samme ASR ved nedsampling fra multi-hastighedsniveau 1 på 24 kHz til multi-hastighedsniveau 2 på 3 kHz.

Det er en almindelig ingeniørpraksis at foretage en antagelse om Gaussisk fordelte signaler. Imidlertid, er mange fænomener i dagligdagen bedst modelleret med såkaldte alfa-stabile fordelings funktioner. Dette gælder også for støjsignaler, der ønskes undertrykt ved hjælp af et aktivt støjdæmpningssystem. Afhandlingen indholder en kort teknisk beskrivelse af de stabile fordelingsfunktioner samt adaptive filter algoritmer for disse type signaler.

Store dele af HMIMOIFFFB systemet samt de udviklede metoder og algoritmer er implementeret i et realtids miljø, der inkluderer en signal processor. I første omgang vil disse blive aftestet på en til formålet designet aktive kontrol testenhed.

ACKNOWLEDGEMENTS

I am grateful to my employer, Terma AS, for formulating and sponsoring this project. In particular I wish to appreciate my colleague Torben Jørgensen who originally proposed the Ph.D. project for his enthusiasm and engagement in making avionics audio system a business area at Terma.

My supervisor Finn Jacobsen is acknowledged for in the first place for daring to take the role as a supervisor for an antenna specialist in the field of acoustics and signal processing and in the second place for dealing with management issues during the course of the project. I am also thankful for his critical review of this manuscript and for providing good comments that have improved the overall readability of the report.

I am also indebted to Jacob Krogh Kristoffersen who has contributed in many practical contexts during the project especially in the development of the Terma noise chamber facility and the DSP implementation of part of the ACSV simulator pertinent for the RTE. Jacob Krogh Kristoffersen is also acknowledged for reviewing Part II and Part III of this report.

I also wish to thank Jakob Krogh-Mayntzhusen[1] for his DSP hardware board design and together with Torben Jørgensen for their assistance during the F-16 noise measurements and rehearses.

My thanks also go to Chlinton Møller Nielsen for many fruitful discussions in the field of signal processing and for taking over the responsibilities related to the transducer selection and test. Moreover, Chlinton Møller Nielsen is thanked for his and Jakob Krogh-Mayntzhusen hard work effort in connection with the Chinook CH-47D helicopter noise recordings. Birger Fauerholt Nielsen is acknowledged for his work on real-time environment (RTE) implementation of the adaptive filter algorithms.

Hans-Jørgen Bjerre is acknowledged for his workmanship in producing the mechanical fixture for the recording system.

Librarian Inge Merete Jensen and Bitten Marie Welling are greatly thanked for their assistance in the acquisition of most of the material listed in the Bibliography.

Mogens Ohlrich is thanked for his engagement as section leader at the institute and teaching me in the field of in structure-borne sound. Finn Agerkvist and Knud Rasmussen are acknowledged for fruitful discussions concerning the choice and design of electroacoustics transducers and recommendations of manufactures. Torben Poulsen is thanked for helpful discussions related to the psychoacoustic part and related to standard test procedures for hearing protection devices.

I am also greatly indebted to Tom Petersen for his assistance with miscellaneous software installations.

The Danish Flight Command is thanked for the cooperation in connection with the F-16 noise measurements. Special thanks shall be given to flight Captain Kasper B. Nielsen (PEL) for his

[1] Formerly known as Jakob Krogh-Sørensen.

enthusiastic effort during the planning of the measurement and for flight. I also grateful for DTU-Ørsted for in the initial phase of the project to lend us one of their PULSE recording systems. The Engineering College of Aarhus is for providing the head and torso simulator (HATS).

I also appreciate the hospitality by the ANR people at Thayer's School of Engineering Dartmouth College, NH, USA during my summer stay 2005. In particular I express my gratefulness to Bob Collier for hosting me and for encouraging us to make joint active noise reduction (ANR) efforts.

Finally, I am deeply indebted to my wife Marianne Astrid Elmkjær, who so generously accepted the extra responsibilities that her husband neglected while authoring this report.

PREFACE

This report is submitted in partial fulfillment of the requirements of the Danish Ph.D. degree. The work has financially supported by Terma and conducted under the supervision of Associate Professor Finn Jacobsen at the Section of Acoustic Technology at Ørsted · DTU, Technical University of Denmark.

CONTENTS

LIST OF FIGURES

LIST OF TABLES

LIST OF MATLAB® SIMULATIONS

NOTATION

The present report is multi-disciplinary involving contributions from many different technology fields. Tentatively, variables should have an unambiguous identity. This goal has partially been achieved. However, in order not to deviate from defacto standards in different communities some reuse of identities has been considered necessary. For example, in signal processing community the symbol λ is used to designate wavelength or an eigenvalue both is also used to designate the so-called forgetting factor in the family of recursive least-squares. However, in the specific context no practical ambiguity will prevail.

We will used bold fonts to designate random variables as opposed to dummy variables designated by plain characters. For scalar quantities the time index is set in parenthesis. A subscript is used to designate the time index of a vector or matrix quantity.

Formally, the tap-weight vector is an estimate of a tap-weight vector subject to a specified cost function. Hence, as in [1] we arguably ought to indicate this, e.g., by applying accent caret to w, that is, $\hat{w}$. However, in order to reduce the notational burden and also be compatible with, e.g., [4] we will suppress the caret and let the estimation process implicitly be understood.

Moreover, in [4] the usual concept of considering the observation vector u as a *column* vector is abandoned and is instead defined as a *row* vector. In our formulation we will employ the column vector definition of the observation vector.

Index origin zero or one. In most programming languages like C or FORTRAN it is customary to use 0 (zero) as index origin in matrix or vector indexing. However, in MATLAB®[2] 1 (one) has (unfortunately) been selected. Moreover, for some quantities, e.g., eigenvalues, poles, zeros the counting always start at 1.

Preferably each symbol should have a unique meaning throughout the report. However, different de facto standards among technical communities represented here add some complication to this. Instead of introducing new symbols or adding subscripts or superscripts to existing symbols, the choice has been made to follow de facto standards and thus allow reuse of symbols for different purposes in this report. For example, a symbol like λ is used for different purposes in different contexts. Moreover, in the Nomenclature every such representation of a symbol is listed. However, it should in most cases from the actual context be clear what is actual meaning of a symbol is.

In the domain of fluid theory, but also to some extent in the domain of elasticity theory the nomenclature from [3] has been used. In the Nomenclature a list of almost every symbol used in this report. This list includes a description of the symbol, a reference to the page where it is defined and for convenience the unit of measurement. Throughout the report, we have applied the Système International d'Unités (SI).

[2] MATLAB® is a trademark of MathWorks Inc.

The mathematical notation applied in this report is to a large extent adapted from [2]. Although the use of subscripts and superscripts etc. to some readers may seem to be overly pedantic, however, this notation has been of great advantage to the author during preparation of this report, in the derivation of the formulas and especially during MATLAB® implementation and subsequent RTE implementation.

This thesis has been typeset using LaTeX 2_ε[3] and using the XY-pic package version 3.7 released 1999/02/16for the construction of most of the figures.

Bibliography

[1] Simon Haykin. *Adaptive Filter Theory*. Prentice-Hall Inc. Upper Saddle River New Jersey 07458, 3rd edition, 1996.

[2] Diederich Hinrichsen and Anthony J. Pritchard. *Mathematical Systems Theory I*. Springer-Verlag, Berlin, 2005.

[3] Christopher L. Morfey. *Dictionary of Acoustics*. Academic Press, London, 2001.

[4] Ali H. Sayed. *Fundamentals of Adaptive Filtering*. John Wiley & Sons, Inc., New York, NY, USA, 2003.

[3] TeXis a trademark of the American Mathematical Society.

1. INTRODUCTION

1.1 Background

Terma A/S, Ørsted-Technical University of Denmark (TUD) and the Engineering College of Aarhus (ECA) have initiated a joint research project in the field of active noise reduction. Terma specializes in development and production of systems for Electronic Warfare Integration and Control, Tactical Reconnaissance, and Environmental Surveillance. Terma is also involved in the design of the next generation of pilot helmets referred to as joint helmet mounted cuing systems (JHMCS), which includes 3-D audio. Existing fighter helmets, e.g., Gentex HGU 55/P yield insufficient low-frequency attenuation. As a consequence, the pilots are exposed to a low-frequency residual sound pressure which typically totals 90 dBA. Therefore, in order to improve the pilot's situational awareness a demand for additional noise countermeasures exists. Similarly in military helicopters the pilot and the crew are exposed to extreme sound pressure levels, that under normal operation condition exceeds $130 - 140$ dB prevail. For such applications the designers are facing a very challenging task that potentially requires man-years of research and development effort.

1.2 Brief Technical Discussion

In this section a brief technical discussion related to hearing protection devices (HPDs), active control (AC) and active noise reduction (ANR) headsets is provided. Readers unfamiliar with the scientific field of AC are strongly recommended to consult some of the excellent textbooks available, e.g., [1–3, 10].

1.2.1 Passive hearing protection device

Hearing protection devices have been used widely for 5-6 decades. A fundamental description of the physical principles was established in the late 1950s by Shaw and Thiessen in their classical papers [8, 9]. The HPD has successfully been modeled as a 2^{nd} order compliance-resistance-mass system. This mechanism is referred to as *passive attenuation* as it involves no active components. In summary, the passive performance of a circumaural HPD is limited by:

1. Hearing Protector Vibration (Non-deformative normal and lateral movements of earcup)
2. Air Leaks (at the interface between the users head and the ear cushion)
3. Material Transmission. (Deformation of earcup, frequency > 1 kHz)
4. Bone and Tissue Conduction

Since the late 1950s the performance has gradually been improved primarily due to the choice of a better material for the ear cushion and the earcups. A comprehensive physical modeling of HPDs was made by Schröter in his Ph.D. [5]. The main results of this work can be found in [6, 7]. In summary, from this work passive HPD usually provide a relative flat attenuation response of $8 - 12$ dB in the low-frequency range from 20 Hz to somewhere between $50 - 250$ Hz where a resonance might be experienced. Above the resonance frequency the attenuation increases by 10 dB/octave until approximately 35 dB beyond which other signal pathes such as bone conduction become more significant and therefore determines the perceived attenuation. Hence, in many applications where the noise is dominated by a high or sometimes an extreme low-frequency content passive HPDs simply provide **insufficient** attenuation capabilities.

1.2.2 Active hearing protection device

In modern HPD design the advantages of active noise control (ANC) have been accommodated in the more expensive range of units. Basically, ANC refers to the technique of:

- Acquisition of a signal with a high coherence with the disturbance, e.g., by a microphone
- Determination of a cancelation response (adaptive filtering, signal processing)
- Activation of the secondary (cancelation) signal, e.g., by a loudspeaker

The field of ANC dates back to the patent claimed by Olson and May [1953] [4]. Active noise cancelation inherently involves a *controller*. It is well known that the achievable performance has been very dependent on the quality of the system model, which in control theory terminology is referred to as the plant model. The plant basically includes the paths from the controller output terminal(s) to the controller input terminal(s) including the transformations from the digital domain to the acoustical domain. In the case of a ANR headset the plant will cover:

- Digital to analogue components
- Loudspeaker(s)
- Acoustical environment experienced by the set of transducers
- Microphone(s)
- Analogue to digital stages

The topology of active noise control systems falls into two categories:

- Feedback
- Feedforward

One of the drawbacks of a feedback system (FBS) is the limitation on control bandwidth, which also is referred to as the *"waterbed effect"*. Basically, the waterbed effect, which stems from the *Bode sensitivity integral*, when applied to our case postulates that attenuation over some frequency ranges necessarily implies amplification over the other frequency ranges. Moreover,

in the field of AC *stability* plays a very significant role in particular in feedback system (FBS) design. Owing to the waterbed effect and the simultaneous requirement of stability in feedback system (FBS) design a trade off between performance, that is, attenuation and robustness to plant uncertainties therefore always will exists. The feedback system (FBS) performance is largely determined by the time-lag that exist between an observation is made by the error sensor and until an appropriately dosed rejection signal is available at the same position.

In contrary, in a feedforward system (FFS) the possibility of *upstream* signal acquisition exists. Accordingly, a quantity that will be referred to as an *acquisition lead time* can obtained. On the other hand reference sensors positioned *down stream* relative to the propagation direction only provide reference signals with an *acquisition lag time*. Feedforward implementations, on the other hand, require a high correlation between the so-called reference signals that are sensed by the reference sensors and the disturbance signals that in turn are sensed by the error sensors. In both feedback system (FBS) and feedforward system (FFS) the error signals provide *performance feedback* to the (adaptive) controller.

The vast majority of AC applications involve the $\mathcal{H}_2$- and the $\mathcal{H}_\infty$-norms. The symbol $\mathcal{H}$ designates the *Hardy space*. More precisely $\mathcal{H}_2$ signifies the Hardy space of transfer functions with bounded 2-norm, that is, *stable and strictly proper* transfer functions. Similarly, $\mathcal{H}_\infty$ denotes Hardy space of transfer functions with bounded ∞-norm, that is, *stable and proper* transfer functions. It should be emphasized that we by the adjective, *optimal*, explicitly understand a $\mathcal{H}_2$ cost function as a statistical criterion.

As discussed above feedback system (FBS) are prone to stability problems due to the direct control feedback. In addition to these exclusive feedback system (FBS) and feedforward system (FFS) specific problems, stability due to imperfect plant modeling and the use of adaptive filters are also of concern in both feedforward system (FFS) and feedback system (FBS) design. Another type of feedback problem exists that is specific to feedforward system (FFS). If the reference sensors are not sufficiently isolated from the signals generated by the actuators the reference signals might be disturbed potentially leading to instability problems.

In recent years hybrid combinations of feedback and feedforward systems have been introduced aimed at taking advantage of both topologies while simultaneously avoiding or at least reducing the shortcomings of each individual topology.

The ANR headsets represent an example of *local active control*. In fact, it can be argued that the desired zones of quiet are very small and limited to the volumes of the earchannels.

The design of HPD with embedded active noise control system is complex requiring synergy between (not prioritized):

① Acoustics

② Transducer Technologies

③ Digital Signal Processing

④ Control

⑤ Vibroacoustics

⑥ Psycho Acoustics

⑦ Microelectronics

⑧ Material Technology

The present Ph.D. project primarily focus on the overall *system design* and scientific issues pertinent to points item ① and item ③.

Traditional ANR headsets are most likely single-input and single-output (SISO) feedback system (FBS) [s] (one per ear). These systems will normally be implemented as continuous-time time systems involving very cheap analogue components in a feedback configuration.

A conventional continuous-time ANR HPD solution satisfying pertinent military standards has also been developed by Terma. This analogue ANR system has been subjected to some tests in our noise chamber facility. Exposed to realistic F-16 Fighting Falcon noise this first prototype system demonstrated reasonable ANR capabilities. In the frequency range from 50 Hz to 300 Hz an active attenuation (as opposed to passive attenuation) exceeding 10 dB was observed. The performance was primary limited by delays in the single channel feedback topology, but also by the stability margins involved. In addition the original earphone (delivered with the Gentex HGU 55/P helmet) was deemed to provide too inefficient low-frequency response. A completely new earcup design was therefore initiated. Recent improvements of the overall continuous-time ANR system have resulted in an attenuation exceeding 10 dB in a frequency band from 100 Hz to 800 Hz.

Early experimentations with adaptive discrete-time (as opposed to continuous-time fixed) filters provided only a marginal overall performance gain. In some cases the upper 0 dB ANR frequency range was reduced from 800 Hz to 650 Hz. This lack of general performance increase can be attributed to the additional delays introduced by the conversion stages involved. Further tests with periodic signals, however, demonstrated the advantages of adaptive filtering over fixed filtering as could be expected. In both cases the system was operating with plant responses close to their nominal values where the continuous-time filter attains its best performance.

Some manufactures of ANR headsets claim to obtain active attenuation figures exceeding 30 dB. Unfortunately, such requirement specifications are usually commercially driven with no due respect to scientific integrity. The specific test conditions are therefore adroitly omitted.

Thorough evaluation of the same ANR headsets under diffuse sound field conditions gave another and less satisfying picture. Large negative deviations from specified attenuation numbers were observed. Moreover, stability problems could rather easily be provoced by a test person walking slowly around in a room with great spatial variation in the sound field. For a high-end product active attenuation of $20-25$ dB in the frequency range $140-300$ Hz, $15-20$ dB in the frequency range $90-400$ Hz and $10-15$ dB in the frequency range $50-530$ Hz was measured.

Hence, the very optimistic attenuation performance numbers proclaimed by some manufactures of ANR headsets are probably obtained under very idealized conditions such as upstream signal acquisition, periodic signals excitation or they stem from experiments with small volume couplers.

In contrary, Terma appreciating the environmental conditions in which our avionics equipment shall operate do comprehensive but **realistic** specification work with our costumers in due respect to their needs.

Although a set of physical and subjective based measurement procedures for passive HPDs exist, unfortunately currently no such standard exists for the test of active HPD.

For practical purposes the ANR HPD supposedly shall work in an often hostile environment with noise incident from almost everywhere and with a significant amount of random signal content. In addition the noise fields usually exhibit a high degree of temporal as well as spatial variation.

Accordingly, but as also confirmed by some of Terma's customers who actually have performed field evaluations of the aforementioned products, **no satisfactory** ANR solutions is currently available for the airborne military platforms.

Some manufactures of ANR headsets add feedforward control functionality by placing a microphone exterior to each earmuff. However, as is proven at various places in this report two reference sensors are often simply not enough to avoid the problem of spatial aliasing in particular under diffuse sound field conditions.

As the physical topology of a headset largely is determined by the humans wearing them, it is relative fixed and only a few possibilities are usually left for the designer. Improvements in transducer design and material technology also are reflected in better ANR designs. Moreover, the fast increase in MIPS provided by modern digital signal processor (DSP) also makes it feasible to implement more and more advanced signal processing algorithms in a discrete-time controller.

In the literature it is often seen that the noise attenuation predicted by a HPD measured by the error microphone in the active control loop exceeds the attenuation obtained from either physical ear channel measurements or psychophysical measurements by as much as 10 dB. Therefore, the acoustical /electro acoustical environment in modern active HPD determines an upper limit to the achievable attenuation figures, which probably is more problematic than the performance limitations associated with bone conduction.

For the signal processing part the least-mean-squares technique has been used extensively. The actual type of application dictates the use of adaptive algorithms in order to cope with an unpredictable noise environment and individual pilot-dependent system responses. Moreover, an adaptation capability also facilitates the use of relative inexpensive transducers which become particular important in more advanced systems involving multiple transducers. In the present case of noise control, the plant inherently introduces a non-negligible delay and possible uncertainty. In order to ensure filter weight convergence a filtered reference signal is used. The filtered reference signal is obtained by passing the reference signal through a plant model. Then the algorithm is referred to as filtered-x least-mean-squares (LMS), abbreviated filtered-x LMS (FxLMS).

In the active noise control literature both time-domain and various transform domain solutions have been proposed. In this project both time-domain and **z**-domain solutions are being considered.

1.3 Motivation

In section 1.2 it was mentioned that an active attenuation of $20-25$ dB is attainable under realistic conditions in the frequency band from 140 Hz to 300 Hz with current high-end ANR HPD. Unfortunately, even by taking passive attenuation into account the total attenuation is still to insufficient in particular in extreme noise cases as often experienced by military personnel.

The present Ph.D. project hopefully represents some initial steps on a probably long passage from this performance level to for example $30-35$ dB **active** diffuse sound field attenuation over a much wider frequency range, e.g., from 20 Hz to 1500 Hz.

However, as is well know among acousticians, antenna designers and active control (AC) engineers increasing system performance - if at all possible - by an order of 10 dB is usually associated with severe difficulties. Popularly phrased, it can be argued that in order to obtain 10 dB noise attenuation then among many other design issues, the designer must be in control of a least 90% of the energy present at the position where noise cancelation shall take place. However, for

20 dB or 30 dB noise attenuation only 1% respective 0.1% of the energy is allowing to be left unmodulated. Quite similar considerations apply to the design of antennas with low or very low side lobe levels (SLLs).

It should also be recalled that the requirement on attenuation performance, however, is very domain dependent and in some cases a smaller bandwidth with even higher achievable attenuation would be more usefull.

Moreover, attenuation capabilities are by no means the only figure of merit in HPD design. Among, other performance criterions we find *dynamic range of operation*, *stability*, *tracking capabilities* etc.

1.4 Research Objectives

Owing to the inherent limitation of feedback control in ANR headsets, in this Ph.D. a - to the author's best knowledge - new technique referred to as confined feedforward (CFF) control in which an array of reference sensors are placed on a surface completely *confining* the *zones of quite* will be investigated. This CFF topology in turn is embedded in a multiple-input and multiple-output (MIMO) system that facilitates both feedforward and feedback control. The general system then referred to as hybrid MIMO confined-feedforward-feedback system (HMIMOCFFFBS) ANR system is depicted in abstract form in Figure 1.1 on the facing page.

The sensor suite comprises N_e error sensors, N_x reference sensors and N_p performance sensors. In total N_y actuators excite the secondary signals. The $\mathcal{S}^x$ reference surface is the (artificial) surface constituted by the reference sensors.

The Ph.D. project, therefore also investigates the benefits of using multi-variable control, that is, a MIMO system configuration. The investigation of a multi-channel ANR system with mixed feedforward and feedback topologies is motivated by the following reasons

1. In diffuse sound fields the sound is by definition incident uniformly from all directions. In the simple feedback configuration part of the disturbance will enter the active control volume before it is sensed by the error microphone. From elementary control theory it is well known that delays in the control path will limit the operational bandwidth of the system. If instead an array of microphones is positioned on a surface enclosing the active control volume, in-time reference signals can be obtained.

2. Collectively, by the use of multiple reference sensors an increase in the multiple coherence function (MCOF) is obtainable. The MCOF provides a measure of the linearity of the system and an indicator of the presence of measurement noise and consequently a measure of the ANR capabilities of a system based on the assumption of a linear control system. By increasing the number of input sensors the rejection signals can more accurately be determined.

3. As the array of reference sensors completely confines the zones of quiescent time-advance reference signals information which in combination with a sufficiently high MCOF improves the ANR attenuation capabilities and operational bandwidth substantially as compared with ordinary feedback system (FBS) solutions in particular for random noise stimuli.

4. In the military domain the trend is to wear complex triple layer hearing protection devices. The first level of protection is provided by the helmet itself. The earcups constitute the

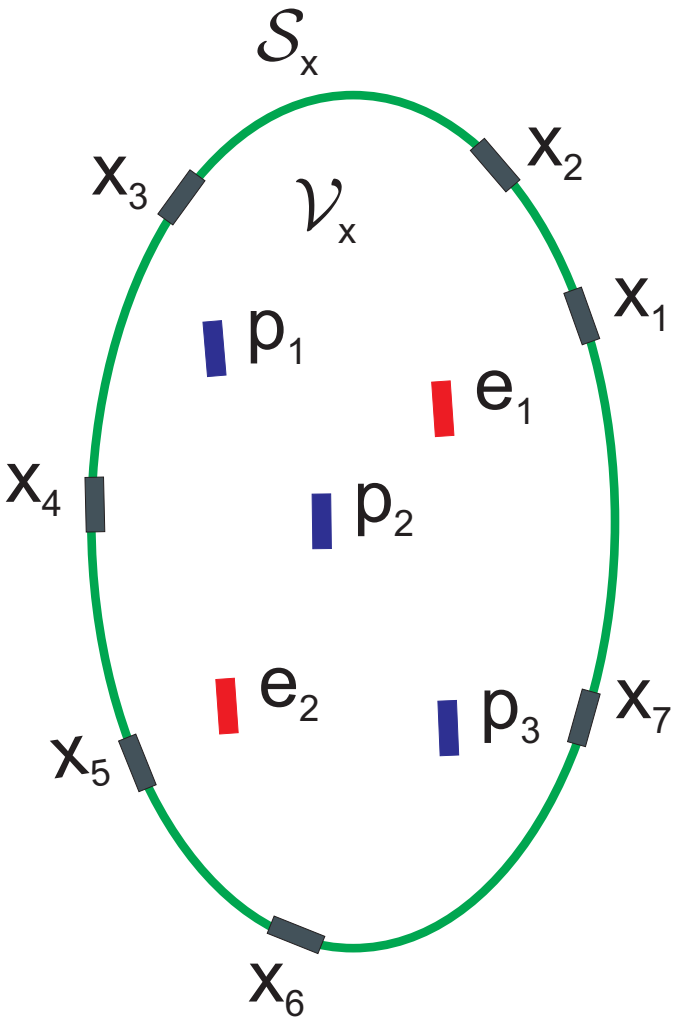

Fig. 1.1: ANR System Topology consisting of $N_x = 7$ reference sensors, $N_e = 2$ error sensors and $N_p = 3$ performance sensors.

second protection layer. The third protection layer is provided by earplugs that are either shallowly or deeply inserted in the earchannel. Both the earcups and the earplugs will be equipped with ANR hardware. A practical instantiation of the HMIMOCFFFBS involves the first and second protection layer in which an array of flush-mounted surface microphones on a helmet, a pair of error microphones in the vicinity of the entrance to the ear channels and a set of earphones that provide the anti-noise signals (rejection signals).

5. Provision for head-tracker capabilities. Terma also produces 3-D audio equipment. Essential to the 3-D audio performance is that the system can track the pilot own-maneuvers. By using a set of exterior sound sources the actual translatoric and angular data needed can then be processed using existing hardware to a large extent.

6. When the positions of the noise sources relative to the zones of quiescent are not static but time-varying the adaptive filters involved should respond accordingly. An audio based head-tracker function provides means to efficiently tune the adaptive filters to new optimal settings.

7. The feedforward part of the system becomes more fault-tolerant as the failure of a single sensor only will lead to some performance degradation especially for a feedforward-feedback system (FFFBS) involving many reference sensors. For single channel FFFBS such failure will imply that the feedforward part of the system simply stops working. The hybrid system, however, will still be vulnerable to failure of the error sensors. The actual F-16 Fighting Falcon and CH-47 Chinook applications are indeed considered mission critical. Hence, system failure cannot be tolerated.

The analysis of stability of MIMO systems with mixed feedback and feedforward topologies is considerably more complicated than in the SISO feedback case. The requirement on using adaptive filters as opposed to fixed (analogue) filters renders the analysis and synthesis of such filters even more challenging.

Although the original problem formulation specifically addresses AC in a HPD context, it has through out the course of the project been the ambition to establish the theory in more abstract and versatile context. The ANR helmet is merely used as an instantiation of this more general applicability of the research.

In order to test and evaluate developed theories and methods it is often very beneficial in engineering practice to work with a reference test unit (RTU) for which highly accurate models can be established. The design of a system for active control of sound and vibration (ACSV) represents no exception from the rule and therefore also pertain to the verification of a complex AC system including hybrid combination of feedforward and feedback system elements like the proposed HMIMOCFFFBS for instance. In contrary, only very crude models are available for helmet based HPDs. Therefore, it may often be difficult to predict very accurately the attenuation achievable when applying AC to such systems.

During initial system test, most likely errors and malfunctions are experienced at least by all honest engineers. The test and debugging of proposed HMIMOCFFFBS is no exception from general observation. During such evaluation phase, the problem is often associated with proper isolation of the fault or problem at hand. Sometimes it might be difficult to trace if a problem is related to the hardware, transducers, the control algorithms or the adaptive filter. Evaluation of the system design to the extent possible on a RTU can greatly help such localisation effort. Moreover, the RTU also serves as framework where a new type of measurement technique might be assessed with respect to obtainable accuracy.

The adaption of the spherical near-field antenna testing (SNFAT) technique discussed in Part I to the domain of acoustics looks as a promising idea in the development of such reference test unit. Accordingly for the development of a test unit for AC acoustical transparent and acoustical semi-transparent-semi-opaque hollow spheres are currently being considered.

A disadvantage of the CFF configuration is related to the requirement on a relative high number of reference sensors required in order to prevent spatial-aliasing of high-frequency components. In practice for the HMIMOCFFFBS applied to a helmet based HPD the minimum number of reference sensors amounts to six to eight. Increasing this number improves performance and in particular raises the upper ANR bandwidth limit. Accordingly, if a of more general framework of sensor data acquisition can be invented this can be beneficial to the HMIMOCFFFBS.

In many signal processing applications a reduction in the computational complexity is required especially whenever finite-duration impulse response (FIR) filters of high order is used. This can be accomplished by using *multi-rate adaptive filters* where the adaptive processing is performed at a lower rate than the incoming rate. The research into the field of multi-rate system design is therefore motivated by a need to keep the requirement on bandwidth requirement at a sufficient low level for the application, which is of particular importance in multi-channel systems. Moreover, multi-rate system design allows the designer to obtain very small delays associated with the conversion stages in the secondary paths.

In the original proposal of the Ph.D. project emphasis was made on the study of adaptive filter algorithms in association with the modified-filtered-x (mFx) technique. However, from the outset the author being a newcomer to the field of AC has been sceptical to this priority of the research activities to be pursued. Early research activities and B.Sc. projects supervised by the author indicated that a variety of already existing adaptive filter candidates are at our disposition. The optimal choice of the underlying parameters and the achievable performance was not surprisingly seen to be governed by the overall structure in which they should work. In particular the achievable performance of ordinary feedback system (FBS) solutions was deemed to be moderate and highly dependent on inherent delays in the secondary path. Moreover, a realistic hardware platform for ANC investigations was expectably first at disposition at a very late stage in this project. It would therefore not be rather beneficial for Terma, that at time of start had no previous experiences with the design of ANC systems, if the Ph.D. has been dwelling all the time in this particular field. Furthermore, it became soon evident that the project supposedly should run autonomously, that is, with a minimum of resource draw elsewhere within the company. It was therefore decided to take a more fundamental and theoretical approach to this research project in which the dependence on hardware for evaluation or the dependence on resource availability in general could be kept at a very low level. Hence, the diversity of the areas studied during the course of the Ph.D. project is probably relative large for this type of project. As a consequence, however, of this approach and the non inexhaustible work capacity of the author only a finite amount of time has been spent in each of the scientific areas investigated.

Although the three branches of physics, acoustics, elasticity and electromagnetics seem quite dissimilar and describe completely different phenomena, however, they are all subjectable to analysis in the mathematical framework of *field theory*. Therefore, by taking the necessary precautions, then results that have been developed for one type of physical system can in some specific cases be adapted to one of the other two physical systems considered. In particular, thorough examination of the governing equations revealed that results for SNFAT as used for more than 30 years for example at Ørsted TUD potentially can be generalized to predict field quantities from sensors being responsive to acoustical as well as elastoric waves. Among such sensors we find ordinary pressure microphones, (radial) velocity microphones and accelerometers.

For this purpose a so-called probe description of the sensor supposedly used for the acquisition of the sensor information must be made. As implicitly appear from the name SNFAT scanning of the fields takes place on a sphere. As discussed in Appendix F the spherical coordinate system is also the only coordinate system in which the vector wave equations separate for all three physical systems considered which in turn greatly simplifies the analysis.

Moreover, the project takes recent improvements in digital signal processing into account. Hence, the use of Kautz/Laguerre filter as possible replacement of FIR filters is investigated.

It is common engineering practice to apply an assumption of Gaussian distributed signals. However, many phenomena encountered in daily life fall into a generalization of the normal distribution and is referred to as α-stable distributions. Noise source encountered in the domain of AC are sometimes best fitted to the family of α-stable distributions. So-called α-stable adaptive filters are therefore also assessed for the use in ANC applications.

As part of the project a MATLAB®-based general purpose tool for analysis and synthesis of ACSV systems and in particular the HMIMOCFFFBS has been developed. This software tool has also largely been used to compensate for the lack of a hardware platform with sufficient channel and processing capability to support the HMIMOCFFFBS.

1.5 Organization of the Thesis

Of course within a single Ph.D. project not every stone can be turned in such multi-disciplinary system design. Hence, such important aspects the psychoacoustical aspects of ANC and in particular related to ANR HPDs. Furthermore, throughout the report it is usually assumed that the systems are strictly linear. Hence, the vast field of adaptive non-linear control is cleverly excluded.

Moreover, some of the chapters are included merely to support the rest of the report. Hence, such chapters are not vital for the overall comprehension of the Ph.D. work and therefore given a low priority (refer to Table 1.1 - 1.2). This report is therefore organized in two volumes. Volume I is the official part of the thesis that will be subject to a formal Ph.D. defense includes the main contribution of the work by the author. Volume II contains a suite of supplementary chapters. The contents of Volume II, however, will not be subjected to the Ph.D. defense.

1.5.1 Organization of Volume I of the Thesis

Volume I in turn is organized in four parts addressing different aspects of an active control of sound (ACS).

Following this introduction chapter 2 - 3 constitute Part I of this report. The performance of a modern complex active noise control system (ANCS) is determined from numerous system parameters. Coherence functions are of particular concern in ANC system design as the achievable ANR performance in a feedforward system (FFS) is to a large extent determined by the degree of *coherence* between the set of reference sensors and the set of error sensors (or performance sensors). The theme of chapter 2 is coherence functions and statistical analysis methods that can be applied to obtain estimates of different types of coherence functions. A quantity referred to as the spatially-weighted-averaged acquisition lead time is introduced to represent the averaged time-advance obtained by each reference sensor relative to each performance sensor involved in a confined feedforward active control (CFFAC) system. A new method for acoustical signal

processing that is referred to as joint-channel residual spectral analysis (JCRSA) is developed. With this method joint signal information including the spatially-weighted-averaged acquisition lead time can be extracted from diffuse sound field measurements.

In chapter 3 the ANR performance limitations as determined from causality constraints will be considered. A key technique to the causality analysis is the *spectral factorization* which therefore will play a main role in this chapter. Another objective pursued is the examination of the performance of two variant Wiener-Hopf (WH) filters that are useful for the analysis of the achievable ANR performance under causality constraints. A suite of examples of increasing complexity is constructed in order to exhibit some of the characteristics related to causality constraints.

Part II includes two chapters related to control system design. In chapter 4 the topology of the overall control system will be introduced. A brief introduction to hybrid continuous-time discrete-time topology (HCTDTT), hybrid feedforward FBS (HFFFBS), internal model control (IMC) and adaptive inverse control (AIC) is provided. The HFFFBS is discussed at length later in chapter 7 directly in a MIMO context. AIC is proposed as a method to achieve *adaptive control* of unknown and possible time-varying systems by using adaptive filters.

In chapter 5 of multi-rate system generally applicable for ACSV is developed. A detailed description of the processing stages involved in *sensing* signals and *actuating* signals respectively is included. This system involves three different sampling rates for maximum trade-off between different design constraints. Moreover, the system is formulated in general ACSV context of a hybrid MIMO feedforward-feedback system (HMIMOFFFBS). A conceptual demonstration of this new multi-rate ANC system is provided.

The theme of the Part III that is constituted by four chapters is adaptive filters for ANC. The objective of chapter 6 is to establish a link between the domain of control system to the domain of adaptive filtering. A description of the well-established *filtered-reference* signal method used to accommodate the presence of a plant is made. The more advanced technique referred to as *modified filtered reference* method is carried out. This method is extensively being used in the simulations. Moreover, this chapter also presents the family of filtered-error (Fe)LMS that provides a cost effective alternative to the mFx in MIMO systems.

In chapter 7 a bottom-up description of the HMIMOFFFBS from basic feedback systems and feedforward systems to the full blown HMIMOCFFFBS including provision for on-line system identification and integrated communication (IC) is made. Moreover, the system includes a scheme that to a large extent can eliminate the effects of feedback signals contaminating the reference signals. In a demonstration off-line simultaneous system identification capabilities of a complex system using different adaptive filter configurations is made.

Then in chapter 8 four different modes of adaptive filtering is presented. The concepts of *cost functions*, *leakage* and *regularization* is discussed. Both **t**-domain- and **z**-domain causally constrained Wiener filters are introduced. The steepest descent (SD) and then subsequently the family of stochastic gradient (SG) are presented. A new and more general variant of the affine projection algorithm has been developed. This adaptive filter algorithm that is denoted by multiple-channel-$\alpha\gamma\Pi\epsilon$-affine projection algorithm includes parameters for *leakage control* and *adaptive tap-weight regularization* as well as *numerical regularization*. A simplification of this algorithm leads to the MC-$\alpha\gamma\Pi\epsilon$-NLMS algorithm that is an extended variant of the NLMS algorithm.

The theme of chapter 9 is an extensive performance analysis of the linear-least-mean-squares estimate (l.l.m.s.e.)-based multiple-channel-$\alpha\gamma\Pi\epsilon$-affine projection algorithm (MC-$\alpha\gamma\Pi\epsilon$-APA) adaptive filter encompassing both dynamic *weight-driven leakage* and dynamic *control-effort-driven*

leakage and numerical regularization as well as weight regularization. Moreover, in our presentation we also allow the step-size μ, the leakage control parameters α, γ and the numerical regularization parameter ϵ to attain matrix-values and to be time-variant. Furthermore the analysis conducted in this chapter uses an advanced random-walk model and also allows a non-vanishing initial weight vector.

Finally, Part IV includes two chapters related to the vibro-electroacoustical part of a HPD. The *passive* operation of circumaural HPDs is addressed in chapter 10. In chapter 11 a discussion of quantities governing the performance of ANR HPDs will be carried out. Moreover, the actual Helmet design including the Terma Earcup system is modeled and suggestions to a less resonant structure is made.

Following our conclusions a total of five appendices are included in Volume I of the thesis. Various ANR attenuation quantities are defined in Appendix A. Among important parameters considered we find the acquisition time, the group delay, aliasing effects, the ordinary coherence function (OCOF) and the MCOF. The obtainable performance as limited by each of these quantities is evaluated. Then in Appendix B random variables (RVs) and random processs (RPs) are formally defined and subsequently set into perspective using the F-16 application as an example. The theme of Appendix C is statistical data analysis (SDA) and in particular an assessment of the errors that result during post processing of the acquired data is made. Results from noise recordings acquired in an F-16/B cockpit and in a CH-47D are presented in Appendix D that also includes a description of the customization process of the Gentex HGU-55/P helmets. Finally, Appendix E describes a pseudo-random noise generator that is used for system identification.

In Table 1.1 a prioritizing of the included chapters of Volume I of the report is listed. Priority 1 is attributed to the chapters that should be read, priority 2 is assigned to the chapters supporting for the overall comprehension of the report and priority 3 indicates that the material might be somewhat outside the main scope of the Ph.D. work or else is at an introductory level.

Chapter	Name	Priority
chapter 1	Introduction	1
chapter 2	Coherence Functions and Spectral Analysis	1
chapter 3	Causality Constraints and Spectral Factorization	1
chapter 4	System Description	2
chapter 5	Multi-rate Systems	2
chapter 6	Adaptive Filtering for Active Control	2
chapter 7	HMIMOFFFBS	2
chapter 8	Adaptive Filtering Algorithms for LTV Systems	1
chapter 9	MC-$\alpha\gamma\Pi\epsilon$-APA Performance Analysis	1
chapter 10	Hearing Protector: Active Attenuation	2
chapter 11	Hearing Protector: Passive Attenuation	2
chapter 12	Conclusions	1
Appendix A	Active Noise Control Performance	2
Appendix B	Random Signals	2
Appendix C	Statistical Data Analysis	2
Appendix D	Analysis of Noise Recordings	2
Appendix E	Random Noise Generation	2

Tab. 1.1: Ph.D. Thesis Chapter Priority Level Volume I.

1.5.2 Organization of Volume II of the Thesis

Volume II of the Thesis is organized in two parts addressing different aspects of an active control (AC) system.

Three chapters constitute Part V that supplement Part I of Volume I of this report. In Appendix F a theory unifying three branches of physics namely acoustics, elasticity theory and electromagnetics is presented. This unifying theory is the mathematical framework of *field theory*. The contents of this chapter should generally be fruitful when attempting to project results obtained in one of the physical systems to one of the other two physical systems. In particular in Appendix G where spherical near-field antenna testing (SNFAT) techniques used primarily for antenna measurement will be accommodated to measurement of acoustical wave fields as well as elastoric wave fields. In order to accomplish this goal, however, some care must be exercised when adapting to results obtained from electromagnectics. Following the presentation of the SNFAT techniques in Appendix G this part of the report concludes with Appendix H that provide some practical examples to where field considerations are of profound concern in the design of an active noise control (ANC) system. The problem related to AC when either of the primary, secondary sources or control volumes are subject to dynamic movements is also addressed. In particular, existing spherical near-field techniques from Appendix G are adapted to cases where the sources are positioned outside the spherical scan surface and time-domain field for which the interior field *inside* the sphere can be determined. These results are used in the design of the aforementioned reference test unit (RTU) dedicated the test and evaluation of methods and techniques developed for active control of sound and vibration (ACSV) systems.

The theme of Part VI that supplements Part III of Volume I is constituted by four chapters is adaptive filters for ANC. The presentation of adaptive filters for AC is proceeded in Appendix I with a discussion of the topology of the filters involved. The topic of Appendix J is fast adaptive filtering algorithms and in particular *order-recursive* algorithms. A detailed derivation of the fast array recursive least-squares (FARLS) is provided. Moreover, an extension to the FARLS algorithm is made allowing a non-vanishing initial condition and a regularization matrix that not necessarily is a diagonal matrix. This adaptive filter is used extensively in many parts of this report. The theme of Appendix K is *orthonormal filters* and in particular Kautz/Laguerre filters. Finally, Appendix L provide insight to the class of α-stable distributions. Various adaptive filter dedicated to this class of probability density functions and in particular the normalized LMpN (NLMpN) algorithm are presented. A total of four appendices namely Appendix M-P are included in Volume II of the thesis.

In Table 1.2 a prioritizing of the included chapters in Volume II of the report is listed.

Chapter	Name	Priority
Appendix F	Acoustic, Electromagnetic and Elastic Field Theory	3
Appendix G	Spherical Near-Field Testing	3
Appendix H	Applied Active Control of Fields	3
Appendix I	Adaptive Filter Topology	3
Appendix J	Adaptive Filtering Fast Algorithms for LTV Systems	3
Appendix K	Orthonormal Filters	3
Appendix L	Alpha-Stable Distributions	3
Appendix M	Fourier Transforms	3
Appendix N	Signal Aliasing Effects	3

Continued on next page

Chapter	Name	Priority
Appendix O	Mathematical Model Dynamical System	3
Appendix P	Terma Noise Chamber Facility	3

Tab. 1.2: Ph.D. Thesis Chapter Priority Level Volume II.

The author has tried to supplement the mathematical derivations and physical ideas by expression in plain English and apology for any deviation from this objective.

Rather than collect all appendices at the end of this report, the author has opted to place each of the domain specific appendices at the end of the chapter where it is called upon. Material of more general character, however, is placed in appendices in the end of the report.

Bibliography

[1] Stephen J. Elliott. *Signal Processing for Active Control*. London: Academic Press, 2001.

[2] Colin H. Hansen and Scott D. Snyder. *Active Control of Noise and Vibration*. E & FN SPON, 1st edition, 1997.

[3] Sen M. Kuo and Dennis R. Morgan. *Active Noise Control Systems Algorithms and DSP Implementations*. John Wiley & Sons, Inc., 1996.

[4] Harry F. Olson and Everett G. May. Electronic sound absorber. *The Journal of the Acoustical Society of America*, 25(6):1130–1136, 1953.

[5] Jürgen Schröter. *Messung der Schalldämmung von Gehörschützern mit einemphysikalischen Verfahren (Kunstkopfmethode) (In German)*. Doctoral thesis, 1983.

[6] Jürgen Schröter. The use of acoustical test fixtures for the measurement of hearing protector attenuation Part I: Review of previous work;design of an improved test fixture. *JASA*, 79 (4):1065–1081, 1986.

[7] Jürgen Schröter and C. Poesselt. The use of acoustical test fixtures for the measurement of hearing protector attenuation. Part II: Modeling: the external ear simulation bone conduction and comparing test fixture and real ear data. *JASA*, 80(2):505–527, 1986.

[8] E. A. G. Shaw and G. J. Thiessen. Improved cushion for ear defenders. *JASA*, 30(No. 1), 1958.

[9] E. A. G. Shaw and G. J. Thiessen. Acoustics of circumaural ear defenders. *JASA*, 34(No. 9), 1962.

[10] Scott D. Snyder. *Active Noise Control Primer*. Springer-Verlag, 2000.

Part I

ACTIVE CONTROL OF FIELDS

2. COHERENCE FUNCTIONS AND SPECTRAL ANALYSIS

2.1 Introduction

The theme of this chapter is coherence functions and statistical analysis methods that can be applied to obtain estimates of different types of coherence functions. Coherence functions are of particular concern in ANC system design as the achievable active noise reduction (ANR) performance in a feedforward system (FFS) is to a large extent determined by the degree of *coherence* between the set of reference sensors and the set of error sensors (or performance sensors).

In section 2.2 on the next page three coherence functions will be introduced, namely the *ordinary coherence function* , the *multiple coherence function* and the *partial coherence function.* Moreover, section 2.2 lists various causes to the lack of coherence between two sensor signals. Expressions for the three coherence functions are provided and for the multiple coherence function and the partial coherence function both an iterative procedure as well as a matrix implementation formulation is presented.

A problem exists when one attempts to model a physical spatially distributed system with no obvious input and output channel definition by a finite lumped-elements multi-channel system. Usually, no unique transfer function exist as the system is not point-wise excited, but excited over an area as in the case of diffuse sound field illumination.

A - to the author's best knowledge - new method for acoustical signal processing that is referred to as joint-channel residual spectral analysis (JCRSA) is developed in section 2.3 on page 29. The JCRSA method is used for the extraction of joint signal information from different observation positions in space. The idea is to separate each spectrum in a *coherent spectrum* and a *residual spectrum.* The contents of the coherent spectrum can be obtained from a linear superposition of the other signals, whereas the residual spectrum bears information that is unique to each specific channel[1]. Moreover, a quantity referred to as the spatially-weighted-averaged acquisition lead time is introduced to represent the averaged time-advance obtained by each reference sensor relative to each performance sensor or error sensor involved in the proposed confined feedforward active control (CFFAC) system.

As will be demonstrated in section 2.4 on page 32 this method has the ability to extract *distinct* channel timing information that is deeply buried in multi-channel interferences in a diffuse sound field. Such timing information is useful for, e.g., the determination of the *spatially-weighted-averaged acquisition lead time.*

[1] In the study of the extent of the diffuse field zone of quiet one may apply a somewhat related idea of separating the primary field at an arbitrary position is space, say, $\mathbf{r}$ into a component that is perfectly *correlated spatially* with primary field (and therefore also secondary field) at the position in space where perfect cancelation is obtained, say, $\mathbf{r}_0$ and an orthogonal field component that is perfectly uncorrelated with this primary field at $\mathbf{r}$ [13] [20, Ch. 11.4]. Hence, spatially decorrelation between two field points $(\mathbf{r}_0, \mathbf{r})$ is considered, whereas the theory developed in this chapter is the natural extension to the multiple field point case. Spatial decorrelation is also considered in subsection 2.4.3 viz. (2.4.2) on page 45.

2.2 Coherence

Coherence functions are measures of linear dependence between random signals or in general *sets* of random signals, say, A and B to be defined later. They represent the correlations between spectral components of random processs (RPs) and are thus functions of frequency. Four types of coherence functions will be considered: the *ordinary coherence function* , the *multiple coherence function* which in turn involves the *partial coherence function* and a *generalized coherence function.* The ordinary coherence function consider two different channels, the multiple coherence function involve one single channel and a number of different channels. The partial coherence function on the other hand consider two different channels and a number of likewise different channels.

In feedforward AC lack of sufficient coherence between the reference sensors and error sensors will directly limit the **obtainable** ANR attenuation. Denoting by $\mathcal{A}_{\gamma^2}$ the *attenuation* limited by (lack of) coherence, the following expression is readily obtainable [12, Ch. 3]

$$\mathcal{A}_{\gamma^2}(f) = 10\log_{10}\big(1-\gamma^2(f)\big) \quad [\text{dB}]. \tag{2.2.1}$$

Many physical systems are extended continuum systems which we, however, model as finite-dimensional continuous-time or discrete-time linear time-invariant (LTI) dynamical systems that can be accessed at different points or channels. As described in Appendix O on page 807 the state-space representation and the *input-output* model is widely used to model a great variety of systems encountered in nature.

Usually in systems theory some of the channels are considered as *inputs* while the remaining channels are considered as *outputs*. Our approach will, however, be more general as often no obvious input output assignment exists. Sometimes the channels[2] naturally fall into two or more sets. Henceforth, we will by A designate one arbitrary subset of the channels and by B designate another arbitrary subset of the channels. Moreover, we will let $\boldsymbol{\psi}_a, \boldsymbol{\psi}_b$ represent *arbitrary* random signals. The signal set membership for these arbitrary random signals is inessential. Typically, $\boldsymbol{\psi}_a$ and $\boldsymbol{\psi}_b$ will be used as surrogates for reference signals, disturbance signals and performance signals.

The total number of channels is henceforth denoted by N_ψ. Accordingly, the system is considered spatially sampled at N_ψ distinct points in space and the corresponding signal as an N_ψ-*multivariate* stationary RP.

2.2.1 Imperfect Coherence

From a literature survey the following reasons for *observed* imperfect coherence has been found[3] [15, Ch. 4], [4, 6, 12]:

Coherence Prob. 1. *Partially Coherent Fields.* A real physical source is not a point source, but has a finite extension, consisting of many elementary radiators. Acoustical sources related to violent fluid motion was discussed in subsection F.3.11 on page 654 represent an example of spatially distributed elementary sources. In optics these elementary sources are atoms. Moreover, a physical source is never constituted by *strictly coherent* elementary sources. This is in particular

[2] We use the words channel and signal synonymously.

[3] The list is most likely not exhaustive and many other causes to imperfect coherence may exist.

the case for the noise generated from violent fluid motion. On the contrary, for some vibrating machinery radiating noise the source points will to a large extent be coherent. Incoherence in turn always implies a finite (though not necessarily wide) spectral range[4]. Accordingly, a physical source is never strictly monochromatic and even the sharpest spectral line has a finite width. At field points many wavelengths away from such extended and partially coherent noise source the amplitude and phase of the radiated field will undergo *temporal* fluctuations, the rapidity of which depends essentially on the width of the spectrum. The characteristic time of the amplitude variations is called the *coherence time* [8, Ch. 10]. Similarly, the field will exhibit *spatial* fluctuations in amplitude and phase, that is, the field points are only *partially coherent*. The spatial extent of the dependence of the field is characterized by the *region of coherence*[5]. Hence, the cause of lack of perfect coherence is an *extended* source of non perfectly coherent elementary elements.

Coherence Prob. 2. Insufficient model order. This is of particular importance when one attempts to model a spatially distributed system as a finite lumped-elements multiple-input and multiple-output (MIMO) system. With increasing frequencies the field necessarily become spatially undersampled and the corresponding spatially-aliased signal components can be considered as extraneous signals.

Coherence Prob. 3. Doppler effects. Consider two sensors as observers that are moving along trajectories with reference to a coordinate system with origo at the position of the noise source. Then at times where a difference in the radial velocity component of the two sensors exists, the sensors will experience different doppler shifts and therefore also a drop in the coherence function.

Hence, 1 and 2 relate to the problem of modeling a physical continuum with a finite-dimensional MIMO system. 1 refers to the reason of the existence of partially coherent fields, whilst 2 refers to the problem of insufficient hardware deployment (for economic and/or practical reasons). Owing to wave nature such considerations apply to the three physical phenomena considered in Appendix F on page 619, that is, acoustics, elasticity theory and optics (electromagnetics). A possible remedy to 3 is to apply doppler filtering techniques well known within the sonar and radar communities.

Coherence Prob. 4. The system relating the $\boldsymbol{\psi}^A(t)$ signals and the $\boldsymbol{\psi}^B(t)$ signals is not linear[6].

Coherence Prob. 5. The system relating the $\boldsymbol{\psi}^A(t)$ signals and the $\boldsymbol{\psi}^B(t)$ signals is not a constant-parameter system.

Deviations from a strictly LTI system is accounted for in 4 and 5. A remedy to this problem is to use non-linear and time-varying AC. However, this will usually increase the complexity considerably. The time-variance is to some extent taken into account by the use of adaptive filters for adaptive control and for plant representation.

[4] In optics the partial coherence is often related to an extended quasi-monochromatic light or polychromatic light source. Such light sources most often imply incoherence.

[5] From optics it is well known that the spectrum of radiation from an extended source changes on propagation unless a certain scaling condition is obeyed by the degree of spectral coherence across the source [8]. For a large class of source-coherence functions the changes may be manifested as shift of spectral lines either towards the longer (red shift) or the shorter (blue shift) wave length. In [7] an acoustical experiment with two small partially correlated sources frequency shifts in tonal contents was observed by this mechanism, which validate this hypothesis in the acoustical domain.

[6] Atmospheric turbulence. This is of particular concern in *aeroacoustic tracking* systems with widely separated sensor arrays [19]. In [25] physics-based models for the associated spatial coherence loss are developed.

Coherence Prob. 6. Finite signal-to-noise ratio (SNR). The presence of extraneous noise that is uncorrelated with $\boldsymbol{\psi}_a(t)$ and $\boldsymbol{\psi}_b(t)$. For example, noise in the receiver electronics will most likely be uncorrelated from one sensor to another. From [6, Ch. 6] we find the ordinary coherence function expressed in terms of the SNR at port a represented by SNR_a and the SNR at port b designated by SNR_b

$$\gamma^2_{\psi_a\psi_b}(f) = \frac{1}{1 + \mathrm{SNR}_a^{-1}(f) + \mathrm{SNR}_b^{-1}(f) + \mathrm{SNR}_a^{-1}(f)\mathrm{SNR}_b^{-1}(f)}. \tag{2.2.2}$$

Accordingly, considering this point isolated high SNRs lead to a coherence function approaching unity.

Coherence Prob. 7. Aliased signal components in discrete-time systems. In AC a trade-off between suppression of aliased signal components and performance loss due to group delays within the anti-aliasing filters (AAFs) therefore often prevails.

Coherence loss associated with the AAF will be discussed in subsection N.2.1 on page 792.

Coherence Prob. 8. Adaptive filter truncation errors. By the use of finite-duration impulse response (FIR) filters for plan model representation some model imperfections necessarily result. *A* remedy to this problem is to use infinite-duration impulse response (IIR) filters. Moreover, by using numerical methods in the determination of fields from an extended source region usually involves an infinite or possibly double infinite sum of terms. In practice an estimate of the field is obtained by truncation of the (double) infinite sum. As a consequence some numerical source contributions are omitted and the coherence function decreases.

Coherence Prob. 9. The underlying RPs are not mean and variance stationary or ergodic.

The analysis presented in this chapter is based on an underlying assumption of mean and variance stationarity. Coherence problem 9 accounts to such model deviations. Lack of stationarity, however, may be compensated for by employing more advanced data analysis schemes.

Coherence Prob. 10. Periodicities in the acquired data set.

Coherence Prob. 11. A nonzero mean in the acquired data set. A finite direct current (DC) offset ïn the acquisition equipment that is not taken properly compensated for may completely overshadow possible subsonic signal content in the first frequency bin.

Coherence problem 10 and coherence problem 11 refer to improper statistical data analysis which may lead to an *underestimation* of the true coherence function.

Moreover, it should, however, be remarked that 1-11 to some extent might be mutually dependent.

In the system identification the coherence function indicates how much of the system output signal is due to the input to the system.

Finally, it should be recalled that the improper statistical analysis of the data set may lead to an erroneous underestimation of the achievable performance. Similarly, imperfections in the performance sensor itself may lead to an underestimation of the ANR performance that will be perceived by humans at the same position.

2.2.2 MIMO channel power spectral density matrix

In the statistical data analysis a MIMO channel power spectral density matrix denoted by $S_{\psi\psi} \in \mathbb{C}^{N_f \times N_\psi \times N_\psi}$, where the diagonal elements are auto spectral density functions and the off-diagonal elements are cross-spectral density functions, is constructed

$$S_{\psi\psi} \triangleq \begin{bmatrix} S_{\psi_1\psi_1} & S_{\psi_1\psi_2} & \cdots & S_{\psi_1\psi_{N_\psi}} \\ S_{\psi_2\psi_1} & S_{\psi_2\psi_2} & \cdots & S_{\psi_2\psi_{N_\psi}} \\ \vdots & \vdots & \ddots & \vdots \\ S_{\psi_{N_\psi}\psi_1} & S_{\psi_{N_\psi}\psi_2} & \cdots & S_{\psi_{N_\psi}\psi_{N_\psi}} \end{bmatrix}. \tag{2.2.3}$$

In the statistical data analysis it is often not required to examine all N_ψ^2 possible channel combinations. Sometimes the data naturally fall into two or more sets. Typically, when considering MIMO systems one subset of signals is designated as input and the other subset of signals is designated as output. Accordingly, we may write the set of all signals denoted by $\boldsymbol{\psi}^S$ as

$$\boldsymbol{\psi}^S = \boldsymbol{\psi}^I \cup \boldsymbol{\psi}^O, \tag{2.2.4}$$

where $\boldsymbol{\psi}^I = \cup_{j \in \underline{N}_\psi^I} \boldsymbol{\psi}_j^I$ denotes the *set of input signals* and N_ψ^I is the number of input channels, and where $\boldsymbol{\psi}^O = \cup_{k \in \underline{N}_\psi^O} \boldsymbol{\psi}_k^O$ similarly denotes the *set of output signals* and N_ψ^O likewise is the number of output channels.

The set of input signals and output signals are by definition always considered *mutually exclusive*, that is, $\boldsymbol{\psi}^I \cap \boldsymbol{\psi}^O = \emptyset$. The number of channels are therefore related by

$$N_\psi = N_\psi^I + N_\psi^O. \tag{2.2.5}$$

Then we may reexpress the MIMO channel power spectral density matrix in terms of block channel matrices according to

$$S_{\psi\psi} \triangleq \begin{bmatrix} S_{\psi^I\psi^I} & S_{\psi^I\psi^O} \\ S_{\psi^O\psi^I} & S_{\psi^O\psi^O} \end{bmatrix}, \tag{2.2.6}$$

where $S_{\psi^I\psi^I} \in \mathbb{C}^{N_f \times N_\psi^I \times N_\psi^I}$ represents the input channel power spectral density matrix, $S_{\psi^O\psi^O} \in \mathbb{C}^{N_f \times N_\psi^O \times N_\psi^O}$ similarly is the output channel power spectral density matrix and $S_{\psi^I\psi^O} = S_{\psi^O\psi^I}^* \in \mathbb{C}^{N_f \times N_\psi^O \times N_\psi^I}$ denotes the input-output cross channel power spectral density matrix. The dependence on the frequency index is suppressed for notational convenience. In full expansion $S_{\psi\psi}$ is

expressed by

$$S_{\psi\psi} = \begin{bmatrix} S_{\psi_1^I\psi_1^I} & S_{\psi_1^I\psi_2^I} & \dots & S_{\psi_1^I\psi^I_{N_\psi^I}} & S_{\psi_1^I\psi_1^O} & S_{\psi_1^I\psi_2^O} & \dots & S_{\psi_1^I\psi^O_{N_\psi^O}} \\ S_{\psi_2^I\psi_1^I} & S_{\psi_2^I\psi_2^I} & \dots & S_{\psi_2^I\psi^I_{N_\psi^I}} & S_{\psi_2^I\psi_1^O} & S_{\psi_2^I\psi_2^O} & \dots & S_{\psi_2^I\psi^O_{N_\psi^O}} \\ \vdots & \vdots & \ddots & \vdots & \vdots & \vdots & \ddots & \vdots \\ S_{\psi^I_{N_\psi^I}\psi_1^I} & S_{\psi^I_{N_\psi^I}\psi_2^I} & \dots & S_{\psi^I_{N_\psi^I}\psi^I_{N_\psi^I}} & S_{\psi^I_{N_\psi^I}\psi_1^O} & S_{\psi^I_{N_\psi^I}\psi_2^O} & \dots & S_{\psi^I_{N_\psi^I}\psi^O_{N_\psi^O}} \\ S_{\psi_1^O\psi_1^I} & S_{\psi_1^O\psi_2^I} & \dots & S_{\psi_1^O\psi^I_{N_\psi^I}} & S_{\psi_1^O\psi_1^O} & S_{\psi_1^O\psi_2^O} & \dots & S_{\psi_1^O\psi^O_{N_\psi^O}} \\ S_{\psi_2^O\psi_1^I} & S_{\psi_2^O\psi_2^I} & \dots & S_{\psi_2^O\psi^I_{N_\psi^I}} & S_{\psi_2^O\psi_1^O} & S_{\psi_2^O\psi_2^O} & \dots & S_{\psi_2^O\psi^O_{N_\psi^O}} \\ \vdots & \vdots & \ddots & \vdots & \vdots & \vdots & \ddots & \vdots \\ S_{\psi^O_{N_\psi^O}\psi_1^I} & S_{\psi^O_{N_\psi^O}\psi_2^I} & \dots & S_{\psi^O_{N_\psi^O}\psi^I_{N_\psi^I}} & S_{\psi^O_{N_\psi^O}\psi_1^O} & S_{\psi^O_{N_\psi^O}\psi_2^O} & \dots & S_{\psi^O_{N_\psi^O}\psi^O_{N_\psi^O}} \end{bmatrix}. \quad (2.2.7)$$

Sometimes such partitioning of the channels is less obvious. For example, at various places in this thesis the mutual relationship between the reference signals, disturbance signals and the performance signals is investigated. However, none of these subsets of signals are physically inputs nor physical outputs, but merely some *sensed* signals. In this specific case, however, it seems natural to consider the reference signals as inputs and the disturbance signals and the performance signals as outputs. For the investigation of mutual relationship between the disturbance signals and the performance signals we may arbitrarily designate the disturbance signals as inputs and the performance signals as outputs.

On the contrary, the aforementioned abstract signal sets A and B may or may not be overlapping. Moreover, the union of A and B will sometimes only constitute a subset of all signals. Hence,

$$\boldsymbol{\psi}^S \supseteq \boldsymbol{\psi}^A \cup \boldsymbol{\psi}^B, \quad (2.2.8)$$

where $\boldsymbol{\psi}^A = \cup_{j\in\underline{N}_\psi^A} \boldsymbol{\psi}_j^A$ denotes the *set of A signals* and N_ψ^A is the number of A channels, and where $\boldsymbol{\psi}^B = \cup_{k\in\underline{N}_\psi^B} \boldsymbol{\psi}_k^B$ similarly denotes the *set of B signals* and N_ψ^B likewise is the number of B channels.

In general, the number of channels is accordingly subject to

$$N_\psi \lesseqgtr N_\psi^A + N_\psi^B. \quad (2.2.9)$$

The equality sign in (2.2.8) and (2.2.9) pertains for example to the case where subsets $\boldsymbol{\psi}^A$ and $\boldsymbol{\psi}^B$ are non-overlapping and include all signals.

Moreover, we introduce the *set of C (conditioning) signals* denoted by $\boldsymbol{\psi}^C = \cup_{l\in\underline{N}_\psi^C} \boldsymbol{\psi}_l^C$ where N_ψ^C is the number of C (conditioning) channels. Important to note is that $\boldsymbol{\psi}^C$ may or may not contain elements from either of $\boldsymbol{\psi}^A$ or $\boldsymbol{\psi}^B$, that is, in general $\boldsymbol{\psi}^C \cap \boldsymbol{\psi}^A \neq \emptyset$ and $\boldsymbol{\psi}^C \cap \boldsymbol{\psi}^B \neq \emptyset$.

For all practical purposes it should suffice to consider signals from three subsets of signals at a time. Then, we may let $\boldsymbol{\psi}^A, \boldsymbol{\psi}^B$and $\boldsymbol{\psi}^C$ be surrogates for application dependent specific subsets.

2.2.3 Ordinary Coherence

The ordinary coherence squared function (or just coherence function) between (arbitrary) random signal $\boldsymbol{\psi}_a$ and (arbitrary) random signal $\boldsymbol{\psi}_b$ denoted by $\gamma^2_{\psi_a\psi_b}(f)$, represents the linear dependence (correlation) in the space-frequency domain between the spectral components of $\boldsymbol{\psi}_a$ and those of $\boldsymbol{\psi}_b$. It is defined from the PSD of signal $\boldsymbol{\psi}_a$ designated by $S_{\psi_a\psi_a}(f)$, the PSD of signal $\boldsymbol{\psi}_b$ denoted by $S_{\psi_b\psi_b}(f)$ and the CPSD between signal $\boldsymbol{\psi}_a$ and signal $\boldsymbol{\psi}_b$ represented by $S_{\psi_a\psi_b}(f)$, that is,

$$\gamma^2_{\psi_a\psi_b}(f) \triangleq \frac{|S_{\psi_a\psi_b}(f)|^2}{S_{\psi_a\psi_a}(f)S_{\psi_b\psi_b}(f)}. \tag{2.2.10}$$

As opposed to the multiple coherence function that will be introduced in subsection 2.2.5 on page 25 the ordinary coherence function consider signals pairwise. The coherence function is zero if the random signals are uncorrelated and equal to one at any frequency index where there exist a linear transformation between $\boldsymbol{\psi}_a$ and $\boldsymbol{\psi}_b$.

In the statistical data analysis presented in Appendix C on page 539 it is useful to introduce the ordinary complex coherence function $\gamma_{\psi_a\psi_b}$ defined by

$$\gamma_{\psi_a\psi_b}(f) = |\gamma_{\psi_a\psi_b}(f)|\mathrm{e}^{\imath\sphericalangle\gamma_{\psi_a\psi_b}(f)}, \tag{2.2.11}$$

where the magnitude and phase are defined by

$$|\gamma_{\psi_a\psi_b}(f)| = +\sqrt{\gamma^2_{\psi_a\psi_b}(f)} \tag{2.2.12}$$

and

$$\sphericalangle\gamma_{\psi_a\psi_b}(f) = \arctan\left(\frac{Q_{\psi_a\psi_b}(f)}{C_{\psi_a\psi_b}(f)}\right) \tag{2.2.13}$$

respectively and where the CoPSD (co-spectrum) $C_{\psi_a\psi_b}(f)$ and QPSD (quad-spectrum) $Q_{\psi_a\psi_b}(f)$ in turn are defined according to

$$S_{\psi_a\psi_b}(f) = C_{\psi_a\psi_b}(f) + \imath Q_{\psi_a\psi_b}(f). \tag{2.2.14}$$

Comparing the definition for the ordinary coherence function in the space-frequency domain (2.2.10) with the definition for the *correlation coefficient* (coherence function in space-time) $\rho_{\psi_a\psi_b}(\tau)$[7].

$$\rho_{\psi_a\psi_b}(\tau) \triangleq \frac{C_{\psi_a\psi_b}(\tau)}{\sqrt{C_{\psi_a\psi_a}(0)}\sqrt{C_{\psi_b\psi_b}(0)}}, \tag{2.2.15}$$

[7] One must distinguish between the *temporal* complex degree of coherence $\rho_{\psi_a\psi_b}(\tau)$ that is a measure of the coherence in the space-time-domain and the *spatial* degree of coherence $\gamma_{\psi_a\psi_b}(f)$ that is a measure of the coherence in the space-frequency-domain [8, Ch. 10].

where $C_{\psi_a\psi_b}(\tau)$ denotes the *cross-covariance function* between two arbitrary continuous-time random signals $\boldsymbol{\psi}_a(t), \boldsymbol{\psi}_b(t)$[8]

$$C_{\psi_a\psi_b}(\tau) \triangleq R_{\psi_a\psi_b}(\tau) - \eta_{\psi_a}\eta^*_{\psi_b}, \tag{2.2.16}$$

and where $R_{\psi_a\psi_b}(\tau)$ in turn denotes the *cross-correlation function* between two arbitrary continuous-time random signals $\boldsymbol{\psi}_a(t), \boldsymbol{\psi}_b(t)$ and η_{ψ_a} in turn denotes the *mean* of arbitrary random signal $\boldsymbol{\psi}_a(t)$, then some interrelations seem to appear. In [17] it is proven that the frequency band coherence can be interpreted as the *squared envelope* of the correlation coefficient at zero time delay for the particular case of pressure and an arbitrary component of the particle velocity vector considered as RPs, that is,

$$\gamma^2_{\psi_a\psi_b}(f) = \rho^2_{\psi_a\psi_b}(0, f_0, \Delta f) + \check{\rho}^2_{\psi_a\psi_b}(0, f_0, \Delta f), \tag{2.2.17}$$

where $\check{\rho}$ in turn designates the *Hilbert transform* of $\rho(\,\cdot\,)$. The relationship between the two degree of coherence is discussed, under more general circumstances in [14, 26]. They found the following relations between the two degrees of coherence[9]

$$\gamma_{\psi_a\psi_b}(\omega) = \frac{1}{2\pi}\frac{1}{\sqrt{s_{\psi_a\psi_a}(\omega)}\sqrt{s_{\psi_b\psi_b}(\omega)}}\int_{-\infty}^{\infty}\rho_{\psi_a\psi_b}(\tau)\mathrm{e}^{-\imath\omega\tau}\,\mathrm{d}\tau, \tag{2.2.18}$$

and

$$\rho_{\psi_a\psi_b}(\tau) = \int_{-\infty}^{\infty}\sqrt{s_{\psi_a\psi_a}(\omega)}\sqrt{s_{\psi_b\psi_b}(\omega)}\gamma_{\psi_a\psi_b}(\omega)\mathrm{e}^{\imath\omega\tau}\,\mathrm{d}\omega, \tag{2.2.19}$$

where $s_{\psi_a\psi_a}(\omega)$ denotes the *normalized* single-sided autospectra

$$s_{\psi_a\psi_a}(\omega) \triangleq \frac{S_{\psi_a\psi_a}(\omega)}{\int_{-\infty}^{\infty}S_{\psi_a\psi_a}(\omega)\,\mathrm{d}\omega}. \tag{2.2.20}$$

Hence, the ordinary complex coherence function is obtained as $\frac{1}{2\pi}$ times the Fourier transform defined in (M.1.3) on page 787 of the correlation coefficient weighted by the inverse product of the square roots of normalized spectral densities. Similarly the correlation coefficient is obtained as 2π times the inverse Fourier transform (see (M.1.5) on page 788) of the ordinary complex coherence function weighted by the product of the square roots of normalized spectral densities.

It should be emphasized that the complex coherence function $\gamma_{\psi_a\psi_b}(f)$ is a measure of coherence in the *space-frequency domain*, whilst the correlation function $\rho_{\psi_a\psi_b}(\tau)$ is a measure of coherence in the *space-time domain*.

The magnitude-squared coherence function is usually determined from periodogram analysis as presented in Appendix C on page 539.

[8] Note, $C_{\psi_a\psi_b}(\tau)$ represents a cross-covariance function whereas $C_{\psi_a\psi_b}(f)$ defined in (2.2.14) is the co-spectrum.

[9] The expressions have been accommodated to the choice of non-unitary Fourier transform pair viz. (M.1.3) and (M.1.5).

2.2.4 Partial Coherence

The partial coherence function is usually most used as an intermediate quantity for the determination of the multiple coherence function. However, we will later make direct use of the partial coherence function in the JCRSA method to be presented in section 2.3 on page 29. The partial coherence function between random signals $\boldsymbol{\psi}_a$ and $\boldsymbol{\psi}_b$ conditioned on the random signal set $\boldsymbol{\psi}^C$ denoted by $\gamma^2_{\psi_a\psi_b\perp\psi^C}$ is defined by[10]

$$\gamma^2_{\psi_a\psi_b\perp\psi^C}(f) \triangleq \frac{S_{\psi_a\psi_b\perp\psi^C}(f)S_{\psi_b\psi_a\perp\psi^C}(f)}{S_{\psi_a\psi_a\perp\psi^C}(f)S_{\psi_b\psi_b\perp\psi^C}(f)}. \tag{2.2.21}$$

By the term *conditioned* is meant the residual components of random signal $\boldsymbol{\psi}_a(t)$ and of random signal $\boldsymbol{\psi}_b(t)$ that remains after removing all components linearly dependent on $\boldsymbol{\psi}^C$. By comparing (2.2.10) and (2.2.21) we recognize that the partial coherence function is the ordinary coherence function of the residual parts of the random signals that follows from conditioning with respect to $\boldsymbol{\psi}^C$. An explicit expression for the partial coherence function is provided in (2.2.28) on page 28.

The partial coherence function is subject is to a double inequality viz. (2.2.31) on page 28. In the development we sometimes are conditioning with an empty set ($\boldsymbol{\psi}^C = \emptyset$), which of course leaves the auto- and cross-spectral density functions unchanged, that is, $S_{\psi_a\psi_a\perp\emptyset} \triangleq S_{\psi_a\psi_a}$ and $S_{\psi_a\psi_b\perp\emptyset} \triangleq S_{\psi_a\psi_b}$.

It is important to note that the partial coherence function involve two single channel signals that may or may not belong to the same channel set and a set of N^C_ψ signals. As such the partial coherence function is more complicated in structure than the multiple coherence function defined in subsection 2.2.5. For the same reason when considering specific pairs of channels, that is, joint-channels and we want to eliminate the interference from a set of other channels, it is therefore the partial coherence function and not the multiple coherence function that will be used.

2.2.5 Multiple Coherence

The multiple magnitude-squared coherence function or more briefly the multiple coherence function is normally only considered in more advanced data analysis.

The MIMO problem has among other authors theoretically been considered by Bendat in [1, 2], Dodds and Robson [11] and Yacoub [27]. Moreover the handbook by Bendat and Piersol [6] provides invaluable insight into the partial coherence function and multiple coherence function.

Somewhat surprisingly, only a few references to the multiple coherence function can be found in the ANC literature. In [9] a diesel engine structural-acoustical problem is modeled by a multiple-input and single-output (MISO) system where the vibration measured at each of the six cylinders constitute the inputs and where the sound pressure measured some distance away represents the output. Using multiple coherence function analysis as opposed to ordinary coherence function it was found that the total noise was almost equal to the coherent noise.

In the present report we will make extensive use of the multiple coherence function in particular for the assessment of the requirement on the amount of reference sensors required in a confined feedforward (CFF) ANC system.

[10] The notion $\psi_a\psi_b \perp \psi^C$ can mnemonically be viewed as the subspace of ψ_a and ψ_b that is orthogonal to ψ^C.

In geophysics the multiple coherence function (MCOF) can be used to separate two stationary components: a signal sequence, which correlates from trace to trace, and an incoherent noise component, which does not correlate from trace to trace [23, 24]. Hence, a single as opposed to multi-channel system is considered, but at multiple times.

The multiple coherence function has also been used as a statistic measure for detection of a common unknown signal component in multiple noisy channels [22]. A discussion of this subject, however, will be deferred until section 2.A on page 102.

The multiple coherence function is not directly available in a MATLAB® package and the engineer or scientist therefore has to implement his own version dedicated to the specific application at hand.

The multiple magnitude-squared coherence function between $\boldsymbol{\psi}_a$ and the set of $\boldsymbol{\psi}^C$ signals that we will denote by[11] $\gamma^2_{\psi_a \cdot \psi^C}$, represents the linear dependence between spectral components of $\boldsymbol{\psi}_a(f)$ and those of the signals $\boldsymbol{\psi}^C_1(f), \boldsymbol{\psi}^C_2(f), \ldots, \boldsymbol{\psi}^C_{N^C_\psi}(f)$. Hence, a *single* signal $\boldsymbol{\psi}_a(t)$ is related to the non-empty set of, e.g., N^C_ψ signals. Some authors prefer to make the size of the conditioning signal set explicit and therefore refer to a N^C_ψ-order multiple coherence function.

At least two different approaches to the determination of the multiple coherence function exist. The first procedure relies on straight forward use of linear algebra and requires no ranking of the input channels nor determination of conditioned spectra or partial coherence functions. The second procedure on the other hand is based on a ranking of the input channels and uses an iterative computation procedure involving conditioned spectra and partial coherence functions. This iterative procedure provides specific insight in to the contribution of the individual signals. Moreover, this second method is relative easy amendable to statistical error analysis as detailed in Appendix C on page 539.

Both methods rely on the construction of a signal set, say, $\boldsymbol{\psi}^A$ as the union of the random signal $\boldsymbol{\psi}_a$ and the set of $\boldsymbol{\psi}^C$ signals, that is, $\boldsymbol{\psi}^A \leftarrow \boldsymbol{\psi}_a \cup \boldsymbol{\psi}^C$. Hence, $N^A_\psi = N^C_\psi + 1$.

From these signals the following $\boldsymbol{\psi}_a - \boldsymbol{\psi}^C$ channel power spectral density matrix denoted by $S_{\psi^A\psi^A} \in \mathbb{C}^{N_f \times N^A_\psi \times N^A_\psi}$ that is obtained from concatenation of the random signal $\boldsymbol{\psi}_a$ and the conditioning signal set $\boldsymbol{\psi}^C$, that is,

$$S_{\psi^A\psi^A} \triangleq \begin{bmatrix} S_{\psi_a\psi_a} & S_{\psi_a\psi^C_1} & S_{\psi_a\psi^C_2} & \cdots & S_{\psi_a\psi^C_{N^C_\psi}} \\ S_{\psi^C_1\psi_a} & S_{\psi^C_1\psi^C_1} & S_{\psi^C_1\psi^C_2} & \cdots & S_{\psi^C_1\psi^C_{N^C_\psi}} \\ S_{\psi^C_2\psi_a} & S_{\psi^C_2\psi^C_1} & S_{\psi^C_2\psi^C_2} & \cdots & S_{\psi^C_2\psi^C_{N^C_\psi}} \\ \vdots & \vdots & \vdots & \ddots & \vdots \\ S_{\psi^C_{N^C_\psi}\psi_a} & S_{\psi^C_{N^C_\psi}\psi^C_1} & S_{\psi^C_{N^C_\psi}\psi^C_2} & \cdots & S_{\psi^C_{N^C_\psi}\psi^C_{N^C_\psi}} \end{bmatrix}. \tag{2.2.22}$$

[11] The notion $\psi_a \cdot \psi^C$ can mnemonically be viewed as the projection of ψ_a on ψ^C.

Multiple Coherence Function Matrix Formulation

In [6, Ch. 7] the multiple magnitude-squared coherence function between the conditioning signal sets $\boldsymbol{\psi}^C$ and random signal $\boldsymbol{\psi}_a$ denoted by $\gamma^2_{\psi_a \cdot \psi^C}$ can be expressed as

$$\boxed{\gamma^2_{\psi_a \cdot \psi^C}(f) = 1 - \frac{|S_{\psi^A \psi^A}(f)|}{S_{\psi_a \psi_a}(f)|S_{\psi^C \psi^C}(f)|}.} \tag{2.2.23}$$

In [21, Ch. 14] a somewhat different expression for the multiple magnitude-squared coherence function is provided

$$\boxed{\gamma^2_{\psi_a \cdot \psi^C}(f) = \frac{S_{\psi_a \psi^C}(f) S^{-1}_{\psi^C \psi^C}(f) S_{\psi^C \psi_a}(f)}{S_{\psi_a \psi_a}(f)},} \tag{2.2.24}$$

where $S_{\psi_a \psi^C}$ and $S_{\psi^C \psi_a}$ are the last N^C_ψ elements of the first row and first column of $S_{\psi^A \psi^A}$ in (2.2.22) respectively. However, applying ordinary rules from linear algebra the equivalence of (2.2.23) and (2.2.24) is easily recognized.

As proven in, e.g., [18] the multiple coherence function is subject to the following double constraints

$$0 \leq \gamma^2_{\psi_a \cdot \psi^C}(f) \leq 1, \tag{2.2.25}$$

where $\gamma^2_{\psi_a \cdot \psi^C}(f)$ attains the lower value 0 when the measured output at the frequency being considered is entirely due to noise and therefore cannot be deduced from the known inputs. Similarly, $\gamma^2_{\psi_a \cdot \psi^C}(f)$ attains the upper value 1 when $\boldsymbol{\psi}_a$ can be completely determined from the $\boldsymbol{\psi}^C$ signals passing through a (virtual) linear noise-free system.

However, the compact forms (2.2.23) and (2.2.24) provide no specific insight into the contribution of the individual signals in $\boldsymbol{\psi}^C$ to the multiple coherence function $\gamma^2_{\psi_a \cdot \psi^C}(f)$.

Multiple Coherence Function Iterative Procedure

In [3, 5, 6] a detailed derivation of the multiple coherence function based on the iterative procedure is provided.

If a large variation among the individual ordinary coherence functions $\gamma^2_{\psi_a \psi^C_l}$ are encountered a ranking of the conditioning signal sets should initially be carried out. Hence, for each frequency index perform a channel ranking with respect to ordinary coherence functions and in descending order, that is,

$$\gamma_{\psi_a \psi^C_{\check{1}(f)}}(f) \geq \gamma_{\psi_a \psi^C_{\check{2}(f)}}(f) \geq \cdots \geq \gamma_{\psi_a \psi^C_{\check{N}^C_{\psi(f)}}}(f), \tag{2.2.26}$$

where $\check{1}(f), \check{2}(f), \ldots, \check{N}^C_{\psi(f)}$ are the corresponding ranking indices in $S_{\psi^A \psi^A}$ defined in (2.2.22). For notational brevity, the explicit dependence of the ranking on the frequency index will subsequently be suppressed.

Then follows the creation of a $N_\psi^A \times N_\psi^A \times N_\psi^C$ MISO channel conditioned power spectral density matrix denoted by $S_{\psi_i\psi_j \perp \psi_{r!}}$ from the following recursive algorithm

$$S_{\psi_i^A\psi_j^A \perp \psi_{l!}^C} = \begin{cases} S_{\psi_{\breve{i}}^A\psi_{\breve{j}}^A} - \frac{S_{\psi_{\breve{1}}^A\psi_{\breve{j}}^A}}{S_{\psi_{\breve{i}}^A\psi_{\breve{1}}^A}} S_{\psi_{\breve{i}}^A\psi_{\breve{1}}^A} & l = 1 \\ S_{\psi_i^A\psi_j^A \perp \psi_{(l-1)!}^C} - \frac{S_{\psi_l^C\psi_j^A \perp \psi_{(l-1)!}^C}}{S_{\psi_l^C\psi_l^C \perp \psi_{(l-1)!}^C}} S_{\psi_i^A\psi_l^C \perp \psi_{(l-1)!}^C} & l > 1; \end{cases} \quad i,j \in N_\psi^A, l \in \underline{N}_\psi^C, l < \min(i,j). \tag{2.2.27}$$

The notion $\boldsymbol{\psi}_{r!} = \cup_{r'=1}^{r} \boldsymbol{\psi}_{r'}$ is introduced as a compact representation of the *accumulated* set of signals.

It should be observed that the link between the iteration variables i, j to the corresponding indices $\breve{i}, \breve{j}$ in the MIMO channel power spectral density matrix $S_{\psi\psi}$ defined in (2.2.22) on page 26 is established by (2.2.26) on the preceding page. In addition by definition $i = N_\psi^A \iff \breve{i} = N_\psi^A$ and a similar relation pertains to j and $\breve{j}$.

Next the partial coherence function $\gamma^2_{\psi_a\psi_l^C \perp \psi_{(l-1)!}^C}$ is likewise determined recursively from

$$\gamma^2_{\psi_a\psi_l^C \perp \psi_{(l-1)!}^C} = \begin{cases} \frac{|S_{\psi_{\breve{l}}\psi_{\breve{j}}}|^2}{S_{\psi_{\breve{l}}\psi_{\breve{l}}} S_{\psi_{\breve{j}}\psi_{\breve{j}}}} & l = 1 \\ \frac{|S_{\psi_a\psi_l^C \perp \psi_{(l-1)!}^C}|^2}{S_{\psi_l^C\psi_l^C \perp \psi_{(l-1)!}^C} S_{\psi_a\psi_a \perp \psi_{(l-1)!}^C}} & l > 1 \end{cases} \quad l \in \underline{N}_\psi^C, j = N_\psi^A. \tag{2.2.28}$$

Finally, the multiple magnitude-squared coherence function is determined from (2.2.28) by

$$\gamma^2_{\psi_a \cdot \psi^C} = 1 - \prod_{l=1}^{N_\psi^C} \big(1 - \gamma^2_{\psi_a\psi_l^C \perp \psi_{(l-1)!}^C}\big). \tag{2.2.29}$$

In [27] it is shown that the multiple coherence function between $\boldsymbol{\psi}_a(t)$ and $\boldsymbol{\psi}^C(t)$ can also be expressed as the sum of N_ψ^C terms each consisting of the product of partial coherence function between $\boldsymbol{\psi}_a(t)$ and the l'th component of $\boldsymbol{\psi}^C(t)$ conditioned on the previous $l-1$ components, and *multiple incoherence* between $\boldsymbol{\psi}_a(t)$ and the conditioning subset of $\boldsymbol{\psi}^C(t)$, that is,

$$\gamma^2_{\psi_a \cdot \psi^C}(f) = \sum_{l=1}^{N_\psi^C} \gamma^2_{\psi_a\psi_l^C \perp \psi_{(l-1)!}^C}(f) \Big(1 - \gamma^2_{\psi_a \cdot \psi_{(l-1)!}^C}(f)\Big). \tag{2.2.30}$$

Hence, $\gamma^2_{\psi_a \cdot \psi^C}$ will be a monotonously non-decreasing function with increasing N_ψ^C.

The partial coherence function defined in subsection 2.2.4 is subject to a double inequality [27]

$$0 \le \gamma^2_{\psi_a\psi_l^C \perp \psi_{\neq l}^C}(f) \le \min\Big\{1; \gamma^2_{\psi_a\psi_l^C}(f) \Big(1 - \gamma^2_{\psi_a \cdot \psi_{\neq l}^C}(f)\Big)^{-1}\Big\}. \tag{2.2.31}$$

In [27] graphical interpretation of the identity (2.2.30) and the inequality (2.2.31) is provided in terms of *coherence diagrams*.

In the special case where the spectral components of $\boldsymbol{\psi}_l^C(f)$ and $\boldsymbol{\psi}_{l'}^C(f)$ are uncorrelated $\forall l \neq l'$, then the multiple coherence function is simply the sum of individual ordinary coherence functions

$$\gamma^2_{\psi_a \cdot \boldsymbol{\psi}^C}(f) = \sum_{l=1}^{N_\psi^C} \gamma^2_{\psi_a \cdot \boldsymbol{\psi}_l^C}(f). \tag{2.2.32}$$

Multiple Coherence Function MIMO *System*

The multiple coherence function is determined by isolating each output channel in turn and by considering the MISO system thus obtained. In the following we assume that channel $\boldsymbol{\psi}_k^O, k \in \underline{N}_\psi^O$ has been selected as output channel. The first step is in accordance with (2.2.22) to assign to the signal set A the union of the k'th output signal and the set of input signals, that is, $\boldsymbol{\psi}_a \leftarrow \boldsymbol{\psi}_k^O$ and $\boldsymbol{\psi}^C \leftarrow \boldsymbol{\psi}^I$ which means $\boldsymbol{\psi}^A \leftarrow \boldsymbol{\psi}_k^O \cup \boldsymbol{\psi}^I$. Hence, in this specific case $N_\psi^A = N_\psi^I + 1$. Accordingly, the multiple coherence function is obtained from the matrix formulations (2.2.23) or (2.2.24) or alternatively are iteratively determined from (2.2.26) to (2.2.29).

For the multiple magnitude-squared coherence function analysis to turn out successfully the following assumptions will be made

MCOF Assump. 1. None of the ordinary coherence functions between any input and the total output should equal unity, that is, $\forall j \in \underline{N}_\psi^I, k \in \underline{N}_\psi^O : \gamma^2_{\psi_j^I \psi_k^O} < 1$. Otherwise the other inputs are superfluous and do not contribute further to the multiple coherence function.

MCOF Assump. 2. None of the multiple coherence functions between any input and the other inputs should equal unity, that is, $\forall j \in \underline{N}_\psi^I : \gamma^2_{\psi_j^I \cdot \boldsymbol{\psi}_{\neq j}^I} < 1$, where we by the notion $\psi_{\neq j}^I = \psi^I \setminus \psi_j^I$ refer to the *subset of input signals obtained from excluding the j'th element* . Otherwise this input is superfluous and can be obtained from a linear combination of the other inputs.

MCOF Assump. 3. Referring to (2.2.1) on page 18 for each output the ordinary coherence function between the output signal and the input signals should exceed, say, 0.9 for 10 dB attenuation, that is, $\forall k \in \underline{N}_\psi^O : \gamma^2_{\psi_k^O \cdot \boldsymbol{\psi}^I} \geq 0.9$.

It should be remarked that MCOF assumption 2 implies that none of the ordinary coherence functions between any pair of input records should equal unity. The MCOF assumptions 1-2 pose no problem for the signals considered in this report. We also appreciate the importance of MCOF Assump. 2 as regards numerical stability of (2.2.23) and (2.2.24). The requirement in MCOF assumption 3 is often of great concern especially at higher frequencies.

Sample statistic for the pairwise and multiple magnitude-squared coherence is considered in [22]. From such sample statistic density functions can be expressed and receiver operating characteristic (ROC) curves deduced, which in turn define the probability of detection versus probability of false alarm for a signal of a given true coherence.

2.3 Joint-Channel-Residual Spectral Analysis

In this section a new method for acoustical signal processing that is referred to as joint-channel residual spectral analysis (JCRSA) is developed. The JCRSA method is used for the extraction of joint signal information from different observation positions in space. The idea is to separate

each spectrum in a *coherent spectrum* and a *residual spectrum*. The contents of the coherent spectrum can be obtained from a linear superposition of the other signals, whereas the residual spectrum bears information that is unique to each specific channel.

As will be demonstrated in section 2.4 on page 32 this method has the ability to extract *distinct* channel response relationships and in particular timing information that may be obscured by the action of the remainder channels. Such timing information is useful for, e.g., the determination of the *spatially-weighted-averaged acquisition lead time.* This quantity is introduced to represent the averaged time-advance obtained by each reference sensor relative to each performance sensor or error sensor involved in the proposed CFFAC system. A formal definition, however, is postponed until section 2.4.3 on page 58.

The idea is to use the results from section 2.2 in particular the concepts of multiple coherence functions and partial coherence functions. Moreover, we will define two sets of mutually exclusive sets of spectra that will be used to describe the joint-channel-conditioned statistics. Hence, we will divide each spectra in two parts. The first part, the *coherent spectrum* or *parallel spectrum*, is the component of the spectrum that could be obtained by the sum of a linear transformation of the conditioning signal. The second part, the *residual spectrum* or *orthogonal spectrum* is that part of the *total spectrum* that is *unique* to the isolated channels. Hence, the residual spectrum is the part that of the total spectrum that remains when the *coherent spectrum* has been subtracted from the total spectrum.

Denoting by $S_{\psi_a\psi_a \cdot \psi^C}(f)$ the *coherent auto spectral density function* of random signal $\boldsymbol{\psi}_a$ conditioned on random signal set $\boldsymbol{\psi}^C$ and denoting by $S_{\psi_a\psi_a \perp \psi^C}(f)$ the *residual auto spectral density function* of random signal $\boldsymbol{\psi}_a$ conditioned on random signal set $\boldsymbol{\psi}^C$ we may express the (total) auto spectral density function as

$$S_{\psi_a\psi_a}(f) \triangleq S_{\psi_a\psi_a \cdot \psi^C}(f) + S_{\psi_a\psi_a \perp \psi^C}(f). \tag{2.3.1}$$

Similarly denoting by $S_{\psi_a\psi_b \cdot \psi^C}(f)$ the *coherent cross-spectral density function* between random signal $\boldsymbol{\psi}_a$ and random signal $\boldsymbol{\psi}_b$ conditioned on random signal set $\boldsymbol{\psi}^C$ and denoting by $S_{\psi_a\psi_b \perp \psi^C}(f)$ the *residual cross-spectral density function* between random signal $\boldsymbol{\psi}_a$ and random signal $\boldsymbol{\psi}_b$ conditioned on random signal set $\boldsymbol{\psi}^C$ we may express the (total) cross-spectral density function as

$$S_{\psi_a\psi_b}(f) \triangleq S_{\psi_a\psi_b \cdot \psi^C}(f) + S_{\psi_a\psi_b \perp \psi^C}(f). \tag{2.3.2}$$

2.3.1 Joint-Channel-Residual Spectral Analysis Matrix Formulation

In the abstract matrix formulation we create the following block matrix

$$S_{\psi\psi} \triangleq \begin{bmatrix} S_{\psi^A\psi^A} & S_{\psi^A\psi^C} \\ S_{\psi^C\psi^A} & S_{\psi^C\psi^C} \end{bmatrix}. \tag{2.3.3}$$

where $S_{\psi^A\psi^A} \in \mathbb{C}^{N_f \times N_\psi^A \times N_\psi^A}$ represents the A channel power spectral density matrix, $S_{\psi^C\psi^C} \in \mathbb{C}^{N_f \times N_\psi^C \times N_\psi^C}$ similarly is the C channel power spectral density matrix and $S_{\psi^A\psi^C} = S^*_{\psi^C\psi^A} \in \mathbb{C}^{N_f \times N_\psi^C \times N_\psi^A}$ denotes the A-C cross channel power spectral density matrix. The dependence on

the frequency index is as usual suppressed for notational convenience. In full expansion $S_{\psi\psi}$ is expressed by

$$S_{\psi\psi} = \begin{bmatrix} S_{\psi_1^A\psi_1^A} & S_{\psi_1^A\psi_2^A} & S_{\psi_1^A\psi_1^C} & S_{\psi_1^A\psi_2^C} & \dots & S_{\psi_1^A\psi^C_{N^C_\psi}} \\ S_{\psi_2^A\psi_1^A} & S_{\psi_2^A\psi_2^A} & S_{\psi_2^A\psi_1^C} & S_{\psi_2^A\psi_2^C} & \dots & S_{\psi_2^A\psi^C_{N^C_\psi}} \\ S_{\psi_1^C\psi_1^A} & S_{\psi_1^C\psi_2^A} & S_{\psi_1^C\psi_1^C} & S_{\psi_1^C\psi_2^C} & \dots & S_{\psi_1^C\psi^C_{N^C_\psi}} \\ S_{\psi_2^C\psi_1^A} & S_{\psi_2^C\psi_2^A} & S_{\psi_2^C\psi_1^C} & S_{\psi_2^C\psi_2^C} & \dots & S_{\psi_2^C\psi^C_{N^C_\psi}} \\ \vdots & \vdots & \vdots & \vdots & \ddots & \vdots \\ S_{\psi^C_{N^C_\psi}\psi_1^A} & S_{\psi^C_{N^C_\psi}\psi_2^A} & S_{\psi^C_{N^C_\psi}\psi_1^C} & S_{\psi^C_{N^C_\psi}\psi_2^C} & \dots & S_{\psi^C_{N^C_\psi}\psi^C_{N^C_\psi}} \end{bmatrix}. \tag{2.3.4}$$

Applying ordinary linear algebra to (2.3.4) we obtain the following expression for the residual cross spectral density matrix $S_{\psi^A\psi^A\perp\psi^C}$

$$\boxed{S_{\psi^A\psi^A\perp\psi^C} = S_{\psi^A\psi^A} - S_{\psi^A\psi^C}S^{-1}_{\psi^C\psi^C}S_{\psi^C\psi^A}.} \tag{2.3.5}$$

2.3.2 Joint-Channel-Residual Spectral Analysis Iterative Procedure

The coherent auto spectral density function[12] is readily available from the multiple coherence function

$$S_{\psi_a\psi_a\cdot\psi^C}(f) = \gamma^2_{\psi_a\cdot\psi^C}(f)S_{\psi_a\psi_a}(f). \tag{2.3.6}$$

Fortunately, we may use the recursive procedure (2.2.27) on page 28 to obtain the residual auto spectral density function and residual cross-spectral density function. Finally, if required, the coherent cross-spectral density function can be derived from insertion of $S_{\psi_a\psi_b\perp\psi^C}$ in (2.3.2).

2.3.3 Joint-Channel-Residual Spectral Analysis MIMO System

The JCRSA method applied to a MIMO system consider each input-output channel combination in turn. The number of such combinations amounts to $N^I_\psi N^O_\psi$. In the following we assume that channel $\boldsymbol{\psi}^I_j, j \in \underline{N}^I_\psi$ and $\boldsymbol{\psi}^O_k, k \in \underline{N}^O_\psi$ have been selected as input and output channel respectively. Accordingly, we make the following assignments: $\boldsymbol{\psi}^A \leftarrow \psi^I_j \cup \psi^O_k$ and $\boldsymbol{\psi}^C \leftarrow \psi^I_{\neq j}$. Now, the spectrum quantities sought after are readily available from instantiating the abstract matrix formulation viz. (2.3.5) or by invoking the iterative procedure viz. (2.2.27) on page 28.

[12] The term *coherent spectrum* is usually used. However, disambiguation of the *coherent autospectrum* and *coherent cross-spectrum* is required here.

2.4 System Identification of Primary Pathes

2.4.1 Motivation

In this demonstration the JCRSA method is used to determine the so-called *primary paths* that mutually link the reference signals to the disturbance signals and performance signals. By the term *primary* an explicit reference is made to the primary sources being responsible for the signals considered. In chapter 7 on page 291 the so-called *secondary paths* that exclusively involve the secondary sources will be determined for the same unit under test (UUT).

In particular we wish to estimate the spatially-weighted-averaged acquisition lead times provided by the reference sensors when positioned on the surface of a Gentex HGU-55/P helmet. By the phrase spatially-weighted-averaged acquisition lead time we refer to some average time value that is obtained in CFFAC topology. This quantity will be more precisely defined in section 2.4.3 on page 58.

In the duct ANR case an upstream reference sensor will provide *lead time* information, that is, $\tau_{acq} > 0$ while a reference sensor positioned *downstream* will provide *lag time* information, that is, $\tau_{acq} < 0$. For an AC system in a diffuse sound field expectably each reference sensor will provide an equal amount of lead time and lag time information. However, this pertains to sound wave propagation in a homogeneous media. For the particular case of the depicted ANR helmet the propagation or leakage of sound waves from the exterior of the helmet to the interior of the earcups involves relative slow vibroacoustic mechanisms. Accordingly, it is expectable that in the average each sensor provide more lead time information than lag time information. The actual time-advance, however, depends on the relative positions of the reference sensor and performance sensor combination.

As only a few accounts to partial coherence functions and residual spectra can be found in the literature, we will discuss residual auto- and cross-spectral density functions, transfer functions and auto- and cross-correlation functions at length in this section. This should hopefully bring new insight to these somewhat abstract quantities.

2.4.2 Measurement Setup

The diffuse sound field measurements were conducted in the Terma Noise Chamber Facility. Some photos illuminating the measurement setup can be found in Figure 2.1 - 2.2 on pages 33–34.

For all statistical analysis the following power spectral density functions parameters defined in Appendix C on page 539 have been chosen: Periodogram, single-sided, $f_s = 65.536$ kHz, $N_{DFT} = 16384, L_{DFT} = 16385, R_{DFT} = 8193$, Hanning, $\Delta f_m = 16$ Hz, $T_{DFT} = 0.25$ s, $N_{f_{DFT}} = 8193, \Delta f_{DFT} = 4$ Hz, $K_{DFT} = 158$.

The system identification uses a random low-pass 4 kHz white noise ($\mathcal{N}(0, 0.2)$) distributed signal. The bandwidth of the statistical analysis has been limited to 900 Hz by using an elliptic LPF ($f_{pass} = 900$ Hz, $f_{stop} = 1$ kHz, $A_{pass} = 1$ dB, $A_{stop} = 40$ dB), f_s =65.536 kHz filter for reasons of bandwidth limitation of the JCRSA method that will be come clear later viz. Simulation 2.4.37 on page 78.

Measurements were acquired over a 30 s time period of which only $0 - 20$ s are used in the analysis. The topology consisted of a total of $N_x = 10$ BK4949 surface microphones flush-mounted on Gentex HGU-55/P helmet mounted on a BK 4128 C head and torso simulator (HATS)

Fig. 2.1: Gentex HGU-55/P helmet with BK 4949 surface microphones mounted on the BK 4128 C HATS. Leftside view.

Fig. 2.2: Gentex HGU-55/P helmet with BK 4949 surface microphones mounted on the BK 4128 C HATS. Backside view.

that in turn includes the BK 4159 C left ear simulator and the BK 4158 C right ear simulator, that is, $N_p = 2$. The performance signals acquired by the left and right ear simulators are denoted by d_1^p and d_2^p respectively. The Terma Earcup Audio System was used on the left ear only. The built-in microphone provides a disturbance signal that will be designated by d_1, that is, $N_e = 1$.

In Figure 2.3 on the facing page the positions of each of the 10 BK 4949 surface microphones flush-mounted on the Gentex HGU-55/P helmet are depicted.

2.4.3 System Identification of Primary Pathes $G_{ex}^{j,m}$

System Identification of Primary Pathes $G_{ex}^{j,m}$, Ordinary Analysis

In Simulation 2.4.1 - 2.4.2 on pages 36–37 the probability density functions (pdfs) for the first reference signal and the disturbance signal, that is, x_1 and d_1 are shown. Apparently, the two pdfs closely resemble zero-mean Gaussian distributions. The same pattern pertains to the other reference signals. This result is expectable as the loudspeakers in the reverberant room are excited by normal distributed signals and as the room acts linearly on the signals. However, some care must be exercised when making conclusion regarding the tail part of a pdf. Accordingly, in order to test for a possible heavy-tail distribution behavior the software package STABLE from Robust Analysis, Inc. was used to obtain estimates of the stable parameters $\mathcal{S}(\alpha, \beta, \gamma, \delta)$ defined in Appendix L on page 773 using the maximum likelihood estimation (MLE). The results are listed Table 2.1

As is well known uncertainty values do not make sense when a parameter is at the boundary of the parameter space, e.g., $\alpha = 2$ and therefore not included. Hence, as the index of stability α is identical to 2 and as the skewness parameter β takes small values this confirms the assumption of normal distributed signals. Having confirmed that the pdfs indeed are Gaussian we use standard statistical tools to estimate the normal parameters $\mathcal{N}(\mu, \sigma^2)$ and the confidence intervals listed

Fig. 2.3: BK 4949 surface microphones flush-mounted on Gentex HGU-55/P helmet mounted on a mannequin (**not** the HATS).

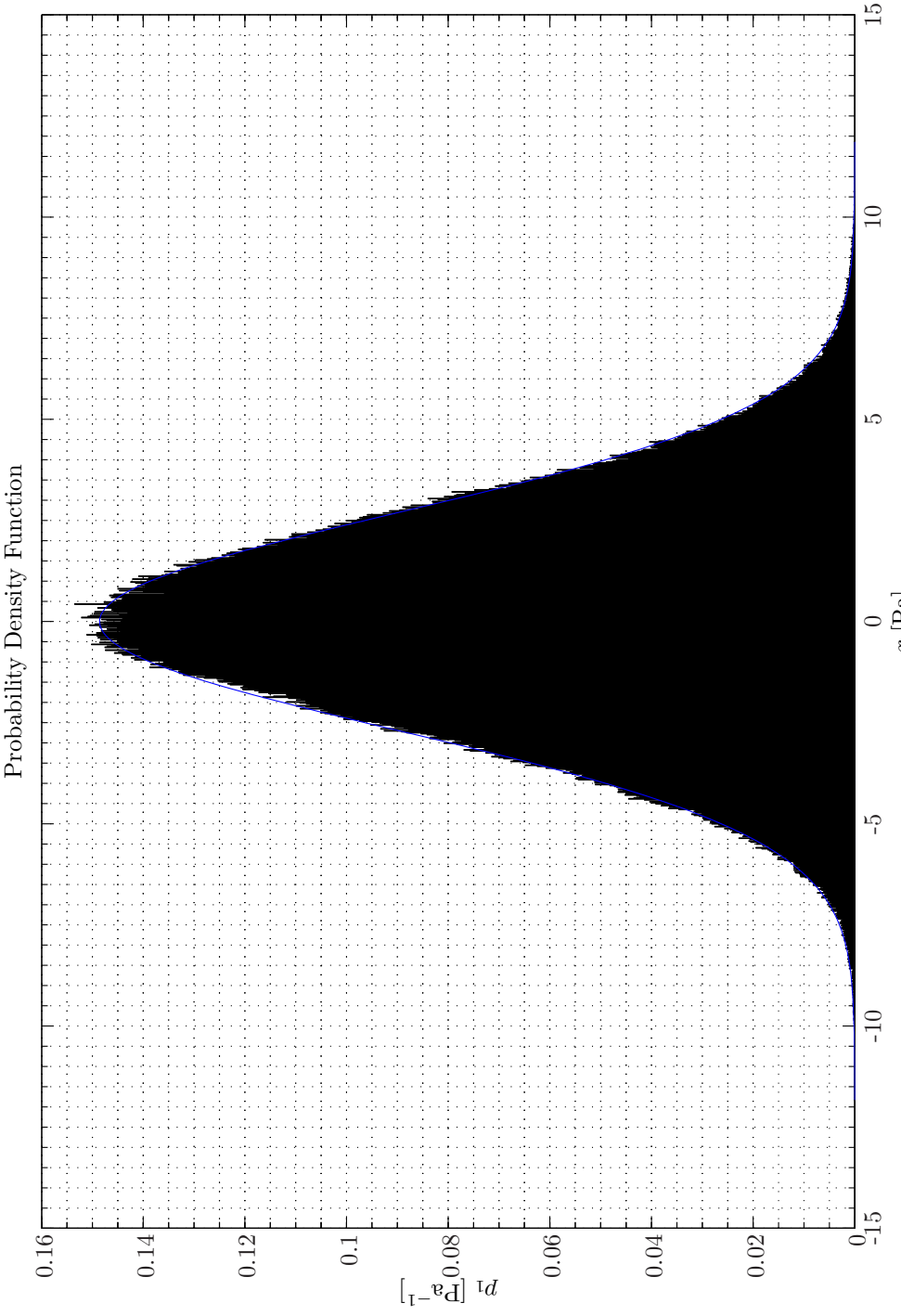

Sim 2.4.1: *Probability Density Functions*: **Statistical Data Analysis**: Single-Sided Modified Periodogram, $f_s = 65.536$ kHz, $N_{DFT} = 16384$, $L_{DFT} = 16385$, $R_{DFT} = 8193$, Hanning, $\Delta f_m = 16$ Hz, $T_{DFT} = 0.25002$ s, $N_{f,DFT} = 8193$, $\Delta f_{DFT} = 4$ Hz, $K_{DFT} = 158$; *System Identification:* (Random Low-Pass (4 kHz) White Noise ($\mathcal{N}(0, 0.2)$), Elliptic LPF ($f_{pass} = 900$ Hz, $f_{stop} = 1$ kHz, $A_{pass} = 1$ dB, $A_{stop} = 40$ dB), f_s =65.536 kHz; Time: $0 - 20$ s; **Topology:** BK 4949 surface microphones flush-mounted on Gentex HGU-55/P helmet mounted on a BK 4128 C HATS, Terma Earcup Audio System (Feedforward, mFx, $N_x = 10, N_e = 1, N_y = 2, N_p = 2$); *Channels:* #1 $\leftarrow x_1$, #2 $\leftarrow x_2$, #3 $\leftarrow x_3$, #4 $\leftarrow x_4$, #5 $\leftarrow x_5$, #6 $\leftarrow x_6$, #7 $\leftarrow x_7$, #8 $\leftarrow x_8$, #9 $\leftarrow x_9$, #10 $\leftarrow x_{10}$, #11 $\leftarrow d_1$; **Scenario:** `SystemIdentification(65536Hz)PrimaryPathes/20070204T112036`.

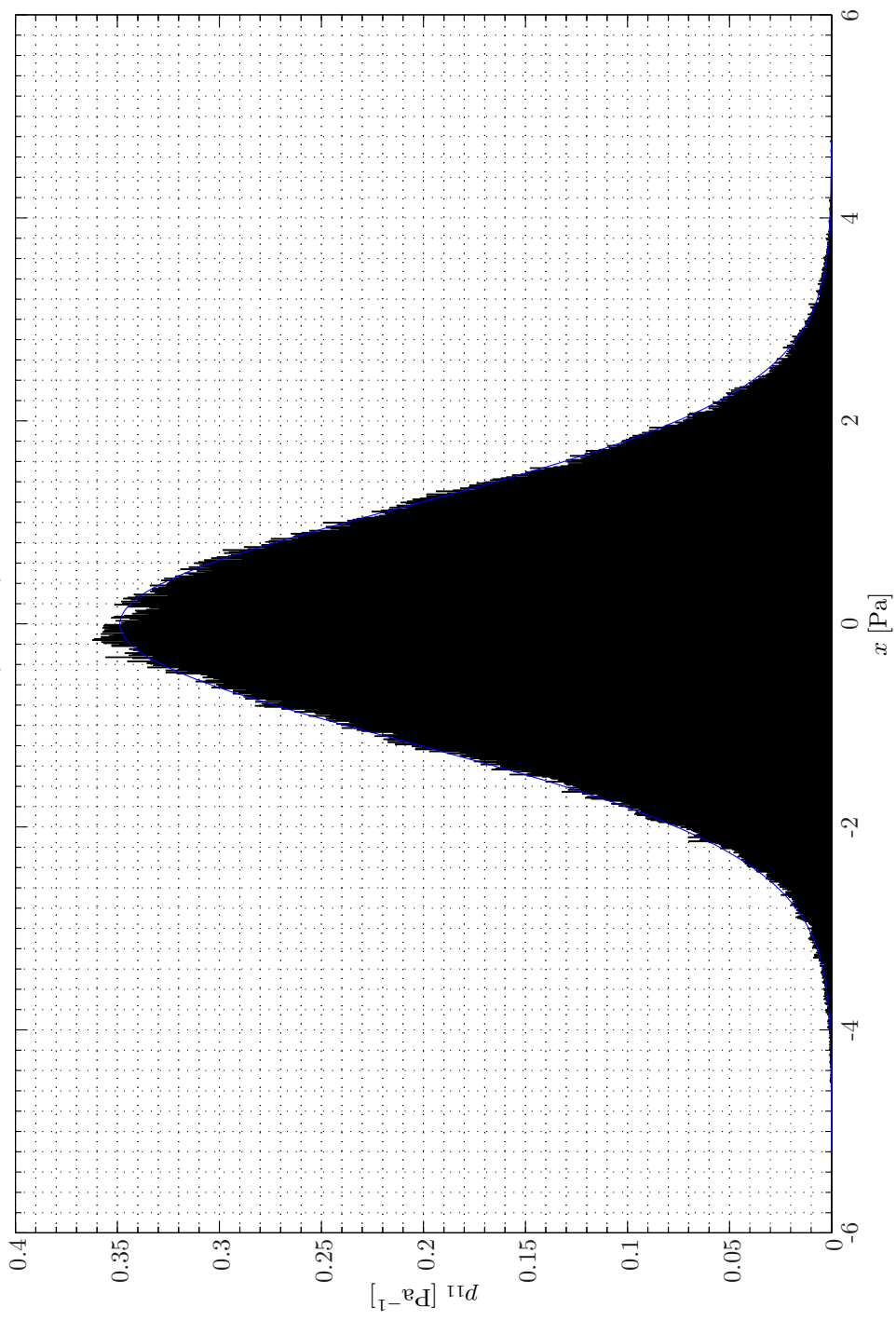

Sim 2.4.2: *Probability Density Functions*: **Statistical Data Analysis**: Single-Sided Modified Periodogram, $f_s = 65.536$ kHz, $N_{DFT} = 16384$, $L_{DFT} = 16385$, $R_{DFT} = 8193$, Hanning; $\Delta f_m = 16$ Hz, $T_{DFT} = 0.25002$ s, $N_{f,DFT} = 8193$, $\Delta f_{DFT} = 4$ Hz, $K_{DFT} = 158$; *System Identification:* (Random Low-Pass (4 kHz) White Noise ($\mathcal{N}(0, 0.2)$), Elliptic LPF ($f_{pass} = 900$ Hz, $f_{stop} = 1$ kHz, $A_{pass} = 1$ dB, $A_{stop} = 40$ dB), f_s =65.536 kHz; Time: $0 - 20$ s; **Topology:** BK 4949 surface microphones flush-mounted on Gentex HGU-55/P helmet mounted on a BK 4128 C HATS, Terma Earcup Audio System (Feedforward, mFx, $N_x = 10, N_e = 1, N_y = 2, N_p = 2$); *Channels:* #1 $\leftarrow x_1$, #2 $\leftarrow x_2$, #3 $\leftarrow x_3$, #4 $\leftarrow x_4$, #5 $\leftarrow x_5$, #6 $\leftarrow x_6$, #7 $\leftarrow x_7$, #8 $\leftarrow x_8$, #9 $\leftarrow x_9$, #10 $\leftarrow x_{10}$, #11 $\leftarrow d_1$; **Scenario:** `SystemIdentification(65536Hz)PrimaryPathes/20070204T112036`.

Signal	x_1	x_2	x_3	x_4	x_5	x_6	x_7	x_8	x_9	x_{10}	d_1
α	2.000	2.000	2.000	2.000	2.000	2.000	2.000	2.000	2.000	2.000	2.000
β	0.000	0.225	0.001	−0.016	−0.055	0.000	0.000	−0.099	0.000	0.010	0.008
γ	1.899	1.781	1.788	1.814	1.840	2.050	2.477	1.914	2.132	1.908	0.809
δ	0.000	0.000	0.000	0.000	0.000	0.000	0.000	0.000	0.000	0.000	0.000

Tab. 2.1: System Identification of Primary Pathes $G_{ex}^{j,m}$, Stable parameters γ, δ re. 20 µPa.

in Table 2.2[13].

Signal	x_1	x_2	x_3	x_4	x_5	x_6	x_7	x_8	x_9	x_{10}	d_1
μ	−0.000	−0.000	−0.000	−0.000	−0.000	−0.000	−0.000	−0.000	−0.000	−0.000	−0.000
σ	2.684	2.518	2.528	2.564	2.601	2.899	3.502	2.706	3.014	2.698	1.143
$\mu - 3\epsilon_\mu$	−0.007	−0.007	−0.007	−0.007	−0.007	−0.008	−0.009	−0.007	−0.008	−0.007	−0.003
$\mu + 3\epsilon_\mu$	0.007	0.006	0.006	0.007	0.007	0.008	0.009	0.007	0.008	0.007	0.002
$\sigma - 3\epsilon_\sigma$	2.679	2.513	2.523	2.559	2.596	2.894	3.495	2.700	3.008	2.693	1.141
$\sigma + 3\epsilon_\sigma$	2.690	2.523	2.533	2.569	2.606	2.905	3.509	2.711	3.020	2.704	1.146

Tab. 2.2: System Identification of Primary Pathes $G_{ex}^{j,m}$, Normal parameters re. 20 µPa.

The auto spectral density functions are shown in Simulation 2.4.3 on the facing page. As expected a relative small variation with frequency above 200 Hz is observed. Unfortunately, the subwoofer that usually is responsible for the generation of very low frequency signals was not at our disposition at the time of measurements. This explains the drop of energy content below 50 Hz. The large variations in auto spectral density functions below 200 Hz experienced by all channels is due to strong resonance behavior of the box-formed reverberant room (see Appendix P on page 809). The variation among the reference sensors is of the order of ±2 dB.

The corresponding averaged sound pressure levels re. 20 µPa can be found in Table 2.3.

Signal	x_1	x_2	x_3	x_4	x_5	x_6	x_7	x_8	x_9	x_{10}	d_1
SPL	102.6	102.0	102.0	102.2	102.3	103.2	104.9	102.6	103.69	102.6	95.2

Tab. 2.3: System Identification of Primary Pathes $G_{ex}^{j,m}$, Sound Pressure Levels re. 20 µPa.

Moreover, as a check of the sound pressure levels listed in Table 2.3 obtained from integration over the frequency band we can obtain identical result within $-0.03, +0$ dB by direct insertion of $p_{rms} = 20\log_{10}(\sigma/20\ \mu\text{Pa})$ in Table 2.2.

The magnitude of the cross-spectral density functions is shown in Simulation 2.4.4 on page 40. Also here very small variations among the individual cross-spectra are observed. Moveover, the troughs and peaks are found at the same frequencies especially below 300 Hz.

The ordinary coherence functions (OCOFs) and related coherence limited attenuation (see (2.2.1) on page 18) are depicted in Simulation 2.4.5 on page 41 and Simulation 2.4.6 on page 42 respectively. Owing to the different relative positions of the reference sensors with respect to the error sensor as large variation in the ordinary coherence functions can be observed. Moreover, each of them exhibit large multiple resonant behavior.

In Simulation 2.4.7 on page 43 and Simulation 2.4.8 on page 44 the specific OCOF details for the sixth reference sensor and the error sensor, that is, $\gamma^2_{x_6 d_1}(f)$ is shown. Both figures include $\pm 3\epsilon$ confidence intervals (refer to subsection C.3.2 on page 542).

[13] As a check from Table 2.1 - 2.2 it can readily be confirmed that the following identity holds: $\mathcal{S}(2, 0, \gamma, \delta) = \mathcal{N}(\delta, 2\gamma^2)$.

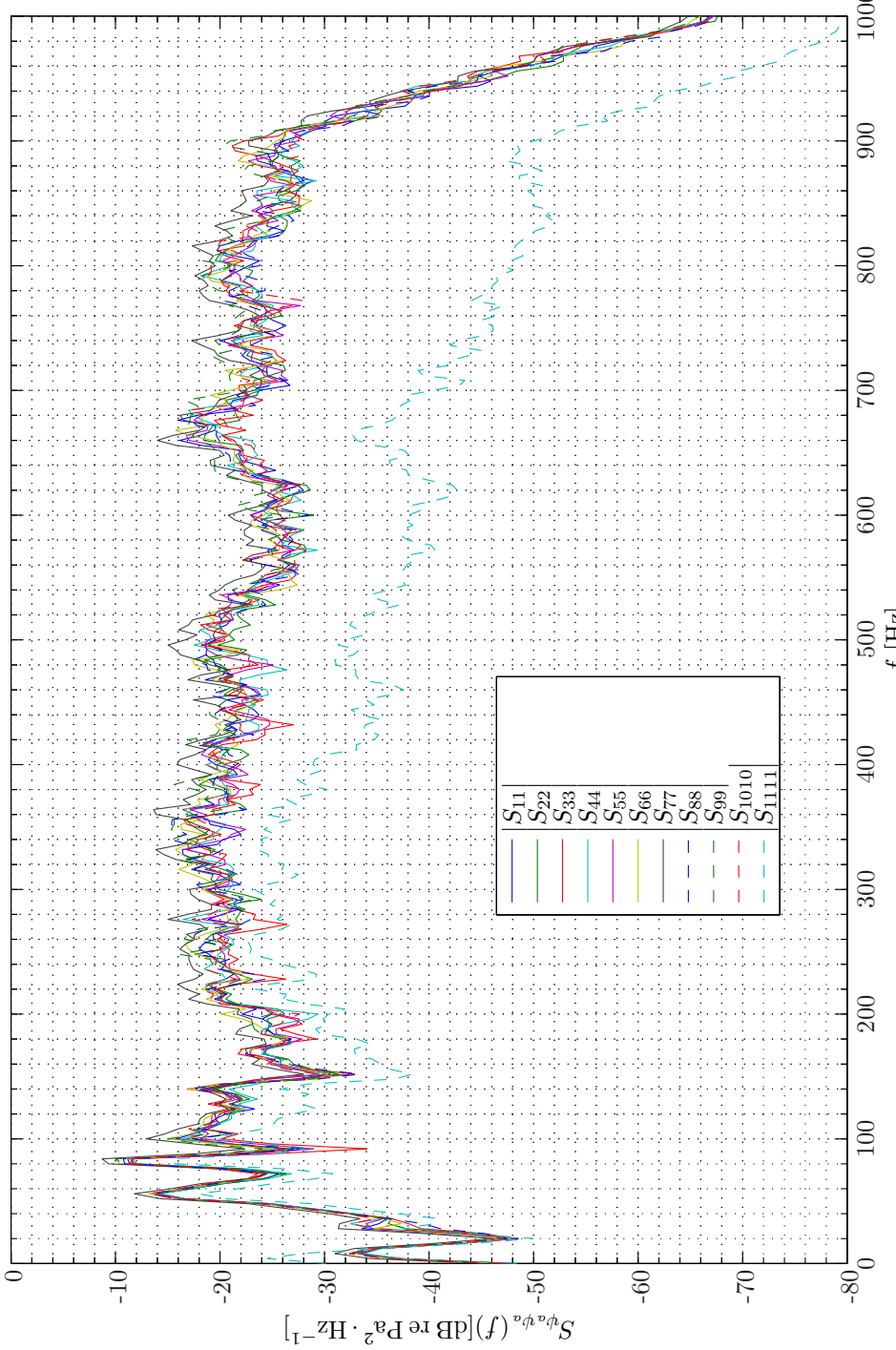

Sim 2.4.3: *Autospectral Density Functions*: **Statistical Data Analysis**: Single-Sided Modified Periodogram, f_s = 65.536 kHz, N_{DFT} = 16384, L_{DFT} = 16385, R_{DFT} = 8193, Hanning, Δf_m = 16 Hz, T_{DFT} = 0.25002 s, $N_{f,DFT}$ = 8193, Δf_{DFT} = 4 Hz, K_{DFT} = 158; *System Identification:* (Random Low-Pass (4 kHz) White Noise ($\mathcal{N}(0, 0.2)$), Elliptic LPF (f_{pass} = 900 Hz, f_{stop} = 1 kHz, A_{pass} = 1 dB, A_{stop} = 40 dB), f_s =65.536 kHz; Time: 0 − 20 s; **Topology:** BK 4949 surface microphones flush-mounted on Gentex HGU-55/P helmet mounted on a BK 4128 C HATS, Terma Earcup Audio System (Feedforward, mFx, $N_x = 10, N_e = 1, N_y = 2, N_p = 2$); *Channels:* #1 ← x_1, #2 ← x_2, #3 ← x_3, #4 ← x_4, #5 ← x_5, #6 ← x_6, #7 ← x_7, #8 ← x_8, #9 ← x_9, #10 ← x_{10}, #11 ← d_1; **Scenario:** `SystemIdentification(65536Hz)PrimaryPathes/20070204T112036`.

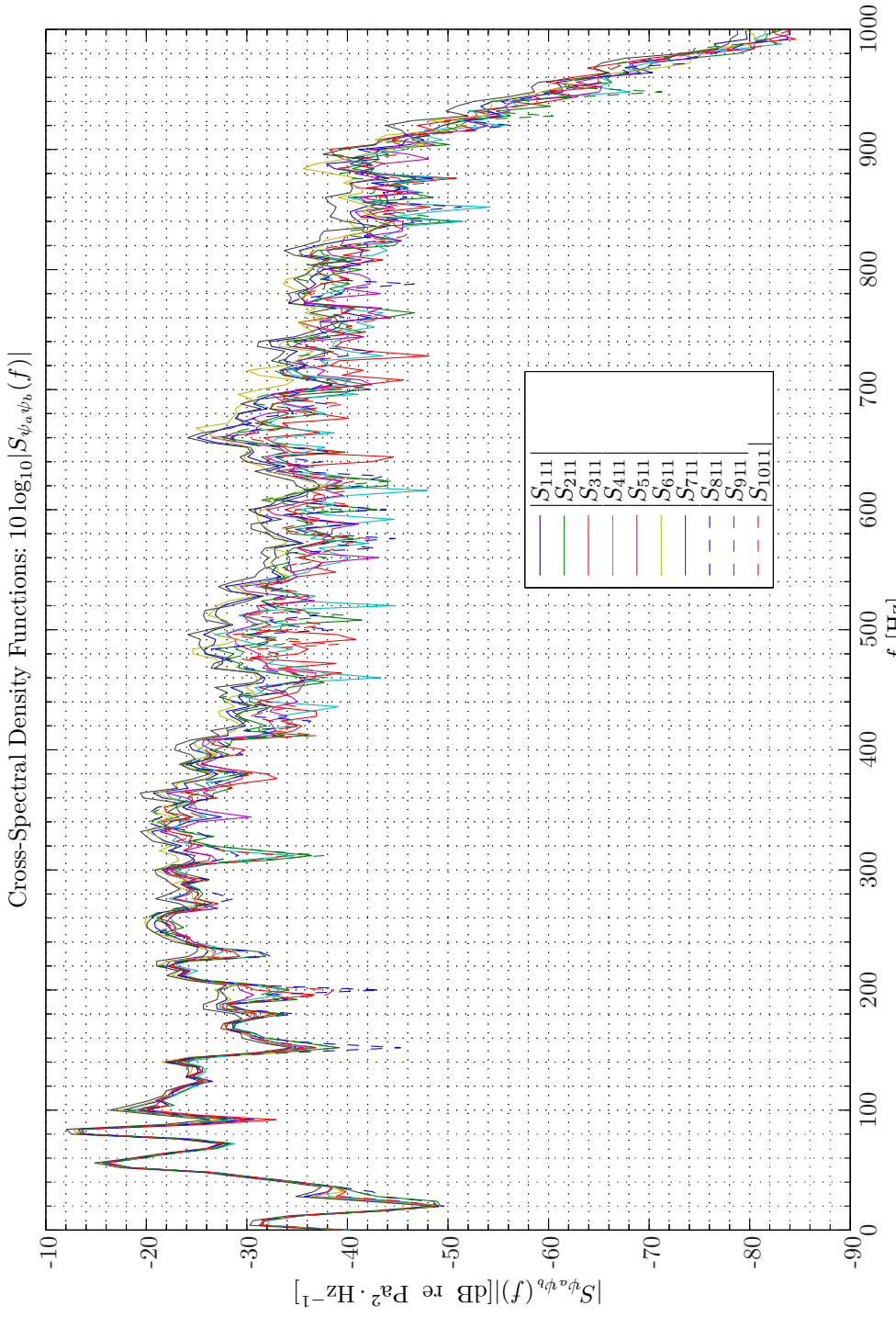

Sim 2.4.4: *Cross-Spectral Density Functions*: **Statistical Data Analysis**: Single-Sided Modified Periodogram, f_s = 65.536 kHz, N_{DFT} = 16384, L_{DFT} = 16385, R_{DFT} = 8193, Hanning, Δf_m = 16 Hz, T_{DFT} = 0.25002 s, $N_{f,DFT}$ = 8193, Δf_{DFT} = 4 Hz, K_{DFT} = 158; *System Identification:* (Random Low-Pass (4 kHz) White Noise ($\mathcal{N}(0, 0.2)$), Elliptic LPF (f_{pass} = 900 Hz, f_{stop} = 1 kHz, A_{pass} = 1 dB, A_{stop} = 40 dB), f_s =65.536 kHz; Time: 0 − 20 s; **Topology:** BK 4949 surface microphones flush-mounted on Gentex HGU-55/P helmet mounted on a BK 4128 C HATS, Terma Earcup Audio System (Feedforward, mFx, $N_x = 10, N_e = 1, N_y = 2, N_p = 2$); *Channels:* #1 ← x_1, #2 ← x_2, #3 ← x_3, #4 ← x_4, #5 ← x_5, #6 ← x_6, #7 ← x_7, #8 ← x_8, #9 ← x_9, #10 ← x_{10}, #11 ← d_1; **Scenario:** `SystemIdentification(65536Hz)PrimaryPathes/20070204T112036`.

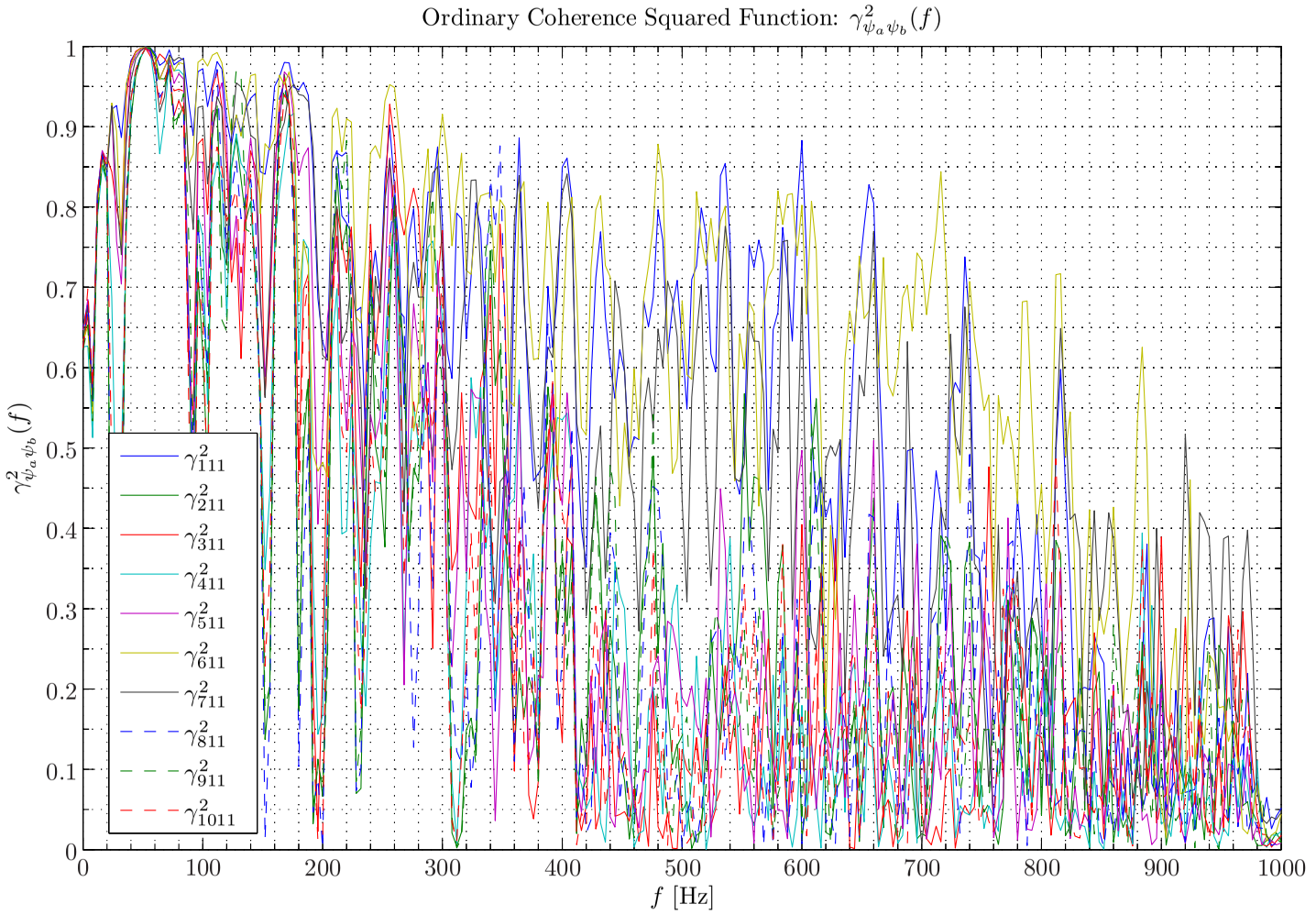

Sim 2.4.5: *Ordinary Coherency-Squared Functions* $\gamma^2_{\psi_a\psi_b}(f)$: **Statistical Data Analysis**: Single-Sided Modified Periodogram, f_s = 65.536 kHz, N_{DFT} = 16384, L_{DFT} = 16385, R_{DFT} = 8193, Hanning, Δf_m = 16 Hz, T_{DFT} = 0.25002 s, $N_{f,DFT}$ = 8193, Δf_{DFT} = 4 Hz, K_{DFT} = 158; *System Identification:* (Random Low-Pass (4 kHz) White Noise ($\mathcal{N}(0, 0.2)$), Elliptic LPF (f_{pass} = 900 Hz, f_{stop} = 1 kHz, A_{pass} = 1 dB, A_{stop} = 40 dB), f_s =65.536 kHz; Time: $0 - 20$ s; **Topology:** BK 4949 surface microphones flush-mounted on Gentex HGU-55/P helmet mounted on a BK 4128 C HATS, Terma Earcup Audio System (Feedforward, mFx, $N_x = 10, N_e = 1, N_y = 2, N_p = 2$); *Channels:* #1 $\leftarrow x_1$, #2 $\leftarrow x_2$, #3 $\leftarrow x_3$, #4 $\leftarrow x_4$, #5 $\leftarrow x_5$, #6 $\leftarrow x_6$, #7 $\leftarrow x_7$, #8 $\leftarrow x_8$, #9 $\leftarrow x_9$, #10 $\leftarrow x_{10}$, #11 $\leftarrow d_1$; **Scenario:** `SystemIdentification(65536Hz)PrimaryPathes/20070204T112036`.

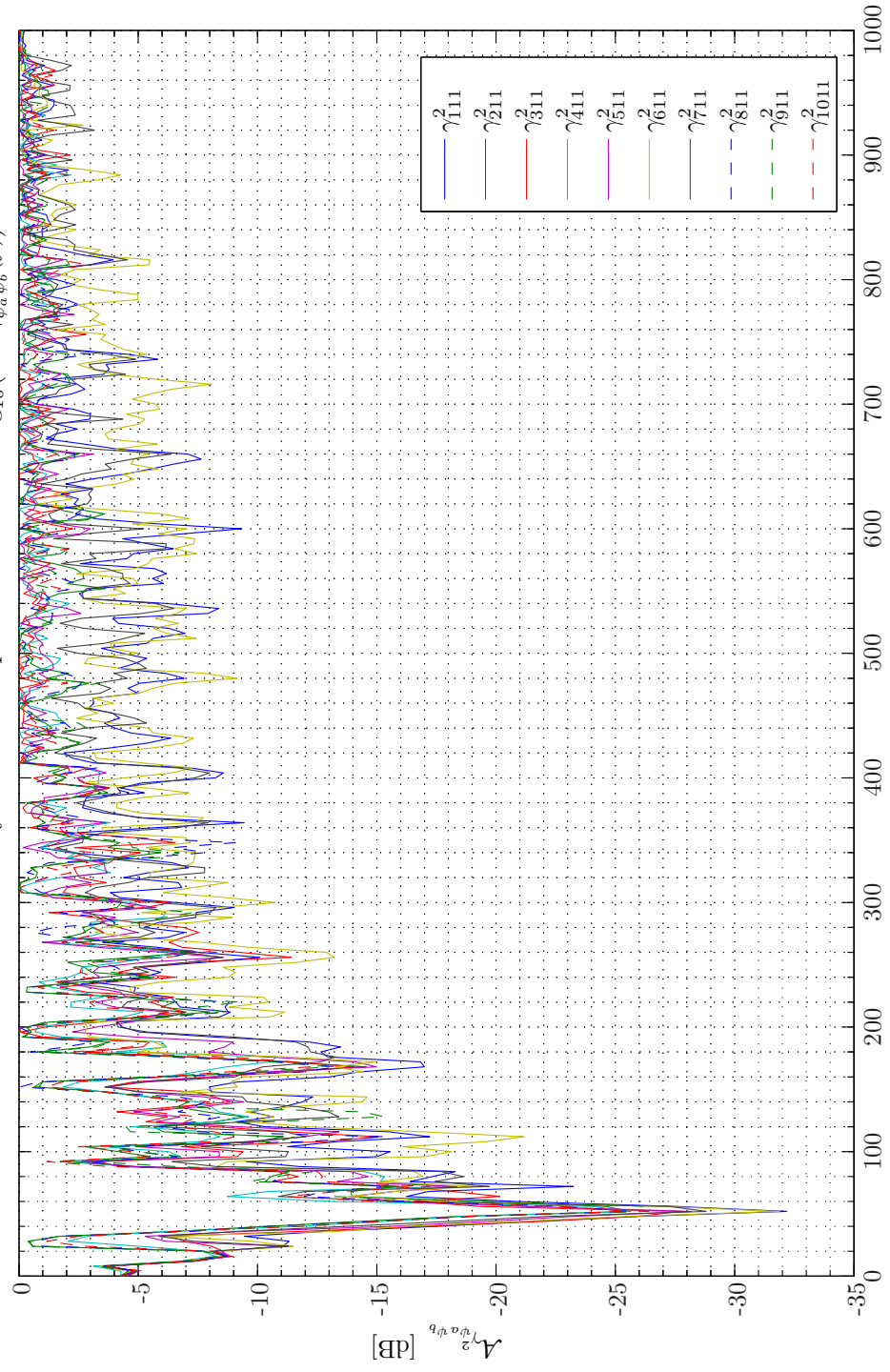

Sim 2.4.6: Attenuation *vs Ordinary Coherency-Squared Functions*: $10\log_{10}(1-\gamma^2_{\psi_a\psi_b}(f))$: **Statistical Data Analysis**: Single-Sided Modified Periodogram, f_s = 65.536 kHz, N_{DFT} = 16384, L_{DFT} = 16385, R_{DFT} = 8193, Hanning, Δf_m = 16 Hz, T_{DFT} = 0.25002 s, $N_{f,DFT}$ = 8193, Δf_{DFT} = 4 Hz, K_{DFT} = 158; *System Identification:* (Random Low-Pass (4 kHz) White Noise ($\mathcal{N}(0,0.2)$), Elliptic LPF (f_{pass} = 900 Hz, f_{stop} = 1 kHz, A_{pass} = 1 dB, A_{stop} = 40 dB), f_s =65.536 kHz; Time: 0 – 20 s; **Topology:** BK 4949 surface microphones flush-mounted on Gentex HGU-55/P helmet mounted on a BK 4128 C HATS, Terma Earcup Audio System (Feedforward, mFx, $N_x = 10, N_e = 1, N_y = 2, N_p = 2$); *Channels:* #1 $\leftarrow x_1$, #2 $\leftarrow x_2$, #3 $\leftarrow x_3$, #4 $\leftarrow x_4$, #5 $\leftarrow x_5$, #6 $\leftarrow x_6$, #7 $\leftarrow x_7$, #8 $\leftarrow x_8$, #9 $\leftarrow x_9$, #10 $\leftarrow x_{10}$, #11 $\leftarrow d_1$; **Scenario:** `SystemIdentification(65536Hz)PrimaryPathes/20070204T112036`.

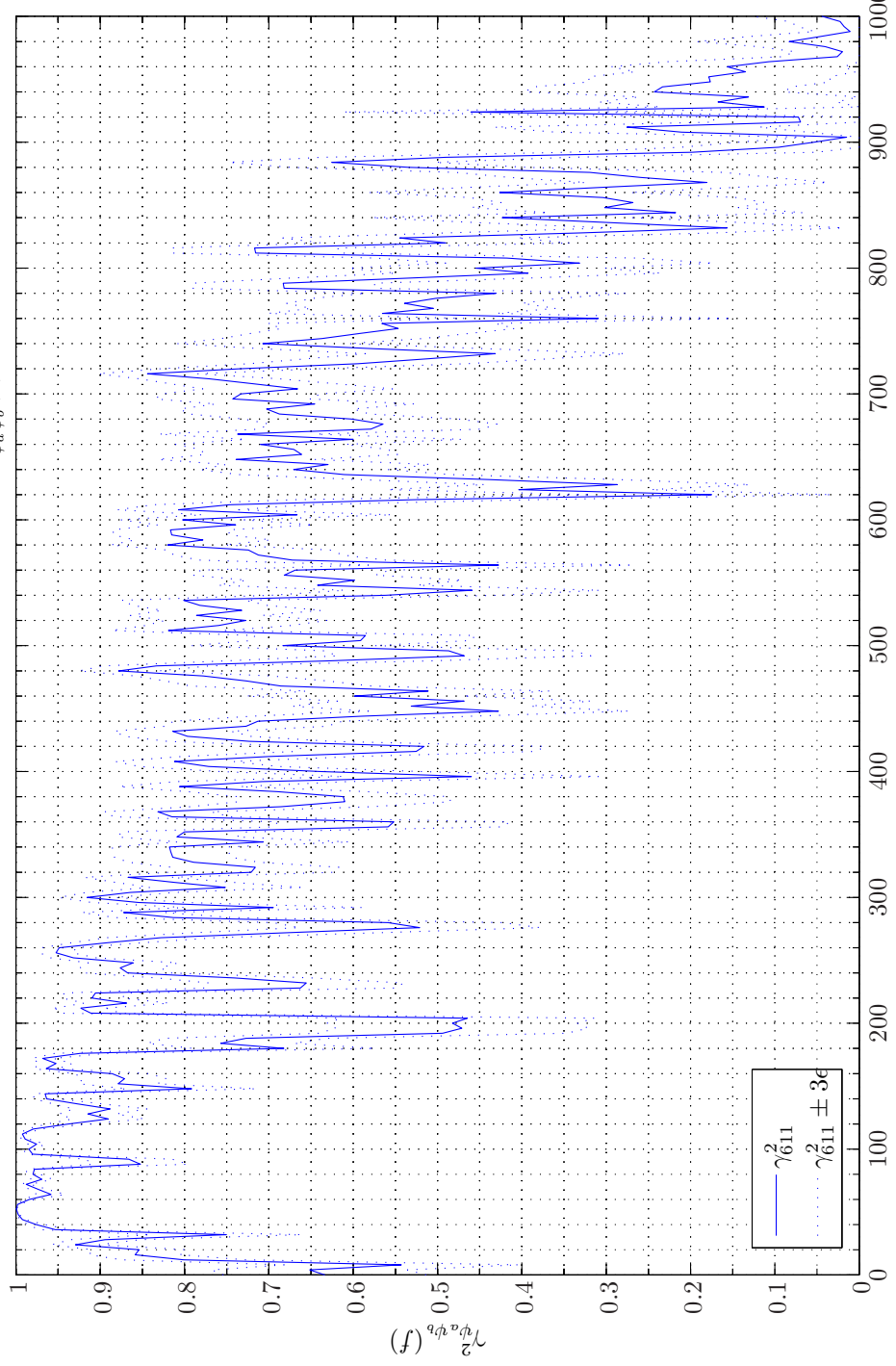

Sim 2.4.7: *Ordinary Coherency-Squared Functions* $\gamma^2_{\psi_a\psi_b}(f)$: **Statistical Data Analysis**: Single-Sided Modified Periodogram, f_s = 65.536 kHz, N_{DFT} = 16384, L_{DFT} = 16385, R_{DFT} = 8193, Hanning, Δf_m = 16 Hz, T_{DFT} = 0.25002 s, $N_{f,DFT}$ = 8193, Δf_{DFT} = 4 Hz, K_{DFT} = 158; *System Identification:* (Random Low-Pass (4 kHz) White Noise ($\mathcal{N}(0, 0.2)$), Elliptic LPF (f_{pass} = 900 Hz, f_{stop} = 1 kHz, A_{pass} = 1 dB, A_{stop} = 40 dB), f_s =65.536 kHz; Time: 0 − 20 s; **Topology:** BK 4949 surface microphones flush-mounted on Gentex HGU-55/P helmet mounted on a BK 4128 C HATS, Terma Earcup Audio System (Feedforward, mFx, $N_x = 10, N_e = 1, N_y = 2, N_p = 2$); *Channels:* #1 ← x_1, #2 ← x_2, #3 ← x_3, #4 ← x_4, #5 ← x_5, #6 ← x_6, #7 ← x_7, #8 ← x_8, #9 ← x_9, #10 ← x_{10}, #11 ← d_1; **Scenario:** `SystemIdentification(65536Hz)PrimaryPathes/20070204T112036`.

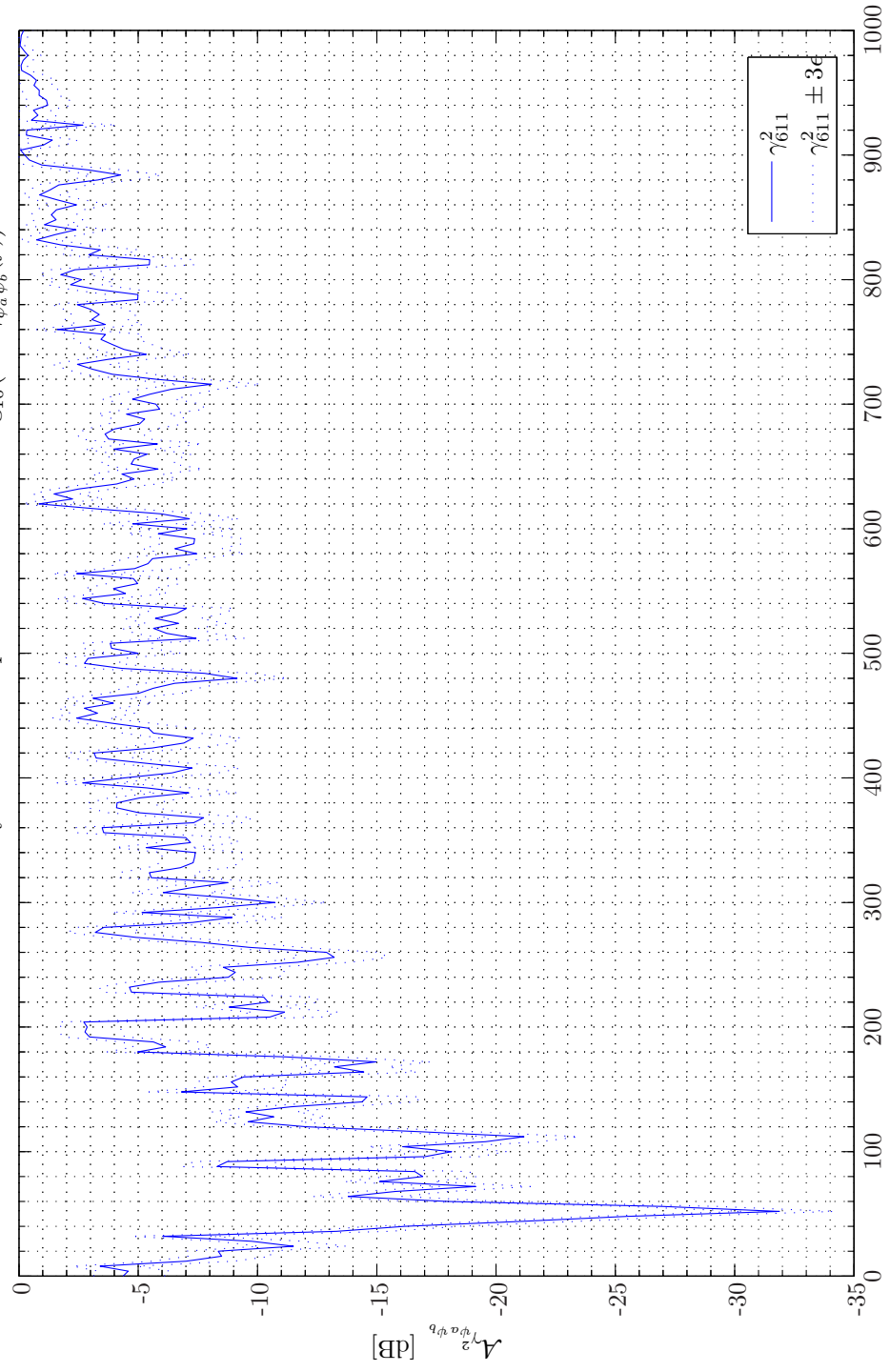

Sim 2.4.8: Attenuation *vs Ordinary Coherency-Squared Functions*: $10\log_{10}(1-\gamma^2_{\psi_a\psi_b}(f))$: **Statistical Data Analysis**: Single-Sided Modified Periodogram, f_s = 65.536 kHz, N_{DFT} = 16384, L_{DFT} = 16385, R_{DFT} = 8193, Hanning, Δf_m = 16 Hz, T_{DFT} = 0.25002 s, $N_{f,DFT}$ = 8193, Δf_{DFT} = 4 Hz, K_{DFT} = 158; *System Identification:* (Random Low-Pass (4 kHz) White Noise ($\mathcal{N}(0, 0.2)$), Elliptic LPF (f_{pass} = 900 Hz, f_{stop} = 1 kHz, A_{pass} = 1 dB, A_{stop} = 40 dB), f_s =65.536 kHz; Time: 0 – 20 s; **Topology:** BK 4949 surface microphones flush-mounted on Gentex HGU-55/P helmet mounted on a BK 4128 C HATS, Terma Earcup Audio System (Feedforward, mFx, $N_x = 10, N_e = 1, N_y = 2, N_p = 2$); *Channels:* #1 $\leftarrow x_1$, #2 $\leftarrow x_2$, #3 $\leftarrow x_3$, #4 $\leftarrow x_4$, #5 $\leftarrow x_5$, #6 $\leftarrow x_6$, #7 $\leftarrow x_7$, #8 $\leftarrow x_8$, #9 $\leftarrow x_9$, #10 $\leftarrow x_{10}$, #11 $\leftarrow d_1$; **Scenario:** `SystemIdentification(65536Hz)PrimaryPathes/20070204T112036`.

Accordingly, from a feedforward based AC system perspective these result might at first glance look disappointing. Hence, attenuation figures above 10 dB is limited to frequencies less than 60 Hz. Deep troughs are observed in the OCOF in the vicinity of 200 Hz, 320 Hz and 370 Hz for some of the reference sensors. Moreover except for reference sensors 1, 6 and 7 coherence is almost absent above 400 Hz. By inspection of Figure 2.3 we observe that reference sensors 1, 6 and 7 indeed are the three reference sensors that are positioned closest to the error sensor at the left ear.

Similarly, in Simulation 2.4.9 - 2.4.10 on pages 46–47 the specific OCOF details for the eighth reference sensor and the error sensor, that is, $\gamma^2_{x_8 d_1}(f)$, which results in the lowest coherence is shown. Hence, by the use of this reference signal alone very poor ANR performance is obtained.

By inspection of the magnitude and phase of the transfer functions from the 10 reference sensors to the performance sensor depicted in Simulation 2.4.11 and Simulation 2.4.12 respectively, it is observed that individual transfer function characteristic is not discernible from some average transfer function except for the phase response at higher frequencies. It could be argued that Simulation 2.4.11 represents the average passive ANR obtained from this hearing protection device (HPD).

The auto- and cross-correlation functions and auto- and cross-spectral density functions constitute Fourier transform pairs. A smoothed-out pattern is therefore also present in the auto- and cross-correlation functions illustrated in Simulation 2.4.13 on page 51 and Simulation 2.4.14 on page 52 respectively. Both the auto- and cross-correlation functions exhibit large temporal side lobes. Different factors contribute to this non-Dirac-impulsively behavior. Firstly, the diffuse sound field in the reverberant room has its imperfections as discussed above. Moreover, by insertion of the UUT, that is, the HATS and helmet (see Figure 2.1 - 2.2 on pages 33–34) large parts of the incident field will be scattered thereby perturbating the pseudo diffuse sound field. Furthermore, the sensors are exposed to random low-pass 4 kHz white noise that is further low-pass filtered with $f_{pass} = 900$ Hz and not to perfect random white noise (RWN). From [6, Ch. 5] we find the following expression for the auto correlation function for low-pass white noise omitting insignificant constants

$$R_{x_j x_j}(\tau) = \mathrm{sinc}(2\pi f_{pass}\tau), \quad j \in 1, 2, \ldots, 10. \tag{2.4.1}$$

Accordingly the zero in the auto correlation function is found at $\tau = \pm\frac{1}{2f_{pass}} \approx 550$ µs. By inspection of the details in Simulation 2.4.13 on page 51 we read the zero-crossing as 560 µs. Hence, the field generally decorrelates in time as predictable from its frequency contents. The first sidelobe level should approximately be $20\log 10\frac{2}{3\pi} \approx -6.7$ dB which agrees reasonably with the results in Simulation 2.4.13 where the sidelobe level is assessed to -9 dB. The auto correlation function for the disturbance signal, that is, $R_{d_1 d_1}(\tau)$ exhibit slower variation due to the low-pass filtering effect from the passive attenuation of the helmet.

Besides the two aforementioned factors *spatial decorrelation* also governs the cross-correlation functions. Cook, Waterhouse, Berendt, Edelman, and M. C. Thomsen [1955] [10] showed theoretically and confirmed experimentally that the normalized cross-correlation function between the sound pressures in a diffuse sound field of narrow bandwidth was equal to

$$\rho_{x_j d_1}(r_{x_j d_1}, \lambda) = \mathrm{sinc}\Big(2\pi\frac{r_{x_j d_1}}{\lambda}\Big), \quad j \in 1, 2, \ldots, 10, \tag{2.4.2}$$

where $r_{x_j d_1}$ is the distance between the j'th reference sensor and the error sensor and λ is

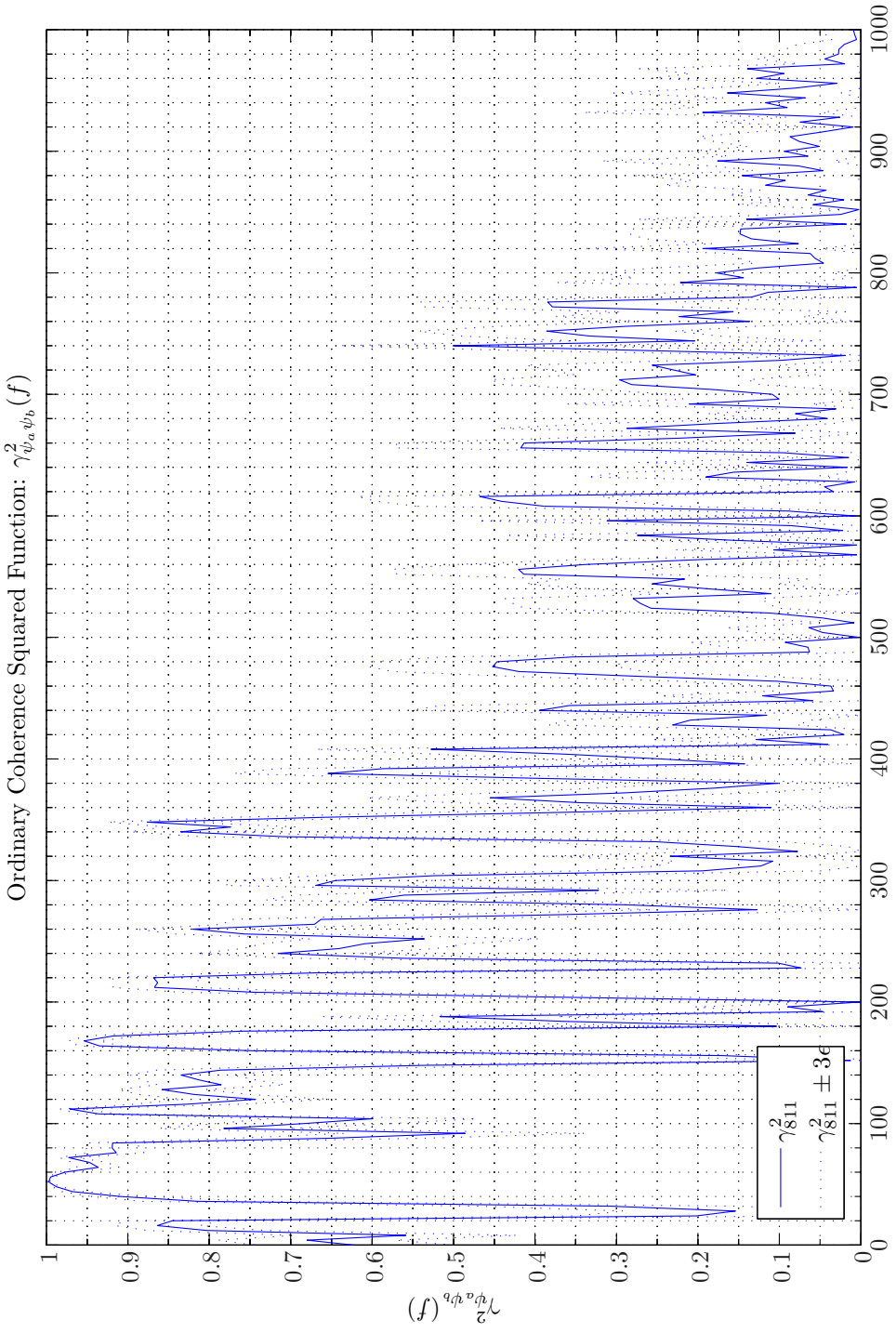

Sim 2.4.9: *Ordinary Coherency-Squared Functions* $\gamma^2_{\psi_a\psi_b}(f)$: **Statistical Data Analysis**: Single-Sided Modified Periodogram, f_s = 65.536 kHz, N_{DFT} = 16384, L_{DFT} = 16385, R_{DFT} = 8193, Hanning, Δf_m = 16 Hz, T_{DFT} = 0.25002 s, $N_{f,DFT}$ = 8193, Δf_{DFT} = 4 Hz, K_{DFT} = 158; *System Identification:* (Random Low-Pass (4 kHz) White Noise ($\mathcal{N}(0, 0.2)$), Elliptic LPF (f_{pass} = 900 Hz, f_{stop} = 1 kHz, A_{pass} = 1 dB, A_{stop} = 40 dB), f_s =65.536 kHz; Time: 0 − 20 s; **Topology:** BK 4949 surface microphones flush-mounted on Gentex HGU-55/P helmet mounted on a BK 4128 C HATS, Terma Earcup Audio System (Feedforward, mFx, $N_x = 10, N_e = 1, N_y = 2, N_p = 2$); *Channels:* #1 ← x_1, #2 ← x_2, #3 ← x_3, #4 ← x_4, #5 ← x_5, #6 ← x_6, #7 ← x_7, #8 ← x_8, #9 ← x_9, #10 ← x_{10}, #11 ← d_1; **Scenario:** SystemIdentification(65536Hz)PrimaryPathes/20070204T112036.

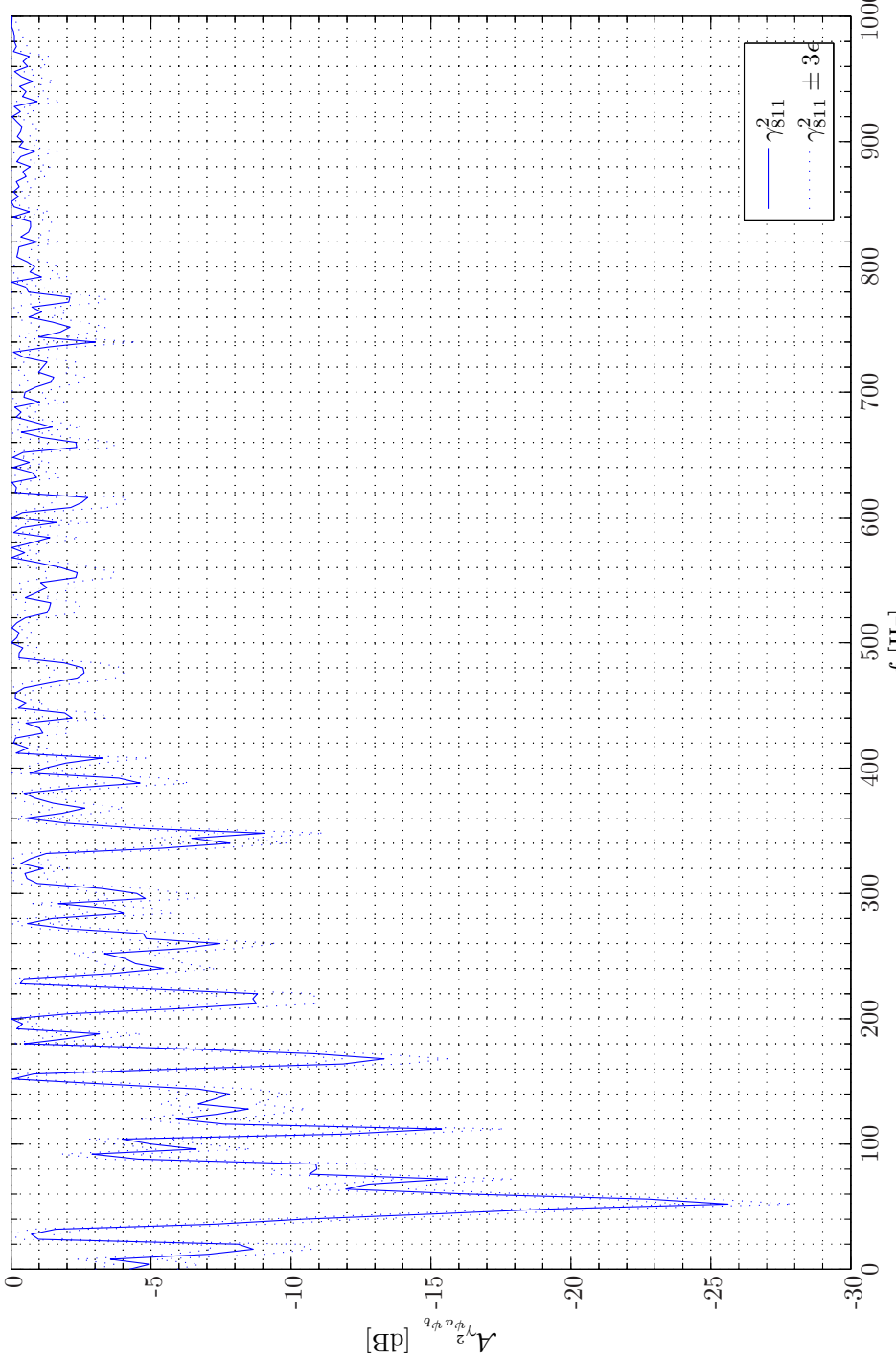

Sim 2.4.10: Attenuation *vs Ordinary Coherency-Squared Functions*: $10\log_{10}(1-\gamma^2_{\psi_a\psi_b}(f))$: **Statistical Data Analysis**: Single-Sided Modified Periodogram, f_s = 65.536 kHz, N_{DFT} = 16384, L_{DFT} = 16385, R_{DFT} = 8193, Hanning, Δf_m = 16 Hz, T_{DFT} = 0.25002 s, $N_{f,DFT}$ = 8193, Δf_{DFT} = 4 Hz, K_{DFT} = 158; *System Identification:* (Random Low-Pass (4 kHz) White Noise ($\mathcal{N}(0, 0.2)$), Elliptic LPF (f_{pass} = 900 Hz, f_{stop} = 1 kHz, A_{pass} = 1 dB, A_{stop} = 40 dB), f_s =65.536 kHz; Time: 0 – 20 s; **Topology:** BK 4949 surface microphones flush-mounted on Gentex HGU-55/P helmet mounted on a BK 4128 C HATS, Terma Earcup Audio System (Feedforward, mFx, $N_x = 10, N_e = 1, N_y = 2, N_p = 2$); *Channels:* #1 $\leftarrow x_1$, #2 $\leftarrow x_2$, #3 $\leftarrow x_3$, #4 $\leftarrow x_4$, #5 $\leftarrow x_5$, #6 $\leftarrow x_6$, #7 $\leftarrow x_7$, #8 $\leftarrow x_8$, #9 $\leftarrow x_9$, #10 $\leftarrow x_{10}$, #11 $\leftarrow d_1$; **Scenario:** `SystemIdentification(65536Hz)PrimaryPathes/20070204T112036`.

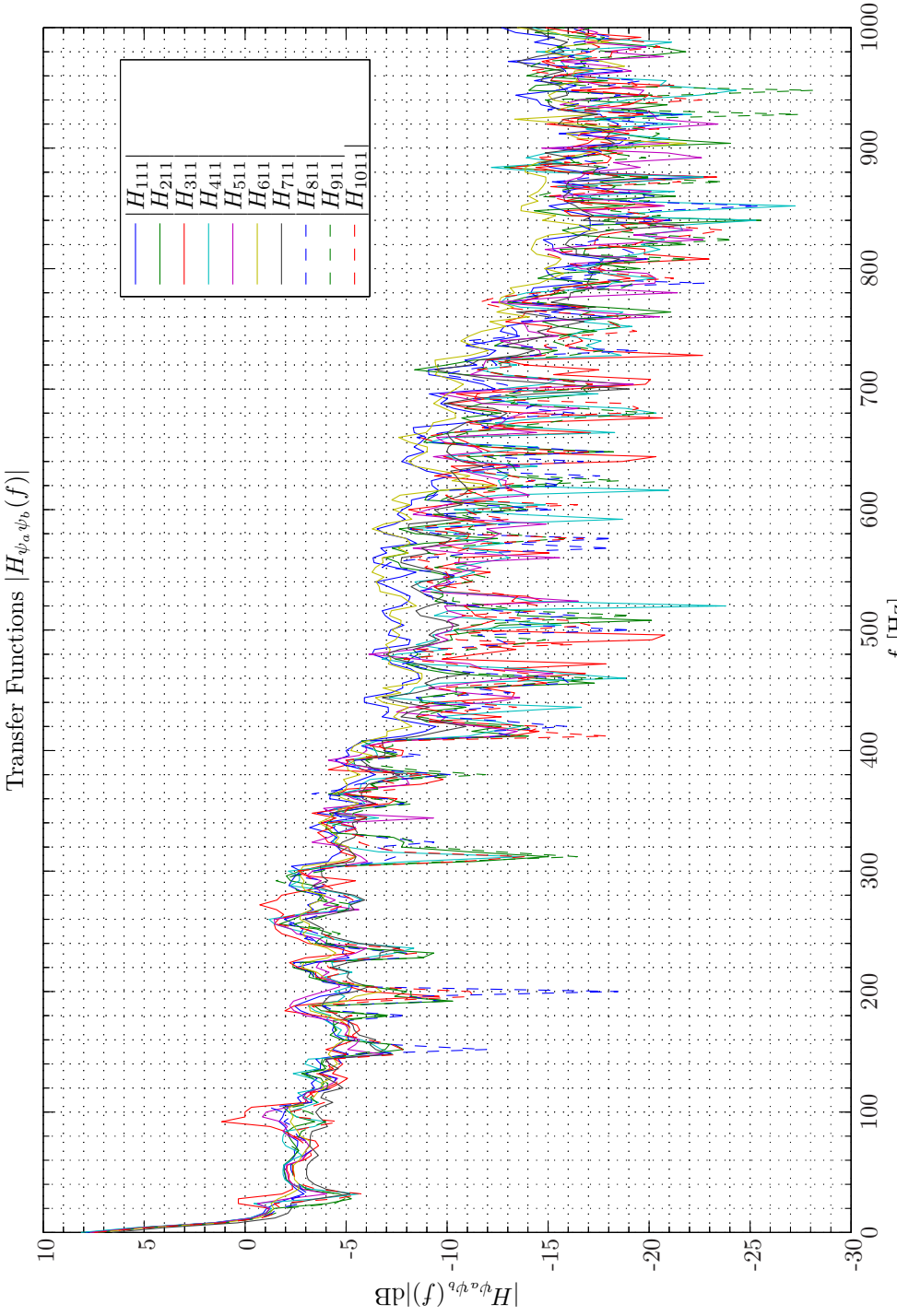

Sim 2.4.11: *Transfer Function, Magnitude:* $|H_{\psi_a\psi_b}(f)|$: **Statistical Data Analysis**: Single-Sided Modified Periodogram, $f_s = 65.536$ kHz, $N_{DFT} = 16384$, $L_{DFT} = 16385$, $R_{DFT} = 8193$, Hanning, $\Delta f_m = 16$ Hz, $T_{DFT} = 0.25002$ s, $N_{f,DFT} = 8193$, $\Delta f_{DFT} = 4$ Hz, $K_{DFT} = 158$; *System Identification:* (Random Low-Pass (4 kHz) White Noise ($\mathcal{N}(0, 0.2)$), Elliptic LPF ($f_{pass} = 900$ Hz, $f_{stop} = 1$ kHz, $A_{pass} = 1$ dB, $A_{stop} = 40$ dB), f_s =65.536 kHz; Time: $0 - 20$ s; **Topology:** BK 4949 surface microphones flush-mounted on Gentex HGU-55/P helmet mounted on a BK 4128 C HATS, Terma Earcup Audio System (Feedforward, mFx, $N_x = 10, N_e = 1, N_y = 2, N_p = 2$); *Channels:* #1 $\leftarrow x_1$, #2 $\leftarrow x_2$, #3 $\leftarrow x_3$, #4 $\leftarrow x_4$, #5 $\leftarrow x_5$, #6 $\leftarrow x_6$, #7 $\leftarrow x_7$, #8 $\leftarrow x_8$, #9 $\leftarrow x_9$, #10 $\leftarrow x_{10}$, #11 $\leftarrow d_1$; **Scenario:** `SystemIdentification(65536Hz)PrimaryPathes/20070204T112036`.

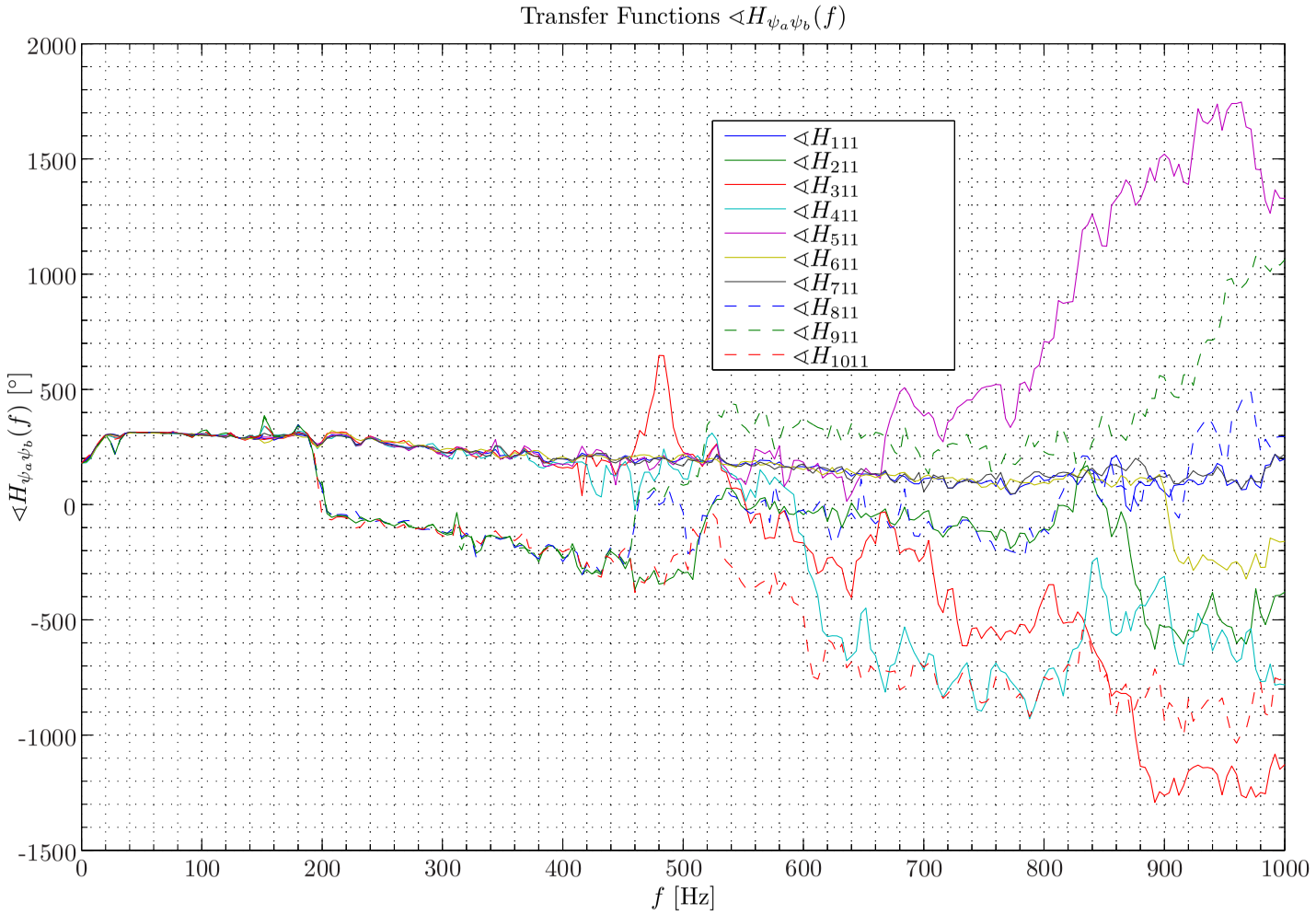

Sim 2.4.12: *Transfer Function, Phase*: $\sphericalangle H_{\psi_a\psi_b}(f)$: **Statistical Data Analysis**: Single-Sided Modified Periodogram, $f_s = 65.536$ kHz, $N_{DFT} = 16384$, $L_{DFT} = 16385$, $R_{DFT} = 8193$, Hanning, $\Delta f_m = 16$ Hz, $T_{DFT} = 0.25002$ s, $N_{f,DFT} = 8193$, $\Delta f_{DFT} = 4$ Hz, $K_{DFT} = 158$; *System Identification:* (Random Low-Pass (4 kHz) White Noise ($\mathcal{N}(0, 0.2)$), Elliptic LPF ($f_{pass} = 900$ Hz, $f_{stop} = 1$ kHz, $A_{pass} = 1$ dB, $A_{stop} = 40$ dB), f_s =65.536 kHz; Time: $0 - 20$ s; **Topology:** BK 4949 surface microphones flush-mounted on Gentex HGU-55/P helmet mounted on a BK 4128 C HATS, Terma Earcup Audio System (Feedforward, mFx, $N_x = 10, N_e = 1, N_y = 2, N_p = 2$); *Channels:* #1 $\leftarrow x_1$, #2 $\leftarrow x_2$, #3 $\leftarrow x_3$, #4 $\leftarrow x_4$, #5 $\leftarrow x_5$, #6 $\leftarrow x_6$, #7 $\leftarrow x_7$, #8 $\leftarrow x_8$, #9 $\leftarrow x_9$, #10 $\leftarrow x_{10}$, #11 $\leftarrow d_1$; **Scenario:** `SystemIdentification(65536Hz)PrimaryPathes/20070204T112036`.

the wavelength. Two important consequences follow from (2.4.2). Firstly, the cross-correlation functions exhibit frequency dependence and secondly the signals from two sensors separated by half a wavelength are completely uncorrelated. Much more details can be found in [16]. It should, however, be recalled that (2.4.2) pertains to propagation in a homogeneous medium and therefore not fully to our UUT. Considering the decorrelation among the reference sensors, however, it seems not unreasonable to assume that (2.4.2) to a first order holds if we ignore scattering effects. In this topology the inter reference sensor distance is uniformly approximately equal to 12 cm. Accordingly, the normalized cross-correlation function between a reference signal and a reference signal that would have been obtained from a reference sensor positioned in the middle between two reference sensors is estimated to be bounded from below by 0.85 at the upper frequency band of 900 Hz. A more advanced analysis would take the correlation effects of the four nearest reference sensors including their mutual correlations into account.

The cross-correlation functions give an indication of an acquisition lead-time of approximately 1 ms.

The corresponding impulse response functions are shown in Simulation 2.4.15 on page 53 which also indicate that time-advance information achievable with the CFF topology. However, the individual timing characteristic is completely smoothed-out. The impulse behavior at $t = 0$ experienced by all the channels may be explained by the large low frequency content in the transfer functions and because such signal content with equal likelihood is present with a time lead and a time lag.

The MCOFs obtained from using both the matrix formulation and the iterative procedure presented in section 2.2.5 on page 27 is displayed in Simulation 2.4.16 - 2.4.17 on pages 54–55. The MCOF corresponding to the disturbance signal taking all ten reference signals into account is designated by $\gamma^2_{d_1 \cdot x_{10!}}(f)$ using the matrix method and the MCOF $\gamma^2_{d_1 \cdot x_{6,1,2,7,10,9,3,4,5,8}}(f)$ applying the iterative procedure. In this simulation the reference signals are sorted in descending order with respect to their ordinary coherence function averaged over the frequency band. Hence, with reference to (2.2.26) on page 27 the following ranking is obtained: $\check{1} \leftarrow 6, \check{2} \leftarrow 1, \ldots, \check{10} \leftarrow 8$.

Within the graphical resolution the two methods give identical results as expected. As seen ANC attenuation figures exceeding 10 dB possible up to approximately 850 Hz is predicted. Moreover, the deep troughs previously observed in some of the ordinary coherence functions are almost absent now in a MCOF analysis. In addition the iterative procedure illuminates the successive increase in the MCOF from increasing the number of reference sensors. Hence, in Simulation 2.4.16 no apparent saturation in MCOF with increasing number of reference sensors is seen. Hence, by including additional reference sensors the upper frequency limit determined by the MCOF would most likely increase as a consequence of closer spatial sampling. It should be emphasized that we in the iterative multiple coherence function procedure successively enable reference signals that exhibit decreasing coherence with the error sensor. If we instead successively add a reference sensor and reoptimized their positions the increase in multiple coherence function would most likely be higher.

In Appendix D very similar pattern in the MCOFs obtained from field measurements in a Chinook CH-47D helicopter will be presented.

The particular details including $\pm 3\epsilon$ confidence intervals for the MCOFs (refer to subsection C.3.4 on page 544) using all ten reference sensors are shown in Simulation 2.4.18 - 2.4.19 on pages 56–57.

We observe that the random errors correspond to an uncertainty in the attenuation estimation of approximately $+1, -1.5$ dB. The relative narrow confidence interval stems from the use of a

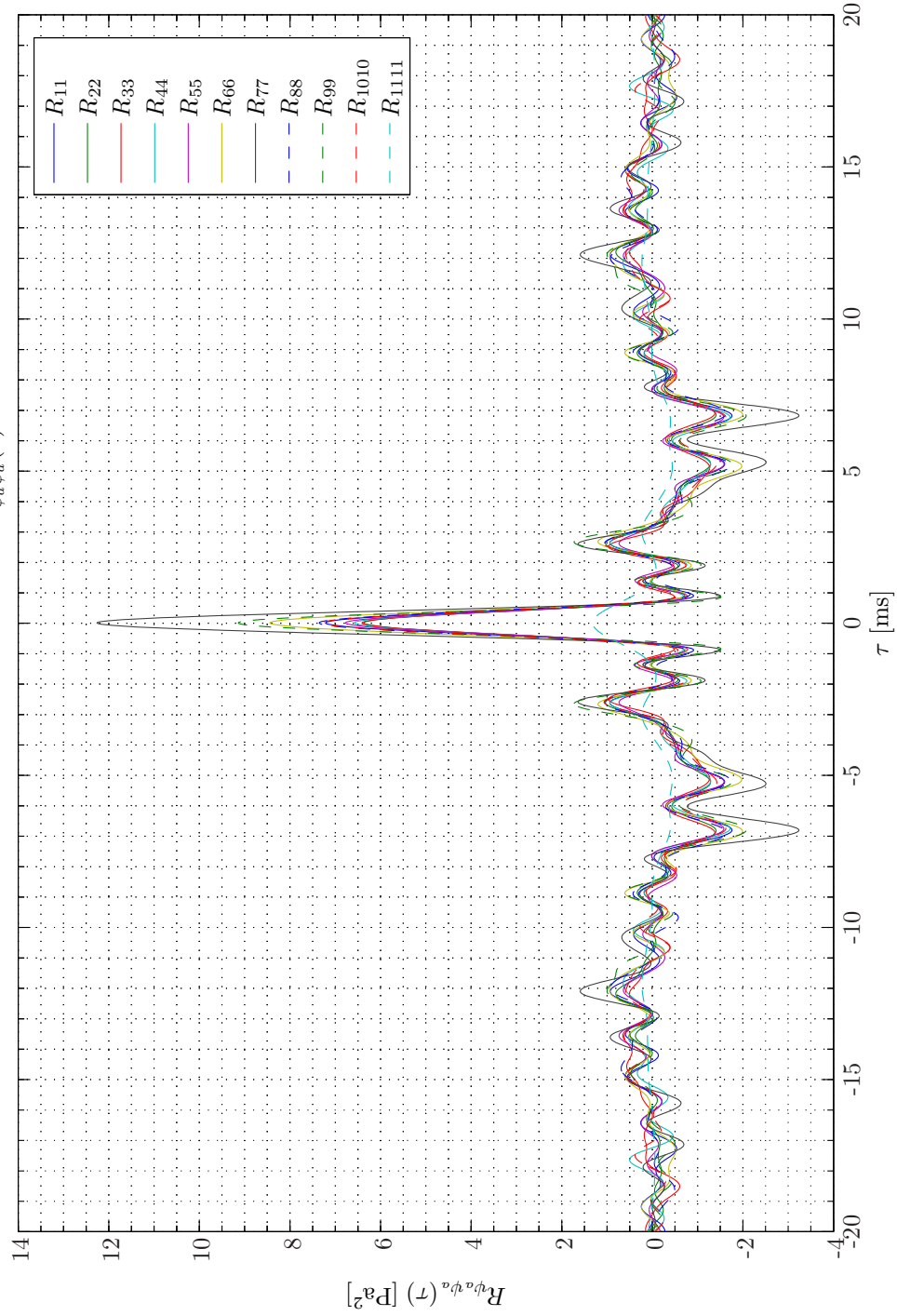

Sim 2.4.13: *Autocorrelation Functions:* $R_{\psi_a\psi_a}(\tau)$: **Statistical Data Analysis**: Single-Sided Modified Periodogram, f_s = 65.536 kHz, N_{DFT} = 16384, L_{DFT} = 16385, R_{DFT} = 8193, Hanning, Δf_m = 16 Hz, T_{DFT} = 0.25002 s, $N_{f,DFT}$ = 8193, Δf_{DFT} = 4 Hz, K_{DFT} = 158; *System Identification:* (Random Low-Pass (4 kHz) White Noise ($\mathcal{N}(0, 0.2)$), Elliptic LPF (f_{pass} = 900 Hz, f_{stop} = 1 kHz, A_{pass} = 1 dB, A_{stop} = 40 dB), f_s =65.536 kHz; Time: 0 − 20 s; **Topology:** BK 4949 surface microphones flush-mounted on Gentex HGU-55/P helmet mounted on a BK 4128 C HATS, Terma Earcup Audio System (Feedforward, mFx, $N_x = 10, N_e = 1, N_y = 2, N_p = 2$); *Channels:* #1 ← x_1, #2 ← x_2, #3 ← x_3, #4 ← x_4, #5 ← x_5, #6 ← x_6, #7 ← x_7, #8 ← x_8, #9 ← x_9, #10 ← x_{10}, #11 ← d_1; **Scenario:** `SystemIdentification(65536Hz)PrimaryPathes/20070204T112036`.

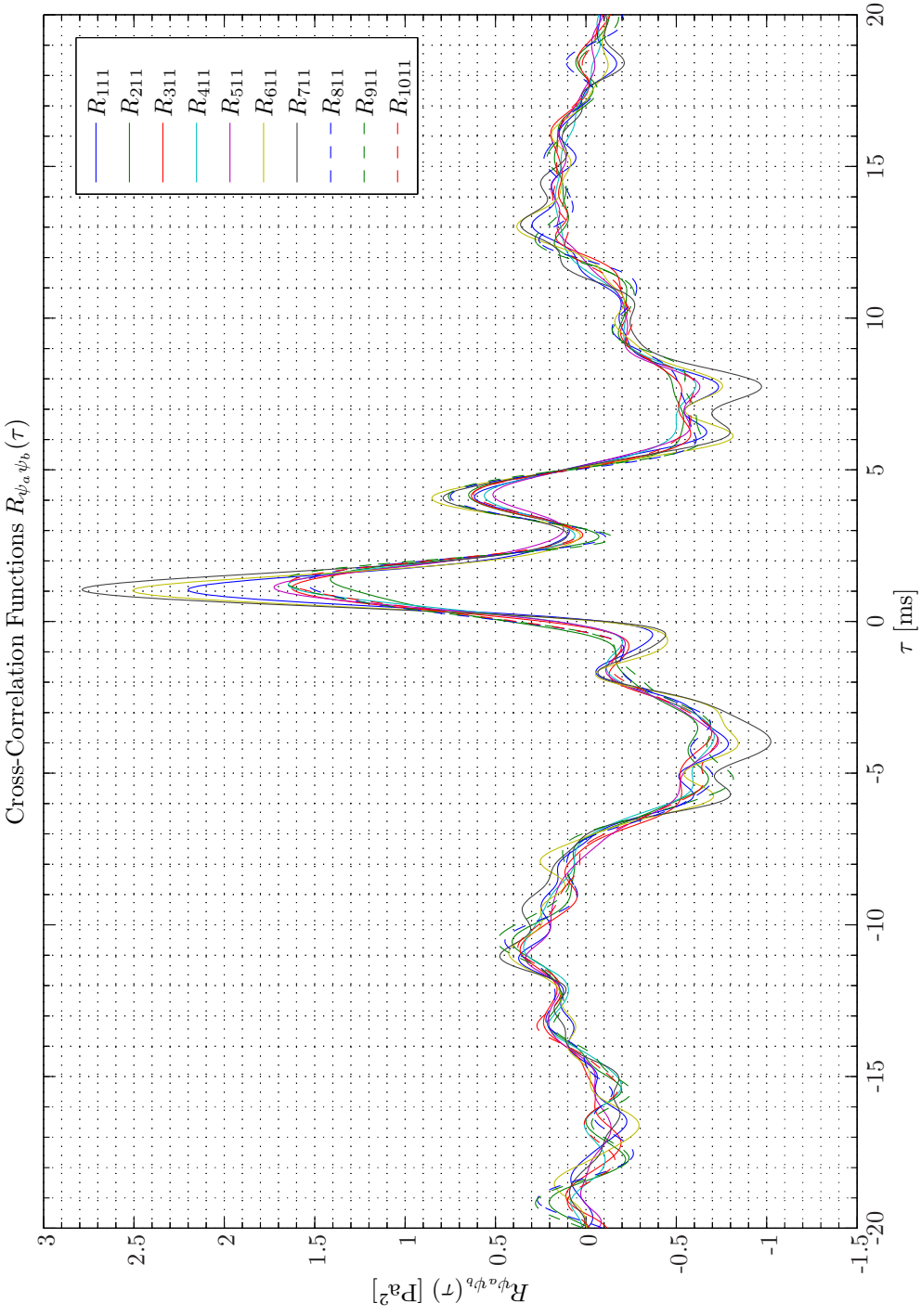

Sim 2.4.14: *Cross-Correlation Functions:* $R_{\psi_a\psi_b}(\tau)$: **Statistical Data Analysis**: Single-Sided Modified Periodogram, $f_s = 65.536$ kHz, $N_{DFT} = 16384$, $L_{DFT} = 16385$, $R_{DFT} = 8193$, Hanning, $\Delta f_m = 16$ Hz, $T_{DFT} = 0.25002$ s, $N_{f,DFT} = 8193$, $\Delta f_{DFT} = 4$ Hz, $K_{DFT} = 158$; *System Identification:* (Random Low-Pass (4 kHz) White Noise ($\mathcal{N}(0, 0.2)$), Elliptic LPF ($f_{pass} = 900$ Hz, $f_{stop} = 1$ kHz, $A_{pass} = 1$ dB, $A_{stop} = 40$ dB), f_s =65.536 kHz; Time: $0 - 20$ s; **Topology:** BK 4949 surface microphones flush-mounted on Gentex HGU-55/P helmet mounted on a BK 4128 C HATS, Terma Earcup Audio System (Feedforward, mFx, $N_x = 10, N_e = 1, N_y = 2, N_p = 2$); *Channels:* #1 $\leftarrow x_1$, #2 $\leftarrow x_2$, #3 $\leftarrow x_3$, #4 $\leftarrow x_4$, #5 $\leftarrow x_5$, #6 $\leftarrow x_6$, #7 $\leftarrow x_7$, #8 $\leftarrow x_8$, #9 $\leftarrow x_9$, #10 $\leftarrow x_{10}$, #11 $\leftarrow d_1$; **Scenario:** `SystemIdentification(65536Hz)PrimaryPathes/20070204T112036`.

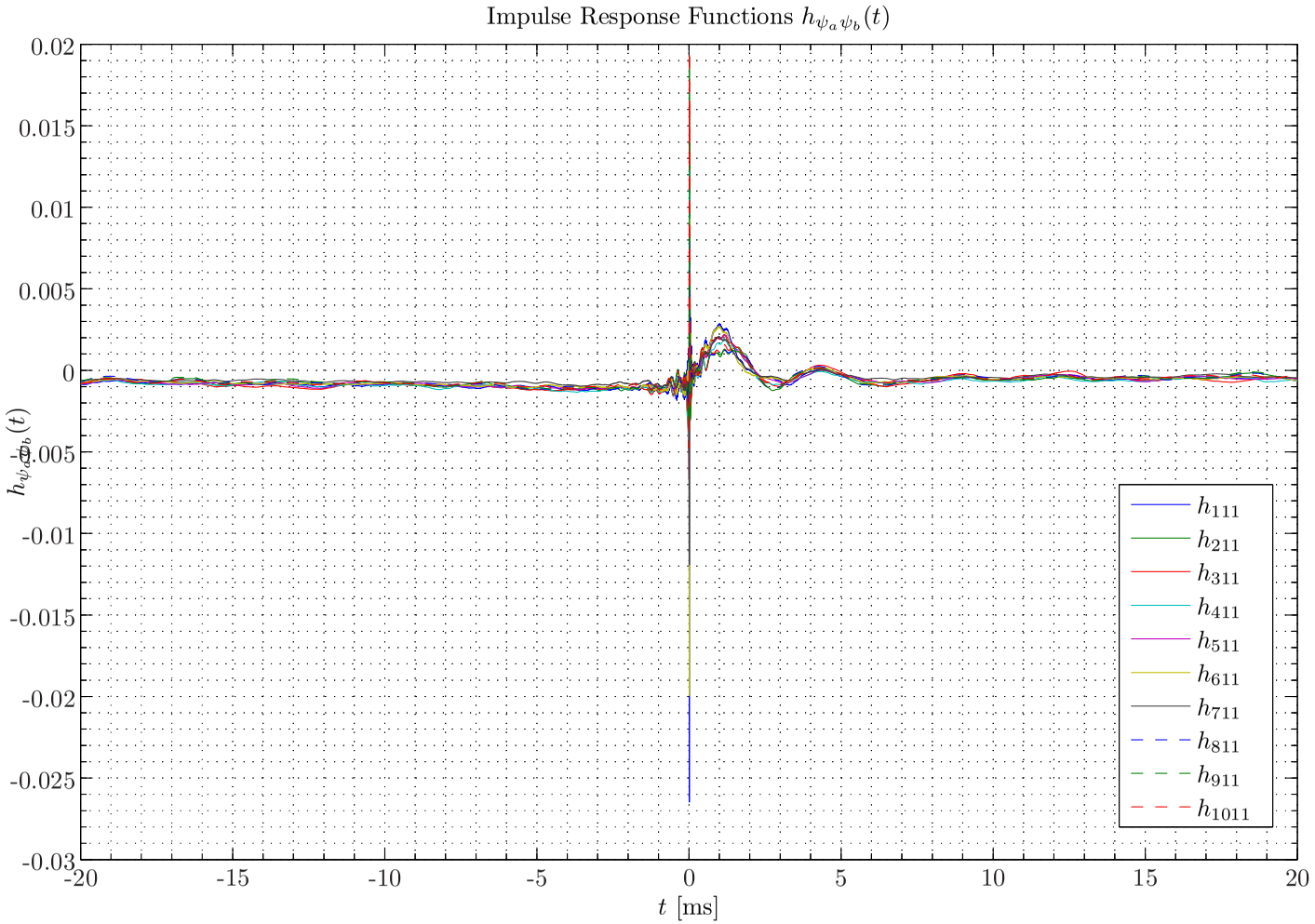

Sim 2.4.15: *Impulse Response Functions*: $h_{\psi_a\psi_b}(t)$: **Statistical Data Analysis**: Single-Sided Modified Periodogram, f_s = 65.536 kHz, N_{DFT} = 16384, L_{DFT} = 16385, R_{DFT} = 8193, Hanning, Δf_m = 16 Hz, T_{DFT} = 0.25002 s, $N_{f,DFT}$ = 8193, Δf_{DFT} = 4 Hz, K_{DFT} = 158; *System Identification:* (Random Low-Pass (4 kHz) White Noise ($\mathcal{N}(0, 0.2)$), Elliptic LPF ($f_{pass} = 900$ Hz, $f_{stop} = 1$ kHz, $A_{pass} = 1$ dB, $A_{stop} = 40$ dB), f_s =65.536 kHz; Time: $0 - 20$ s; **Topology:** BK 4949 surface microphones flush-mounted on Gentex HGU-55/P helmet mounted on a BK 4128 C HATS, Terma Earcup Audio System (Feedforward, mFx, $N_x = 10, N_e = 1, N_y = 2, N_p = 2$); *Channels:* #1 $\leftarrow x_1$, #2 $\leftarrow x_2$, #3 $\leftarrow x_3$, #4 $\leftarrow x_4$, #5 $\leftarrow x_5$, #6 $\leftarrow x_6$, #7 $\leftarrow x_7$, #8 $\leftarrow x_8$, #9 $\leftarrow x_9$, #10 $\leftarrow x_{10}$, #11 $\leftarrow d_1$; **Scenario:** `SystemIdentification(65536Hz)PrimaryPathes/20070204T112036`.

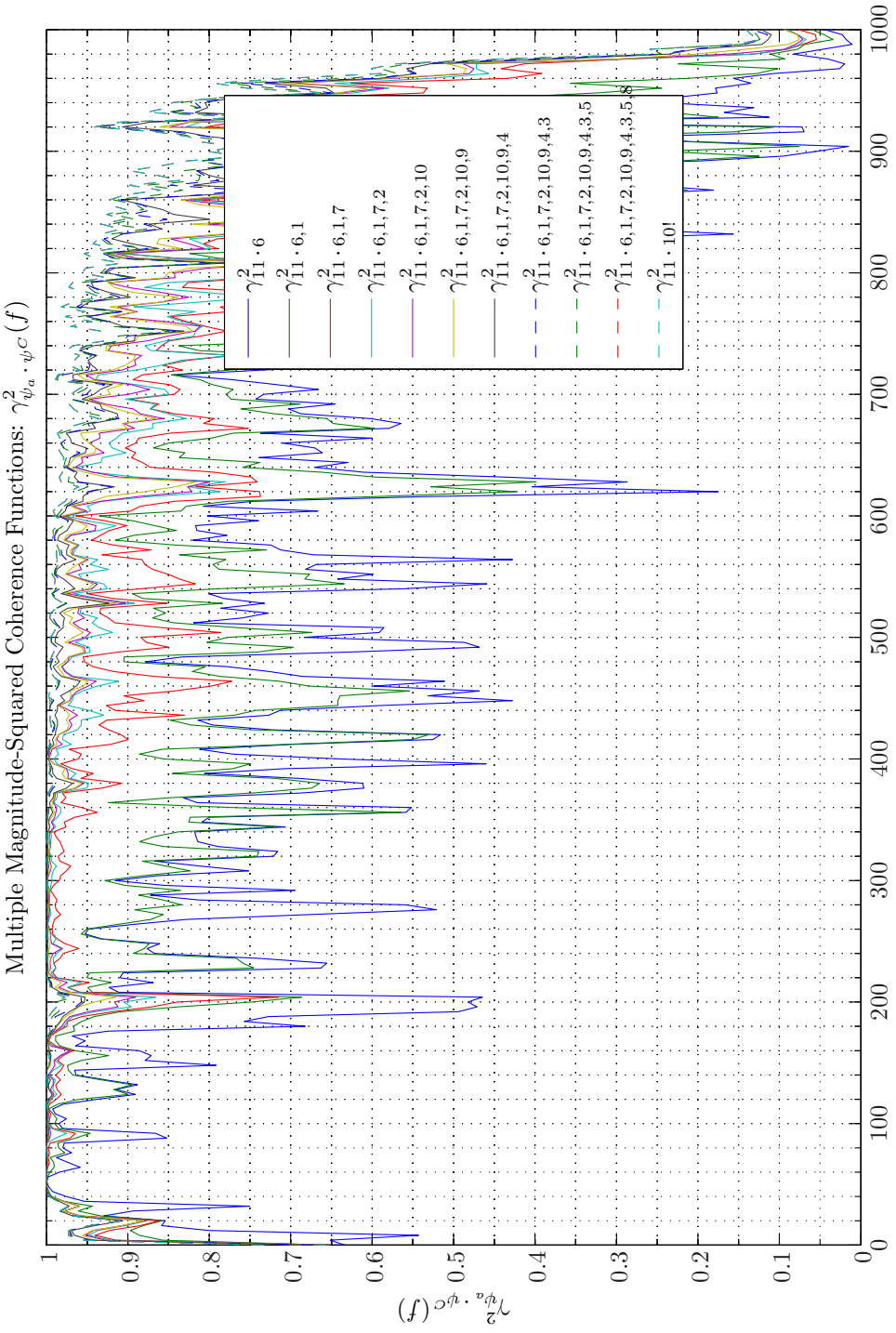

Sim 2.4.16: *Multiple Magnitude-Squared Coherence Functions* $\gamma^2_{\psi_a \cdot \psi^C}(f)$: **Statistical Data Analysis**: Single-Sided Modified Periodogram, f_s = 65.536 kHz, N_{DFT} = 16384, L_{DFT} = 16385, R_{DFT} = 8193, Hanning, Δf_m = 16 Hz, T_{DFT} = 0.25002 s, $N_{f,DFT}$ = 8193, Δf_{DFT} = 4 Hz, K_{DFT} = 158; *System Identification:* (Random Low-Pass (4 kHz) White Noise ($\mathcal{N}(0, 0.2)$), Elliptic LPF (f_{pass} = 900 Hz, f_{stop} = 1 kHz, A_{pass} = 1 dB, A_{stop} = 40 dB), f_s =65.536 kHz; Time: 0 – 20 s; **Topology:** BK 4949 surface microphones flush-mounted on Gentex HGU-55/P helmet mounted on a BK 4128 C HATS, Terma Earcup Audio System (Feedforward, mFx, $N_x = 10, N_e = 1, N_y = 2, N_p = 2$); *Channels:* #1 $\leftarrow x_1$, #2 $\leftarrow x_2$, #3 $\leftarrow x_3$, #4 $\leftarrow x_4$, #5 $\leftarrow x_5$, #6 $\leftarrow x_6$, #7 $\leftarrow x_7$, #8 $\leftarrow x_8$, #9 $\leftarrow x_9$, #10 $\leftarrow x_{10}$, #11 $\leftarrow d_1$; **Scenario:** `SystemIdentification(65536Hz)PrimaryPathes/20070204T112036`.

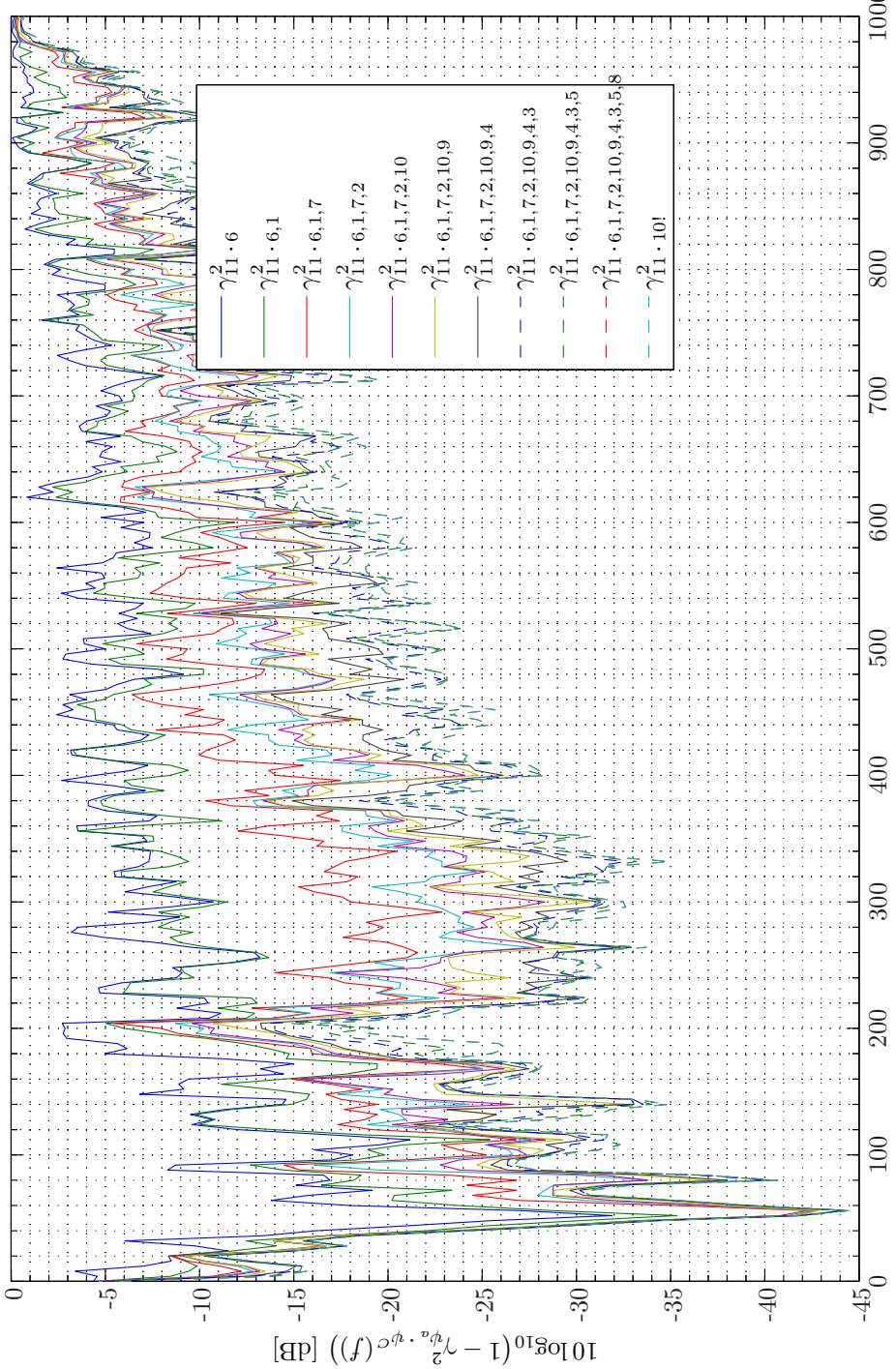

Sim 2.4.17: *Attenuation vs Multiple Magnitude-Squared Coherence Functions* $10\log_{10}(1-\gamma^2_{\psi_a\cdot\psi^C}(f))$: **Statistical Data Analysis**: Single-Sided Modified Periodogram, f_s = 65.536 kHz, N_{DFT} = 16384, L_{DFT} = 16385, R_{DFT} = 8193, Hanning, Δf_m = 16 Hz, T_{DFT} = 0.25002 s, $N_{f,DFT}$ = 8193, Δf_{DFT} = 4 Hz, K_{DFT} = 158; *System Identification:* (Random Low-Pass (4 kHz) White Noise ($\mathcal{N}(0,0.2)$), Elliptic LPF (f_{pass} = 900 Hz, f_{stop} = 1 kHz, A_{pass} = 1 dB, A_{stop} = 40 dB), f_s =65.536 kHz; Time: 0 − 20 s; **Topology:** BK 4949 surface microphones flush-mounted on Gentex HGU-55/P helmet mounted on a BK 4128 C HATS, Terma Earcup Audio System (Feedforward, mFx, $N_x = 10, N_e = 1, N_y = 2, N_p = 2$); *Channels:* #1 ← x_1, #2 ← x_2, #3 ← x_3, #4 ← x_4, #5 ← x_5, #6 ← x_6, #7 ← x_7, #8 ← x_8, #9 ← x_9, #10 ← x_{10}, #11 ← d_1; **Scenario:** `SystemIdentification(65536Hz)PrimaryPathes/20070204T112036`.

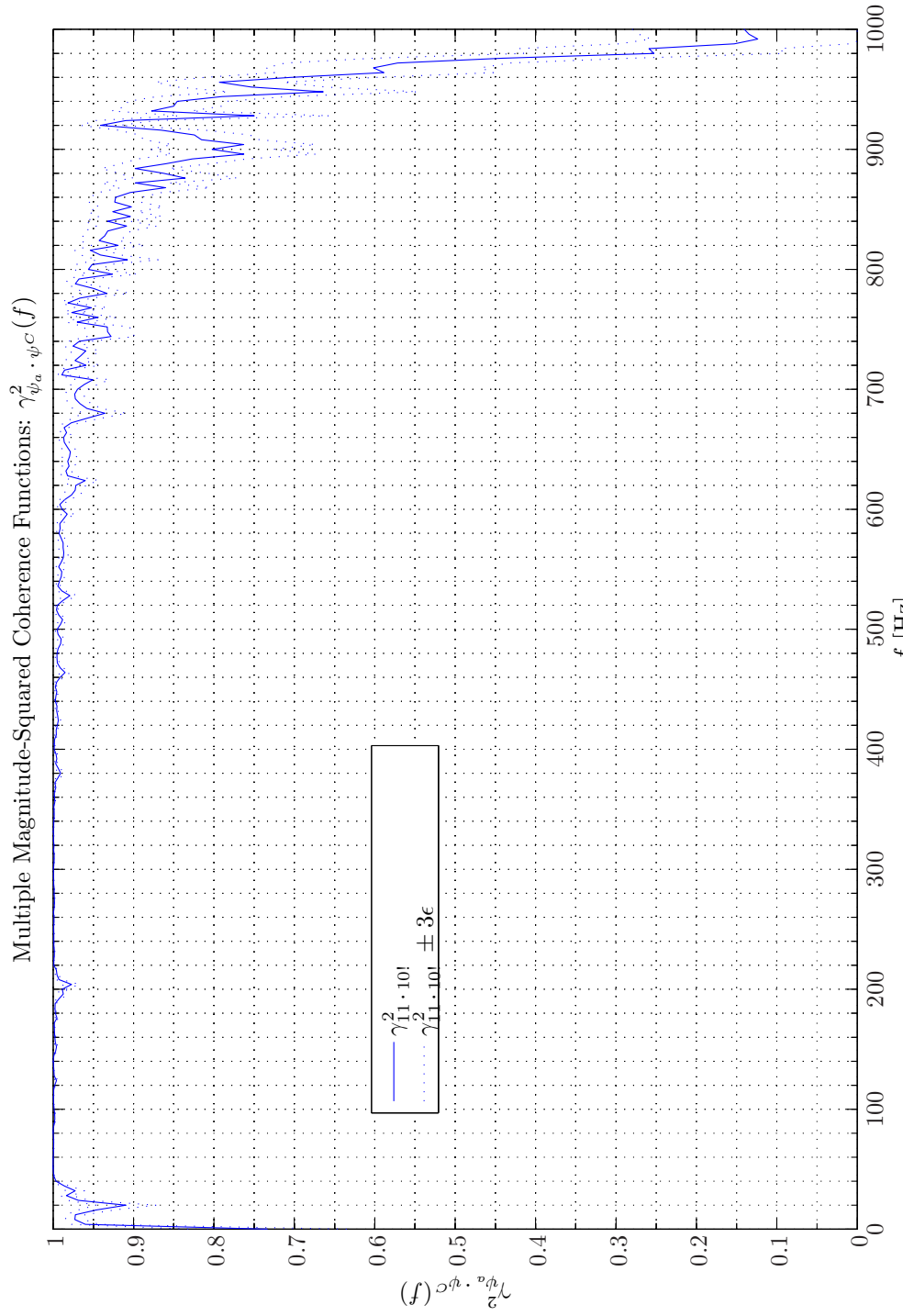

Sim 2.4.18: *Multiple Magnitude-Squared Coherence Functions* $\gamma^2_{\psi_a \cdot \psi^C}(f)$: **Statistical Data Analysis**: Single-Sided Modified Periodogram, f_s = 65.536 kHz, N_{DFT} = 16384, L_{DFT} = 16385, R_{DFT} = 8193, Hanning, Δf_m = 16 Hz, T_{DFT} = 0.25002 s, $N_{f,DFT}$ = 8193, Δf_{DFT} = 4 Hz, K_{DFT} = 158; *System Identification:* (Random Low-Pass (4 kHz) White Noise ($\mathcal{N}(0, 0.2)$), Elliptic LPF (f_{pass} = 900 Hz, f_{stop} = 1 kHz, A_{pass} = 1 dB, A_{stop} = 40 dB), f_s =65.536 kHz; Time: 0 – 20 s; **Topology:** BK 4949 surface microphones flush-mounted on Gentex HGU-55/P helmet mounted on a BK 4128 C HATS, Terma Earcup Audio System (Feedforward, mFx, $N_x = 10, N_e = 1, N_y = 2, N_p = 2$); *Channels:* #1 $\leftarrow x_1$, #2 $\leftarrow x_2$, #3 $\leftarrow x_3$, #4 $\leftarrow x_4$, #5 $\leftarrow x_5$, #6 $\leftarrow x_6$, #7 $\leftarrow x_7$, #8 $\leftarrow x_8$, #9 $\leftarrow x_9$, #10 $\leftarrow x_{10}$, #11 $\leftarrow d_1$; **Scenario:** `SystemIdentification(65536Hz)PrimaryPathes/20070204T112036`.

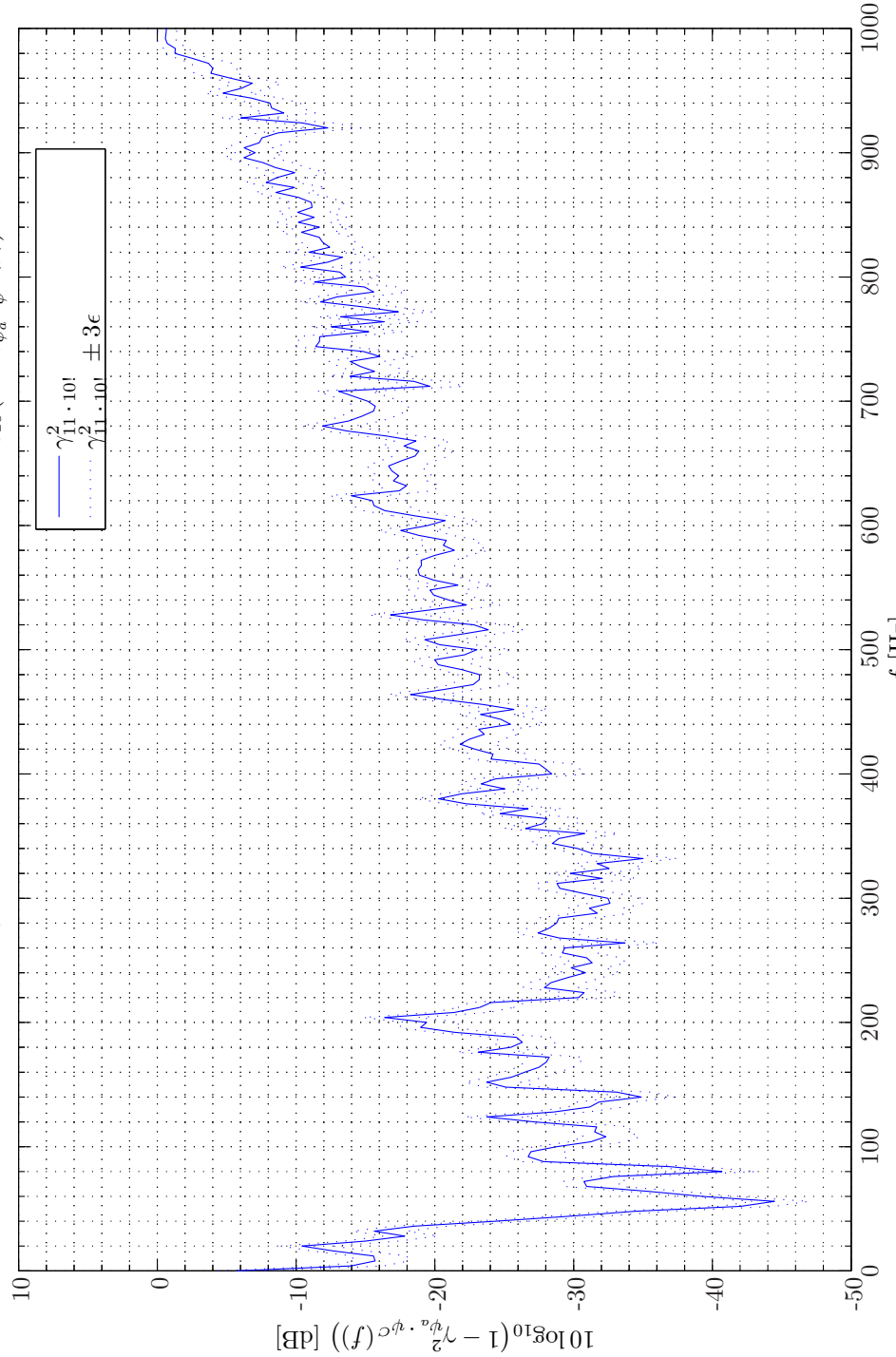

Sim 2.4.19: *Attenuation vs Multiple Magnitude-Squared Coherence Functions* $10\log_{10}(1-\gamma^2_{\psi_a\cdot\psi^C}(f))$: **Statistical Data Analysis**: Single-Sided Modified Periodogram, f_s = 65.536 kHz, N_{DFT} = 16384, L_{DFT} = 16385, R_{DFT} = 8193, Hanning, Δf_m = 16 Hz, T_{DFT} = 0.25002 s, $N_{f,DFT}$ = 8193, Δf_{DFT} = 4 Hz, K_{DFT} = 158; *System Identification:* (Random Low-Pass (4 kHz) White Noise ($\mathcal{N}(0,0.2)$), Elliptic LPF (f_{pass} = 900 Hz, f_{stop} = 1 kHz, A_{pass} = 1 dB, A_{stop} = 40 dB), f_s =65.536 kHz; Time: 0 − 20 s; **Topology:** BK 4949 surface microphones flush-mounted on Gentex HGU-55/P helmet mounted on a BK 4128 C HATS, Terma Earcup Audio System (Feedforward, mFx, $N_x = 10, N_e = 1, N_y = 2, N_p = 2$); *Channels:* #1 ← x_1, #2 ← x_2, #3 ← x_3, #4 ← x_4, #5 ← x_5, #6 ← x_6, #7 ← x_7, #8 ← x_8, #9 ← x_9, #10 ← x_{10}, #11 ← d_1; **Scenario:** `SystemIdentification(65536Hz)PrimaryPathes/20070204T112036`.

large number of averages ($K_{DFT} = 158$) and because the multiple coherence function is exceeding 0.9 up to 850 Hz. The uncertainty in the attenuation estimation is relatively constant over the frequency band. This is a consequence of two opposing factors. Firstly, when the multiple coherence function is close to unity, that is, $\gamma^2_{\psi^a \cdot \psi^C} \lessapprox 1$ the uncertainty is very low viz. (C.3.10) on page 544 and Simulation 2.4.18. Secondly, when the multiple coherence function is close to unity large negative (dB) attenuation numbers are predicted which in turn is associated with large estimation uncertainties. This second determining factor to some extent counterbalances the first factor. Off course a formal derivation of the relative uncertainty in the attenuation estimation that could be obtained from insertion of (2.2.1) on page 18 in (C.3.10) would lead to the same conclusions.

From this ordinary analysis it can be concluded that in general much care should be exercised when interpreting the result from applying single-input and single-output (SISO) model to a spatially distributed physical system. The consequence of using an insufficient number of spatial samples was predicted in Coherence Prob. 2 on page 19.

System Identification of Primary Pathes $G^{j,m}_{ex}$, JCRSA

Next we use the JCRSA method as described in section 2.3 on page 29 to obtain more distinctive channel and in particular timing information.

By comparing the residual spectra shown in Simulation 2.4.20 - 2.4.21 on pages 59–60 with the total spectra in Simulation 2.4.3 - 2.4.4 on pages 39–40 we observe that by conditioning the spectra by the contents of the other channels effectively acts as a high-pass filter. The reason for this effect can be attributed to the fact that at lower frequencies the fields at the position of the reference sensors are indeed coherent. With increasing frequency, however, the coherence decreases which in turn leads to an increase in the information that is unique for each specific reference sensor. The difference between Simulation 2.4.20 - 2.4.21 and Simulation 2.4.3 - 2.4.4 are the coherent auto and cross-spectral density functions respectively.

The partial coherence functions (PCOFs) and related coherence limited attenuation (see (2.2.1) on page 18) are depicted in Simulation 2.4.22 on page 61 and Simulation 2.4.23 on page 62 respectively. A large individual variation with frequency as well as variation among the channels themselves are observed.

In Simulation 2.4.24 - 2.4.27 on pages 63–66 the specific PCOF details for the sixth and eighth reference sensor and the error sensor, that is, $\gamma^2_{x_6 d_1 \perp 1,2,3,4,5,7,8,9,10}(f)$, and $\gamma^2_{x_8 d_1 \perp 1,2,3,4,5,6,7,9,10}(f)$ including $\pm 3\epsilon$ confidence intervals are shown.

It should be recalled that the sixth reference sensor is the one closest to the position of the error sensor in the left ear cf. Figure 2.3 on page 35. However, due to imperfection the partial coherence function estimate over some frequencies exceeds 1. As a consequence the attenuation estimate erroneously becomes complex.

In Simulation 2.4.28 on page 67 the partial coherence function $\gamma^2_{d_1 \cdot x_{6,1,2,7,10,9,3,4,5,8}}(f)$ obtained from increasing the number of independent discrete Fourier transform (DFT) averages from 158 to 638 is shown. From this it can be concluded that the overestimate of the partial coherence function is not due to an insufficient number of averages, but related to inherent numerical limitations of the use of this estimate. It is for the same reason that we sort the reference signals with respect to the ordinary coherence function in *descending order*. Hence, a reference signal having a high coherence with respect to the disturbance signal is not conditioned with respect to

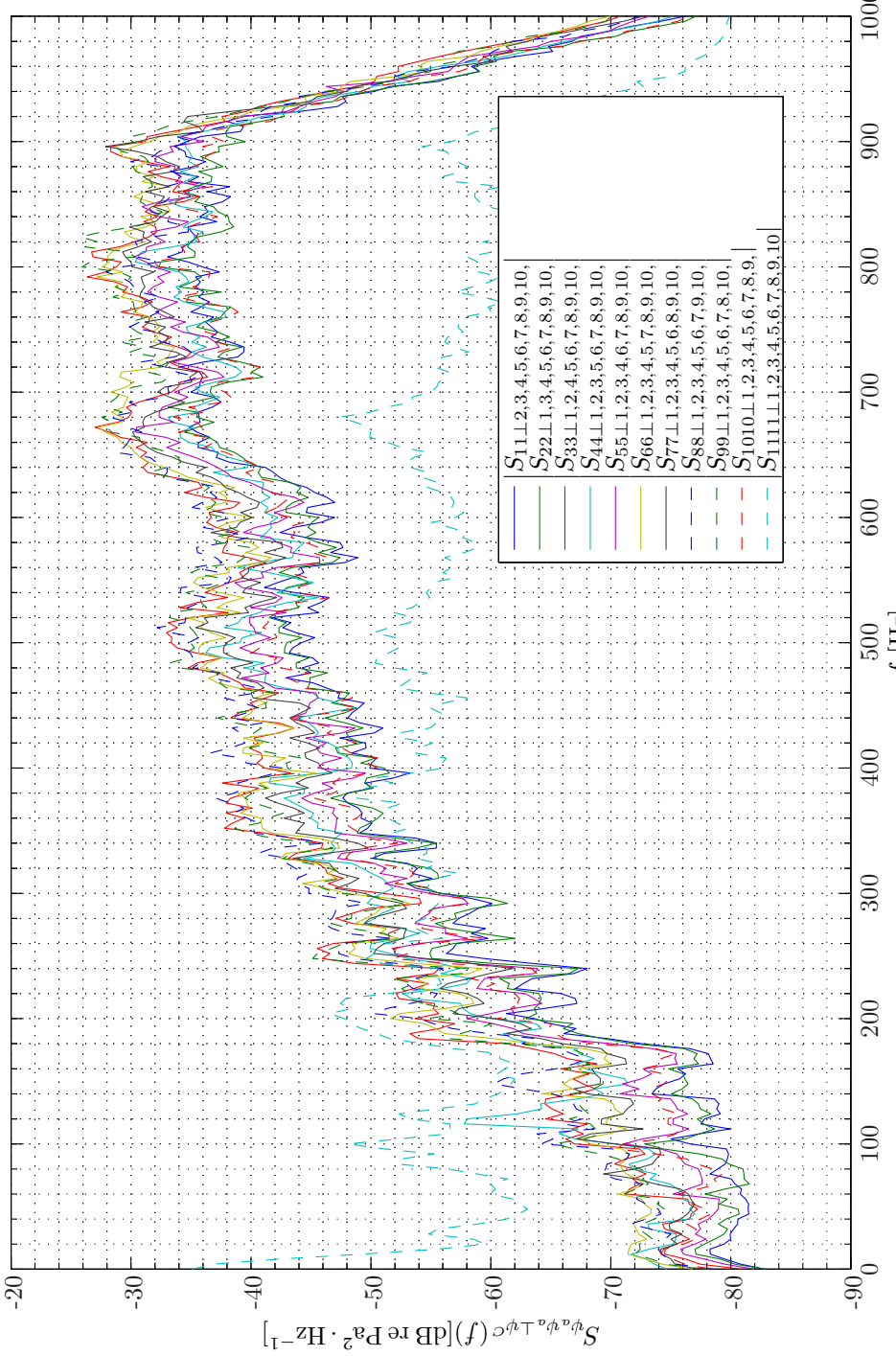

Sim 2.4.20: *Residual Autospectral Density Functions* JCRSA: **Statistical Data Analysis**: Single-Sided Modified Periodogram, f_s = 65.536 kHz, N_{DFT} = 16384, L_{DFT} = 16385, R_{DFT} = 8193, Hanning, Δf_m = 16 Hz, T_{DFT} = 0.25002 s, $N_{f,DFT}$ = 8193, Δf_{DFT} = 4 Hz, K_{DFT} = 158; *System Identification:* (Random Low-Pass (4 kHz) White Noise ($\mathcal{N}(0, 0.2)$), Elliptic LPF (f_{pass} = 900 Hz, f_{stop} = 1 kHz, A_{pass} = 1 dB, A_{stop} = 40 dB), f_s =65.536 kHz; Time: 0 − 20 s; **Topology:** BK 4949 surface microphones flush-mounted on Gentex HGU-55/P helmet mounted on a BK 4128 C HATS, Terma Earcup Audio System (Feedforward, mFx, $N_x = 10, N_e = 1, N_y = 2, N_p = 2$); *Channels:* #1 ← x_1, #2 ← x_2, #3 ← x_3, #4 ← x_4, #5 ← x_5, #6 ← x_6, #7 ← x_7, #8 ← x_8, #9 ← x_9, #10 ← x_{10}, #11 ← d_1; **Scenario:** `SystemIdentification(65536Hz)PrimaryPathes/20070204T112036`.

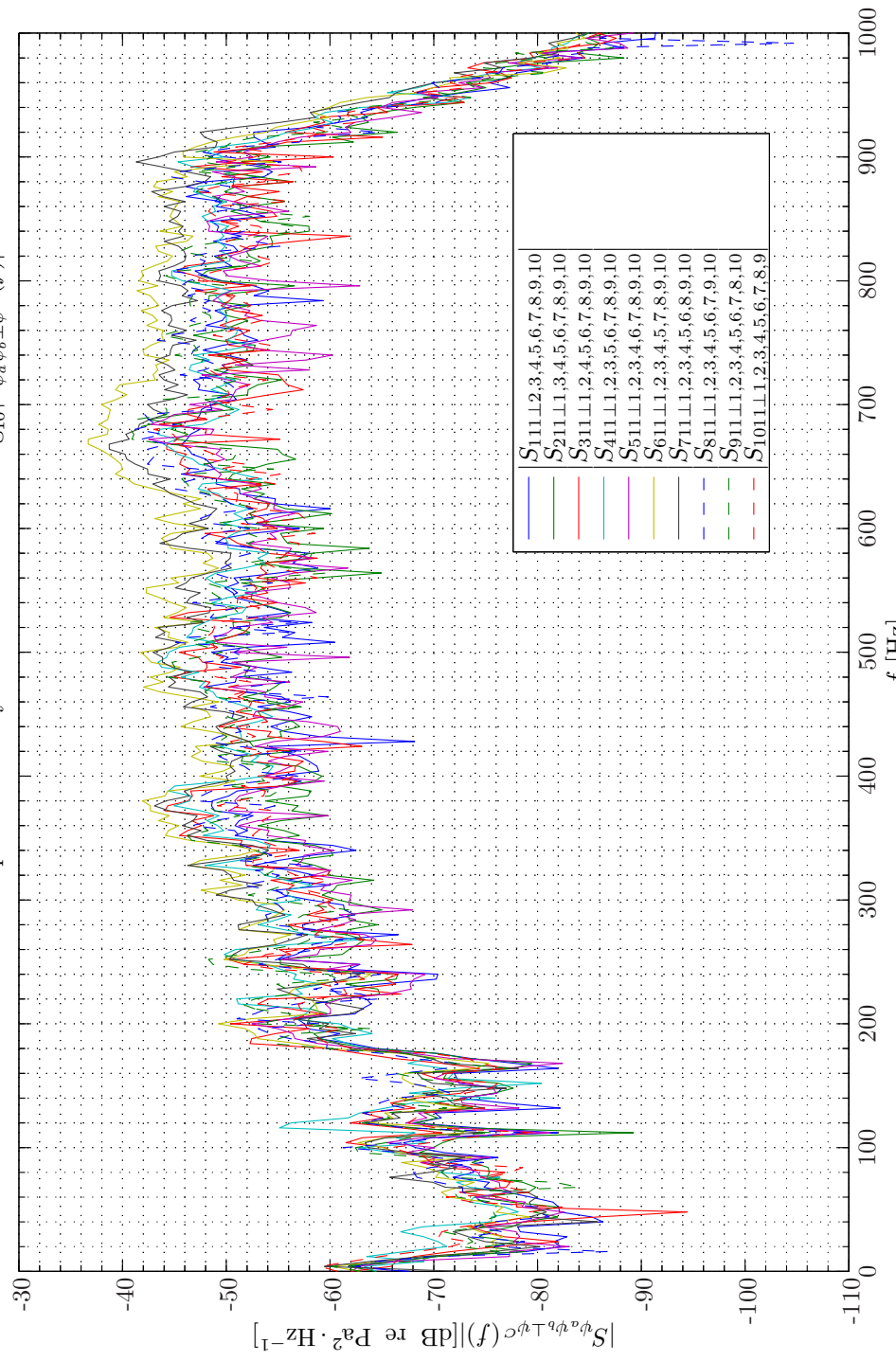

Sim 2.4.21: *Residual Cross-Spectral Density Functions* JCRSA: **Statistical Data Analysis**: Single-Sided Modified Periodogram, f_s = 65.536 kHz, N_{DFT} = 16384, L_{DFT} = 16385, R_{DFT} = 8193, Hanning, Δf_m = 16 Hz, T_{DFT} = 0.25002 s, $N_{f,DFT}$ = 8193, Δf_{DFT} = 4 Hz, K_{DFT} = 158; *System Identification:* (Random Low-Pass (4 kHz) White Noise ($\mathcal{N}(0, 0.2)$), Elliptic LPF (f_{pass} = 900 Hz, f_{stop} = 1 kHz, A_{pass} = 1 dB, A_{stop} = 40 dB), f_s =65.536 kHz; Time: 0 − 20 s; **Topology:** BK 4949 surface microphones flush-mounted on Gentex HGU-55/P helmet mounted on a BK 4128 C HATS, Terma Earcup Audio System (Feedforward, mFx, $N_x = 10, N_e = 1, N_y = 2, N_p = 2$); *Channels:* #1 ← x_1, #2 ← x_2, #3 ← x_3, #4 ← x_4, #5 ← x_5, #6 ← x_6, #7 ← x_7, #8 ← x_8, #9 ← x_9, #10 ← x_{10}, #11 ← d_1; **Scenario:** `SystemIdentification(65536Hz)PrimaryPathes/20070204T112036`.

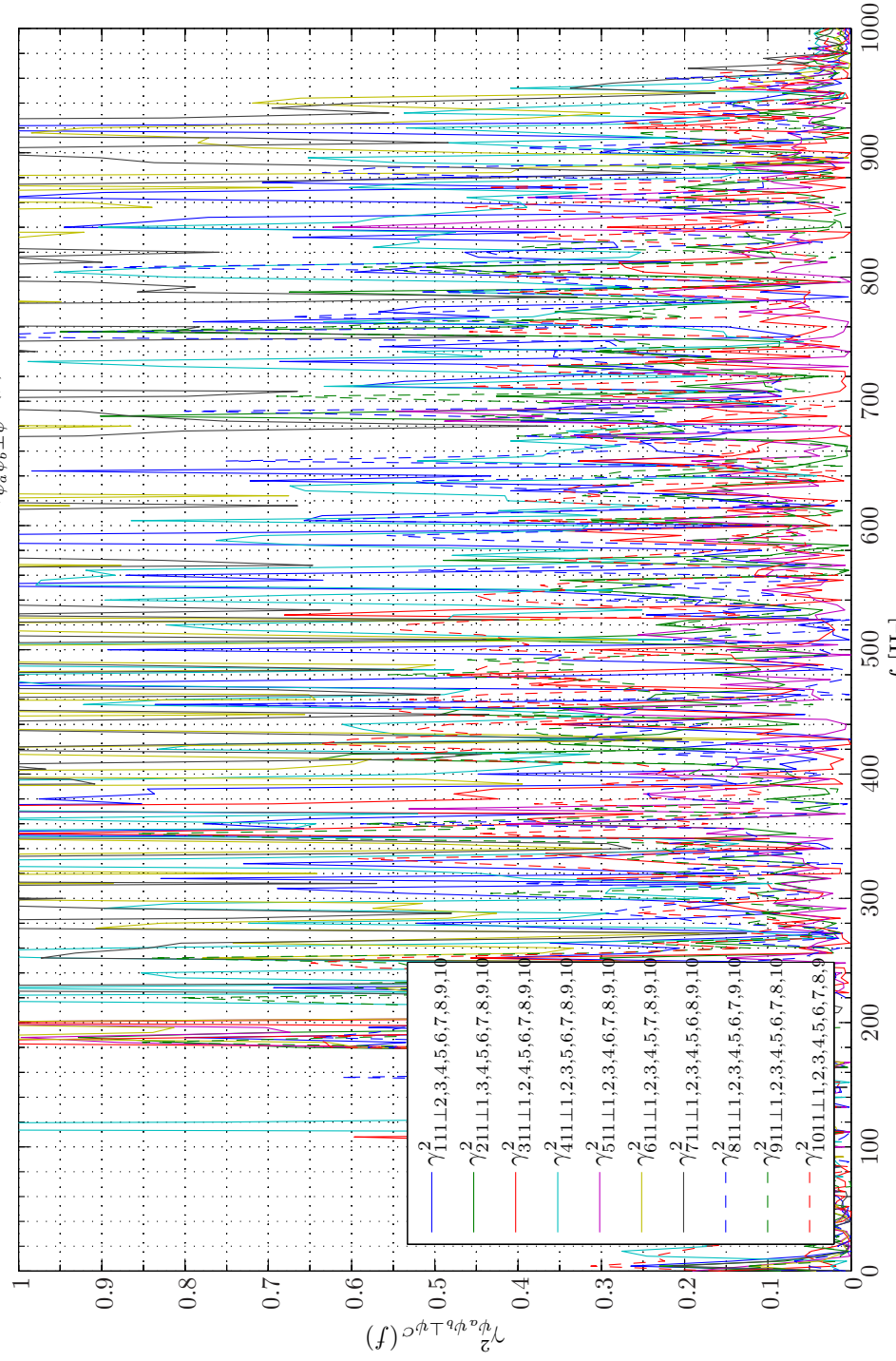

Sim 2.4.22: *Partial Coherency-Squared Functions* $\gamma^2_{\psi_a\psi_b\perp\psi^C}(f)$: **Statistical Data Analysis**: Single-Sided Modified Periodogram, f_s = 65.536 kHz, N_{DFT} = 16384, L_{DFT} = 16385, R_{DFT} = 8193, Hanning, Δf_m = 16 Hz, T_{DFT} = 0.25002 s, $N_{f,DFT}$ = 8193, Δf_{DFT} = 4 Hz, K_{DFT} = 158; *System Identification:* (Random Low-Pass (4 kHz) White Noise ($\mathcal{N}(0, 0.2)$), Elliptic LPF (f_{pass} = 900 Hz, f_{stop} = 1 kHz, A_{pass} = 1 dB, A_{stop} = 40 dB), f_s =65.536 kHz; Time: 0 – 20 s; **Topology:** BK 4949 surface microphones flush-mounted on Gentex HGU-55/P helmet mounted on a BK 4128 C HATS, Terma Earcup Audio System (Feedforward, mFx, $N_x = 10, N_e = 1, N_y = 2, N_p = 2$); *Channels:* #1 $\leftarrow x_1$, #2 $\leftarrow x_2$, #3 $\leftarrow x_3$, #4 $\leftarrow x_4$, #5 $\leftarrow x_5$, #6 $\leftarrow x_6$, #7 $\leftarrow x_7$, #8 $\leftarrow x_8$, #9 $\leftarrow x_9$, #10 $\leftarrow x_{10}$, #11 $\leftarrow d_1$; **Scenario:** SystemIdentification(65536Hz)PrimaryPathes/20070204T112036.

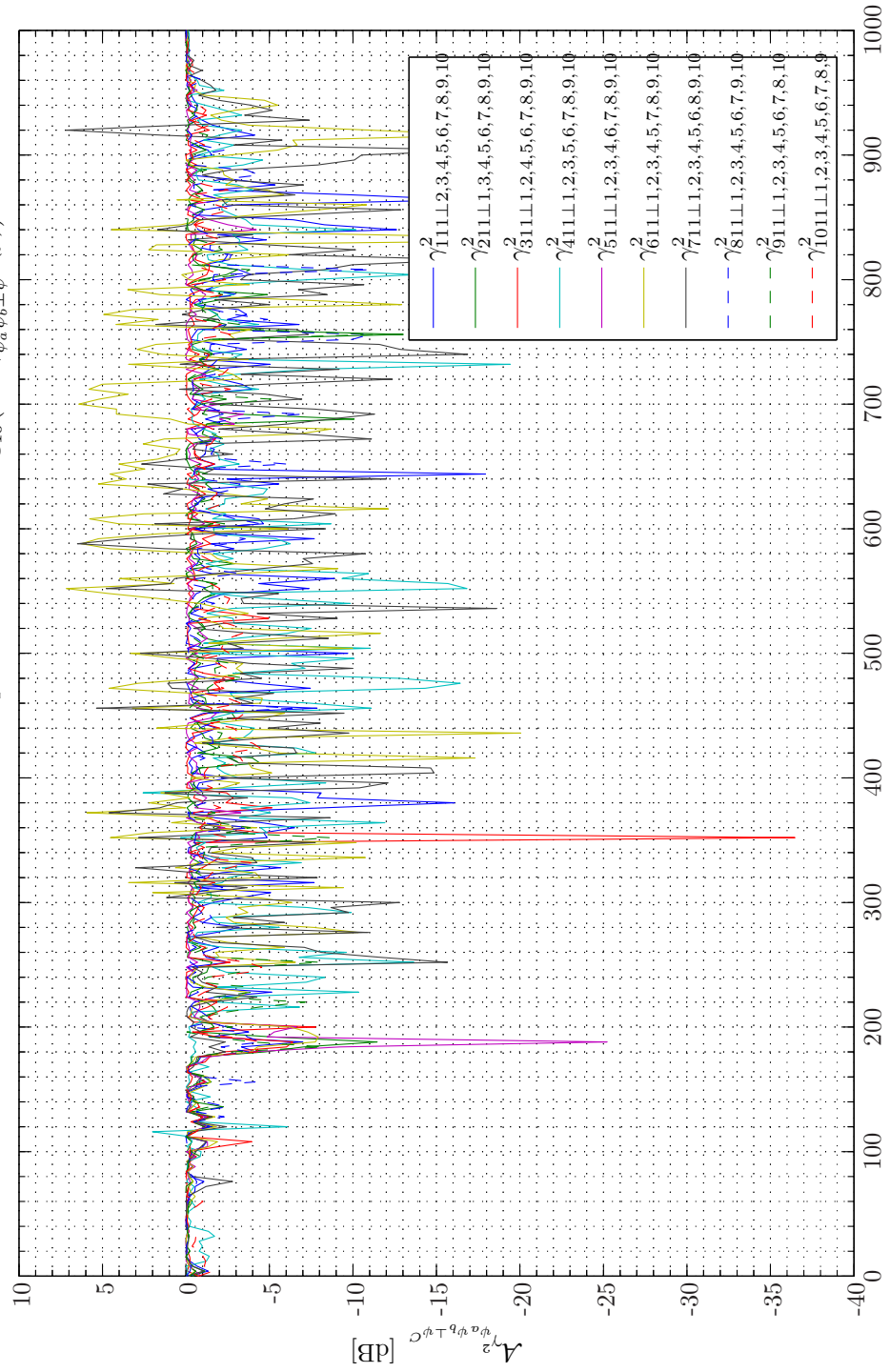

Sim 2.4.23: Attenuation *vs Partial Coherency-Squared Functions* JCRSA: $10\log_{10}(1-\gamma^2_{\psi_a\psi_b\perp\psi^C}(f))$: **Statistical Data Analysis**: Single-Sided Modified Periodogram, $f_s = 65.536$ kHz, $N_{DFT} = 16384$, $L_{DFT} = 16385$, $R_{DFT} = 8193$, Hanning, $\Delta f_m = 16$ Hz, $T_{DFT} = 0.25002$ s, $N_{f,DFT} = 8193$, $\Delta f_{DFT} = 4$ Hz, $K_{DFT} = 158$; *System Identification:* (Random Low-Pass (4 kHz) White Noise ($\mathcal{N}(0, 0.2)$), Elliptic LPF ($f_{pass} = 900$ Hz, $f_{stop} = 1$ kHz, $A_{pass} = 1$ dB, $A_{stop} = 40$ dB), f_s =65.536 kHz; Time: $0 - 20$ s; **Topology:** BK 4949 surface microphones flush-mounted on Gentex HGU-55/P helmet mounted on a BK 4128 C HATS, Terma Earcup Audio System (Feedforward, mFx, $N_x = 10, N_e = 1, N_y = 2, N_p = 2$); *Channels:* #1 $\leftarrow x_1$, #2 $\leftarrow x_2$, #3 $\leftarrow x_3$, #4 $\leftarrow x_4$, #5 $\leftarrow x_5$, #6 $\leftarrow x_6$, #7 $\leftarrow x_7$, #8 $\leftarrow x_8$, #9 $\leftarrow x_9$, #10 $\leftarrow x_{10}$, #11 $\leftarrow d_1$; **Scenario:** `SystemIdentification(65536Hz)PrimaryPathes/20070204T112036`.

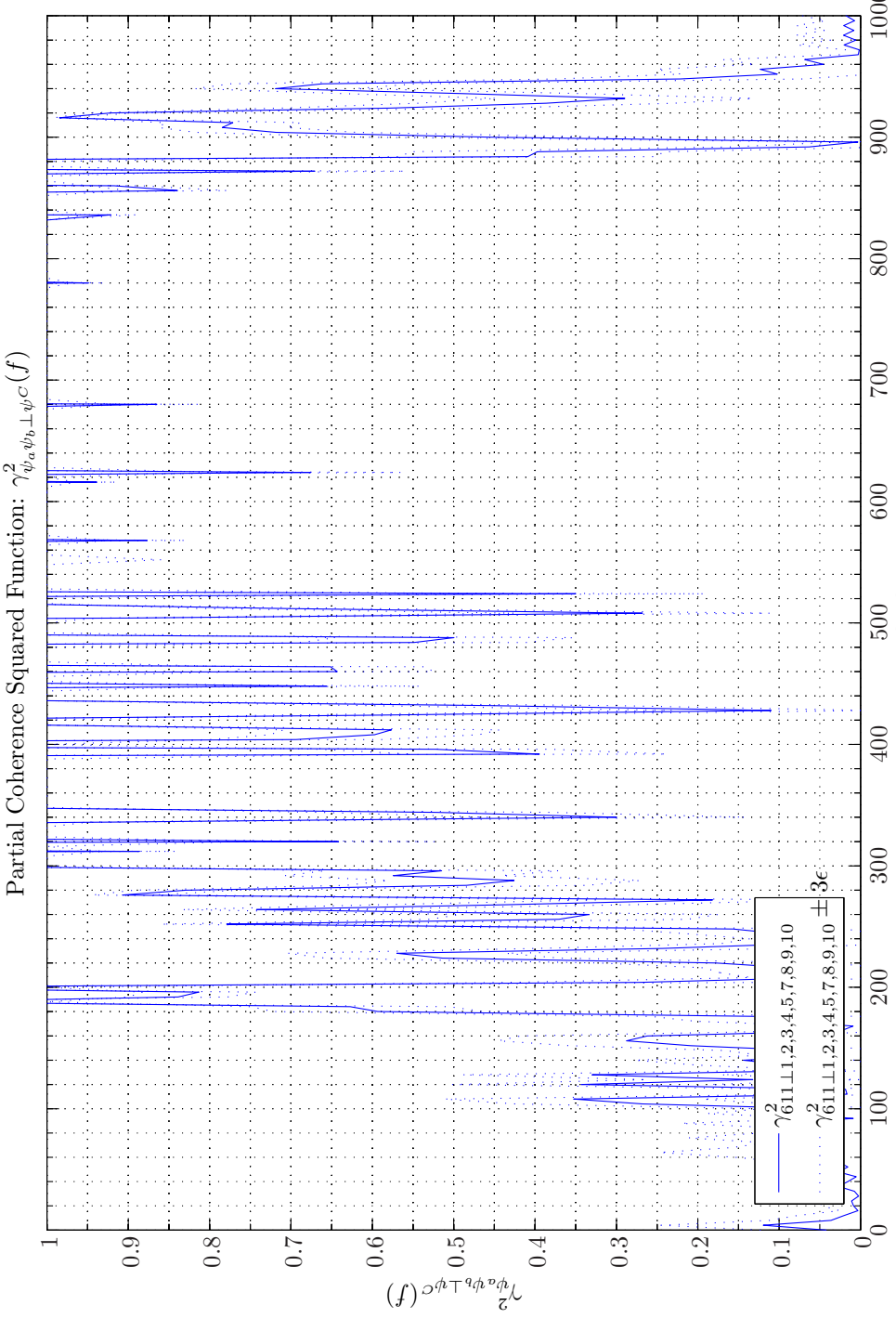

Sim 2.4.24: *Partial Coherency-Squared Functions* $\gamma^2_{\psi_a\psi_b\perp\psi^C}(f)$: **Statistical Data Analysis**: Single-Sided Modified Periodogram, f_s = 65.536 kHz, N_{DFT} = 16384, L_{DFT} = 16385, R_{DFT} = 8193, Hanning, Δf_m = 16 Hz, T_{DFT} = 0.25002 s, $N_{f,DFT}$ = 8193, Δf_{DFT} = 4 Hz, K_{DFT} = 158; *System Identification:* (Random Low-Pass (4 kHz) White Noise ($\mathcal{N}(0, 0.2)$), Elliptic LPF (f_{pass} = 900 Hz, f_{stop} = 1 kHz, A_{pass} = 1 dB, A_{stop} = 40 dB), f_s =65.536 kHz; Time: 0 – 20 s; **Topology:** BK 4949 surface microphones flush-mounted on Gentex HGU-55/P helmet mounted on a BK 4128 C HATS, Terma Earcup Audio System (Feedforward, mF×, $N_x = 10, N_e = 1, N_y = 2, N_p = 2$); *Channels:* #1 ← x_1, #2 ← x_2, #3 ← x_3, #4 ← x_4, #5 ← x_5, #6 ← x_6, #7 ← x_7, #8 ← x_8, #9 ← x_9, #10 ← x_{10}, #11 ← d_1; **Scenario:** `SystemIdentification(65536Hz)PrimaryPathes/20070204T112036`.

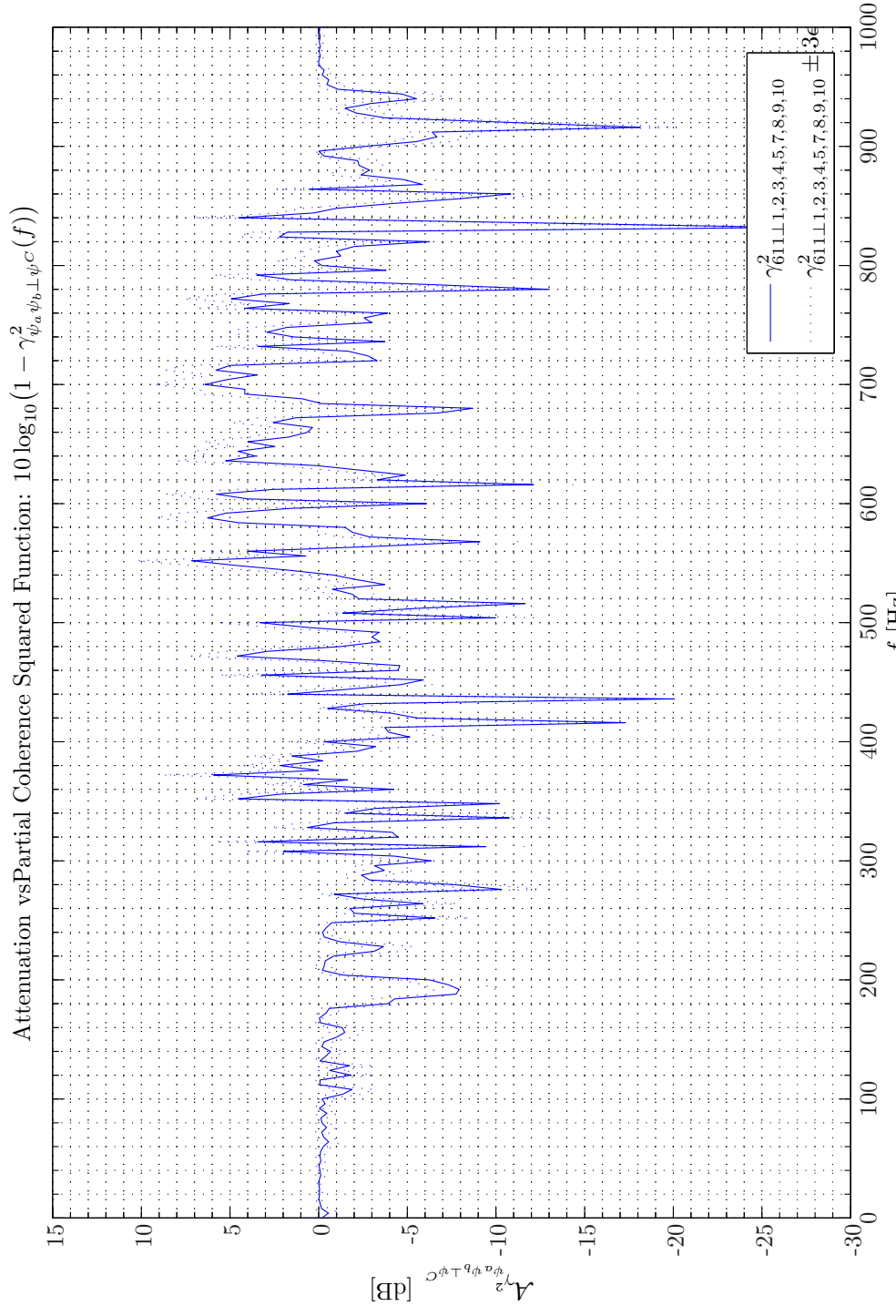

Sim 2.4.25: Attenuation *vs Partial Coherency-Squared Functions* JCRSA: $10\log_{10}(1-\gamma^2_{\psi_a\psi_b\perp\psi^C}(f))$: **Statistical Data Analysis**: Single-Sided Modified Periodogram, $f_s = 65.536$ kHz, $N_{DFT} = 16384$, $L_{DFT} = 16385$, $R_{DFT} = 8193$, Hanning, $\Delta f_m = 16$ Hz, $T_{DFT} = 0.25002$ s, $N_{f,DFT} = 8193$, $\Delta f_{DFT} = 4$ Hz, $K_{DFT} = 158$; *System Identification:* (Random Low-Pass (4 kHz) White Noise ($\mathcal{N}(0, 0.2)$), Elliptic LPF ($f_{pass} = 900$ Hz, $f_{stop} = 1$ kHz, $A_{pass} = 1$ dB, $A_{stop} = 40$ dB), f_s =65.536 kHz; Time: $0 - 20$ s; **Topology:** BK 4949 surface microphones flush-mounted on Gentex HGU-55/P helmet mounted on a BK 4128 C HATS, Terma Earcup Audio System (Feedforward, mFx, $N_x = 10, N_e = 1, N_y = 2, N_p = 2$); *Channels:* #1 $\leftarrow x_1$, #2 $\leftarrow x_2$, #3 $\leftarrow x_3$, #4 $\leftarrow x_4$, #5 $\leftarrow x_5$, #6 $\leftarrow x_6$, #7 $\leftarrow x_7$, #8 $\leftarrow x_8$, #9 $\leftarrow x_9$, #10 $\leftarrow x_{10}$, #11 $\leftarrow d_1$; **Scenario:** `SystemIdentification(65536Hz)PrimaryPathes/20070204T112036`.

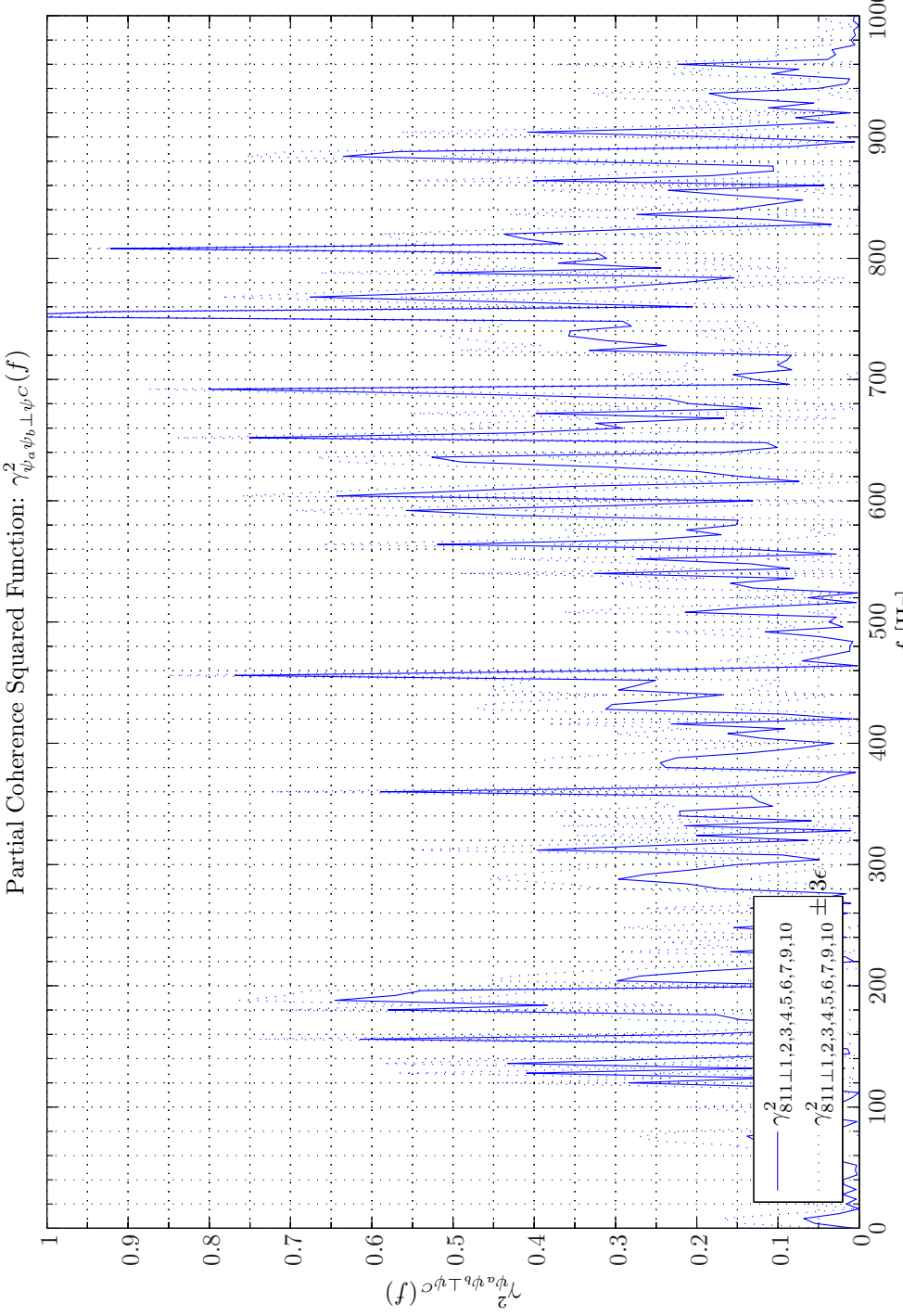

Sim 2.4.26: *Partial Coherency-Squared Functions* $\gamma^2_{\psi_a\psi_b\perp\psi^C}(f)$: **Statistical Data Analysis**: Single-Sided Modified Periodogram, f_s = 65.536 kHz, N_{DFT} = 16384, L_{DFT} = 16385, R_{DFT} = 8193, Hanning, Δf_m = 16 Hz, T_{DFT} = 0.25002 s, $N_{f,DFT}$ = 8193, Δf_{DFT} = 4 Hz, K_{DFT} = 158; *System Identification:* (Random Low-Pass (4 kHz) White Noise ($\mathcal{N}(0, 0.2)$), Elliptic LPF (f_{pass} = 900 Hz, f_{stop} = 1 kHz, A_{pass} = 1 dB, A_{stop} = 40 dB), f_s =65.536 kHz; Time: 0 − 20 s; **Topology:** BK 4949 surface microphones flush-mounted on Gentex HGU-55/P helmet mounted on a BK 4128 C HATS, Terma Earcup Audio System (Feedforward, mFx, $N_x = 10, N_e = 1, N_y = 2, N_p = 2$); *Channels:* #1 ← x_1, #2 ← x_2, #3 ← x_3, #4 ← x_4, #5 ← x_5, #6 ← x_6, #7 ← x_7, #8 ← x_8, #9 ← x_9, #10 ← x_{10}, #11 ← d_1; **Scenario:** `SystemIdentification(65536Hz)PrimaryPathes/20070204T112036`.

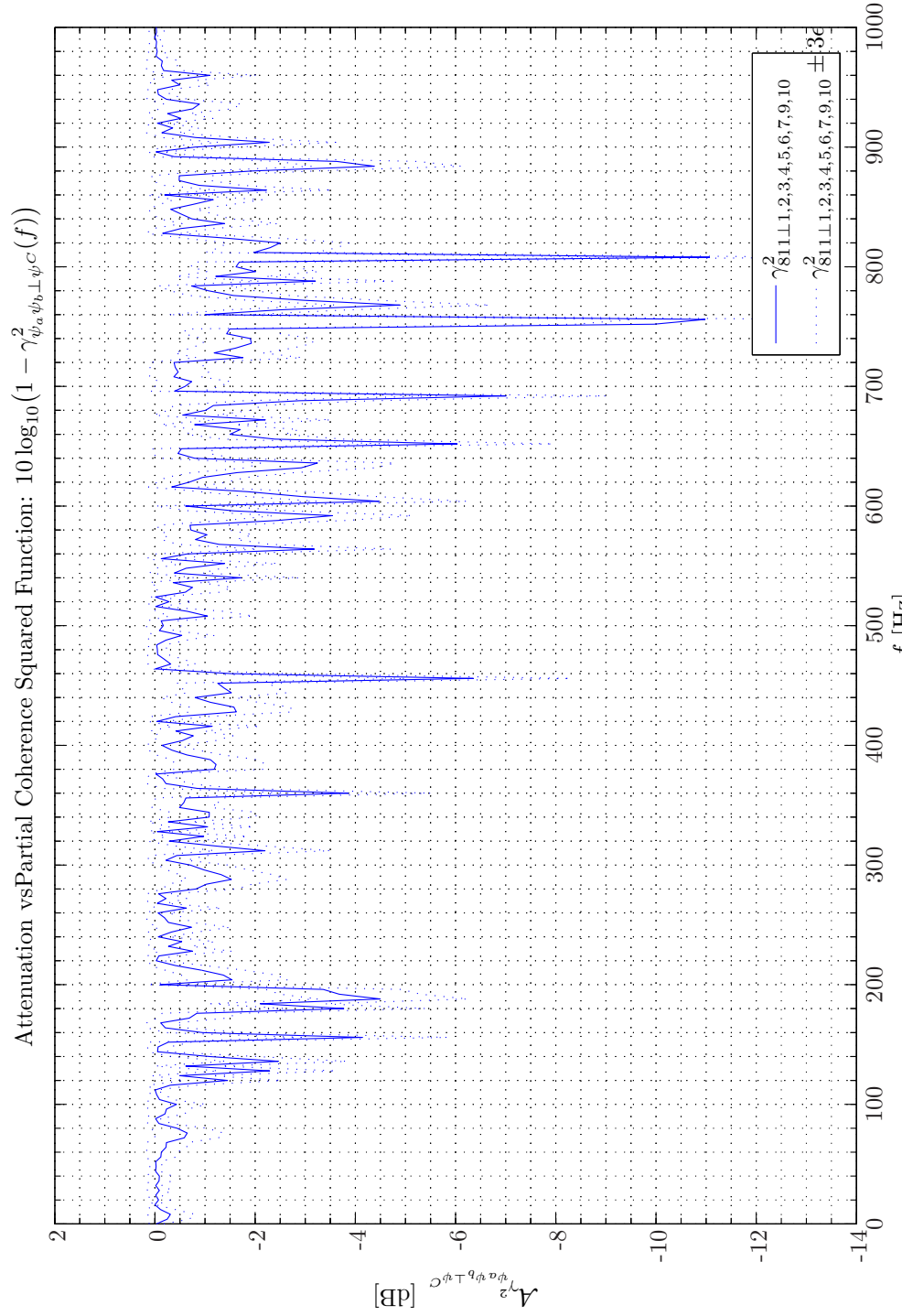

Sim 2.4.27: Attenuation *vs Partial Coherency-Squared Functions* JCRSA: $10\log_{10}(1-\gamma^2_{\psi_a\psi_b\perp\psi^C}(f))$: **Statistical Data Analysis**: Single-Sided Modified Periodogram, $f_s = 65.536$ kHz, $N_{DFT} = 16384$, $L_{DFT} = 16385$, $R_{DFT} = 8193$, Hanning, $\Delta f_m = 16$ Hz, $T_{DFT} = 0.25002$ s, $N_{f,DFT} = 8193$, $\Delta f_{DFT} = 4$ Hz, $K_{DFT} = 158$; *System Identification:* (Random Low-Pass (4 kHz) White Noise ($\mathcal{N}(0, 0.2)$), Elliptic LPF ($f_{pass} = 900$ Hz, $f_{stop} = 1$ kHz, $A_{pass} = 1$ dB, $A_{stop} = 40$ dB), f_s =65.536 kHz; Time: $0 - 20$ s; **Topology:** BK 4949 surface microphones flush-mounted on Gentex HGU-55/P helmet mounted on a BK 4128 C HATS, Terma Earcup Audio System (Feedforward, mFx, $N_x = 10, N_e = 1, N_y = 2, N_p = 2$); *Channels:* #1 $\leftarrow x_1$, #2 $\leftarrow x_2$, #3 $\leftarrow x_3$, #4 $\leftarrow x_4$, #5 $\leftarrow x_5$, #6 $\leftarrow x_6$, #7 $\leftarrow x_7$, #8 $\leftarrow x_8$, #9 $\leftarrow x_9$, #10 $\leftarrow x_{10}$, #11 $\leftarrow d_1$; **Scenario:** `SystemIdentification(65536Hz)PrimaryPathes/20070204T112036`.

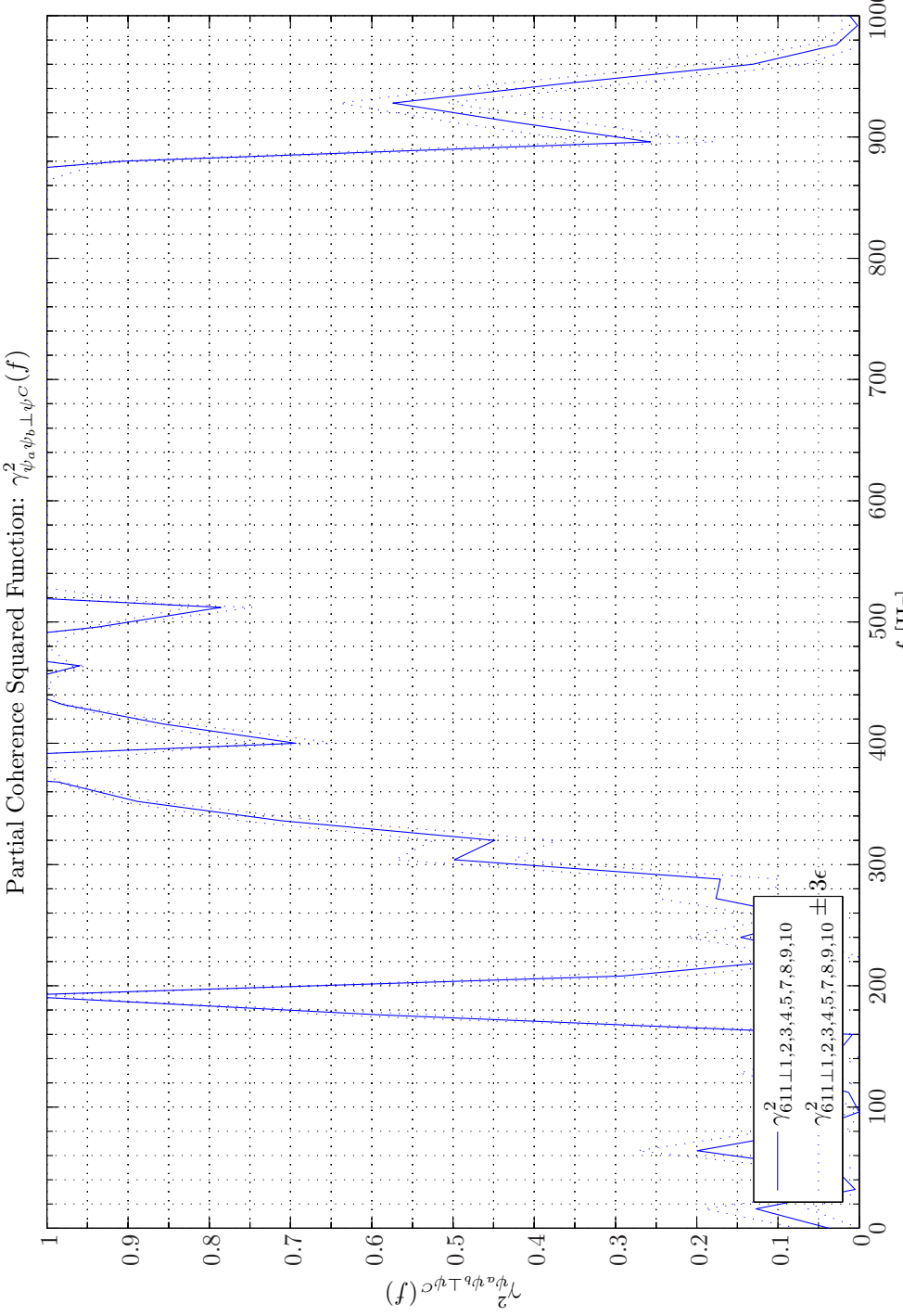

Sim 2.4.28: *Partial Coherency-Squared Functions* $\gamma^2_{\psi_a\psi_b\perp\psi^C}(f)$: **Statistical Data Analysis**: Single-Sided Modified Periodogram, f_s = 65.536 kHz, N_{DFT} = 4096, L_{DFT} = 4097, R_{DFT} = 2049, Hanning, Δf_m = 64 Hz, T_{DFT} = 0.062515 s, $N_{f,DFT}$ = 2049, Δf_{DFT} = 16 Hz, K_{DFT} = 638; *System Identification:* (Random Low-Pass (4 kHz) White Noise ($\mathcal{N}(0, 0.2)$), Elliptic LPF (f_{pass} = 900 Hz, f_{stop} = 1 kHz, A_{pass} = 1 dB, A_{stop} = 40 dB), f_s =65.536 kHz; Time: 0 − 20 s; **Topology:** BK 4949 surface microphones flush-mounted on Gentex HGU-55/P helmet mounted on a BK 4128 C HATS, Terma Earcup Audio System (Feedforward, mFx, $N_x = 10, N_e = 1, N_y = 2, N_p = 2$); *Channels:* #1 ← x_1, #2 ← x_2, #3 ← x_3, #4 ← x_4, #5 ← x_5, #6 ← x_6, #7 ← x_7, #8 ← x_8, #9 ← x_9, #10 ← x_{10}, #11 ← d_1; **Scenario:** `SystemIdentification(65536Hz)PrimaryPathes/20070204T181457`.

the reference signals with low coherence. Instead the reference signal having a low coherence with respect to the disturbance signal is conditioned with respect to the reference signals with a high coherence. However, the relative high partial coherence function numbers in Simulation 2.4.24 indicate that provided that a narrow acoustical beam could be constructed such as only reference sensor 6 would be illuminated this sensor alone would provide sufficient coherence for the ANR attenuation predicted in Simulation 2.4.25.

Next consider the eighth reference sensor which lead to the poorest ordinary coherence function values depicted in Simulation 2.4.9 on page 46. As expected the corresponding partial coherence function depicted in Simulation 2.4.26 reveal even lower coherence values. It should be remembered that in the construction of the partial coherence function we are conditioning on the other reference signals thereby subtracting that part of the coherent spectrum that is also coherent with these sensors.

By inspection of Simulation 2.4.29 - 2.4.30 on pages 69–70 we appreciate that more distinctive gain and phase factors of the transfer functions from the ten reference sensors to the error sensor are provided by the JCRSA method.

The JCRSA based auto- and cross-correlation functions are shown in Simulation 2.4.31 on page 71 and Simulation 2.4.33 on page 73 respectively. As expected the use of residual spectra accentuates individual channel characteristics. Moreover, the sidelobe is much more reduced as compared with the ordinary analysis in Simulation 2.4.13 - 2.4.14 on pages 51–52. The detailed information is illuminated in Simulation 2.4.32 on page 72 and Simulation 2.4.34 - 2.4.36 on pages 74–76.

Now we are in a position to formally define the acquisition lead-time and spatially-weighted-averaged acquisition lead time.

Definition 2.1. Each input-output channel combination of a MIMO system consisting of N_ψ^I inputs and N_ψ^O outputs is considered in turn. Assume for now that channel $\boldsymbol{\psi}_j^I, j \in \underline{N}_\psi^I$ and $\boldsymbol{\psi}_k^O, k \in \underline{N}_\psi^O$ have been selected as input and output channel respectively. Apply the assignments: $\boldsymbol{\psi}^A \leftarrow \psi_j^I \cup \psi_k^O$ and $\boldsymbol{\psi}^C \leftarrow \psi_{\neq j}^I$ and subsequently determine the JCRSA based residual cross-spectral density function $S_{\psi_j^I \psi_k^O \perp \psi_{\neq j}^I}(f)$ as outlined in subsection 2.3.3. The JCRSA based cross-correlation functions is $R_{\psi_j^I \psi_k^O \perp \psi_{\neq j}^I}(\tau) \triangleq \mathcal{F}^{-1}\{S_{\psi_j^I \psi_k^O \perp \psi_{\neq j}^I}(f)\}$. Then the acquisition lead-time between input signal ψ_j^I and output signal ψ_k^O denoted by $\tau_{\psi_j^I \psi_k^O}$ is defined as the time where $R_{\psi_j^I \psi_k^O \perp \psi_{\neq j}^I}(\tau)$ attains its numerical peak value.

It should be observed that the acquisition lead-time defined in Definition 2.1 is a general system theoretic quantity without any assumption on the physical nature of the excitation of the system. The spatially-weighted-averaged acquisition lead time defined next, however, is an instantiation to the domain of acoustics.

Definition 2.2. Assume in addition to the conditions stated in Definition 2.1 that the MIMO is subject to diffuse sound field incidence, then the acquisition lead-time becomes the spatially-weighted-averaged acquisition lead time between input signal ψ_j^I and output signal ψ_k^O that also will be denoted by $\tau_{\psi_j^I \psi_k^O}$.

Applying Definition 2.2 the calculated spatially-weighted-averaged acquisition lead times are tabulated in Table 2.4

Hence, except for reference sensors 5 and 9 the spatially-weighted-averaged acquisition lead time exceeds 0.8 ms. This is very important as such large lead times to a very large extent

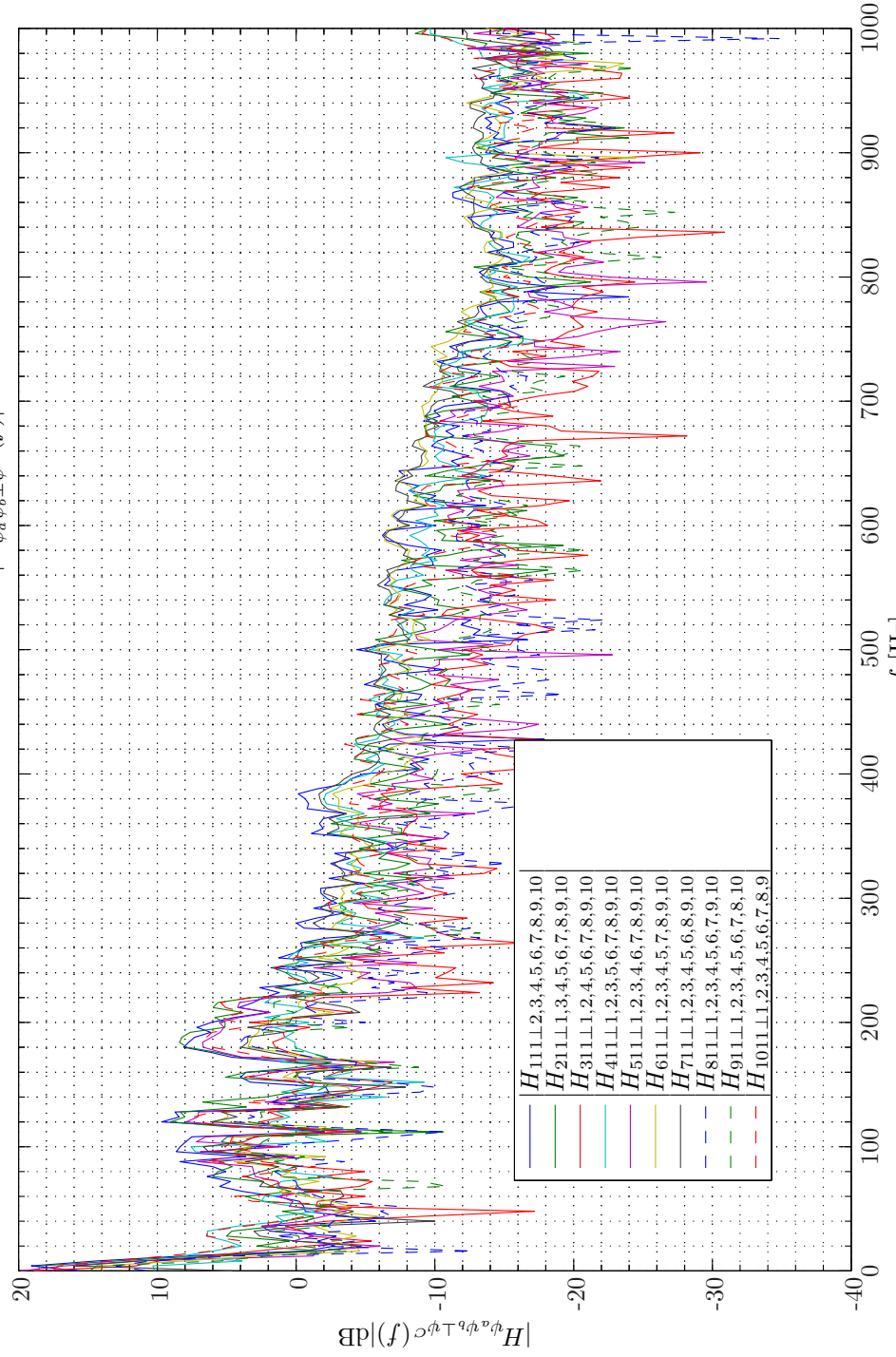

Sim 2.4.29: *Residual Transfer Function, Magnitude* JCRSA: $|H_{\psi_a\psi_b\perp\psi^C}(f)|$: **Statistical Data Analysis**: Single-Sided Modified Periodogram, f_s = 65.536 kHz, N_{DFT} = 16384, L_{DFT} = 16385, R_{DFT} = 8193, Hanning, Δf_m = 16 Hz, T_{DFT} = 0.25002 s, $N_{f,DFT}$ = 8193, Δf_{DFT} = 4 Hz, K_{DFT} = 158; *System Identification:* (Random Low-Pass (4 kHz) White Noise ($\mathcal{N}(0, 0.2)$), Elliptic LPF (f_{pass} = 900 Hz, f_{stop} = 1 kHz, A_{pass} = 1 dB, A_{stop} = 40 dB), f_s =65.536 kHz; Time: 0 − 20 s; **Topology:** BK 4949 surface microphones flush-mounted on Gentex HGU-55/P helmet mounted on a BK 4128 C HATS, Terma Earcup Audio System (Feedforward, mFx, $N_x = 10, N_e = 1, N_y = 2, N_p = 2$); *Channels:* #1 ← x_1, #2 ← x_2, #3 ← x_3, #4 ← x_4, #5 ← x_5, #6 ← x_6, #7 ← x_7, #8 ← x_8, #9 ← x_9, #10 ← x_{10}, #11 ← d_1; **Scenario:** SystemIdentification(65536Hz)PrimaryPathes/20070204T112036.

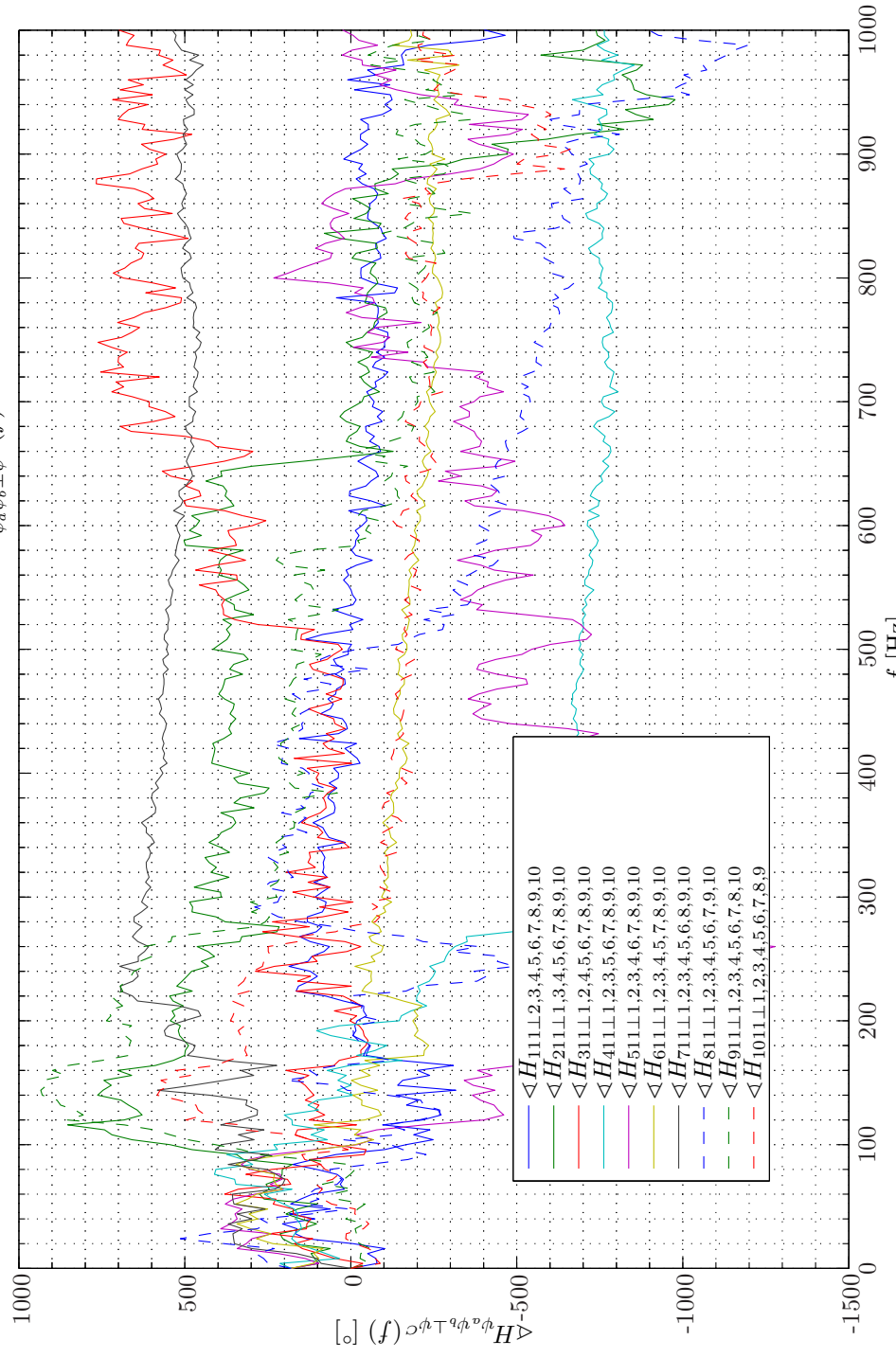

Sim 2.4.30: *Transfer Function, Phase* JCRSA: $\lhd H_{\psi_a \psi_b \perp \psi^C}(f)$: **Statistical Data Analysis**: Single-Sided Modified Periodogram, f_s = 65.536 kHz, N_{DFT} = 16384, L_{DFT} = 16385, R_{DFT} = 8193, Hanning, Δf_m = 16 Hz, T_{DFT} = 0.25002 s, $N_{f,DFT}$ = 8193, Δf_{DFT} = 4 Hz, K_{DFT} = 158; *System Identification:* (Random Low-Pass (4 kHz) White Noise ($\mathcal{N}(0, 0.2)$), Elliptic LPF (f_{pass} = 900 Hz, f_{stop} = 1 kHz, A_{pass} = 1 dB, A_{stop} = 40 dB), f_s =65.536 kHz; Time: 0 − 20 s; **Topology:** BK 4949 surface microphones flush-mounted on Gentex HGU-55/P helmet mounted on a BK 4128 C HATS, Terma Earcup Audio System (Feedforward, mFx, $N_x = 10, N_e = 1, N_y = 2, N_p = 2$); *Channels:* #1 ← x_1, #2 ← x_2, #3 ← x_3, #4 ← x_4, #5 ← x_5, #6 ← x_6, #7 ← x_7, #8 ← x_8, #9 ← x_9, #10 ← x_{10}, #11 ← d_1; **Scenario:** SystemIdentification(65536Hz)PrimaryPathes/20070204T112036.

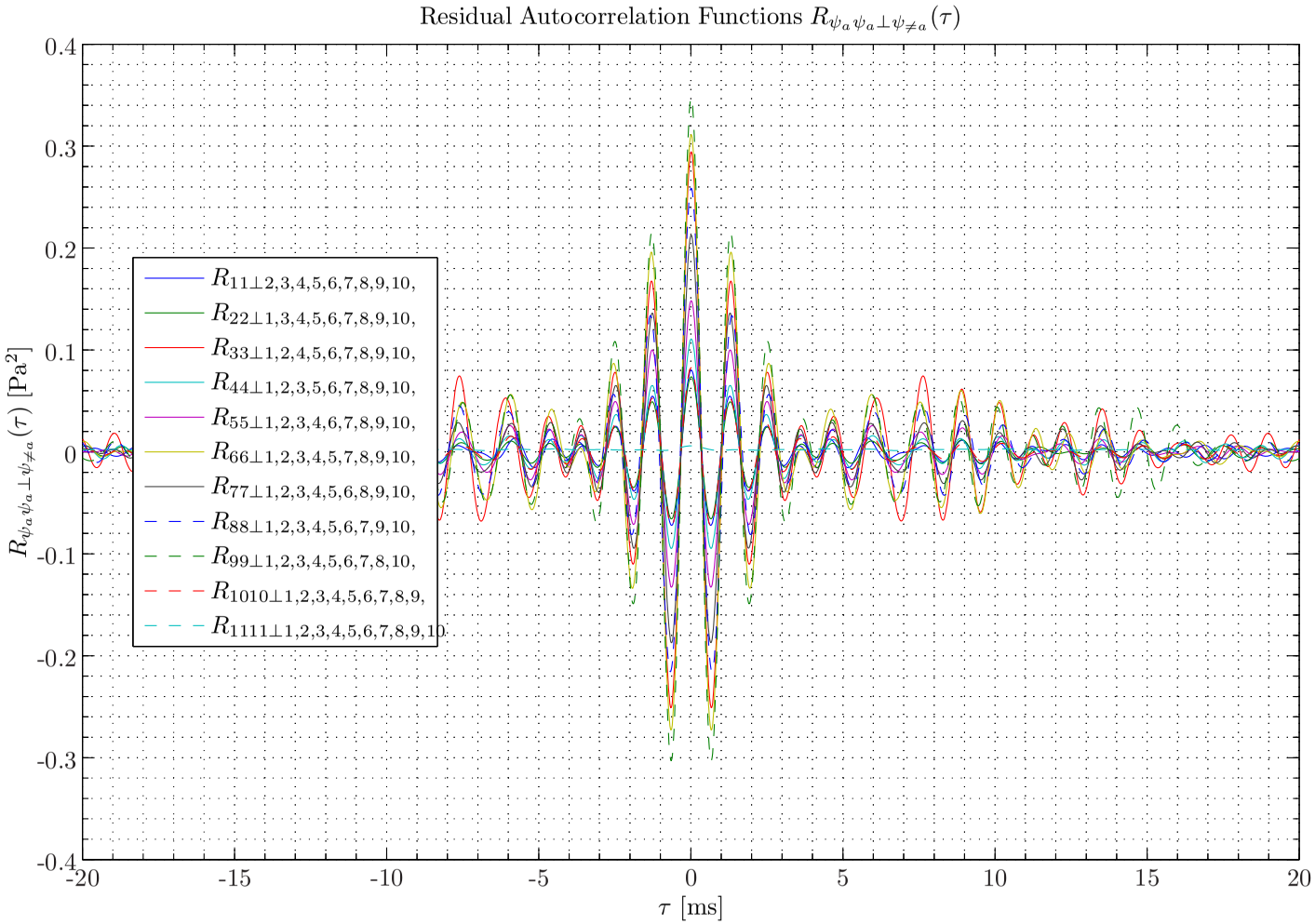

Sim 2.4.31: *Residual Autocorrelation Functions* JCRSA: $R_{\psi_a \psi_a \perp \psi_{\neq a}}(\tau)$: **Statistical Data Analysis**: Single-Sided Modified Periodogram, $f_s = 65.536$ kHz, $N_{DFT} = 16384$, $L_{DFT} = 16385$, $R_{DFT} = 8193$, Hanning, $\Delta f_m = 16$ Hz, $T_{DFT} = 0.25002$ s, $N_{f,DFT} = 8193$, $\Delta f_{DFT} = 4$ Hz, $K_{DFT} = 158$; *System Identification:* (Random Low-Pass (4 kHz) White Noise ($\mathcal{N}(0, 0.2)$), Elliptic LPF ($f_{pass} = 900$ Hz, $f_{stop} = 1$ kHz, $A_{pass} = 1$ dB, $A_{stop} = 40$ dB), f_s =65.536 kHz; Time: $0 - 20$ s; **Topology:** BK 4949 surface microphones flush-mounted on Gentex HGU-55/P helmet mounted on a BK 4128 C HATS, Terma Earcup Audio System (Feedforward, mFx, $N_x = 10, N_e = 1, N_y = 2, N_p = 2$); *Channels:* #1 $\leftarrow x_1$, #2 $\leftarrow x_2$, #3 $\leftarrow x_3$, #4 $\leftarrow x_4$, #5 $\leftarrow x_5$, #6 $\leftarrow x_6$, #7 $\leftarrow x_7$, #8 $\leftarrow x_8$, #9 $\leftarrow x_9$, #10 $\leftarrow x_{10}$, #11 $\leftarrow d_1$; **Scenario:** `SystemIdentification(65536Hz)PrimaryPathes/20070204T112036`.

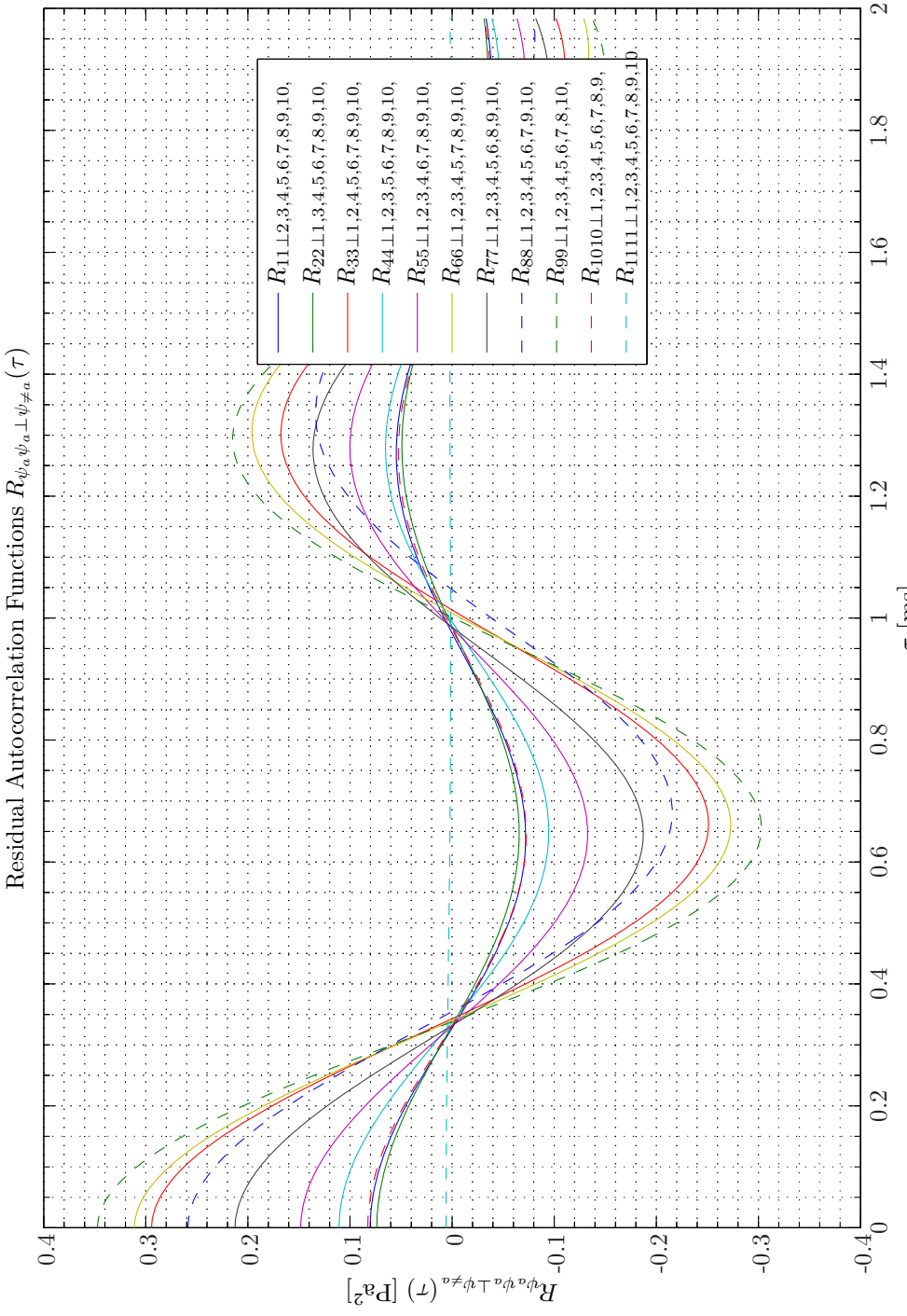

Sim 2.4.32: *Residual Autocorrelation Functions* JCRSA: $R_{\psi_a \psi_a \perp \psi_{\neq a}}(\tau)$: **Statistical Data Analysis:** Single-Sided Modified Periodogram, $f_s = 65.536$ kHz, $N_{DFT} = 16384$, $L_{DFT} = 16385$, $R_{DFT} = 8193$, Hanning, $\Delta f_m = 16$ Hz, $T_{DFT} = 0.25002$ s, $N_{f,DFT} = 8193$, $\Delta f_{DFT} = 4$ Hz, $K_{DFT} = 158$; *System Identification:* (Random Low-Pass (4 kHz) White Noise ($\mathcal{N}(0, 0.2)$), Elliptic LPF ($f_{pass} = 900$ Hz, $f_{stop} = 1$ kHz, $A_{pass} = 1$ dB, $A_{stop} = 40$ dB), f_s =65.536 kHz; Time: $0 - 20$ s; **Topology:** BK 4949 surface microphones flush-mounted on Gentex HGU-55/P helmet mounted on a BK 4128 C HATS, Terma Earcup Audio System (Feedforward, mFx, $N_x = 10, N_e = 1, N_y = 2, N_p = 2$); *Channels:* #1 $\leftarrow x_1$, #2 $\leftarrow x_2$, #3 $\leftarrow x_3$, #4 $\leftarrow x_4$, #5 $\leftarrow x_5$, #6 $\leftarrow x_6$, #7 $\leftarrow x_7$, #8 $\leftarrow x_8$, #9 $\leftarrow x_9$, #10 $\leftarrow x_{10}$, #11 $\leftarrow d_1$; **Scenario:** SystemIdentification(65536Hz)PrimaryPathes/20070204T112036.

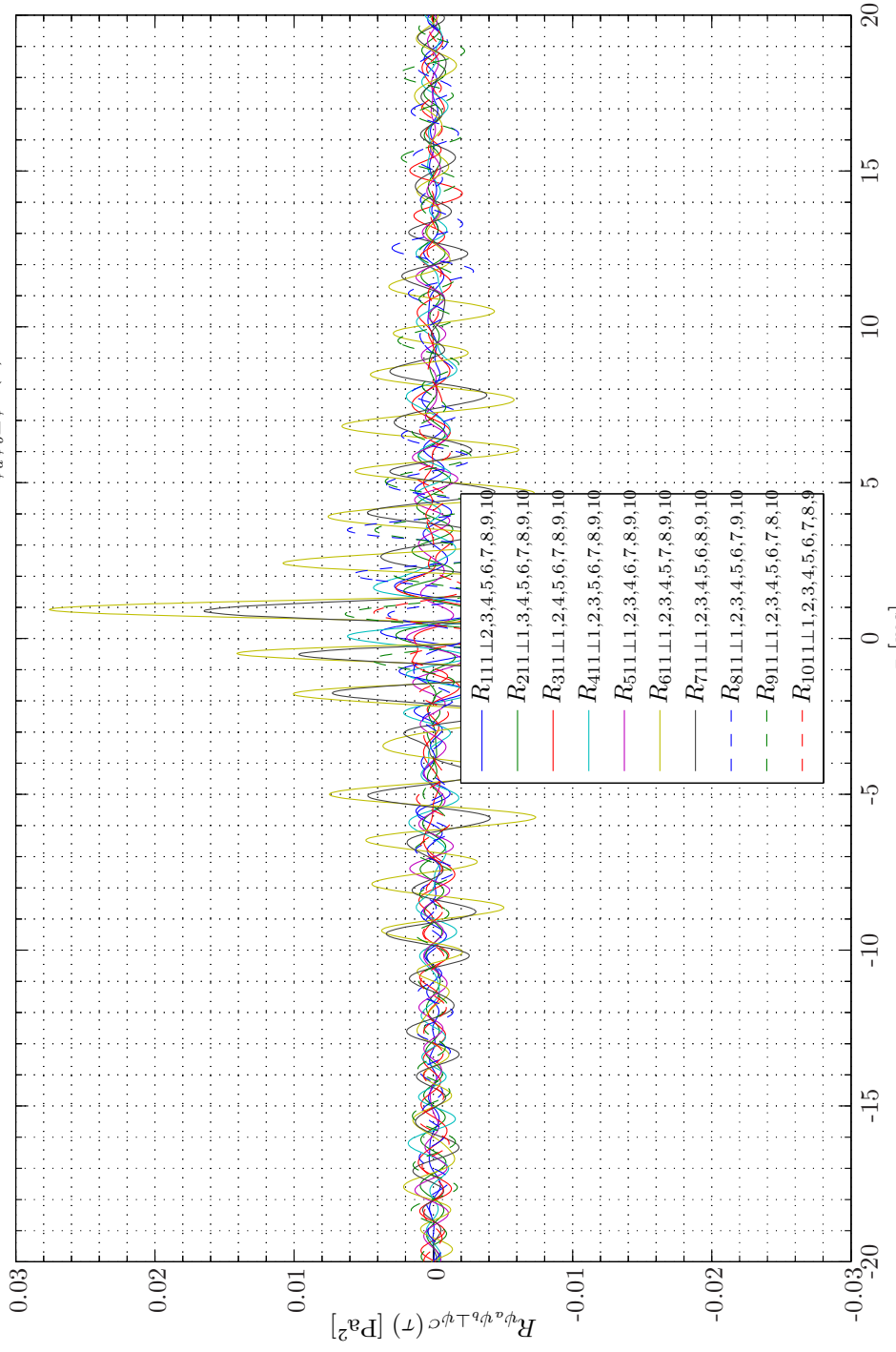

Sim 2.4.33: *Residual Cross-Correlation Functions* JCRSA: $R_{\psi_a\psi_b\perp\psi^C}(\tau)$: **Statistical Data Analysis**: Single-Sided Modified Periodogram, f_s = 65.536 kHz, N_{DFT} = 16384, L_{DFT} = 16385, R_{DFT} = 8193, Hanning, Δf_m = 16 Hz, T_{DFT} = 0.25002 s, $N_{f,DFT}$ = 8193, Δf_{DFT} = 4 Hz, K_{DFT} = 158; *System Identification:* (Random Low-Pass (4 kHz) White Noise ($\mathcal{N}(0, 0.2)$), Elliptic LPF (f_{pass} = 900 Hz, f_{stop} = 1 kHz, A_{pass} = 1 dB, A_{stop} = 40 dB), f_s =65.536 kHz; Time: 0 − 20 s; **Topology:** BK 4949 surface microphones flush-mounted on Gentex HGU-55/P helmet mounted on a BK 4128 C HATS, Terma Earcup Audio System (Feedforward, mFx, $N_x = 10, N_e = 1, N_y = 2, N_p = 2$); *Channels:* #1 ← x_1, #2 ← x_2, #3 ← x_3, #4 ← x_4, #5 ← x_5, #6 ← x_6, #7 ← x_7, #8 ← x_8, #9 ← x_9, #10 ← x_{10}, #11 ← d_1; **Scenario:** `SystemIdentification(65536Hz)PrimaryPathes/20070204T112036`.

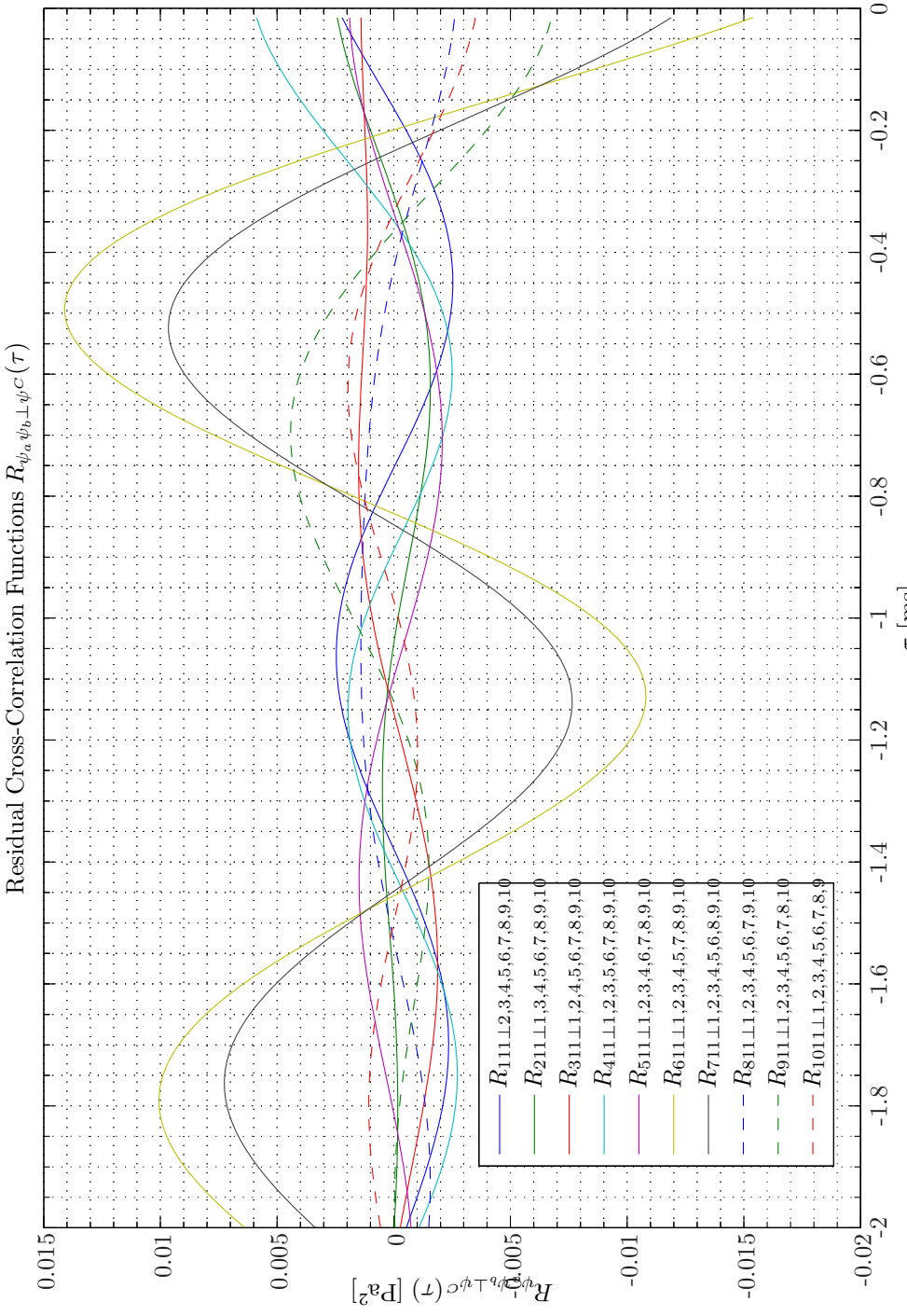

Sim 2.4.34: *Residual Cross-Correlation Functions* JCRSA: $R_{\psi_a \psi_b \perp \psi^C}(\tau)$: **Statistical Data Analysis**: Single-Sided Modified Periodogram, $f_s = 65.536$ kHz, $N_{DFT} = 16384$, $L_{DFT} = 16385$, $R_{DFT} = 8193$, Hanning, $\Delta f_m = 16$ Hz, $T_{DFT} = 0.25002$ s, $N_{f,DFT} = 8193$, $\Delta f_{DFT} = 4$ Hz, $K_{DFT} = 158$; *System Identification:* (Random Low-Pass (4 kHz) White Noise ($\mathcal{N}(0, 0.2)$), Elliptic LPF ($f_{pass} = 900$ Hz, $f_{stop} = 1$ kHz, $A_{pass} = 1$ dB, $A_{stop} = 40$ dB), f_s =65.536 kHz; Time: $0 - 20$ s; **Topology:** BK 4949 surface microphones flush-mounted on Gentex HGU-55/P helmet mounted on a BK 4128 C HATS, Terma Earcup Audio System (Feedforward, mFx, $N_x = 10, N_e = 1, N_y = 2, N_p = 2$); *Channels:* #1 $\leftarrow x_1$, #2 $\leftarrow x_2$, #3 $\leftarrow x_3$, #4 $\leftarrow x_4$, #5 $\leftarrow x_5$, #6 $\leftarrow x_6$, #7 $\leftarrow x_7$, #8 $\leftarrow x_8$, #9 $\leftarrow x_9$, #10 $\leftarrow x_{10}$, #11 $\leftarrow d_1$; **Scenario:** `SystemIdentification(65536Hz)PrimaryPathes/20070204T112036`.

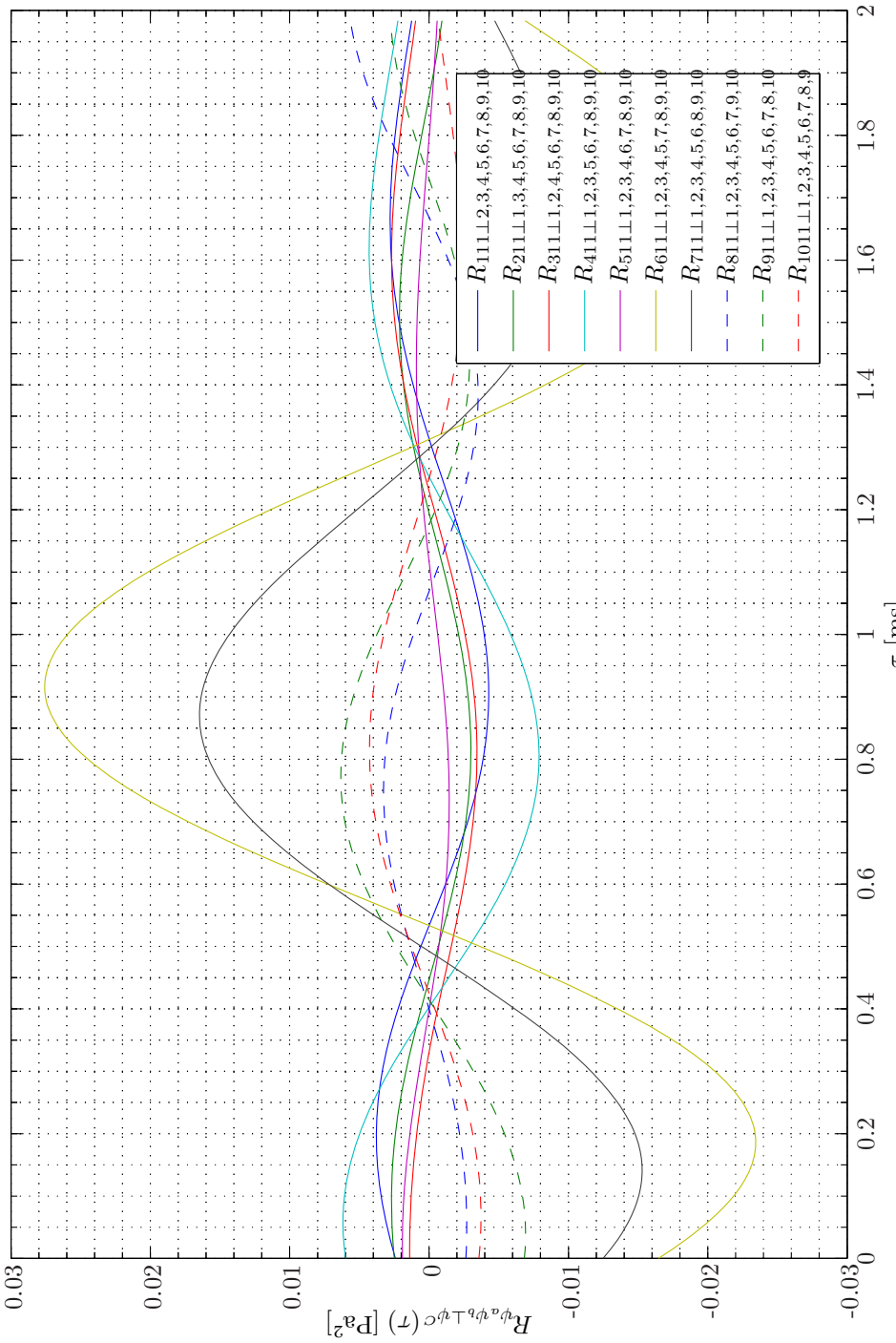

Sim 2.4.35: *Residual Cross-Correlation Functions* JCRSA: $R_{\psi_a\psi_b\perp\psi^C}(\tau)$: **Statistical Data Analysis**: Single-Sided Modified Periodogram, $f_s = 65.536$ kHz, $N_{DFT} = 16384$, $L_{DFT} = 16385$, $R_{DFT} = 8193$, Hanning, $\Delta f_m = 16$ Hz, $T_{DFT} = 0.25002$ s, $N_{f,DFT} = 8193$, $\Delta f_{DFT} = 4$ Hz, $K_{DFT} = 158$; *System Identification:* (Random Low-Pass (4 kHz) White Noise ($\mathcal{N}(0, 0.2)$), Elliptic LPF ($f_{pass} = 900$ Hz, $f_{stop} = 1$ kHz, $A_{pass} = 1$ dB, $A_{stop} = 40$ dB), f_s =65.536 kHz; Time: $0 - 20$ s; **Topology:** BK 4949 surface microphones flush-mounted on Gentex HGU-55/P helmet mounted on a BK 4128 C HATS, Terma Earcup Audio System (Feedforward, mFx, $N_x = 10, N_e = 1, N_y = 2, N_p = 2$); *Channels:* #1 $\leftarrow x_1$, #2 $\leftarrow x_2$, #3 $\leftarrow x_3$, #4 $\leftarrow x_4$, #5 $\leftarrow x_5$, #6 $\leftarrow x_6$, #7 $\leftarrow x_7$, #8 $\leftarrow x_8$, #9 $\leftarrow x_9$, #10 $\leftarrow x_{10}$, #11 $\leftarrow d_1$; **Scenario:** `SystemIdentification(65536Hz)PrimaryPathes/20070204T112036`.

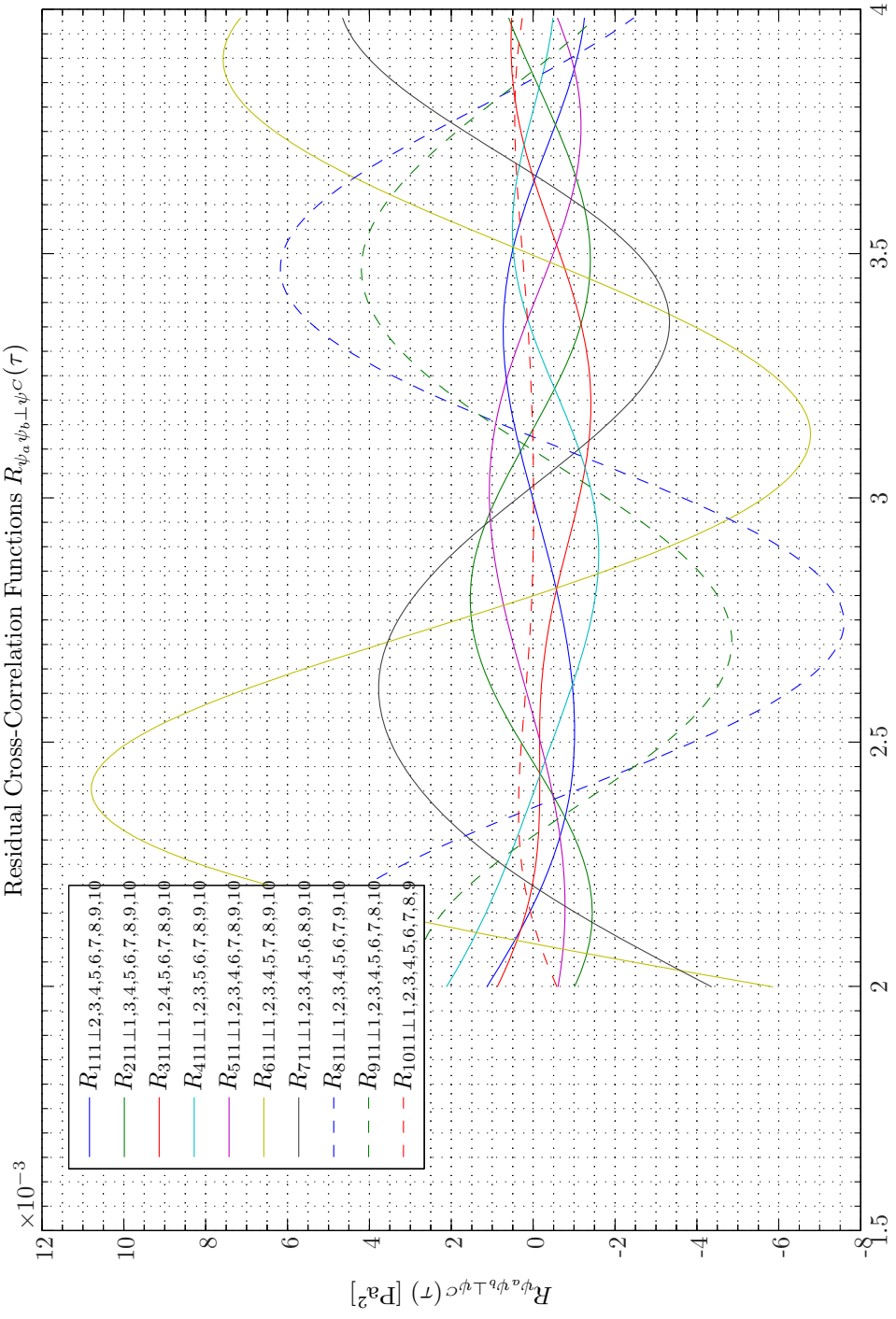

Sim 2.4.36: *Residual Cross-Correlation Functions* JCRSA: $R_{\psi_a \psi_b \perp \psi^C}(\tau)$: **Statistical Data Analysis**: Single-Sided Modified Periodogram, $f_s = 65.536$ kHz, $N_{DFT} = 16384$, $L_{DFT} = 16385$, $R_{DFT} = 8193$, Hanning, $\Delta f_m = 16$ Hz, $T_{DFT} = 0.25002$ s, $N_{f,DFT} = 8193$, $\Delta f_{DFT} = 4$ Hz, $K_{DFT} = 158$; *System Identification:* (Random Low-Pass (4 kHz) White Noise ($\mathcal{N}(0, 0.2)$), Elliptic LPF ($f_{pass} = 900$ Hz, $f_{stop} = 1$ kHz, $A_{pass} = 1$ dB, $A_{stop} = 40$ dB), f_s =65.536 kHz; Time: $0 - 20$ s; **Topology:** BK 4949 surface microphones flush-mounted on Gentex HGU-55/P helmet mounted on a BK 4128 C HATS, Terma Earcup Audio System (Feedforward, mFx, $N_x = 10, N_e = 1, N_y = 2, N_p = 2$); *Channels:* #1 $\leftarrow x_1$, #2 $\leftarrow x_2$, #3 $\leftarrow x_3$, #4 $\leftarrow x_4$, #5 $\leftarrow x_5$, #6 $\leftarrow x_6$, #7 $\leftarrow x_7$, #8 $\leftarrow x_8$, #9 $\leftarrow x_9$, #10 $\leftarrow x_{10}$, #11 $\leftarrow d_1$; **Scenario:** SystemIdentification(65536Hz)PrimaryPathes/20070204T112036.

Signal	x_1	x_2	x_3	x_4	x_5	x_6	x_7	x_8	x_9	x_{10}
τ_{xd_1}	0.91	0.82	0.81	0.81	−0.70	0.92	0.87	2.75	0.05	0.82

Tab. 2.4: System Identification of Primary Pathes $G_{ex}^{j,m}$, Acquisition Lead Times in ms.

can compensate for the delays in the secondary paths (refer to section 11.5 on page 489) as discussed in Appendix A on page 529. The acquisition time lag between reference sensor 5 and the error sensor can probably be attributed to the lack of coherence between these signals cf. Simulation 2.4.5 on page 41. By inspection of Simulation 2.4.34 - 2.4.36 on pages 74–76 we appreciate that the cross-correlation function for this channel pair, that is, $R_{x_5 d_1}$ is very flat with no significant peaks. Accordingly, this spatially-weighted-averaged acquisition lead time is very uncertain. The same considerations apply to the large spatially-weighted-averaged acquisition lead time predicted for reference sensor 8. The vanishing spatially-weighted-averaged acquisition lead time provided by reference sensor 9 as depicted in Figure 2.3 on page 35 may be attributed to the high temporal sidelobes rendering the maximum response insignificant.

Now returning to the use of a low-pass filter (LPF) for bandwidth limitation proclaimed in section 2.4 on page 32. The coresponding results for the cross-correlation functions without a LPF are illuminated in Simulation 2.4.37 - 2.4.40 on pages 78–81.

The calculated spatially-weighted-averaged acquisition lead times are tabulated in Table 2.5

Signal	x_1	x_2	x_3	x_4	x_5	x_6	x_7	x_8	x_9	x_{10}
τ_{xd_1}	0.85	0.76	0.87	0.71	0.03	0.87	0.79	2.65	−0.04	0.73

Tab. 2.5: System Identification of Primary Pathes $G_{ex}^{j,m}$, Acquisition Lead Times in ms.

By comparison of Table 2.4 and Table 2.5 we see that the predicted spatially-weighted-averaged acquisition lead times are very similar except for reference sensor 5. Hence, by excluding the frequency band above 900 Hz from the analysis essentially no loss in information takes place. It should, however, be emphasized that the nature of the problem cannot be fully described in terms of a single time quantity. In a more advanced analysis we should also consider the first, say, two temporal sidelobes. However, it can readily be observed that the main part of the energy is present with a lead time.

With the availability of estimates of the propagation delays that prevail between the reference sensors and the error sensor, it is time to assess if these delays could lead to potential bias errors in the ordinary coherence function estimates. As discussed in subsection C.3.2 on page 542 negative bias is introduced to the estimates of cross-spectral density functions, transfer functions and ordinary coherence functions (and therefore also to the multiple coherence functions) if such delays form a small but non-negligible fractions of the DFT time. We may use (C.3.6c) to obtain a factor by which the ordinary coherence function is underestimated: $\frac{\hat{\gamma}^2_{\psi_a\psi_b}(f)}{\gamma^2_{\psi_a\psi_b}(f)} = \left(1 - \frac{1\text{ ms}}{250\text{ ms}}\right)^2 \approx 0.992$. Accordingly, even if a perfect ordinary coherence function between a reference sensor and an error sensor actually is present, if this propagation delay is not taken into account, we may erroneously conclude that the attenuation cannot to exceed 21 dB. However, this estimate represents a sort of worst case bias estimate based on the assumption that two neighboring DFT records are completely decorrelated. In an earlier analysis with $T_{DFT} = 64$ ms the bias was underestimated by a factor $\left(1 - \frac{1\text{ ms}}{64\text{ ms}}\right)^2 \approx 0.969$ corresponding to a 15 dB attenuation floor.

The corresponding conditioned impulse response functions are shown in Simulation 2.4.41 on page 83. The impulse nature owing to the large gain factor $|H_{\phi_a\phi_b\perp\phi^C}|$ at low frequencies shown

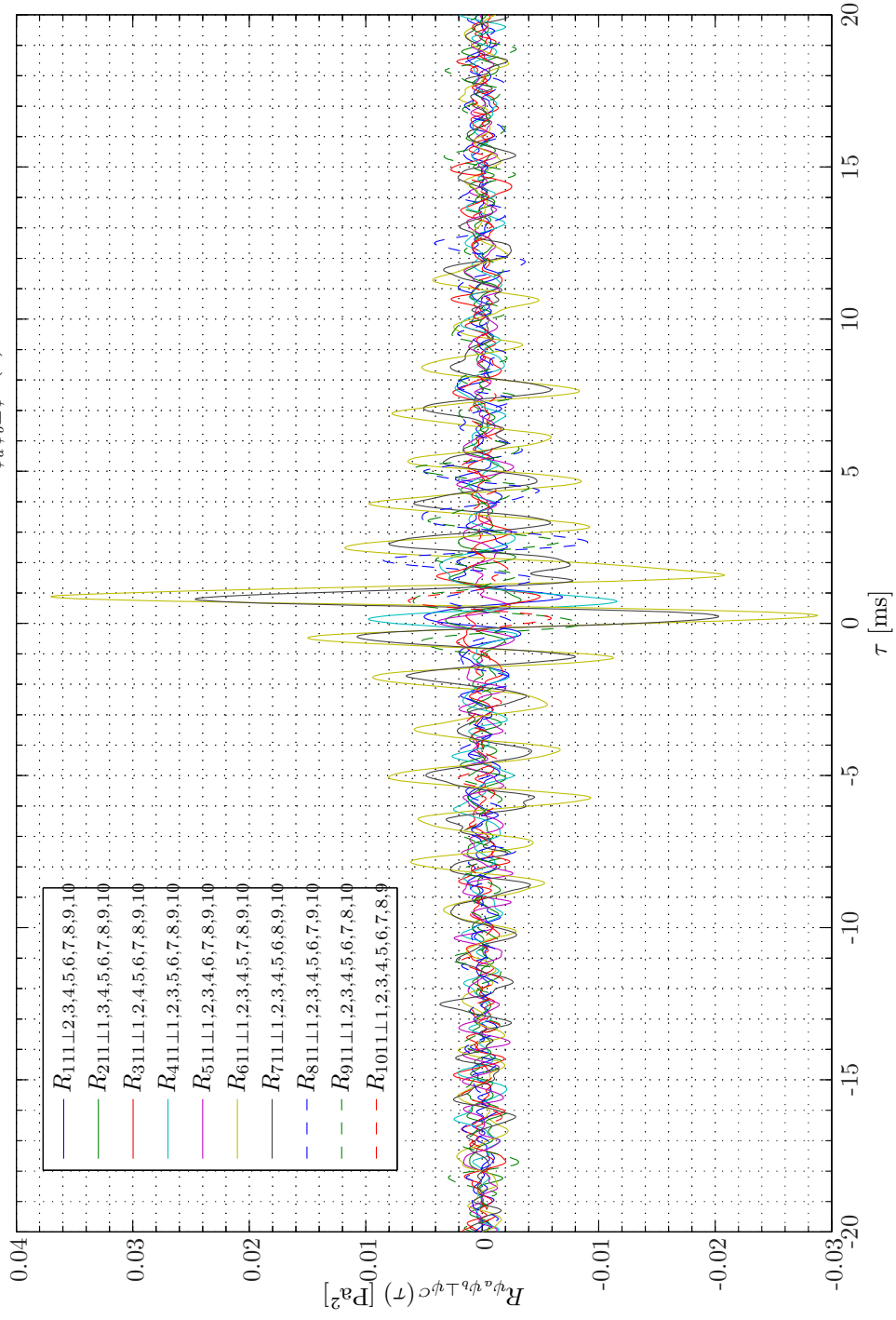

Sim 2.4.37: *Residual Cross-Correlation Functions* JCRSA: $R_{\psi_a \psi_b \perp \psi^C}(\tau)$: **Statistical Data Analysis**: Single-Sided Modified Periodogram, $f_s = 65.536$ kHz, $N_{DFT} = 16384$, $L_{DFT} = 16385$, $R_{DFT} = 8193$, Hanning, $\Delta f_m = 16$ Hz, $T_{DFT} = 0.25002$ s, $N_{f,DFT} = 8193$, $\Delta f_{DFT} = 4$ Hz, $K_{DFT} = 158$; *System Identification:* (Random Low-Pass (4 kHz) White Noise ($\mathcal{N}(0, 0.2)$),f_s =65.536 kHz; Time: $0 - 20$ s; **Topology:** BK 4949 surface microphones flush-mounted on Gentex HGU-55/P helmet mounted on a BK 4128 C HATS, Terma Earcup Audio System (Feedforward, mFx, $N_x = 10, N_e = 1, N_y = 2, N_p = 2$); *Channels:* #1 $\leftarrow x_1$, #2 $\leftarrow x_2$, #3 $\leftarrow x_3$, #4 $\leftarrow x_4$, #5 $\leftarrow x_5$, #6 $\leftarrow x_6$, #7 $\leftarrow x_7$, #8 $\leftarrow x_8$, #9 $\leftarrow x_9$, #10 $\leftarrow x_{10}$, #11 $\leftarrow d_i$; **Scenario:** `SystemIdentification(65536Hz)PrimaryPathes/20070204T143126`.

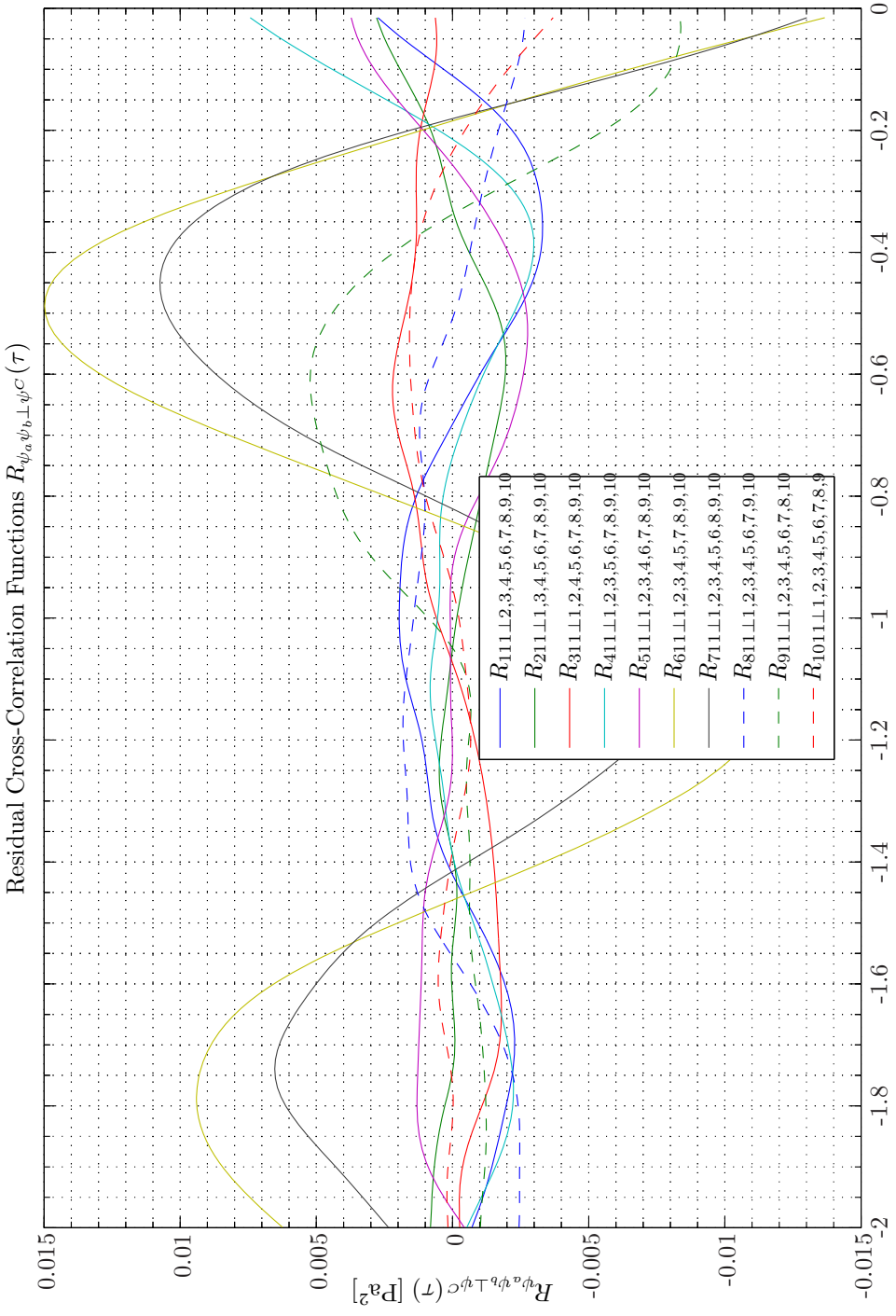

Sim 2.4.38: *Residual Cross-Correlation Functions* JCRSA: $R_{\psi_a\psi_b\perp\psi^C}(\tau)$: **Statistical Data Analysis**: Single-Sided Modified Periodogram, $f_s = 65.536$ kHz, $N_{DFT} = 16384$, $L_{DFT} = 16385$, $R_{DFT} = 8193$, Hanning, $\Delta f_m = 16$ Hz, $T_{DFT} = 0.25002$ s, $N_{f,DFT} = 8193$, $\Delta f_{DFT} = 4$ Hz, $K_{DFT} = 158$; *System Identification:* (Random Low-Pass (4 kHz) White Noise ($\mathcal{N}(0, 0.2)$),f_s =65.536 kHz; Time: 0 − 20 s; **Topology:** BK 4949 surface microphones flush-mounted on Gentex HGU-55/P helmet mounted on a BK 4128 C HATS, Terma Earcup Audio System (Feedforward, mFx, $N_x = 10$, $N_e = 1$, $N_y = 2$, $N_p = 2$); *Channels:* #1 ← x_1, #2 ← x_2, #3 ← x_3, #4 ← x_4, #5 ← x_5, #6 ← x_6, #7 ← x_7, #8 ← x_8, #9 ← x_9, #10 ← x_{10}, #11 ← d_1; **Scenario:** `SystemIdentification(65536Hz)PrimaryPathes/20070204T143126`.

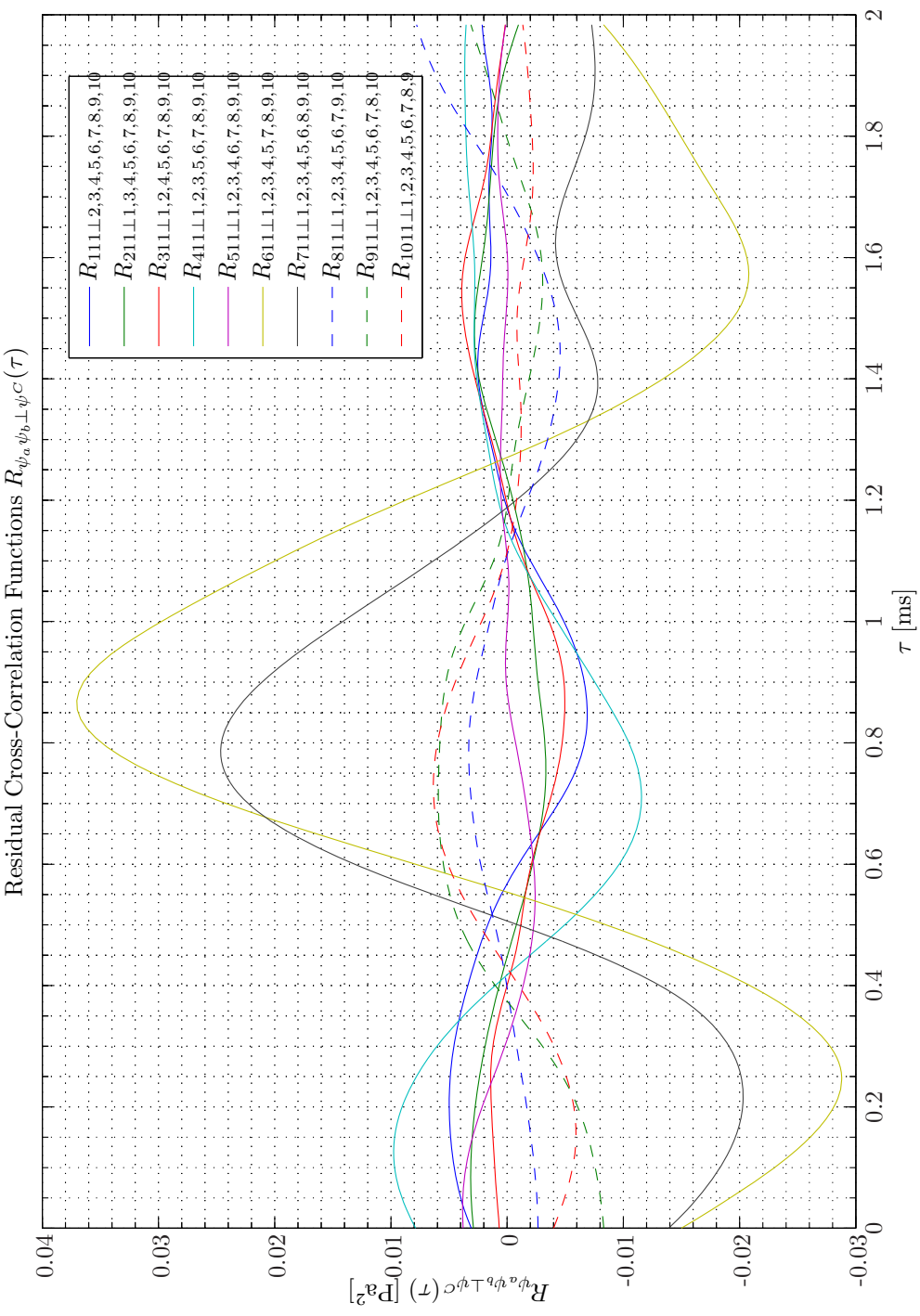

Sim 2.4.39: *Residual Cross-Correlation Functions* JCRSA: $R_{\psi_a \psi_b \perp \psi^C}(\tau)$: **Statistical Data Analysis**: Single-Sided Modified Periodogram, $f_s = 65.536$ kHz, $N_{DFT} = 16384$, $L_{DFT} = 16385$, $R_{DFT} = 8193$, Hanning, $\Delta f_m = 16$ Hz, $T_{DFT} = 0.25002$ s, $N_{f,DFT} = 8193$, $\Delta f_{DFT} = 4$ Hz, $K_{DFT} = 158$; *System Identification:* (Random Low-Pass (4 kHz) White Noise ($\mathcal{N}(0, 0.2)$),f_s =65.536 kHz; Time: $0 - 20$ s; **Topology:** BK 4949 surface microphones flush-mounted on Gentex HGU-55/P helmet mounted on a BK 4128 C HATS, Terma Earcup Audio System (Feedforward, mFx, $N_x = 10, N_e = 1, N_y = 2, N_p = 2$); *Channels:* #1 $\leftarrow x_1$, #2 $\leftarrow x_2$, #3 $\leftarrow x_3$, #4 $\leftarrow x_4$, #5 $\leftarrow x_5$, #6 $\leftarrow x_6$, #7 $\leftarrow x_7$, #8 $\leftarrow x_8$, #9 $\leftarrow x_9$, #10 $\leftarrow x_{10}$, #11 $\leftarrow d_1$; **Scenario:** `SystemIdentification(65536Hz)PrimaryPathes/20070204T143126`.

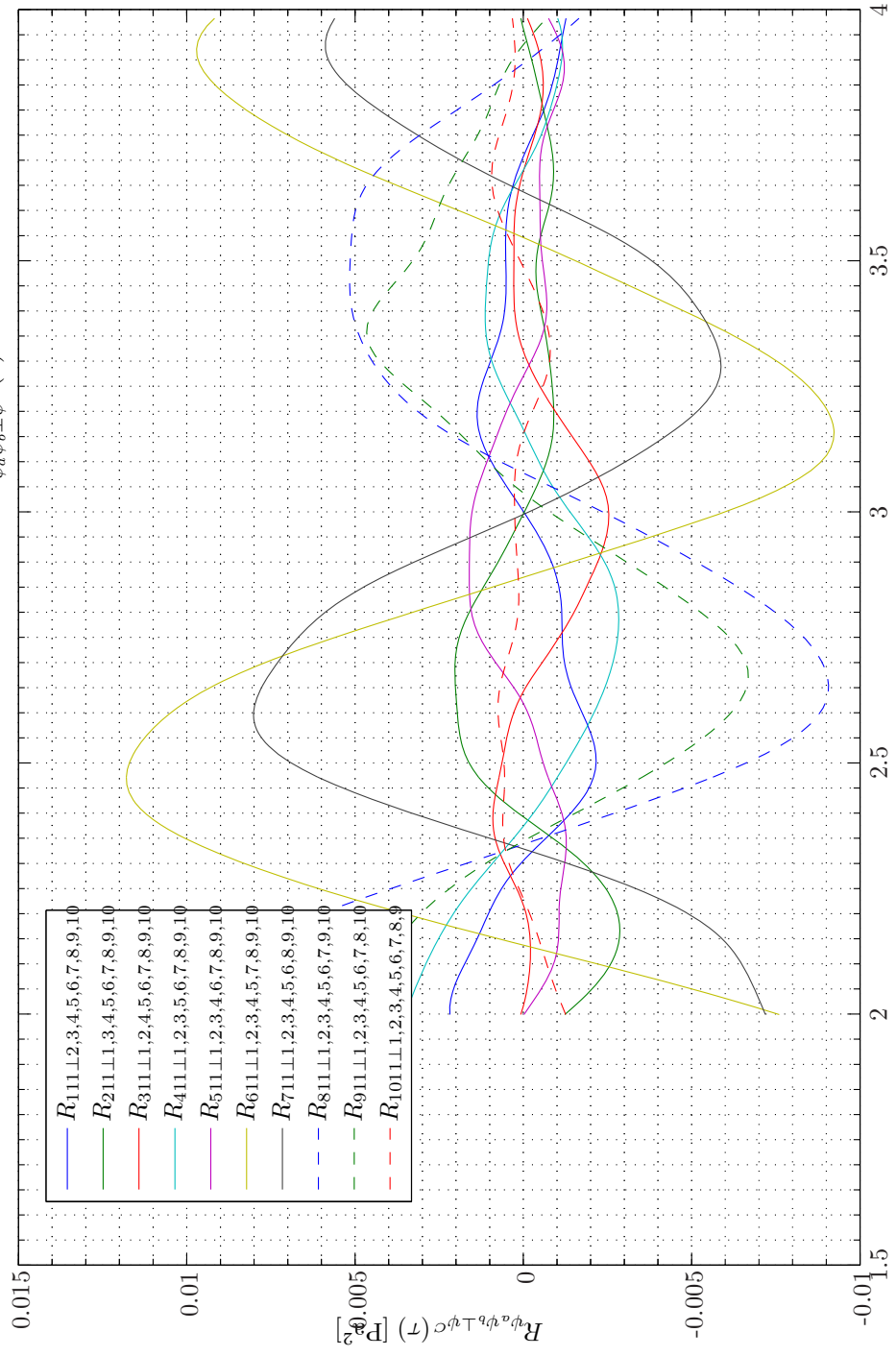

Sim 2.4.40: *Residual Cross-Correlation Functions* JCRSA: $R_{\psi_a\psi_b\perp\psi^C}(\tau)$: **Statistical Data Analysis**: Single-Sided Modified Periodogram, $f_s = 65.536$ kHz, $N_{DFT} = 16384$, $L_{DFT} = 16385$, $R_{DFT} = 8193$, Hanning, $\Delta f_m = 16$ Hz, $T_{DFT} = 0.25002$ s, $N_{f,DFT} = 8193$, $\Delta f_{DFT} = 4$ Hz, $K_{DFT} = 158$; *System Identification:* (Random Low-Pass (4 kHz) White Noise ($\mathcal{N}(0, 0.2)$),f_s =65.536 kHz; Time: $0 - 20$ s; **Topology:** BK 4949 surface microphones flush-mounted on Gentex HGU-55/P helmet mounted on a BK 4128 C HATS, Terma Earcup Audio System (Feedforward, mFx, $N_x = 10, N_e = 1, N_y = 2, N_p = 2$); *Channels:* #1 $\leftarrow x_1$, #2 $\leftarrow x_2$, #3 $\leftarrow x_3$, #4 $\leftarrow x_4$, #5 $\leftarrow x_5$, #6 $\leftarrow x_6$, #7 $\leftarrow x_7$, #8 $\leftarrow x_8$, #9 $\leftarrow x_9$, #10 $\leftarrow x_{10}$, #11 $\leftarrow d_1$; **Scenario:** `SystemIdentification(65536Hz)PrimaryPathes/20070204T143126`.

in Simulation 2.4.29 on page 69 completely dominates.

In Appendix A on page 529 we will consider the concept of group delays as representing delays encountered in primary the electrical circuitry of an ANR system. This is useful for the assessment of delay limited performance which is of particular importance in feedback system (FBS). For comparison with previous results the group delays estimates are depicted in Simulation 2.4.42 - 2.4.43 on pages 84–85. From these figures it is evidently clear that the concept of group delays provide little information regarding the delay encountered in a physical spatially extended system.

System Identification of Primary Pathes $G_{px}^{j,k}$

System Identification of Primary Performance Pathes $G_{px}^{j,k}$, Ordinary Analysis

For the UUT depicted in Figure 2.1 - 2.2 on pages 33–34 the pair of performance sensors and error sensors are positioned relative close to one another as seen from the 10 reference sensors. Accordingly the primary performance paths $G_{px}^{j,k}$ expectably will exhibit similar coherence behavior as for the primary paths $G_{ex}^{j,m}$ described in subsection 2.4.3 on page 34. We will therefore only accentuate the main results.

The MCOFs for the first performance sensor, that is, d_1^p are displayed in Simulation 2.4.44 - 2.4.47 on pages 86–89 and for the second performance sensor, that is, d_2^p in Simulation 2.4.48 - 2.4.51 on pages 90–93.

As observed, attenuation above 10 dB is predicted attainable up to $800 - 900$ Hz for both the left and the right ear system. Also for the primary paths no apparent saturation in the MCOF with increasing number of reference sensors is seen. Hence, by including additional reference sensors the upper frequency limit determined by the MCOF would most likely increase as a consequence of closer spatial sampling.

It should be observed that the ordinary coherence function-based reference signal sorting order is the same for the left ear performance signal, that is, d_1^p as for the left ear error signal in Simulation 2.4.5 - 2.4.6 on pages 41–42. Hence, owing to different positions of the two performance sensors relative to the 10 reference sensors the reference signal sorting order for the right ear performance signal, that is, d_2^p is different.

System Identification of Primary Pathes $G_{px}^{j,k}$, JCRSA

The calculated spatially-weighted-averaged acquisition lead times are tabulated in Table 2.6.

Signal	x_1	x_2	x_3	x_4	x_5	x_6	x_7	x_8	x_9	x_{10}
$\tau_{xd_1^p}$	0.89	0.79	0.78	0.79	-0.72	0.89	0.85	2.73	0.03	0.79
$\tau_{xd_2^p}$	2.69	0.96	1.50	1.89	7.49	2.66	2.56	1.01	0.96	2.72

Tab. 2.6: System Identification of Primary Pathes $G_{px}^{j,k}$, Acquisition Lead Times in ms.

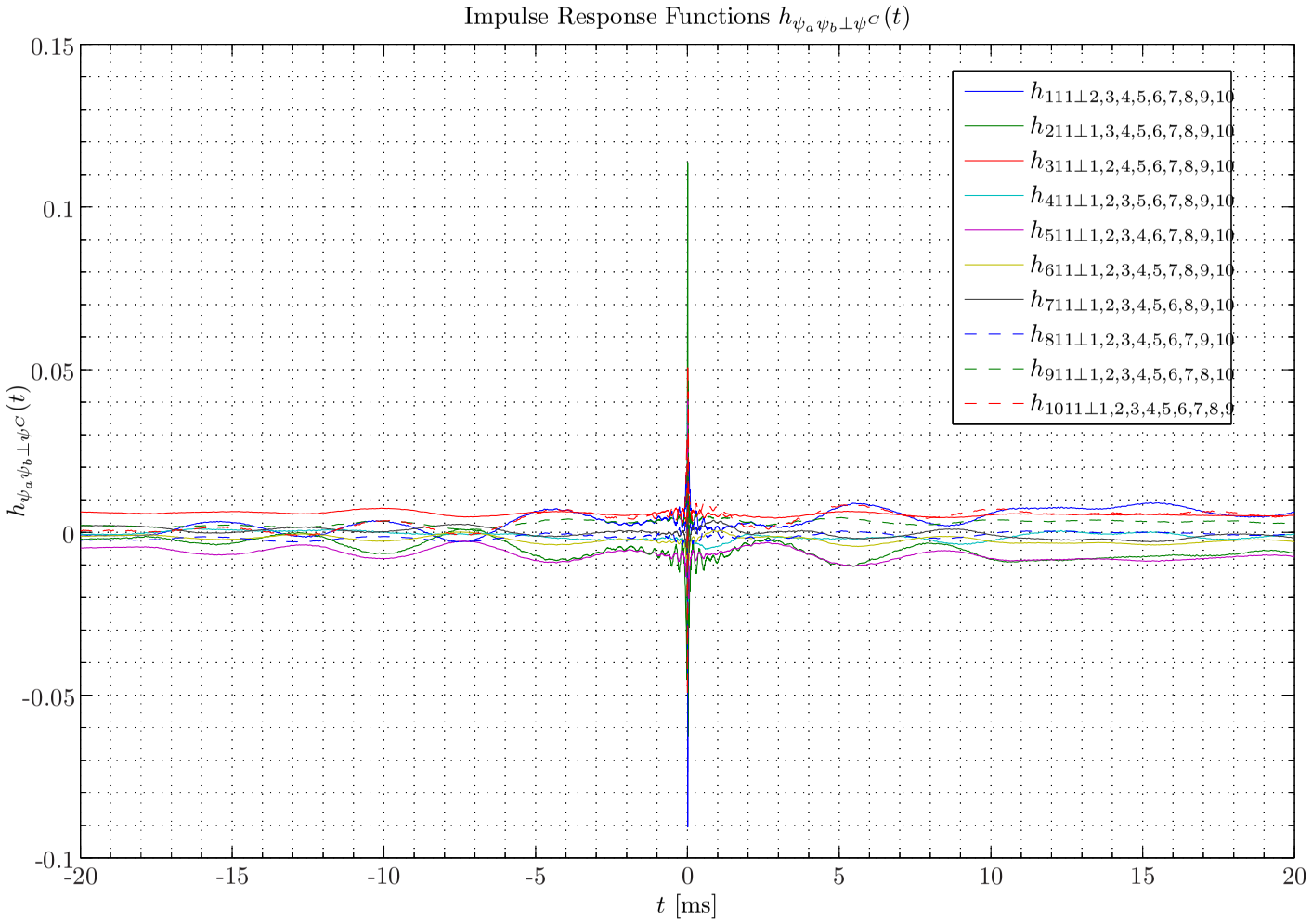

Sim 2.4.41: *Impulse Response Functions* JCRSA: $h_{\psi_a\psi_b\perp\psi^C}(t)$: **Statistical Data Analysis**: Single-Sided Modified Periodogram, f_s = 65.536 kHz, N_{DFT} = 16384, L_{DFT} = 16385, R_{DFT} = 8193, Hanning, Δf_m = 16 Hz, T_{DFT} = 0.25002 s, $N_{f,DFT}$ = 8193, Δf_{DFT} = 4 Hz, K_{DFT} = 158; *System Identification:* (Random Low-Pass (4 kHz) White Noise ($\mathcal{N}(0, 0.2)$), Elliptic LPF (f_{pass} = 900 Hz, f_{stop} = 1 kHz, A_{pass} = 1 dB, A_{stop} = 40 dB), f_s =65.536 kHz; Time: $0 - 20$ s; **Topology:** BK 4949 surface microphones flush-mounted on Gentex HGU-55/P helmet mounted on a BK 4128 C HATS, Terma Earcup Audio System (Feedforward, mFx, $N_x = 10, N_e = 1, N_y = 2, N_p = 2$); *Channels:* #1 $\leftarrow x_1$, #2 $\leftarrow x_2$, #3 $\leftarrow x_3$, #4 $\leftarrow x_4$, #5 $\leftarrow x_5$, #6 $\leftarrow x_6$, #7 $\leftarrow x_7$, #8 $\leftarrow x_8$, #9 $\leftarrow x_9$, #10 $\leftarrow x_{10}$, #11 $\leftarrow d_1$; **Scenario:** `SystemIdentification(65536Hz)PrimaryPathes/20070204T112036`.

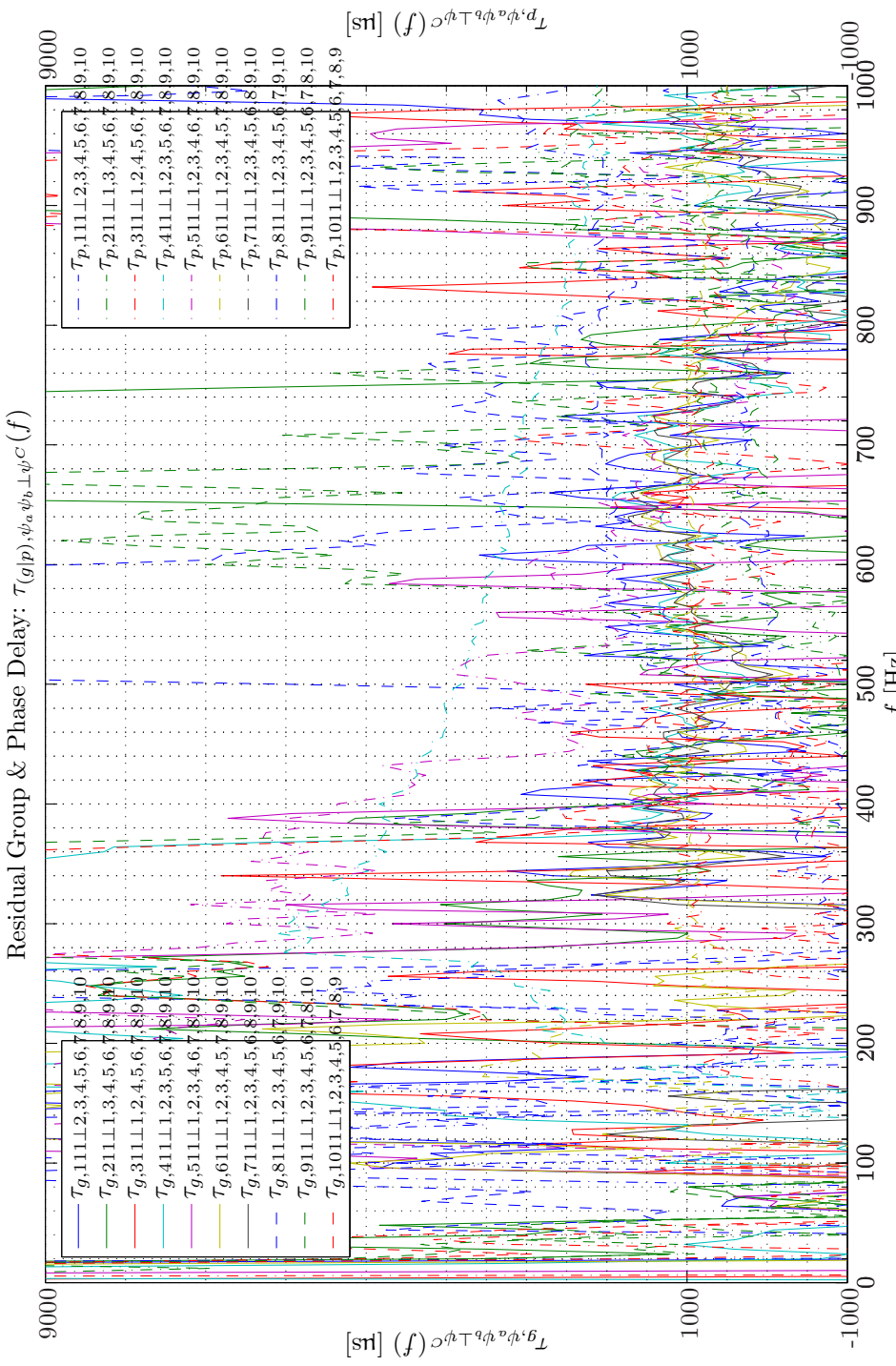

Sim 2.4.42: *Residual Group & Phase Delay* JCRSA: $\tau_{(g|p),\psi_a\psi_b\perp\psi^C}(f)$: **Statistical Data Analysis**: Single-Sided Modified Periodogram, $f_s = 65.536$ kHz, $N_{DFT} = 16384$, $L_{DFT} = 16385$, $R_{DFT} = 8193$, Hanning, $\Delta f_m = 16$ Hz, $T_{DFT} = 0.25002$ s, $N_{f,DFT} = 8193$, $\Delta f_{DFT} = 4$ Hz, $K_{DFT} = 158$; *System Identification:* (Random Low-Pass (4 kHz) White Noise ($\mathcal{N}(0, 0.2)$), Elliptic LPF ($f_{pass} = 900$ Hz, $f_{stop} = 1$ kHz, $A_{pass} = 1$ dB, $A_{stop} = 40$ dB), f_s =65.536 kHz; Time: $0 - 20$ s; **Topology:** BK 4949 surface microphones flush-mounted on Gentex HGU-55/P helmet mounted on a BK 4128 C HATS, Terma Earcup Audio System (Feedforward, mFx, $N_x = 10, N_e = 1, N_y = 2, N_p = 2$); *Channels:* #1 $\leftarrow x_1$, #2 $\leftarrow x_2$, #3 $\leftarrow x_3$, #4 $\leftarrow x_4$, #5 $\leftarrow x_5$, #6 $\leftarrow x_6$, #7 $\leftarrow x_7$, #8 $\leftarrow x_8$, #9 $\leftarrow x_9$, #10 $\leftarrow x_{10}$, #11 $\leftarrow d_1$; **Scenario:** `SystemIdentification(65536Hz)PrimaryPathes/20070204T112036`.

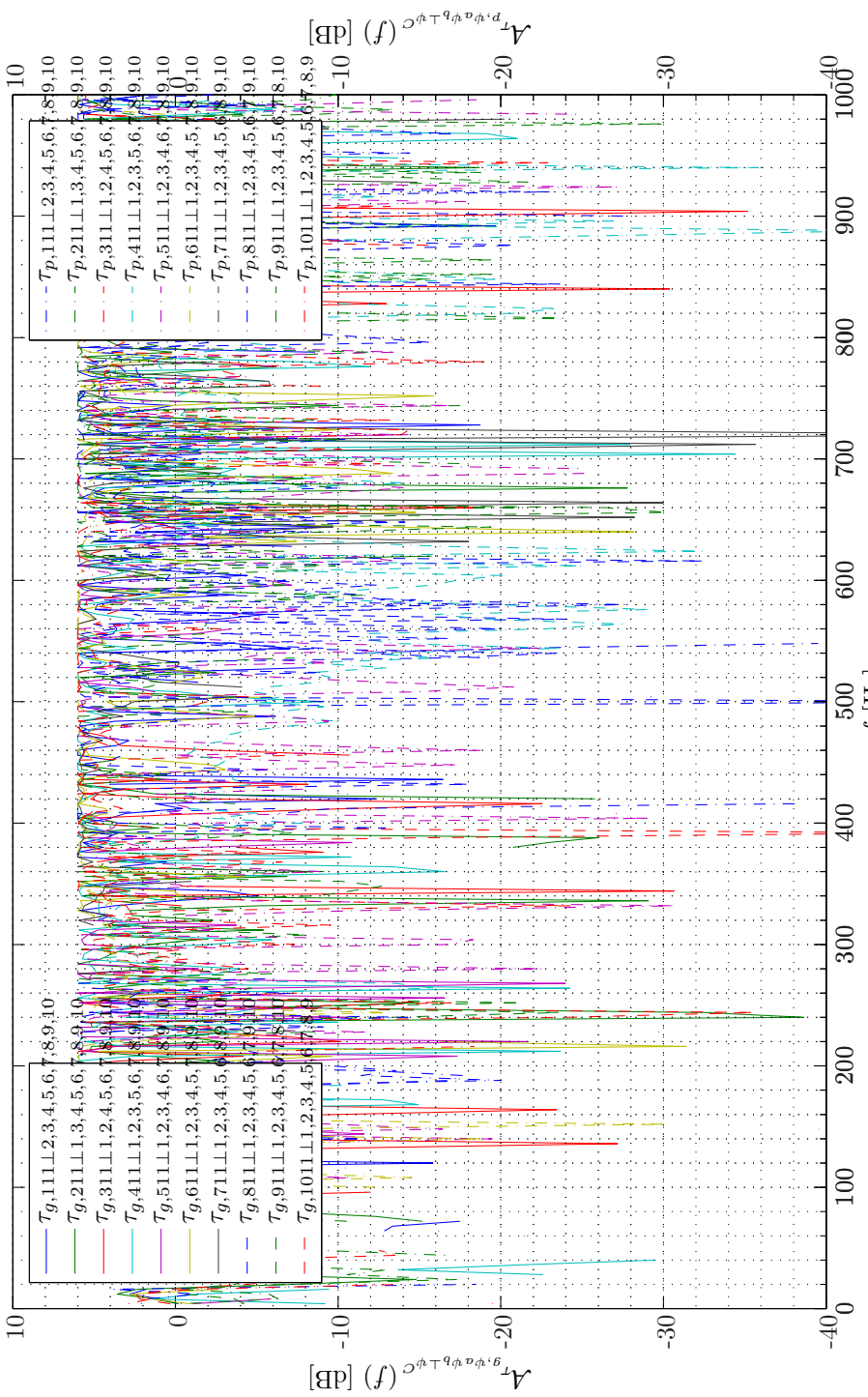

Sim 2.4.43: *Residual Attenuation vs Group & Phase Delay* $20\log_{10}|1-\mathrm{e}^{-\imath 2\pi f \tau_g}|$: **Statistical Data Analysis**: Single-Sided Modified Periodogram, f_s = 65.536 kHz, N_{DFT} = 16384, L_{DFT} = 16385, R_{DFT} = 8193, Hanning, Δf_m = 16 Hz, T_{DFT} = 0.25002 s, $N_{f,DFT}$ = 8193, Δf_{DFT} = 4 Hz, K_{DFT} = 158; *System Identification:* (Random Low-Pass (4 kHz) White Noise ($\mathcal{N}(0,0.2)$), Elliptic LPF (f_{pass} = 900 Hz, f_{stop} = 1 kHz, A_{pass} = 1 dB, A_{stop} = 40 dB), f_s =65.536 kHz; Time: 0 − 20 s; **Topology:** BK 4949 surface microphones flush-mounted on Gentex HGU-55/P helmet mounted on a BK 4128 C HATS, Terma Earcup Audio System (Feedforward, mFx, $N_x = 10, N_e = 1, N_y = 2, N_p = 2$); *Channels:* #1 ← x_1, #2 ← x_2, #3 ← x_3, #4 ← x_4, #5 ← x_5, #6 ← x_6, #7 ← x_7, #8 ← x_8, #9 ← x_9, #10 ← x_{10}, #11 ← d_1; **Scenario:** SystemIdentification(65536Hz)PrimaryPathes/20070204T112036.

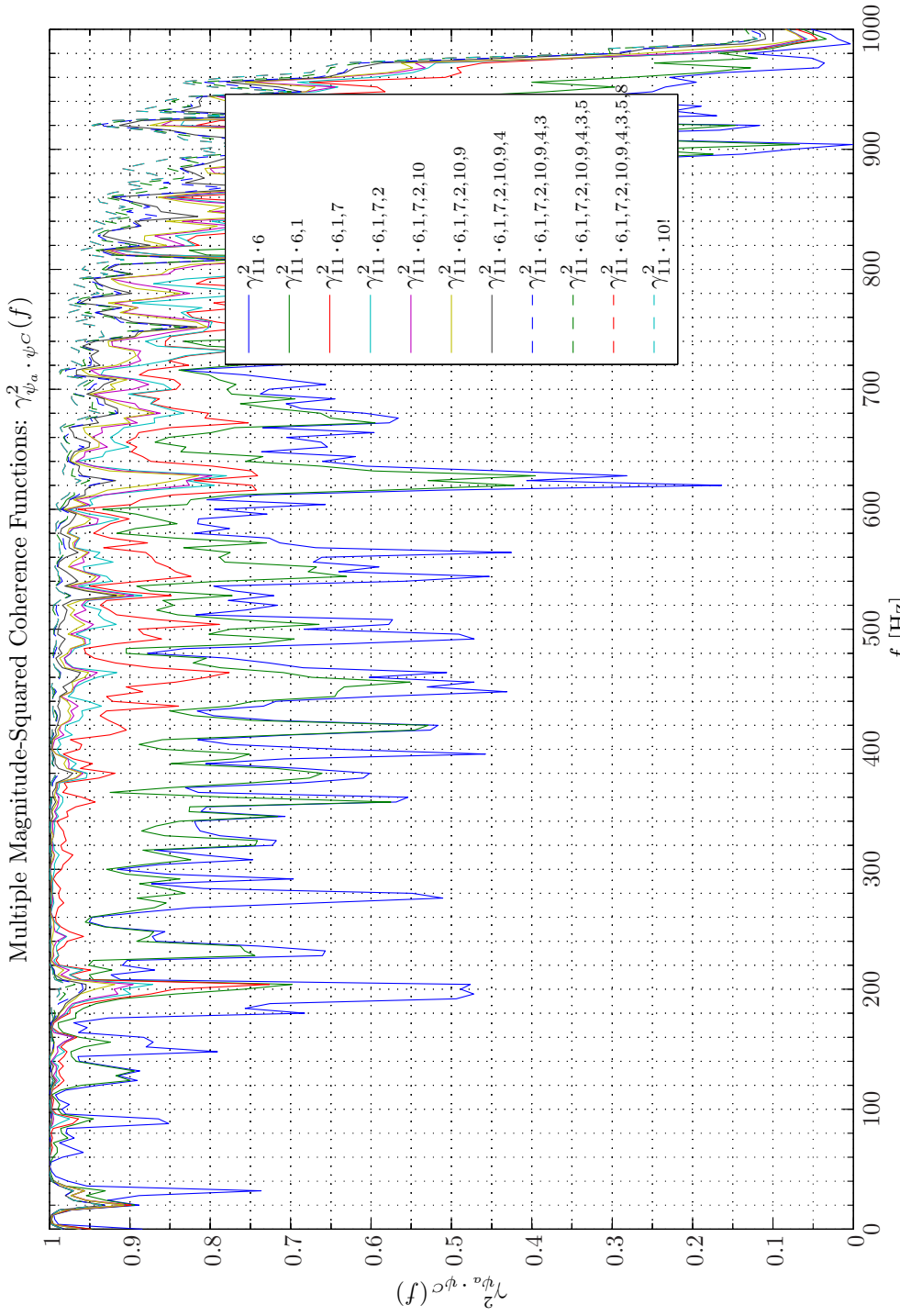

Sim 2.4.44: *Multiple Magnitude-Squared Coherence Functions* $\gamma^2_{\psi_a \cdot \psi^C}(f)$: **Statistical Data Analysis**: Single-Sided Modified Periodogram, f_s = 65.536 kHz, N_{DFT} = 16384, L_{DFT} = 16385, R_{DFT} = 8193, Hanning, Δf_m = 16 Hz, T_{DFT} = 0.25002 s, $N_{f,DFT}$ = 8193, Δf_{DFT} = 4 Hz, K_{DFT} = 158; *System Identification:* (Random Low-Pass (4 kHz) White Noise ($\mathcal{N}(0, 0.2)$), Elliptic LPF (f_{pass} = 900 Hz, f_{stop} = 1 kHz, A_{pass} = 1 dB, A_{stop} = 40 dB), f_s =65.536 kHz; Time: 0 − 20 s; **Topology:** BK 4949 surface microphones flush-mounted on Gentex HGU-55/P helmet mounted on a BK 4128 C HATS, Terma Earcup Audio System (Feedforward, mFx, $N_x = 10, N_e = 1, N_y = 2, N_p = 2$); *Channels:* $\#1 \leftarrow x_1$, $\#2 \leftarrow x_2$, $\#3 \leftarrow x_3$, $\#4 \leftarrow x_4$, $\#5 \leftarrow x_5$, $\#6 \leftarrow x_6$, $\#7 \leftarrow x_7$, $\#8 \leftarrow x_8$, $\#9 \leftarrow x_9$, $\#10 \leftarrow x_{10}$, $\#11 \leftarrow d_1^P$, $\#12 \leftarrow d_2^P$; **Scenario:** SystemIdentification(65536Hz)PrimaryPathes/20070203T142219.

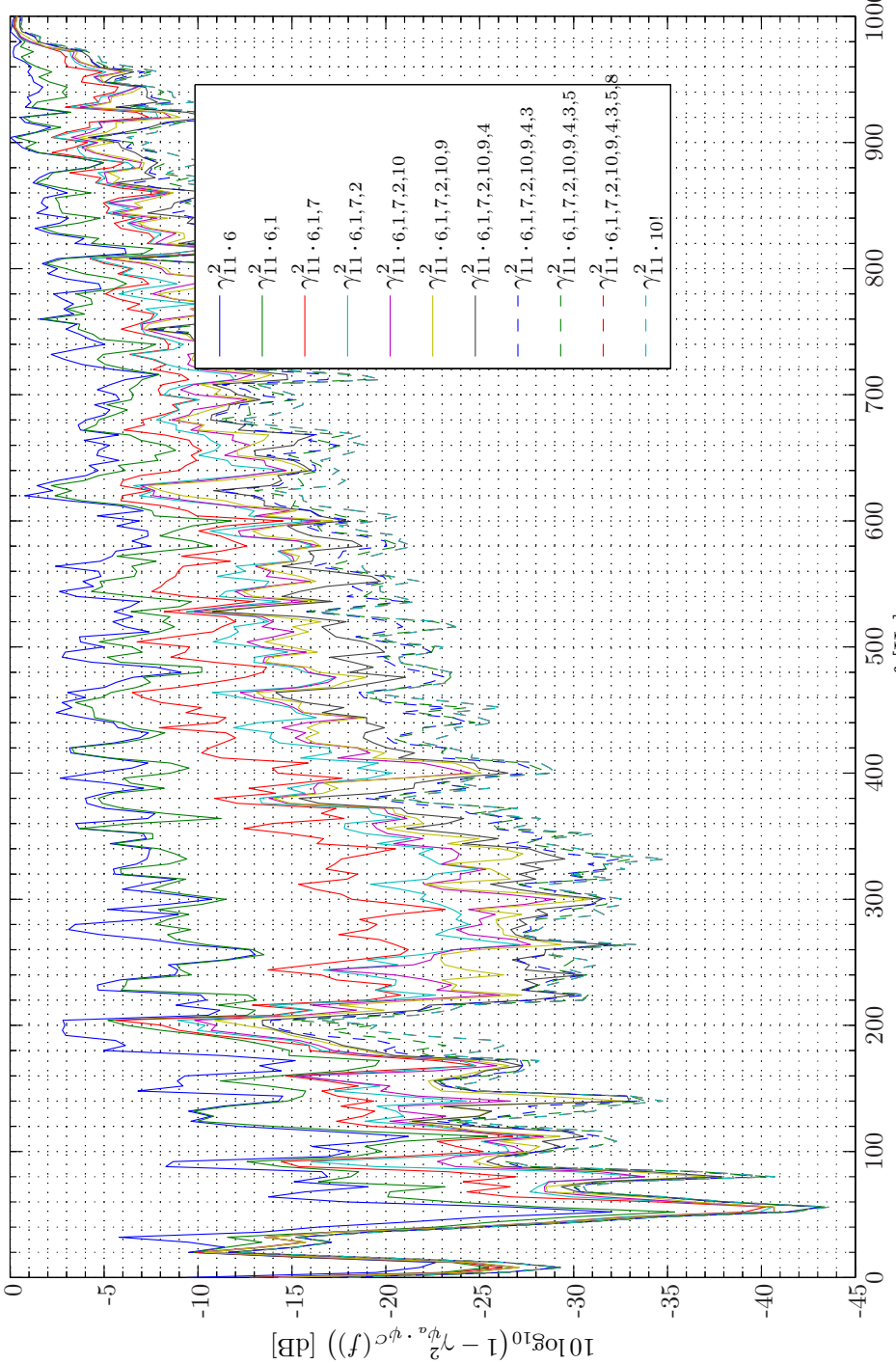

Sim 2.4.45: *Attenuation vs Multiple Magnitude-Squared Coherence Functions* $10\log_{10}\big(1-\gamma^2_{\psi_a\cdot\psi^C}(f)\big)$: **Statistical Data Analysis**: Single-Sided Modified Periodogram, f_s = 65.536 kHz, N_{DFT} = 16384, L_{DFT} = 16385, R_{DFT} = 8193, Hanning, Δf_n = 16 Hz, T_{DFT} = 0.25002 s, $N_{f,DFT}$ = 8193, Δf_{DFT} = 4 Hz, K_{DFT} = 158; *System Identification:* (Random Low-Pass (4 kHz) White Noise ($\mathcal{N}(0,0.2)$), Elliptic LPF (f_{pass} = 900 Hz, f_{stop} = 1 kHz, A_{pass} = 1 dB, A_{stop} = 40 dB), f_s =65.536 kHz; Time: 0 − 20 s; **Topology:** BK 4949 surface microphones flush-mounted on Gentex HGU-55/P helmet mounted on a BK 4128 C HATS, Terma Earcup Audio System (Feedforward, mFx, $N_x = 10, N_e = 1, N_y = 2, N_p = 2$); *Channels:* #1 ← x_1, #2 ← x_2, #3 ← x_3, #4 ← x_4, #5 ← x_5, #6 ← x_6, #7 ← x_7, #8 ← x_8, #9 ← x_9, #10 ← x_{10}, #11 ← d_1^p, #12 ← d_2^p; **Scenario:** `SystemIdentification(65536Hz)PrimaryPathes/20070203T142219`.

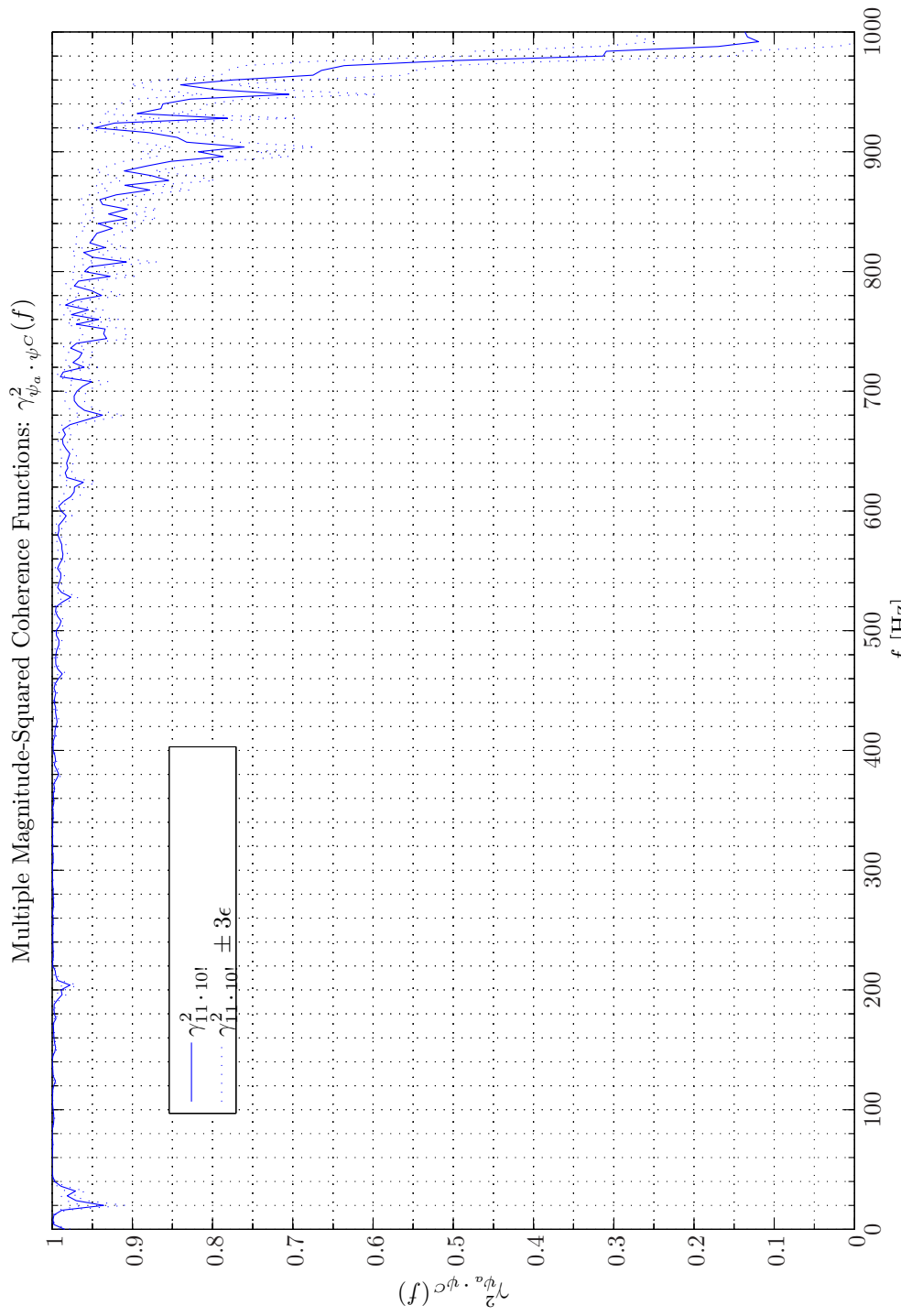

Sim 2.4.46: *Multiple Magnitude-Squared Coherence Functions* $\gamma^2_{\psi_a \cdot \psi^C}(f)$: **Statistical Data Analysis**: Single-Sided Modified Periodogram, f_s = 65.536 kHz, N_{DFT} = 16384, L_{DFT} = 16385, R_{DFT} = 8193, Hanning, Δf_m = 16 Hz, T_{DFT} = 0.25002 s, $N_{f,DFT}$ = 8193, Δf_{DFT} = 4 Hz, K_{DFT} = 158; *System Identification:* (Random Low-Pass (4 kHz) White Noise ($\mathcal{N}(0, 0.2)$), Elliptic LPF (f_{pass} = 900 Hz, f_{stop} = 1 kHz, A_{pass} = 1 dB, A_{stop} = 40 dB), f_s =65.536 kHz; Time: 0 – 20 s; **Topology:** BK 4949 surface microphones flush-mounted on Gentex HGU-55/P helmet mounted on a BK 4128 C HATS, Terma Earcup Audio System (Feedforward, mFx, $N_x = 10, N_e = 1, N_y = 2, N_p = 2$); *Channels:* #1 $\leftarrow x_1$, #2 $\leftarrow x_2$, #3 $\leftarrow x_3$, #4 $\leftarrow x_4$, #5 $\leftarrow x_5$, #6 $\leftarrow x_6$, #7 $\leftarrow x_7$, #8 $\leftarrow x_8$, #9 $\leftarrow x_9$, #10 $\leftarrow x_{10}$, #11 $\leftarrow d_1^p$, #12 $\leftarrow d_2^p$; **Scenario:** `SystemIdentification(65536Hz)PrimaryPathes/20070203T142219`.

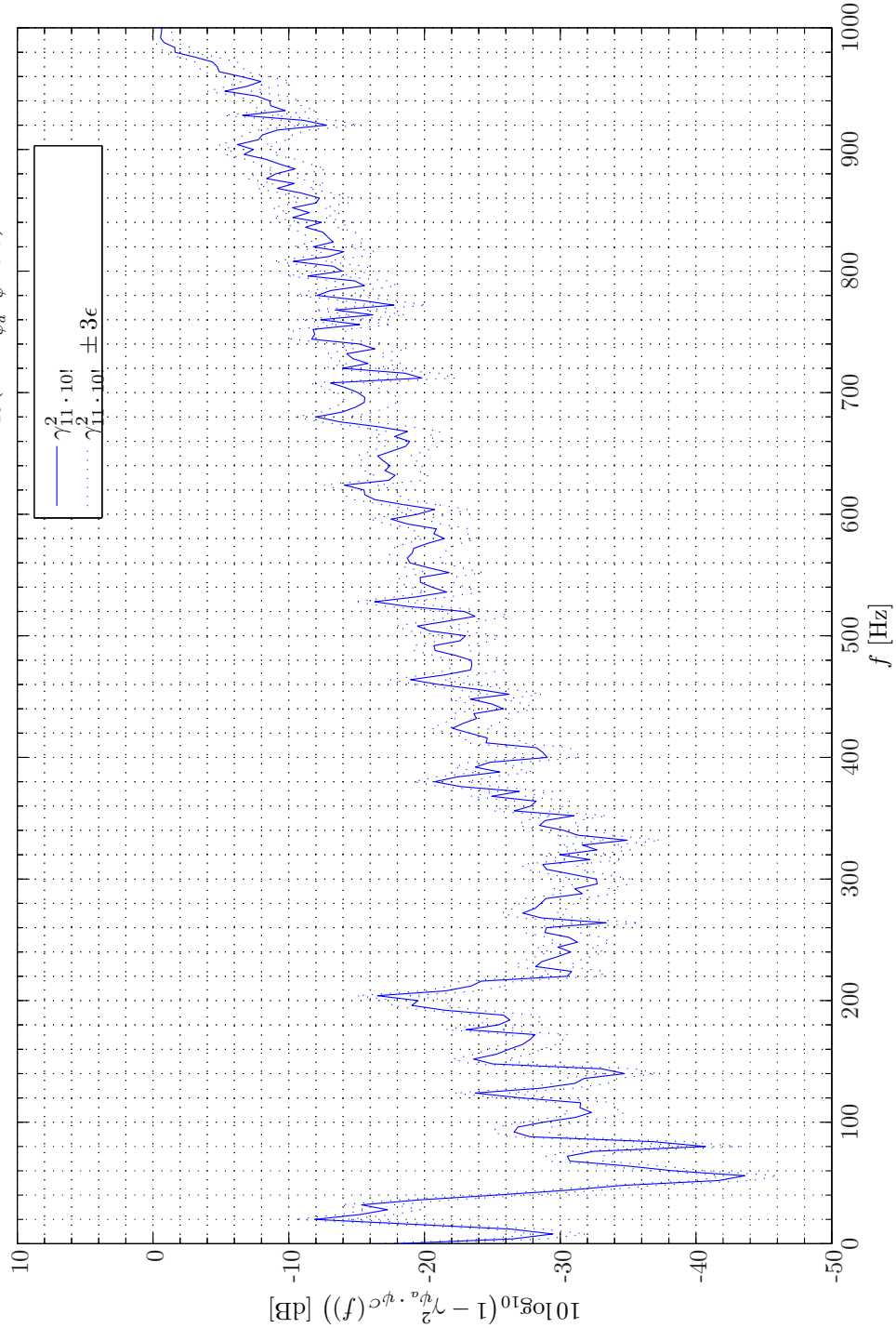

Sim 2.4.47: *Attenuation vs Multiple Magnitude-Squared Coherence Functions* $10\log_{10}(1-\gamma^2_{\psi_a\cdot\psi^C}(f))$: **Statistical Data Analysis**: Single-Sided Modified Periodogram, f_s = 65.536 kHz, N_{DFT} = 16384, L_{DFT} = 16385, R_{DFT} = 8193, Hanning, Δf_n = 16 Hz, T_{DFT} = 0.25002 s, $N_{f,DFT}$ = 8193, Δf_{DFT} = 4 Hz, K_{DFT} = 158; *System Identification:* (Random Low-Pass (4 kHz) White Noise ($\mathcal{N}(0,0.2)$), Elliptic LPF (f_{pass} = 900 Hz, f_{stop} = 1 kHz, A_{pass} = 1 dB, A_{stop} = 40 dB), f_s =65.536 kHz; Time: 0 − 20 s; **Topology:** BK 4949 surface microphones flush-mounted on Gentex HGU-55/P helmet mounted on a BK 4128 C HATS, Terma Earcup Audio System (Feedforward, mFx, $N_x = 10, N_e = 1, N_y = 2, N_p = 2$); *Channels:* #1 ← x_1, #2 ← x_2, #3 ← x_3, #4 ← x_4, #5 ← x_5, #6 ← x_6, #7 ← x_7, #8 ← x_8, #9 ← x_9, #10 ← x_{10}, #11 ← d_1^p, #12 ← d_2^p; **Scenario:** `SystemIdentification(65536Hz)PrimaryPathes/20070203T142219`.

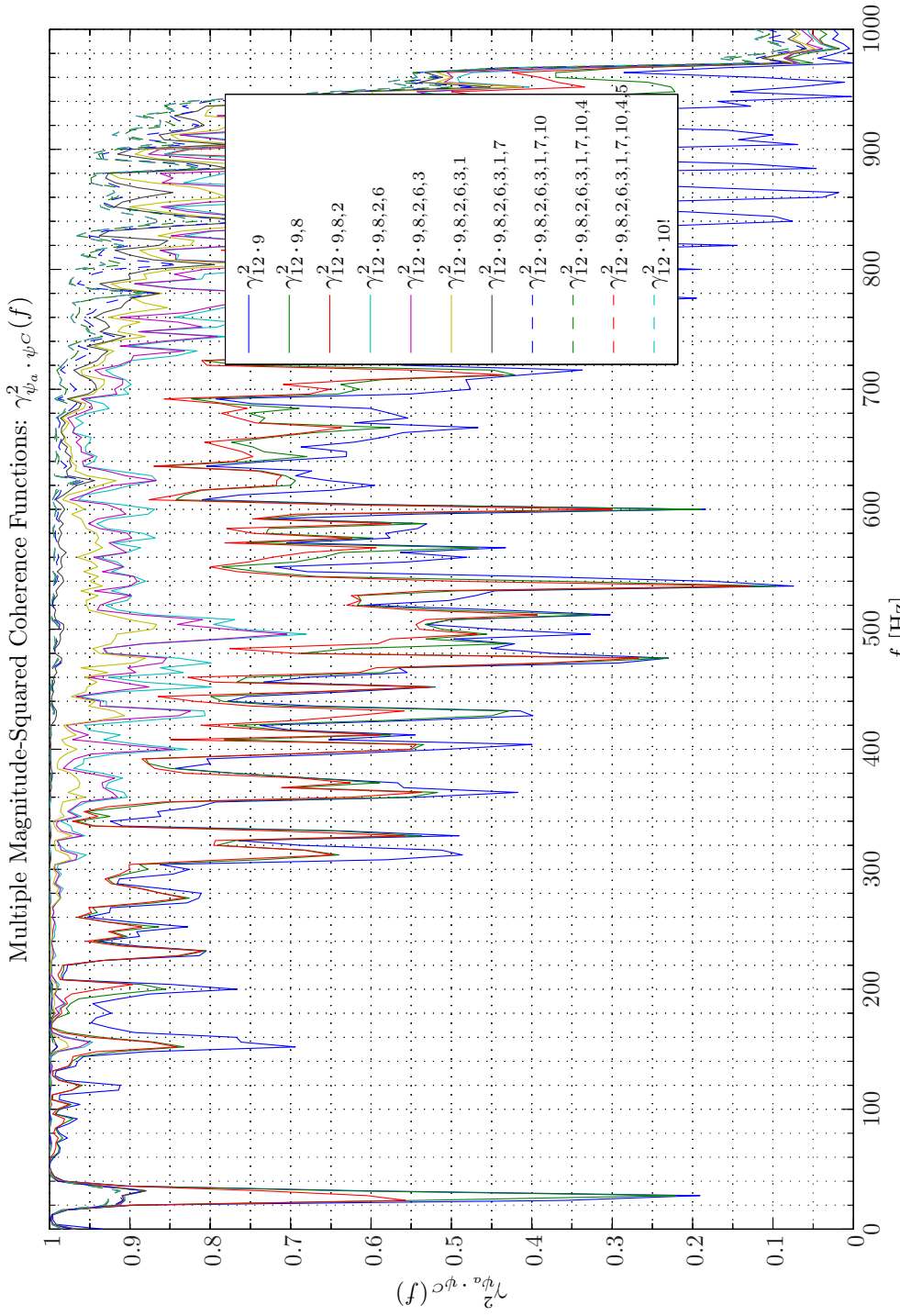

Sim 2.4.48: *Multiple Magnitude-Squared Coherence Functions* $\gamma^2_{\psi_a \cdot \psi^C}(f)$: **Statistical Data Analysis**: Single-Sided Modified Periodogram, f_s = 65.536 kHz, N_{DFT} = 16384, L_{DFT} = 16385, R_{DFT} = 8193, Hanning, Δf_m = 16 Hz, T_{DFT} = 0.25002 s, $N_{f,DFT}$ = 8193, Δf_{DFT} = 4 Hz, K_{DFT} = 158; *System Identification:* (Random Low-Pass (4 kHz) White Noise ($\mathcal{N}(0, 0.2)$), Elliptic LPF (f_{pass} = 900 Hz, f_{stop} = 1 kHz, A_{pass} = 1 dB, A_{stop} = 40 dB), f_s =65.536 kHz; Time: 0 − 20 s; **Topology:** BK 4949 surface microphones flush-mounted on Gentex HGU-55/P helmet mounted on a BK 4128 C HATS, Terma Earcup Audio System (Feedforward, mFx, $N_x = 10, N_e = 1, N_y = 2, N_p = 2$); *Channels:* #1 ← x_1, #2 ← x_2, #3 ← x_3, #4 ← x_4, #5 ← x_5, #6 ← x_6, #7 ← x_7, #8 ← x_8, #9 ← x_9, #10 ← x_{10}, #11 ← d_1^P, #12 ← d_2^P; **Scenario:** `SystemIdentification(65536Hz)PrimaryPathes/20070203T142219`.

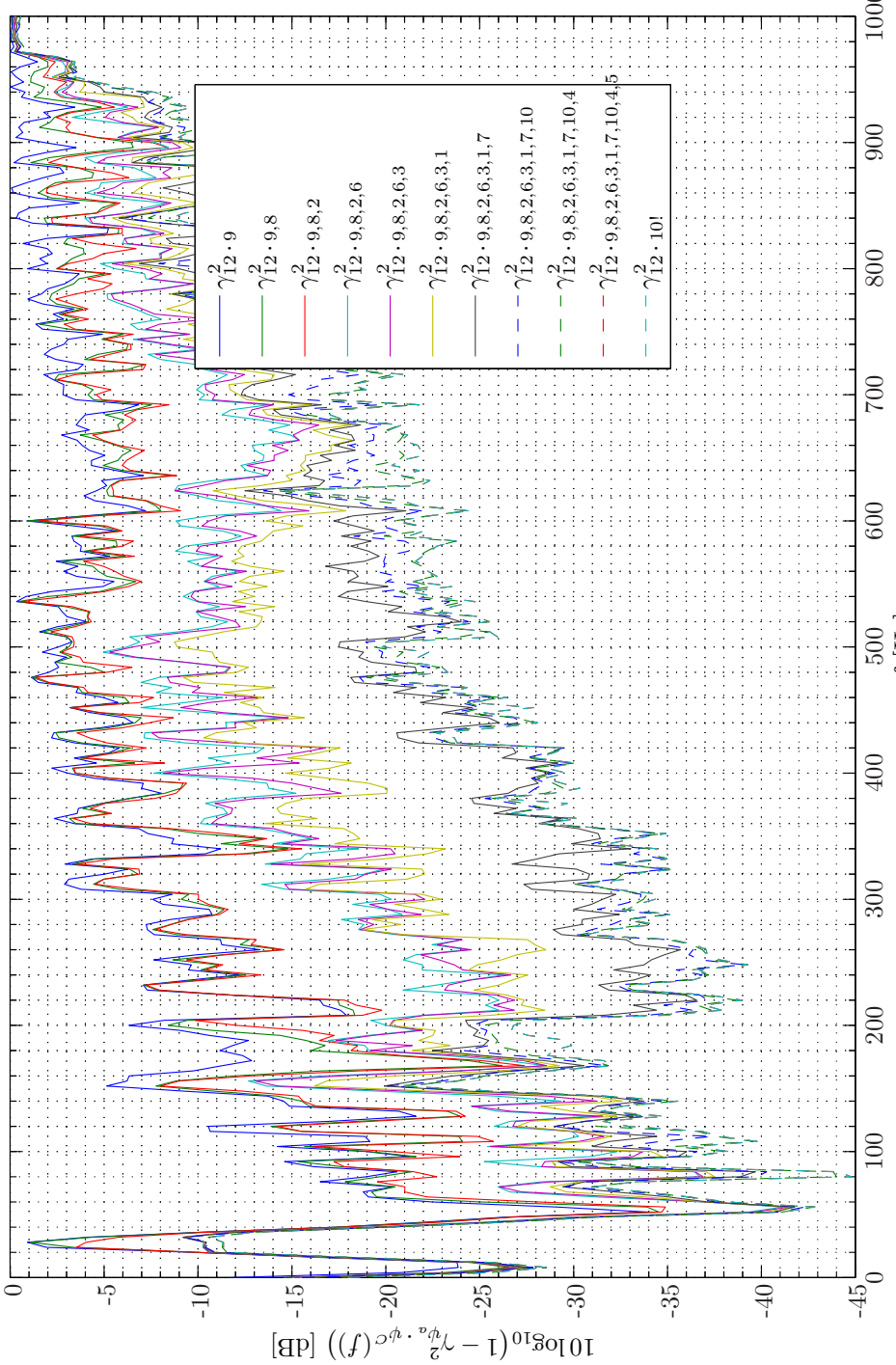

Sim 2.4.49: *Attenuation vs Multiple Magnitude-Squared Coherence Functions* $10\log_{10}(1-\gamma^2_{\psi_a\cdot\psi^C}(f))$: **Statistical Data Analysis**: Single-Sided Modified Periodogram, f_s = 65.536 kHz, N_{DFT} = 16384, L_{DFT} = 16385, R_{DFT} = 8193, Hanning, Δf_n = 16 Hz, T_{DFT} = 0.25002 s, $N_{f,DFT}$ = 8193, Δf_{DFT} = 4 Hz, K_{DFT} = 158; *System Identification:* (Random Low-Pass (4 kHz) White Noise ($\mathcal{N}(0,0.2)$), Elliptic LPF (f_{pass} = 900 Hz, f_{stop} = 1 kHz, A_{pass} = 1 dB, A_{stop} = 40 dB), f_s =65.536 kHz; Time: 0 − 20 s; **Topology:** BK 4949 surface microphones flush-mounted on Gentex HGU-55/P helmet mounted on a BK 4128 C HATS, Terma Earcup Audio System (Feedforward, mFx, $N_x = 10, N_e = 1, N_y = 2, N_p = 2$); *Channels:* #1 ← x_1, #2 ← x_2, #3 ← x_3, #4 ← x_4, #5 ← x_5, #6 ← x_6, #7 ← x_7, #8 ← x_8, #9 ← x_9, #10 ← x_{10}, #11 ← d_1^p, #12 ← d_2^p; **Scenario:** `SystemIdentification(65536Hz)PrimaryPathes/20070203T142219`.

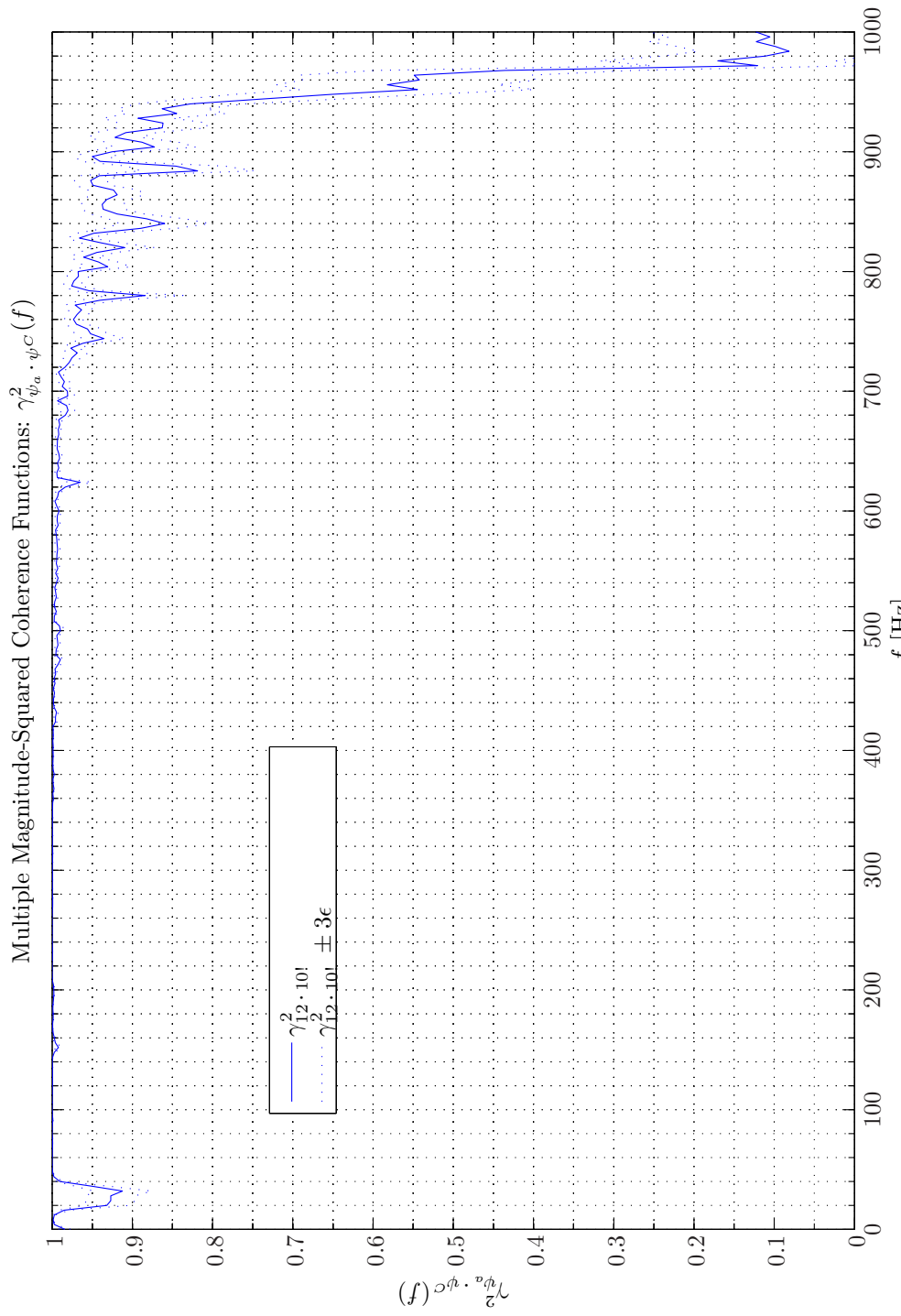

Sim 2.4.50: *Multiple Magnitude-Squared Coherence Functions* $\gamma^2_{\psi_a \cdot \psi^C}(f)$: **Statistical Data Analysis**: Single-Sided Modified Periodogram, f_s = 65.536 kHz, N_{DFT} = 16384, L_{DFT} = 16385, R_{DFT} = 8193, Hanning, Δf_m = 16 Hz, T_{DFT} = 0.25002 s, $N_{f,DFT}$ = 8193, Δf_{DFT} = 4 Hz, K_{DFT} = 158; *System Identification:* (Random Low-Pass (4 kHz) White Noise ($\mathcal{N}(0, 0.2)$), Elliptic LPF (f_{pass} = 900 Hz, f_{stop} = 1 kHz, A_{pass} = 1 dB, A_{stop} = 40 dB), f_s =65.536 kHz; Time: 0 – 20 s; **Topology:** BK 4949 surface microphones flush-mounted on Gentex HGU-55/P helmet mounted on a BK 4128 C HATS, Terma Earcup Audio System (Feedforward, mFx, $N_x = 10, N_e = 1, N_y = 2, N_p = 2$); *Channels:* $\#1 \leftarrow x_1$, $\#2 \leftarrow x_2$, $\#3 \leftarrow x_3$, $\#4 \leftarrow x_4$, $\#5 \leftarrow x_5$, $\#6 \leftarrow x_6$, $\#7 \leftarrow x_7$, $\#8 \leftarrow x_8$, $\#9 \leftarrow x_9$, $\#10 \leftarrow x_{10}$, $\#11 \leftarrow d_1^p$, $\#12 \leftarrow d_2^p$; **Scenario:** `SystemIdentification(65536Hz)PrimaryPathes/20070203T142219`.

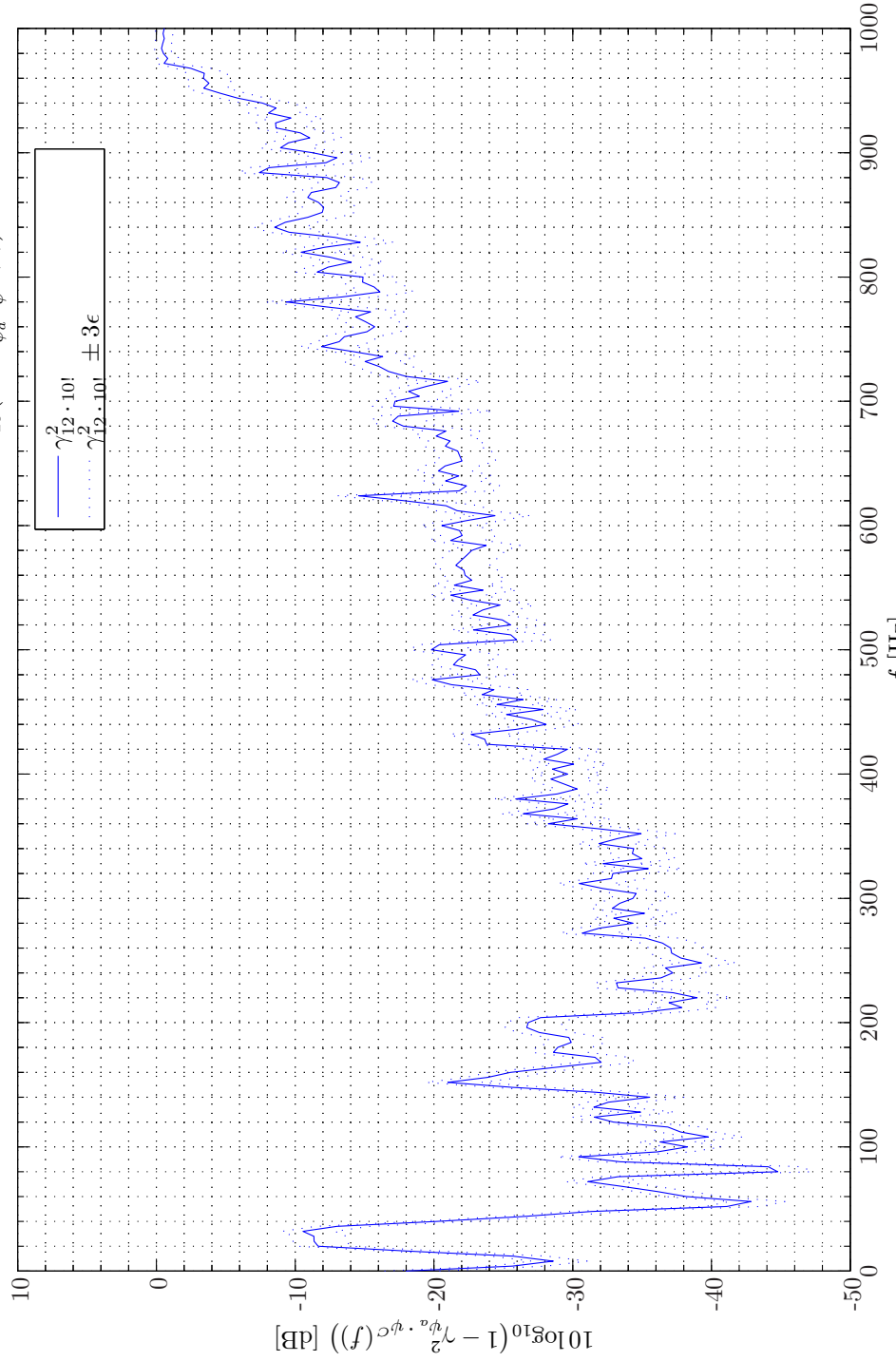

Sim 2.4.51: *Attenuation vs Multiple Magnitude-Squared Coherence Functions* $10\log_{10}(1-\gamma^2_{\psi_a\cdot\psi^C}(f))$: **Statistical Data Analysis**: Single-Sided Modified Periodogram, f_s = 65.536 kHz, N_{DFT} = 16384, L_{DFT} = 16385, R_{DFT} = 8193, Hanning, Δf_n = 16 Hz, T_{DFT} = 0.25002 s, $N_{f,DFT}$ = 8193, Δf_{DFT} = 4 Hz, K_{DFT} = 158; *System Identification:* (Random Low-Pass (4 kHz) White Noise ($\mathcal{N}(0, 0.2)$), Elliptic LPF (f_{pass} = 900 Hz, f_{stop} = 1 kHz, A_{pass} = 1 dB, A_{stop} = 40 dB), f_s =65.536 kHz; Time: 0 − 20 s; **Topology:** BK 4949 surface microphones flush-mounted on Gentex HGU-55/P helmet mounted on a BK 4128 C HATS, Terma Earcup Audio System (Feedforward, mFx, $N_x = 10, N_e = 1, N_y = 2, N_p = 2$); *Channels:* #1 ← x_1, #2 ← x_2, #3 ← x_3, #4 ← x_4, #5 ← x_5, #6 ← x_6, #7 ← x_7, #8 ← x_8, #9 ← x_9, #10 ← x_{10}, #11 ← d_1^p, #12 ← d_2^p; **Scenario:** `SystemIdentification(65536Hz)PrimaryPathes/20070203T142219`.

System Identification of Primary Pathes $G_{pe}^{m,k}$

System Identification of Primary Pathes $G_{pe}^{m.k}$, Ordinary Analysis

Ideally, a performance signal should be fully coherent with the corresponding error signal for optimal performance. However, it is well known (see, e.g., (2.4.2) on page 45) that a finite interspacing between the performance sensor and the error sensor leads to a decrease in their ordinary coherence function in a diffuse sound field. However, for the particular case of an acoustical field inside an earcup the field will to a large extent exhibit cavity behavior, where the field in the limit will be fully coherent *everywhere*.

The auto- and cross-spectral density functions for the error sensor and the two performance sensors presented previously are included in Simulation 2.4.52 - 2.4.54 on pages 95–97 for convenience

The OCOFs and related attenuation are depicted in Simulation 2.4.55 - 2.4.56 on pages 98–99 respectively.

It should be observed that for frequencies above 700 Hz the coherence between the left ear error sensor and performance sensor gradually decreases and the same therefore also applies to the predicted ANR capabilities. Hence, for a nominal 20 dB ANR system this lack of coherence becomes a problem at frequencies exceeding 800 Hz.

Not surprisingly, very poor coherence exist between the left ear error sensor and the right ear performance sensor. Hence, the signal content in one earcup is not representative of the signal content in the opposite earcup. As a consequence, if a malfunction enters one of the error sensors, it is very difficult to maintain ANR performance by using the opposite error sensor for performance feedback.

The HATS is designed for the test of hearing aids and for binaural experiments in general. It models accurately scattering of waves by a human head (without a helmet) and torso, but also the transfer function from the pinna to the eardrum. However, the HATS does not model the vibroacoustic mechanisms involved in the energy transfer from the sound field exterior to the helmet and the sound field interior to each earcup. Hence, the ordinary coherence function between the signal sensed by an error sensor in a ANR system and the field at the eardrum might deviate substantially from the results presented.

2.5 Conclusions

In this chapter the *ordinary coherence function* , the *multiple coherence function* and the *partial coherence function* have been introduced. Various general causes for the lack of coherence between two sensor signals encountered in practice were listed. Expressions for the three coherence functions have been provided and for the multiple coherence function and the partial coherence function both an iterative procedure as well as a matrix implementation formulation was presented. The concepts of *coherent spectrum* and *residual spectrum* were subsequently introduced. Then the joint-channel residual spectral analysis (JCRSA) method was developed and expressions for both an iterative procedure as well as expressions for a matrix based formulation provided.

The JCRSA method can used for the extraction of joint signal information from different observation positions in space. In a demonstration the JCRSA method was used to determine the spatially-weighted-averaged acquisition lead times provided by the reference sensors positioned

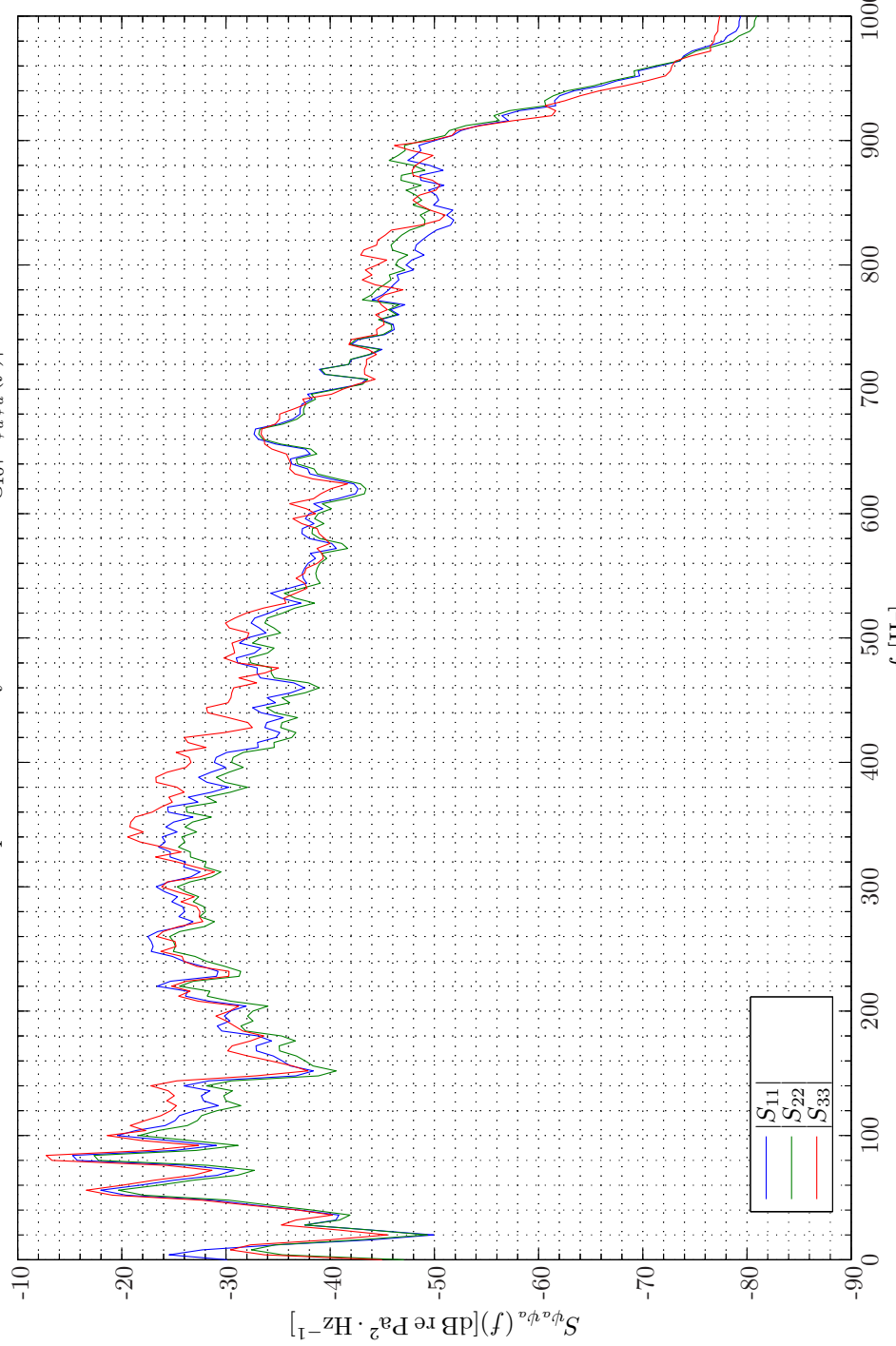

Sim 2.4.52: *Autospectral Density Functions*: **Statistical Data Analysis**: Single-Sided Modified Periodogram, f_s = 65.536 kHz, N_{DFT} = 16384, L_{DFT} = 16385, R_{DFT} = 8193, Hanning, Δf_m = 16 Hz, T_{DFT} = 0.25002 s, $N_{f,DFT}$ = 8193, Δf_{DFT} = 4 Hz, K_{DFT} = 158; *System Identification:* (Random Low-Pass (4 kHz) White Noise ($\mathcal{N}(0, 0.2)$), Elliptic LPF (f_{pass} = 900 Hz, f_{stop} = 1 kHz, A_{pass} = 1 dB, A_{stop} = 40 dB), f_s =65.536 kHz; Time: 0 – 20 s; **Topology:** BK 4949 surface microphones flush-mounted on Gentex HGU-55/P helmet mounted on a BK 4128 C HATS, Terma Earcup Audio System (Feedforward, mFx, $N_x = 10, N_e = 1, N_y = 2, N_p = 2$); *Channels:* #1 $\leftarrow d_1$, #2 $\leftarrow d_1^p$, #3 $\leftarrow d_2^p$; **Scenario:** `SystemIdentification(65536Hz)PrimaryPathes/20070203T151206`.

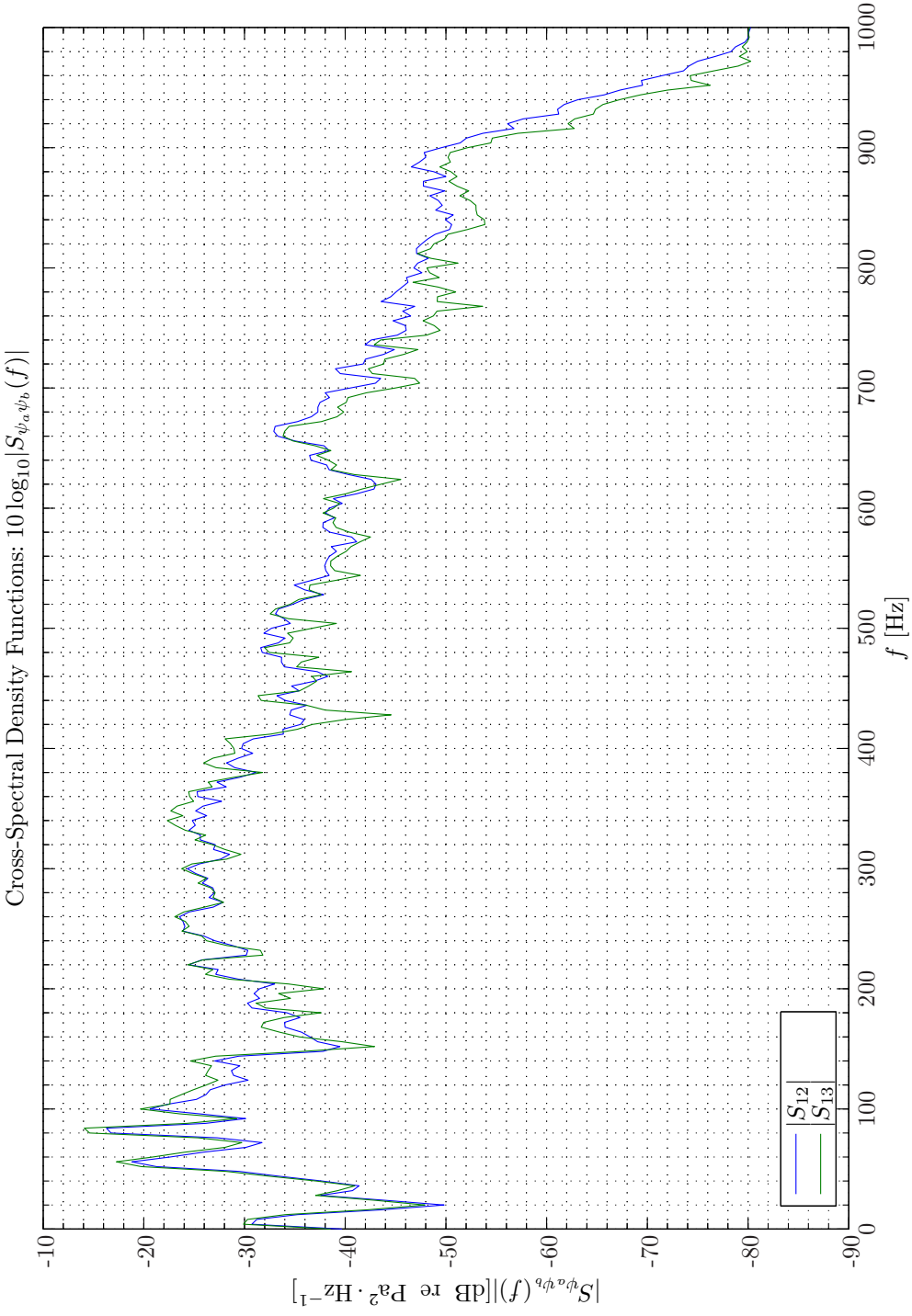

Sim 2.4.53: *Cross-Spectral Density Functions*: **Statistical Data Analysis**: Single-Sided Modified Periodogram, f_s = 65.536 kHz, N_{DFT} = 16384, L_{DFT} = 16385, R_{DFT} = 8193, Hanning, Δf_m = 16 Hz, T_{DFT} = 0.25002 s, $N_{f,DFT}$ = 8193, Δf_{DFT} = 4 Hz, K_{DFT} = 158; *System Identification:* (Random Low-Pass (4 kHz) White Noise ($\mathcal{N}(0, 0.2)$), Elliptic LPF (f_{pass} = 900 Hz, f_{stop} = 1 kHz, A_{pass} = 1 dB, A_{stop} = 40 dB), f_s =65.536 kHz; Time: 0 − 20 s; **Topology:** BK 4949 surface microphones flush-mounted on Gentex HGU-55/P helmet mounted on a BK 4128 C HATS, Terma Earcup Audio System (Feedforward, mFx, $N_x = 10, N_e = 1, N_y = 2, N_p = 2$); *Channels:* #1 $\leftarrow d_1$, #2 $\leftarrow d_1^p$, #3 $\leftarrow d_2^p$; **Scenario:** `SystemIdentification(65536Hz)PrimaryPathes/20070203T151206`.

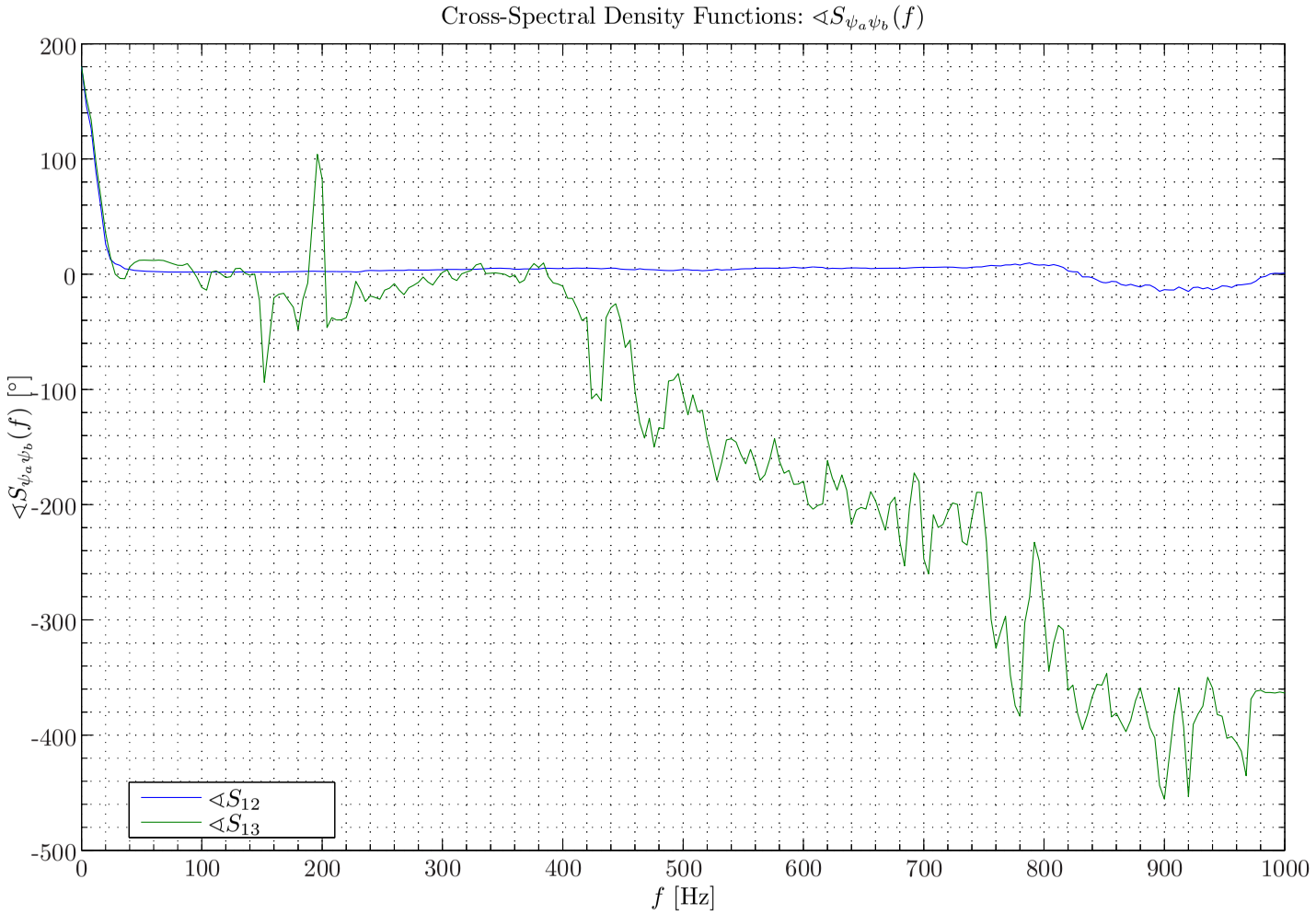

Sim 2.4.54: *Cross-Spectral Density Functions*: **Statistical Data Analysis**: Single-Sided Modified Periodogram, f_s = 65.536 kHz, N_{DFT} = 16384, L_{DFT} = 16385, R_{DFT} = 8193, Hanning, Δf_m = 16 Hz, T_{DFT} = 0.25002 s, $N_{f,DFT}$ = 8193, Δf_{DFT} = 4 Hz, K_{DFT} = 158; *System Identification:* (Random Low-Pass (4 kHz) White Noise ($\mathcal{N}(0, 0.2)$), Elliptic LPF (f_{pass} = 900 Hz, f_{stop} = 1 kHz, A_{pass} = 1 dB, A_{stop} = 40 dB), f_s =65.536 kHz; Time: $0 - 20$ s; **Topology:** BK 4949 surface microphones flush-mounted on Gentex HGU-55/P helmet mounted on a BK 4128 C HATS, Terma Earcup Audio System (Feedforward, mFx, $N_x = 10, N_e = 1, N_y = 2, N_p = 2$); *Channels:* $\#1 \leftarrow d_1$, $\#2 \leftarrow d_1^p$, $\#3 \leftarrow d_2^p$; **Scenario:** `SystemIdentification(65536Hz)PrimaryPathes/20070203T151206`.

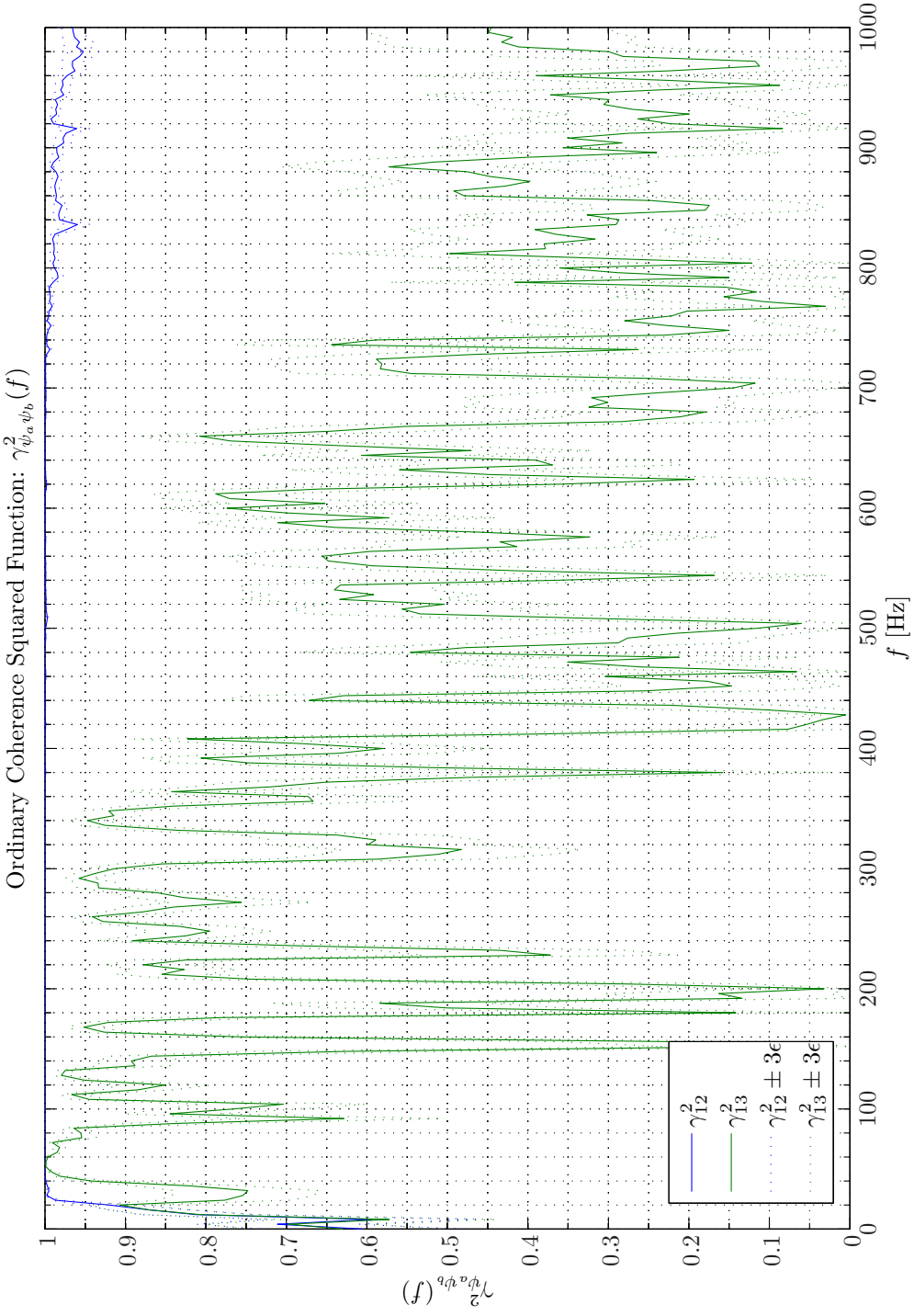

Sim 2.4.55: *Ordinary Coherency-Squared Functions* $\gamma^2_{\psi_a\psi_b}(f)$: **Statistical Data Analysis:** Single-Sided Modified Periodogram, f_s = 65.536 kHz, N_{DFT} = 16384, L_{DFT} = 16385, R_{DFT} = 8193, Hanning, Δf_m = 16 Hz, T_{DFT} = 0.25002 s, $N_{f,DFT}$ = 8193, Δf_{DFT} = 4 Hz, K_{DFT} = 158; *System Identification:* (Random Low-Pass (4 kHz) White Noise ($\mathcal{N}(0, 0.2)$), Elliptic LPF (f_{pass} = 900 Hz, f_{stop} = 1 kHz, A_{pass} = 1 dB, A_{stop} = 40 dB), f_s =65.536 kHz; Time: 0 − 20 s; **Topology:** BK 4949 surface microphones flush-mounted on Gentex HGU-55/P helmet mounted on a BK 4128 C HATS, Terma Earcup Audio System (Feedforward, mFx, $N_x = 10, N_e = 1, N_y = 2, N_p = 2$); *Channels:* #1 ← d_1, #2 ← d_1^p, #3 ← d_2^p; **Scenario:** SystemIdentification(65536Hz)PrimaryPathes/20070203T151206.

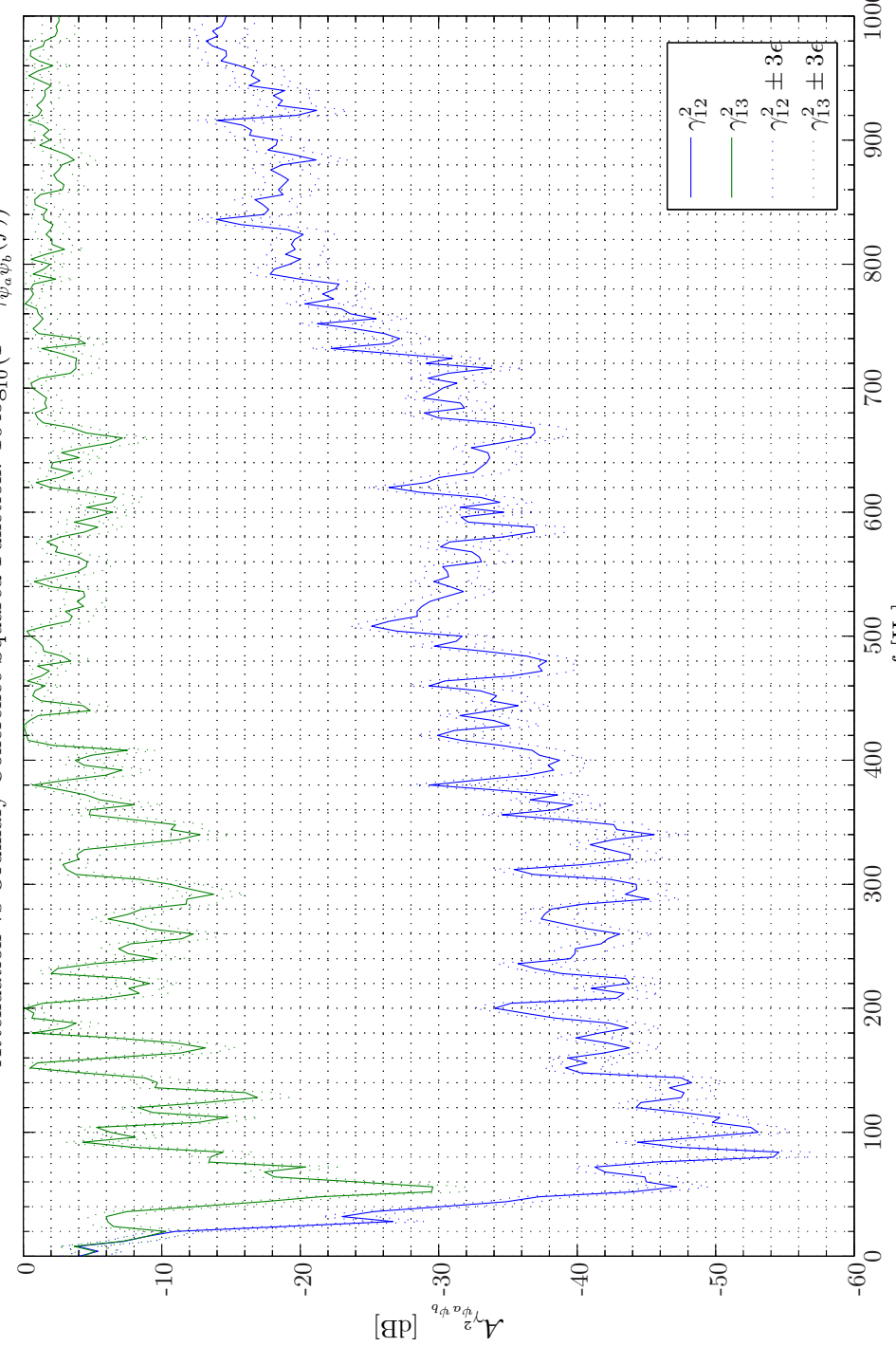

Sim 2.4.56: Attenuation *vs Ordinary Coherency-Squared Functions*: $10\log_{10}\left(1-\gamma^2_{\psi_a\psi_b}(f)\right)$: **Statistical Data Analysis**: Single-Sided Modified Periodogram, f_s = 65.536 kHz, N_{DFT} = 16384, L_{DFT} = 16385, R_{DFT} = 8193, Hanning, Δf_m = 16 Hz, T_{DFT} = 0.25002 s, $N_{f,DFT}$ = 8193, Δf_{DFT} = 4 Hz, K_{DFT} = 158; *System Identification:* (Random Low-Pass (4 kHz) White Noise ($\mathcal{N}(0, 0.2)$), Elliptic LPF (f_{pass} = 900 Hz, f_{stop} = 1 kHz, A_{pass} = 1 dB, A_{stop} = 40 dB), f_s =65.536 kHz; Time: $0-20$ s; **Topology:** BK 4949 surface microphones flush-mounted on Gentex HGU-55/P helmet mounted on a BK 4128 C HATS, Terma Earcup Audio System (Feedforward, mFx, $N_x = 10, N_e = 1, N_y = 2, N_p = 2$); *Channels:* $\#1 \leftarrow d_1$, $\#2 \leftarrow d_1^p$, $\#3 \leftarrow d_2^p$; **Scenario:** `SystemIdentification(65536Hz)PrimaryPathes/20070203T151206`.

on the surface of a ANR helmet employing the CFF topology. Owing to the relative slow mechanisms involved in the propagation or rather leakage of sound waves from the exterior of the helmet to the interior of the earcups most of the reference sensors provide an acquisition lead-time in the order of 0.8 ms.

The key function to the determination of the channel distinctive timing information is the residual cross-correlation functions. The conditioned impulse response functions, however, provide no such insight. The reason for this apparent paradox can be explained as follows. The cross-correlation function and cross-spectral density function constitute a Fourier transform pair. Likewise do the impulse response function and the transfer function constitute a Fourier transform pair. However, recalling that the transfer function is obtained as the ratio of cross-spectral density function to auto spectral density function the very small residual low-frequency auto spectral density function content will totally dominate the characteristics in the residual impulse response function. As the field is almost perfectly coherent at low frequencies no distinctive information are therefore really provided by the residual impulse response functions. The residual cross-correlation functions on the other hand provide the unfiltered timing information. Assuming negligible dispersion effects the acquisition lead-time represent an average acquisition lead-time over the measurement bandwidth.

As no reasonably accurate vibroacoustic model is available for this hardware, it is indeed difficult to assess the accuracy of the obtained results. With the completion of the RTU for AC described in section H.2 on page 720 a rigorous analysis and assessment of the JCRSA method can be made.

In order analytically to determine the number of reference sensors required for a certain attenuation-bandwidth combination an expression for the integrated normalized correlation function obtained from sampling the (diffuse) field at equidistant positions over a sphere should be derived.

The primary path measurements did also reveal that a nonunity coherence function between the error signal and performance signal within the same earcup prevails at frequencies above 700 Hz. Objective measurements where a person wearing the ANR helmet is equipped with a microphone in the ear (MIE) should examine more realistically to which extent this lack of coherence also will limit the achievable performance in practice. Of course subjective ANR measurement can be used to relate *monitored* ANR performance from the error sensor and the actually *perceived* ANR performance by a humans wearing the helmet.

Bibliography

[1] Julius S. Bendat. Solutions for the multiple input/output problem. *Sound and Vibration*, 44(3):311–325, 1976.

[2] Julius S. Bendat. System identification for multiple input/output data. *Sound and Vibration*, 49(3):293–308, 1976.

[3] Julius S. Bendat. Modern analysis procedures for multiple input/output problems. *JASA*, 68(2):1655–1687, 1980.

[4] Julius S. Bendat. *Nonlinear System Techniques and Applications*. Wiley-Interscience, New York, 1998.

[5] Julius S. Bendat and Allan G. Piersol. *Engineering Applications of Correlations and Spectral Analysis*. Wiley-Interscience, New York, 2nd edition, 1993.

[6] Julius S. Bendat and Allan G. Piersol. *Random data Analysis and measurement procedures*. John Wiley & Sons, Inc., 3rd edition, 2000.

[7] Mark F. Bocko, David H. Douglass, and Robert S. Knox. Observation of frequency shifts of spectral lines due to source correlations. *Phys.Rev. Lett.*, 58(25):2649/2651, 1987.

[8] Max Born and Emil Wolf. *Principles of Optics. Electromagnetic Theory of Propagation, Interference and Diffraction of Light*. Cambridge University Press, 7th edition, 2002.

[9] J. Y. Chung, Malcolm J. Crocker, and James F . Hamilton. Measurement of frequency responses and the multiple coherence function of the noise-generation system of a diesel engine. *JASA*, 58(3):635–642, 1975.

[10] Richard K. Cook, R. V. Waterhouse, R. D. Berendt, Seymour Edelman, and Jr. M. C. Thomsen. Measurement of correlation coeflicients in-reverberant sound fields. *The Journal of the Acoustical Society of America*, 27:1072–1077, 1955.

[11] C. J. Dodds and J. D. Robson. Pariel coherence in multivariaternadom processes. *Journal of Sound and Vibration*, 42(2):243–249, 1975.

[12] Stephen J. Elliott. *Signal Processing for Active Control*. London: Academic Press, 2001.

[13] Stephen J. Elliott, P. Joseph, A. J. Bullmore, and Philip A. Nelson. Active cancellation at a point in a pure tone diffuse sound field. *Journal of Sound and Vibration*, 120(1):183–189, 1988.

[14] Ari T. Friberg and Emil Wolf. Relationships between the complex degrees of coherence in the space-time and in the space-frequency domain. *Optics Letters*, 20(6):623–625, 1995.

[15] Colin H. Hansen and Scott D. Snyder. *Active Control of Noise and Vibration*. E & FN SPON, 1st edition, 1997.

[16] Finn Jacobsen. The diffuse sound field. Technical report, Technical University of Denmark, 1979.

[17] Finn Jacobsen and T. G. Nielsen. Spatial correlation and coherence in a reverberant sound field. *Journal of Sound and Vibration*, 118(1):175–180, 1987.

[18] Gwilym M. Jenkins and Donald Watts. *Spectral Analysis and Its Applications*. Emerson-Adams Press, 1998.

[19] Richard J. Kozick and Brian M. Sadler. Source localization with distributed sensor arrays and partial spatial coherence. *IEEE Transactions on Signal Processing*, 52(3):601–616, 2004.

[20] Philip A. Nelson and Stephen J. Elliott. *Active Control of Sound*. Academic Press, 1992.

[21] D. E. Newland. *An Introduction to Random Vibrations, Spectral and Wavelet Analysis*. Addison-Wesley Longman, Harlow Essex England, 3rd edition, 1993.

[22] R. D. Trueblood and D. L. Alspach. Multiple coherence as a detection statistic. Technical Report 265, Naval Ocean Syst. Center, 1978.

[23] Roy E. White. The estimation of signal spectra and related quantities by means of the multiple coherence function. *Geophysical Prospecting*, 21(4):660–703, 1973.

[24] Roy E. White. Signal and noise estimation from seismic reflection data using spectral coherence methods. *Proceedings of the IEEE*, 72(10):1340–1359, 1984.

[25] D. Keith Wilson. Performance bounds for acoustic direction-of-arrival arrays operating in atmospheric turbulence. *JASA*, 103(3):1306–1319, 1998.

[26] Emil Wolf. Young's interference fringes with narrow-band light. *Optics Letters*, 8(5):250–252, 1983.

[27] Kamal Yacoub. Relationship between multiple and partial coherence functions. *IEEE Transactions on Information Theory*, 16(6):668–672, 1970.

2.A *Multiple-Channel Signal Detection and Generalized Coherence*[14]

Detection theory usually involves two mutually exclusive hypothesis:

$$\begin{cases} H_0: & x_i(t) = n_i(t) \\ H_1: & x_i(t) = s(t) + n_i(t) \end{cases}, \quad \forall i \in \underline{N}_\psi. \tag{2.A.1}$$

Hence, hypothesis H_0 refers to the case of only noise $n(t)$ present at each of the channels, that is, the signal absent case. The H_1 hypothesis refers to the hypothesis that both a signal $s(t)$ and noise are present in the channels. Of course, the channel statistic will be different for the two hypothesis. A detection threshold $\gamma^2_{th}(p_{fa}, p_d)$ that is a function of the probability of false alarm p_{fa} and the probability of detection p_d is used to select between H_0 and H_1 according to

$$\begin{cases} H_0 : \hat{\gamma}^2(t) < \gamma^2_{th} \\ H_1 : \hat{\gamma}^2(t) \geq \gamma^2_{th}. \end{cases} \tag{2.A.2}$$

The target location usually involves time-delay estimation [1] to establish a time difference of arrival (TDOA) map. In [2, 3] analytical expressions for the statistics of the two-channel estimate involving two random stationary Gaussian processes were presented. From the pdf of the magnitude-squared coherence function denoted by $f_{\gamma^2}(\gamma^2)$ detection thresholds γ^2_{th} corresponding to predetermined probability of false alarm values can then be deduced.

The invariance of the magnitude-squared coherence estimate with respect to the statistics of one of the channels has been investigated in several studies. In [8] it was demonstrated that $f_{\gamma^2}(\gamma^2)$ does not depend on the distribution of a channel in the magnitude-squared coherence function (two-channel) estimate provided that the other channel contains only zero-mean stationary Gaussian noise and the RPs involved in the two channels are statistically independent of each other. Such invariance results have importance in *active* radar or sonar applications where an exact replica of the transmitted signal typically is at disposition for detection of the radar/sonar returns. Similarly, *passive* radar or sonar applications might benefit from reserving one of the channels as a reference channel. Using geometric arguments it was further shown in [7] that even the Gaussian assumption on one of the channels for the invariance of the second-channel statistics in the two-channel estimate is not necessary. Hence, threshold corresponding to particular false probabilities can be computed under the mild condition that, say, $f_{\psi_1}(\psi_1)$ is

[14] This subsection provides supplementary that, however, can be skipped on a first reading.

spherically symmetric [15] and statistically independent on $f_{\psi_2}(\psi_2)$. Such invariance extends the utility of the magnitude-squared coherence function estimate based detection from passive to active applications where one of the N_ψ channels is an exact replica of a transmitted waveform thereby providing a multiple-channel matched filter.

The generalized coherence (GC) estimate was proposed by Cochran, Gish, and Sinno [6] as a natural extension to the magnitude-squared coherence (MSC) estimate for *multi-channel detection*. Adapted to the nomenclature used in this report the GC estimate is defined by $\hat{\gamma}^2(f)$

$$\hat{\gamma}^2(f) \triangleq 1 - \frac{g(S_{11}, \cdots, S_{N_\psi N_\psi})}{\|S_{11}\|^2 \cdots \|S_{N_\psi N_\psi}\|^2}, \tag{2.A.3}$$

where $g(S_{11}, \cdots, S_{N_\psi N_\psi})$ denotes the *Gram determinant* of a $N_\psi \times N_\psi$ Gram matrix which coincides with the MIMO channel power spectral density matrix defined in (2.2.3) on page 21, that is,

$$g(S_{11}, \cdots, S_{N_{\psi N \psi}}) \triangleq \|S_{\psi\psi}\|. \tag{2.A.4}$$

The main difference between the generalized coherence function (2.A.3) and the multiple coherence function presented in subsection 2.2.5 on page 25 relies in the former using one of the channels as a reference. The GC estimate can be used for multiple-channel matched filtering with applications to radar and sonar and seismography [10]. In these applications the ability to detect and locate a common signal present on two or more channels is crucial.

For the particular examples studied in [4, 6] the GC estimate provided better ROC curves than by MSC estimation [9]. This means that for the same p_d the GC estimate will in average provide a smaller probability of false alarm than by MSC estimation. Similarly for a fixed p_{fa} the GC estimate will provide a higher probability of detection than by MSC estimation.

In [5] it is proved that the GC estimate likewise the magnitude-squared coherence function estimate is invariant to the distribution in one channel provided that remaining channels contain only white Gaussian noise and that all channels are independent. The analysis of the GC estimate as a multiple-channel detection statistic, however, in general is rather complicated. The pdf is difficult to evaluate under the H_0 hypothesis and is unknown under the H_1 hypothesis. In [4] asymptotic ($K_{DFT} \to \infty$) a model for the signal present hypothesis H_1 statistics in the multi-channel. Likewise an efficient closed-form asymptotic model for the target absent hypothesis H_0 case was developed for multi-channel systems.

Bibliography

[1] G. Cliford Carter. Coherence and time delay estimation. *Proceedings of the IEEE*, 75(2): 236–255, 1987.

[2] G. Cliford Carter, Charles H. Knapp, and Albert H. Nuttall. Estimation of the magnitude-squared coherence function via overlapped fast fourier transform processing. *IEEE Transactions on Audio and Electroacoustics*, 21(4):337–344, 1973.

[15] A pdf, say $f_z(z_1, \ldots z_N)$, $z \in \mathbb{C}^N$ is spherically symmetric if the N-dimensional multivariate distribution can be substituted by a one-dimension distribution where the value depends only on the distance form the origin and not on the direction, that is, $f_z(z_1, \ldots z_N) = f_{\|z\|^2}(\|z\|^2)$.

[3] G. Cliford Carter, Charles H. Knapp, and Albert H. Nuttall. Statistics of the estimate of the magnitude-coherence function. *IEEE Transactions on Audio and Electroacoustics*, 21 (4):388–389, 1973.

[4] Axel Clausen. Asymptotic analysis of the generalized coherence estimate. *IEEE Transactions on Signal Processing*, 49(1):45–53, 2001.

[5] Axel Clausen and Douglas Cochran. An invariance property of the generalized coherence estimate. *IEEE Transactions on Signal Processing*, 45(4):1065–1067, 1997.

[6] Douglas Cochran, Herbert Gish, and Dana Sinno. A geometric approach to multiple-channel signal detection. *IEEE Transactions on Signal Processing*, 43(9):2049–2057, 1995.

[7] Herbert Gish and Douglas Cochran. Invariance of the magnitude-squared coherence estimate with respect to second-channel statistics. *IEEE Transactions on Acoustics, Speech, and Signal Processing*, 35(12):1774–1776, 1987.

[8] A. H. Nutall. Invariance of distribution of coherence estimate to second-channel statistics. *IEEE Transactions on Acoustics, Speech, and Signal Processing*, ASSP-29(1):120–122, 1981.

[9] R. D. Trueblood and D. L. Alspach. Multiple coherence as a detection statistic. Technical Report 265, Naval Ocean Syst. Center, 1978.

[10] Roy E. White. Signal and noise estimation from seismic reflection data using spectral coherence methods. *Proceedings of the IEEE*, 72(10):1340–1359, 1984.

3. CAUSALITY CONSTRAINTS AND SPECTRAL FACTORIZATION

3.1 Introduction

The performance of a modern complex active noise control system (ANCS) is determined from numerous system parameters as detailed in Appendix A on page 529. In chapter 2 on page 17 the active noise reduction (ANR) performance as a function of the multiple coherence function was examined in detail. In particular, it was found that in the ANR helmet application the spatially-weighted-averaged acquisition lead time is approximately 0.9 ms. A natural question is therefore, whether this lead time sufficiently can compensate for delays associated with the secondary paths in relation to the frequency spectrum of the noise. Hence, in this chapter the ANR performance limitations as determined from causality constraints will be considered.

In special situations, however, it might be possible to avoid considering causality constraints. For example, if we experimentally could set up a noise scenario and then acquire the primary signals, post process these signals and determine the control output signals, then provided that the experiment is conducted in a controlled environment where the primary noise fields can be reproduced with high accuracy we could excite the secondary fields from those previously determined control output signals. Of course such system is useful for system test but not for practical real-time ANR operation.

A key technique to the causality analysis is the *spectral factorization* which therefore will play a main role in this chapter.

Another objective pursued in this chapter is to examine the performance of two variant Wiener-Hopf (WH) filters that are useful for the analysis of the achievable ANR performance under causality constraints. These WH filters are formally defined in chapter 8 on page 371 where adaptive filtering algorithms for linear time-variant systems are considered. The first method that will be referred to as the **t**-domain WH method estimates the optimal causally constrained filter weights when presented to random white noise signals. The second WH method referred to as the **z**-domain WH filter returns the optimal causally constrained filter weights *independent* of the colorization of the regressor signals. This method, however, is more complex and is relying on a spectral factorization that can be quite involved in particular for multiple-channel (MC) systems.

3.1.1 Chapter Outline

Following these introductory remarks the theme of section 3.2 is spectral factorization. This section starts with a formal definition of z-spectra and the spectral factorization will then formally be defined. Spectral factorization in active control (AC) context is subsequently addressed and the importance of the most significant parameters discussed. In particular a formula that defines the optimal causally constrained weight vector and that involves the so-called plus operator is

the kernel for much of the development in that section.

In many ANR applications the reference signals and the disturbance signals will tentatively be very correlated as the system will possess some underlying structure. We will exploit the existence of such structure in section 3.3 and in particular, specific expressions for the optimal causally constrained weight vector for systems governed by primary paths and for FBS are provided.

Hitherto, the chapter has included examples involving mathematically constructed plants in order to make our exhibitions of the causality constraints more clear. Then in section 3.4 we will consider causality constraints pertaining to the Gentex HGU-55/P helmet closed-back headset system employing the Terma earcup system.

Instructive examples should hopefully help to make these somewhat abstract concepts more comprehendible. To the author's best knowledge no such or similar calculations can be found in the open literature.

The theme of section 3.5 is spectral factorization methods for active control of sound and vibration (ACSV) applications. In subsection 3.5.1 the *cepstral* method for single-channel (SC) spectral factorization is introduced. This method is rather simple and straightforward to use. The cepstral method is applied in the examples to divide the secondary paths into their all-pass component and minimum-phase components. A more versatile framework, however, is required for MC spectral factorization. One such candidate for MC spectral factorization that involves a prediction error filter (PEF) is presented in subsection 3.5.2. Moreover, some design guides for successful operation of this more complex procedure that we henceforth will refer to as the multiple-channel prediction error filter spectral factorization (MCPEFSF) algorithm is provided.

The main results of this chapter are summarized in section 3.6.

Finally, in appendix 3.A an attempt is made to carry out in hand the spectral factorization of simple ANR system involving two reference sensors that are exposed to pink noise.

3.2 Spectral Factorization

Spectral factorization is a signal processing technique that has applications to stable inverse filter design, linear quadratic estimation and also to the design of optimal causally constrained (nonanticipatory) filters for AC. In spectral factorization the minimum-phase part of a signal is constructed from the auto correlation function or directly from the auto spectral density function. Owing to its wide spread applicability a variety of methods have been developed for the computation of the *canonical spectral factors* in particular for scalar-valued signals. A survey of spectral factorization methods can be found in [13], that also establishes a link between the somewhat scattered results in this field. Unfortunately, generalization of the spectral factorization methods to the case of vector-valued signals is not straightforward. Some methods have been reported in the literature for computing the matrix-valued spectral factorization also including a technique that involves solving the discrete-time algebraic Riccati equation (DARE) [9] (see also [8, Ch. 6] and the references herein). However, a common problem associated with these factorization methods is that they generally rely on accurate modeling of the MIMO systems in terms of state-space (SS) form, which is extremely difficult for high order systems frequently encountered in active noise and vibration control (ANVC) problems.

Examples with increasing complexity will be used to explain in details the underlying mechanism of MC spectral factorization applied to active control of sound (ACS). These examples establish a link to more realistic systems.

The PEF based method for obtaining the MC spectral factors only requires a discrete-frequency version of the auto- and cross-spectral density functions and is thus well suited for AC applications whether applied to experimental data or simulated data.

3.2.1 z-Spectra

Signal analysis often involves examination of the z-autospectrum and z-cross-spectrum. For two arbitrary but *stationary*[1] random sequences (RSs) $\psi_a(n), \psi_b(n)$ the z-autospectrum and z-cross-spectrum are defined as the bilateral **z**-transform of the discrete-time ACS respective the discrete-time CCS, that is,

$$S_{\psi_a\psi_a}(z) \triangleq \sum_{n=-\infty}^{\infty} R_{\psi_a\psi_a}(n) z^{-n} = \mathrm{E}\,\tilde{\boldsymbol{\psi}}_a(z)\tilde{\boldsymbol{\psi}}_a^*(z^{-*}) \tag{3.2.1a}$$

$$S_{\psi_a\psi_b}(z) \triangleq \sum_{n=-\infty}^{\infty} R_{\psi_a\psi_b}(n) z^{-n} = \mathrm{E}\,\tilde{\boldsymbol{\psi}}_a(z)\tilde{\boldsymbol{\psi}}_b^*(z^{-*}) \tag{3.2.1b}$$

respectively, where the discrete-time ACS and CCS $R_{\psi_a\psi_a}(n)$ and $R_{\psi_a\psi_b}(n)$ in turn are defined in (N.2.14) on page 796. The last equation in (3.2.1a) to (3.2.1b) are obtained from interchanging the expectation operator $\mathrm{E}(\,\cdot\,)$ and the **z**-transform operator $\tilde{\psi}_a(z) = (\mathcal{Z}\psi_a)(z)$. A sufficient requirement for the existence of the z-auto-cross-spectrum is that the ACS respectively the CCS are *exponentially bounded*, namely that at all time n there exist a constant positive-definite (p.d.) matrix K and a constant ν such that

$$\exists K \succ 0, 0 < \nu < 1 : \forall n \in \mathbb{Z} \quad R_{\psi_a\psi_a}(n), R_{\psi_a\psi_b}(n) \prec K\nu^{|n|}. \tag{3.2.2}$$

The region of convergence (ROC) of (3.2.1a) and (3.2.1b) is the annular ring defined by $\nu \leq |z| \leq \nu^{-1}$, that includes the unit circle.

3.2.2 Spectral Factorization Definition

The spectral factorization of the z-auto-cross-spectrum[2] $S_{xx}(z)$ of a finite-power possibly vector-valued sequence $x(n)$ is defined by [8, Ch. 6]

$$S_{xx}(z) = L(z)R_eL^*(z^{-*}), \tag{3.2.3}$$

where the quantity $L(z) \in \mathbb{C}^{N_x \times N_x}$ is a *minimum phase* function (modeling filter) that can be expanded as

$$L(z) = \sum_{k=0}^{\infty} L_k z^{-k}, \tag{3.2.4}$$

[1] Formally, stationarity is meant as *stationarity in a autocorrelation sequence (ACS) sense* and *stationarity in a cross correlation sequence (CCS) sense* respectively (refer to footnote 3 on page 796 and [11]).

[2] We deliberately use the term z-auto-cross-spectrum in the MC case as S_{xx} involves both self-terms in the diagonal (z-autospectrum) and cross-terms outside the diagonal (z-cross-spectrum).

where each spectral factor $L_k \in \mathbb{K}^{N_x \times N_x}$ and $L_0 = \mathrm{I}$. The quantity $L^*(z^{-*})$ denotes the *para-Hermitian conjugate* of $L(z)$ (whitening filter) that when evaluated on the unit circle $\delta\mathbb{D}$ becomes the usual Hermitian conjugate. The parameter[3] z^{-*} is just the *conjugate-reciprocal* of z (reflection of z about the uc). In this formulation $R_e \in \mathbb{R}^{N_x \times N_x} \succ 0$ is a normalization matrix (constant) that ensures that $L(z)$ is normalized to the identity matrix at infinity, that is, $L(\infty) = \mathrm{I}$. This in turn makes the *canonical spectral factorization*[4] in (3.2.3) unique.

For scalar-valued signals it is in principle straightforward to calculate the *canonical spectral factorization*: Compute the poles and zeros and retain the stable ones in the canonical factor and use their conjugate reciprocals for the para-Hermitian conjugate. In this case R_e is simply the variance of the signal. However, for vector-valued signals $L(z)$ becomes matrix-valued and can therefore not alone be determined from zeros and poles. In addition *transmission zeros* must be considered.

The conditions under which such spectral factorization exists will be dependent on whether *rational* z-autospectra or *nonrational* z-autospectra are considered.

Spectral Factorization of Processes with Rational z-Spectra

In general for MCAC systems the z-autospectrum matrix $S_{xx}(z)$ may be globally rank deficient, that is, $S_{xx}(\mathrm{e}^{\imath\omega})$ is rank deficient at infinitely many points on the unit circle. In such a globally rank deficient case a spectral factorization of the form [8, Ch. 6]

$$S_{xx}(z) = \bar{L}(z)\bar{R}_e\bar{L}^*(z^{-*}), \tag{3.2.6}$$

can always be performed, where

1. $\bar{L}(z) \in \mathbb{C}^{N_x \times n_x}$ is a *minimum phase* rational matrix sequence (modeling filter), that is analytic[5] on and outside the unit circle (uc), i.e., for $z \in \mathbb{D}_+$.

2. The normalization matrix $\bar{R}_e \in \mathbb{R}^{n_x \times n_x} \succeq 0$ is only positive-semidefinite (p.s.d.).

The quantity $n_x \in \mathbb{N}^*$ is the rank of $S_{xx}(\mathrm{e}^{\imath\omega})$, that is, $\operatorname{rank}\big(S_{xx}(\mathrm{e}^{\imath\omega})\big) = n_x < N_x$ *a.e.*; $\omega \in [-\pi;\pi]$.

For example, for collocated reference sensors the reference signal content in, say, two reference sensors may be very redundant especially in the low frequency region leading to $n_x = N_x - 1$. A remedy to such global rank deficiency is (artificially) to superpose the reference signals with some uncorrelated noise. In this global rank deficient case the pseudo inverse of $\bar{L}(z)$ denoted by

[3] Recall that z^{-1} is the *reciprocal* of z (reflection of z about the uc and reflection of the result hereof about the real axis).

[4] By the term *canonical* we explicitly refer to a unique solution to (3.2.3). However, we may obtain a *basic spectral factorization* $S_{xx}(z) = QL(z)R_eL^*(z^{-*})Q^*$ for some orthonormal matrix Q. In the literature the basic spectral factorization is often expressed by

$$S_{xx}(z) = L_+(z)L_-^*(z^{-*}), \tag{3.2.5}$$

where $L_+(z)$ is *a* spectral factor (minimum phase, modeling filter) and $L_-(z)$ is the para-Hermitian conjugate of $L_+(z)$.

[5] Basically, an *analytic function* is an infinitely differentiable function such that the Taylor series at any point z_0 in its domain is convergent for z close enough to z_0 and its value equals $f(z)$.

$\bar{L}^{\dagger}(z)$ should be inserted in (3.2.3) instead of $L^{-1}(z)$ (and accordingly in (3.2.11) on the following page).

Now excluding the possibility of global rank deficiency, then for a *rational* z-autospectrum $S_{xx}(\mathrm{e}^{\imath\omega})$ can only be rank deficient at finitely many points on the unit circle, that is, rank $\big(S_{xx}(\mathrm{e}^{\imath\omega})\big) = N_x$ *a.e.*; $\omega \in [-\pi;\pi]$, the existence of the spectral factorization (3.2.3) is then always guaranteed, where

1. $L(z) \in \mathbb{C}^{N_x \times N_x}$ is rational matrix sequence, that is analytic on and outside the uc, i.e., for $z \in \mathbb{D}_+$.

2. $L^{-1}(z) \in \mathbb{C}^{N_x \times N_x}$ is rational matrix sequence that is analytic outside the uc, i.e., for $z \in \mathbb{D}_+^* \; \{z \in \mathbb{C}; |z| > 1\}$.

3. $L(\infty) = \mathrm{I}$.

4. The normalization matrix is p.d., that is, $R_e \succ 0$.

Furthermore, if we explicitly assume that $S_{xx}(z)$ has full rank *everywhere* on the unit circle, that is, $S_{xx}(\mathrm{e}^{\imath\omega})$ has no unit-circle zeros then point 2 should be replaced by

1. $L^{-1}(z) \in \mathbb{C}^{N_x \times N_x}$ is rational matrix sequence for $z \in \mathbb{D}_+$.

Hence, as both $L(z)$ and $L^{-1}(z)$ are analytic in the domain $\mathbb{D}_+$, $L(z)$ therefore has all its zeros and poles strictly inside the unit circle, that is, for $z \in \mathbb{D}_-^* \; \{z \in \mathbb{C}; |z| < 1\}$ and is therefore a *rational minimum phase function*. By excluding the possibility of global rank deficiency the uniqueness is guaranteed and we refer (3.2.3) to as a *canonical spectral factorization*.

Spectral Factorization of Processes with Nonrational z*-Spectra*

In contrary to the case of *rational* z*-spectra* where both $L(z)$ and $L^{-1}(z)$ are analytic both on the unit circle and outside the unit circle, that is, for $|z| \geq 1$ this analyticity, however, does only pertain to the region $|z| > 1$ in the case of *nonrational* z*-spectra*. In practice this means that although the impulse response of $L(z)$ $l(n)$ is square-summable, that is, $\sum_{n=1}^{\infty} |l(n)|^2 < \infty$ this cannot in general be guaranteed for the impulse response of $L^{-1}(z)$.

However, if and only if $S_{xx}(\mathrm{e}^{\imath\omega})$ satisfies the *finite power condition*

$$R_{xx}(0) \triangleq \frac{1}{2\pi} \int_{-\pi}^{\pi} S_{xx}(\mathrm{e}^{\imath\omega}) \, \mathrm{d}\omega < \infty \tag{3.2.7}$$

and the so-called *Paley-Wiener condition*

$$\frac{1}{2\pi} \int_{-\pi}^{\pi} \ln\big(S_{xx}(\mathrm{e}^{\imath\omega})\big) \, \mathrm{d}\omega > -\infty, \tag{3.2.8}$$

then the existence of a spectral factorization of the form (3.2.3), where $L(z)$ and $L^{-1}(z)$ are analytic in $\mathcal{D}_+^*$, is guaranteed. The finite power condition which is the same as the condition of $S_{xx}(\mathrm{e}^{\imath\omega})$ being absolute integrable is satisfied by virtue of the assumption of exponentially bounded sequences (3.2.2). More importantly, however, in many engineering applications the Paley-Wiener condition is not satisfied. For example, for band-width limited signals $S_{xx}(\mathrm{e}^{\imath\omega}) = 0$ at infinitely many points.

3.2.3 Spectral Factorization in Active Control

In subsection 8.5.4 on page 389 viz. (8.5.19) an expression for the **t**-domain WH filter optimal weight vector for a cost function $J^{\alpha\gamma\Pi}(w_{i_B})$ that include weight-effort-driven leakage, control-effor-driven leakage and weight regularization is provided and repeated here for convenience

$$\boxed{w_{i_B}^o = \big[R_{u,i}^{W_e} + \alpha_{i_\alpha} + R_{x,i}^{\gamma} + \Pi_{i_\Pi}\big]^{-1}\big(R_{du,i}^{W_e} + \Pi_{i_\Pi}\bar{w}_{i_{\bar{w}}}\big).} \tag{3.2.9}$$

In order to accommodate the corresponding **z**-domain WH solution (8.5.20) for AC applications in addition to the spectral factorization of the reference signals we also need to decompose the secondary paths into their minimum-phase/all-pass components, that is,

$$\boxed{\tilde{g}_{ey}(z) = \tilde{g}_{ey,\min}(z)\tilde{g}_{ey,\mathrm{all}}(z).} \tag{3.2.10}$$

In the transform domain the optimal weights - in a linear-least-mean-squares estimate (l.l.m.s.e.) sense - are obtained from[6]

$$\boxed{\tilde{w}^o(z) = -\tilde{g}_{ey,\min}^{-1}(z)\big\{L^{-1}(z^{-*})S_{xd}(z^{-*})\tilde{g}_{ey,\mathrm{all}}(z^{-*})\big\}_+^* R_e^{-1}L^{-1}(z),} \tag{3.2.11}$$

where the *plus operator* $\big\{\,\cdot\,\big\}_+$ determines the *causal part* of the sequence whose Fourier transform is inside the curlets and where the notion $\big\{\,\cdot\,\big\}_+^*$ is used instead of $\big(\big\{\,\cdot\,\big\}_+\big)^*$ for notational convenience.

Expression (3.2.11) represents an extension to (8.5.20) in subsection 8.5.4 on page 389 by accomodating the plant. For notational brevity, however, in this chapter we use $S_{xx}(z)$ and $L(z)$ as surrogates for $S_{uuxx}^{\alpha\gamma W_e}(z)$ and $L_{ux}^{\alpha\gamma W_e}(z)$ defined in (8.5.21) to (8.5.22).

We recognize that the following three components all evaluated in a time-reversed sense are subject to the plus operator $\big\{\,\cdot\,\big\}_+$:

1. $L^{-1}(z^{-*})$ that is the inverse of the minimum phase function $L(z)$ evaluated in a time-reversed sense. As $L^*(z^{-*})$ by the definition (3.2.3) is anti-causal the same applies to its reciprocal. Hence this factor (matrix) will *increase* the number of terms within the plus operator, but therefore also increase the number of terms discarded by the action of the plus operator as the signals become more and more colored. At first glance this might seem counter-intuitive, but might be explained by the fact that white signals require relative few weights in the time-domain representation (in principle only a Dirac impulse) while in order to represent colored signals more weights are required half of which extent in to the past.

[6] This expression is slightly different from [5, Ch. 5] owing to the different definition of z-cross-spectrum.

On the other hand white noise signals are generally substantially more difficult to control by a feedback system (FBS) topology than colored signals.

2. The z-cross-spectrum matrix between the reference sensors and the error sensors $S_{xd}(z^{-*})$ evaluated in a time-reversed sense. From the definition of z-cross-spectrum (3.2.1b) on page 107 $S_{xd}(z)$ will include z-terms raised to a *positive* power corresponding to the number of samples signals are acquired in advance by the reference sensors before they are acquired by the error sensors. Hence, the time-reversed version hereof, that is, $S_{xd}(z^{-*})$ will include *causal* terms corresponding to such acquisition lead-time and will therefore act to increase the number of terms remaining after the plus operation.

3. $\tilde{g}_{ey,\text{all}}(z^{-*})$ that is the time-reversed all-pass component of the plants. This matrix consists therefore of anti-causal elements that will *decrease* the number of terms remaining on under causality constraints.

It should be recalled that the operation of the plus operator is associated with a performance decrease as compared with the unconstrained case[7]. In conclusion, causally constrained filtering is of most concern in AC of colored random signals involving "slowly" reacting plants (secondary paths) and with negligible acquisition lead-times. On the contrary, for random white noise (RWN) signals with responsive plants and with a feedforward topology that ensure large acquisition lead-times fewer terms will be discarded by the plus operator in (3.2.11). For periodic signals the causality constraints as applied in (3.2.11) are not of concern.

The following examples will hopefully shed some light on the underlying nature of the expression for the optimal weights (3.2.11).

Example 3.2.1 (Feedforward System)**.** In this example we consider a very rudimentary feedforward system (FFS) consisting of two reference sensors, one error sensor and one actuator, that is, $N_x = 2, N_e = 1$ and $N_y = 1$. An acoustical field is established by two uncorrelated random white noise sources (1 Hz-3 kHz) of unit variance each. The propagation direction of these fields are along the negative and positive x-axis respectively, that is, $\hat{\boldsymbol{s}}_1^C = (-1, 0, 0)$ and $\hat{\boldsymbol{s}}_2^C = (1, 0, 0)$, where $\hat{\boldsymbol{s}}_s^C$ is the propagation direction of the s'th clutter signal (see Figure 3.1). The vector $\hat{\boldsymbol{s}}_s^S$ denotes the propagation direction of the s'th periodic signal. The reference sensors and the error sensor are positioned at $\mathbf{r}_{x_1} = (517.5, 0, 0)$mm and $\mathbf{r}_{x_2} = (-517.5, 0, 0)$mm and $\mathbf{r}_{d_1} = (57.5, 0, 0)$mm respectively. With a speed of sound $c = 345\,\text{m}\cdot\text{s}^{-1}$ and a sampling frequency of f_s^2=6 kHz these interspacings under the assumption of free space (FS) propagation correspond to a delay of exactly 8 samples from the reference sensor x_1 to error sensor d_1, 10 samples delay from reference sensor x_2 to d_1 and 18 samples delay from x_1 to x_2.

The position of the actuator is inessential but implicitly included in the plant response that we assume is a simple delay of 4 samples, that is, $\tilde{g}_{ey}(z) \equiv \tilde{g}_{e_1y_1}(z) = z^{-4}$. Hence, $\tilde{g}_{ey,\text{all}}(z) \equiv \tilde{g}_{e_1y_1,\text{all}}(z) = z^{-4}$ and $\tilde{g}_{ey,\text{min}}(z) \equiv \tilde{g}_{e_1y_1,\text{min}}(z) = 1$. Moreover, for simplicity of the analysis we exclude any feedback paths, that is, $\tilde{g}_{xy}(z) = 0$.

The cross-correlation functions $r_{x_1d_1}(\tau), r_{x_2d_1}(\tau), r_{x_1x_1}(\tau), r_{x_2x_2}(\tau)$ and $r_{x_1x_2}(\tau)$ therefore become

[7] An example where noncausal filtering is applied is when *smoothing* signals.

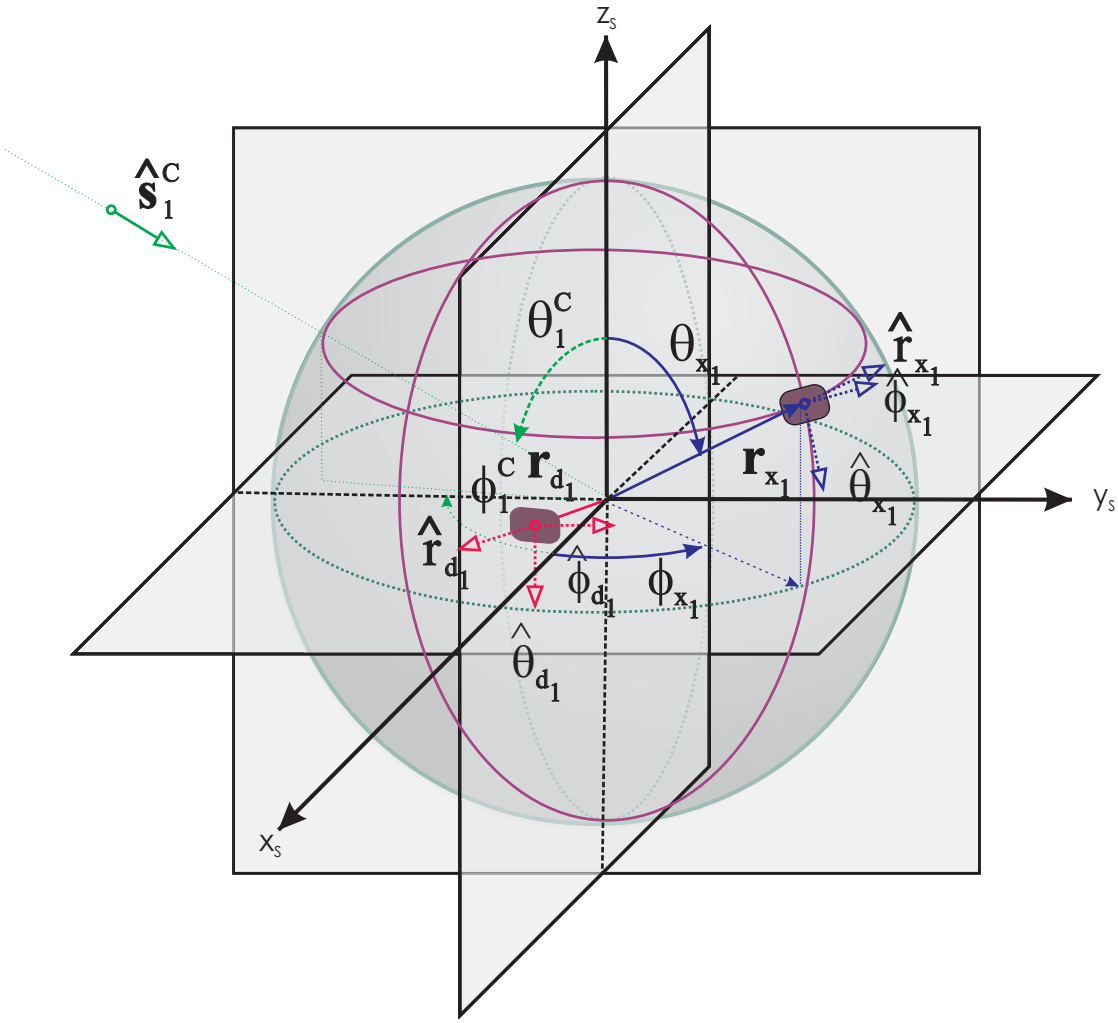

Fig. 3.1: Scenario Coordinate System.

$$r_{x_1d_1}(\tau) = \begin{cases} 1; & \tau = \pm 8 \\ 0; & \text{else} \end{cases} \tag{3.2.12a}$$

$$r_{x_2d_1}(\tau) = \begin{cases} 1; & \tau = \pm 10 \\ 0; & \text{else} \end{cases} \tag{3.2.12b}$$

$$r_{x_1x_1}(\tau) = r_{x_2x_2}(\tau) = \begin{cases} 2; & \tau = 0 \\ 0; & \text{else} \end{cases} \tag{3.2.12c}$$

$$r_{x_1x_2}(\tau) = r^*_{x_2x_1}(-\tau) = \begin{cases} 1; & \tau = \pm 18 \\ 0; & \text{else.} \end{cases} \tag{3.2.12d}$$

The z-auto-cross-spectrum matrices are therefore

$$S_{xx}(z) = \begin{bmatrix} 2 & z^{18} + z^{-18} \\ z^{18} + z^{-18} & 2 \end{bmatrix} \tag{3.2.13}$$

and

$$S_{xd}(z) = \begin{bmatrix} z^8 + z^{-8} \\ z^{10} + z^{-10} \end{bmatrix}. \tag{3.2.14}$$

Although two RWN signals of unit variance each are used the z-auto-cross-spectrum matrix does not coincide with two times the identity matrix owing to the cross-coupling between the reference sensors.

By using Euler's formula we may express $S_{xx}(\mathrm{e}^{\imath\omega})$ on the unit circle as

$$S_{xx}(\mathrm{e}^{\imath\omega}) = 2 \begin{bmatrix} 1 & \cos(36\pi f/f_s) \\ \cos(36\pi f/f_s) & 1 \end{bmatrix}. \tag{3.2.15}$$

From (3.2.15) we identify the frequency points where $S_{xx}(\mathrm{e}^{\imath\omega})$ might be rank-deficient to be obtained from $f = \frac{n}{18}\frac{f_s}{2} = n166.67\,\mathrm{Hz}, n \in \mathbb{Z}$. We therefore appreciate that $S_{xx}(\mathrm{e}^{\imath\omega})$ does **not** comply with our requirements on $S_{xx}(\mathrm{e}^{\imath\omega}) \succ 0$ as $S_{xx}(\mathrm{e}^{\imath\omega})$ is rank-deficient for $f = \frac{n}{18}\frac{f_s}{2}, n \in \mathbb{Z}$. We will return later to the consequences of the lack of positive-definiteness. It should, however, be noticed that as the elements of $S_{xx}(z)$ are rational functions of z $S_{xx}(\mathrm{e}^{\imath\omega})$ will only have a finite number of such *transmission zeros*, that is, $S_{xx}(\mathrm{e}^{\imath\omega}) \succ 0$ a.e. on the UC. However, ignoring this problem for a moment we readily identify the *unique* spectral factorization of $S_{xx}(z)$ namely,

$$L(z) = \begin{bmatrix} 1 & z^{-18} \\ z^{-18} & 1 \end{bmatrix}; \quad R_e = \mathrm{I}; \quad L^*(z^{-*}) = \begin{bmatrix} 1 & z^{18} \\ z^{18} & 1 \end{bmatrix}. \tag{3.2.16}$$

We appreciate that $L(z)$ basically has an 18^{th} order pole at the origo and no zeros outside the UC (at all) and therefore presents a causal stable sequence. On the contrary $L^*(z^{-*})$ has an 18^{th} order pole at infinity and also no zeros inside the UC (at all) and therefore presents a anti-causal unstable sequence.

From (3.2.16) the inverse of $L(z)$ and $L^*(z^{-*})$ are

$$L^{-1}(z) = \tfrac{1}{1-z^{-36}} \begin{bmatrix} 1 & -z^{-18} \\ -z^{-18} & 1 \end{bmatrix}; \quad L^{-*}(z^{-*}) = \tfrac{1}{1-z^{36}} \begin{bmatrix} 1 & -z^{18} \\ -z^{18} & 1 \end{bmatrix}. \tag{3.2.17}$$

Note that $L^{-1}(z)$ and $L^{-*}(z^{-*})$ are causal and anti-causal sequences respectively. Accordingly, by insertion of (3.2.14) and (3.2.17) in (3.2.11) we obtain

$$\begin{aligned} \tilde{w}^o(z) &= -\left\{ \tfrac{1}{1-z^{*36}} \begin{bmatrix} 1 & -z^{*18} \\ -z^{*18} & 1 \end{bmatrix} \begin{bmatrix} z^{*8} + z^{-*8} \\ z^{*10} + z^{-*10} \end{bmatrix} z^{*4} \right\}_+^* \tfrac{1}{1-z^{-36}} \begin{bmatrix} 1 & -z^{-18} \\ -z^{-18} & 1 \end{bmatrix} \\ &= -\left\{ \tfrac{1}{1-z^{*36}} \begin{bmatrix} z^{*8} + z^{-*8} - z^{*28} - z^{*8} \\ z^{*10} + z^{-*10} - z^{*26} - z^{*10} \end{bmatrix} z^{*4} \right\}_+^* \tfrac{1}{1-z^{-36}} \begin{bmatrix} 1 & -z^{-18} \\ -z^{-18} & 1 \end{bmatrix} \\ &= -\left\{ \tfrac{1}{1-z^{36}} \begin{bmatrix} z^{-4} - z^{32} & z^{-6} - z^{30} \end{bmatrix} \right\}_+ \tfrac{1}{1-z^{-36}} \begin{bmatrix} 1 & -z^{-18} \\ -z^{-18} & 1 \end{bmatrix}, \end{aligned} \tag{3.2.18}$$

where we for notational compactness use z^{*18} instead of $(z^{18})^*$. Now by applying the Taylor expansion $(1 - z^{\pm 36})^{-1} = 1 + z^{\pm 36} + z^{\pm 72} + z^{\pm 108} \dots$ to the terms inside the $\{\cdot\}_+$ operator in (3.2.18) we see that only a single term in each element remains. Accordingly the optimal weights are obtained from

$$\begin{aligned} \tilde{w}^o(z) &= -(1 + z^{-36} + z^{-72} + z^{-108} + \dots) \begin{bmatrix} z^{-4} & z^{-6} \end{bmatrix} \begin{bmatrix} 1 & -z^{-18} \\ -z^{-18} & 1 \end{bmatrix} \\ &= -(1 + z^{-36} + z^{-72} + z^{-108} + \dots) \begin{bmatrix} z^{-4} - z^{-24} & z^{-6} - z^{-22} \end{bmatrix}. \end{aligned} \tag{3.2.19}$$

We readily observe from (3.2.19) that w^o is constituted by two infinite sequences of weights. The weight vector $\underset{\sim}{w}^{1,1}$ that links the first reference signal to the control output signal has two "fundamental" weights, namely the 4'th weight and the 24'th weight that in turn both are repeated an infinite number of times shifted 36 positions each time. The weight vector $\underset{\sim}{w}^{2,1}$ that links the second reference signal to the control output signal similarly has its 6'th and the 22'th weight as "fundamental" weights and these weights are also repeated an infinite number of times shifted 36 positions each time.

The results from applying the two causality-finite-order-constrained WH filters, that is, the **t**-domain and the **z**-domain WH filter defined in (3.2.9) and (3.2.11) respectively to the setup in this example will be presented next. For the **z**-domain method we have employed the MCPEFSF described in subsection 3.5.2 on page 206.

The auto spectral density functions are shown in Simulation 3.2.1. Hence, for a one-sided spectra the $S_{xx}(f) = S_{ee}(f) = 10\log_{10}(2/(f_s/2)) \approx -31.76\,\mathrm{dBHz}^{-1}$. The signals have been averaged over 180 s resulting in $K_{\mathrm{DFT}} = 1438$ averages and the fluctuations are therefore confined within fractions of a dB. In Simulation 3.2.2 very deep troughs are observed in the multiple coherence function $\gamma_{d_1 \cdot x!}$ at frequency points where $S_{xx}(\mathrm{e}^{\imath\omega})$ is rank-deficient, namely for $f = \frac{n}{18}\frac{f_s}{2}, n \in \mathbb{Z}$, as previously predicted from (3.2.15). Hence, at these frequencies the system is blind as regards the reference signals and no ANR is possible. The cross-correlation functions are depicted in Simulation 3.2.3. The pulses occur at times ± 133 µs and ± 167 µs in agreement with (3.2.12a)

to (3.2.12b) for a sampling frequency of f_s^2=6 kHz. The finite width and the spill-over to time-domain side-lobes of the "Dirac" impulse is due to the finite bandwidth of 3 kHz. The spill-over effects are also responsible for the peak values being marginally lower than unity.

When only 130 weights are used we readily identify the non-zero weights predicted from (3.2.19) in Simulation 3.2.4 - 3.2.5. The first non-zero weights of $\underset{\sim}{\overset{\frown}{w}}^{1,1}$ and $\underset{\sim}{\overset{\frown}{w}}^{2,1}$ corresponding to the z^{-4} and z^{-6} terms in (3.2.19) can easily physically be explained as follows. When reference sensor x_1 receives the incident field with propagation direction $\hat{\boldsymbol{s}}_1^C$ it has an acquisition lead time of 8 samples. That lead time in combination with 4 samples delay in the secondary path leads to choice of a "wait delay" in the weight vector of 4 samples. Similarly, arguments explains the "wait delay" in weight vector $\underset{\sim}{\overset{\frown}{w}}^{2,1}$ of 6 samples when the incident field with propagation direction $\hat{\boldsymbol{s}}_2^C$ is received as the acquisition lead-time for reference sensor x_2 amounts to 10 samples. By considering the case where each reference sensor is only "responsible" for a single incident field, that is, reference sensor x_1 and x_2 are only responsive to the fields with propagation direction $\hat{\boldsymbol{s}}_1^C$ and $\hat{\boldsymbol{s}}_2^C$ respectively, we appreciate that no more active weights would be needed. However, both reference signals $x_1(t)$ and $x_2(t)$ are superpositions of both primary fields $s_1^C(t)$ and $s_2^C(t)$. One may argue that reference sensor x_1 should "take some actions" on $s_2^C(t)$. However, this signal is received 8 samples after it has been received by the error sensor and for a causal secondary path and a random white noise signal nothing can be done. This term is therefore correctly discarded by the plus operator.

In general, a superposition of the secondary fields that are generated in response to those primary fields on the reference signals should be considered. However, we have explicitly assumed that no such feedback path exists.

The second non-zero weights of $\underset{\sim}{\overset{\frown}{w}}^{1,1}$ and $\underset{\sim}{\overset{\frown}{w}}^{2,1}$ corresponding to the z^{-24} and z^{-22} terms in (3.2.19) are consequences of the superposition of the primary and secondary fields at the error sensor. For example, as the component of the primary field at reference sensor x_1 caused by $s_2^C(t)$ provides no useful information the controller should estimate this contribution and subtract it from the corresponding reference signal. This also explains the infinite and repetitive weight pattern in (3.2.19) where z^{-36} corresponds to the turn-around time $x_1 \leftrightarrows x_2$. The z^{-24} and z^{-22} terms correspond to the initial weight delays z^{-6} and z^{-4} associated with the opposite reference sensor and subsequent propagation delays $x_1 \leftarrow x_2$ and $x_1 \rightarrow x_2$ respectively that both count for z^{-18}. This operation is obtained from inverse filtering (cross-channel-whitening) by $L^{-1}(z)$.

In Simulation 3.2.6 - 3.2.7 the weight vectors $\underset{\sim}{\overset{\frown}{w}}^{1,1}$ and $\underset{\sim}{\overset{\frown}{w}}^{2,1}$ are shown for the **t**-domain WH method for $M_{\underset{\sim}{\overset{\frown}{w}}^{1,1}} = M_{\underset{\sim}{\overset{\frown}{w}}^{2,1}} = M_w = 2048$. Both of these weight vectors are seen to be tapered such that, e.g., $\underset{\sim}{\overset{\frown}{w}}_{M_w-1} \approx 0$. The white-noise-independent WH method, that is, the **z**-domain WH method described in subsection 8.4.2 on page 387 is more sensitive to truncation effects as evident from Simulation 3.2.8 - 3.2.9 and in accordance with [6].

The weights supposedly being equal to unity at infinitely many points, however are numerically decaying from 0.8 for the first weights to 0.1 for the last weights. This might be explained by truncation effects. Elliott and Rafaely [6] investigated frequency-domain domain adaptation of causal digital filters for SC systems and we will augment their findings to the MC case without a formal proof. Hence, according to [6] when employing the cepstral method the operation of the plus operator taking per frequency bin, that is,

$$\boxed{\tilde{w}^o(k) = -\tilde{g}_{ey,\min}^{-1}(k)\big\{L^{-1}(k)S_{xd}(k)\tilde{g}_{ey,\text{all}}(k)\big\}_+^* R_e^{-1}L^{-1}(k),} \tag{3.2.20}$$

then the accuracy of (3.2.20) will only be equal to the continuous frequency version of the

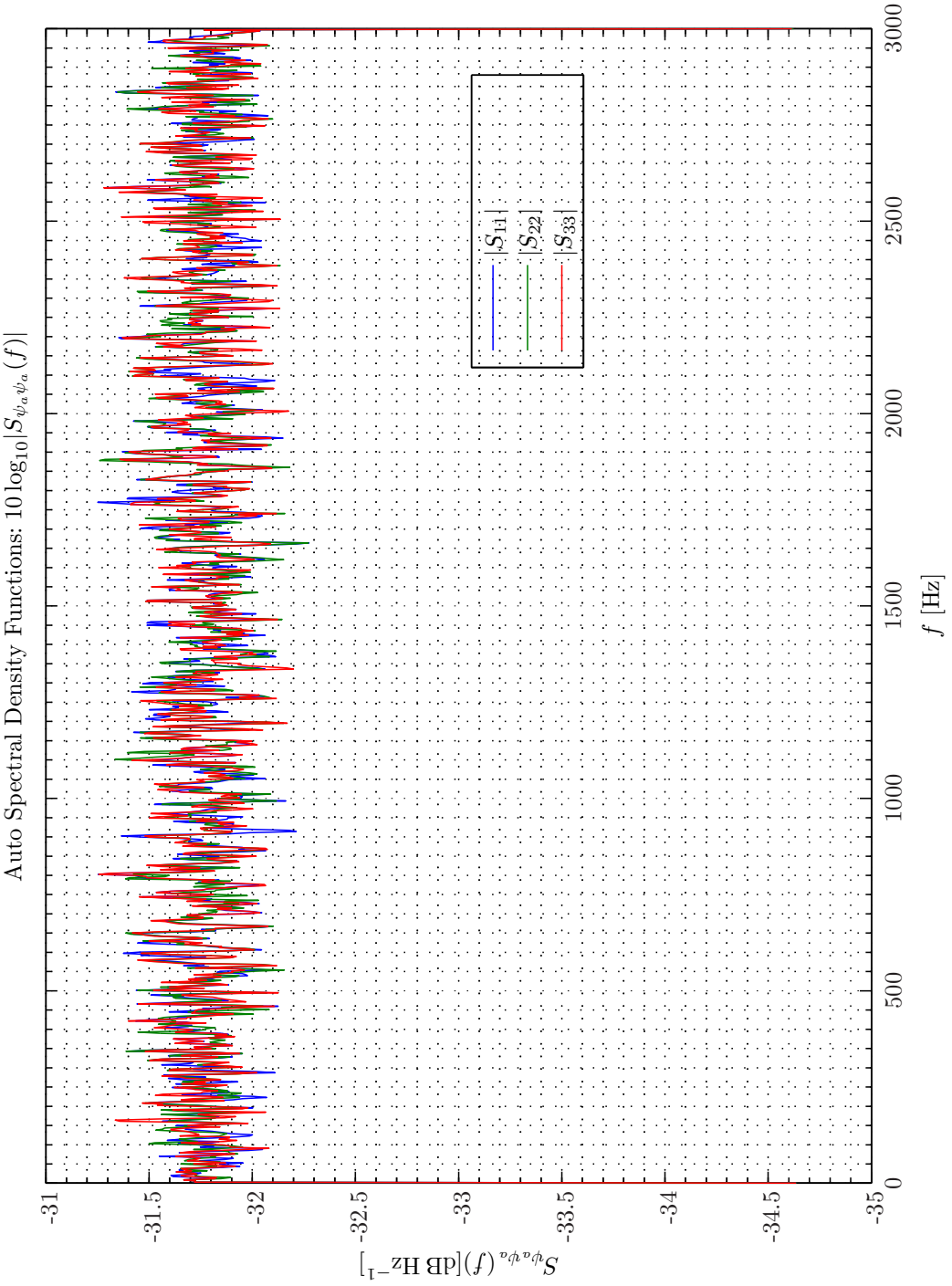

Sim 3.2.1: *Autospectral Density Functions*: **Statistical Data Analysis**: Single-Sided Modified Periodogram, $f_s = 6$ kHz, $N_{DFT} = 2048$, $L_{DFT} = 1501$, $R_{DFT} = 751$, Hanning, $\Delta f_m = 16$ Hz, $T_{DFT} = 0.25017$ s, $N_{f,DFT} = 1025$, $\Delta f_{DFT} = 2.9297$ Hz, $K_{DFT} = 1438$; **Signals:** Time: $0 - 180$ s. Refer to SigIDLaT. ; *Channels:* $\#1 \leftarrow x_1, \#2 \leftarrow x_2, \#3 \leftarrow d_1$. **Scenario:** `MultipleSinusoidalsAddiativeNoiseFeedforwardNx2Ne1Ny1Np0/20080210T213818.`.

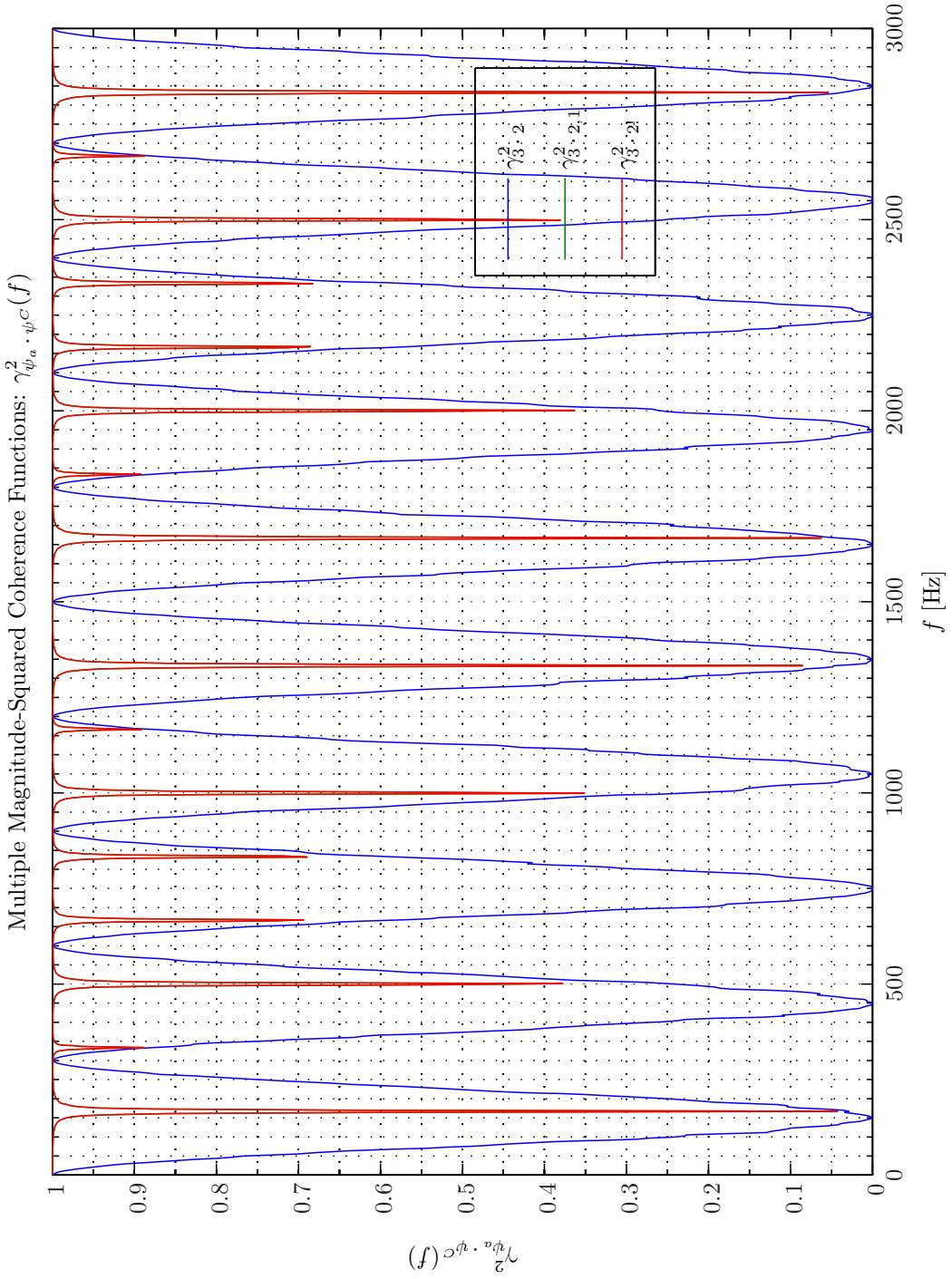

Sim 3.2.2: *Multiple Magnitude-Squared Coherence Functions* $\gamma^2_{\psi_a \cdot \psi^C}(f)$: **Statistical Data Analysis**: Single-Sided Modified Periodogram, $f_s = 6$ kHz, $N_{DFT} = 2048$, $L_{DFT} = 1501$, $R_{DFT} = 751$, Hanning, $\Delta f_m = 16$ Hz, $T_{DFT} = 0.25017$ s, $N_{f,DFT} = 1025$, $\Delta f_{DFT} = 2.9297$ Hz, $K_{DFT} = 1438$; **Signals:** Time: $0 - 180$ s. Refer to SigIDLaT. ; *Channels:* #1 $\leftarrow x_1$, #2 $\leftarrow x_2$, #3 $\leftarrow d_1$. **Scenario:** `MultipleSinusoidalsAddiativeNoiseFeedforwardNx2Ne1Ny1Np0/20080210T213818.`; .

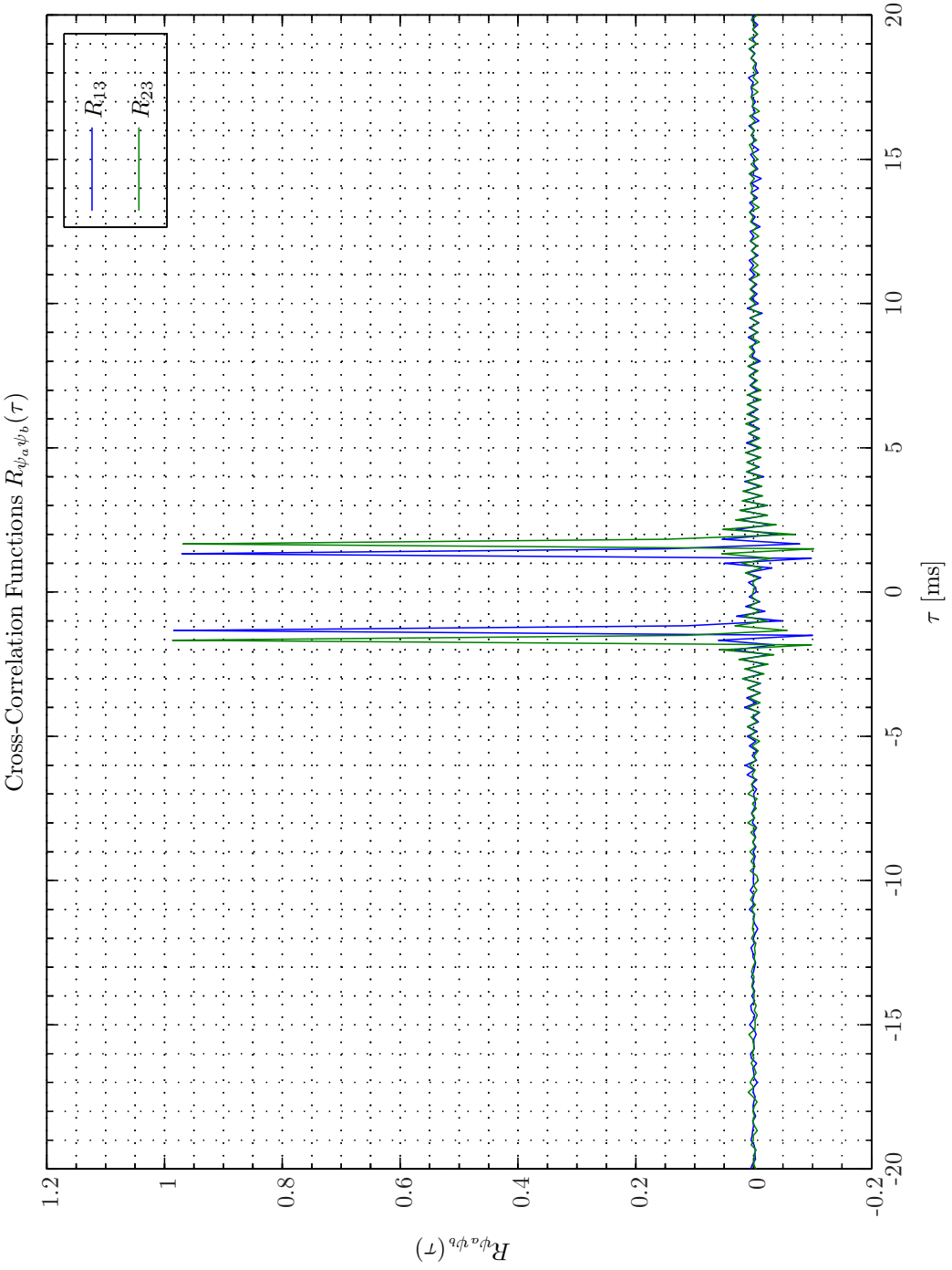

Sim 3.2.3: *Cross-Correlation Functions:* $R_{\psi_a\psi_b}(\tau)$: **Statistical Data Analysis**: Single-Sided Modified Periodogram, $f_s = 6$ kHz, $N_{DFT} = 2048$, $L_{DFT} = 1501$, $R_{DFT} = 751$, Hanning, $\Delta f_m = 16$ Hz, $T_{DFT} = 0.25017$ s, $N_{f,DFT} = 1025$, $\Delta f_{DFT} = 2.9297$ Hz, $K_{DFT} = 1438$; **Signals:** Time: $0 - 180$ s. Refer to SigIDLaT.; *Channels:* #1 $\leftarrow x_1$, #2 $\leftarrow x_2$, #3 $\leftarrow d_1$. **Scenario:** `MultipleSinusoidalsAddiativeNoiseFeedforwardNx2Ne1Ny1Np0/20080210T213818.;` .

optimum filter (3.2.11) at the frequencies $f = k\Delta f_{\text{DFT}}$, where $-N_{f,\text{DFT}} + 1 \leq k \leq N_{f,\text{DFT}}$ provided that the causal part of the inverse discrete-time Fourier transform of each entity in $\left\{L^{-1}(\mathrm{e}^{\imath\omega})S_{xd}(\mathrm{e}^{\imath\omega})\tilde{g}_{ey,\text{all}}(\mathrm{e}^{\imath\omega})\right\}_+$ has a duration less than $N_{DFT}/2$ samples. However, we cannot make the discrete Fourier transform (DFT) size sufficiently large enough for the causal part of the impulse response entities to have decayed to zero at $N_{DFT}/2$ samples as we need an infinite number of weights for perfect operation for this topology. An indication of this type of problem can also be seen as a "reflection" of $\underset{\sim}{w}^{1,1}$ and $\underset{\sim}{w}^{2,1}$ at $M_{\underset{\sim}{w}^{1,1}} = 2048$. By increasing the DFT size N_{DFT} from 4096 to 16382 the tapering is less pronounced and the last weight in $\underset{\sim}{w}^{1,1}$ increases numerically from $|\underset{\sim}{w}_{M_w-1}| \approx 0.1$ to $0.35 \ll 1$ and similar observations apply to $\underset{\sim}{w}^{2,1}$.

The performance is depicted in Simulation 3.2.10. It is readily observed that the performance is heavily dependent on the number of weights used, that is, $M_{\underset{\sim}{w}^{1,1}}$ and $M_{\underset{\sim}{w}^{2,1}}$.

This simple example revealed that even though the acquisition lead-times are larger than the plant delays at least three problems limit the achievable ANR performance. Firstly, the solution (3.2.19) is only optimal in a mean-square error (m.s.e.) sense under causality constraints. Without considering causality many more terms would be included, however, with a negative time-index. The second problem is related to the use of finite filter orders. It was demonstrated for this particular example that the **t**-domain WH method is more robust to truncation errors than the **z**-domain WH counterpart. The third problem identified is the lack of directivity of the reference sensors. This problem in turn accentuates the problem of using filters of insufficient order as will be seen next.

The discussion above suggests that by using reference sensors with element directivity more successful ANR performance is achievable. In the next example we will therefore investigate the benefits of element directivity.

Example 3.2.2 (Feedforward System, Reference Sensors with Directivity)**.** We assume in this example that each reference sensor but not the error sensor possess elementary directivity. Referring to Figure 3.1 we will assume a uniform directivity in the elevation plane (θ) and that the sensitivity varies as a cosine-on-a-pedestal function in the azimuthal plane (ϕ), that is,

$$g_{x_j}(\theta_{j,s},\phi_{j,s}) = \begin{cases} \max(\cos(\theta_{j,s}), b_{x_j}); & \theta_{j,s} \in [0;\pi/2]; \\ b_{x_j}; & \theta_{j,s} \in [\pi/2;\pi]; \end{cases} \quad \phi_{j,s} \in [-\pi,\pi]; \quad j = 1,2; s = 1,2, \tag{3.2.21}$$

where $g_{x_j}(\theta_{j,s},\phi_{j,s})$ is the elementary directivity of the j'th reference sensor $\theta_{j,s},\phi_{j,s}$ denote the angles of incidence of the s'th field relative to the j'th reference sensor and b_{x_j} is the minimum directivity of the j'th reference sensor ($0 \leq b_{x_j} \leq 1$).

Hence, for the same two incident fields with propagation directions $\hat{\boldsymbol{s}}_1^C$ and $\hat{\boldsymbol{s}}_2^C$ respectively and the same two reference sensor positions $\mathbf{r}_{x_1}$ and $\mathbf{r}_{x_2}$ as in Example 3.2.1 the element directivities become $g_{x_1}(\theta_{1,1},\phi_{1,1}) = g_{x_1}(0,0) = 1$, $g_{x_1}(\theta_{1,2},\phi_{1,2}) = g_{x_1}(\pi,0) = b_x$, $g_{x_2}(\theta_{2,1},\phi_{2,1}) = g_{x_2}(\pi,0) = b_x$ and $g_{x_2}(\theta_{2,2},\phi_{2,2}) = g_{x_2}(0,0) = 1$ respectively.

Proceeding as in Example 3.2.1 we readily obtain

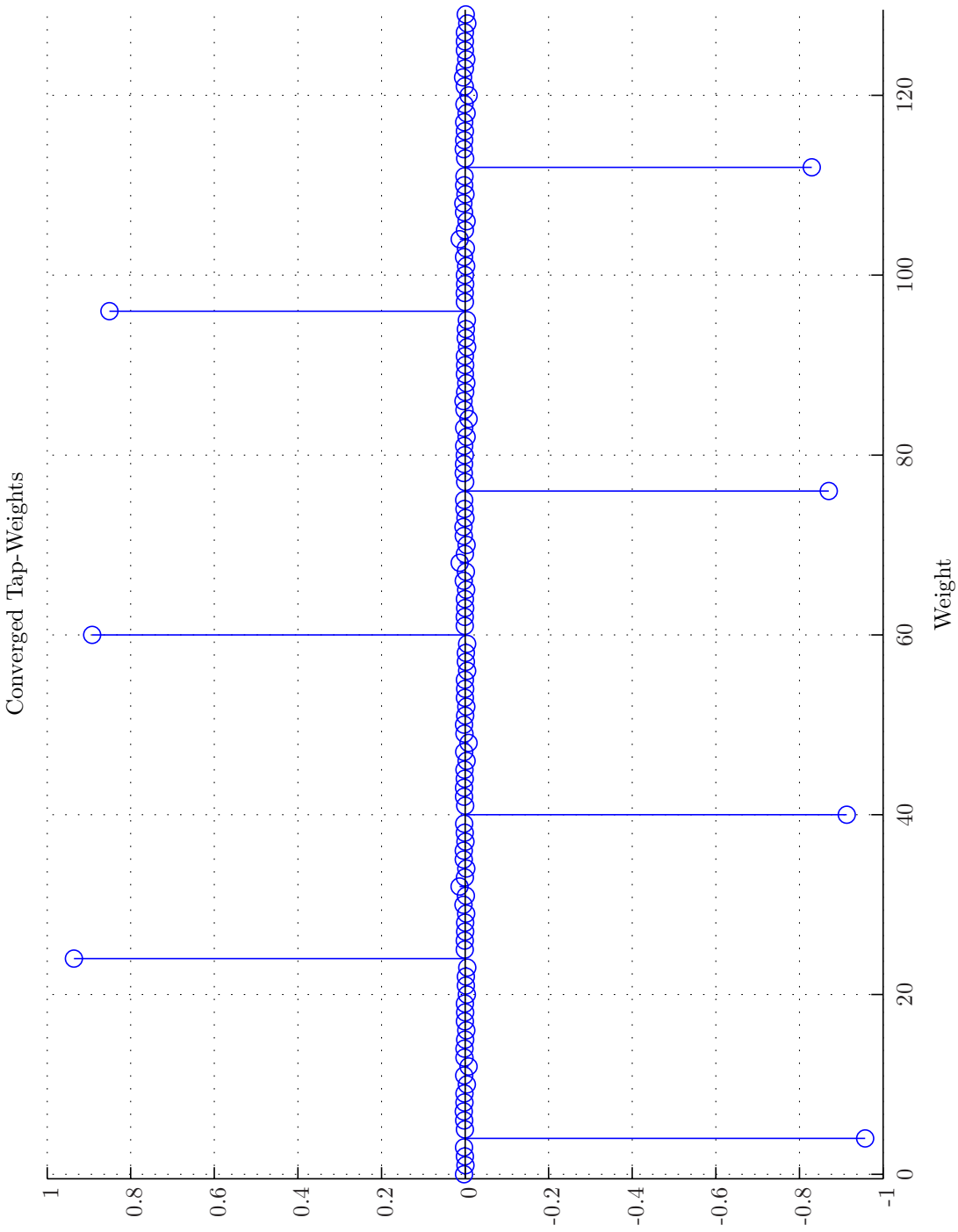

Sim 3.2.4: *Converged Tap-weights.* **Adaptive Filter** $\underset{\sim}{w}$: $\underset{\sim}{w}^{1,1}$: Wiener Hopf ($M = 130, \alpha = 1e-005, T_{WSS} = 0$,**z**-domain); **Main:** $f_s^0 = 192$ kHz, $f_s^1 = 6$ kHz, $R_\updownarrow^1 = \frac{1}{32} = 0.03125$, Elliptic LPF ($f_s = 192$ kHz, $f_{pass} = 2.75$ kHz, $f_{stop} = 3$ kHz, $A_{pass} = 2$ dB, $A_{stop} = 40$ dB), $f_s^2 = 6$ kHz, $R_\updownarrow^2 = \frac{1}{1} = 1$, Dummy; **Topology:** (Feedforward, mFx, $N_x = 2, N_e = 1, N_y = 1, N_p = 0, N_v = 2$); **Plants:** ($g_{xy}^{1,1}$: (FIR : $M_{gxy}^{1,1} = 1$), $g_{xy}^{1,2}$: (FIR : $M_{gxy}^{1,2} = 1$), $g_{ey}^{1,1}$: Delayed Sampled System: ($f_s = 6$ kHz, $t_d = 500$ µs, $\tau = 0$ µs) (FIR : $M_{gey}^{1,1} = 4$)); **Signals:** Time: $0 - 2$ s. Refer to SigIDLaT. ; **Scenario:** `MultipleSinusoidalsAddiativeNoiseFeedforwardNx2Ne1Ny1Np0/20080210T231832`.

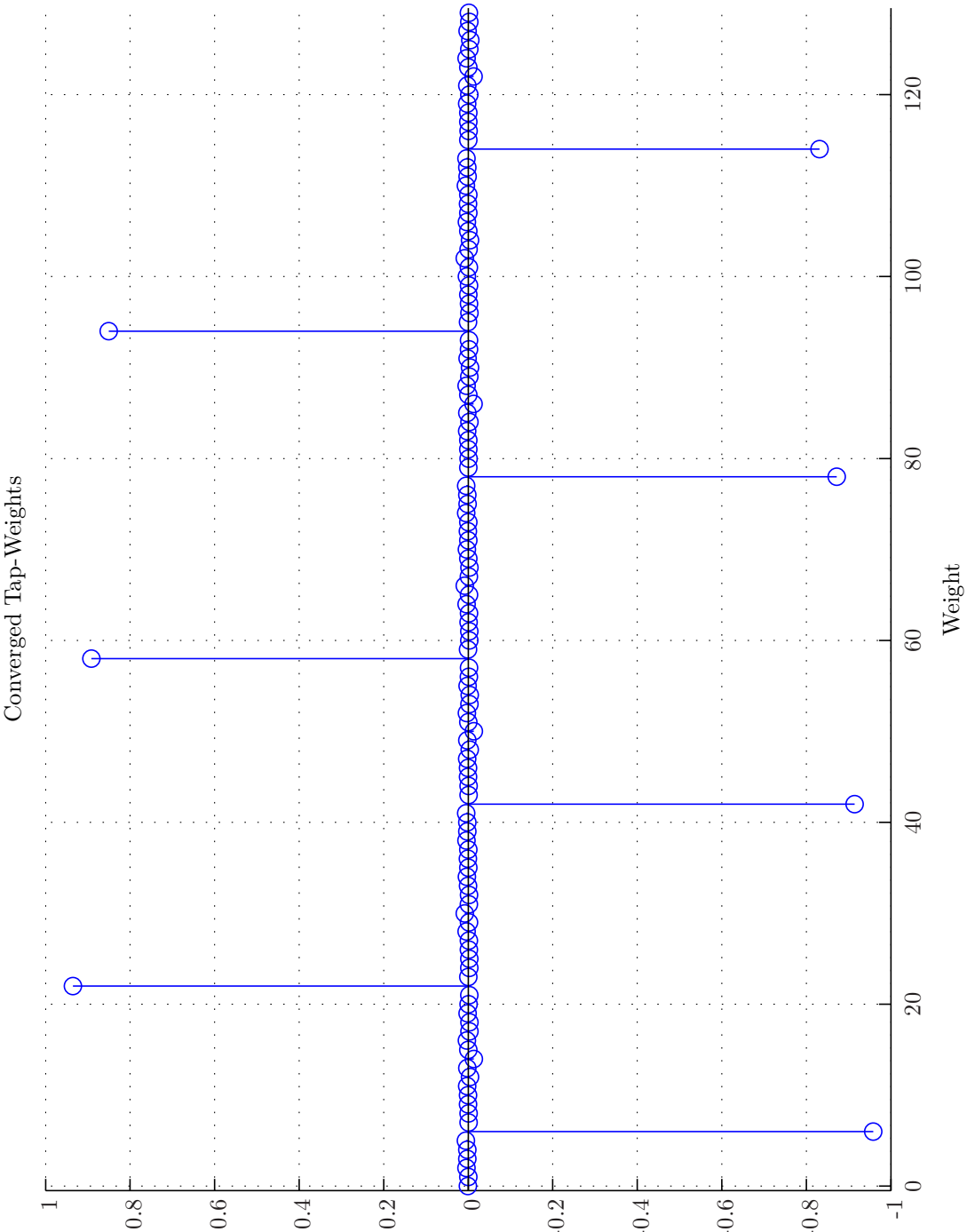

Sim 3.2.5: *Converged Tap-weights.* **Adaptive Filter** $\underset{\sim}{w}$: $\underset{\sim}{w}^{2,1}$: Wiener Hopf ($M = 130, \alpha = 1e-005, T_{WSS} = 0$,**z**-domain); **Main:** $f_s^0 = 192$ kHz, $f_s^1 = 6$ kHz, $R_{\updownarrow}^1 = \frac{1}{32} = 0.03125$, Elliptic LPF ($f_s = 192$ kHz, $f_{pass} = 2.75$ kHz, $f_{stop} = 3$ kHz, $A_{pass} = 2$ dB, $A_{stop} = 40$ dB), $f_s^2 = 6$ kHz, $R_{\updownarrow}^2 = \frac{1}{1} = 1$, Dummy; **Topology:** (Feedforward, mFx, $N_x = 2, N_e = 1, N_y = 1, N_p = 0, N_v = 2$); **Plants:** ($g_{xy}^{1,1}$: (FIR : $M_{gxy}^{1,1} = 1$), $g_{xy}^{1,2}$: (FIR : $M_{gxy}^{1,2} = 1$), $g_{ey}^{1,1}$: Delayed Sampled System: ($f_s = 6$ kHz, $t_d = 500$ µs, $\tau = 0$ µs) (FIR : $M_{gey}^{1,1} = 4$)); **Signals:** Time: $0 - 2$ s. Refer to SigIDLaT. ; **Scenario:** `MultipleSinusoidalsAddiativeNoiseFeedforwardMx2Ne1Ny1Np0/20080210T231832`.

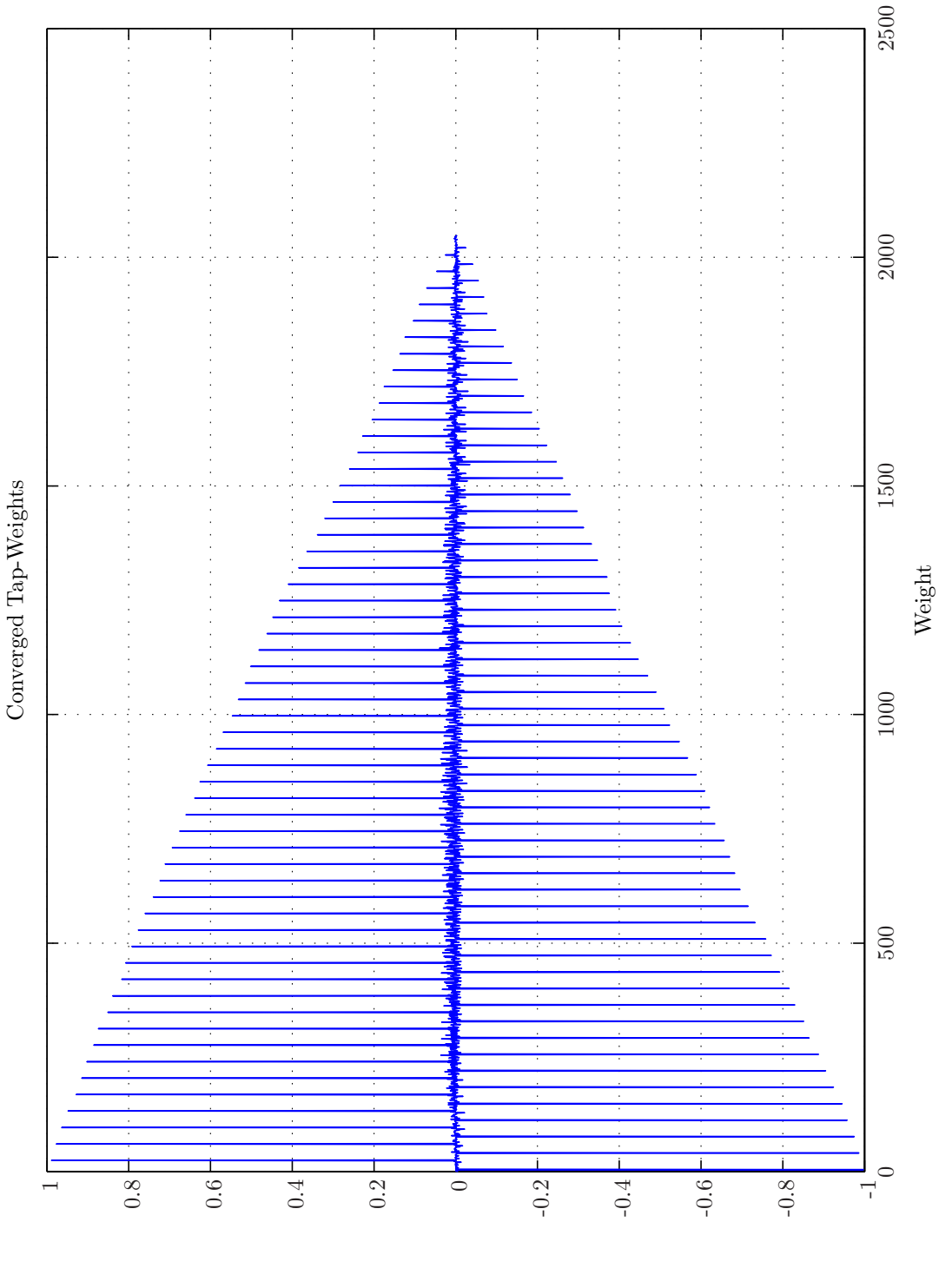

Sim 3.2.6: *Converged Tap-weights.* **Adaptive Filter** $\underset{\sim}{w}$: $\underset{\sim}{w}^{1,1}$: Wiener Hopf ($M = 2048, \alpha = 1e-005, Tw_{SS} = 0$,**t**-domain); **Main:** $f_s^0 = 192$ kHz, $f_s^1 = 6$ kHz, $R_\updownarrow^1 = \frac{1}{32} = 0.03125$, Elliptic LPF ($f_s = 192$ kHz, $f_{pass} = 2.75$ kHz, $f_{stop} = 3$ kHz, $A_{pass} = 2$ dB, $A_{stop} = 40$ dB), $f_s^2 = 6$ kHz, $R_\updownarrow^2 = \frac{1}{1} = 1$, Dummy; **Topology:** (Feedforward, mFx, $N_x = 2, N_e = 1, N_y = 1, N_p = 0, N_v = 2$); **Plants:** $(g_{xy}^{1,1}$: (FIR : $M_{gxy}^{1,1} = 1)$, $g_{xy}^{1,2}$: (FIR : $M_{gxy}^{1,2} = 1)$, $g_{ey}^{1,1}$: Delayed Sampled System: ($f_s = 6$ kHz, $t_d = 500$ µs, $\tau = 0$ µs) (FIR : $M_{gey}^{1,1} = 4)$); **Signals:** Time: $0 - 2$ s. Refer to SigIDLaT.; **Scenario:** `MultipleSinusoidalsAddiativeNoiseFeedforwardNx2Ne1Ny1Np0/20080210T231832`.

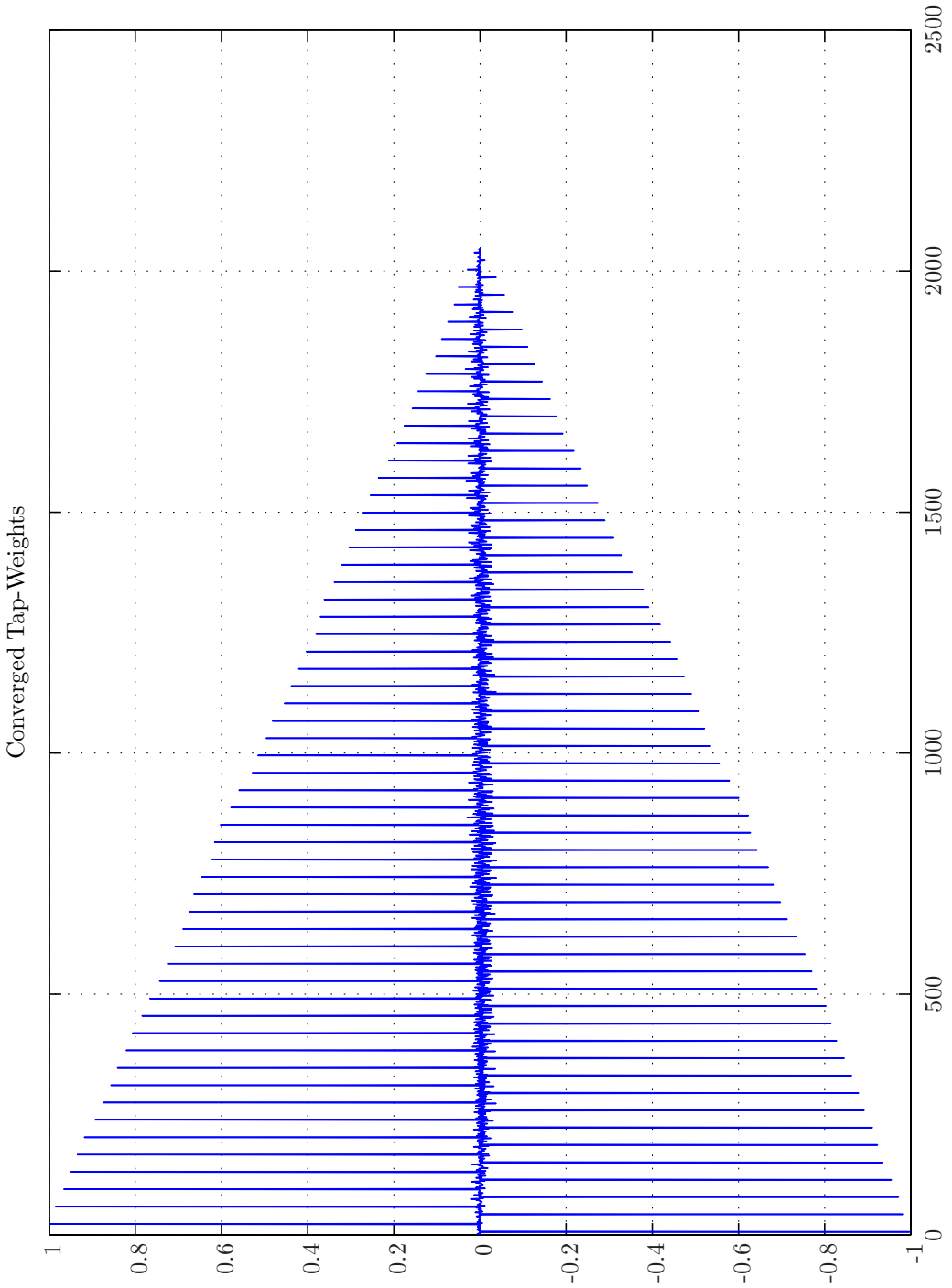

Sim 3.2.7: *Converged Tap-weights.* **Adaptive Filter** $\underset{\sim}{w}$: $\underset{\sim}{w}^{2,1}$: Wiener Hopf ($M = 2048, \alpha = 1e-005, T_{WSS} = 0$,**t**-domain); **Main:** $f_s^0 = 192$ kHz, $f_s^1 = 6$ kHz, $R_\updownarrow^1 = \frac{1}{32} = 0.03125$, Elliptic LPF ($f_s = 192$ kHz, $f_{pass} = 2.75$ kHz, $f_{stop} = 3$ kHz, $A_{pass} = 2$ dB, $A_{stop} = 40$ dB), $f_s^2 = 6$ kHz, $R_\updownarrow^2 = \frac{1}{1} = 1$, Dummy; **Topology:** (Feedforward, mFx, $N_x = 2, N_e = 1, N_y = 1, N_p = 0, N_v = 2$); **Plants:** ($g_{xy}^{1,1}$: (FIR : $M_{gxy}^{1,1} = 1$), $g_{xy}^{1,2}$: (FIR : $M_{gxy}^{1,2} = 1$), $g_{ey}^{1,1}$: Delayed Sampled System: ($f_s = 6$ kHz, $t_d = 500$ µs, $\tau = 0$ µs) (FIR : $M_{gey}^{1,1} = 4$)); **Signals:** Time: $0 - 2$ s. Refer to SigIDLaT. ; **Scenario:** `MultipleSinusoidalsAddiativeNoiseFeedforwardMx2Ne1Ny1Np0/20080210T231832`.

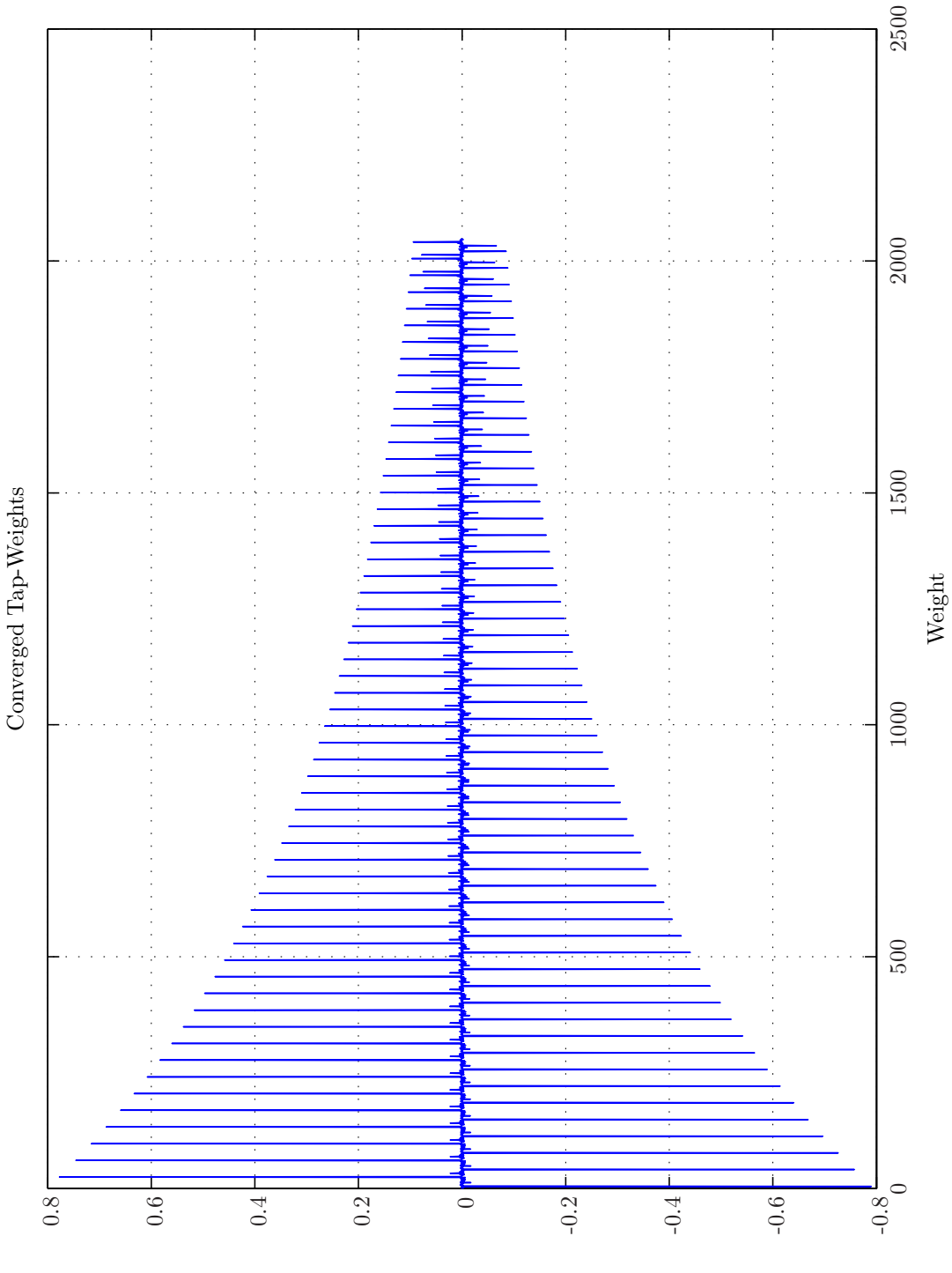

Sim 3.2.8: *Converged Tap-weights.* **Adaptive Filter** $\underset{\sim}{w}$: $\underset{\sim}{w}^{1,1}$: Wiener Hopf ($M = 2048, \alpha = 1e-005, T_{WSS} = 0$,**z**-domain); **Main:** $f_s^0 = 192$ kHz, $f_s^1 = 6$ kHz, $R_\updownarrow^1 = \frac{1}{32} = 0.03125$, Elliptic LPF ($f_s = 192$ kHz, $f_{pass} = 2.75$ kHz, $f_{stop} = 3$ kHz, $A_{pass} = 2$ dB, $A_{stop} = 40$ dB), $f_s^2 = 6$ kHz, $R_\updownarrow^2 = \frac{1}{1} = 1$, Dummy; **Topology:** (Feedforward, mFx, $N_x = 2, N_e = 1, N_y = 1, N_p = 0, N_v = 2$); **Plants:** ($g_{xy}^{1,1}$: (FIR : $M_{gxy}^{1,1} = 1$), $g_{xy}^{1,2}$: (FIR : $M_{gxy}^{1,2} = 1$), $g_{ey}^{1,1}$: Delayed Sampled System: ($f_s = 6$ kHz, $t_d = 500$ µs, $\tau = 0$ µs) (FIR : $M_{gey}^{1,1} = 4$)); **Signals:** Time: $0 - 2$ s. Refer to SigIDLaT.; **Scenario:** `MultipleSinusoidalsAddiativeNoiseFeedforwardNx2Ne1Ny1Np0/20080210T231832`.

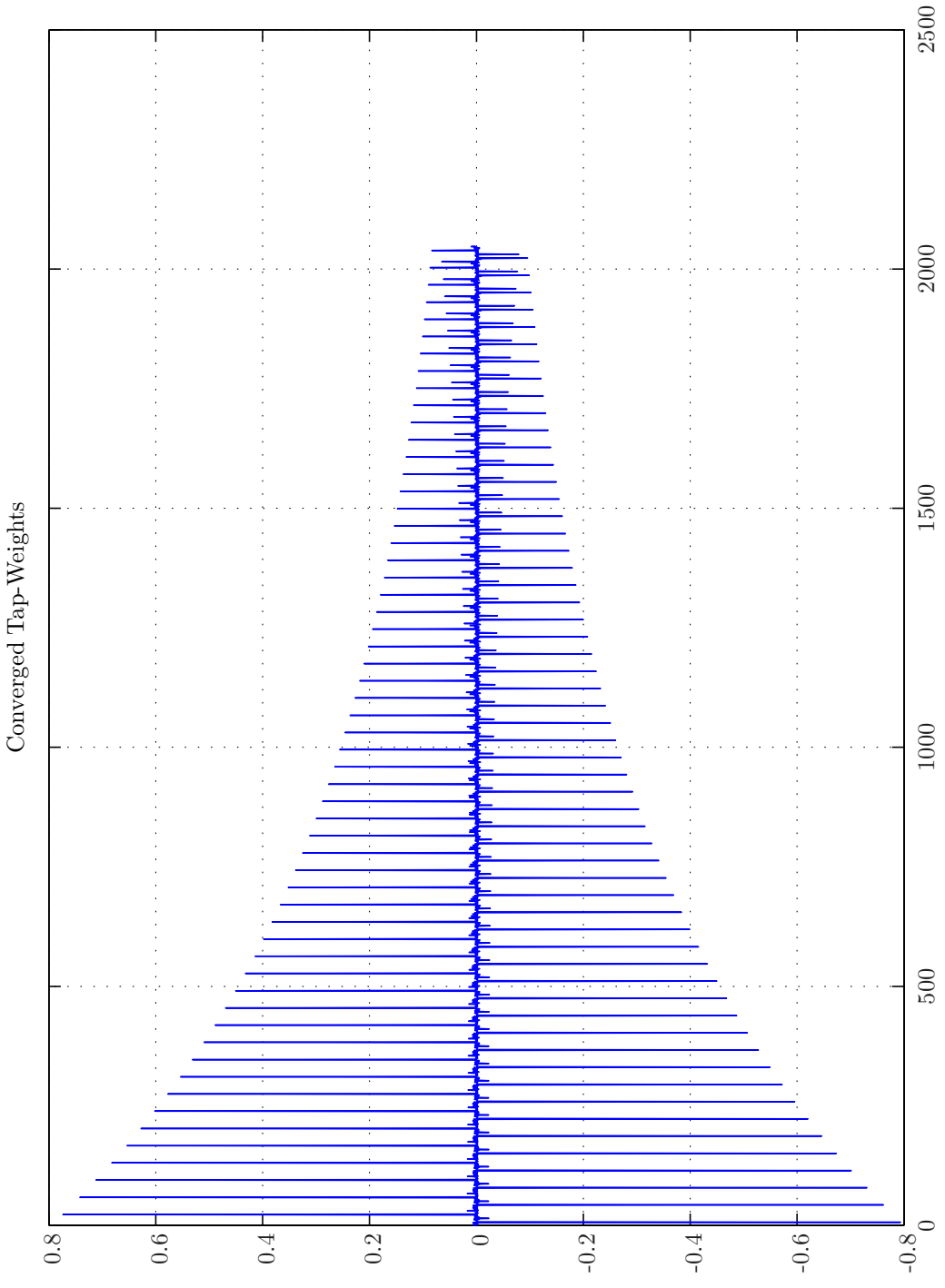

Sim 3.2.9: *Converged Tap-weights.* **Adaptive Filter** $\underset{\sim}{w}$: $\underset{\sim}{w}^{2,1}$: Wiener Hopf ($M = 2048, \alpha = 1e-005, T_{WSS} = 0$,**z**-domain); **Main:** $f_s^0 = 192$ kHz, $f_s^1 = 6$ kHz, $R_\updownarrow^1 = \frac{1}{32} = 0.03125$, Elliptic LPF ($f_s = 192$ kHz, $f_{pass} = 2.75$ kHz, $f_{stop} = 3$ kHz, $A_{pass} = 2$ dB, $A_{stop} = 40$ dB), $f_s^2 = 6$ kHz, $R_\updownarrow^2 = \frac{1}{1} = 1$, Dummy; **Topology:** (Feedforward, mFx, $N_x = 2, N_e = 1, N_y = 1, N_p = 0, N_v = 2$); **Plants:** ($g_{xy}^{1,1}$: (FIR : $M_{gxy}^{1,1} = 1$), $g_{xy}^{1,2}$: (FIR : $M_{gxy}^{1,2} = 1$), $g_{ey}^{1,1}$: Delayed Sampled System: ($f_s = 6$ kHz, $t_d = 500$ µs, $\tau = 0$ µs) (FIR : $M_{gey}^{1,1} = 4$)); **Signals:** Time: $0 - 2$ s. Refer to SigIDLaT. ; **Scenario:** `MultipleSinusoidalsAddiativeNoiseFeedforwardNx2Ne1Ny1Np0/20080210T231832`.

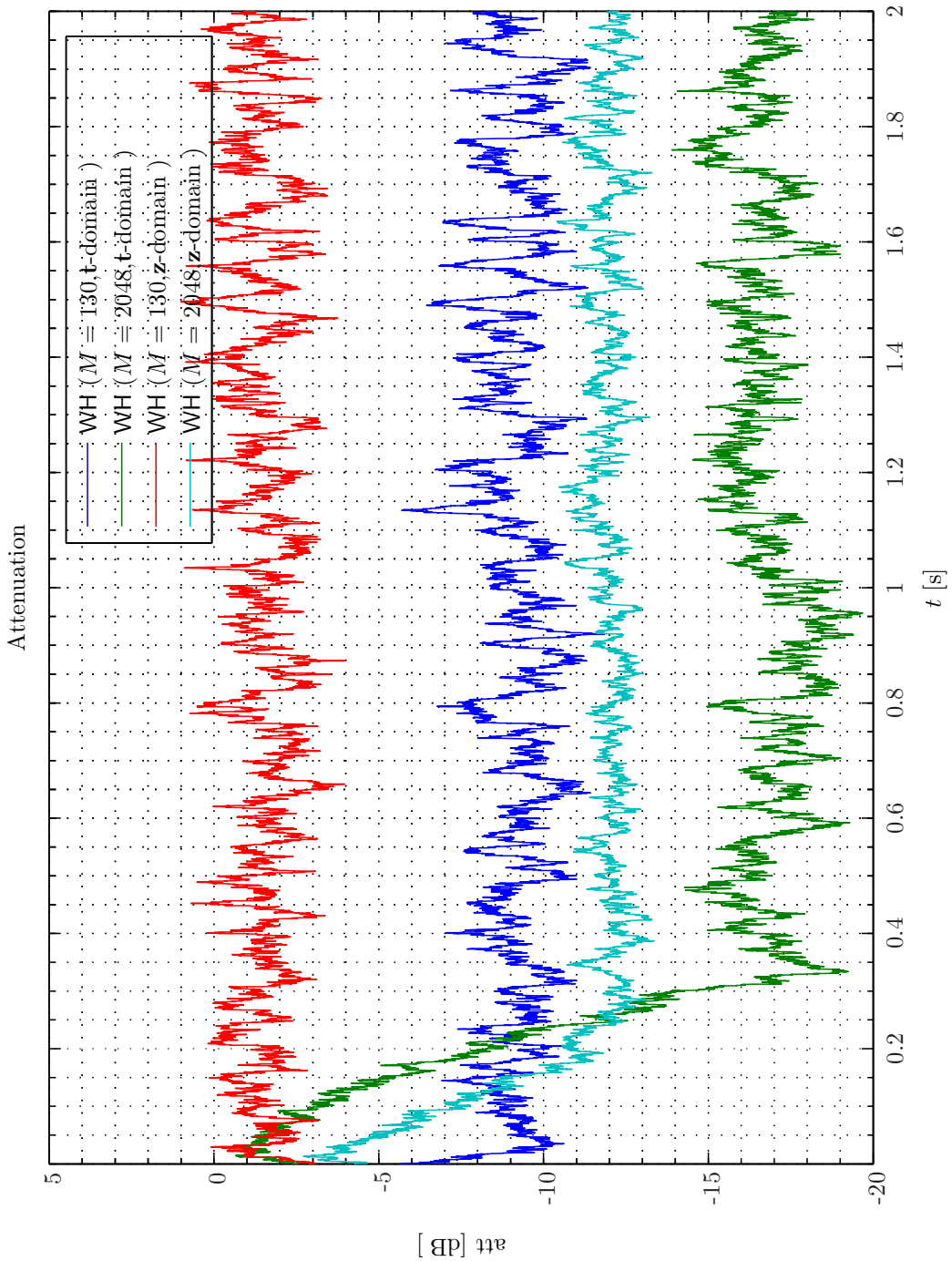

Sim 3.2.10: *Time-Domain: Attenuation.* **Adaptive Filter** $\underset{\sim}{w}$: $\underset{\sim}{w}^{1,1}$: WH ($\alpha = 1e-005, T_{WSS} = 0$); **Main:** $f_s^0 = 192$ kHz, $f_s^1 = 6$ kHz, $R_\downarrow^1 = \frac{1}{32} = 0.03125$, Elliptic LPF ($f_s = 192$ kHz, $f_{pass} = 2.75$ kHz, $f_{stop} = 3$ kHz, $A_{pass} = 2$ dB, $A_{stop} = 40$ dB), $f_s^2 = 6$ kHz, $R_\downarrow^2 = \frac{1}{1} = 1$, Dummy; **Topology:** (Feedforward, mFx, $N_x = 2, N_e = 1, N_y = 1, N_p = 0, N_v = 2$); **Plants:** ($g_{xy}^{1,1}$: (FIR : $M_{gxy}^{1,1} = 1$), $g_{xy}^{1,2}$: (FIR : $M_{gxy}^{1,2} = 1$), $g_{ey}^{1,1}$: Delayed Sampled System: ($f_s = 6$ kHz, $t_d = 500$ µs, $\tau = 0$ µs) (FIR : $M_{gey}^{1,1} = 4$)); **Signals:** Time: $0 - 2$ s. Refer to SigIDLaT. ; **Scenario:** `MultipleSinusoidalsAddiativeNoiseFeedforwardNx2Ne1Ny1Np0/20080210T231832`.

$$r_{x_1d_1}(\tau) = \begin{cases} 1; & \tau = -8 \\ b_x; & \tau = 8 \\ 0; & \text{else} \end{cases} \tag{3.2.22a}$$

$$r_{x_2d_1}(\tau) = \begin{cases} 1; & \tau = -10 \\ b_x; & \tau = 10 \\ 0; & \text{else} \end{cases} \tag{3.2.22b}$$

$$r_{x_1x_1}(\tau) = r_{x_2x_2}(\tau) = \begin{cases} 1 + b_x^2; & \tau = 0 \\ 0; & \text{else} \end{cases} \tag{3.2.22c}$$

$$r_{x_1x_2}(\tau) = r^*_{x_2x_1}(-\tau) = \begin{cases} b_x; & \tau = \pm 18 \\ 0; & \text{else.} \end{cases} \tag{3.2.22d}$$

The z-cross-spectrum matrix $S_{xd}(z)$ and z-auto-cross-spectrum matrix $S_{xx}(z)$ are therefore

$$S_{xd}(z) = \begin{bmatrix} z^8 + b_x z^{-8} \\ z^{10} + b_x z^{-10} \end{bmatrix} \tag{3.2.23}$$

and

$$S_{xx}(z) = \begin{bmatrix} 1 + b_x^2 & b_x(z^{18} + z^{-18}) \\ b_x(z^{18} + z^{-18}) & 1 + b_x^2 \end{bmatrix}. \tag{3.2.24}$$

On the unit circle $S_{xx}(\mathrm{e}^{\imath\omega})$ can be expressed by

$$S_{xx}(\mathrm{e}^{\imath\omega}) = \begin{bmatrix} 1 + b_x^2 & 2b_x \cos(36\pi f/f_s) \\ 2b_x \cos(36\pi f/f_s) & 1 + b_x^2 \end{bmatrix}. \tag{3.2.25}$$

The frequency points where $S_{xx}(\mathrm{e}^{\imath\omega})$ might be rank-deficient can be obtained from $f = \frac{n}{18}\frac{f_s}{2}\cos^{-1}(\frac{1+b_x^2}{2b_x}), n \in \mathbb{Z}$. Hence, as by assumption $0 \leq b_x \leq 1$ the case $b_x = 1$, that is, without element directivity is the only case where the lack of positive-definiteness on the uc exists.

We observe that in the limit $\lim_{b_x \to 0}$ the z-auto-cross-spectrum matrix will coincide with the identity matrix.

For the present case of directional reference sensors we may guess the spectral factorization of $S_{xx}(z)$ to be of the form

$$L(z) = \begin{bmatrix} 1 & b'_x z^{-18} \\ b'_x z^{-18} & 1 \end{bmatrix}; \quad R_e = \operatorname{diag}\{d_x^{-1}\}; \quad L^*(z^{-*}) = \begin{bmatrix} 1 & b'_x z^{18} \\ b'_x z^{18} & 1 \end{bmatrix}. \tag{3.2.26}$$

It can readily be deduced that (3.2.26) has the following two solutions for the normalization constant d_x and the quantity b'_x

$$d_x = \begin{cases} 1 \\ b_x^{-2} \end{cases} \quad ; \qquad b'_x = d_x b_x. \tag{3.2.27}$$

For $b_x = 1$ the two solutions in (3.2.27) coincide and the spectral factorization coincide with Example 3.2.1 viz. (3.2.16), where $R_e = \mathrm{I}$. However, as $L^{-1}(z)$ also should be analytic in $\mathcal{D}_+$ this rules out the $d_x = b_x^{-2}$ solution in (3.2.27). The inverse of $L(z)$ and $L^*(z^{-*})$ are therefore

$$L^{-1}(z) = \tfrac{1}{1-b_x^2 z^{-36}} \begin{bmatrix} 1 & -b_x z^{-18} \\ -b_x z^{-18} & 1 \end{bmatrix}; \quad L^{-*}(z^{-*}) = \tfrac{1}{1-b_x^2 z^{36}} \begin{bmatrix} 1 & -b_x z^{18} \\ -b_x z^{18} & 1 \end{bmatrix}. \quad (3.2.28)$$

By insertion of (3.2.23) and (3.2.28) in (3.2.11) we obtain

$$\begin{aligned}
\tilde{w}^o(z) &= -\left\{ \tfrac{1}{1-b_x^2 z^{*36}} \begin{bmatrix} 1 & -b_x z^{*18} \\ -b_x z^{*18} & 1 \end{bmatrix} \begin{bmatrix} b_x z^{*8} + z^{-*8} \\ b_x z^{*10} + z^{-*10} \end{bmatrix} z^{*4} \right\}_+^* \tfrac{1}{1-b_x^2 z^{-36}} \begin{bmatrix} 1 & -b_x z^{-18} \\ -b_x z^{-18} & 1 \end{bmatrix} \\
&= -\left\{ \tfrac{1}{1-b_x^2 z^{*36}} \begin{bmatrix} z^{-*8} - b_x^2 z^{*28} \\ z^{-*10} - b_x^2 z^{*26} \end{bmatrix} z^{*4} \right\}_+^* \tfrac{1}{1-b_x^2 z^{-36}} \begin{bmatrix} 1 & -b_x z^{-18} \\ -b_x z^{-18} & 1 \end{bmatrix} \\
&= -\left\{ \tfrac{1}{1-b_x^2 z^{36}} \begin{bmatrix} z^{-4} - b_x^2 z^{32} & z^{-6} - b_x^2 z^{30}) \end{bmatrix} \right\}_+ \tfrac{1}{1-b_x^2 z^{-36}} \begin{bmatrix} 1 & -b_x z^{-18} \\ -b_x z^{-18} & 1 \end{bmatrix} \\
&= -(1 + b_x^2 z^{-36} + b_x^4 z^{-72} + b_x^6 z^{-108} + \dots) \begin{bmatrix} z^{-4} & z^{-6} \end{bmatrix} \begin{bmatrix} 1 & -b_x z^{-18} \\ -b_x z^{-18} & 1 \end{bmatrix} \\
&= -(1 + b_x^2 z^{-36} + b_x^4 z^{-72} + b_x^6 z^{-108} + \dots) \begin{bmatrix} z^{-4} - b_x z^{-24} & z^{-6} - b_x z^{-22} \end{bmatrix}.
\end{aligned} \quad (3.2.29)$$

Hence, from (3.2.29) we observe that element directivity may lead to an adaptive filter (AF) solution of finite order as the weight-vector sequences $\underset{\sim}{w}^{1,1}$ and $\underset{\sim}{w}^{2,1}$ both decrease rapidly with increasing weight number even for a modest value of $b_x = 0.5$ as in this example.

The auto spectral density functions are shown in Simulation 3.2.11. Hence, for a one-sided spectra the $S_{xx}(f) = 10\log_{10}(1.25/(f_s/2)) \approx -33.80$ dBHz^{-1}, while $S_{ee}(f) \approx -31.76$ dBHz^{-1} as in Example 3.2.1. In Simulation 3.2.12 the multiple coherence functions $\gamma_{d_1 \cdot x!}$ is depicted. The deep troughs from Simulation 3.2.2 on page 117 are now barely observed. The cross-correlation functions depicted in Simulation 3.2.13 are now asymmetric in agreement with (3.2.22a) to (3.2.22b).

In Simulation 3.2.14 - 3.2.15 on pages 132–133 we readily identify the weights $\underset{\sim}{w}^{1,1}$ and $\underset{\sim}{w}^{2,1}$ predicted from (3.2.29) for the $b_x = 0.5$ case.

These weights were again obtained from time-averaging of the reference signals and the disturbance signal over a period of 180 s. Moreover, in this case the effects of the plus operator are less pronounced as the discarded terms related to the ratio $\frac{1}{1-b_x^2 z^{36}}$, that is, $\sum_{k=1}^{\infty}(b_x^2 z^{36})^k$ are rapidly decaying with increasing k by the presence of the b_x^2 factor. Expectably, we will be much more successful with the ANR operation as illustrated in Simulation 3.2.16 showing the attenuation performance for the **t**-domain and the **z**-domain WH filter defined in (3.2.9) and (3.2.11) respectively. For the **z**-domain method we have employed the MCPEFSF described in subsection 3.5.2 on page 206.

As seen the attenuation fluctuates in the vicinity of $\mathcal{A}_1^e(t) \approx 31 - 35$ dB for the **t**-domain WH method and $\mathcal{A}_1^e(t) \approx 40 - 44$ dB for the **z**-domain WH method[8]. Hence, employing the PEF

[8] In all the time-domain attenuation plots presented in this report the power of the disturbance signals and the error signals have been subject an exponentially weighted average with an integration time of approximately 200 ms.

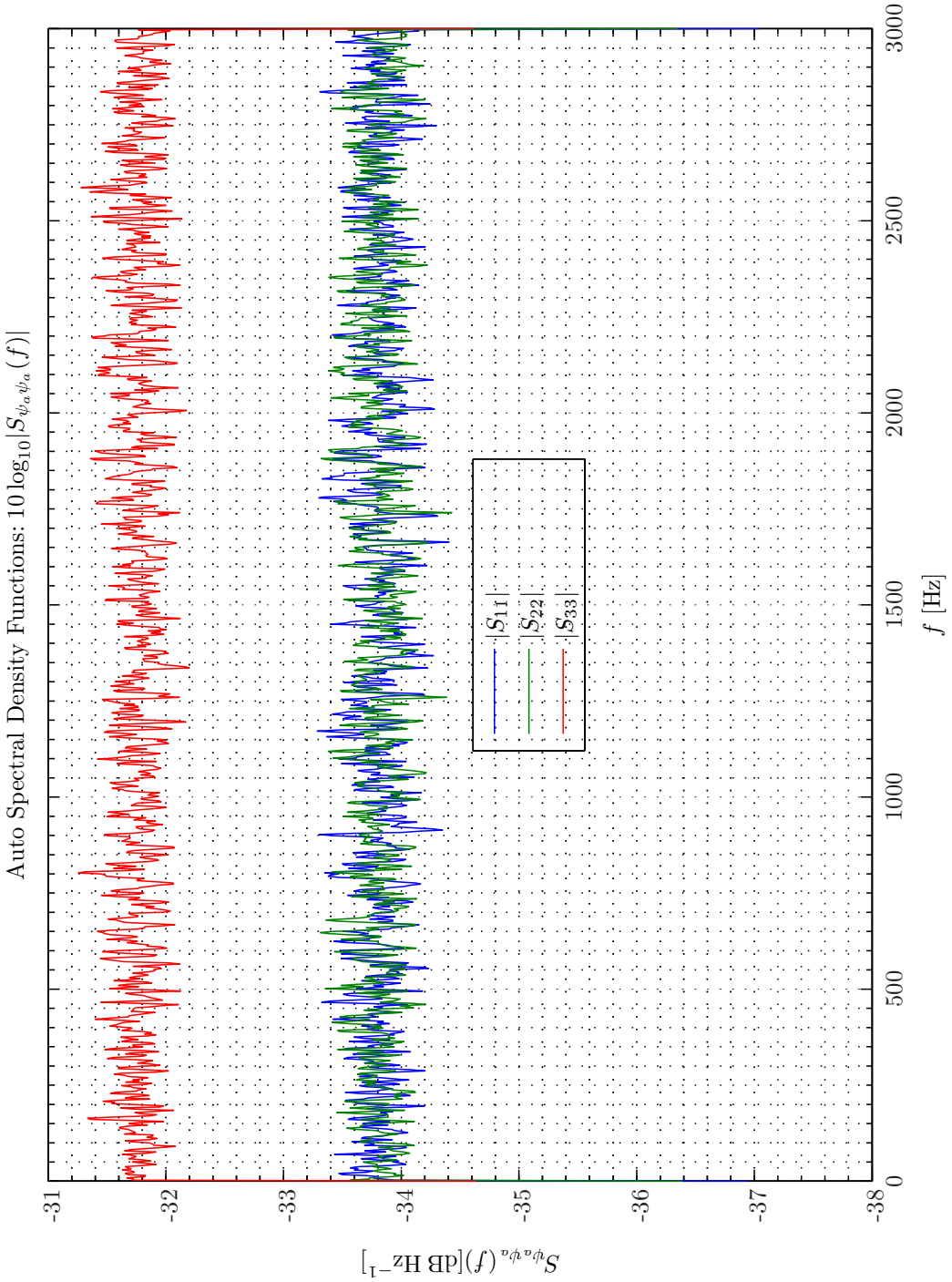

Sim 3.2.11: *Autospectral Density Functions*: **Statistical Data Analysis**: Single-Sided Modified Periodogram, $f_s = 6$ kHz, $N_{DFT} = 2048$, $L_{DFT} = 1501$, $R_{DFT} = 751$, Hanning, $\Delta f_m = 16$ Hz, $T_{DFT} = 0.25017$ s, $N_{f,DFT} = 1025$, $\Delta f_{DFT} = 2.9297$ Hz, $K_{DFT} = 1438$; **Signals:** Time: $0 - 180$ s. Refer to SigIDLaT. ; *Channels:* $\#1 \leftarrow x_1$, $\#2 \leftarrow x_2$, $\#3 \leftarrow d_1$. **Scenario:** `MultipleSinusoidalsAddiativeNoiseFeedforwardNx2Ne1Ny1Np0/20080131T152118.`.

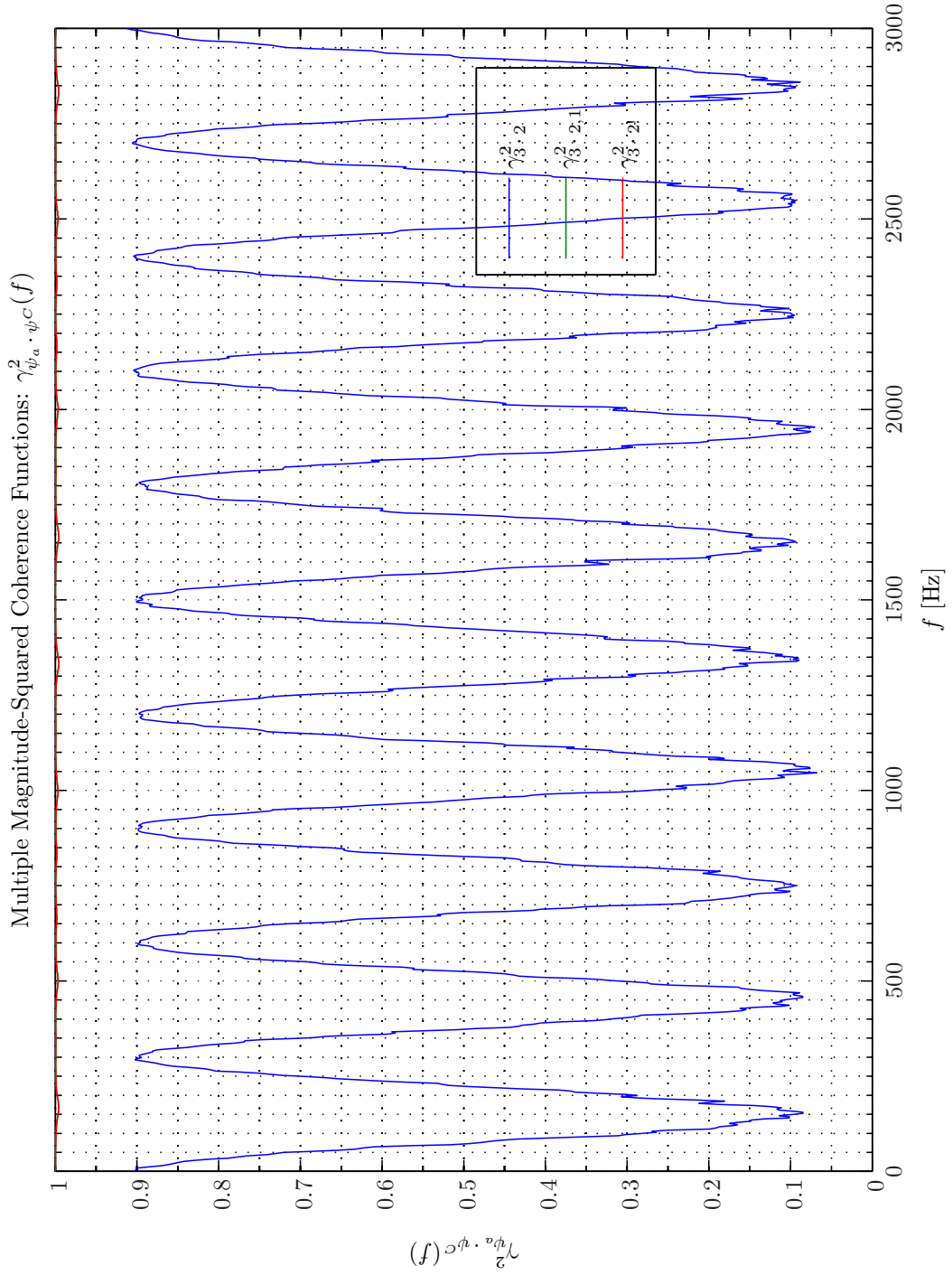

Sim 3.2.12: *Multiple Magnitude-Squared Coherence Functions* $\gamma^2_{\psi_a \cdot \psi^C}(f)$: **Statistical Data Analysis**: Single-Sided Modified Periodogram, $f_s = 6$ kHz, $N_{DFT} = 2048$, $L_{DFT} = 1501$, $R_{DFT} = 751$, Hanning, $\Delta f_m = 16$ Hz, $T_{DFT} = 0.25017$ s, $N_{f,DFT} = 1025$, $\Delta f_{DFT} = 2.9297$ Hz, $K_{DFT} = 1438$; **Signals:** Time: $0 - 180$ s. Refer to SigIDLaT. ; *Channels:* $\#1 \leftarrow x_1$, $\#2 \leftarrow x_2$, $\#3 \leftarrow d_1$. **Scenario:** `MultipleSinusoidalsAddiativeNoiseFeedforwardNx2Ne1Ny1Np0/20080131T152118.;` .

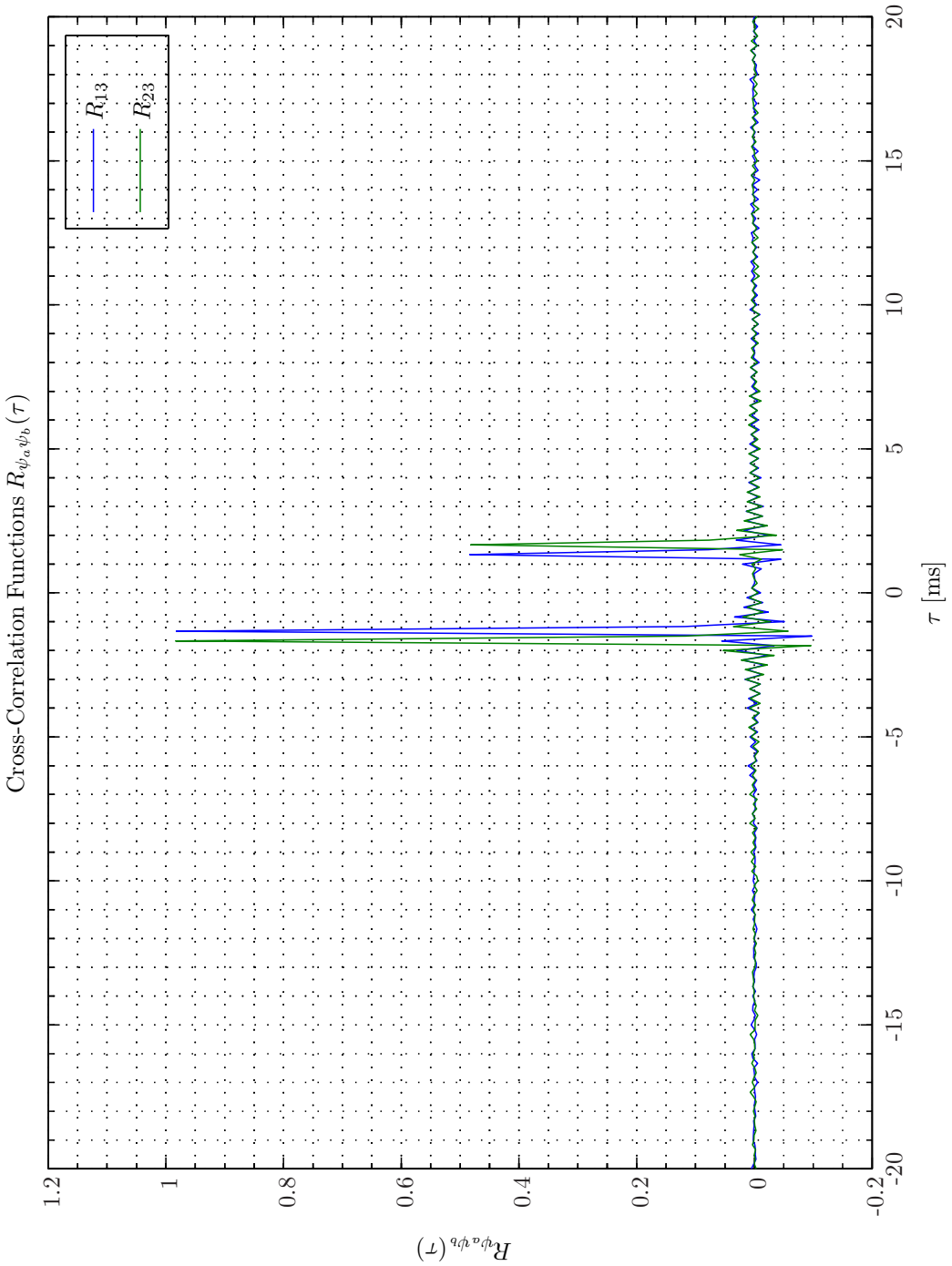

Sim 3.2.13: *Cross-Correlation Functions:* $R_{\psi_a\psi_b}(\tau)$: **Statistical Data Analysis:** Single-Sided Modified Periodogram, $f_s = 6$ kHz, $N_{DFT} = 2048$, $L_{DFT} = 1501$, $R_{DFT} = 751$, Hanning, $\Delta f_m = 16$ Hz, $T_{DFT} = 0.25017$ s, $N_{f,DFT} = 1025$, $\Delta f_{DFT} = 2.9297$ Hz, $K_{DFT} = 1438$; **Signals:** Time: $0 - 180$ s. Refer to SigIDLaT. ; *Channels:* #1 $\leftarrow x_1$, #2 $\leftarrow x_2$, #3 $\leftarrow d_1$. **Scenario:** `MultipleSinusoidalsAddiativeNoiseFeedforwardNx2Ne1Ny1Np0/20080131T152118.`; .

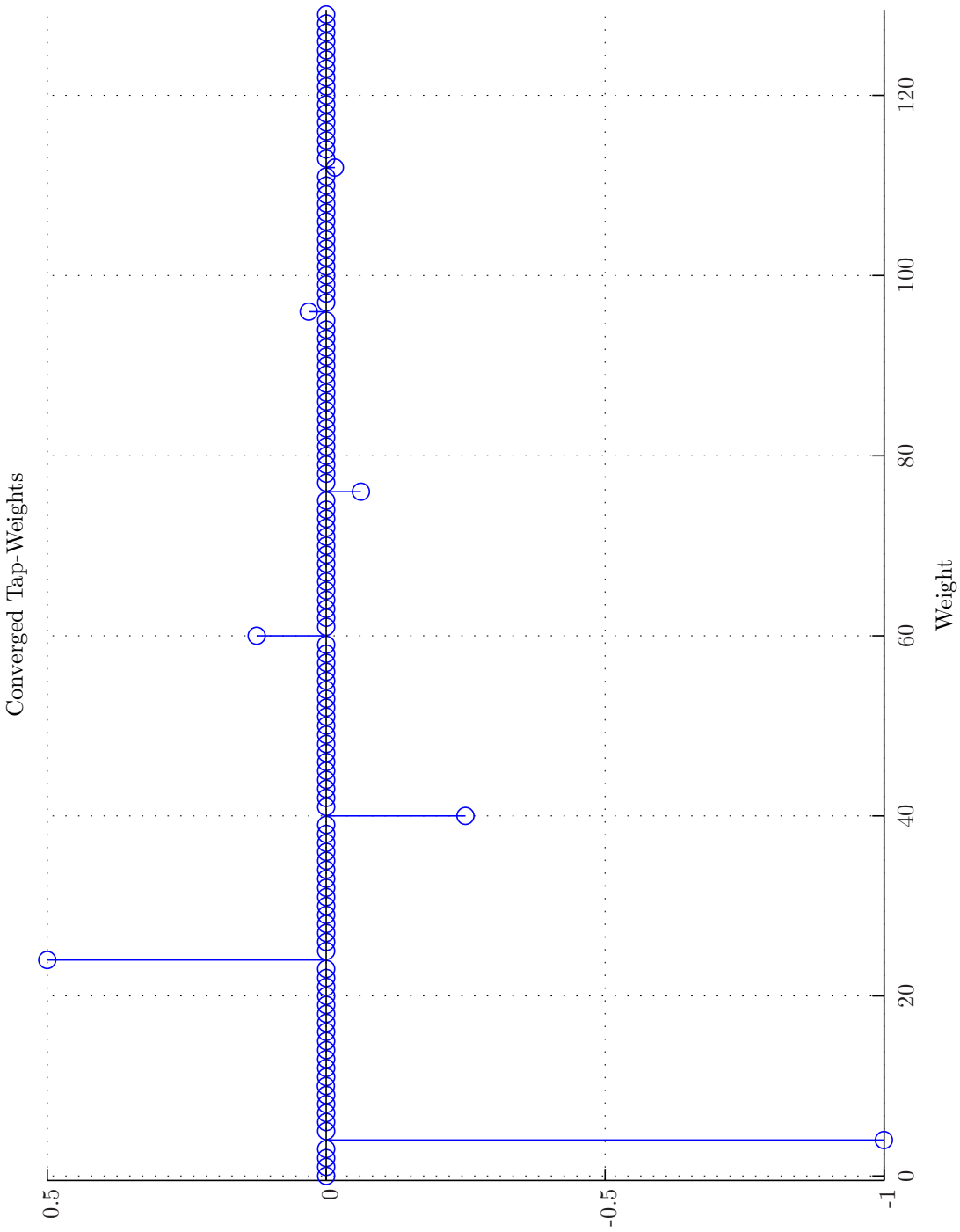

Sim 3.2.14: *Converged Tap-weights.* **Adaptive Filter** $\underset{\sim}{w}$: $\underset{\sim}{w}^{1,1}$: Wiener Hopf ($M = 130, \alpha = 1e-005, T_{WSS} = 0$,**z**-domain); **Main:** $f_s^0 = 192$ kHz, $f_s^1 = 6$ kHz, $R_{\updownarrow}^1 = \frac{1}{32} = 0.03125$, Elliptic LPF ($f_s = 192$ kHz, $f_{pass} = 2.75$ kHz, $f_{stop} = 3$ kHz, $A_{pass} = 2$ dB, $A_{stop} = 40$ dB), $f_s^2 = 6$ kHz, $R_{\updownarrow}^2 = \frac{1}{1} = 1$, Dummy; **Topology:** (Feedforward, mFx, $N_x = 2, N_e = 1, N_y = 1, N_p = 0, N_v = 2$); **Plants:** ($g_{xy}^{1,1}$: (FIR : $M_{gxy}^{1,1} = 1$), $g_{xy}^{1,2}$: (FIR : $M_{gxy}^{1,2} = 1$), $g_{ey}^{1,1}$: Delayed Sampled System: ($f_s = 6$ kHz, $t_d = 500$ µs, $\tau = 0$ µs) (FIR : $M_{gey}^{1,1} = 4$)); **Signals:** Time: $0 - 2$ s. Refer to SigIDLaT. ; **Scenario:** `MultipleSinusoidalsAddiativeNoiseFeedforwardNx2Ne1Ny1Np0/20080210T205456`.

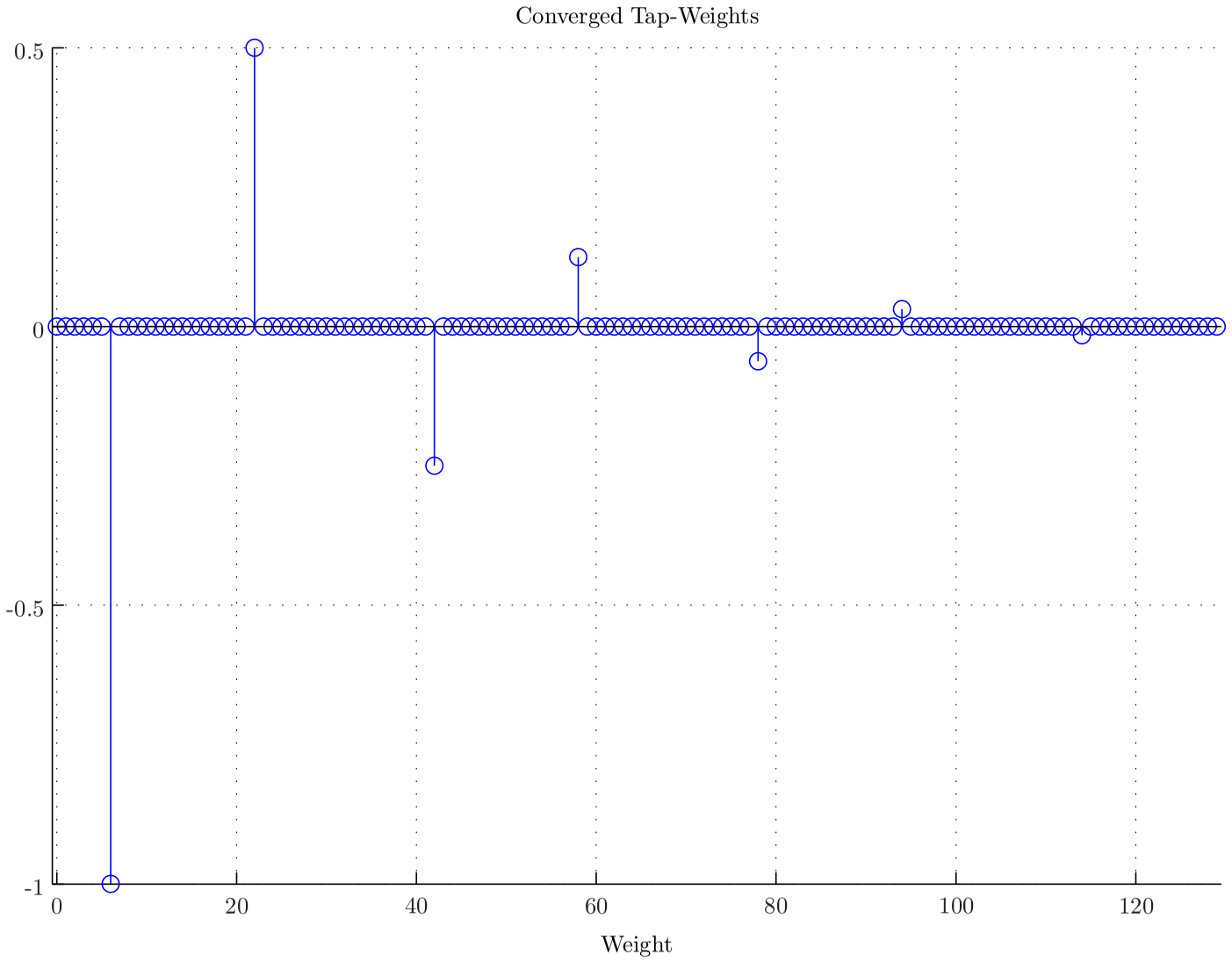

Sim 3.2.15: *Converged Tap-weights.* **Adaptive Filter** $\underset{\sim}{w}$: $\underset{\sim}{w}^{2,1}$: Wiener Hopf ($M = 130, \alpha = 1e-005, T_{WSS} = 0$,**z**-domain); **Main:** $f_s^0 = 192$ kHz, $f_s^1 = 6$ kHz, $R_{\downarrow}^1 = \frac{1}{32} = 0.03125$, Elliptic LPF ($f_s = 192$ kHz, $f_{pass} = 2.75$ kHz, $f_{stop} = 3$ kHz, $A_{pass} = 2$ dB, $A_{stop} = 40$ dB), $f_s^2 = 6$ kHz, $R_{\downarrow}^2 = \frac{1}{1} = 1$, Dummy; **Topology:** (Feedforward, mFx, $N_x = 2, N_e = 1, N_y = 1, N_p = 0, N_v = 2$); **Plants:** ($g_{xy}^{1,1}$: (FIR : $M_{gxy}^{1,1} = 1$), $g_{xy}^{1,2}$: (FIR : $M_{gxy}^{1,2} = 1$), $g_{ey}^{1,1}$: Delayed Sampled System: ($f_s = 6$ kHz, $t_d = 500$ µs, $\tau = 0$ µs) (FIR : $M_{gey}^{1,1} = 4$)); **Signals:** Time: $0 - 2$ s. Refer to SigIDLaT. ; **Scenario:** `MultipleSinusoidalsAddiativeNoiseFeedforwardNx2Ne1Ny1Np0/20080210T205456`.

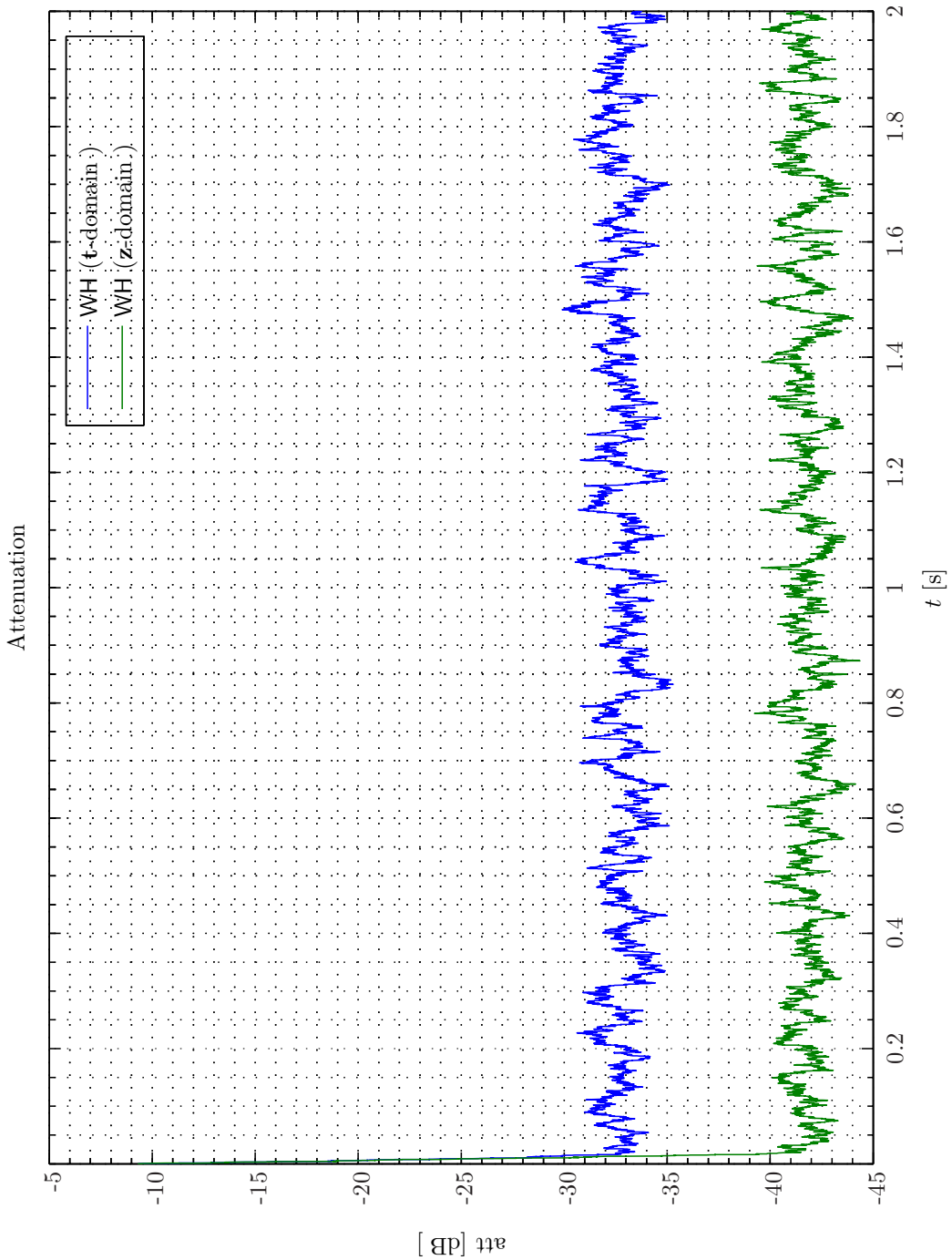

Sim 3.2.16: *Time-Domain: Attenuation.* **Adaptive Filter** $\underset{\sim}{w}$: $\underset{\sim}{w}^{1,1}$: WH ($M = 130, \alpha = 1e{-}005, T_{WSS} = 0$); **Main:** $f_s^0 = 192$ kHz, $f_s^1 = 6$ kHz, $R_\updownarrow^1 = \frac{1}{32} = 0.03125$, Elliptic LPF ($f_s = 192$ kHz, $f_{pass} = 2.75$ kHz, $f_{stop} = 3$ kHz, $A_{pass} = 2$ dB, $A_{stop} = 40$ dB), $f_s^2 = 6$ kHz, $R_\updownarrow^2 = \frac{1}{1} = 1$, Dummy; **Topology:** (Feedforward, mFx, $N_x = 2, N_e = 1, N_y = 1, N_p = 0, N_v = 2$); **Plants:** ($g_{xy}^{1,1}$: (FIR : $M_{gxy}^{1,1} = 1$), $g_{xy}^{1,2}$: (FIR : $M_{gxy}^{1,2} = 1$), $g_{ey}^{1,1}$: Delayed Sampled System: ($f_s = 6$ kHz, $t_d = 500$ µs, $\tau = 0$ µs) (FIR : $M_{gey}^{1,1} = 4$)); **Signals:** Time: $0 - 2$ s. Refer to SigIDLaT.; **Scenario:** `MultipleSinusoidalsAddiativeNoiseFeedforwardNx2Ne1Ny1Np0/20080210T205456`.

described in subsection 3.5.2 on page 206 for the **z**-domain WH method even outperformed the **t**-domain WH filter tailored to such flat spectral excitation. This might be explained by the fact that although the **t**-domain WH method works on random white noise signals the channels are cross-coupled leading to a channel-cross colorization.

3.3 Decomposition of Reference Signals and Disturbance Signals

As described in details in chapter 2 on page 17 the performance of a feedforward based ACSV system is very dependent on the coherence between the set of reference sensors and the set of error sensors. Accordingly, the reference signals and the disturbance signals will tentatively be very correlated and the system is designed to possess some underlying structure. In this section we will exploit the existence of such structure and in particular new expressions for the optimal weights in a causally constrained system will be derived. This should also provide new insights to the actions of the plus operator $\{\cdot\}_+$.

Hence, referring to Figure 3.1 we will consider the incident primary noise field as constituted from a number of random white noise signals that amount to N_v and that are assumed mutually uncorrelated and with unit variance. Accordingly, $L_{wv}(z)$ is a diagonal matrix. A *minimum phase* function (modeling filter) that we will denote by $L_v(z) \in \mathbb{C}^{N_v \times N_v}$ is responsible for *colorization* of the random white noise signals

$$\tilde{w}(z) = L_{wv}(z)\tilde{v}(z), \tag{3.3.1}$$

where $w(t) \in \mathbb{C}^{N_v \times 1}$ is the vector of random colored noise signals. Although the random colored noise signals are *individually* correlated they are assumed *mutually* uncorrelated. The random colored noise signals are considered acquired by set of N_v virtual sensors that are positioned on an (imaginary) surface $\mathcal{S}^v$. The number of virtual sensors equals the number of random white noise signals and each virtual sensor is positioned on $\mathcal{S}^v$ in a direction opposite to the propagation direction of the corresponding incident field, that is, $\hat{\boldsymbol{r}}_n^C \cdot \hat{\boldsymbol{s}}_n^C = -1, n \in \underline{N}_v$ (refer to Figure 3.1 on page 112).

Another *minimum phase* function (modeling filter) $L_{xw}(z) \in \mathbb{C}^{N_x \times N_v}$ establishes a link between the random colored noise signals and the reference signals

$$\tilde{x}(z) = L_{xw}(z)\tilde{w}(z). \tag{3.3.2}$$

The number of reference sensors equals the number of reference signals and each reference sensor is positioned on the possibly virtual surface $\mathcal{S}^x$. Similarly, the random colored noise signals and the disturbance signals are related by the *minimum phase* function (modeling filter) $L_{dw}(z) \in \mathbb{C}^{N_d \times N_v}$

$$\tilde{d}(z) = L_{dw}(z)\tilde{w}(z). \tag{3.3.3}$$

The causality of $L_{dw}(z)$ is obtained from requiring that the virtual sensor surface $\mathcal{S}^v$ is entirely circumscribing the surface spanned by the reference sensors that we will designate by $\mathcal{S}^x$ and is also entirely circumscribing the surface spanned by the error sensors that we denote by $\mathcal{S}^d$. This is equivalently to the conditions $\mathcal{V}^x \subset \mathcal{V}^v$ and $\mathcal{V}^d \subset \mathcal{V}^v$, where $\mathcal{V}^v, \mathcal{V}^x, \mathcal{V}^d$ are the interior

volumes of $\mathcal{S}^v, \mathcal{S}^x, \mathcal{S}^d$ respectively. The reference sensors and error sensors are therefore entirely inside $\mathcal{V}^v$ and every incident primary field is acquired first by one of the virtual sensors.

It should be noticed that in Example 3.2.1 - 3.2.2 the reference sensor and virtual sensor positions coincide, that is, $N_x = N_v = 2, \mathbf{r}_{x_1} = \mathbf{r}_{v_1}$ and $\mathbf{r}_{x_2} = \mathbf{r}_{v_2}$.

The model described above will be of general applicability provided that the following points are taking into account.

1. The *primary sources* responsible for the random white noise signals are positioned *exterior* to the imaginary surface $\mathcal{S}^v$.

2. A sufficient number of random white noise signals are used in order to establish a sound field with the required diffuseness.

3. A sufficient number of virtual sensors/reference sensors are used in order to prevent spatially undersampling of the incident fields.

According to (3.3.1) to (3.3.3) we may express the reference signal vector and the disturbance signal vector in the transform domain as

$$\tilde{\mathbf{x}}(z) = L_x(z)\tilde{\mathbf{v}}(z) = L_{xw}(z)L_{wv}(z)\tilde{\mathbf{v}}(z) \tag{3.3.4a}$$

$$\tilde{\mathbf{d}}(z) = L_d(z)\tilde{\mathbf{v}}(z) = L_{dw}(z)L_{wv}(z)\tilde{\mathbf{v}}(z). \tag{3.3.4b}$$

By using (3.3.4) we may the express the z-cross-spectrum (3.2.1b) as

$$\begin{aligned} S_{xd}(z) &= \mathrm{E}\,\tilde{\mathbf{x}}(z)\tilde{\mathbf{d}}^*(z^{-*}) \\ &= \mathrm{E}\,L_{xw}(z)L_{wv}(z)\tilde{\mathbf{v}}(z)\tilde{\mathbf{v}}^*(z^{-*})L_{wv}^*(z^{-*})L_{dw}^*(z^{-*}) \\ &= L_{xw}(z)L_{wv}(z)L_{wv}^*(z^{-*})L_{dw}^*(z^{-*}), \end{aligned} \tag{3.3.5}$$

where we have used that by definition $\mathrm{E}\,\tilde{\mathbf{v}}(z)\tilde{\mathbf{v}}^*(z^{-*}) = \mathrm{I}$. Hence, from (3.3.4a) and (3.3.5) we get

$$\begin{aligned} L_x^{-1}(z^{-*})S_{xd}(z^{-*}) &= L_{wv}^{-1}(z^{-*})L_{xw}^{-1}(z^{-*})L_{xw}(z^{-*})L_{wv}(z^{-*})L_{wv}^*(z)L_{dw}^*(z) \\ &= L_{wv}^*(z)L_{dw}^*(z). \end{aligned} \tag{3.3.6}$$

Then by insertion of (3.3.4a) and (3.3.6) in (3.2.11) we obtain

$$\boxed{\tilde{w}^o(z) = -\tilde{g}_{ey,\min}^{-1}(z)\big\{\tilde{g}_{ey,\mathrm{all}}^*(z^{-*})L_{dw}(z)L_{wv}(z)\big\}_+ R_e^{-1}L_{wv}^{-1}(z)L_{xw}^{-1}(z).} \tag{3.3.7}$$

By using (3.3.7) the results in Example 3.2.1 - 3.2.2 viz. (3.2.19) and (3.2.29) can be obtained in a somewhat more straightforward manner as we will see in Example 3.3.1.

Moreover, if the primary paths $\tilde{g}_{ex}(z)$ that link the reference signals to the disturbance signals are known we may express (3.3.7) as

$$\boxed{\tilde{w}^o(z) = -\tilde{g}^{-1}_{ey,\min}(z)\big\{\tilde{g}^*_{ey,\text{all}}(z^{-*})\tilde{g}_{ex}(z)L_{xw}(z)L_{wv}(z)\big\}_+ R_e^{-1}L^{-1}_{wv}(z)L^{-1}_{xw}(z).} \tag{3.3.8}$$

We appreciate from (3.3.8) that the all-pass component $\tilde{g}_{ey,\text{all}}(z)$ counteracts the benefit of large acquisition lead-times provided by the primary paths $\tilde{g}_{ex}(z)$ in CFF. Finally, it should be remarked that for a FBS using internal model control (IMC) described in section 4.6 on page 244 the reference signals and disturbance signals are entirely correlated to the point of the accuracy of the secondary path models. Hence, by insertion of $\tilde{x}(z) = \tilde{\tilde{d}}(z)$ in (3.3.7) we obtain

$$\boxed{\tilde{w}^o(z) \approx -\tilde{g}^{-1}_{ey,\min}(z)\big\{\tilde{g}^*_{ey,\text{all}}(z^{-*})L_{\hat{d}}(z)\big\}_+ R_e^{-1}L^{-1}_{\hat{d}}(z).} \tag{3.3.9}$$

We will return to consequences of (3.3.9) on this page in Example 3.4.2 on page 163.

Example 3.3.1 (Feedforward System, Reference Sensors with Directivity, Colored Noise)**.** In the audio and signal processing communities reference is often made to various types of colored noise governed by a constant rate of increase/decrease in the auto spectral density function per decade or octave. For example, within these aforementioned communities it has become standard to let the terms *purple noise*, *blue noise*, *white noise*, *pink noise* and *brown noise* refer to a slope in the auto spectral density function of $+20, +10, 0, -10$ and -20 dB/decade respectively.

In the preceding examples we obtained closed-form *canonical spectral factorization* of the form (3.2.3) for white noise signals that subsequently could be inserted in (3.2.11) leading to the determination of the optimal causally-constrained filter weights. However, as demonstrated in section 3.A on page 231 such spectral factorization unfortunately is not easily amendable to the other colorization types mentioned above.

Before entering details, we will first discuss the effects of colorization governed by $L_{wv}(z)$ when applied to Example 3.2.1 - 3.2.2. By using (3.3.7) instead of (3.2.11) in Example 3.2.2 (where $L_{wv}(z) = \mathrm{I}$) and by insertion of $L_{dw}(z) = \begin{bmatrix} z^{-8} & z^{-10} \end{bmatrix}$ and by using that $L_{xw}(z)$ coincides with $L_x(z)$ in Example 3.2.2 on page 119 then from insertion in (3.3.7) we obtain

$$\begin{aligned} \tilde{w}^o(z) &= -\big\{z^4 \begin{bmatrix} z^{-8} & z^{-10} \end{bmatrix} L_{wv}(z)\big\}_+ L^{-1}_{wv}(z) \tfrac{1}{1-b_x^2 z^{-36}} \begin{bmatrix} 1 & -b_x z^{-18} \\ -b_x z^{-18} & 1 \end{bmatrix} \\ &= -(1 + b_x^2 z^{-36} + b_x^4 z^{-72} + b_x^6 z^{-108} + \dots) \begin{bmatrix} z^{-4} - b_x z^{-24} & z^{-6} - b_x z^{-22} \end{bmatrix}. \end{aligned} \tag{3.3.10}$$

This expression coincides with (3.2.29) in Example 3.2.2. Hence, for this very ordinary delay system involving a simple secondary path *any* type of colorization will lead to the same optimal causally constrained weights. This is due to the fact that $\tilde{g}^*_{ey,\text{all}}(z^{-*})L_{dw}(z)$ is already causal and no truncation effects occur and $L_{wv}(z)L^{-1}_{wv}(z) = \mathrm{I}$ cancel out.

Now in order to verify these findings instead of random white noise signal we will use *pink noise* (1 Hz-3 kHz) in this example. The results from applying the **t**-domain and the **z**-domain WH filters are shown in Simulation 3.3.1 - 3.3.4 on pages 138–141. For the **t**-domain WH filter in Simulation 3.3.1 - 3.3.2 the weight estimates are somewhat noisy. However, for the **z**-domain approach shown in Simulation 3.3.3 - 3.3.4 we readily identify the weights $\underset{\sim}{w}^{1,1}$ and $\underset{\sim}{w}^{2,1}$ predicted from (3.2.29) for the $b_x = 0.5$ case.

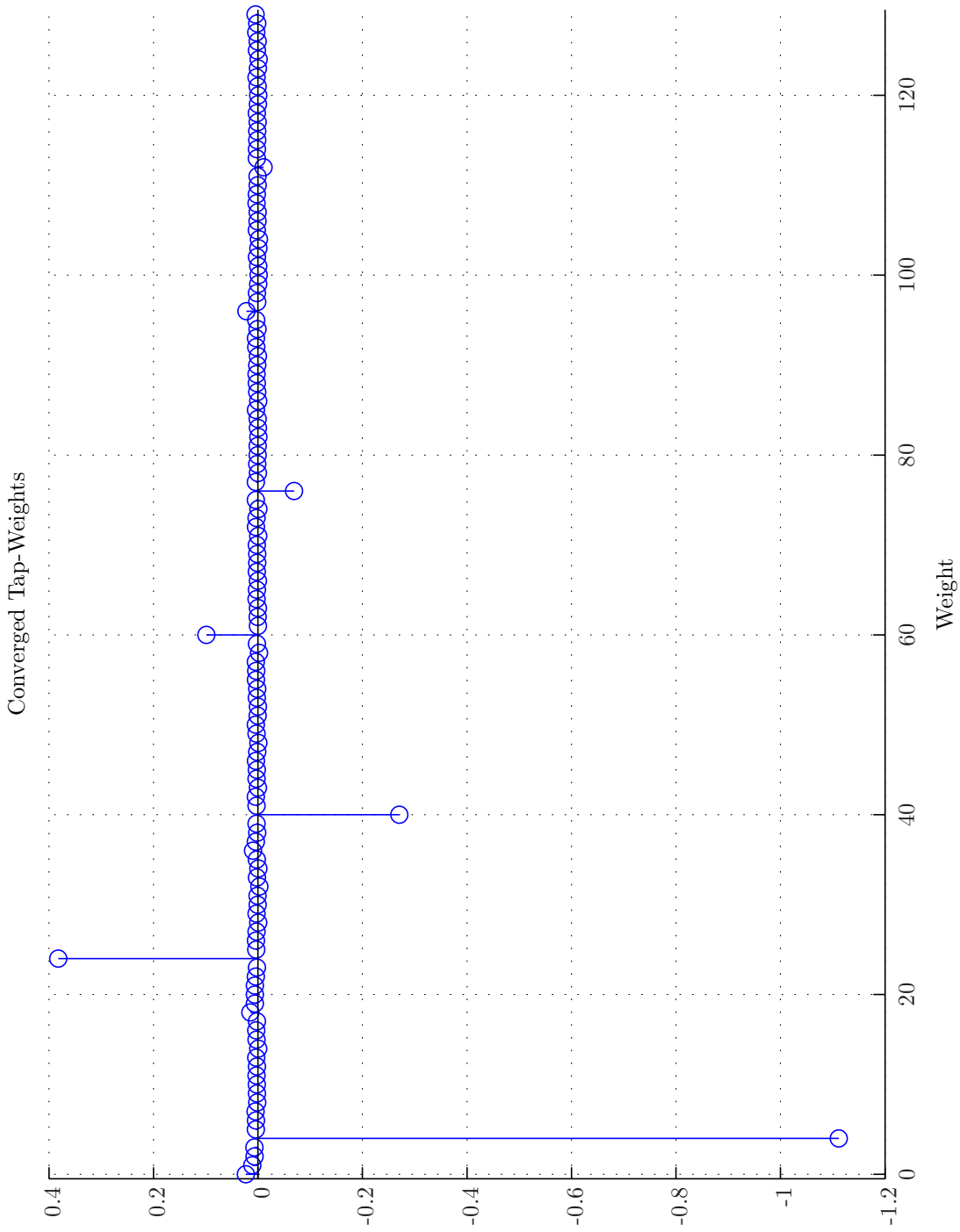

Sim 3.3.1: *Converged Tap-weights.* **Adaptive Filter** $\underset{\sim}{w}$: $\underset{\sim}{w}^{1,1}$: Wiener Hopf ($M = 130, \alpha = 1e-005, T_{WSS} = 0$,**t**-domain); **Main:** $f_s^0 = 192$ kHz, $f_s^1 = 6$ kHz, $R_\updownarrow^1 = \frac{1}{32} = 0.03125$, Elliptic LPF ($f_s = 192$ kHz, $f_{pass} = 2.75$ kHz, $f_{stop} = 3$ kHz, $A_{pass} = 2$ dB, $A_{stop} = 40$ dB), $f_s^2 = 6$ kHz, $R_\updownarrow^2 = \frac{1}{1} = 1$, Dummy; **Topology:** (Feedforward, mFx, $N_x = 2, N_e = 1, N_y = 1, N_p = 0, N_v = 2$); **Plants:** ($g_{xy}^{1,1}$: (FIR : $M_{gxy}^{1,1} = 1$), $g_{xy}^{1,2}$: (FIR : $M_{gxy}^{1,2} = 1$), $g_{ey}^{1,1}$: Delayed Sampled System: ($f_s = 6$ kHz, $t_d = 500$ µs, $\tau = 0$ µs) (FIR : $M_{gey}^{1,1} = 4$)); **Signals:** Time: $0 - 2$ s. Refer to SigIDLaT. ; **Scenario:** `MultipleSinusoidalsAddiativeNoiseFeedforwardNx2Ne1Ny1Np0/20080209T180449`.

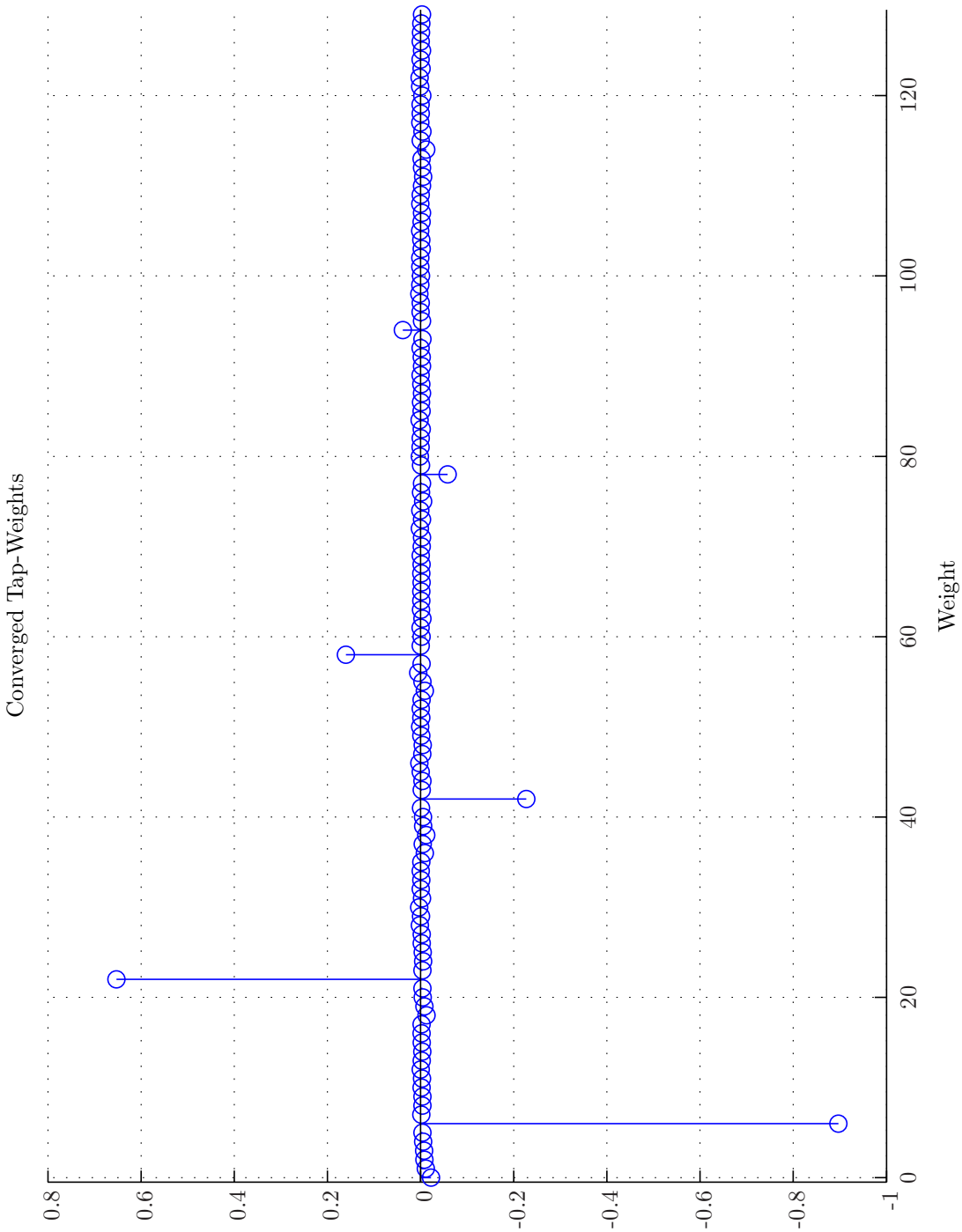

Sim 3.3.2: *Converged Tap-weights.* **Adaptive Filter** $\underset{\sim}{y}$: $\underset{\sim}{y}^{2,1}$: Wiener Hopf ($M = 130, \alpha = 1e-005, T_{WSS} = 0$,**t**-domain); **Main:** $f_s^0 = 192$ kHz, $f_s^1 = 6$ kHz, $R_{\updownarrow}^1 = \frac{1}{32} = 0.03125$, Elliptic LPF ($f_s = 192$ kHz, $f_{pass} = 2.75$ kHz, $f_{stop} = 3$ kHz, $A_{pass} = 2$ dB, $A_{stop} = 40$ dB), $f_s^2 = 6$ kHz, $R_{\updownarrow}^2 = \frac{1}{1} = 1$, Dummy; **Topology:** (Feedforward, mFx, $N_x = 2, N_e = 1, N_y = 1, N_p = 0, N_v = 2$); **Plants:** ($g_{xy}^{1,1}$: (FIR : $M_{gxy}^{1,1} = 1$), $g_{xy}^{1,2}$: (FIR : $M_{gxy}^{1,2} = 1$), $g_{ey}^{1,1}$: Delayed Sampled System: ($f_s = 6$ kHz, $t_d = 500$ µs, $\tau = 0$ µs) (FIR : $M_{gey}^{1,1} = 4$)); **Signals:** Time: $0 - 2$ s. Refer to SigIDLaT. ; **Scenario:** `MultipleSinusoidalsAddiativeNoiseFeedforwardMx2Ne1Ny1Np0/20080209T180449`.

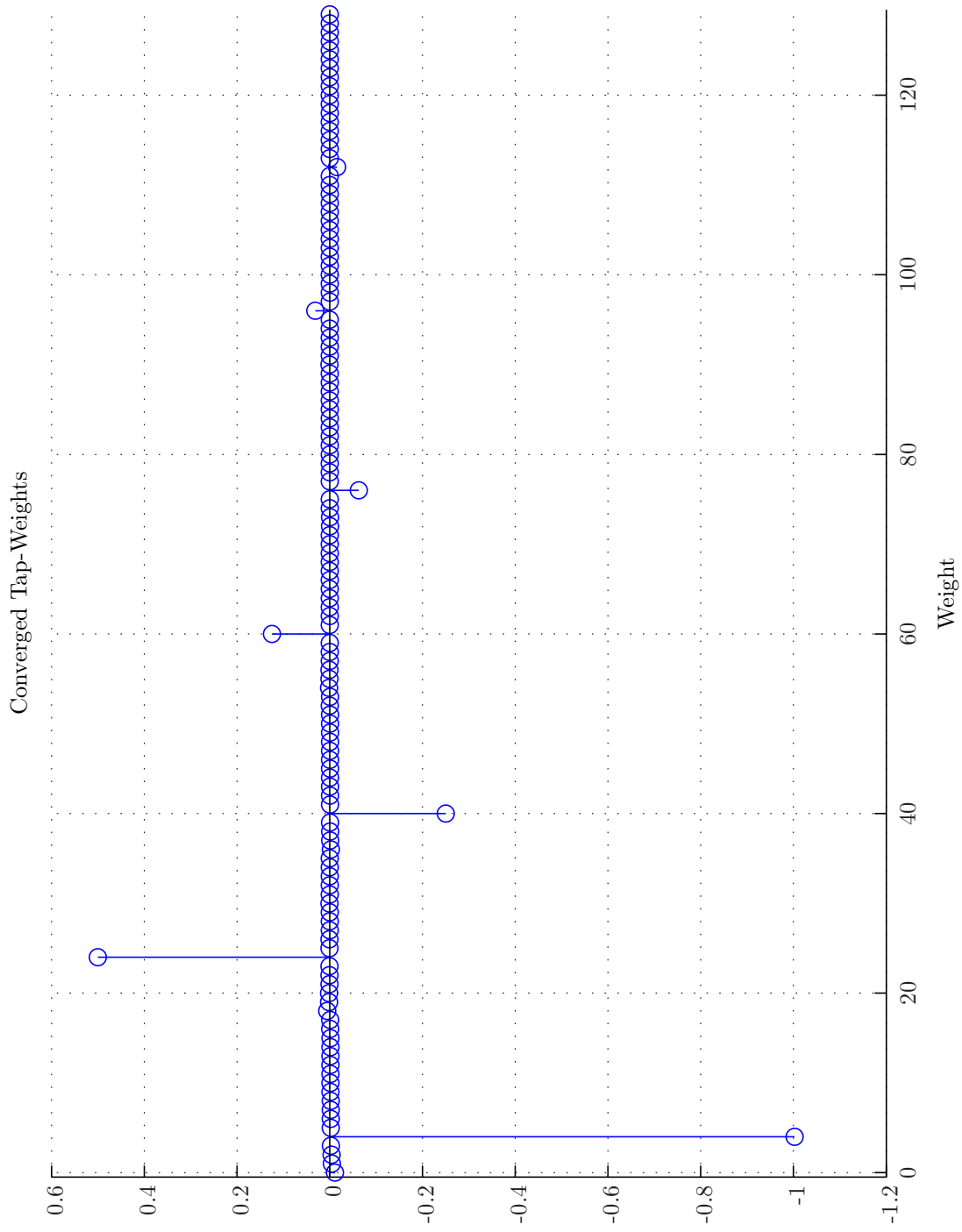

Sim 3.3.3: *Converged Tap-weights.* **Adaptive Filter** $\underset{\sim}{w}$: $\underset{\sim}{w}^{1,1}$: Wiener Hopf ($M = 130, \alpha = 1e-005, T_{WSS} = 0$,**z**-domain); **Main:** $f_s^0 = 192$ kHz, $f_s^1 = 6$ kHz, $R_{\updownarrow}^1 = \frac{1}{32} = 0.03125$, Elliptic LPF ($f_s = 192$ kHz, $f_{pass} = 2.75$ kHz, $f_{stop} = 3$ kHz, $A_{pass} = 2$ dB, $A_{stop} = 40$ dB), $f_s^2 = 6$ kHz, $R_{\updownarrow}^2 = \frac{1}{1} = 1$, Dummy; **Topology:** (Feedforward, mFx, $N_x = 2, N_e = 1, N_y = 1, N_p = 0, N_v = 2$); **Plants:** ($g_{xy}^{1,1}$: (FIR : $M_{gxy}^{1,1} = 1$), $g_{xy}^{1,2}$: (FIR : $M_{gxy}^{1,2} = 1$), $g_{ey}^{1,1}$: Delayed Sampled System: ($f_s = 6$ kHz, $t_d = 500$ µs, $\tau = 0$ µs) (FIR : $M_{gey}^{1,1} = 4$)); **Signals:** Time: $0 - 2$ s. Refer to SigIDLaT. ; **Scenario:** `MultipleSinusoidalsAddiativeNoiseFeedforwardNx2Ne1Ny1Np0/20080209T180449`.

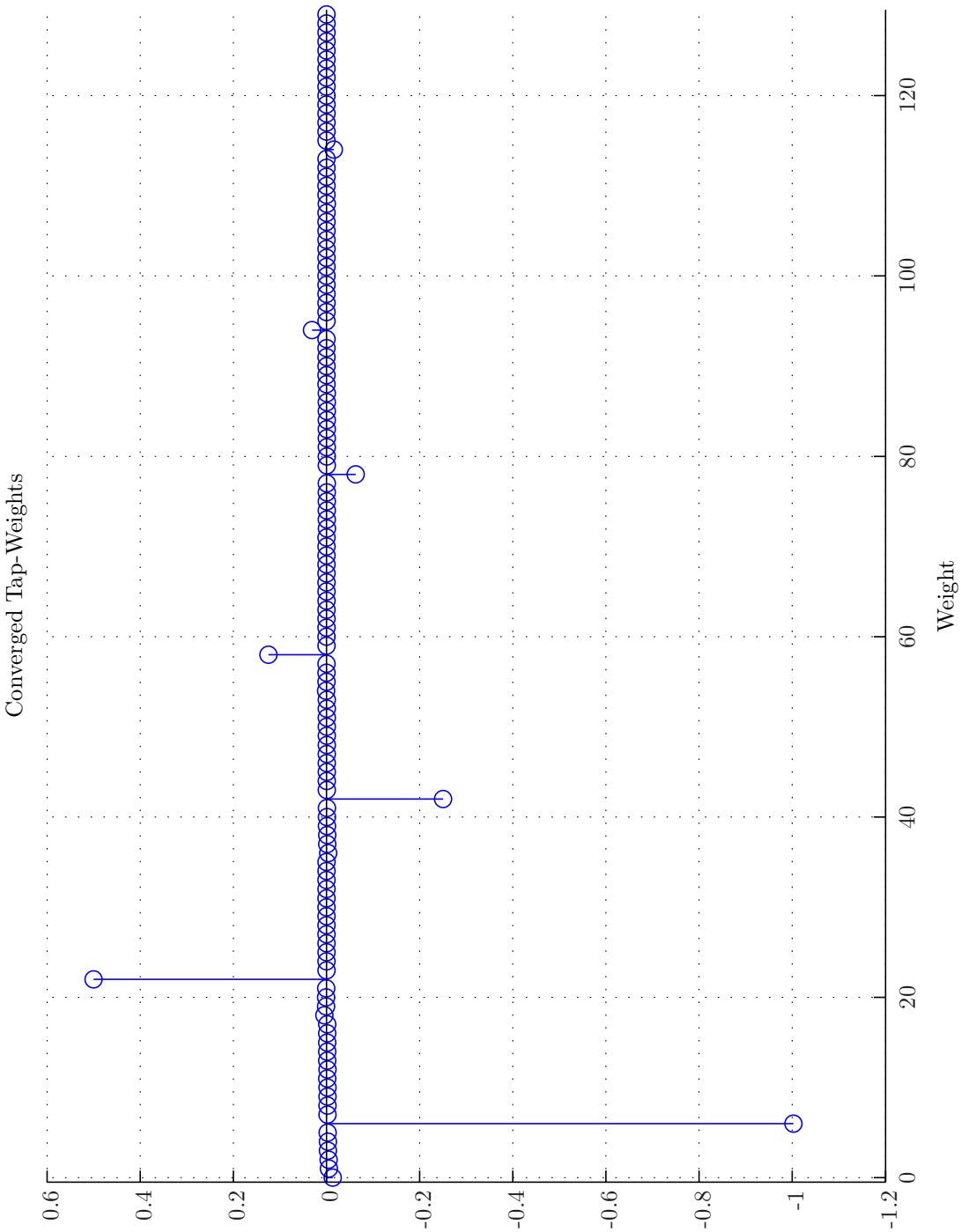

Sim 3.3.4: *Converged Tap-weights.* **Adaptive Filter** $\underset{\sim}{w}$: $\underset{\sim}{w}^{2,1}$: Wiener Hopf ($M = 130, \alpha = 1e-005, T_{WSS} = 0$,**z**-domain); **Main:** $f_s^0 = 192$ kHz, $f_s^1 = 6$ kHz, $R_{\updownarrow}^1 = \frac{1}{32} = 0.03125$, Elliptic LPF ($f_s = 192$ kHz, $f_{pass} = 2.75$ kHz, $f_{stop} = 3$ kHz, $A_{pass} = 2$ dB, $A_{stop} = 40$ dB), $f_s^2 = 6$ kHz, $R_{\updownarrow}^2 = \frac{1}{1} = 1$, Dummy; **Topology:** (Feedforward, mFx, $N_x = 2, N_e = 1, N_y = 1, N_p = 0, N_v = 2$); **Plants:** ($g_{xy}^{1,1}$: (FIR : $M_{gxy}^{1,1} = 1$), $g_{xy}^{1,2}$: (FIR : $M_{gxy}^{1,2} = 1$), $g_{ey}^{1,1}$: Delayed Sampled System: ($f_s = 6$ kHz, $t_d = 500$ µs, $\tau = 0$ µs) (FIR : $M_{gey}^{1,1} = 4$)); **Signals:** Time: $0 - 2$ s. Refer to SigIDLaT. ; **Scenario:** `MultipleSinusoidalsAddiativeNoiseFeedforwardMx2Ne1Ny1Np0/20080209T180449`.

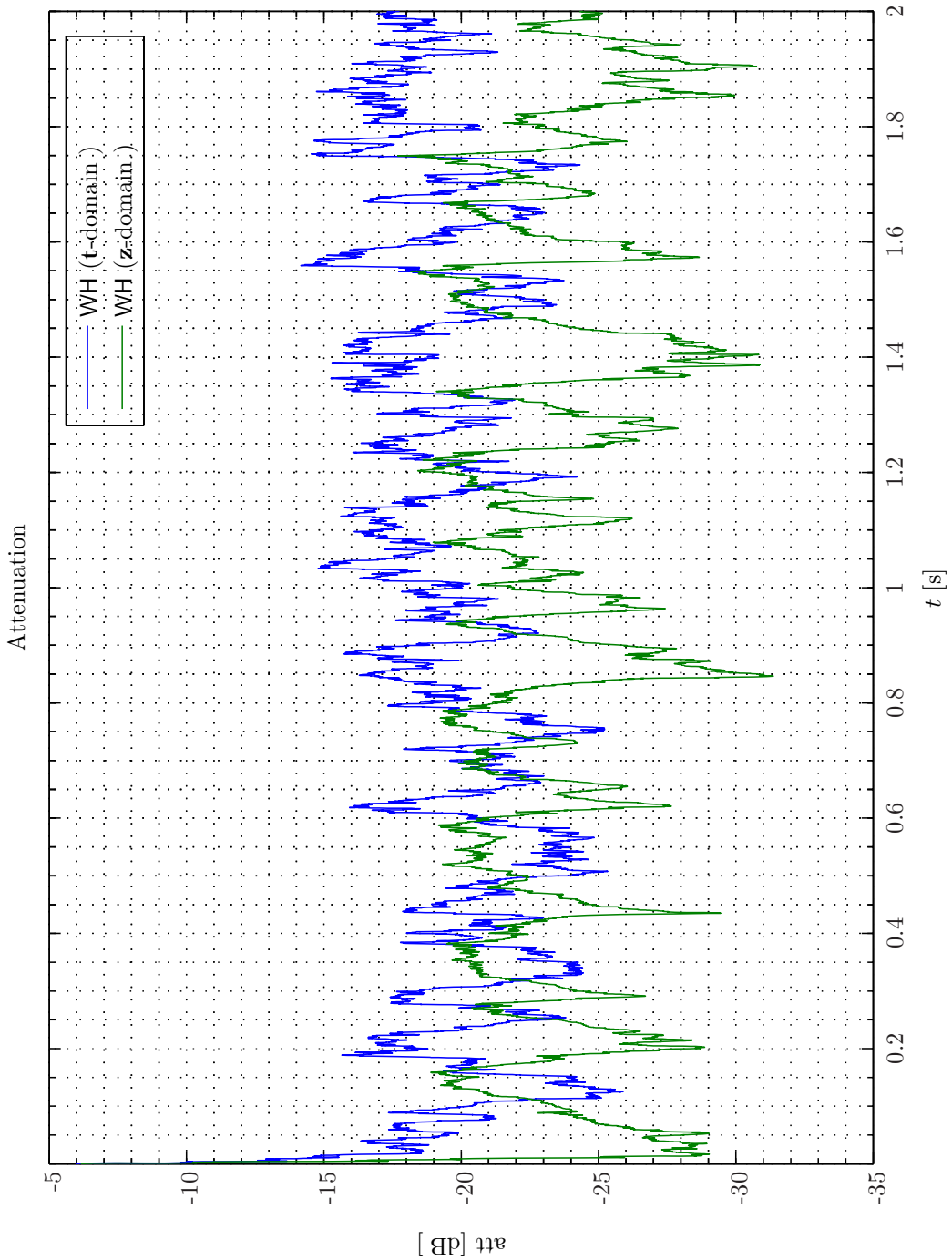

Sim 3.3.5: *Time-Domain: Attenuation.* **Adaptive Filter** $\underset{\sim}{w}$: $\underset{\sim}{w}^{1,1}$: WH ($M = 130, \alpha = 1e-005, T_{WSS} = 0$); **Main:** $f_s^0 = 192$ kHz, $f_s^1 = 6$ kHz, $R_\downarrow^1 = \frac{1}{32} = 0.03125$, Elliptic LPF ($f_s = 192$ kHz, $f_{pass} = 2.75$ kHz, $f_{stop} = 3$ kHz, $A_{pass} = 2$ dB, $A_{stop} = 40$ dB), $f_s^2 = 6$ kHz, $R_\downarrow^2 = \frac{1}{1} = 1$, Dummy; **Topology:** (Feedforward, mFx, $N_x = 2, N_e = 1, N_y = 1, N_p = 0, N_v = 2$); **Plants:** ($g_{xy}^{1,1}$: (FIR : $M_{gxy}^{1,1} = 1$), $g_{xy}^{1,2}$: (FIR : $M_{gxy}^{1,2} = 1$), $g_{ey}^{1,1}$: Delayed Sampled System: ($f_s = 6$ kHz, $t_d = 500$ µs, $\tau = 0$ µs) (FIR : $M_{gey}^{1,1} = 4$)); **Signals:** Time: $0 - 2$ s. Refer to SigIDLaT.; **Scenario:** `MultipleSinusoidalsAddiativeNoiseFeedforwardNx2Ne1Ny1Np0/20080209T180449`.

As expected, the **z**-domain WH method (3.2.11) outperforms the **t**-domain WH method (3.2.9). This can be seen in Simulation 3.3.5 where the attenuation for the former method fluctuates in the vicinity of $\mathcal{A}_1^e(t) = 20 - 30$ dB, while the attenuation for the latter method fluctuates in the vicinity $\mathcal{A}_1^e(t) = 15 - 25$ dB. That is, when the reference sensors are illuminated by random pink noise signals the achieved performance is approximately 5 dB better for the **z**-domain WH method.

In practice, however, it is rarely possible to proceed as in Example 3.2.1 - 3.3.1 and obtain closed-form expressions for the optimal weight vector as will be demonstrated in the next example.

Example 3.3.2 (Feedforward System, Reference Sensors with Directivity, Pink Noise, Extended Secondary Path)**.** In this example we will demonstrate that truncation effects caused by the plus operator are often more pronounced for colored signals than for random white noise signals. In order to make this exhibition we appreciate that from Example 3.3.1 and (3.3.7) we need to extent the duration of the *all-pass* component of the impulse response of the secondary path. Hence, in this example an exponential decaying/growing pulse with an initial delay of t_d samples and a duration of t_w samples will be considered as the impulse response $g_{ey}(t)$. The **z**-transform of $g_{ey}(t)$ is then

$$\tilde{g}_{ey}(z) = (\kappa z)^{-t_d} \sum_{k=0}^{t_w} (\kappa z)^{-k} = (\kappa z)^{-t_d} \frac{1 - (\kappa z)^{-(t_w+1)}}{1 - (\kappa z)^{-1}}, \tag{3.3.11}$$

where the second equation in (3.3.11) is obtained from rules on geometric series. The complex constant κ can be used to regularize the exponential decay/grow of the amplitude over the pulse duration t_w ($\kappa > 1/\kappa < 1$) while $\kappa = 1$ corresponds to a rectangular pulse. Whenever, κ is complex the plant exhibits oscillatory behavior. From (3.3.11) it can be observed that $\tilde{g}_{ey}(z)$ has a t_d-order pole at the origin and t_w+1 zeros at $z = \kappa^{-1}\mathrm{e}^{\imath\frac{2n\pi}{t_w+1}}, n = 1, 2, \ldots, t_w+1$. The reflection of those zeros about the uc are $z^{-*} = \kappa\mathrm{e}^{\imath\frac{2n\pi}{t_w+1}}, n = 1, 2, \ldots, t_w+1$. Hence, the expressions for the all-pass component $\tilde{g}_{ey,\mathrm{all}}(z)$ and the minimum-phase component $\tilde{g}_{ey,\min}(z)$ differ in the regimes $|\kappa| < 1$ and $|\kappa| \geq 1$

$$\tilde{g}_{ey,\mathrm{all}}(z) = \begin{cases} z^{-t_d}\kappa^{t_w}\frac{\sum_{k=0}^{t_w}(\kappa z)^{-k}}{\sum_{k=0}^{t_w}(\kappa^{-1}z)^{-k}} = z^{-t_d}\kappa^{t_w} & \frac{1-(\kappa z)^{-(t_w+1)}}{1-(\kappa^{-1}z)^{-(t_w+1)}}\frac{1-(\kappa^{-1}z)^{-1}}{1-(\kappa z)^{-1}}; \quad |\kappa| < 1 \\ z^{-t_d}; \qquad |\kappa| \geq 1 \end{cases} \tag{3.3.12}$$

and

$$\tilde{g}_{ey,\min}(z) = \begin{cases} \kappa^{-(t_d+t_w)}\sum_{k=0}^{t_w}(\kappa^{-1}z)^{-k} & = \kappa^{-(t_d+t_w)}\frac{1-(\kappa^{-1}z)^{-(t_w+1)}}{1-(\kappa^{-1}z)^{-1}}; \quad |\kappa| < 1 \\ \kappa^{-t_d}\sum_{k=0}^{t_w}(\kappa z)^{-k} & = \kappa^{-t_d}\frac{1-(\kappa z)^{-(t_w+1)}}{1-(\kappa z)^{-1}}; \qquad |\kappa| \geq 1. \end{cases} \tag{3.3.13}$$

The factor κ^{t_w} in (3.3.12) and (3.3.13) ensures that $g^*_{ey,\mathrm{all}}(z^{-*})g_{ey,\mathrm{all}}(z) = \mathrm{I}_1 = 1$. Moreover, it can easily be shown that the inverse of $\tilde{g}_{ey,\min}(z)$ in (3.3.13) is expressed as

$$\tilde{g}^{-1}_{ey,\min}(z) = \begin{cases} \kappa^{(t_d+t_w)}z^{t_d}\big(1-(\kappa^{-1}z)^{-1}\big)\sum_{k=0}^{\infty}(\kappa^{-1}z)^{-k(t_w+1)}; & |\kappa| < 1 \\ \kappa^{t_d}z^{t_d}\big(1-(\kappa z)^{-1}\big)\sum_{k=0}^{\infty}(\kappa z)^{-k(t_w+1)}; & |\kappa| \geq 1. \end{cases} \tag{3.3.14}$$

Hence, for the special case of a rectangular pulse ($\kappa = 1$) the inverse of the minimum-phase component is constituted from an infinite sum of non converging terms. We may therefore expect that a very large filter order in a finite-duration impulse response (FIR) implementation is required for successful performance with such a plant involved. This is demonstrated in Simulation 3.3.6 on the facing page showing the weights $\underset{\sim}{w}^{1,1}$ for $t_d = 4, t_w = 6, \kappa = 1$ and a *pink noise* (1 Hz-3 kHz) signal excitation. The weight vector $\underset{\sim}{w}^{2,1}$ exhibits a similar lack of convergence. The ANR attenuation is negligble in this case.

Now returning to the objective of extending the duration of the *all-pass* component of the impulse response of the secondary path it is evident from (3.3.12) that we must choose $|\kappa| < 1$. Having determined the secondary path components $\tilde{g}_{ey,\mathrm{all}}(z)$ and $\tilde{g}^{-1}_{ey,\mathrm{min}}(z)$ we still need to determine the colorization modeling filter $L_{wv}(z)$ in (3.3.7). For uncolored signals $L_{wv}(z) = \mathrm{I}$. Unfortunately, however, spectral factorization as carried out in the preceding examples is not easily amendable to a pink noise excitation. Instead of attempting to obtain a rigoristic expression for $L_{wv}(z)$ (refer to section 3.A on page 231) we may take a more pragmatic approach and use an estimate hereof. For pink noise experimental evidence (see Simulation 3.5.5 on page 212) suggests that within the first few, say 10 samples the auto correlation sequence can be approximated by $R_{xx}(\tau) \approx \mathrm{e}^{-a|\tau|}$ for $a \approx 450\,\mathrm{s}^{-1}$. Hence, the minimum phase coloring filter may be approximated by

$$L_{wv}(z) \approx \sum_{k=0}^{\infty} \mathrm{e}^{-ak} z^{-k} \mathrm{I}. \tag{3.3.15}$$

Then from insertion of the extended secondary path impulse response function (3.3.11) and the colorisation approximation (3.3.15) in (3.3.7) using (3.3.12) and (3.3.14) we obtain

$$\begin{aligned}\tilde{w}^o(z) = -\kappa^{t_d+t_w} z^{t_d} \big(1 - (\kappa^{-1}z)^{-1}\big) \sum_{k=0}^{\infty} (\kappa^{-1}z)^{-(t_w+1)} \\ \left\{ \kappa^{t_w} (\kappa z)^{t_d} \sum_{k=0}^{t_w} (\kappa^{-1}z)^{-k} \Big(\sum_{k=0}^{t_w} (\kappa^{-1}z)^{-k} \Big)^{-1} \begin{bmatrix} z^{-8} & z^{-10} \end{bmatrix} \sum_{k'=0}^{\infty} \mathrm{e}^{a|k|} z^{-k} \mathrm{I} \right\}_+ \\ \Big(\sum_{k'=0}^{\infty} \mathrm{e}^{ak} z^{-k} \Big)^{-1} \mathrm{I}_{\frac{1}{1-b_x^2 z^{-36}}} \begin{bmatrix} 1 & -b_x z^{-18} \\ -b_x z^{-18} & 1 \end{bmatrix}.\end{aligned} \tag{3.3.16}$$

Comparing expression (3.3.16) with (3.2.29) where a Dirac-impulse ($t_w = 0$) is used for the secondary path, we see that colorization of the reference signals and the use of an extended plant response leads to a considerably more involved expression for the optimal weight vector. We do, therefore, not attempt to process (3.3.16) further in hand.

From (3.3.16), however, it is expectable that the discrete nonvanishing weights to be smeared out by comparing expression for the extended secondary path. Moreover, it is expectable that the plus operator will lead to some truncation of the contribution of the colorization modeling filter $L_{wv}(z)$ such that $\underset{\sim}{w}^{1,1}$ and $\underset{\sim}{w}^{2,1}$ will follow a decaying pattern with increasing weight number. Both of these predictions are confirmed by inspection of the weight $\underset{\sim}{w}^{1,1}$ and $\underset{\sim}{w}^{2,1}$ pattern for the two WH filter methods shown in Simulation 3.3.7 - 3.3.10 on pages 147–150. The set of optimal weight vectors from the two methods now deviate substantially from each other.

Expectably, as compared with the $\kappa = 1$ case above we will be more successful with the ANR operation as illustrated in Simulation 3.3.11 where the attenuation performance for the two

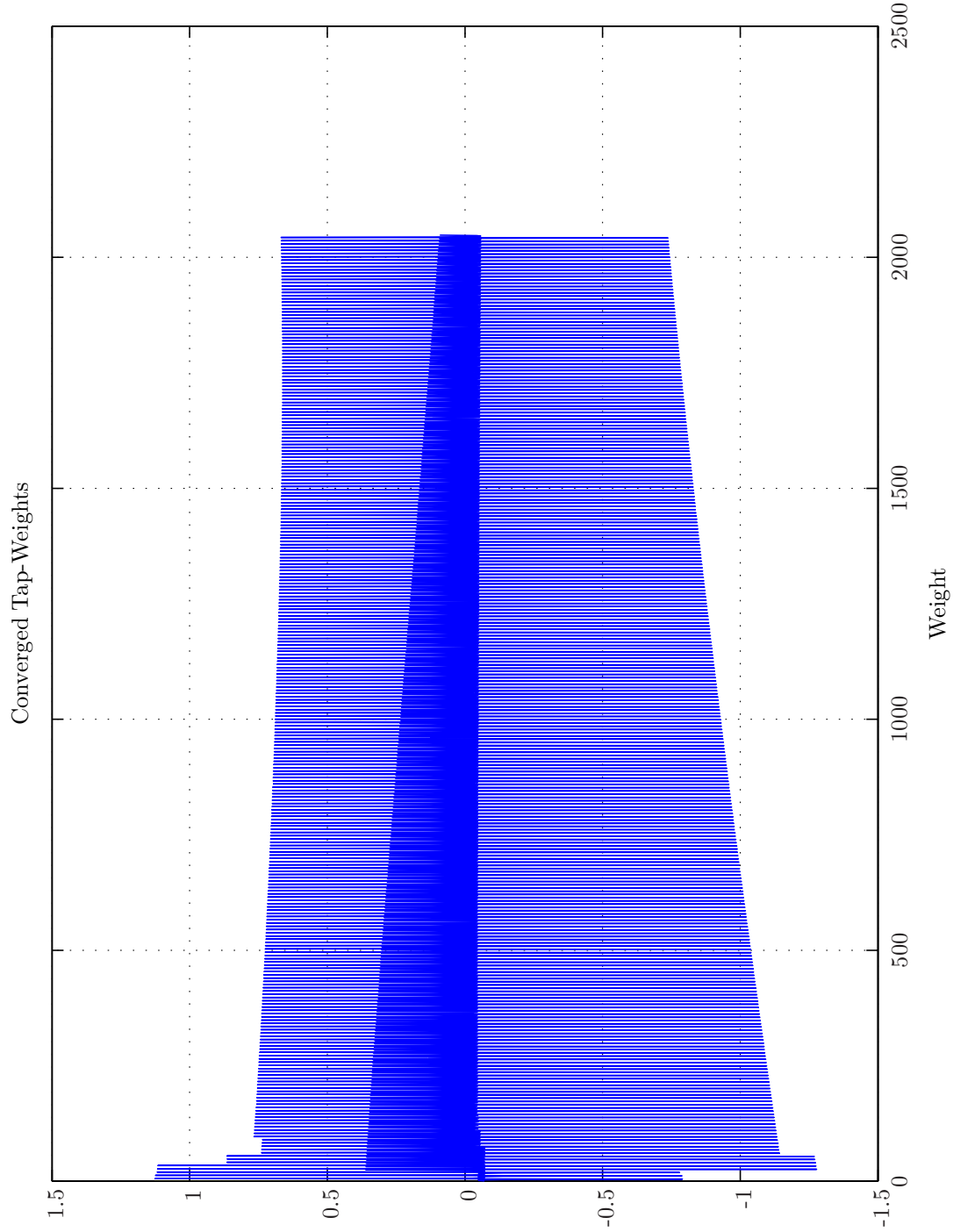

Sim 3.3.6: *Converged Tap-weights.* **Adaptive Filter** $\underset{\sim}{w}$: $\underset{\sim}{w}^{1,1}$: Wiener Hopf ($M = 2048, \alpha = 1e-005, T_{WSS} = 0$,**z**-domain); **Main:** $f_s^0 = 192$ kHz, $f_s^1 = 6$ kHz, $R_\downarrow^1 = \frac{1}{32} = 0.03125$, Elliptic LPF ($f_s = 192$ kHz, $f_{pass} = 2.75$ kHz, $f_{stop} = 3$ kHz, $A_{pass} = 2$ dB, $A_{stop} = 40$ dB), $f_s^2 = 6$ kHz, $R_\downarrow^2 = \frac{1}{1} = 1$, Dummy; **Topology:** (Feedforward, mFx, $N_x = 2, N_e = 1, N_y = 1, N_p = 0, N_v = 2$); **Plants:** ($g_{xy}^{1,1}$: (FIR : $M_{gxy}^{1,1} = 1$), $g_{xy}^{1,2}$: (FIR : $M_{gxy}^{1,2} = 1$), $g_{ey}^{1,1}$: Delayed Sampled System: ($f_s = 6$ kHz, $t_d = 500$ µs, $\tau = 1000$ µs, $\kappa = 1.0$) (FIR : $M_{gey}^{1,1} = 10$)); **Signals:** Time: $0 - 2$ s. Refer to SigIDLaT. ; **Scenario:** `MultipleSinusoidalsAddiativeNoiseFeedforwardNx2Ne1Ny1Np0/20080210T013311`.

causality WH filters is shown. As seen the attenuation fluctuates in the vicinity of $\mathcal{A}_1^e(t) = -2 - 8$ dB for the **t**-domain WH filter (3.2.9) while the attenuation is confined to the interval $\mathcal{A}_1^e(t) = 4 - 14$ dB for the **z**-domain WH method (3.2.11). Hence, as expected when the reference sensors are illuminated by random pink noise signals the achieved performance is much better for the latter method.

Moreover, the time-domain attenuation somewhat hiddens the real benefits of using the more advanced colorization-dependent WH filter. This can be seen in Simulation 3.3.12 - 3.3.13 on pages 152–153 displaying the frequency-domain attenuation $\mathcal{A}^e(f)$ achieved by the two WH methods. Plant delays effectively limits the upper ANR frequency to 800 Hz. Accordingly, only marginal ANR performance is achievable in the frequency range $800 - 3000$ Hz which even for a pink noise signal clearly limits the time-domain attenuation $\mathcal{A}^e(t)$.

The operational difference between the two WH methods investigated is probably most clearly exhibited in Simulation 3.3.14 - 3.3.15 on pages 154–155 displaying the auto spectral density functions of the disturbance signals and resulting error signals from applying the WH filters. While the **t**-domain method fails to produce a white noise error signal when exposed to colored noise the **z**-domain method successfully takes the spectral distribution of the reference signals into account and produces a RWN error signal.

Finally, in Simulation 3.3.16 the attenuation performance for the two WH filters when *white noise* (1 Hz-3 kHz) signals are used instead. As expected the two different WH methods yield an almost identical attenuation capability that in turn is much poorer than for the *pink noise* (1 Hz-3 kHz signal in Simulation 3.3.11).

3.4 Causality Constraints in a Closed-Back Headset System

In the preceding examples we have used mathematically determined plants in order to make our exhibitions of the causality constraints more clear. In this section we will investigate the impact of causality constraints pertinent to the helmet based ANR system (see Figure 2.1 - 2.2 on pages 33–34).

3.4.1 Vibro-Acoustical Model Helmet Closed-Back Headset System

Various theoretical models for the primary path and secondary path transfer functions exist as explained in chapter 10 - 11 on pages 471–481 and practical measurement data is also at our disposal (see section 2.4 on page 32). Accordingly, we will use (3.3.8) instead of (3.3.7) for the determination of the optimal causally constrained weights.

We do not attempt to establish an *exact* vibro-acoustical model for the Gentex HGU-55/P helmet. Instead we will use the main findings from chapter 10 - 11 regarding the primary paths and secondary paths transfer functions in combination with an elementary spherical model for the helmet that takes propagation delays and spatial decorrelation effects into account. The applicability of the results obtained in this report are therefore heavily dependent on simulations and actual measurements. It is therefore important that the test scenarios obtained from the simulations closely resemble realistic noise data. As will be demonstrated, by using a sufficient number of random white noise signals and a colorization filter we may obtain a sound field with the required diffuseness and reference signals and disturbance signals with the desired characteristics.

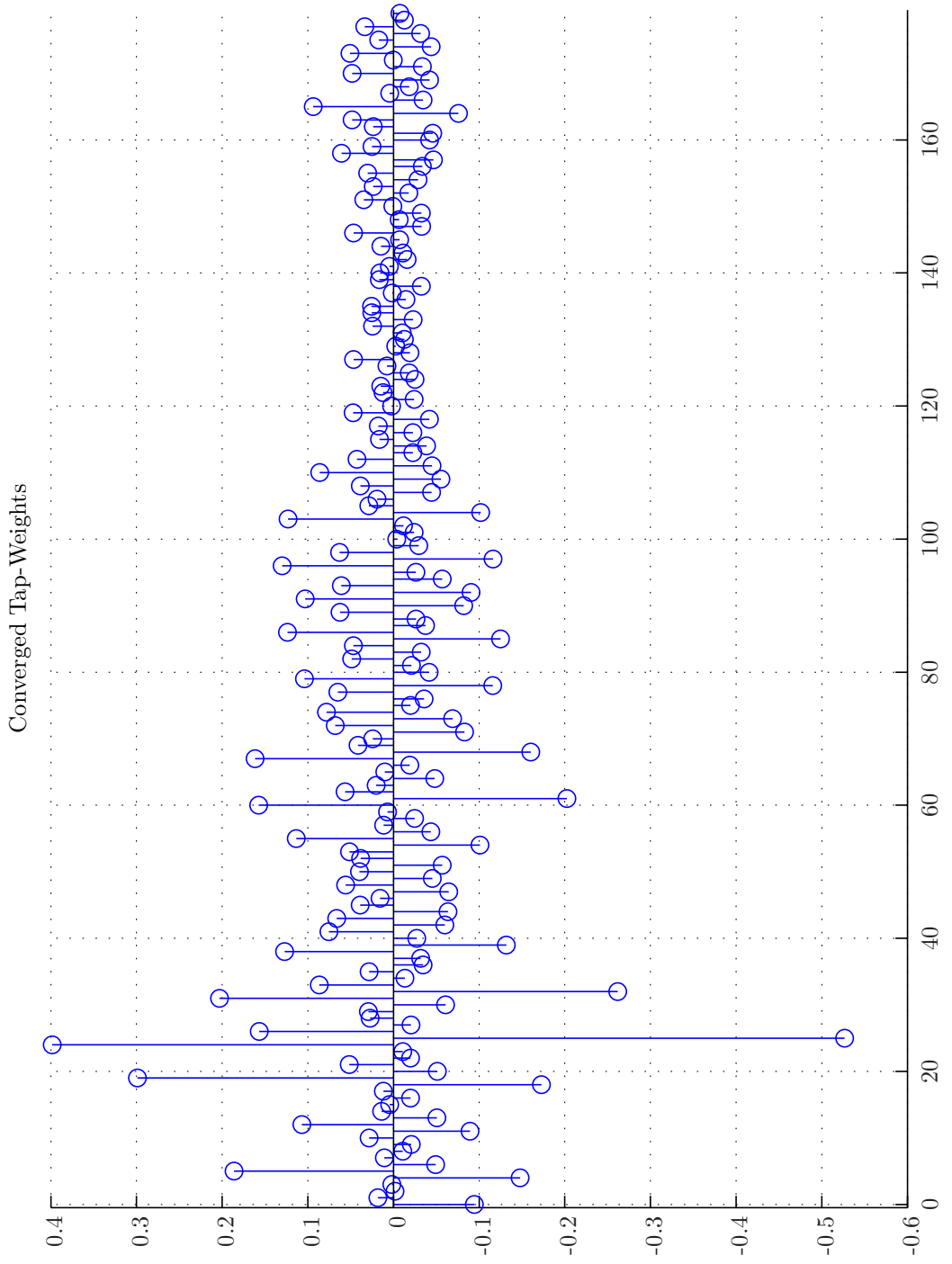

Sim 3.3.7: *Converged Tap-weights.* **Adaptive Filter** $\underset{\chi}{w}$: $\underset{\chi}{w}^{1,1}$: Wiener Hopf ($M = 180, \alpha = 1e-005, T_{WSS} = 0$,**t**-domain); **Main:** $f_s^0 = 192$ kHz, $f_s^1 = 6$ kHz, $R_\updownarrow^1 = \frac{1}{32} = 0.03125$, Elliptic LPF ($f_s = 192$ kHz, $f_{pass} = 2.75$ kHz, $f_{stop} = 3$ kHz, $A_{pass} = 2$ dB, $A_{stop} = 40$ dB), $f_s^2 = 6$ kHz, $R_\updownarrow^2 = \frac{1}{1} = 1$, Dummy; **Topology:** (Feedforward, mFx, $N_x = 2, N_e = 1, N_y = 1, N_p = 0, N_v = 2$); **Plants:** ($g_{xy}^{1,1}$: (FIR : $M_{gxy}^{1,1} = 1$), $g_{xy}^{1,2}$: (FIR : $M_{gxy}^{1,2} = 1$), $g_{ey}^{1,1}$: Delayed Sampled System: ($f_s = 6$ kHz, $t_d = 500$ µs, $\tau = 1000$ µs, $\kappa = 0.9$) (FIR : $M_{gey}^{1,1} = 10$)); **Signals:** Time: 0 − 2 s. Refer to SigIDLaT. ; **Scenario:** `MultipleSinusoidalsAddiativeNoiseFeedforwardNx2Ne1Ny1Np0/20080210T185714`.

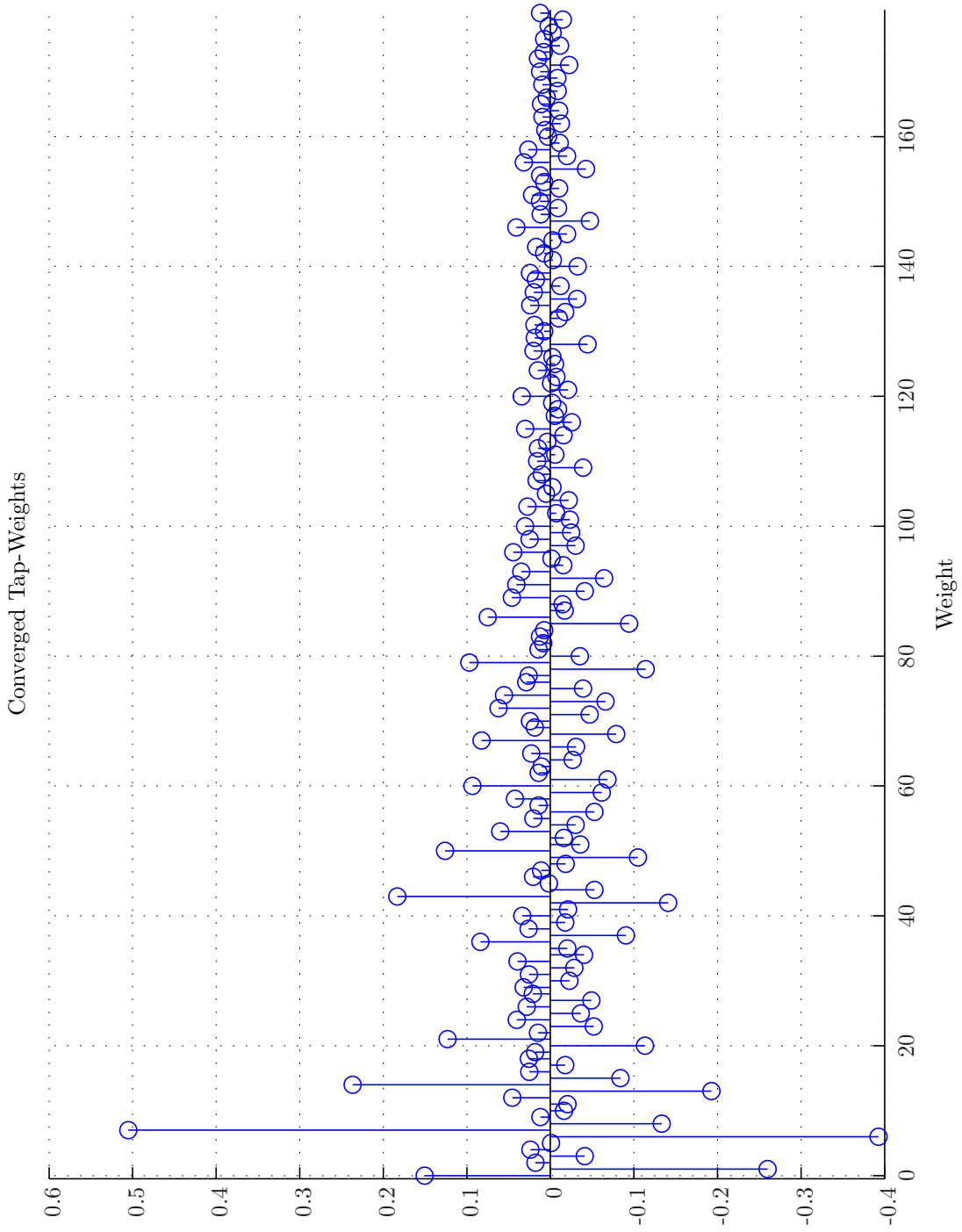

Sim 3.3.8: *Converged Tap-weights.* **Adaptive Filter** $\underset{\sim}{w}$: $\underset{\sim}{w}^{2,1}$: Wiener Hopf ($M = 180, \alpha = 1e-005, T_{WSS} = 0$,**t**-domain); **Main:** $f_s^0 = 192$ kHz, $f_s^1 = 6$ kHz, $R_\downarrow^1 = \frac{1}{32} = 0.03125$, Elliptic LPF ($f_s = 192$ kHz, $f_{pass} = 2.75$ kHz, $f_{stop} = 3$ kHz, $A_{pass} = 2$ dB, $A_{stop} = 40$ dB), $f_s^2 = 6$ kHz, $R_\downarrow^2 = \frac{1}{1} = 1$, Dummy; **Topology:** (Feedforward, mFx, $N_x = 2, N_e = 1, N_y = 1, N_p = 0, N_v = 2$); **Plants:** ($g_{xy}^{1,1}$: (FIR : $M_{gxy}^{1,1} = 1$), $g_{xy}^{1,2}$: (FIR : $M_{gxy}^{1,2} = 1$), $g_{ey}^{1,1}$: Delayed Sampled System: ($f_s = 6$ kHz, $t_d = 500$ µs, $\tau = 1000$ µs, $\kappa = 0.9$) (FIR : $M_{gey}^{1,1} = 10$)); **Signals:** Time: $0 - 2$ s. Refer to SigIDLaTeX.; **Scenario:** `MultipleSinusoidalsAddiativeNoiseFeedforwardNx2Ne1Ny1Np0/20080210T185714`.

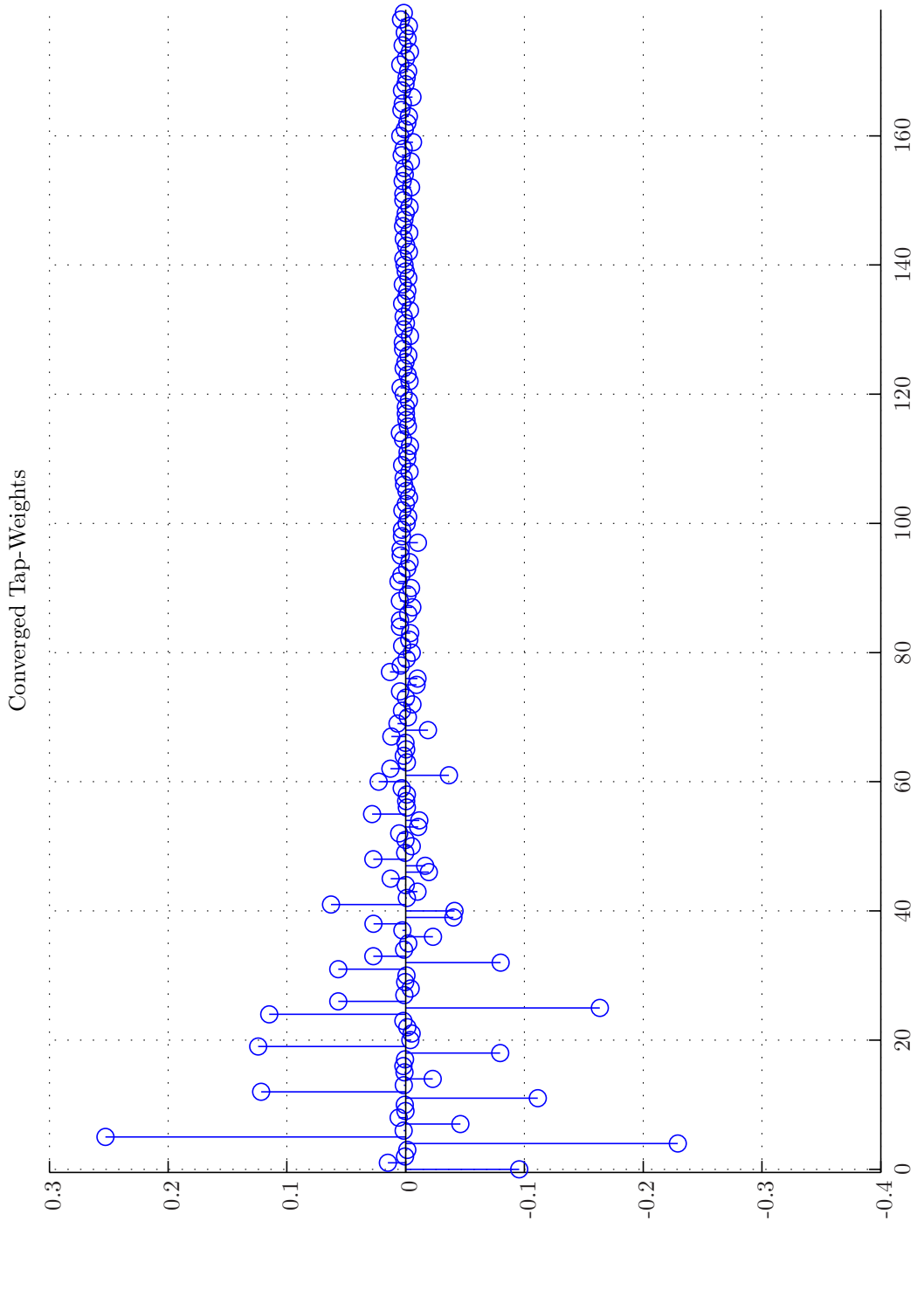

Sim 3.3.9: *Converged Tap-weights.* **Adaptive Filter** $\underset{\sim}{w}$: $\underset{\sim}{w}^{1,1}$: Wiener Hopf ($M = 180, \alpha = 1e-005, T_{WSS} = 0$,**z**-domain); **Main:** $f_s^0 = 192$ kHz, $f_s^1 = 6$ kHz, $R_\updownarrow^1 = \frac{1}{32} = 0.03125$, Elliptic LPF ($f_s = 192$ kHz, $f_{pass} = 2.75$ kHz, $f_{stop} = 3$ kHz, $A_{pass} = 2$ dB, $A_{stop} = 40$ dB), $f_s^2 = 6$ kHz, $R_\updownarrow^2 = \frac{1}{1} = 1$, Dummy; **Topology:** (Feedforward, mFx, $N_x = 2, N_e = 1, N_y = 1, N_p = 0, N_v = 2$); **Plants:** ($g_{xy}^{1,1}$: (FIR : $M_{gxy}^{1,1} = 1$), $g_{xy}^{1,2}$: (FIR : $M_{gxy}^{1,2} = 1$), $g_{ey}^{1,1}$: Delayed Sampled System: ($f_s = 6$ kHz, $t_d = 500$ µs, $\tau = 1000$ µs, $\kappa = 0.9$) (FIR : $M_{gey}^{1,1} = 10$)); **Signals:** Time: 0 − 2 s. Refer to SigIDLaT. ; **Scenario:** `MultipleSinusoidalsAddiativeNoiseFeedforwardNx2Ne1Ny1Np0/20080210T185714`.

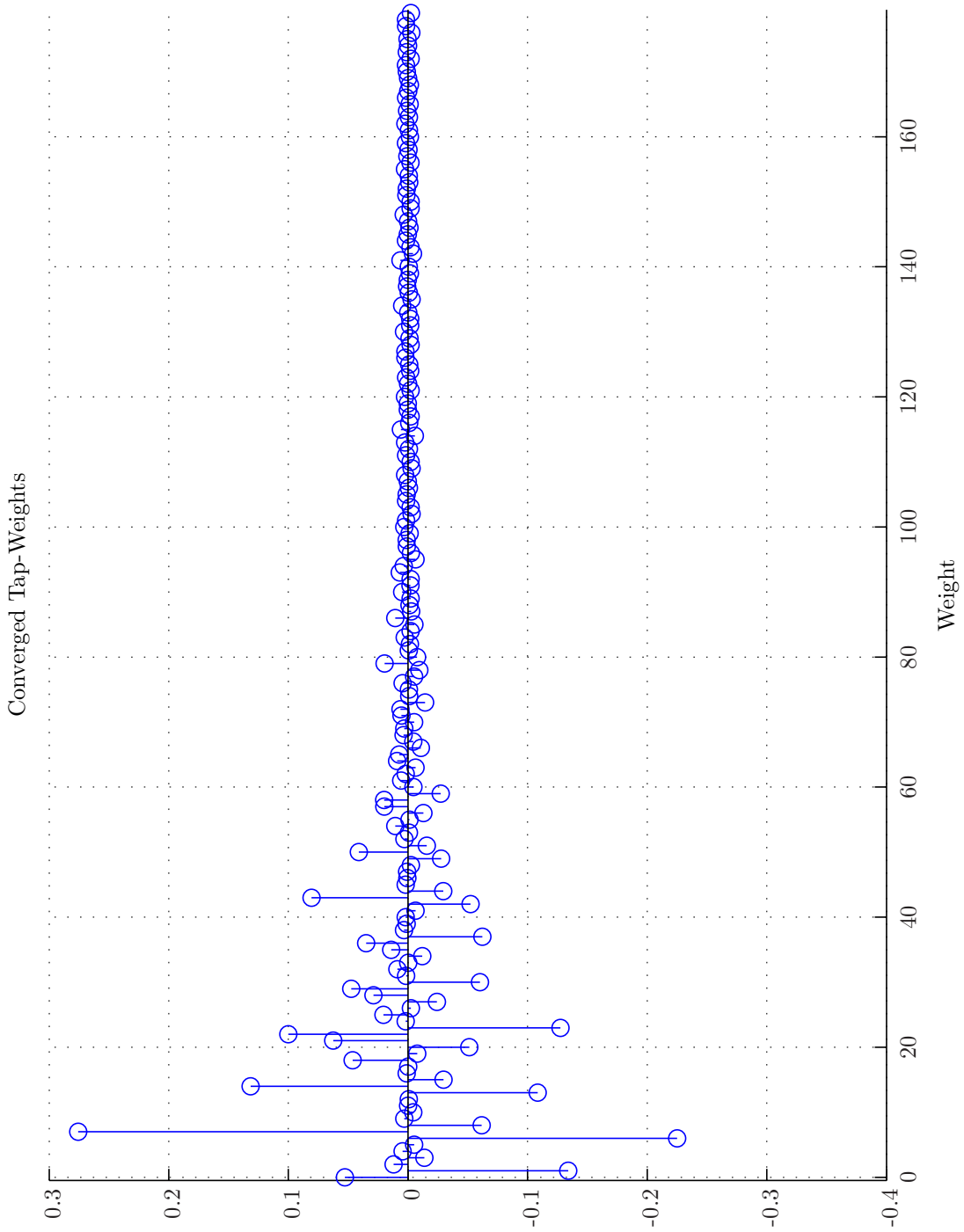

Sim 3.3.10: *Converged Tap-weights.* **Adaptive Filter** $\underset{\sim}{w}$: $\underset{\sim}{w}^{2,1}$: Wiener Hopf ($M = 180, \alpha = 1e-005, Tw_{SS} = 0$,$\mathbf{z}$-domain); **Main:** $f_s^0 = 192$ kHz, $f_s^1 = 6$ kHz, $R_{\downarrow}^1 = \frac{1}{32} = 0.03125$, Elliptic LPF ($f_s = 192$ kHz, $f_{pass} = 2.75$ kHz, $f_{stop} = 3$ kHz, $A_{pass} = 2$ dB, $A_{stop} = 40$ dB), $f_s^2 = 6$ kHz, $R_{\downarrow}^2 = \frac{1}{1} = 1$, Dummy; **Topology:** (Feedforward, mFx, $N_x = 2, N_e = 1, N_y = 1, N_p = 0, N_v = 2$); **Plants:** ($g_{xy}^{1,1}$: (FIR : $M_{gxy}^{1,1} = 1$), $g_{xy}^{1,2}$: (FIR : $M_{gxy}^{1,2} = 1$), $g_{ey}^{1,1}$: Delayed Sampled System: ($f_s = 6$ kHz, $t_d = 500$ µs, $\tau = 1000$ µs, $\kappa = 0.9$) (FIR : $M_{gey}^{1,1} = 10$)); **Signals:** Time: $0 - 2$ s. Refer to SigIDLaT. ; **Scenario:** `MultipleSinusoidalsAddiativeNoiseFeedforwardNx2Ne1Ny1Np0/20080210T185714`.

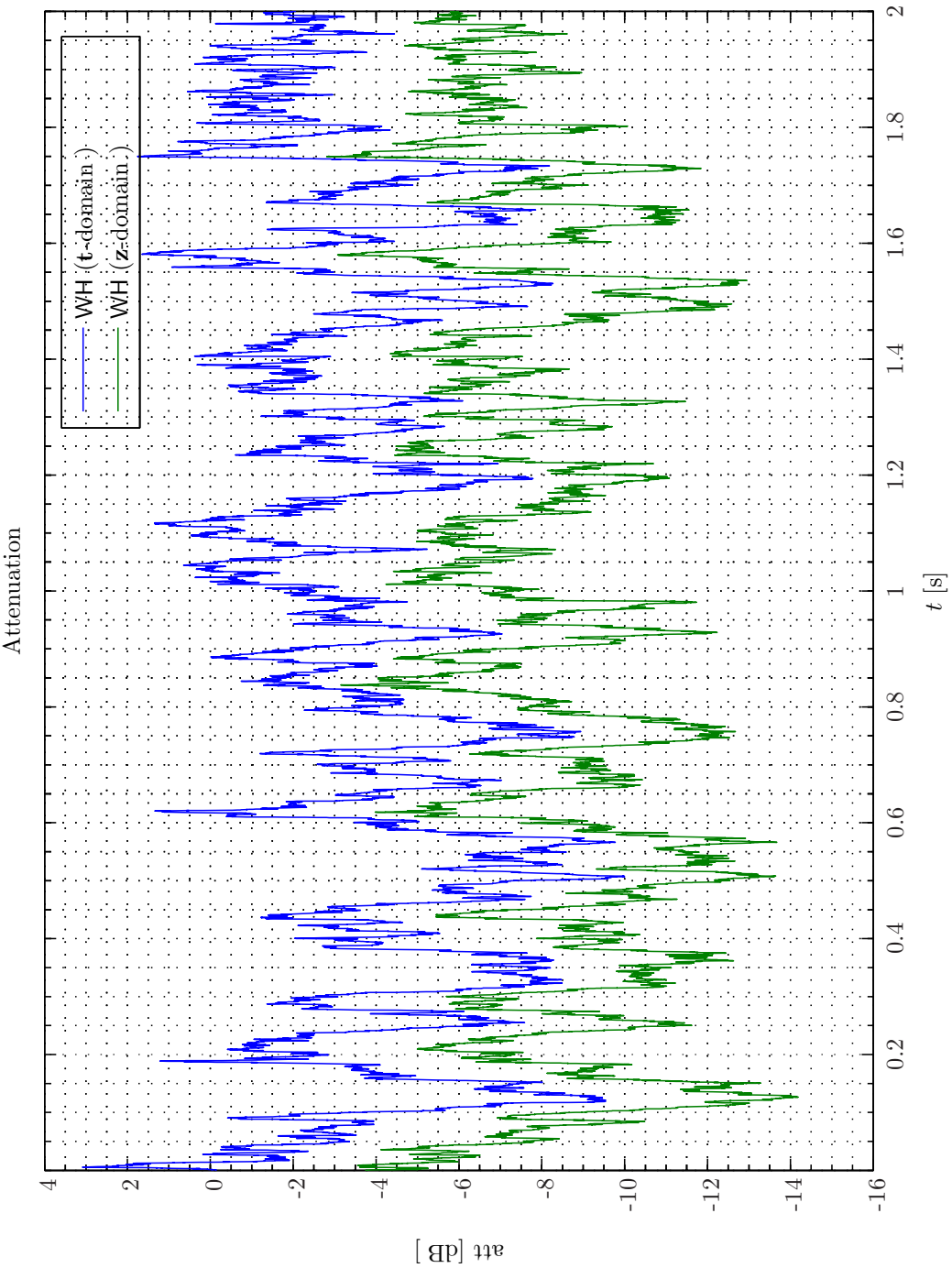

Sim 3.3.11: *Time-Domain: Attenuation.* **Adaptive Filter** $\underset{\sim}{w}$: $\underset{\sim}{w}^{1,1}$: WH ($M = 180, \alpha = 1e{-}005, T_{WSS} = 0$); **Main:** $f_s^0 = 192$ kHz, $f_s^1 = 6$ kHz, $R_\downarrow^1 = \frac{1}{32} = 0.03125$, Elliptic LPF ($f_s = 192$ kHz, $f_{pass} = 2.75$ kHz, $f_{stop} = 3$ kHz, $A_{pass} = 2$ dB, $A_{stop} = 40$ dB), $f_s^2 = 6$ kHz, $R_\downarrow^2 = \frac{1}{1} = 1$, Dummy; **Topology:** (Feedforward, mFx, $N_x = 2, N_e = 1, N_y = 1, N_p = 0, N_v = 2$); **Plants:** ($g_{xy}^{1,1}$: (FIR : $M_{gxy}^{1,1} = 1$), $g_{xy}^{1,2}$: (FIR : $M_{gxy}^{1,2} = 1$), $g_{ey}^{1,1}$: Delayed Sampled System: ($f_s = 6$ kHz, $t_d = 500$ µs, $\tau = 1000$ µs, $\kappa = 0.9$) (FIR : $M_{gey}^{1,1} = 10$)); **Signals:** Time: $0 - 2$ s. Refer to SigIDLaT.; **Scenario:** `MultipleSinusoidalsAddiativeNoiseFeedforwardMx2Ne1Ny1Np0/20080210T185714`.

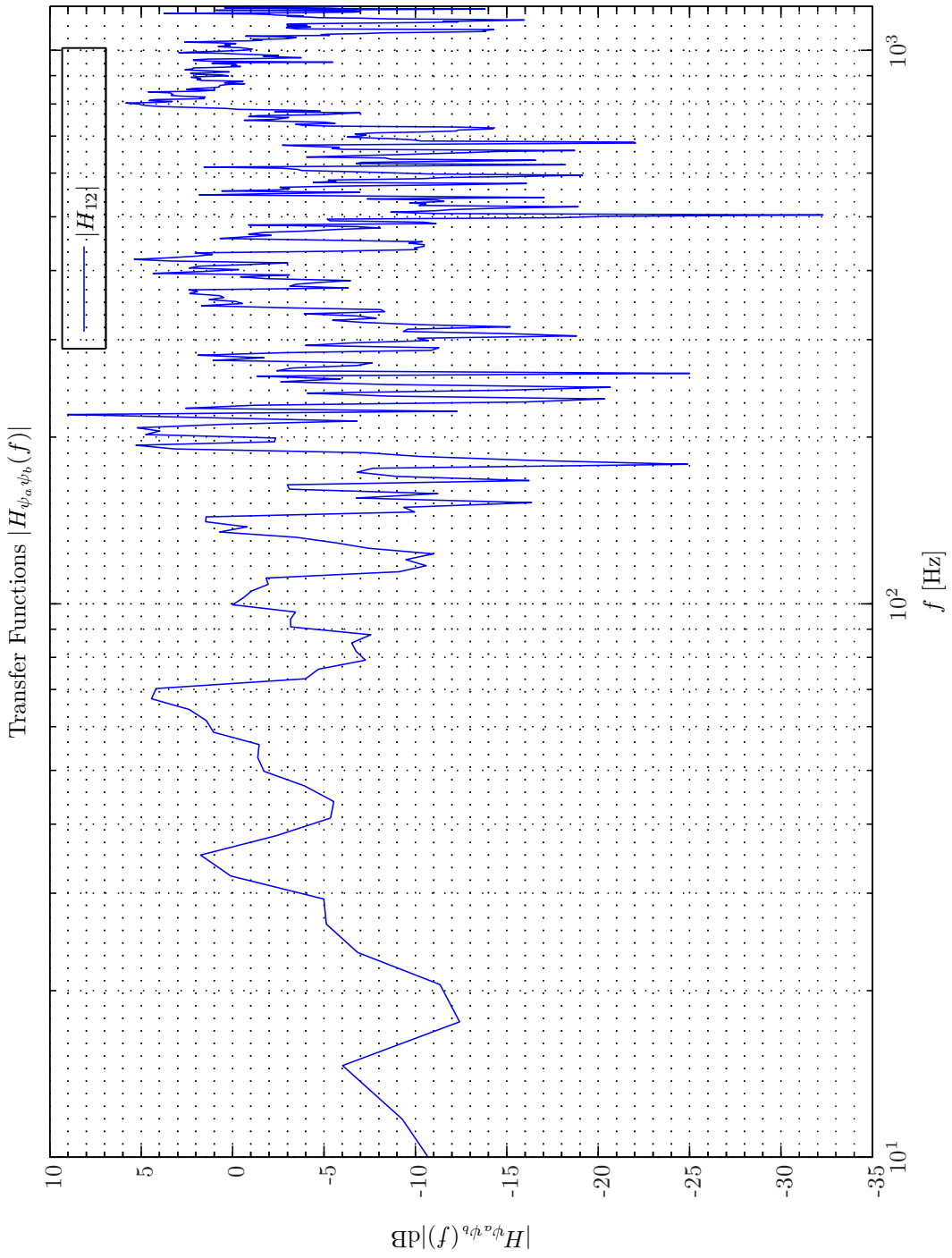

Sim **3.3.12:** *Transfer Function, Magnitude:* $|H_{\psi_a\psi_b}(f)|$: **Statistical Data Analysis**: Single-Sided Modified Periodogram, $f_s = 6$ kHz, $N_{DFT} = 2048$, $L_{DFT} = 1501$, $R_{DFT} = 751$, Hanning, $\Delta f_m = 16$ Hz, $T_{DFT} = 0.25017$ s, $N_{f,DFT} = 1025$, $\Delta f_{DFT} = 2.9297$ Hz, $K_{DFT} = 2$; **Adaptive Filter** $\underset{\sim}{w}$: Wiener Hopf ($M = 180, \alpha = 1e-005, T_{WSS} = 0$,**t**-domain); **Main:** $f_s^0 = 192$ kHz, $f_s^1 = 6$ kHz, $R_\downarrow^1 = \frac{1}{32} = 0.03125$, Elliptic LPF ($f_s = 192$ kHz, $f_{pass} = 2.75$ kHz, $f_{stop} = 3$ kHz, $A_{pass} = 2$ dB, $A_{stop} = 40$ dB), $f_s^2 = 6$ kHz, $R_\downarrow^2 = \frac{1}{1} = 1$, Dummy; **Topology:** (Feedforward, mFx, $N_x = 2, N_e = 1, N_y = 1, N_p = 0, N_v = 2$); **Plants:** $(g_{xy}^{1,1}$: (FIR : $M_{gxy}^{1,1} = 1$), $g_{xy}^{1,2}$: (FIR : $M_{gxy}^{1,2} = 1$), $g_{ey}^{1,1}$: Delayed Sampled System: ($f_s = 6$ kHz, $t_d = 500$ µs, $\tau = 1000$ µs, $\kappa = 0.9$) (FIR : $M_{gey}^{1,1} = 10$)); **Signals:** Time: $0 - 2$ s. Refer to SigIDLaT. ; **Scenario:** `MultipleSinusoidalsAddiativeNoiseFeedforwardNx2Ne1Ny1Np0/20080210T185714`; *Channels:* #1 $\leftarrow d_1(t_1^1)$, #2 $\leftarrow e_1(t_1^1)$.: .

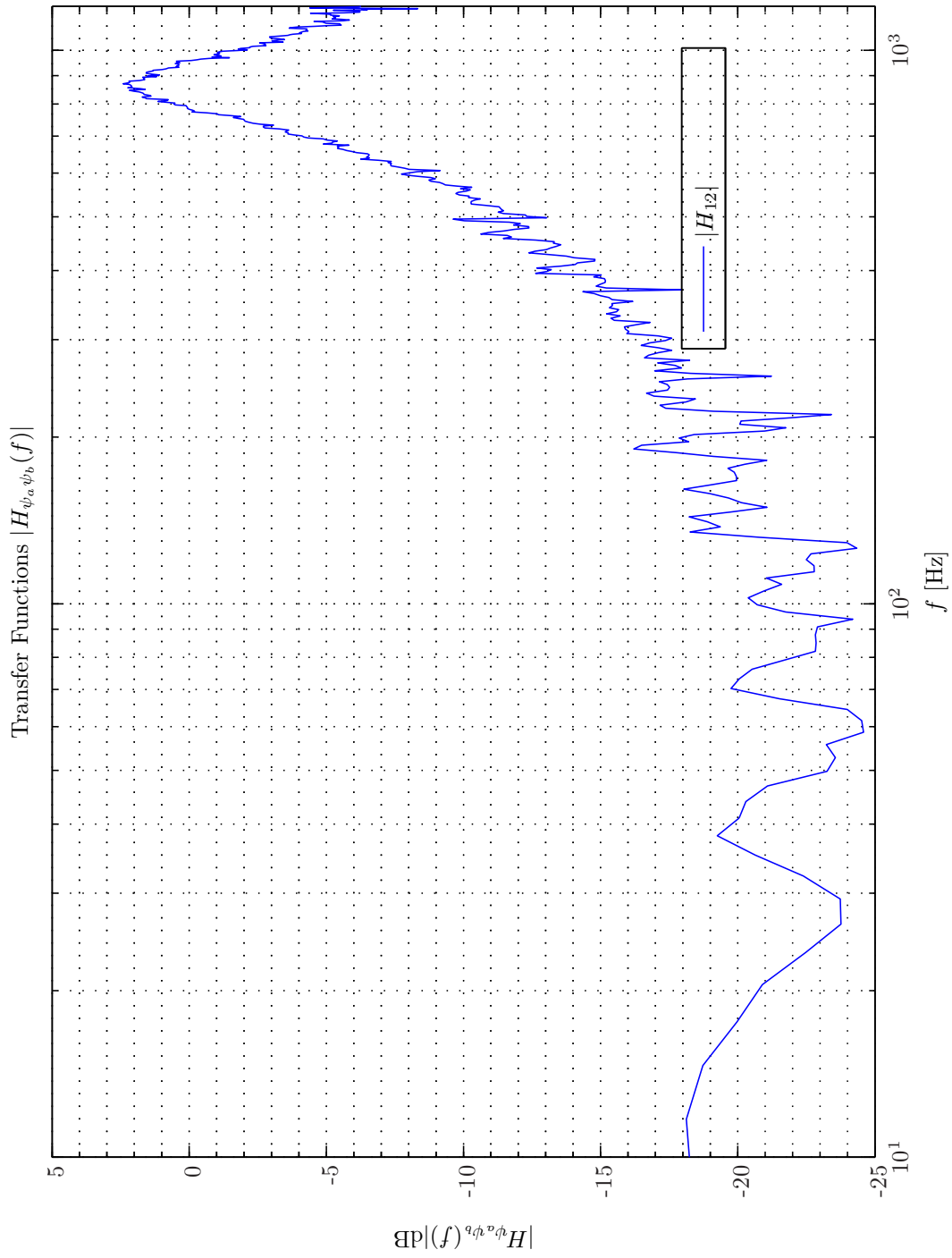

Sim 3.3.13: *Transfer Function, Magnitude:* $|H_{\psi_a\psi_b}(f)|$: **Statistical Data Analysis**: Single-Sided Modified Periodogram, $f_s = 6$ kHz, $N_{DFT} = 2048$, $L_{DFT} = 1501$, $R_{DFT} = 751$, Hanning, $\Delta f_m = 16$ Hz, $T_{DFT} = 0.25017$ s, $N_{f,DFT} = 1025$, $\Delta f_{DFT} = 2.9297$ Hz, $K_{DFT} = 2$; **Adaptive Filter** $\underset{\sim}{w}$: Wiener Hopf ($M = 180, \alpha = 1e-005, T_{WSS} = 0.$**z**-domain); **Main:** $f_s^0 = 192$ kHz, $f_s^1 = 6$ kHz, $R_\updownarrow^1 = \frac{1}{32} = 0.03125$, Elliptic LPF ($f_s = 192$ kHz, $f_{pass} = 2.75$ kHz, $f_{stop} = 3$ kHz, $A_{pass} = 2$ dB, $A_{stop} = 40$ dB), $f_s^2 = 6$ kHz, $R_\updownarrow^2 = \frac{1}{1} = 1$, Dummy; **Topology:** (Feedforward, mFx, $N_x = 2, N_e = 1, N_y = 1, N_p = 0, N_v = 2$); **Plants:** $(g_{xy}^{1,1}$: (FIR : $M_{gxy}^{1,1} = 1$), $g_{xy}^{1,2}$: (FIR : $M_{gxy}^{1,2} = 1$), $g_{ey}^{1,1}$: Delayed Sampled System: ($f_s = 6$ kHz, $t_d = 500$ µs, $\tau = 1000$ µs, $\kappa = 0.9$) (FIR : $M_{gey}^{1,1} = 10$)); **Signals:** Time: $0 - 2$ s. Refer to SigIDLaT. ; **Scenario:** `MultipleSimusoidalsAddiativeNoiseFeedforwardNx2Ne1Ny1Np0/20080210T185714`; *Channels:* #1 $\leftarrow d_1(t_1^1)$, #2 $\leftarrow e_1(t_1^1)$.: .

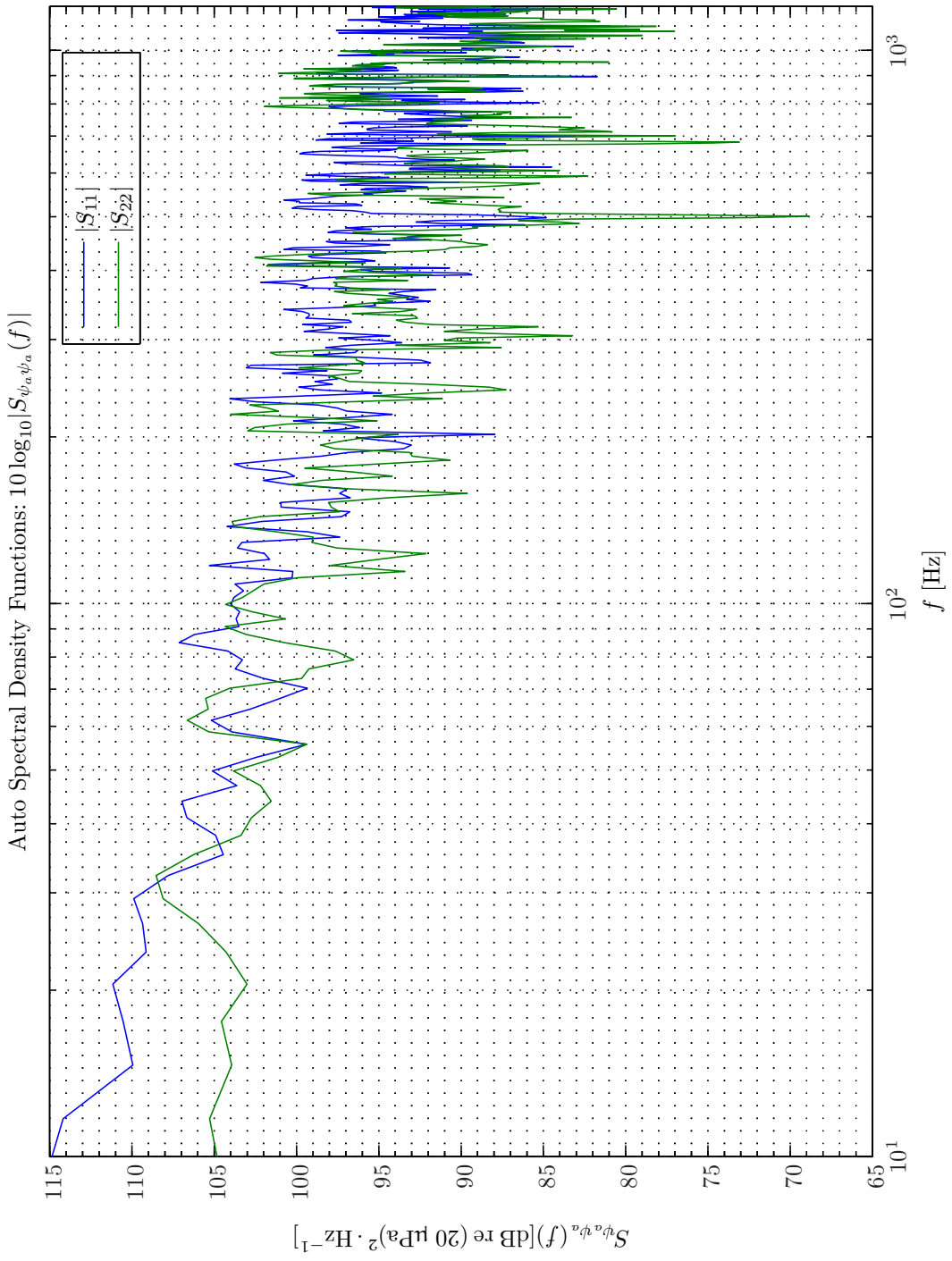

Sim 3.3.14: *Autospectral Density Functions:* **Statistical Data Analysis:** Single-Sided Modified Periodogram, $f_s = 6$ kHz, $N_{DFT} = 2048$, $L_{DFT} = 1501$, $R_{DFT} = 751$, Hanning, $\Delta f_m = 16$ Hz, $T_{DFT} = 0.25017$ s, $N_{f,DFT} = 1025$, $\Delta f_{DFT} = 2.9297$ Hz, $K_{DFT} = 2$; **Adaptive Filter** $\underset{\sim}{w}$: Wiener Hopf ($M = 180$, $\alpha = 1e{-}005$, $T_{WSS} = 0$,**t**-domain); **Main:** $f_s^0 = 192$ kHz, $f_s^1 = 6$ kHz, $R_\updownarrow^1 = \frac{1}{32} = 0.03125$, Elliptic LPF ($f_s = 192$ kHz, $f_{pass} = 2.75$ kHz, $f_{stop} = 3$ kHz, $A_{pass} = 2$ dB, $A_{stop} = 40$ dB), $f_s^2 = 6$ kHz, $R_\updownarrow^2 = \frac{1}{1} = 1$, Dummy; **Topology:** (Feedforward, mFx, $N_x = 2, N_e = 1, N_y = 1, N_p = 0, N_v = 2$); **Plants:** ($g_{xy}^{1,1}$: (FIR : $M_{gxy}^{1,1} = 1$), $g_{xy}^{1,2}$: (FIR : $M_{gxy}^{1,2} = 1$), $g_{ey}^{1,1}$: Delayed Sampled System: ($f_s = 6$ kHz, $t_d = 500$ µs, $\tau = 1000$ µs, $\kappa = 0.9$) (FIR : $M_{gey}^{1,1} = 10$)); **Signals:** Time: $0 - 2$ s. Refer to SigIDLaT. ; **Scenario:** `MultipleSinusoidalsAddiativeNoiseFeedforwardNx2Ne1Ny1Np0/20080210T185714`; *Channels:* #1 $\leftarrow d_1(t_1^1)$, #2 $\leftarrow e_1(t_1^1)$; .

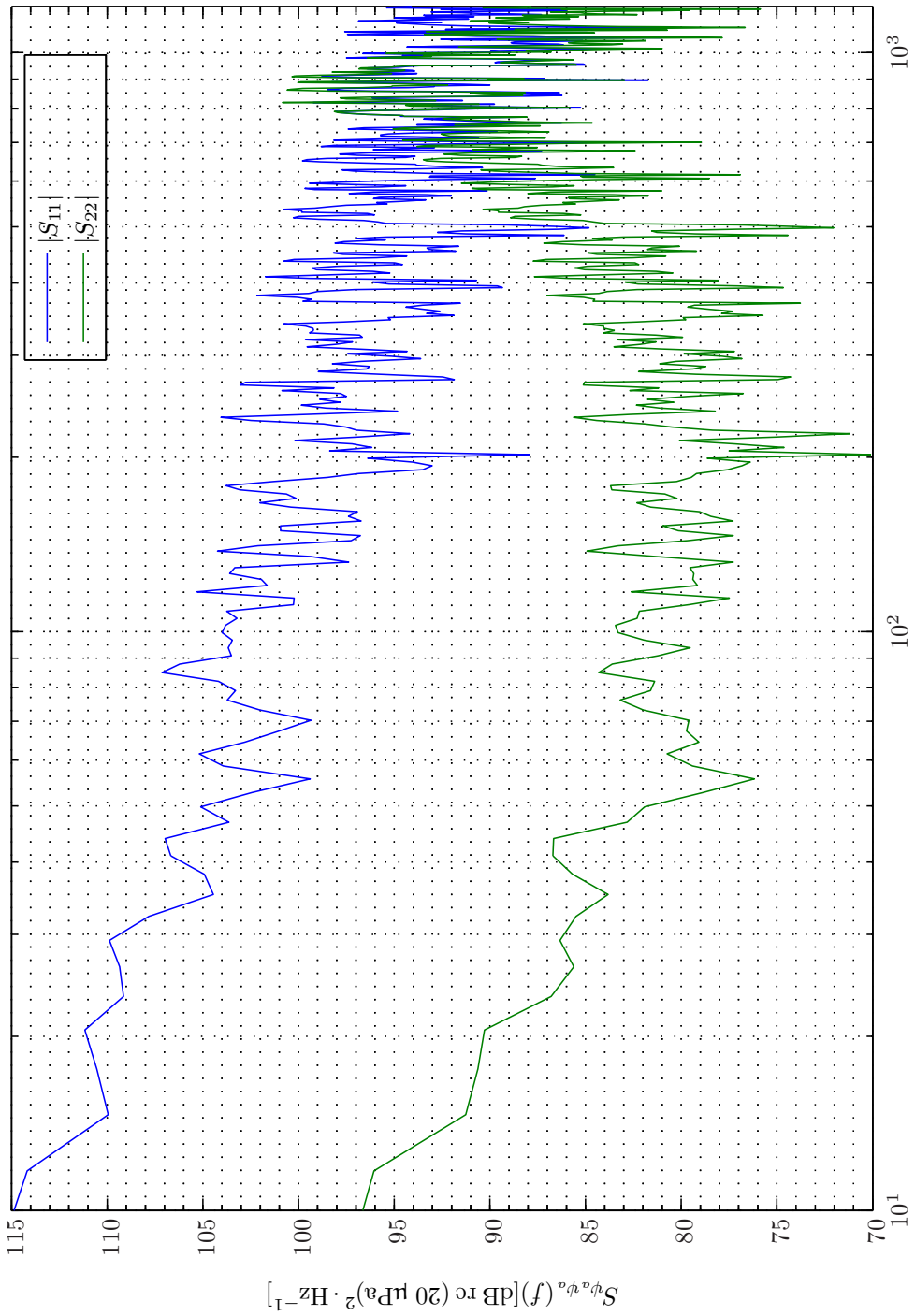

Sim 3.3.15: *Autospectral Density Functions:* **Statistical Data Analysis:** Single-Sided Modified Periodogram, f_s = 6 kHz, N_{DFT} = 2048, L_{DFT} = 1501, R_{DFT} = 751, Hanning, Δf_m = 16 Hz, T_{DFT} = 0.25017 s, $N_{f,DFT}$ = 1025, Δf_{DFT} = 2.9297 Hz, K_{DFT} = 2; **Adaptive Filter** $\underset{\sim}{w}$: Wiener Hopf (M = 180, α = 1e−005, T_{WSS} = 0,**z**-domain); **Main:** f_s^0 = 192 kHz, f_s^1 = 6 kHz, $R_\updownarrow^1 = \frac{1}{32}$ = 0.03125, Elliptic LPF (f_s = 192 kHz, f_{pass} = 2.75 kHz, f_{stop} = 3 kHz, A_{pass} = 2 dB, A_{stop} = 40 dB), f_s^2 = 6 kHz, $R_\updownarrow^2 = \frac{1}{1}$ = 1, Dummy; **Topology:** (Feedforward, mFx, N_x = 2, N_e = 1, N_y = 1, N_p = 0, N_v = 2); **Plants:** ($g_{xy}^{1,1}$: (FIR : $M_{gxy}^{1,1}$ = 1), $g_{xy}^{1,2}$: (FIR : $M_{gxy}^{1,2}$ = 1), $g_{ey}^{1,1}$: Delayed Sampled System: (f_s = 6 kHz, t_d = 500 µs, τ = 1000 µs, κ = 0.9) (FIR : $M_{gey}^{1,1}$ = 10)); **Signals:** Time: 0 − 2 s. Refer to SigIDLaT. ; **Scenario:** `MultipleSinusoidalsAddiativeNoiseFeedforwardNx2Ne1Ny1Np0/20080210T185714`; *Channels:* #1 ←$d_1(t_1^1)$, #2 ←$e_1(t_1^1)$.;.

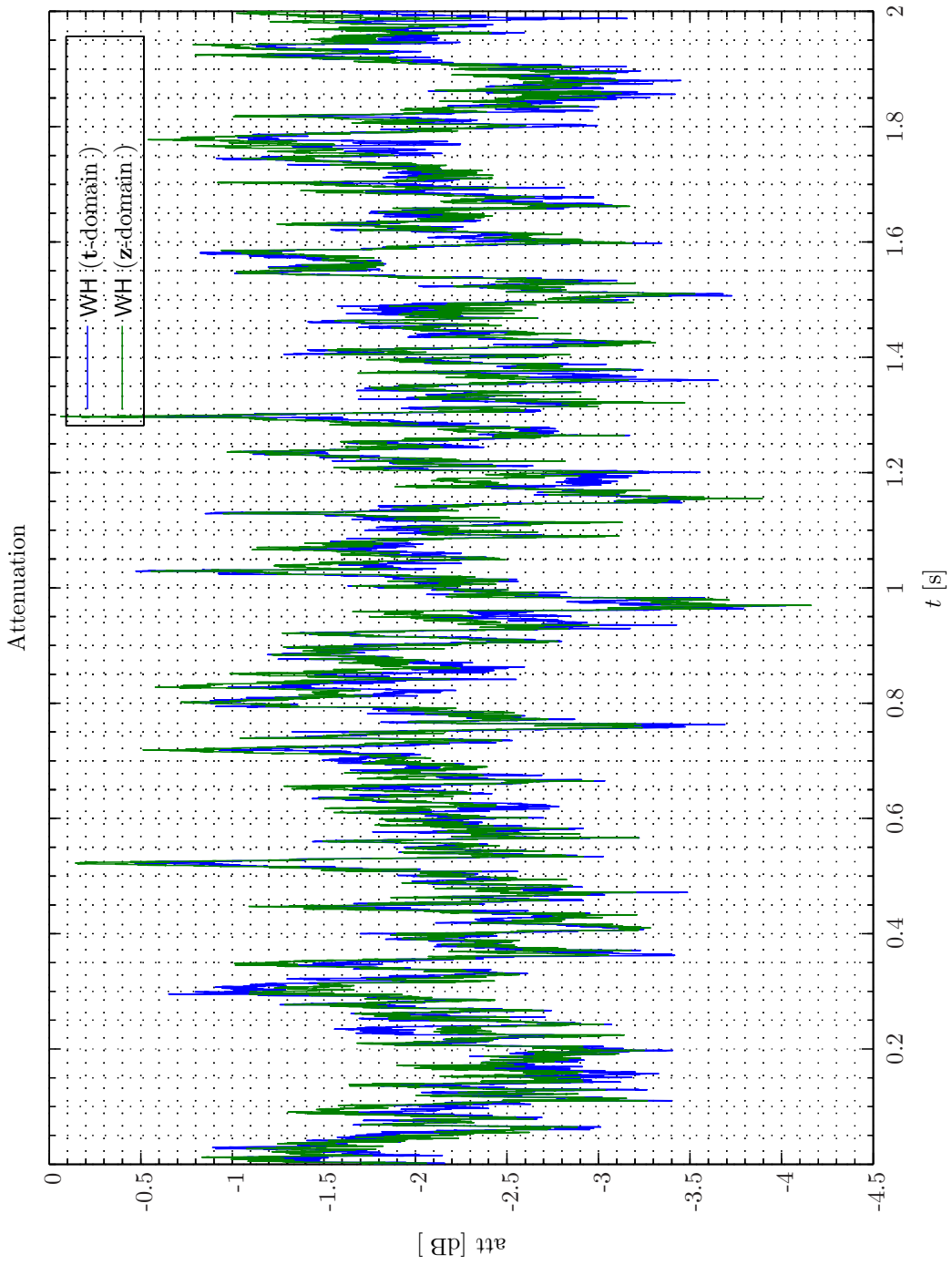

Sim 3.3.16: *Time-Domain: Attenuation.* **Adaptive Filter** $\underset{\sim}{w}$: $\underset{\sim}{w}^{1,1}$: WH ($M = 180, \alpha = 1e{-}005, T_{WSS} = 0$); **Main:** $f_s^0 = 192$ kHz, $f_s^1 = 6$ kHz, $R_\downarrow^1 = \frac{1}{32} = 0.03125$, Elliptic LPF ($f_s = 192$ kHz, $f_{pass} = 2.75$ kHz, $f_{stop} = 3$ kHz, $A_{pass} = 2$ dB, $A_{stop} = 40$ dB), $f_s^2 = 6$ kHz, $R_\downarrow^2 = \frac{1}{1} = 1$, Dummy; **Topology:** (Feedforward, mFx, $N_x = 2, N_e = 1, N_y = 1, N_p = 0, N_v = 2$); **Plants:** ($g_{xy}^{1,1}$: (FIR : $M_{gxy}^{1,1} = 1$), $g_{xy}^{1,2}$: (FIR : $M_{gxy}^{1,2} = 1$), $g_{ey}^{1,1}$: Delayed Sampled System: ($f_s = 6$ kHz, $t_d = 500$ µs, $\tau = 1000$ µs) (FIR : $M_{gey}^{1,1} = 10$)); **Signals:** Time: $0 - 2$ s. Refer to SigIDLaT. ; **Scenario:** `MultipleSinusoidalsAddiativeNoiseFeedforwardNx2Ne1Ny1Np0/20080210T192948`.

The confined feedforward (CFF) ANR topology involve the surface spanned by the virtual sensors $\mathcal{S}^v$, that circumscribes both the surface spanned by the reference sensors $\mathcal{S}^x$ and the surface spanned by the error sensors that we denote by $\mathcal{S}^d$. This is equivalently to the conditions $\mathcal{V}^x \subset \mathcal{V}^v$ and $\mathcal{V}^d \subset \mathcal{V}^v$, where $\mathcal{V}^v, \mathcal{V}^x, \mathcal{V}^d$ are the interior volumes of $\mathcal{S}^v, \mathcal{S}^x, \mathcal{S}^d$ respectively.

We first want to validate our simulation data by considering coinciding virtual sensor and reference sensor spherical surfaces equipped with a total of $N_v = 14$ virtual sensors and $N_x = 10$ reference sensors respectively. The radius of the spherical surface virtual sensor and reference sensor surface $\mathcal{S}_v, \mathcal{S}_x$ that we designate by R_v, R_x and that equal an average radius of the non-spherical Gentex HGU-55/P helmet of $R_v = R_x = 150$ mm. Both the set of virtual sensors and the set of reference sensors are assumed equidistantly positioned on the sphere. These positions have be obtained from using the spherical design tool provided by Hardin and Sloane [7]. The simulation results of using the vibro-acoustical model closed-back headset system described above will be presented next.

The auto spectral density functions are shown in Simulation 3.4.1. These results comply fairly well with similar data obtained in a noise chamber under diffuse sound field conditions in Simulation 2.4.3 on page 39 and the F-16 measurements in Simulation D.3.5 on page 564 and the CH-47 measurements in Simulation D.4.5 on page 581 respectively. In the present analysis of causality constraints, however, we have deliberately chosen to use reference signals with a less dominant low frequency contents than actually present in, e.g., the CH-47 measurements. Therefore, a *blue noise* $0 - 400$ Hz, *pink noise* $400 - 1000$ Hz and *brown noise* $1000 - 12000$ Hz signal is used for the reference signals. In Simulation 3.4.2 - 3.4.3 the multiple coherence functions are depicted. Again a fairly close match exist to the results in Simulation 2.4.16 - 2.4.17 on pages 54–55 for the diffuse sound field in the noise chamber and Simulation D.4.10 - D.4.13 on pages 587–590 for the helicopter noise. The joint-channel residual spectral analysis (JCRSA) based cross-correlation functions are shown in Simulation 3.4.4 on page 161 and the details in Simulation 3.4.5 on page 162. By inspection of similar results in Simulation 2.4.33 on page 73 the validity of the results are confirmed.

In conclusion, we have demonstrated that the simulator on three critical points for our analysis has been able to reproduce experimentally obtained data. Firstly, the colorization of the reference signals and the disturbance signals were obtained from a combination of the colorization filter $L_{wv}(\mathrm{e}^{\imath\omega})$ and a model for the closed-back headset system described in chapter 10 on page 471. Secondly, it was estimated that in order to produce the experimentally determined multiple coherence function as a function of frequency a total of 14 uncorrelated uniformly spatially distributed primary noise sources should used for the choice of 10 reference sensors. Thirdly, by using the JCRSA based method developed in chapter 2 on page 17 the auto- and cross-correlation functions should result in acquisition lead-time of the order of 0.8 ms.

In order to provide a smooth transition to the confined feedforward system (CFFS) ANR system we will first consider the simple two-reference sensor case that has also been considered by, e.g., Rafaely and Jones [12].

3.4.2 Causality Constraints in a Closed-Back Headset System, 2 Reference Sensors

Example 3.4.1 (Confined Feedforward ANR System, Pink Noise, Helmet)**.** We will use the same reference signals as in subsection 3.4.1, that is, *blue noise* $0 - 400$ Hz, *pink noise* $400 - 1000$ Hz and *brown noise* $1000 - 12000$ Hz. As primary paths we will use the model presented in chapter 10 and for the secondary path we will use the results from a system identification applied to the

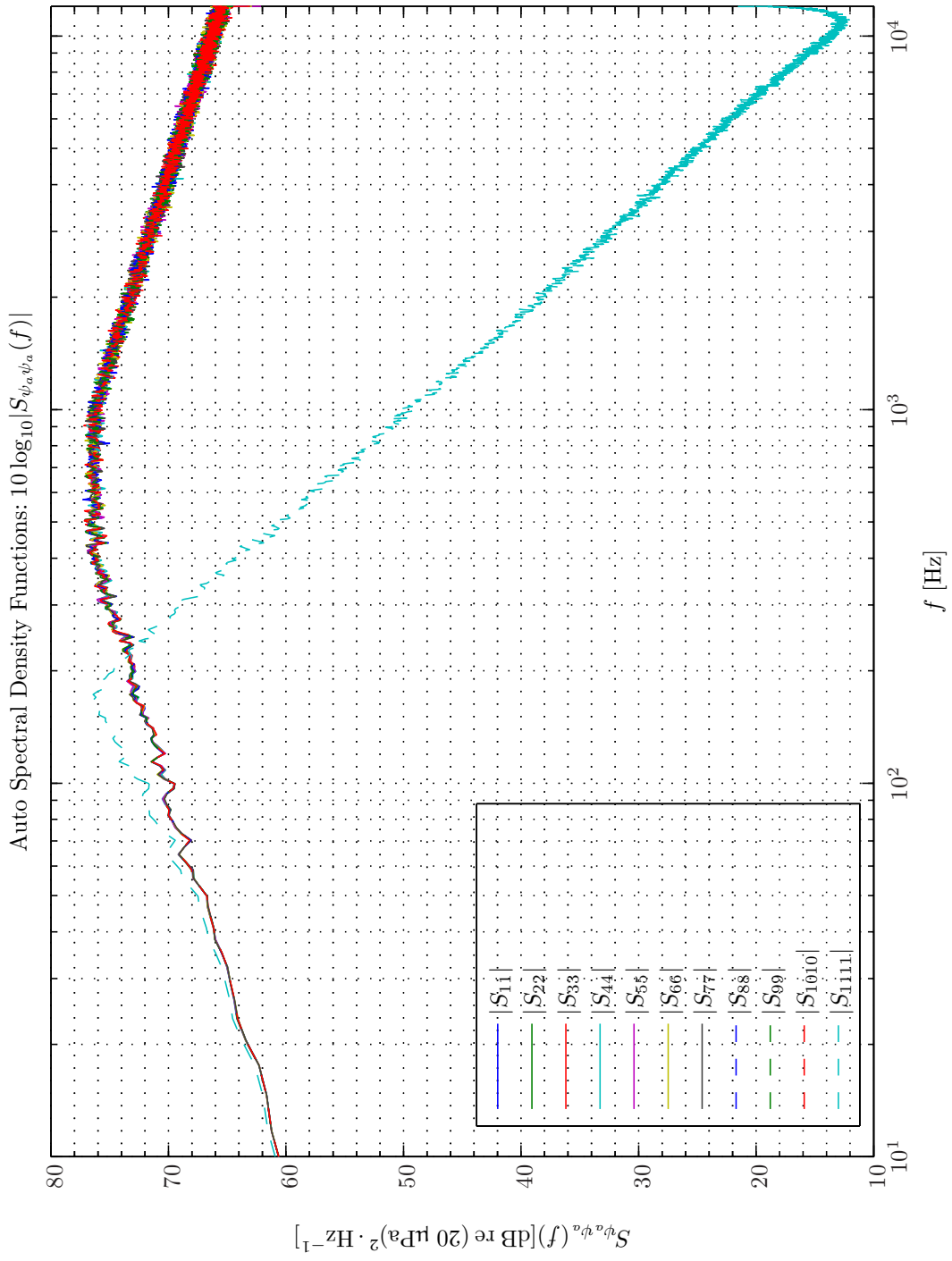

Sim 3.4.1: *Autospectral Density Functions:* **Statistical Data Analysis:** Single-Sided Modified Periodogram, f_s = 24 kHz, N_{DFT} = 8192, L_{DFT} = 6001, R_{DFT} = 3001, Hanning, Δf_m = 16 Hz, T_{DFT} = 0.25004 s, $N_{f,DFT}$ = 4097, Δf_{DFT} = 2.9297 Hz, K_{DFT} = 238; **Signals:** Time: 0 – 30 s. Refer to SigIDLaT.; *Channels:* #1 ← x_1, #2 ← x_2, #3 ← x_3, #4 ← x_4, #5 ← x_5, #6 ← x_6, #7 ← x_7, #8 ← x_8, #9 ← x_9, #10 ← x_{10}, #11 ← d_1. **Scenario:** `MultipleSinusoidalsAddiativeNoiseFeedforwardNx10Ne1Ny1Np0/20080114T141949.;` .

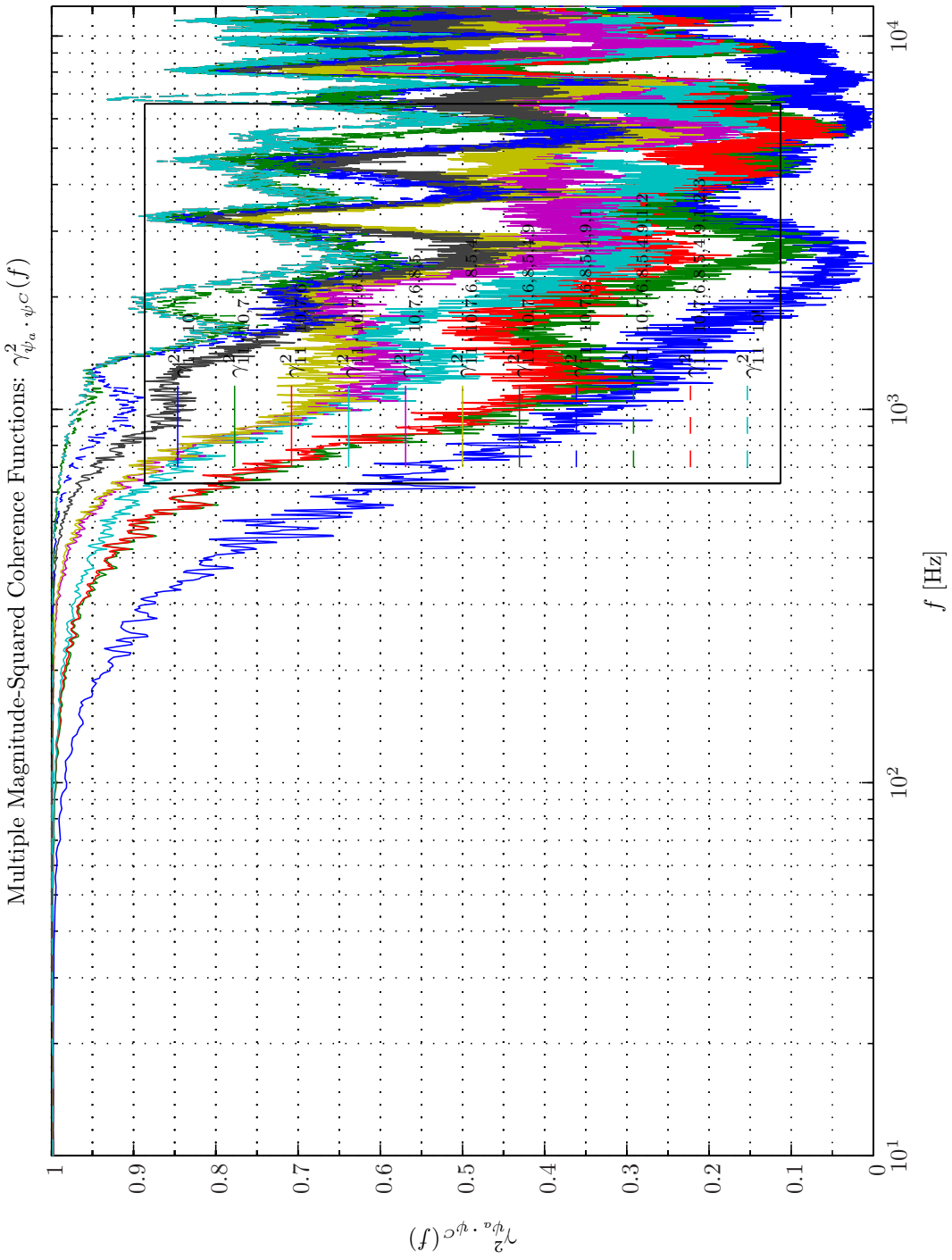

Sim 3.4.2: *Multiple Magnitude-Squared Coherence Functions* $\gamma^2_{\psi_a \cdot \psi^C}(f)$: **Statistical Data Analysis**: Single-Sided Modified Periodogram, $f_s = 24$ kHz, $N_{DFT} = 8192$, $L_{DFT} = 6001$, $R_{DFT} = 3001$, Hanning, $\Delta f_m = 16$ Hz, $T_{DFT} = 0.25004$ s, $N_{f\,DFT} = 4097$, $\Delta f_{DFT} = 2.9297$ Hz, $K_{DFT} = 238$; **Signals:** Time: $0 - 30$ s. Refer to SigIDLaT. ; *Channels:* $\#1 \leftarrow x_1, \#2 \leftarrow x_2, \#3 \leftarrow x_3, \#4 \leftarrow x_4, \#5 \leftarrow x_5, \#6 \leftarrow x_6, \#7 \leftarrow x_7, \#8 \leftarrow x_8, \#9 \leftarrow x_9, \#10 \leftarrow x_{10}, \#11 \leftarrow d_1$. **Scenario:** `MultipleSinusoidalsAddiativeNoiseFeedforwardNx10Ne1Ny1Np0/20080114T141949.`; .

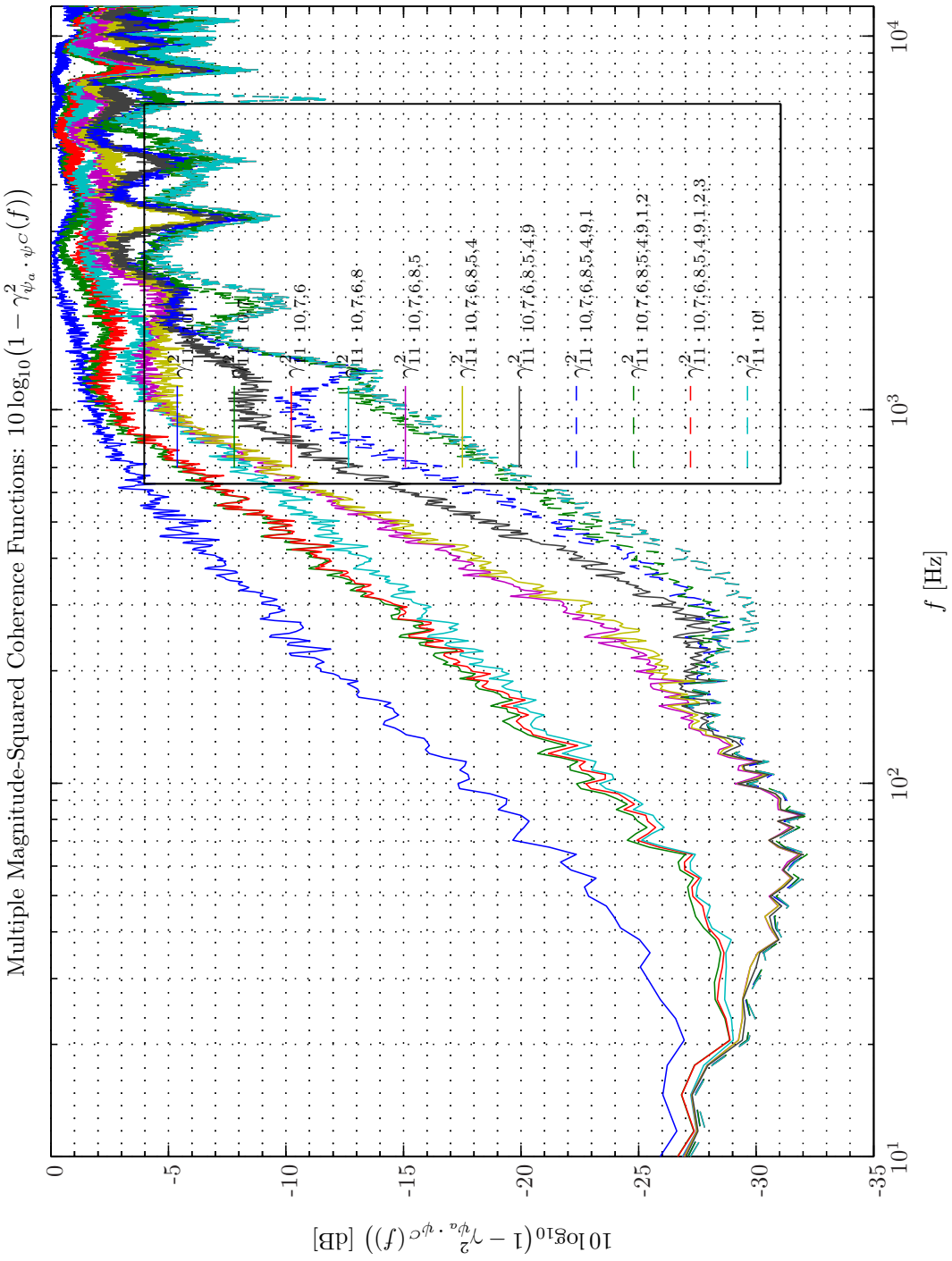

Sim 3.4.3: *Attenuation vs Multiple Magnitude-Squared Coherence Functions* $10\log_{10}(1-\gamma^2_{\psi_a\cdot\psi^C}(f))$: **Statistical Data Analysis:** Single-Sided Modified Periodogram, $f_s = 24$ kHz, $N_{DFT} = 8192$, $L_{DFT} = 6001$, $R_{DFT} = 3001$, Hanning, $\Delta f_m = 16$ Hz, $T_{DFT} = 0.25004$ s, $N_{f,DFT} = 4097$, $\Delta f_{DFT} = 2.9297$ Hz, $K_{DFT} = 238$; **Signals:** Time: $0 - 30$ s. Refer to SigIDLaT. ; *Channels:* $\#1 \leftarrow x_1$, $\#2 \leftarrow x_2$, $\#3 \leftarrow x_3$, $\#4 \leftarrow x_4$, $\#5 \leftarrow x_5$, $\#6 \leftarrow x_6$, $\#7 \leftarrow x_7$, $\#8 \leftarrow x_8$, $\#9 \leftarrow x_9$, $\#10 \leftarrow x_{10}$, $\#11 \leftarrow d_1$. **Scenario:** `MultipleSinusoidalsAddiativeNoiseFeedforwardNx10Ne1Ny1Np0/20080114T141949:` .

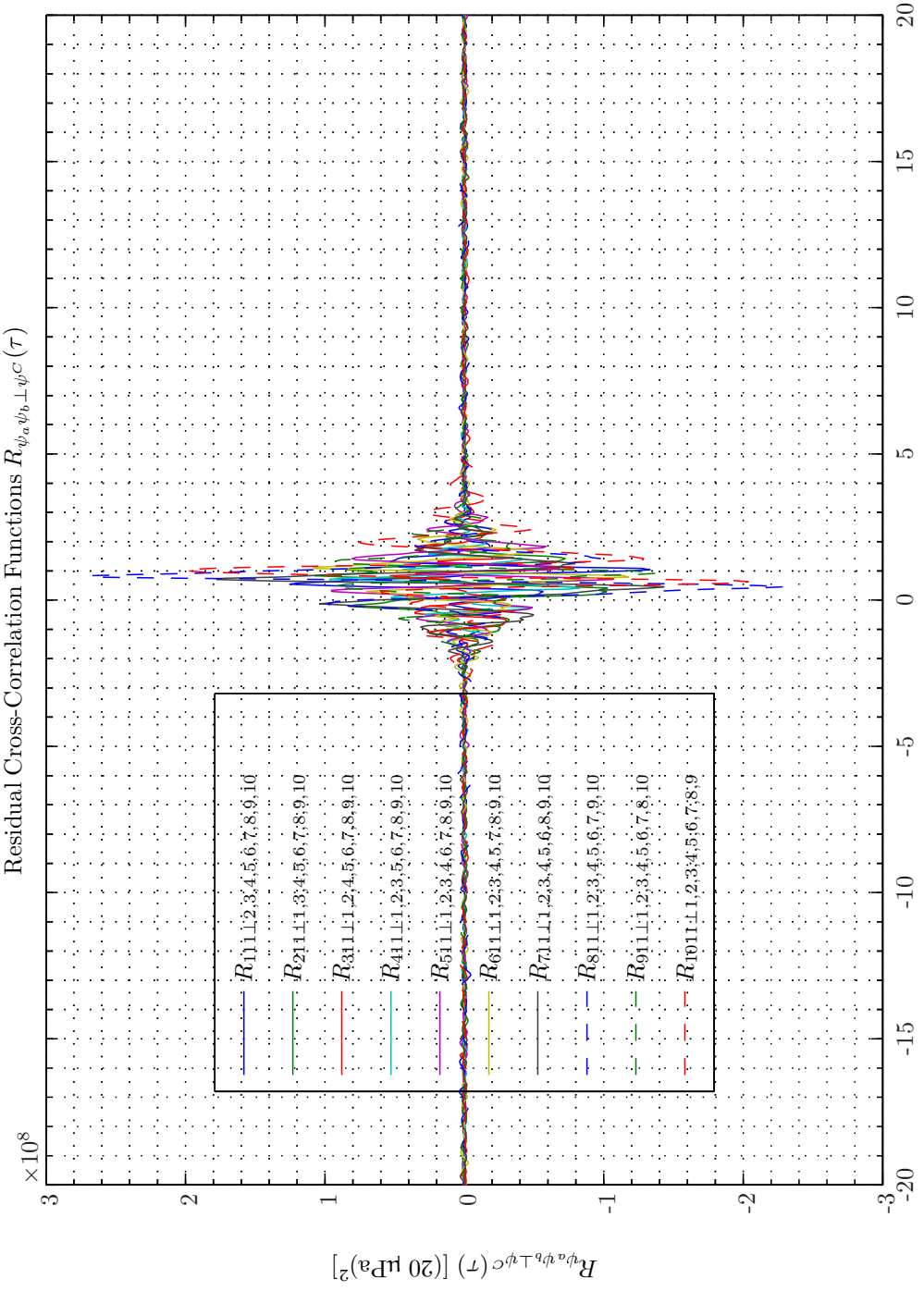

Sim 3.4.4: *Residual Cross-Correlation Functions* JCRSA: $R_{\psi_a\psi_b\perp\psi^C}(\tau)$: **Statistical Data Analysis**: Single-Sided Modified Periodogram, $f_s = 24$ kHz, $N_{DFT} = 8192$, $L_{DFT} = 6001$, $R_{DFT} = 3001$, Hanning, $\Delta f_m = 16$ Hz, $T_{DFT} = 0.25004$ s, $N_{f,DFT} = 4097$, $\Delta f_{DFT} = 2.9297$ Hz, $K_{DFT} = 238$; **Signals:** Time: $0 - 30$ s. Refer to SigIDLaT.; *Channels:* #1 $\leftarrow x_1$, #2 $\leftarrow x_2$, #3 $\leftarrow x_3$, #4 $\leftarrow x_4$, #5 $\leftarrow x_5$, #6 $\leftarrow x_6$, #7 $\leftarrow x_7$, #8 $\leftarrow x_8$, #9 $\leftarrow x_9$, #10 $\leftarrow x_{10}$, #11 $\leftarrow d_1$. **Scenario:** `MultipleSinusoidalsAddiativeNoiseFeedforwardNx10Ne1Ny1Np0/20080114T141949;` .

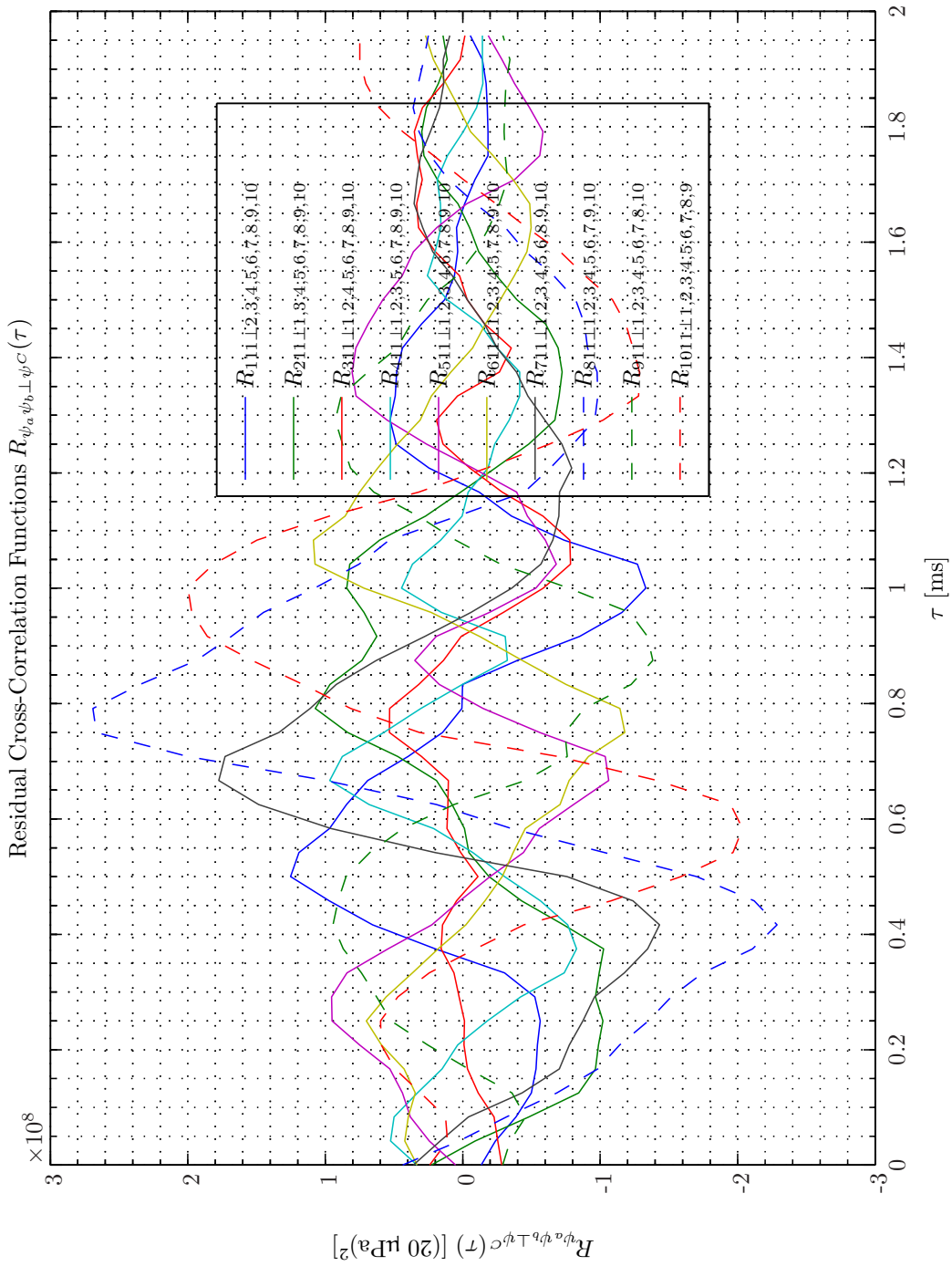

Sim 3.4.5: *Residual Cross-Correlation Functions* JCRSA: $R_{\psi_a \psi_b \perp \psi^C}(\tau)$: **Statistical Data Analysis**: Single-Sided Modified Periodogram, $f_s = 24$ kHz, $N_{DFT} = 8192$, $L_{DFT} = 6001$, $R_{DFT} = 3001$, Hanning, $\Delta f_m = 16$ Hz, $T_{DFT} = 0.25004$ s, $N_{f\,DFT} = 4097$, $\Delta f_{DFT} = 2.9297$ Hz, $K_{DFT} = 238$; **Signals:** Time: $0 - 30$ s. Refer to SigIDLaT. ; *Channels:* #1 $\leftarrow x_1$, #2 $\leftarrow x_2$, #3 $\leftarrow x_3$, #4 $\leftarrow x_4$, #5 $\leftarrow x_5$, #6 $\leftarrow x_6$, #7 $\leftarrow x_7$, #8 $\leftarrow x_8$, #9 $\leftarrow x_9$, #10 $\leftarrow x_{10}$, #11 $\leftarrow d_1$. **Scenario:** `MultipleSinusoidalsAddiativeNoiseFeedforwardNx10Ne1Ny1Np0/20080114T141949.` ; .

current version of the Terma Earcup System that is detailed in section 7.7 on page 333.

The analysis comprises both the **t**-domain WH method and the **z**-domain WH method with $M_{\underset{\sim}{w}^{1,1}} = M_{\underset{\sim}{w}^{2,1}} = M_w = 2048$ and $\alpha = 1e-5$. As independent reference adaptive filter the multiple-channel-$\alpha\gamma\Pi\epsilon$-NLMS (MC-$\alpha\gamma\Pi\epsilon$-NLMS) algorithm with M_w equal to 1024 and $\mu = 0.15$ is tested in parallel. The time span of the simulations is $0-10$ s.

Although the two reference sensors coincide with the two virtual sensors and therefore should not lead to any spatial aliasing effects, owing to the passive attenuation rate of 40 dB $\cdot$ decade^{-1} and the finite precission in our calculations the multiple coherence function $\gamma^2_{d_1x!}$ starts to deviate from unity above 2000 Hz as depicted in Simulation 3.4.6 on the next page. Hence, an upper limit (≈ 5000 Hz) to the validity of the simulated ANR therefore exist as shown in Simulation 3.4.7 on page 165.

The time-domain attenuation results can be found in Simulation 3.4.8 on page 166. Apparently, the **t**-domain WH method provides better ANR performance ($\mathcal{A}^e(t) = 11 \pm 6$ dB) than the **z**-domain WH method ($\mathcal{A}^e(t) = 6 \pm 4$ dB). However, from inspection of the weight vectors $\underset{\sim}{w}^{1,1}$ and $\underset{\sim}{w}^{2,1}$ for the two WH filters shown in Simulation 3.4.9 - 3.4.12 we appreciate that all of these four weight vectors exhibit similar highly fluctuating pattern[9] and that the optimal weight vector predicted by the **t**-domain WH method but not by the **z**-domain WH method is tapered such that, e.g., $\underset{\sim}{w}_{M_w-1} \approx 0$. Further analysis revealed that by doubling the number of weights, that is, $M_{\underset{\sim}{w}^{1,1}} = M_{\underset{\sim}{w}^{2,1}} = M_w = 4096$ would lead to $\underset{\sim}{w}^{2,1}_{M_w-1} \approx 0$ but still not to $\underset{\sim}{w}^{1,1}_{M_w-1} \approx 0$. Refering to Example 3.2.1 on page 111 this also explains why better ANR performance is obtained by the **t**-domain WH method than by the **z**-domain WH method.

We also observe that it takes the $\alpha\gamma\Pi\epsilon$-NLMS ($\alpha\gamma\Pi\epsilon$-NLMS) algorithm more than the entire time span from $0-10$ s to converge.

The auto spectral density functions and frequency-domain attenuation of the **t**-domain based WH filter is depicted in Simulation 3.4.13 on page 171 and Simulation 3.4.14 on page 172 respectively. The plus 10 dB attenuation range extent from 50 Hz up to 5000 Hz as also predicted by the multiple coherence function in Simulation 3.4.7 on page 165.

Example 3.4.2 (Feedback ANR System, Pink Noise Helmet)**.** In this example we will examine the ANR performance provided by a FBS solution when using the same real plant and when exposed to the same representative disturbance signal as in the preceding example. Moreover, in order exclusively to focus on causality constraints we do not enforce the FBS to be robustly stable in the examples presented in this chapter. Hence, in practice $\mathcal{H}_\infty$ adaptive control should be applied, e.g., by incorporating stability margins as explained in section 8.A on page 404. Accordingly, the achievable ANR attenuation provided by a practical feedback systems will be lower than predicted here in particular at higher frequencies.

The following candidate adaptive filters are considered:

1. WH (**t**-domain,**z**-domain , $\alpha = 1e-5, T_{WSS} = 0, M = 1024$);

2. $\alpha\gamma\Pi\epsilon$-NLMS ($M = 512, L_B = 1, \mu = 0.15, \alpha = 1e-5, \gamma = 1e-5, \Pi = 0, \epsilon = 1e-006, \breve{w} = 0, W_e = \mathrm{I}, T_{Eu} = 20$);

[9] Such oscillatory pattern could be caused by the presence of a factor $(1 - z^{-1})$.

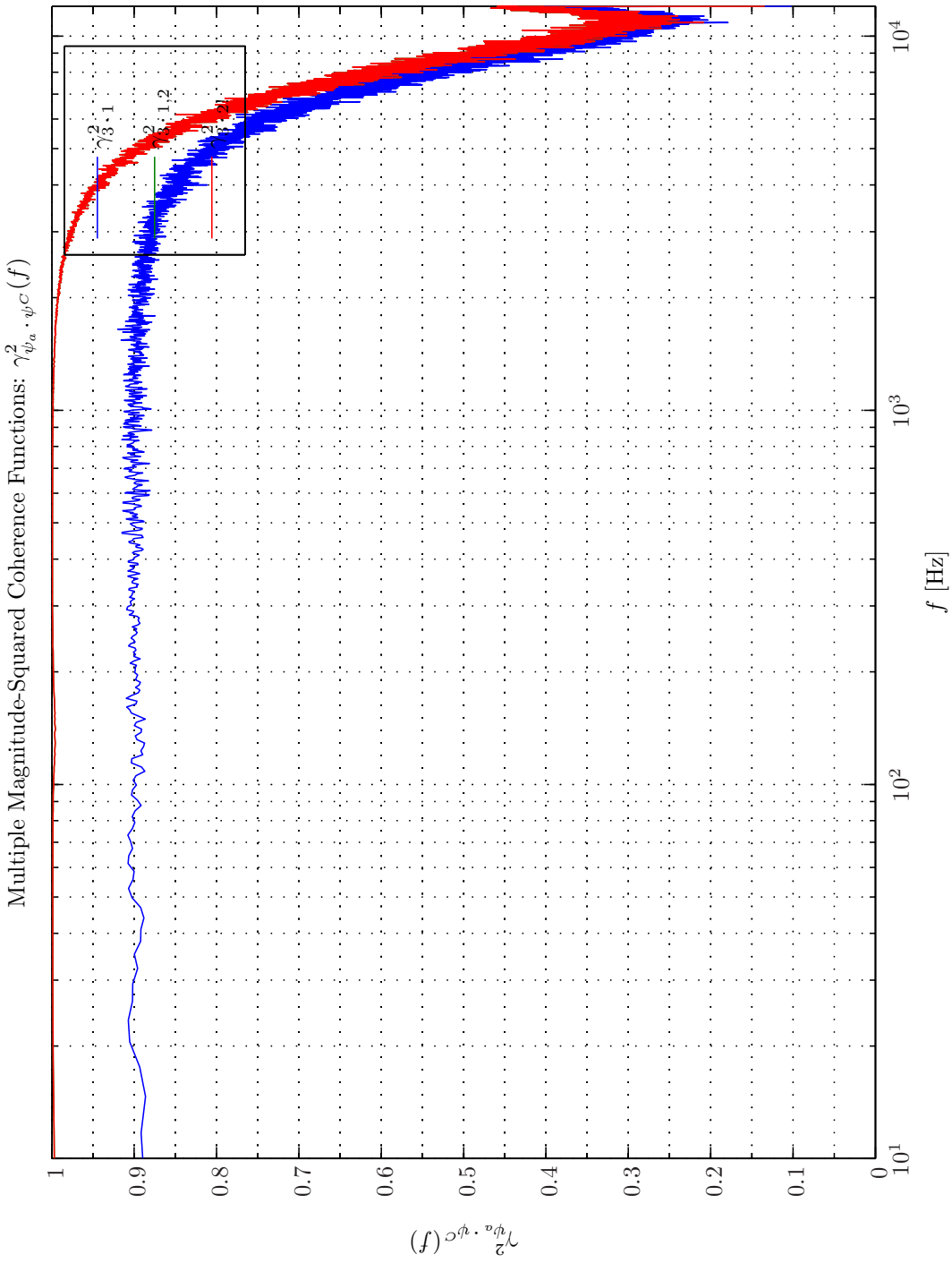

Sim 3.4.6: *Multiple Magnitude-Squared Coherence Functions* $\gamma^2_{\psi_a \cdot \psi^C}(f)$: **Statistical Data Analysis**: Single-Sided Modified Periodogram, $f_s = 24$ kHz, $N_{DFT} = 8192$, $L_{DFT} = 6001$, $R_{DFT} = 3001$, Hanning, $\Delta f_m = 16$ Hz, $T_{DFT} = 0.25004$ s, $N_{f,DFT} = 4097$, $\Delta f_{DFT} = 2.9297$ Hz, $K_{DFT} = 478$; **Signals:** Time: $0 - 60$ s. Refer to SigIDLaT. ; *Channels:* $\#1 \leftarrow x_1$, $\#2 \leftarrow x_2$, $\#3 \leftarrow d_1$. **Scenario:** `MultipleSinusoidalsAddiativeNoiseFeedforwardNx2NelNy1NpO/20080310T184652;` .

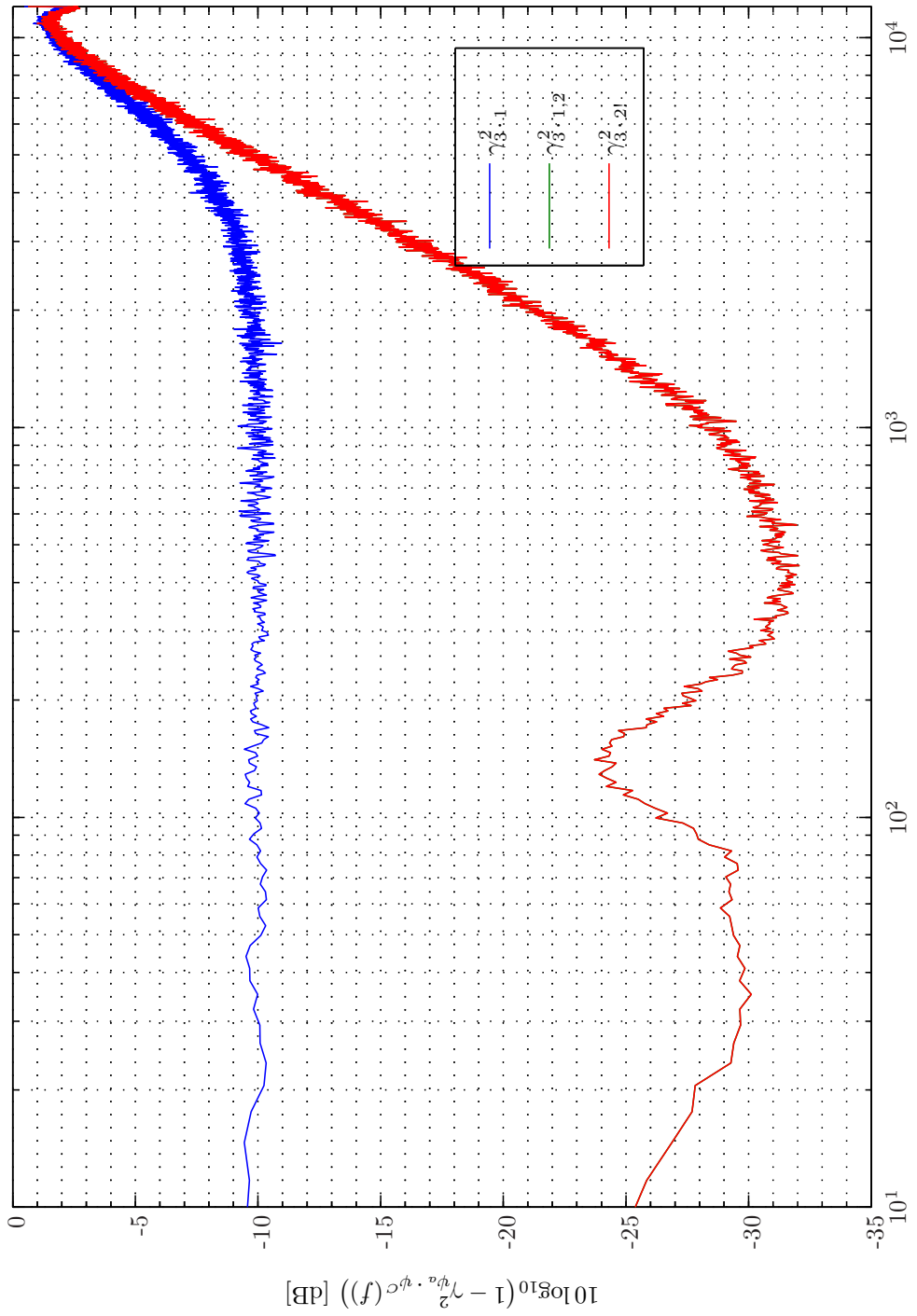

Sim 3.4.7: *Attenuation vs Multiple Magnitude-Squared Coherence Functions* $10\log_{10}(1-\gamma^2_{\psi_a\cdot\psi^C}(f))$: **Statistical Data Analysis:** Single-Sided Modified Periodogram, f_s = 24 kHz, N_{DFT} = 8192, L_{DFT} = 6001, R_{DFT} = 3001, Hanning, Δf_m = 16 Hz, T_{DFT} = 0.25004 s, $N_{f,DFT}$ = 4097, Δf_{DFT} = 2.9297 Hz, K_{DFT} = 478; **Signals:** Time: 0 − 60 s. Refer to SigIDLaT.; *Channels:* #1 ← x_1, #2 ← x_2, #3 ← d_1. **Scenario:** `MultipleSinusoidalsAddiativeNoiseFeedforwardNx2Ne1Ny1Np0/20080310T184652;`.

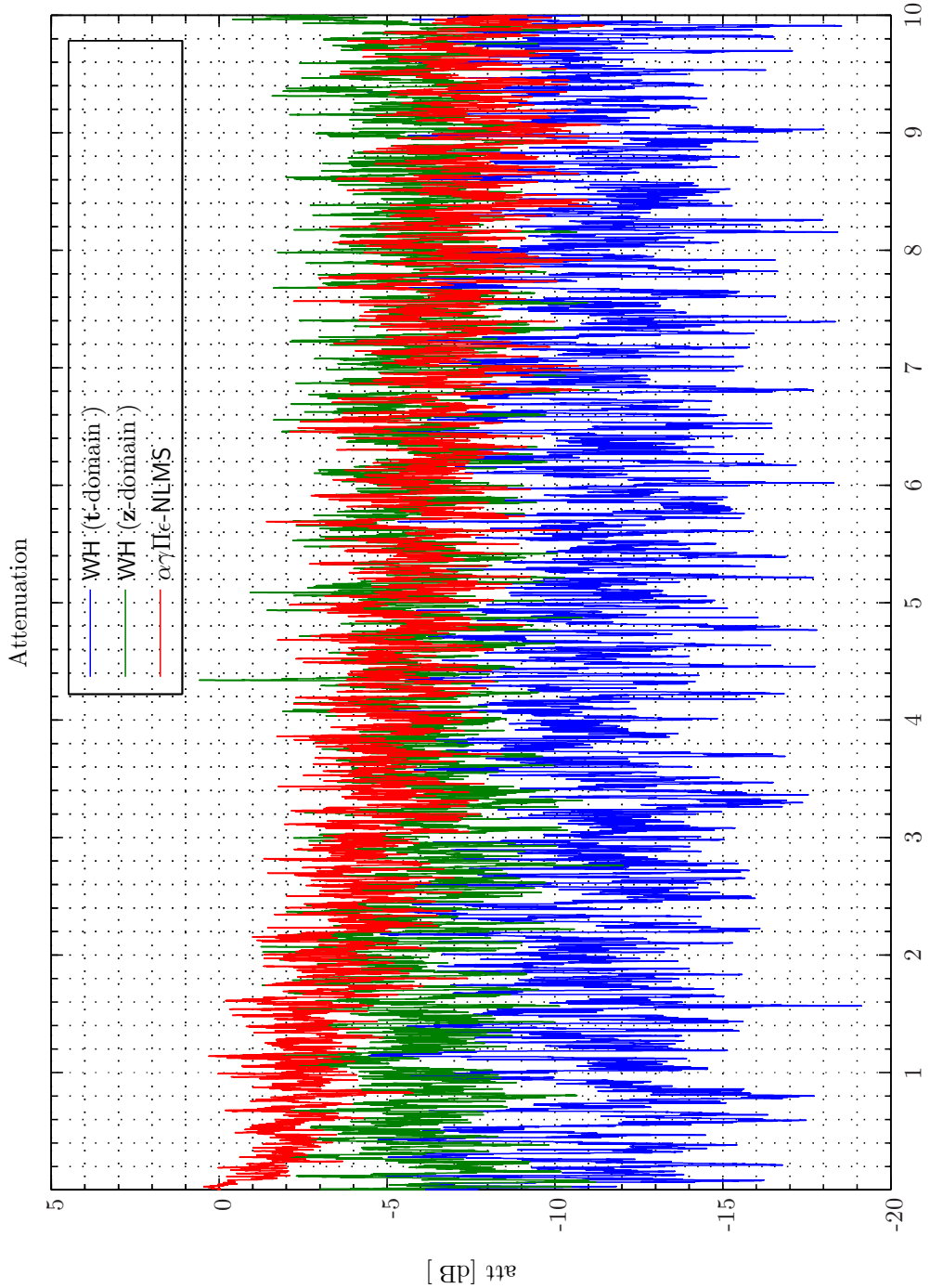

Sim 3.4.8: *Time-Domain: Attenuation.* **Adaptive Filter** $\underset{\sim}{w}$: $\underset{\sim}{w}^{1,1}$: WH ($M = 2048, \alpha = 1e-005, T_{WSS} = 0$);$\alpha\gamma\Pi\varepsilon$-NLMS ($M = 1024, L_B = 1, \mu = 0.15, \alpha = 1e-005, \epsilon = 1e-006, T_{Eu} = 400$); **Main:** $f_s^0 = 192$ kHz, $f_s^1 = 24$ kHz, $R_\downarrow^1 = \frac{1}{8} = 0.125$, Elliptic LPF ($f_s = 192$ kHz, $f_{pass} = 11$ kHz, $f_{stop} = 12$ kHz, $A_{pass} = 2$ dB, $A_{stop} = 40$ dB), $f_s^2 = 24$ kHz, $R_\downarrow^2 = \frac{1}{1} = 1$, Dummy; **Topology:** (Feedforward, mFx, $N_x = 2, N_e = 1, N_y = 1, N_p = 0, N_v = 2$); **Plants:** SysID/20080113T014624 ($g_{xy,\infty}^{1,1}$: (FIR : $M_{gxy}^{1,1} = 481$), $g_{xy,\infty}^{1,2}$: (FIR : $M_{gxy}^{1,2} = 481$), $g_{ey,\infty}^{1,1}$: (FIR : $M_{gey}^{1,1} = 71$), $g_{py,\infty}^{1,1}$: (FIR : $M_{gpy}^{1,1} = 410$), $g_{py,\infty}^{1,2}$: (FIR : $M_{gpy}^{1,2} = 410$)); **Signals:** Time: $0 - 10$ s. Refer to SigIDLaT. ; **Scenario:** `MultipleSinusoidalsAddiativeNoiseFeedforwardNx2Ne1Ny1Np0/20080309T220501`.

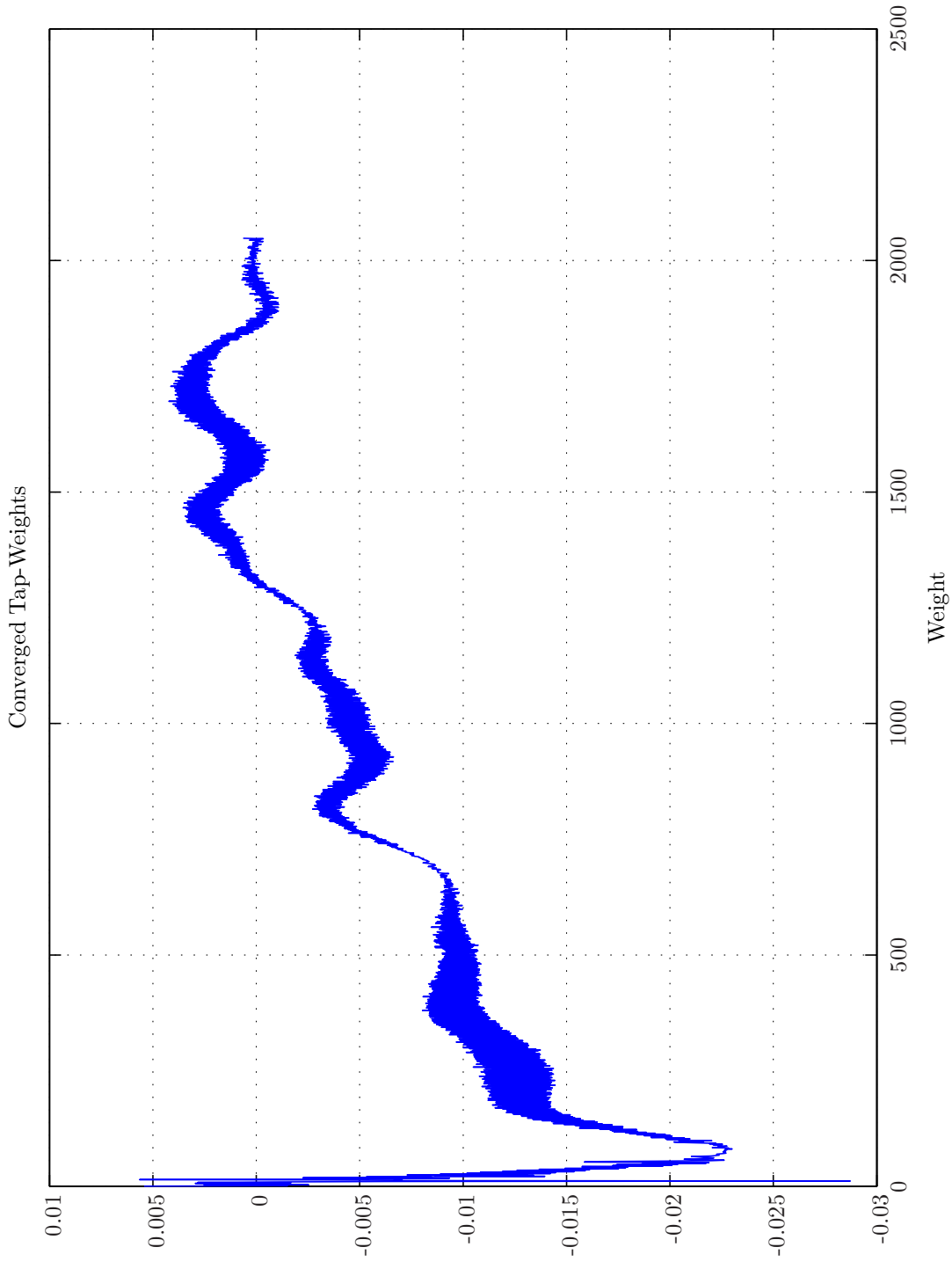

Sim 3.4.9: *Converged Tap-weights.* **Adaptive Filter** $\underset{\sim}{w}$: $\underset{\sim}{w}^{1,1}$: Wiener Hopf ($M = 2048, \alpha = 1e-005, T_{WSS} = 0$,**t**-domain); **Main:** $f_s^0 = 192$ kHz, $f_s^1 = 24$ kHz, $R_{\downarrow}^1 = \frac{1}{8} = 0.125$, Elliptic LPF ($f_s = 192$ kHz, $f_{pass} = 11$ kHz, $f_{stop} = 12$ kHz, $A_{pass} = 2$ dB, $A_{stop} = 40$ dB), $f_s^2 = 24$ kHz, $R_{\downarrow}^2 = \frac{1}{1} = 1$, Dummy; **Topology:** (Feedforward, mFx, $N_x = 2, N_e = 1, N_y = 1, N_p = 0, N_v = 2$); **Plants:** SysID/20080113T014624 ($g_{xy,\infty}^{1,1}$: (FIR : $M_{gxy}^{1,1} = 481$), $g_{xy,\infty}^{1,2}$: (FIR : $M_{gxy}^{1,2} = 481$), $g_{ey,\infty}^{1,1}$: (FIR : $M_{gey}^{1,1} = 71$), $g_{py,\infty}^{1,1}$: (FIR : $M_{gpy}^{1,1} = 410$), $g_{py,\infty}^{1,2}$: (FIR : $M_{gpy}^{1,2} = 410$)); **Signals:** Time: $0 - 10$ s. Refer to SigIDLaT. ; **Scenario:** `MultipleSinusoidalsAddiativeNoiseFeedforwardNx2Ne1Ny1Np0/20080309T220501`.

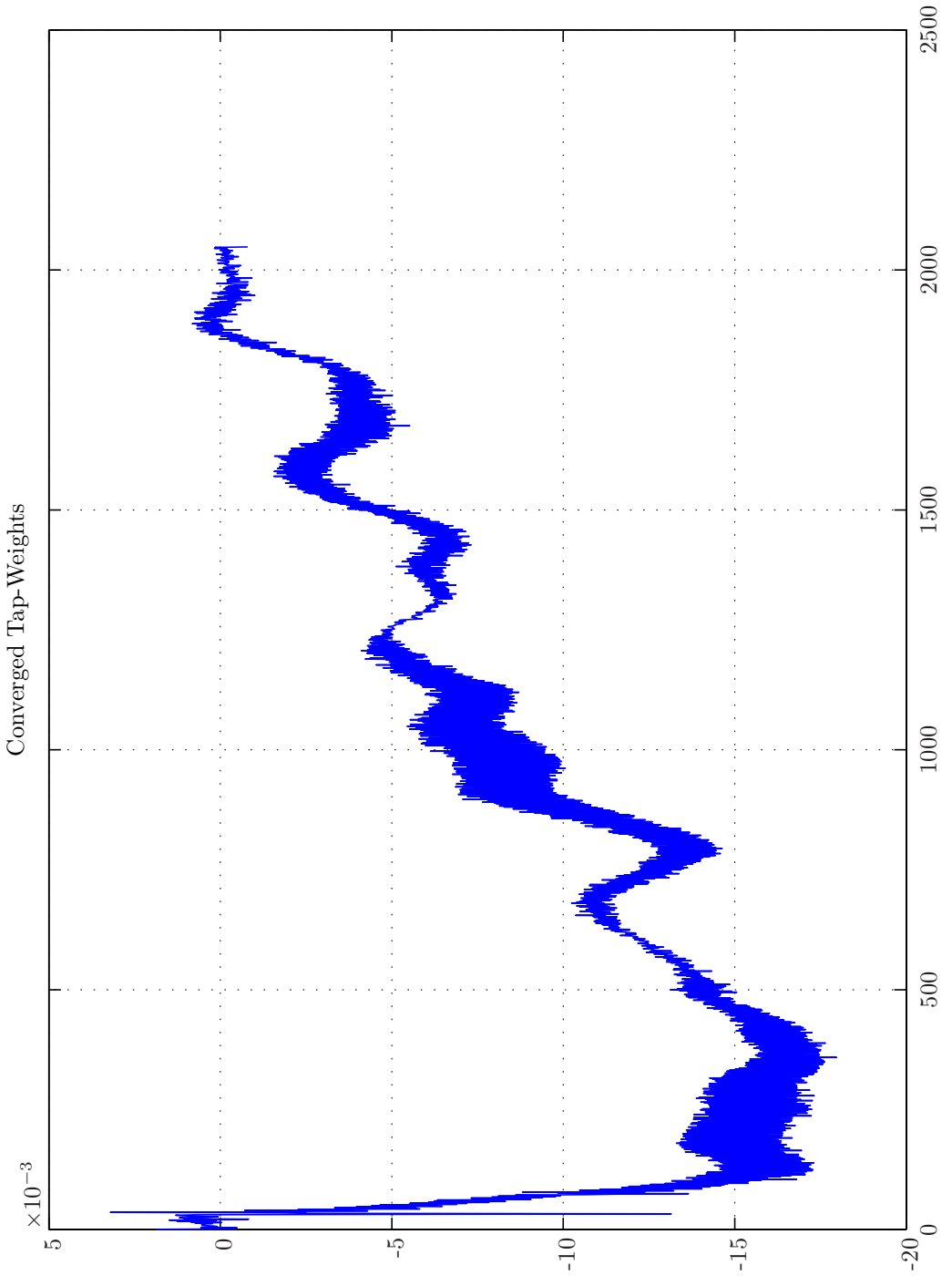

Sim 3.4.10: *Converged Tap-weights.* **Adaptive Filter** $\underset{\sim}{w}$: $\underset{\sim}{w}^{2,1}$: Wiener Hopf ($M = 2048, \alpha = 1e-005, T_{WSS} = 0$,**t**-domain); **Main:** $f_s^0 = 192$ kHz, $f_s^1 = 24$ kHz, $R_\updownarrow^1 = \frac{1}{8} = 0.125$, Elliptic LPF ($f_s = 192$ kHz, $f_{pass} = 11$ kHz, $f_{stop} = 12$ kHz, $A_{pass} = 2$ dB, $A_{stop} = 40$ dB), $f_s^2 = 24$ kHz, $R_\updownarrow^2 = \frac{1}{1} = 1$, Dummy; **Topology:** (Feedforward, mFx, $N_x = 2, N_e = 1, N_y = 1, N_p = 0, N_v = 2$); **Plants:** SysID/20080113T014624 ($g_{xy,\infty}^{1,1}$: (FIR : $M_{gxy}^{1,1} = 481$), $g_{xy,\infty}^{1,2}$: (FIR : $M_{gxy}^{1,2} = 481$), $g_{ey,\infty}^{1,1}$: (FIR : $M_{gey}^{1,1} = 71$), $g_{py,\infty}^{1,1}$: (FIR : $M_{gpy}^{1,1} = 410$), $g_{py,\infty}^{1,2}$: (FIR : $M_{gpy}^{1,2} = 410$)); **Signals:** Time: $0 - 10$ s. Refer to SigIDLaT. ; **Scenario:** `MultipleSinusoidalsAddiativeNoiseFeedforwardNx2Ne1Ny1Np0/20080309T220501`.

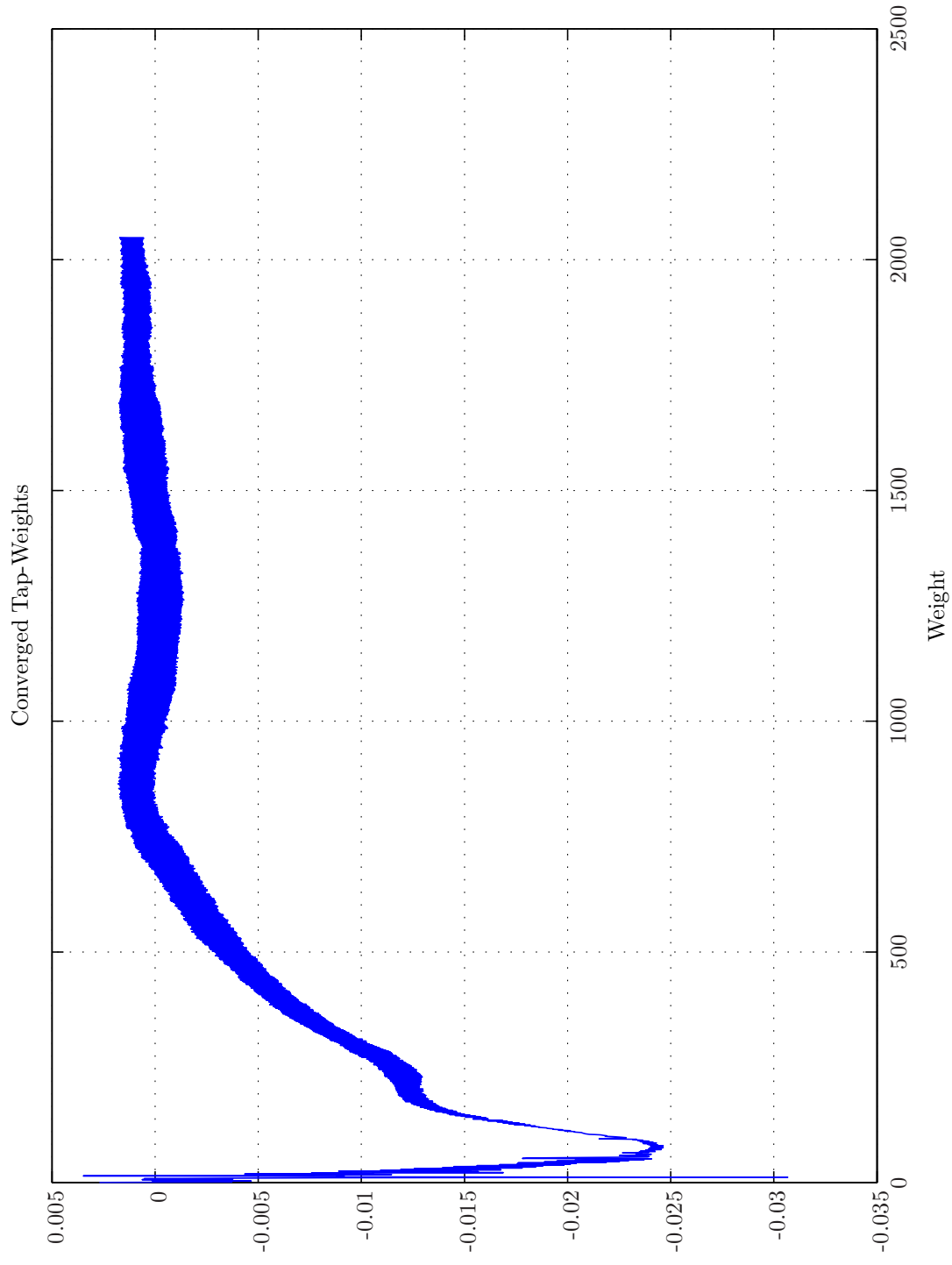

Sim 3.4.11: *Converged Tap-weights.* **Adaptive Filter** $\underset{\sim}{w}$: $\underset{\sim}{w}^{1,1}$; Wiener Hopf ($M = 2048, \alpha = 1e-005, T_{WSS} = 0$,**z**-domain); **Main:** $f_s^0 = 192$ kHz, $f_s^1 = 24$ kHz, $R_\updownarrow^1 = \frac{1}{8} = 0.125$, Elliptic LPF ($f_s = 192$ kHz, $f_{pass} = 11$ kHz, $f_{stop} = 12$ kHz, $A_{pass} = 2$ dB, $A_{stop} = 40$ dB), $f_s^2 = 24$ kHz, $R_\updownarrow^2 = \frac{1}{1} = 1$, Dummy; **Topology:** (Feedforward, mFx, $N_x = 2, N_e = 1, N_y = 1, N_p = 0, N_v = 2$); **Plants:** SysID/20080113T014624 ($g_{xy,\infty}^{1,1}$: (FIR : $M_{gxy}^{1,1} = 481$), $g_{xy,\infty}^{1,2}$: (FIR : $M_{gxy}^{1,2} = 481$), $g_{ey,\infty}^{1,1}$: (FIR : $M_{gey}^{1,1} = 71$), $g_{py,\infty}^{1,1}$: (FIR : $M_{gpy}^{1,1} = 410$), $g_{py,\infty}^{1,2}$: (FIR : $M_{gpy}^{1,2} = 410$)); **Signals:** Time: $0 - 10$ s. Refer to SigIDLaT. ; **Scenario:** `MultipleSinusoidalsAddiativeNoiseFeedforwardNx2Ne1Ny1Np0/20080309T220501`.

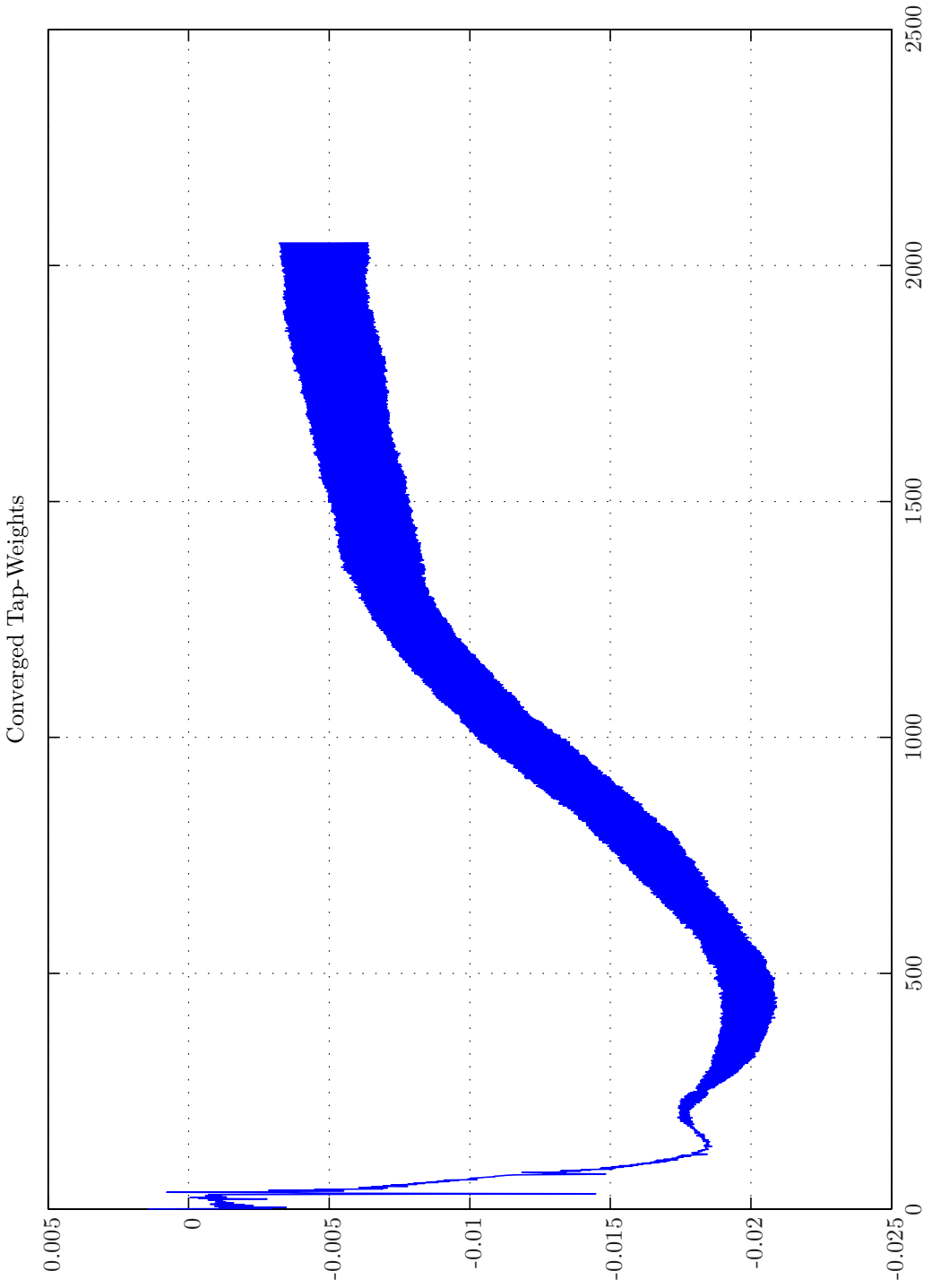

Sim 3.4.12: *Converged Tap-weights.* **Adaptive Filter** $\underset{\sim}{w}$: $\underset{\sim}{w}^{2,1}$: Wiener Hopf ($M = 2048, \alpha = 1e-005, T_{WSS} = 0$,**z**-domain); **Main:** $f_s^0 = 192$ kHz, $f_s^1 = 24$ kHz, $R_\updownarrow^1 = \frac{1}{8} = 0.125$, Elliptic LPF ($f_s = 192$ kHz, $f_{pass} = 11$ kHz, $f_{stop} = 12$ kHz, $A_{pass} = 2$ dB, $A_{stop} = 40$ dB), $f_s^2 = 24$ kHz, $R_\updownarrow^2 = \frac{1}{1} = 1$, Dummy; **Topology:** (Feedforward, mFx, $N_x = 2, N_e = 1, N_y = 1, N_p = 0, N_v = 2$); **Plants:** SysID/20080113T014624 ($g_{xy,\infty}^{1,1}$: (FIR : $M_{gxy}^{1,1} = 481$), $g_{xy,\infty}^{1,2}$: (FIR : $M_{gxy}^{1,2} = 481$), $g_{ey,\infty}^{1,1}$: (FIR : $M_{gey}^{1,1} = 71$), $g_{py,\infty}^{1,1}$: (FIR : $M_{gpy}^{1,1} = 410$), $g_{py,\infty}^{1,2}$: (FIR : $M_{gpy}^{1,2} = 410$)); **Signals:** Time: $0 - 10$ s. Refer to SigIDLaT. ; **Scenario:** `MultipleSinusoidalsAddiativeNoiseFeedforwardNx2Ne1Ny1Np0/20080309T220501`.

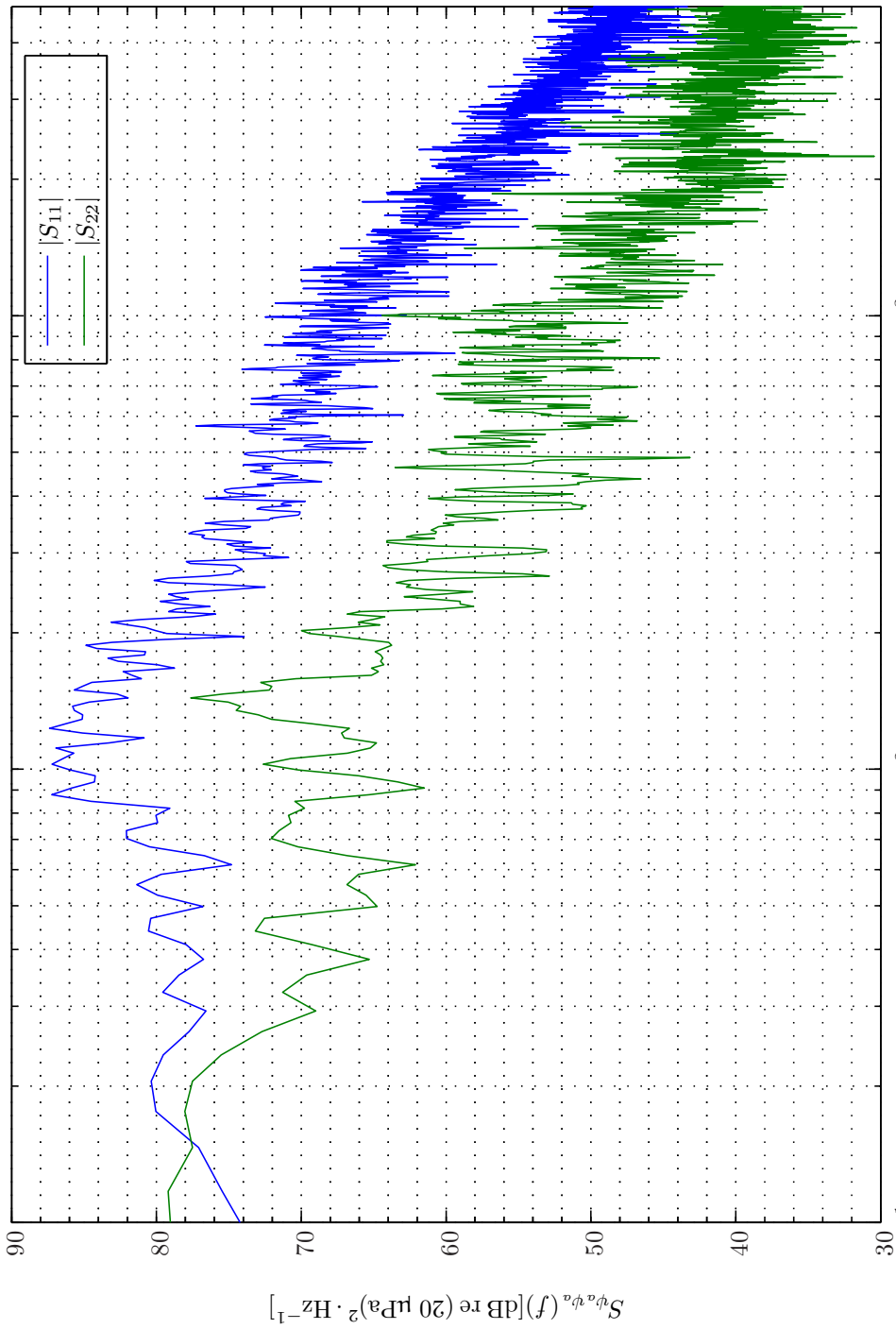

Sim 3.4.13: *Autospectral Density Functions:* **Statistical Data Analysis:** Single-Sided Modified Periodogram, f_s = 24 kHz, N_{DFT} = 8192, L_{DFT} = 6001, R_{DFT} = 3001, Hanning, Δf_m = 16 Hz, T_{DFT} = 0.25004 s, $N_{f,DFT}$ = 4097, Δf_{DFT} = 2.9297 Hz, K_{DFT} = 4; **Adaptive Filter** $\underline{w}$: Wiener Hopf (M = 2048, $\alpha = 1e-005$, T_{WSS} = 0.t-domain); **Main:** f_s^0 = 192 kHz, f_s^1 = 24 kHz, $R_\downarrow^1 = \frac{1}{8} = 0.125$, Elliptic LPF ($f_s$ = 192 kHz, f_{pass} = 11 kHz, f_{stop} = 12 kHz, A_{pass} = 2 dB, A_{stop} = 40 dB), f_s^2 = 24 kHz, $R_\downarrow^2 = \frac{1}{1} = 1$, Dummy; **Topology:** (Feedforward, mFx, $N_x = 2, N_e = 1, N_y = 1, N_p = 0, N_v = 2$); **Plants:** SysID/20080113T014624 ($g_{xy,\infty}^{1,1}$: (FIR : $M_{gxy}^{1,2}$ = 481), $g_{xy,\infty}^{1,2}$: (FIR : $M_{gxy}^{1,2}$ = 481), $g_{ey,\infty}^{1,1}$: (FIR : $M_{gey}^{1,1}$ = 71), $g_{py,\infty}^{1,1}$: (FIR : $M_{gpy}^{1,1}$ = 410), $g_{py,\infty}^{1,2}$: (FIR : $M_{gpy}^{1,2}$ = 410)); **Signals:** Time: 0 − 10 s. Refer to SigIDLaT. ; **Scenario:** MultipleSinusoidalsAddiativeNoiseFeedforwardNx2Ne1Ny1Np0/20080309T220501; *Channels:* #1 ←$d_1(t_1^1)$, #2 ←$e_1(t_1^1)$.: .

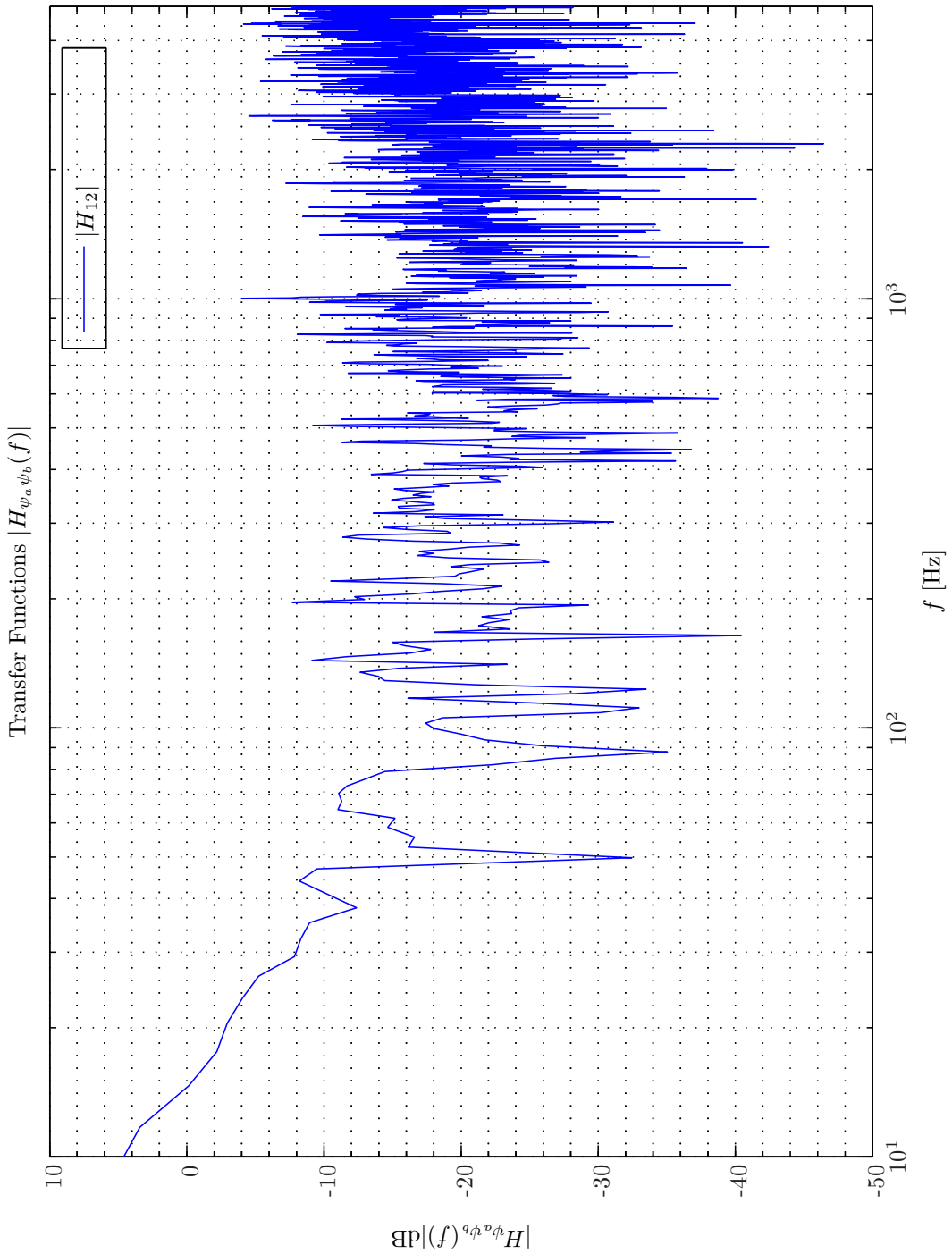

Sim 3.4.14: *Transfer Function, Magnitude:* $|H_{\psi_a\psi_b}(f)|$: **Statistical Data Analysis:** Single-Sided Modified Periodogram, $f_s = 24$ kHz, $N_{DFT} = 8192$, $L_{DFT} = 6001$, $R_{DFT} = 3001$, Hanning, $\Delta f_m = 16$ Hz, $T_{DFT} = 0.25004$ s, $N_{f,DFT} = 4097$, $\Delta f_{DFT} = 2.9297$ Hz, $K_{DFT} = 4$; **Adaptive Filter** $\underset{\sim}{w}$: Wiener Hopf ($M = 2048$, $\alpha = 1e-005$, $T_{WSS} = 0$,**t**-domain); **Main:** $f_s^0 = 192$ kHz, $f_s^1 = 24$ kHz, $R_\downarrow^1 = \frac{1}{8} = 0.125$, Elliptic LPF ($f_s = 192$ kHz, $f_{pass} = 11$ kHz, $f_{stop} = 12$ kHz, $A_{pass} = 2$ dB, $A_{stop} = 40$ dB), $f_s^2 = 24$ kHz, $R_\downarrow^2 = \frac{1}{1} = 1$, Dummy; **Topology:** (Feedforward, mFx, $N_x = 2$, $N_e = 1$, $N_y = 1$, $N_p = 0$, $N_v = 2$); **Plants:** SysID/20080113T014624 ($g_{xy,\infty}^{1,1}$: (FIR : $M_{gxy}^{1,1} = 481$), $g_{xy,\infty}^{1,2}$: (FIR : $M_{gxy}^{1,2} = 481$), $g_{ey,\infty}^{1,1}$: (FIR : $M_{gey}^{1,1} = 71$), $g_{py,\infty}^{1,1}$: (FIR : $M_{gpy}^{1,1} = 410$), $g_{py,\infty}^{1,2}$: (FIR : $M_{gpy}^{1,2} = 410$)); **Signals:** Time: $0 - 10$ s. Refer to SigIDLaT. ; **Scenario:** `MultipleSinusoidalsAddiativeNoiseFeedforwardNx2Ne1Ny1Np0/20080309T220501`; *Channels:* #1 $\leftarrow d_1(t_1^1)$, #2 $\leftarrow e_1(t_1^1)$.; .

3. $\alpha\gamma\Pi\epsilon$-APA ($M = 512, L_B = 1, \mu = 0.15, K = 2, 4, \Delta = 1, \alpha = 1e-5, \gamma = 1e-5, \Pi = 0, \epsilon = 1e-006, \breve{w} = 0, W_e = \mathrm{I}$);

4. FARLS ($M = 512, L_B = 1, \lambda = 0.9999, 0.99995, 0.99999, \eta = 0.125, \alpha = 1e-5, T_{SW} = 0, \mathrm{Calc} = 1$);

The time span of the simulations is again $0 - 10$ s.

In Simulation 3.4.15 - 3.4.17 on pages 174–176 the time-domain attenuation convergence for the entire $0 - 10$ s period and the details for the first 100 ms and the last 20 ms respectively are displayed.

The two WH methods investigated provide almost identical ANR performance ($\mathcal{A}^e(t) = 8 \pm 6$ dB), while $\mathcal{A}^e(t) = 6 \pm 4$ dB, 0 ± 3 dB and 3 ± 3 dB for the $\alpha\gamma\Pi\epsilon$-NLMS and the $\alpha\gamma\Pi\epsilon$-affine projection algorithm ($\alpha\gamma\Pi\epsilon$-APA) upon convergence. The attenuation provided by the fast array recursive least-squares (FARLS) varies as $\mathcal{A}^e(t) = 5 \pm 2$ dB for $\lambda = 0.99999$ and $\mathcal{A}^e(t) = 8 \pm 4$ dB for $\lambda = 0.9999, 0.99995$. Moreover, in comparison with the FFS in Example 3.2.1 owing to the fewer weights involved ($M_{\overset{\circ}{w}^{1,1}} = 512$ while $M_{\underset{\sim}{w}^{1,1}} = M_{\underset{\sim}{w}^{2,1}} = 1024$) the $\alpha\gamma\Pi\epsilon$-NLMS algorithm converges within 2.5 s.

Apparently the two $\alpha\gamma\Pi\epsilon$-APA filters initally provide fast convergence, but then lead to a performance that seems to decrease somewhat with time. The reason for this behavior is currently not understood. Finally, the three FARLS variants provide almost identical fast convergence of 0.6 s.

Although, the reference signal for the FBS, that is, the estimated disturbance signal deviates substantially from RWN the **t**-domain and **z**-domain WH filters give very similar results. The weight vector $\overset{\circ}{w}^{1,1}$ for the two WH filters is shown in Simulation 3.4.18 - 3.4.19. We appreciate that the two weight vectors exhibit similar pattern and that the energy is almost entirely confined to the first 150 weights. The very much identical performance of the two WH filters may be explained as follows. From the **z**-domain WH filter expression for the optimal causally-constrained weights viz. (3.3.9) on page 137 we appreciate that if the plus operator only leads to minor truncation effects then we get $\tilde{w}^o(z) \approx -\tilde{g}_{ey}^{-1}(z)$ which coincide with the expression for the **t**-domain WH filter. Concerning the terms that enter the plus operator in (3.3.9), that is, $\tilde{g}_{ey,\mathrm{all}}^*(z^{-*})L_{\hat{d}}(z)$, it should be recalled that only in the order of 50 weights are used to represent the secondary path. However, from the auto spectral density function in Simulation 3.4.1 on page 158 we appreciate that the disturbance signal is primarily confined to the low-frequency range $0 - 200$ Hz and the order of the colorization filter $L_x(z)$ therefore exceeds 120 samples for a sampling frequency $f_s^1 = 24$ kHz. Hence, owing to the low-frequency characteristics of the reference signal used in a helmet based FBS, the difference between **z**-domain and the **t**-domain WH filter is less pronounced than for the FFS considered in Example 3.4.1.

Moreover, by comparison the weight vector $\underset{\sim}{w}^{1,1}$ obtained by the $\alpha\gamma\Pi\epsilon$-NLMS, $\alpha\gamma\Pi\epsilon$-APA ($K = 2$) algorithms depicted in Simulation 3.4.20 - 3.4.21 deviate substantially from the optimally constrained weight vector in Simulation 3.4.19 while, e.g., the FARLS ($\lambda = 0.99995$) shown in Simulation 3.4.22 constitute a fairly close match.

The auto spectral density functions for the two WH filters are shown in Simulation 3.4.23 - 3.4.24. As readily seen except for the low frequency range $10 - 500$ Hz the resulting error spectra are very flat in contrast to the error spectra of the FFS in Simulation 3.4.13 that exhibit pink noise characteristics.

The dominant low-frequency ANR capabilities of the feedback topology is clearly exhibited in

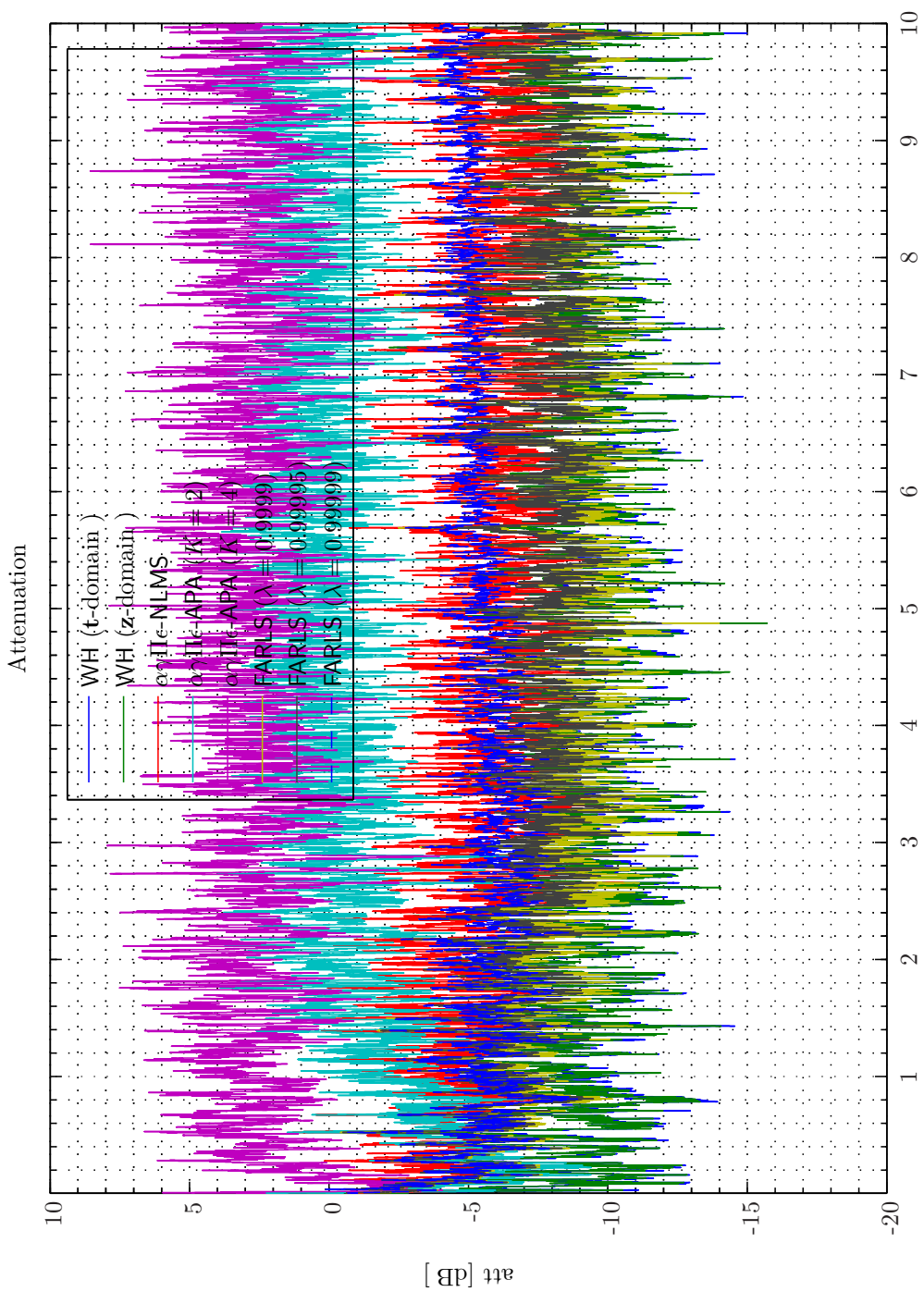

Sim 3.4.15: *Time-Domain: Attenuation.* **Adaptive Filter** y: $\overset{1,1}{\bigcirc}\overset{1,1}{\bigcirc}$: WH ($M = 1024, \alpha = 1e-005, T_{WSS} = 0$);αγΠε-NLMS ($M = 512, L_B = 1, \mu = 0.15, \alpha = 1e-005, \epsilon = 1e-006, T_{Eu} = 400$);αγΠε-APA ($M = 512, L_B = 1, \mu = 0.15, \Delta = 1, \alpha = 1e-005, \gamma = 1e-005, \Pi = 0, \epsilon = 1e-006, \breve{w} = 0, W_e = 1$);FARLS ($M = 512, L_B = 1, \eta = 0.125, \alpha = 1e-005, T_{SW} = 0$, Calc = 1); **Main:** $f_s^0 = 192$ kHz, $f_s^1 = 24$ kHz, $R_\updownarrow^1 = \frac{1}{8} = 0.125$, Elliptic LPF ($f_s = 192$ kHz, $f_{pass} = 11$ kHz, $f_{stop} = 12$ kHz, $A_{pass} = 2$ dB, $A_{stop} = 40$ dB), $f_s^2 = 24$ kHz, $R_\updownarrow^2 = \frac{1}{1} = 1$, Dummy; **Topology:** (Feedback, mFx, $N_e = 1, N_y = 1, N_p = 0, N_v = 2$); **Plants:** SysID/20080321T134130 ($g_{xy,\infty}^{1,1}$: (FIR : $M_{gxy}^{1,1} = 700$), $g_{xy,\infty}^{1,2}$: (FIR : $M_{gxy}^{1,2} = 700$), $g_{ey,\infty}^{1,1}$: (FIR : $M_{gey}^{1,1} = 120$), $g_{py,\infty}^{1,1}$: (FIR : $M_{gpy}^{1,1} = 200$), $g_{py,\infty}^{1,2}$: (FIR : $M_{gpy}^{1,2} = 200$)); **Signals:** Time: $0 - 10$ s. Refer to SigIDLaT. ; **Scenario:** `MultipleSinusoidalsAddiativeNoiseFeedbackN2Ne1Ny1Np0/20080408T070449`.

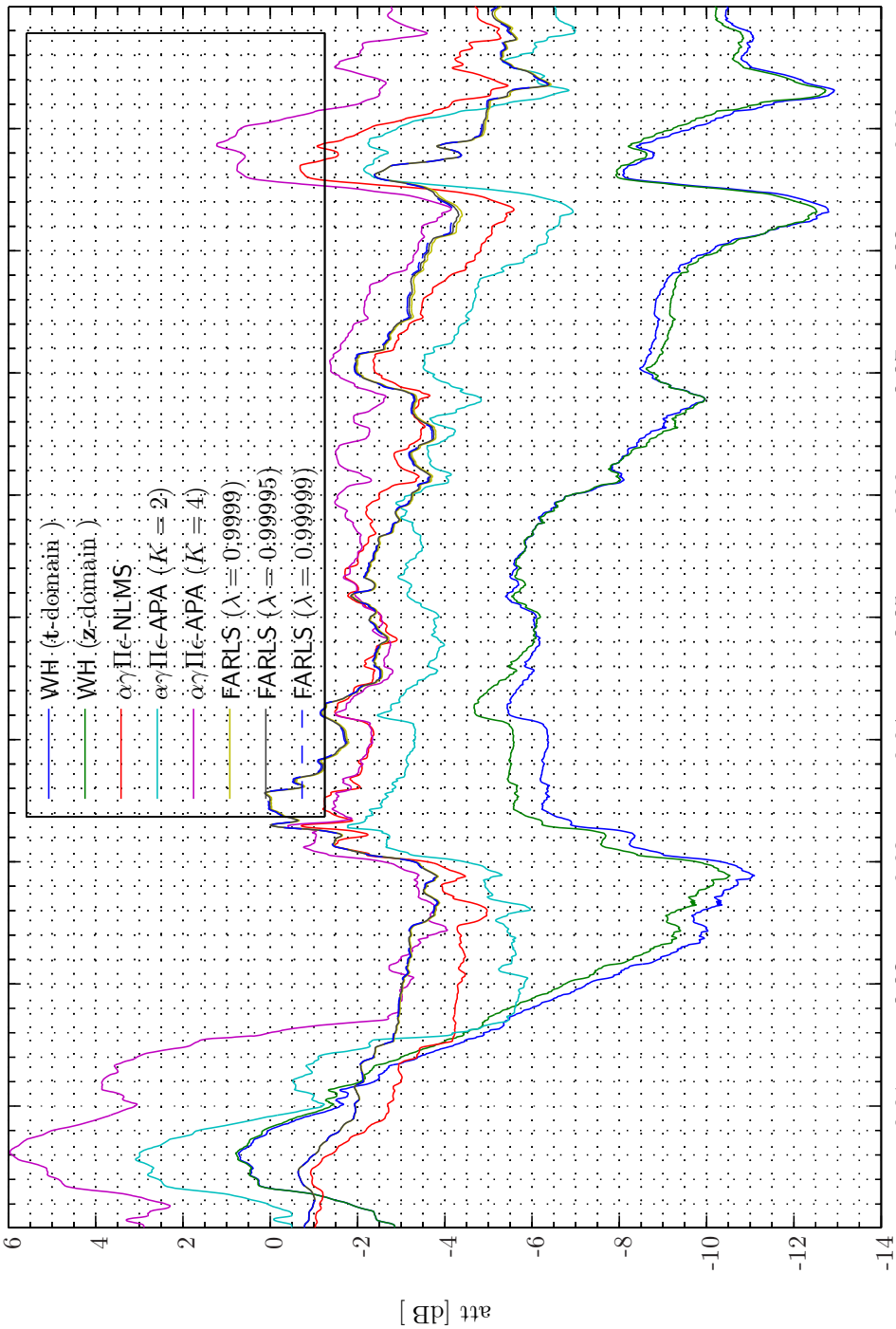

Sim 3.4.16: *Time-Domain: Attenuation Initial.* **Adaptive Filter** $\underset{\circlearrowleft}{w}$: $w^{1,1}$: WH ($M = 1024, \alpha = 1e-005, T_{WSS} = 0$);αγΠϵ-NLMS ($M = 512, L_B = 1, \mu = 0.15, \alpha = 1e-005, \epsilon = 1e-006, T_{Eu} = 400$);αγΠϵ-APA ($M = 512, L_B = 1, \mu = 0.15, \Delta = 1, \alpha = 1e-005, \gamma = 1e-005, \Pi = 0, \epsilon = 1e-006, \breve{w} = 0, W_e = 1$);FARLS ($M = 512, L_B = 1, \eta = 0.125, \alpha = 1e-005, T_{SW} = 0$, Calc = 1); **Main:** $f_s^0 = 192$ kHz, $f_s^1 = 24$ kHz, $R_{\updownarrow}^1 = \frac{1}{8} = 0.125$, Elliptic LPF ($f_s = 192$ kHz, $f_{pass} = 11$ kHz, $f_{stop} = 12$ kHz, $A_{pass} = 2$ dB, $A_{stop} = 40$ dB), $f_s^2 = 24$ kHz, $R_{\updownarrow}^2 = \frac{1}{1} = 1$, Dummy; **Topology:** (Feedback, mFx, $N_e = 1, N_y = 1, N_p = 0, N_v = 2$); **Plants:** SysID/20080321T134130 ($g_{xy,\infty}^{1,1}$: (FIR : $M_{gxy}^{1,2} = 700$), $g_{xy,\infty}^{1,2}$: (FIR : $M_{gxy}^{1,2} = 700$), $g_{ey,\infty}^{1,1}$: (FIR : $M_{gey}^{1,1} = 120$), $g_{py,\infty}^{1,1}$: (FIR : $M_{gpy}^{1,1} = 200$), $g_{py,\infty}^{1,2}$: (FIR : $M_{gpy}^{1,2} = 200$)); **Signals:** Time: $0 - 10$ s. Refer to SigIDLaT. ; **Scenario:** `MultipleSinusoidalsAddiativeNoiseFeedbackNx2Ne1Ny1Np0/20080408T070449`.

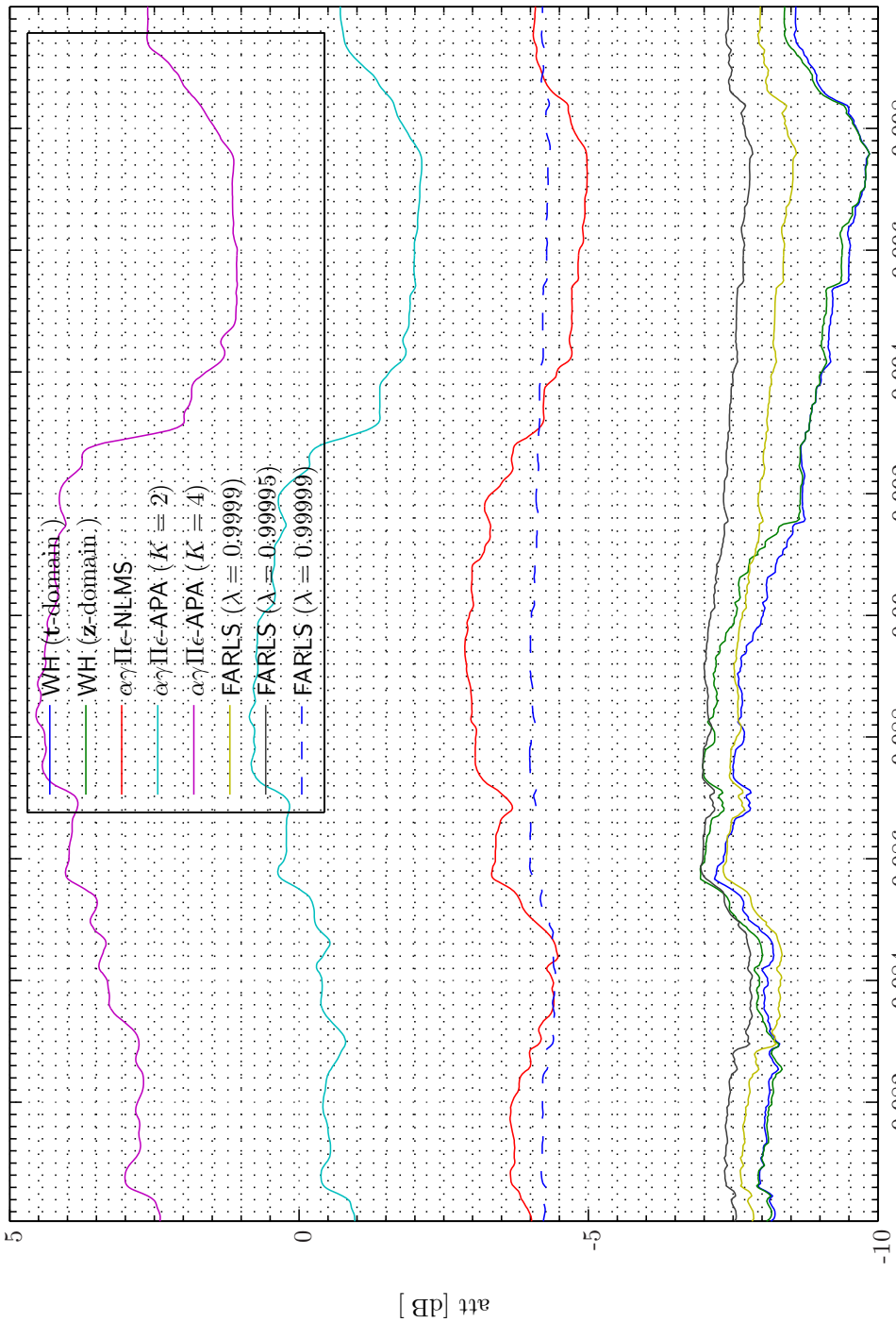

Sim 3.4.17: *Time-Domain: Attenuation Final.* **Adaptive Filter** w: $\overset{\circ}{w}^{1,1}$: WH ($M = 1024, \alpha = 1e-005, T_{WSS} = 0$);αγΠϵ-NLMS ($M = 512, L_B = 1, \mu = 0.15, \alpha = 1e-005, \epsilon = 1e-006, T_{Eu} = 400$);αγΠϵ-APA ($M = 512, L_B = 1, \mu = 0.15, \Delta = 1, \alpha = 1e-005, \gamma = 1e-005, \Pi = 0, \epsilon = 1e-006, \mathring{w} = 0, W_e = 1$);FARLS ($M = 512, L_B = 1, \eta = 0.125, \alpha = 1e-005, T_{SW} = 0,$ Calc = 1); **Main:** $f_s^0 = 192$ kHz, $f_s^1 = 24$ kHz, $R_\updownarrow^1 = \frac{1}{8} = 0.125$, Elliptic LPF ($f_s = 192$ kHz, $f_{pass} = 11$ kHz, $f_{stop} = 12$ kHz, $A_{pass} = 2$ dB, $A_{stop} = 40$ dB), $f_s^2 = 24$ kHz, $R_\updownarrow^2 = \frac{1}{1} = 1$, Dummy; **Topology:** (Feedback, mFx, $N_e = 1, N_y = 1, N_p = 0, N_v = 2$); **Plants:** SysID/20080321T134130 ($g_{xy,\infty}^{1,1}$: (FIR : $M_{gxy}^{1,1} = 700$), $g_{xy,\infty}^{1,2}$: (FIR : $M_{gxy}^{1,2} = 700$), $g_{ey,\infty}^{1,1}$: (FIR : $M_{gey}^{1,1} = 120$), $g_{py,\infty}^{1,1}$: (FIR : $M_{gpy}^{1,1} = 200$), $g_{py,\infty}^{1,2}$: (FIR : $M_{gpy}^{1,2} = 200$)); **Signals:** Time: $0 - 10$ s. Refer to SigIDLaT. ; **Scenario:** MultipleSinusoidalsAddiativeNoiseFeedbackN2Ne1Ny1Np0/20080408T070449.

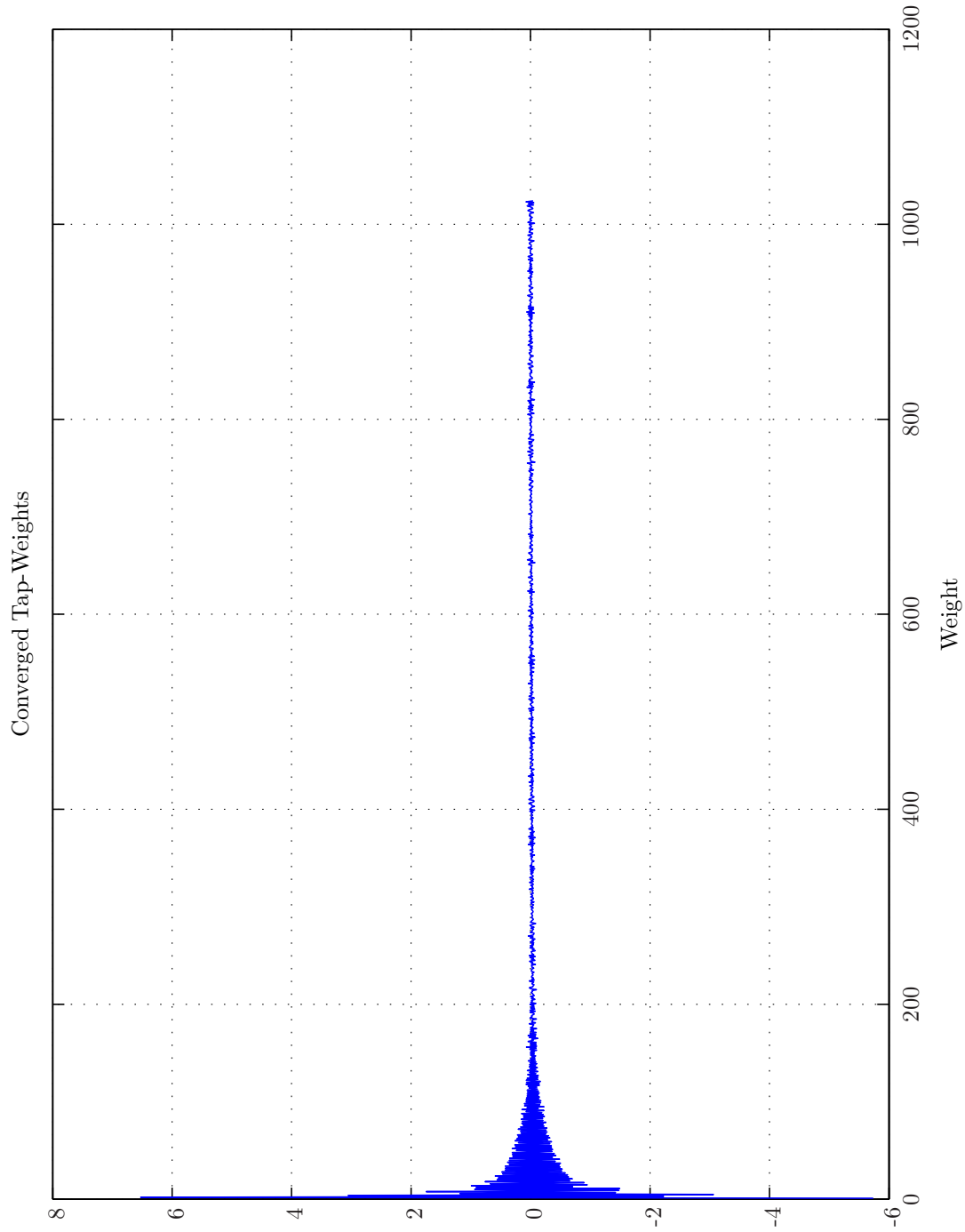

Sim 3.4.18: *Converged Tap-weights.* **Adaptive Filter** w: $w^{1,1}_{\circlearrowleft}$: Wiener Hopf ($M = 1024, \alpha = 1e-005, T_{WSS} = 0$,**t**-domain); **Main:** $f^0_s = 192$ kHz, $f^1_s = 24$ kHz, $R^1_{\updownarrow} = \frac{1}{8} = 0.125$, Elliptic LPF ($f_s = 192$ kHz, $f_{pass} = 11$ kHz, $f_{stop} = 12$ kHz, $A_{pass} = 2$ dB, $A_{stop} = 40$ dB), $f^2_s = 24$ kHz, $R^2_{\updownarrow} = \frac{1}{1} = 1$, Dummy; **Topology:** (Feedback, mFx, $N_e = 1, N_y = 1, N_p = 0, N_v = 2$); **Plants:** SysID/20080321T134130 ($g^{1,1}_{xy,\infty}$: (FIR : $M^{1,1}_{gxy} = 700$), $g^{1,2}_{xy,\infty}$: (FIR : $M^{1,2}_{gxy} = 700$), $g^{1,1}_{ey,\infty}$: (FIR : $M^{1,1}_{gey} = 120$), $g^{1,1}_{py,\infty}$: (FIR : $M^{1,1}_{gpy} = 200$), $g^{1,2}_{py,\infty}$: (FIR : $M^{1,2}_{gpy} = 200$)); **Signals:** Time: $0 - 10$ s. Refer to SigIDLaT. ; **Scenario:** `MultipleSinusoidalsAddiativeNoiseFeedbackNx2Ne1Ny1Np0/20080408T070449`.

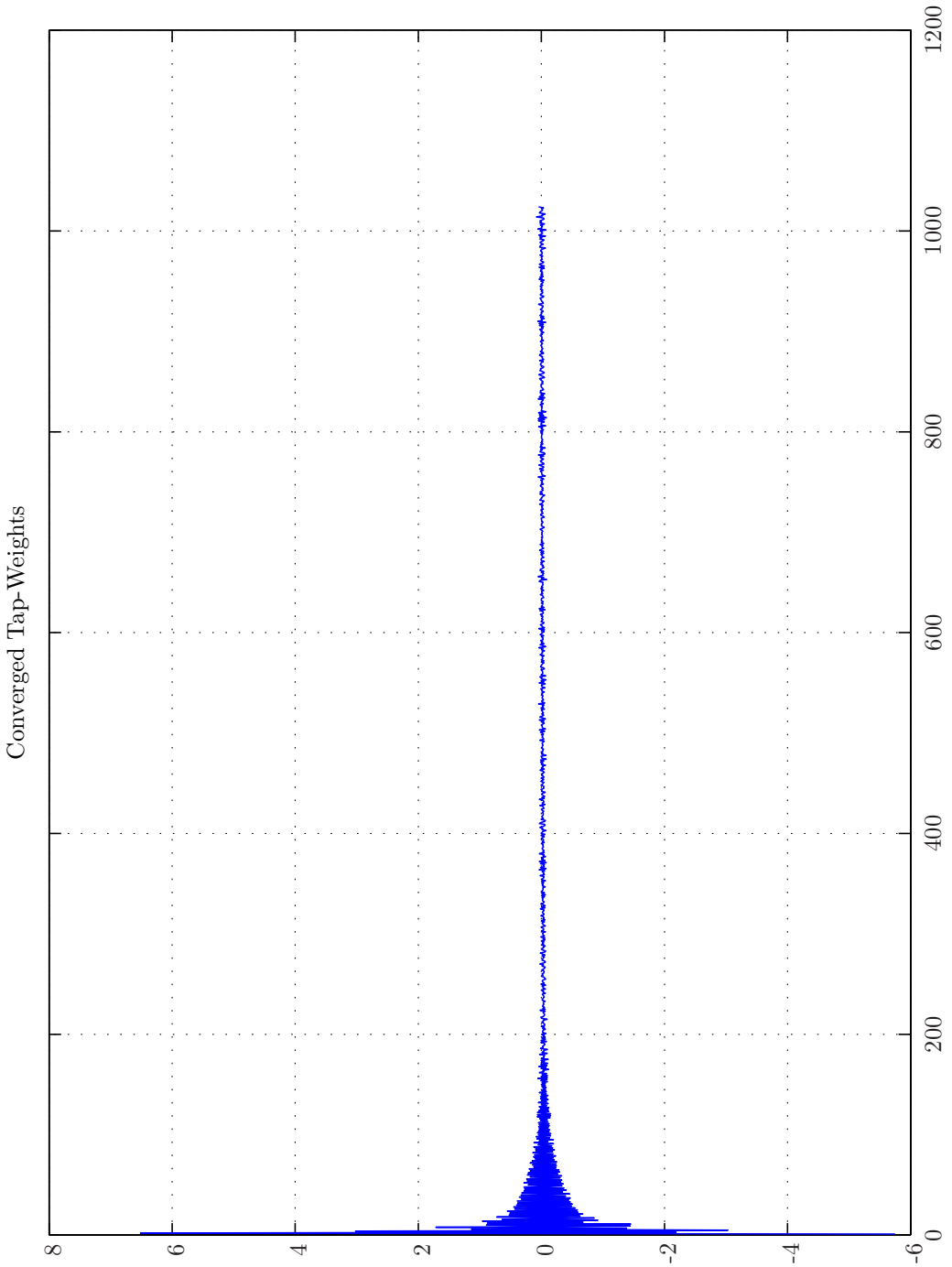

Sim 3.4.19: *Converged Tap-weights.* **Adaptive Filter** w: $\overset{\circ}{w}^{1,1}$: Wiener Hopf ($M = 1024, \alpha = 1e-005, T_{WSS} = 0$,**z**-domain); **Main:** $f_s^0 = 192$ kHz, $f_s^1 = 24$ kHz, $R_\updownarrow^1 = \frac{1}{8} = 0.125$, Elliptic LPF ($f_s = 192$ kHz, $f_{pass} = 11$ kHz, $f_{stop} = 12$ kHz, $A_{pass} = 2$ dB, $A_{stop} = 40$ dB), $f_s^2 = 24$ kHz, $R_\updownarrow^2 = \frac{1}{1} = 1$, Dummy; **Topology:** (Feedback, mFx, $N_e = 1, N_y = 1, N_p = 0, N_v = 2$); **Plants:** SysID/20080321T134130 ($g_{xy,\infty}^{1,1}$: (FIR : $M_{gxy}^{1,1} = 700$), $g_{xy,\infty}^{1,2}$: (FIR : $M_{gxy}^{1,2} = 700$), $g_{ey,\infty}^{1,1}$: (FIR : $M_{gey}^{1,1} = 120$), $g_{py,\infty}^{1,1}$: (FIR : $M_{gpy}^{1,1} = 200$), $g_{py,\infty}^{1,2}$: (FIR : $M_{gpy}^{1,2} = 200$)); **Signals:** Time: $0 - 10$ s. Refer to SigIDLaT. ; **Scenario:** `MultipleSinusoidalsAddiativeNoiseFeedbackNx2Ne1Ny1Np0/20080408T070449`.

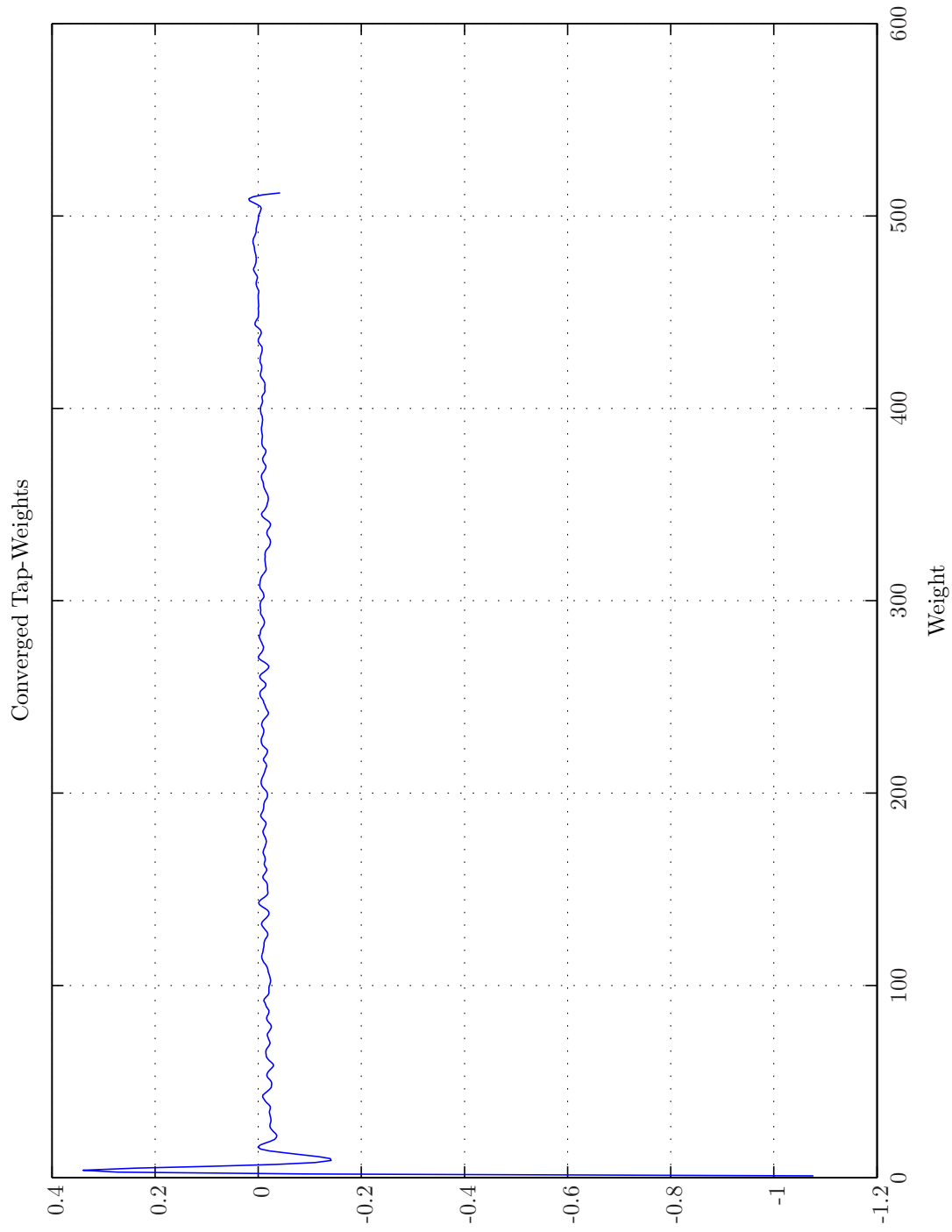

Sim 3.4.20: *Converged Tap-weights.* **Adaptive Filter** w: $w^{1,1}_{\circlearrowleft}$: $\alpha\gamma\Pi$e-Normalized Least-Mean-Squares ($M = 512, L_B = 1, \mu = 0.15, \alpha = 1e-005, \epsilon = 1e-006, T_{Eu} = 400$); **Main:** $f^0_s = 192$ kHz, $f^1_s = 24$ kHz, $R^1_{\updownarrow} = \frac{1}{8} = 0.125$, Elliptic LPF ($f_s = 192$ kHz, $f_{pass} = 11$ kHz, $f_{stop} = 12$ kHz, $A_{pass} = 2$ dB, $A_{stop} = 40$ dB), $f^2_s = 24$ kHz, $R^2_{\updownarrow} = \frac{1}{1} = 1$, Dummy; **Topology:** (Feedback, mFx, $N_e = 1, N_y = 1, N_p = 0, N_v = 2$); **Plants:** SysID/20080321T134130 ($g^{1,1}_{xy,\infty}$: (FIR : $M^{1,1}_{gxy} = 700$), $g^{1,2}_{xy,\infty}$: (FIR : $M^{1,2}_{gxy} = 700$), $g^{1,1}_{ey,\infty}$: (FIR : $M^{1,1}_{gey} = 120$), $g^{1,1}_{py,\infty}$: (FIR : $M^{1,1}_{gpy} = 200$), $g^{1,2}_{py,\infty}$: (FIR : $M^{1,2}_{gpy} = 200$)); **Signals:** Time: $0 - 10$ s. Refer to SigIDLaT. ; **Scenario:** `MultipleSinusoidalsAddiativeNoiseFeedbackNx2Ne1Ny1Np0/20080408T070449`.

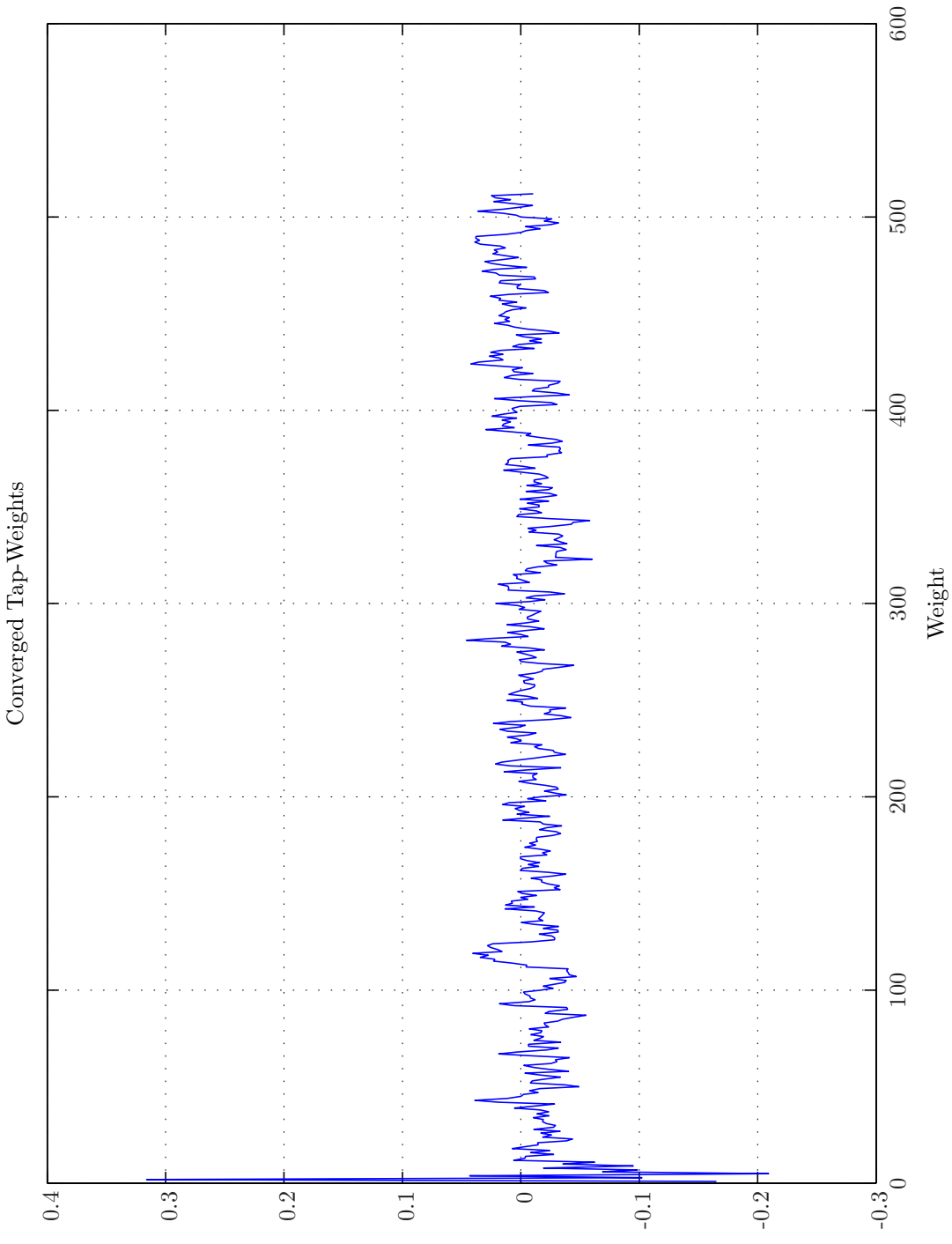

Sim 3.4.21: *Converged Tap-weights.* **Adaptive Filter** y: $\overset{\circlearrowleft}{0}{}^{1,1}_{w}$, $\alpha\gamma\Pi\epsilon$-Affine Projection Algorithm ($M = 512, L_B = 1, \mu = 0.15, K = 2, \Delta = 1, \alpha = 1e-005, \gamma = 1e-005, \Pi = 0, \epsilon = 1e-006, \ddot{w} = 0, W_e = 1$); **Main:** $f_s^0 = 192$ kHz, $f_s^1 = 24$ kHz, $R_\updownarrow^1 = \frac{1}{8} = 0.125$, Elliptic LPF ($f_s = 192$ kHz, $f_{pass} = 11$ kHz, $f_{stop} = 12$ kHz, $A_{pass} = 2$ dB, $A_{stop} = 40$ dB), $f_s^2 = 24$ kHz, $R_\updownarrow^2 = \frac{1}{1} = 1$, Dummy; **Topology:** (Feedback, mFx, $N_e = 1, N_y = 1, N_p = 0, N_v = 2$); **Plants:** SysID/20080321T134130 ($g_{xy,\infty}^{1,1}$: (FIR : $M_{gxy}^{1,1} = 700$), $g_{xy,\infty}^{1,2}$: (FIR : $M_{gxy}^{1,2} = 700$), $g_{ey,\infty}^{1,1}$: (FIR : $M_{gey}^{1,1} = 120$), $g_{py,\infty}^{1,1}$: (FIR : $M_{gpy}^{1,1} = 200$), $g_{py,\infty}^{1,2}$: (FIR : $M_{gpy}^{1,2} = 200$)); **Signals:** Time: $0 - 10$ s. Refer to SigIDLaT. ; **Scenario:** `MultipleSinusoidalsAddiativeNoiseFeedbackNx2Ne1Ny1Np0/20080408T070449`.

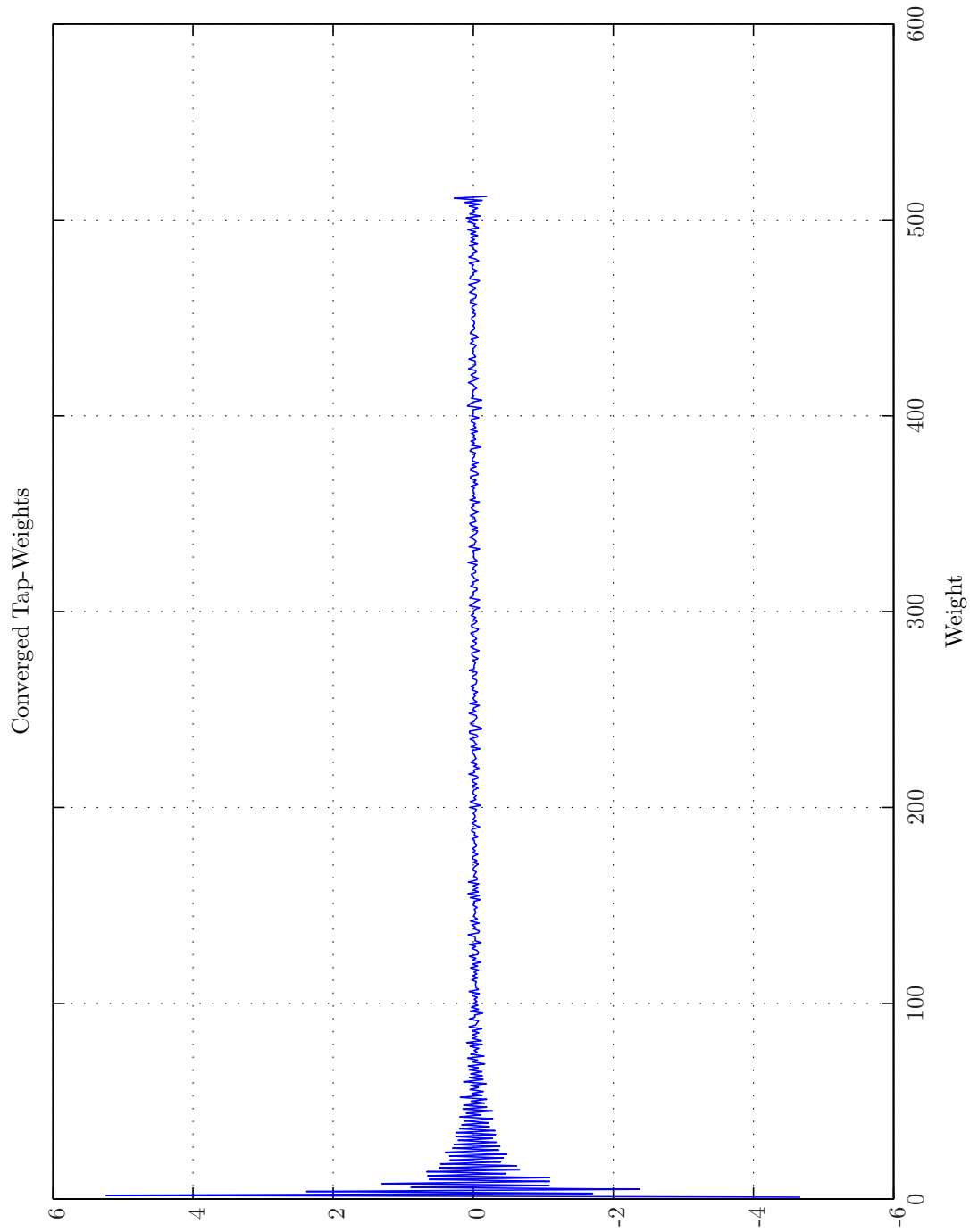

Sim 3.4.22: *Converged Tap-weights.* **Adaptive Filter** w: $\overset{\circ}{w}^{1,1}$: Fast Array RLS ($M = 512, L_B = 1, \lambda = 0.99995, \eta = 0.125, \alpha = 1e-005, T_{SW} = 0$, Calc $= 1$); **Main:** $f_s^0 = 192$ kHz, $f_s^1 = 24$ kHz, $R_\updownarrow^1 = \frac{1}{8} = 0.125$, Elliptic LPF ($f_s = 192$ kHz, $f_{pass} = 11$ kHz, $f_{stop} = 12$ kHz, $A_{pass} = 2$ dB, $A_{stop} = 40$ dB), $f_s^2 = 24$ kHz, $R_\updownarrow^2 = \frac{1}{1} = 1$, Dummy; **Topology:** (Feedback, mFx, $N_e = 1, N_y = 1, N_p = 0, N_v = 2$); **Plants:** SysID/20080321T134130 ($g_{xy,\infty}^{1,1}$: (FIR : $M_{gxy}^{1,1} = 700$), $g_{xy,\infty}^{1,2}$: (FIR : $M_{gxy}^{1,2} = 700$), $g_{ey,\infty}^{1,1}$: (FIR : $M_{gey}^{1,1} = 120$), $g_{py,\infty}^{1,1}$: (FIR : $M_{gpy}^{1,1} = 200$), $g_{py,\infty}^{1,2}$: (FIR : $M_{gpy}^{1,2} = 200$)); **Signals:** Time: $0 - 10$ s. Refer to SigIDLaT. ; **Scenario:** `MultipleSinusoidalsAddiativeNoiseFeedbackNx2Ne1Ny1Np0/20080408T070449`.

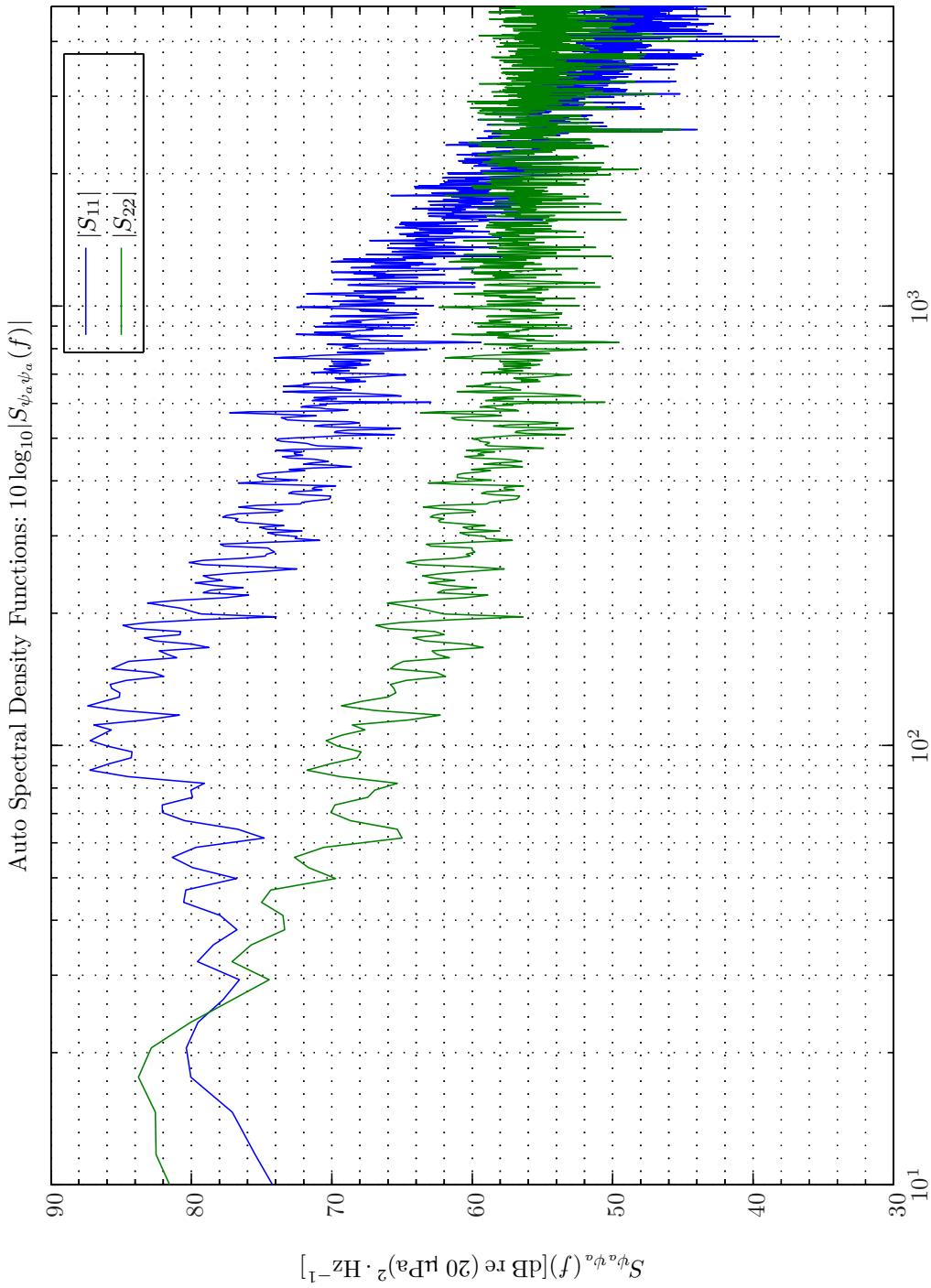

Sim 3.4.23: *Autospectral Density Functions*: **Statistical Data Analysis**: Single-Sided Modified Periodogram, $f_s = 24$ kHz, $N_{DFT} = 8192$, $L_{DFT} = 6001$, $R_{DFT} = 3001$, Hanning, $\Delta f_m = 16$ Hz, $T_{DFT} = 0.25004$ s, $N_{f,DFT} = 4097$, $\Delta f_{DFT} = 2.9297$ Hz, $K_{DFT} = 4$; **Adaptive Filter** *w*: Wiener Hopf ($M = 1024$, $\alpha = 1e-005$, $T_{WSS} =$ 0.t-domain); **Main:** $f_s^0 = 192$ kHz, $f_s^1 = 24$ kHz, $R_\downarrow^1 = \frac{1}{8} = 0.125$, Elliptic LPF ($f_s = 192$ kHz, $f_{pass} = 11$ kHz, $f_{stop} = 12$ kHz, $A_{pass} = 2$ dB, $A_{stop} = 40$ dB), $f_s^2 = 24$ kHz, $R_\downarrow^2 = \frac{1}{1} = 1$, Dummy; **Topology:** (Feedback, mFx, $N_e = 1, N_y = 1, N_p = 0, N_v = 2$); **Plants:** SysID/20080321T134130 ($g_{xy,\infty}^{1,1}$: (FIR : $M_{gxy}^{1,1} = 700$), $g_{xy,\infty}^{1,2}$: (FIR : $M_{gxy}^{1,2} = 700$), $g_{ey,\infty}^{1,1}$: (FIR : $M_{gey}^{1,1} = 120$), $g_{py,\infty}^{1,1}$: (FIR : $M_{gpy}^{1,1} = 200$), $g_{py,\infty}^{1,2}$: (FIR : $M_{gpy}^{1,2} = 200$)); **Signals:** Time: $0 - 10$ s. Refer to SigIDLaT. ; **Scenario:** `MultipleSinusoidalsAddiativeNoiseFeedbackNx2Ne1Ny1Np0/20080408T070449`; *Channels:* $\#1 \leftarrow d_1(t_1^1)$; $\#2 \leftarrow e_1(t_1^1)$.;

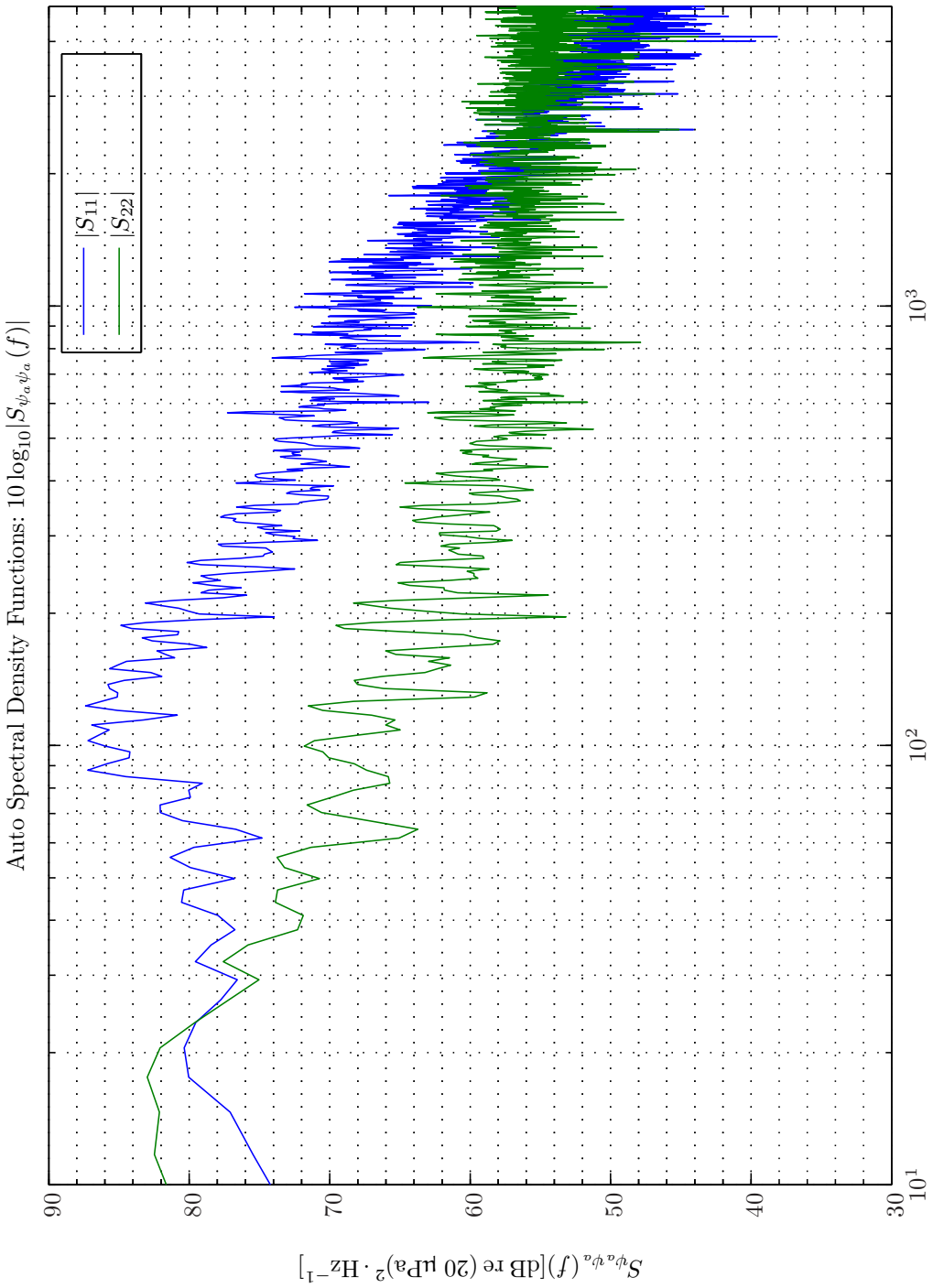

Sim 3.4.24: *Autospectral Density Functions:* **Statistical Data Analysis**: Single-Sided Modified Periodogram, f_s = 24 kHz, N_{DFT} = 8192, L_{DFT} = 6001, R_{DFT} = 3001, Hanning, Δf_m = 16 Hz, T_{DFT} = 0.25004 s, $N_{f,DFT}$ = 4097, Δf_{DFT} = 2.9297 Hz, K_{DFT} = 4; **Adaptive Filter** $\underset{\circ}{w}$: Wiener Hopf (M = 1024, $\alpha = 1e-005$, T_{WSS} = 0.**z**-domain); **Main:** f_s^0 = 192 kHz, f_s^1 = 24 kHz, $R_\downarrow^1 = \frac{1}{8}$ = 0.125, Elliptic LPF (f_s = 192 kHz, f_{pass} = 11 kHz, f_{stop} = 12 kHz, A_{pass} = 2 dB, A_{stop} = 40 dB), f_s^2 = 24 kHz, $R_\downarrow^2 = \frac{1}{1}$ = 1, Dummy; **Topology:** (Feedback, mFx, $N_e = 1, N_y = 1, N_p = 0, N_v = 2$); **Plants:** SysID/20080321T134130 ($g_{xy,\infty}^{1,1}$: (FIR : $M_{gxy}^{1,1}$ = 700), $g_{xy,\infty}^{1,2}$: (FIR : $M_{gxy}^{1,2}$ = 700), $g_{ey,\infty}^{1,1}$: (FIR : $M_{gey}^{1,1}$ = 120), $g_{py,\infty}^{1,1}$: (FIR : $M_{gpy}^{1,1}$ = 200), $g_{py,\infty}^{1,2}$: (FIR : $M_{gpy}^{1,2}$ = 200)); **Signals:** Time: 0 − 10 s. Refer to SigIDLaT.; **Scenario:** `MultipleSinusoidalsAddiativeNoiseFeedbackNx2Ne1Ny1Np0/20080408T070449`; *Channels:* #1 $\leftarrow d_1(t_1^1)$; #2 $\leftarrow e_1(t_1^1)$.;.

Simulation 3.4.25 on the next page for the **z**-domain WH filter. The plus 10 dB attenuation range spans the frequency range from 60 Hz up to 950 Hz, while noise amplification takes place below 25 Hz and above 2200 Hz.

The performance of the two variants of the $\alpha\gamma\Pi\epsilon$-APA is disappointing as no noise reduction is obtained. On the contrary, some noise amplification actually takes place for the $K = 4$ case. In order to check if this lack of performance can be attributed to the choice of a to large value of the step size parameter μ a new simulation with the following $\alpha\gamma\Pi\epsilon$-APA variants has been conducted:

1. $\alpha\gamma\Pi\epsilon$-APA $(M = 512, L_B = 1, \mu = 0.01, 0.05, 0.15, K = 1, 2, \Delta = 1, \alpha = 1e-5, \gamma = 1e-5, \Pi = 0, \epsilon = 1e-006, \breve{w} = 0, W_e = \mathrm{I})$;

The corresponding time-domain attenuation convergence results for these $\alpha\gamma\Pi\epsilon$-APA variants are depicted in Simulation 3.4.26 - 3.4.28 on pages 186–188.

Hence, except for the $K = 1$ case where the affine projection algorithm (APA) filter virtually become a normalized LMS (NLMS) filter (see section 8.5 on page 388) no ANR benefits are obtained even for very small values of the step size parameter. However, as will turn out from section 7.7 on page 333 the $\alpha\gamma\Pi\epsilon$-APA is indeed very suited for system identification. The two adaptive filtering modes, however, differ as also discussed in section 8.2 on page 373. In the system identification a RWN signal is often applied for which (see in chapter 8 on page 371) the eigenvalue spread of the regressor signal is unity ($\mathcal{X}(R_u) = 1$). In the AC case, however, we apply the modified-filtered-x (mFx) method (see chapter 6 on page 273) in order to take the presence of the plant into account. By filtering the colored disturbance signal by the dynamic plant the eigenvalue spread becomes as high as $\mathcal{X}(R_u) = 1.4e7$. This also explains why the FARLS variants converged substantially faster than the least-mean-squares (LMS) algorithm. In order to clarify on this seemingly contradictory behavior an intensive performance analysis that is reported in chapter 9 on page 417 has been initiated. From this analysis viz. Theorem 1 on page 451 we conclude that the performance of the $\alpha\gamma\Pi\epsilon$-APA depends on the eigenvalues, however, in a rather complicated way.

Finally, from a comparison of Simulation 3.4.8 with Simulation 3.4.15 and Simulation 3.4.14 with Simulation 3.4.25 we conclude that in general somewhat better AC performance is obtainable with the FFS than with the FBS in particular if we use a FIR filter of higher order for the **z**-domain WH filter and also consider to enforce the FBS to be robustly stable. However, the FBS provides the fastest convergence.

Example 3.4.3 (Confined Feedforward ANR System, Pink Noise, Helmet Model)**.** In this example we will use the parameters settings of the ordinary lumped element model in chapter 10 - 11 on pages 471–481 that lead to primary path and secondary path transfer functions that most closely resemble practical evidence, that is, the compliance-resistance-mass system constituted by $K_a = 26\ \mathrm{kN \cdot m^{-1}}$, $K_c = 100\ \mathrm{kN \cdot m^{-1}}$, $R_c = 80\ \mathrm{N \cdot s \cdot m^{-1}}$, $Z_l^A = (1 + \frac{2\omega_l}{\imath\omega})1.26\mathrm{e}7\ \mathrm{N \cdot s \cdot m^{-5}}$, $M_s = 0.16$ kg that in turn determine the passive attenuation and that jointly with the cross-over network parameters $Q_t = 1.6$, $f_t = 870$ Hz determine the active attenuation of the hearing protection device (HPD).

The time-domain attenuation for this simulated HPD is shown in Simulation 3.4.29 on page 189 for the same three investigated filters as in Example 3.4.1. Now, the **z**-domain WH method provides much better ANR performance ($\mathcal{A}^e(t) = 10 - 18$ dB) than the **t**-domain WH method ($\mathcal{A}^e(t) = -2 - 11$ dB) .

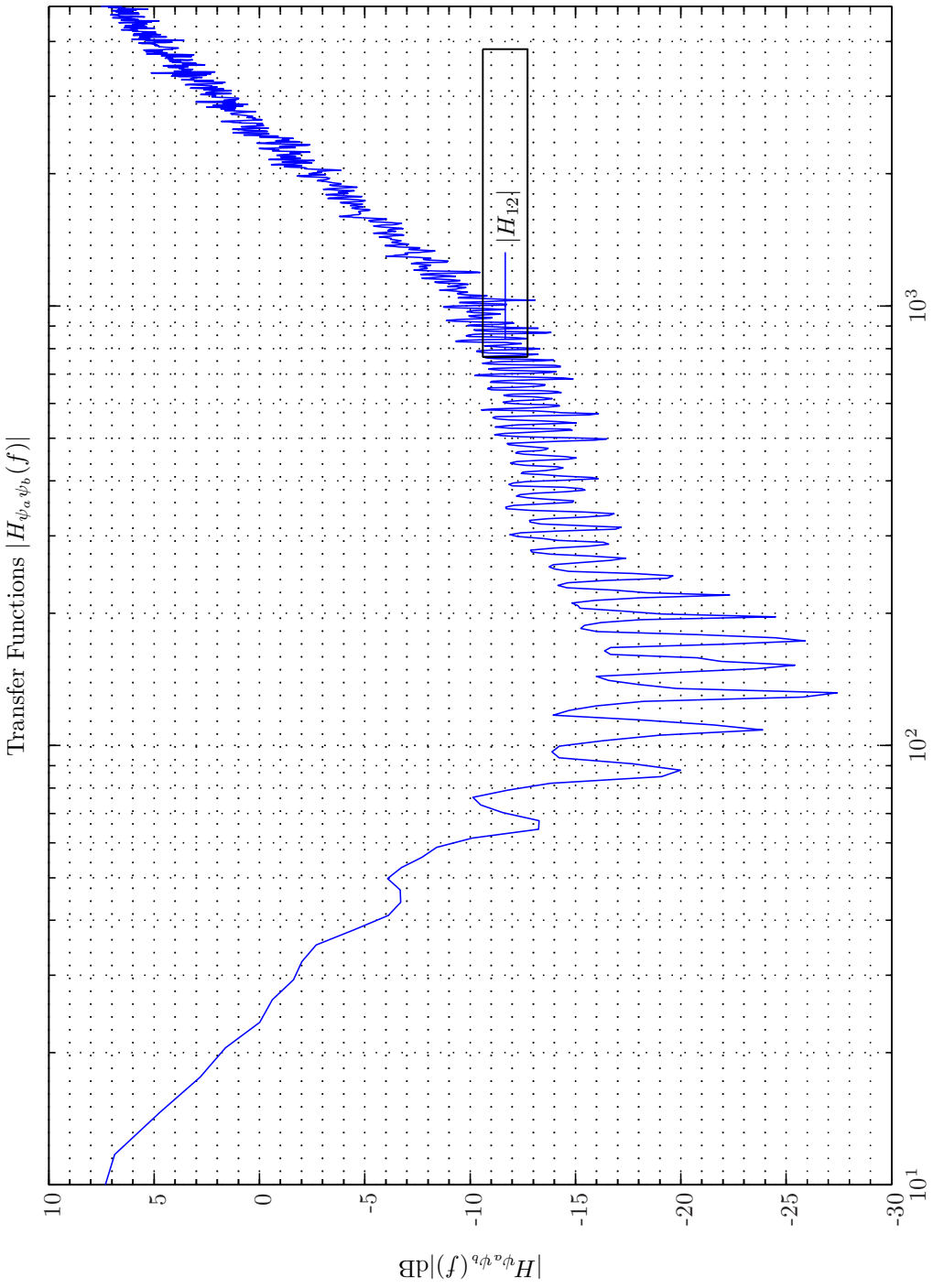

Sim 3.4.25: *Transfer Function, Magnitude:* $|H_{\psi_a\psi_b}(f)|$: **Statistical Data Analysis**: Single-Sided Modified Periodogram, $f_s = 24$ kHz, $N_{DFT} = 8192$, $L_{DFT} = 6001$, $R_{DFT} = 3001$, Hanning, $\Delta f_m = 16$ Hz, $T_{DFT} = 0.25004$ s, $N_{f,DFT} = 4097$, $\Delta f_{DFT} = 2.9297$ Hz, $K_{DFT} = 4$; **Adaptive Filter** $\underset{\circ}{w}$: Wiener Hopf ($M = 1024, \alpha = 1e-005, T_{WSS} = 0.$**z**-domain); **Main:** $f_s^0 = 192$ kHz, $f_s^1 = 24$ kHz, $R_\updownarrow^1 = \frac{1}{8} = 0.125$, Elliptic LPF ($f_s = 192$ kHz, $f_{pass} = 11$ kHz, $f_{stop} = 12$ kHz, $A_{pass} = 2$ dB, $A_{stop} = 40$ dB), $f_s^2 = 24$ kHz, $R_\updownarrow^2 = \frac{1}{1} = 1$, Dummy; **Topology:** (Feedback, mFx, $N_e = 1, N_y = 1, N_p = 0, N_v = 2$); **Plants:** SysID/20080321T134130 ($g_{xy,\infty}^{1,1}$: (FIR : $M_{gxy}^{1,2} = 700$), $g_{xy,\infty}^{1,2}$: (FIR : $M_{gxy}^{1,2} = 700$), $g_{ey,\infty}^{1,1}$: (FIR : $M_{gey}^{1,1} = 120$), $g_{py,\infty}^{1,1}$: (FIR : $M_{gpy}^{1,1} = 200$), $g_{py,\infty}^{1,2}$: (FIR : $M_{gpy}^{1,2} = 200$)); **Signals:** Time: $0 - 10$ s. Refer to SigIDLaT. ; **Scenario:** MultipleSinusoidalsAddiativeNoiseFeedbackNx2Ne1Ny1Np0/20080408T070449; *Channels:* #1 $\leftarrow d_1(t_1^1)$, #2 $\leftarrow e_1(t_1^1)$; .

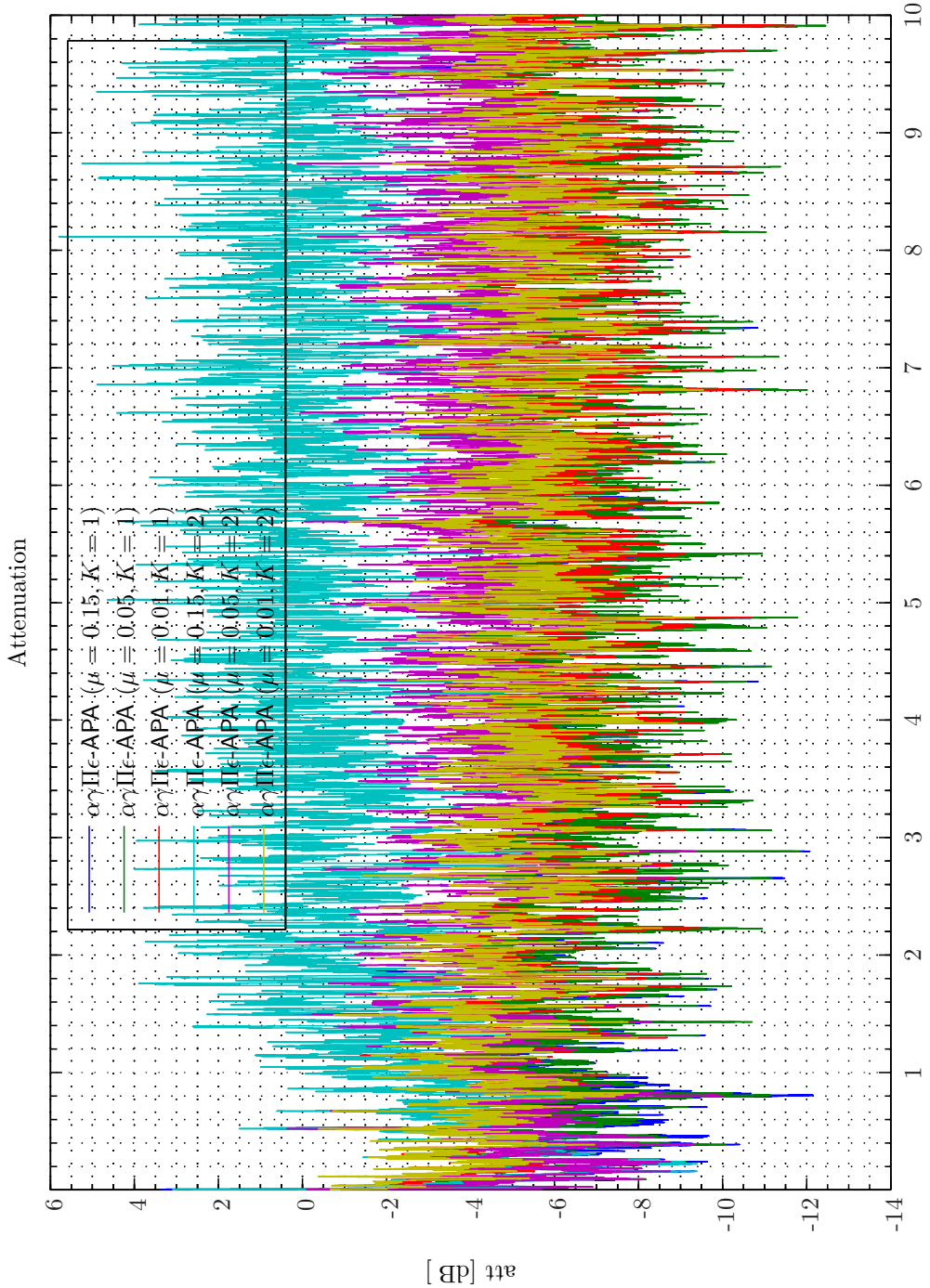

Sim 3.4.26: *Time-Domain: Attenuation.* **Adaptive Filter** y: $\overset{\circ}{y}^{1,1}$: $\alpha\gamma\Pi\epsilon$-APA ($M = 512, L_B = 1, \Delta = 1, \alpha = 1e-005, \gamma = 1e-005, \Pi = 0, \epsilon = 1e-006, \breve{w} = 0, W_e = 1$); **Main:** $f_s^0 = 192$ kHz, $f_s^1 = 24$ kHz, $R_\updownarrow^1 = \frac{1}{8} = 0.125$, Elliptic LPF ($f_s = 192$ kHz, $f_{pass} = 11$ kHz, $f_{stop} = 12$ kHz, $A_{pass} = 2$ dB, $A_{stop} = 40$ dB), $f_s^2 = 24$ kHz, $R_\updownarrow^2 = \frac{1}{1} = 1$, Dummy; **Topology:** (Feedback, mFx, $N_e = 1, N_y = 1, N_p = 0, N_v = 2$); **Plants:** SysID/20080321T134130 ($g_{xy,\infty}^{1,1}$: (FIR : $M_{gxy}^{1,1} = 700$), $g_{xy,\infty}^{1,2}$: (FIR : $M_{gxy}^{1,2} = 700$), $g_{ey,\infty}^{1,1}$: (FIR : $M_{gey}^{1,1} = 120$), $g_{py,\infty}^{1,1}$: (FIR : $M_{gpy}^{1,1} = 200$), $g_{py,\infty}^{1,2}$: (FIR : $M_{gpy}^{1,2} = 200$)); **Signals:** Time: $0 - 10$ s. Refer to SigIDLaT.; **Scenario:** `MultipleSinusoidalsAddiativeNoiseFeedbackNx2Ne1Ny1Np0/20080408T172720`.

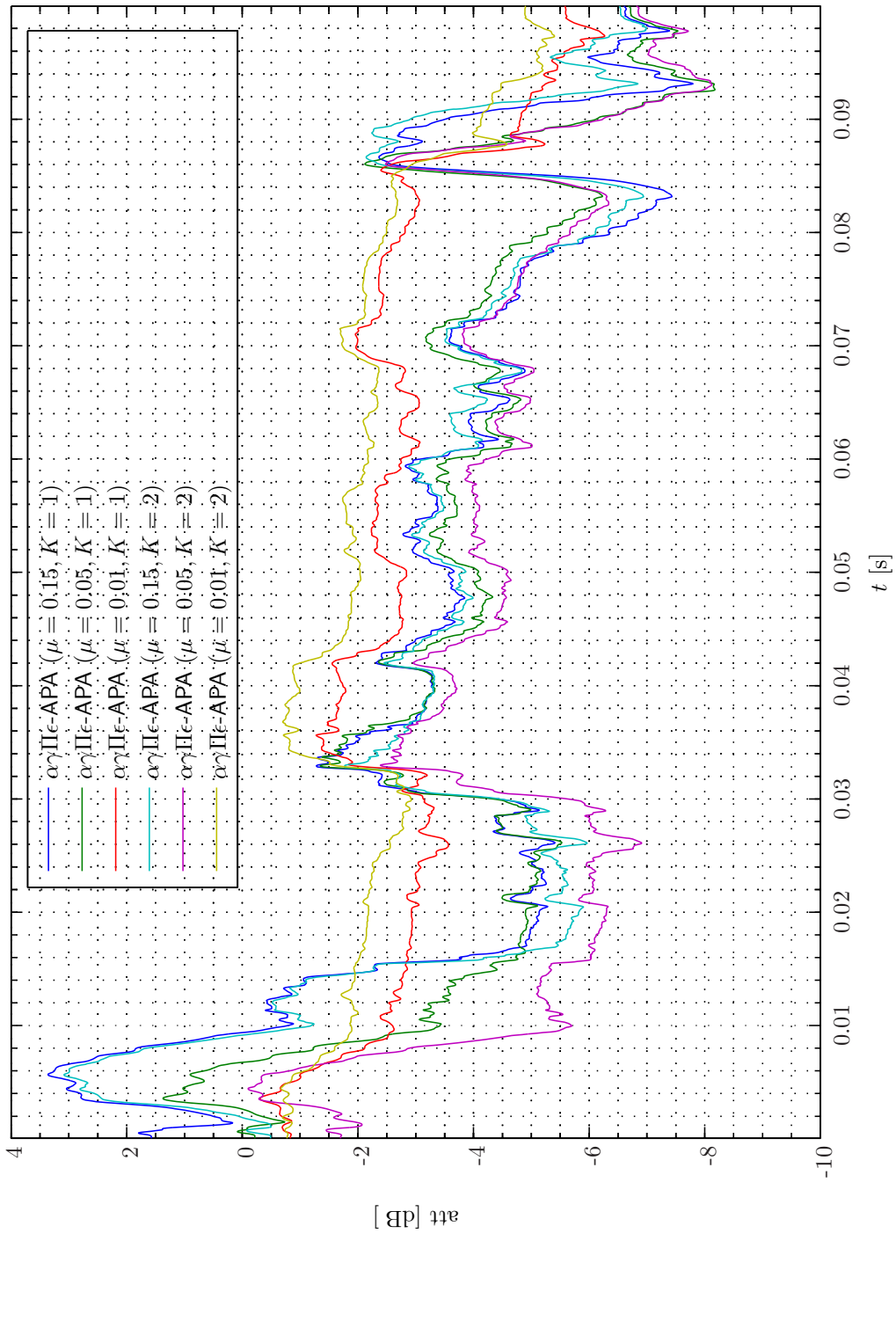

Sim 3.4.27: *Time-Domain: Attenuation Initial.* **Adaptive Filter** w: $\overset{\circ}{w}^{1,1}$: $\alpha\gamma\Pi\epsilon$-APA ($M = 512, L_B = 1, \Delta = 1, \alpha = 1e-005, \gamma = 1e-005, \Pi = 0, \epsilon = 1e-006, \breve{w} = 0, W_e = 1$); **Main:** $f_s^0 = 192$ kHz, $f_s^1 = 24$ kHz, $R_\downarrow^1 = \frac{1}{8} = 0.125$, Elliptic LPF ($f_s = 192$ kHz, $f_{pass} = 11$ kHz, $f_{stop} = 12$ kHz, $A_{pass} = 2$ dB, $A_{stop} = 40$ dB), $f_s^2 = 24$ kHz, $R_\downarrow^2 = \frac{1}{1} = 1$, Dummy; **Topology:** (Feedback, mFx, $N_e = 1, N_y = 1, N_p = 0, N_v = 2$); **Plants:** SysID/20080321T134130 ($g_{xy,\infty}^{1,1}$: (FIR : $M_{gxy}^{1,1} = 700$), $g_{xy,\infty}^{1,2}$: (FIR : $M_{gxy}^{1,2} = 700$), $g_{ey,\infty}^{1,1}$: (FIR : $M_{gey}^{1,1} = 120$), $g_{py,\infty}^{1,1}$: (FIR : $M_{gpy}^{1,1} = 200$), $g_{py,\infty}^{1,2}$: (FIR : $M_{gpy}^{1,2} = 200$)); **Signals:** Time: $0 - 10$ s. Refer to SigIDLaT. ; **Scenario:** `MultipleSinusoidalsAddiativeNoiseFeedbackNx2Ne1Ny1Np0/20080408T172720`.

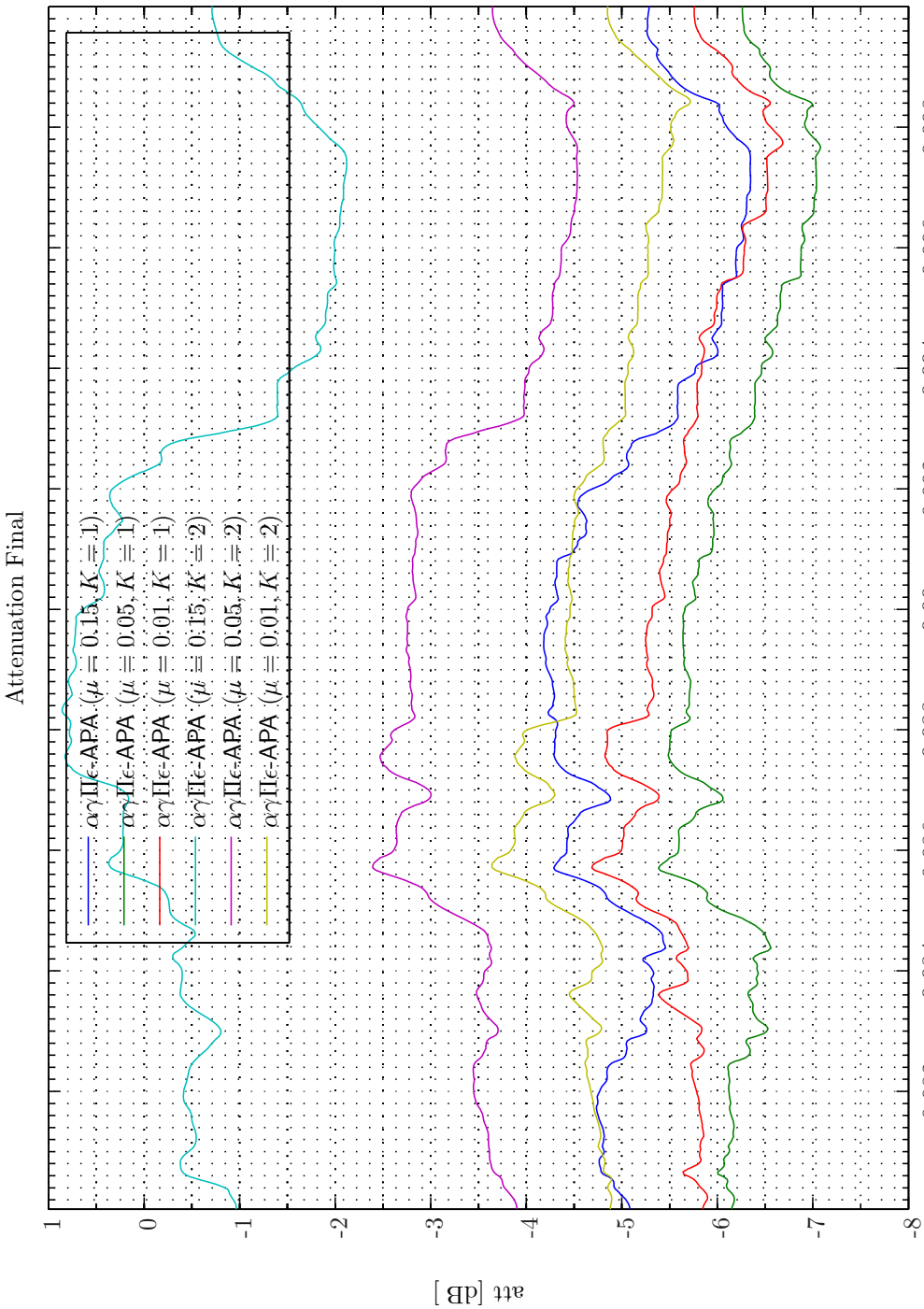

Sim 3.4.28: *Time-Domain: Attenuation Final.* **Adaptive Filter** w: $w^{1,1}_{\mathring{\circ}}$: $\alpha\gamma\Pi\epsilon$-APA ($M = 512, L_B = 1, \Delta = 1, \alpha = 1e-005, \gamma = 1e-005, \Pi = 0, \epsilon = 1e-006, \breve{w} = 0, W_e = 1$); **Main:** $f^0_s = 192$ kHz, $f^1_s = 24$ kHz, $R^1_{\updownarrow} = \frac{1}{8} = 0.125$, Elliptic LPF ($f_s = 192$ kHz, $f_{pass} = 11$ kHz, $f_{stop} = 12$ kHz, $A_{pass} = 2$ dB, $A_{stop} = 40$ dB), $f^2_s = 24$ kHz, $R^2_{\updownarrow} = \frac{1}{1} = 1$, Dummy; **Topology:** (Feedback, mFx, $N_e = 1, N_y = 1, N_p = 0, N_v = 2$); **Plants:** SysID/20080321T134130 ($g^{1,1}_{xy,\infty}$: (FIR : $M^{1,1}_{gxy} = 700$), $g^{1,2}_{xy,\infty}$: (FIR : $M^{1,2}_{gxy} = 700$), $g^{1,1}_{ey,\infty}$: (FIR : $M^{1,1}_{gey} = 120$), $g^{1,1}_{py,\infty}$: (FIR : $M^{1,1}_{gpy} = 200$), $g^{1,2}_{py,\infty}$: (FIR : $M^{1,2}_{gpy} = 200$)); **Signals:** Time: $0 - 10$ s. Refer to SigIDLaT.; **Scenario:** `MultipleSinusoidalsAddiativeNoiseFeedbackNx2Ne1Ny1Np0/20080408T172720`.

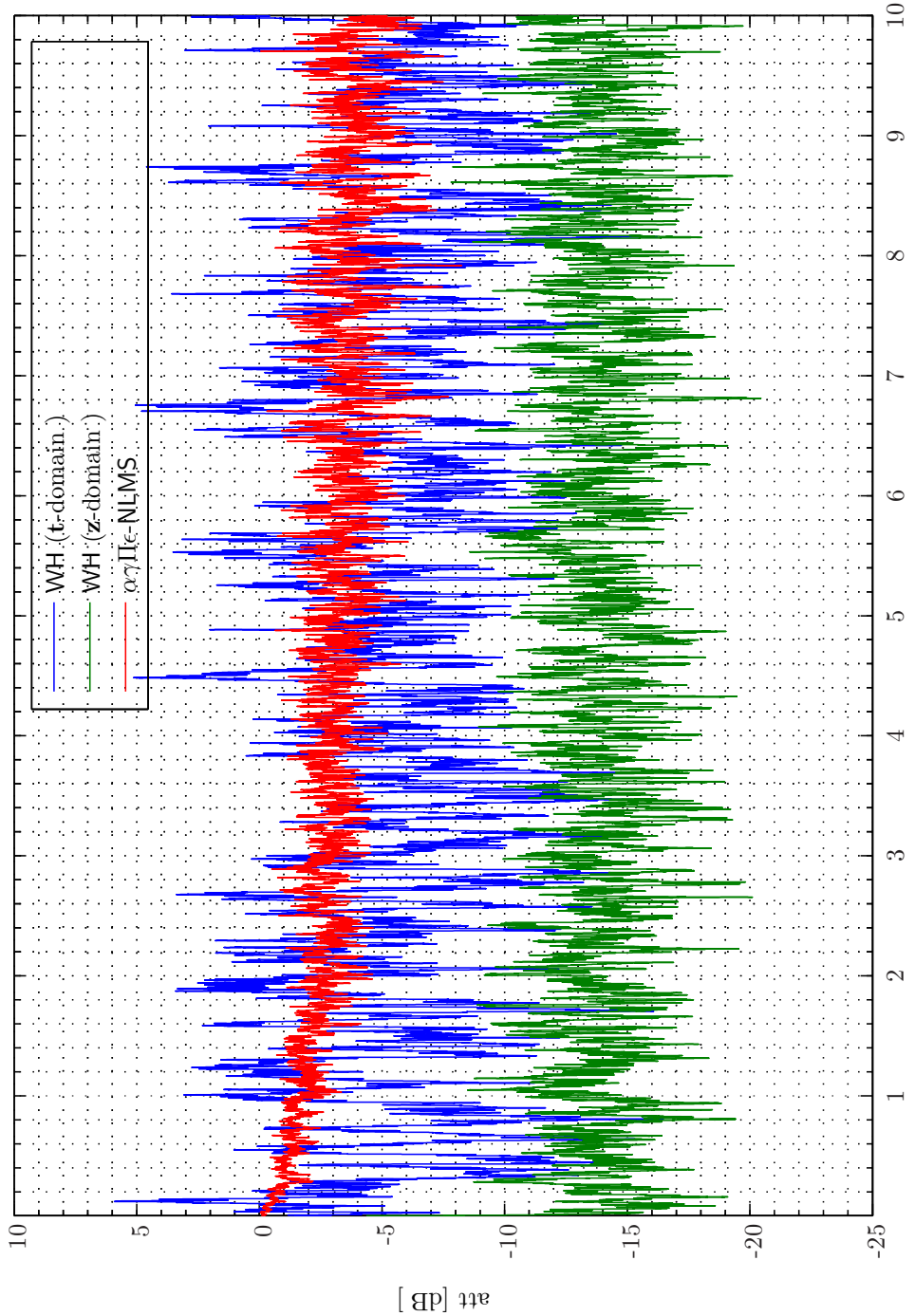

Sim 3.4.29: *Time-Domain: Attenuation.* **Adaptive Filter** $\underset{\sim}{w}$: $\underset{\sim}{w}^{1,1}$. WH ($M = 2048, \alpha = 1e-005, T_{WSS} = 0$);$\alpha\gamma\Pi\epsilon$-NLMS ($M = 1024, L_B = 1, \mu = 0.15, \alpha = 1e-005, \epsilon = 1e-006, T_{Eu} = 400$); **Main:** $f_s^0 = 192$ kHz, $f_s^1 = 24$ kHz, $R_{\downarrow}^1 = \frac{1}{8} = 0.125$, Elliptic LPF ($f_s = 192$ kHz, $f_{pass} = 11$ kHz, $f_{stop} = 12$ kHz, $A_{pass} = 2$ dB, $A_{stop} = 40$ dB), $f_s^2 = 24$ kHz, $R_{\downarrow}^2 = \frac{1}{1} = 1$, Dummy; **Topology:** (Feedforward, mFx, $N_x = 2, N_e = 1, N_y = 1, N_p = 0, N_v = 2$); **Plants:** ($g_{xy}^{1,1}$: (FIR : $M_{gxy}^{1,1} = 1$), $g_{xy}^{1,2}$: (FIR : $M_{gxy}^{1,2} = 1$), $g_{ey}^{1,1}$: Closed-Back Headset System Shaw Thiessen: ($f_s = 24$ kHz, $K_a = 26\ \mathrm{N \cdot m^{-1}}, K_c = 100\ \mathrm{kN \cdot m^{-1}}, f_0 = 141.236$ Hz, $R_c = 80\ \mathrm{N \cdot s \cdot m^{-1}}, M_s = 0.16$ kg, $R_l^A = 1.26\mathrm{e}+007\ \mathrm{N \cdot s \cdot m^{-5}}, f_t = 870$ Hz, $R_{Et} = 2\ \Omega, Q_t = 1.6$ (FIR : $M_{gey}^{1,1} = 97$)); **Signals:** Time: $0 - 10$ s. Refer to SigIDLaT. ; **Scenario:** `MultipleSinusoidalsAddiativeNoiseFeedforwardNx2Ne1Ny1Np0/20080309T233655`.

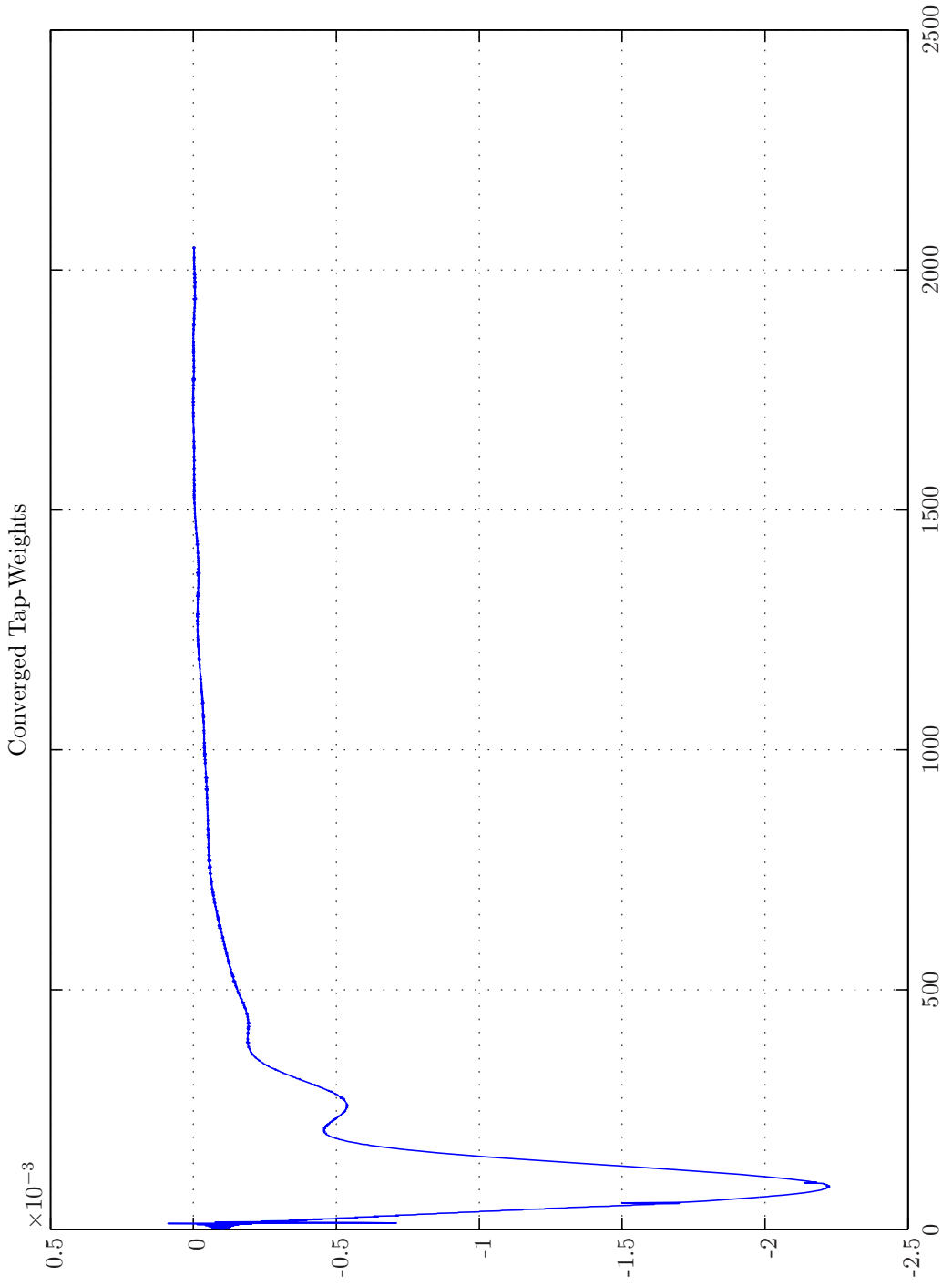

Sim 3.4.30: *Converged Tap-weights.* **Adaptive Filter** $\underset{\sim}{w}$: $\underset{\sim}{w}^{1,1}$: Wiener Hopf ($M = 2048, \alpha = 1e-005, T_{WSS} = 0$,**z**-domain); **Main:** $f_s^0 = 192$ kHz, $f_s^1 = 24$ kHz, $R_\updownarrow^1 = \frac{1}{8} = 0.125$, Elliptic LPF ($f_s = 192$ kHz, $f_{pass} = 11$ kHz, $f_{stop} = 12$ kHz, $A_{pass} = 2$ dB, $A_{stop} = 40$ dB), $f_s^2 = 24$ kHz, $R_\updownarrow^2 = \frac{1}{1} = 1$, Dummy; **Topology:** (Feedforward, mFx, $N_x = 2, N_e = 1, N_y = 1, N_p = 0, N_v = 2$); **Plants:** $(g_{xy}^{1,1}$: (FIR : $M_{gxy}^{1,1} = 1)$, $g_{xy}^{1,2}$: (FIR : $M_{gxy}^{1,2} = 1)$, $g_{ey}^{1,1}$: Closed-Back Headset System Shaw Thiessen: ($f_s = 24$ kHz, $K_a = 26$ N $\cdot$ s $\cdot$ m^{-1}, $K_c = 100$ kN $\cdot$ m^{-1}, $f_0 = 141.236$ Hz, $R_c = 80$ N $\cdot$ s $\cdot$ m^{-1}, $M_s = 0.16$ kg, $R_l^A = 1.26\text{e}+007$ N $\cdot$ s $\cdot$ m^{-5}, $f_t = 870$ Hz, $R_{Et} = 2\ \Omega$, $Q_t = 1.6$ (FIR : $M_{gey}^{1,1} = 97$)); **Signals:** Time: $0 - 10$ s. Refer to SigIDLaT. ; **Scenario:** `MultipleSinusoidalsAddiativeNoiseFeedforwardNx2Ne1Ny1Np0/20080309T233655`.

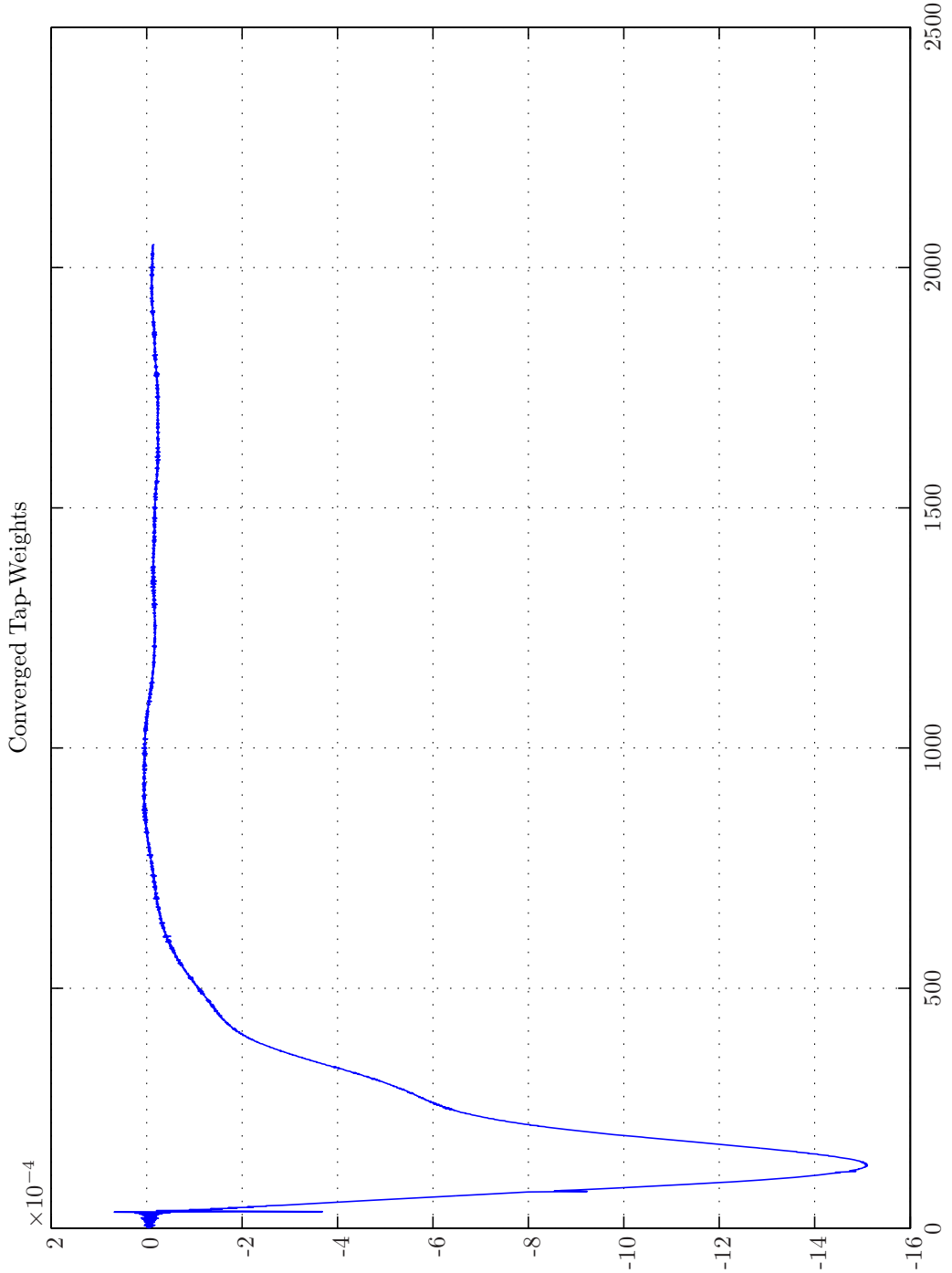

Sim 3.4.31: *Converged Tap-weights.* **Adaptive Filter** $\underset{\sim}{w}$: $\underset{\sim}{w}^{2,1}$: Wiener Hopf ($M = 2048, \alpha = 1e-005, T_{WSS} = 0$,**z**-domain); **Main:** $f_s^0 = 192$ kHz, $f_s^1 = 24$ kHz, $R_{\updownarrow}^1 = \frac{1}{8} = 0.125$, Elliptic LPF ($f_s = 192$ kHz, $f_{pass} = 11$ kHz, $f_{stop} = 12$ kHz, $A_{pass} = 2$ dB, $A_{stop} = 40$ dB), $f_s^2 = 24$ kHz, $R_{\updownarrow}^2 = \frac{1}{1} = 1$, Dummy; **Topology:** (Feedforward, mFx, $N_x = 2, N_e = 1, N_y = 1, N_p = 0, N_v = 2$); **Plants:** ($g_{xy}^{1,1}$: (FIR : $M_{gxy}^{1,1} = 1$), $g_{xy}^{1,2}$: (FIR : $M_{gxy}^{1,2} = 1$), $g_{ey}^{1,1}$: Closed-Back Headset System Shaw Thiessen: ($f_s = 24$ kHz, $K_a = 26\ \mathrm{N \cdot m^{-1}}$, $K_c = 100\ \mathrm{kN \cdot m^{-1}}$, $f_0 = 141.236$ Hz, $R_c = 80\ \mathrm{N \cdot s \cdot m^{-1}}$, $M_s = 0.16$ kg, $R_t^A = 1.26\mathrm{e}+007\ \mathrm{N \cdot s \cdot m^{-5}}$, $f_t = 870$ Hz, $R_{Et} = 2\ \Omega$, $Q_t = 1.6$ (FIR : $M_{gey}^{1,1} = 97$)); **Signals:** Time: 0 − 10 s. Refer to SigIDLaT. ; **Scenario:** `MultipleSinusoidalsAddiativeNoiseFeedforwardNx2Ne1Ny1Np0/20080309T233655`.

The condition $\underset{\sim}{w}_{M_w-1} \approx 0$ is now also satisfied for the **z**-domain WH method as seen in Simulation 3.4.30 - 3.4.31 . For the the **z**-domain WH method the weight vector $\underset{\sim}{w}^{1,1}$ is somewhat similar to Simulation 3.4.11 in Example 3.4.1, while $\underset{\sim}{w}^{2,1}$ deviates substantially from Simulation 3.4.12. Moreover, we appreciate that both $\underset{\sim}{w}^{1,1}$ and $\underset{\sim}{w}^{2,1}$ are very slowly varying and may very likely be more efficiently represented by Lageurre/Kautz filters described in Appendix K on page 759.

The frequency-domain attenuation of the **z**-domain based WH filter is depicted in Simulation 3.4.33 on page 194. The plus 25 dB attenuation range now extent from 10 Hz up to 200 Hz. Owing to the large discrepancy between the group delay of the real plant depicted in Simulation 11.5.10 on page 506 and that by the plant model in Simulation 11.4.3 on page 488 below 200 Hz the filter now provides considerably more low frequency attenuation than in Example 3.4.1 on page 157. However, this higher low-frequency ANR attenuation occurs at the expense of medium frequency range $400 - 1500$ Hz where less than 10 dB attenuation is achieved. Referring to Simulation 11.4.4 - 11.4.5 on pages 490–491 this lack of ANR capabilities can be explained by the very large group delays of the plant in the frequency range $700 - 1000$ Hz. In the high-frequency range, however, 10 dB attenuation is provided by the FFS up to 5000 Hz.

Example 3.4.4 (Feedback ANR System, Pink Noise, Helmet Model)**.** For the same helmet model as in Example 3.4.3 the time-domain attenuation performance obtained by the FBS is shown in Simulation 3.4.34 - 3.4.36 on pages 195–197.

The two WH methods investigated provide almost identical ANR performance in agreement with our discussion in Example 3.4.2. Hence, $\mathcal{A}^e(t) = 18 \pm 4$ dB which is 10 dB better than in Example 3.4.2. The $\alpha\gamma\Pi\epsilon$-APA following a very short initial convergence then departs from the optimal settings. This behavior is most pronounced for the $K = 4$ variant. It is also observed that for the FARLS with $\lambda = 0.99999$ is showing signs of instability. The ANR capabilities in the frequency-domain of the feedback topology is exhibited in Simulation 3.4.37 on page 198 and in comparison with the transfer function in Simulation 3.4.25 on page 185 in Example 3.4.2 it is readily observed that a much higher attenuation is achieved. Moreover, noise amplification only takes places for frequencies above 4 kHz.

From this example and Example 3.4.1 - 3.4.3 we appreciate that the secondary path is of profound importance for the achievable ANR performance. Hence, although a fairly close match between measurements and simulation data of a lumped-element model is reported in chapter 10 - 11 on pages 471–481 this similarity does not completely hold when the achievable ANR performance is being considered.

Finally, from a comparison of Simulation 3.4.29 with Simulation 3.4.34 and Simulation 3.4.33 with Simulation 3.4.37 we conclude that from ignoring requirements on robust stability then the best ANR performance is delivered by the FBS in the frequency range $20 - 1500$ Hz while the FFS provides the best solution at frequencies above 1500 Hz.

Example 3.4.5 (Confined Feedforward ANR System, Pink Noise Optimized Helmet)**.** In this example we want to demonstrate that by increasing the damping of the 2nd order compliance-resistance-mass system and by lowering the Q-factor of the cross-over network in the HPD a better ANR performance is achievable. Hence, we increase the resistance of the cushion from $R_c = 80\ \mathrm{N \cdot s \cdot m^{-1}}$ to $R_c = 120\ \mathrm{N \cdot s \cdot m^{-1}}$ and decrease the Q-factor of the cross-over network from $Q_t = 1.6$ to $Q_t = 0.5$.

The time-domain attenuation for this simulated HPD are shown in Simulation 3.4.38 on page 199. By comparison with similar results for the non-optimized HPD in Example 3.4.3 viz. Simulation 3.4.29 on page 189 it is readily observed that the $\alpha\gamma\Pi\epsilon$-NLMS algorithm converges faster and that in particular the **t**-domain WH filter provides better results.

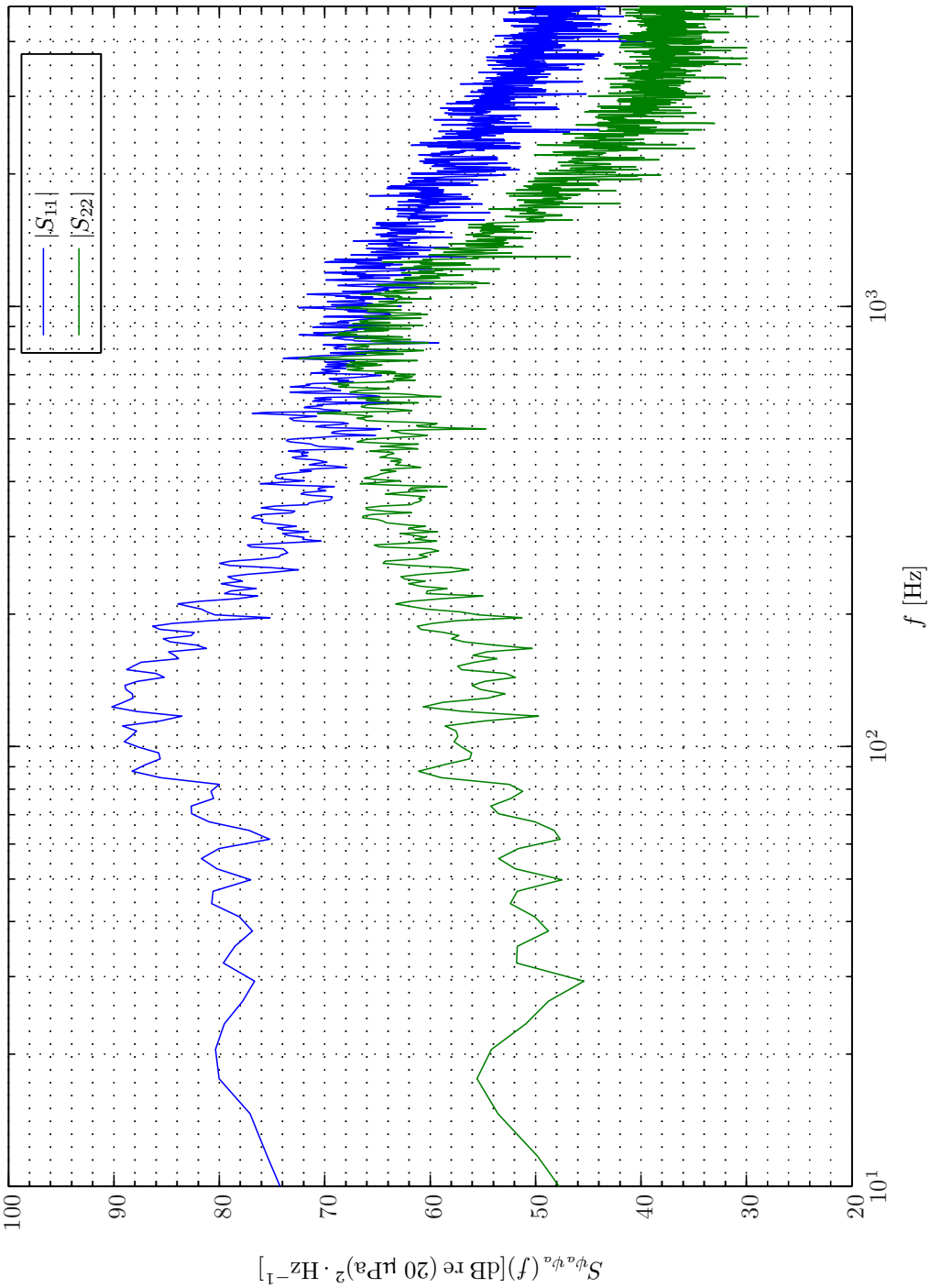

Sim 3.4.32: *Autospectral Density Functions*: **Statistical Data Analysis**: Single-Sided Modified Periodogram, $f_s = 24$ kHz, $N_{DFT} = 8192$, $L_{DFT} = 6001$, $R_{DFT} = 3001$, Hanning, $\Delta f_m = 16$ Hz, $T_{DFT} = 0.25004$ s, $N_{f,DFT} = 4097$, $\Delta f_{DFT} = 2.9297$ Hz, $K_{DFT} = 4$; **Adaptive Filter** $\underset{\sim}{w}$: Wiener Hopf ($M = 2048$, $\alpha = 1e-005$, $T_{WSS} = 0.\mathbf{z}$-domain); **Main:** $f_s^0 = 192$ kHz, $f_s^1 = 24$ kHz, $R_\downarrow^1 = \frac{1}{8} = 0.125$, Elliptic LPF ($f_s = 192$ kHz, $f_{pass} = 11$ kHz, $f_{stop} = 12$ kHz, $A_{pass} = 2$ dB, $A_{stop} = 40$ dB), $f_s^2 = 24$ kHz, $R_\downarrow^2 = \frac{1}{1} = 1$, Dummy; **Topology:** (Feedforward, mFx, $N_x = 2, N_c = 1, N_y = 1, N_p = 0, N_v = 2$); **Plants:** ($g_{xy}^{1,1}$: (FIR : $M_{gxy}^{1,1} = 1$), $g_{xy}^{1,2}$: (FIR : $M_{gxy}^{1,2} = 1$), $g_{ey}^{1,1}$: Closed-Back Headset System Shaw Thiessen: ($f_s = 24$ kHz, $K_a = 26$ N $\cdot$ m^{-1}, $K_c = 100$ kN $\cdot$ m^{-1}, $f_0 = 141.236$ Hz, $R_c = 80$ N $\cdot$ s $\cdot$ m^{-1}, $M_s = 0.16$ kg, $R_t^A = 1.26\text{e}+007$ N $\cdot$ s $\cdot$ m^{-5}, $f_t = 870$ Hz, $R_{Et} = 2\,\Omega, Q_t = 1.6$ (FIR : $M_{gey}^{1,1} = 97$)); **Signals:** Time: $0-10$ s. Refer to SigIDLaT. ; **Scenario:** `MultipleSinusoidalsAddiativeNoiseFeedforwardNx2Ne1Ny1Np0/20080309T233655`; *Channels:* #1 $\leftarrow d_1(t_1^1)$, #2 $\leftarrow e_1(t_1^1)$.; .

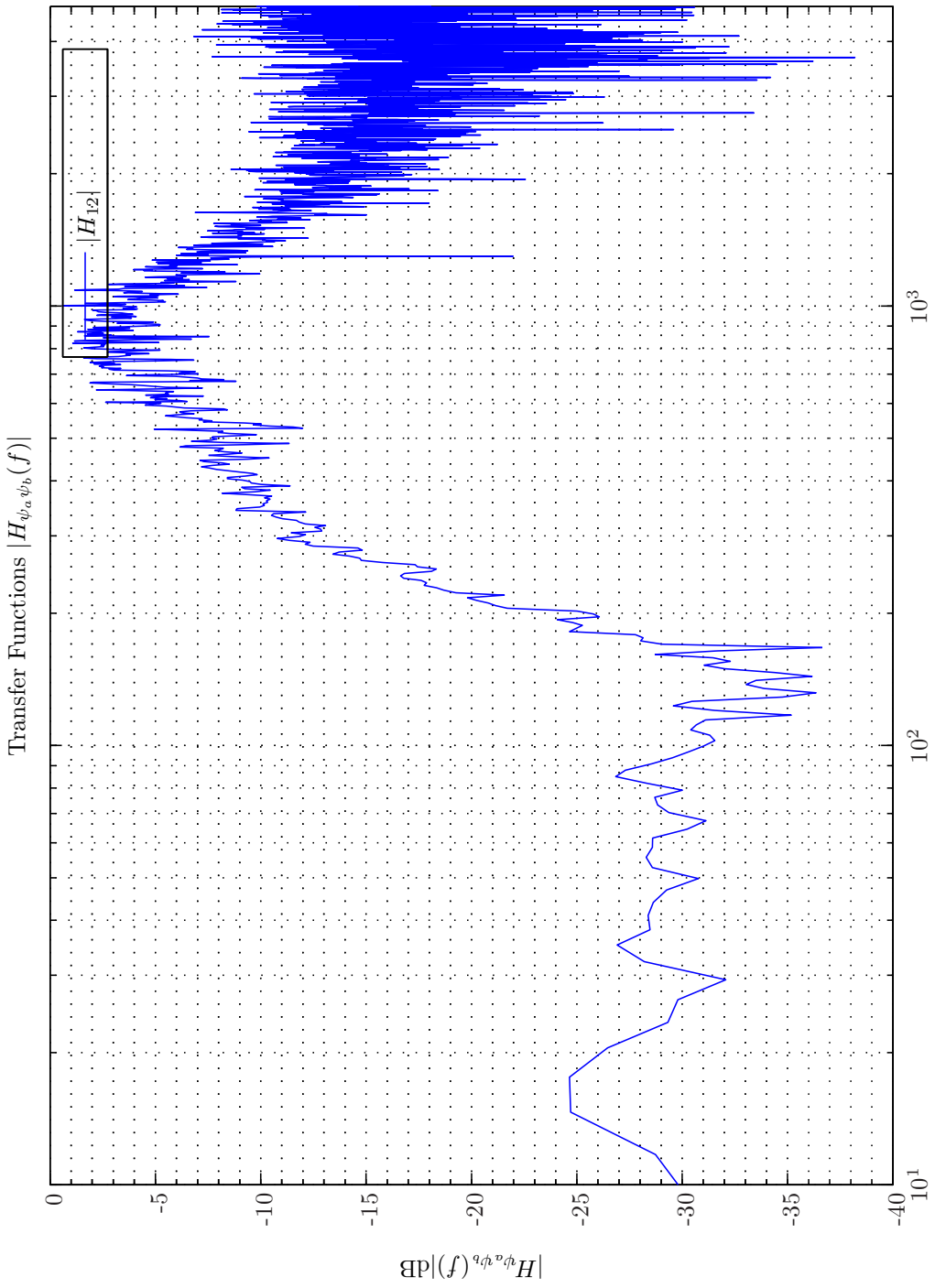

Sim 3.4.33: *Transfer Function, Magnitude:* $|H_{\psi_a\psi_b}(f)|$: **Statistical Data Analysis:** Single-Sided Modified Periodogram, $f_s = 24$ kHz, $N_{DFT} = 8192$, $L_{DFT} = 6001$, $R_{DFT} = 3001$, Hanning, $\Delta f_m = 16$ Hz, $T_{DFT} = 0.25004$ s, $N_{f,DFT} = 4097$, $\Delta f_{DFT} = 2.9297$ Hz, $K_{DFT} = 4$; **Adaptive Filter** $\underset{\sim}{w}$: Wiener Hopf ($M = 2048, \alpha = 1e-005, T_{WSS} = 0$,**z**-domain); **Main:** $f_s^0 = 192$ kHz, $f_s^1 = 24$ kHz, $R_\updownarrow^1 = \frac{1}{8} = 0.125$, Elliptic LPF ($f_s = 192$ kHz, $f_{pass} = 11$ kHz, $f_{stop} = 12$ kHz, $A_{pass} = 2$ dB, $A_{stop} = 40$ dB), $f_s^2 = 24$ kHz, $R_\updownarrow^2 = \frac{1}{1} = 1$, Dummy; **Topology:** (Feedforward, mFx, $N_x = 2, N_e = 1, N_y = 1, N_p = 0, N_v = 2$); **Plants:** $(g_{xy}^{1,1}$: (FIR : $M_{gxy}^{1,1} = 1$), $g_{xy}^{1,2}$: (FIR : $M_{gxy}^{1,2} = 1$), $g_{ey}^{1,1}$: Closed-Back Headset System Shaw Thiessen: ($f_s = 24$ kHz, $K_a = 26$ N $\cdot$ m^{-1}, $K_c = 100$ kN $\cdot$ m^{-1}, $f_0 = 141.236$ Hz, $R_c = 80$ N $\cdot$ s $\cdot$ m^{-1}, $M_s = 0.16$ kg, $R_l^A = 1.26e+007$ N $\cdot$ s $\cdot$ m^{-5}, $f_t = 870$ Hz, $R_{Et} = 2\ \Omega, Q_t = 1.6$ (FIR : $M_{gey}^{1,1} = 97$)); **Signals:** Time: $0 - 10$ s. Refer to SigIDLaT. ; **Scenario:** `MultipleSinusoidalsAddiativeNoiseFeedforwardNx2Ne1Ny1Np0/20080309T233655`; *Channels:* #1 $\leftarrow d_1(t_1^1)$, #2 $\leftarrow e_1(t_1^1)$: .

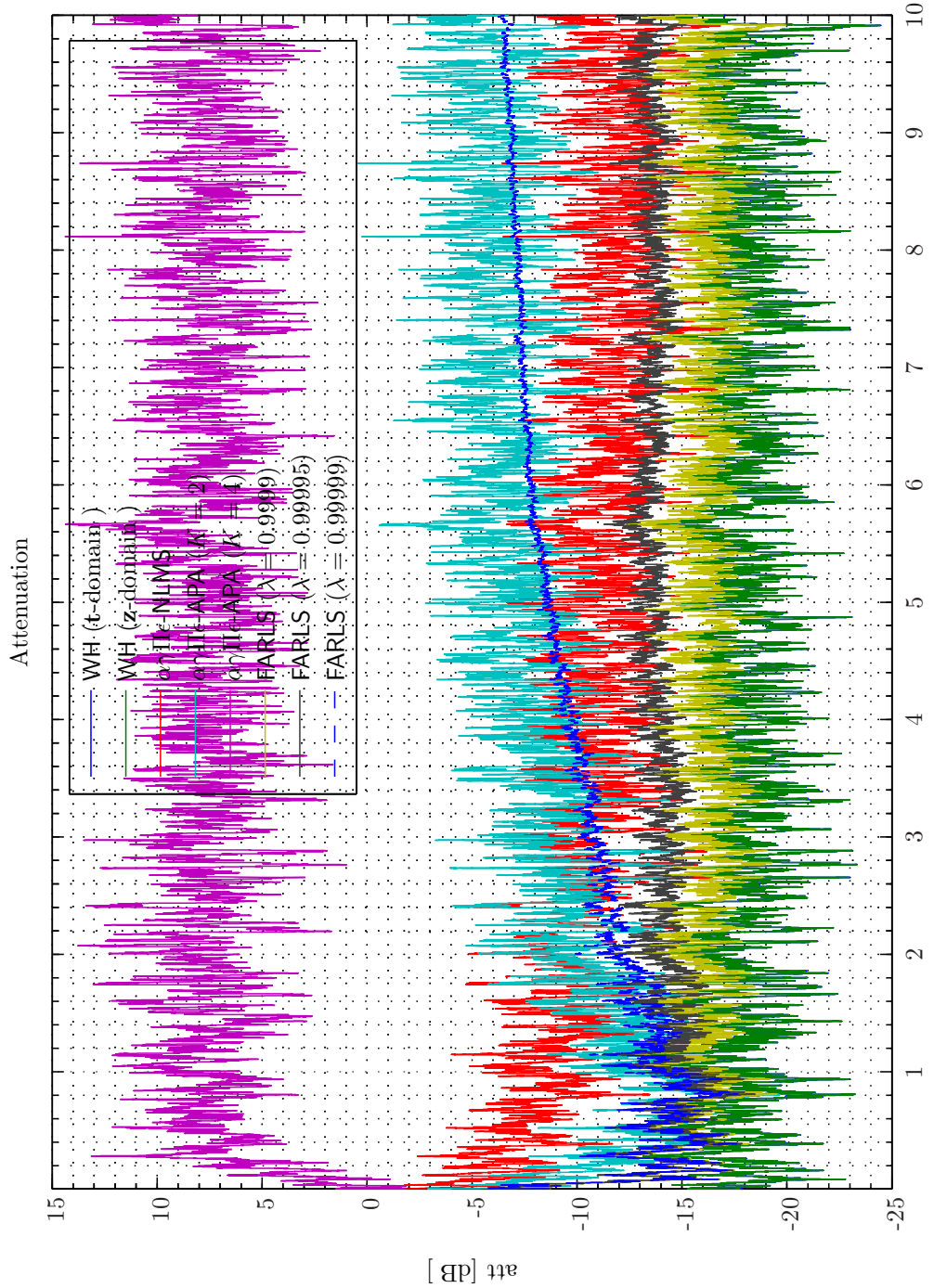

Sim 3.4.34: *Time-Domain: Attenuation.* **Adaptive Filter** $\underset{\circ}{w}^{1,1}$: WH ($M = 1024, \alpha = 1e-005, T_{WSS} = 0$);αγΠe-NLMS ($M = 512, L_B = 1, \mu = 0.15, \alpha = 1e-005, \epsilon = 1e-006, T_{Eu} = 400$);αγΠe-APA ($M = 512, L_B = 1, \mu = 0.15, \Delta = 1, \alpha = 1e-005, \gamma = 1e-005, \Pi = 0, \epsilon = 1e-006, \breve{w} = 0, W_e = 1$);FARLS ($M = 512, L_B = 1, \eta = 0.125, \alpha = 1e-005, T_{SW} = 0$, Calc = 1); **Main:** $f_s^0 = 192$ kHz, $f_s^1 = 24$ kHz, $R_\updownarrow^1 = \frac{1}{8} = 0.125$, Elliptic LPF ($f_s = 192$ kHz, $f_{pass} = 11$ kHz, $f_{stop} = 12$ kHz, $A_{pass} = 2$ dB, $A_{stop} = 40$ dB), $f_s^2 = 24$ kHz, $R_\updownarrow^2 = \frac{1}{1} = 1$, Dummy; **Topology:** (Feedback, mFx, $N_e = 1, N_y = 1, N_p = 0, N_v = 2$); **Plants:** $(g_{xy}^{1,1}$: (FIR : $M_{gxy}^{1,1} = 1$), $g_{xy}^{1,2}$: (FIR : $M_{gxy}^{1,2} = 1$), $g_{ey}^{1,1}$: Closed-Back Headset System Shaw Thiessen: ($f_s = 24$ kHz, $K_a = 26$ N $\cdot$ m^{-1}, $K_c = 100$ kN $\cdot$ m^{-1}, $f_0 = 141.236$ Hz, $R_c = 80$ N $\cdot$ s $\cdot$ m^{-1}, $M_s = 0.16$ kg, $R_l^A = 1.26e+007$ N $\cdot$ s $\cdot$ m^{-5}, $f_t = 870$ Hz, $R_{Et} = 2\ \Omega$, $Q_t = 1.6$ (FIR : $M_{gey}^{1,1} = 97$)); **Signals:** Time: $0 - 10$ s. Refer to SigIDLaT. ; **Scenario:** `MultipleSinusoidalsAddiativeNoiseFeedbackNx2Ne1Ny1Np0/20080409T160241`.

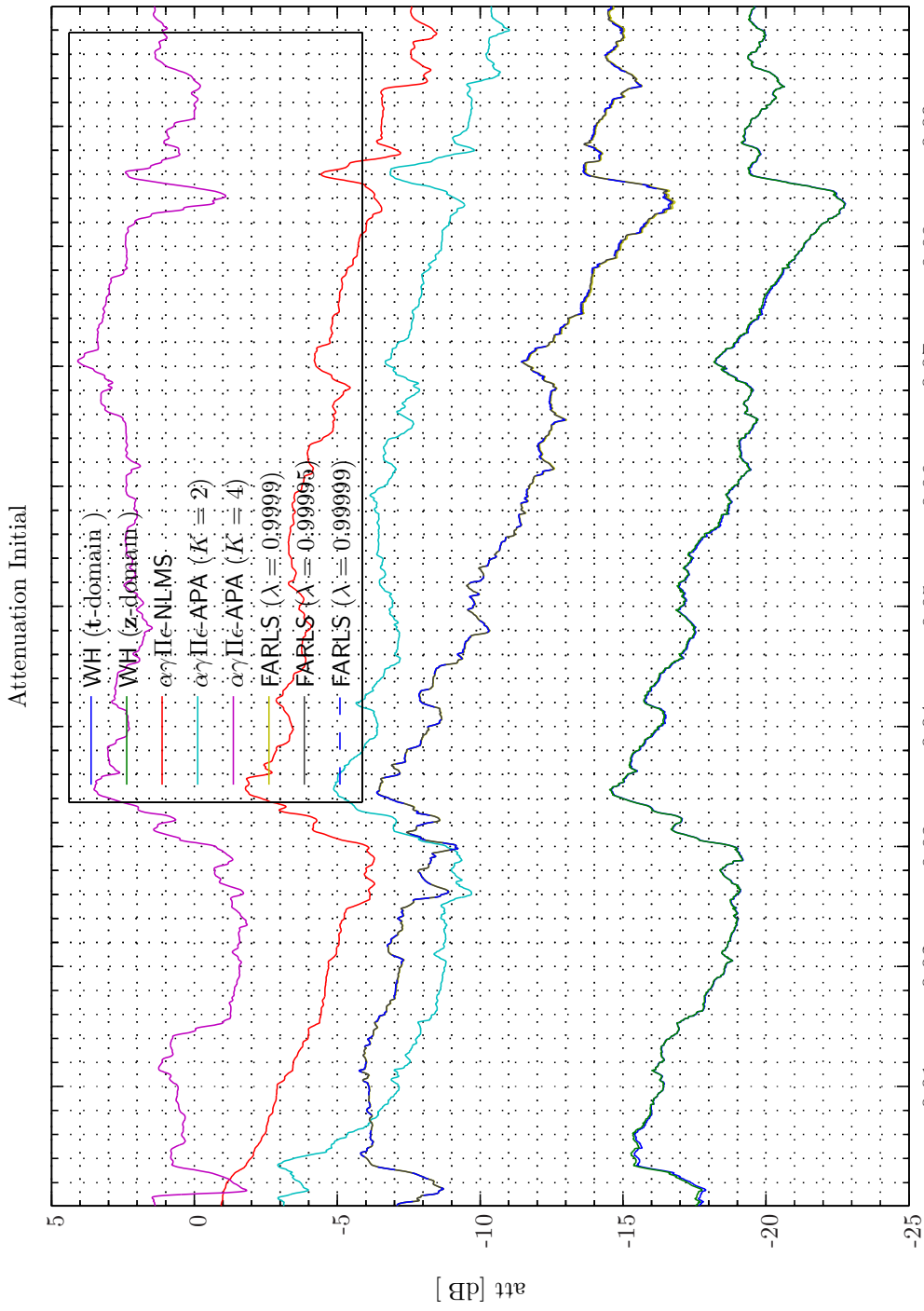

Sim 3.4.35: *Time-Domain: Attenuation Initial.* **Adaptive Filter** $\overset{w}{\circlearrowleft}$: $w^{1,1}$: WH ($M = 1024, \alpha = 1e-005, T_{WSS} = 0$);αγΠϵ-NLMS ($M = 512, L_B = 1, \mu = 0.15, \alpha = 1e-006, \epsilon = 1e-005, L_B = 1, \mu = 0.15, \Delta = 1, \alpha = 1e-005, \gamma = 1e-005, \Pi = 0, \epsilon = 1e-006, \ddot{w} = 0, W_e = 1$);FARLS ($M = 512, L_B = 1, \eta = 0.125, \alpha = 1e-005, T_{SW} = 0$, Calc = 1); **Main:** $f_s^0 = 192$ kHz, $f_s^1 = 24$ kHz, $R_{\updownarrow}^1 = \frac{1}{8} = 0.125$, Elliptic LPF ($f_s = 192$ kHz, $f_{pass} = 11$ kHz, $f_{stop} = 12$ kHz, $A_{pass} = 2$ dB, $A_{stop} = 40$ dB), $f_s^2 = 24$ kHz, $R_{\updownarrow}^2 = \frac{1}{1} = 1$, Dummy; **Topology:** (Feedback, mFx, $N_e = 1, N_y = 1, N_p = 0, N_v = 2$); **Plants:** $(g_{xy}^{1,1}$: (FIR : $M_{gxy}^{1,1} = 1$), $g_{xy}^{1,2}$: (FIR : $M_{gxy}^{1,2} = 1$), $g_{ey}^{1,1}$: Closed-Back Headset System Shaw Thiessen: ($f_s = 24$ kHz, $K_a = 26$ N · m^{-1}, $K_c = 100$ kN · m^{-1}, $f_0 = 141.236$ Hz, $R_c = 80$ N · s · m^{-1}, $M_s = 0.16$ kg, $R_l^A = 1.26e+007$ N · s · m^{-5}, $f_t = 870$ Hz, $R_{Et} = 2\ \Omega$, $Q_t = 1.6$ (FIR : $M_{gey}^{1,1} = 97$)); **Signals:** Time: $0 - 10$ s. Refer to SigIDLaT. ; **Scenario:** `MultipleSinusoidalsAddiativeNoiseFeedbackNx2Ne1Ny1Np0/20080409T160241`.

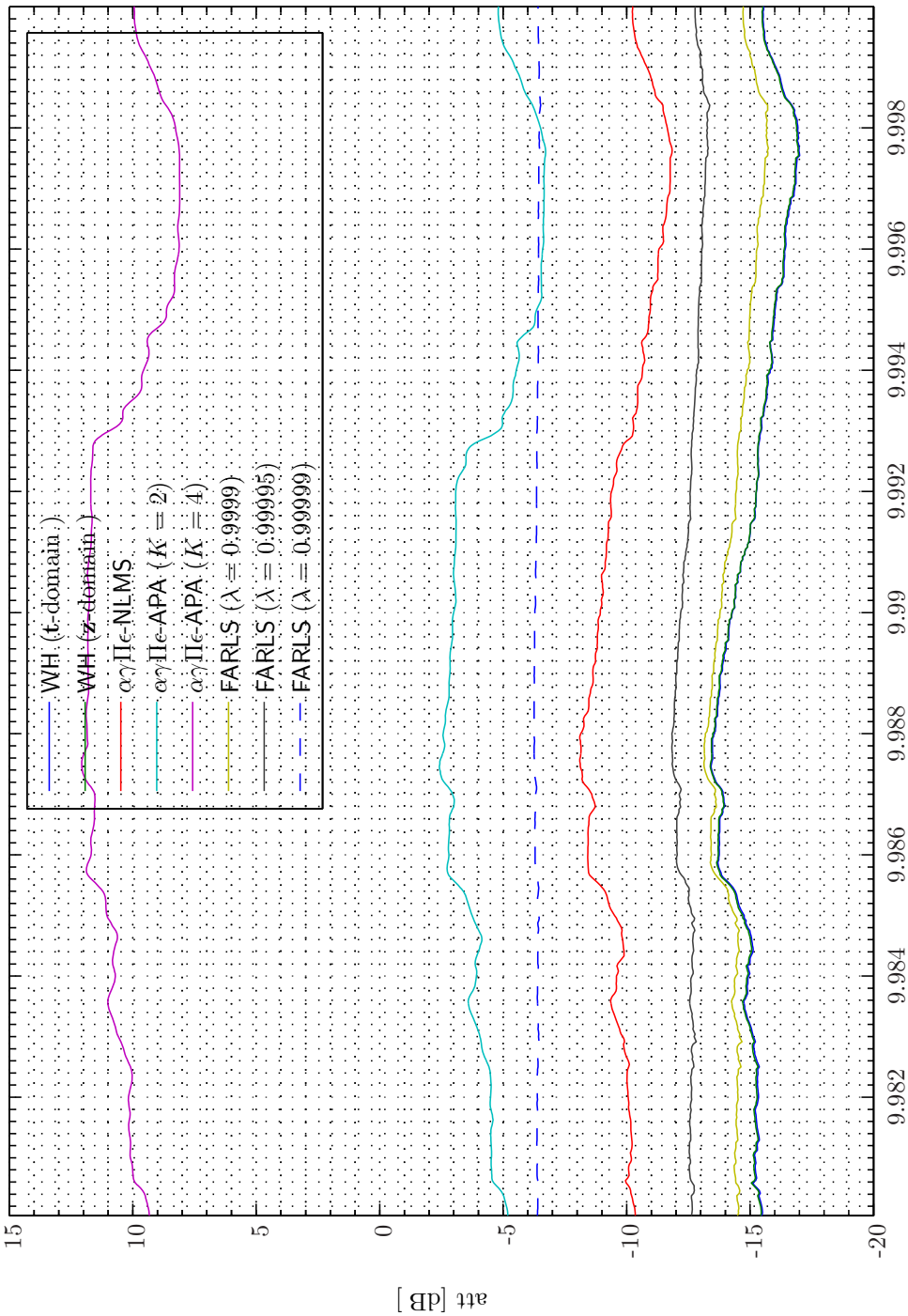

Sim 3.4.36: *Time-Domain: Attenuation Final.* **Adaptive Filter** w: $\overset{\circ}{w}^{1,1}$: WH ($M = 1024, \alpha = 1e-005, T_{WSS} = 0$);αγΠε-NLMS ($M = 512, L_B = 1, \mu = 0.15, \alpha = 1e-005, \epsilon = 1e-006, T_{Eu} = 400$);αγΠε-APA ($M = 512, L_B = 1, \mu = 0.15, \Delta = 1, \alpha = 1e-005, \gamma = 1e-005, \Pi = 0, \epsilon = 1e-006, \breve{w} = 0, W_e = 1$);FARLS ($M = 512, L_B = 1, \eta = 0.125, \alpha = 1e-005, T_{SW} = 0$, Calc = 1); **Main:** $f_s^0 = 192$ kHz, $f_s^1 = 24$ kHz, $R_\updownarrow^1 = \frac{1}{8} = 0.125$, Elliptic LPF ($f_s = 192$ kHz, $f_{pass} = 11$ kHz, $f_{stop} = 12$ kHz, $A_{pass} = 2$ dB, $A_{stop} = 40$ dB), $f_s^2 = 24$ kHz, $R_\updownarrow^2 = \frac{1}{1} = 1$, Dummy; **Topology:** (Feedback, mFx, $N_e = 1, N_y = 1, N_p = 0, N_v = 2$); **Plants:** $(g_{xy}^{1,1}$: (FIR : $M_{gxy}^{1,1} = 1$), $g_{xy}^{1,2}$: (FIR : $M_{gxy}^{1,2} = 1$), $g_{ey}^{1,1}$: Closed-Back Headset System Shaw Thiessen: ($f_s = 24$ kHz, $K_a = 26$ N · m^{-1}, $K_c = 100$ kN · m^{-1}, $f_0 = 141.236$ Hz, $R_c = 80$ N · s · m^{-1}, $M_s = 0.16$ kg, $R_l^A = 1.26e+007$ N · s · m^{-5}, $f_t = 870$ Hz, $R_{Et} = 2\,\Omega$, $Q_t = 1.6$ (FIR : $M_{gey}^{1,1} = 97$)); **Signals:** Time: 0 − 10 s. Refer to SigIDLaT. ; **Scenario:** `MultipleSinusoidalsAddiativeNoiseFeedbackNx2Ne1Ny1Np0/20080409T160241`.

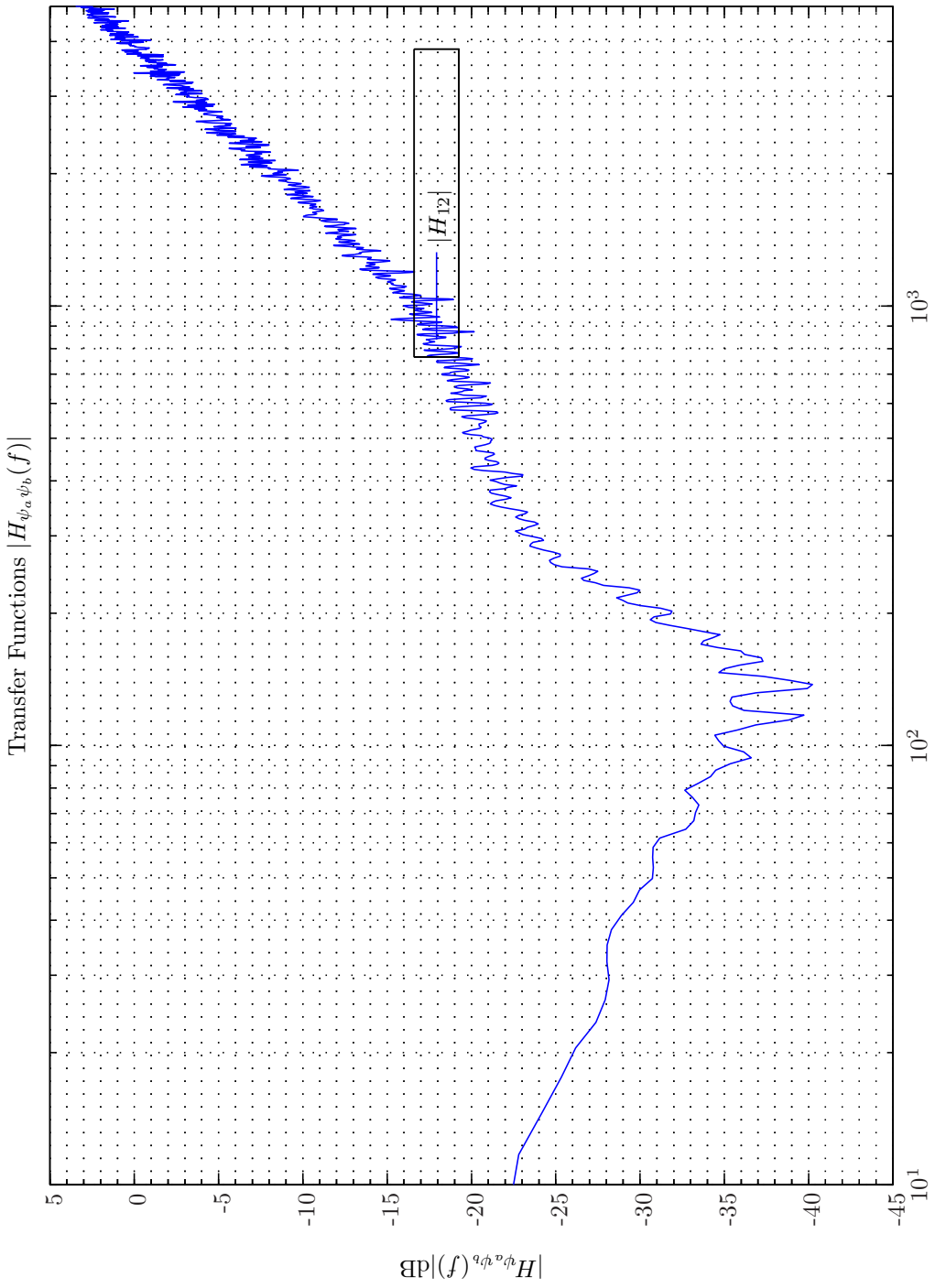

Sim 3.4.37: *Transfer Function, Magnitude*: $|H_{\psi_a\psi_b}(f)|$: **Statistical Data Analysis**: Single-Sided Modified Periodogram, $f_s = 24$ kHz, $N_{DFT} = 8192$, $L_{DFT} = 6001$, $R_{DFT} = 3001$, Hanning, $\Delta f_m = 16$ Hz, $T_{DFT} = 0.25004$ s, $N_{f,DFT} = 4097$, $\Delta f_{DFT} = 2.9297$ Hz, $K_{DFT} = 4$; **Adaptive Filter** $\overset{w}{\circlearrowleft}$: Wiener Hopf ($M = 1024, \alpha = 1e-005, T_{WSS} = 0.$**z**-domain); **Main:** $f_s^0 = 192$ kHz, $f_s^1 = 24$ kHz, $R_\updownarrow^1 = \frac{1}{8} = 0.125$, Elliptic LPF ($f_s = 192$ kHz, $f_{pass} = 11$ kHz, $f_{stop} = 12$ kHz, $A_{pass} = 2$ dB, $A_{stop} = 40$ dB), $f_s^2 = 24$ kHz, $R_\updownarrow^2 = \frac{1}{1} = 1$, Dummy; **Topology:** (Feedback, mFx, $N_e = 1, N_y = 1, N_p = 0, N_v = 2$); **Plants:** ($g_{xy}^{1,1}$: (FIR : $M_{gxy}^{1,1} = 1$), $g_{xy}^{1,2}$: (FIR : $M_{gxy}^{1,2} = 1$), $g_{ey}^{1,1}$: Closed-Back Headset System Shaw Thiessen: ($f_s = 24$ kHz, $K_a = 26$ N $\cdot$ m^{-1}, $K_c = 100$ kN $\cdot$ m^{-1}, $f_0 = 141.236$ Hz, $R_c = 80$ N $\cdot$ s $\cdot$ m^{-1}, $M_s = 0.16$ kg, $R_l^A = 1.26e+007$ N $\cdot$ s $\cdot$ m^{-5}, $f_t = 870$ Hz, $R_{Et} = 2\,\Omega, Q_t = 1.6$ (FIR : $M_{gey}^{1,1} = 97$)); **Signals:** Time: $0 - 10$ s. Refer to SigIDLaT. ; **Scenario:** `MultipleSinusoidalsAddiativeNoiseFeedbackNx2Ne1Ny1Np0/20080409T160241`; *Channels:* #1 $\leftarrow d_1(t_1^1)$, #2 $\leftarrow e_1(t_1^1)$; .

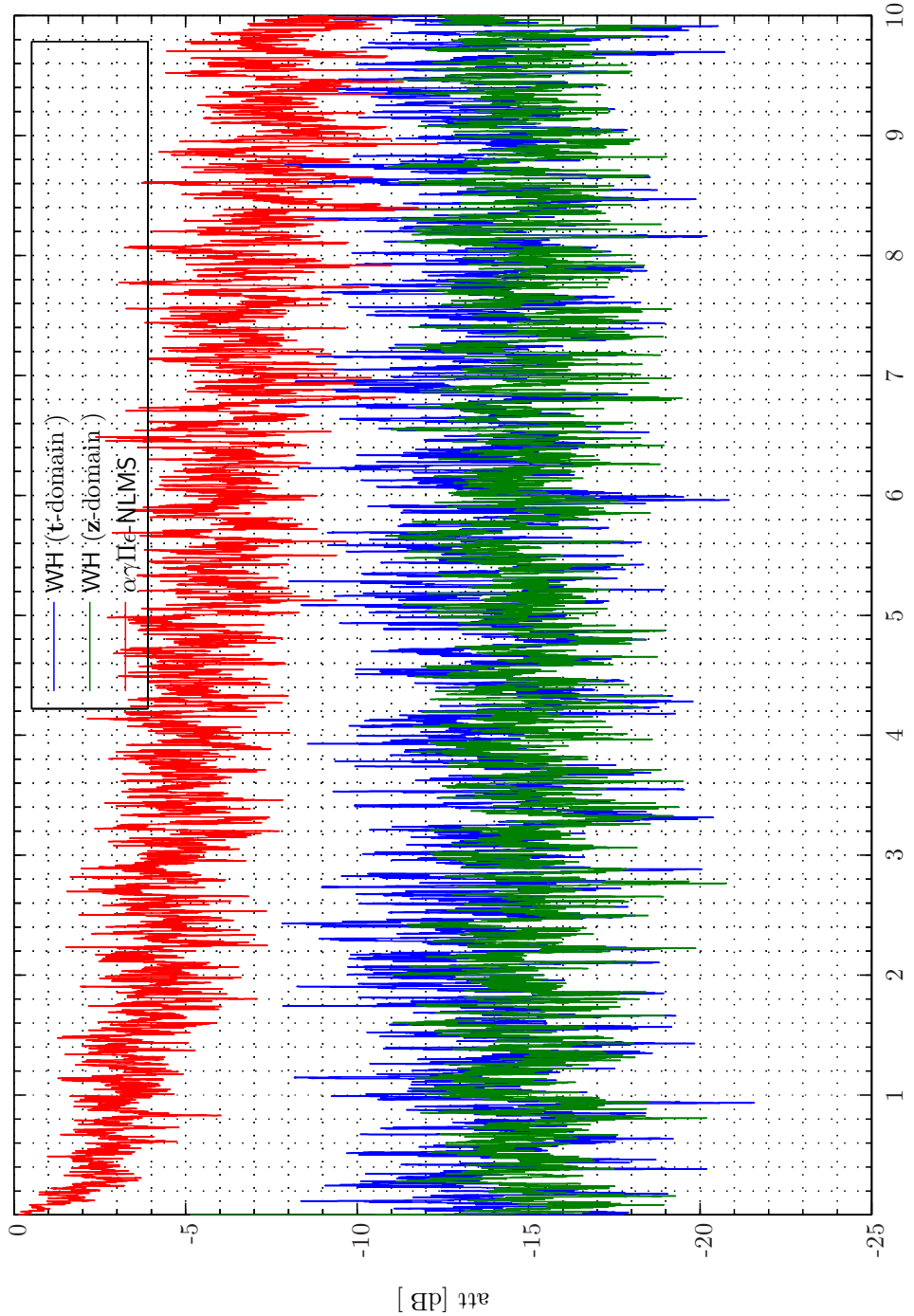

Sim 3.4.38: *Time-Domain: Attenuation.* **Adaptive Filter** $\underset{\sim}{w}$: $\underset{\sim}{w}^{1,1}$. WH ($M = 2048, \alpha = 1e-005, T_{WSS} = 0$);$\alpha\gamma\Pi\epsilon$-NLMS ($M = 1024, L_B = 1, \mu = 0.15, \alpha = 1e-005, \epsilon = 1e-006, T_{Eu} = 400$); **Main:** $f_s^0 = 192$ kHz, $f_s^1 = 24$ kHz, $R_\downarrow^1 = \frac{1}{8} = 0.125$, Elliptic LPF ($f_s = 192$ kHz, $f_{pass} = 11$ kHz, $f_{stop} = 12$ kHz, $A_{pass} = 2$ dB, $A_{stop} = 40$ dB), $f_s^2 = 24$ kHz, $R_\updownarrow^2 = \frac{1}{1} = 1$, Dummy; **Topology:** (Feedforward, mFx, $N_x = 2, N_e = 1, N_y = 1, N_p = 0, N_v = 2$); **Plants:** ($g_{xy}^{1,1}$: (FIR : $M_{gxy}^{1,1} = 1$), $g_{xy}^{1,2}$: (FIR : $M_{gxy}^{1,2} = 1$), $g_{ey}^{1,1}$: Closed-Back Headset System Shaw Thiessen: ($f_s = 24$ kHz, $K_a = 26$ N $\cdot$ m^{-1}, $K_c = 100$ kN $\cdot$ m^{-1}, $f_0 = 141.236$ Hz, $R_c = 120$ N $\cdot$ s $\cdot$ m^{-1}, $M_s = 0.16$ kg, $R_l^A = 1.26e+007$ N $\cdot$ s $\cdot$ m^{-5}, $f_t = 870$ Hz, $R_{Et} = 2\ \Omega, Q_t = 0.5$ (FIR : $M_{gey}^{1,1} = 97$)); **Signals:** Time: $0-10$ s. Refer to SigIDLaT.; **Scenario:** `MultipleSinusoidalsAddiativeNoiseFeedforwardNx2Ne1Ny1Np0/20080309T202849`.

The optimal weight vectors for the **z**-domain WH method depicted in Simulation 3.4.39 - 3.4.40 exhibit a very smooth pattern and is therefore amendable to Lageurre/Kautz filter implementation.

The frequency-domain attenuation of the **z**-domain based WH filter is depicted in Simulation 3.4.41 on page 203. Also by comparison with similar results for the non-optimized earcup system in Example 3.4.3 viz. Simulation 3.4.33 on page 194 we appreciate that the reduction in the group delay (see chapter 11 on page 481) manifests itself in terms of a higher noise attenuation in the frequency range $300 - 1500$ Hz.

Example 3.4.6 (Feedback ANR System, Pink Noise Optimized Helmet)**.** In this example will we examine the ANR FBS solution for the same disturbance signal as in the preceding examples. In Simulation 3.4.42 on page 204 the time-domain attenuation convergence is shown.

The two WH methods investigated provide almost identical ANR performance ($\mathcal{A}^e(t) = 13 - 21$ dB) while $\mathcal{A}^e(t) = 9 - 14$ dB for the $\alpha\gamma\Pi\epsilon$-NLMS algorithm. Moreover, owing to the fewer weights involved ($M_{\overset{\circ}{w}^{1,1}} = 512$ while $M_{\underset{\sim}{w}^{1,1}} = M_{\underset{\sim}{w}^{2,1}} = M_w = 2048$ in the preceding FFS examples) the $\alpha\gamma\Pi\epsilon$-NLMS algorithm converges within 2.5 s.

The low-frequency ANR capabilities of the feedback topology is clearly exhibited in Simulation 3.4.43 on page 205. By comparison with similar results for the non-optimized earcup system in Example 3.4.4 viz. Simulation 3.4.37 on page 198 we appreciate that by lowering the Q-factor of the compliance-resistance-mass system the attenution barely increases for the FBS in contrast to the improvements obtained from such hardware change in the FFS. However, a less resonant design is in favor when considering the gain magins of the plant.

The reason why the **t**-domain WH filter and the **z**-domain WH filter yield similar ANR performance in the FBS but not for the FFS is explained in Example 3.4.2.

Finally, by comparing Simulation 3.4.38 with Simulation 3.4.42 and Simulation 3.4.41 with Simulation 3.4.43 leads us to essentially the same conclusions regarding the relative performance of FFS and a FBS solution as made in Example 3.4.4.

3.5 Spectral Factorization Method

In this section we will present two methods for spectral factorization for ACSV applications.

3.5.1 Cepstral Method

In AC applications the spectral factorization of scalar-valued reference signals or scalar-valued secondary paths is often accomplished by using the *cepstral* method [10, Ch. 10] that works in the discrete frequency-domain and involves the *Hilbert transform*. The cepstral method has been used in the chapter in the examples to divide the secondary paths into their all-pass component and minimum-phase components. The basic spectral factor is obtained from

$$L_+(k) = \exp\Big(\text{fft}\,\Big(c(n)\,\text{ifft}\ln\big(S_{xx}(k)\big)\Big)\Big), \tag{3.5.1}$$

where $c(n) = 0$ for $n < 0$, $c(n) = \frac{1}{2}$ for $n = 0$ and $c(n) = 1$ for $n > 0$. Unfortunately, to the author's best knowledge no extension of the cepstral method to the vector-valued signals is yet

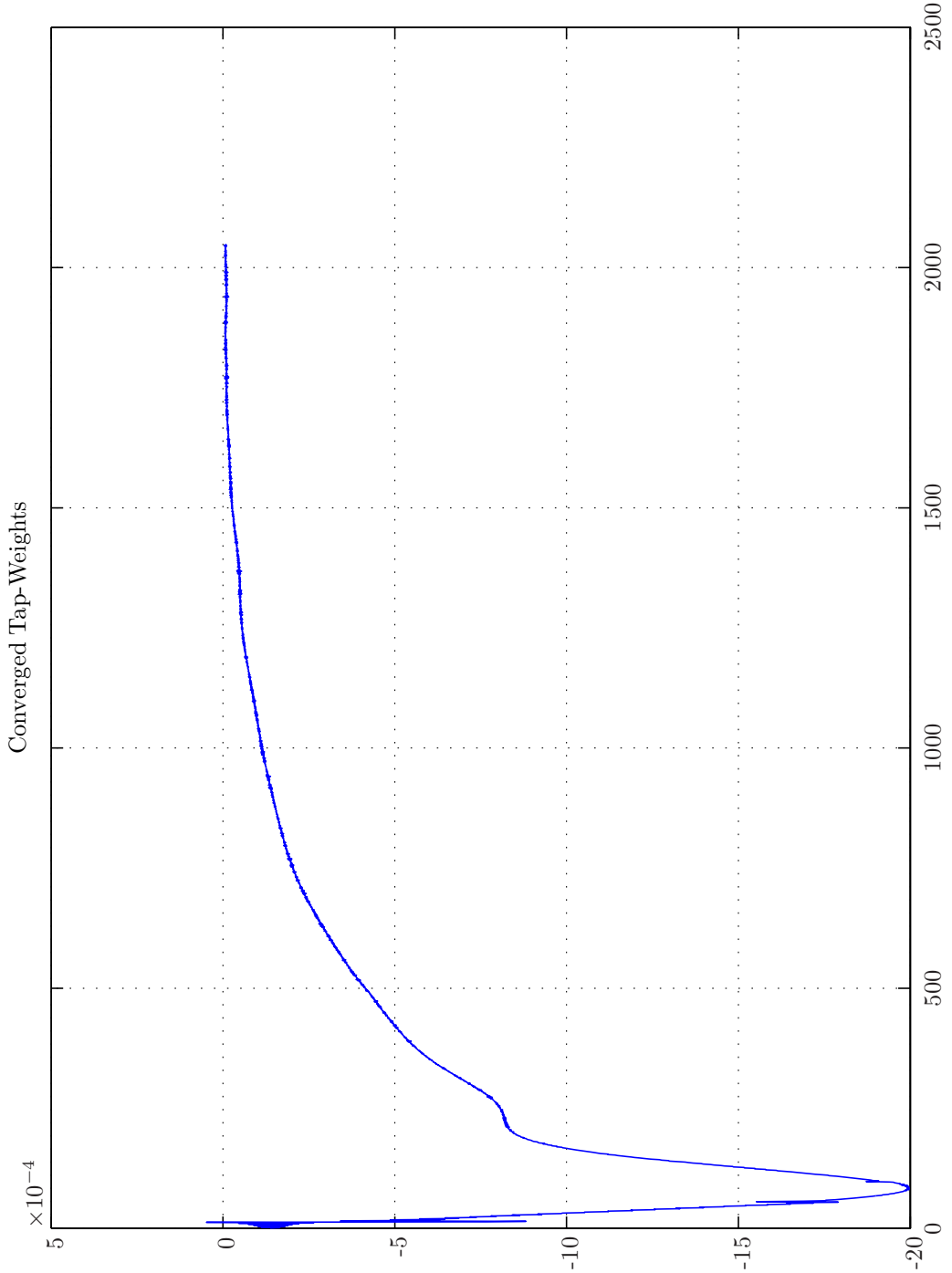

Sim 3.4.39: *Converged Tap-weights.* **Adaptive Filter** $\underset{\sim}{w}$: $\underset{\sim}{w}^{1,1}$: Wiener Hopf ($M = 2048, \alpha = 1e-005, T_{WSS} = 0$,**z**-domain); **Main:** $f_s^0 = 192$ kHz, $f_s^1 = 24$ kHz, $R_{\updownarrow}^1 = \frac{1}{8} = 0.125$, Elliptic LPF ($f_s = 192$ kHz, $f_{pass} = 11$ kHz, $f_{stop} = 12$ kHz, $A_{pass} = 2$ dB, $A_{stop} = 40$ dB), $f_s^2 = 24$ kHz, $R_{\updownarrow}^2 = \frac{1}{1} = 1$, Dummy; **Topology:** (Feedforward, mFx, $N_x = 2, N_e = 1, N_y = 1, N_p = 0, N_v = 2$); **Plants:** $(g_{xy}^{1,1}$: (FIR : $M_{gxy}^{1,1} = 1)$, $g_{xy}^{1,2}$: (FIR : $M_{gxy}^{1,2} = 1)$, $g_{ey}^{1,1}$; Closed-Back Headset System Shaw Thiessen: ($f_s = 24$ kHz, $K_a = 26$ N $\cdot$ m^{-1}, $K_c = 100$ kN $\cdot$ m^{-1}, $f_0 = 141.236$ Hz, $R_c = 120$ N $\cdot$ s $\cdot$ m^{-1}, $M_s = 0.16$ kg, $R_l^A = 1.26\text{e}+007$ N $\cdot$ s $\cdot$ m^{-5}, $f_t = 870$ Hz, $R_{Et} = 2\ \Omega, Q_t = 0.5$ (FIR : $M_{gey}^{1,1} = 97)$); **Signals:** Time: $0 - 10$ s. Refer to SigIDLaT. ; **Scenario:** `MultipleSinusoidalsAddiativeNoiseFeedforwardNx2Ne1Ny1Np0/20080309T202849`.

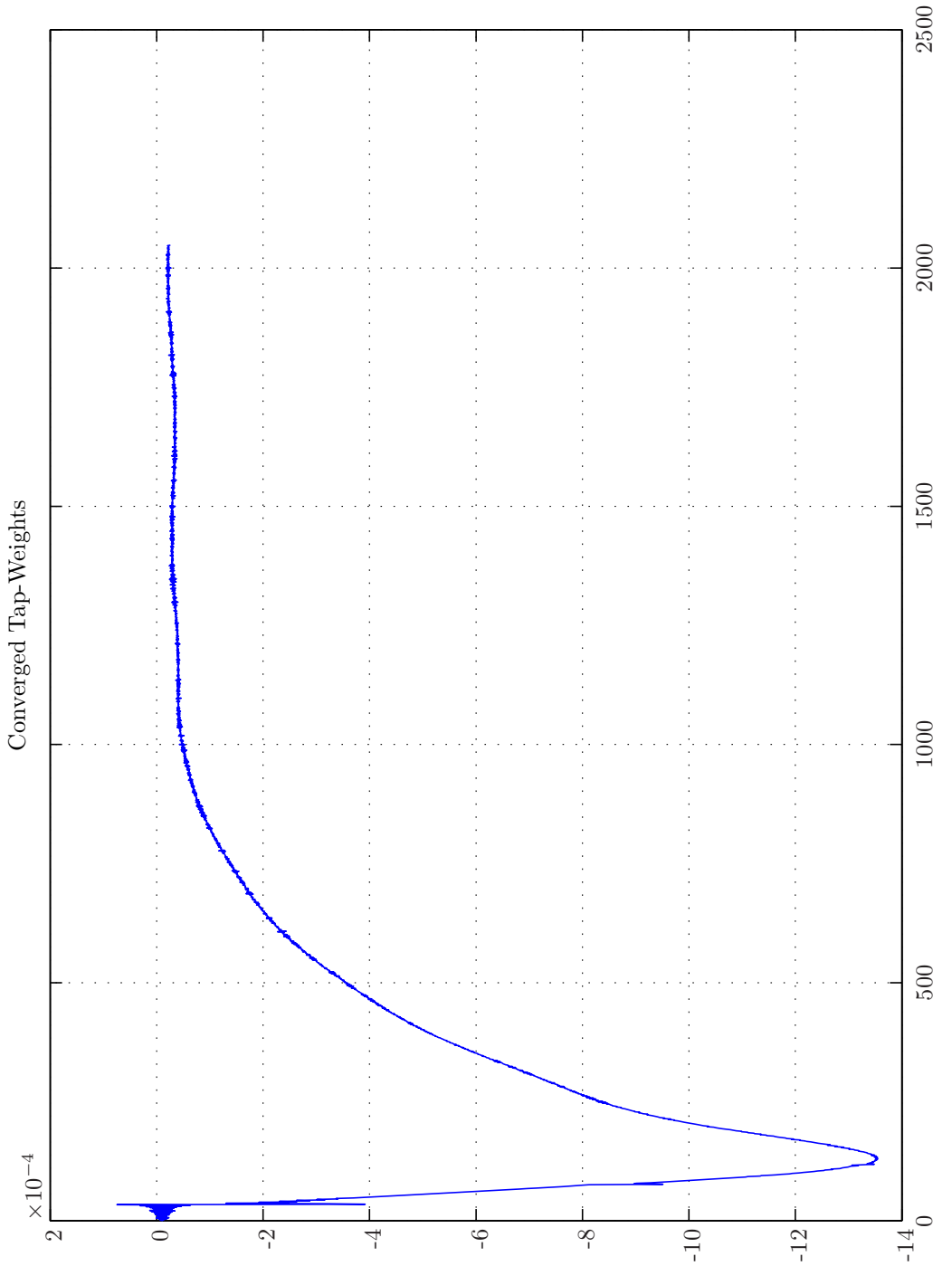

Sim 3.4.40: *Converged Tap-weights.* **Adaptive Filter** $\underset{\sim}{w}$: $\underset{\sim}{w}^{2,1}$: Wiener Hopf ($M = 2048, \alpha = 1e-005, T_{WSS} = 0$,**z**-domain); **Main:** $f_s^0 = 192$ kHz, $f_s^1 = 24$ kHz, $R_\updownarrow^1 = \frac{1}{8} = 0.125$, Elliptic LPF ($f_s = 192$ kHz, $f_{pass} = 11$ kHz, $f_{stop} = 12$ kHz, $A_{pass} = 2$ dB, $A_{stop} = 40$ dB), $f_s^2 = 24$ kHz, $R_\updownarrow^2 = \frac{1}{1} = 1$, Dummy; **Topology:** (Feedforward, mFx, $N_x = 2, N_e = 1, N_y = 1, N_p = 0, N_v = 2$); **Plants:** ($g_{xy}^{1,1}$: (FIR : $M_{gxy}^{1,1} = 1$), $g_{xy}^{1,2}$: (FIR : $M_{gxy}^{1,2} = 1$), $g_{ey}^{1,1}$: Closed-Back Headset System Shaw Thiessen: ($f_s = 24$ kHz, $K_a = 26$ N $\cdot$ s $\cdot$ m^{-1}, $K_c = 100$ kN $\cdot$ m^{-1}, $f_0 = 141.236$ Hz, $R_c = 120$ N $\cdot$ s $\cdot$ m^{-1}, $M_s = 0.16$ kg, $R_l^A = 1.26\text{e}+007$ N $\cdot$ s $\cdot$ m^{-5}, $f_t = 870$ Hz, $R_{Et} = 2\ \Omega$, $Q_t = 0.5$ (FIR : $M_{gey}^{1,1} = 97$)); **Signals:** Time: $0 - 10$ s. Refer to SigIDLaT. ; **Scenario:** `MultipleSinusoidalsAddiativeNoiseFeedforwardNx2Ne1Ny1Np0/20080309T202849`.

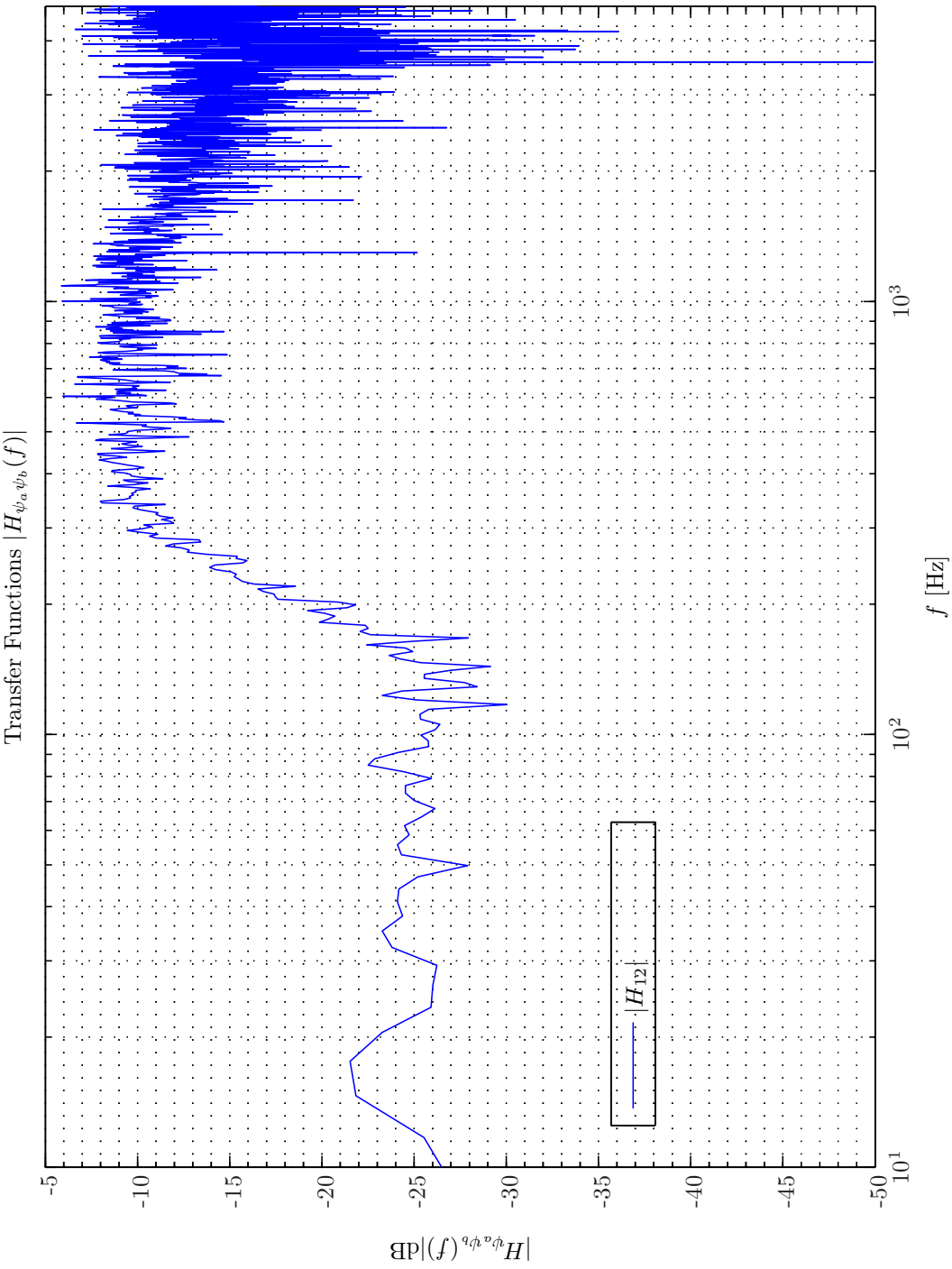

Sim 3.4.41: *Transfer Function, Magnitude*: $|H_{\psi_a\psi_b}(f)|$: **Statistical Data Analysis**: Single-Sided Modified Periodogram, $f_s = 24$ kHz, $N_{DFT} = 8192$, $L_{DFT} = 6001$, $R_{DFT} = 3001$, Hanning, $\Delta f_m = 16$ Hz, $T_{DFT} = 0.25004$ s, $N_{f,DFT} = 4097$, $\Delta f_{DFT} = 2.9297$ Hz, $K_{DFT} = 4$; **Adaptive Filter** $\mathcal{W}$: Wiener Hopf ($M = 2048, \alpha = 1e-005, T_{WSS} = 0.$**z**-domain); **Main:** $f_s^0 = 192$ kHz, $f_s^1 = 24$ kHz, $R_\updownarrow^1 = \frac{1}{8} = 0.125$, Elliptic LPF ($f_s = 192$ kHz, $f_{pass} = 11$ kHz, $f_{stop} = 12$ kHz, $A_{pass} = 2$ dB, $A_{stop} = 40$ dB), $f_s^2 = 24$ kHz, $R_\updownarrow^2 = \frac{1}{1} = 1$, Dummy; **Topology:** (Feedforward, mFx, $N_x = 2, N_e = 1, N_y = 1, N_p = 0, N_v = 2$); **Plants:** $(g_{xy}^{1,1}$: (FIR : $M_{gxy}^{1,1} = 1$), $g_{xy}^{1,2}$: (FIR : $M_{gxy}^{1,2} = 1$), $g_{ey}^{1,1}$: Closed-Back Headset System Shaw Thiessen: ($f_s = 24$ kHz, $K_a = 26$ N $\cdot$ m^{-1}, $K_c = 100$ kN $\cdot$ m^{-1}, $f_0 = 141.236$ Hz, $R_c = 120$ N $\cdot$ s $\cdot$ m^{-1}, $M_s = 0.16$ kg, $R_l^A = 1.26e+007$ N $\cdot$ s $\cdot$ m^{-5}, $f_t = 870$ Hz, $R_{Et} = 2\ \Omega, Q_t = 0.5$ (FIR : $M_{gey}^{1,1} = 97$)); **Signals:** Time: $0-10$ s. Refer to SigIDLaT. ; **Scenario:** `MultipleSinusoidalsAddiativeNoiseFeedforwardNx2Ne1Ny1Np0/20080309T202849`; *Channels:* #1 $\leftarrow d_1(t_1^1)$, #2 $\leftarrow e_1(t_1^1)$.; .

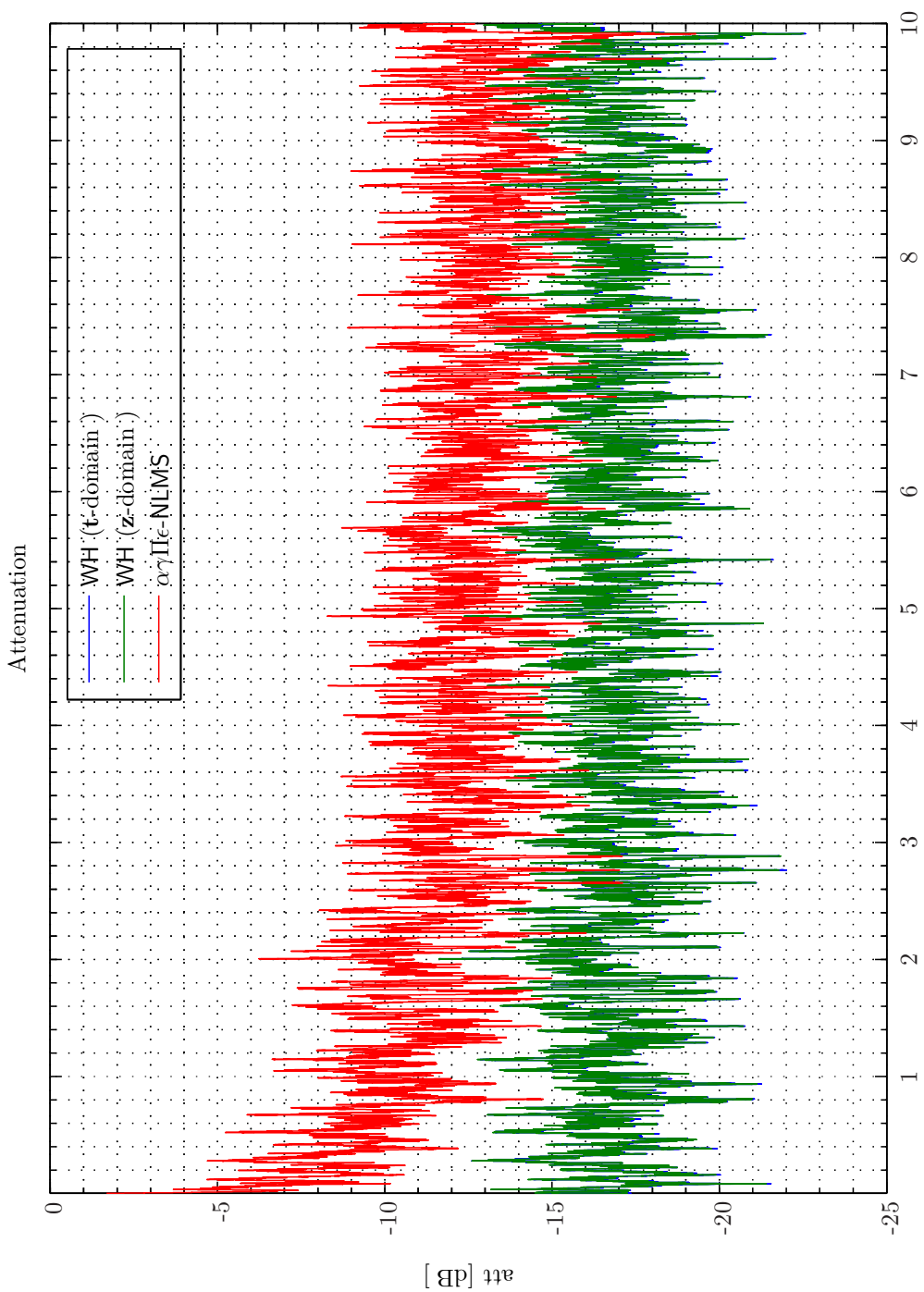

Sim 3.4.42: *Time-Domain: Attenuation.* **Adaptive Filter** w: $w^{1,1}_{\bigcirc}$: WH ($M = 1024, \alpha = 1e-005, T_{WSS} = 0$);αγΠe-NLMS ($M = 512, L_B = 1, \mu = 0.15, \alpha = 1e-005, \epsilon = 1e-006, T_{Eu} = 400$); **Main:** $f^0_s = 192$ kHz, $f^1_s = 24$ kHz, $R^1_{\updownarrow} = \frac{1}{8} = 0.125$, Elliptic LPF ($f_s = 192$ kHz, $f_{pass} = 11$ kHz, $f_{stop} = 12$ kHz, $A_{pass} = 2$ dB, $A_{stop} = 40$ dB), $f^2_s = 24$ kHz, $R^2_{\updownarrow} = \frac{1}{1} = 1$, Dummy; **Topology:** (Feedback, mFx, $N_e = 1, N_y = 1, N_p = 0, N_v = 2$); **Plants:** ($g^{1,1}_{xy}$: (FIR : $M^{1,1}_{gxy} = 1$), $g^{1,2}_{xy}$: (FIR : $M^{1,2}_{gxy} = 1$), $g^{1,1}_{ey}$: Closed-Back Headset System Shaw Thiessen: ($f_s = 24$ kHz, $K_a = 26$ N $\cdot$ m^{-1}, $K_c = 100$ kN $\cdot$ m^{-1}, $f_0 = 141.236$ Hz, $R_c = 120$ N $\cdot$ s $\cdot$ m^{-1}, $M_s = 0.16$ kg, $R^A_l = 1.26e+007$ N $\cdot$ s $\cdot$ m^{-5}, $f_t = 870$ Hz, $R_{Et} = 2\ \Omega$, $Q_t = 0.5$ (FIR : $M^{1,1}_{gey} = 97$)); **Signals:** Time: $0-10$ s. Refer to SigIDLaT.; **Scenario:** `MultipleSinusoidalsAddiativeNoiseFeedbackNx2Ne1Ny1Np0/20080311T002609`.

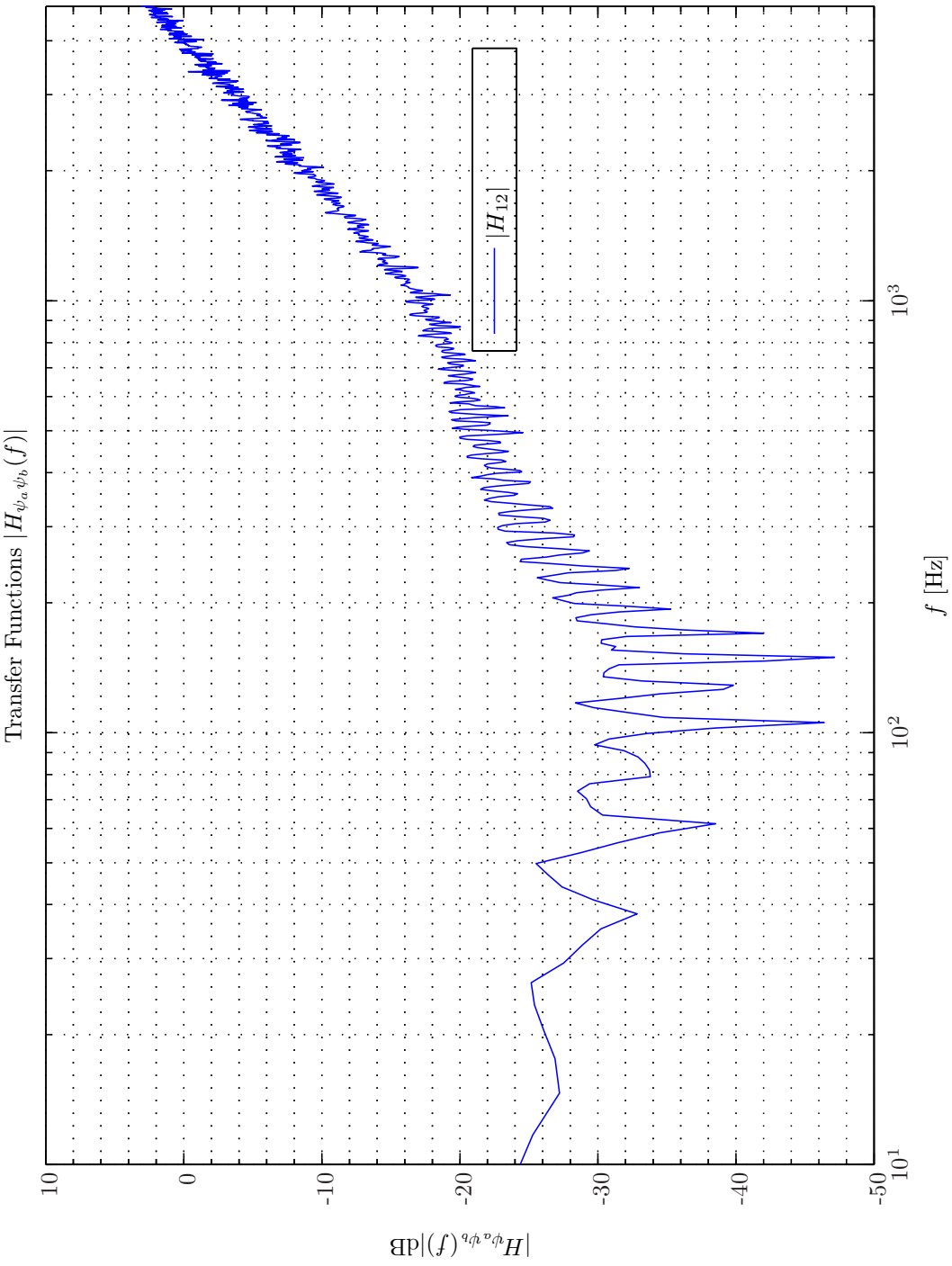

Sim 3.4.43: *Transfer Function, Magnitude:* $|H_{\psi_a\psi_b}(f)|$: **Statistical Data Analysis**: Single-Sided Modified Periodogram, $f_s = 24$ kHz, $N_{DFT} = 8192$, $L_{DFT} = 6001$, $R_{DFT} = 3001$, Hanning, $\Delta f_m = 16$ Hz, $T_{DFT} = 0.25004$ s, $N_{f,DFT} = 4097$, $\Delta f_{DFT} = 2.9297$ Hz, $K_{DFT} = 4$; **Adaptive Filter** $\overset{w}{\bigcirc}$: Wiener Hopf ($M = 1024, \alpha = 1e-005, T_{WSS} = 0$.**z**-domain); **Main:** $f_s^0 = 192$ kHz, $f_s^1 = 24$ kHz, $R_\updownarrow^1 = \frac{1}{8} = 0.125$, Elliptic LPF ($f_s = 192$ kHz, $f_{pass} = 11$ kHz, $f_{stop} = 12$ kHz, $A_{pass} = 2$ dB, $A_{stop} = 40$ dB), $f_s^2 = 24$ kHz, $R_\updownarrow^2 = \frac{1}{1} = 1$, Dummy; **Topology:** (Feedback, mFx, $N_e = 1, N_y = 1, N_p = 0, N_v = 2$); **Plants:** ($g_{xy}^{1,1}$: (FIR : $M_{gxy}^{1,1} = 1$), $g_{xy}^{1,2}$: (FIR : $M_{gxy}^{1,2} = 1$), $g_{ey}^{1,1}$: Closed-Back Headset System Shaw Thiessen: ($f_s = 24$ kHz, $K_a = 26$ N $\cdot$ m^{-1}, $K_c = 100$ kN $\cdot$ m^{-1}, $f_0 = 141.236$ Hz, $R_c = 120$ N $\cdot$ s $\cdot$ m^{-1}, $M_s = 0.16$ kg, $R_l^A = 1.26e+007$ N $\cdot$ s $\cdot$ m^{-5}, $f_t = 870$ Hz, $R_{Et} = 2\ \Omega, Q_t = 0.5$ (FIR : $M_{gey}^{1,1} = 97$)); **Signals:** Time: $0 - 10$ s. Refer to SigIDLaT.; **Scenario:** `MultipleSinusoidalsAddiativeNoiseFeedbackNx2Ne1Ny1Np0/20080311T002609`; *Channels:* ,:; .

available. This might be explained by the fact that although the cepstral method effectively operates on zeros and poles *transmission zeros* also enter the characterization of MC signals as discussed in subsection 3.2.2 on page 107.

A more versatile framework is therefore required for MC ACSV systems. A candidate for MC spectral factorization is provided by a method that involves a PEF.

3.5.2 Multi-Channel Prediction Error Filter Spectral Factorization Method

The connection between the PEF and the spectral factorization was investigated by Cook and Elliott [4]. In this section we will demonstrate how actually to use a PEF to accomplish the MC *canonical spectral factorization* in practice.

The PEF based method for obtaining the MC spectral factors MCPEFSF is constituted from two parts. In the first part the PEF filters out any predictable part of the reference signals. In the second part an estimate of the causal whitening filter $L^{-1}(\mathrm{e}^{\imath\omega})$ is obtained directly from the resulting auto- and cross-spectral density functions. This filter has a stable causal inverse namely the modeling filter $L(\mathrm{e}^{\imath\omega})$. Actually, for MCWH filtering it suffice to determine $L^{-1}(\mathrm{e}^{\imath\omega})$ as evident from (3.2.11) and (3.3.7).

A brief description of the operation of the PEF follows next. For more details the reader should consult the original reference [4]. The PEF takes as input the set of reference signals and outputs a set of error signals that are the unpredictable parts of the reference signal. In this section (and only here) the term error signal accordingly will refer to the parts of the reference signals that remain following the operation of the PEF and **not** to a signal acquired by an error sensor. Hence, the operation of the PEF should not be confused with the operation of the ANCS.

In order to get acquainted with the first part of the MC spectral factorization we will next present the results from applying the method to Example 3.3.1 where two reference sensors are exposed to pink noise excitation.

For the topology in Example 3.2.1 - 3.3.1 the action of the PEF can be explained as follows: The first reference signal, that is, $x_1(t)$ is constituted as a superposition of the random signals $s_1^C(t)$ and $s_2^C(t)$ with propagation direction $\hat{\boldsymbol{s}}_1^C = (-1,\, 0,\, 0)$ and $\hat{\boldsymbol{s}}_2^C = (1,\, 0,\, 0)$ respectively. Provided that filters with a sufficient high order are used, the PEF is in principle capable of removing any predictable part of those signals[10]. Now reference sensor x_1 itself can predict any part of both signals with a strictly positive time lag which for a pink noise signal almost amounts to one half of the signal energy contents, but amounts to nothing for a RWN signal. In addition reference sensor x_2 can predict $s_2^C(t)$ with a lead time of 18 samples (3 ms), which corresponds to all part of a RWN signal and more than the half of the energy in a pink noise signal. Moreover, that part of random signal $s_1^C(t)$ with time lag exceeding 18 samples can also be predicted by reference sensor x_2. This however, is of little use as reference sensor x_1 offers much better predictability for random signal s_1^C.

A WH filter with parameters $M = 2048, \alpha = 10^{-5}, \gamma = 0, W_e = \mathrm{I}, \Pi = 0$ was selected for the actual implementation of the PEF.

The auto spectral density functions in Simulation 3.5.1 demonstrate that the PEF effectively turns the constant-slope pink noise spectra into a flat white noise spectra as desired. The magnitude

[10] A finite bandwidth, however, tends to smear the Dirac impulses such that a fraction of the energy in the auto correlation functions appears with negative time index (see Appendix C on page 539 for details concerning statistical data analysis (SDA)).

and the phase of the cross-spectral density functions are illuminated in Simulation 3.5.2 - 3.5.3 respectively. As the reference signals are pink noise signals while the error signals are white noise signal the magnitude of the cross-spectral density functions follows a pink noise spectral density function. We can confirm that the phase of a reference signal and the corresponding error signal coincide while a linear phase progression between cross reference sensors exists equivalent to a propagation delay of 18 samples between the two reference sensors. The magnitude of the error signal cross-spectral density function $S_{e_1e_2}(f)$ depicted in Simulation 3.5.4 is seen to be more than 20 dB lower than the auto spectral density functions $S_{e_1e_1}(f)$ and $S_{e_2e_2}(f)$.

Finally, from the auto- and cross-correlation functions depicted in Simulation 3.5.5 - 3.5.6 we observe the slow decorrelation pattern of the pink noise reference signals $(R_{x_1x_1}(\tau), R_{x_2x_2}(\tau))$ in contrast with the Dirac-like impulse associated with the white noise error signals $(R_{e_1e_1}(\tau), R_{e_2e_2}(\tau))$. Moreover, a very characteristic behavior of the PEF, namely the completely anti-symmetric cross-correlation functions $(R_{x_1e_1}(\tau), R_{x_1e_2}(\tau), R_{x_2e_1}(\tau), R_{x_2e_2}(\tau))$ is also clearly exhibited. Hence, considering the cross-correlation function between, e.g., the first reference signal and the first error signal $R_{x_1e_1}(\tau)$ the PEF removes the part with negative time lag as expected. Similarly, considerations apply to $R_{x_2e_2}(\tau)$. The cross-correlation function subsequently follows the pink noise decorrelation pattern. For the cross-correlation function between the first reference signal and the second error signal $R_{x_1e_2}(\tau)$ is shifted 3 ms or 18 samples as expected. The benefit of the 3 ms acquisition lead-time can also be observed in terms of an increased high-frequency predicability. This explains why the peak value of $R_{x_1e_2}(\tau)$ is almost twice as small as the peak value of $R_{x_1e_1}(\tau)$. For large time lags corresponding to the low-frequency signal contents the two cross-correlation functions more or less coincide. Similarly, discussion applies to $R_{x_2e_1}(\tau)$.

The ordinary coherence function $\gamma^2_{e_1e_2}(f)$ is as seen in Simulation 3.5.8 on page 215 within the graphically solution identical to zero. This vanishing coherence between the error signals together with the cross-correlation function in Simulation 3.5.6 provide evidence that very little correlation between the two error signals exists as desired.

In conclusion, following the operation of the PEF each error signal is uncorrelated with its past values or with the past values of any other error signal, that is, $R_{e_1e_1}(\tau) = R_{e_2e_2}(\tau) = R_{e_1e_2}(\tau) = R_{e_2e_1}(\tau) = 0$ and recalling that $R_{e_1e_2}(-\tau) = R_{e_2e_1}(\tau)$ this pertains to $\tau \lessgtr 0$. This in turn implies that the entities in the error power spectral density matrix $S_{ee}(\mathrm{e}^{\imath\omega})$ are all white.

We are now in a position to step to the second part of the PEF based MC spectral factorization procedure, namely the determination of the whitening filter $L^{-1}(\mathrm{e}^{\imath\omega})$ that is used in (3.2.11) and (3.3.7). This part is not addressed in [4] and we will in the subsequent text provide a method that to the authors experience works satisfactorily.

The transfer function of the PEF denoted by $\tilde{w}_{\mathrm{PEF}}(z)$ is obtained from the whitening filter $L^{-1}(z)$ and the *power term* $L_0(z)$, that is, the first term in the expansion of the $L(z)$ (refer to (3.2.4)) according to

$$\tilde{w}_{\mathrm{PEF}}(z) = L_0(z)L^{-1}(z). \tag{3.5.2}$$

The transfer function (TF) of a linear time-invariant (LTI) filter can be determined from the input spectra, output spectra and cross-input-output spectra according to[11]

[11] This definition is a consequence of the definition of z-cross-spectrum in Equation 3.2.1b on page 107 and therefore deviates from, e.g., [2].

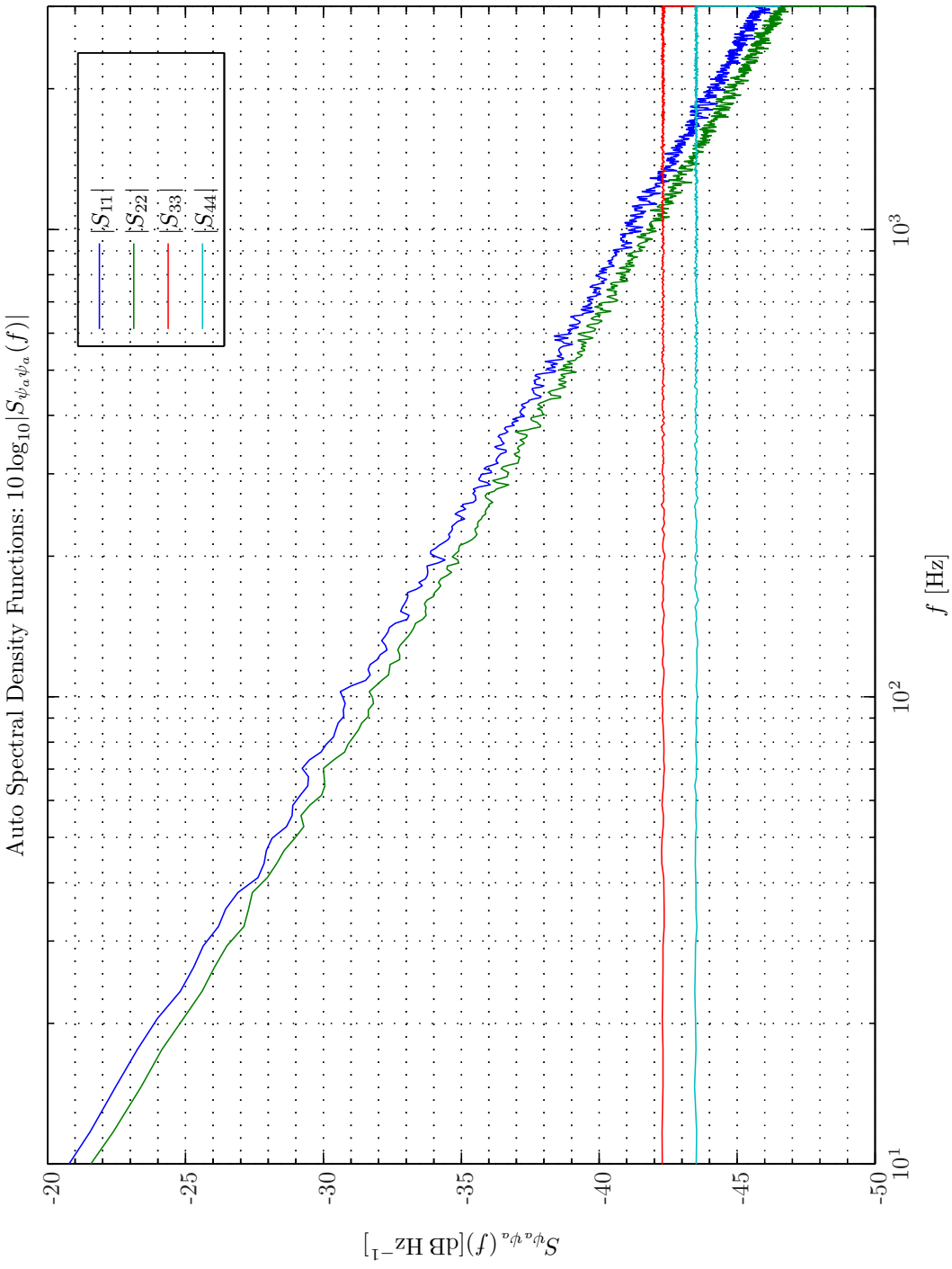

Sim 3.5.1: *Autospectral Density Functions*: **Statistical Data Analysis**: Single-Sided Modified Periodogram, $f_s = 6$ kHz, $N_{DFT} = 2048$, $L_{DFT} = 1501$, $R_{DFT} = 751$, Hanning, $\Delta f_m = 16$ Hz, $T_{DFT} = 0.25017$ s, $N_{f,DFT} = 1025$, $\Delta f_{DFT} = 2.9297$ Hz, $K_{DFT} = 1597$; Linear Prediction Error Filter; *Channels:* #1 $\leftarrow x_1$, #2 $\leftarrow x_2$, #3 $\leftarrow e_1$, #4 $\leftarrow e_2$. **Scenario:** `MultipleSinusoidalsAddiativeNoiseFeedforwardNx2Ne1Ny1Np0/20080213T165541.;` .

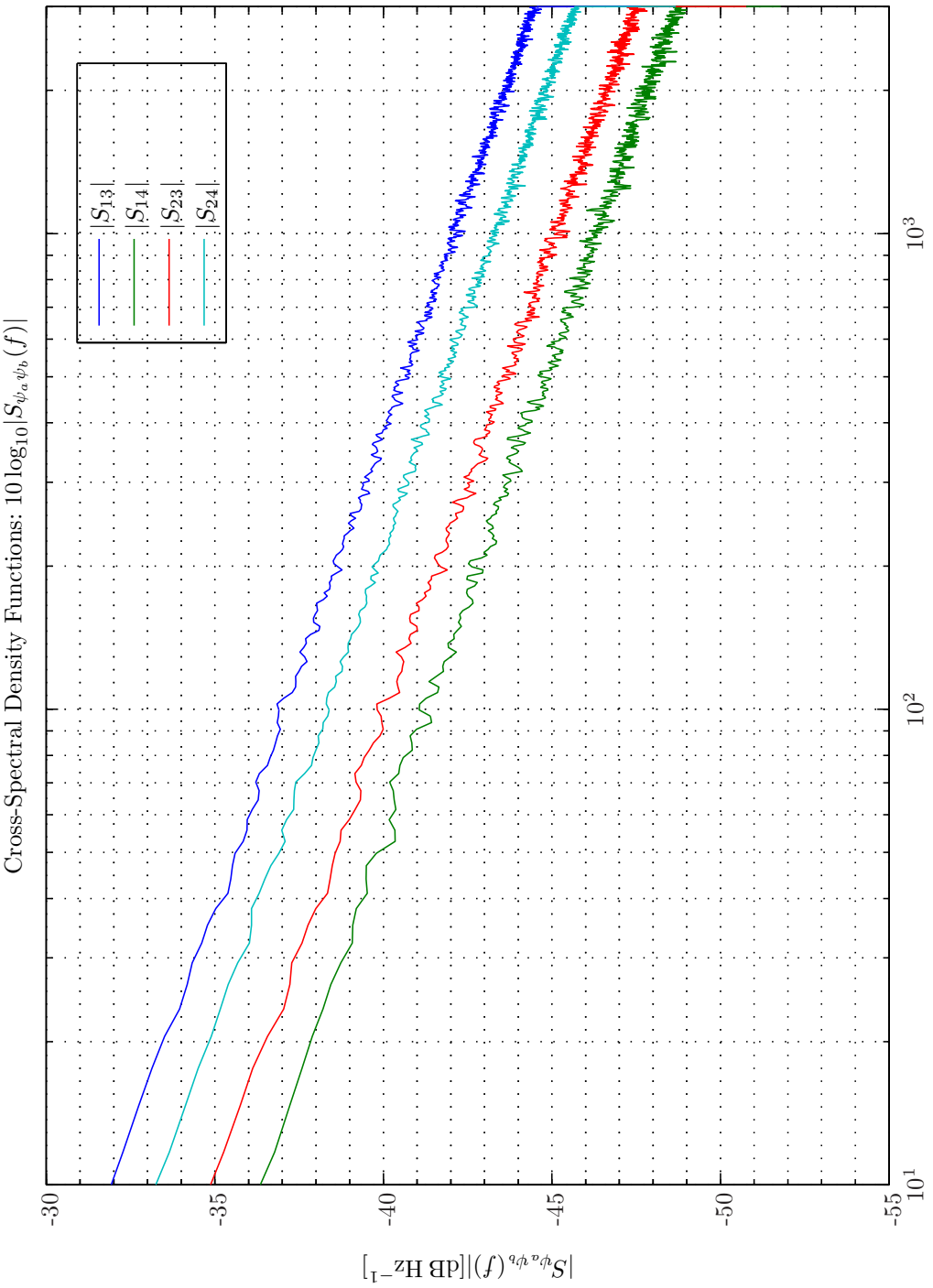

Sim 3.5.2: *Cross-Spectral Density Functions*: **Statistical Data Analysis**: Single-Sided Modified Periodogram, $f_s = 6$ kHz, $N_{DFT} = 2048$, $L_{DFT} = 1501$, $R_{DFT} = 751$, Hanning, $\Delta f_m = 16$ Hz, $T_{DFT} = 0.25017$ s, $N_{f,DFT} = 1025$, $\Delta f_{DFT} = 2.9297$ Hz, $K_{DFT} = 1597$; Linear Prediction Error Filter; *Channels:* $\#1 \leftarrow x_1$, $\#2 \leftarrow x_2$, $\#3 \leftarrow e_1$, $\#4 \leftarrow e_2$. **Scenario:** `MultipleSimusoidalsAddiativeNoiseFeedforwardNx2Ne1Ny1Np0/20080213T165541.;` .

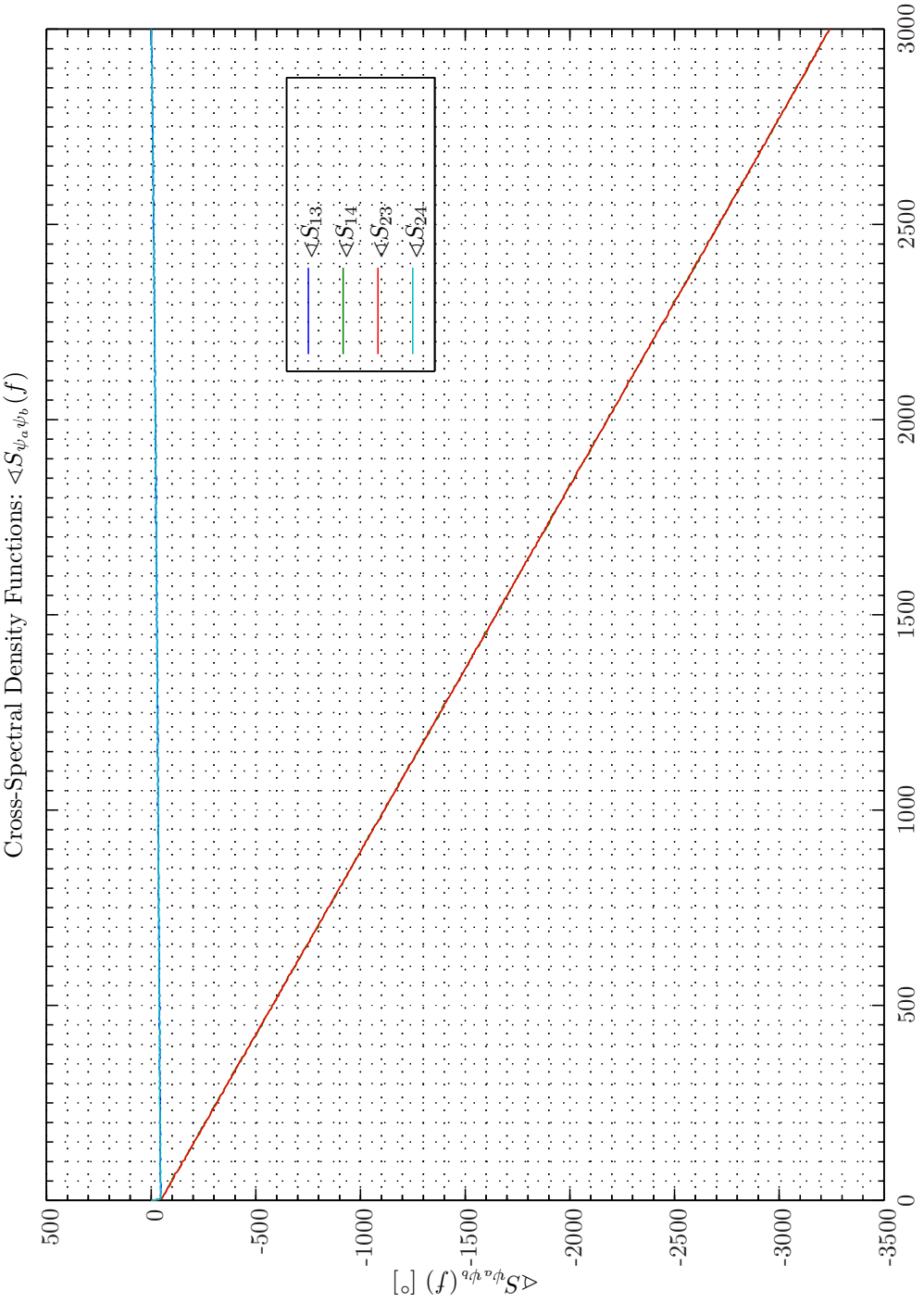

Sim 3.5.3: *Cross-Spectral Density Functions*: **Statistical Data Analysis**: Single-Sided Modified Periodogram, $f_s = 6$ kHz, $N_{DFT} = 2048$, $L_{DFT} = 1501$, $R_{DFT} = 751$, Hanning, $\Delta f_m = 16$ Hz, $T_{DFT} = 0.25017$ s, $N_{f,DFT} = 1025$, $\Delta f_{DFT} = 2.9297$ Hz, $K_{DFT} = 1597$; Linear Prediction Error Filter; *Channels:* $\#1 \leftarrow x_1$, $\#2 \leftarrow x_2$, $\#3 \leftarrow e_1$, $\#4 \leftarrow e_2$. **Scenario:** `MultipleSinusoidalsAddiativeNoiseFeedforwardNx2Ne1Ny1Np0/20080213T165541.`.

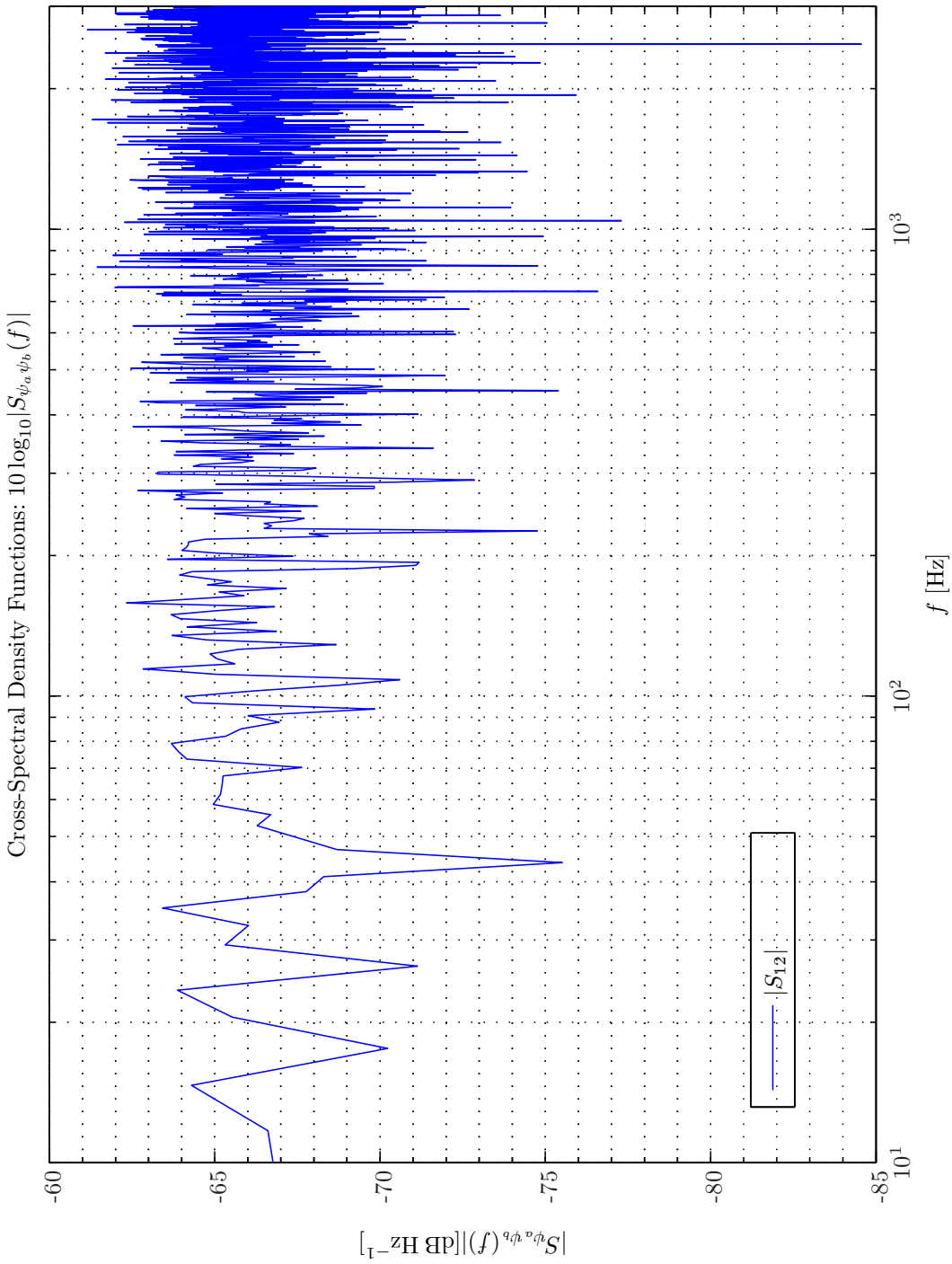

Sim 3.5.4: *Cross-Spectral Density Functions*: **Statistical Data Analysis**: Single-Sided Modified Periodogram, f_s = 6 kHz, N_{DFT} = 2048, L_{DFT} = 1501, R_{DFT} = 751, Hanning, Δf_m = 16 Hz, T_{DFT} = 0.25017 s, $N_{f,DFT}$ = 1025, Δf_{DFT} = 2.9297 Hz, K_{DFT} = 1597; Linear Prediction Error Filter; *Channels:* #1 $\leftarrow e_1$; #2 $\leftarrow e_2$;.

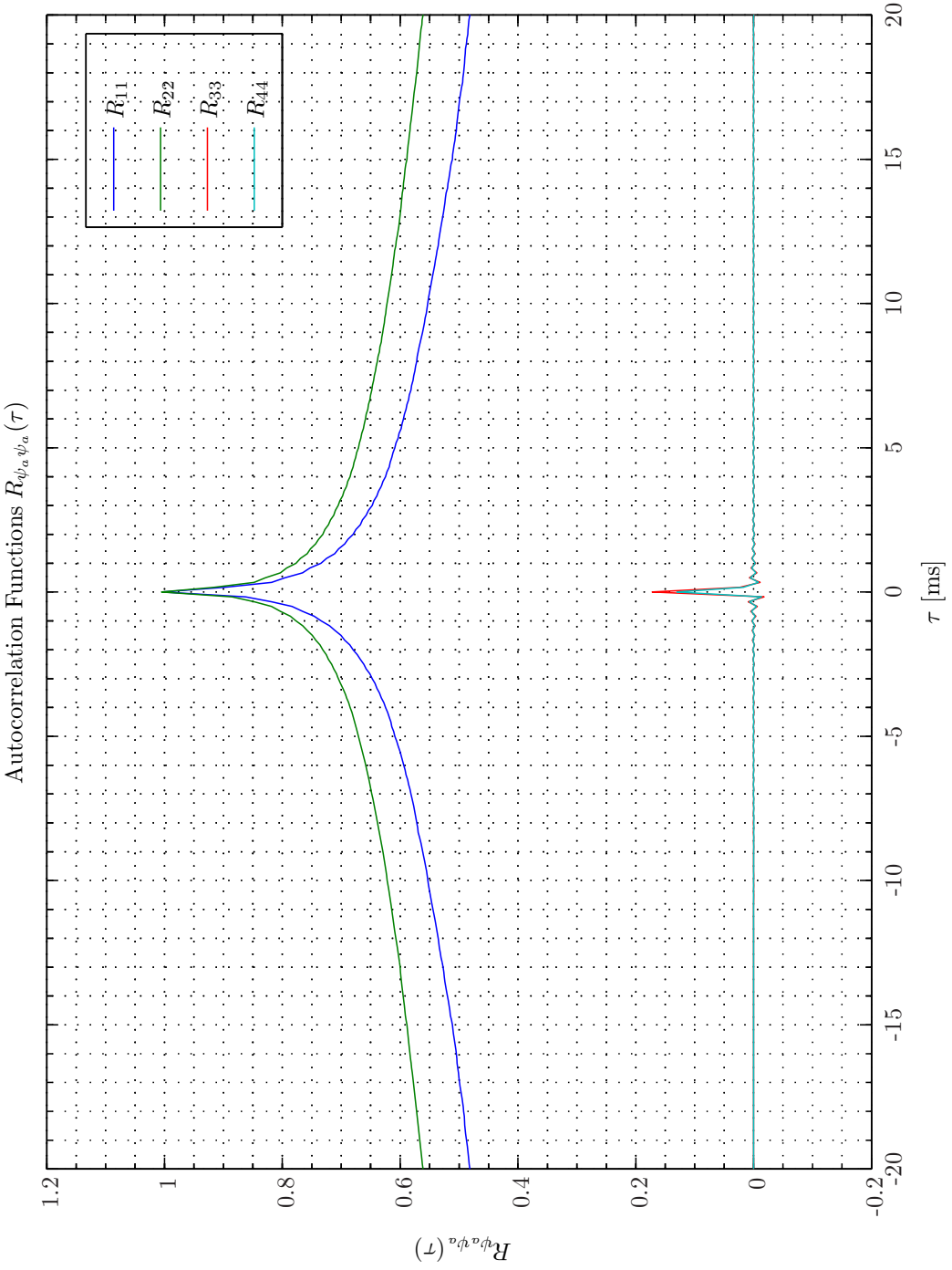

Sim 3.5.5: *Autocorrelation Functions:* $R_{\psi_a\psi_a}(\tau)$: **Statistical Data Analysis**: Single-Sided Modified Periodogram, $f_s = 6$ kHz, $N_{DFT} = 2048, L_{DFT} = 1501, R_{DFT} = 751$, Hanning, $\Delta f_m = 16$ Hz, $T_{DFT} = 0.25017$ s, $N_{f,DFT} = 1025$, $\Delta f_{DFT} = 2.9297$ Hz, $K_{DFT} = 1597$; Linear Prediction Error Filter; *Channels:* #1 $\leftarrow x_1$, #2 $\leftarrow x_2$, #3 $\leftarrow e_1$, #4 $\leftarrow e_2$. **Scenario:** `MultipleSinusoidalsAddiativeNoiseFeedforwardNx2Ne1Ny1Np0/20080213T165541.`.

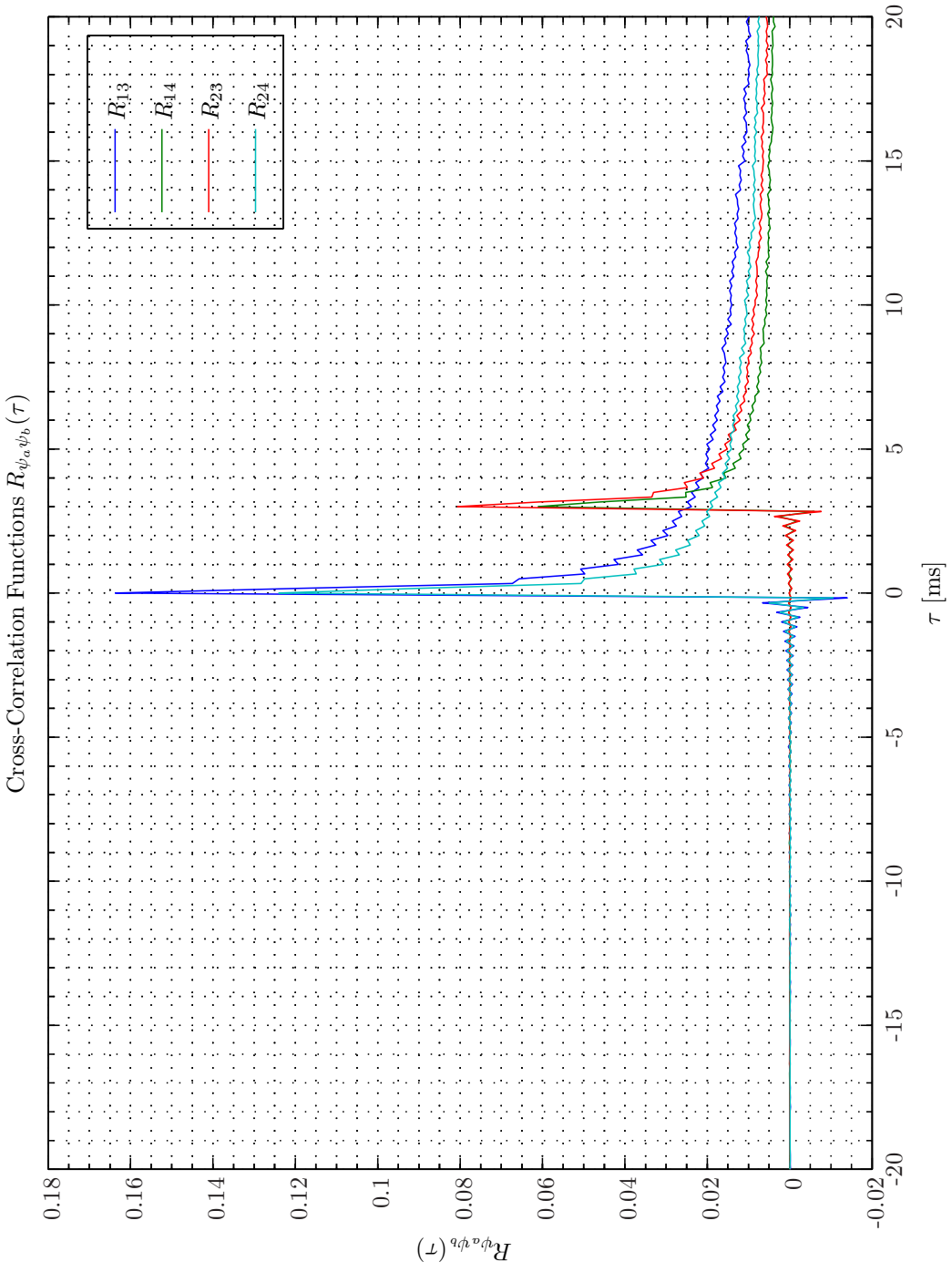

Sim 3.5.6: *Cross-Correlation Functions:* $R_{\psi_a\psi_b}(\tau)$: **Statistical Data Analysis**: Single-Sided Modified Periodogram, f_s = 6 kHz, N_{DFT} = 2048, L_{DFT} = 1501, R_{DFT} = 751, Hanning, Δf_m = 16 Hz, T_{DFT} = 0.25017 s, $N_{f,DFT}$ = 1025, Δf_{DFT} = 2.9297 Hz, K_{DFT} = 1597; Linear Prediction Error Filter; *Channels:* #1 $\leftarrow x_1$, #2 $\leftarrow x_2$, #3 $\leftarrow e_1$, #4 $\leftarrow e_2$. **Scenario:** `MultipleSinusoidalsAdditiveNoiseFeedforwardNx2Ne1Ny1Np0/20080213T165541.;` .

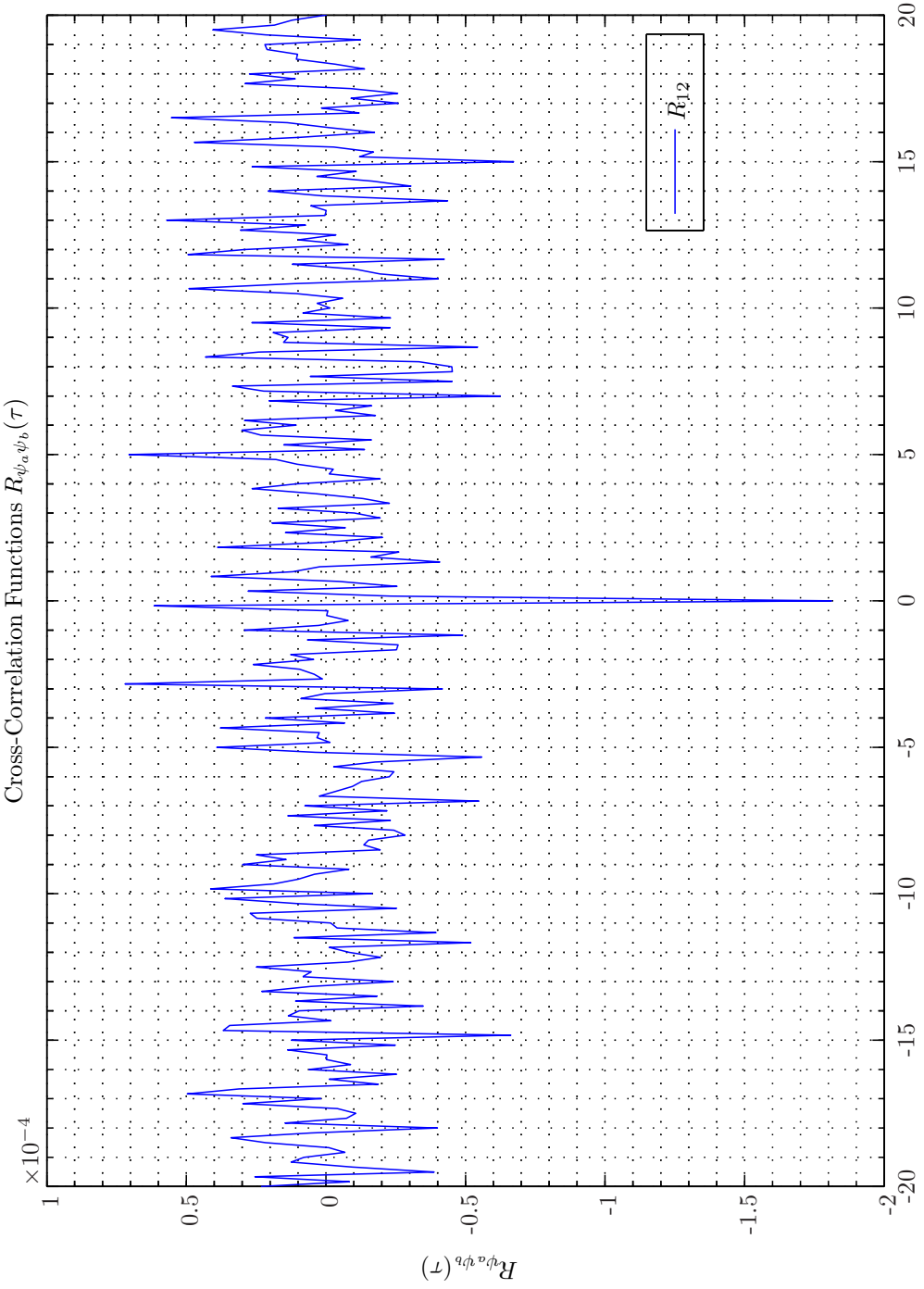

Sim 3.5.7: *Cross-Correlation Functions:* $R_{\psi_a\psi_b}(\tau)$: **Statistical Data Analysis**: Single-Sided Modified Periodogram, f_s = 6 kHz, N_{DFT} = 2048, L_{DFT} = 1501, R_{DFT} = 751, Hanning, Δf_m = 16 Hz, T_{DFT} = 0.25017 s, $N_{f,DFT}$ = 1025, Δf_{DFT} = 2.9297 Hz, K_{DFT} = 1597; Linear Prediction Error Filter; *Channels:* #1 ← e_1; #2 ← e_2; .

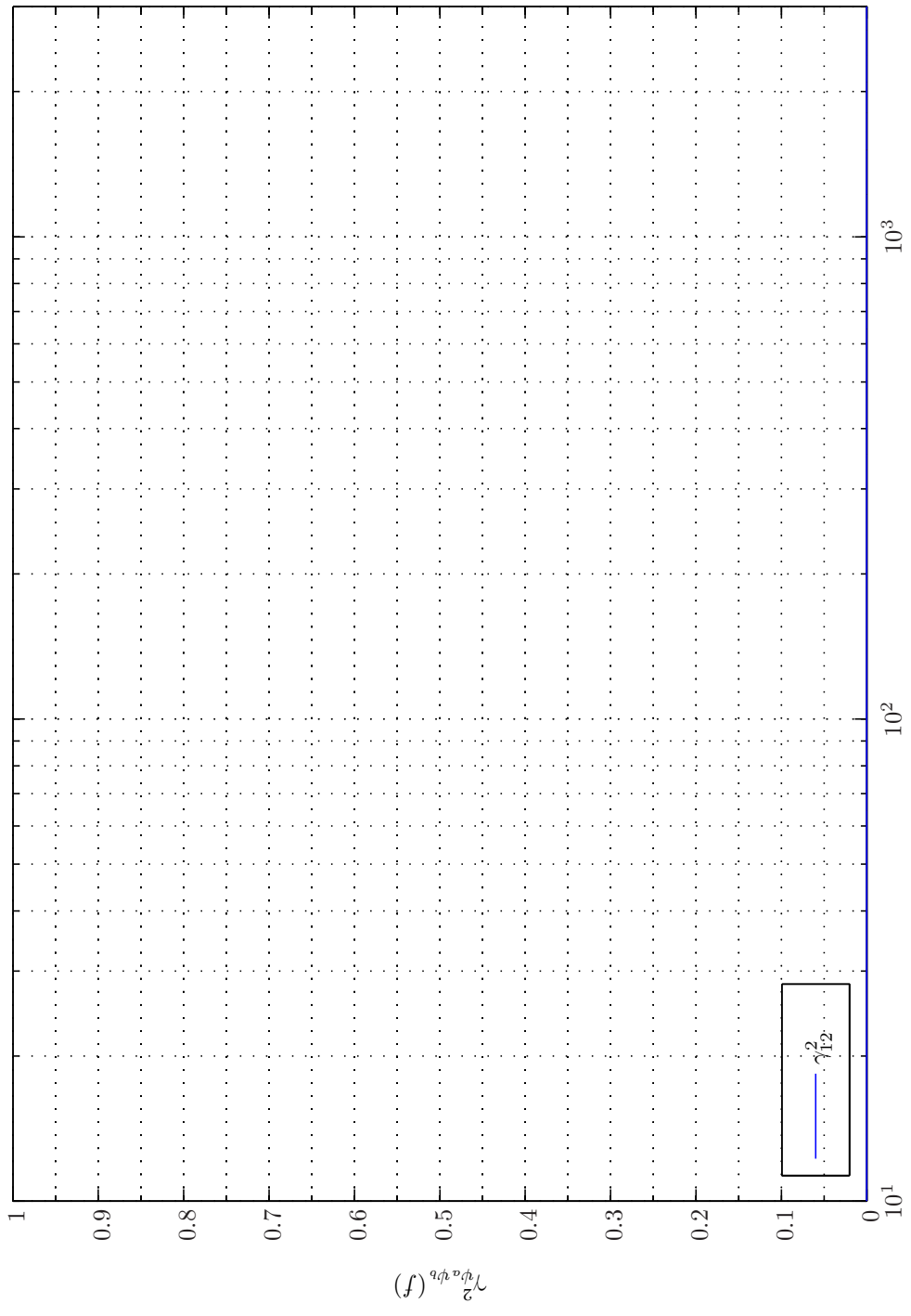

Sim 3.5.8: *Ordinary Coherency-Squared Functions* $\gamma^2_{\psi_a\psi_b}(f)$: **Statistical Data Analysis**: Single-Sided Modified Periodogram, $f_s = 6$ kHz, $N_{DFT} = 2048$, $L_{DFT} = 1501$, $R_{DFT} = 751$, Hanning, $\Delta f_m = 16$ Hz, $T_{DFT} = 0.25017$ s, $N_{f,DFT} = 1025$, $\Delta f_{DFT} = 2.9297$ Hz, $K_{DFT} = 1597$; Linear Prediction Error Filter; *Channels:* #1 $\leftarrow e_1$; #2 $\leftarrow e_2$; .

$$\tilde{w}^{(1)}_{\text{PEF}}(\mathrm{e}^{\imath\omega}) = S_{ee}(\mathrm{e}^{\imath\omega})S^{-1}_{xe}(\mathrm{e}^{\imath\omega}) \tag{3.5.3a}$$

$$\tilde{w}^{(2)}_{\text{PEF}}(\mathrm{e}^{\imath\omega}) = S^{*}_{xe}(\mathrm{e}^{\imath\omega})S^{-1}_{xx}(\mathrm{e}^{\imath\omega}), \tag{3.5.3b}$$

provide that the matrix inverse exists. In the present case the number of input channels equals the number of output channels. Otherwise, the pseudo-inverse replaces the matrix inverse in (3.5.3). The two methods in (3.5.3a) to (3.5.3b) have their own advantages and disadvantages depending on, e.g., the signal-to-noise ratio (SNR) at the input/output channels (refer to [2]).

For the purpose of MC spectral factorization we will use some heuristic SC arguments and propose two variants of (3.5.3). Sometimes it happens that the transfer function obtained from method (3.5.3a) and method (3.5.3b) are of equal magnitude but with opposite arguments. Hence, it is straightforward to define another transfer function as the average of $\tilde{w}^{(1)}_{\text{PEF}}(\mathrm{e}^{\imath\omega})$ and $\tilde{w}^{(2)}_{\text{PEF}}(\mathrm{e}^{\imath\omega})$, that is,

$$\tilde{w}^{(3)}_{\text{PEF}}(\mathrm{e}^{\imath\omega}) = \tfrac{1}{2}\big(\tilde{w}^{(1)}_{\text{PEF}}(\mathrm{e}^{\imath\omega}) + \tilde{w}^{(2)}_{\text{PEF}}(\mathrm{e}^{\imath\omega})\big). \tag{3.5.4}$$

In other situations it might be that over certain frequency intervals that method $\tilde{w}^{(1)}_{\text{PEF}}(\mathrm{e}^{\imath\omega})$ and $\tilde{w}^{(2)}_{\text{PEF}}(\mathrm{e}^{\imath\omega})$ are overestimating respectively underestimating the magnitude of the transfer functions or vice-versa. This suggests that a better and more robust estimate might be obtained from taking the square-root (in a matrix-sense) of the product of the transfer functions defined in (3.5.3), that is,

$$\tilde{w}^{(4)}_{\text{PEF}}(\mathrm{e}^{\imath\omega}) = S^{1/2}_{ee}(\mathrm{e}^{\imath\omega})S^{-1/2}_{xe}(\mathrm{e}^{\imath\omega})S^{*/2}_{xe}(\mathrm{e}^{\imath\omega})S^{-1/2}_{xx}(\mathrm{e}^{\imath\omega}). \tag{3.5.5}$$

In the multiple-input and multiple-output (MIMO) case the transfer function is matrix-valued ($\tilde{w}_{\text{PEF}}(\mathrm{e}^{\imath\omega}) \in \mathbb{C}^{N_x \times N_x}$) which complicates the error analysis considerably. Nevertheless, we will next establish some performance measures in order to assess the four transfer function estimation methods (3.5.3) to (3.5.5).

In [4] the power term $L_0(\mathrm{e}^{\imath\omega})$ introduced in (3.5.2) is expressed as

$$L_0(\mathrm{e}^{\imath\omega}) = Q_e\Lambda_e^{1/2}, \tag{3.5.6}$$

where Q_e is the matrix of real eigenvectors of $S_{ee}(\mathrm{e}^{\imath\omega})$ and Λ_e represents the diagonal matrix of real eigenvalues of $S_{ee}(\mathrm{e}^{\imath\omega})$, that is, $S_{ee}(\mathrm{e}^{\imath\omega}) = Q_e\Lambda_eQ_e^{\top}$. The elements of $e(z)$ are decorrelated by $Q^{\top}$ while $\Lambda^{-1/2}$ normalizes their variances. However, some care should be exercised as (3.5.6) presents ambiguity in terms of the order of the eigenvalues/eigenvectors[12].

A more straightforward approach is to obtain $L_0(\mathrm{e}^{\imath\omega})$ from

$$L_0(\mathrm{e}^{\imath\omega}) \triangleq S^{1/2}_{ee}(\mathrm{e}^{\imath\omega}) = Q_e\Lambda_e^{1/2}Q_e^{-1}. \tag{3.5.7}$$

It can readily be verified that this procedure for obtaining the power term is insensitive to permutations in the eigenvalues/eigenvectors.

[12]Suppose $Q = \begin{bmatrix} q_1 & q_2 \end{bmatrix}$ and $\Lambda = \operatorname{diag}\{\lambda_1, \lambda_2\}$ is a solution to $A = Q\Lambda Q^{\top}$. Then, another solution is obtained from permutations of the eigenvalues and eigenvectors, that is, $A = Q'\Lambda'Q'^{\top}$ for $Q' = \begin{bmatrix} q_2 & q_1 \end{bmatrix}$ and $\Lambda' = \operatorname{diag}\{\lambda_2, \lambda_1\}$. However, in general $Q\Lambda \neq Q'\Lambda'$.

A natural question is then, how should we actually measure the performance of the spectral factorization? In a general context a candidate *figure of merit* for the spectral factorization procedure could be the relative spectral factorization error that we denote by $\Delta s_{xx}(\mathrm{e}^{\imath\omega})$ and define by

$$\Delta s_{xx}(\mathrm{e}^{\imath\omega}) \triangleq \frac{\|\Delta S_{xx}(\mathrm{e}^{\imath\omega})\|}{\|S_{xx}(\mathrm{e}^{\imath\omega})\|}, \tag{3.5.8}$$

where the spectral factorization error $\Delta S_{xx}(\mathrm{e}^{\imath\omega})$ in turn is defined by

$$\Delta S_{xx}(\mathrm{e}^{\imath\omega}) \triangleq \hat{L}(\mathrm{e}^{\imath\omega}) R_e \hat{L}^*(\mathrm{e}^{\imath\omega}) - S_{xx}(\mathrm{e}^{\imath\omega}) \tag{3.5.9}$$

and evaluated over the frequency range $0 \leq f \leq \frac{f_s}{2}$. Moreover, the spectral factorization is nonunique (see Footnote 4 on page 108).

Our main objective in this chapter is to establish an analysis method by which we can estimate the performance of MC active noise control (ANC) systems as limited by the requirement on causal operation of the system. Hence, we should consider the equation governing the optimal causally constrained weights (3.2.11) or (3.3.7). In both these equations it is the whitening filter $L^{-1}(z)$ and not the modeling filter $L(z)$ that is used. Moreover, $L^{-1}(z)$ enters both inside the plus operator (in a time reversed sense) and outside the plus operator. Concerning the later term, that is, $L^{-1}(z)$ outside the plus operator we may argue that the weight estimation error is linearly related to the whitening filter error $\Delta L(z)$ that we define by

$$\Delta L^{-1}(z) \triangleq \widehat{L^{-1}}(z) - L^{-1}(z), \tag{3.5.10}$$

where $\widehat{L^{-1}}(z)$ is the whitening filter estimate.

It should, however, be recalled that the plus operator is nonlinear. In practice this means that even a small factorization error might lead to relative large erroneous truncation effects. It might, however, also be that even for a relative poor spectral factorization quality that the effects on the estimated optimally constrained weights are negligible. It is therefore exceedingly difficult to establish exact requirements to the quality of the spectral factorization.

Instead we will measure the efficiency of the spectral factorization method as the ability to determine a whitening filter $L^{-1}(\mathrm{e}^{\imath\omega})$ that when excited by the reference signals produce random white noise signals $v(t)$ that are mutually uncorrelated.

We may then define spectral factorization error averaged norm ΔS_{vv} by

$$\Delta S_{vv} = \tfrac{1}{N_{\mathrm{DFT}}} \sum_{k=1}^{N_{\mathrm{DFT}}} \|S_{vv}(k) - \mathrm{I}\|^2, \tag{3.5.11}$$

where the random white noise signal vector in turn is obtained from $\tilde{v}(z) = L^{-1}(z)\tilde{x}(z)$, that is, the deviation from the identity matrix. The matrix norm (largest singular value) of the deviation is then averaged over the frequency bins.

We may now present the results from estimating the MC spectral factorization (3.5.2) using each of the proposed methods for estimating the transfer functions of the PEF (3.5.3) (3.5.4) and (3.5.5).

The auto spectral density functions of the supposedly random white noise signals $v_1(t), v_2(t)$ using $\tilde{w}^{(1)}_{\mathrm{PEF}}(\mathrm{e}^{\imath\omega}) - \tilde{w}^{(4)}_{\mathrm{PEF}}(\mathrm{e}^{\imath\omega})$ can be found in Simulation 3.5.9 - 3.5.12 on pages 219–222. The spectra are not perfectly flat, but exhibit ripples ranging from ± 0.5 dB in peak-to-peak values Δv_{pp} by method (1) and up to ± 4 dB for method (2). Recalling that the for unit variance the auto spectral density function should be $10\log_{10}(f_s/2)$=-34.77 dBHz^{-1} we conclude that only method (1) provides a unbiased estimate. Moreover, it can be observed that the minimum/maximum values of the ripples in the auto spectral density functions occur at $f = \frac{n}{18}\frac{f_s}{2}, n \in \mathbb{Z}$. Referring to Simulation 3.2.2 on page 117 and Simulation 3.2.12 on page 130 we recognize these frequencies as the same frequency points where very deep troughs in the multiple coherence function for the system without element directivity respectively small deviations from unity multiple coherence function for the system with element directivity are observed. Accordingly, we may attribute the periodicities in the auto spectral density functions as related to a potential rank-deficient auto-spectral density matrix $S_{xx}(\mathrm{e}^{\imath\omega})$.

From inspection of the four different transfer function definitions (3.5.3) (3.5.4) and (3.5.5) it can readily be observed that method (1) is less dependent on reference signal contents than the other methods. This in turn explains why method (1) provides the best MC spectral factorization results. The spectral factorization quality measure defined in (3.5.11) is ranging from 0.14 to 0.45 for method (1) and method (2) respectively. These findings are summarized in Table 3.1

Signal	$\tilde{w}^{(1)}_{\mathrm{PEF}}$	$\tilde{w}^{(2)}_{\mathrm{PEF}}$	$\tilde{w}^{(3)}_{\mathrm{PEF}}$	$\tilde{w}^{(4)}_{\mathrm{PEF}}$
Δv_{pp}[dB]	± 0.5	± 1.0	± 1.0	± 0.8
ΔS_{vv}	0.14	0.45	0.25	0.21

Tab. 3.1: Quality Measures of Spectral Factorization, Transfer Functions.

In conclusion, method (1) provides the best MC spectral factorization results. It leads to unbiased unit variance random white noise signals $v_1(t), v_2(t)$ smallest ripples and also the smallest quality number as defined in (3.5.11).

Henceforth, we will apply method (1), $\tilde{w}_{\mathrm{PEF}}(\mathrm{e}^{\imath\omega}) \equiv \tilde{w}^{(1)}_{\mathrm{PEF}}(\mathrm{e}^{\imath\omega})$. In the subsequent text we present more detailed results of the spectral factorization obtained from this method.

Ideally, the z-autospectrum matrix $S_{vv}(\mathrm{e}^{\imath\omega}) \approx \mathrm{I}$. We therefore expect a vanishing cross-spectral density function. From Simulation 3.5.13 on page 223 we see that the cross-spectral density function is suppressed by approximately $8 - 25$ dB. as compared with the auto spectral density functions in Simulation 3.5.9 on the next page. The marginal correlateness between v_1 and v_2 is exhibited in the staircase pattern of phase of the cross-spectral density function in Simulation 3.5.14 on page 224.

Some imperfections can be also seen in the auto correlation functions $(R_{v_1v_1}(\tau), R_{v_2v_2}(\tau)$ depicted in Simulation 3.5.15 where small time-domain side lobes can be observed at ± 6 ms corresponding to the turn-around time of 36 samples.

From the ordinary coherence function in Simulation 3.5.16 on page 226 and the cross-correlation function in Simulation 3.5.17 on page 227 it can be observed that the two random white noise signals are marginally correlated.

Finally, we return to the actual behavior of the modeling filter $L(\mathrm{e}^{\imath\omega})$. The magnitude and phase are shown in Simulation 3.5.18 and Simulation 3.5.19 respectively. It can be observed that the direct channel excitation is approximately 6 dB higher than the cross-channel excitation independent of the frequency which agrees with the minimum element sensitivity $b_x = \frac{1}{2}$. The

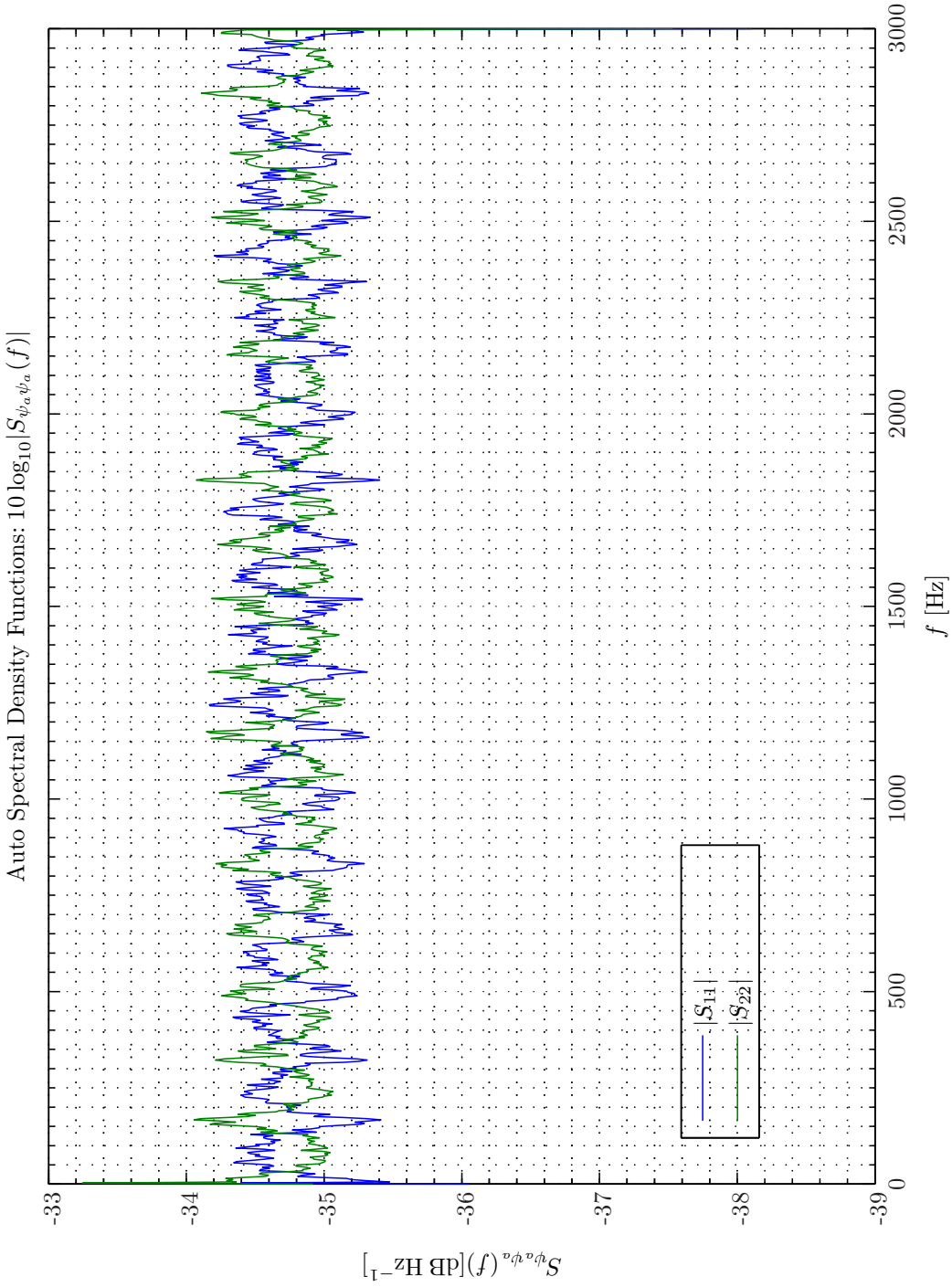

Sim 3.5.9: *Autospectral Density Functions*: **Statistical Data Analysis**: Single-Sided Modified Periodogram, $f_s = 6$ kHz, $N_{DFT} = 2048$, $L_{DFT} = 1501$, $R_{DFT} = 751$, Hanning, $\Delta f_m = 16$ Hz, $T_{DFT} = 0.25017$ s, $N_{f,DFT} = 1025$, $\Delta f_{DFT} = 2.9297$ Hz, $K_{DFT} = 1597$; Wiener Hopf Modeling Filter; *Channels:* $\#1 \leftarrow v_1$; $\#2 \leftarrow v_2$; .

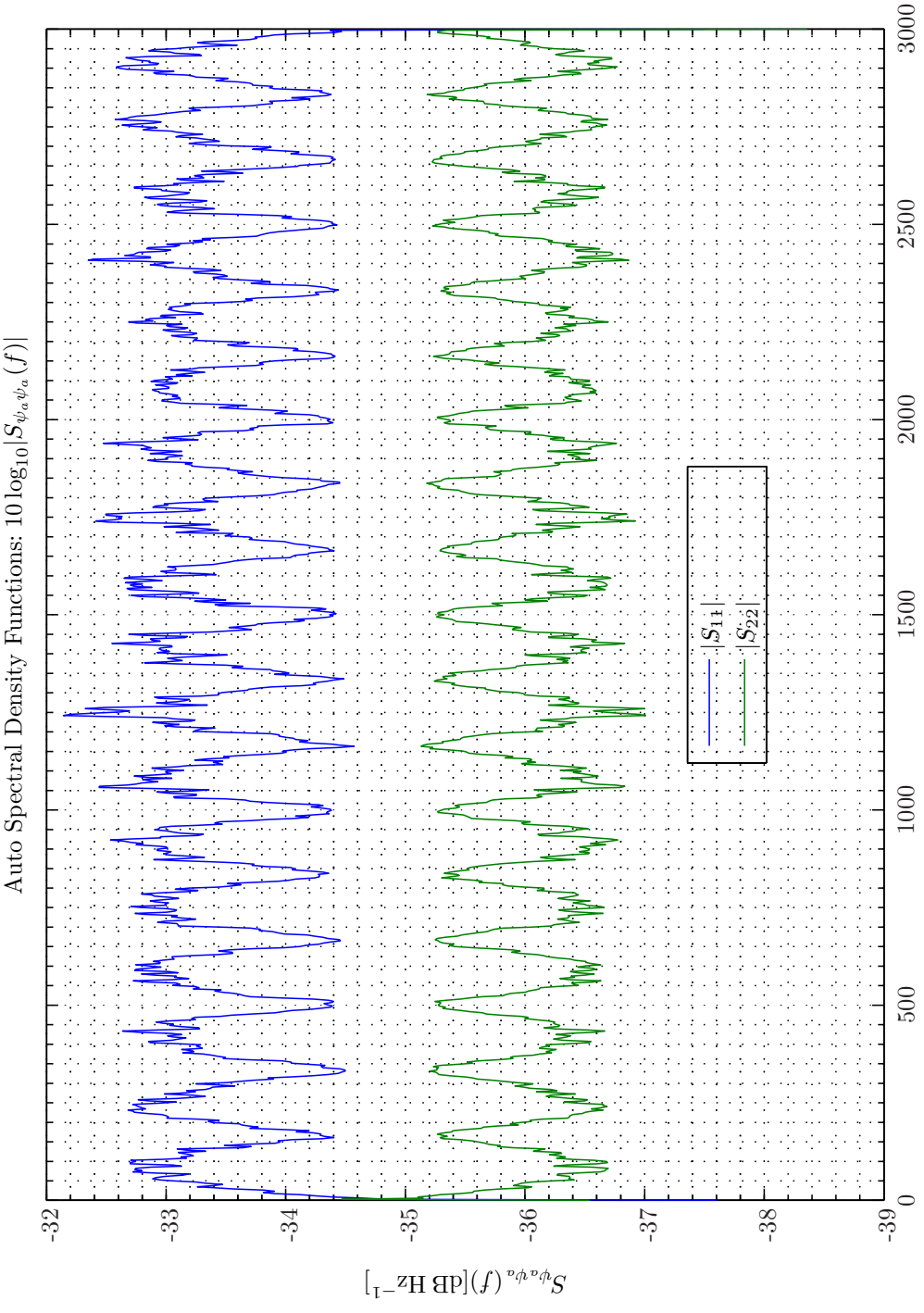

Sim 3.5.10: *Autospectral Density Functions*: **Statistical Data Analysis**: Single-Sided Modified Periodogram, $f_s = 6$ kHz, $N_{DFT} = 2048$, $L_{DFT} = 1501$, $R_{DFT} = 751$, Hanning, $\Delta f_m = 16$ Hz, $T_{DFT} = 0.25017$ s, $N_{f,DFT} = 1025$, $\Delta f_{DFT} = 2.9297$ Hz, $K_{DFT} = 1597$; Wiener Hopf Modeling Filter; *Channels:* $\#1 \leftarrow v_1$; $\#2 \leftarrow v_2$. **Scenario:** `MultipleSinusoidalsAddiativeNoiseFeedforwardNx2Ne1Ny1Np0/20080214T130939:`.

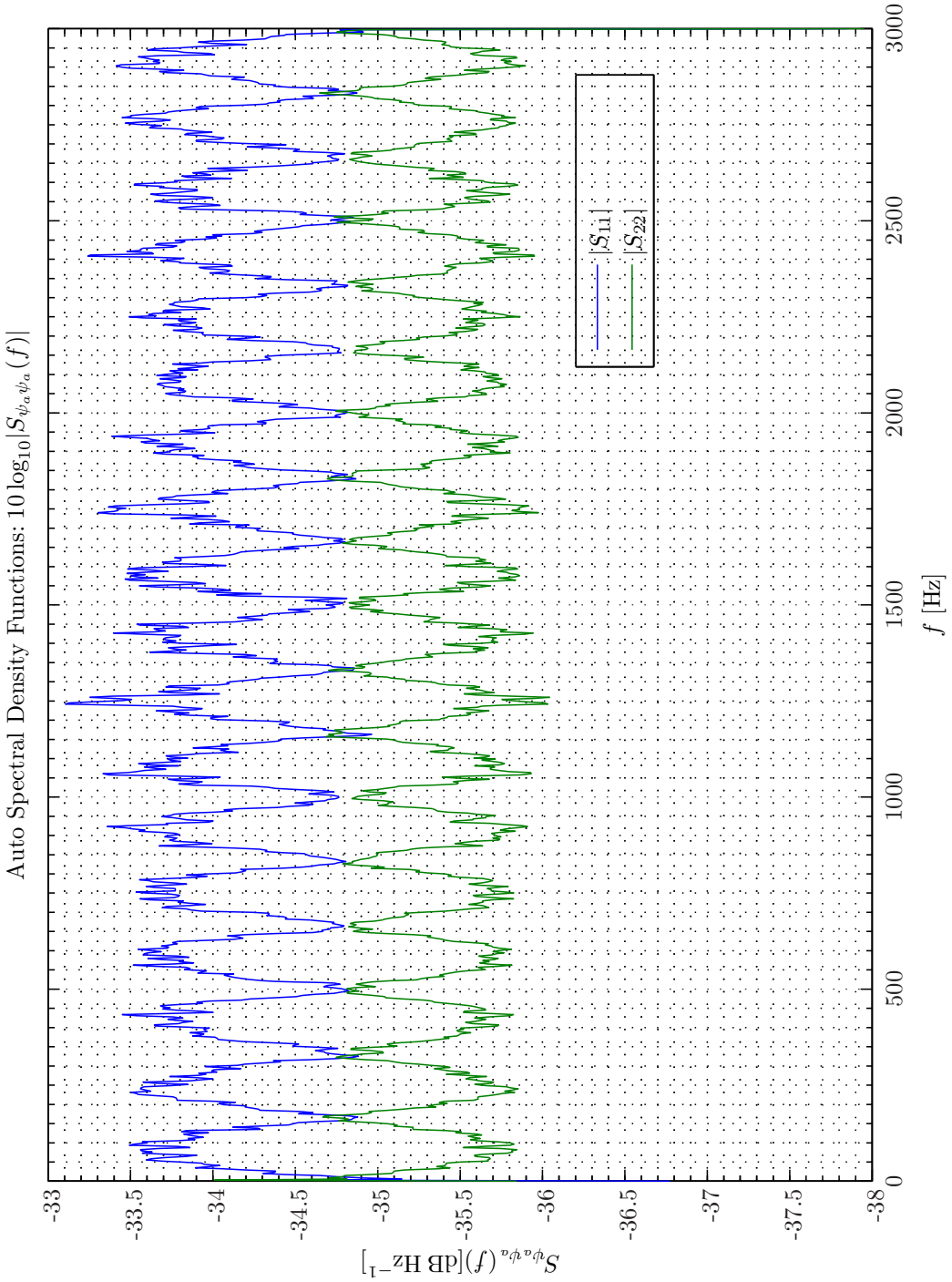

Sim 3.5.11: *Autospectral Density Functions*: **Statistical Data Analysis**: Single-Sided Modified Periodogram, f_s = 6 kHz, N_{DFT} = 2048, L_{DFT} = 1501, R_{DFT} = 751, Hanning, Δf_m = 16 Hz, T_{DFT} = 0.25017 s, $N_{f,DFT}$ = 1025, Δf_{DFT} = 2.9297 Hz, K_{DFT} = 1597; Wiener Hopf Modeling Filter; *Channels:* #1 ← v_1; #2 ← v_2. **Scenario:** `MultipleSinusoidalsAddiativeNoiseFeedforwardNx2Ne1Ny1Np0/20080214T134004.`.

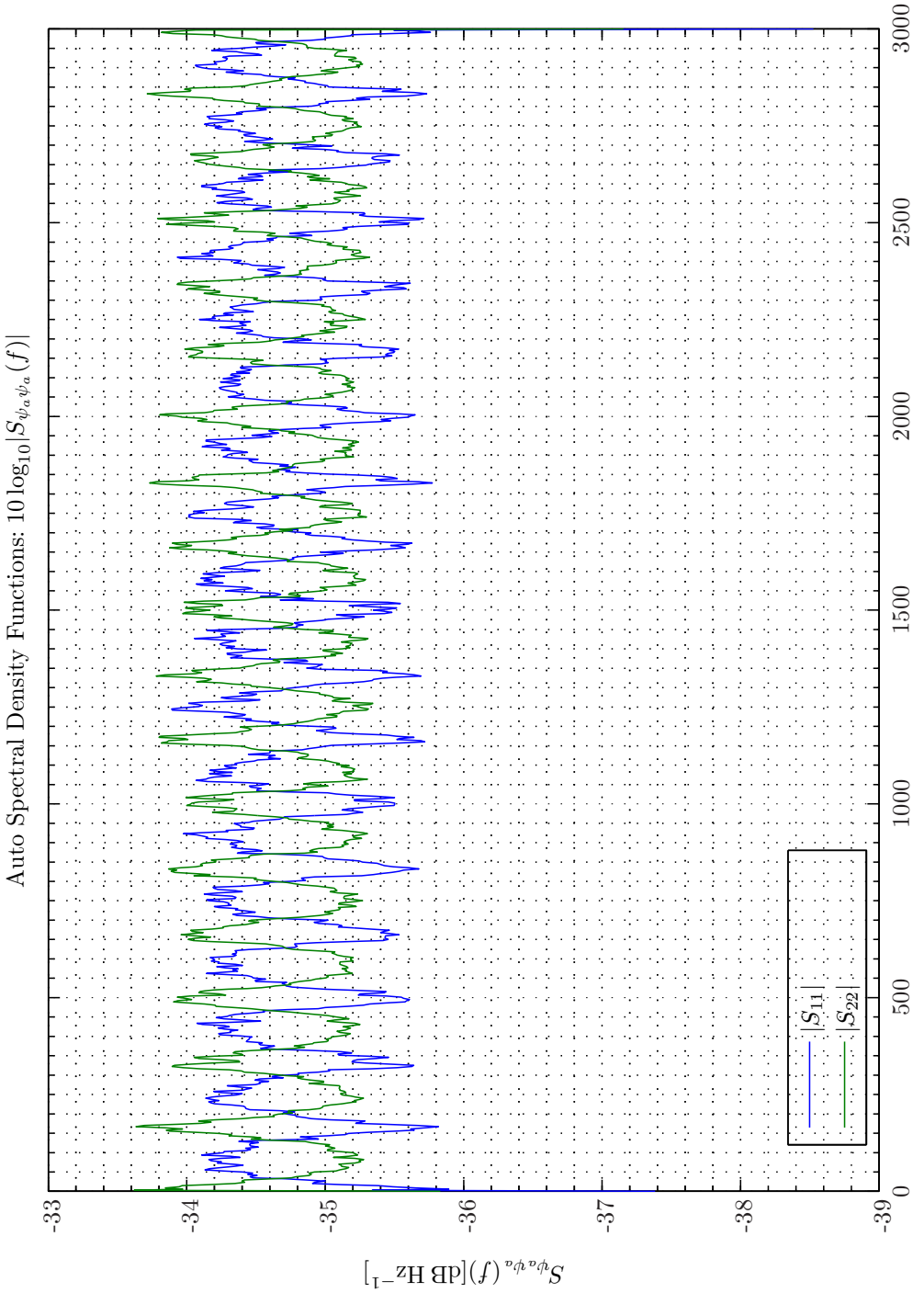

Sim 3.5.12: *Autospectral Density Functions*: **Statistical Data Analysis**: Single-Sided Modified Periodogram, f_s = 6 kHz, N_{DFT} = 2048, L_{DFT} = 1501, R_{DFT} = 751, Hanning, Δf_m = 16 Hz, T_{DFT} = 0.25017 s, $N_{f,DFT}$ = 1025, Δf_{DFT} = 2.9297 Hz, K_{DFT} = 1597; Wiener Hopf Modeling Filter; *Channels*: #1 $\leftarrow v_1$; #2 $\leftarrow v_2$; .

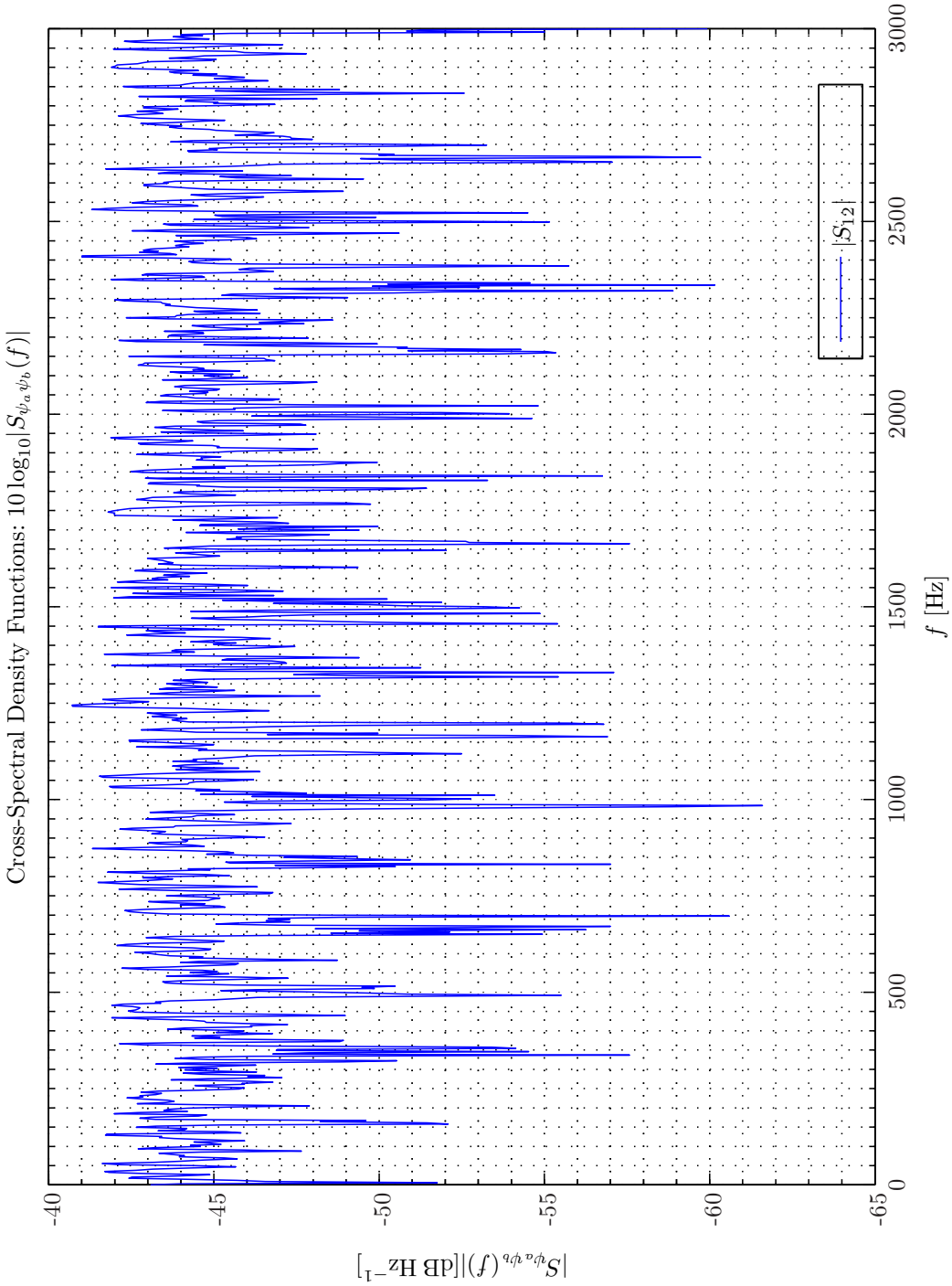

Sim 3.5.13: *Cross-Spectral Density Functions*: **Statistical Data Analysis**: Single-Sided Modified Periodogram, $f_s = 6$ kHz, $N_{DFT} = 2048$, $L_{DFT} = 1501$, $R_{DFT} = 751$, Hanning, $\Delta f_m = 16$ Hz, $T_{DFT} = 0.25017$ s, $N_{f,DFT} = 1025$, $\Delta f_{DFT} = 2.9297$ Hz, $K_{DFT} = 1597$; Wiener Hopf Modeling Filter; *Channels:* $\#1 \leftarrow v_1$; $\#2 \leftarrow v_2$; .

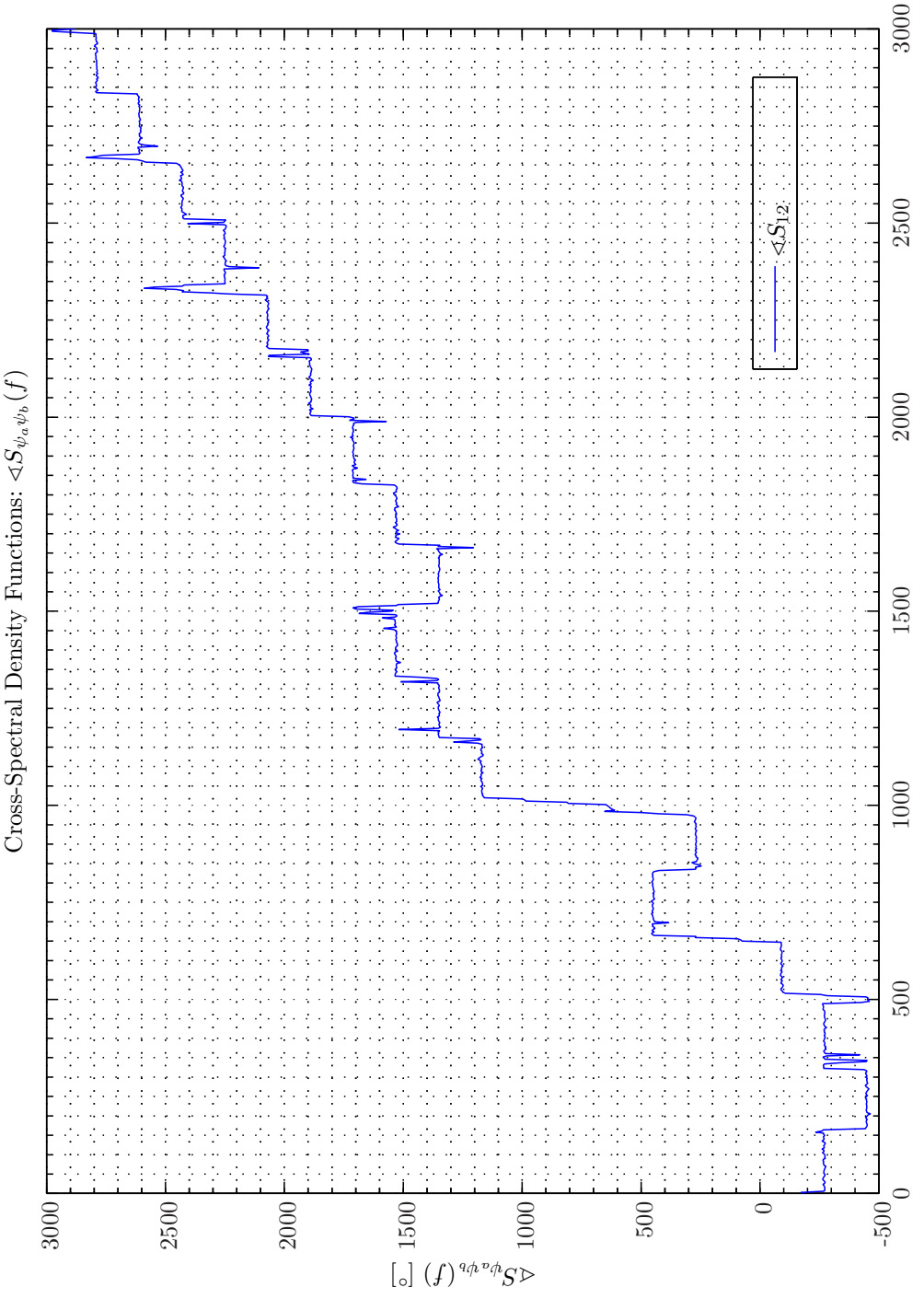

Sim 3.5.14: *Cross-Spectral Density Functions*: **Statistical Data Analysis**: Single-Sided Modified Periodogram, $f_s = 6$ kHz, $N_{DFT} = 2048$, $L_{DFT} = 1501$, $R_{DFT} = 751$, Hanning, $\Delta f_m = 16$ Hz, $T_{DFT} = 0.25017$ s, $N_{f,DFT} = 1025$, $\Delta f_{DFT} = 2.9297$ Hz, $K_{DFT} = 1597$; Wiener Hopf Modeling Filter; *Channels:* $\#1 \leftarrow v_1; \#2 \leftarrow v_2;$.

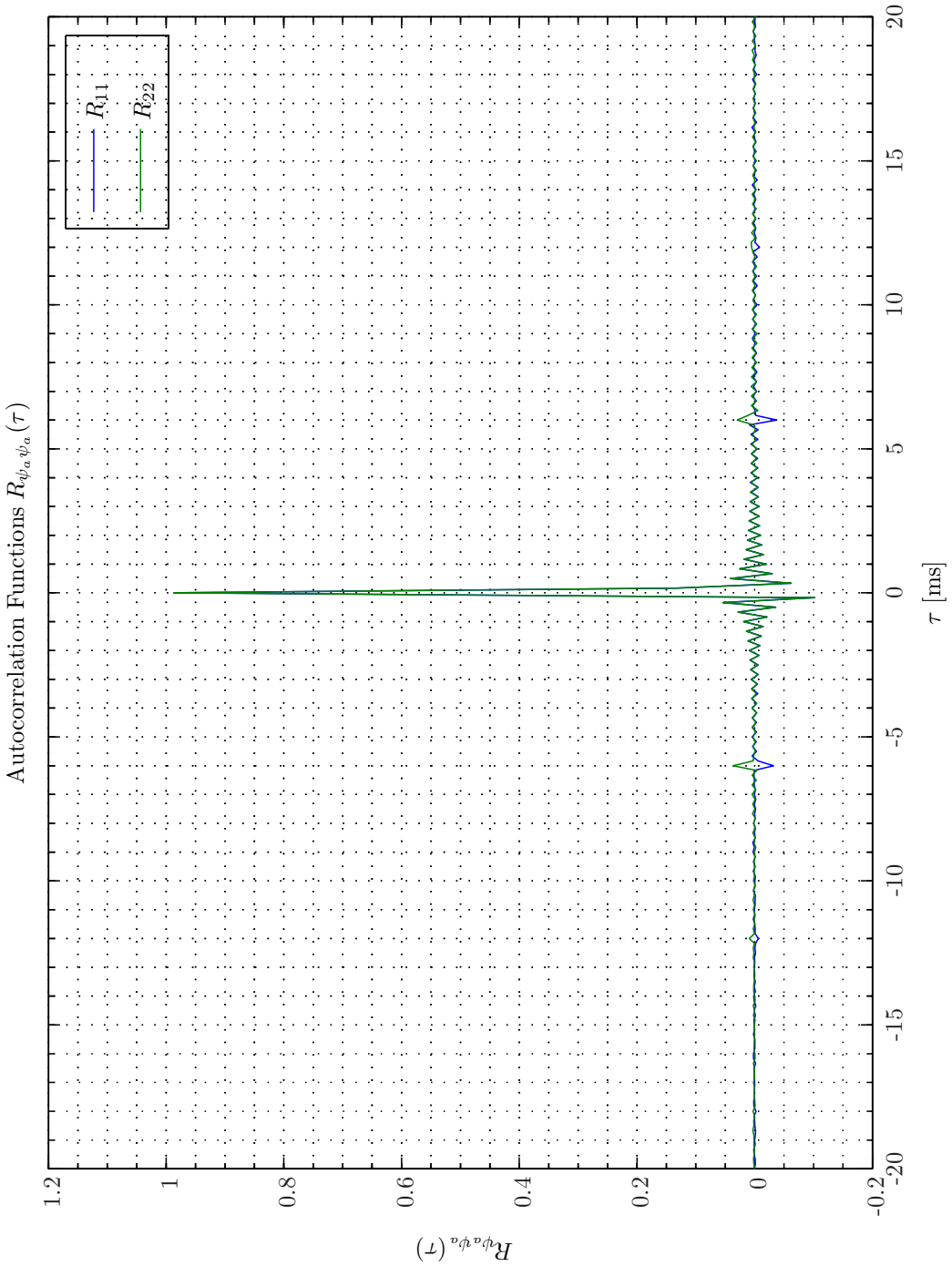

Sim 3.5.15: *Autocorrelation Functions:* $R_{\psi_a\psi_a}(\tau)$: **Statistical Data Analysis**: Single-Sided Modified Periodogram, $f_s = 6$ kHz, $N_{DFT} = 2048$, $L_{DFT} = 1501$, $R_{DFT} = 751$, Hanning, $\Delta f_m = 16$ Hz, $T_{DFT} = 0.25017$ s, $N_{f,DFT} = 1025$, $\Delta f_{DFT} = 2.9297$ Hz, $K_{DFT} = 1597$; Wiener Hopf Modeling Filter; *Channels:* $\#1 \leftarrow v_1$; $\#2 \leftarrow v_2$; .

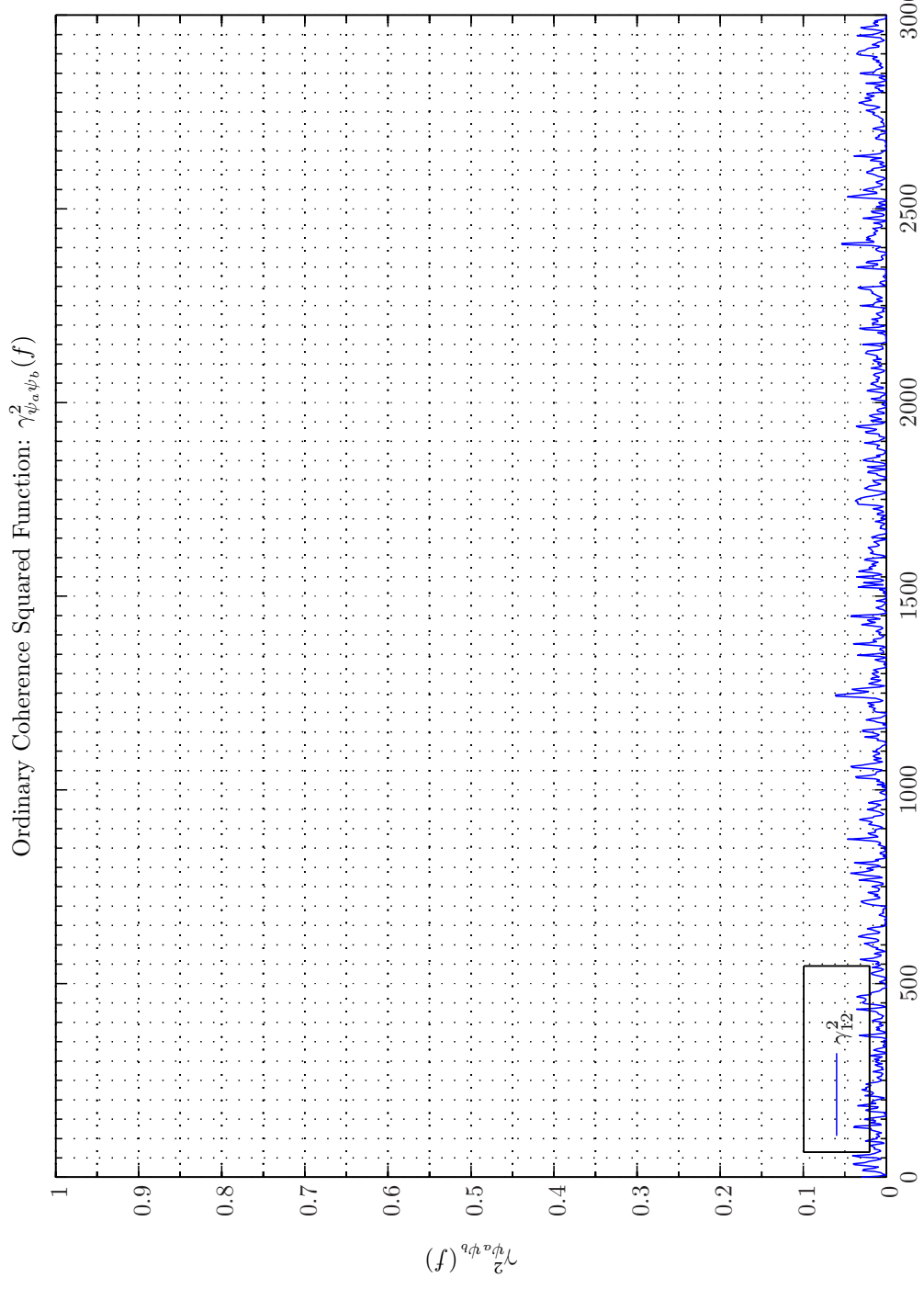

Sim 3.5.16: *Ordinary Coherency-Squared Functions* $\gamma^2_{\psi_a\psi_b}(f)$: **Statistical Data Analysis**: Single-Sided Modified Periodogram, $f_s = 6$ kHz, $N_{DFT} = 2048$, $L_{DFT} = 1501$, $R_{DFT} = 751$, Hanning, $\Delta f_m = 16$ Hz, $T_{DFT} = 0.25017$ s, $N_{f,DFT} = 1025$, $\Delta f_{DFT} = 2.9297$ Hz, $K_{DFT} = 1597$; Wiener Hopf Modeling Filter; *Channels:* $\#1 \leftarrow v_1$; $\#2 \leftarrow v_2$; .

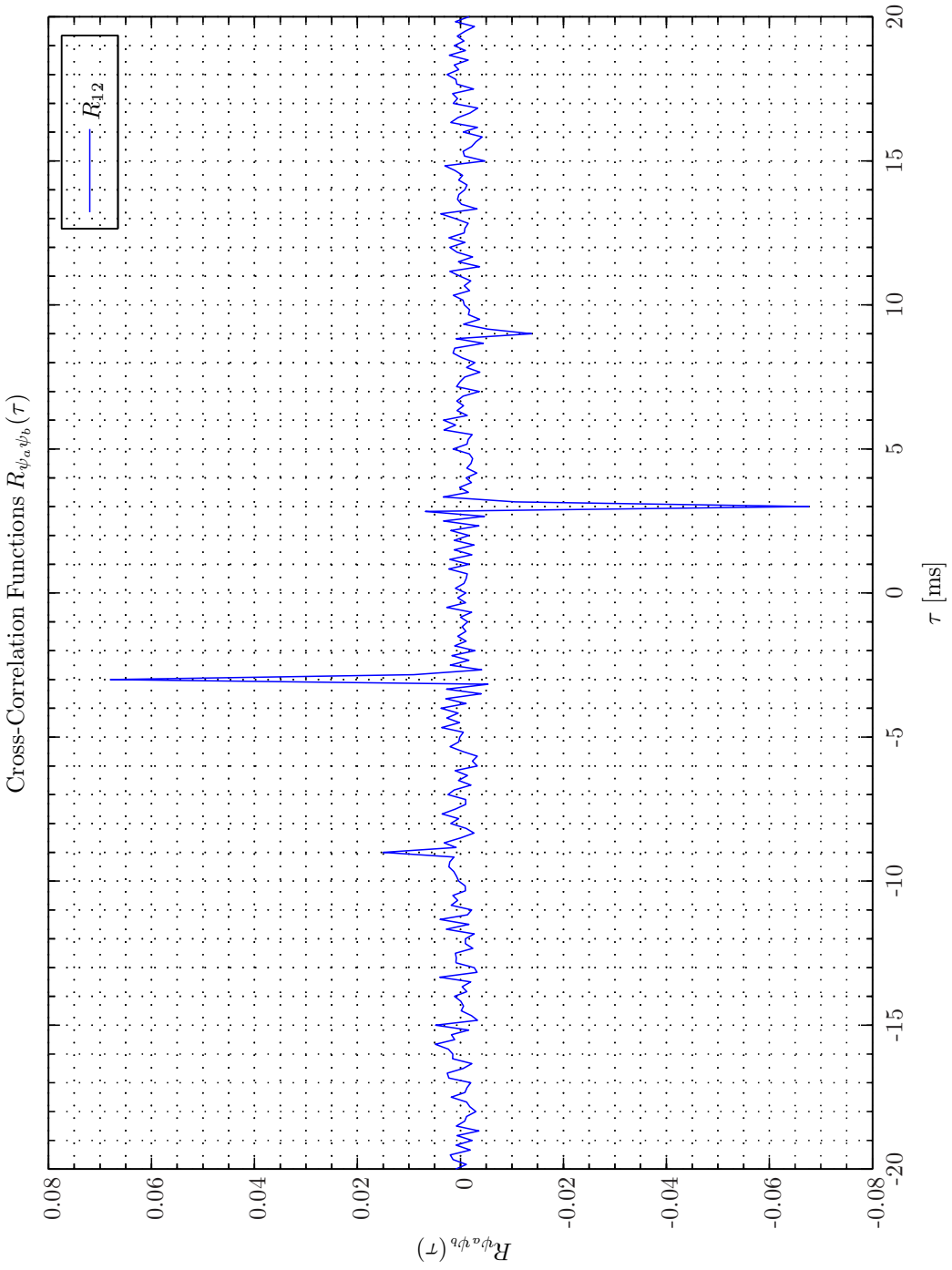

Sim 3.5.17: *Cross-Correlation Functions:* $R_{\psi_a\psi_b}(\tau)$: **Statistical Data Analysis**: Single-Sided Modified Periodogram, f_s = 6 kHz, N_{DFT} = 2048, L_{DFT} = 1501, R_{DFT} = 751, Hanning, Δf_m = 16 Hz, T_{DFT} = 0.25017 s, $N_{f,DFT}$ = 1025, Δf_{DFT} = 2.9297 Hz, K_{DFT} = 1597; Wiener Hopf Modeling Filter; *Channels:* #1 ← v_1; #2 ← v_2; .

phase of $L(\mathrm{e}^{\imath\omega})$ is decreasing and the phase shift amounts to $-18 \cdot 180^\circ = 3240^\circ$ at $f = f_s/2$ as desired (it is therefore $L(z)$ and not $L^{-*}(z^{-*})$ that we end up with). Close examination of the phase function of all four entities in $L(\mathrm{e}^{\imath\omega})$ reveals a function that decreases from 45° at $f = 0$ to 0° at $f = f_s/2$. The initial phase lead of 45° can probably be attributed the fact that the PEF is almost completely removing any low frequency contents. In the high frequency range, however, the reference signal just passes by the PEF.

3.6 Conclusions

The theme of this chapter has been causality constraints pertaining to active control (AC). Fundamental to the casuality analysis is the so-called plus operator that enters the formula that defines the optimal causally constrained weight vector. Constructed examples, have revealed some of the technicalities associated with the use of the nonlinear plus operator. Accordingly, new insights to the actions of the plus operator $\left\{ \cdot \right\}_+$ was provided. Moreover, a new expression for the optimally constrained weight vector for a system that possess underlying structure was obtained.

A practical framework for multiple-channel (MC) spectral factorization using the prediction error filter (PEF) was developed. This technique is referred to as the multiple-channel prediction error filter spectral factorization algorithm. For the purpose of MC spectral factorization a variant of existing transfer function definitions was proposed. By using this definition more robust estimates of the transfer function of the PEF was obtained. This multiple-channel prediction error filter spectral factorization (MCPEFSF) algorithm has been used in all the presented examples in this chapter. Another objective pursued in the chapter was to examine the consequence of using the ordinary **t**-domain Wiener-Hopf (WH) filter instead of the more computational intensive **z**-domain WH filter. It was demonstrated that by using the MCPEFSF algorithm that the associated **z**-domain WH filter when exposed to random white noise signals even outperformed the **t**-domain WH filter that is tailored to such flat spectral excitation. Moreover, for the single-channel (SC) case the MCPEFSF algorithm even outperformed the *cepstral* method. However, the requirement on a sufficient high filter order may be prohibitive in terms of realizable DFT sizes. Finally, from the practical hearing protection device (HPD) with active noise reduction (ANR) system the two WHs differed only marginally.

A suite of examples of increasing complexity was constructed in order to exhibit some of the characteristics related to causality constraints. In order to make this exhibition more clear the feedforward system (FFS) examples mainly considered the use of two reference sensors.

In one example the advantage of even small reference sensor directivity was exhibited. By introducing element gain an underlying infinite sum of terms is shifted to an exponentially decaying series with a decay constant that depends on the element directivity. In particular, the decay constant coincides with the minimum directivity for an assumed cosine-on-a-pedestal azimuthal pattern.

In another example, it was demonstrated that for a secondary path with a impulse response function that takes form of a rectangular pulse, the inverse of the minimum-phase component is constituted from an infinite sum of non converging terms. We may therefore expect that a very large filter order in finite-duration impulse response (FIR) implementation is required for successful ANR performance with such a plant involved. In a general context it can be concluded that the inverse of the minimum-phase component of the plant is of profound importance.

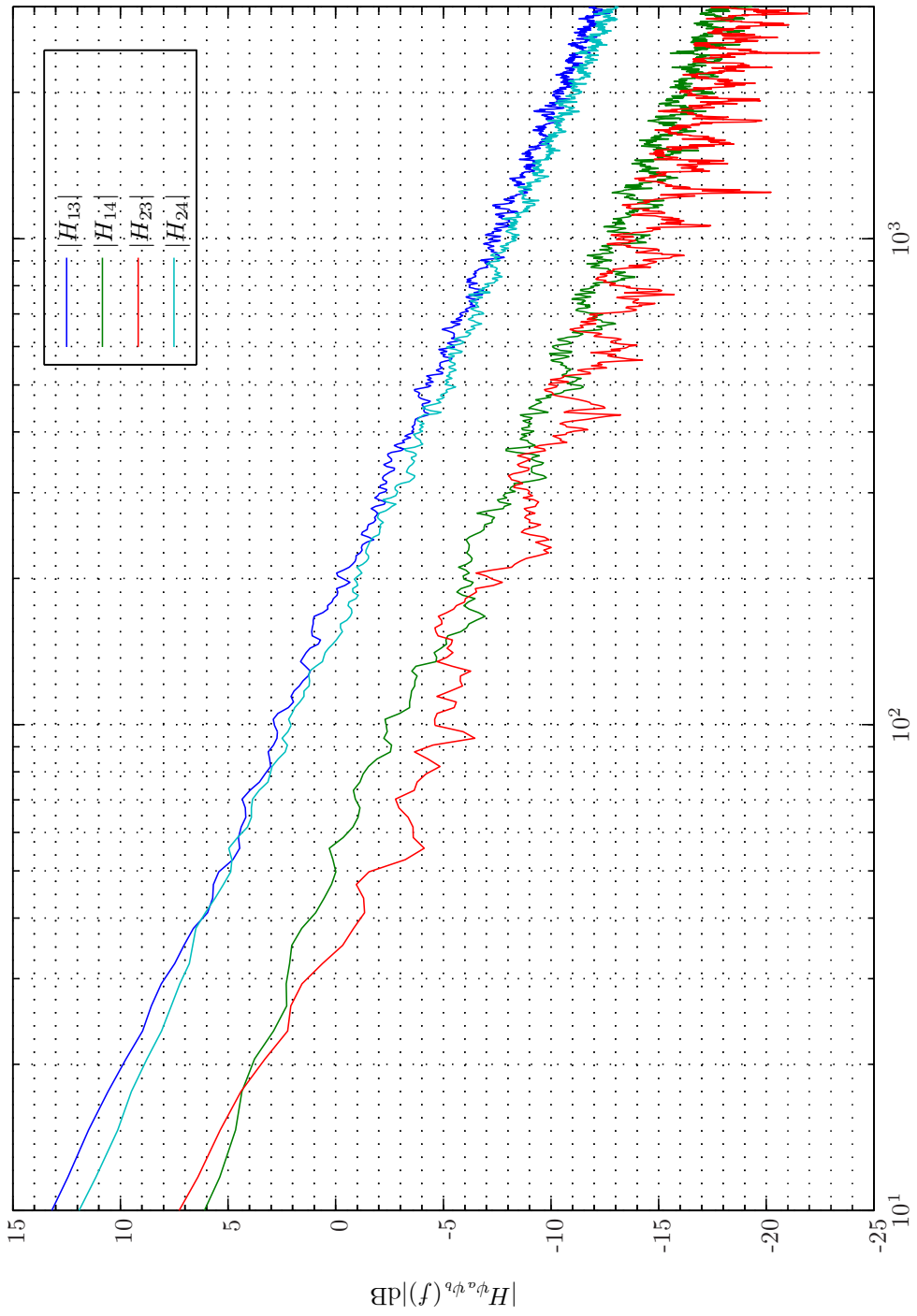

Sim 3.5.18: *Transfer Function, Magnitude:* $|H_{\psi_a\psi_b}(f)|$: **Statistical Data Analysis**: Single-Sided Modified Periodogram, f_s = 6 kHz, N_{DFT} = 2048, L_{DFT} = 1501, R_{DFT} = 751, Hanning, Δf_m = 16 Hz, T_{DFT} = 0.25017 s, $N_{f,DFT}$ = 1025, Δf_{DFT} = 2.9297 Hz, K_{DFT} = 1597; Wiener Hopf Modeling Filter; *Channels:* #1 ← v_1, #2 ← v_2, #3 ← x_1, #4 ← x_2. **Scenario:** `MultipleSinusoidalsAddiativeNoiseFeedforwardNx2Ne1Ny1Np0/20080214T115450:,`.

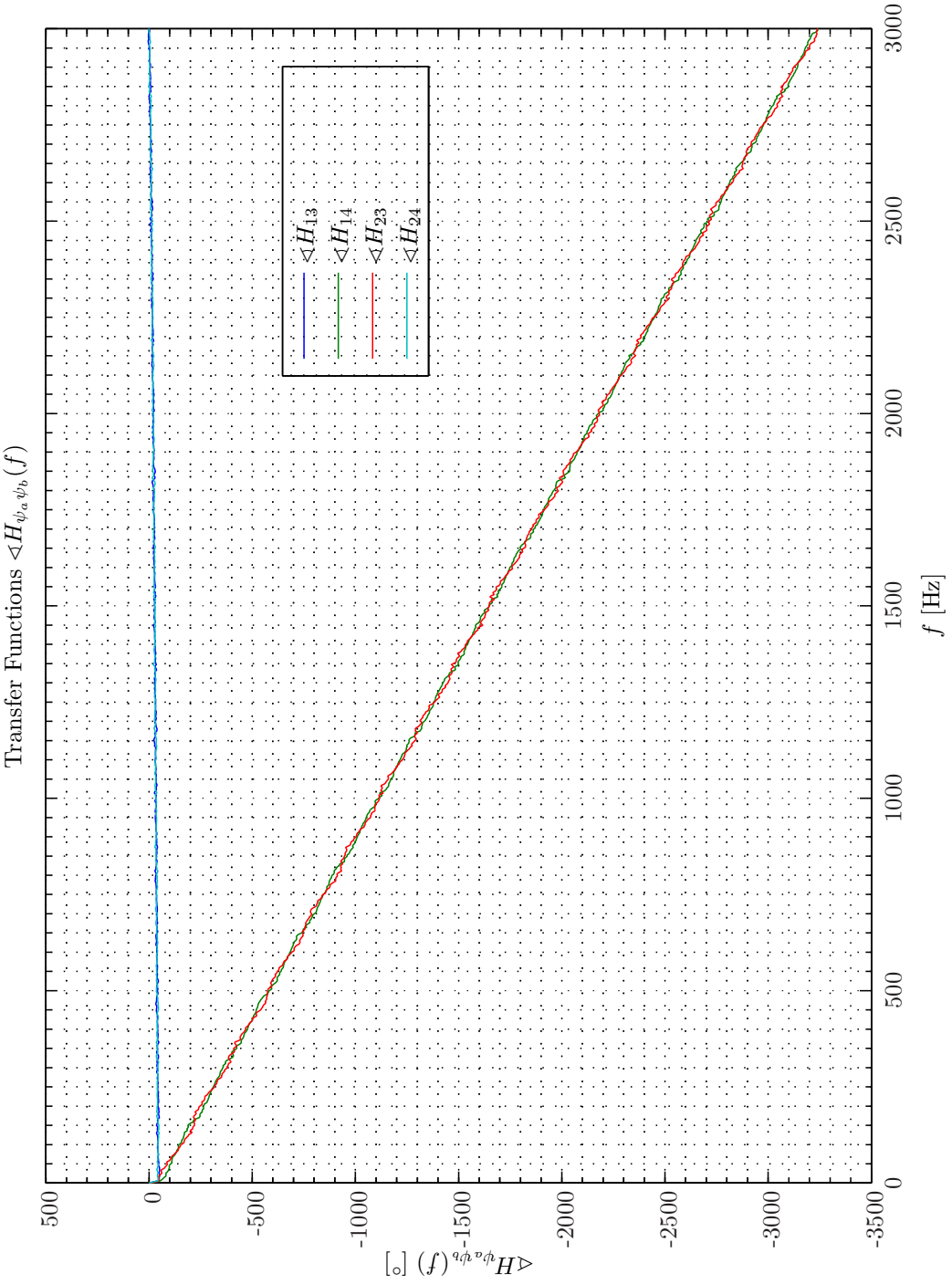

Sim 3.5.19: *Transfer Function, Phase:* $\sphericalangle H_{\psi_a\psi_b}(f)$: **Statistical Data Analysis**: Single-Sided Modified Periodogram, f_s = 6 kHz, N_{DFT} = 2048, L_{DFT} = 1501, R_{DFT} = 751, Hanning, Δf_m = 16 Hz, T_{DFT} = 0.25017 s, $N_{f,DFT}$ = 1025, Δf_{DFT} = 2.9297 Hz, K_{DFT} = 1597; Wiener Hopf Modeling Filter; *Channels:* #1 ← v_1, #2 ← v_2, #3 ← x_1, #4 ← x_2. **Scenario:** `MultipleSinusoidalsAddiativeNoiseFeedforwardNx2Ne1Ny1Np0/20080214T115450:`, .

The all-pass component of the secondary path $\tilde{g}_{ey,\mathrm{all}}(z)$ counteracts the benefits of the acquisition lead time in $\tilde{g}_{ex}(z)$ provided by CFF.

Group delays are often considered in an initial design phase in order to assess the ANR capability of a system. However, such analysis is often deemed to be to primitive and will often lead to an underestimation of the achievable performance. It was, however, confirmed that the discrete-time group delays have a direct impact on the achievable performance while the impact of continuous-time group delays is less predictable. Hence, the performance analysis should preferably be based on simulations involving one of the expressions for the optimal causally constrained and finite-order constrained weight vector for the MC **z**-domain WH filter presented in this chapter.

The analysis also revealed that the *current* version of the Terma Earcup System is rather unfortunate being insufficiently damped. However, simulations did reveal that by decreasing the Q-factors associated with the resonance of the passive spring-mass-damper system and the Q-factor associated with the cross-over network of the tweeter unit would significantly improve the ANR performance of the helmet system. Such improved design is beneficial both for a feedback system (FBS) and a FFS.

In conclusion, a considerably amount of ANR performance is often available from a well-designed HPD in particular the plant that in the present case coincides with the Terma Earcup system. Accordingly, in the design of an active HPD the optimal choice of the secondary path and in particular the resulting inverse of the minimum-phase component is crucial and should receive much attention in the design phase.

Considering, the proposed confined feedforward system (CFFS) it was found that for the actual HPD owing to the acquisition lead times provided this topology a higher AC attenuation is in general obtained than by a FBS in particular if we use a FIR filter of sufficiently high order and enforce the FBS to be robustly stable. However, owing to the fewer total weights involved the FBS provides the fastest convergence. The examples also revealed that by optimizing the HPD as discussed above the FBS will then typically provide the best ANR performance in the low-frequency range while the CFFS is in favour at higher frequencies. Requirement on robust stability, however, may severely limit the upper operational band width of the FBS.

3.A Spectral Factorization of a Pink Noise Signal[13]

We assume that an equal amount of colorization is present in the reference signals and the disturbance signals. Accordingly, applying the model in section 3.3 we may in this example consider the modeling filter $L_x(z)$ as constituted by a cascade coupling of a colorization filter $L_{wv}(z)$ and a channel delay filter $L_{xw}(z)$ that in turn coincides with $L_x(z)$ in Example 3.2.2 on page 119. Both modeling filter components are linear time-invariant (LTI) filters and $L_x(z)$ can therefore expressed as $L(z) = L_{xw}(z)L_{wv}(z)$, where $L_{wv}(z)$ in turn equals $L_{wv,1}(z)\mathrm{I}$ for some scalar-valued colorization filter $L_{wv,1}(z)$. Accordingly, we may express the z-autospectrum of the random colored noise signals by

$$S_{ww}(z) = L_{wv}(z)L_{wv}^{*}(z^{-*}) \tag{3.A.1}$$

and we wish to obtain an expression for $L_{wv,1}(z)$ and therefore first consider the aspect of

[13] This appendix provides an attempt to carry out the spectral factorization of a pink noise signal in-hand that, however, can be skipped on a first reading.

colorization on a single channel. For pink noise signals we may obtain the z-autospectrum as follows. On the unit circle the auto spectral density functions are given by

$$S(\mathrm{e}^{\imath\omega}) = S(\mathrm{e}^{-\imath\omega}) = \begin{cases} A|\omega_1|^{-1}; & \omega \leq \omega_1 \\ A|\omega|^{-1}; & \omega > \omega_1 \end{cases} \tag{3.A.2}$$

for some normalization constant A, that for a unit variance signal and a two-sided spectrum is obtained from

$$\int_{-\pi}^{\pi} S(\mathrm{e}^{\imath\omega})\,\mathrm{d}\omega = 2\int_0^{\omega_1} A\omega_1^{-1}\,\mathrm{d}\omega + 2\int_{\omega_1}^{\pi} A\omega^{-1}\,\mathrm{d}\omega = 2A\Big[1 - \ln\Big(\frac{\omega_1}{\pi}\Big)\Big] = 1, \tag{3.A.3}$$

where $\omega_1 > 0$ is a lower cut-off frequency of the pink noise excitation that ensures the convergence of the third integral in (3.A.3). Then using the relation $\omega = \frac{2f}{f_s}\pi$ and that $\ln(z)$ evaluates to $\imath\omega$ on the unit circle we obtain

$$S(z) = \frac{2\pi\imath}{f_s \ln\frac{f_s}{2f_1}\ln(z)}, \quad z \notin \cup\{0, C_{\pm\omega_1}\}, \tag{3.A.4}$$

where $C_{\pm\omega_1}$ refers to the circular arc on the unit circle from $-\omega_1$ to ω_1[14]. In order to proceed we may use the following Taylor expansion for $\ln(z)$ [1]

$$\begin{aligned} \ln(z) &= 2\Big[\Big(\frac{z-1}{z+1}\Big) + \frac{1}{3}\Big(\frac{z-1}{z+1}\Big)^3 + \frac{1}{5}\Big(\frac{z-1}{z+1}\Big)^5 \dots\Big] \\ &= 2\sum_{k=0}^{\infty} \frac{1}{2k+1}\Big(\frac{z-1}{z+1}\Big)^{2k+1}; \quad \Re\{z\} \geq 0, z \neq 0. \end{aligned} \tag{3.A.5}$$

Moreover, as $\ln(-z) = \ln^*(z)$ (3.A.5) can be used everywhere except for $z = 0$. By insertion of (3.A.5) in (3.A.4) we get

$$S(z) = \begin{cases} \pi\imath\Big[f_s \ln\frac{f_s}{2f_1}\sum_{k=0}^{\infty}\frac{1}{2k+1}\big(\frac{z-1}{z+1}\big)^{2k+1}\Big]^{-1}; & \Re\{z\} \geq 0, z \notin C_{+\omega_1} \\ \pi\imath\Big[f_s \ln\frac{f_s}{2f_1}\sum_{k=0}^{\infty}\frac{1}{2k+1}\big(\frac{z^*+1}{z^*-1}\big)^{2k+1}\Big]^{-1}; & \Re\{z\} < 0 z \notin C_{-\omega_1}. \end{cases} \tag{3.A.6}$$

It can be shown that the following scalar-valued canonical spectral factorization holds

$$L_{11}(z) = \ln^{-1/2}(z); \quad r_e = \frac{\pi}{f_s \ln\frac{f_s}{2f_1}}; \quad L^*(z^{-*}) = \ln^{-*/2}(z^{-*}). \tag{3.A.7}$$

Using the Taylor expansion (3.A.5) the modeling filter $L(z)$ becomes

$$L_{11}(z) = 2^{-\frac{1}{2}}\left(\sum_{k=0}^{\infty}\frac{1}{2k+1}\Big(\frac{z-1}{z+1}\Big)^{2k+1}\right)^{-\frac{1}{2}}; \quad \Re\{z\} \geq 0, z \neq 0. \tag{3.A.8}$$

[14] We ignore for a moment the problem related to the lack of analyticity in (3.A.2) at the points $z = \mathrm{e}^{\pm\imath\omega_1}$.

Although we have obtained a closed-form factorization of (3.A.6) in order to proceed we should take the inverse of (3.A.8) evaluated in a time-reversed sense, that is,

$$L_{11}^{-1}(z^{-1}) = 2^{\frac{1}{2}}\left(\sum_{k=0}^{\infty}\frac{-1}{2k+1}\Big(\frac{z-1}{z+1}\Big)^{2k+1}\right)^{\frac{1}{2}};\quad \Re\{z\}\geq 0, z\neq 0 \tag{3.A.9}$$

and applying a Taylor expansion for $(1+z)^{\frac{1}{2}}$ and subsequently inserting the expression obtained in that way in (3.2.11). In addition the remarks made in Equation 14 concerning analyticity, that is, the limited range of the pink noise excitation also has to be considered. Altogether, however, this seems be a quite challenging task.

Moreover, we also appreciate that the normalization constraint $L(\infty) = 1$ cannot be satisfied. This is due to fact that $S(z)$ has a nonrational z-spectrum. From section 3.2.2 the existence of the spectral factorization is guaranteed provided $S_{xx}(\mathrm{e}^{\imath\omega})$ satisfies the finite-power requirement and the Paley-Wiener condition. The finite-power requirement (3.2.7) is evidently satisfied. The latter requirement can easily be verified from insertion of (3.A.2) in (3.2.8)

$$\begin{aligned}\frac{1}{2\pi}\int_{-\pi}^{\pi}\ln\big(S_{xx}(\mathrm{e}^{\imath\omega})\big)\,\mathrm{d}\omega &= \frac{1}{\pi}\int_{0}^{\omega_1}\ln\big(A\omega_1^{-1}\big)\,\mathrm{d}\omega + \frac{1}{\pi}\int_{\omega_1}^{\pi}\ln\big(A\omega^{-1}\big)\,\mathrm{d}\omega\\ &= \frac{1}{\pi}\omega_1\ln\big(A\omega_1^{-1}\big) + \frac{1}{\pi}\big[\omega\ln A - \omega\ln\omega + \omega\big]_{\omega_1}^{\pi}\\ &= \frac{1}{\pi}\Big[\omega_1\ln\big(A\omega_1^{-1}\big) + (1+\ln A)(\pi-\omega_1) + \omega_1\ln\omega_1 - \pi\ln\pi\Big]\\ &= \ln\big(A\pi^{-1}\big) + 1 - \frac{\omega_1}{\pi}\end{aligned}$$

insertion of (3.A.3) gives

$$\frac{1}{2\pi}\int_{-\pi}^{\pi}\ln\big(S_{xx}(\mathrm{e}^{\imath\omega})\big)\,\mathrm{d}\omega = 1 - \ln\left(2\pi\left[1-\ln\Big(\frac{\omega_1}{\pi}\Big)\right]\right) - \frac{\omega_1}{\pi} > -\infty \tag{3.A.10}$$

for any value of $\omega_1 \geq 0$ and the Paley-Wiener condition (3.2.8) is therefore evidently satisfied. Hence, the choice of a lower cut-off frequency ω_1 for the pink noise excitation to be strictly greater than zero is only necessary for the finite power requirement. Then r_e can be obtained from the *Szegö formula*

$$r_e = \exp\Big[\frac{1}{2\pi}\int_{-\pi}^{\pi}\ln\big(S_{xx}(\mathrm{e}^{\imath\omega})\big)\,\mathrm{d}\omega\Big]. \tag{3.A.11}$$

By insertion of (3.A.2) in the Szegö formula (3.A.11) and using (3.A.10) we readily obtain

$$r_e = \frac{1}{2\pi}\left[1-\ln\Big(\frac{\omega_1}{\pi}\Big)\right]^{-1}\exp\Big(1-\frac{\omega_1}{\pi}\Big). \tag{3.A.12}$$

Still, the determination $L_{11}(z)$ remains. Although a closed-form expression for the basic spectral

factorization involving an *outer function* and the Herglotz-Riesz transform can be found in, e.g., [3]

$$L_+(z) = \sqrt{\exp\left[\frac{1}{2\pi}\int_{-\pi}^{\pi} \ln\big(S_{xx}(\mathrm{e}^{\imath\omega})\big)\frac{\mathrm{e}^{-\imath\omega}+z}{\mathrm{e}^{-\imath\omega}-z}\,\mathrm{d}\omega\right]}, \tag{3.A.13}$$

the evaluation hereof and subsequent insertion of the expression obtained in that way in (3.2.11) is rather difficult and most of all does not provide us with readily explainable terms as in the preceding examples.

This Appendixhas revealed that the spectral factorization in general is exceedingly difficult to carry out by "hand calculations". We could, however, construct colored signals with known z-autospectrum as exponentially correlated signals.

Bibliography

[1] Milton Abramowitz and Irene A. Stegun. *Handbook of Mathematical Functions*. U.S. Government Printing Office, 6th edition, 1984.

[2] Julius S. Bendat and Allan G. Piersol. *Random data Analysis and measurement procedures*. John Wiley & Sons, Inc., 3rd edition, 2000.

[3] Holger Boche and Volker Pohl. Structural properties of the wiener filter - stability, smoothness properties, and fir approximation behavior. *IEEE Transactions on Information Theory*, 52(9):4272–4282, 2006.

[4] J. G. Cook and Stephen J. Elliott. Connection between mutichannel prediction error filter and spectral factorisation. *IEE, Electronics letters*, 35(15):1218–1220, 1999.

[5] Stephen J. Elliott. *Signal Processing for Active Control*. London: Academic Press, 2001.

[6] Stephen J. Elliott and Boaz Rafaely. Frequency-domain adaptation of causal digital filters. *IEEE Transactions on Signal Processing*, 48(5):1354–1364, 2000.

[7] R. H. Hardin and N. J. A. Sloane. Mclaren's improved snub cube and other new spherical designs in three dimensions. *Discrete and Computational Geometry*, 15:429–441, 1996.

[8] Thomas Kailath, Ali H. Sayed, and Babak Hassabi. *Linear Estimation*. Printice Hall, Upper Saddle River, New Jersey, 2000.

[9] D. N. Prabhakar Murthy. Factorization of discrete-process spectral matrices. *IEEE Transactions on Information Theory*, 19(5):693–696, 1973.

[10] Alan V. Oppenheim and Ronald W. Schafer. *Digital Signal Processing*. Prentice Hall International Inc., 1975.

[11] Athanasios Papoulis and S. Unnikrishna Pillai. *Probability, Random Variables and Stochastic Processes*. McGraw-Hill, New York, 4th edition, 2002.

[12] Boaz Rafaely and Matthew Jones. Combined feedback-feedforward active noise-reducing headset -the effect of the acoustics on broadband performance. *The Journal of the Acoustical Society of America*, 112(3):981–989, 2002.

[13] Ali H. Sayed and Thomas Kailath. A survey of spectral factorization methods. *Numerical Linear Algebra with Applications*, 8:467–496, 2001.

Part II

ACTIVE NOISE CONTROLLER

4. SYSTEM DESCRIPTION

4.1 Introduction

In this chapter the control subsystem involved in the active noise control (ANC) system depicted in Figure 1.1 on page 7 will be presented. The aim is to set the hybrid MIMO feedforward-feedback system (HMIMOFFFBS) presented in chapter 6 into an overall system perspective.

4.1.1 Chapter Outline

First section 4.2 introduces the topology of the overall control system. Next in section 4.3 a description of the continuous-time controller part of the hybrid continuous-time discrete-time topology (HCTDTT) is provided. Then section 4.4 considers the discrete-time controller part of the HCTDTT. The advantages of combining a feedback- and a feedforward control system is the theme of section 4.5. The internal model control (IMC) used in the discrete-time feedback controller is presented in section 4.6. Finally, the use of an adaptive inverse controller is treated in section 4.7.

4.2 Hybrid Continuous-Time Discrete-Time Topology

The single-input and single-output (SISO) controller topology depicted in Figure 4.1 on page 241 encompasses a *hybrid*[1] feedback continuous-time and feedback discrete-time controller consisting of an continuous-time inner loop and a discrete-time outer control loop [1, Ch. 7.5]. The continuous-time controller (sometimes referred to as analogue controller) consists of the continuous-time plant, $G_C(s)$, the continuous-time feedback filter $H_C(s)$. The digital to analogue converter $T_{DAC}(s)$ in cascade with the reconstruction filter $T_{RF}(s)$, the analogue controller, the anti-aliasing filter $T_{AAF}(s)$ and finally the analogue to digital converter $T_{ADC}(s)$ constitute together a physical plant denoted by $\tilde{g}(z)$[2]. As seen in Figure 4.1 the physical plant, $\tilde{g}(z)$, is connected in cascade with a *plant correction filter*, $\hat{C}(z)$. This plant correction filter (discussed in more details in section 4.7 on page 245) is part of an *adaptive inverse controller* that is depicted in Figure 4.4 on page 247. The purpose of the adaptive inverse controller is to maintain the effective plant experienced by the digital controller at some prescribed reference transfer function, $\tilde{g}_{ref}(z)$.

[1] The term *hybrid* is ambiguous as it is used within the active control (AC) community with different and context dependent meanings. Hybrid may as here refer to the combination of continuous-time and discrete-time controllers. In other contexts hybrid means a combination of feedback and feedforward control strategies (as in chapter 6). Finally, the term hybrid sometimes refers to the combination of passive and active noise reduction strategies.

[2] We will relax on notation and allow use of mixed domain representation of the various transfer functions involved.

In feedback control design a trade-off between noise suppression and stability will always exist. By adaptively maintaining the effective plant at the prescribed frequency response or at least reducing the variation from this level experienced during operation of the system we can effectively reduce the controller margins normally enforced in a feedback design in order to ensure robust stability. Hence, by reducing the requirement on stability margins the digital controller can achieve a higher level of noise attenuation.
The adaptive inverse control will be pursued in more details in section 4.7.

The aim of combining continuous-time and discrete-time controllers can be found in [1, Ch. 7.5] and summarized here:

HCTDTT 1. By using complementary advantages of a continuous-time controller and a discrete-time controller better active noise reduction (ANR) performance can be achieved as compared with either of the controllers operating alone. For *stationary broad band* noise signals a *fixed* continuous-time controller may provide a cost effective solution. Therefore, by far most of the ANR implementations for headsets hitherto have been based on pure analogue circuitry design. For *nonstationary* disturbances, however, adaptivity becomes important. This functionality is provided by an *adaptive* discrete-time controller. Inherent processing delays but also group delays encountered in the anti-aliasing filter (AAF), analogue to digital converter (ADC), digital to analogue converter (DAC) and reconstruction filter (RF) will limit the operational bandwidth as explained in details in section A.3 on page 532. In a confined feedforward-feedback system as presented in chapter 6 these delays, however, become less significant to the system performance.

HCTDTT 2. Reduction of impulse response time of plant $\tilde{g}(z)$ due to the presence of the continuous-time controller.

HCTDTT 3. Reduction of the variability of the plant response due to continuous-time feedback. This reduction in plant uncertainty, however, is more important in systems that do apply adaptive inverse control (AIC).

Hence, in principle the continuous-time controller is responsible for attenuation of *stationary broad band* disturbances. This basically requires a relative smooth frequency response without delays. The digital controller is responsible for suppression of any residual non-stationary deterministic (narrow band) noise signal not sufficiently attenuated by the action of the analogue controller.

For testing purposes the analogue controller and the digital controller should both be able to operate in stand-alone mode.

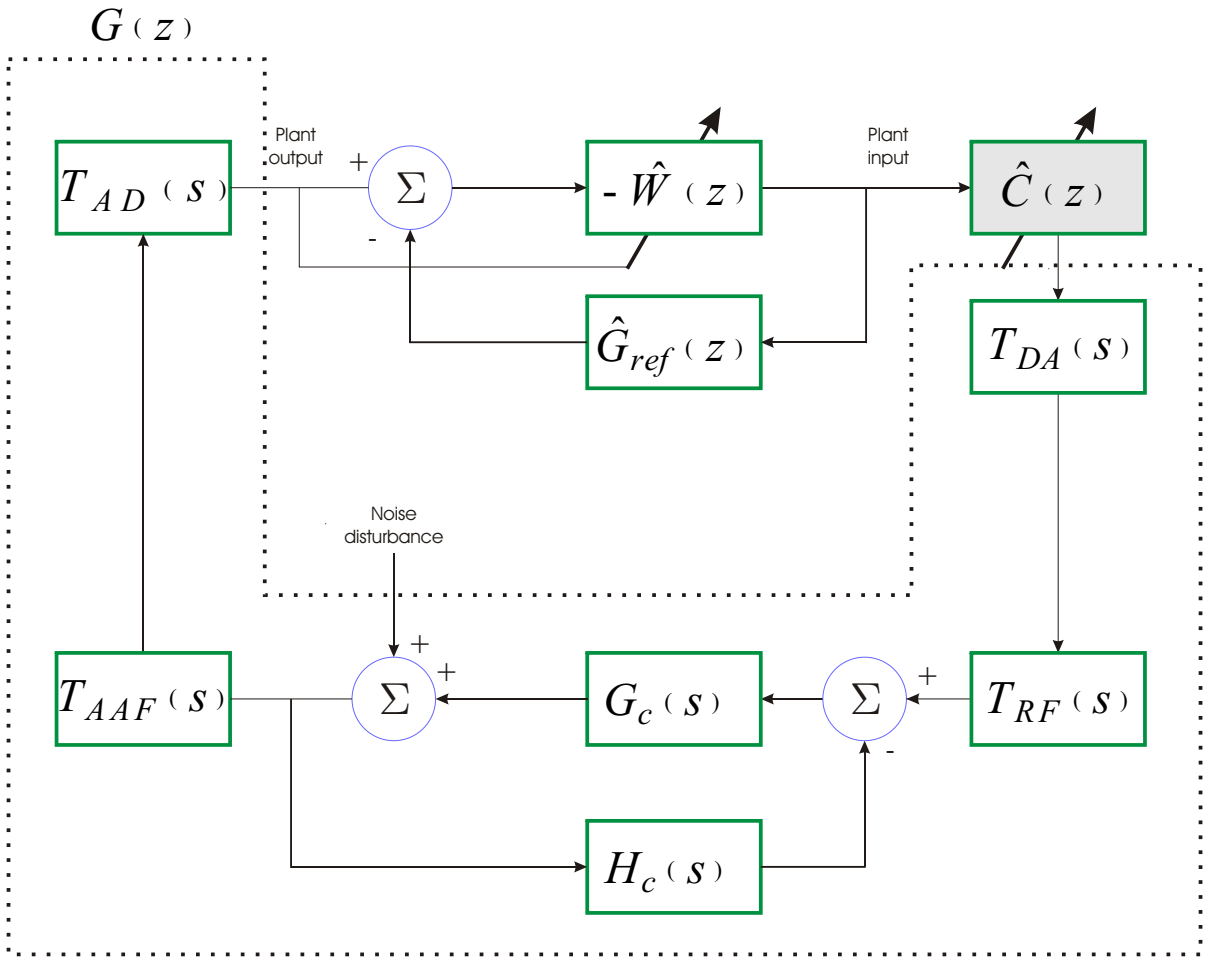

Fig. 4.1: Hybrid Continuous-Time Discrete-Time Controller.

This type of hybrid topology is also amendable to continuous-time feedback discrete-time feedforward-feedback controller and to multiple-input and multiple-output (MIMO) cases as presented in chapter 6 on page 273.

4.3 Continuous-Time Controller

The continuous-time controller is currently under development under a contract with Royal Danish Air Force (RDAF) and will not be further detailed here.

4.4 Discrete-Time Controller

The HMIMOFFFBS will be presented in details in chapter 6.

4.5 Hybrid Feedforward-Feedback Control

The feedforward-feedback topology is illuminated in Figure 4.2 and detailed in chapter 6.

As stated in [1, Ch. 7] and also in [2, Ch. 6] by combining the advantages of feedback and feedforward topologies a better active control performance can be achieved. The effective system (plant) as seen from the adaptive feedforward controller is modified by the operation of a fixed or adaptive feedback system. This can beneficial in the following ways:

FFFBS Pro.# 1. Provision of time-advanced information by the feedforward system (FFS) not available to the stand alone feedback system. Accordingly the upper frequency of AC can be increased (see section A.3 on page 532).

FFFBS Pro.# 2. Reduction of variability with time of effective plant response. This claim, however, should be reconsidered if the feedback controller is adaptive.

FFFBS Pro.# 3. Reduction of amplitude in plant resonances rendering the system easier to be controlled by the feedforward system.

FFFBS Pro.# 4. Reduction of convergence time in an adaptive feedforward system due to a reduction in the effective transient response.

FFFBS Pro.# 5. The feedback system (FBS) can complement the operation of a stand alone FFS that is dependent on the coherence function between the error sensors and the reference sensors. Hence, even with the confined feedforward-feedback active control system (CFFFBACS) topology the multiple coherence function will attain values less than unity at certain frequencies. In a multiple source environment and in particular in a diffuse sound field spatial under sampling will eventually take place with increasing frequency viz. (G.4.9) on page 714. Another potential source of a nonunity multiple coherence function is the presence of nonlinearities and sensing noise in feedforward system viz. section 2.2 on page 18. Moreover, in some ANC applications the reference sensors might be exposed to very high sound pressure levels or vibration levels beyond the linear dynamic range of these sensors. The error sensors, however, are often exposed to a reduced sound pressure level (SPL) due to the passive attenuation provided by the system and by the operation of the active controller.

In such nonunity multiple coherence environment the feedback controller will the be responsible for attenuation of high-frequency noise components, but might also provide supplementary attenuation in the lower and middle frequency range.

However, the following disadvantage is encountered:

FFFBS Con.# 1. Increase in system complexity.

In AC applications using adaptive filters a filtered-x (Fx) method is usually applied to compensate for the group delay and frequency transfer function of the plant as explained in section 6.3 on page 275. But when the effective plant seen from either of the feedback- or the feedforward-controller is modified by the actions of the other controller which plant transfer function should be invoked when applying the Fx. We will return to this issue in chapter 6 on page 273.

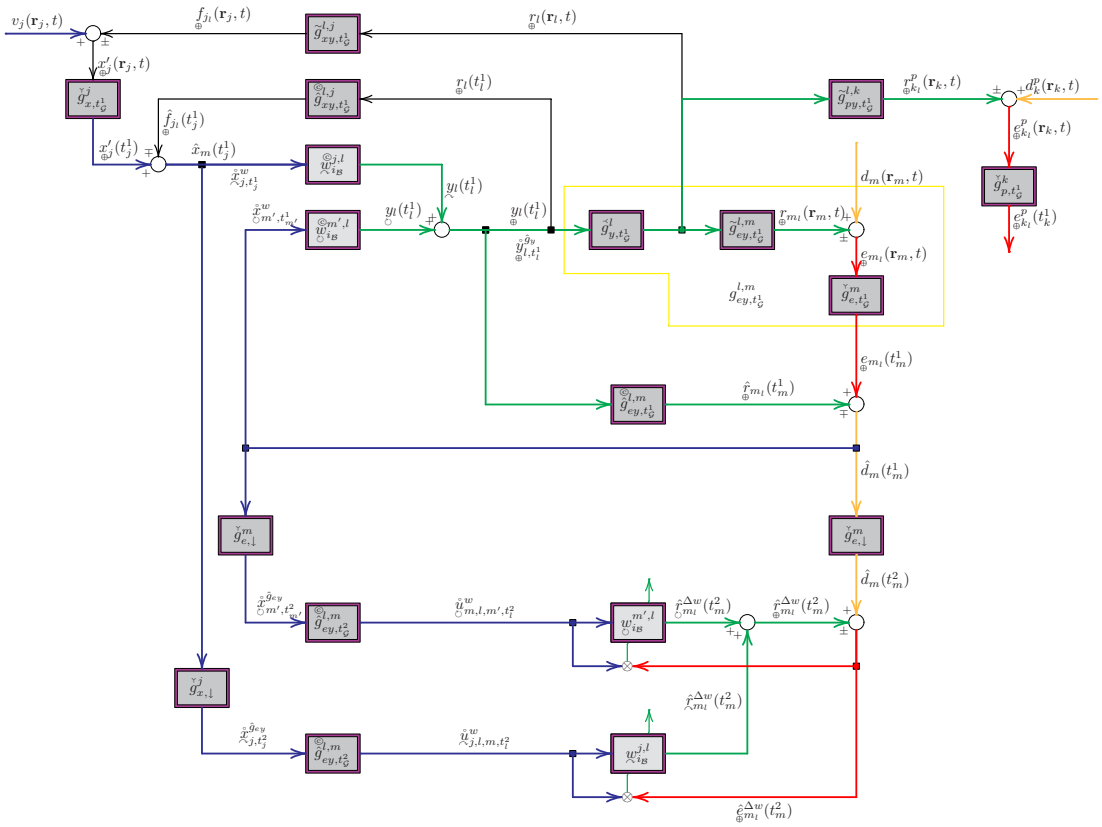

Fig. 4.2: Hybrid Feedforward-Feedback Controller.

4.6 Internal Model Control

The digital controller is based on an internal model control IMC architecture [3, Ch. 3] and [1, Ch. 6-7] depicted in Figure 4.3. The IMC architecture is used to transform the adaptive filter feedback topology into an apparent feedforward topology. The main advantages of implementing the IMC model in a feedback system is that the system then is guaranteed to be stable provided that the plant model is sufficiently accurate, that is, $\hat{\tilde{g}}(z) \approx \tilde{g}(z)$.

As stated in [1, Ch. 6-7] the adaptive filter weights are able to compensate for small deviations in the plant model. However, as the filtered-reference signal is obtained by filtering the reference signal by a *model* of a plant response and not the plant response itself the gradient estimates will become more noisy with increasing level of plant modeling error. As a consequence the adaptive process will converge to a non-optimal point and the estimate can no longer be assumed unbiased. The elements in the weight-error covariance matrix are similarly increased from their values obtained under the assumption of a perfect plant model.

A point of more concern in connection with an imperfect plant model is that the feedback system will not be perfectly transformed into a FFS. Hence, a residual level of feedback will remain. A loop gain, $\tilde{l}(z)$, around the control filter that is proportional to the plant error, $\Delta\tilde{g}(z)$ will exist

$$\tilde{l}(z) = \Delta\tilde{g}(z)\tilde{w}(z). \tag{4.6.1}$$

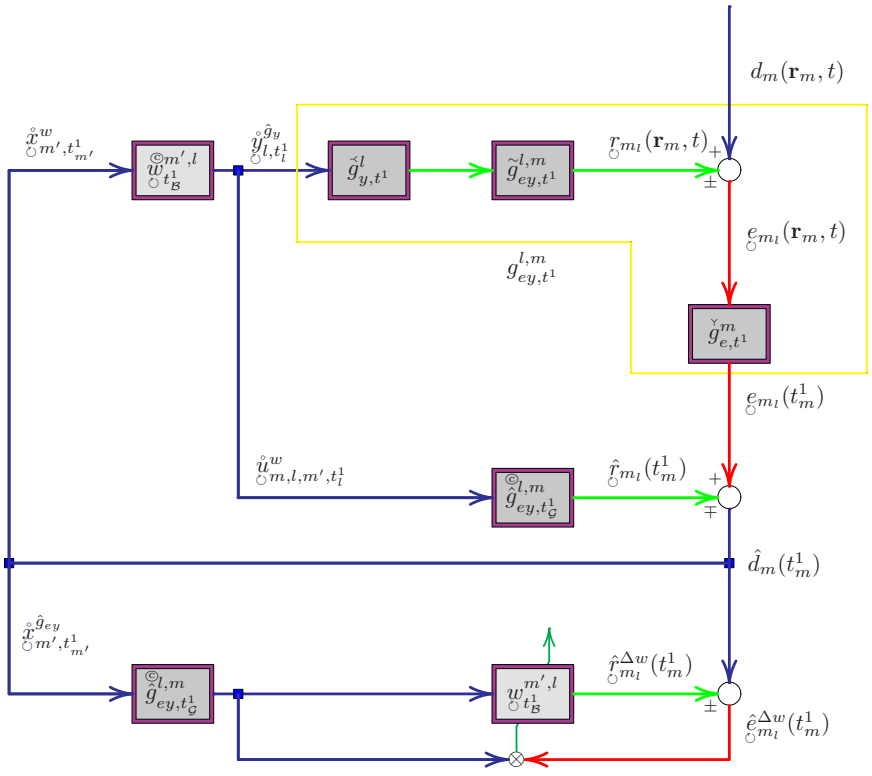

Fig. 4.3: Internal Model Control.

As a consequence the system may be become unstable. Moreover, as the discrete-time adaptive controller during the adaptation process involves a convergence along a noisy error curve this only increases the sensitivity of the system to such imperfect plant modeling. Therefore, an otherwise stable system might transverse into an unstable region during adaptation.

A plant identification procedure must therefore be invoked in order to avoid problems associated with an imperfect plant model described above. The plant identification should be repeated on a regular basis depending on practical experiences with the time interval between successive changes of plant response functions. Alternatively, an adaptive inverse controller can be used to reduce the excursion made by the system from the nominal frequency response curve. As explained in more details in section 4.7 the adaptive inverse control also requires system identification from time to time.

Finally, it should be remarked that the IMC controller involving two adaptive processes namely for plant identification and for control filter adjustment respectively including feedback loops poses great analytical challenges.

4.7 Adaptive Inverse Plant Correction

The concept of AIC was proposed by Widrow and Walach as a method to achieve *adaptive control* of unknown and possible time-varying systems by using adaptive filters. The objective of the plant correction transfer function $\hat{C}(z)$ is in cascade with the actual plant transfer function $P(z)$ to obtain a plant that seen from the digital controller equals the transfer function of a predetermined $P_{ref}(z)$ reference plant transfer function. Hence,

$$P_{ref}(z) = \hat{C}(z)P(z). \tag{4.7.1}$$

Such construction is referred to as *model-reference control*. The principle of AIC is illustrated in Figure 4.4 on page 247. The estimated plant correction, $\hat{C}$, is obtained using available control input. The adaptive process for obtaining $\hat{C}(z)$ will always be lagging behind that for obtaining $P(z)$. To allow the adaptive process for $\hat{C}(z)$ to keep up with the changes in $\hat{P}(z)$ without lag an *offline* system identification process could be used [4, Ch. 5]. Moreover, by using white or colored noise in an offline system identification process the sensitivity to nonstationarity and insufficient spectral excitation in the control output signal can be avoided.

The *dither scheme* C in [4] is used for plant identification. Other configurations offering different functionality and at various degree of complexity can be found in [4].

The purpose of introducing the AIC in an active control of sound and vibration (ACSV) system for secondary path correction is twofold. Firstly, and as already argued in section 4.2 the adaptive inverse controller can improve noise cancelation capabilities by relaxing requirements on stability margins. Conversely, for the same ANR attenuation performance the system can be made more tolerant to changes in the secondary path. However, it must be recalled that the stability analysis is difficult due to the presence of (1) an inner loop constituted by the feedback controller, (2) an outer loop in the adaptive filtering. Moreover, on-line addition of identification noise further complicates the analysis. Secondly, the adaptive filtering process employing one kind of the Fx method or the filtered-error (Fe) method discussed in section 6.3 - 6.4 involves filtering of the disturbance with an estimated plant response. Then if this plant response is subject to control the level of gradient bias will be reduced. The gradient based adaptive filters will be introduced in chapter 8 of this report. Moreover, the loop gain $\tilde{l}(z)$ in (4.6.1) can be reduced. In adaptive

inverse control a potential risk of obtaining a biased plant response estimate from using an insufficient number of tap-weights exists. However, as demonstrated in [4, Ch. 7] the adaptive inverse control scheme C proves to be rather insensitive to possible truncation effects associated with the choice of $M_{\hat{P}}$ and $M_{\hat{C}}$ corresponding to the number of tap-weights used in model of $\hat{P}(z)$ and $\hat{C}(z)$ respectively.

The price to be paid for the integration of an AIC is additional system complexity and processing delays, but also group delay in $\hat{C}(z)$.

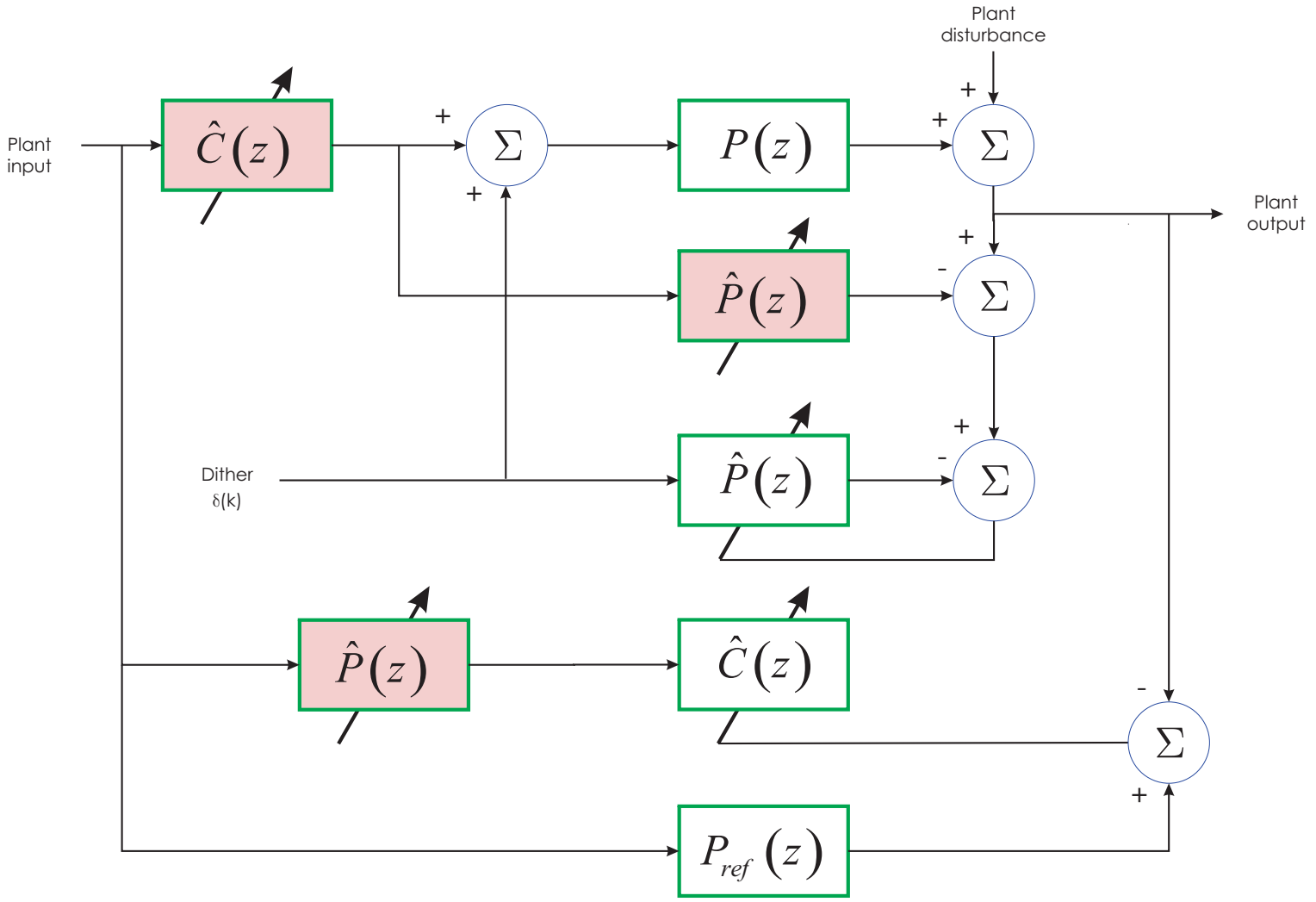

Fig. 4.4: Adaptive Inverse Plant Controller using dither scheme C (from [4, Fig. 7.2]).

Finally is should be mentioned that the AIC benefits from feedforward-feedback integrated communication on-line system identification system (FFFBICIDS) topology presented in section 7.6 on page 326 providing time-advanced communication signal. The AIC system using the *model reference* involves an inverse of the model-reference plant transfer function [4, Ch. 5]. However, the plant is usually nonminimum-phase. In a causal system the model-reference plant will consequently also be nonminimum phase. However, as is well known inverse of a nonminimum-phase transfer function is unstable although causal. Instead a noncausal expansion of the inverse should be made and the noncausal terms discarded which in turn leads to truncation effects and performance degradation. Now if the communication signal is time-advanced by, say Δ samples the number of terms discarded will decrease by Δ thereby improving the accuracy of the inverse model-reference plant.

Bibliography

[1] Stephen J. Elliott. *Signal Processing for Active Control*. London: Academic Press, 2001.

[2] Sen M. Kuo and Dennis R. Morgan. *Active Noise Control Systems Algorithms and DSP Implementations*. John Wiley & Sons, Inc., 1996.

[3] Manfred Morari and Evanghelos Zafiriou. *Robust Process Control*. Prentice Hall, 1989.

[4] Bernard Widrow and Eugene Walach. *Adaptive Inverse Control*. Prentice Hall, 1996.

5. MULTIRATE SYSTEMS

5.1 Introduction

Multirate signal processing is the branch of signal processing that deals with concepts, algorithms, and architectures that embed sample rate changes at one or more sites in the signal flow path. The ability to process signals at multiple sampling rates has made it possible to reduce costs and improve performance in applications ranging from signal compression to wireless systems, consumer entertainment products, laboratory instruments, cable modems and sensor networks. Moreover, many systems have a sampled-data structure which is necessarily multirate to fit in with the use of different data buses and digital sensors and actuators. Such systems therefore lend themselves to multirate implementations. Accordingly the field of multirate signal processing has witnessed a great deal of progress and an increasingly wide range of applications since the publication of the first textbook by Crochiere and Rabiner [1983] [6].

5.1.1 Chapter Outline

Following this introduction a review of some application fields of multi-rate systems (MRSs) is provided in section 5.2. Subsequently the theme of section 5.3 and section 5.4 is the processing stages involved in *sensing* signals and *actuating* signals respectively. A general multirate system scheme for active control of sound and vibration (ACSV) applications is developed. This system involves three different sampling rates for maximum trade-off between different design constraints. Moreover, the system is formulated in general ACSV context of a general hybrid MIMO feedforward-feedback system (HMIMOFFFBS). In section 5.5 a decomposition of the total group delay into individual group delays is carried out. A practical example of group delays versus sampling frequencies encountered in a MRS is provided. Appendix 5.A is reserved for more detailed information on group delays and phase delays.

5.2 Multirate System Applications

In the traditional DSP perspective, the sample rate is selected to satisfy the Nyquist criterion but is otherwise incidental to the problem. In multirate signal processing, selection and modification of the sample rate are primary considerations and options in the signal processing chain. Another application of multirate systems is in realizing *convolution algorithms* with a reduced average number of multiplications per output sample with some compromise in the average number of additions per output sample [24]. In [9] a multirate architecture based on multirate subsystems for such reduced multiplicative complexity is proposed.

In the control community multirate controllers have been used since the late 1950s. The overall objective is to take into account that a system may involve multiple actuators operating at

different bandwidths. Hence instead of designing a *single-rate* system that operates at the highest sample rate required by the high bandwidth loops, a *multirate* control system where different and bandwidth-dependent update rates should be considered as an alternative solution.

Usually we refer to either continuous-time or discrete-time systems. However, in between an important class of so-called sampled-data control systems (SDCSs) exists. Systems involving nonconventional sampling like multirate and/or nonsynchronous sampling belong to this class. In SDCSs the times of input stimuli, state evaluation and output acquisition do not necessarily coincide. In [1] a block multirate input-output (BMIO) and control design methodology for such systems is presented. Matrix relations between *controllability*, *observability*, and impulse response matrices, and those formed by transfer function coefficients are established.

An example of an everyday application of multirate control is found in personal computers (PCs). Modern magnetic hard disc drive (HDD) storage technology often employ multirate techniques for head positioning control. The ever increasing capacity densities implies that the control engineer faces a similar increase in the requirement on estimation accuracy and robustness to parameter uncertainty and unmodelled dynamics. Typically, for HDD control the measurement sampling frequency is limited while a higher control input update rate is used for smoother control input and wider control bandwidth. In [7, 12] it is demonstrated that the multirate implementations achieve regulation performance of the position error signal at about the same level of the single-rate implementation while realizing significant computation saving. A more elaborate multirate control scheme including proportional integral and discontinuous error feedback is proposed in [14]. It was experimentally verified that this seeking control scheme effectively reduces the level of unwanted chattering.

Multirate solutions have also been considered within the ultrasound community. Owing to the short wavelengths the characterization of a transducer for ultrasonic measurement usually involves a large number of field points in order to satisfy Nyquist sampling criterion. In [16] a multirate algorithm is developed in which the discretization of the velocity potential occurs at a variable sampling rate, based specifically on the spatial coordinate. The complex acoustic sound pressure is determined from this nonuniformly sampled field and the computational savings of this *zoom FFT* technique was of the order of a factor 15 to 30.

In some applications, for instance, photonics, it may be expensive or even impossible to build a measurement sensor with high enough sampling rate. In such cases the signal characteristics like the power spectral density (PSD) is not directly obtainable but might instead be determined by merging the information contained in a set of low-rate measurements. By considering a *multirate observer* or *multirate sensor* system that outputs low-rate measurements of an unobservable signal and by using the principle of maximum entropy (ME) Jahromi, Francis, and Kwong [11] showed that now a unique solution for the PSD can determined. Some work on existence and stability, however, remains. Other applications fields for such multirate sensor systems include radar, remote sensing and sensor networks.

In many signal processing applications a reduction in the computational complexity is required especially whenever finite-duration impulse response (FIR) filters of high order are used. This can be accomplished by using *multirate adaptive filters* where the adaptive processing is performed at a lower rate than the incoming rate. Both multirate time-domain adaptive filters (TDAFs) and multirate frequency-domain adaptive filters (FDAFs) are at our disposition. The TDAF based multirate system for active control (AC) to be presented next ensures shortest possible group delays while trying to balance requirements on computational savings and tracking capabilities to nonstationary data. Two classes of FDAF employing different frequency-domain-transformation exist. One class of FDAF use *subband* filtering techniques where the signals are filtered be a set

of filter banks [20, Ch. 5]. In *subband adaptive filtering* the input data are first processed by a bank of narrow-band bandpass filters, that are approximately nonoverlapping. The transformed signals are then decimated by a factor that depends on the degree of aliasing that can be tolerated, resulting in computational savings. The other class of FDAF utilizes that efficient convolution (linear or circular) is provided by the discrete Fourier transform (DFT). The advantage of FDAF is in terms of the parallel configuration that often result in faster convergence rates than the time-domain counterparts and they are more amenable to hardware implementations. However, as the tap weights are frozen while a block of data is accumulated this might compromise tracking capabilities. Moreover, in AC the effective group delay accompanied by this blocking process might reduce the bandwidth of the system. An overview of several FDAFs is presented by Shynk [19].

To the author's best knowledge only a few records on multirate solutions to active noise control (ANC) problems can be found in the open literature. Brammer, Pan, and Crabtree [4] proposed a dual-rate system for helicopter active noise reduction (ANR) headsets [25]. Bai, Lin, and Lai [2] investigated a fixed digital dual-rate system for a duct application. An oversampling factor of 8 (2/16 kHz) was used leading to a reduction in the delays in the analogue to digital converter (ADC), digital to analogue converter (DAC) and computation delays together with avoidance of an analogue low-pass filter. Such reduction in electrical delays is discussed in section A.3 lead to an increased bandwidth and/or to a more physically compact system.

In section 5.3 and section 5.4 a general multirate system scheme for ACSV applications is described. This system involves three different sampling rates for maximum trade-off between different design constraints. Moreover, the system is formulated in a general ACSV context of a HMIMOFFFBS. The details for multirate implementation in a HMIMOFFFBS, however, is postponed until chapter 6.

In section A.3 we appreciate how delays in the discrete-time part of the plants may compromise the performance of an AC system. This pertains both to feedback systems and to feedforward systems.

The novel general multirate (triple-rate) system for ACSV applications that is based on TDAF will demonstrate the following advantages:

1. By using a very fast system (zeroth level) sampling frequency almost negligible conversion delays are obtained viz. Table 5.1 on page 266.

2. Active control is conducted at a slower downsampled (first level) speed which, however, is still largely oversampled compared with the operational bandwidth of the system. The one sample control output delay viz Table 5.1 is therefore small while preserving the computational effort required for the generation of the control output signals at an acceptable level.

3. Tap-weight adaptation takes place at an even slower downsampled (second level) speed. This sampling frequency is selected as a compromise between the computational burden involved in the adaptive tap-weight updates and the requirement on fast update rates to ensure fast convergence and tracking capabilities to nonstationary signals. Moreover, by limiting the bandwidth subject to adaptive control well below the full frequency span corresponding to the highest sampling frequency, potential problems of large eigenvalue spread and poor frequency resolution leading to poor tap-weight convergence rates can be alleviated. Furthermore, instead of operating at the highest sample rates but by restricting

the bandwidth of adaptive control the corresponding requirement of very long FIR filters for adaptive tap-weights and plant representation can be avoided.

4. By enforcing some reasonable constraints the multirate system can be employed in a HMIMOFFFBS.

5.3 Sensed Signals

In the active noise control system (ANCS) signals are *sensed* by the reference sensors, error sensors and possible performance sensors. The aim in this section is to describe the different stages involved in the sensing process at these sensors. The process of sensing for the case of an error sensor is depicted in Figure 5.1 on the facing page. Reference and performance signals are processed in similar way.

In the following we let $\boldsymbol{\psi}(\mathbf{r}_m, t)$ represent an arbitrary scalar-valued continuous-time random signal at position $\mathbf{r}_m$ in space of the m-th error sensor at time t. The error signal will always include both the disturbance and the rejection signal provided that the ANR system is switched on. There is no provision of separating the disturbance and reference signals. Only estimates of these signal quantities can be made. Similarly, the reference signals could also be subject to contamination of rejection signals due to undesired feedback.

The sensors will transduce some physical continuous-time and spatially-distributed quantity into an equivalent electrical signal represented here by $\boldsymbol{\psi}_m^{\mathcal{M}}(t)$. For example, if we use a microphone as error sensor we could use the pressure distribution over the membrane as reference. This analogue, possibly noisy, nonlinear[1] and also possibly time-variant *transduction* operation of the sensor is represented by the function $\mathcal{M}_m(A_m, t)$

$$\boldsymbol{\psi}_m^{\mathcal{M}}(t) \xleftarrow{\mathcal{M}_m(A_m,t)} \boldsymbol{\psi}_m(\mathbf{r}_m, t), \quad t \in \mathbb{R}_+, \tag{5.3.1}$$

where $\boldsymbol{\psi}_m^{\mathcal{M}}(t)$ denotes the transduced m-th error signal at time t. The system time starts at $t_0 = 0$.

The system might be constituted from different sensor front-ends among the reference sensors, error sensors and performance sensors, but also among these types of sensors themselves. Hence, in general for $m_1 \neq m_2, j_1 \neq j_2$ and $k_1 \neq k_2$, we have

$$\mathcal{M}_{m_1} \neq \mathcal{M}_{m_2} \neq \mathcal{M}_{j_1} \neq \mathcal{M}_{j_2} \neq \mathcal{M}_{k_1} \neq \mathcal{M}_{k_2}, \quad m_1, m_2 \in \underline{N}_e, j_1, j_2 \in \underline{N}_x, k_1, k_2 \in \underline{N}_p. \tag{5.3.2}$$

The quantity A_m denotes the amplitude of a physical parameter, e.g., an instantaneous sound pressure $p(t)$ measured at the m-th error microphone[2]. Typically, signal preamplification and conditioning will take place here.

The discrete-time controller operates on *sampled* (in time) signals. Moreover, the signals will be quantized in amplitude level due to a finite number of bits in the ADC N_{ADC} . The sampling

[1] Nonlinearities are difficult to model in general. The specific nonlinearity should be properly accounted for.
[2] A complete model of a sensor would involve many parameters omitted here for simplicity.

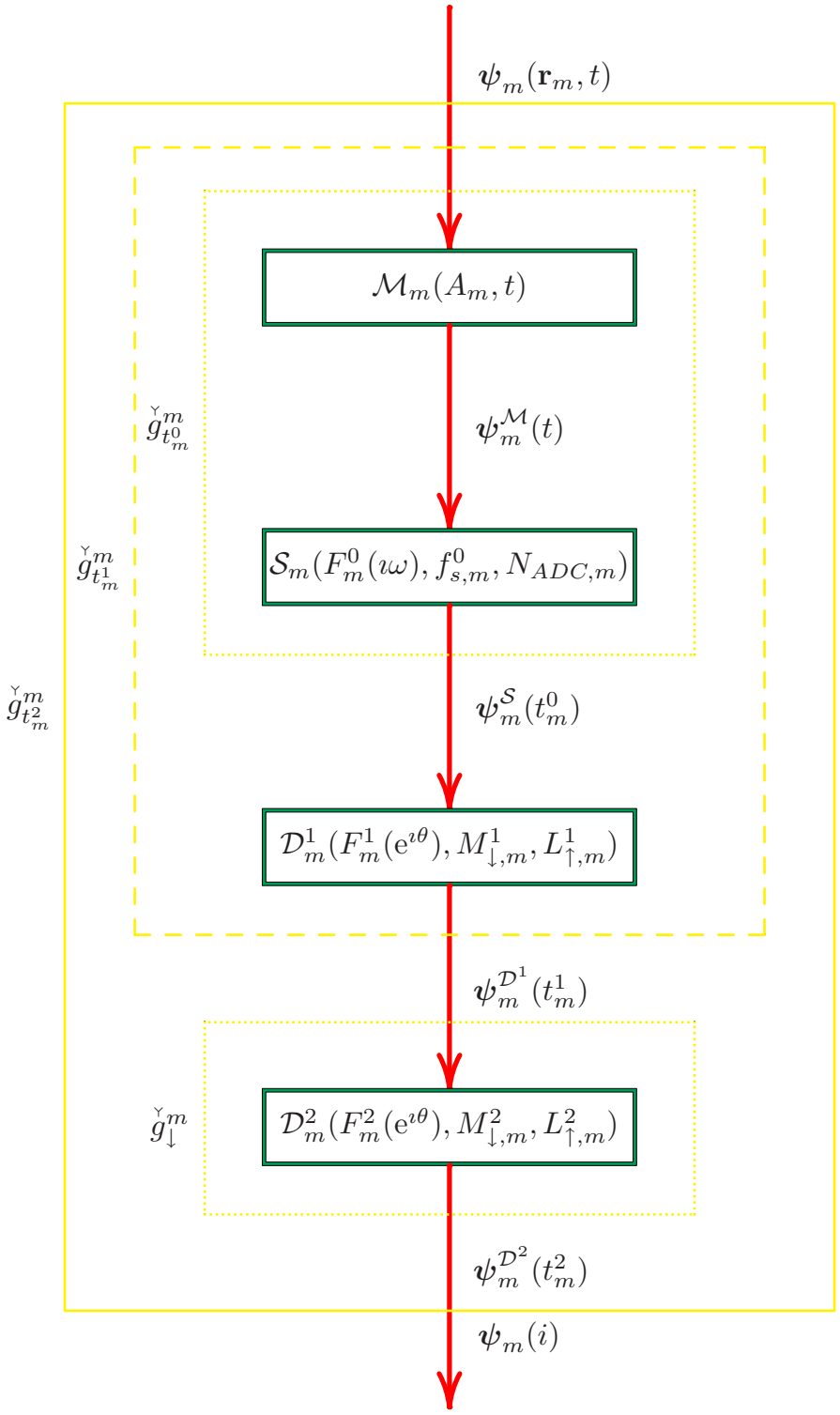

Fig. 5.1: Plant Receive Part.

operation that also involves a sample and hold operation is represented by the (time-independent) $\mathcal{S}_m(\,\cdot\,)$ sampling function. By $\boldsymbol{\psi}_m^{\mathcal{S}}(t_m^0)$ we will refer to the sampled m-th error signal

$$\boldsymbol{\psi}_m^{\mathcal{S}}(t_m^0) \xleftarrow{\mathcal{S}_m(F_m^0(\imath\omega),f_{s,m}^0,N_{ADC,m})} \boldsymbol{\psi}_m^{\mathcal{M}}\big(\big](t_m^0-1)T_m^0;t_m^0T_m^0\big]\big), \quad t_m^0\in\mathbb{N}, \tag{5.3.3}$$

where t_m^0 is the sample index, $f_{s,m}^0$ is the sampling frequency which is the reciprocal of the sampling period T_m^0 ($T_m^0 \triangleq 1/f_{s,m}^0$). The superscript 0 refers to the 0^{th} multirate level. The semi-open interval $\big](t_m^0-1)T_m^0;t_m^0T_m^0\big]$ represents the time interval from the previous sampling operation to the current sampling time. In the present case involving oversampled A/D conversion [15, Ch. 4.8] $\mathcal{S}_m$ includes a simple continuous-time anti-aliasing filter (AAF) $F_m^0(\imath\omega)$. Sometimes the sensor transduction $\mathcal{M}_m$ itself might provide sufficient high-frequency attenuation to avoid aliasing problems. Nevertheless, because of the possibility of high-frequency noise in the sensing system and the severe consequences of aliasing, it is recommended that analog low-pass filtering be performed on all sensors prior to the analog-to-digital conversion, no matter how high the sampling rate.

The clock generator that is responsible for f_s^0 is usually implemented in hardware in order to avoid performance loss and instability problems associated with sampling jitter due to variable-length loops. All reference sensors and error sensors will use the same system clock. The performance sensors, however, do not partake in the control and may use their own system clock. Hence, in general

$$f_{s,m_1}^0 = f_{s,m_2}^0 = f_{s,j_1}^0 = f_{s,j_2}^0 \neq f_{s,k_1}^0 = f_{s,k_2}^0, \quad m_1,m_2\in\underline{N}_e, \quad j_1,j_2\in\underline{N}_x, \quad k_1,k_2\in\underline{N}_p. \tag{5.3.4}$$

The same considerations apply to the number of conversion bits N_{ADC}. Following the discussion in section N.3 on page 803 different requirements on the AAFs function among the reference sensors, error sensors and performance sensors exist, but not among these types of sensors themselves. Hence, in general

$$F_{m_1}^0(\imath\omega) = F_{m_2}^0(\imath\omega) \neq F_{j_1}^0(\imath\omega) = F_{j_2}^0(\imath\omega) \neq F_{k_1}^0(\imath\omega) = F_{k_2}^0(\imath\omega), \quad m_1,m_2\in\underline{N}_e, \quad j_1,j_2\in\underline{N}_x, \quad k_1,k_2\in\underline{N}_p. \tag{5.3.5}$$

and accordingly

$$\mathcal{S}_{m_1} = \mathcal{S}_{m_2} \neq \mathcal{S}_{j_1} = \mathcal{S}_{j_2} \neq \mathcal{S}_{k_1} = \mathcal{S}_{k_2}, \quad m_1,m_2\in\underline{N}_e, \quad j_1,j_2\in\underline{N}_x, \quad k_1,k_2\in\underline{N}_p. \tag{5.3.6}$$

It should be recalled that in a single-rate ACSV application $\boldsymbol{\psi}_m^{\mathcal{S}}(t_m^0)$ is used both for control and control weight adaptation. However, a multirate system involves discrete-time signals at different sampling rates. In order to comply with computational constraints control will take place at the reduced sampling frequency $f_{s,m}^1$ with corresponding sampling period $T_m^1 \triangleq 1/f_{s,m}^1$. The superscript 1 refers to the 1^{st} multirate level where a sample index t_m^1 will be used.

As depicted in Figure 5.1 this input sampling rate shift is accomplished by the time-independent resampling function $\mathcal{D}_m^1(\,\cdot\,)$ that in turn takes three arguments. The first argument is the discrete-time decimation interpolation filter (DIF) $F_m^1(\mathrm{e}^{\imath\theta})$. The second and third arguments are the

downsampling factor in resampling $M^1_{\downarrow,m}$ and the upsampling factor in resampling $L^1_{\uparrow,m}$ that together determine the resampling factor $R^1_{\updownarrow,m}$ according to $R^1_{\updownarrow,m} \triangleq \frac{f^1_{s,m}}{f^0_{s,m}} = \frac{L^1_{\uparrow,m}}{M^1_{\downarrow,m}}$. Hence $R^1_{\updownarrow,m}$ is a rational number ($R^1_{\updownarrow,m} \in \mathbb{Q}$).

We may then write

$$\boldsymbol{\psi}^{\mathcal{D}^1}_m(t^1_m) \xleftarrow{\mathcal{D}^1_m(F^1_m(\mathrm{e}^{\imath\theta}),M^1_{\downarrow,m},L^1_{\uparrow,m})} \boldsymbol{\psi}^{\mathcal{S}}_m(t^0_m), \quad t^1_m \in \mathbb{N}, \tag{5.3.7}$$

where $\boldsymbol{\psi}^{\mathcal{D}^1}_m(t^1_m)$ denotes the resampled (1^{st} level) m-th error signal at sample index t^1_m.

For computational efficiency a *polyphase* implementation of the DIF which for our application is a low-pass filter (LPF) is employed [21, Ch. 4], [22]. The concept of polyphase was developed by Bellanger, Bonnerot, and Coudreuse [3] and Vary [23]. The basic idea of the polyphase implementation is to commute the filtering operation to a low sampling rate whereby the computational efficiency is achieved. The polyphase technique work well for reasonable sample rate changes, but not for very large decimation or interpolation factors.

Multistage decimators and *interpolators* were introduced by Rabiner and Crochiere [17] [5]. It was demonstrated that multistage implementation can lead to a greatly reduced number of multiplications per second in the realization over standard direct form implementations. An efficient method for general sampling conversion by a *rational number* as opposed to an *integer number* was devised by Hsiao [10]. Murakami [13] proposed a cyclic sampling rate conversion system by a rational factor that due to the inherent DFT is computational more efficient than the polyphase implementation when the filter length is large. Ramstad [18] presented filtering methods for interfacing time-discrete systems with different sampling frequencies. The methods developed are applicable for sampling rate conversion between *any* two sampling frequencies. For the ANR application we will use the ordinary polyphase implementation for integer decimation or integer interpolation [21, Ch. 4]. For sampling conversion by a rational number the scheme by Hsiao will be used as only small rational resampling ratios are considered.

In order to achieve a high degree of flexibility and to reduce the computational burden different sampling rates might be used at the error sensors and reference sensors. This could, for instance, allow us to operate the feedforward and feedback controllers in a hybrid continuous-time discrete-time topology (HCTDTT) at different speeds. However, in order to reduce the complexity of the multirate system feedforward and feedback control will operate at the same sampling frequency. Moreover, as already mentioned the performance sensors do not partake in the control and may use their own sampling rates. Hence,

$$f^1_{s,m_1} = f^1_{s,m_2} = f^1_{s,j_1} = f^1_{s,j_2} \neq f^1_{s,k_1} = f^1_{s,k_2}, \quad m_1, m_2 \in \underline{N}_e, \quad j_1, j_2 \in \underline{N}_x, \quad k_1, k_2 \in \underline{N}_p. \tag{5.3.8}$$

The constraints on the sampling frequencies (5.3.8) therefore also apply to the resampling functions. Hence, in general

$$\mathcal{D}^1_{m_1} = \mathcal{D}^1_{m_2} = \mathcal{D}^1_{j_1} = \mathcal{D}^1_{j_2} \neq \mathcal{D}^1_{k_1} = \mathcal{D}^1_{k_2}, \quad m_1, m_2 \in \underline{N}_e, j_1, j_2 \in \underline{N}_x, k_1, k_2 \in \underline{N}_p. \tag{5.3.9}$$

Similar considerations therefore also apply to $F^1_m(\mathrm{e}^{\imath\theta})$, $M^1_{\downarrow,m}$ and $L^1_{\uparrow,m}$.

Adaptation of the tap-weights in control filters takes place at a lower sampling frequency $f^2_{s,m}$

with corresponding sampling period $T_m^2 \triangleq 1/f_{s,m}^2$. The superscript 2 refers to the 2nd multirate level where a sample index t_m^2 will be used. The second level of input sampling rate in the multirate system is as depicted in Figure 5.1 accomplished by the time-independent resampling function $\mathcal{D}_m^2(\,\cdot\,)$ that takes arguments $F_m^2(\mathrm{e}^{\imath\theta})$, $M_{\downarrow,m}^2$ and $L_{\uparrow,m}^2$ similar to $\mathcal{D}_m^1(\,\cdot\,)$ and the $R_{\updownarrow,m}^2 \triangleq \frac{f_{s,m}^2}{f_{s,m}^1} = \frac{L_{\uparrow,m}^2}{M_{\downarrow,m}^2}$ is defined as resampling factor (2nd level).

Formally, we then write

$$\boldsymbol{\psi}_m^{\mathcal{D}^2}(t_m^2) \xleftarrow{\mathcal{D}_m^2(F_m^2(\mathrm{e}^{\imath\theta}),M_{\downarrow,m}^2,L_{\uparrow,m}^2)} \boldsymbol{\psi}_m^{\mathcal{D}^1}(t_m^1), \quad t_m^1, t_m^2 \in \mathbb{N}, \tag{5.3.10}$$

where $\boldsymbol{\psi}_m^{\mathcal{D}^2}(t_m^2)$ denotes the resampled (2nd level) m-th error signal at sample index t_m^2.

The remarks made above concerning the benefits of operating the feedforward and feedback controllers in a HCTDTT at different speeds also apply to the adaptive part. But, again in order not to increase the complexity of the multirate system further feedforward- and feedback adaptive control will operate at the same sampling frequency. We therefore enforce the following constraints on the second level sampling frequencies

$$f_{s,m_1}^2 = f_{s,m_2}^2 = f_{s,j_1}^2 = f_{s,j_2}^2 \neq f_{s,k_1}^2 = f_{s,k_2}^2, \quad m_1, m_2 \in \underline{N}_e, \quad j_1, j_2 \in \underline{N}_x, \quad k_1, k_2 \in \underline{N}_p. \tag{5.3.11}$$

The constraints on the sampling frequencies (5.3.11) therefore also apply to the resampling functions. Hence, in general

$$\mathcal{D}_{m_1}^2 = \mathcal{D}_{m_2}^2 = \mathcal{D}_{j_1}^2 = \mathcal{D}_{j_2}^2 \neq \mathcal{D}_{k_1}^2 = \mathcal{D}_{k_2}^2, \quad m_1, m_2 \in \underline{N}_e, j_1, j_2 \in \underline{N}_x, k_1, k_2 \in \underline{N}_p. \tag{5.3.12}$$

Similar considerations therefore also apply to $F_m^2(\mathrm{e}^{\imath\theta})$, $M_{\downarrow,m}^2$ and $L_{\uparrow,m}^2$.

A single rate system can easily be configured by selecting unity for the up- and downsampling factors and by omitting the DIFs

$$F_m^1(\mathrm{e}^{\imath\theta}) = F_m^2(\mathrm{e}^{\imath\theta}) = F_j^1(\mathrm{e}^{\imath\theta}) = F_j^2(\mathrm{e}^{\imath\theta}) = F_k^1(\mathrm{e}^{\imath\theta}) = F_k^2(\mathrm{e}^{\imath\theta}) = 1, \quad \theta \in [-\pi, \pi] \tag{5.3.13}$$

and

$$M_{\downarrow,m}^1 = L_{\uparrow,m}^1 = M_{\downarrow,m}^2 = L_{\uparrow,m}^2 = 1, \quad m \in \underline{N}_e, \tag{5.3.14a}$$
$$M_{\downarrow,j}^1 = L_{\uparrow,j}^1 = M_{\downarrow,j}^2 = L_{\uparrow,j}^2 = 1, \quad j \in \underline{N}_x, \tag{5.3.14b}$$
$$M_{\downarrow,k}^1 = L_{\uparrow,k}^1 = M_{\downarrow,k}^2 = L_{\uparrow,k}^2 = 1, \quad k \in \underline{N}_p. \tag{5.3.14c}$$

In this case the time indices coincide ($t_m^0 = t_m^1 = t_m^2$) and the same applies to the sensed signals, that is, $\boldsymbol{\psi}_m^{\mathcal{S}} = \boldsymbol{\psi}_m^{\mathcal{D}^1} = \boldsymbol{\psi}_m^{\mathcal{D}^2}$.

In Part III we will replace the sample index t_m^2 by the *iteration index* i as it is customary in the literature on adaptive filtering, that is,

$$\boldsymbol{\psi}_m^{\mathcal{D}^2}(t_m^2) \rightarrow \boldsymbol{\psi}_m(i) \rightarrow \boldsymbol{\psi}(i), \tag{5.3.15}$$

where $\psi_m(i) \triangleq \boldsymbol{\psi}_m^{\mathcal{D}^2}(t_m^2)$ also represents the m-th error signal at sample index i. We may also as indicated suppress the sensor index for notational convenience.

Referring to Figure 5.1 the collective effects of $\mathcal{M}_m(\cdot)$ and $\mathcal{S}_m(\cdot)$ constitute the receiver (0^{th} level) part of plants $\overset{\vee}{g}{}_{t_m^0}^m$. The cascade-coupling of $\overset{\vee}{g}{}_{t_m^0}^m$ and $\mathcal{D}_m^1(\cdot)$ is the receiver (1^{st} level) part of plants $\overset{\vee}{g}{}_{t_m^1}^m$. Finally, the cascade-coupling of $\overset{\vee}{g}{}_{t_m^1}^m$ and $\mathcal{D}_m^2(\cdot)$ in turn constitutes the receiver (2^{nd} level) part of plants denoted by $\overset{\vee}{g}{}_{t_m^2}^m$. The time-independent function $\mathcal{D}_m^2(\cdot)$ will also be referred to as receiver (down conversion) part of plants involving the m'th error sensor $\overset{\vee}{g}{}_{\downarrow}^m$. The receiver part of a plant will be subject to further discussions in chapter 6 on page 273.

5.4 Actuated Signals

In the ANCS control output signals are *actuated* by the controllers. The aim in this section is to describe the different stages involved in the process actuating as illuminated in Figure 5.2.

As depicted in the bottom of Figure 5.2 provision is made for upsampling of some discrete-time low-frequency signal represented by l-th control output signal $\psi_l(j) \triangleq \boldsymbol{\psi}_l^{\mathcal{U}^2}(t_l^2)$.

Let $f_{s,l}^2$ represent sampling frequency with corresponding sampling period $T_l^2 \triangleq 1/f_{s,l}^2$. The superscript 2 refers to the 2^{nd} multirate level where a sample index t_l^2 will be used.

The first multirate level on both the input and output sides is reserved for the control output generation. Accordingly we have the following constraints on the sample frequencies pertaining to the error sensors, reference sensors and actuators for $m_1 \neq m_2, j_1 \neq j_2$ and $l_1 \neq l_2$:

$$f_{s,m_1}^1 = f_{s,m_2}^1 = f_{s,j_1}^1 = f_{s,j_2}^1 = f_{s,l_1}^1 = f_{s,l_2}^1, \quad m_1, m_2 \in \underline{N}_e, \quad j_1, j_2 \in \underline{N}_x, \quad l_1, l_2 \in \underline{N}_y, \tag{5.4.1}$$

where we by $f_{s,l}^1$ refer to the sampling frequency with corresponding sampling period $T_l^1 \triangleq 1/f_{s,l}^1$. The superscript 1 refers to the 1^{st} multirate level where a sample index t_l^1 will be used.

The constraints in (5.4.1) also apply to the sample indices

$$t_{m_1}^1 = t_{m_2}^1 = t_{j_1}^1 = t_{j_2}^1 = t_{l_1}^1 = t_{l_2}^1, \quad m_1, m_2 \in \underline{N}_e, \quad j_1, j_2 \in \underline{N}_x, \quad l_1, l_2 \in \underline{N}_y. \tag{5.4.2}$$

The transition from the second to the first level of output sampling rate in the multirate system is as depicted in Figure 5.2 accomplished by the time-independent resampling function $\mathcal{U}_l^2(\cdot)$ that takes arguments $F_l^2(\mathrm{e}^{\imath\theta})$, $M_{\downarrow,l}^2$ and $L_{\uparrow,l}^2$ similar to $\mathcal{D}_m^2(\cdot)$ defined in (5.3.10) on the preceding page and $R_{\downarrow,l}^2 \triangleq \frac{f_{s,l}^1}{f_{s,l}^2} = \frac{L_{\uparrow,l}^2}{M_{\downarrow,l}^2}$ is the resampling factor (2^{nd} level). Hence,

$$\boldsymbol{\psi}_l^{\mathcal{U}^1}(t_l^1) \xleftarrow{\mathcal{U}_l^2(F_l^2(\mathrm{e}^{\imath\theta}), M_{\downarrow,l}^2, L_{\uparrow,l}^2)} \boldsymbol{\psi}_l^{\mathcal{U}^2}(t_l^2), \quad t_l^1, t_l^2 \in \mathbb{N}, \tag{5.4.3}$$

where $\boldsymbol{\psi}_l^{\mathcal{U}^1}(t_l^1)$ denotes the resampled (1^{st} level) l-th control output signal at sample index t_l^1.

The conversion between the continuous-time and discrete-time part of the system takes place at the zeroth multirate level on both the input and output sides. Accordingly we have the

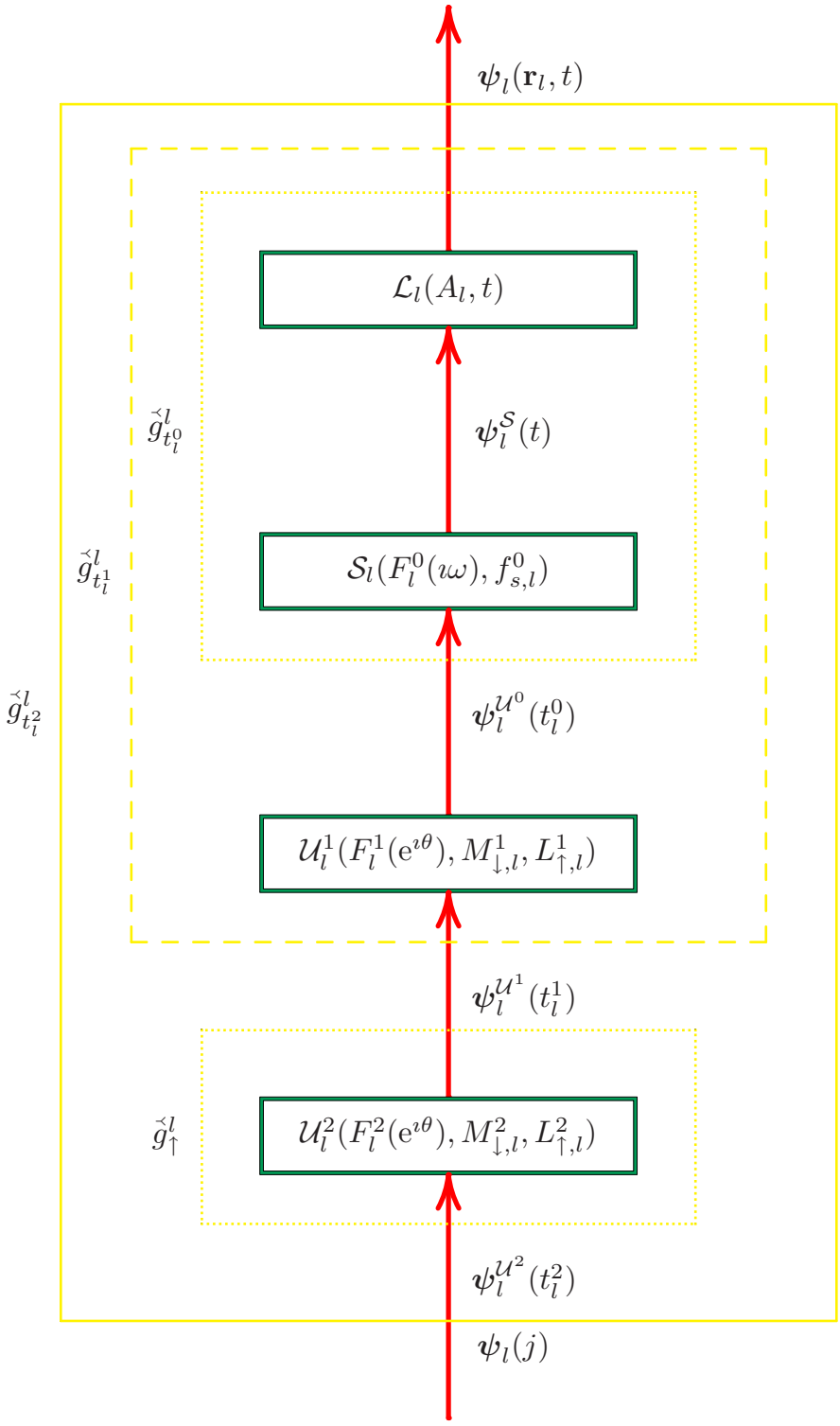

Fig. 5.2: Plant Transmit Part

following constraints on the sample frequencies pertaining to the error sensors, reference sensors and actuators for $m_1 \neq m_2, j_1 \neq j_2$ and $l_1 \neq l_2$:

$$f^0_{s,m_1} = f^0_{s,m_2} = f^0_{s,j_1} = f^0_{s,j_2} = f^0_{s,l_1} = f^0_{s,l_2}, \quad m_1, m_2 \in \underline{N}_e, \quad j_1, j_2 \in \underline{N}_x, \quad l_1, l_2 \in \underline{N}_y. \tag{5.4.4}$$

where we by $f^0_{s,l}$ refer to the sampling frequency with corresponding sampling period $T^0_l \triangleq 1/f^0_{s,l}$. The superscript 0 refers to the 0^{th} multirate level where a sample index t^0_l will be used.

The constraints in (5.4.4) also apply to the sample indices

$$t^0_{m_1} = t^0_{m_2} = t^0_{j_1} = t^0_{j_2} = t^0_{l_1} = t^0_{l_2}, \quad m_1, m_2 \in \underline{N}_e, \quad j_1, j_2 \in \underline{N}_x, \quad l_1, l_2 \in \underline{N}_y. \tag{5.4.5}$$

Now in order to minimize conversion delays, we will as depicted in Figure 5.2 upsample $\boldsymbol{\psi}_l^{\mathcal{U}^1}(t^1_l)$ to the zeroth level of output sampling rate in the multirate system by means of the time-independent resampling function $\mathcal{U}^1_l(\,\cdot\,)$ that takes arguments $F^1_l(\mathrm{e}^{\imath\theta})$, $M^1_{\downarrow,l}$ and $L^1_{\uparrow,l}$ similar to $\mathcal{D}^1_m(\,\cdot\,)$ defined in (5.3.7) on page 255 and $R^1_{\updownarrow,l} \triangleq \frac{f^0_{s,l}}{f^1_{s,l}} = \frac{L^1_{\uparrow,l}}{M^1_{\downarrow,l}}$ is defined as a resampling factor (1^{st} level)

$$\boldsymbol{\psi}_l^{\mathcal{U}^0}(t^0_l) \xleftarrow{\mathcal{U}^1_l(F^1_l(\mathrm{e}^{\imath\theta}),M^1_{\downarrow,l},L^1_{\uparrow,l})} \boldsymbol{\psi}_l^{\mathcal{U}^1}(t^1_l), \tag{5.4.6}$$

where $\boldsymbol{\psi}_l^{\mathcal{U}^0}(t^0_l)$ denotes the resampled (0^{th} level) l-th control output signal at sample index t^0_l.

The conversion from the discrete-time domain to the continuous-time domain is governed by the hold function in DAC (0^{th} order) represented by $H_l(\imath\omega)$ and by the reconstruction filter (RF) (lowpass filter) represented by $F^0_l(\imath\omega)$ that smoothes the output from the DAC

$$\boldsymbol{\psi}_l^{\mathcal{S}}(t) \xleftarrow{\mathcal{S}_l(H_l(\imath\omega),F^0_l(\imath\omega),f^0_{s,l})} \boldsymbol{\psi}_l^{\mathcal{U}^0}(t^0_l), \tag{5.4.7}$$

where $\mathcal{S}_l(\,\cdot\,)$ denotes the sampling function. The actuators will transduce an electrical signal represented here by $\boldsymbol{\psi}_l^{\mathcal{S}}(t)$ into some equivalent physical parameter (, e.g., sound pressure). This analogue, possibly nonlinear and also possibly time-variant operation of the actuator is represented by the function $\mathcal{L}_m(A_l, t)$. The output is represented by scalar-valued continuous-time signal $\boldsymbol{\psi}(\mathbf{r}_l, t)$ *present* at position $\mathbf{r}_l$ in space at time t. The control output signal will include both the rejection signal (provided that the ANR system switched on) and possibly a control output signal

$$\boldsymbol{\psi}_l(\mathbf{r}_l, t) \xleftarrow{\mathcal{L}_m(A_l,t)} \boldsymbol{\psi}_l^{\mathcal{S}}(t). \tag{5.4.8}$$

The quantity A_l denotes the amplitude of physical parameter, e.g., an instantaneous voltage $v(t)$ applied to a loudspeaker[3].

Referring to Figure 5.2 the collective effects of $\mathcal{L}_l(\,\cdot\,)$ and $\mathcal{S}_l(\,\cdot\,)$ constitute the transmitter (0^{th} level) part of plants $\overleftarrow{g}^l_{t^0_l}$. The cascade-coupling of $\overleftarrow{g}^l_{t^0_l}$ and $\mathcal{U}^1_l(\,\cdot\,)$ is the transmitter (1^{st} level) part of plants $\overleftarrow{g}^l_{t^1_l}$. Finally, the cascade-coupling of $\overleftarrow{g}^l_{t^1_l}$ and $\mathcal{U}^2_l(\,\cdot\,)$ in turn constitutes the transmitter

[3] A complete model of an actuator would involve many parameters omitted here for simplicity.

(2^{nd} level) part of plants denoted by $\overset{\prec}{g}{}^{l}_{t_l^2}$. The time-independent function $\mathcal{U}_l^2(\,\cdot\,)$ will also be referred to as transmitter (up conversion) part of plants involving the l'th actuator $\overset{\prec}{g}{}^{l}_{\uparrow}$. The transmitter part of a plant will be subject to further discussions in chapter 6 on page 273.

5.5 Group Delays

5.5.1 Decomposition of Group Delays

The total group delay τ_g exhibited by a plant is obtained as the sum[4] of the group delay from transmitter part of plant $\overset{\prec}{\tau}_g$, the group delay from propagation part of plant $\widetilde{\tau}_g$ and the group delay from receiver part of plant $\overset{\succ}{\tau}_g$[5], that is,

$$\tau_g = \overset{\prec}{\tau}_g + \widetilde{\tau}_g + \overset{\succ}{\tau}_g. \tag{5.5.1}$$

In some cases it is useful to express the total group delay as the sum of the group delay τ_g^{ct} and τ_g^{dt} contributed by the continuous-time part and discrete-time part of the plant respectively:

$$\tau_g = \tau_g^{ct} + \tau_g^{dt}. \tag{5.5.2}$$

In the design of the stand alone continuous-time controller or a continuous-time controller employed in the hybrid continuous-time discrete-time controller presented in section 4.5 on page 242 only the continuous-time part of the plant is considered.

The group delay caused by the discrete-time part of the system, however, can normally be estimated using fairly reasonable arguments as will be explained in the subsequent text. Then using (A.3.1), (A.3.2) in Appendix A on page 529 and (5.5.1) it can be assessed if an ANC-system with sufficient low group delay can be synthesized. We may decompose the delays in the continuous-time part of the plant by

$$\tau_g^{ct} = \overset{\prec}{\tau}_g{}^{ct} + \widetilde{\tau}_g + \overset{\succ}{\tau}_g{}^{ct}, \tag{5.5.3}$$

where $\overset{\prec}{\tau}_g^{ct}$ denotes the group delay from transmitter part of the continuous-time part of plant and $\overset{\succ}{\tau}_g^{ct}$ is the group delay from receiver part of the continuous-time part of plant.

These group delays in turn coincide with the group delay associated with transduction in the transmitter part of the plant $\tau_g^{\mathcal{L}}$ and group delay associated with transduction in the receiver part of the plant $\tau_g^{\mathcal{M}}$ respectively (see section 5.3 - 5.4), that is,

$$\overset{\prec}{\tau}_g^{ct} = \tau_g^{\mathcal{L}} \tag{5.5.4a}$$

$$\overset{\succ}{\tau}_g^{ct} = \tau_g^{\mathcal{M}}. \tag{5.5.4b}$$

[4]For a linear cascade-coupled system the magnitude and the phase of the resulting transfer functions is obtained as the product and sum respectively of the individual system elements. Hence, the group delays and phase delays are also obtained as a linear sum of the individual delays.

[5]Refer to subsection 7.2.1 on page 292 and subsection 7.3.1 on page 303.

We may similarly break down the delays encountered in the discrete-time part of the system as

$$\tau_g^{dt} = \overset{\prec}{\tau}_g^{\,dt} + \tau_g^w + \overset{\succ}{\tau}_g^{\,dt}, \tag{5.5.5}$$

where $\overset{\prec}{\tau}_g^{dt}$ denotes the group delay from transmitter part of the discrete-time part of plant, τ_g^w represents the group delay associated with the generation of the control output and $\overset{\succ}{\tau}_g^{dt}$ is the group delay from receiver part of the discrete-time part of plant. In our MRS described in section 5.3 - 5.4 τ_g^w will coincide with the sampling period at the 1st multirate level, that is, $\tau_g^w = 1/f_s^1$. Referring to section 5.4 the *total* group delay from transmitter part of the discrete-time part of plant $\overset{\prec}{\tau}_g^{dt,tot}$, is the sum of the group delays involved in the upsampling stages and the sample and hold stage of the plant $\tau_g^{\mathcal{U}^2}, \tau_g^{\mathcal{U}^1}, \tau_g^{\mathcal{H}}$, that is,

$$\overset{\prec}{\tau}_g^{dt,tot} = \tau_g^{\mathcal{U}^2} + \tau_g^{\mathcal{U}^1} + \tau_g^{\mathcal{H}}. \tag{5.5.6}$$

The *total* group delay from receiver part of the discrete-time part of plant $\overset{\succ}{\tau}_g^{dt,tot}$ consists of the group delays involved in the sampling stage and downsampling stages of the plant $\tau_g^{\mathcal{S}}, \tau_g^{\mathcal{D}^1}, \tau_g^{\mathcal{D}^2}$ (see section 5.3 on page 252)

$$\overset{\succ}{\tau}_g^{dt,tot} = \tau_g^{\mathcal{S}} + \tau_g^{\mathcal{D}^1} + \tau_g^{\mathcal{D}^2}. \tag{5.5.7}$$

Now, the total transmit and receive group delay are pertinent to *adaptive control*. However, the control loop itself does not involve the 2nd multirate level. Hence, for the assessment of the attenuation capabilities of the ANCS it is $\overset{\prec}{\tau}_g^{dt}, \overset{\succ}{\tau}_g^{dt}$ that are obtained from

$$\overset{\prec}{\tau}_g^{dt} = \tau_g^{\mathcal{U}^1} + \tau_g^{\mathcal{H}} \tag{5.5.8}$$

and

$$\overset{\succ}{\tau}_g^{dt} = \tau_g^{\mathcal{S}} + \tau_g^{\mathcal{D}^1} \tag{5.5.9}$$

respectively and not $\overset{\prec}{\tau}_g^{dt,tot}, \overset{\succ}{\tau}_g^{dt,tot}$ that should be considered.

5.5.2 Examples of Group Delays

In the subsequent text we will present practical group delay decomposition results for the MRS employed in the Terma Earcup Audio System installed on a Gentex HGU-55/P helmet.

Unlike the design in [2] where FIR filters are considered for decimation and interpolation, we will use elliptic infinite-duration impulse response (IIR) filters due to their low group delay well below the transition band. Moreover, we choose to use the same decimation filter (DF) and interpolation filter (IF), that is, $\mathcal{F}_m^1(e^{\imath\theta}) = \mathcal{F}_j^1(e^{\imath\theta}) = \mathcal{F}_l^1(e^{\imath\theta})$ and $\mathcal{F}_m^2(e^{\imath\theta}) = \mathcal{F}_j^2(e^{\imath\theta}) = \mathcal{F}_l^1(e^{\imath\theta}), m \in \underline{N}_e, j \in \underline{N}_x, l \in \underline{N}_y$. The following emperically determined parameters are used: Elliptic LPF ($f_{stop} = \frac{L_\uparrow}{M_\downarrow}\frac{f_s}{2}, f_{pass} = \frac{11}{12}f_{stop}, A_{pass} = 2$ dB, $A_{stop} = 40$ dB).

In Simulation 5.5.1 - 5.5.2 on pages 262–263 the magnitude response and group delay for $\mathcal{F}^1(e^{\imath\theta})$ are shown. The corresponding results for $\mathcal{F}^2(e^{\imath\theta})$ are shown in Simulation 5.5.3 - 5.5.4 on pages 264–265.

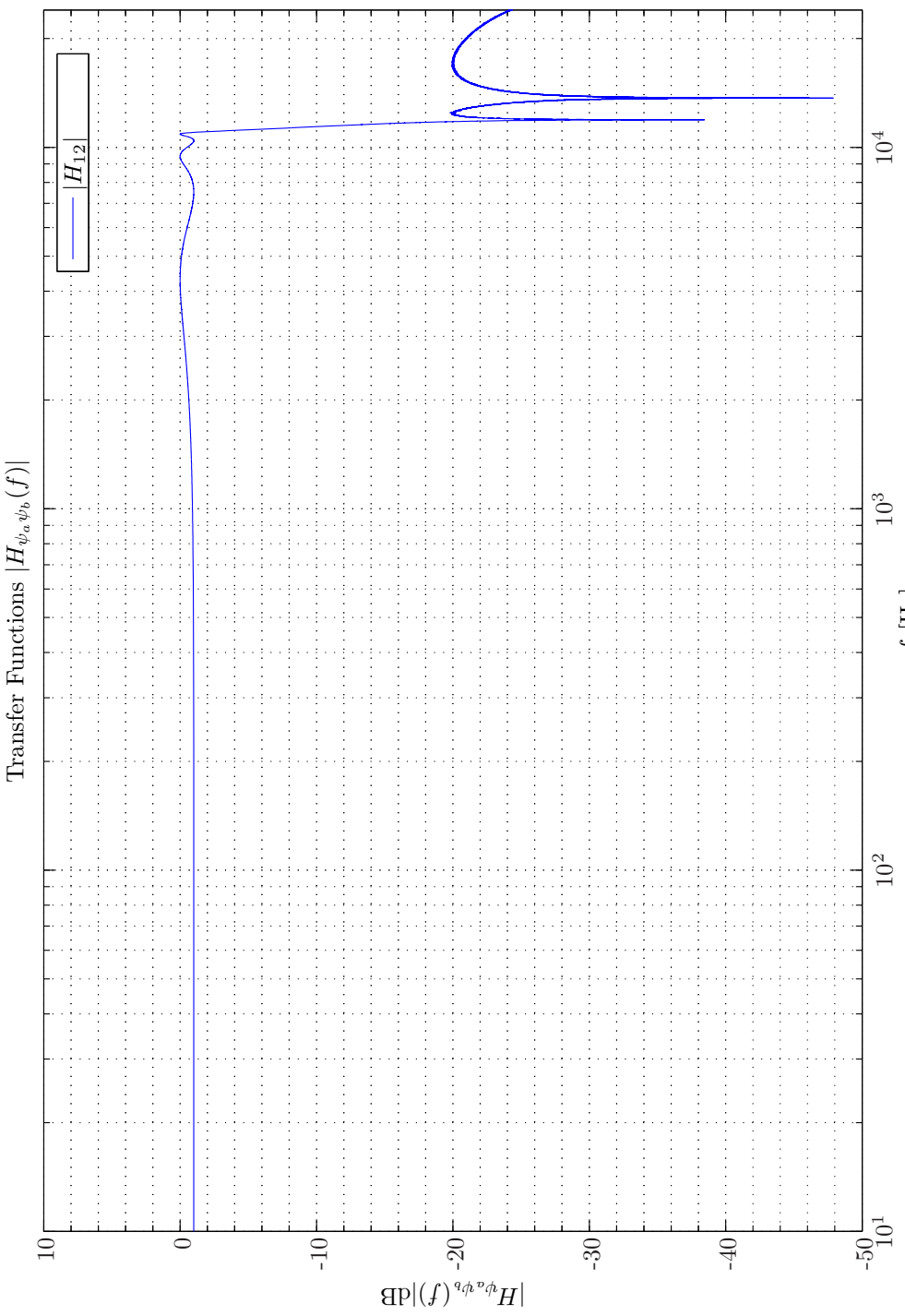

Sim 5.5.1: *Transfer Function, Magnitude:* $|H_{\psi_a\psi_b}(f)|$: **Statistical Data Analysis**: Single-Sided Modified Periodogram, f_s = 192 kHz, N_{DFT} = 65536, L_{DFT} = 48001, R_{DFT} = 24001, Hamming, Δf_m = 16 Hz, T_{DFT} = 0.25001 s, $N_{f,DFT}$ = 32769, Δf_{DFT} = 2.9297 Hz, K_{DFT} = 40; **Signals:** Elliptic LPF (f_s = 192 kHz, f_{pass} = 11 kHz, f_{stop} = 12 kHz, A_{pass} = 2 dB, A_{stop} = 40 dB); *Channels:* #1 ← x, #2 ← y; .

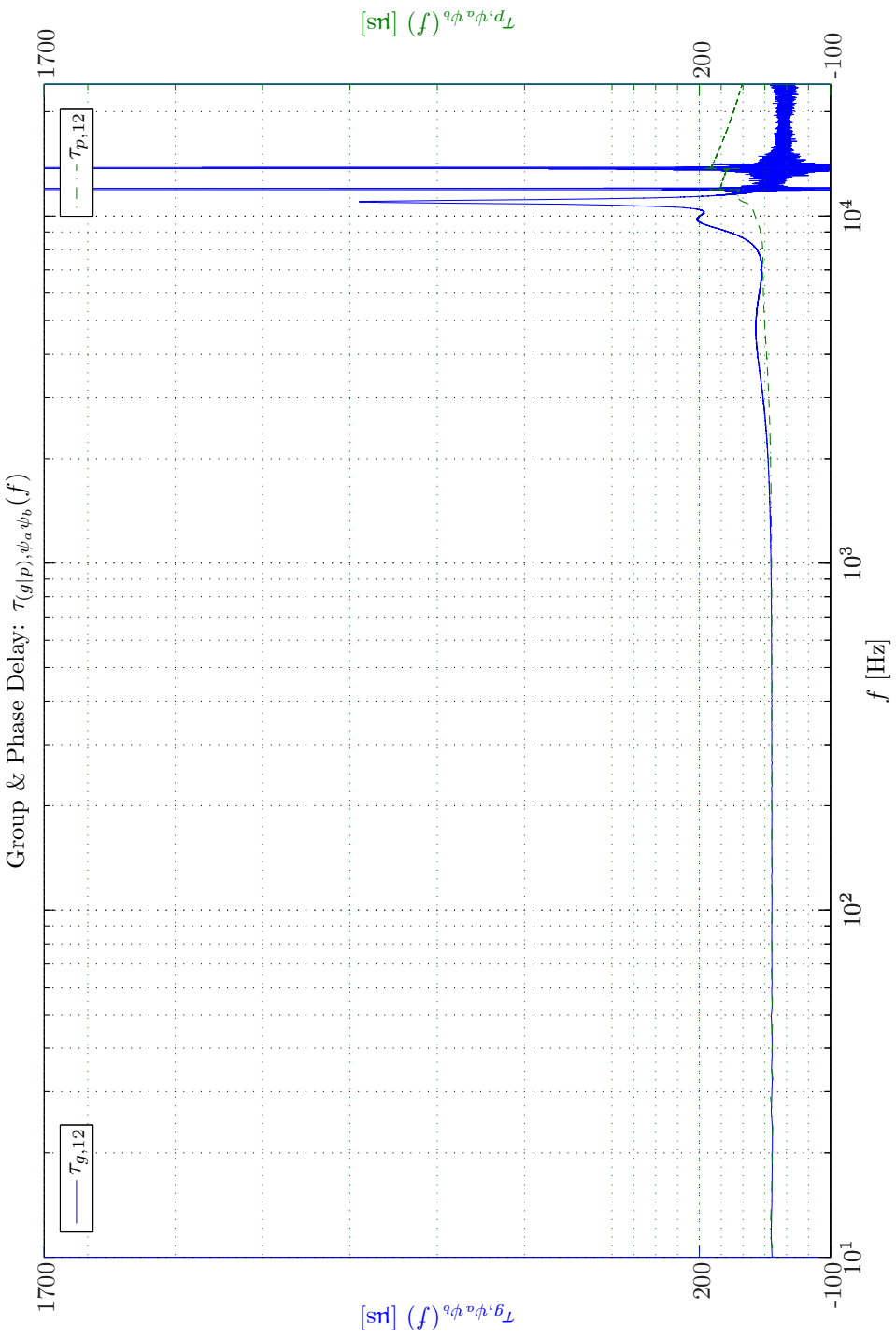

Sim 5.5.2: *Group & Phase Delay:* $\tau_{(g|p),\psi_a\psi_b}(f)$: **Statistical Data Analysis**: Single-Sided Modified Periodogram, f_s = 192 kHz, N_{DFT} = 65536, L_{DFT} = 48001, R_{DFT} = 24001, Hanning, Δf_m = 16 Hz, T_{DFT} = 0.25001 s, $N_{f,DFT}$ = 32769, Δf_{DFT} = 2.9297 Hz, K_{DFT} = 40; **Signals:** Elliptic LPF (f_s = 192 kHz, f_{pass} = 11 kHz, f_{stop} = 12 kHz, A_{pass} = 2 dB, A_{stop} = 40 dB); *Channels:* #1 ← x, #2 ← y.; .

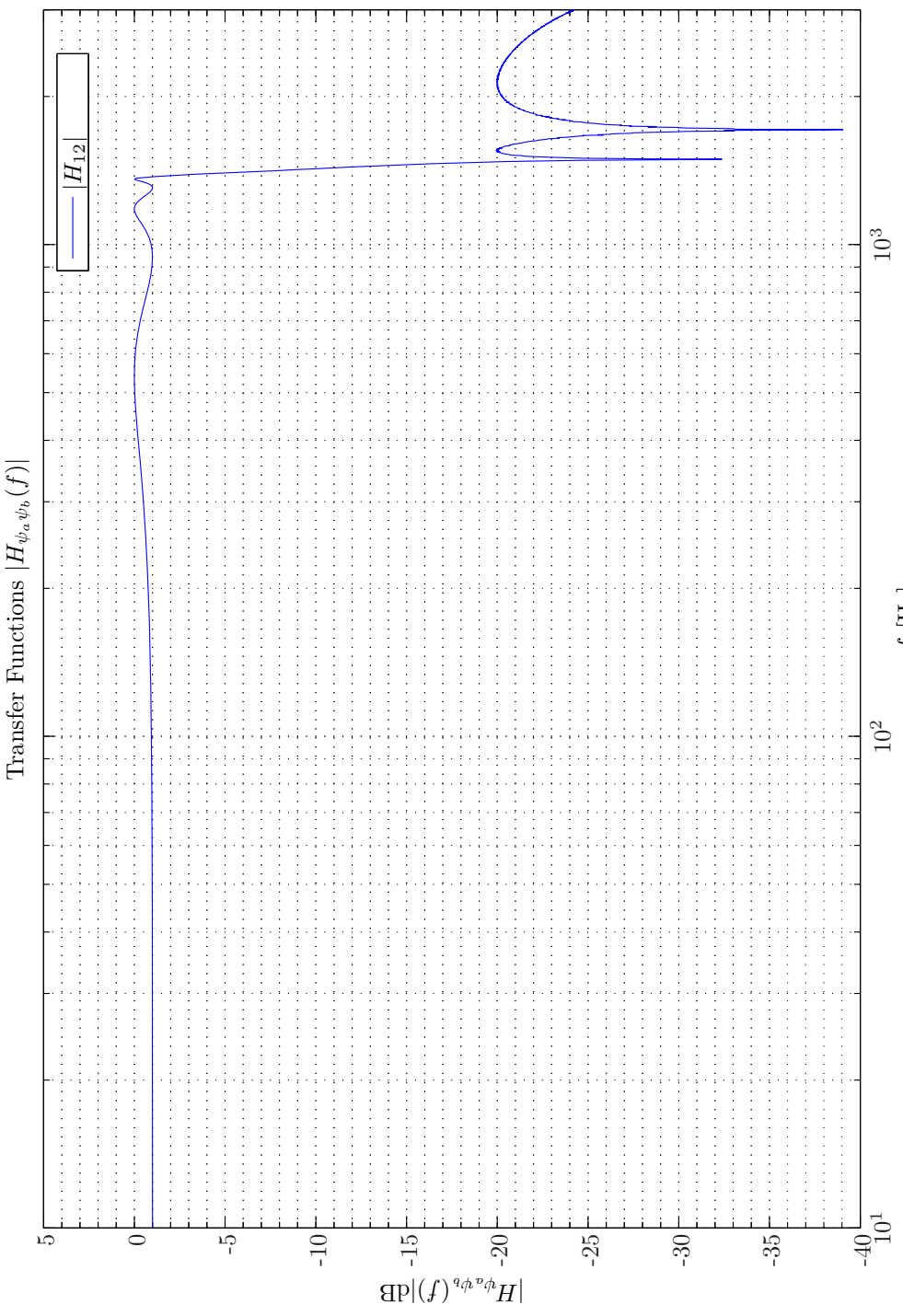

Sim 5.5.3: *Transfer Function, Magnitude:* $|H_{\psi_a\psi_b}(f)|$: **Statistical Data Analysis**: Single-Sided Modified Periodogram, f_s = 24 kHz, N_{DFT} = 8192, L_{DFT} = 6001, R_{DFT} = 3001, Hanning, Δf_m = 16 Hz, T_{DFT} = 0.25004 s, $N_{f,DFT}$ = 4097, Δf_{DFT} = 2.9297 Hz, K_{DFT} = 332; **Signals:** Elliptic LPF (f_s = 24 kHz, f_{pass} = 1.375 kHz, f_{stop} = 1.5 kHz, A_{pass} = 2 dB, A_{stop} = 40 dB); *Channels:* #1 ← x, #2 ← y;.

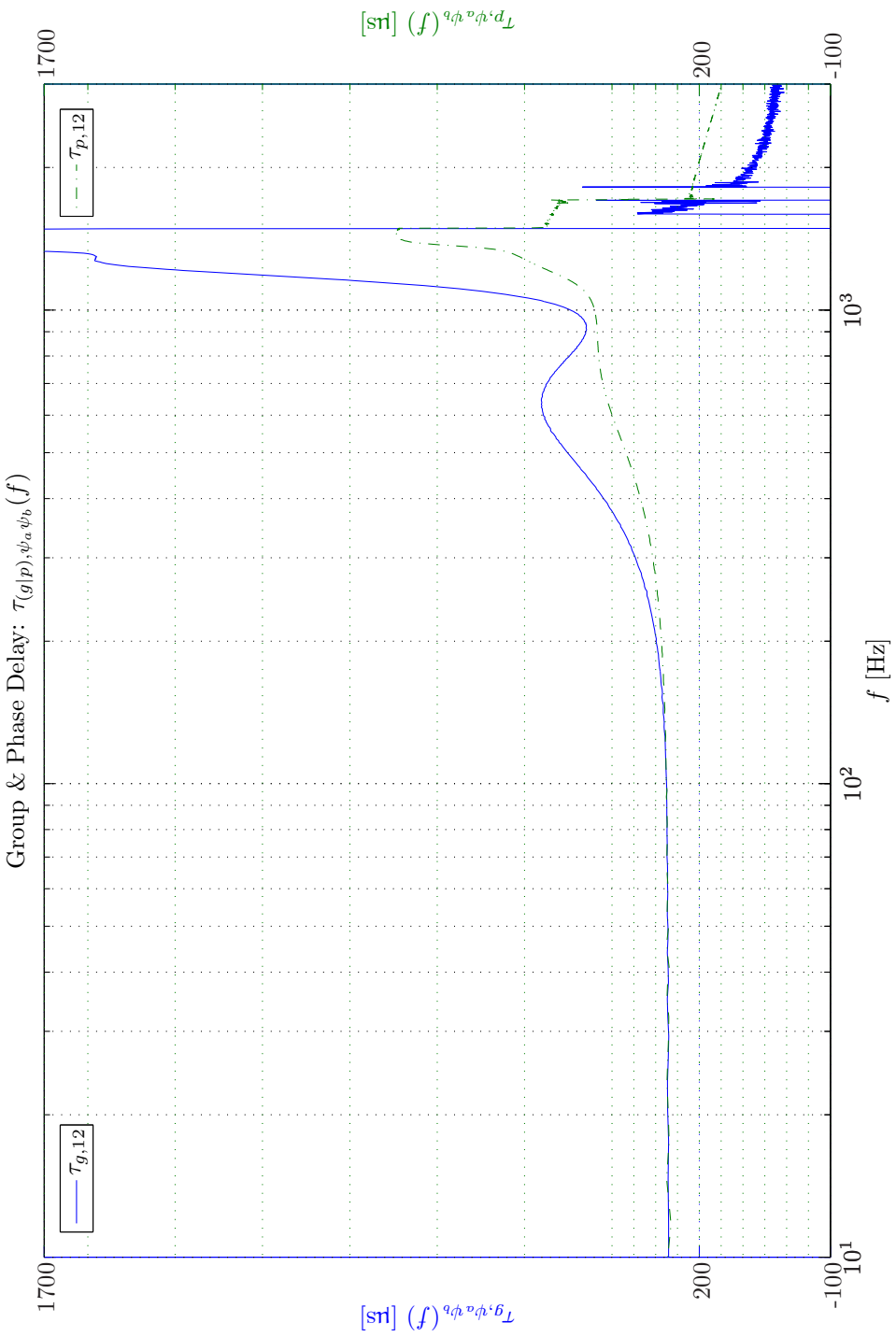

Sim 5.5.4: *Group & Phase Delay:* $\tau_{(g|p),\psi_a\psi_b}(f)$: **Statistical Data Analysis:** Single-Sided Modified Periodogram, f_s = 24 kHz, N_{DFT} = 8192, L_{DFT} = 6001, R_{DFT} = 3001, Hanning, Δf_m = 16 Hz, T_{DFT} = 0.25004 s, $N_{f,DFT}$ = 4097, Δf_{DFT} = 2.9297 Hz, K_{DFT} = 332; **Signals:** Elliptic LPF (f_s = 24 kHz, f_{pass} = 1.375 kHz, f_{stop} = 1.5 kHz, A_{pass} = 2 dB, A_{stop} = 40 dB); *Channels:* #1 ← x, #2 ← y; .

In Table 5.1 group delays for three different choice of sampling rate combinations, namely $(f_s^0, f_s^1, f_s^2) = (192, 48, 6)$ kHz, $(192, 24, 3)$ kHz and $(192, 12, 3)$ kHz are presented.

f_s^0	f_s^1	f_s^2	$\tau_g^{\mathcal{S}}$	$\tau_g^{\mathcal{D}^1}$	$\tau_g^{\mathcal{D}^2}$	τ_g^w	$\tau_g^{\mathcal{U}^2}$	$\tau_g^{\mathcal{U}^1}$	$\tau_g^{\mathcal{H}}$	τ_g^{dt}
192	48	6	5.2	16.7	136	20.8	136	16.7	2.6	62
192	24	3	5.2	33.3	271	41.7	271	33.3	2.6	116
192	12	3	5.2	66.7	262	83.3	262	66.7	2.6	224

Tab. 5.1: Group Delay Decomposition, MRS, Terma Earcup Audio System, Gentex HGU-55/P helmet. Sampling frequencies in kHz, delays in µs.

Owing to the close to unity ratio between f_{pass} and f_{stop} the group delays obtained here are roughly one half the group delays predicted in [8, Ch. 10]. We find that the upsampling and downsampling delays $\tau_g^{\mathcal{U}^2}, \tau_g^{\mathcal{U}^1}, \tau_g^{\mathcal{D}^1}$ and $\tau_g^{\mathcal{D}^2}$ may be approximated by

$$\tau_g^{\mathcal{U}^1} = \tau_g^{\mathcal{D}^1} \approx \frac{3.2}{8 f_{stop}^1} \tag{5.5.10a}$$

$$\tau_g^{\mathcal{U}^2} = \tau_g^{\mathcal{D}^2} \approx \frac{3.2}{8 f_{stop}^2}. \tag{5.5.10b}$$

These results should be compared with the group delays in a single-rate system (SRS) as listed in Table 5.2

f_s	$\tau_g^{\mathcal{S}}$	τ_g^w	$\tau_g^{\mathcal{H}}$	τ_g^{dt}
192	5.2	5.2	2.6	13.0
48	20.8	20.8	10.4	52.0
24	41.7	41.7	20.8	104
12	83.3	83.3	41.7	208
6	167	167	83.3	416

Tab. 5.2: Group Delay Decomposition, Terma Earcup Audio System, Gentex HGU-55/P helmet. Sampling frequency in kHz, delays in µs.

From a system identification to be carried out in section 11.5 on page 489, however, we will indeed see that τ_g^{ct} and therefore also τ_g will exhibit considerably variation with the frequency.

Bibliography

[1] P. Albertos. Block multirate input-output model for sampled-data control systems. *IEEE Transactions on Automatic Control*, 35(9):1085–1088, 1990.

[2] Mingsian Bai, Yuanpei Lin, and Jienwen Lai. Reduction of electronic delay in active noise control system. a multirate signal processing approach. *Journal of the Acoustical Society of America*, 111(2):916–924, 2002.

[3] Maurice G. Bellanger, Georges Bonnerot, and Michel Coudreuse. Digital filtering by polyphase network:application to sample-rate alteration and filter banks. *IEEE Transactions on Acoustics, Speech, and Signal Processing*, 24(2):109–114, 1976.

[4] A. J. Brammer, G. J. Pan, and R. B. Crabtree. Adaptive feedforward active noise reduction headset for low frequency noise. In *ACTIVE97*, pages 365–372, Budapest, 1997.

[5] Ronald E. Crochiere and Lawrence. R. Rabiner. Optimum FIR digital filter implementations for decimation, interpolation, and narrow-band filtering. *IEEE Transactions on Acoustics, Speech, and Signal Processing*, ASSP-23(5):444–456, 1975.

[6] Ronald E. Crochiere and Lawrence R. Rabiner. *Multirate Digital Signal Processing*. Prentice Hall, 1st edition, 1983.

[7] Jiagen Ding, Federica Marcassa, Shang-Chen Wu, and Masayoshi Tomizuka. Multirate control for computation saving. *IEEE Transactions on Control Systems Technology*, 14(1): 165–169, 2006.

[8] Stephen J. Elliott. *Signal Processing for Active Control*. London: Academic Press, 2001.

[9] Vikram M. Gadre and R. K. Patney. Some novel multirate architectures for filter realization with reduced multiplicative complexity. *IEEE Transactions on Signal Processing*, 42(9): 2492–2495, 1994.

[10] Chia-Chuan Hsiao. Polyphase filter matrix for rational sampling rate conversions. *ICASSP'87*, 12:2173–2176, 1987.

[11] O.S. Jahromi, B.A. Francis, and R.H Kwong. Spectrum estimation using multirate observations. *IEEE Transactions on Signal Processing*, 52(7):1878–1890, 2004.

[12] Seung-Hi Lee. Multirate digital control system design and its application to computer disk drives. *IEEE Transactions on Control Systems Technology*, 14(1):124–132, 2006.

[13] Hideo Murakami. Sampling rate conversion systems using a new generalized form of the discrete fourier transform. *IEEE Transactions on Signal Processing*, 43(9):20952102, 1995.

[14] Keitaro Ohno and Roberto Horowitz. A variable structure multirate state estimator for seeking control of HDDs. *IEEE Transactions on Control Systems Technology*, 13(2):233–245, 2005.

[15] Alan V. Oppenheim and Ronald W. Schafer. *Discrete-Time Signal Processing*. Prentice Hall International Inc., 2nd edition, 1999.

[16] Donald P. Orofino and Pder C. Pedersen. Multirate digital signal processing algorithm to calculate complex acoustic pressure fields. *JASA*, 92(1):563–582, 1992.

[17] Lawrence. R. Rabiner and Ronald E. Crochiere. A novel implementation for narrow-band FIR digital filters. *IEEE Transactions on Acoustics, Speech, and Signal Processing*, ASSP-23 (5):457–464, 1975.

[18] Tor A. Ramstad. Digital methods for conversion between arbitrary sampling frequencies. *IEEE Transactions on Acoustics, Speech, and Signal Processing*, ASSP-32(3):577–591, 1984.

[19] J. J. Shynk. Frequency domain and multirate adaptive filtering. *IEEE Signal Processing Magazine*, pages 14–37, 1992.

[20] P. P. Vaidyanathan. Quadrature mirror filter banks, m-band -extensions and perfect-reconstruction techniques. *IEEE ASSP Magazine*, ASSP-35(3):356–372, 1987.

[21] P. P. Vaidyanathan. *Multirate Systems and Filter Banks*. Prentice Hall Signal Processing Series. Prentice-Hall Inc., Upper Saddle River, New Jersey, 1993.

[22] P.P Vaidyanathan. Multirate digital filters, filter banks, polyphase networks, and applications: A tutorial. *Proceedings of the IEEE*, 78(1):56–93, 1990.

[23] P. Vary. On the design of digital filter banks based on a modified principle of polyphase. *AEU*, 33:293–300, 1979.

[24] Martin Vetterli. Running FIR and IIR filtering using multirate filter banks. *IEEE Transactions on Acoustics, Speech, and Signal Processing*, ASSP-36(5):730–738, 1988.

[25] Jeong-Hyeon Yun, Young-Cheol Park, and Dae-Hee Youn. Subband active noise control algorithm based on a delayless subband adaptive filter architecture. In *ICASSP*, volume 1, pages 391–394, 1997.

5.A Group and Phase Delays

In general an information bearing signal is characterized by a carrier frequency enveloped by some modulating signal. This signal when transmitted through a media or some filter will experience two related but different types of delays. The propagation delay of the *carrier* is determined by the phase delay $\tau_p(\omega)$ whereas the propagation delay of the *envelope* is determined by the group delay $\tau_g(\omega)$.

In audio system design the group delay is often used as a measure of the *phase linearity* of a device. Since a phase delay occurs at the output of a filter, it is important to know if this phase shift is linear with frequency. If the phase shift is nonlinear with frequency the output waveform will be distorted.

The group delay is defined as the negative derivative of the phase shift versus frequency [2, Ch. 5]

$$\tau_g(\omega) \triangleq -\frac{\mathrm{d}}{\mathrm{d}\omega}\sphericalangle H(\imath\omega), \tag{5.A.1}$$

where ω denotes the continuous-time angular frequency and $H(\imath\omega)$ is the transfer function. A linear phase shift will result in a constant group delay, since the derivative of a linear function is a constant.

The phase delay gives the time delay in seconds experienced by each sinusoidal component of the input signal

$$\tau_p(\omega) \triangleq -\frac{1}{\omega}\sphericalangle H(\imath\omega). \tag{5.A.2}$$

Similarly, in the discrete-time domain the group delay $\tau_g(\theta)$ and the phase delay $\tau_p(\theta)$ are defined according to

$$\tau_g(\theta) \triangleq -\frac{\mathrm{d}}{\mathrm{d}\theta}\sphericalangle H(\imath\theta) \tag{5.A.3}$$

and

$$\tau_p(\theta) \triangleq -\frac{1}{\theta}\sphericalangle H(\imath\theta), \tag{5.A.4}$$

where θ denotes the discrete-time angular frequency ($\theta \in [-\pi, \pi]$).

The continuous-time and discrete-time angular frequencies are linked through the sampling period T:

$$\theta = \omega T = 2\pi f T, \tag{5.A.5}$$

where the sampling frequency ω is obtained as

$$\omega = 2\pi / T. \tag{5.A.6}$$

5.A.1 Anti-Aliasing and Decimation/Interpolation Filter Constraints

As a rule of thumb the following relation between the group delay and the number of filter poles N_p and the number of filter zeroes N_z

$$\tau_g(f) \approx \begin{cases} \frac{N_p T}{8}; & 0 \leq f \lessapprox f_{stop}; \quad \text{IIR filter}, \\ \frac{N_z T}{2}; & 0 \leq f \leq f_s/2; \quad \text{FIR filter} \end{cases} \tag{5.A.7}$$

could be used, however, with some precautions as Tchebychev and elliptic filters exhibit large group delays at f_{stop}.

In ANC applications analogue filters are predominantly used for AAF and RF. Anti-imaging functionality can also be obtain by digitally filtering the control output signals. Digital low-order Butterworth filter (BWF) are often suitable as they provide a low-pass response with a relative flat group delay characteristic. Such group delay can then initially be estimated from (5.A.7).

The group delay involved in the sampling stage $\mathcal{S}(\imath\omega)$ is

$$\tau_g^{\mathcal{S}}(f) = \tau_g^{\mathcal{S}} = T^0. \tag{5.A.8}$$

Referring to the discussion in chapter 6 the output from the digital controller is first to the disposition to the outside at the next iteration cycle. The digital controller therefore contributes by a one sample delay. Hence, the associated group delay τ_g^w is then

$$\tau_g^w(f) = \tau_g^w = T^1. \tag{5.A.9}$$

Most DACs have a built-in zero-order sample and hold device. Such devices increase the overall phase corresponding to half a sample-time. Hence, the group delay of the zero-order sample and hold device $\mathcal{H}(\imath\omega)$ is then

$$\tau_g^{\mathcal{H}}(f) = \tau_g^{\mathcal{H}} = \frac{T^0}{2}. \tag{5.A.10}$$

From the expressions for the group delay τ_g^w, $\tau_g^{\mathcal{S}}(f)$ and $\tau_g^{\mathcal{H}}$ all exhibit linear proportionality with the common sample period T in a single-rate system. Hence, by doubling the sampling frequency these group delays will all be halved. However, doubling the sampling frequency will

approximately lead to a quadrupling of the computational requirements [1, Ch. 10]. A doubling of the computational requirements occur since the time available has been halved. The second doubling of the computational effort stems from the expressions involving the quantity $M_{\hat{g}_y^t}^{max}$ involved in obtaining the filtered-reference signal. But now each plant model requires twice as many tap-weight as before for the same amount of time represented by $\hat{g}_{ey}$. Now by employing MRS design we can maintain low values of $\tau_g^{\mathcal{S}}$ and $\tau_g^{\mathcal{H}}$ and to some extent also τ_g^w while preserving a the computational effort at an acceptable level.

However, this argumentation only applies to the use of FIR filter representation of the plants. The main problem with the FIR filter topology is that each tap-weight effectively only represents a short fraction of time $T = 1/f_s$ of the full plant response. In Appendix I we will introduce more computational efficient filter topologies that can represent the entire plant response for a fixed number of tap-weights independent of the sampling frequency.

From a practical viewpoint we can use (5.A.11) presented next in order to estimate the collective contributions to τ_g^{ct}. If we make a system identification with a very high sampling frequency ($f_s \gg f_u$) and defer from using AAFs and RFs then we obtain a plant estimate and therefore also a group delay estimate from system identification $\hat{\tau}_g^{SI}$

$$\hat{\tau}_g^{SI}(f) = \tau_g^{\mathcal{H}} + \tau_g^{ct}(f) + \tau_g^w. \tag{5.A.11}$$

Then $\tau_g^{ct}(f)$ can readily be obtained from (5.A.11) by subtraction of $\tau_g^{\mathcal{H}}$ and τ_g^w using (5.A.10) and (5.A.9).

Bibliography

[1] Stephen J. Elliott. *Signal Processing for Active Control*. London: Academic Press, 2001.

[2] Alan V. Oppenheim and Ronald W. Schafer. *Discrete-Time Signal Processing*. Prentice Hall International Inc., 2nd edition, 1999.

Part III

ADAPTIVE FILTERS FOR ACTIVE NOISE CONTROL

6. ADAPTIVE FILTERING FOR ACTIVE CONTROL OF SOUND AND VIBRATION

6.1 Introduction

Before entering a more detailed description of the adaptive filtering processing schemes considered in the subsequent chapters of this Part III some remarks, however, should be made in general on the application of adaptive filtering algorithms to the domain of active control of sound and vibration. This chapter establishes a link between the domain of control system to the domain of adaptive filtering. The pertinent terminology will also be established.

The main body of the literature in the field of adaptive digital filtering exclusively consider purely electrical problems that are characterized by the absence of a *physical plant*.

Briefly described for a digital controller the plant is defined as the transfer function between the output of the adaptive filter and the sensed error signal. Hence, the plant in a pure electrical system is constituted by the transformation from the sampled-time domain to the continuous-time physical domain and back to the sampled-time domain. The plant therefore includes the digital to analogue converter, reconstruction filter, anti-aliasing filter and analogue to digital converter. However, in active control of sound or vibration systems a physical plant will inevitably also be present. A more exhaustive description of the concept of a plant is provided in Part II of this report.

Unfortunately, in practice the physical plant will be non-minimum phase due to propagation delays and possibly exhibit non-linear behavior. Moreover, the physical plant is unknown and in general time-varying and therefore repeatedly has to be identified. Therefore, as compared with their purely electrical counterparts adaptive robust control of sound and vibration poses a considerably amount of extra challenges to the designer.

If the plant response is not adopted then the ordinary least-mean-squares (LMS), normalized LMS (NLMS) and recursive least-squares (RLS) algorithms described in chapter 8 will degrade in performance in terms of a lower convergence rate, an increased residual power and will possibly exhibit instability problems. The main problem arise due to the lack of synchronization between the output $y(\cdot)$ of the adaptive filter and the resulting error $e(\cdot)$ due to the filtering and inherent time-delays caused by the plant. In all of the adaptive filtering algorithm presented in chapter 8 the disturbance $d(\cdot)$ is referred to a point coinciding with the output terminal of the adaptive filter viz. Figure I.1 on page 731 in contrast to active control (AC) systems presented in chapter 7 on page 291.

6.1.1 Chapter Outline

After this introduction some general remarks on the accommodation of the plants for adaptive filters is made in section 6.2. Next the well-established *filtered-reference signal* method and the more advanced variant hereof referred to as the *modified filtered-reference signal* method used to accommodate the presence of a plant is described in section 6.3. Owing to the fast convergence property of the *modified filtered reference* signal method this method will extensively be used in the subsequent chapters. Next the theme of section 6.4 is the family of *filtered-error* methods that provide cost effective alternatives to the modified-filtered-x (mFx) method which is of particular importance in multiple-input and multiple-output (MIMO) systems. In AC acoustical and structural feedback from the control output signals to the reference signals may present a threat to the overall system performance. In section 6.5 the problem of acoustical and structural feedback is detailed. Both the family of filtered-reference methods and the family of filtered-error methods rely on estimates of the secondary pathes involved in the AC system. Accordingly section 6.6 discusses the aspects of the system identification of these plants. Next in section 6.7 some discussions of the use of infinite-duration impulse response (IIR) filters for AC is made. Finally, in section 6.8 some comments on the use of non-linear AC is made.

A review of the filtered-reference methods can be found in [19, Ch. 3] and [37, Ch. 3].

6.2 Accommodation of Plants for Adaptive Filters

Hitherto the physical plant has been accommodated in the adaptive filtering algorithms by incorporating a model of the plant response. The *stochastic* gradient methods used for adaptive filtering, e.g., the famous least-mean-squares are all based on instantaneously estimating the local gradient of the ensemble-averaged error-surface with respect to the tap-weights. However, in active noise control applications, the measured error stems from a control output signal that is filtered by virtue of the presence of the plant. The same lack of alignment between the measured error and the error used for tap-weight recursion also applies to the *deterministic* ('exact') methods.

The adaptive processing schemes discussed in the subsequent chapters of this Part III will all apply an *performance feedback* scheme as discussed in section I.1. What basically differentiates the methods presented in this chapter is the specific error signal used for tap-weight update denoted here by $e^{\Delta w}(\,\cdot\,)$, the reference signal used for tap-weight update represented by $u^{\Delta w}(\,\cdot\,)$ and the tap-weight update time that we designate by $i^{\Delta w}(\,\cdot\,)$. Hence, we can generally write the tap-weight adaptation process as $\Delta\mathcal{W}(t_B^2, \{u^{\Delta w}\}, \{e^{\Delta w}\})$, where t_B^2 designates the block index time that corresponds to the time where the tap-weight are updated. As will be detailed in Appendix J in the literature it is customary to use w_{i-1}, where i denotes the iteration number, to signify that the error $e(i)$ is an *a priori* error, that is, the error is calculated on the basis of previous tap-weights [57]. Moreover, we also make provision for *time-block update* as presented in Appendix J. For adaptive filtering not using block-time update the tap-weight update time is identical to the previous iteration, that is, $t_B^2 = i - 1$. In the general case the two iteration are subject to $t_B^2 < i$.

In the development we will address the "plant-less" case as a special case for which the plant response equals unity, that is, in the $\mathbf{z}$-domain $\tilde{g}(z) \triangleq 1$. The plant-less control system will also be identified as *electrical control* as opposed to *acoustical/structural control system* or just *active control system*. If the adaptive filter (AF) is used in a plant-less case the measured error $e(\,\cdot\,)$ and

$e^{\Delta w}(\,\cdot\,)$ will coincide.

6.3 Family of Filtered-x Method

In the family of filtered reference methods the reference signal used for tap-weight update is obtained from filtering the original reference signal with a *model* of the physical plant response. Historically the input signal or reference signal has been denoted by x. Hence, the notation filtered-x (Fx).

6.3.1 Ordinary Filtered-x Method

The fundamental assumption made in the ordinary filtered-x method is that the system is linear and the tap-weights vary slowly, so that

$$w_{t_B^2} \approx w_{t_B^2-1} \approx \ldots \approx w_{t_B^2-M_{\hat{g}_{ey}}+1}, \quad t_B^2 < i \tag{6.3.1}$$

holds. The filter order used to represent the secondary path is denoted by $M_{\hat{g}_{ey}}$. This assumption of "slow" adaptation means that the controller → plant response can be replaced by plant → controller response [19, Ch. 3]. Strictly speaking, however, this interchange operation is only valid in *linear time-invariant*(LTI) *systems.*

The applicability of this assumption will be dependent both on the adaptation rate and the duration of the plant response. Therefore (6.3.1) will usually apply better for the least-mean-squares than the recursive least-squares. For fast adaptation rates and long impulse responses more advanced Fx-methods discussed in the subsequent sections will provide better performance.

In the Fx method the error signal $e^{\Delta w}$ used for tap-weight recursion will coincide with the measured error

$$e^{\Delta w}(i) = e(i). \tag{6.3.2}$$

6.3.2 Modified Filtered-x Method

Although the filtered reference technique was originally developed for *stochastic* gradient based methods it also works with algorithms with roots in deterministic problem formulation provided that the adaptation rate is sufficiently slow [10, 29]. In order to extend the applicability of the filtered-reference technique to situations were the enforcement on the requirement on a slow adaptation (6.3.1) is prohibitive as may be the case with the recursive least-squares algorithm the *modified filtered reference* approach abbreviated mFx has been invented [10, 29, 55].

Instead of using the *measured* error signal $e(i)$ for tap-weight recursion it is arguable more correct to use an estimate of what the error signal would have been provided that the tap-weights had been frozen for a period corresponding to the impulse response of the plant. Then $e^{\Delta w}(i) \triangleq e(i|w_{i'} = w_{t_B^2}), \quad i' = i - M_{\hat{g}_{ey}}, i - M_{\hat{g}_{ey}} + 1, \ldots, i-1$. This error in turn is obtained by superposing the disturbance estimate at time i $\hat{d}(i)$ and the cancelation signal estimate (frozen filter) at time i $\hat{r}^{\Delta w}(i)$ defined by $\hat{r}^{\Delta w}(i) \triangleq r(i|w_{i'} = w_{t_B^2}), \quad i' = i - M_{\hat{g}_{ey}}, i - M_{\hat{g}_{ey}} + 1, \ldots, i-1$ where $M_{\hat{g}_{ey}}$ introduced in (6.3.1) denotes the order of the secondary path model.

The details of the mFx technique will be revealed during the presentation of the multi-channel feedback and feedforward systems in section 7.2 and section 7.3.

Finally, $\hat{e}^{\Delta w}(i)$ is obtained from

$$\hat{e}^{\Delta w}(i) = \hat{d}(i) + \hat{r}^{\Delta w}(i). \tag{6.3.3}$$

This technique is also referred to as *modified error algorithm* [19]. A (minor) disadvantage of the mFx method in general is associated with the additional calculation of $\hat{d}_m(i)$ and $\hat{r}_m^{\Delta w}(i)$. In a feedback IMC configuration $\hat{d}_m(i)$, however, should be determined anyway. The FxLMS requires $2\underset{\frown}{M} + M_{\hat{g}_{ey}}$ or $2(\underset{\circ}{M} + M_{\hat{g}_{ey}})$ operations per update cycle in a feedforward implementation and in a feedback IMC configuration respectively. For the same case the mFxLMS requires of the order of $3\underset{\frown}{M} + 2M_{\hat{g}_{ey}}$ respectively $3\underset{\circ}{M} + 2M_{\hat{g}_{ey}}$ operations per cycle. For the ordinary (as opposed to FAST) recursive least-squares the extra computational load of mFxRLS over the ordinary FxFx is usually acceptable.

A major problem associated with the filtered-x technique is encountered in large multi-channel applications [18] where computational difficulties arise. Moreover, the multi-channel filtered-x LMS algorithm also suffers from excessive data storage requirements. In the literature other methods have therefore been proposed to account for the presence of the plant. In [55] two variants of the mFx approach referred to as mFxLMS-1 and mFxLMS-2 respectively were presented. The main advantages of applying the proposed mFxLMS-1 and mFxLMS-2 approaches are computational and storage savings. The computational effort can be reduced from $3M + 2M_{\hat{g}_{ey}}^{l,m}$ to $2(M + M_{\hat{g}_{ey}}^{l,m})$ while simultaneously reducing the requirement on storage from $3M + M_{\hat{g}_{ey}}^{l,m}$ to $M + M_{\hat{g}_{ey}}^{l,m}$ as compared with the ordinary mFxLMS technique. Moreover, in [55] conditions for robustness and optimal choice of step-size parameter is derived.

Bibliographic Notes on Filtered Reference Techniques[1]

The analysis of the adaptive filters based on an instantaneous stochastic gradient estimation in general is a very complicated task as treated in more detailed in chapter 8. Moreover, the presence of a plant and the subsequent application of the filtered reference technique further complicates the analysis even under the assumption of the availability of a perfect plant model. By invoking an assumption of the input data to stem from a *spherical invariant random process* Bjarnason [5] made a *stochastic* analysis of the convergence behavior and steady-state performance of the FxLMS algorithm. The expressions governing the convergence/stability behavior and excess error are quite involved and depends heavily on the plant response that commonly is modeled by a FIR filter. Particular emphasis was given to simple delay systems.

The presence of the secondary path also has an impact on the optimal *adaptation rates*. It is well known from LMS adaptive filter theory that the maximum adaptation coefficient is determined by the eigenvalues of the signal and the filter length [57]. However, in AC the system operates with delayed adaptation. As studied in details in [20], [42], [43] and [59] the maximum stable value of the convergence coefficient is greatly influenced by the time delay that occurs between a change in the digital filter and the change being reflected in the error signal. In [63] the AC performance of a lightly damped structural single-input and single-output (SISO) feedforward

[1] This subsection provides supplementary bibliographic information on filtered reference techniques that, however, can be skipped on a first reading.

FxLMS system was assessed with regards to final mean square error, speed of convergence and excitation of unreferenced frequency components. By simply calculating the tap-weight update each N sample and discarding the interim $(N-1)$ samples different update rates were obtained from varying N. For this system it was found that by using every sample has the undesired effect of greatly reducing the maximum stable value of the convergence speed. This in turn implied that the weight updates were stucked by quantization effects. As a consequence better attenuation figures could obtained be discarding 4 out of 5 samples. The time required to reach steady state with optimized values of the adaptation coefficient was quite insensitive to the discardation of input samples. The reason is that the use of larger adaptation coefficient counterbalanced for the lack of interim tap-weight updates. During the adaptation process the filter will exhibit time-variance and process the input nonlinearly. As a consequence the error signal is to some degree *heterodyned* over the reference signal on its path to the signal output. From applications involving adaptive notch filters it is well known that the bandwidth increases with adaptation rate and the magnitude of the adaptation coefficient [31]. Consequently, it was found that by slowing the adaptation rate can improve the system performance by reducing the level of excitation of unreferenced signal components. The investigations in [63], however, were restricted to a specific lightly damped system using ordinary FxLMS. Hence, the conclusions are not directly amendable to broad band system using, e.g., mFxNLMS with floating point precision. On the other hand it can indeed be stated that faster adaptation rates in general does not necessarily imply better system performance.

The adaptive delay filter (ADF) has been developed for feedforward narrow band applications where it suffice to iteratively to determine the gain and delay of the controller that in turn compensates for the ratio of primary path to secondary path gain and difference in delays encountered in the primary path and secondary path [36]. In applications involving a periodic noise that contains several harmonics, multiple ADFs connected in parallel to form a cost-effective active noise control (ANC) system has been proposed [36].

The influence of the eigenvalue contribution and the associated slow convergence speed of a lightly damped system under using FxLMS has been analyzed [46] and is derived from computer simulations in [60].

It should also be remarked that FxLMS and filtered-error (Fe)LMS find use in adaptive inverse control (AIC) in order largely to reduce the dependence of the inverse controller $C(z)$ on the estimate of the plant g_{ey} [72, Ch. 7].

Suggested literature on the mFx method includes [2, 5, 6, 8, 13, 16, 17, 21–23, 25, 27, 33, 33, 38, 42, 44, 48, 50, 51, 54, 67] and [71, Ch. 8].

6.4 Family of Filtered-Error Method[2]

The family of FeLMS algorithms is widely used in MIMO ANC systems as an alternative to FxLMS to reduce the computational complexity and memory requirements. As discussed in section 6.3 the aim of the Fx- and mFx is to establish synchronization between the reference signal and the error signal. Instead of filtering the reference signal with an estimate of the secondary path we could filter the error signal by an error filter denoted by $A(z)$. In the subsequent text two commonly available FeLMS methods will be described; the adjoint LMS (ALMS) [69], [49] and the secondary

[2]The algorithms presented in this section are considered candidate methods for accommodating the plants in a multiple-channel (MC)active noise control system (ANCS). However, these algorithms are currently not implemented and the section can therefore be skipped on a first reading.

path equalization (SPE) [45] [37, Sec. 3.3.3]. Next the hybrid Fe (HFe)LMS method introduced recently [14] will be presented.

6.4.1 Adjoint LMS

The derivation of the FeLMS algorithm can be found in [19, Sec. 3.4.6, 5.4.2]. The error signal $e^{\Delta w}$ used for tap-weight recursion is now obtained by *causally* filtering the measured error signal using a *time-reversed* version of the estimated plant response. The update time $i^{\Delta w}$ has a time lag of $M_{\hat{g}_{ey}} - 1$ samples compared with the current time i in order to ensure causality. The reference signal used for the tap-weight update $u^{\Delta w}$ is an in time aligned version of x. Hence,

$$e^{\Delta w}(i) = \sum_{j=0}^{M_{\hat{g}_{ey}}-1} \hat{g}_{M_{\hat{g}_{ey}}-1-j} e(i-j), \tag{6.4.1}$$

$$u_i^{\Delta w} = x_{i-M_{\hat{g}_{ey}}+1}, \quad i^{\Delta w} = i - M_{\hat{g}_{ey}} + 1. \tag{6.4.2}$$

Accordingly in the **z**-domain we may express the error filter in terms of the adjoint (time-reversed) secondary path function as

$$A(z) = z^{-\beta} \tilde{\hat{g}}_{ey}(z^{-1}), \tag{6.4.3}$$

where the delay number is determined from

$$\beta = M_{\hat{g}_{ey}}. \tag{6.4.4}$$

A disadvantage of the FeLMS algorithm is the $M_{\hat{g}_y} - 1$ delay introduced in (6.4.1) to (6.4.2) in order to ensure causal filtered error operation. This further reduces the maximum convergence speed as compared with the ordinary In [69] it is demonstrated that FxLMS and FeLMS algorithms lead to similar active noise reduction (ANR) performance provided that the convergence rate is sufficiently slow.

6.4.2 Secondary Path Equalization

The error filter in the SPELMS method is obtained from.

$$A(z) = \{z^{-\beta} \tilde{\hat{g}}_{ey}^{-1}(z)\}_+, \tag{6.4.5}$$

where the delay number is determined from

$$\beta = C M_{\hat{g}_{ey,max}} + M_{\hat{g}_{ey,UC}} \tag{6.4.6}$$

and C is a constant chosen as to approximate $\tilde{\hat{g}}_{ey}^{-1}(z)$.

$$e^{\Delta w}(i) = \sum_{j=0}^{M_{\hat{g}_{ey}}-1} \hat{g}_{M_{\hat{g}_{ey}}-1-j} e(i-j), \tag{6.4.7}$$

$$u_i^{\Delta w} = x_{i-M_{\hat{g}_{ey}}+1}, \quad i^{\Delta w} = i - M_{\hat{g}_{ey}} + 1. \tag{6.4.8}$$

The main disadvantages of the SPELMS method is that an error-weighting filter explicitly is invoked viz. (6.4.5). Hence the SPELMS algorithm minimize the error filtered by $\tilde{\hat{g}}_{ey}^{-1}(z)$ rather than the (unfiltered) error. As remarked in [37, Sec. 3.3.3] if there is a dip in $\tilde{\hat{g}}_{ey}^{-1}(\omega)$ there will be no content in $e^{\Delta w}(\omega)$ at this frequency and the disturbance noise therefore left unattenuated.

6.4.3 Hybrid FeLMS

The FeLMS algorithms described above, however, introduce significant delays in updating the adaptive filter coefficients that slow the convergence rate. Recently an algorithm called the HFeLMS aimed at (1) increasing the convergence rate, (2) reducing the excess-mean-square error (EMSE) and (3) shaping the excess noise power as compared with the ordinary FeLMS has been introduced [14].

The central point in the development of the hybrid FeLMS (HFeLMS) technique is to exploit that the system function of any finite-duration impulse response (FIR) linear phase system, say, $H(z)$ can be factored into a minimum-phase lag term $H_{min}(z)$, a maximum-phase lag term $H_{max}(z)$ and a delay term $H_{UC}(z)$ containing only zeros on the unit circle [47, ch. 5], that is,

$$H(z) = H_{min}(z)H_{UC}(z)H_{max}(z). \tag{6.4.9}$$

Moreover the HFeLMS technique relies on factorizing the error filter $A(z)$ into parts related to the ALMS- and SPE methods respectively according to the overall system objectives

$$A(z) = A_{ALMS}(z)A_{SPE}(z), \tag{6.4.10}$$

where the ALMS part of error filter in HFeLMS $A_{ALMS}(z)$ is similarly defined by

$$A_{ALMS}(z) = \prod_i z^{-\beta_i^{ALMS}} \tilde{\hat{g}}_{ey,i}(z^{-1}) \tag{6.4.11}$$

and $H(z^{-1})$ denotes the adjoint (time-reversed) transfer function of $H(z)$,

and where SPE part of error filter in HFeLMS $A_{SPE}(z)$ is defined by

$$A_{SPE}(z) = \prod_i z^{-\beta_i^{SPE}} \tilde{\hat{g}}_{ey,i}^{-1}(z). \tag{6.4.12}$$

Now in order to reduce the delays due to the presence of a nonminimum secondary path as far as possible the contribution from the minimum phase lag part should be addressed by the SPE algorithm as the $\beta^{SPE} = 0$ in this case. Accordingly $\tilde{\hat{g}}_{ey}$ is divided as in (6.4.9) into three parts. The error filter $A(z)$ is chosen as the combination of the adjoint of the maximum phase part ($A_{ALMS}(z) = \tilde{\hat{g}}_{ey,max}(z^{-1})$), the inverse of the minimum phase part and the delay ($A_{SPE,1}(z) = z^{-\beta_1^{SPE}} \tilde{\hat{g}}_{ey,min}(z)$, $A_{SPE,2}(z) = \{z^{-\beta_2^{ALMS}} \tilde{\hat{g}}_{ey,UC}(z)\}_+$) where $\beta_1^{ALMS} = M_{\hat{g}_{ey,max}}$ and $\beta_1^{SPE} = 0, \beta_2^{SPE} = CM_{\hat{g}_{ey,min}}$. Other design objectives are possible with this method [14].

As regards computational load in a MIMO system the HFeLMS will be in favor of mFx. Unfortunately no comparison with the mFx was conducted in [14]. For the practical use in a ANR-system where requirements on system identification of the secondary paths usually exist, a method automatically to factorize $\tilde{\hat{g}}_{ey}$ must be found. The inverse of a transfer function is readily obtainable using adaptive filtering techniques, e.g., [72, Ch. 5]. Although as reported in [14] the ALMS and FxLMS exhibit similar convergence performance for a simple secondary path ($M_{\hat{g}_{ey}} = 6$), it is an open question whether this statement also applies when the notorious slow-converging LMS is replaced by one of the so-called fast algorithms, e.g., fast array recursive least-squares (FARLS) in particular for secondary paths with a large nonminimum-phase lag part is doubtful[3].

6.5 Solutions to Acoustic or Structural Feedback

In feedforward ANC applications and in particular the duct ANR systems the control output signals might contaminate the reference sensors thereby formally transferring the feedforward system into a feedback system. It has been found from theory and confirmed by experimental investigations that the acoustical feedback significantly complicates the control design and degrades the performance and stability of the active control system. In fact the feedback path g_{xy} turns an else stationary (in some sense) reference signal $x(t)$ into a nonstationary reference signal $x'(t)$ during tap-weight adaptation and presents a source of instability.

By introducing close-loop poles to the system the feedback path might have a destabilizing effect on the ANC system if the feedback loop gain becomes too large. In addition, it changes the direction of the adaptive control filter updating. Since the primary noise is highly correlated with the anti-noise and therefore also the feedback signals, the adaptation of the feedback neutralization filter must be inhibited when the ANC system is in operation [28].

Simple steady-state analysis of a SISO feedforward ANR-system we can express the transformed error $\tilde{e}(z)$ as

$$\tilde{e}(z) = \tilde{g}_{ex}(z)\tilde{x'}(z) - \tilde{g}_{ey}(z)\tilde{y}(z) \tag{6.5.1}$$

$$= \tilde{g}_{ex}(z)\tilde{x'}(z) - \tilde{g}_{ey}(z)\frac{\tilde{\underset{\sim}{w}}(z)\tilde{x'}(z)}{1 - \tilde{\underset{\sim}{w}}(z)\tilde{x'}(z)}. \tag{6.5.2}$$

From [53] and [37, Ch. 3] we find the following expression for the optimal feedforward steady-state tap-weights transfer function $\tilde{\underset{\sim}{w}}^o(z)$ in SISO case (using our terminology)

$$\tilde{\underset{\sim}{w}}^o(z) = \frac{\beta(z)\tilde{g}_{ex}(z)}{\tilde{g}_{ey}(z) + \beta(z)\tilde{g}_{ex}(z)\tilde{g}_{xy}(z)}, \tag{6.5.3}$$

where

$$\beta(z) = \frac{\mathrm{SNR}_x(z)}{1 + \mathrm{SNR}_x(z)} \tag{6.5.4}$$

and SNR_x denotes the signal-to-noise ratio at the reference sensor.

[3] Information from [37, Ch. 3.7], [35, 68] to be included

From (6.5.3) we see that when the open-loop phase-lag $\angle\beta(\mathrm{e}^{\imath\omega})\tilde{g}_{ex}(\mathrm{e}^{\imath\omega})\tilde{g}_{xy}(\mathrm{e}^{\imath\omega})$ reaches 180 degrees while the open-loop gain $|\beta(\mathrm{e}^{\imath\omega})\tilde{g}_{ex}(\mathrm{e}^{\imath\omega})\tilde{g}_{xy}(\mathrm{e}^{\imath\omega})|$ is greater than unity *instability* occurs.

Some remedies to the feedback problem have been presented in the literature including the use of directional microphones and loudspeakers, *neutralization filter*, dual microphone reference sensors, use of the FuLMS algorithm, *nonacoustic sensors*, motional feedback loudspeakers etc. [37, Ch. 3]. The first *adaptive* feedback canceling architecture for AC was proposed by Warnaka, Poole, and Tichy [70]. In this scheme, however, due to the operation of the ANR-system the primary noise, that is, the reference signal is highly correlated with the feedback signal.

Another technique to compensate for the acoustic or structural feedback is to use an adaptive IIR filter [26].

Bai and Wu [4] applying *modal matching* and adopting Youla's parameterizations [74] expressions for the controller that guarantees internal stability of the closed loop system and minimizing with the residual pressure with respect to either of the l_1- or l_2-norm was derived. In an industrial duct setup the system was tested with various noise stimuli and the performance of the l_1-norm based optimization was compared with filtered-u (Fu)LMS method. Depending on the noise excitation the proposed methods performed equally to FuLMS method, but exhibited transient noise suppression capabilities as opposed to the FuLMS algorithm.

In a recent paper [1] an architecture involving a threefold of adaptive filters for on-line system identification in an feedforward SISO ANR system is proposed.

6.6 System Identification: Plants

6.6.1 Motivation

Modern AC systems usually use plant estimates for various purposes. This also applies to the rather complex hybrid MIMO feedforward-feedback system (HMIMOFFFBS) presented in chapter 7 on page 291. From section 6.3 - 6.4 we appreciate that both the family of filtered-reference methods and the family of filtered-error methods rely on estimates of the secondary pathes involved in the AC system. Moreover, in feedback system (FBS) design the internal model control (IMC) technique (refer to section 4.6) is usually employed to cast the FBS to a feedforward system (FFS). The IMC involves an estimate of the secondary path $\hat{g}_{ey}$. Similarly, as discussed in section 6.5 in FFS a feedback cancelation scheme that requires an estimate of the feedback paths is used to compensate for the corruption by feedback from the actuators on the reference sensors.

6.6.2 Performance

In [59, 61] an analysis of the effect of transfer function estimation errors on the FxLMS is provided.

The performance of the system identification process is determined by

SID 1. The number of tap-weights used to represent the theoretical infinite impulse response function of the plant ($M_{\hat{g}} < \infty$). Hence, $M_{\hat{g}}$ should be sufficiently large to contain almost the entire energy content of the plant response function. On the other hand the covariance of the error vector of a LMS-based adaptation scheme varies linearly with the number of tap-weights [72, App. A].

SID 2. Sufficient spectral excitation of the signal applied for system identification. Dither noise may be used for persistent excitation However, the effect of dither noise will experienced at the error sensors and most likely also at the performance sensors which can cause annoyance. In [72, Ch. 4] three different dither schemes referred to as A, B and C representing distinctively different approaches to the use of dither signals for plant modeling can be found. The introduction of such schemes, however, is at the expense of some extra system complexity.

SID 3. Insufficient time span for the system identification preventing steady-state convergence. This is particular important if the LMS algorithm is used and a large eigenvalue-value spread is present in the system identification signal. The remedy to this problem is to use white noise dither and/or a higher adaptation coefficient (LMS case) or to use the FARLS algorithm. In all cases a sufficient amount of time for the process should be allowed. The resulting convergence time of course should be smaller than the time-constant of the plant disturbances.

SID 4. In an ANC system the disturbance signal "surviving" the operation of the control system that correlates with system identification signal represents noise to the system identification process. Moreover, if the power ratio of system identification signal to disturbance signal is to small convergence in the adaptive filter process might not occur.

With the adaption coefficient μ selected, the dither power may then be selected. Usually, a small dither power will result in a large time constant, and by increasing the dither power, the adaptive process will converge more rapidly. Reducing the dither power will reduce the contribution of dither power at the performance sensors but slow down the adaption process. Since the uncanceled disturbance is irreducible, there is no point in making the output dither noise power substantially less than the uncanceled disturbance power. A reasonable compromise between the objectives of fast adaptation and low residual noise power would be to make the dither power equal to the uncanceled disturbance power.

Bibliographic Notes on Secondary Path Modeling Errors[4]

An estimate of the plant response will normally be obtained from a system identification procedure. Any imperfect plant modeling will lead to bias error and possible instability problems. Loosely speaking for small plant estimate errors the performance degradation will be small, but for large inaccuracies the result can be disastrous [30, Ch. 7].

Unfortunately the secondary path may be noisy, that is, subject to disturbances. As discussed in section 4.7 on page 245 the plant uncertainty can largely be compensated for by using an AIC. Hereby, the cascade of the inverse controller $C(z)$ and the plant g_{ey}. In any case system identification of the time-varying secondary path is required at regular intervals depending on the rate of fluctuations.

In one of the earlier investigations of the least-mean-squares (LMS) involving an "auxiliary path" it was found that convergence a fairly mild criteria of the phase error being numerical less than 90° prevails [45].

The limits on the adaptation coefficient in a FxLMS configuration subject to secondary path modeling errors for a single sinusoidal was examined in [59]. If the magnitude of the frequency response $|\tilde{g}_{ey}(\mathrm{e}^{\imath\omega})|$ deviates from the correct value the maximum allowable tap-weight update

[4] This subsection provides supplementary bibliographic information on secondary path modeling errors that, however, can be skipped on a first reading.

coefficient μ_{max} decreases inversely proportional to the magnitude error which follows directly from the tap-weight update recursion viz. (8.6.30) on page 402.

In [56] the performance degradation versus plant modeling error was investigated through simulations for a vehicle cabin equipped with a SISO feedforward FxLMS system designed to cancel random noise. Invoking the independence theory (IT) assumption analytical expressions for stability, convergence performance and noise cancelation was developed. As described the Fx scheme involves a filtering of the reference signal with an estimate of the secondary path. However, if the secondary path is not perfectly modeled a pertubated filtered-reference signal u' which generally differs from the "correct" filtered-reference signal u. Essential to the analysis is the cross-correlation matrix between the correct filtered-reference signal and the pertubated filtered-reference signal, $R_{uu'}(i)$, and the cross-correlation between the pertubated filtered-reference signal and the desired response $R_{du'}(i)$ defined in (B.1.2) on page 537. In fact convergence analysis of the gradient-based adaptive filters discussed in details in chapter 8 should be based on $R_{uu'}(i)$ which in general is complex instead of the real autocorrelation matrix $R_{uu}(i)$. The aforementioned criteria on the phase error was deduced by considering eigenvalues of $R_{uu'}$. As regards ANR performance it is shown that provided that the cross-correlation matrix $R_{uu'}$ is nonsingular and the primary path can be expressed as a cascade coupling of the adaptive filter operating with optimal tap-weights and the secondary path (which would be the case in the duct case) then the adaptive filter in principle exactly can compensate for the modeling errors. The ANR system had a nominal performance of 9 dB noise reduction. The analysis revealed performance robustness to even large modeling errors. However, as will be shown through the course of this report such conclusions cannot in general be transferred to system with a nominal performance of, say $20 - 25$ dB.

The secondary path is usually estimated using an adaptive system identification procedure as described in section 7.6 using white noise as excitation signal which, however, in tends to be annoying. Instead as demonstrated in [39] music can be used for secondary path and feedback path modeling. In this reference an excellent secondary path estimation accuracy was obtained using music as excitation source. The convergence time as compared with white noise excitation, however, was not reported.

6.7 Active Control using IIR Filters[5]

Owing to the inherent stability FIR filters have most commonly been employed in the AC community for the adaptive tap-weights and for secondary path and feedback path modeling. However, it has also been proposed instead to use potentially more efficient IIR filters [26] [25] and [37, Ch. 3.6], [19, Ch. 2.9] and [30, Sec. 6.12]. As is well known and detailed in section I.3 an IIR filter employs both direct and recursive coefficients. For the direct coefficients the Fx or the mFx might be employed to the reference signals to obtain filtered-reference signals. Similarly the recursive tap-weight update uses the control output signals filtered by the secondary paths.

The main benefit of using IIR filter instead of FIR filter is that the same response can be obtained with a IIR filter using fewer adaptive tap-weights. In Appendix K on page 759 a class of so-called *orthonormal filters* with large inherent modeling capabilities are presented.

In particular, the recursive LMS (RLMS) algorithm discussed in section I.3 has received much

[5]The algorithms presented in this section are considered candidate methods for accommodating the plants in a MCANCS. However, these algorithms are currently not implemented and the section can therefore be skipped on a first reading.

attention over the years. The same arguments made in section 6.2 for the use of filtering methods to take the presence of the plant into account for the least-mean-squares (LMS) apply to the RLMS algorithm. The Furecursive LMS (RLMS)[6] algorithm was developed in [24] based on a crude gradient estimate and the filtered-v RLMS (FuRLMS) algorithm [12] using a more correct gradient estimate. However, both the filtered-u RLMS (FuRLMS) and FuRLMS may converge to a *local* minima on the error surface. The FuRLMS can also be used to compensate for the influence of feedback from control output signal to reference signal in a feedforward system. An algorithm that under the assumption of a perfect plant model and noise free measurements ensures global convergence was proposed in [66]. A Steiglitz-McBride-type adaptive IIR filter algorithm [52] that according to the authors guarantees global convergence while ensuring robustness to imperfect secondary path modeling errors and measurement noise provided that no feedback signals are present was proposed in [65].

Laugesen and Elliott [41] presented an adaptive IIR filter algorithm referred to as multiple error recursive leaky LMS (MERLLMS) for multi-channel ($N_x = 1$, $N_y = 4, N_e = 8$) active control (AC) of random noise in a reverberant room. The details can be found in [40]. It was found that for this particular reverberant room that was excited by a loudspeaker inside the room that no apparent benefit in terms of global cost function of using an IIR filter with $M_a = M_b = 32$ as compared with a FIR filter $M = 32$ was obtained. However, it is an open question if a smaller IIR filter, say $M_a = M_b = 16$, could have been used without sacrificing the performance. For the secondary paths, however, only FIR filters of the order $M_{g_{ey}} = 32$ were considered. An IIR filter expectably has the potential to model the secondary paths with fewer tap-weights. However, system identification of secondary paths was not specifically investigated in this reference. In an other arrangement where a more complicated primary path was obtained by moving the loudspeaker to an adjoining room coupling to the receiving room through a plywood panel. In this case very long impulse responses of the controller were required. The practical benefit of using an adaptive IIR filter in this particular setup was clearly demonstrated. Hence, adaptive IIR filters or the class of orthonormal filters discussed in Appendix K most likely and in particular in reverberant cases constitute cost effective alternatives to the FIR filter implementations.

Additional readings on the use of IIR filter for system identification and for AC can be found in [25] [27] [23] [15] [64] [58] [34] [3] [32] [73].

6.8 Bibliographic Notes on Nonlinear Active Control[7]

As mentioned previously the actuators used in active control systems might exhibit nonlinear characteristics, or in some cases a structure to be controlled exhibits a nonlinear behavior. In such cases *nonlinear active controllers* may be required. For active control of sound and vibration, the use of *neural networks* as nonlinear control structures has been reported in [62]. In [9] and [7] training algorithms for a multilayer perceptron (MLP) artificial neural network (ANN) based nonlinear active control structure were investigated. The control structure comprised two MLP feedforward ANN (one as a nonlinear controller and one as a nonlinear plant model). *Steepest descent* algorithms based on two distinct gradient approaches were introduced for the training of the controller network. Experiments of feedforward active sound control in a duct using a nonlinear actuator with linear and nonlinear controllers were performed. Control results also

[6] We will consistently use the term RLMS instead of LMS to signify the underlying recursive topology of the filter.

[7] This subsection provides some bibliographic information on nonlinear AC. However, these algorithms are currently not implemented and the section can therefore be skipped on a first reading.

showed that a multilayered perceptron neural-network control structure could outperform linear controllers for the experimental nonlinear system. Learning rates and computational load for various ANN algorithms were compared.

In [11] a Fx Cerebellar Model Articulation Controller (CMAC) ANN is analyzed. As compared with the aforementioned MLP based solution the CMAC controller exhibits better convergence properties and at the same time with less computational effort.

Bibliography

[1] Muhammad Tahir Akhtar, Masahide Abe, and Masayuki Kawamata. On active noise control systems with online acoustic feedback path modeling. *IEEE Transactions on Acoustics, Speech, and Signal Processing*, 2006.

[2] T. Auspitzer, D. Guicking, and Elliot S, J. Using a fast-recursive-least squared algorithm in a feedback controller. In *IEEE Workshop on Applications of Signal Processing to Audio and Acoustics*, New Platz, NY, 1995.

[3] Mingsian R. Bai and Jienwen Lai. Broadband spatially feedforward active noise control algorithms using a comb filter. *Journal of Vibration and Acoustics*, 125(1):18–23, 2003.

[4] Mingsian R. Bai and Tianyau Wu. Study of the acoustic feedback problem of active noise control by using the l_1 and l_2 vector space optimization approaches. *The Journal of the Acoustical Society of America*, 102(2):1004–1012, 1997.

[5] E. Bjarnason. Analysis of the filtered-XLMS algorithm. *IEEE Transactions on Speech and Audio Processing*, 3:504–514, 1995.

[6] M. Bouchard and B. Paillard. An alternative feedback structure for the adaptive active control of periodic and time-varying periodic disturbances. *Journal of Sound and Vibration*, 210:517–527, 1998.

[7] Martin Bouchard. New recursive-least-squares algorithms for nonlinear active control of sound and vibration using neural networks. *IEEE Transactions on Neural Networks*, 12(1): 135–147, 2001.

[8] Martin Bouchard and Yu Feng. Inverse structure for active noise control and combined active noise control/sound reproduction systems. *IEEE Transactions on Speech and Audio Processing*, 9(2):141–151, 2001.

[9] Martin Bouchard, Bruno Paillard, and Chon Tan Le Dinh. Improved training of neural networks for the nonlinear active control of sound and vibration. *IEEE Transactions on Neural Networks*, 10(2):391–401, 1999.

[10] M. Bronzel. *Aktive Beeinflussung nich-stationärer schallfelder midt adaptiven Digitalfiltern.* Phd, Göttingen, 1993.

[11] John Canfield, L. Gordon Kraft, Paul Latham, and Andrew Kun. Filtered-X CMAC: An efficient algorithm for active disturbance cancellation in nonlinear dynamical systems. In *IEEE Internation Symposium on Inteligent Control*, 2003.

[12] David H. Crawford and Robert W. Stewart. Adaptive IIR filtered-v algorithms for active noise control. *JASA*, 101(4):1097–1103, 1997.

[13] Aniruddha Datta and James Ochoa. Adaptive internal model control: $\mathcal{H}_2$ optimisation for stable plant. *Automatica*, 34:75–82, 1998.

[14] Victor E. DeBrunner and Dayong Zhou. Hybrid filtered error lms algorithm: Another alternative to filtered-x LMS. *IEEE Transactions on Circuits and Systems—Part I: Fundamental Theory and Applications*, 53(3):653–661, 2006.

[15] N. Doelman. *Design of Systems for Active Sound Control*. Ph.D., Technische Universiteit Delft, The Netherlands, 1993.

[16] Scott C. Douglas. Fast exact filtered-X LMS and LMS algorithms for multichannel active noise control. In *IEEE ICASSP*, pages 399–402, Munich, Germany, 1997.

[17] Scott C. Douglas. An efficient implementation of the modified filtered-XLMS algorithm. *IEEE Signal Processing Letters*, 4(10):286–288, 1997.

[18] Scott C. Douglas. Fast implementations of the filtered-XLMS and LMS algorithm for multichannel active noise control. *IEEE Transactions on Speech and Audio Processing*, 7(4): 454–465, 1999.

[19] Stephen J. Elliott. *Signal Processing for Active Control*. London: Academic Press, 2001.

[20] Stephen J. Elliott, Ian M. Stothers, and Phillip A. Nelson. A a multiple error LMS algorithm and its application to the active control of sound and vibration. *IEEE Transactions on Speech and Audio Processing*, 35:1423–1434, 1987.

[21] Stephen. J. Elliott, Nelson Phillip A, Ian M. Stothers, and C. C. Boucher. Preliminary results of in-flight experiments on the active control of propeller-induced cabin noise. *Journal of Sound and Vibration*, 128(2):355–357, 1989.

[22] Stephen. J. Elliott, Nelson Phillip A, Ian M. Stothers, and C. C. Boucher. In-flight experiments on the active control of propeller-induced cabin noise. *Journal of Sound and Vibration*, 140(2):219–238, 1989.

[23] L. J. Eriksson. *Active Sound Attenuation Using Adaptive Digital Signal Processing Techniques*. PhD thesis, University of Wisconsin-Madison, 1991.

[24] L. J. Eriksson. Development of the filtered-u algorithm for active noise control. *JASA*, 89: 257–265, 1991.

[25] L. J. Eriksson and M. C. Allie. Use of random noise for on-line transducer modeling in an adaptive active attenuation system. *JASA*, 85(2):797–802, 1989.

[26] L. J. Eriksson, M. C. Allie, and R. A. Greiner. The selection and application of an IIR adaptive filter for use in active sound attention. *IEEE Transactions on Acoustics, Speech, and Signal Processing*, 35:433–437, 1987.

[27] L. J. Eriksson, M. C. Allie, and R. A. Grenier. The selection and application of an iir adaptive filter for use in active sound attenuation. *IEEE Transactions on Acoustics, Speech, and Signal Processing*, 35(4):433–437, 1987.

[28] E. Esmailzadeh, A. R. Ohadi, and A. Alasty. Multi-channel adaptive feedforward control of noise in an acoustic duct. *Journal of Dynamic Systems, Measurement, and Control*, 126(2): 406–415, 2004.

[29] S. J. Flockton. Fast adaptation algorithms in active noise control. In *Second Conference on Recent Advances in the Active Control of Sound and Vibration*, pages 802–810, Virgina, 1993.

[30] Colin H. Hansen and Scott D. Snyder. *Active Control of Noise and Vibration*. E & FN SPON, 1st edition, 1997.

[31] Jr. John R. Glover. Adaptive noise canceling applied to sinusoidal interferences. *IEEE Transactions on Speech and Audio Processing*, 25(6):484–491, 1977.

[32] Masaki Kamata, Yuhsuke Ohta, and Akira Sano. New direct adaptive algorithm for multi-channel active noise control and sound reproduction. In *Eusipco*, pages 717–720, 2004.

[33] In-Soo Kim, Hee-Seung Na, Kwang-Joon Kim, and Youngjin Park. Constraint filtered-x and filtered-u least-mean-square algorithms for the active control of noise in ducts. *JASA*, 95(6):3379–3389, 1994.

[34] Xuan Kong, Pu Liu, and Sen M. Kuo. Multiple channel hybrid active noise control systems. *IEEE Transactions on Control Systems Technology*, 6(6):719–729, 1998.

[35] S. M. Kuo and J. Tsai. Acoustical mechanism and performance of various active duct noise control system. *Applied Acoustics*, 41:81–91, 1994.

[36] Sen M. Kuo. Narrowband active noise control using adaptive delay filter. *IEEE Signal Processing Letters*, 5(12):309–311, 1998.

[37] Sen M. Kuo and Dennis R. Morgan. *Active Noise Control Systems Algorithms and DSP Implementations*. John Wiley & Sons, Inc., 1996.

[38] Sen M. Kuo, Xuan Kong, and Woon S. Gan. Applications of adaptive feedback active noise control system. *IEEE Transactions on Control Systems Technology*, 11(2):216–220, 2003.

[39] Sen M. Kuo, Sohini Mitra, and Woon-Seng Gan. Active noise control system for headphone applications. *IEEE Transactions on Control Systems Technology*, 14(2):331–335, 2006.

[40] Søren Laugesen and Stephen J. Elliott. A demonstration of multichannel broadband active control in a small reverberent room. Technical Memorandum 709, University of Southampton, Institute of Sound and Vibration Research, 1991.

[41] Søren Laugesen and Stephen J. Elliott. Multichannel active control of random noise in a small reverberent room. *IEEE Transactions on Signal Processing*, 1:241–249, 1993.

[42] Gouzho Long, Fuyun Ling, and John G. Proakis. The LMS algorithm with delayed coefficient adaption. *IEEE Transactions on Acoustics, Speech, and Signal Processing*, 37(9):1397–1405, 1989.

[43] Gouzho Long, Fuyun Ling, and John G. Proakis. Corrections to: The LMS algorithm with delayed coefficient adaption. *IEEE Transactions on Acoustics, Speech, and Signal Processing*, 40(1):230–232, 1992.

[44] L. Meirovitch and M. A. Norris. Sensitivity of distributed structures to model order in feedback control. *Journal of Sound and Vibration*, 144(3):365–380, 1991.

[45] Dennis R. Morgan. An analysis of multiple correlation cancellation loops with filter in the auxiliary path. *IEEE Transactions on Acoustics, Speech, and Signal Processing*, 28(4): 454–467, 1980.

[46] Dennis R. Morgan and Charles Sanford. A control theory approach to the stability and transient analysis of the filtered-x lms adaptive notch filter. *IEEE Transactions on Signal Processing*, 40(9):2341–2346, 1992.

[47] Alan V. Oppenheim and Ronald W. Schafer. *Discrete-Time Signal Processing*. Prentice Hall International Inc., 2nd edition, 1999.

[48] Marek Pawelczyk, Stephen J. Elliott, and Boaz Rafaely. Active noise control using feedback fixed and adaptive controllers. Technical Memorandum 822, University of Southampton, Institute of Sound and Vibration Research, 1997.

[49] S. R. Popovich. A simplified parameter update identification of multiple input, multiple output systems. In *International Congress on Noise Engineering*, volume 2, pages 1229–1232, Yokohama, Japan, 1994.

[50] Boaz Rafaely and Stephen J. Elliott. Active noise control using feedback fixed and adaptive controllers. Technical Memorandum 776, University of Southampton, Institute of Sound and Vibration Research, 1996.

[51] Boaz Rafaely and Matthew Jones. Combined feedback-feedforward active noise-reducing headset -the effect of the acoustics on broadband performance. *The Journal of the Acoustical Society of America*, 112(3):981–989, 2002.

[52] P. A. Regalia. *Adaptive IIR Filtering in Signal Processing and Control*. Marcel Dekker, New York, 1995.

[53] A. Roure. Self-adaptive broadband active sound control systems. *Journal of Sound and Vibration*, 101:429–441, 1985.

[54] M. Rupp. Saving complexity of modified filtered-XLMS and delayed update LMS algorithms. *IEEE Transactions on Circuits and Systems—Part II: Analog and Digital Signal Processing*, 44:45–48, 1997.

[55] M. Rupp and A. H. Sayed. Robust fxlms algorithms with improved convergence performance. *IEEE Transactions on Speech and Audio Processing*, 6:78–85, 1998.

[56] N. Saito and T. Sone. Influence of modelling error on noise reduction performance of active control system using filtered-XLMS algorithm. *JASA of Japan*, 17:195–202, 1996.

[57] Ali H. Sayed. *Fundamentals of Adaptive Filtering*. John Wiley & Sons, Inc., New York, NY, USA, 2003.

[58] JP Smith, RA Burdisso, CR Fuller, and RG Gibson. Active control of low-frequency broadband jet engine exhaust noise. *Noise Contr. Eng.*, 44(1):45–52, 1996.

[59] Scott D. Snyder and Colin H. Hansen. The influence of transducer transfer functions and acoustic time delays on the LMS algorithm in active control systems. *Sound and Vibration*, 140:409–424, 1990.

[60] Scott D. Snyder and Colin H. Hansen. Design considerations for active noise control systems implementing the multiple input, multiple output LMS algorithm. *Journal of Sound and Vibration*, 159:157–174, 1992.

[61] Scott D. Snyder and Colin H. Hansen. The effect of transfer function estimation errors on the filtered-x LMS algorithm. *IEEE Transactions on Signal Processing*, 42(4):950–953, 1994.

[62] Scott D. Snyder and Nobuo Tanaka. Active control of vibration using a neural network. *IEEE Transactions on Neural Networks*, 6(4):819–828, 1995.

[63] Scott D. Snyder and Nobuo Tanaka. Algorithm adaptation rate in active control: Is faster necessarily better? *IEEE Transactions on Speech and Audio Processing*, 5(4):378–381, 1997.

[64] S. D. Sommerfeldt. Multi-channel adaptive control of structural vibration. *Noise Contr. Eng.*, 37(2):77–89, 1991.

[65] X. Sun and Guang Meng. Steiglitz-mcbride type adaptive IIR algorithm for active noise control. *Journal of Sound and Vibration*, 273(4):441–450, 2004.

[66] Xu Sun and D. Chen. A new infinite impulse response filter-based adaptive algorithm for active noise control. *Journal of Sound and Vibration*, 258(2):385–397, 2002.

[67] Orlando J. Tobias, José Carlos M. Bermudez, and Neil J. Bershad. Mean weight behaviour of the filtered-XLMS algorithm. *IEEE Transactions on Signal Processing*, 48(4):1061–1075, 2000.

[68] J. Tsai. *Active Noise Control Systems: Secondary Source Arrangements Frequency Shaping and Electroacoustic Path Modelling*. M. sc., Northern Illinois University DeKalb, 1993.

[69] Eric A. Wan. Adjoint LMS: An efficient alternative to the filtered-x ms multiple error LMS algorithms. In *IEEE Int. Conf. Acoust., Speech, Signal Processing*, volume 3, pages 1842–1845, Atlanta, GA, 1996.

[70] G. E. Warnaka, L. A. Poole, and J. Tichy. Applications for active noise control, 25 September 1984.

[71] Bernard Widrow and Samuel D. Stearns. *Adaptive Signal Processing*. Prentice-Hall, New Jersey, 1985.

[72] Bernard Widrow and Eugene Walach. *Adaptive Inverse Control*. Prentice Hall, 1996.

[73] Tuk Keuizg Yeuizg and Sze Fong Yuu. Feedforward ANC system using adaptive FIR filters with on-line secondary path identification. pages 675–678, 1999.

[74] Dante C. Youla, Jr. Joseph J. Bongiorno, and Hamid A. Jabr. Modern wiener -hopf design of optimal controllers part ii: The multivariate case. *IEEE Transactions on Automatic Control*, 21(3):319–338, 1976.

7. HYBRID MULTIPLE-INPUT-MULTIPLE-OUTPUT FEEDFORWARD FEEDBACK SYSTEM

7.1 Introduction

The active noise reduction (ANR) system is shown in Figure 1.1. The sensor suite comprises N_e error sensors, N_x reference sensors and N_p performance monitoring sensors. A total of N_y actuators excite the secondary signals. We will present the general multi-channel multirate case right away. The superscripts j, k, l and m will be used to designate reference sensor-, performance-, actuator- and error sensor index respectively. These indices are subject to the constraints $j \in \underline{N}_x$, $k \in \underline{N}_p$, $l \in \underline{N}_y$ and $m \in \underline{N}_e$. Moreover, in order to prevent ambiguity between feedback and feedforward quantities we will apply an underaccent$_{\circ}$ to indicate a feedback topology quantity and similarly an underaccent$_{\frown}$ to indicate a feedforward topology quantity. For feedforward-feedback signals we will use an underaccent$_{\oplus}$ and finally for signals that include the contributions from signal sources an underaccent$_{\circledast}$ will be used. For pure signals an underaccent$_{\copyright}$ will be employed. For ease of presentation we may suppress the explicit reference of superscripts j, l, k and m.

7.1.1 Chapter Outline

After this introduction from section 7.2 to section 7.6 we gradually build the multi-channel feedforward-feedback integrated communication on-line system identification system (FFFBICIDS). section 7.2 presents the topology of the *multi-channel adaptive feedback controller*. In addition a detailed discussion of the various signals involved is provided. Then in section 7.3 we similarly describe the employed *multi-channel adaptive feedforward controller*. Some quantities specific to the feedforward system (FFS) are also defined. After presentation of the feedback- and the feedforward controller the road is paved for the introduction of the combination of the two which is referred to as a *multi-channel adaptive feedforward-feedback controller* in section 7.4. A requirement of distortion-free transmission of communication signals is often imposed on modern ANR headset equipment. In section 7.5 a technique to prevent unintentional suppression of such signals is presented. In section 7.6 we add provision for on-line system identification. This system will be referred to as a multi-channel FFFBICIDS. Finally, in section 7.7 and section 7.8 some simulation results of system identification and active control (AC) will be presented. In the Appendix 7.A an array description of the feedforward-feedback system (FFFBS) is provided.

7.2 Feedback Controller - Adaptive Filter Topology

7.2.1 Introduction

The feedback controller - adaptive filtering - interface is depicted in Figure 7.1 on the next page. Specifically, Figure 7.1 illuminates the *error feedback* (refer to section I.1) interaction between the l'th secondary source and the m'th error sensor. In total $N_e \times N_y$ such controller-error sensor combinations exist. The system uses a *multirate* structure as detailed in chapter 5. The zeroth multirate level (refer to Figure 5.1 and Figure 5.2) contains the conversion stages that are operated at high sampling rates leading to very low delays. The non-adaptive controller constitute the first multirate level where moderate sampling speeds prevail. The first multirate level is still highly oversampled compared with the operational bandwidth of the system. As discussed in chapter 5 a tradeoff between delay and computation effort determines these sampling frequencies. The tap-weight adaptation takes place at the slower downsampled second multirate level. This sampling frequency is selected as a compromise between the computational burden involved in the adaptive tap-weight updates and the requirement on fast update rates to ensure fast convergence and tracking capabilities to nonstationary signals. Furthermore, by restricting the bandwidth of adaptive control the corresponding requirement on very long finite-duration impulse response (FIR) filters for adaptive tap-weights and plant representation can be avoided.

In order to achieve a high degree of flexibility and to reduce the computational burden different sampling rates might be used at the error sensors and reference sensors. This could, for instance, allow us to operate the feedforward and feedback controllers in a hybrid continuous-time discrete-time topology (HCTDTT) at different speeds. The presentation of the hybrid MIMO feedforward-feedback system (HMIMOFFFBS) to follow has partly been prepared for such advanced system configuaration. However, in order to reduce the complexity of the multirate system feedforward and feedback control will operate at the same sampling frequency. Moreover, as already mentioned the performance sensors do not partake in the control and may use their own sampling rates. These constraints also apply to the sample indices. Hence, for $m_1 \neq m_2, j_1 \neq j_2$ and $l_1 \neq l_2$

$$t^1_{m_1} = t^1_{m_2} = t^1_{j_1} = t^1_{j_2} = t^1_{l_1} = t^1_{l_2}, \quad m_1, m_2 \in \underline{N}_e, \quad j_1, j_2 \in \underline{N}_x, \quad l_1, l_2 \in \underline{N}_y. \tag{7.2.1}$$

The system comprises a *physical plant* $g^{l,m}_{ey,t^1} \in \mathbb{K}^{M_{g^{l,m}_{ey}}}$ linking the l'th secondary source output to the m'th error sensor input, the *estimate* of $g^{l,m}_{ey,t^1}$ (copy weights) at multirate level 1 denoted by $\overset{\copyright}{\hat{g}}{}^{l,m}_{ey,t^1_G} \in \mathbb{K}^{M_{g^{l,m}_{ey}}}$ and the *estimate* of $g^{l,m}_{ey,t^1}$ (copy weights) at multirate level 2 denoted by $\overset{\copyright}{\hat{g}}{}^{l,m}_{ey,t^2_G} \in \mathbb{K}^{M_{g^{l,m}_{ey}}}$, the *physical plant* $g^{l,k}_{py,t^1} \in \mathbb{K}^{M_{g^{l,k}_{ey}}}$ linking the l'th secondary source output to the k'th performance sensor input, the *adaptive tap-weights* $\underset{\circlearrowleft}{w}{}^{m',l}_{t^2_B} \in \mathbb{K}^{M^{m',l}_{\circlearrowleft}}$ at multirate level 2, where adjustability is indicated by an arrow through the box in Figure 7.1, and the *adaptive tap-weights copy* of $\underset{\circlearrowleft}{w}{}^{m',l}_{t^2_B}$ at multirate level 1 represented by $\overset{\copyright}{\underset{\circlearrowleft}{w}}{}^{m',l}_{t^1_B} \in \mathbb{K}^{M^{m',l}_{\circlearrowleft}}$.

The number of adaptive controller units amounts to $N_e \times N_y$. Moreover, we will allow each controller unit to employ an individual adaptive filtering paradigm. The plant subscript $_{ey}$ establishes the link between an error input e in response to a control output signal y. In total $N_e \times N_y$ secondary plant and tap-weight vectors exist. The time indices $t^1_G \in \mathbb{N}, t^2_G \in \mathbb{N}$ are used as a plant estimation counter and therefore also emphasize the possible time-variance of the

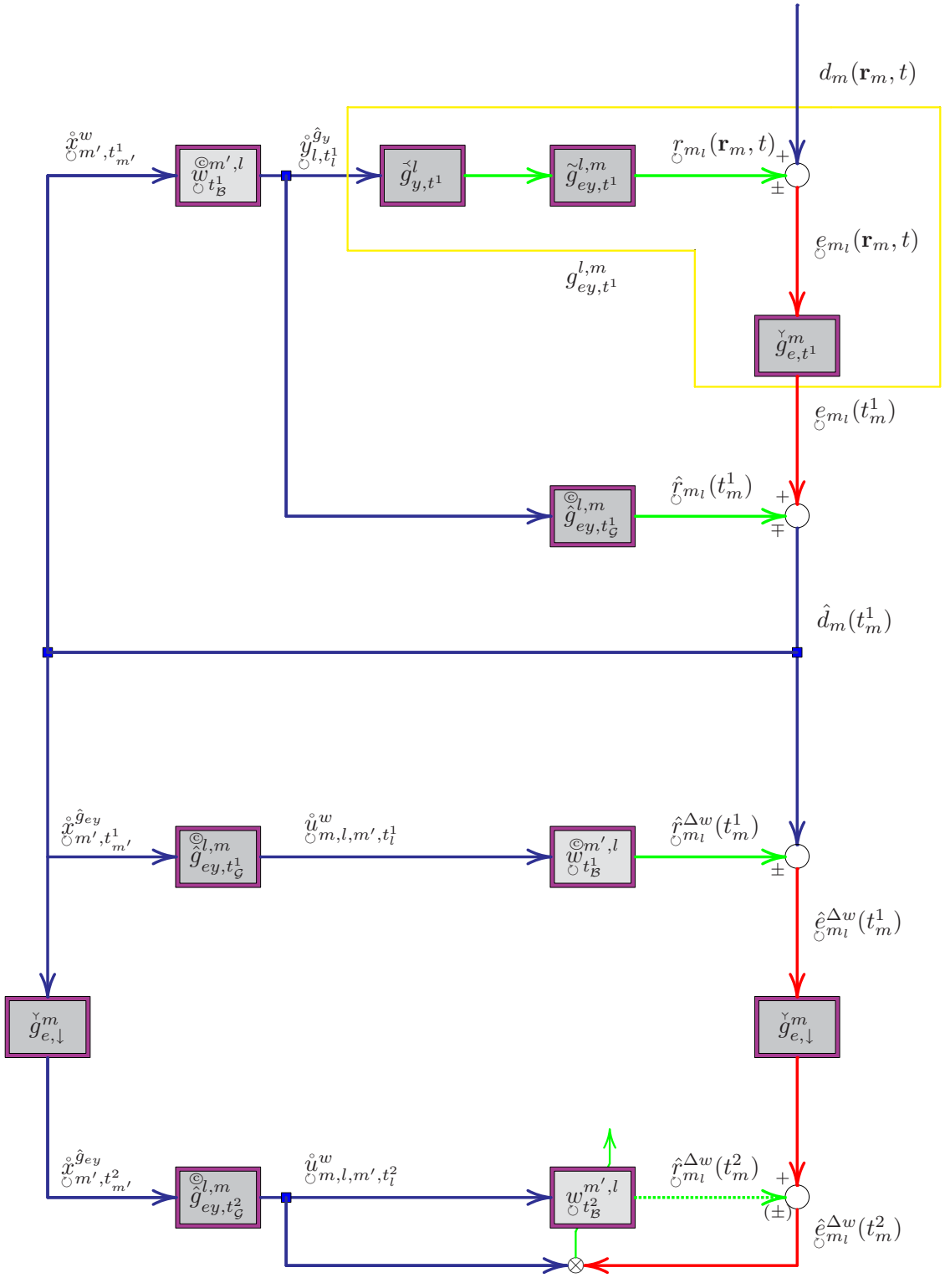

Fig. 7.1: Feedback Multirate Controller using IMC and mFx based Adaptive Filter.

plant. The plant estimation scheme is detailed in section 7.6. The time indices $t_B^1 \in \mathbb{N}, t_B^2 \in \mathbb{N}$ refer to the time of block-update of the adaptive tap-weight.

The physical plant in turn has been divided into a transmission part $\overset{\curvearrowright}{g}{}^l_{y,t^1}$, a propagation part $\widetilde{g}^{l,m}_{ey,t^1}$ and a receive part $\overset{\curvearrowleft}{g}{}^m_{e,t^1}$. The transmission part of the plant $\overset{\curvearrowright}{g}{}^l_{y,t^1}$ links a scalar quantity namely the digital control output signal $y(t_l^1)$ to some actuator depending spatial-distributed continuous-time physical quantity represented here by $y(\mathbf{r}_l, t)$. By $\mathbf{r}_l$ we refer to a position in space of the l'th actuator and t denotes the time. For example for a loudspeaker we could let the volume velocity source distribution over the surface of the membrane in the present context be represented by $y(\mathbf{r}_l, t)$ appreciating the underlying spatially-distributed nature of such signal (refer to Appendix F on page 619). The transmission part of the plant is common to all secondary paths $g^{l,m}_{ey}, \quad m \in \underline{N}_e$ comprises the digital to analogue converter (DAC), interpolation filter (IF), reconstruction filter (RF), amplification stage, and some transducer characteristics.

The propagation part of the plant $\widetilde{g}^{l,m}_{ey,t^1}$ links the aforementioned generally spatially-distributed signal provided by the l'th secondary source to some likewise spatially-distributed continuous-time physical quantity at the m'th error sensor. By $\mathbf{r}_m$ we refer to the position in space of the m'th error sensor. For example if we use a microphone as error sensor we could use the pressure distribution over the membrane as reference. The propagation part will be dependent on the physical environment surrounding the secondary source and the error sensor. In the acoustical field theory the propagation part could mathematically be modeled in terms of *Green functions* [3, Ch. 9] and Appendix F of this report. The receive part $\overset{\curvearrowleft}{g}{}^m_{e,t^1}$ takes us back from the physical domain to a scalar quantity namely the error signal $e(t_m^l)$. The receive part that is common to all secondary paths $g^{l,m}_{ey}, \quad l \in \underline{N}_y$ comprises some transducer characteristic, anti-aliasing filter (AAF), decimation filter (DF), the analogue to digital converter (ADC) and pre-amplification stage. Often the propagation part mainly contributes in terms of delays. We will return to the physical models of the various plants involved in much more details in Part I of this report. Finally, Figure 7.1 depicts the physical plant $g^{l,k}_{py,t^1_G}$ that links the l'th secondary source to the k'th performance monitoring sensor. In total $N_p \times N_y$ such control-performance path combinations exist. This control-performance path in turn is constituted by the transmission part $\overset{\curvearrowright}{g}{}^l_{t^1_G}$, a propagation path $\widetilde{g}^{l,k}_{py,t^1_G}$ and a receive part $\overset{\curvearrowleft}{g}{}^k_{p,t^1}$. The transmission part $\overset{\curvearrowright}{g}{}^l_{t^1_G}$ is therefore also common to all performance pathes $g^{l,k}_{py}, \quad l \in \underline{N}_y$. The receive part is likewise common to all secondary paths $g^{l,k}_{py}, \quad j \in \underline{N}_p$. It should be emphasized that performance sensors by definition are only *monitoring* the performance of the active control system. Hence, there will be **no** *error feedback* (refer to section I.1) from any of the N_p performance sensors to the control system.

The quantities and signals depicted in Figure 7.1 on the previous page will be introduced along the presentation to follow. It is the authors experience that some students experience difficulties in identifying the order of signal flow in active control configuration similar to the one depicted in Figure 7.1 on the preceding page. Hopefully, this should be clarified during the course of this presentation. Firstly, we will use the first multirate level iteration index t^1 to signify when the signal actually is *available*. It should be emphasized that this definition has an impact on the computation of the control output signal $\underset{\circlearrowright}{y}(t_l^1 + 1)$ and rejection signal $\underset{\circlearrowright}{r}_m(t_m^1 + 1)$ defined in subsection 7.2.6 and subsection 7.2.7 respectively. Although both $\underset{\circlearrowright}{y}(t_l^1 + 1)$ and $\underset{\circlearrowright}{r}_m(t_m^1 + 1)$ are determined in the i'th iteration following the adaptive weight update they are first at the *disposition* to the control hardware at the next iteration. Secondly, it should be recalled that due to the sampling function or more precisely time-discretization the first element in any plant impulse response will always be zero i.e. $g(0) = 0$. As a consequence there will be no *instantaneous feedback* . The signals can then relative easily be determined sequently from one

iteration to the next iteration. The active control system will typically be embedded in real-time platform that facilitates interrupt driven I/O control. For simplicity we consider all N_e error signals as well as all N_y control output signals to be driven by the same interrupt. Each iteration cycle then commence following such an interrupt.

7.2.2 Error Signals

The feedback error signal $\underset{\circ}{e}_m(t_m^1)$ is a *sensed* signal cf. section 5.3. Referring to Figure 7.1 we identify viz. (5.3.15)

$$e_m^{\mathcal{D}^1}(t_m^1) \rightarrow \underset{\circ}{e}_m(t_m^1). \tag{7.2.2}$$

The error signal is the result of the *superposition* of the disturbance signal $d_m(t_m^1)$ and the total rejection signal $\underset{\circ}{r}_m(t_m^1)$

$$\underset{\circ}{e}_m(t_m^1) = d_m(t_m^1) \pm \underset{\circ}{r}_m(t_m^1). \tag{7.2.3}$$

The disturbance signal $d_m(t_m^1)$ will be discussed in subsection 7.2.3. The rejection signal $\underset{\circ}{r}_m(t_m^1)$ in turn is a superposition of in total N_y secondary source driven rejection signals $\underset{\circ}{r}_{m_l}(t_m^1)$. The rejection signal is subject for discussion in subsection 7.2.7 and an expression for $\underset{\circ}{r}_m(t_m^1)$ can be found in (7.2.29).

In the active control community no firm sign convention exists for the summation of $d_m(t_m^1)$ and $\underset{\circ}{r}_m(t_m^1)$. For example in [1] a + sign is used while [2] applies the − sign. In order to enforce compatibility with results from both definitions and in order to reuse the mathematical expression and derived software we will apply the ± notation where the upper + signifies superposition of two physical signals, which is arguably more correct in the domain of active control of sound and vibration (ACSV). The lower − sign indicates subtraction, which is the convention most often used when adaptive filters are applied to pure electrical signals. This issue will be further commented in section I.2.

7.2.3 Disturbance Signals

The number of disturbance signals $d_m(t_m^1)$ corresponding to $d_m(\mathbf{r}_m, t)$ equals N_e. It should be remarked that the disturbance signal $d_m(t_m^1)$ is only *directly* measurable when the rejection signals are turned-off[1].

Importantly, is should be recalled that in a feedback system (FBS) employing the internal model control (IMC) the feedback reference signal at multirate level 1 $\underset{\circ}{x}_{m'}(t_{m'}^1) \in \mathbb{K}$ and the *estimated* disturbance coincide, that is,

$$\underset{\circ}{x}_{m'}(t_{m'}^1) \triangleq \hat{d}_m(t_m^1). \tag{7.2.4}$$

[1]The disturbance $d_m(t_m^1)$ is considered a *source signal*. Hence, it is **independent** of the operation of the active control system.

Therefore the number of reference signals equals N_e. The reason for using both unprimed and primed m indices will be explained soon. A disturbance signal estimate at multirate level 1 $\hat{d}_m(t_m^1) \in \mathbb{K}$ can be computed as

$$\hat{d}_m(t_m^1) = \underset{\circ}{e}_m(t_m^1) \mp \hat{\underset{\circ}{r}}_m(t_m^1). \tag{7.2.5}$$

The estimated rejection signal $\hat{\underset{\circ}{r}}_m(t_m^1)$ will be defined in subsection 7.2.7 viz. (7.2.26). Moreover, the $\mp$ signs correspond to the $\pm$ signs in (7.2.3).

In the multirate system introduced in chapter 5 on page 249 the disturbance signal estimate at multirate level 2 $\hat{d}_m(t_m^2) \in \mathbb{K}$ is obtained from

$$\hat{d}_m(t_m^2) \xleftarrow{\mathcal{D}_m^2(F_m^2(\theta), M_{\downarrow,m}^2, L_{\uparrow,m}^2)} \hat{d}_m(t_m^1), \tag{7.2.6}$$

where the downsampling function $\mathcal{D}_m^2(F_m^2(\theta), M_{\downarrow,m}^2, L_{\uparrow,m}^2)$ in turn was introduced in section 5.3 on page 252 and is represented by the receive (down conversion) plant part $\check{g}_{e,\downarrow}^m$ in Figure 7.1.

We appreciate the following identity between the feedback reference signal $\underset{\circ}{x}_{m'}(t_{m'}^2)$ and the decimated disturbance estimate

$$\underset{\circ}{x}_{m'}(t_{m'}^2) \triangleq \hat{d}_m(t_m^2). \tag{7.2.7}$$

7.2.4 Unfiltered and Filtered Reference Signals

For later use in subsection 7.2.6 it is useful to create a *unfiltered* reference signal time-reversed buffer at multirate level 1 $\underset{\circ}{\mathring{x}}^w_{m',t_{m'}^1} \in \mathbb{K}^{\underset{\circ}{M}^{\max}_{w^{m'}}}$ according to

$$\underset{\circ}{\mathring{x}}^w_{m',t_{m'}^1} = \Big[\underset{\circ}{x}_{m'}(t_{m'}^1) \quad \underset{\circ}{x}_{m'}(t_{m'}^1 - 1) \quad \dots \quad \underset{\circ}{x}_{m'}(t_{m'}^1 - \underset{\circ}{M}^{\max}_{w^{m'}} + 1)\Big]. \tag{7.2.8}$$

The superscript ^{w} indicates that the reference signal is used in connection with the copy tap-weights. In the general case each of the controllers might apply a different adaptive filtering paradigm and consequently also use different model order $\underset{\circ}{M}^{m',l}_{w,1}$. The quantity $\underset{\circ}{M}^{\max}_{w^{m'}} \in \mathbb{N}^{N_e}$ represents the maximum filter order used for the adaptive tap-weights $\underset{\circ}{\overset{\copyright}{w}}^{m',l}_{t_B^1}$ and is obtained from[2]

$$\underset{\circ}{M}^{\max}_{w^{m'}} \triangleq \max_{1 \le l \le N_y} \{\underset{\circ}{M}^{m',l}_{w,1}\}. \tag{7.2.9}$$

All filtered reference methods will be based on creating a *filtered-reference signal* at multirate level 2 $\underset{\circ}{u}(t_l^2)$.

Each triplet of elements $\underset{\circ}{u}_{m,l,m'}(t_l^2) \in \mathbb{K}$ *filtered-reference signal* at multirate level 2 where m' refers to the reference sensor and l, m refer to the secondary path is obtained by *filtering*

[2] In the literature the controller algorithms will normally be assumed identical and the same applies to the model order viz. $\underset{\circ}{M}^{\max}_{w^{m'}} \triangleq M$.

the m'th *reference signal* by the secondary path estimate $\overset{\copyright}{\hat{g}}{}^{l,m}_{ey}$. It is necessary here also to use a prime in order to distinguish the reference signal, that as discussed in subsection 7.2.3 stems from the error sensor, from the destination of secondary path that also is at an error sensor. In general, however, the two error sensors differ i.e., $m' \neq m$ (in Figure 7.1 on page 293, however, $m' = m$). Therefore, a total of $N_e^2 \times N_y$ filtered-reference signals exists. However, as $\underset{\circ}{u}_{m,l,m'}(t_l^2) = \underset{\circ}{u}_{m,l,m'}(t_l^2)$ only $\frac{N_e \times N_y \times (N_e+1)}{2}$ will be different. The filtering operation by the plant is modeled by $\hat{\mathcal{G}}_{ey}^{l,m}(y, t_G^2)$

$$\underset{\circ}{u}_{m,l,m'}(t_l^2) \xleftarrow{\hat{\mathcal{G}}_{ey}^{l,m}(x,t_G^2)} \underset{\circ}{x}_{m'}(t_m^2). \tag{7.2.10}$$

If $\mathcal{G}_{ey}^{l,m}(x, t_G^2)$ can be modeled by a *linear* FIR filter then $\underset{\circ}{u}_{m,l,m'}(t_l^2)$ is simply obtained by multiplying an auxiliary *reference signal time-reversed buffer* $\mathring{\underset{\circ}{x}}{}^{\hat{g}_{ey}}_{m',t_{m'}^2} \in \mathbb{K}^{M_{\hat{g}_{ey}}^{\max}}$ defined as

$$\mathring{\underset{\circ}{x}}{}^{\hat{g}_{ey}}_{m',t_{m'}^2} = \begin{bmatrix} \underset{\circ}{x}_{m'}(t_{m'}^2) & \underset{\circ}{x}_{m'}(t_{m'}^2 - 1) & \dots & \underset{\circ}{x}_{m'}(t_{m'}^2 - M_{\hat{g}_{ey}}^{\max} + 1) \end{bmatrix} \tag{7.2.11}$$

and $\overset{\copyright}{\hat{g}}{}^{l,m}_{ey,t_G^2}$, that is,

$$\underset{\circ}{u}_{m,l,m'}(t_l^2) = \mathring{\underset{\circ}{x}}{}^{\hat{g}_{ey}}_{m',t_{m'}^2}(1 : M_{\hat{g}_{ey}}^{l,m,2}) \overset{\copyright}{\hat{g}}{}^{l,m}_{ey,t_G^2}, \tag{7.2.12}$$

where $\mathring{\underset{\circ}{x}}{}^{\hat{g}_{ey}}_{m',t_{m'}^2}(1 : M_{\hat{g}_{ey}}^{l,m,2})$ refers to the first $M_{\hat{g}_{ey}}^{l,m,2}$ elements of $\mathring{\underset{\circ}{x}}{}^{\hat{g}_{ey}}_{m',t_{m'}^2}$. The accent $\mathring{}$ signifies that reference signal possesses shift-structure and possibly lends itself to a computational efficient ring buffer implementation.

The quantity $M_{\hat{g}_{ey}}^{\max} \in \mathbb{N}$ is the maximum filter order used in the secondary path models. Hence,

$$M_{\hat{g}_{ey}}^{\max} \triangleq \max_{\substack{1 \leq m \leq N_e \\ 1 \leq l \leq N_y}} \{ M_{\hat{g}_{ey}}^{l,m,2} \}. \tag{7.2.13}$$

We will also create a collection of $(N_e \times N_y \times N_e)$ time-reversed *filtered* auxiliary reference signals $\mathring{\underset{\circ}{u}}{}^{w}_{m,l,m',t_l^2}$ ($1 \times \underset{\circ}{M}{}_u^{\max}$ row vectors) defined by

$$\mathring{\underset{\circ}{u}}{}^{w}_{m,l,m',t_l^2} = \begin{bmatrix} \underset{\circ}{u}_{m,l,m'}(t_l^2) & \underset{\circ}{u}_{m,l,m'}(t_l^2 - 1) & \dots & \underset{\circ}{u}_{m,l,m'}(t_l^2 - \underset{\circ}{M}{}_u^{\max} + 1) \end{bmatrix}. \tag{7.2.14}$$

For each reference signal m' an amount of $\underset{\circ}{M}{}_u^{\max}$ elements is required. The quantity $\underset{\circ}{M}{}_u^{\max} \in \mathbb{N}$ is the maximum *regressor* length involved in the adaptive tap-weights update for each $m = 1, 2, \dots, N_e$ error sensor and $l = 1, 2, \dots, N_y$ combination. Hence,

$$\underset{\circ}{M}{}_u^{\max} \triangleq \max_{\substack{1 \leq m' \leq N_e \\ 1 \leq l \leq N_y}} \{ \underset{\circ}{M}{}_u^{m',l,2} \}, \tag{7.2.15}$$

where the quantity $\underset{\circ}{M}{}_u^{m',l,2} \in \mathbb{N}$ in turn is the regressor length used for adaptive tap-weights

$\overset{\circ}{w}{}^{m',l}_{t_B^1}$ that is closely link to the corresponding weight length

$$\overset{\circ}{M}{}^{m',l,2}_{u} = \begin{cases} \overset{\circ}{M}{}^{m',l,2}_{w} + 1, & \textsf{FARLS} \\ \overset{\circ}{M}{}^{m',l,2}_{w}, & \text{else.} \end{cases} \tag{7.2.16}$$

7.2.5 Tap-Weight Update Signals

The adaptive tap-weight update will take place at each block-update time. We will use the adaptive tap-weight time index multirate level 1 $t_B^1 \in \mathbb{N}$ and adaptive tap-weight time index multirate level 2 $t_B^2 \in \mathbb{N}$ to represent the time where the adaptive tap-weight update takes place.

The error used for tap-weight adaptation $e(i)$ coincides with $\overset{\circ}{\hat{e}}{}^{\Delta w}_{m}(t_m^2)$, that in turn is obtained from

$$\overset{\circ}{\hat{e}}{}^{\Delta w}_{m}(t_m^2) = \hat{d}_m(t_m^2) \pm \overset{\circ}{\hat{r}}{}^{\Delta w}_{m}(t_m^2), \tag{7.2.17}$$

where $\overset{\circ}{\hat{r}}{}^{\Delta w}_{m}(t_m^2)$ will be defined in subsection 7.2.7 viz. (7.2.31) and the $\pm$ signs correspond to the $\pm$ signs in (7.2.3).

In the remaining part of Part III extensive references will be made to the *reference signal* or *regressor* u_i that is a $1 \times M_u$ row vector. In the domain of *active control* it is the filtered-reference signal $\overset{\circ}{u}{}^{w}_{t_l^2}$ that will be used for tap-weights update, that is,

$$u_i \leftarrow \overset{\circ}{u}{}^{w}_{m,l,m',t_l^2} \quad \text{AC.} \tag{7.2.18}$$

7.2.6 Control Output

In general the adaptive filter output (control output signal) $\overset{\circ}{y}_{l}(t_l^1)$ depicted in Figure 7.1 on page 293 is obtained as a summation of control output signal $\overset{\circ}{y}_{l_m}(t_l^1)$ components in response to the N_e reference signals. Each component $\overset{\circ}{y}_{l_m}(t_l^1)$ in turn is obtained by filtering the reference signal $\overset{\circ}{x}_{m',t^1_{m'}}$ in some possible non-linear and indeed time varying sense, that is,

$$\overset{\circ}{y}_{l_{m'}}(t_l^1 + 1) \xleftarrow{\overset{\circ}{\mathcal{W}}{}^{m',l}(x,t^1_{m'},t^1_l)} \overset{\circ}{x}_{m',t^1_{m'}}. \tag{7.2.19}$$

The adaptive filtering function is described by the function $\overset{\circ}{\mathcal{W}}{}^{m',l}(x, t^1_{m'}, t^1_l)$.

Similarly to the discussion above, if $\overset{\circ}{\mathcal{W}}{}^{m',l}(x, t^1_{m'}, t^1_l)$ is of finite-duration and *linear* we can use $\overset{\circ}{\mathring{x}}{}^{w}_{m',t^1_{m'}}$ defined in (7.2.8). For a FIR filter implementation $\overset{\circ}{y}_{l'_m}(t_l^1 + 1)$ is simply obtained by multiplying $\overset{\circ}{\mathring{x}}{}^{w}_{m',t^1_{m'}}$ defined in (7.2.8) and $\overset{\circ}{\textcircled{w}}{}^{m',l}_{t_B^1}$, that is,

$$\overset{\circ}{y}_{l_m}(t_l^1 + 1) = \overset{\circ}{\mathring{x}}{}^{w}_{m',t^1_{m'}} \overset{\circ}{\textcircled{w}}{}^{m',l}_{t_B^1}. \tag{7.2.20}$$

The total control output signal delivered by the l'th secondary source is under the assumption of linearity obtained by summing the contribution from each of the N_e reference signals

$$\underset{\circ}{y}_l(t_l^1+1)=\sum_{m'=1}^{N_e}\underset{\circ}{\mathring{x}}^{w}_{m',t_{m'}^1}\overset{\copyright}{\underset{\circ}{w}}^{m',l}_{t_B^1}. \tag{7.2.21}$$

For later use we will define a set of N_y auxiliary time-reversed control output signal buffers $\underset{\circ}{\mathring{y}}^{\hat{g}_y}_{l,t_l^1+1}$ ($1\times M^{\max}_{\hat{g}_y^l}$ row vectors) according to

$$\underset{\circ}{\mathring{y}}^{\hat{g}_y}_{l,t_l^1+1}=\Big[\underset{\circ}{y}_l(t_l^1+1)\quad \underset{\circ}{y}_l(t_l^1)\quad \dots\quad \underset{\circ}{y}_l(t_l^1-M^{\max}_{\hat{g}_y^l}+2)\Big], \tag{7.2.22}$$

where the superscript $^{\hat{g}_y}$ indicates that reference signal is used in connection with an estimate of the plant (secondary path). The quantity $M^{\max}_{\hat{g}_y^l}$ will be defined in subsection 7.2.8 viz. (7.2.34).

7.2.7 Rejection Signals

The *rejection signal* component $\underset{\circ}{r}_{m_l}(t_m^1+1)$ depicted in Figure 7.1 on page 293 sensed by the m'th error sensor is a consequence of the control output signal $\underset{\circ}{y}_l$ up to time (t_l^1+1) that subsequently is filtered in some possible non-linear and time varying sense by the plant. As in subsection 7.2.4 the filtering operation by the plant is described by $\mathcal{G}_{ey}^{l,m}(y,t^1)$

$$\underset{\circ}{r}_{m_l}(t_m^1+1)\xleftarrow{\mathcal{G}_{ey}^{l,m}(y,t^1)}\underset{\circ}{y}_l(t_l^1+1). \tag{7.2.23}$$

The rejection signal is also commonly referred to as *cancelation* signal or *anti-noise* signal. Usually perfect knowledge of $\mathcal{G}_{ey}^{l,m}(y,t^1)$ is unavailable and has instead to be estimated from some system identification process. If we by $\hat{\mathcal{G}}_{ey}^{l,m}(y,t_G^1)$ denote the estimate of $\mathcal{G}_{ey}^{l,m}(y,t^1)$ we can obtain an estimate of the anti-noise signal $\underset{\circ}{\hat{r}}_m(t_m^1+1)$ by

$$\underset{\circ}{\hat{r}}_m(t_m^1+1)\xleftarrow{\hat{\mathcal{G}}_{ey}^{l,m}(y,t_G^1)}\underset{\circ}{y}_l(t_l^1+1). \tag{7.2.24}$$

If the digital controller is based on an IMC architecture depicted in Figure 4.3 an estimate of the cancelation signal $\underset{\circ}{\hat{r}}_m(t_m^1+1)$ is required anyway.

If $\mathcal{G}_{ey}^{l,m}(y,t^1)$ is of finite-duration we can use $\underset{\circ}{\mathring{y}}^{\hat{g}_y}_{l,t_l^1+1}$ defined in (7.2.22). It should be recalled that each control output signal $y_l(t_l^1+1)$ is linked to N_e error sensors by the secondary plants. Different plant model order $M^{l,m,1}_{\hat{g}_{ey}}$ might exist, but it suffices to store the first $M^{\max}_{\hat{g}_{ey}^l}\triangleq\max_{1\le m\le N_e}\{M^{l,m,1}_{\hat{g}_{ey}}\}$ control output signal $\underset{\circ}{y}^l$ elements for each $l=1,2,\dots,N_y$ actuator.

Moreover, if $\mathcal{G}_{ey}^{l,m}(y,t^1)$ can be modeled by a *linear* FIR filter then $\underset{\circ}{\hat{r}}_m(t_m^1+1)$ is simply obtained by multiplying the first $M^{l,m,1}_{\hat{g}_{ey}}$ elements of $\underset{\circ}{\mathring{y}}^{\hat{g}_y}_{l,t_l^1+1}$ and $\overset{\copyright}{\hat{g}}_{ey,t_G^1}$, that is,

$$\underset{\circ}{\hat{r}}_{m_l}(t_m^1+1)=\underset{\circ}{\mathring{y}}^{\hat{g}_y}_{l,t_l^1+1}(1:M^{l,m,1}_{\hat{g}_{ey}})\overset{\copyright}{\hat{g}}^{l,m}_{ey,t_G^1}. \tag{7.2.25}$$

An estimate of the total rejection signal present at the m'th error sensor is then obtained as a superposition of the contribution from each of the N_y secondary sources

$$\hat{\underset{\circ}{r}}_m(t_m^1+1)=\sum_{l=1}^{N_y}\overset{\hat{g}_y}{\underset{\circ}{y}}_{l,t_l^1+1}(1:M_{\hat{g}_{ey}}^{l,m,1})\overset{\copyright}{\hat{g}}_{ey,t_G^1}^{l,m}. \tag{7.2.26}$$

Similarly, for evaluation purposes and assuming perfect knowledge of the plant response the "true" cancelation term $\underset{\circ}{r}_m(t_m^1+1)$ output $\underset{\circ}{y}_{l_m}(t_l^1+1)$ by the physical plant $g_{ey,t^1}^{l,m}$ according to

$$\underset{\circ}{r}_{m_l}(t_m^1+1)=\overset{\hat{g}_y}{\underset{\circ}{y}}_{l,t_l^1+1}(1:M_{g_{ey}}^{l,m})g_{ey,t^1}^{l,m}, \tag{7.2.27}$$

where $\overset{\hat{g}_y}{\underset{\circ}{y}}_{l,t_l^1+1}$ was defined in (7.2.22), but the requirement $M_{\hat{g}_{ey}^l}^{\max}$ on $M_{\hat{g}_y^l}^{\max}$ should now be computed as

$$M_{\hat{g}_{ey}^l}^{\max}\triangleq\max\Big\{\max_{1\le m\le N_e}\{M_{\hat{g}_{ey}}^{l,m,2}\},\max_{1\le m\le N_e}\{M_{g_{ey}}^{l,m}\}\Big\},\quad l=1,2,\ldots,N_y. \tag{7.2.28}$$

The total rejection signal present at the m'th error sensor is likewise obtained as a superposition of the contribution from each of the N_y secondary sources

$$\underset{\circ}{r}_m(t_m^1+1)=\sum_{l=1}^{N_y}\overset{\hat{g}_y}{\underset{\circ}{y}}_{l,t_l^1+1}(1:M_{g_{ey}}^{l,m})g_{ey,t^1}^{l,m}. \tag{7.2.29}$$

Finally, we will estimate the artificial rejection signal $\hat{\underset{\circ}{r}}_m^{\Delta w}(t_m^2+1)$ used for the computation of $\hat{\underset{\circ}{e}}_m^{\Delta w}(t_m^2+1)$. If the system is linear then the principle of interchanging the plant and the controller discussed in connection with filtered-x (Fx)-assumption viz. (6.3.1) applies and $\hat{\underset{\circ}{r}}_{m_l}^{\Delta w}(t_m^2+1)$ then is readily obtainable from (7.2.14)

$$\hat{\underset{\circ}{r}}_{m_l}^{\Delta w}(t_m^2+1)=\sum_{m'=1}^{N_e}\overset{w}{\underset{\circ}{u}}_{m,l,m',t_l^2}(1:\underset{\circ}{M}_u^{m',l,2})\underset{\circ}{w}_{t_B^2}^{m',l}. \tag{7.2.30}$$

By inspection of (7.2.11), (7.2.12) and (7.2.14) we observe that elements of $\underset{\circ}{x}_m$ dating back up to $\underset{\circ}{M}_u^{\max}+M_{\hat{g}_{ey}^{l,m,2}}-1$ iterations back in time are used. The total rejection signal $\hat{\underset{\circ}{r}}_m^{\Delta w}(t_m^2+1)$ "received" by the m'th error sensor is under an assumption of linearity obtained by summing the contribution from each of the N_y rejection signals

$$\hat{\underset{\circ}{r}}_m^{\Delta w}(t_m^2+1)=\sum_{l=1}^{N_y}\sum_{m'=1}^{N_e}\overset{w}{\underset{\circ}{u}}_{m,l,m',t_l^2}(1:\underset{\circ}{M}_u^{m',l,2})\underset{\circ}{w}_{t_B^2}^{m',l}. \tag{7.2.31}$$

7.2.8 Performance Signals

By inspection of Figure 7.1 on page 293 we recognize that the resulting performance error at the k'th performance sensor $\underset{\circ}{e}_k^p(t_k^1)$ is obtained as the *superposition* of the disturbance signal $d_k^p(t_k^1)$

and the total rejection signal $\underset{\circ}{r}{}_k^p(t_k^1)$

$$\underset{\circ}{e}{}_k^p(t_k^1) = d_k^p(t_k^1) \pm \underset{\circ}{r}{}_k^p(t_k^1), \tag{7.2.32}$$

where $r_k^p(t_k^1)$ in turn is obtained from an expression equivalent to (7.2.29)

$$\underset{\circ}{r}{}_k^p(t_k^1+1) = \sum_{l=1}^{N_y} \underset{\circ}{\mathring{y}}{}_{l,t_l^1+1}^{\hat{g}_y}(1 : M_{g_{py}}^{l,k}) g_{py,t_G^1}^{l,k}. \tag{7.2.33}$$

Here it suffices to store the first $M_{g_{py}^l}^{\max} \triangleq \max\limits_{1\le k\le N_p}\{M_{g_{py}^{l,k}}\}$ control output signal $\underset{\circ}{y}{}^l$ elements for each $l = 1, 2, \ldots, N_y$ actuator. Now we are in a position to determine $M_{\hat{g}_y^l}^{\max}$ introduced in subsection 7.2.6 viz. (7.2.22) that defines the buffer size of $\underset{\circ}{\mathring{y}}{}_{l,t_l^1+1}^{\hat{g}_y}$

$$M_{\hat{g}_y^l}^{\max} \triangleq \max\left\{M_{\hat{g}_{ey}^l}^{\max}, M_{g_{py}^l}^{\max}\right\}, \quad l = 1, 2, \ldots, N_y, \tag{7.2.34}$$

where the requirement $M_{\hat{g}_{ey}^l}^{\max}$ for the secondary paths was defined in (7.2.28).

7.2.9 Tap-Weight Estimates Copying

When the weights $\underset{\circ}{w}{}_{t_B^2}^{m',l}$ have converged the copy weights $\underset{\circ}{\overset{\copyright}{w}}{}_{t_B^1}^{m',l}$ are updated using the upsampling function $\mathcal{U}_l^2(F_l^2(\theta), M_{\downarrow,l}^2, L_{\uparrow,l}^2)$ defined in section 5.4 on page 257

$$\underset{\circ}{\overset{\copyright}{w}}{}_{t_B^1}^{m',l} \xleftarrow{\mathcal{U}_l^2(F_l^2(\theta), M_{\downarrow,l}^2, L_{\uparrow,l}^2)} \underset{\circ}{w}{}_{t_B^2}^{m',l}. \tag{7.2.35}$$

7.2.10 Feedback Algorithm Summary

The feedback control adaptive filtering algorithm is constituted by first sensing the error signal $\underset{\circ}{e}_m(t_m^1)$ (7.2.2) then estimating the disturbances $\hat{d}_m(t_m^1)$ (7.2.5) and $\hat{d}_m(t_m^2)$ (7.2.6), next creating the unfiltered reference buffers $\underset{\circ}{\mathring{x}}{}_{m',t_{m'}^1}^{w}$ (7.2.8) and $\underset{\circ}{\mathring{x}}{}_{m',t_{m'}^2}^{\hat{g}_{ey}}$ (7.2.11). Thereafter the filtered reference triplet $\underset{\circ}{u}_{m,l,m'}(t_l^2)$ (7.2.12) is determined leading to $\underset{\circ}{\mathring{u}}{}_{m,l,m',t_l^2}^{w}$ (7.2.14). Next $\underset{\circ}{\hat{e}}{}_m^{\Delta w}(t_m^2)$ used for tap-weight adaptation is determined viz. (7.2.17). The tap-weights $\underset{\circ}{w}{}_{t_B^2}^{m',l}$ are subsequently updated (at least at each block-update time) following one of the algorithms detailed in chapter 8 and Appendix J. Then the control output signals $\underset{\circ}{y}_l(t_l^1+1)$ provided by the system at the next iteration are computed (7.2.21) followed by the creation of $\underset{\circ}{\mathring{y}}{}_{l,t_l^1+1}^{\hat{g}_y}$ in (7.2.22). Finally, also in preparation for the next iteration the rejection signals $\underset{\circ}{\hat{r}}_m(t_m^1+1)$ and successively $\underset{\circ}{\hat{r}}{}_m^{\Delta w}(t_m^2+1)$ are determined from (7.2.26) and (7.2.31). At regular intervals the copy weights $\underset{\circ}{\overset{\copyright}{w}}{}_{t_B^1}^{m',l}$ are updated from (7.2.35).

For simulation purpose we also need the error signals $\underset{\circ}{e}_m(t_m^1)$ (7.2.3), rejection signals $\underset{\circ}{r}_m(t_m^1+1)$ and $\underset{\circ}{r}{}_k^p(t_k^1+1)$ determined from (7.2.29) and (7.2.33) respectively. Finally, (7.2.32) provides a performance assessment.

7.2.11 Feedback Algorithm Computational Considerations

In order to assess the computational burden we will next rewrite our expressions. Starting with the expression (7.2.11) involving the reference signal time-reversed buffer used in connection with the plant estimate filtering $\mathring{\underset{\circ}{x}}^{\hat{g}_{ey}}_{m',t^2_{m'}}$, that in turn is constituted from feedback reference signal $\underset{\circ}{x}_{m'}(t^2_{m'})$. The feedback reference signal are obtained from decimation of the disturbance signal estimate cf. (7.2.5), (7.2.6) and (7.2.7). Essential for the determination of $\hat{d}_m(t^1_m)$ and therefore also of $\mathring{\underset{\circ}{u}}^{w}_{m,l,m',t^2_l}$ is the estimate of the rejection signal $\hat{r}_m(t^1_m)$ which will be done below.

From (7.2.26) the expression for $\hat{\underset{\circ}{r}}_m(t^1_m)$ is

$$\hat{\underset{\circ}{r}}_m(t^1_m+1)=\sum_{l=1}^{N_y}\mathring{\underset{\circ}{y}}^{\hat{g}_y}_{l,t^1_l+1}(1:M^{l,m,1}_{\hat{g}_{ey}})\hat{\overset{\copyright}{g}}^{l,m}_{ey,t^1_G}$$

insertion of (7.2.22) gives

$$\hat{\underset{\circ}{r}}_m(t^1_m+1)=\sum_{l=1}^{N_y}\sum_{i_g=1}^{M^{l,m,1}_{\hat{g}_{ey}}}\underset{\circ}{y}_l(t^1_l-i_g+2)\hat{\overset{\copyright}{g}}^{l,m}_{ey,t^1_G}(i_g)$$

using (7.2.21) leads to

$$\hat{\underset{\circ}{r}}_m(t^1_m+1)=\sum_{l=1}^{N_y}\sum_{i_g=1}^{M^{l,m,1}_{\hat{g}_{ey}}}\sum_{m'=1}^{N_e}\mathring{\underset{\circ}{x}}^{w}_{m,t^1_{m'}-i_g+1}\overset{\copyright m',l}{\underset{\circ}{w}}_{t^1_B}\hat{\overset{\copyright}{g}}^{l,m}_{ey,t^1_G}(i_g)$$

finally by insertion of (7.2.8) we obtain

$$\hat{\underset{\circ}{r}}_m(t^1_m+1)=\sum_{l=1}^{N_y}\sum_{i_g=1}^{M^{l,m,1}_{\hat{g}_{ey}}}\sum_{m'=1}^{N_e}\sum_{i_w=1}^{\underset{\circ}{M}^{m',l}}\underset{\circ}{x}_{m'}(t^1_{m'}-i_g-i_w+1)\overset{\copyright m',l}{\underset{\circ}{w}}_{t^1_B}(i_w)\hat{\overset{\copyright}{g}}^{l,m}_{ey,t^1_G}(i_g).\tag{7.2.36}$$

We appreciate from (7.2.36) that in order to obtain an estimate of the rejection signals used by the IMC the amount of multiplications is determined from the upper limits in the quadruple summation, that is, $N_y, M^{l,m,1}_{\hat{g}_{ey}}, N_e$ and $\underset{\circ}{M}^{m',l}$. Hence, if we had used matrix structures instead of cell structures the computational effort would have been proportional to the product $N_y \times M^{\max}_{\hat{g}_{ey}} \times N_e \times \underset{\circ}{M}^{\max}_{w^{m'}}$. Accordingly, if both the number of feedback weights and the number of weights used to represent the secondary paths are uniformly distributed between $0.5\underset{\circ}{M}^{\max}_{w^{m'}}-\underset{\circ}{M}^{\max}_{w^{m'}}$ and $0.5M^{\max}_{\hat{g}_{ey}}-M^{\max}_{\hat{g}_{ey}}$ respectively then the computational savings of the proposed cell structure approach would be approximately 37.5%.

Actually, (7.2.36) also implictly accounts for calculations that lead to the expression (7.2.14) for the filtered-reference signal buffer $\underset{\circ}{\overset{\circ}{u}}{}^{w}_{m,l,m',t_l^2}$ that is used by the mFx scheme.

7.3 Feedforward Controller - Adaptive Filter Topology

7.3.1 Introduction

The FFS - adaptive filtering - interface is depicted in Figure 7.2 on the following page.

By comparison with Figure 7.1 on page 293 we see that the two topologies are very alike. Therefore, we will primarily focus on the differences between the FFS and FBS.

Also for the feedforward controller we have decided to illuminate the *error feedback* (refer to section I.1) interaction between the l'th secondary source and the m'th error sensor and the k'th performance sensor. Moreover, only the j'th reference sensor is included. By $\mathbf{r}_j$ we refer to the position in space of the j'th reference sensor. In total $N_e \times N_y$ such control-performance path and $N_p \times N_y$ controller-performance sensor combinations exist.

As in the FBS case the FFS comprises a physical plant $g^{l,m}_{ey,t^1}$, the two models of the plant (copy weights) $\overset{\copyright}{\hat{g}}{}^{l,m}_{ey,t^1_G}$ and $\overset{\copyright}{\hat{g}}{}^{l,m}_{ey,t^2_G}$ and the physical controller-performance path g^{lk}_{py,t^1_G}. Moreover, the FFS includes the *adaptive tap-weights* $\underset{\sim}{w}{}^{j,l}_{t^2_B} \in \mathbb{K}^{M^{j,l}}_{\sim}$ at multirate level 2, where adjustability is indicated by an arrow through the box in Figure 7.2, and the *adaptive tap-weights copy* of $\underset{\sim}{w}{}^{j,l}_{t^2_B}$ at multirate level 1 represented by $\overset{\copyright}{\underset{\sim}{w}}{}^{j,l}_{t^1_B} \in \mathbb{K}^{M^{j,l}}_{\sim}$. In addition to the FBS the FFS uses in total N_x reference sensors to obtain time-advanced information to the control system. Moreover, the potential feedback of the control output signal to the reference sensors are modeled by the physical plant

physical feedback plant $g^{l,j}_{xy,t^1} \in \mathbb{K}^{M_{g^{l,j}_{xy}}}$ linking the l'th secondary source output to the j'th reference sensor input, the *estimate* of $g^{l,j}_{xy,t^1}$ (copy weights) at multirate level 1 denoted by $\overset{\copyright}{\hat{g}}{}^{l,j}_{xy,t^1_G} \in \mathbb{K}^{M_{\hat{g}^{l,j}_{ey}}}$ The plant subscript $_{xy}$ establishes the link between an reference input x in response to a control output signal y. The number of adaptive controller units amounts to $N_x \times N_y$. Moreover, we will allow each controller unit to employ an individual adaptive filtering paradigm.

The physical feedback plant in turn has also been divided into a transmission part $\overset{\backsim}{g}{}^{l}_{t^1_G}$, a propagation part $\widetilde{g}^{l,j}_{xy,t^1_G}$ and a receive part $\overset{\curlyvee}{g}{}^{j}_{x,t^1}$. The transmission part that is common to all secondary paths $g^{l,m}_{ey}, \quad m \in \underline{N}_e$ but also to all feedback paths $g^{l,j}_{xy}, \quad j \in \underline{N}_x$. The same remarks made to the propagation part $\widetilde{g}^{l,m}_{ey}$ in subsection 7.2.1 applies to the feedback paths $\widetilde{g}^{l,j}_{xy}$. Finally, the receive part $\overset{\curlyvee}{g}{}^{j}$ is common to all feedback pathes $g^{l,j}_{xy}, \quad l \in \underline{N}_y$.

The feedback path is normally undesired as it left alone can lead to performance degradation and more seriously to instability problems. Therefore, a feedback cancelation scheme [4–6] will be employed.

The quantities and signals depicted in Figure 7.2 on the following page will be introduced along the presentation to follow. The same remarks made to the signal flow made in subsection 7.2.1 applies to Figure 7.2.

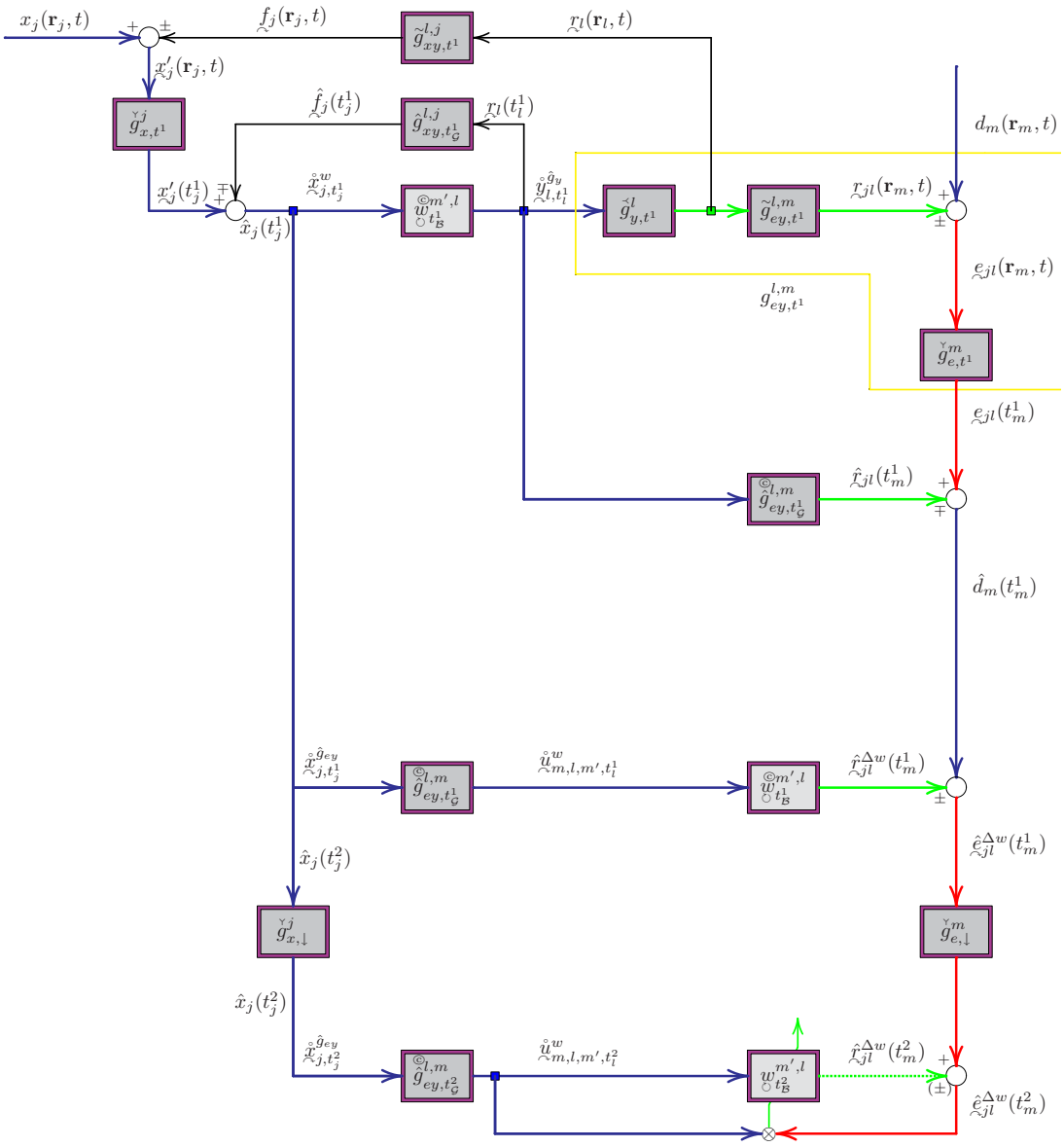

Fig. 7.2: Feedforward Multirate Controller using IMC and mFx based Adaptive Filter.

7.3.2 Error Signals

The error signal $\underset{\sim}{e}_m(t_m^1)$ is a *sensed* signal cf. section 5.3. Referring to Figure 7.2 we identify viz. (5.3.15)

$$e_m^{\mathcal{D}^1}(t_m^1) \rightarrow \underset{\sim}{e}_m(t_m^1). \tag{7.3.1}$$

The error signal is the result of the *superposition* of the disturbance signal $d_m(t_m^1)$ and the total rejection signal $\underset{\sim}{r}_m(t_m^1)$

$$\underset{\sim}{e}_m(t_m^1) = d_m(t_m^1) \pm \underset{\sim}{r}_m(t_m^1). \tag{7.3.2}$$

The disturbance signal $d_m(t_m^1)$ is discussed in subsection 7.3.3. The rejection signal $\underset{\sim}{r}_m(t_m^1)$ in turn is a superposition of in total N_y secondary source driven rejection signals $\underset{\sim}{r}_{m_l}(t_m^1)$. The rejection signal is subject for discussion in subsection 7.3.7 and an expression for $\underset{\sim}{r}_m(t_m^1)$ can be found in (7.3.29). The sign convention is described in subsection 7.2.2.

7.3.3 Disturbance Signals

The disturbance signals are only *directly* measurable when the rejection signals are turned-off. In the FFS the feedforward reference signal are as discussed in subsection 7.3.4 derived from the *sensed* reference signal and should therefore not be internally generated from the *estimated* disturbance as in the feedback topology employing the IMC. A disturbance signal estimate at multirate level 1 $\hat{d}_m(t_m^1) \in \mathbb{K}$, however, is still required for the mFx algorithm and is computed as

$$\hat{d}_m(t_m^1) = \underset{\sim}{e}_m(t_m^1) \mp \underset{\sim}{\hat{r}}_m(t_m^1). \tag{7.3.3}$$

In (7.3.3) the estimated rejection signal $\underset{\sim}{\hat{r}}_m(t_m^1)$ defined in subsection 7.3.7 viz. (7.3.27) was introduced. Moreover, the $\mp$ signs correspond to the $\pm$ signs in (7.3.2).

In the multirate system introduced in chapter 5 on page 249 we also need the downsampled version of the disturbance estimate $\hat{d}_m(t_m^2)$

$$\hat{d}_m(t_m^2) \xleftarrow{\mathcal{D}_m^2(F_m^2(\theta), M_{\downarrow,m}^2, L_{\uparrow,m}^2)} \hat{d}_m(t_m^1), \tag{7.3.4}$$

where the downsampling function $\mathcal{D}_m^2(F_m^2(\theta), M_{\downarrow,m}^2, L_{\uparrow,m}^2)$ in turn was introduced in section 5.3 on page 252.

7.3.4 Unfiltered and Filtered Reference Signals

The number of reference signals $x_j(t_j^1)$ corresponding to $x_j(\mathbf{r}_j, t)$ equals N_x. The reference signal $\underset{\sim}{x}'_j(t_j^1)$ is a *sensed* signal cf. section 5.3. Referring to Figure 7.2 we identify viz. (5.3.15)

$$\underset{\sim}{x}_j^{'\mathcal{D}^1}(t_j^1) \rightarrow \underset{\sim}{x}'_j(t_j^1). \tag{7.3.5}$$

Due to the feedback the actual reference signal *sensed* $\underset{\sim}{x}'_j(t_j^1)$ is a perturbed version of $x_j(t_j^1)$

$$\underset{\sim}{x}'_j(t_j^1) = x_j(t_j^1) \pm \underset{\sim}{f}_j(t_j^1), \tag{7.3.6}$$

where, the $\pm$ signs follows the sign convention in (7.3.2).

An estimate of the undisturbed reference signal is available from

$$\hat{x}_j(t_j^1) = \underset{\sim}{x}'_j(t_j^1) \mp \underset{\sim}{\hat{f}}_j(t_j^1). \tag{7.3.7}$$

The calculation of $\underset{\sim}{\hat{f}}_j(t_j^1)$ is described in subsection 7.3.8 viz. (7.3.35).

Importantly, is should be recalled that in a FFS employing the feedback cancelation scheme the reference signal $\underset{\sim}{x}_j(t_j^1)$ and the *estimated* reference signal coincide, that is,

$$\underset{\sim}{x}_j(t_j^1) \triangleq \hat{x}_j(t_j^1). \tag{7.3.8}$$

Therefore the number of reference signals equals N_x. For the multirate system a downsampled version of the undisturbed reference signal estimate $\hat{x}_j(t_j^2)$ is similarly obtained from

$$\hat{x}_j(t_j^2) \xleftarrow{\mathcal{D}_j^2(F_j^2(\theta), M_{\downarrow,j}^2, L_{\uparrow,j}^2)} \hat{x}_j(t_j^1), \tag{7.3.9}$$

where the downsampling function $\mathcal{D}_j^2(F_j^2(\theta), M_{\downarrow,j}^2, L_{\uparrow,j}^2)$ in turn was introduced in section 5.3 on page 252 and is represented by the receive (down conversion) plant part $\overset{\curlyvee j}{g}_{x,\downarrow}$ in Figure 7.2.

For later use in subsection 7.3.6 it is useful to create a *unfiltered* reference signal time-reversed buffer at multirate level 1 $\underset{\sim}{\overset{\circ}{x}}^w_{j,t_j^1} \in \mathbb{K}^{\underset{\sim}{M}_{w^j}^{\max}}$ according to

$$\underset{\sim}{\overset{\circ}{x}}^w_{j,t_j^1} = \begin{bmatrix} \hat{\underset{\sim}{x}}_j(t_j^1) & \hat{\underset{\sim}{x}}_j(t_j^1 - 1) & \dots & \hat{\underset{\sim}{x}}_j(t_j^1 - \underset{\sim}{M}_{w^j}^{\max} + 1) \end{bmatrix}. \tag{7.3.10}$$

The superscript ^{w} indicates that the reference signal is used in connection with the tap-weights. In the general case each of the controllers might apply a different adaptive filtering paradigm and consequently also use different model order $\underset{\sim}{M}^{j,l}$. The quantity $\underset{\sim}{M}_{w^j}^{\max} \in \mathbb{N}^{N_x}$ represents the maximum filter order used for the adaptive tap-weights $\underset{\sim}{\overset{\copyright}{w}}^{j,l}_{t_B^1}$ and is obtained from[3]

$$\underset{\sim}{M}_{w^j}^{\max} \triangleq \max_{1 \le l \le N_y} \{\underset{\sim}{M}^{j,l}\}. \tag{7.3.11}$$

Equivalent to the FBS a triplet of elements $\underset{\sim}{u}_{l,m,j}(t_l^2)$ constitute the *filtered reference* signal $\underset{\sim}{u}(t_l^2)$. Each element in turn is obtained by *filtering* the j'th *reference signal* by the secondary path estimate $\overset{\copyright}{\hat{g}}^{l,m}_{ey}$. A total of $N_x \times N_y \times N_e$ filtered-reference signals exists. The filtering operation by the plant is described by $\mathcal{G}_{ey}^{l,m}(x, t_G^2)$

$$\underset{\sim}{u}_{l,m,j}(t_l^2) \xleftarrow{\hat{\mathcal{G}}_{ey}^{l,m}(x,t_G^2)} \underset{\sim}{x}_j(t_j^2). \tag{7.3.12}$$

[3] In the literature the controller algorithms will normally be assumed identical and the same applies to the model order viz. $\underset{\sim}{M}_{w^j}^{\max} \triangleq M$.

If $\mathcal{G}_{ey}^{l,m}(x,t_G^2)$ can be modeled by a *linear* FIR filter then $\underset{\sim}{u}_{l,m,j}(t_l^2)$ is simply obtained by multiplying an auxiliary *unfiltered* reference signal ($1\times M_{\hat{g}_{ey}}^{\max}$ row vector) $\mathring{\underset{\sim}{x}}_{j,t_j^2}^{\hat{g}_{ey}}$ defined as

$$\mathring{\underset{\sim}{x}}_{j,t_j^2}^{\hat{g}_{ey}} = \Big[\underset{\sim}{x}_j(t_j^2) \quad \underset{\sim}{x}_j(t_j^2-1) \quad \dots \quad \underset{\sim}{x}_j(t_j^2-M_{\hat{g}_{ey}}^{\max}+1)\Big] \tag{7.3.13}$$

and $\hat{g}_{ey,t_G^2}^{l,m}$, that is,

$$\underset{\sim}{u}_{l,m,j}(t_l^2) = \mathring{\underset{\sim}{x}}_{j,t_j^2}^{\hat{g}_{ey}}(1:M_{\hat{g}_{ey}}^{l,m,2})\overset{\circledcirc}{\hat{g}}_{ey,t_G^2}^{l,m}, \tag{7.3.14}$$

where $\mathring{\underset{\sim}{x}}_{j,t_j^2}^{\hat{g}_{ey}}(1:M_{\hat{g}_{ey}}^{l,m,2})$ refers to the first $M_{\hat{g}_{ey}}^{l,m,2}$ elements of $\mathring{\underset{\sim}{x}}_{j,t_j^2}^{\hat{g}_{ey}}$.

The quantity $M_{\hat{g}_{ey}}^{\max}$ defined in subsection 7.2.4 is the maximum filter order used in the secondary path models .

We will also create a collection of $(N_x\times N_y\times N_e)$ time-reversed *filtered* auxiliary reference signals $\mathring{\underset{\sim}{u}}_{l,m,j,t_l^2}^{w}$ ($1\times \underset{\sim}{M}_u^{\max}$ row vectors) defined by

$$\mathring{\underset{\sim}{u}}_{l,m,j,t_l^2}^{w} = \big[\underset{\sim}{u}_{l,m,j}(t_l^2) \quad \underset{\sim}{u}_{l,m,j}(t_l^2-1) \quad \dots \quad \underset{\sim}{u}_{l,m,j}(t_l^2-\underset{\sim}{M}_u^{\max}+1)\big]. \tag{7.3.15}$$

For each reference signal j an amount of $\underset{\sim}{M}_u^{\max}$ elements is required. The quantity $\underset{\sim}{M}_u^{\max}\in\mathbb{N}$ is the maximum *regressor* length involved in the adaptive tap-weights representation $\underset{\sim}{w}_{t_B^2}^{j,l}$. update for each $j=1,2,\dots,N_x$ reference sensor and $l=1,2,\dots,N_y$ combination. Hence,

$$\underset{\sim}{M}_u^{\max} \triangleq \max_{\substack{1\le j\le N_x\\ 1\le l\le N_y}}\{\underset{\sim}{M}_u^{j,l}\}, \tag{7.3.16}$$

where the quantity $\underset{\sim}{M}_u^{j,l}\in\mathbb{N}$ is the regressor length used for the update of the adaptive tap-weights $\underset{\sim}{w}_{t_B^1}^{j,l}$ in turn is the *regressor* length used for the update of the adaptive tap-weights $\underset{\sim}{w}_{t_B^1}^{j,l}$ that is closely link to the corresponding weight length

$$\underset{\sim}{M}_u^{j,l,2} = \begin{cases} \underset{\sim}{M}_w^{j,l,2}+1, & \textsf{FARLS}\\ \underset{\sim}{M}_w^{j,l,2}, & \text{else.}\end{cases} \tag{7.3.17}$$

7.3.5 Tap-Weight Update Signals

The error $\hat{\underset{\sim}{e}}_m^{\Delta w}(t_m^2)$ used for tap-weight adaptation is obtained from

$$\hat{\underset{\sim}{e}}_m^{\Delta w}(t_m^2) = \hat{d}_m(t_m^2) \pm \hat{\underset{\sim}{r}}_m^{\Delta w}(t_m^2), \tag{7.3.18}$$

where $\hat{\underset{\sim}{r}}_m^{\Delta w}(t_m^2)$ will be defined in subsection 7.3.7 viz. (7.3.31) and the $\pm$ signs correspond to the $\pm$ signs in (7.3.2).

In the remaining part of Part III extensive references will be made to the *reference signal* or *regressor* u_i that is a $1 \times M_u$ row vector. As discussed in subsection 7.2.5 in the domain of *active control* it is the filtered-reference signal $\underset{\sim}{\mathring{u}}_i^w$ that will be used for tap-weights update, that is,

$$u_i \leftarrow \underset{\sim}{\mathring{u}}_{l,m,j,t_l^2}^w \quad \text{AC.} \tag{7.3.19}$$

7.3.6 Control Output

In general the adaptive filter output (control output signal) $\underset{\sim}{y}_l(t_l^1)$ depicted in Figure 7.2 on page 304 is obtained as a summation of control output signal $\underset{\sim}{y}_{l_j}(t_l^1)$ components in response to the N_x reference signals. Each component $\underset{\sim}{y}_{l_j}(t_l^1)$ in turn is obtained by filtering the reference signal $\underset{\sim}{x}_{j,i}$ in some possible non-linear and indeed time varying sense, that is,

$$\underset{\sim}{y}_{l_j}(t_l^1 + 1) \xleftarrow{\underset{\sim}{\mathcal{W}}^{j,l}(x,t_j^1,t_l^1)} \underset{\sim}{x}_{j,i}. \tag{7.3.20}$$

The adaptive filtering function is described by the function $\underset{\sim}{\mathcal{W}}^{j,l}(x, t_j^1, t_l^1)$.

Similarly to the discussion above, if $\underset{\sim}{\mathcal{W}}^{j,l}(x, i)$ is of finite-duration and *linear* we can apply a FIR filter implementation and $\underset{\sim}{y}_{l_j}(t_l^1 + 1)$ is simply obtained by multiplying $\underset{\sim}{\mathring{x}}_{j,t_j^1}^w$ defined in (7.3.10) and $\underset{\sim}{\overset{\copyright}{w}}_{t_B^1}^{j,l}$, that is,

$$\underset{\sim}{y}_{l_j}(t_l^1 + 1) = \underset{\sim}{\mathring{x}}_{j,t_j^1}^w \underset{\sim}{\overset{\copyright}{w}}_{t_B^1}^{j,l}. \tag{7.3.21}$$

The total control output signal delivered by the l'th secondary source is under the assumption of linearity obtained by summing the contribution from each of the N_x reference signals

$$\underset{\sim}{y}_l(t_l^1 + 1) = \sum_{j=1}^{N_x} \underset{\sim}{\mathring{x}}_{j,t_j^1}^w \underset{\sim}{\overset{\copyright}{w}}_{t_B^1}^{j,l}. \tag{7.3.22}$$

For later use we will define a set of N_y auxiliary time-reversed control output signal buffers $\underset{\sim}{\mathring{y}}_{l,t_l^1+1}^{\hat{g}_y}$ ($1 \times M_{\hat{g}_y^l}^{\max}$ row vectors) according to

$$\underset{\sim}{\mathring{y}}_{l,t_l^1+1}^{\hat{g}_y} = \Big[\underset{\sim}{y}_l(t_l^1 + 1) \quad \underset{\sim}{y}_l(t_l^1) \quad \dots \quad \underset{\sim}{y}_l(t_l^1 - M_{\hat{g}_y^l}^{\max} + 2)\Big]. \tag{7.3.23}$$

The quantity $M_{\hat{g}_y^l}^{\max}$ will be defined in subsection 7.3.9 viz. (7.3.41).

7.3.7 Rejection Signals

The *rejection signal* component $\underset{\sim}{r}_{m_l}(t_m^1 + 1)$ depicted in Figure 7.2 on page 304 sensed by the m'th error sensor is a consequence of the control output signal $\underset{\sim}{y}_l$ up to time $(t_l^1 + 1)$ that

subsequently is filtered in some possible non-linear and time varying sense by the plant. As in subsection 7.3.4 the filtering operation by the plant is described by $\mathcal{G}_{ey}^{l,m}(y,t^1)$

$$\underset{\sim}{r}_{m_l}(t_m^1+1) \xleftarrow{\mathcal{G}_{ey}^{l,m}(y,t^1)} \underset{\sim}{y}_l(t_l^1+1). \tag{7.3.24}$$

Using the same arguments as in subsection (7.2.7) for the FBS we will obtain an estimate of the anti-noise signal $\underset{\sim}{\hat{r}}_m(t_m^1+1)$ by

$$\underset{\sim}{\hat{r}}_m(t_m^1+1) \xleftarrow{\hat{\mathcal{G}}_{ey}^{l,m}(y,t_G^1)} \underset{\sim}{y}_l(t_l^1+1). \tag{7.3.25}$$

If the digital controller is based on an IMC architecture depicted in Figure 4.3 an estimate of the cancelation signal $\underset{\sim}{\hat{r}}_m(t_m^1+1)$ is required anyway.

If $\mathcal{G}_{ey}^{l,m}(y,t^1)$ is of finite-duration we can use $\underset{\sim}{\overset{\circ}{y}}_{l,t_l^1+1}^{\hat{g}_y}$ defined in (7.3.23). Moreover, if $\mathcal{G}_{ey}^{l,m}(y,t^1)$ can be modeled by a *linear* FIR filter then $\underset{\sim}{\hat{r}}_m(t_m^1+1)$ is simply obtained by multiplying the first $M_{\hat{g}_{ey}}^{l,m,1}$ elements of $\underset{\sim}{\overset{\circ}{y}}_{l,t_l^1+1}^{\hat{g}_y}$ and $\overset{\copyright}{\hat{g}}_{ey,t_G^1}^{l,m}$, that is,

$$\underset{\sim}{\hat{r}}_{m_l}(t_m^1+1) = \underset{\sim}{\overset{\circ}{y}}_{l,t_l^1+1}^{\hat{g}_y}(1:M_{\hat{g}_{ey}}^{l,m,1})\overset{\copyright}{\hat{g}}_{ey,t_G^1}^{l,m}. \tag{7.3.26}$$

An estimate of the total rejection signal present at the m'th error sensor is then obtained as a superposition of the contribution from each of the N_y secondary sources

$$\underset{\sim}{\hat{r}}_m(t_m^1+1) = \sum_{l=1}^{N_y} \underset{\sim}{\overset{\circ}{y}}_{l,t_l^1+1}^{\hat{g}_y}(1:M_{\hat{g}_{ey}}^{l,m,1})\overset{\copyright}{\hat{g}}_{ey,t_G^1}^{l,m}. \tag{7.3.27}$$

Similarly, for evaluation purposes and assuming perfect knowledge of the plant response the "true" cancelation term $\underset{\sim}{r}_m(t_m^1+1)$ is obtained by filtering the control output signal $\underset{\sim}{y}_{l_j}(t_l^1+1)$ by the physical plant $g_{ey,t^1}^{l,m}$ according to

$$\underset{\sim}{r}_{m_l}(t_m^1+1) = \underset{\sim}{\overset{\circ}{y}}_{l,t_l^1+1}^{\hat{g}_y}(1:M_{g_{ey}}^{l,m})g_{ey,t^1}^{l,m}, \tag{7.3.28}$$

where $\underset{\sim}{\overset{\circ}{y}}_{l,t_l^1+1}^{\hat{g}_y}$ was defined in (7.3.23) but the requirement $M_{\hat{g}_{ey}^l}^{\max}$ on $M_{\hat{g}_y^l}^{\max}$ should be computed from (7.2.28).

The total rejection signal present at the m'th error sensor is likewise obtained as a superposition of the contribution from each of the N_y secondary sources

$$\underset{\sim}{r}_m(t_m^1+1) = \sum_{l=1}^{N_y} \underset{\sim}{\overset{\circ}{y}}_{l,t_l^1+1}^{\hat{g}_y}(1:M_{g_{ey}}^{l,m})g_{ey,t^1}^{l,m}. \tag{7.3.29}$$

Finally, we will estimate the artificial rejection signal $\underset{\sim}{\hat{r}}_m^{\Delta w}(t_m^2+1)$ used for the computation of $\underset{\sim}{\hat{e}}_m^{\Delta w}(t_m^2+1)$. If the system is linear then the principle of interchanging the plant and the

controller discussed in connection with Fx-assumption viz. (6.3.1) applies and $\hat{\underset{\sim}{r}}^{\Delta w}_{m_l}(t^2_m+1)$ then is readily obtainable from (7.3.15)

$$\hat{\underset{\sim}{r}}^{\Delta w}_{m_l}(t^2_m+1)=\sum_{j=1}^{N_x}\mathring{\underset{\sim}{u}}^{w}_{l,m,j,t^2_l}(1:\underset{\sim}{M}^{j,l,2}_{u})\underset{\sim}{w}^{j,l}_{t^2_B}. \tag{7.3.30}$$

By inspection of (7.3.13), (7.3.14) and (7.3.15) we observe that elements of $\underset{\sim}{x}_m$ dating back up to $\underset{\sim}{M}^{\max}_{u}+M_{\hat{g}^{l,m,2}_{ey}}-1$ iterations back in time are used. The total rejection signal $\hat{\underset{\sim}{r}}^{\Delta w}_{m}(t^2_m+1)$ "received" by the m'th error sensor is under an assumption of linearity obtained by summing the contribution from each of the N_y rejection signals

$$\hat{\underset{\sim}{r}}^{\Delta w}_{m}(t^2_m+1)=\sum_{l=1}^{N_y}\sum_{j=1}^{N_x}\mathring{\underset{\sim}{u}}^{w}_{l,m,j,t^2_l}(1:\underset{\sim}{M}^{j,l,2}_{u})\underset{\sim}{w}^{j,l}_{t^2_B}. \tag{7.3.31}$$

7.3.8 Feedback Signals

The *feedback signal* component $\underset{\sim}{f}_{jl}(t^1_j+1)$ depicted in Figure 7.2 on page 304 sensed by the j'th sensor is a consequence of the control output signal $\underset{\sim}{y}_l$ up to time (t^1_l+1) that subsequently is filtered in some possible non-linear and time varying sense by the feedback plant. By analogy with subsection 7.3.4 the filtering operation by the feedback plant is described by $\mathcal{G}^{l,j}_{xy}(y,t^1_G)$.

$$\underset{\sim}{f}_{jl}(t^1_j+1)\xleftarrow{\mathcal{G}^{l,j}_{xy}(y,t^1_G)}\underset{\sim}{y}_l(t^1_l+1). \tag{7.3.32}$$

Usually perfect knowledge of $\mathcal{G}^{l,j}_{xy}(y,t^1_G)$ is unavailable and has to be estimated from some system identification process. If we by $\hat{\mathcal{G}}^{l,j}_{xy}(y,t^1_G)$ denote the estimate of $\mathcal{G}^{l,j}_{xy}(y,t^1_G)$ we can obtain an estimate of the feedback signal $\hat{\underset{\sim}{f}}_j(t^1_j+1)$ by

$$\hat{\underset{\sim}{f}}_j(t^1_j+1)\xleftarrow{\hat{\mathcal{G}}^{l,j}_{xy}(y,t^1_G)}\underset{\sim}{y}_l(t^1_l+1). \tag{7.3.33}$$

If $\mathcal{G}^{l,j}_{xy}(y,t^1_G)$ is of finite-duration we can use $\mathring{\underset{\sim}{y}}^{\hat{g}_y}_{t_l+1}$ defined in (7.3.23). It should be recalled that each control output signal $y_l(t^1_l+1)$ is linked to N_x reference sensors by the feedback plants. Different plant model order $M^{l,j}_{\hat{g}_{xy}}$ might exist, but it suffices to store the first $M^{\max}_{\hat{g}^l_{xy}}\triangleq\max_{1\le j\le N_x}\{M^{l,j}_{\hat{g}_{xy}}\}$ control output signal $\underset{\sim}{y}^l$ elements for each $l=1,2,\ldots,N_y$ actuator.

Moreover, if $\mathcal{G}^{l,j}_{xy}(y,t^1_G)$ can be modeled by a *linear* FIR filter then $\hat{\underset{\sim}{f}}_j(t^1_j+1)$ is simply obtained by multiplying the first $M^{l,j}_{\hat{g}_{xy}}$ elements of $\mathring{\underset{\sim}{y}}^{\hat{g}^{l,j}_{xy}}_{l,t^1_l+1}$ and $\overset{\copyright}{\hat{g}}^{l,j}_{xy,t^1_G}$, that is,

$$\hat{\underset{\sim}{f}}_{jl}(t^1_j+1)=\mathring{\underset{\sim}{y}}^{\hat{g}_y}_{l,t^1_l+1}(1:M^{l,j}_{\hat{g}_{xy}})\overset{\copyright}{\hat{g}}^{l,j}_{xy,t^1_G}. \tag{7.3.34}$$

An estimate of the total feedback signal present at the j'th reference sensor is then obtained as

a superposition of the contribution from each of the N_y secondary sources

$$\underset{\sim}{\hat{f}}_j(t_j^1+1) = \sum_{l=1}^{N_y} \underset{\sim}{\overset{\circ}{y}}{}^{\hat{g}_y}_{l,t_l^1+1}(1:M_{\hat{g}_{xy}}^{l,j})\overset{\copyright}{\hat{g}}{}^{l,j}_{xy,t_G^1}. \tag{7.3.35}$$

Similarly, for evaluation purposes and assuming perfect knowledge of the plant response the "true" feedback term $\underset{\sim}{f}_{jl}(t_j^1+1)$ is obtained by filtering the control output $\underset{\sim}{y}_{l_j}(t_l^1+1)$ by the physical plant $g^{l,j}_{xy,t_G^1}$ according to

$$\underset{\sim}{f}_{jl}(t_j^1+1) = \underset{\sim}{\overset{\circ}{y}}{}^{\hat{g}_y}_{l,t_l^1+1}(1:M_{g_{xy}}^{l,j})g^{l,j}_{xy,t_G^1}, \tag{7.3.36}$$

where $\underset{\sim}{\overset{\circ}{y}}{}^{\hat{g}_y}_{l,t_l^1+1}$ was defined in (7.3.23) but the requirement $M_{\hat{g}_{xy}^l}^{\max}$ on $M_{\hat{g}_y^l}^{\max}$ should be computed as

$$M_{\hat{g}_{xy}^l}^{\max} \triangleq \max\left\{\max_{1\le j\le N_x}\{M_{\hat{g}_{xy}}^{l,j}\}, \max_{1\le j\le N_x}\{M_{g_{xy}}^{l,j}\}\right\}, \quad l=1,2,\ldots,N_y. \tag{7.3.37}$$

The total feedback signal $\underset{\sim}{f}_j(t_j^1+1)$ present at the j'th reference sensor is likewise obtained as a superposition of the contribution from each of the N_y secondary sources

$$\underset{\sim}{f}_j(t_j^1+1) = \sum_{l=1}^{N_y} \underset{\sim}{\overset{\circ}{y}}{}^{\hat{g}_y}_{l,t_l^1+1}(1:M_{g_{xy}}^{l,j})g^{l,j}_{xy,t_G^1}. \tag{7.3.38}$$

7.3.9 Performance Signals

By inspection of Figure 7.2 on page 304 we recognize that the resulting performance error at the k'th performance sensor $\underset{\sim}{e}_k^p(t_k^1)$ is obtained as the *superposition* of the disturbance signal $d_k^p(t_k^1)$ and the total rejection signal $\underset{\sim}{r}_k^p(t_k^1)$

$$\underset{\sim}{e}_k^p(t_k^1) = d_k^p(t_k^1) \pm \underset{\sim}{r}_k^p(t_k^1), \tag{7.3.39}$$

where $\underset{\sim}{r}_k^p(t_k^1)$ in turn is obtained from an expression equivalent to (7.3.29)

$$\underset{\sim}{r}_k^p(t_k^1+1) = \sum_{l=1}^{N_y} \underset{\sim}{\overset{\circ}{y}}{}^{\hat{g}_y}_{l,t_l^1+1}(1:M_{g_{py}}^{l,k})g^{l,k}_{py,t_G^1}. \tag{7.3.40}$$

Now we are in a position to determine $M_{\hat{g}_y^l}^{\max}$ introduced in subsection 7.3.6 viz. (7.3.23) that defines the buffer size of $\underset{\sim}{\overset{\circ}{y}}{}^{\hat{g}_y}_{l,t_l^1+1}$

$$M_{\hat{g}_y^l}^{\max} \triangleq \max\left\{M_{\hat{g}_{ey}^l}^{\max}, M_{\hat{g}_{xy}^l}^{\max}, \max_{1\le k\le N_p}\{M_{g_{py}}^{l,k}\}\right\}, \quad l=1,2,\ldots,N_y, \tag{7.3.41}$$

where the requirement $M_{\hat{g}_{ey}^l}^{\max}$ and $M_{\hat{g}_{xy}^l}^{\max}$ pertinent to the secondary paths and feedback paths were defined in (7.2.28) and (7.3.37) respectively.

7.3.10 Tap-Weight Estimates Copying

When the weights have converged the copy weights $\underset{\sim}{\overset{\copyright j,l}{w}}_{t_B^1}$ are updated with the new values using the upsampling function $\mathcal{U}_l^2(F_l^2(\theta), M_{\downarrow,l}^2, L_{\uparrow,l}^2)$ described in section 5.4 on page 257

$$\underset{\sim}{\overset{\copyright j,l}{w}}_{t_B^1} \xleftarrow{\mathcal{U}_l^2(F_l^2(\theta),M_{\downarrow,l}^2,L_{\uparrow,l}^2)} \underset{\sim}{w}_{t_B^2}^{j,l}. \tag{7.3.42}$$

7.3.11 Feedforward Algorithm Summary

The feedforward control adaptive filtering algorithm is constituted by first sensing the error signal $\underset{\sim}{e}_m(t_m^1)$ (7.3.1) then estimating the disturbances $\hat{d}_m(t_m^1)$ (7.3.3) and $\hat{d}_m(t_m^2)$ (7.3.4) and estimating the reference signals $\hat{x}_j(t_j^1)$ (7.3.7) and downsampled $\hat{x}_j(t_j^2)$ (7.3.9); next creating the unfiltered reference buffers $\underset{\sim}{\mathring{x}}_{j,t_j^1}^{w}$ (7.3.10) and $\underset{\sim}{\mathring{x}}_{j,t_j^2}^{\hat{g}_{ey}}$ (7.3.13). Thereafter the filtered reference triplet $\underset{\sim}{u}_{l,m,j}(t_l^2)$ (7.3.14) is determined leading to $\underset{\sim}{\mathring{u}}_{l,m,j,t_l^2}^{w}$ (7.3.15). Next $\underset{\sim}{\hat{e}}_m^{\Delta w}(t_m^2)$ used for tap-weight adaptation is determined viz. (7.3.18). The tap-weights $\underset{\sim}{w}_{t_B^2}^{j,l}$ are subsequently updated (at least at each block-update time) following one of the algorithms detailed in chapter 8 and Appendix J. Then the control output signals $\underset{\sim}{y}_l(t_l^1+1)$ provided by the system at the next iteration are computed (7.3.22) followed by the creation of $\underset{\sim}{\mathring{y}}_{l,t_l^1+1}^{\hat{g}_y}$ in (7.3.23). Moreover, the rejection signals $\underset{\sim}{\hat{r}}_m(t_m^1+1)$ and successively $\underset{\sim}{\hat{r}}_m^{\Delta w}(t_m^2+1)$ are determined from (7.3.27) and (7.3.31). Finally, also in preparation for the next iteration the feedback signals $\underset{\sim}{\hat{f}}_j(t_j^1+1)$ are computed from (7.3.35). At regular intervals the copy weights $\underset{\sim}{\overset{\copyright j,l}{w}}_{t_B^1}$ are updated from (7.3.42).

For simulation purpose we also need the error signals $\underset{\sim}{e}_m(t_m^1)$ (7.3.2), the reference signal $\underset{\sim}{x}'_j(t_j^1)$ (7.3.6), rejection signals $\underset{\sim}{r}_m(t_m^1+1)$ determined from (7.3.29), feedback signals $\underset{\sim}{f}_{j_l}(t_j^1+1)$ (7.3.38).

7.3.12 FeedForward Algorithm Computational Considerations

Following the same procedure as subsection 7.2.11 we will here use (7.3.27) to reexpress $\hat{\underset{\sim}{r}}_m(t_m^1)$

$$\hat{\underset{\sim}{r}}_m(t_m^1+1)=\sum_{l=1}^{N_y}\mathring{\underset{\sim}{y}}^{\hat{g}_y}_{l,t_l^1+1}(1:M_{\hat{g}_{ey}}^{l,m,1})\overset{\copyright}{\hat{g}}{}^{l,m}_{ey,t_G^1}$$

insertion of (7.3.23) gives

$$\hat{\underset{\sim}{r}}_m(t_m^1+1)=\sum_{l=1}^{N_y}\sum_{i_g=1}^{M_{\hat{g}_{ey}}^{l,m,1}}\underset{\sim}{y}_l(t_l^1-i_g+2)\overset{\copyright}{\hat{g}}{}^{l,m}_{ey,t_G^1}(i_g)$$

using (7.3.22) leads to

$$\hat{\underset{\sim}{r}}_m(t_m^1+1)=\sum_{l=1}^{N_y}\sum_{i_g=1}^{M_{\hat{g}_{ey}}^{l,m,1}}\sum_{j=1}^{N_x}\mathring{\underset{\sim}{x}}^{w}_{m,t_j^1-i_g+1}\overset{\copyright}{\underset{\sim}{w}}{}^{j,l}_{t_B^1}\overset{\copyright}{\hat{g}}{}^{l,m}_{ey,t_G^1}(i_g)$$

finally by insertion of (7.3.10) we obtain

$$\hat{\underset{\sim}{r}}_m(t_m^1+1)=\sum_{l=1}^{N_y}\sum_{i_g=1}^{M_{\hat{g}_{ey}}^{l,m,1}}\sum_{j=1}^{N_x}\sum_{i_w=1}^{\underset{\sim}{M}^{j,l}}\underset{\sim}{x}_j(t_j^1-i_g-i_w+1)\overset{\copyright}{\underset{\sim}{w}}{}^{j,l}_{t_B^1}(i_w)\overset{\copyright}{\hat{g}}{}^{l,m}_{ey,t_G^1}(i_g).\tag{7.3.43}$$

We appreciate from (7.3.43) that in order to obtain an estimate of the rejection signals used by the IMC the amount of multiplications is determined from the upper limits in the quadruple summation, that is, $N_y, M_{\hat{g}_{ey}}^{l,m,1}, N_x$ and $\underset{\sim}{M}^{j,l}$. Hence, if we had used matrix structures instead of cell structures the computational effort would have been proportional to the product $N_y\times M_{\hat{g}_{ey}}^{\max}\times N_x\times \underset{\sim}{M}_{w^j}^{\max}$. Accordingly, if both the number of feedback weights and the number of weights used to represent the secondary paths are uniformly distributed between $0.5\underset{\sim}{M}_{w^j}^{\max}-\underset{\sim}{M}_{w^j}^{\max}$ and $0.5M_{\hat{g}_{ey}}^{\max}-M_{\hat{g}_{ey}}^{\max}$ respectively then the computational savings of the proposed cell structure approach would be approximately 37.5%.

Actually, (7.3.43) also implictly accounts for calculations that lead to the expression (7.3.15) for the filtered-reference signal buffer $\mathring{\underset{\sim}{u}}^{w}_{m,l,j,t_l^2}$ that is used by the mFx scheme. Moreover, for the FFS the same degree of computational savings in the determination of the feedback signals are obtained.

7.4 Feedforward Feedback Controller - Adaptive Filter Topology

7.4.1 Introduction

The FFFBS - adaptive filtering - interface is depicted in Figure 7.3 on the next page.

By comparison with Figure 7.1 on page 293 and Figure 7.2 on page 304 it is observed that the FFFBS is basically obtained by combining the FBS and FFS topologies. As mentioned in the introduction in section 7.1 an underaccent$_{\oplus}$ will be enforced to signify that both the FBS and the FFS contribute to the pertinent signals.

Also for the feedforward-feedback controller we illuminate the interaction between the l'th secondary source, the j'th feedforward reference sensor and the m'th error sensor. In total $N_x \times N_y$ such reference sensor- secondary source and $N_y \times N_e$ secondary source-error sensor combinations exist. By employing feedforward-feedback technique the estimated disturbance signals are also used as reference signal in the feedback part as discussed in subsection 7.2.1. The effective number of reference sensors amounts to

$$N_{ex} = N_e + N_x. \tag{7.4.1}$$

For a description of the various components depicted in Figure 7.3 the reader should consult subsection 7.2.1 and subsection 7.3.1. In total $N_{ex} \times N_y$ reference to control output signal tap-weight vectors exist.

In the presentation to follow we will explain how the various feedback and feedforward signals should be combined.

7.4.2 Error Signals

The error signal $\underset{\oplus}{e}(t_m^1)$ is a *sensed* signal cf. section 5.3. Referring to Figure 7.3 we identify viz. (5.3.15)

$$e_m^{\mathcal{D}^1}(t_m^1) \rightarrow \underset{\oplus}{e}_m(t_m^1). \tag{7.4.2}$$

The error signal is the result of the *superposition* of the disturbance signal $d_m(t_m^1)$ and the total rejection signal $\underset{\oplus}{r}_m(t_m^1)$

$$\underset{\oplus}{e}_m(t_m^1) = d_m(t_m^1) \pm \underset{\oplus}{r}_m(t_m^1). \tag{7.4.3}$$

The disturbance signal $d_m(t_m^1)$ is discussed in subsection 7.4.3. The rejection signal $\underset{\oplus}{r}_m(t_m^1)$ in turn is a superposition of in total N_y secondary source driven rejection signals $\underset{\oplus}{r}_{m_l}(t_m^1)$. The rejection signal is subject for discussion in subsection 7.4.7 and an expression for $\underset{\oplus}{r}_m(t_m^1)$ can be found in (7.4.14). The sign convention is described in subsection 7.2.2.

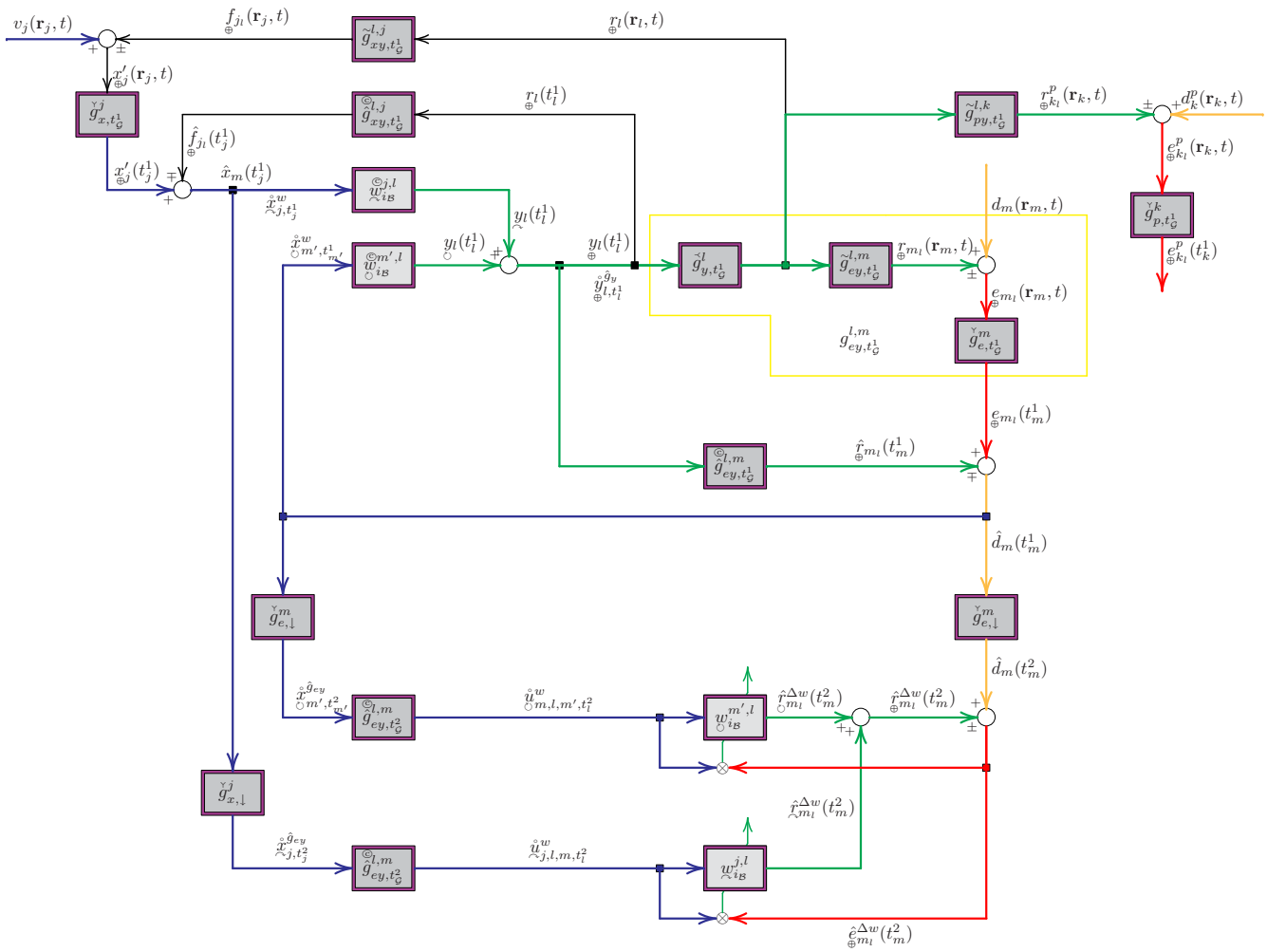

Fig. 7.3: Feedforwardback Controller using IMC and mFx based Adaptive Filter.

7.4.3 Disturbance Signals

The disturbance signals are only *directly* measurable when the rejection signals are turned-off.

In the FFFBS the feedforward part $\underset{\sim}{x}(t_j^1)$ of the reference signal is a *sensed* signal but the feedback part supposedly employing the IMC $\underset{\circ}{x}(t_m^1)$ should be internally generated from the *estimated* disturbance.

A disturbance signal estimate at multirate level 1 $\hat{d}_m(t_m^1) \in \mathbb{K}$, however, is required anyway for the mFx algorithm. It is computed as

$$\hat{d}_m(t_m^1) = \underset{\oplus}{e}_m(t_m^1) \mp \hat{\underset{\oplus}{r}}_m(t_m^1). \tag{7.4.4}$$

In (7.4.4) the estimated rejection signal $\hat{\underset{\oplus}{r}}_m(t_m^1)$ defined in subsection 7.4.7 viz. (7.4.13) was introduced. Moreover, the $\mp$ signs correspond to the $\pm$ signs in (7.4.3).

7.4.4 Unfiltered and Filtered Reference Signals

The set of reference signals in a FFFBS is constituted by the union of the set $\underset{\circ}{x}(t_m^1)$ of feedback reference signals and the set $\underset{\sim}{x}(t_j^1)$ of feedforward reference signals. In a FFFBS the feedback signal and feedforward signals will be mutually coupled. This also applies to the reference signals. Therefore, some corrections to the equations for the feedback and feedforward reference signal provided in subsection 7.2.4 and subsection 7.3.4 respectively should be made.

Unfiltered and Filtered Reference Signals Feedback Part

In analogy with the discussion in subsection 7.2.4 we obtain the reference signals $\underset{\circ}{x}_{m'}(t_m^1)$ as in (7.2.4), but now taking the effects of the feedforward system into account

$$\underset{\circ}{x}_{m'}(t_m^1) \triangleq \hat{d}_m(t_m^1), \tag{7.4.5}$$

where $\hat{d}_m$ is obtained from (7.4.4).

The time-reversed *unfiltered* auxiliary reference feedback signal buffers $\mathring{\underset{\circ}{x}}^{\hat{g}_{ey}}_{m',t_{m'}^2}$ and $\mathring{\underset{\circ}{x}}^{w}_{m',t_{m'}^1}$ are obtained from (7.2.11) and (7.2.8) respectively. From (7.2.12) and (7.2.14) we obtain the filtered reference feedback triplet $\underset{\circ}{u}_{m,l,m'}(t_l^2)$ and filtered feedback reference buffer $\mathring{\underset{\circ}{u}}^{w}_{m,l,m',t_l^2}$.

Unfiltered and Filtered Reference Signals Feedforward Part

In subsection 7.4.8 the calculation of the feedback terms $\hat{\underset{\oplus}{f}}_m(t_j^1)$ and $\underset{\oplus}{f}_j(t_j^1)$ including the effects of the FFFBS will be made viz. (7.4.15) and (7.4.16).

From subsection 7.3.4 we have the following expressions for the sensed reference signals $\underset{\oplus}{x}'_j(t_j^1)$ and estimate of the undisturbed reference signals $\hat{x}_j(t_j^1)$ viz. (7.3.6) and (7.3.7), included here

for convenience

$$\underset{\oplus}{x'_j}(t_j^1) = x_j(t_j^1) \pm \underset{\oplus}{f_j}(t_j^1) \tag{7.4.6}$$

$$\hat{x}_j(t_j^1) = \underset{\oplus}{x'_j}(t_j^1) \mp \underset{\oplus}{\hat{f}_m}(t_j^1). \tag{7.4.7}$$

The feedback terms $\underset{\oplus}{\hat{f}_m}(t_j^1)$ and $\underset{\oplus}{f_j}(t_j^1)$, however, should now be determined from (7.4.15) and (7.4.16) respectively (see subsection 7.4.8).

Also in the FFFBS employing the feedback cancelation scheme $\underset{\sim}{x_j}(t_j^1)$ will be used as reference signal, that is,

$$\underset{\sim}{x_j}(t_j^1) \triangleq \hat{x}_j(t_j^1). \tag{7.4.8}$$

The time-reversed *unfiltered* auxiliary reference feedforward signal buffers $\underset{\sim}{\mathring{x}}^{\hat{g}_{ey}}_{j,t^2_{m'}}$ and $\underset{\sim}{\mathring{x}}^{w}_{j,t^1_{m'}}$ are obtained from (7.3.13) and (7.3.10) respectively. From (7.3.14) and (7.3.15) we obtain the filtered reference feedforward triplet $\underset{\sim}{u_{l,m,j}}(t_l^2)$ and filtered feedforward reference buffer $\underset{\sim}{\mathring{u}}^{w}_{l,m,j,t_l^2}$.

7.4.5 Tap-Weight Update Signals

We will first estimate $\underset{\oplus}{\hat{r}}^{\Delta w}_m(t_m^2)$ used for the determination of $\underset{\oplus}{\hat{e}}^{\Delta w}_m(t_m^2)$. If the system is linear we can superpose the feedback $\underset{\circ}{\hat{r}}^{\Delta w}_m(t_m^2)$ and feedforward $\underset{\sim}{r}^{\Delta w}_m(t_m^2)$ contributions to the rejection signal. Moreover, due to the assumption of frozen tap-weights the system can be considered time-invariant and then the principle of interchanging the plant and the controller discussed in connection with Fx-assumption viz. (6.3.1) applies and $\underset{\oplus}{\hat{r}}^{\Delta w}_m(t_m^2)$ then is readily obtainable from (7.2.31) and (7.3.31)

$$\underset{\oplus}{\hat{r}}^{\Delta w}_m(t_m^2) = \underset{\circ}{\hat{r}}^{\Delta w}_m(t_m^2) + \underset{\sim}{\hat{r}}^{\Delta w}_m(t_m^2). \tag{7.4.9}$$

Finally, $\underset{\oplus}{\hat{e}}^{\Delta w}_m(t_m^2)$ is obtained from

$$\underset{\oplus}{\hat{e}}^{\Delta w}_m(t_m^2) = \hat{d}_m(t_m^2) \pm \underset{\oplus}{\hat{r}}^{\Delta w}_m(t_m^2), \tag{7.4.10}$$

where the $\pm$ signs correspond to the $\pm$ signs in (7.4.3). The *reference signal* u_i used for adaptive tap-weights update follows from the discussion made in subsection 7.2.5 and subsection 7.3.5 viz. (7.2.18) on page 298 and (7.3.19) on page 308.

7.4.6 Control Output

The adaptive filter output (control output signal) $\underset{\oplus}{y_l}(t_l^1 + 1)$ depicted in Figure 7.3 on page 315 is obtained under the assumption of linearity as the sum of the feedback control output signal $\underset{\circ}{y_l}(t_l^1 + 1)$ and the feedforward control output signal $\underset{\sim}{y_l}(t_l^1 + 1)$

$$\underset{\oplus}{y_l}(t_l^1 + 1) = \underset{\circ}{y_l}(t_l^1 + 1) + \underset{\sim}{y_l}(t_l^1 + 1), \tag{7.4.11}$$

where $\underset{\circlearrowleft}{y_l}(t_l^1+1)$ and $\underset{\frown}{y_l}(t_l^1+1)$ in turn are determined in (7.2.21) and (7.3.22) respectively.

For later use we will define a set of N_y auxiliary time-reversed control output signal buffers $\overset{\circ}{\underset{\oplus}{y}}{}^{\hat{g}_y}_{l,t_l^1+1}$ $(1 \times M^l_{\hat{g}_y}$ row vectors) according to

$$\overset{\circ}{\underset{\oplus}{y}}{}^{\hat{g}_y}_{l,t_l^1+1} = \Big[\underset{\oplus}{y_l}(t_l^1+1) \quad \underset{\oplus}{y_l}(t_l^1) \quad \dots \quad \underset{\oplus}{y_l}(t_l^1 - M^{\max}_{\hat{g}_y^l}+2)\Big]. \tag{7.4.12}$$

The quantity $M^{\max}_{\hat{g}_y^l}$ was defined in subsection 7.3.8 viz. (7.3.41).

7.4.7 Rejection Signals

The *rejection signal* $\underset{\oplus}{r_m}(t_m^1+1)$ depicted in Figure 7.3 on page 315 sensed by the m'th sensor is a consequence of the combined control output signals $\underset{\oplus}{y_l}$ up to time (t_l^1+1) that subsequently is filtered in some possible non-linear and time varying sense by the plant.

In analogy with subsection 7.2.7 and subsection 7.3.7 an estimate of the total rejection signal $\underset{\oplus}{\hat{r}_m}(t_m^1+1)$ present at the m'th error sensor is obtained as a superposition of the contribution from each of the N_y secondary sources

$$\underset{\oplus}{\hat{r}_m}(t_m^1+1) = \sum_{l=1}^{N_y} \overset{\circ}{\underset{\oplus}{y}}{}^{\hat{g}_y}_{l,t_l^1+1}(1 : M^{l,m,1}_{\hat{g}_{ey}}) \overset{\copyright}{\hat{g}}{}^{l,m}_{ey,t_G^1}, \tag{7.4.13}$$

where $\overset{\circ}{\underset{\oplus}{y}}{}^{\hat{g}_y}_{l,t_l^1+1}$ is expressed in (7.4.12). Similarly, for evaluation purposes and assuming perfect knowledge of the plant response the "true" total rejection signal $\underset{\oplus}{r_m}(t_m^1+1)$ present at the m'th error sensor is likewise obtained as a superposition of the contribution from each of the N_y secondary sources

$$\underset{\oplus}{r_m}(t_m^1+1) = \sum_{l=1}^{N_y} \overset{\circ}{\underset{\oplus}{y}}{}^{\hat{g}_y}_{l,t_l^1+1}(1 : M^{l,m}_{g_{ey}}) g^{l,m}_{ey,t^1}. \tag{7.4.14}$$

7.4.8 Feedback Signals

The *feedback signal* component $\underset{\oplus}{f_{j_l}}(t_j^1+1)$ depicted in Figure 7.3 on page 315 sensed by the j'th sensor is a consequence of the combined control output signals $\underset{\oplus}{y_l}$ up to time (t_l^1+1) that subsequently is filtered in some possible non-linear and time varying sense by the feedback plant. By analogy with subsection 7.3.8 we can under the usual assumption of linearity determine an estimate of the total feedback signal $\underset{\oplus}{\hat{f}_j}(t_j^1+1)$ present at the j'th reference sensor as a superposition of the contribution from each of the N_y secondary sources

$$\underset{\oplus}{\hat{f}_j}(t_j^1+1) = \sum_{l=1}^{N_y} \overset{\circ}{\underset{\oplus}{y}}{}^{\hat{g}_y}_{l,t_l^1+1}(1 : M^{l,j}_{\hat{g}_{xy}}) \overset{\copyright}{\hat{g}}{}^{l,j}_{xy,t_G^1}. \tag{7.4.15}$$

Similarly, for evaluation purposes and assuming perfect knowledge of the plant response the "true" total feedback signal $\underset{\oplus}{f}_j(t_j^1+1)$ present at the j'th reference sensor is likewise obtained as a superposition of the contribution from each of the N_y secondary sources

$$\underset{\oplus}{f}_j(t_j^1+1) = \sum_{l=1}^{N_y} \underset{\oplus}{\overset{\circ}{y}}{}^{\hat{g}_y}_{l,t_l^1+1}(1 : M_{g_{xy}}^{l,j}) g_{xy,t_G^1}^{l,j}, \tag{7.4.16}$$

where $\underset{\oplus}{\overset{\circ}{y}}{}^{\hat{g}_y}_{l,t_l^1+1}$ is defined in subsection 7.4.6 viz. (7.4.12).

7.4.9 Performance Signals

By inspection of Figure 7.3 on page 315 we recognize that the resulting performance error at the k'th performance sensor $\underset{\oplus}{e}{}^p_k(t_k^1)$ is obtained as the *superposition* of the disturbance signal $d_k^p(t_k^1)$ and the total rejection signal $\underset{\oplus}{r}{}^p_k(t_k^1+1)$

$$\underset{\oplus}{e}{}^p_k(t_k^1) = d_k^p(t_k^1) \pm \underset{\oplus}{r}{}^p_k(t_k^1), \tag{7.4.17}$$

where $\underset{\oplus}{r}{}^p_k(t_k^1)$ in turn is obtained from an expression equivalent to (7.4.14)

$$\underset{\oplus}{r}{}^p_k(t_k^1+1) = \sum_{l=1}^{N_y} \underset{\oplus}{\overset{\circ}{y}}{}^{\hat{g}_y}_{l,t_l^1+1}(1 : M_{g_{py}}^{l,k}) g_{py,t_G^1}^{l,k}, \tag{7.4.18}$$

where $\underset{\oplus}{\overset{\circ}{y}}{}^{\hat{g}_y}_{l,t_l^1+1}$ is defined in subsection 7.4.6 viz. (7.4.12).

7.4.10 Feedforwardback Algorithm Summary

The feedforward-feedback control adaptive filtering algorithm is constituted by first sensing the error signal $\underset{\oplus}{e}_m(t_m^1)$ (7.4.2) then estimating the disturbances $\hat{d}_m(t_m^1)$ (7.4.4) and estimating the reference signals $\underset{\oplus}{\hat{x}}'_j(t_j^1)$ (7.4.7); next creating the unfiltered reference buffers $\underset{\circlearrowleft}{\overset{\circ}{x}}{}^{\hat{g}_{ey}}_{m',t_{m'}^2}$ and $\underset{\curvearrowright}{\overset{\circ}{x}}{}^{\hat{g}_{ey}}_{j,t_{m'}^2}$ from (7.2.11) and (7.3.13); $\underset{\circlearrowleft}{\overset{\circ}{x}}{}^{w}_{m',t_{m'}^1}$ and $\underset{\curvearrowright}{\overset{\circ}{x}}{}^{w}_{j,t_j^1}$ from (7.2.8) and (7.3.10).

Thereafter the filtered reference triplets $\underset{\circlearrowleft}{u}_{m,l,m'}(t_l^2)$ and $\underset{\curvearrowright}{u}_{l,m,j}(t_l^2)$ are computed from (7.2.12) and (7.3.14) leading to the filtered buffers $\underset{\circlearrowleft}{\overset{\circ}{u}}{}^{w}_{m,l,m',t_l^2}$ and $\underset{\curvearrowright}{\overset{\circ}{u}}{}^{w}_{l,m,j,t_l^2}$ from (7.2.14) and (7.3.15).

Next $\underset{\oplus}{\hat{r}}{}^{\Delta w}_m(t_m^2)$ and successively $\underset{\oplus}{\hat{e}}{}^{\Delta w}_m(t_m^2)$ used for tap-weight adaptation are determined viz. (7.4.9) and (7.4.10). The tap-weights are subsequently updated (at least at each block-update time) following one of the algorithms detailed in chapter 8 and Appendix J. Then the control output signals $\underset{\oplus}{y}_l(t_l^1+1)$ provided by the system at the next iteration are computed (7.4.11) followed by the creation of $\underset{\oplus}{\overset{\circ}{y}}{}^{\hat{g}_y}_{l,t_l^1+1}$ in (7.4.12). Moreover, the rejection signals $\underset{\oplus}{\hat{r}}_m(t_m^1+1)$ are determined from (7.4.13). Finally, also in preparation for the next iteration the feedback signals $\underset{\oplus}{\hat{f}}_j(t_j^1+1)$ are computed from (7.4.15).

For simulation purpose we also need the error signals $\underset{\oplus}{e}_m(t_m^1)$ (7.4.3), the reference signal $\underset{\oplus}{x'}_j(t_j^1)$ (7.4.6), rejection signals $\underset{\oplus}{r}_m(t_m^1+1)$ and $\underset{\oplus}{r}_k^p(t_k^1+1)$ determined from (7.4.14) and (7.4.18), feedback signals $\underset{\sim}{f}_{jl}(t_j^1+1)$ (7.3.38). Finally, the performance measure $\underset{\oplus}{e}_k(t_k^1)$ can be assessed from (7.4.17).

7.5 Feedforwardback Integrated Communication Controller - Adaptive Filter Topology

7.5.1 Introduction

In practical ANR systems a side requirement of distortion free transmission of communication signals, audio signals etc. is often posed on the system. For example for airborne operation one of the objective of introducing active noise reduction is to improve the speech intelligibility, but also to increase the benefits from 3-D audio cuing signals. Another example is found in cars equipped with an ANR facility. Here the system should provide substantial noise suppression while preserving high fidelity sound in the entertainment system. Hence, the ANR-system shall be designed so as to avoid cancelation of such information bearing signals. In this section we will present a technique that was originally proposed in [7] that we will augment to the multi-channel FFFBS that can be applied to warrant the objective of distortion free transmission communication signals. Moreover, online-system identification which is the topic of section 7.6 on page 326 also requires the introduction of a well known identification signal without this leading to a perceivable performance degradation. Hence, the following discussion also applies to the ANR part of a FFFBICIDS.

The feedforward-feedback integrated communication system (FFFBICS) - adaptive filtering - interface is depicted in Figure 7.4 on the next page.

In addition to the plain FFFBS topology in Figure 7.3 on page 315 the FFFBICS is basically obtained by adding provision for communication. In center of Figure 7.4 we see the symbol Ⓢ which refers to the signal source in a FFFBICS. In order to reduce the overall system complexity and costs the communication signals are assumed to use existing hardware provided by the secondary sources. In general a total of N_y signal sources exist.

For a description of the various components depicted in Figure 7.4 the reader should consult subsection 7.2.1, subsection 7.3.1 and subsection 7.4.1. As mentioned in the introduction in section 6.1 underaccent $\underset{\circledS}{}$ is used to signify a pure signal source and an underaccent $\underset{\circledast}{}$ will be enforced to signify that contributions from the signal sources are included in the pertinent signals in **addition** to the contributions from the plain FFFBS.

In the presentation to follow we will explain how the integrated communication (IC)-system and the ANR-system successfully can operate simultaneously together.

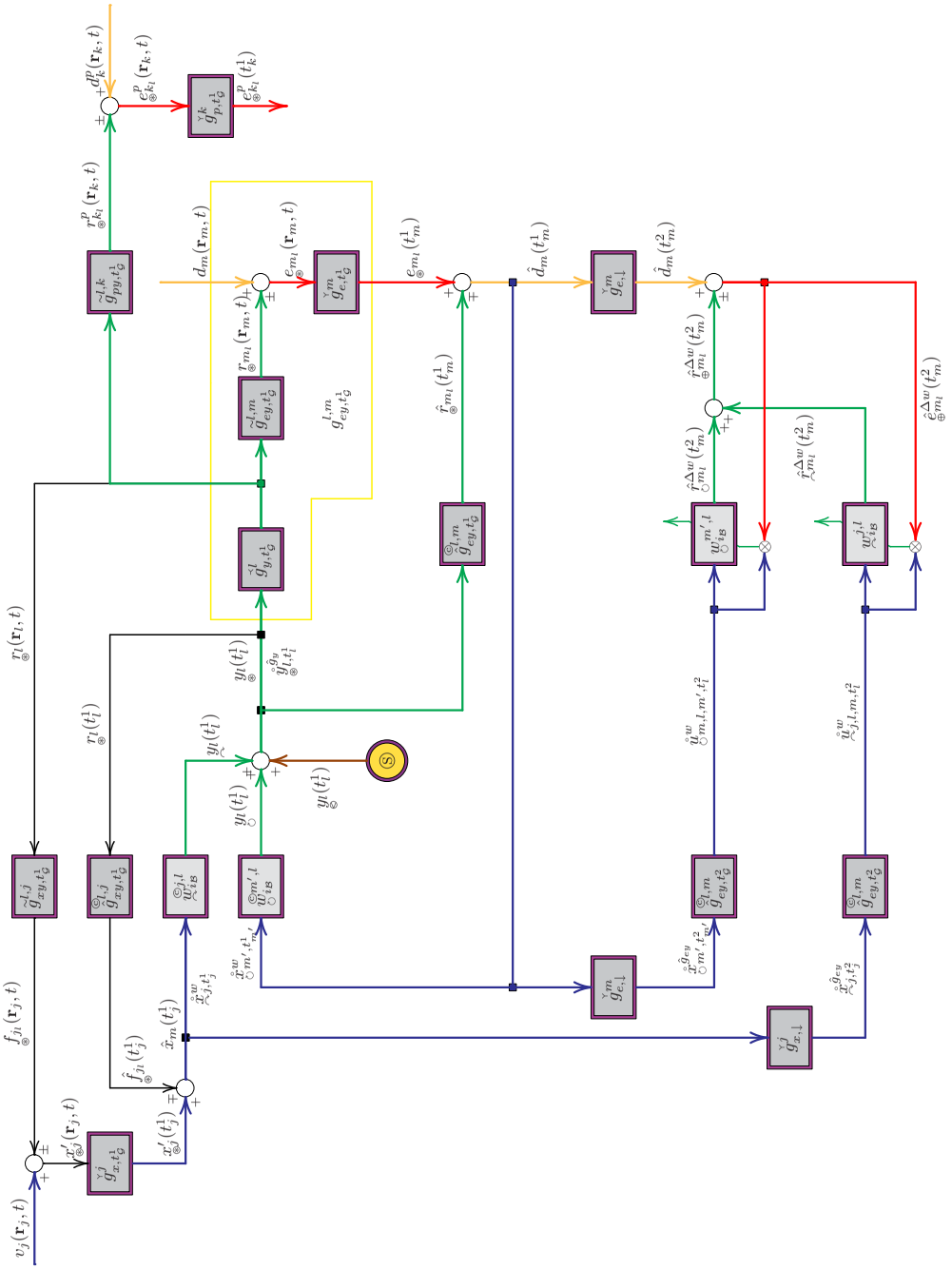

Fig. 7.4: Feedforwardback Integrated Communication Controller using IMC and mFx based Adaptive Filter.

7.5.2 Error Signals

The error signal $\underset{\circledast}{e}(t_m^1)$ is a *sensed* signal cf. section 5.3. Referring to Figure 7.4 we identify viz. (5.3.15)

$$e_m^{\mathcal{D}^1}(t_m^1) \rightarrow \underset{\circledast}{e}_m(t_m^1). \tag{7.5.1}$$

The error signal is the result of the *superposition* of the disturbance signal $d_m(t_m^1)$ and the total rejection signal $\underset{\circledast}{r}_m(t_m^1)$

$$\underset{\circledast}{e}_m(t_m^1) = d_m(t_m^1) \pm \underset{\circledast}{r}_m(t_m^1). \tag{7.5.2}$$

The disturbance signal $d_m(t_m^1)$ is discussed in subsection 7.5.3. The rejection signal $\underset{\circledast}{r}_m(t_m^1)$ in turn is a superposition of in total N_y secondary source driven rejection signals $\underset{\circledast}{r}_{m_l}(t_m^1)$. The rejection signal is subject for discussion in subsection 7.5.7 and an expression for $\underset{\circledast}{r}_m(t_m^1)$ can be found in (7.5.10). The sign convention is described in subsection 7.2.2

7.5.3 Disturbance Signals

The disturbance signals are only *directly* measurable when the rejection signals **and** the signal sources are turned-off.

In the FFFBICS the feedforward part $\underset{\sim}{x}(t_j^1)$ of the reference signal is a *sensed* signal but the feedback part supposedly employing the IMC $\underset{\circ}{x}(t_m^1)$ should be internally generated from the *estimated* disturbance.

A disturbance signal estimate at multirate level 1 $\hat{d}_m(t_m^1) \in \mathbb{K}$, however, is required anyway for the mFx algorithm. It is computed as

$$\hat{d}_m(t_m^1) = \underset{\circledast}{e}_m(t_m^1) \mp \underset{\circledast}{\hat{r}}_m(t_m^1). \tag{7.5.3}$$

In (7.5.3) the estimated rejection signal $\underset{\circledast}{\hat{r}}_m(t_m^1)$ defined in subsection 7.5.7 viz. (7.5.9) was introduced. Moreover, the $\mp$ signs correspond to the $\pm$ signs in (7.5.2). From Figure 7.4 it can be observed that by employing the IMC the contribution from the signal source is automatically canceled in the estimate $\hat{d}_m(t_m^1)$ of the disturbance $d_m(t_m^1)$ provided that the secondary source model is sufficiently accurate.

7.5.4 Unfiltered and Filtered Reference Signals

The generation of the unfiltered- and filtered-reference signals follows the procedure in subsection 7.4.4. Hence, we will reestablish the pertinent equation and comment on the changes to be made.

Unfiltered and Filtered Reference Signals Feedback Part

The reference signals $\underset{\circlearrowleft}{x}_{m'}(t_m^1)$ is obtained as in (7.2.4), but now taking the effects of the feedforward system **and** the effects of the audio signals into account

$$\underset{\circlearrowleft}{x}_{m'}(t_m^1) \triangleq \hat{d}_m(t_m^1), \tag{7.5.4}$$

where $\hat{d}_m$ is obtained from (7.5.3).

The time-reversed *unfiltered* auxiliary reference feedback signal buffers $\underset{\circlearrowleft}{\mathring{x}}^{\hat{g}_{ey}}_{m',t_{m'}^2}$ and $\underset{\circlearrowleft}{\mathring{x}}^{w}_{m',t_{m'}^1}$ are obtained from (7.2.11) and (7.2.8) respectively. From (7.2.12) and (7.2.14) we obtain the filtered reference feedback triplet $\underset{\circlearrowleft}{u}_{m,l,m'}(t_l^2)$ and filtered feedback reference buffer $\underset{\circlearrowleft}{\mathring{u}}^{w}_{m,l,m',t_l^2}$.

Unfiltered and Filtered Reference Signals Feedforward Part

From subsection 7.3.4 we have the following expressions for the sensed reference signals $\underset{\sim}{x}'_j(t_j^1)$ and estimate of the undisturbed reference signals $\hat{x}_j(t_j^1)$ viz. (7.3.6) and (7.3.7), included here for convenience

$$\underset{\circledast}{x}'_j(t_j^1) = \underset{\sim}{x}_j(t_j^1) \pm \underset{\circledast}{f}_j(t_j^1) \tag{7.5.5}$$

$$\hat{x}_j(t_j^1) = \underset{\sim}{x}'_j(t_j^1) \mp \underset{\circledast}{\hat{f}}_m(t_j^1). \tag{7.5.6}$$

The feedback terms $\underset{\circledast}{\hat{f}}_m(t_j^1)$ and $\underset{\circledast}{f}_j(t_j^1)$, however, should now be determined from (7.5.11) and (7.5.12) respectively (see subsection 7.5.8).

The time-reversed *unfiltered* auxiliary reference feedforward signal buffers $\underset{\sim}{\mathring{x}}^{\hat{g}_{ey}}_{j,t_{m'}^2}$ and $\underset{\sim}{\mathring{x}}^{w}_{j,t_{m'}^1}$ are obtained from (7.3.13) and (7.3.10) respectively. From (7.3.14) and (7.3.15) we obtain the filtered reference feedforward triplet $\underset{\sim}{u}_{l,m,j}(t_l^2)$ and filtered feedforward reference buffer $\underset{\sim}{\mathring{u}}^{w}_{l,m,j,t_l^2}$.

The *reference signal* u_i used for adaptive tap-weights update follows from the discussion made in subsection 7.2.4 and subsection 7.3.4 viz. (7.2.18) on page 298 and (7.3.19) on page 308.

7.5.5 Tap-Weight Update Signals

Recalling from the discussion made in subsection 6.3.2 in connection with the mFx technique that instead of using the *measured* error signal $e(i)$ for tap-weight recursion it is arguable more correct to use an estimate of what the error signal would have been provided that the tap-weights had been frozen for a period corresponding to the impulse response of the plant. In addition the error shall not include contributions from the signal sources. By applying the same arguments concerning the use of the IMC model as in subsection 7.5.3 we can therefore conclude that the expression (7.4.10) for $\underset{\oplus}{\hat{e}}^{\Delta w}_m(t_m^2)$ for the tap-weight update holds for the FFFBICS provided that $hat g_{ey}$ is sufficient accurate.

7.5.6 Combined Control and Signal Source Output

In the FFFBICS the combined output $\underset{\circledast}{y_l}(t_l^1+1)$ depicted in Figure 7.4 on page 321 contain the control output signal contribution $\underset{\oplus}{y_l}(t_l^1+1)$ from the plain FFFBS as well as the signal source $\underset{\copyright}{y_l}(t_l^1+1)$. Under the usual assumption of linearity $\underset{\circledast}{y_l}(t_l^1+1)$ is obtained as the sum of the feedforward-feedback control output signal $\underset{\oplus}{y_l}(t_l^1+1)$ and the signal source $\underset{\copyright}{y_l}(t_l^1+1)$

$$\underset{\circledast}{y_l}(t_l^1+1) = \underset{\oplus}{y_l}(t_l^1+1) + \underset{\copyright}{y_l}(t_l^1+1), \tag{7.5.7}$$

where $\underset{\oplus}{y_l}(t_l^1+1)$ in turn is determined in (7.4.11).

For later use we will define a set of N_y auxiliary time-reversed control output signal buffers $\underset{\circledast}{\mathring{y}}^{\hat{g}_y}_{l,t_l^1+1}$ ($1 \times M^l_{\hat{g}_y}$ row vectors) according to

$$\underset{\circledast}{\mathring{y}}^{\hat{g}_y}_{l,t_l^1+1} = \Big[\underset{\circledast}{y_l}(t_l^1+1) \quad \underset{\circledast}{y_l}(t_l^1) \quad \dots \quad \underset{\circledast}{y_l}(t_l^1 - M^{\max}_{\hat{g}_y^l}+2)\Big]. \tag{7.5.8}$$

The quantity $M^{\max}_{\hat{g}_y^l}$ was defined in subsection 7.3.8 viz. (7.3.41).

7.5.7 Rejection Signals

The *rejection signal* $\underset{\circledast}{r}_m(t_m^1+1)$ depicted in Figure 7.4 on page 321 sensed by the m'th sensor is a consequence of the combined control output signals $\underset{\circledast}{y_l}$ up to time (t_l^1+1) that subsequently is filtered in some possible non-linear and time varying sense by the plant.

In analogy with subsection 7.2.7 and subsection 7.3.7 an estimate of the total rejection signal $\underset{\circledast}{\hat{r}}_m(t_m^1+1)$ present at the m'th error sensor is obtained as a superposition of the contribution from each of the N_y secondary sources

$$\underset{\circledast}{\hat{r}}_m(t_m^1+1) = \sum_{l=1}^{N_y} \underset{\circledast}{\mathring{y}}^{\hat{g}_y}_{l,t_l^1+1}(1 : M^{l,m,1}_{\hat{g}_{ey}}) \overset{\copyright}{\hat{g}}^{l,m}_{ey,t_G^1}, \tag{7.5.9}$$

where $\underset{\circledast}{\mathring{y}}^{\hat{g}_y}_{l,t_l^1+1}$ is expressed in (7.5.8). Similarly, for evaluation purposes and assuming perfect knowledge of the plant response the "true" total rejection signal $\underset{\circledast}{r}_m(t_m^1+1)$ present at the m'th error sensor is likewise obtained as a superposition of the contribution from each of the N_y secondary sources

$$\underset{\circledast}{r}_m(t_m^1+1) = \sum_{l=1}^{N_y} \underset{\circledast}{\mathring{y}}^{\hat{g}_y}_{l,t_l^1+1}(1 : M^{l,m}_{g_{ey}}) g^{l,m}_{ey,t^1}. \tag{7.5.10}$$

7.5.8 Feedback Signals

The *feedback signal* component $\underset{\circledast}{f}_{jl}(t_j^1+1)$ depicted in Figure 7.4 on page 321 sensed by the j'th sensor is a consequence of the combined control output signals $\underset{\circledast}{y}_l$ up to time (t_l^1+1) that subsequently is filtered in some possible non-linear and time varying sense by the feedback plant. By analogy with subsection 7.3.8 we can under the usual assumption of linearity determine an estimate of the total feedback signal $\underset{\circledast}{\hat{f}}_j(t_j^1+1)$ present at the j'th reference sensor as a superposition of the contribution from each of the N_y secondary sources

$$\underset{\circledast}{\hat{f}}_j(t_j^1+1)=\sum_{l=1}^{N_y}\underset{\circledast}{\mathring{y}}^{\hat{g}_y}_{l,t_l^1+1}(1:M^{l,j}_{\hat{g}_{xy}})\overset{\copyright}{\hat{g}}^{l,j}_{xy,t_G^1}. \tag{7.5.11}$$

Similarly, for evaluation purposes and assuming perfect knowledge of the plant response the "true" total feedback signal $\underset{\circledast}{f}_j(t_j^1+1)$ present at the j'th reference sensor is likewise obtained as a superposition of the contribution from each of the N_y secondary sources

$$\underset{\circledast}{f}_j(t_j^1+1)=\sum_{l=1}^{N_y}\underset{\circledast}{\mathring{y}}^{\hat{g}_y}_{l,t_l^1+1}(1:M^{l,j}_{g_{xy}})g^{l,j}_{xy,t_G^1}, \tag{7.5.12}$$

where $\underset{\circledast}{\mathring{y}}^{\hat{g}_y}_{l,t_l^1+1}$ is defined in subsection 7.5.6 viz. (7.5.8).

7.5.9 Performance Signals

By inspection of Figure 7.4 on page 321 we recognize that the resulting performance error at the k'th performance sensor $\underset{\circledast}{e}^p_k(t_k^1)$ is obtained as the *superposition* of the disturbance signal $d^p_k(t_k^1)$ and the total rejection signal $\underset{\circledast}{r}^p_k(t_k^1+1)$

$$\underset{\circledast}{e}^p_k(t_k^1)=d^p_k(t_k^1)\pm\underset{\circledast}{r}^p_k(t_k^1), \tag{7.5.13}$$

where $r^p_k(t_k^1)$ in turn is obtained from an expression equivalent to (7.5.10)

$$\underset{\circledast}{r}^p_k(t_k^1+1)=\sum_{l=1}^{N_y}\underset{\circledast}{\mathring{y}}^{\hat{g}_y}_{l,t_l^1+1}(1:M^{l,k}_{g_{py}})g^{l,k}_{py,t_G^1}, \tag{7.5.14}$$

where $\underset{\circledast}{\mathring{y}}^{\hat{g}_y}_{l,t_l^1+1}$ is defined in subsection 7.5.6 viz. (7.5.8).

7.5.10 Feedforwardback Algorithm Summary

The feedforward-feedback integrated communication control adaptive filtering algorithm is constituted by first sensing the error signal $\underset{\circledast}{e}_m(t_m^1)$ (7.5.1) then estimating the disturbances $\hat{d}_m(t_m^1)$ (7.5.3) and estimating the reference signals $\underset{\circledast}{\hat{x}'}_j(t_j^1)$ (7.5.6); next creating the unfiltered reference buffers $\underset{\circlearrowleft}{\mathring{x}}^{\hat{g}_{ey}}_{m',t^2_{m'}}$ and $\underset{\curvearrowright}{\mathring{x}}^{\hat{g}_{ey}}_{j,t^2_{m'}}$ from (7.2.11) and (7.3.13); $\underset{\circlearrowleft}{\mathring{x}}^{w}_{m',t^1_{m'}}$ and $\underset{\curvearrowright}{\mathring{x}}^{w}_{j,t^1_j}$ from (7.2.8) and (7.3.10).

Thereafter the filtered reference triplets $\underset{\circ}{u}_{m,l,m'}(t_l^2)$ and $\underset{\sim}{u}_{l,m,j}(t_l^2)$ are computed from (7.2.12) and (7.3.14) leading to the filtered buffers $\underset{\circ}{\mathring{u}}^w_{m,l,m',t_l^2}$ and $\underset{\sim}{\mathring{u}}^w_{l,m,j,t_l^2}$ from (7.2.14) and (7.3.15).

Next $\underset{\oplus}{\hat{r}}_m^{\Delta w}(t_m^2)$ and successively $\underset{\oplus}{\hat{e}}_m^{\Delta w}(t_m^2)$ used for tap-weight adaptation are determined viz. (7.4.9) and (7.4.10). The tap-weights are subsequently updated (at least at each block-update time) following one of the algorithms detailed in chapter 8 and Appendix J. Then the control output signals $\underset{\circledast}{y}_l(t_l^1+1)$ provided by the system at the next iteration are computed (7.5.7) followed by the creation of $\underset{\circledast}{\mathring{y}}^{\hat{g}_y}_{l,t_l^1+1}$ in (7.5.8). Moreover, the rejection signals $\underset{\circledast}{\hat{r}}_m(t_m^1+1)$ are determined from (7.5.9). Finally, also in preparation for the next iteration the feedback signals $\underset{\circledast}{\hat{f}}_j(t_j^1+1)$ are computed from (7.5.11).

For simulation purpose we also need the error signals $\underset{\circledast}{e}_m(t_m^1)$ (7.5.2), the reference signal $\underset{\circledast}{x'_j}(t_j^1)$ (7.5.5), rejection signals $\underset{\circledast}{r}_m(t_m^1+1)$ and $\underset{\circledast}{r}^p_k(t_k^1+1)$ determined from (7.5.10) and (7.5.14), feedback signals $\underset{\sim}{f}_{jl}(t_j^1+1)$ (7.3.38). Finally, the performance measure $\underset{\circledast}{e}_k(t_k^1)$ can be assessed from (7.5.13).

7.6 Feedforwardback Integrated Communication Controller On-Line System Identification - Adaptive Filter Topology

7.6.1 Introduction

In this section we will demonstrate how on-line system identification functionality can be added to the FFFBICS. The main challenge is to achieve convergence of the system identification process despite the effects of the operating ANR-system. The similar problem encountered when introducing a signal source to an ANR-system was described in section 7.5.

The feedforward-feedback integrated communication control system including system identification- adaptive filtering - interface is depicted in Figure 7.5 on the next page.

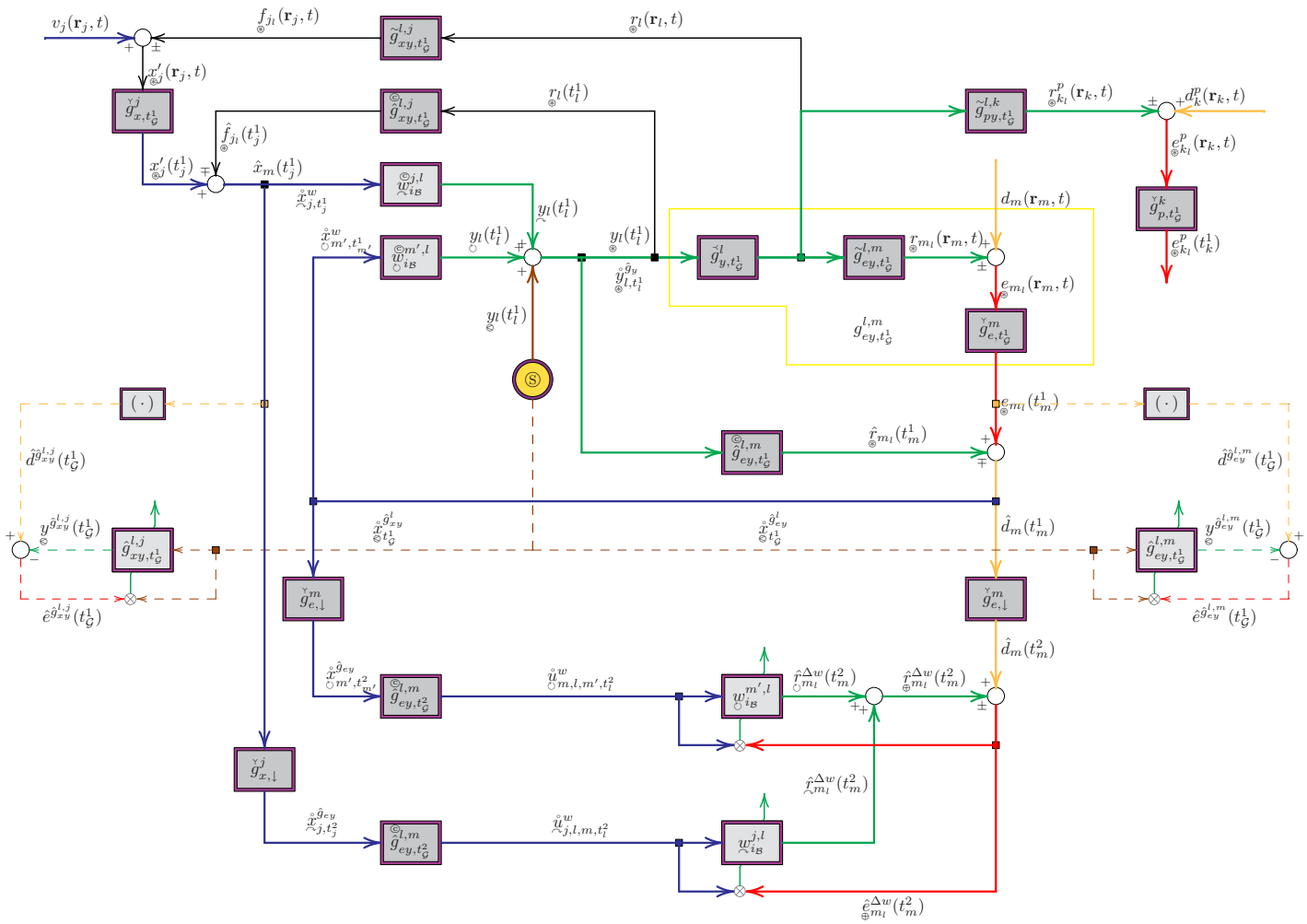

Fig. 7.5: Feedforwardback Integrated Communication Controller using IMC and mFx based Adaptive Filter with on-line system identification.

By comparison with Figure 7.4 on page 321 we observe that the FFFBICIDS is basically obtained by adding provision for system identification to the plain FFFBICS topology. For a description of the various components depicted in Figure 7.5 the reader should consult subsection 7.2.1, subsection 7.3.1, subsection 7.4.1 and subsection 7.5.1.

In Figure 7.5 we observe (indicated by a dashed line) that the identification signal $\underset{\circledS}{y_l}(t_G^1)$ is feed into an adaptive filter on the right where the tap-weights are identical to $\hat{g}_{ey}^{l,m}(t_G^1)$ for secondary path estimation. The number of such secondary path estimation adaptive filters amounts to $N_y \times N_e$. At the same time the identification signal $\underset{\circledS}{y_l}(t_G^1)$ is feed into an adaptive filter on the left where the tap-weights are identical to $\hat{g}_{xy}^{l,j}(t_G^1)$ for feedback path estimation. The number of such feedback path estimation adaptive filters amounts to $N_y \times N_x$. In system identification the plant is to be *estimated* and the process can be considered pure electrical ("plantless") as regards the adaptive filter as opposed to the active noise control (ANC) adaptive filter.

The system identification of the secondary paths and feedback paths will take place at regular, but highly application dependent intervals. We will use the plant estimation time index multirate level 1 $t_G^1 \in \mathbb{N}$ and plant estimation time index multirate level 2 $t_G^2 \in \mathbb{N}$ to represent the time where a system identification process is taking place. In the presentation to follow we will explain how the system identification can operate *on-line* (as opposed to off-line) inside an ANR-system.

7.6.2 Reference Signals

The identification signals $\underset{\circledS}{x}^{\hat{g}_{ey}^{l,m}}(t_G^1)$ and $\underset{\circledS}{x}^{\hat{g}_{xy}^{l,j}}(t_G^1)$ that may include communication signal, 3-D audio information etc. coincide with the reference signals for system identification, that is,

$$\underset{\circledS}{x}^{\hat{g}_{ey}^{l}}(t_G^1) = \underset{\circledS}{x}^{\hat{g}_{xy}^{l}}(t_G^1) \triangleq \underset{\circledS}{y_l}(t_G^1), \quad l \in \underline{N}_y. \tag{7.6.1}$$

For each secondary source we will constitute a time-reversed *unfiltered* auxiliary reference signal buffer $\underset{\circledS}{\hat{x}}_{t_G^1}^{\hat{g}_y^l}$ ($1 \times (M_{\hat{g}_y^l}^{\max} + 1)$ row vector) according to

$$\underset{\circledS}{\hat{x}}_{l,t_G^1}^{\hat{g}_y^l} = \begin{bmatrix} \underset{\circledS}{x_l}(t_G^1) & \underset{\circledS}{x_l}(t_G^1 - 1) & \dots & \underset{\circledS}{x_l}(t_G^1 - M_{\hat{g}_y^l}^{\max}) \end{bmatrix}, \quad l \in \underline{N}_y, \tag{7.6.2}$$

where the quantity $M_{\hat{g}_y^l}^{\max}$ was defined in subsection 7.3.8 viz. (7.3.41). The superscript $^{\hat{g}_y^l}$ indicates that the reference signal is used in connection with plant estimates involving the l'th secondary source. In the general case each of the controllers might apply a different adaptive filtering paradigm and consequently also use different model order $M_{\hat{g}_{ey}}^{l,m}$ and $M_{\hat{g}_{xy}}^{l,j}$. The reason for using a $1 \times (M_{\hat{g}_y^l}^{\max} + 1)$ row vector is to accommodate adaptive filter algorithms that use a regressor length $M_u = M + 1$ as detailed in Appendix J on page 737.

As no external pathes are involved in the two adaptive filters no filtering of reference signals is required.

7.6.3 Desired Signals

For single-input and single-output (SISO) and single-input and multiple-output (SIMO) systems the system identification procedure will usually involve one of the adaptive filter processing

schemes described in chapter 8, Appendix J and Appendix L. In system identification the disturbance signals are normally obtained as the outputs from stimulating the plants to be identified with some reference signals, e.g., $\underset{\circledcirc}{x}^{\hat{g}^l_{ey}}(t^1_G)$. As the adaptive filters during the adaptation phase should converge to the same output the disturbance signals are also referred to as *desired signals*. This choice of name will also be used in this report to avoid possible ambiguity between AC disturbance terms and system identification disturbance terms. The disturbance signals $d_m(\mathbf{r}_m, t)$ and reference signals $x_j(\mathbf{r}_j, t)$ depicted in Figure 7.5 on page 327 are considered as measurement noise terms for the system identification. Unfortunately, however, in an ANR-system the external disturbances can normally not be turned-off during the time of system identification.

For the system identification of SIMO MIMO systems some precautions most be taking. In the SIMO and multiple-input and multiple-output (MIMO) case at least two possibilities for obtaining estimates of all the plants involved exist. In a *sequential system identification* process only a single output is activated at a time. During system identification all the adaptive filter corresponding to the secondary paths and feedback paths involving only, say, the l_1'th actuator, that is G^{m,l_1}_{ey} and G^{j,l_1}_{xy} are then brought into an adaptive mode while the adaptive filters associated with the remaining secondary paths and feedback paths are fixed. Upon converging actuator l_2 is excited by an identification signal $\underset{\circledcirc}{x}^{\hat{g}^{l_2}_{ey}}(t^1_G)$. The N_y actuators are then sequentially activated in this manner. In a *parallel system identification* process all actuators are simultaneously excited but with uncorrelated identification signals. Briefly speaking the *parallel system identification* scheme will normally provide the fastest plant estimation of the $N_y \times N_e$ secondary paths and $N_y \times N_x$ feedback paths while the *sequential system identification* scheme will be more robust and provide more accurate results.

Desired Signals Secondary Pathes

Fortunately, however, during on-line operation of the ANR-system rejection signals tentatively seek to minimize the resulting error signals. If the ANR-system should facilitate simultaneous multi-channel system identification contributions from other secondary source identification signals will also be present and should accordingly be taking into account.

An estimate of the desired signal $\hat{d}^{\hat{g}^{l,m}_{ey}}(t^1_G)$ can be derived from the error signal $\underset{\circledast}{e}_m(t^1_G)$ by subtracting the identification signal[4] contributions from other secondary sources

$$\hat{d}^{\hat{g}^{l,m}_{ey}}(t^1_G) = \underset{\circledast}{e}_m(t^1_m) - \underset{\circledcirc}{\hat{r}}_{m_{-l}}(t^1_m), \tag{7.6.3}$$

where the quantity $\underset{\circledcirc}{\hat{r}}_{m_{-l}}(t^1_m)$ is an estimate of the total rejection signal caused by the identification signals **excluding** the self term. In subsection 7.6.7 an expression for $\underset{\circledast}{\hat{r}}_{m_{-l}}(t^1_G)$ is provided viz. (7.6.10).

Desired Signals Feedback Pathes

During on-line operation of the ANR-system the feedback signals are a consequence of the control output signals being appropriately dosed such as to minimize the resulting error signals. The feedback signals will therefore pertubate the reference signals, but generally not decrease the level of the reference signals. Hence the on-line system identification of the feedback paths normally

[4] By definition an identification signal does not take part of the AC.

present a greater identification challenge to the system design as compared with on-line of the secondary paths. On the other hand if the feedback signals are veak their influence on the ANR performance will be marginal.

The desired signal $\hat{d}^{\hat{g}^{l,j}_{xy}}(t^1_G)$ is then readily available from the estimated feedforward reference signal defined in (7.5.6)

$$\hat{d}^{\hat{g}^{l,j}_{xy}}(t^1_G) = \underset{\circledast}{\hat{x}'_j}(t^1_j) - \underset{\circledcirc}{\hat{f}}_{j-l}(t^1_j), \tag{7.6.4}$$

where the quantity $\underset{\circledcirc}{\hat{f}}_{j-l}(t^1_j)$ is an estimate of the total feedback signal caused by the identification signals **excluding** the self term. In subsection 7.6.7 an expression for $\underset{\circledast}{\hat{f}}_{j-l}(t^1_G)$ is provided viz. (7.6.12).

The performance of the system identification process will largely be dependent on the degree of correlation between the identification signals and the disturbance signals and the feedback signals pertinent to the secondary paths and feedback paths estimation respectively.

7.6.4 Output

The filtering operation by the plants are generally described by the functions $\mathcal{G}^{l,m}_{ey}(y, t^1_G)$ and $\mathcal{G}^{l,j}_{xy}(y, t^1_G)$ pertinent for the secondary path and feedback path respectively. Similarly to the discussion made in subsection 7.2.6 and subsection 7.3.6 we will assume $\mathcal{G}^{l,m}_{ey}(y, t^1_G)$ and $\mathcal{G}^{l,j}_{xy}(y, t^1_G)$ to be of finite-duration and *linear*. By applying a FIR filter implementation the secondary path system identification output signal $\underset{\circledcirc}{y}^{\hat{g}^{l,m}_{ey}}(t^1_G + 1)$ and the feedback path system identification output signal $\underset{\circledcirc}{y}^{\hat{g}^{l,j}_{xy}}(t^1_G + 1)$ are simply obtained by multiplying $\underset{\circledcirc}{\mathring{x}}^{\hat{g}^l_y}_{t^1_G}$ defined in (7.6.2) by $\hat{g}^{l,m}_{ey,t^1_G}$ and $\hat{g}^{l,j}_{xy,t^1_G}$ respectively

$$\underset{\circledcirc}{y}^{\hat{g}^{l,m}_{ey}}(t^1_G) = \underset{\circledcirc}{\mathring{x}}^{\hat{g}^l_y}_{t^1_G}(1 : M^{l,m,1}_{\hat{g}_{ey}})\hat{g}^{l,m}_{ey,t^1_G} \tag{7.6.5}$$

and

$$\underset{\circledcirc}{y}^{\hat{g}^{l,j}_{xy}}(t^1_G) = \underset{\circledcirc}{\mathring{x}}^{\hat{g}^l_y}_{t^1_G}(1 : M^{l,j,1}_{\hat{g}_{xy}})\hat{g}^{l,j}_{xy,t^1_G}. \tag{7.6.6}$$

The plant model order quantities $M^{l,m,1}_{\hat{g}_{ey}}$ and $M^{l,j,1}_{\hat{g}_{xy}}$ were introduced in subsection 7.2.7 and subsection 7.3.7 respectively.

7.6.5 Error Signals

The secondary path and feedback path estimation error signals $e^{\hat{g}^{l,m}_{ey}}(t^1_G)$ and $e^{\hat{g}^{l,j}_{xy}}(t^1_G)$ are estimated by *subtracting*[5] the system identification output signals $\underset{\circledcirc}{y}^{\hat{g}^{l,m}_{ey}}(t^1_G)$, $\underset{\circledcirc}{y}^{\hat{g}^{l,j}_{xy}}(t^1_G)$ from the

[5]To the authors best knowledge the - sign is always applied in system identification.

disturbance signals $\hat{d}^{\hat{g}^{l,m}_{ey}}(t^1_G)$ and $\hat{d}^{\hat{g}^{l,j}_{xy}}(t^1_G)$ respectively

$$\underset{\circledast}{e}^{\hat{g}^{l,m}_{ey}}(t^1_G) = \hat{d}^{\hat{g}^{l,m}_{ey}}(t^1_G) - \underset{\circledcirc}{y}^{\hat{g}^{l,m}_{ey}}(t^1_G) \tag{7.6.7}$$

and

$$\underset{\circledast}{e}^{\hat{g}^{l,j}_{xy}}(t^1_G) = \hat{d}^{\hat{g}^{l,j}_{xy}}(t^1_G) - \underset{\circledcirc}{y}^{\hat{g}^{l,j}_{xy}}(t^1_G). \tag{7.6.8}$$

The disturbance signal $\hat{d}^{\hat{g}^{l,m}_{ey}}(t^1_G)$ and $\hat{d}^{\hat{g}^{l,j}_{xy}}(t^1_G)$ were introduced in subsection 7.6.3 viz. (7.6.3) and (7.6.4). The control output signal $\underset{\circledcirc}{y}^{\hat{g}^{l,m}_{ey}}(t^1_G)$ and $\underset{\circledcirc}{y}^{\hat{g}^{l,j}_{xy}}(t^1_G)$ were subject for discussion in subsection 7.6.4 viz. (7.6.5) and (7.6.6).

7.6.6 Tap-Weight Update Signals

Recalling from the discussion made in subsection 6.3.2 the argument for employing the mFx technique was to avoid performance degradation in terms of a lower convergence rate, an increased residual power and possibly instability. This problem was attributed to the lack of synchronization between the output $y(i)$ of the adaptive filter and the resulting error $e(i)$ due to the filtering and inherent time-delays caused by the plant. However, in the 'plantless' case the system identification output signal and error signal are in full synchronization. The estimated errors $\underset{\circledast}{\hat{e}}^{\hat{g}^{l,m}_{ey}}(t^1_G)$ and $\underset{\circledast}{\hat{e}}^{\hat{g}^{l,j}_{xy}}(t^1_G)$ provided in (7.6.7) and (7.6.8) will therefore be used for tap-weight update for the secondary path and feedback path estimation respectively.

In the domain of *electrical control* the adaptive filters use the unfiltered-reference signal $\underset{\circlearrowleft}{\mathring{x}}^{w}_{i}$.

$$u_i = \begin{cases} \underset{\circledcirc}{x}^{\hat{g}^{l,m}_{ey}}(t^1_G) & \text{secondary paths,} \\ \underset{\circledcirc}{x}^{\hat{g}^{l,j}_{xy}}(t^1_G) & \text{feedback paths.} \end{cases} \tag{7.6.9}$$

7.6.7 Identification Signal Cross Terms

As discussed in subsection 7.6.3 a non-vanishing correlation between the individual identification signals can lead to degradation of the system identification. However, by the subtracting the *estimated* effects from the other identification signals on the desired signals this can largely be compensated for. Following a procedure equivalent to subsection 7.5.7 an estimate of the total identification signal-driven rejection signal $\underset{\circledcirc}{\hat{r}}_{m_{-l}}(t^1_G + 1)$ present at the m'th error sensor but excluding the l'th secondary source is obtained as a superposition of the identification signal contribution from each of the $N_y - 1$ other secondary sources

$$\hat{\underset{\copyright}{r}}_{j-l}(t_G^1+1) = \sum_{\substack{l'=1 \\ l'\neq l}}^{N_y} \mathring{\underset{\copyright}{x}}_{t_G^1}^{\hat{g}_y^{l'}} (1 : M_{\hat{g}_{ey}}^{l',m}) \hat{g}_{ey,t_G^1}^{l',m} \tag{7.6.10}$$

$$= \sum_{\substack{l'=1 \\ l'\neq l}}^{N_y} \underset{\copyright}{y}^{\hat{g}_{ey}^{l',m}} (t_G^1+1), \tag{7.6.11}$$

where $\mathring{\underset{\copyright}{x}}_{t_G^1}^{\hat{g}_y^l}$ is defined in (7.6.2).

Similarly, an estimate of the total identification signal-driven feedback signal $\hat{\underset{\copyright}{f}}_{j-l}(t_G^1+1)$ present at the j'th reference sensor but excluding the l'th secondary source is obtained as a superposition of the identification signal contribution from each of the $N_y - 1$ other secondary sources

$$\hat{\underset{\copyright}{f}}_{j-l}(t_G^1+1) = \sum_{\substack{l'=1 \\ l'\neq l}}^{N_y} \mathring{\underset{\copyright}{x}}_{t_G^1}^{\hat{g}_y^{l'}} (1 : M_{\hat{g}_{xy}}^{l',j}) \hat{g}_{xy,t_G^1}^{l',j} \tag{7.6.12}$$

$$= \sum_{\substack{l'=1 \\ l'\neq l}}^{N_y} \underset{\copyright}{y}^{\hat{g}_{xy}^{l',j}} (t_G^1+1). \tag{7.6.13}$$

These terms vanish if the N_y actuators are invoked in a sequential system identification scheme.

7.6.8 Plant Estimates Copying

When the system identification has converged the copy plant estimates $\overset{\copyright}{\hat{g}}_{ey,t_G^1}^{l,m}$ and $\overset{\copyright}{\hat{g}}_{xy,t_G^1}^{l,j}$ are updated with the new values

$$\overset{\copyright}{\hat{g}}_{ey,t_G^1}^{l,m} = \hat{g}_{ey,t_G^1}^{l,m}. \tag{7.6.14}$$

and

$$\overset{\copyright}{\hat{g}}_{xy,t_G^1}^{l,j} = \hat{g}_{xy,t_G^1}^{l,j}. \tag{7.6.15}$$

Moreover, the corresponding decimated plant estimates are obtained from

$$\overset{\copyright}{\hat{g}}_{ey,t_G^2}^{l,m} \xleftarrow{\mathcal{D}_l^2(F_j^2(\theta),M_{\downarrow,l}^2,L_{\uparrow,l}^2)} \hat{g}_{ey,t_G^1}^{l,m} \tag{7.6.16}$$

and

$$\overset{\copyright}{\hat{g}}_{xy,t_G^2}^{l,j} \xleftarrow{\mathcal{D}_j^2(F_j^2(\theta),M_{\downarrow,j}^2,L_{\uparrow,j}^2)} \hat{g}_{xy,t_G^1}^{l,j}, \tag{7.6.17}$$

where the function $\mathcal{D}_l^2(F_j^2(\theta), M_{\downarrow,l}^2, L_{\uparrow,l}^2)$ and $\mathcal{D}_j^2(F_j^2(\theta), M_{\downarrow,j}^2, L_{\uparrow,j}^2)$ were defined in section 5.3.

7.6.9 System Identification Algorithm Summary

The ANC system identification adaptive filtering algorithm is constituted by first generating the stimuli $\underset{\circledcirc}{y_l}(t_G^1)$ and using the identity (7.6.1) to form the reference signals $\underset{\circledcirc}{x}^{\hat{g}_{ey}^l}(t_G^1)$ and $\underset{\circledcirc}{x}^{\hat{g}_{xy}^l}(t_G^1)$, next creating the unfiltered reference buffer $\underset{\circledcirc}{\mathring{x}}_{t_G^1}^{\hat{g}_y^l}$ from (7.6.2); then estimating the desired signals $\hat{d}^{\hat{g}_{ey}^{l,m}}(t_G^1)$ and $\hat{d}^{\hat{g}_{xy}^{l,j}}(t_G^1)$ from (7.6.3) and (7.6.4). Thereafter the identification signal-driven control output signals $\underset{\circledcirc}{y}^{\hat{g}_{ey}^{l,m}}(t_G^1)$ and $\underset{\circledcirc}{y}^{\hat{g}_{xy}^{l,j}}(t_G^1)$ provided by the system at the next iteration are computed (7.6.5) and (7.6.6). The error signals $\underset{\circledast}{\hat{e}}^{\hat{g}_{ey}^{l,m}}(t_G^1)$ and $\underset{\circledast}{\hat{e}}^{\hat{g}_{xy}^{l,j}}(t_G^1)$ are subsequently determined from (7.6.7) and (7.6.8).

The tap-weights are subsequently updated (at least at each block-update time) following one of the algorithms detailed in chapter 8 and Appendix J.

Finally, in preparation of the next iteration the mutual coupling between the secondary sources-driven identification signals i.e., $\underset{\circledcirc}{\hat{r}}_{m-l}(t_G^1+1)$ and $\underset{\circledcirc}{\hat{f}}_{j-l}(t_G^1+1)$ are estimated from (7.6.10) and (7.6.12) respectively.

Upon convergence of the system identification process the plant copies $\overset{\copyright}{\hat{g}}_{ey,t_G^1}^{l,m}$ and $\overset{\copyright}{\hat{g}}_{xy,t_G^1}^{l,j}$ are updated according to (7.6.14) and (7.6.15) and the corresponding decimated plant estimates $\overset{\copyright}{\hat{g}}_{ey,t_G^2}^{l,m}$ and $\overset{\copyright}{\hat{g}}_{xy,t_G^2}^{l,j}$ are then obtained from (7.6.16) and (7.6.17) respectively.

7.7 System Identification of Secondary Pathes

The objective of the system identification is multilateral. The first objective is to verify that the system identification results obtained from statistical data analysis (SDA) reported in section 11.5 on page 489 can be reproduced by the adaptive system identification approach described in section 7.6 on page 326. A second objective is to examine the potential benefits of using the $\alpha\gamma\Pi\epsilon$-affine projection algorithm ($\alpha\gamma\Pi\epsilon$-APA) and the fast array recursive least-squares (FARLS) algorithms instead of the least-mean-squares (LMS) algorithm most frequently employed in the active control community. A third objective is to determine the filter orders required for FIR filter implementation of the various secondary paths considered. For this purpose three different filter orders ($M_{\hat{g}_{ey}^{1,1}} = 55, 70, 100$) are selected for the $\mathbf{t}$-domain Wiener-Hopf (WH) filter. A fourth objective is to obtain specific data for the group delays involved in the secondary paths. As discussed in chapter 5 on page 249 it is important that group delays are sufficiently small as they otherwise ultimatively can limit the achievable ANR performance.

The topology consists of ten reference sensors ($N_x = 10$) BK4949 surface microphones flush-mounted on a Gentex HGU-55/P helmet mounted on a BK 4128 C head and torso simulator (HATS) that in turn includes the BK 4159 C left ear simulator and the BK 4158 C right ear simulator. Hence, the amount of performance sensors amounts to two, that is, $N_p = 2$. The performance signals acquired by the left and right ear simulator are designated by $d_1^p(t)$ and $d_2^p(t)$ respectively. The ten reference signals are designated by $x_1(t), \ldots, x_{10}(t)$. Due to the inherent symmetry of the system the Terma Earcup Audio System is used on the left ear only. Accordingly, only a

single actuator (earphone) and a single error sensor are used ($N_y = N_e = 1$). The disturbance signal is designated by $d_1(t)$.

Hence, the system identification includes a total of $N_y(N_x + N_e + N_p) = 1(10 + 1 + 2) = 13$ different secondary paths.

All system identification processes are conducted at multi-rate level 1 with $f_s^1 = 24$ kHz. For this purpose the source signal with f_s =65.536 kHz is resampled prior to the system identification.

7.7.1 Reference Plants for System Identification

In order to assess the quality of the system identification presented next a reference system identification is obtained from using a large (sufficient) number of weights over an extended 8.0 s period corresponding to 192000 samples and for a 5 V (peak) signal excitation level. The resulting weights, that is, the impulse response functions for $g_{ey}^{1,1}, g_{xy}^{1,1}, g_{xy}^{1,5}$ and $g_{py}^{1,1}$ are depicted in Simulation 7.7.1 - 7.7.4 on pages 335–338. The number of weights amounts to $M_{g_{ey}^{l,m}} = 120, M_{g_{xy}^{l,j}} = 700$ and $M_{g_{py}^{l,k}} = 200$ respectively.

Hence, in the subsequent analysis we will use $g_{ey}^{l,m}, g_{xy}^{l,j}$ and $g_{py}^{l,k}$ determined from this reference measurement as "true" secondary paths.

7.7.2 System Identification of Secondary Pathes $g_{ey}^{l,m}$

As $N_e = N_y = 1$ only the $\hat{g}_{ey}^{l,m} = \hat{g}_{ey}^{1,1}$ secondary path is considered. The system identification process is examined for a $0 - 0.8$ s period. The earphone is excited by a 5 V (peak) random white noise (RWN) Gaussian distributed signal. The following candidate adaptive filters are considered:

1. **t**-domain WH ($\alpha = 1e-4, 1e-5, 1e-6, T_{WSS} = 0, M = 55, 70, 100, 120$);

2. $\alpha\gamma\Pi\epsilon$-NLMS ($M = 70, L_B = 1, \mu = 0.15, \alpha = 1e-5, \gamma = 1e-5, \Pi = 0, \epsilon = 1e-006, \breve{w} = 0, W_e = \mathrm{I}), T_{Eu} = 20$);

3. $\alpha\gamma\Pi\epsilon$-APA ($M = 70, L_B = 1, \mu = 0.15, \alpha = 1e-5, \gamma = 1e-5, \Pi = 0, \epsilon = 1e-006, \breve{w} = 0, W_e = \mathrm{I}$);

4. FARLS ($M = 70, L_B = 1, \lambda = 0.998, 0.999, 0.9995, \eta = 0.125, \alpha = 1e-5, T_{SW} = 0, \mathrm{Calc} = 1$);

System Identification of Secondary Pathes $g_{ey}^{l,m}$ **t**-domain WH

In order to determine the order of the FIR filter necessary the system identification first employed the **t**-domain WH for $\alpha = 1e-4, 1e-5, 1e-6, T_{WSS} = 0, M = 55, 70, 100, 120$. The results are summarized in Simulation 7.7.5 on page 339. It can readily be seen that only marginal improvements are available from using more than 70 weights. Hence, also recalling that a FBS employing the IMC is relative robust to plant model imperfections, the secondary path is accordingly modeled by a FIR filter with $M_{g_{ey}}^{1,1} = 70$. This also agrees with the result in Simulation 7.7.1 on the next page, where only negligible contribution to the impulse response function is made by

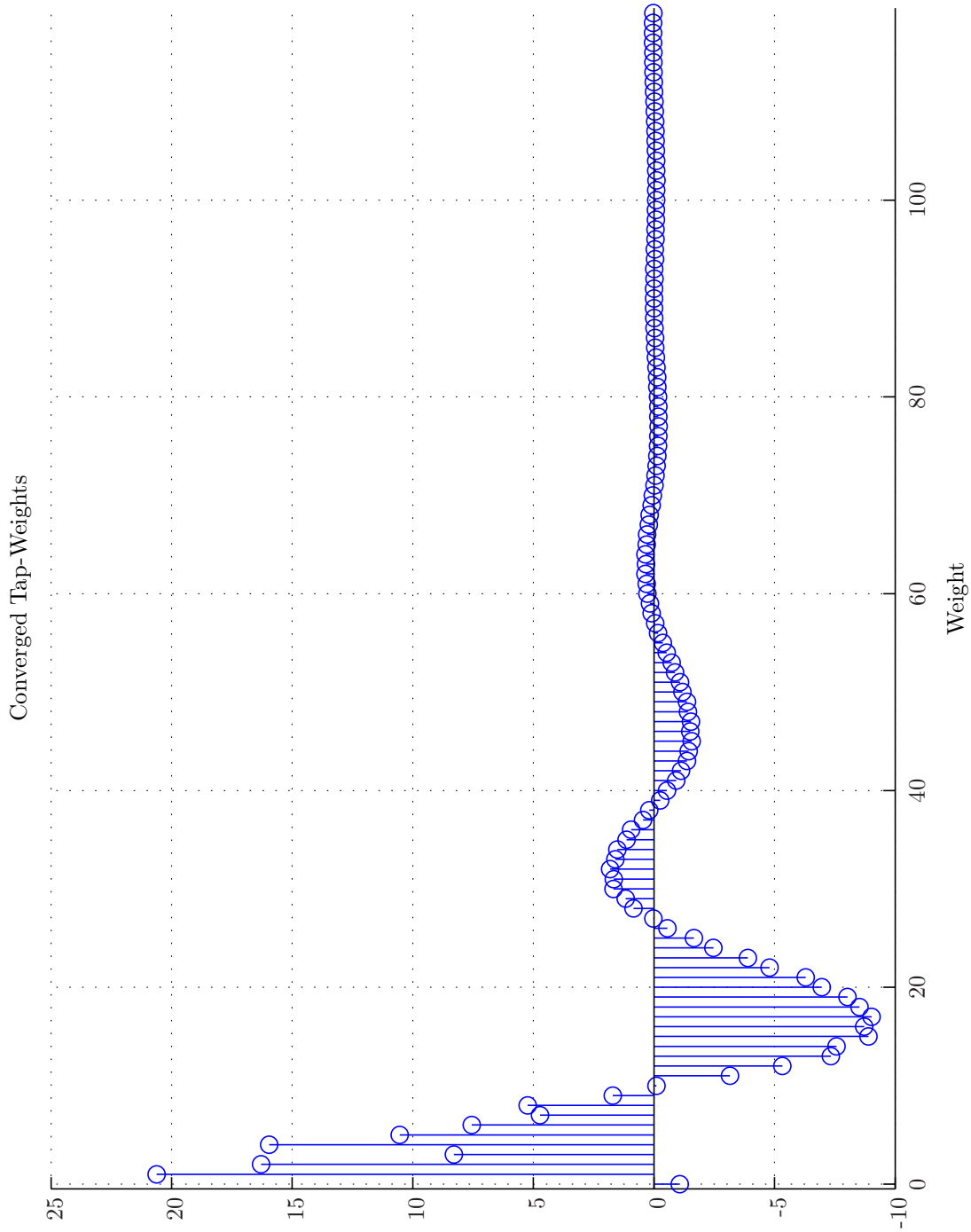

Sim 7.7.1: *Converged Tap-weights.* **Adaptive Filter** $\hat{g}_{ey}$: $\hat{g}_{ey}^{1,1}$: Wiener Hopf ($M = 120, \alpha = 1e-005$, $T_{WSS} = 0$,**t**-domain); **Main:** $f_s^0 = 192$ kHz, $f_s^1 = 24$ kHz, $R_{\downarrow}^1 = \frac{1}{8} = 0.125$, Elliptic LPF ($f_s = 192$ kHz,$f_{pass} = 11$ kHz,$f_{stop} = 12$ kHz, $A_{pass} = 2$ dB, $A_{stop} = 40$ dB), $f_s^2 = 24$ kHz, $R_{\downarrow}^2 = \frac{1}{1} = 1$, Dummy; **Topology:** BK 4949 surface microphones flush-mounted on Gentex HGU-55/P helmet mounted on a BK 4128 C HATS, Terma Earcup Audio System (Feedforwardback, mFx, $N_x = 10, N_e = 2, N_y = 1, N_p = 2, N_v = 0$); **Plants:** SysID/20080113T014624 ($g_{xy,\infty}^{1,1}$: (FIR : $M_{gxy}^{1,1} = 481$), $g_{xy,\infty}^{1,2}$: (FIR : $M_{gxy}^{1,2} = 481$), $g_{xy,\infty}^{1,3}$: (FIR : $M_{gxy}^{1,3} = 481$), $g_{xy,\infty}^{1,4}$: (FIR : $M_{gxy}^{1,4} = 481$), $g_{xy,\infty}^{1,5}$: (FIR : $M_{gxy}^{1,5} = 481$), $g_{xy,\infty}^{1,6}$: (FIR : $M_{gxy}^{1,6} = 481$), $g_{xy,\infty}^{1,7}$: (FIR : $M_{gxy}^{1,7} = 481$), $g_{xy,\infty}^{1,8}$: (FIR : $M_{gxy}^{1,8} = 481$), $g_{xy,\infty}^{1,9}$: (FIR : $M_{gxy}^{1,9} = 481$), $g_{xy,\infty}^{1,10}$: (FIR : $M_{gxy}^{1,10} = 481$), $g_{ey,\infty}^{1,1}$: (FIR : $M_{gey}^{1,1} = 71$), $g_{ey,\infty}^{1,2}$: (FIR : $M_{gey}^{1,2} = 71$), $g_{py,\infty}^{1,1}$: (FIR : $M_{gpy}^{1,1} = 151$), $g_{py,\infty}^{1,2}$: (FIR : $M_{gpy}^{1,2} = 151$)); **Signals:** *System Identification:* Random White Noise ($\mathcal{N}(0, 0.2)$), Output: 5 V, $f_s = 65.536$ kHz; Time: $0 - 8$ s; **Scenario:** `SystemIdentification(65536Hz)/20080317T021401`.

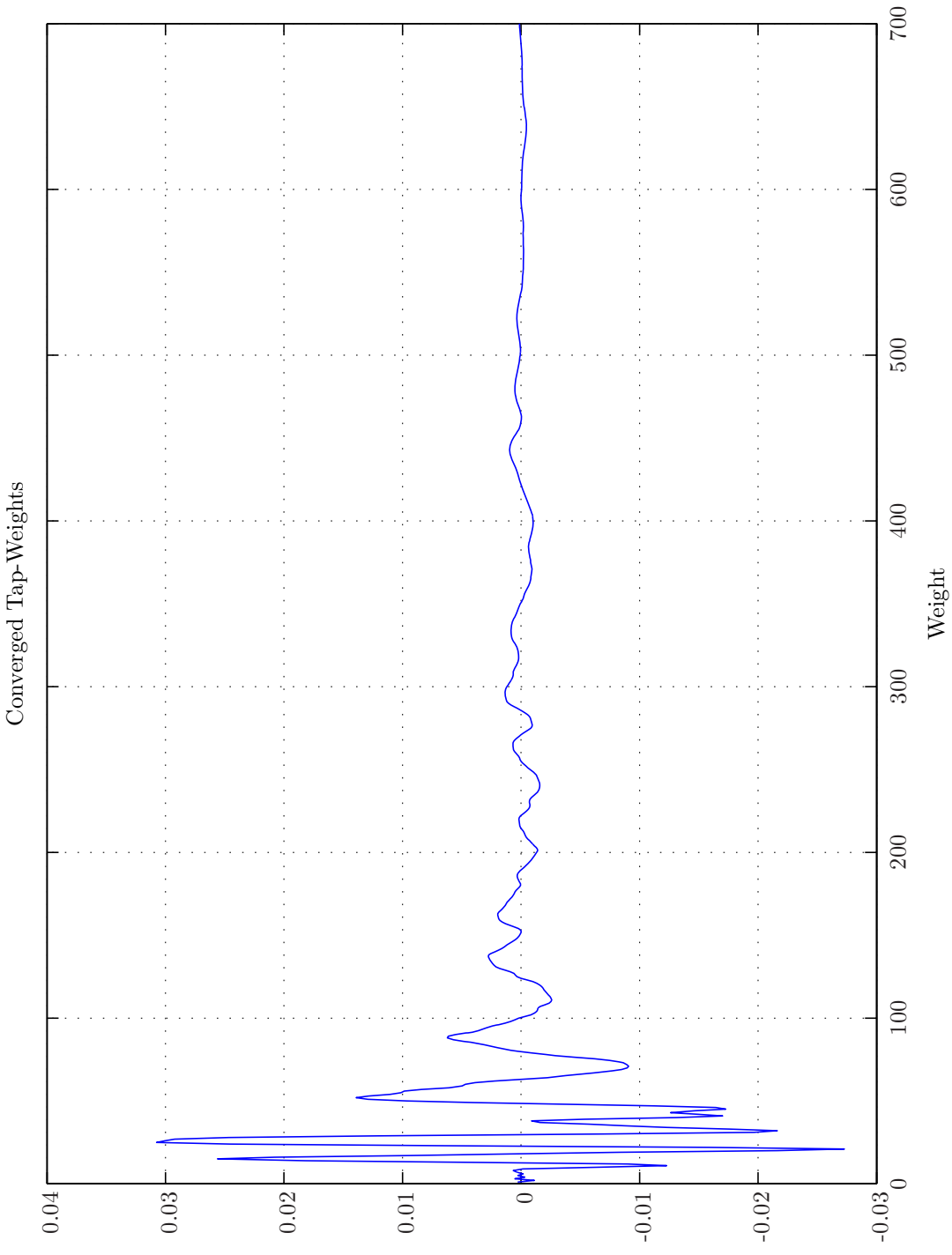

Sim 7.7.2: *Converged Tap-weights.* **Adaptive Filter** $\hat{g}_{xy}$: $\hat{g}^{1,1}_{xy}$: Wiener Hopf ($M = 700, \alpha = 1e-005, T_{WSS} = 0.1$**t**-domain); **Main:** $f^0_s = 192$ kHz, $f^1_s = 24$ kHz, $R^1_\updownarrow = \frac{1}{8} = 0.125$, Elliptic LPF ($f_s = 192$ kHz, $f_{pass} = 11$ kHz, $f_{stop} = 12$ kHz, $A_{pass} = 2$ dB, $A_{stop} = 40$ dB), $f^2_s = 24$ kHz, $R^2_\updownarrow = \frac{1}{1} = 1$, Dummy; **Topology:** BK 4949 surface microphones flush-mounted on Gentex HGU-55/P helmet mounted on a BK 4128 C HATS, Terma Earcup Audio System (Feedforwardback, mFx, $N_x = 10, N_e = 2, N_y = 1, N_p = 2, N_v = 0$); **Plants:** SysID/20080113T014624 ($g^{1,1}_{xy,\infty}$: (FIR : $M^{1,1}_{gxy} = 481$), $g^{1,2}_{xy,\infty}$: (FIR : $M^{1,2}_{gxy} = 481$), $g^{1,3}_{xy,\infty}$: (FIR : $M^{1,3}_{gxy} = 481$), $g^{1,4}_{xy,\infty}$: (FIR : $M^{1,4}_{gxy} = 481$), $g^{1,5}_{xy,\infty}$: (FIR : $M^{1,5}_{gxy} = 481$), $g^{1,6}_{xy,\infty}$: (FIR : $M^{1,6}_{gxy} = 481$), $g^{1,7}_{xy,\infty}$: (FIR : $M^{1,7}_{gxy} = 481$), $g^{1,8}_{xy,\infty}$: (FIR : $M^{1,8}_{gxy} = 481$), $g^{1,9}_{xy,\infty}$: (FIR : $M^{1,9}_{gxy} = 481$), $g^{1,10}_{xy,\infty}$: (FIR : $M^{1,10}_{gxy} = 481$), $g^{1,1}_{ey,\infty}$: (FIR : $M^{1,1}_{gey} = 71$), $g^{1,2}_{ey,\infty}$: (FIR : $M^{1,2}_{gey} = 71$), $g^{1,1}_{py,\infty}$: (FIR : $M^{1,1}_{gpy} = 151$), $g^{1,2}_{py,\infty}$: (FIR : $M^{1,2}_{gpy} = 151$)); **Signals:** *System Identification:* Random White Noise ($\mathcal{N}(0, 0.2)$), Output: 5 V, $f_s = 65.536$ kHz; Time: $0 - 8$ s; **Scenario:** SystemIdentification(65536Hz)/20080317T021401.

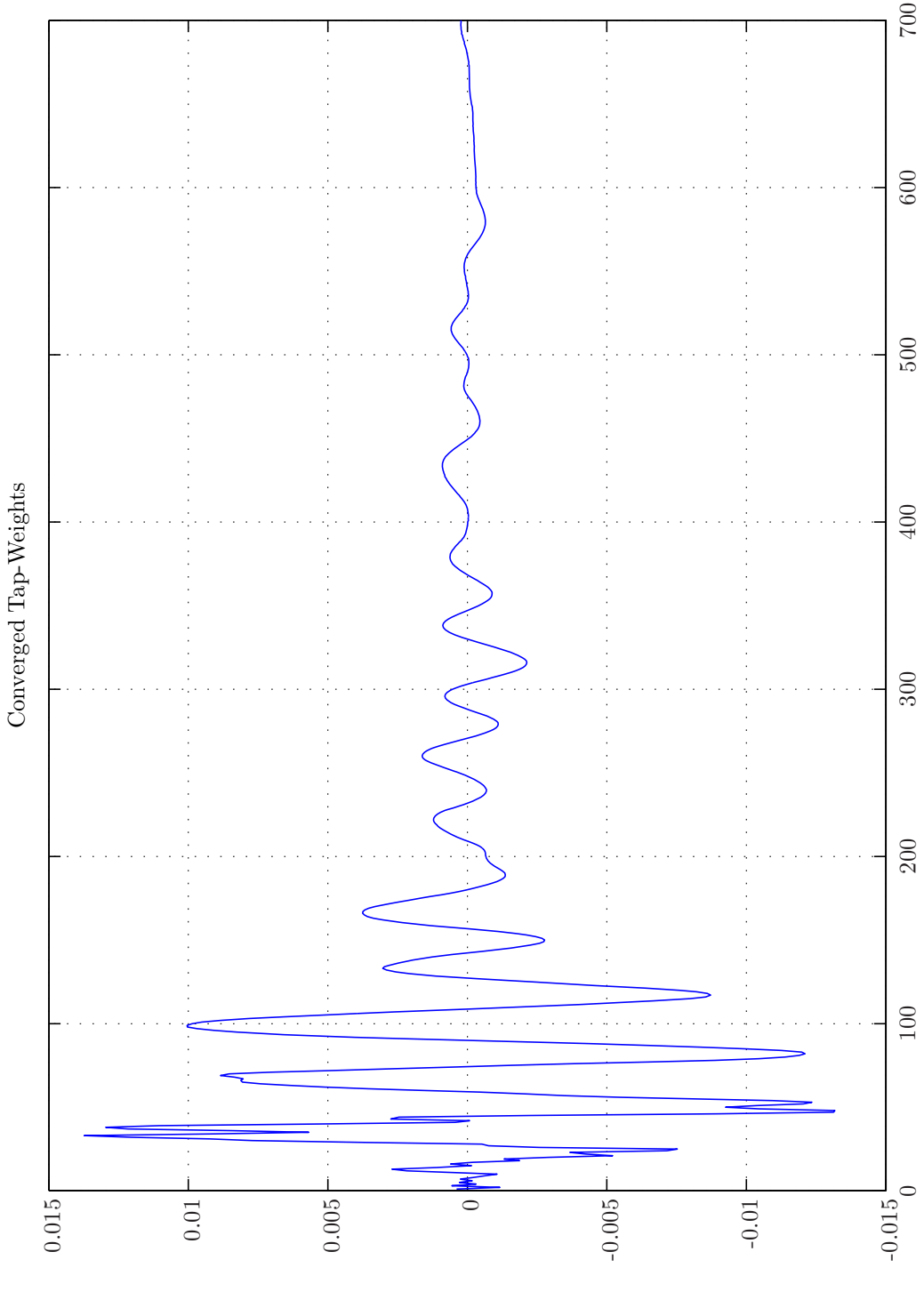

Sim 7.7.3: *Converged Tap-weights.* **Adaptive Filter** $\hat{g}_{xy}$: $\hat{g}_{xy}^{1,5}$: Wiener Hopf ($M = 700, \alpha = 1e-005, T_{WSS} = 0$,**t**-domain); **Main:** $f_s^0 = 192$ kHz, $f_s^1 = 24$ kHz, $R_{\downarrow}^1 = \frac{1}{8} = 0.125$, Elliptic LPF ($f_s = 192$ kHz, $f_{pass} = 11$ kHz, $f_{stop} = 12$ kHz, $A_{pass} = 2$ dB, $A_{stop} = 40$ dB), $f_s^2 = 24$ kHz, $R_{\downarrow}^2 = \frac{1}{1} = 1$, Dummy; **Topology:** BK 4949 surface microphones flush-mounted on Gentex HGU-55/P helmet mounted on a BK 4128 C HATS, Terma Earcup Audio System (Feedforwardback, mFx, $N_x = 10$, $N_e = 2, N_y = 1, N_p = 2, N_v = 0$); **Plants:** SysID/20080113T014624 ($g_{xy,\infty}^{1,1}$: (FIR : $M_{gxy}^{1,1} = 481$), $g_{xy,\infty}^{1,2}$: (FIR : $M_{gxy}^{1,2} = 481$), $g_{xy,\infty}^{1,3}$: (FIR : $M_{gxy}^{1,3} = 481$), $g_{xy,\infty}^{1,4}$: (FIR : $M_{gxy}^{1,4} = 481$), $g_{xy,\infty}^{1,5}$: (FIR : $M_{gxy}^{1,5} = 481$), $g_{xy,\infty}^{1,6}$: (FIR : $M_{gxy}^{1,6} = 481$), $g_{xy,\infty}^{1,7}$: (FIR : $M_{gxy}^{1,7} = 481$), $g_{xy,\infty}^{1,8}$: (FIR : $M_{gxy}^{1,8} = 481$), $g_{xy,\infty}^{1,9}$: (FIR : $M_{gxy}^{1,9} = 481$), $g_{xy,\infty}^{1,10}$: (FIR : $M_{gxy}^{1,10} = 481$), $g_{ey,\infty}^{1,1}$: (FIR : $M_{gey}^{1,1} = 71$), $g_{ey,\infty}^{1,2}$: (FIR : $M_{gey}^{1,2} = 71$), $g_{py,\infty}^{1,1}$: (FIR : $M_{gpy}^{1,1} = 151$), $g_{py,\infty}^{1,2}$: (FIR : $M_{gpy}^{1,2} = 151$)); **Signals:** *System Identification:* Random White Noise ($\mathcal{N}(0, 0.2)$), Output: 5 V, $f_s = 65.536$ kHz; Time: $0 - 8$ s; **Scenario:** `SystemIdentification(65536Hz)/20080317T021401`.

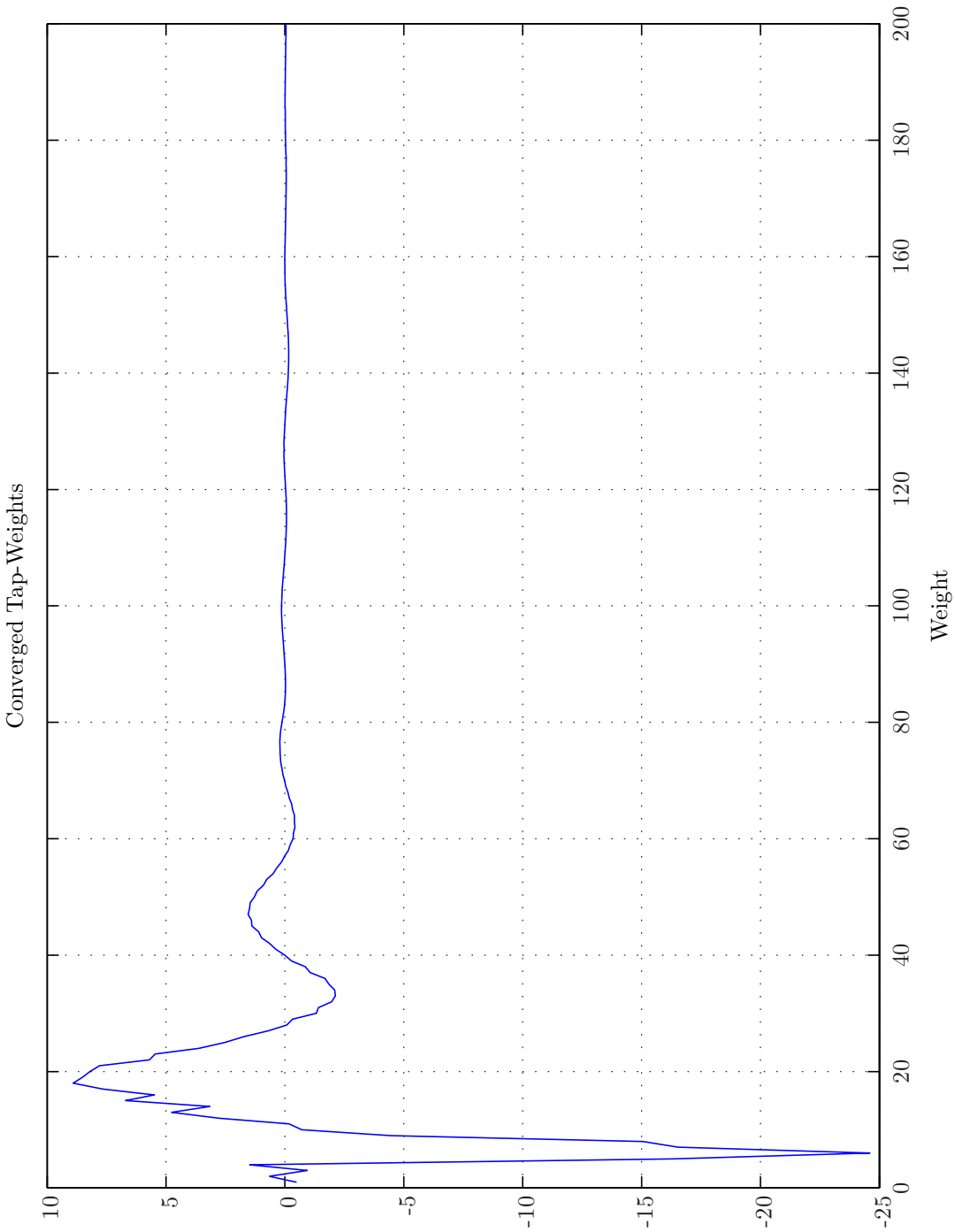

Sim 7.7.4: *Converged Tap-weights.* **Adaptive Filter** $\hat{g}_{py}$: $\hat{g}_{py}^{1,1}$: Wiener Hopf ($M = 200, \alpha = 1e-005, T_{WSS} = 0.1$**t**-domain); **Main:** $f_s^0 = 192$ kHz, $f_s^1 = 24$ kHz, $R_{\updownarrow}^1 = \frac{1}{8} = 0.125$, Elliptic LPF ($f_s = 192$ kHz, $f_{pass} = 11$ kHz, $f_{stop} = 12$ kHz, $A_{pass} = 2$ dB, $A_{stop} = 40$ dB), $f_s^2 = 24$ kHz, $R_{\updownarrow}^2 = \frac{1}{1} = 1$, Dummy; **Topology:** BK 4949 surface microphones flush-mounted on Gentex HGU-55/P helmet mounted on a BK 4128 C HATS, Terma Earcup Audio System (Feedforwardback, mFx, $N_x = 10, N_e = 2, N_y = 1, N_p = 2, N_v = 0$); **Plants:** SysID/20080113T014624 ($g_{xy,\infty}^{1,1}$: (FIR : $M_{gxy}^{1,1} = 481$), $g_{xy,\infty}^{1,2}$: (FIR : $M_{gxy}^{1,2} = 481$), $g_{xy,\infty}^{1,3}$: (FIR : $M_{gxy}^{1,3} = 481$), $g_{xy,\infty}^{1,4}$: (FIR : $M_{gxy}^{1,4} = 481$), $g_{xy,\infty}^{1,5}$: (FIR : $M_{gxy}^{1,5} = 481$), $g_{xy,\infty}^{1,6}$: (FIR : $M_{gxy}^{1,6} = 481$), $g_{xy,\infty}^{1,7}$: (FIR : $M_{gxy}^{1,7} = 481$), $g_{xy,\infty}^{1,8}$: (FIR : $M_{gxy}^{1,8} = 481$), $g_{xy,\infty}^{1,9}$: (FIR : $M_{gxy}^{1,9} = 481$), $g_{xy,\infty}^{1,10}$: (FIR : $M_{gxy}^{1,10} = 481$), $g_{ey,\infty}^{1,1}$: (FIR : $M_{gey}^{1,1} = 71$), $g_{ey,\infty}^{1,2}$: (FIR : $M_{gey}^{1,2} = 71$), $g_{py,\infty}^{1,1}$: (FIR : $M_{gpy}^{1,1} = 151$), $g_{py,\infty}^{1,2}$: (FIR : $M_{gpy}^{1,2} = 151$)); **Signals:** *System Identification:* Random White Noise ($\mathcal{N}(0, 0.2)$), Output: 5 V, $f_s = 65.536$ kHz; Time: $0 - 8$ s; **Scenario:** SystemIdentification(65536Hz)/20080317T021401.

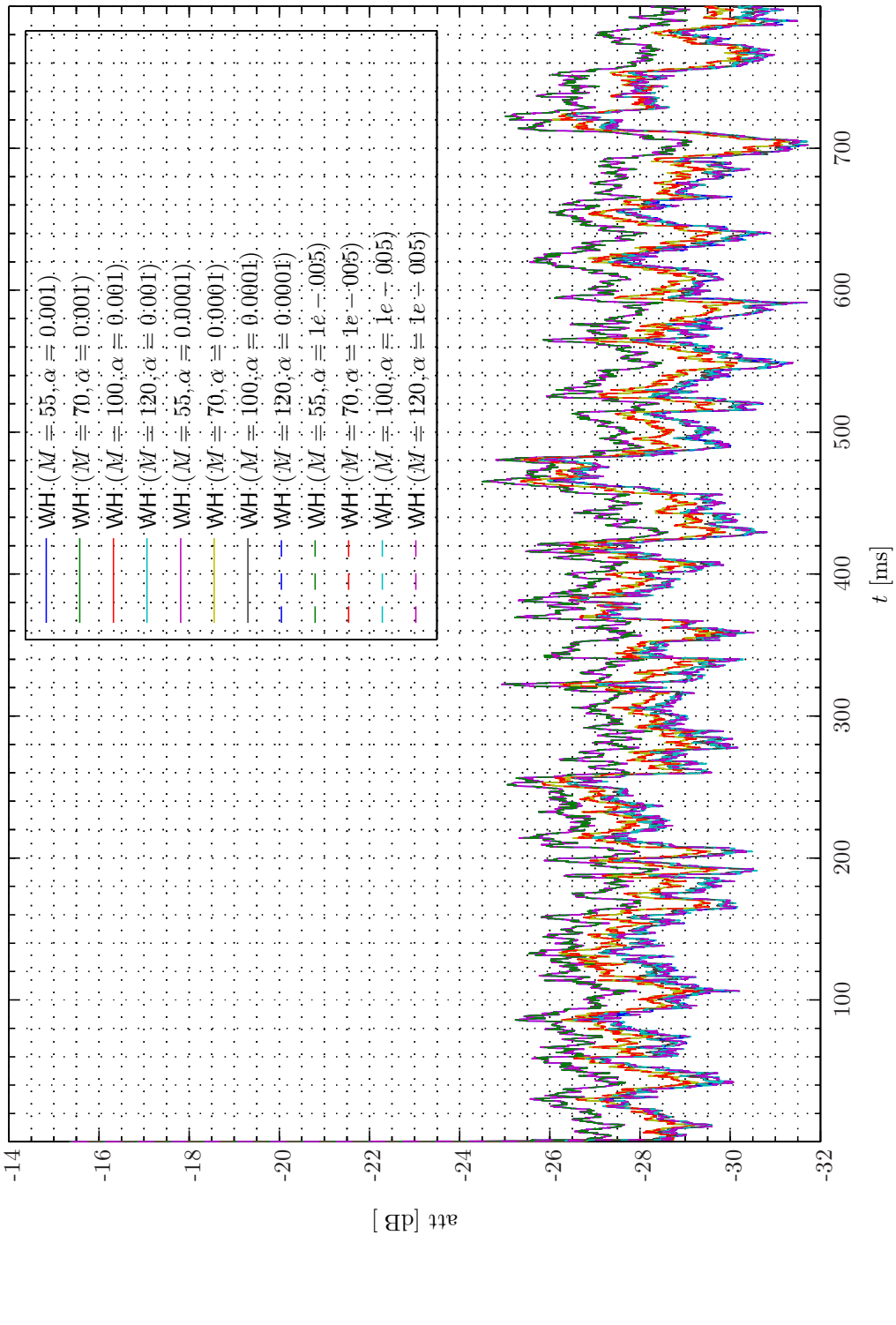

Sim 7.7.5: *Time-Domain: Attenuation.* **Adaptive Filter** $\hat{g}_{ey}$: $\hat{g}_{ey}^{1,1}$: WH ($T_{WSS} = 0, domain = 0$); **Main:** $f_s^0 = 192$ kHz, $f_s^1 = 24$ kHz, $R_\downarrow^1 = \frac{1}{8} = 0.125$, Elliptic LPF ($f_s = 192$ kHz, $f_{pass} = 11$ kHz, $f_{stop} = 12$ kHz, $A_{pass} = 2$ dB, $A_{stop} = 40$ dB), $f_s^2 = 24$ kHz, $R_\uparrow^2 = \frac{1}{1} = 1$, Dummy; **Topology:** BK 4949 surface microphones flush-mounted on Gentex HGU-55/P helmet mounted on a BK 4128 C HATS, Terma Earcup Audio System (Feedforward, mFx, $N_x = 10, N_e = 1, N_y = 1, N_p = 2, N_v = 0$); **Plants:** SysID/20080321T134130 ($g_{xy,\infty}^{1,1}$: (FIR : $M_{gxy}^{1,1} = 700$), $g_{xy,\infty}^{1,2}$: (FIR : $M_{gxy}^{1,2} = 700$), $g_{xy,\infty}^{1,3}$: (FIR : $M_{gxy}^{1,3} = 700$), $g_{xy,\infty}^{1,4}$: (FIR : $M_{gxy}^{1,4} = 700$), $g_{xy,\infty}^{1,5}$: (FIR : $M_{gxy}^{1,5} = 700$), $g_{xy,\infty}^{1,6}$: (FIR : $M_{gxy}^{1,6} = 700$), $g_{xy,\infty}^{1,7}$: (FIR : $M_{gxy}^{1,7} = 700$), $g_{xy,\infty}^{1,8}$: (FIR : $M_{gxy}^{1,8} = 700$), $g_{xy,\infty}^{1,9}$: (FIR : $M_{gxy}^{1,9} = 700$), $g_{xy,\infty}^{1,10}$: (FIR : $M_{gxy}^{1,10} = 700$), $g_{ey,\infty}^{1,1}$: (FIR : $M_{gey}^{1,1} = 120$), $g_{py,\infty}^{1,1}$: (FIR : $M_{gpy}^{1,2} = 200$), $g_{py,\infty}^{1,2}$: (FIR : $M_{gpy}^{1,2} = 200$)); **Signals:** *System Identification:* Random White Noise ($\mathcal{N}(0, 0.2)$), Output: 5 V, $f_s = 65.536$ kHz; Time: $0 - 0.8$ s; **Scenario:** SystemIdentification(65536Hz)/20080321T202249.

the weights above 70 as also confirmed by the impulse response function obtained from SDA viz. Simulation 11.5.9 on page 505 only a marginal better performance is obtained by increasing the filter order to $M_{g_{ey}}^{1,1} = 100$ corresponding to 2.4 ms. Moreover, it can be observed that increasing the leakage from a small value $\alpha = 1 - e5$ to a relative large value $\alpha = 1e - 3$ does not change the quality of the system identification appreciably. The reason is that even for $\alpha = 1e - 3$ the corresponding random white noise signal is an order of magnitude lower than the excitation signal.

The results from a SDA conducted on the converged adaptive filter are presented in Simulation 7.7.6 - 7.7.8 on pages 341–343. The following modified single-sided periodogram parameters are used: $f_s = 24\,\text{kHz}, N_{DFT} = 8192, L_{DFT} = 4800, R_{DFT} = 2400, \text{Hanning}, \Delta f_m = 20\,\text{Hz}, T_{DFT} = 0.2\,\text{s}, N_{f,DFT} = 4097, \Delta f_{DFT} = 2.93\,\text{Hz}, K_{DFT} = 1$. In Simulation 7.7.6 the auto spectral density functions for $d^{\hat{g}_{ey}^{1,1}}(t)$ and $e^{\hat{g}_{ey}^{1,1}}(t)$ are illuminated. The error spectrum, that is, $S_{e^{\hat{g}_{ey}^{1,1}} e^{\hat{g}_{ey}^{1,1}}}(f)$ exhibits white noise characteristics as expected. Being excited by a RWN signal the desired signal spectrum, that is, $S_{d^{\hat{g}_{ey}^{1,1}} d^{\hat{g}_{ey}^{1,1}}}(f)$ closely matches the secondary path transfer function as obtained from a purely SDA in Simulation 11.5.3 - 11.5.4 on pages 499–500. The pseudo transfer function linking the desired signal $d^{\hat{g}_{ey}^{1,1}}(t)$ to the error signal $e^{\hat{g}_{ey}^{1,1}}(t)$ is depicted in Simulation 7.7.7 - 7.7.8 on pages 342–343. From these figures it can be concluded that the adaptive filter provides best system identification in the frequency region from 600 Hz to 800 Hz. This corresponds also the frequency region where the secondary path attains a resonance, that is, where the best signal-to-noise ratio (SNR) is available for the system identification process.

System Identification of Secondary Pathes $g_{ey}^{l,m}$ $\alpha\gamma\Pi\epsilon$-NLMS

In the subsequent text the detailed results from a simulation using an adaptive LMS filter with the following parameters: $\alpha\gamma\Pi\epsilon$-NLMS ($M = 70, L_B = 1, \mu = 0.15, \alpha = 1e - 5, \gamma = 1e - 5, \Pi = 0, \epsilon = 1e - 006, \breve{w} = 0, W_e = \text{I}), T_{Eu} = 20$) defined in chapter 8 on page 371 is presented.

In Simulation 7.7.9 on page 344 the time-domain convergence of the adaptive filter over the 800 ms is shown. Specifically, the desired-, output-, error signals and attenuation, that is, $d^{\hat{g}_{ey}^{1,1}}(t), y^{\hat{g}_{ey}^{1,1}}(t), e^{\hat{g}_{ey}^{1,1}}(t)$ and $\mathcal{A}^{\hat{g}_{ey}^{1,1}}(t)$ introduced in Figure 7.5 on page 327 are displayed. It is observed that the attenuation curve for the LMS adaptive filter follows an almost constant slope while adapting and the converging time is approximately 50 ms (see Simulation 7.7.19 on page 356). The attenuation $\mathcal{A}^{\hat{g}_{ey}^{1,1}}(t) \approx -27$ dB corresponding to a match of $1 - 10^{-2.7} \approx 0.998$ to 1.

Finally, the converged adaptive tap-weights that resemble the impulse response function of the secondary path are shown in Simulation 7.7.10. By comparison with Simulation 11.5.9 we recognize a quite similar impulse response function as obtained from the statistical data analysis.

System Identification of Secondary Pathes $g_{ey}^{l,m}$ $\alpha\gamma\Pi\epsilon$-APA

The adaptive affine projection algorithm (APA) filter uses the following fixed parameters: $\alpha\gamma\Pi\epsilon$-affine projection algorithm ($M = 70, L_B = 1, \mu = 0.15, \alpha = 1e - 5, \gamma = 1e - 5, \Pi = 0, \epsilon = 1e - 006, \breve{w} = 0, W_e = 1$) that are defined in section 8.6 on page 396. In total six combinations are examined, namely for $K = 1, 2, 4$ (number of samples to estimate the ensemble-averaged covariance matrices) and for $\Delta = 1, 4$ (number of samples used for inter-block decorrelation).

In Simulation 7.7.11 the time-domain convergence of the adaptive filter with $K = 4$ and $\Delta = 1$

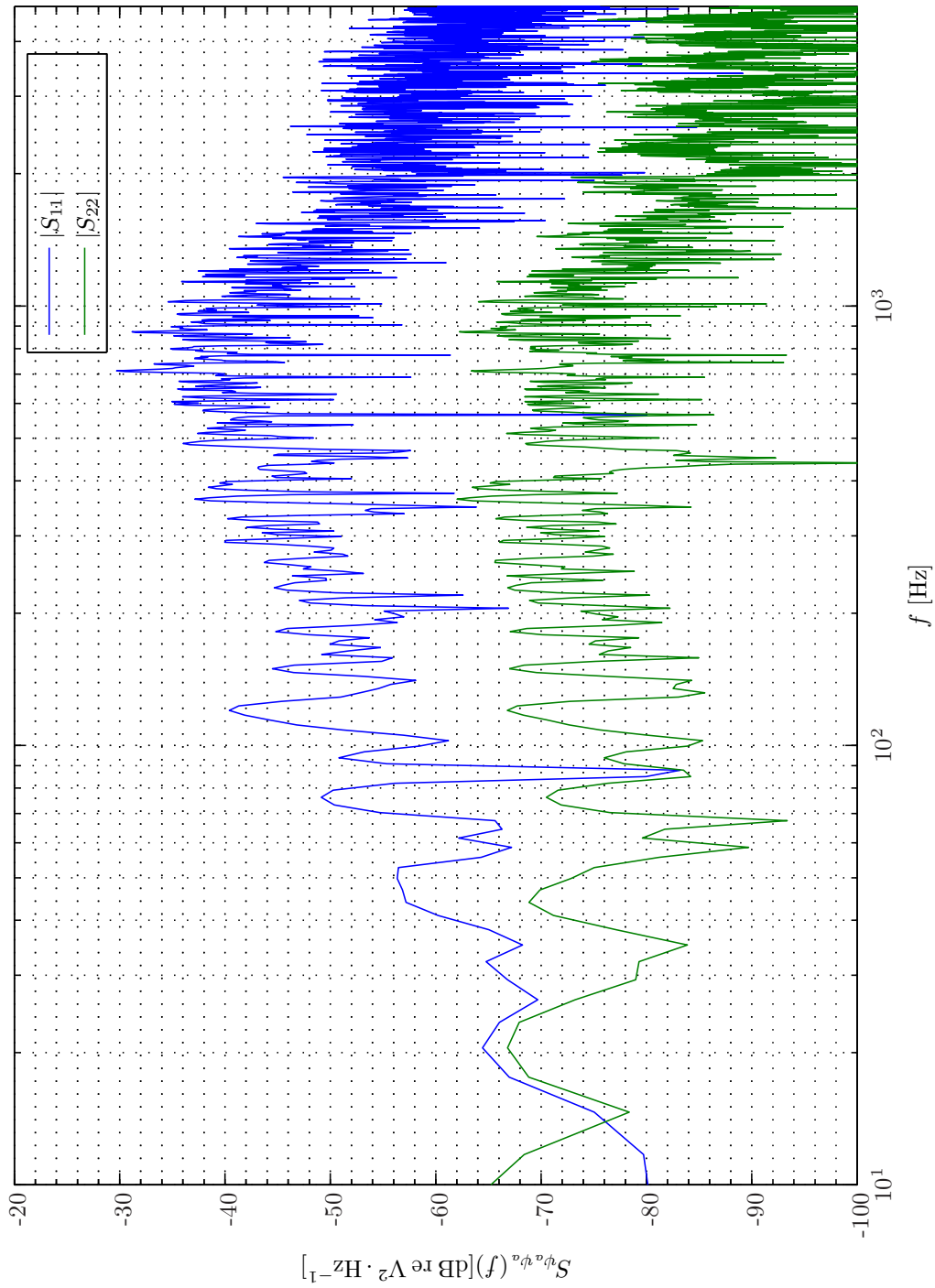

Sim 7.7.6: *Autospectral Density Functions*: **Statistical Data Analysis**: Single-Sided Modified Periodogram, $f_s = 24$ kHz, $N_{DFT} = 8192$, $L_{DFT} = 4800$, $R_{DFT} = 2400$, Hanning, $\Delta f_m = 20.0042$ Hz, $T_{DFT} = 0.2$ s, $N_{f,DFT} = 4097$, $\Delta f_{DFT} = 2.9297$ Hz, $K_{DFT} = 1$; **Adaptive Filter** $\hat{g}_{ey}$: Wiener Hopf ($M = 55, \alpha = 1e-005, T_{WSS} = 0$,**t**-domain); **Main:** $f_s^0 = 192$ kHz, $f_s^1 = 24$ kHz, $R_\updownarrow^1 = \frac{1}{8} = 0.125$, Elliptic LPF ($f_s = 192$ kHz, $f_{pass} = 11$ kHz, $f_{stop} = 12$ kHz, $A_{pass} = 2$ dB, $A_{stop} = 40$ dB), $f_s^2 = 24$ kHz, $R_\updownarrow^2 = \frac{1}{1} = 1$, Dummy; **Topology:** BK 4949 surface microphones flush-mounted on Gentex HGU-55/P helmet mounted on a BK 4128 C HATS, Terma Earcup Audio System (Feedforward, mFx, $N_x = 10, N_e = 1, N_y = 1, N_p = 2, N_v = 0$); **Plants:** SysID/20080321T134130 ($g_{xy,\infty}^{1,1}$: (FIR : $M_{gxy}^{1,1} = 700$), $g_{xy,\infty}^{1,2}$: (FIR : $M_{gxy}^{1,2} = 700$), $g_{xy,\infty}^{1,3}$: (FIR : $M_{gxy}^{1,3} = 700$), $g_{xy,\infty}^{1,4}$: (FIR : $M_{gxy}^{1,4} = 700$), $g_{xy,\infty}^{1,5}$: (FIR : $M_{gxy}^{1,5} = 700$), $g_{xy,\infty}^{1,6}$: (FIR : $M_{gxy}^{1,6} = 700$), $g_{xy,\infty}^{1,7}$: (FIR : $M_{gxy}^{1,7} = 700$), $g_{xy,\infty}^{1,8}$: (FIR : $M_{gxy}^{1,8} = 700$), $g_{xy,\infty}^{1,9}$: (FIR : $M_{gxy}^{1,9} = 700$), $g_{xy,\infty}^{1,10}$: (FIR : $M_{gxy}^{1,10} = 700$), $g_{ey,\infty}^{1,1}$: (FIR : $M_{gey}^{1,1} = 120$), $g_{py,\infty}^{1,1}$: (FIR : $M_{gpy}^{1,1} = 200$), $g_{py,\infty}^{1,2}$: (FIR : $M_{gpy}^{1,2} = 200$)); **Signals:** *System Identification:* Random White Noise ($\mathcal{N}(0, 0.2)$), Output: 5 V, $f_s = 65.536$ kHz; Time: $0 - 0.8$ s; **Scenario:** SystemIdentification(65536Hz)/20080321T183021; *Channels:* $\#1 \leftarrow d^{\hat{g}_{ey}^{1,1}}(t)$, $\#2 \leftarrow e^{\hat{g}_{ey}^{1,1}}(t)$.;.

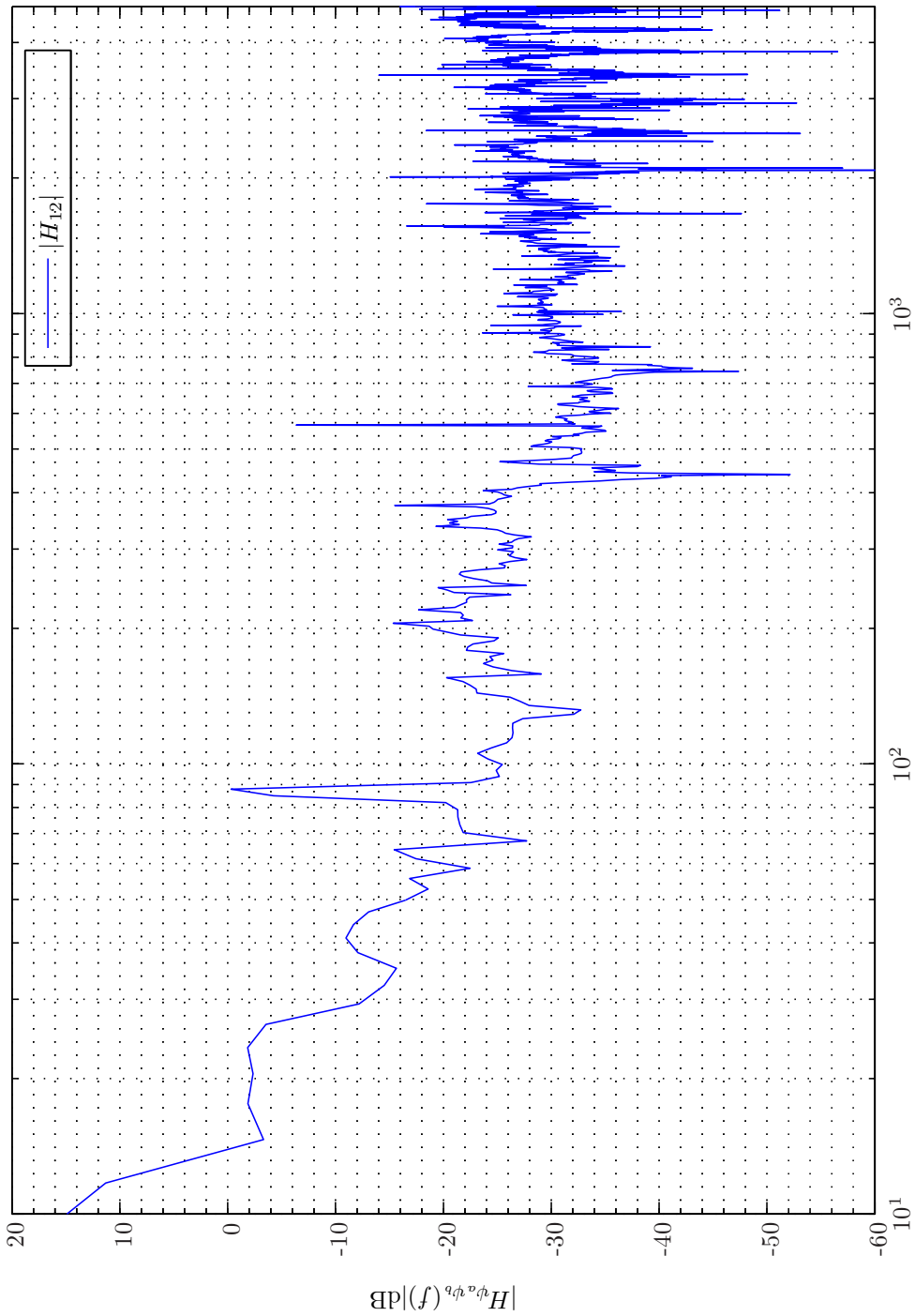

Sim 7.7.7: *Transfer Function, Magnitude:* $|H_{\psi_a\psi_b}(f)|$: **Statistical Data Analysis**: Single-Sided Modified Periodogram, f_s = 24 kHz, N_{DFT} = 8192, L_{DFT} = 4800, R_{DFT} = 2400, Hanning, Δf_m = 20.0042 Hz, T_{DFT} = 0.2 s, $N_{f,DFT}$ = 4097, Δf_{DFT} = 2.9297 Hz, K_{DFT} = 1; **Adaptive Filter** $\hat{g}_{ey}$: Wiener Hopf (M = 55, $\alpha = 1e-005, T_{WSS}$ = 0,**t**-domain); **Main:** f_s^0 = 192 kHz, f_s^1 = 24 kHz, $R_\updownarrow^1 = \frac{1}{8}$ = 0.125, Elliptic LPF (f_s = 192 kHz, f_{pass} = 11 kHz, f_{stop} = 12 kHz, A_{pass} = 2 dB, A_{stop} = 40 dB), f_s^2 = 24 kHz, $R_\updownarrow^2 = \frac{1}{1}$ = 1, Dummy; **Topology:** BK 4949 surface microphones flush-mounted on Gentex HGU-55/P helmet mounted on a BK 4128 C HATS, Terma Earcup Audio System (Feedforward, mFx, N_x = 10, N_e = 1, N_y = 1, N_p = 2, N_v = 0); **Plants:** SysID/20080321T134130 ($g_{xy,\infty}^{1,1}$: (FIR : $M_{gxy}^{1,1}$ = 700), $g_{xy,\infty}^{1,2}$: (FIR : $M_{gxy}^{1,2}$ = 700), $g_{xy,\infty}^{1,3}$: (FIR : $M_{gxy}^{1,3}$ = 700), $g_{xy,\infty}^{1,4}$: (FIR : $M_{gxy}^{1,4}$ = 700), $g_{xy,\infty}^{1,5}$: (FIR : $M_{gxy}^{1,5}$ = 700), $g_{xy,\infty}^{1,6}$: (FIR : $M_{gxy}^{1,6}$ = 700), $g_{xy,\infty}^{1,7}$: (FIR : $M_{gxy}^{1,7}$ = 700), $g_{xy,\infty}^{1,8}$: (FIR : $M_{gxy}^{1,8}$ = 700), $g_{xy,\infty}^{1,9}$: (FIR : $M_{gxy}^{1,9}$ = 700), $g_{xy,\infty}^{1,10}$: (FIR : $M_{gxy}^{1,10}$ = 700), $g_{ey,\infty}^{1,1}$: (FIR : $M_{gey}^{1,1}$ = 120), $g_{py,\infty}^{1,1}$: (FIR : $M_{gpy}^{1,1}$ = 200), $g_{py,\infty}^{1,2}$: (FIR : $M_{gpy}^{1,2}$ = 200)); **Signals:** *System Identification:* Random White Noise ($\mathcal{N}(0, 0.2)$), Output: 5 V, f_s = 65.536 kHz; Time: 0 − 0.8 s; **Scenario:** SystemIdentification(65536Hz)/20080321T183021; *Channels:* #1 ← $d^{\hat{g}_{ey}^{1,1}}(t)$, #2 ← $e^{\hat{g}_{ey}^{1,1}}(t)$.;.

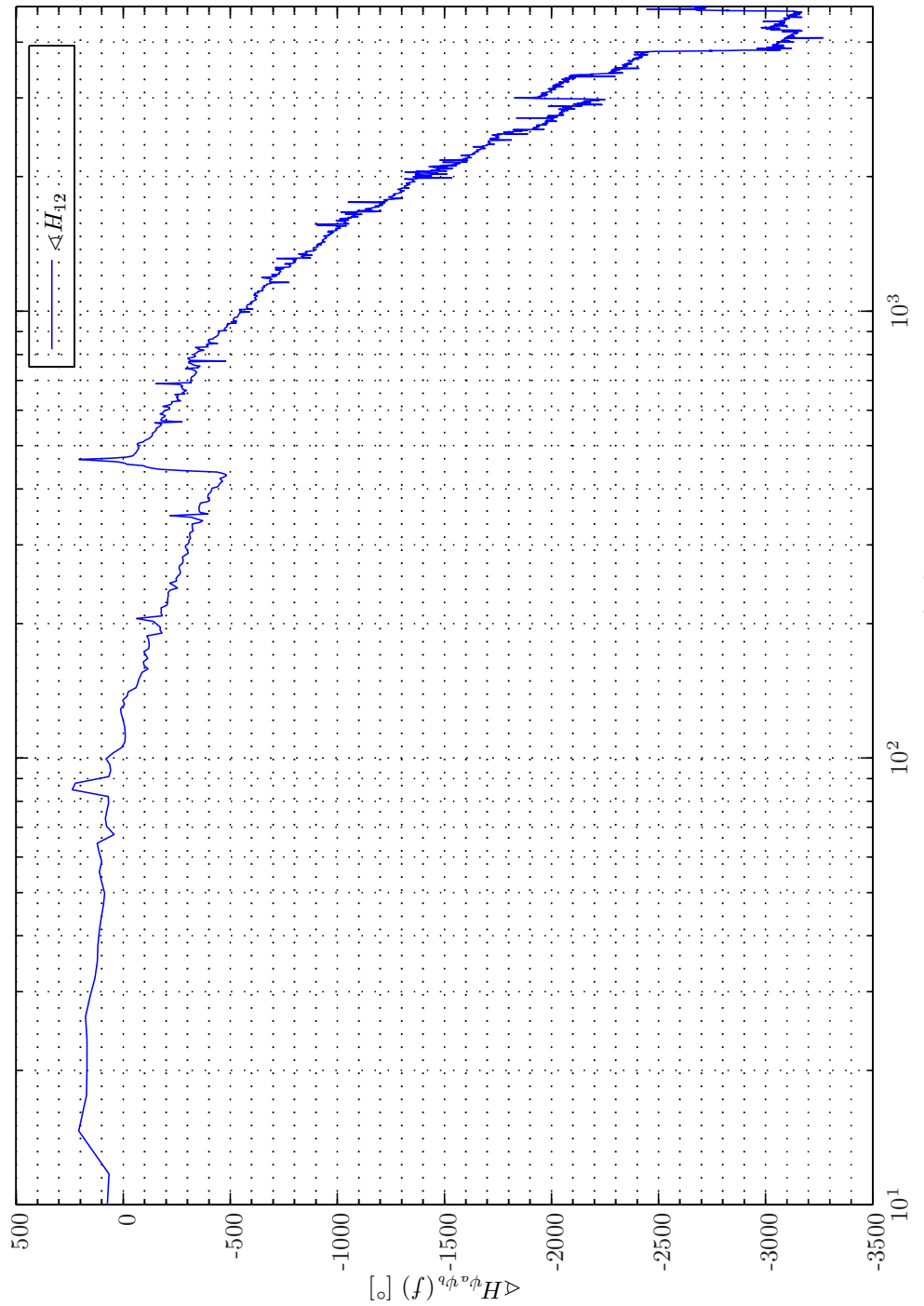

Sim 7.7.8: *Transfer Function, Phase:* $\sphericalangle H_{\psi_a\psi_b}(f)$: **Statistical Data Analysis:** Single-Sided Modified Periodogram, $f_s = 24$ kHz, $N_{DFT} = 8192$, $L_{DFT} = 4800$, $R_{DFT} = 2400$, Hanning, $\Delta f_m = 20.0042$ Hz, $T_{DFT} = 0.2$ s, $N_{f,DFT} = 4097$, $\Delta f_{DFT} = 2.9297$ Hz, $K_{DFT} = 1$; **Adaptive Filter** $\hat{g}_{ey}$: Wiener Hopf ($M = 55, \alpha = 1e-005, T_{WSS} = 0$,t-domain); **Main:** $f_s^0 = 192$ kHz, $f_s^1 = 24$ kHz, $R_\updownarrow^1 = \frac{1}{8} = 0.125$, Elliptic LPF ($f_s = 192$ kHz, $f_{pass} = 11$ kHz, $f_{stop} = 12$ kHz, $A_{pass} = 2$ dB, $A_{stop} = 40$ dB), $f_s^2 = 24$ kHz, $R_\updownarrow^2 = \frac{1}{1} = 1$, Dummy; **Topology:** BK 4949 surface microphones flush-mounted on Gentex HGU-55/P helmet mounted on a BK 4128 C HATS, Terma Earcup Audio System (Feedforward, mFx, $N_x = 10, N_e = 1, N_y = 1, N_p = 2, N_v = 0$); **Plants:** SysID/20080321T134130 ($g_{xy,\infty}^{1,1}$: (FIR : $M_{gxy}^{1,1} = 700$), $g_{xy,\infty}^{1,2}$: (FIR : $M_{gxy}^{1,2} = 700$), $g_{xy,\infty}^{1,3}$: (FIR : $M_{gxy}^{1,3} = 700$), $g_{xy,\infty}^{1,4}$: (FIR : $M_{gxy}^{1,4} = 700$), $g_{xy,\infty}^{1,5}$: (FIR : $M_{gxy}^{1,5} = 700$), $g_{xy,\infty}^{1,6}$: (FIR : $M_{gxy}^{1,6} = 700$), $g_{xy,\infty}^{1,7}$: (FIR : $M_{gxy}^{1,7} = 700$), $g_{xy,\infty}^{1,8}$: (FIR : $M_{gxy}^{1,8} = 700$), $g_{xy,\infty}^{1,9}$: (FIR : $M_{gxy}^{1,9} = 700$), $g_{xy,\infty}^{1,10}$: (FIR : $M_{gxy}^{1,10} = 700$), $g_{ey,\infty}^{1,1}$: (FIR : $M_{gey}^{1,1} = 120$), $g_{py,\infty}^{1,1}$: (FIR : $M_{gpy}^{1,1} = 200$), $g_{py,\infty}^{1,2}$: (FIR : $M_{gpy}^{1,2} = 200$)); **Signals:** *System Identification:* Random White Noise ($\mathcal{N}(0, 0.2)$), Output: 5 V, $f_s = 65.536$ kHz; Time: $0 - 0.8$ s; **Scenario:** SystemIdentification(65536Hz)/20080321T183021; *Channels:* #1 $\leftarrow d^{\hat{g}_{ey}^{1,1}}(t)$, #2 $\leftarrow e^{\hat{g}_{ey}^{1,1}}(t)$.;.

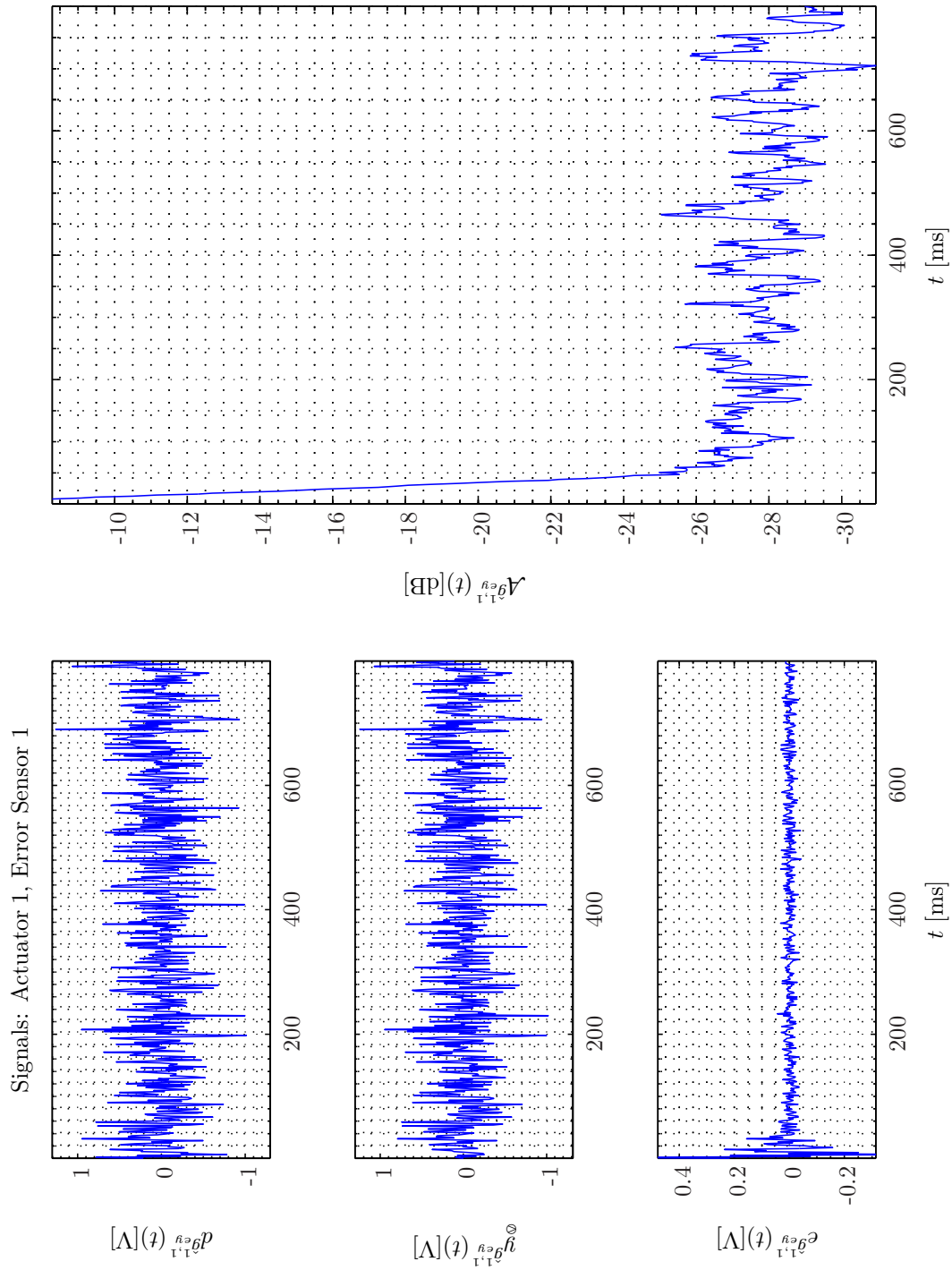

Sim 7.7.9: *Time-Domain:* Actuator 1, Error Sensor 1. Desired, output, error signals and attenuation. **Adaptive Filter** $\hat{g}_{ey}$: $\hat{g}_{ey}^{1,1}$: $\alpha\gamma\Pi$e-Normalized Least-Mean-Squares ($M = 70, L_B = 1, \mu = 0.15, \alpha = 1e-005, \epsilon = 1e-006, T_{Eu} = 20$); **Main:** $f_s^0 = 192$ kHz, $f_s^1 = 24$ kHz, $R_\updownarrow^1 = \frac{1}{8} = 0.125$, Elliptic LPF ($f_s = 192$ kHz, $f_{pass} = 11$ kHz, $f_{stop} = 12$ kHz, $A_{pass} = 2$ dB, $A_{stop} = 40$ dB), $f_s^2 = 24$ kHz, $R_\updownarrow^2 = \frac{1}{1} = 1$, Dummy; **Topology:** BK 4949 surface microphones flush-mounted on Gentex HGU-55/P helmet mounted on a BK 4128 C HATS, Terma Earcup Audio System (Feedforward, mFx, $N_x = 10, N_e = 1, N_y = 1, N_p = 2, N_v = 0$); **Plants:** SysID/20080321T134130 ($g_{xy,\infty}^{1,1}$: (FIR : $M_{gxy}^{1,1} = 700$), $g_{xy,\infty}^{1,2}$: (FIR : $M_{gxy}^{1,2} = 700$), $g_{xy,\infty}^{1,3}$: (FIR : $M_{gxy}^{1,3} = 700$), $g_{xy,\infty}^{1,4}$: (FIR : $M_{gxy}^{1,4} = 700$), $g_{xy,\infty}^{1,5}$: (FIR : $M_{gxy}^{1,5} = 700$), $g_{xy,\infty}^{1,6}$: (FIR : $M_{gxy}^{1,6} = 700$), $g_{xy,\infty}^{1,7}$: (FIR : $M_{gxy}^{1,7} = 700$), $g_{xy,\infty}^{1,8}$: (FIR : $M_{gxy}^{1,8} = 700$), $g_{xy,\infty}^{1,9}$: (FIR : $M_{gxy}^{1,9} = 700$), $g_{xy,\infty}^{1,10}$: (FIR : $M_{gxy}^{1,10} = 700$), $g_{ey,\infty}^{1,1}$: (FIR : $M_{gey}^{1,1} = 120$), $g_{py,\infty}^{1,1}$: (FIR : $M_{gpy}^{1,1} = 200$), $g_{py,\infty}^{1,2}$: (FIR : $M_{gpy}^{1,2} = 200$)); **Signals:** *System Identification:* Random White Noise ($\mathcal{N}(0, 0.2)$), Output: 5 V, $f_s = 65.536$ kHz; Time: $0 - 0.8$ s; **Scenario:** SystemIdentification(65536Hz)/20080321T183021.

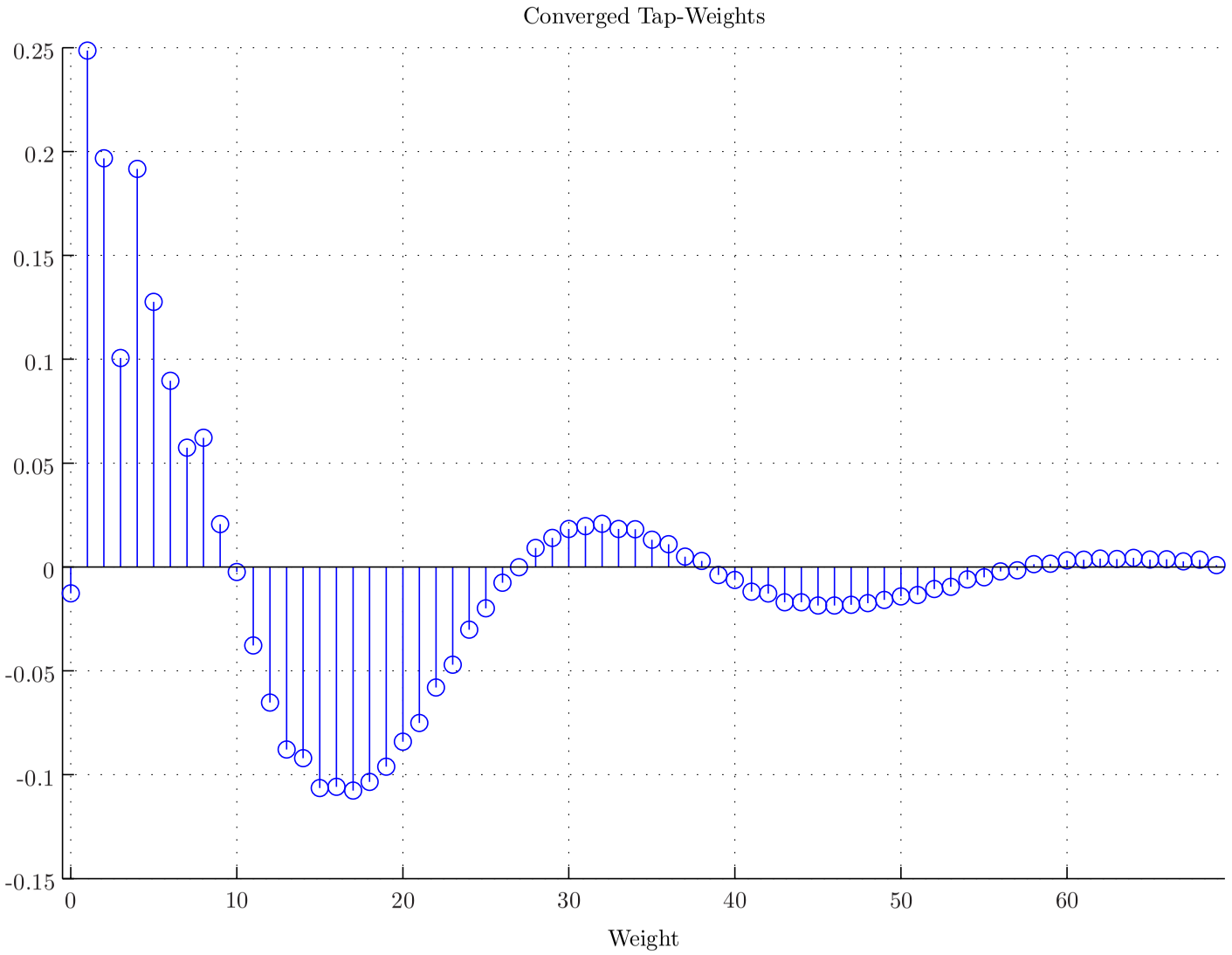

Sim 7.7.10: *Converged Tap-weights.* **Adaptive Filter** $\hat{g}_{ey}$: $\hat{g}_{ey}^{1,1}$: $\alpha\gamma\Pi\epsilon$-Normalized Least-Mean-Squares ($M = 70, L_B = 1, \mu = 0.15, \alpha = 1e{-}005, \epsilon = 1e{-}006, T_{Eu} = 20$); **Main:** $f_s^0 = 192$ kHz, $f_s^1 = 24$ kHz, $R_\downarrow^1 = \frac{1}{8} = 0.125$, Elliptic LPF ($f_s = 192$ kHz, $f_{pass} = 11$ kHz, $f_{stop} = 12$ kHz, $A_{pass} = 2$ dB, $A_{stop} = 40$ dB), $f_s^2 = 24$ kHz, $R_\updownarrow^2 = \frac{1}{1} = 1$, Dummy; **Topology:** BK 4949 surface microphones flush-mounted on Gentex HGU-55/P helmet mounted on a BK 4128 C HATS, Terma Earcup Audio System (Feedforward, mFx, $N_x = 10, N_e = 1, N_y = 1, N_p = 2, N_v = 0$); **Plants:** SysID/20080321T134130 ($g_{xy,\infty}^{1,1}$: (FIR : $M_{gxy}^{1,1} = 700$), $g_{xy,\infty}^{1,2}$: (FIR : $M_{gxy}^{1,2} = 700$), $g_{xy,\infty}^{1,3}$: (FIR : $M_{gxy}^{1,3} = 700$), $g_{xy,\infty}^{1,4}$: (FIR : $M_{gxy}^{1,4} = 700$), $g_{xy,\infty}^{1,5}$: (FIR : $M_{gxy}^{1,5} = 700$), $g_{xy,\infty}^{1,6}$: (FIR : $M_{gxy}^{1,6} = 700$), $g_{xy,\infty}^{1,7}$: (FIR : $M_{gxy}^{1,7} = 700$), $g_{xy,\infty}^{1,8}$: (FIR : $M_{gxy}^{1,8} = 700$), $g_{xy,\infty}^{1,9}$: (FIR : $M_{gxy}^{1,9} = 700$), $g_{xy,\infty}^{1,10}$: (FIR : $M_{gxy}^{1,10} = 700$), $g_{ey,\infty}^{1,1}$: (FIR : $M_{gey}^{1,1} = 120$), $g_{py,\infty}^{1,1}$: (FIR : $M_{gpy}^{1,1} = 200$), $g_{py,\infty}^{1,2}$: (FIR : $M_{gpy}^{1,2} = 200$)); **Signals:** *System Identification:* Random White Noise ($\mathcal{N}(0, 0.2)$), Output: 5 V, $f_s = 65.536$ kHz; Time: $0 - 0.8$ s; **Scenario:** `SystemIdentification(65536Hz)/20080321T183021`.

is shown. The attenuation for the APA adaptive filter follows a relative constant slope curve reaching a -28 dB attenuation level at approximately 24 ms.

The results from a SDA conducted on the converged adaptive filter provide no new insight is provided as compared with the WH filter.

The converged adaptive tap-weights shown in Simulation 7.7.12 are therefore also as expected quite similar to the adaptive tap-weights from the LMS system identification.

System Identification of Secondary Pathes $g_{ey}^{l,m}$ FARLS

The adaptive FARLS filter uses the following fixed parameters: FARLS ($M = 70, L_B = 1, \eta = 0.125, \alpha = 1e-5, T_{SW} = 0, \text{Calc} = 1$) and three different values of the forgetting factor $\lambda = 0.998, 0.999, 0.9995$ that are defined in Appendix J on page 737.

In Simulation 7.7.13 the time-domain convergence of the adaptive filter for $\lambda = 0.998$ is shown. The attenuation for the FARLS adaptive filter follows a constant slope curve reaching a -28 dB attenuation level already after approximately 15 ms. Also here no new insight from a SDA conducted on the converged adaptive filter is provided as compared with the WH filter.

The converged adaptive tap-weights shown in Simulation 7.7.14 are therefore also as expected quite similar to the adaptive tap-weights from the LMS system identification.

System Identification of Secondary Pathes $g_{ey}^{l,m}$ WH, $\alpha\gamma\Pi\epsilon$-NLMS, $\alpha\gamma\Pi\epsilon$-APA, FARLS

The performance for the four selected adaptive filters and their variants is illuminated in Simulation 7.7.15 - 7.7.17 on pages 351–353 displaying the entire $0 - 0.8$ s period and the details for the first 100 ms and the last 20 ms respectively. As reference for the system identification the **t**-domain WH filter defined in section 8.4 on page 385 for the filter orders $M = 55, 70$ and 100 is used.

As expected the **t**-domain WH filters with $M_{g_{ey}}^{1,1} = 100, 70$ provide best and second best performance respectively in terms of. However, all the $M_{g_{ey}}^{1,1} = 70$ adaptive filters upon converging provide a system identification match within $0 - 2$ dB. The fastest convergence is provided by the FARLS filter. Only marginal differences are observed among the three variants hereof. The $\alpha\gamma\Pi\epsilon$-APA filter is seen to provide faster system identification than the $\alpha\gamma\Pi\epsilon$-NLMS almost approaching the speed of the FARLS filter. In particular the choice $K = 4, \Delta = 1$ seems to provide a good trade-off between convergence and excess error.

Concerning the convergence time the FARLS is approximately twice as fast as the LMS for $M_{g_{ey}}^{1,1} = 100$ and a half time faster for $M_{g_{ey}}^{1,1} = 70$. Now the alert reader may ask to which extent the achieved -28 dB match of the secondary path represent an upper limit to what can be obtained. Well, again the coherence function discussed at length in chapter 2 on page 17 provide an answer to this question. From Simulation 11.5.1 - 11.5.2 on pages 497–498 we appreciate that the ordinary coherence function predicts an attenuation exceeding 35 dB for frequencies above approximately 200 Hz. However, for decreasing frequencies the achievable attenuation decreases reaching only -5 dB at 10 Hz. Hence, the -28 dB level represents a frequency average of the ordinary coherence function. with decreasing frequency. As such the gain factor of the pseudo transfer function that links the desired signal $d^{\hat{g}_{ey}^{1,1}}(t)$ to the error signal $e^{\hat{g}_{ey}^{1,1}}(t)$ is to some extent the reverse of the gain factor of the secondary path transfer function depicted in Simulation 11.5.3 on page 499.

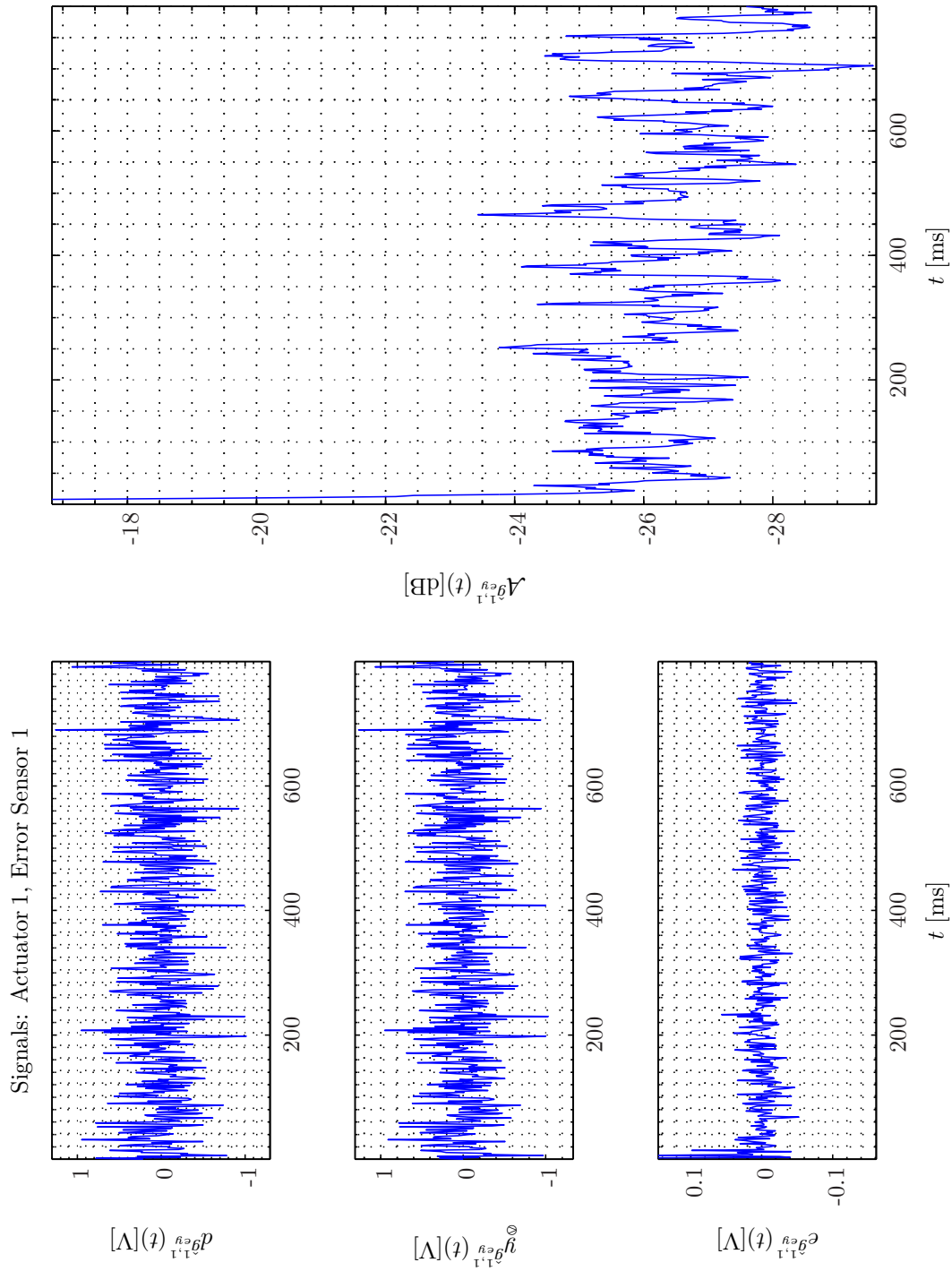

Sim 7.7.11: *Time-Domain:* Actuator 1, Error Sensor 1. Desired, output, error signals and attenuation. **Adaptive Filter** $\hat{g}_{ey}$: $\hat{g}_{ey}^{1,1}$: $\alpha\gamma\Pi\epsilon$-Affine Projection Algorithm ($M = 70, L_B = 1, \mu = 0.15, K = 4, \Delta = 1, \alpha = 1e-005, \gamma = 1e-005, \Pi = 0, \epsilon = 1e-006, \dot{w} = 0, W_e = 1$); **Main:** $f_s^0 = 192$ kHz, $f_s^1 = 24$ kHz, $R_\downarrow^1 = \frac{1}{8} = 0.125$, Elliptic LPF ($f_s = 192$ kHz, $f_{pass} = 11$ kHz, $f_{stop} = 12$ kHz, $A_{pass} = 2$ dB, $A_{stop} = 40$ dB), $f_s^2 = 24$ kHz, $R_\downarrow^2 = \frac{1}{1} = 1$, Dummy; **Topology:** BK 4949 surface microphones flush-mounted on Gentex HGU-55/P helmet mounted on a BK 4128 C HATS, Terma Earcup Audio System (Feedforward, mFx, $N_x = 10, N_e = 1, N_y = 1, N_p = 2, N_v = 0$); **Plants:** SysID/20080321T134130 ($g_{x,\infty}^{1,1}$: (FIR : $M_{gxy}^{1,1} = 700$), $g_{xy,\infty}^{1,2}$: (FIR : $M_{gxy}^{1,2} = 700$), $g_{xy,\infty}^{1,3}$: (FIR : $M_{gxy}^{1,3} = 700$), $g_{xy,\infty}^{1,4}$: (FIR : $M_{gxy}^{1,4} = 700$), $g_{xy,\infty}^{1,5}$: (FIR : $M_{gxy}^{1,5} = 700$), $g_{xy,\infty}^{1,6}$: (FIR : $M_{gxy}^{1,6} = 700$), $g_{xy,\infty}^{1,7}$: (FIR : $M_{gxy}^{1,7} = 700$), $g_{xy,\infty}^{1,8}$: (FIR : $M_{gxy}^{1,8} = 700$), $g_{xy,\infty}^{1,9}$: (FIR : $M_{gxy}^{1,9} = 700$), $g_{xy,\infty}^{1,10}$: (FIR : $M_{gxy}^{1,10} = 700$), $g_{ey,\infty}^{1,1}$: (FIR : $M_{gey}^{1,1} = 120$), $g_{py,\infty}^{1,1}$: (FIR : $M_{gpy}^{1,1} = 200$), $g_{py,\infty}^{1,2}$: (FIR : $M_{gpy}^{1,2} = 200$)); **Signals:** *System Identification:* Random White Noise ($\mathcal{N}(0, 0.2)$), Output: 5 V, $f_s = 65.536$ kHz; Time: $0 - 0.8$ s; **Scenario:** `SystemIdentification(65536Hz)/20080321T183021`.

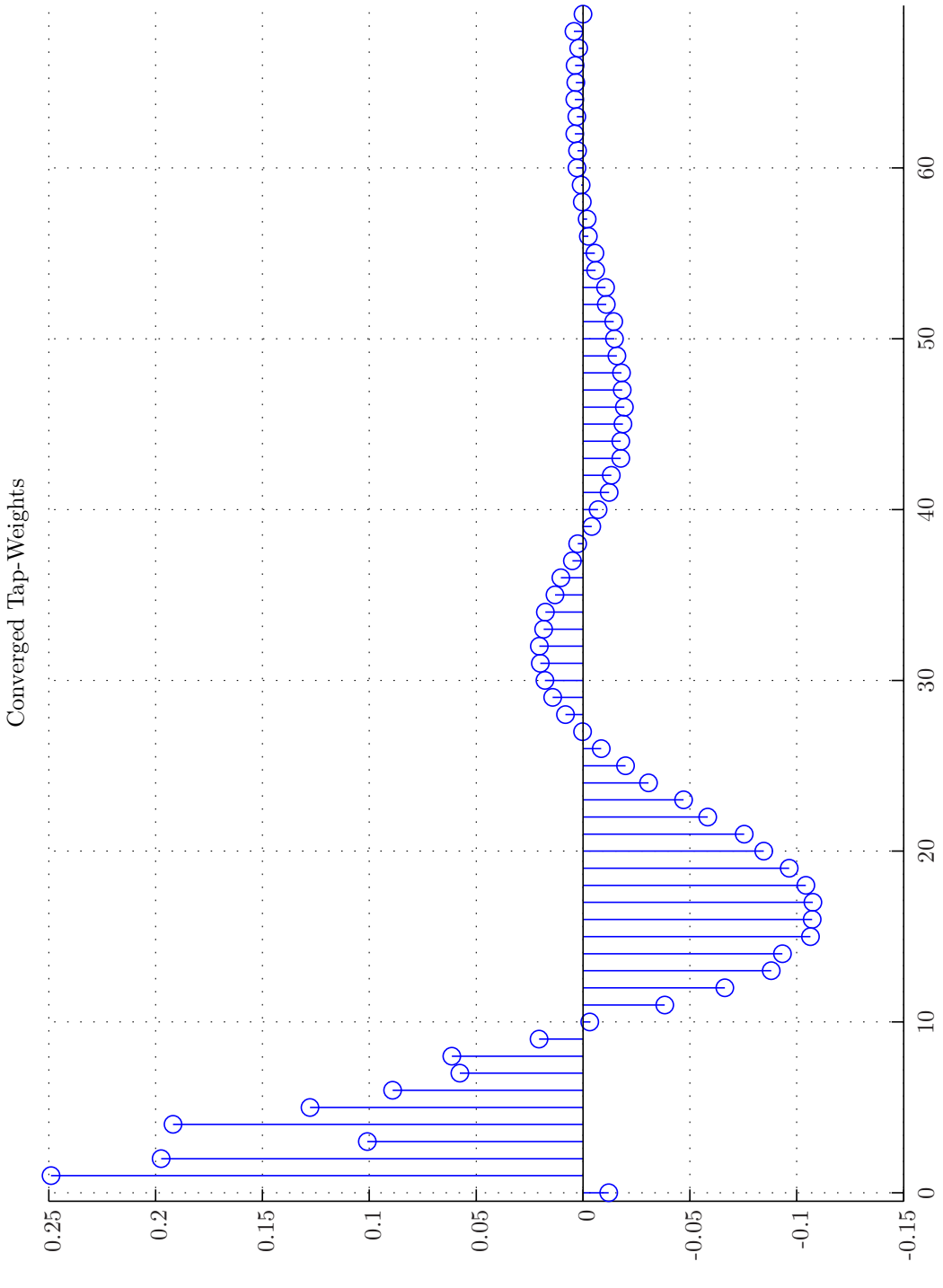

Sim 7.7.12: *Converged Tap-weights.* **Adaptive Filter** $\hat{g}_{ey}$: $\hat{g}_{ey}^{1,1}$: $\alpha\gamma\Pi\epsilon$-Affine Projection Algorithm ($M = 70, L_B = 1, \mu = 0.15, K = 2, \Delta = 4, \alpha = 1e-005, \gamma = 1e-005, \Pi = 0, \epsilon = 1e-006, \breve{w} = 0, W_e = 1$); **Main:** $f_s^0 = 192$ kHz, $f_s^1 = 24$ kHz, $R_\downarrow^1 = \frac{1}{8} = 0.125$, Elliptic LPF ($f_s = 192$ kHz, $f_{pass} = 11$ kHz, $f_{stop} = 12$ kHz, $A_{pass} = 2$ dB, $A_{stop} = 40$ dB), $f_s^2 = 24$ kHz, $R_\downarrow^2 = \frac{1}{1} = 1$, Dummy; **Topology:** BK 4949 surface microphones flush-mounted on Gentex HGU-55/P helmet mounted on a BK 4128 C HATS, Terma Earcup Audio System (Feedforward, mFx, $N_x = 10, N_e = 1, N_y = 1, N_p = 2, N_v = 0$); **Plants:** SysID/20080321T134130 ($g_{xy,\infty}^{1,1}$: (FIR : $M_{gxy}^{1,1} = 700$), $g_{xy,\infty}^{1,2}$: (FIR : $M_{gxy}^{1,2} = 700$), $g_{xy,\infty}^{1,3}$: (FIR : $M_{gxy}^{1,3} = 700$), $g_{xy,\infty}^{1,4}$: (FIR : $M_{gxy}^{1,4} = 700$), $g_{xy,\infty}^{1,5}$: (FIR : $M_{gxy}^{1,5} = 700$), $g_{xy,\infty}^{1,6}$: (FIR : $M_{gxy}^{1,6} = 700$), $g_{xy,\infty}^{1,7}$: (FIR : $M_{gxy}^{1,7} = 700$), $g_{xy,\infty}^{1,8}$: (FIR : $M_{gxy}^{1,8} = 700$), $g_{xy,\infty}^{1,9}$: (FIR : $M_{gxy}^{1,9} = 700$), $g_{xy,\infty}^{1,10}$: (FIR : $M_{gxy}^{1,10} = 700$), $g_{ey,\infty}^{1,1}$: (FIR : $M_{gey}^{1,1} = 120$), $g_{py,\infty}^{1,1}$: (FIR : $M_{gpy}^{1,1} = 200$), $g_{py,\infty}^{1,2}$: (FIR : $M_{gpy}^{1,2} = 200$)); **Signals:** *System Identification:* Random White Noise ($\mathcal{N}(0, 0.2)$), Output: 5 V, $f_s = 65.536$ kHz; Time: $0 - 0.8$ s; **Scenario:** `SystemIdentification(65536Hz)/20080321T183021`.

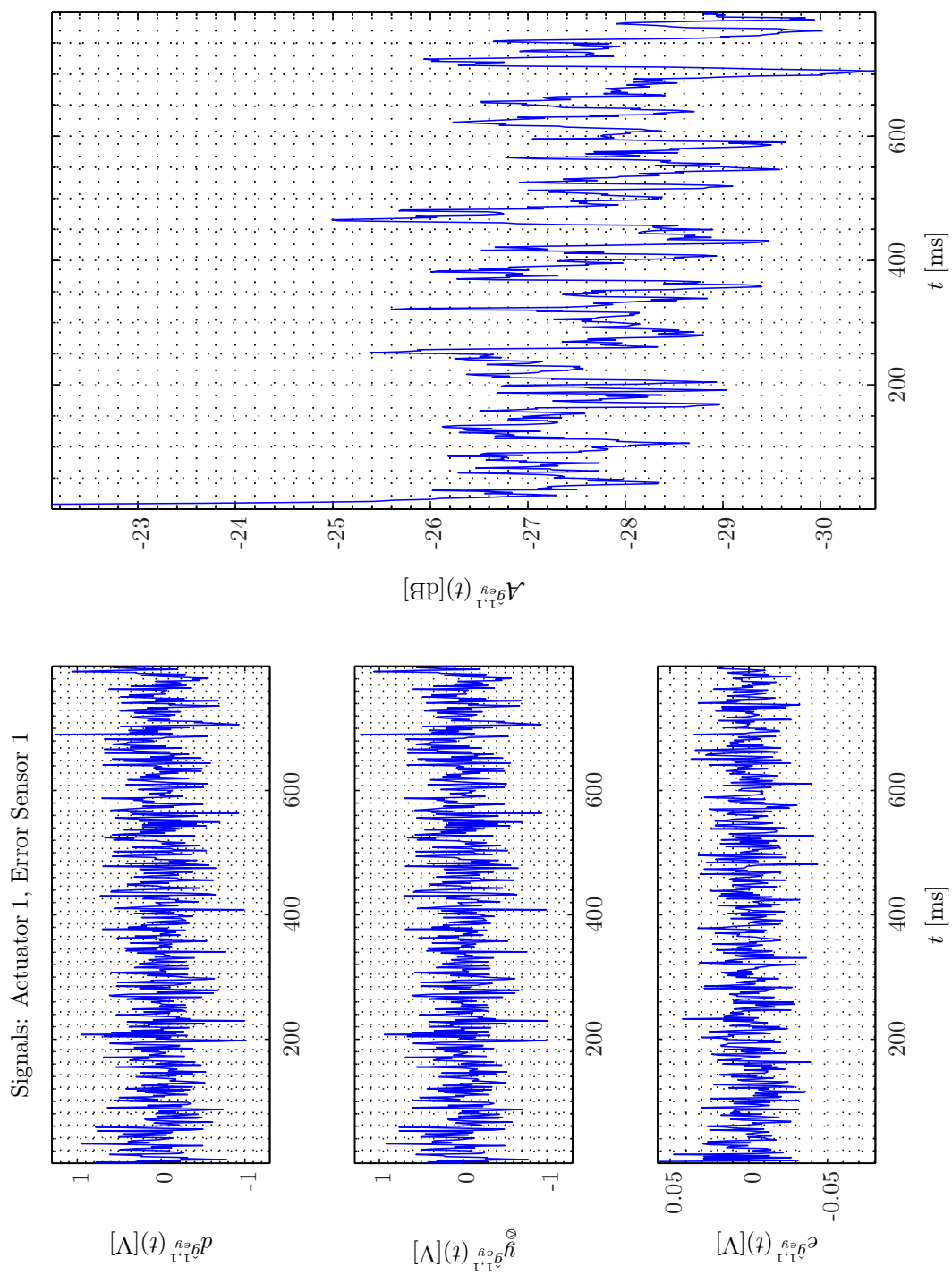

Sim 7.7.13: *Time-Domain:* Actuator 1, Error Sensor 1. Desired, output, error signals and attenuation. **Adaptive Filter** $\hat{g}_{ey}$: $\hat{g}_{ey}^{1,1}$: Fast Array RLS ($M = 70, L_B = 1, \lambda = 0.998, \eta = 0.125, \alpha = 1e-005, T_{SW} = 0, Calc = 1$); **Main:** $f_s^0 = 192$ kHz, $f_s^1 = 24$ kHz, $R_\downarrow^1 = \frac{1}{8} = 0.125$, Elliptic LPF ($f_s = 192$ kHz, $f_{pass} = 11$ kHz, $f_{stop} = 12$ kHz, $A_{pass} = 2$ dB, $A_{stop} = 40$ dB), $f_s^2 = 24$ kHz, $R_\downarrow^2 = \frac{1}{1} = 1$, Dummy; **Topology:** BK 4949 surface microphones flush-mounted on Gentex HGU-55/P helmet mounted on a BK 4128 C HATS, Terma Earcup Audio System (Feedforward, mFx, $N_x = 10, N_e = 1, N_y = 1, N_p = 2, N_v = 0$); **Plants:** SysID/20080321T134130 ($g_{x,\infty}^{1,1}$: (FIR : $M_{gxy}^{1,1} = 700$), $g_{xy,\infty}^{1,2}$: (FIR : $M_{gxy}^{1,2} = 700$), $g_{xy,\infty}^{1,3}$: (FIR : $M_{gxy}^{1,3} = 700$), $g_{xy,\infty}^{1,4}$: (FIR : $M_{gxy}^{1,4} = 700$), $g_{xy,\infty}^{1,5}$: (FIR : $M_{gxy}^{1,5} = 700$), $g_{xy,\infty}^{1,6}$: (FIR : $M_{gxy}^{1,6} = 700$), $g_{xy,\infty}^{1,7}$: (FIR : $M_{gxy}^{1,7} = 700$), $g_{xy,\infty}^{1,8}$: (FIR : $M_{gxy}^{1,8} = 700$), $g_{x,\infty}^{1,9}$: (FIR : $M_{gxy}^{1,9} = 700$), $g_{x,\infty}^{1,10}$: (FIR : $M_{gxy}^{1,10} = 700$), $g_{e,\infty}^{1,1}$: (FIR : $M_{gey}^{1,1} = 120$), $g_{py,\infty}^{1,1}$: (FIR : $M_{gpy}^{1,1} = 200$), $g_{py,\infty}^{1,2}$: (FIR : $M_{gpy}^{1,2} = 200$)); **Signals:** *System Identification:* Random White Noise ($\mathcal{N}(0, 0.2)$), Output: 5 V, $f_s = 65.536$ kHz; Time: $0 - 0.8$ s; **Scenario:** `SystemIdentification(65536Hz)/20080321T183021`.

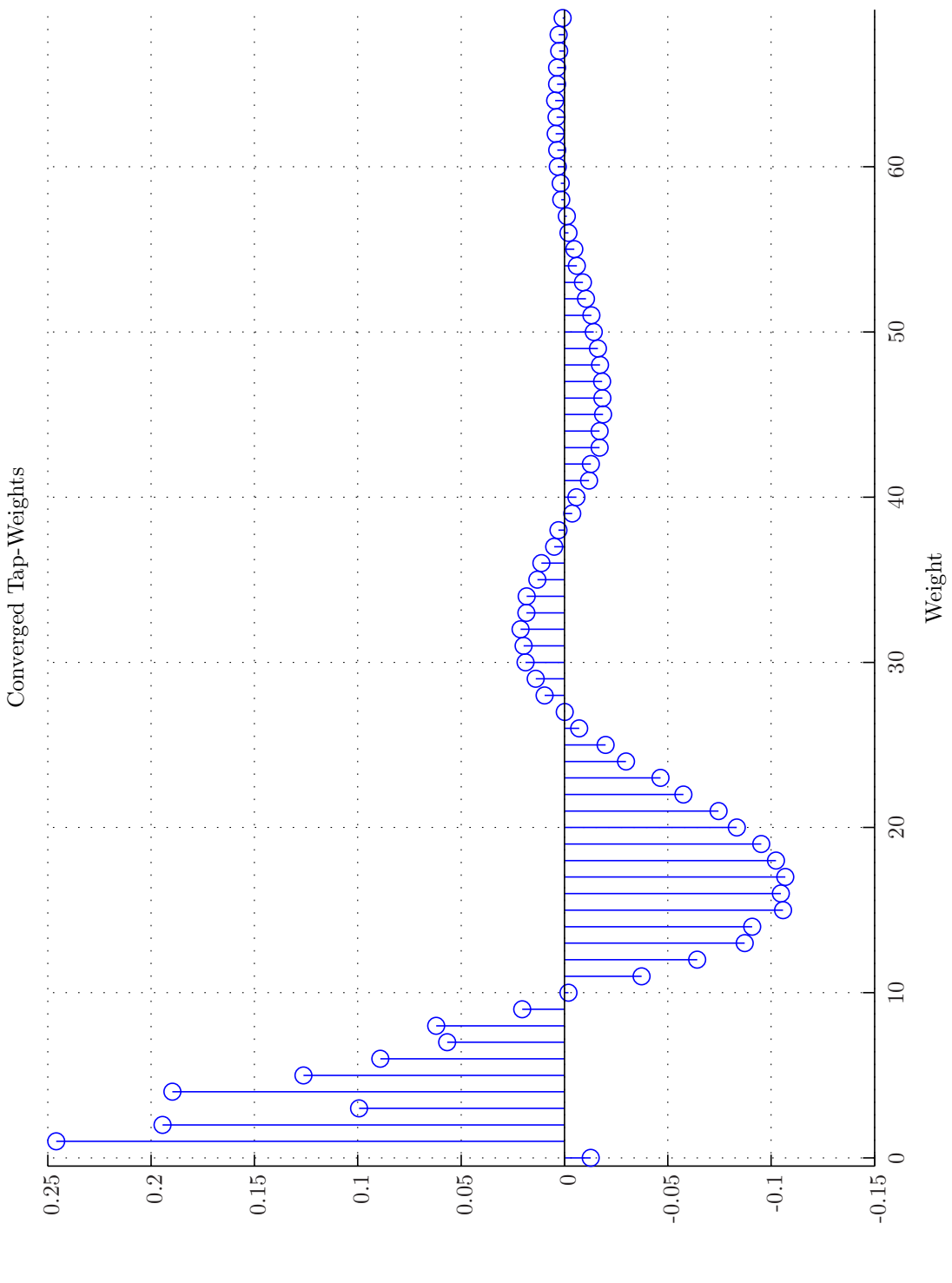

Sim 7.7.14: *Converged Tap-weights.* **Adaptive Filter** $\hat{g}_{ey}$: $\hat{g}_{ey}^{1,1}$: Fast Array RLS ($M = 70, L_B = 1, \lambda = 0.998, \eta = 0.125, \alpha = 1e-005, T_{SW} = 0, Calc = 1$); **Main:** $f_s^0 = 192$ kHz, $f_s^1 = 24$ kHz, $R_\updownarrow^1 = \frac{1}{8} = 0.125$, Elliptic LPF ($f_s = 192$ kHz, $f_{pass} = 11$ kHz, $f_{stop} = 12$ kHz, $A_{pass} = 2$ dB, $A_{stop} = 40$ dB), $f_s^2 = 24$ kHz, $R_\updownarrow^2 = \frac{1}{1} = 1$, Dummy; **Topology:** BK 4949 surface microphones flush-mounted on Gentex HGU-55/P helmet mounted on a BK 4128 C HATS, Terma Earcup Audio System (Feedforward, mFx, $N_x = 10, N_e = 1, N_y = 1, N_p = 2, N_v = 0$); **Plants:** SysID/20080321T134130 ($g_{xy,\infty}^{1,1}$: (FIR : $M_{gxy}^{1,1} = 700$), $g_{xy,\infty}^{1,2}$: (FIR : $M_{gxy}^{1,2} = 700$), $g_{xy,\infty}^{1,3}$: (FIR : $M_{gxy}^{1,3} = 700$), $g_{xy,\infty}^{1,4}$: (FIR : $M_{gxy}^{1,4} = 700$), $g_{xy,\infty}^{1,5}$: (FIR : $M_{gxy}^{1,5} = 700$), $g_{xy,\infty}^{1,6}$: (FIR : $M_{gxy}^{1,6} = 700$), $g_{xy,\infty}^{1,7}$: (FIR : $M_{gxy}^{1,7} = 700$), $g_{xy,\infty}^{1,8}$: (FIR : $M_{gxy}^{1,8} = 700$), $g_{xy,\infty}^{1,9}$: (FIR : $M_{gxy}^{1,9} = 700$), $g_{xy,\infty}^{1,10}$: (FIR : $M_{gxy}^{1,10} = 700$), $g_{ey,\infty}^{1,1}$: (FIR : $M_{gey}^{1,1} = 120$), $g_{py,\infty}^{1,1}$: (FIR : $M_{gpy}^{1,1} = 200$), $g_{py,\infty}^{1,2}$: (FIR : $M_{gpy}^{1,2} = 200$)); **Signals:** *System Identification:* Random White Noise ($\mathcal{N}(0, 0.2)$), Output: 5 V, $f_s = 65.536$ kHz; Time: $0 - 0.8$ s; **Scenario:** SystemIdentification(65536Hz)/20080321T183021.

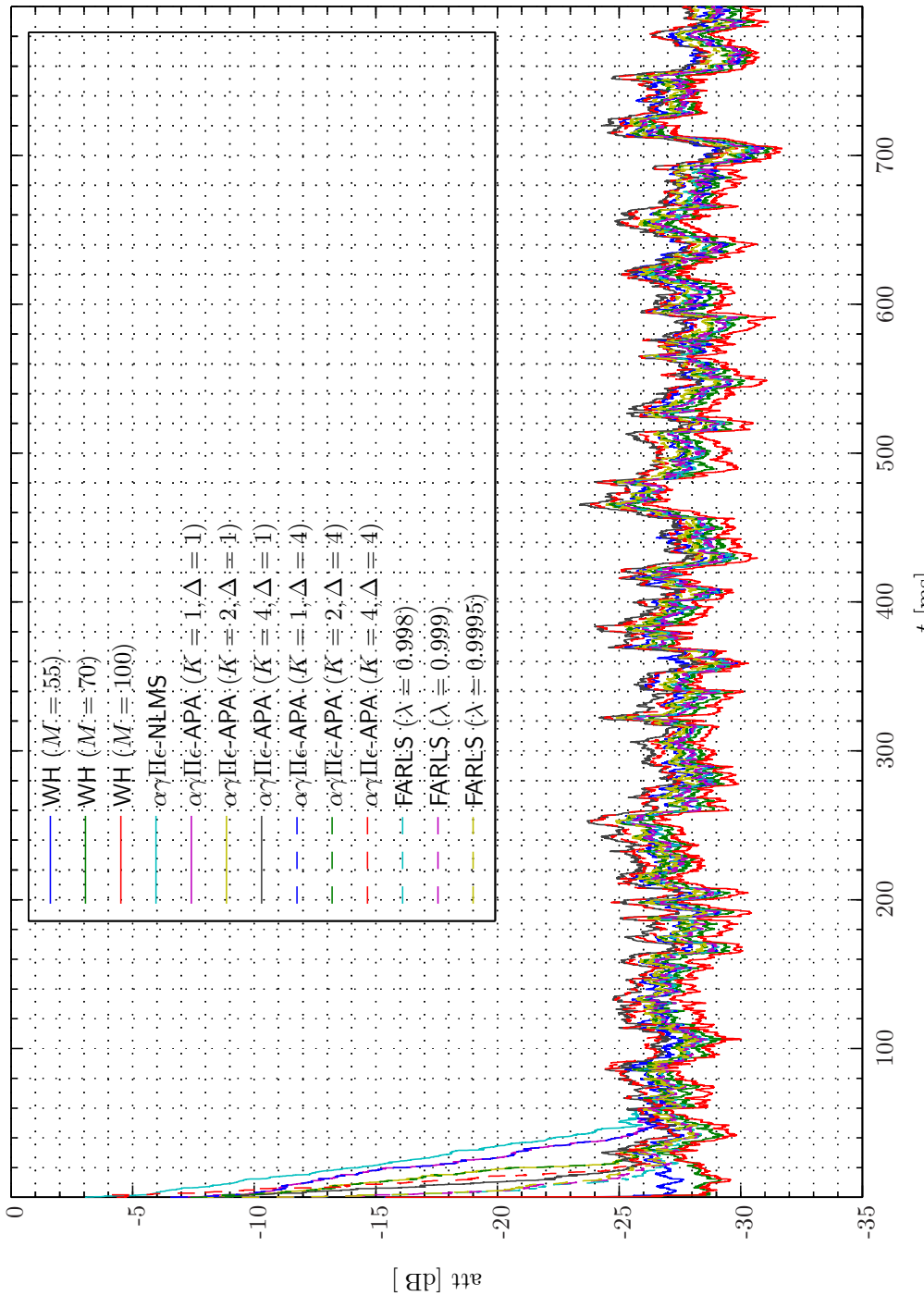

Sim 7.7.15: *Time-Domain: Attenuation.* **Adaptive Filter** $\hat{g}_{ey}$: $\hat{g}_{ey}^{1,1}$: WH ($\alpha = 1e-005, T_{WSS} = 0$,**t**-domain);$\alpha\gamma\Pi\epsilon$-NLMS ($M = 70, L_B = 1, \mu = 0.15, \alpha = 1e-005, \epsilon = 1e-006, T_{Eu} = 20$);$\alpha\gamma\Pi\epsilon$-APA ($M = 70, L_B = 1, \mu = 0.15, \alpha = 1e-005, \gamma = 1e-005, \Pi = 0, \epsilon = 1e-006, \check{w} = 0, W_e = 1$);FARLS ($M = 70, L_B = 1, \eta = 0.125, \alpha = 1e-005, T_{SW} = 0, Calc = 1$); **Main:** $f_s^0 = 192$ kHz, $f_s^1 = 24$ kHz, $R_{\updownarrow}^1 = \frac{1}{8} = 0.125$, Elliptic LPF ($f_s = 192$ kHz, $f_{pass} = 11$ kHz, $f_{stop} = 12$ kHz, $A_{pass} = 2$ dB, $A_{stop} = 40$ dB), $f_s^2 = 24$ kHz, $R_{\updownarrow}^2 = \frac{1}{1} = 1$, Dummy; **Topology:** BK 4949 surface microphones flush-mounted on Gentex HGU-55/P helmet mounted on a BK 4128 C HATS, Terma Earcup Audio System (Feedforward, mFx, $N_x = 10, N_e = 1, N_y = 1, N_p = 2, N_v = 0$); **Plants:** SysID/20080321T134130 ($g_{xy,\infty}^{1,1}$: (FIR : $M_{gxy}^{1,1} = 700$), $g_{xy,\infty}^{1,2}$: (FIR : $M_{gxy}^{1,2} = 700$), $g_{xy,\infty}^{1,3}$: (FIR : $M_{gxy}^{1,3} = 700$), $g_{xy,\infty}^{1,4}$: (FIR : $M_{gxy}^{1,4} = 700$), $g_{xy,\infty}^{1,5}$: (FIR : $M_{gxy}^{1,5} = 700$), $g_{xy,\infty}^{1,6}$: (FIR : $M_{gxy}^{1,6} = 700$), $g_{xy,\infty}^{1,7}$: (FIR : $M_{gxy}^{1,7} = 700$), $g_{xy,\infty}^{1,8}$: (FIR : $M_{gxy}^{1,8} = 700$), $g_{xy,\infty}^{1,9}$: (FIR : $M_{gxy}^{1,9} = 700$), $g_{xy,\infty}^{1,10}$: (FIR : $M_{gxy}^{1,10} = 700$), $g_{ey,\infty}^{1,1}$: (FIR : $M_{gey}^{1,1} = 120$), $g_{py,\infty}^{1,1}$: (FIR : $M_{gpy}^{1,1} = 200$), $g_{py,\infty}^{1,2}$: (FIR : $M_{gpy}^{1,2} = 200$)); **Signals:** *System Identification:* Random White Noise ($\mathcal{N}(0, 0.2)$), Output: 5 V, $f_s = 65.536$ kHz; Time: $0 - 0.8$ s; **Scenario:** SystemIdentification(65536Hz)/20080321T183021.

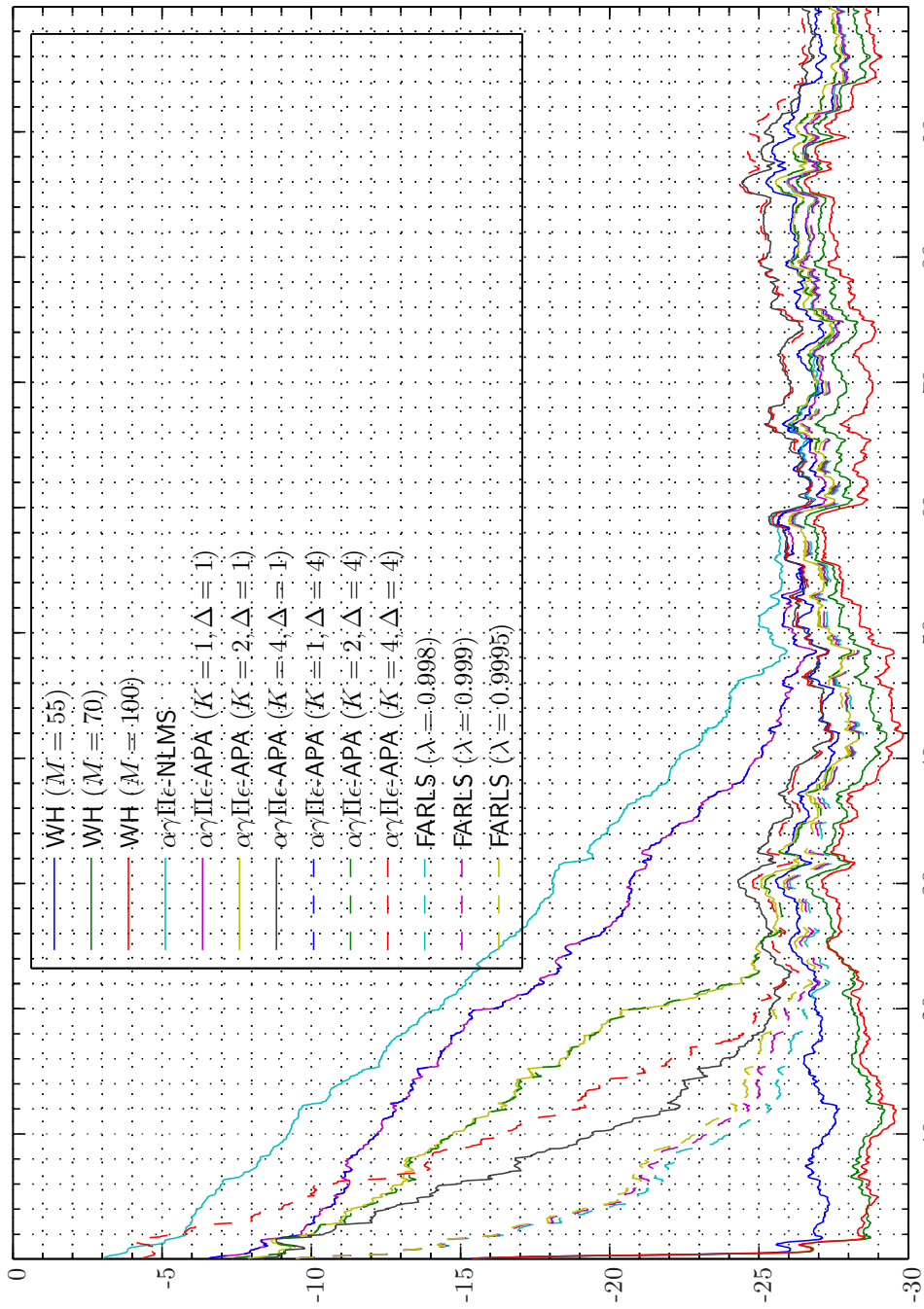

Sim 7.7.16: *Time-Domain: Attenuation Initial.* **Adaptive Filter** $\hat{g}_{ey}$: $\hat{g}_{ey}^{1,1}$: WH ($\alpha = 1e-005, T_{WSS} = 0$,**t**-domain);$\alpha\gamma\Pi\epsilon$-NLMS ($M = 70, L_B = 1, \mu = 0.15, \alpha = 1e-005, \epsilon = 1e-006, T_{Eu} = 20$);$\alpha\gamma\Pi\epsilon$-APA ($M = 70, L_B = 1, \mu = 0.15, \alpha = 1e-005, \gamma = 1e-005, \Pi = 0, \epsilon = 1e-006, \check{w} = 0, W_e = 1$);FARLS ($M = 70, L_B = 1, \eta = 0.125, \alpha = 1e-005, T_{SW} = 0, Calc = 1$); **Main:** $f_s^0 = 192$ kHz, $f_s^1 = 24$ kHz, $R_\updownarrow^1 = \frac{1}{8} = 0.125$, Elliptic LPF ($f_s = 192$ kHz, $f_{pass} = 11$ kHz, $f_{stop} = 12$ kHz, $A_{pass} = 2$ dB, $A_{stop} = 40$ dB), $f_s^2 = 24$ kHz, $R_\updownarrow^2 = \frac{1}{1} = 1$, Dummy; **Topology:** BK 4949 surface microphones flush-mounted on Gentex HGU-55/P helmet mounted on a BK 4128 C HATS, Terma Earcup Audio System (Feedforward, mFx, $N_x = 10, N_e = 1, N_y = 1, N_p = 2, N_v = 0$); **Plants:** SysID/20080321T134130 ($g_{x,\infty}^{1,1}$: (FIR : $M_{gxy}^{1,1} = 700$), $g_{xy,\infty}^{1,2}$: (FIR : $M_{gxy}^{1,2} = 700$), $g_{xy,\infty}^{1,3}$: (FIR : $M_{gxy}^{1,3} = 700$), $g_{xy,\infty}^{1,4}$: (FIR : $M_{gxy}^{1,4} = 700$), $g_{xy,\infty}^{1,5}$: (FIR : $M_{gxy}^{1,5} = 700$), $g_{xy,\infty}^{1,6}$: (FIR : $M_{gxy}^{1,6} = 700$), $g_{xy,\infty}^{1,7}$: (FIR : $M_{gxy}^{1,7} = 700$), $g_{xy,\infty}^{1,8}$: (FIR : $M_{gxy}^{1,8} = 700$), $g_{xy,\infty}^{1,9}$: (FIR : $M_{gxy}^{1,9} = 700$), $g_{xy,\infty}^{1,10}$: (FIR : $M_{gxy}^{1,10} = 700$), $g_{ey,\infty}^{1,1}$: (FIR : $M_{gey}^{1,1} = 120$), $g_{py,\infty}^{1,1}$: (FIR : $M_{gpy}^{1,1} = 200$), $g_{py,\infty}^{1,2}$: (FIR : $M_{gpy}^{1,2} = 200$)); **Signals:** *System Identification:* Random White Noise ($\mathcal{N}(0, 0.2)$), Output: 5 V, $f_s = 65.536$ kHz; Time: $0 - 0.8$ s; **Scenario:** `SystemIdentification(65536Hz)/20080321T183021`.

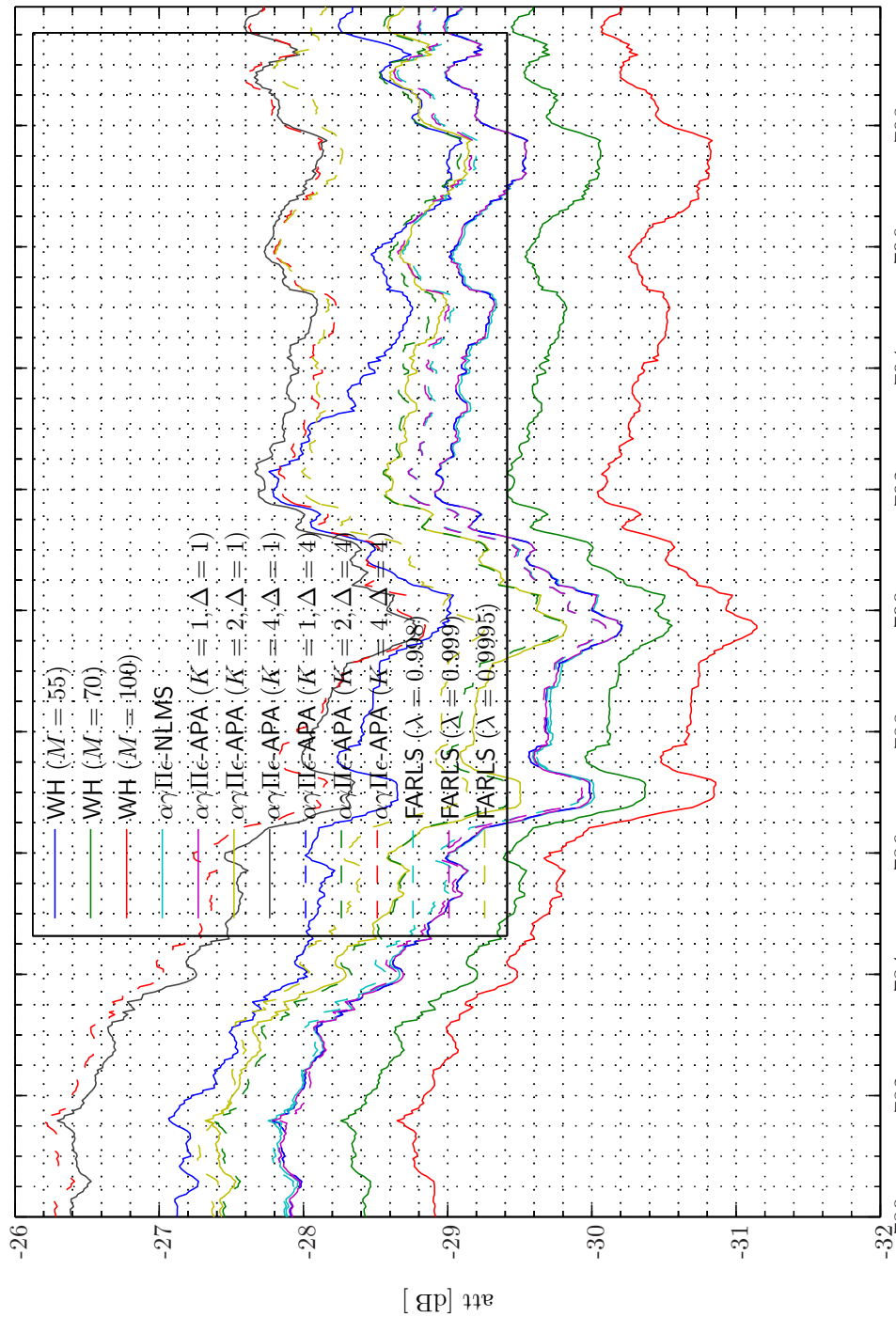

Sim 7.7.17: *Time-Domain: Attenuation Final.* **Adaptive Filter** $\hat{g}_{ey}$: $\hat{g}_{ey}^{1,1}$: WH ($\alpha = 1e-005, T_{WSS} = 0$,**t**-domain);$\alpha\gamma\Pi\epsilon$-NLMS ($M = 70, L_B = 1, \mu = 0.15, \alpha = 1e-005, \epsilon = 1e-006, T_{Eu} = 20$);$\alpha\gamma\Pi\epsilon$-APA ($M = 70, L_B = 1, \mu = 0.15, \alpha = 1e-005, \gamma = 1e-005, \Pi = 0, \epsilon = 1e-006, \tilde{w} = 0, W_e = 1$);FARLS ($M = 70, L_B = 1, \eta = 0.125, \alpha = 1e-005, T_{SW} = 0, Calc = 1$); **Main:** $f_s^0 = 192$ kHz, $f_s^1 = 24$ kHz, $R_\updownarrow^1 = \frac{1}{8} = 0.125$, Elliptic LPF ($f_s = 192$ kHz, $f_{pass} = 11$ kHz, $f_{stop} = 12$ kHz, $A_{pass} = 2$ dB, $A_{stop} = 40$ dB), $f_s^2 = 24$ kHz, $R_\updownarrow^2 = \frac{1}{1} = 1$, Dummy; **Topology:** BK 4949 surface microphones flush-mounted on Gentex HGU-55/P helmet mounted on a BK 4128 C HATS, Terma Earcup Audio System (Feedforward, mFx, $N_x = 10, N_e = 1, N_y = 1, N_p = 2, N_v = 0$); **Plants:** SysID/20080321T134130 ($g_{xy,\infty}^{1,1}$: (FIR : $M_{gxy}^{1,1} = 700$), $g_{xy,\infty}^{1,2}$: (FIR : $M_{gxy}^{1,2} = 700$), $g_{xy,\infty}^{1,3}$: (FIR : $M_{gxy}^{1,3} = 700$), $g_{xy,\infty}^{1,4}$: (FIR : $M_{gxy}^{1,4} = 700$), $g_{xy,\infty}^{1,5}$: (FIR : $M_{gxy}^{1,5} = 700$), $g_{xy,\infty}^{1,6}$: (FIR : $M_{gxy}^{1,6} = 700$), $g_{xy,\infty}^{1,7}$: (FIR : $M_{gxy}^{1,7} = 700$), $g_{xy,\infty}^{1,8}$: (FIR : $M_{gxy}^{1,8} = 700$), $g_{xy,\infty}^{1,9}$: (FIR : $M_{gxy}^{1,9} = 700$), $g_{xy,\infty}^{1,10}$: (FIR : $M_{gxy}^{1,10} = 700$), $g_{ey,\infty}^{1,1}$: (FIR : $M_{gey}^{1,1} = 120$), $g_{py,\infty}^{1,1}$: (FIR : $M_{gpy}^{1,1} = 200$), $g_{py,\infty}^{1,2}$: (FIR : $M_{gpy}^{1,2} = 200$)); **Signals:** *System Identification:* Random White Noise ($\mathcal{N}(0, 0.2)$), Output: 5 V, $f_s = 65.536$ kHz; Time: $0 - 0.8$ s; **Scenario:** SystemIdentification(65536Hz)/20080321T183021.

System Identification of Secondary Pathes $g_{ey}^{l,m}$ WH, $\alpha\gamma\Pi\epsilon$-NLMS, $\alpha\gamma\Pi\epsilon$-APA, FARLS, Small Signal

Next we investigate if a less annoying random white noise signal can be used without detoriating the system identification performance. Hence, for the earphone is now excited by a 0.5 V (peak) RWN signal corresponding to a sound pressure level (SPL) reduction of 20 dB in comparison with the previous experiment. The performance for the four selected adaptive filters and their variants is illuminated in Simulation 7.7.18 - 7.7.20 on pages 355–357.

In comparison with the 5.0 V (peak) signal we appreciate that except for the FARLS filter variants that in this case exhibit slow convergence the performance is practical intact. The reason for the poor behavior of the FARLS in this case, however, is in the moment of writing not understood.

7.7.3 System Identification of Feedback Pathes $g_{xy}^{l,j}$

As $N_x = 10$ and $N_y = 1$ the capability of the system identification for the ten feedback paths $\hat{g}_{xy}^{l,j} = \hat{g}_{xy}^{1,1} - \hat{g}_{xy}^{1,10}$ are considered.

The performance for the four selected adaptive filters and their variants applied to the feedback paths $g_{xy}^{1,1}, g_{xy}^{1,5}$ is illuminated in Simulation 7.7.21 - 7.7.26 on pages 358–363.

As expected the convergence time of the feedback paths is considerably slower than for the simple secondary path. Also here the two FARLS filter variants exhibit slower convergence than the other adaptive filters. The best choice for the system identification in terms of convergence and excess error is provided by the $\alpha\gamma\Pi\epsilon$-APA with $K = 4, \Delta = 1$.

7.8 Active Control Simulations

The developed hybrid MIMO confined-feedforward-feedback system (HMIMOCFFFBS) is used in the examples provided in chapter 3 on page 105.

Bibliography

[1] Stephen J. Elliott. *Signal Processing for Active Control*. London: Academic Press, 2001.

[2] Sen M. Kuo and Dennis R. Morgan. *Active Noise Control Systems Algorithms and DSP Implementations*. John Wiley & Sons, Inc., 1996.

[3] Philip M. Morse and K. Uno Ingard. *Theoretical Acoustics*. Princeton University Press Princeton New Jersey, 1968.

[4] W. Ren and P. R. Kumar. Adaptive active noise control: Structures, algorithms and convergence analysis. In *Inter-noise*, pages 435–440, 1989.

[5] W. Ren and P. R. Kumar. Stochastic parallel model adaption: Theory and application to active noise cancelling, feedforward control IIR filtering and identification. *IEEE Transactions on Automatic Control*, 37:566–578, 1992.

[6] G. E. Warnaka, L. A. Poole, and J. Tichy. Applications for active noise control, 25 September 1984.

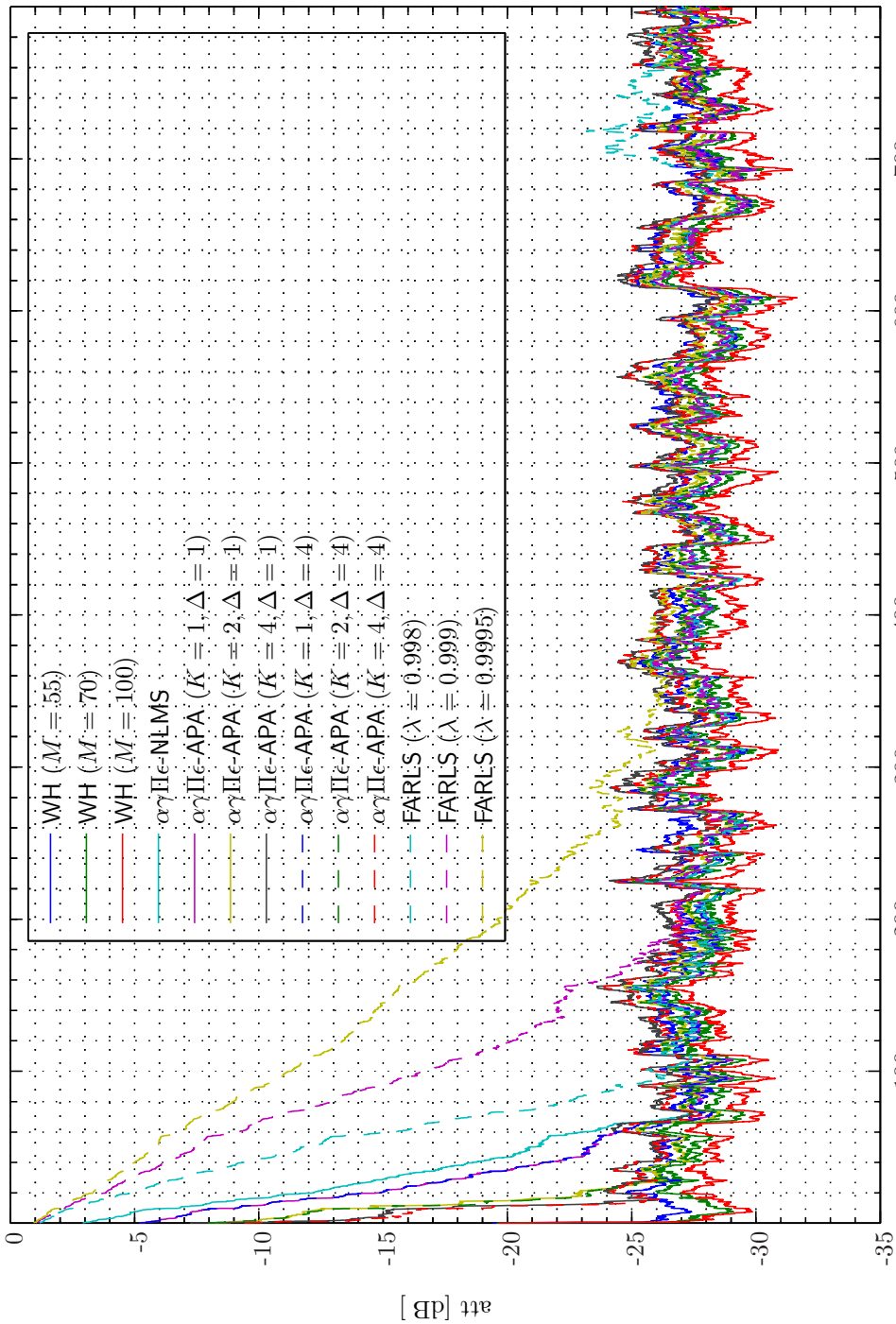

Sim 7.7.18: *Time-Domain: Attenuation.* **Adaptive Filter** $\hat{g}_{ey}$: $\hat{g}_{ey}^{1,1}$: WH ($\alpha = 1e-005, T_{WSS} = 0$,t-domain);$\alpha\gamma\Pi\epsilon$-NLMS ($M = 70, L_B = 1, \mu = 0.15, \alpha = 1e-005, \epsilon = 1e-006, T_{Eu} = 20$);$\alpha\gamma\Pi\epsilon$-APA ($M = 70, L_B = 1, \mu = 0.15, \alpha = 1e-005, \gamma = 1e-005, \Pi = 0, \epsilon = 1e-006, \check{w} = 0, W_e = 1$);FARLS ($M = 70, L_B = 1, \eta = 0.125, \alpha = 1e-005, T_{SW} = 0, Calc = 1$); **Main:** $f_s^0 = 192$ kHz, $f_s^1 = 24$ kHz, $R_{\updownarrow}^1 = \frac{1}{8} = 0.125$, Elliptic LPF ($f_s = 192$ kHz, $f_{pass} = 11$ kHz, $f_{stop} = 12$ kHz, $A_{pass} = 2$ dB, $A_{stop} = 40$ dB), $f_s^2 = 24$ kHz, $R_{\updownarrow}^2 = \frac{1}{1} = 1$, Dummy; **Topology:** BK 4949 surface microphones flush-mounted on Gentex HGU-55/P helmet mounted on a BK 4128 C HATS, Terma Earcup Audio System (Feedforward, mFx, $N_x = 10, N_e = 1, N_y = 1, N_p = 2, N_v = 0$); **Plants:** SysID/20080321T134130 ($g_{xy,\infty}^{1,1}$: (FIR : $M_{gxy}^{1,1} = 700$), $g_{xy,\infty}^{1,2}$: (FIR : $M_{gxy}^{1,2} = 700$), $g_{xy,\infty}^{1,3}$: (FIR : $M_{gxy}^{1,3} = 700$), $g_{xy,\infty}^{1,4}$: (FIR : $M_{gxy}^{1,4} = 700$), $g_{xy,\infty}^{1,5}$: (FIR : $M_{gxy}^{1,5} = 700$), $g_{xy,\infty}^{1,6}$: (FIR : $M_{gxy}^{1,6} = 700$), $g_{xy,\infty}^{1,7}$: (FIR : $M_{gxy}^{1,7} = 700$), $g_{xy,\infty}^{1,8}$: (FIR : $M_{gxy}^{1,8} = 700$), $g_{xy,\infty}^{1,9}$: (FIR : $M_{gxy}^{1,9} = 700$), $g_{xy,\infty}^{1,10}$: (FIR : $M_{gxy}^{1,10} = 700$), $g_{ey,\infty}^{1,1}$: (FIR : $M_{gey}^{1,1} = 120$), $g_{py,\infty}^{1,1}$: (FIR : $M_{gpy}^{1,1} = 200$), $g_{py,\infty}^{1,2}$: (FIR : $M_{gpy}^{1,2} = 200$)); **Signals:** *System Identification:* Random White Noise ($\mathcal{N}(0, 0.2)$), Output: 0.5 V, $f_s = 65.536$ kHz; Time: $0 - 0.8$ s; **Scenario:** `SystemIdentification(65536Hz)/20080321T172917`.

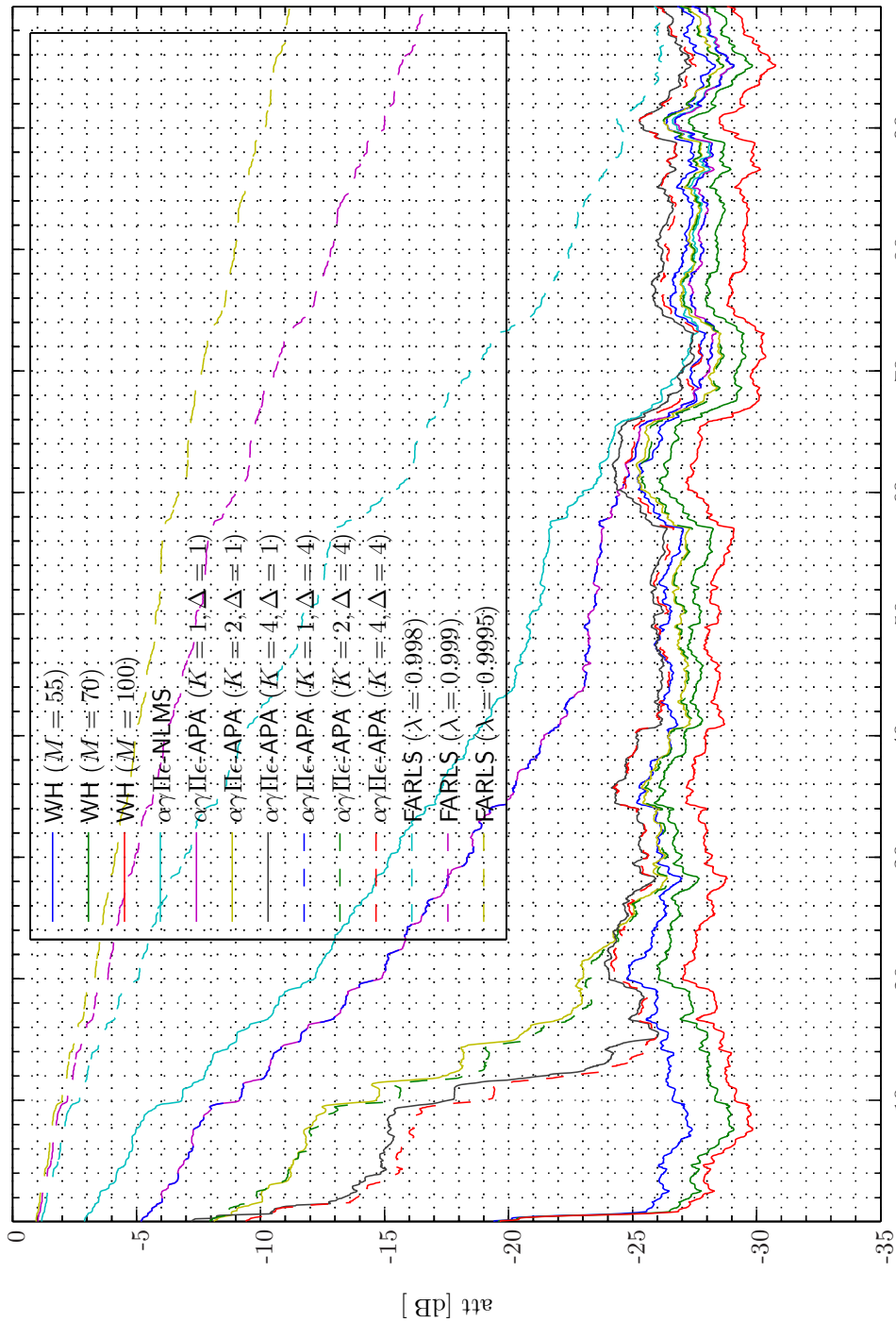

Sim 7.7.19: *Time-Domain: Attenuation Initial.* **Adaptive Filter** $\hat{g}_{ey}$: $\hat{g}_{ey}^{1,1}$: WH ($\alpha = 1e-005, T_{WSS} = 0$,**t**-domain);$\alpha\gamma\Pi\epsilon$-NLMS ($M = 70, L_B = 1, \mu = 0.15, \alpha = 1e-005, \epsilon = 1e-006, T_{Eu} = 20$);$\alpha\gamma\Pi\epsilon$-APA ($M = 70, L_B = 1, \mu = 0.15, \alpha = 1e-005, \gamma = 1e-005, \Pi = 0, \epsilon = 1e-006, \dot{w} = 0, W_e = 1$);FARLS ($M = 70, L_B = 1, \eta = 0.125, \alpha = 1e-005, T_{SW} = 0, Cadc = 1$); **Main:** $f_s^0 = 192$ kHz, $f_s^1 = 24$ kHz, $R_\updownarrow^1 = \frac{1}{8} = 0.125$, Elliptic LPF ($f_s = 192$ kHz, $f_{pass} = 11$ kHz, $f_{stop} = 12$ kHz, $A_{pass} = 2$ dB, $A_{stop} = 40$ dB), $f_s^2 = 24$ kHz, $R_\updownarrow^2 = \frac{1}{1} = 1$, Dummy; **Topology:** BK 4949 surface microphones flush-mounted on Gentex HGU-55/P helmet mounted on a BK 4128 C HATS, Terma Earcup Audio System (Feedforward, mFx, $N_x = 10, N_e = 1, N_y = 1, N_p = 2, N_v = 0$); **Plants:** SysID/20080321T134130 ($g_{xy}^{1,1}$: (FIR : $M_{gxy}^{1,1} = 700$), $g_{xy,\infty}^{1,2}$: (FIR : $M_{gxy}^{1,2} = 700$), $g_{xy,\infty}^{1,3}$: (FIR : $M_{gxy}^{1,3} = 700$), $g_{xy,\infty}^{1,4}$: (FIR : $M_{gxy}^{1,4} = 700$), $g_{xy,\infty}^{1,5}$: (FIR : $M_{gxy}^{1,5} = 700$), $g_{xy,\infty}^{1,6}$: (FIR : $M_{gxy}^{1,6} = 700$), $g_{xy,\infty}^{1,7}$: (FIR : $M_{gxy}^{1,7} = 700$), $g_{xy,\infty}^{1,8}$: (FIR : $M_{gxy}^{1,8} = 700$), $g_{xy,\infty}^{1,9}$: (FIR : $M_{gxy}^{1,9} = 700$), $g_{xy,\infty}^{1,10}$: (FIR : $M_{gxy}^{1,10} = 700$), $g_{ey,\infty}^{1,1}$: (FIR : $M_{geu}^{1,1} = 120$), $g_{py,\infty}^{1,1}$: (FIR : $M_{gpy}^{1,1} = 200$), $g_{py,\infty}^{1,2}$: (FIR : $M_{gpy}^{1,2} = 200$)); **Signals:** *System Identification:* Random White Noise ($\mathcal{N}(0, 0.2)$), Output: 0.5 V, $f_s = 65.536$ kHz; Time: $0 - 0.8$ s; **Scenario:** `SystemIdentification(65536Hz)/20080321T172917`.

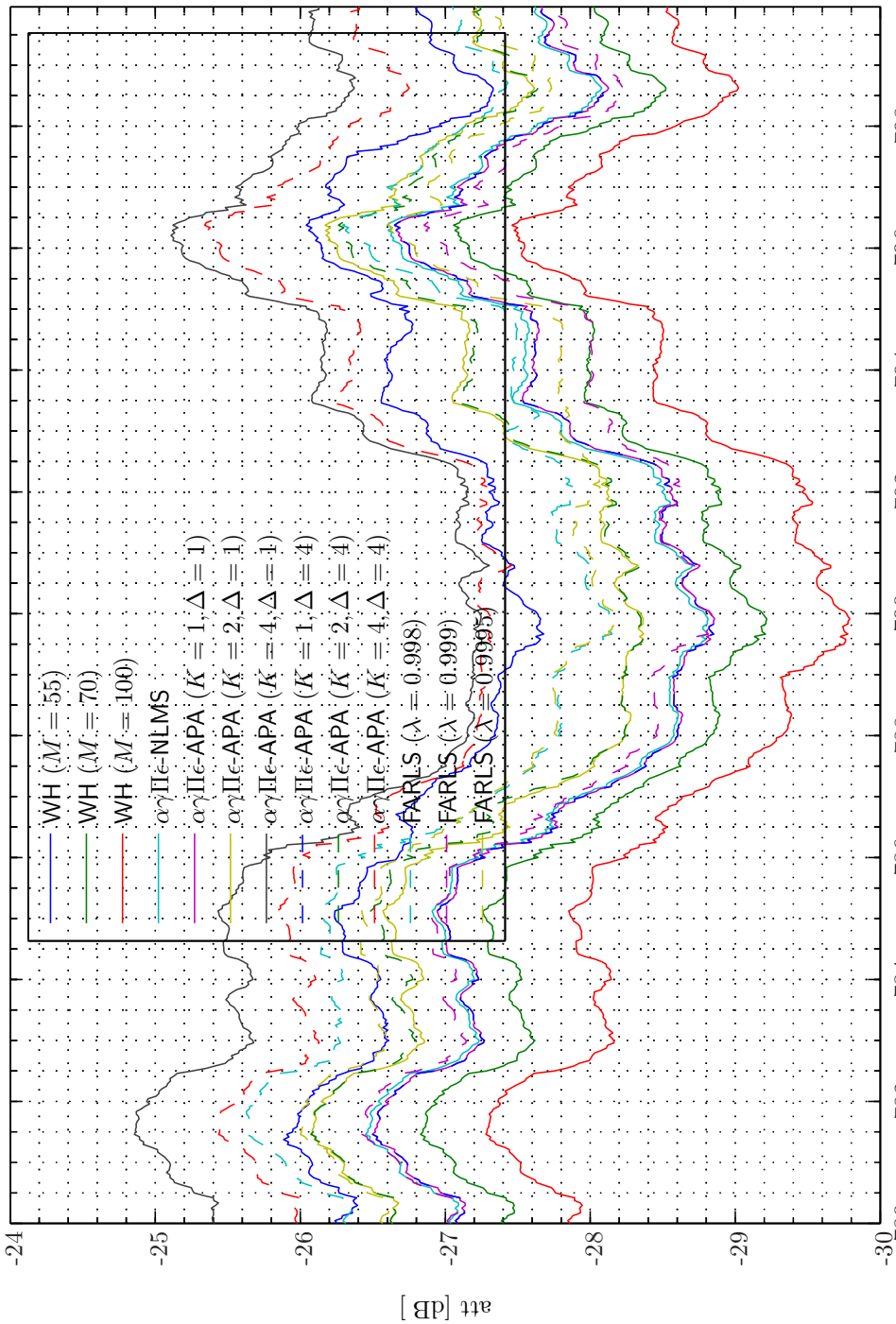

Sim 7.7.20: *Time-Domain: Attenuation Final.* **Adaptive Filter** $\hat{g}_{ey}$: $\hat{g}_{ey}^{1,1}$: WH ($\alpha = 1e-005, T_{WSS} = 0$,**t**-domain);$\alpha\gamma\Pi\epsilon$-NLMS ($M = 70, L_B = 1, \mu = 0.15, \alpha = 1e-005, \epsilon = 1e-006, T_{Eu} = 20$);$\alpha\gamma\Pi\epsilon$-APA ($M = 70, L_B = 1, \mu = 0.15, \alpha = 1e-005, \gamma = 1e-005, \Pi = 0, \epsilon = 1e-006, \check{w} = 0, W_e = 1$);FARLS ($M = 70, L_B = 1, \eta = 0.125, \alpha = 1e-005, T_{SW} = 0, Calc = 1$); **Main:** $f_s^0 = 192$ kHz, $f_s^1 = 24$ kHz, $R_{\updownarrow}^1 = \frac{1}{8} = 0.125$, Elliptic LPF ($f_s = 192$ kHz, $f_{pass} = 11$ kHz, $f_{stop} = 12$ kHz, $A_{pass} = 2$ dB, $A_{stop} = 40$ dB), $f_s^2 = 24$ kHz, $R_{\updownarrow}^2 = \frac{1}{1} = 1$, Dummy; **Topology:** BK 4949 surface microphones flush-mounted on Gentex HGU-55/P helmet mounted on a BK 4128 C HATS, Terma Earcup Audio System (Feedforward, mFx, $N_x = 10, N_e = 1, N_y = 1, N_p = 2, N_v = 0$); **Plants:** SysID/20080321T134130 ($g_{xy,\infty}^{1,1}$: (FIR : $M_{gxy}^{1,1} = 700$), $g_{xy,\infty}^{1,2}$: (FIR : $M_{gxy}^{1,2} = 700$), $g_{xy,\infty}^{1,3}$: (FIR : $M_{gxy}^{1,3} = 700$), $g_{xy,\infty}^{1,4}$: (FIR : $M_{gxy}^{1,4} = 700$), $g_{xy,\infty}^{1,5}$: (FIR : $M_{gxy}^{1,5} = 700$), $g_{xy,\infty}^{1,6}$: (FIR : $M_{gxy}^{1,6} = 700$), $g_{xy,\infty}^{1,7}$: (FIR : $M_{gxy}^{1,7} = 700$), $g_{xy,\infty}^{1,8}$: (FIR : $M_{gxy}^{1,8} = 700$), $g_{xy,\infty}^{1,9}$: (FIR : $M_{gxy}^{1,9} = 700$), $g_{xy,\infty}^{1,10}$: (FIR : $M_{gxy}^{1,10} = 700$), $g_{ey,\infty}^{1,1}$: (FIR : $M_{gey}^{1,1} = 120$), $g_{py,\infty}^{1,1}$: (FIR : $M_{gpy}^{1,1} = 200$), $g_{py,\infty}^{1,2}$: (FIR : $M_{gpy}^{1,2} = 200$)); **Signals:** *System Identification:* Random White Noise ($\mathcal{N}(0, 0.2)$), Output: 0.5 V, $f_s = 65.536$ kHz; Time: $0 - 0.8$ s; **Scenario:** `SystemIdentification(65536Hz)/20080321T172917`.

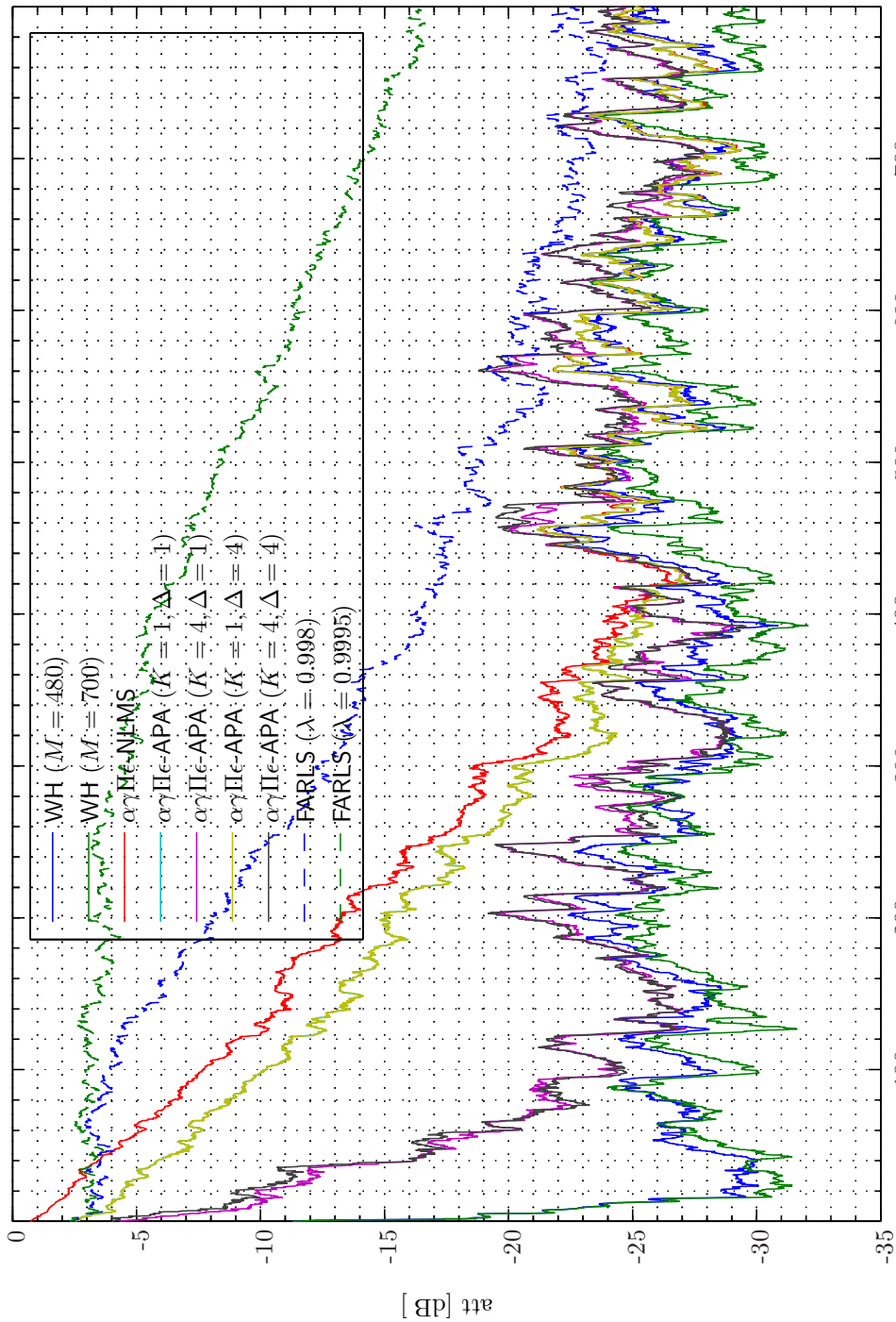

Sim 7.7.21: *Time-Domain: Attenuation.* **Adaptive Filter** $\hat{g}_{xy}$: $\hat{g}^{1,1}_{xy}$: WH ($\alpha = 1e-005, T_{WSS} = 0$,**t**-domain);$\alpha\gamma\Pi\epsilon$-NLMS ($M = 480, L_B = 1, \mu = 0.15, \alpha = 1e-005, \epsilon = 1e-006, T_{Eu} = 20$);$\alpha\gamma\Pi\epsilon$-APA ($M = 480, L_B = 1, \mu = 0.15, \alpha = 1e-005, \gamma = 1e-005, \Pi = 0, \epsilon = 1e-006, \breve{w} = 0, W_e = 1$);FARLS ($M = 480, L_B = 1, \eta = 0.125, \alpha = 1e-005, T_{SW} = 0, Cadc = 1$); **Main:** $f^0_s = 192$ kHz, $f^1_s = 24$ kHz, $R^1_{\updownarrow} = \frac{1}{8} = 0.125$, Elliptic LPF ($f_s = 192$ kHz, $f_{pass} = 11$ kHz, $f_{stop} = 12$ kHz, $A_{pass} = 2$ dB, $A_{stop} = 40$ dB), $f^2_s = 24$ kHz, $R^2_{\updownarrow} = \frac{1}{1} = 1$, Dummy; **Topology:** BK 4949 surface microphones flush-mounted on Gentex HGU-55/P helmet mounted on a BK 4128 C HATS, Terma Earcup Audio System (Feedforward, mFx, $N_x = 10, N_e = 1, N_y = 1, N_p = 2, N_v = 0$); **Plants:** SysID/20080321T134130 ($g^{1,1}_{xy,\infty}$: (FIR : $M^{1,1}_{gxy} = 700$), $g^{1,2}_{xy,\infty}$: (FIR : $M^{1,2}_{gxy} = 700$), $g^{1,3}_{xy,\infty}$: (FIR : $M^{1,3}_{gxy} = 700$), $g^{1,4}_{xy,\infty}$: (FIR : $M^{1,4}_{gxy} = 700$), $g^{1,5}_{xy,\infty}$: (FIR : $M^{1,5}_{gxy} = 700$), $g^{1,6}_{xy,\infty}$: (FIR : $M^{1,6}_{gxy} = 700$), $g^{1,7}_{xy,\infty}$: (FIR : $M^{1,7}_{gxy} = 700$), $g^{1,8}_{xy,\infty}$: (FIR : $M^{1,8}_{gxy} = 700$), $g^{1,9}_{xy,\infty}$: (FIR : $M^{1,9}_{gxy} = 700$), $g^{1,10}_{xy,\infty}$: (FIR : $M^{1,10}_{gxy} = 700$), $g^{1,1}_{ey,\infty}$: (FIR : $M^{1,1}_{gey} = 120$), $g^{1,1}_{py,\infty}$: (FIR : $M^{1,1}_{gpy} = 200$), $g^{1,2}_{py,\infty}$: (FIR : $M^{1,2}_{gpy} = 200$)); **Signals:** *System Identification:* Random White Noise ($\mathcal{N}(0, 0.2)$), Output: 5 V, $f_s = 65.536$ kHz; Time: $0 - 0.8$ s; **Scenario:** SystemIdentification(65536Hz)/20080322T003613.

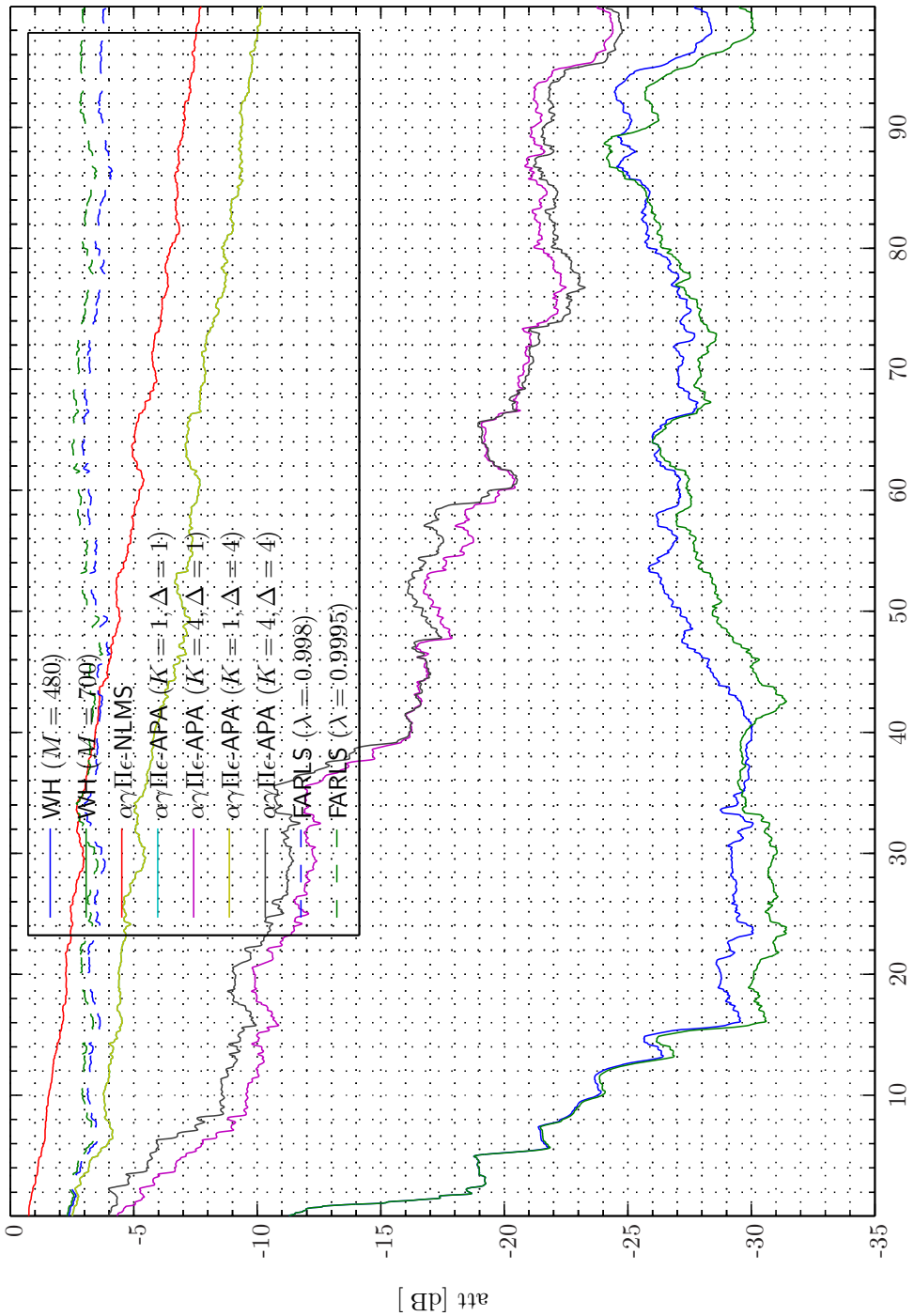

Sim 7.7.22: *Time-Domain: Attenuation Initial.* **Adaptive Filter** $\hat{g}_{xy}$: $\hat{g}_{xy}^{1,1}$: WH ($\alpha = 1e-005, T_{WSS} = 0$,**t**-domain);$\alpha\gamma\Pi\epsilon$-NLMS ($M = 480, L_B = 1, \mu = 0.15, \alpha = 1e-006, T_{Eu} = 20$);$\alpha\gamma\Pi\epsilon$-APA ($M = 480, L_B = 1, \mu = 0.15, \alpha = 1e-005, \gamma = 1e-005, \Pi = 0, \epsilon = 1e-006, \vec{w} = 0, W_e = 1$);FARLS ($M = 480, L_B = 1, \eta = 0.125, \alpha = 1e-005, T_{SW} = 0, Calc = 1$); **Main:** $f_s^0 = 192$ kHz, $f_s^1 = 24$ kHz, $R_\downarrow^1 = \frac{1}{8} = 0.125$, Elliptic LPF ($f_s = 192$ kHz, $f_{pass} = 11$ kHz, $f_{stop} = 12$ kHz, $A_{pass} = 2$ dB, $A_{stop} = 40$ dB), $f_s^2 = 24$ kHz, $R_\downarrow^2 = \frac{1}{1} = 1$, Dummy; **Topology:** BK 4949 surface microphones flush-mounted on Gentex HGU-55/P helmet mounted on a BK 4128 C HATS, Terma Earcup Audio System (Feedforward, mFx, $N_x = 10, N_e = 1, N_y = 1, N_p = 2, N_v = 0$); **Plants:** SysID/20080321T134130 ($g_{xy,\infty}^{1,1}$: (FIR : $M_{gxy}^{1,1} = 700$), $g_{xy,\infty}^{1,2}$: (FIR : $M_{gxy}^{1,2} = 700$), $g_{xy,\infty}^{1,3}$: (FIR : $M_{gxy}^{1,3} = 700$), $g_{xy,\infty}^{1,4}$: (FIR : $M_{gxy}^{1,4} = 700$), $g_{xy,\infty}^{1,5}$: (FIR : $M_{gxy}^{1,5} = 700$), $g_{xy,\infty}^{1,6}$: (FIR : $M_{gxy}^{1,6} = 700$), $g_{xy,\infty}^{1,7}$: (FIR : $M_{gxy}^{1,7} = 700$), $g_{xy,\infty}^{1,8}$: (FIR : $M_{gxy}^{1,8} = 700$), $g_{xy,\infty}^{1,9}$: (FIR : $M_{gxy}^{1,9} = 700$), $g_{xy,\infty}^{1,10}$: (FIR : $M_{gxy}^{1,10} = 700$), $g_{ey,\infty}^{1,1}$: (FIR : $M_{gey}^{1,1} = 120$), $g_{py,\infty}^{1,1}$: (FIR : $M_{gpy}^{1,1} = 200$), $g_{py,\infty}^{1,2}$: (FIR : $M_{gpy}^{1,2} = 200$)); **Signals:** *System Identification:* Random White Noise ($\mathcal{N}(0, 0.2)$), Output: 5 V, $f_s = 65.536$ kHz; Time: $0 - 0.8$ s; **Scenario:** SystemIdentification(65536Hz)/20080322T003613.

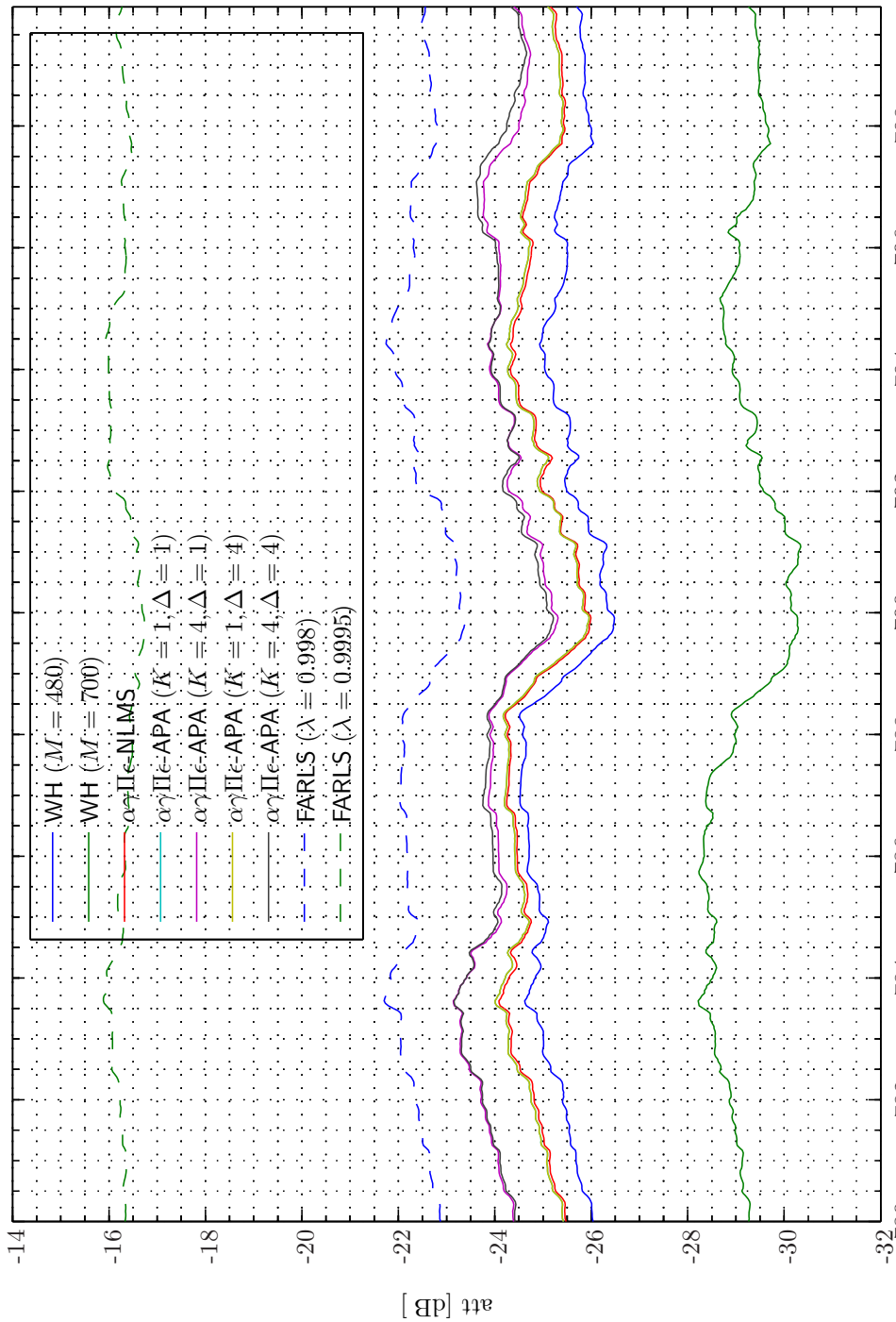

Sim 7.7.23: *Time-Domain: Attenuation Final.* **Adaptive Filter** $\hat{g}_{xy}$: $\hat{g}^{1,1}_{xy}$: WH ($\alpha = 1e-005, T_{WSS} = 0$,**t**-domain);$\alpha\gamma\Pi\epsilon$-NLMS ($M = 480, L_B = 1, \mu = 0.15, \epsilon = 1e-006, T_{Eu} = 20$);$\alpha\gamma\Pi\epsilon$-APA ($M = 480, L_B = 1, \mu = 0.15, \alpha = 1e-005, \gamma = 1e-005, \Pi = 0, \epsilon = 1e-006, \check{w} = 0, W_e = 1$);FARLS ($M = 480, L_B = 1, \eta = 0.125, \alpha = 1e-005, T_{SW} = 0, Calc = 1$); **Main:** $f^0_s = 192$ kHz, $f^1_s = 24$ kHz, $R^1_\updownarrow = \frac{1}{8} = 0.125$, Elliptic LPF ($f_s = 192$ kHz, $f_{pass} = 11$ kHz, $f_{stop} = 12$ kHz, $A_{pass} = 2$ dB, $A_{stop} = 40$ dB), $f^2_s = 24$ kHz, $R^2_\updownarrow = \frac{1}{1} = 1$, Dummy; **Topology:** BK 4949 surface microphones flush-mounted on Gentex HGU-55/P helmet mounted on a BK 4128 C HATS, Terma Earcup Audio System (Feedforward, mFx, $N_x = 10, N_e = 1, N_y = 1, N_p = 2, N_v = 0$); **Plants:** SysID/20080321T134130 ($g^{1,1}_{xy,\infty}$: (FIR : $M^{1,1}_{g_{xy}} = 700$), $g^{1,2}_{xy,\infty}$: (FIR : $M^{1,2}_{g_{xy}} = 700$), $g^{1,3}_{xy,\infty}$: (FIR : $M^{1,3}_{g_{xy}} = 700$), $g^{1,4}_{xy,\infty}$: (FIR : $M^{1,4}_{g_{xy}} = 700$), $g^{1,5}_{xy,\infty}$: (FIR : $M^{1,5}_{g_{xy}} = 700$), $g^{1,6}_{xy,\infty}$: (FIR : $M^{1,6}_{g_{xy}} = 700$), $g^{1,7}_{xy,\infty}$: (FIR : $M^{1,7}_{g_{xy}} = 700$), $g^{1,8}_{xy,\infty}$: (FIR : $M^{1,8}_{g_{xy}} = 700$), $g^{1,9}_{xy,\infty}$: (FIR : $M^{1,9}_{g_{xy}} = 700$), $g^{1,10}_{xy,\infty}$: (FIR : $M^{1,10}_{g_{xy}} = 700$), $g^{1,1}_{ey,\infty}$: (FIR : $M^{1,1}_{ge_y} = 120$), $g^{1,1}_{py,\infty}$: (FIR : $M^{1,1}_{gpy} = 200$), $g^{1,2}_{py,\infty}$: (FIR : $M^{1,2}_{gpy} = 200$)); **Signals:** *System Identification:* Random White Noise ($\mathcal{N}(0, 0.2)$), Output: 5 V, $f_s = 65.536$ kHz; Time: $0 - 0.8$ s; **Scenario:** `SystemIdentification(65536Hz)/20080322T003613`.

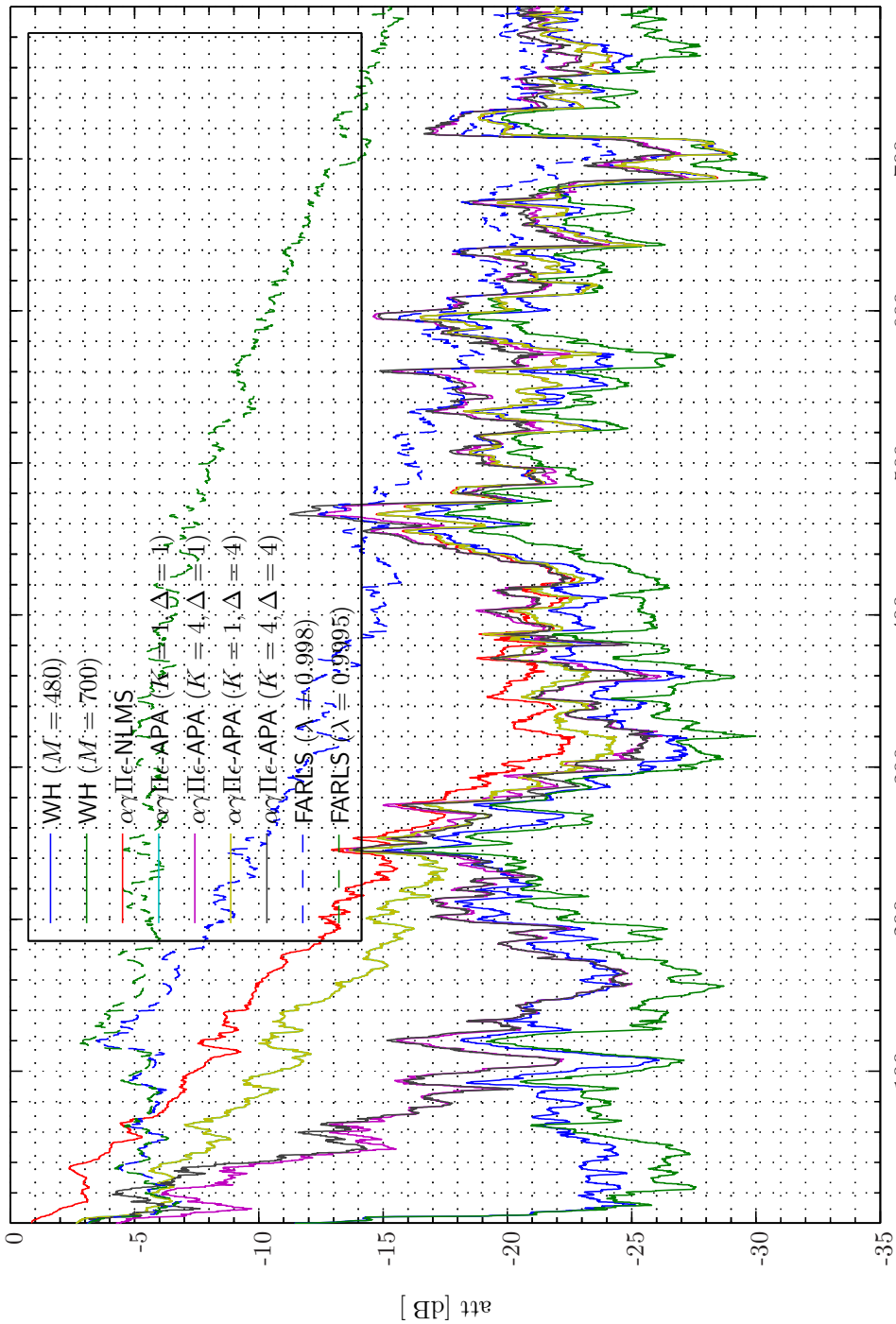

Sim 7.7.24: *Time-Domain: Attenuation.* **Adaptive Filter** $\hat{g}_{xy}$: $g_{xy}^{1,5}$: WH ($\alpha = 1e-005, T_{WSS} = 0$,t-domain);$\alpha\gamma\Pi\epsilon$-NLMS ($M = 480, L_B = 1, \mu = 0.15, \alpha = 1e-005, \epsilon = 1e-006, T_{Eu} = 20$);$\alpha\gamma\Pi\epsilon$-APA ($M = 480, L_B = 1, \mu = 0.15, \alpha = 1e-005, \gamma = 1e-005, \Pi = 0, \epsilon = 1e-006, \check{w} = 0, W_e = 1$);FARLS ($M = 480, L_B = 1, \eta = 0.125, \alpha = 1e-005, T_{SW} = 0, Calc = 1$); **Main:** $f_s^0 = 192$ kHz, $f_s^1 = 24$ kHz, $R_\updownarrow^1 = \frac{1}{8} = 0.125$, Elliptic LPF ($f_s = 192$ kHz, $f_{pass} = 11$ kHz, $f_{stop} = 12$ kHz, $A_{pass} = 2$ dB, $A_{stop} = 40$ dB), $f_s^2 = 24$ kHz, $R_\updownarrow^2 = \frac{1}{1} = 1$, Dummy; **Topology:** BK 4949 surface microphones flush-mounted on Gentex HGU-55/P helmet mounted on a BK 4128 C HATS, Terma Earcup Audio System (Feedforward, mFx, $N_x = 10, N_e = 1, N_y = 1, N_p = 2, N_v = 0$); **Plants:** SysID/20080321T134130 ($g_{xy,\infty}^{1,1}$: (FIR : $M_{gxy}^{1,1} = 700$), $g_{xy,\infty}^{1,2}$: (FIR : $M_{gxy}^{1,2} = 700$), $g_{xy,\infty}^{1,3}$: (FIR : $M_{gxy}^{1,3} = 700$), $g_{xy,\infty}^{1,4}$: (FIR : $M_{gxy}^{1,4} = 700$), $g_{xy,\infty}^{1,5}$: (FIR : $M_{gxy}^{1,5} = 700$), $g_{xy,\infty}^{1,6}$: (FIR : $M_{gxy}^{1,6} = 700$), $g_{xy,\infty}^{1,7}$: (FIR : $M_{gxy}^{1,7} = 700$), $g_{xy,\infty}^{1,8}$: (FIR : $M_{gxy}^{1,8} = 700$), $g_{xy,\infty}^{1,9}$: (FIR : $M_{gxy}^{1,9} = 700$), $g_{xy,\infty}^{1,10}$: (FIR : $M_{gxy}^{1,10} = 700$), $g_{ey,\infty}^{1,1}$: (FIR : $M_{gey}^{1,1} = 120$), $g_{py,\infty}^{1,1}$: (FIR : $M_{gpy}^{1,1} = 200$), $g_{py,\infty}^{1,2}$: (FIR : $M_{gpy}^{1,2} = 200$)); **Signals:** *System Identification:* Random White Noise ($\mathcal{N}(0, 0.2)$), Output: 5 V, $f_s = 65.536$ kHz; Time: $0 - 0.8$ s; **Scenario:** SystemIdentification(65536Hz)/20080322T003613.

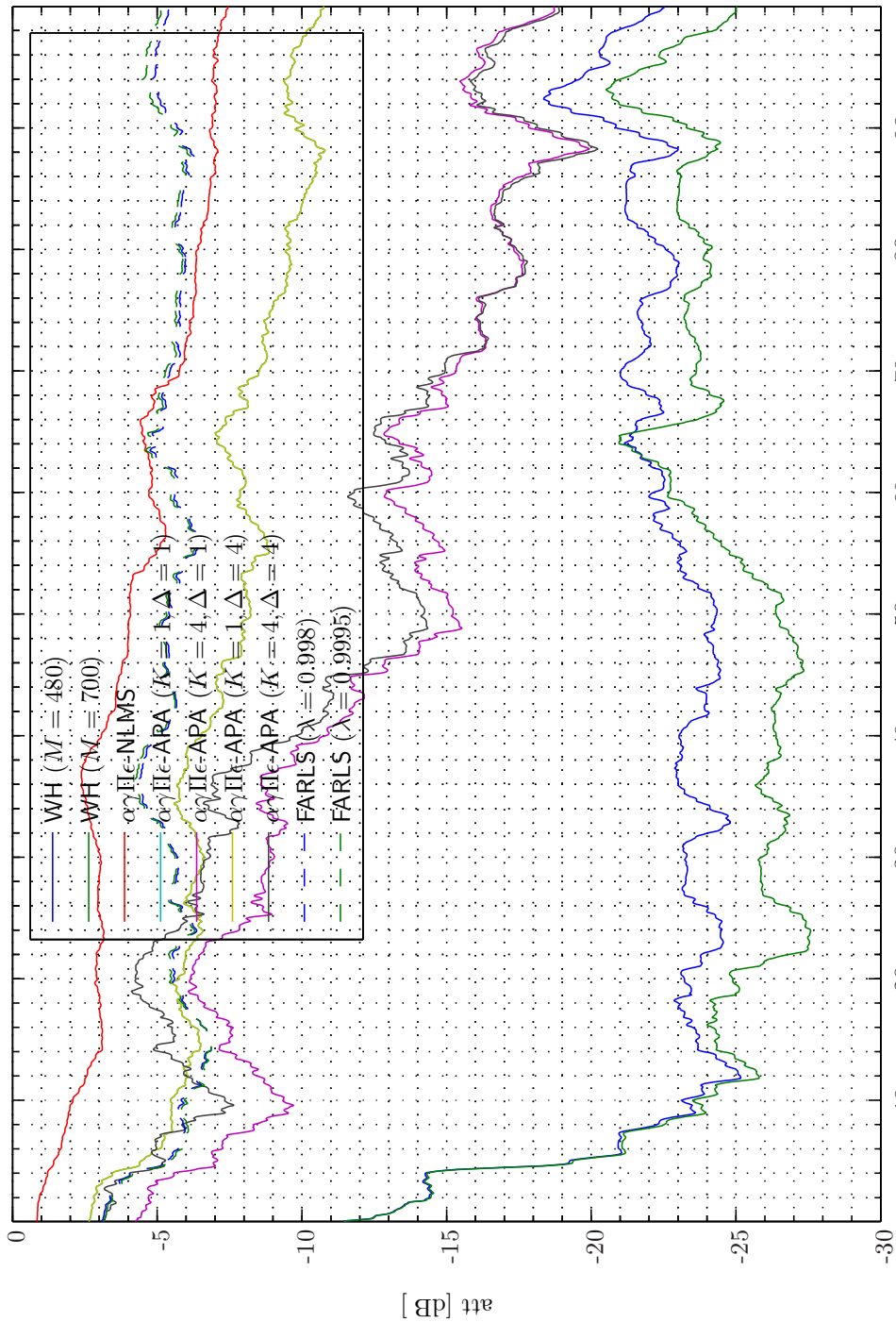

Sim 7.7.25: *Time-Domain: Attenuation Initial.* **Adaptive Filter** $\hat{g}_{xy}$: $\hat{g}_{xy}^{1,5}$: WH ($\alpha = 1e-005, T_{WSS} = 0$,**t**-domain):$\alpha\gamma\Pi\epsilon$-NLMS ($M = 480, L_B = 1, \mu = 0.15, \alpha = 1e-005, \epsilon = 1e-006, T_{Eu} = 20$);$\alpha\gamma\Pi\epsilon$-APA ($M = 480, L_B = 1, \mu = 0.15, \alpha = 1e-005, \gamma = 1e-005, \Pi = 0, \epsilon = 1e-006, \check{w} = 0, W_e = 1$);FARLS ($M = 480, L_B = 1, \eta = 0.125, \alpha = 1e-005, T_{SW} = 0, Calc = 1$); **Main:** $f_s^0 = 192$ kHz, $f_s^1 = 24$ kHz, $R_\updownarrow^1 = \frac{1}{8} = 0.125$, Elliptic LPF ($f_s = 192$ kHz, $f_{pass} = 11$ kHz, $f_{stop} = 12$ kHz, $A_{pass} = 2$ dB, $A_{stop} = 40$ dB), $f_s^2 = 24$ kHz, $R_\updownarrow^2 = \frac{1}{1} = 1$, Dummy; **Topology:** BK 4949 surface microphones flush-mounted on Gentex HGU-55/P helmet mounted on a BK 4128 C HATS, Terma Earcup Audio System (Feedforward, mFx, $N_x = 10, N_e = 1, N_y = 1, N_p = 2, N_v = 0$); **Plants:** SysID/20080321T134130 ($g_{xy,\infty}^{1,1}$: (FIR : $M_{g_{xy}}^{1,1} = 700$), $g_{xy,\infty}^{1,2}$: (FIR : $M_{g_{xy}}^{1,2} = 700$), $g_{xy,\infty}^{1,3}$: (FIR : $M_{g_{xy}}^{1,3} = 700$), $g_{xy,\infty}^{1,4}$: (FIR : $M_{g_{xy}}^{1,4} = 700$), $g_{xy,\infty}^{1,5}$: (FIR : $M_{g_{xy}}^{1,5} = 700$), $g_{xy,\infty}^{1,6}$: (FIR : $M_{g_{xy}}^{1,6} = 700$), $g_{xy,\infty}^{1,7}$: (FIR : $M_{g_{xy}}^{1,7} = 700$), $g_{xy,\infty}^{1,8}$: (FIR : $M_{g_{xy}}^{1,8} = 700$), $g_{xy,\infty}^{1,9}$: (FIR : $M_{g_{xy}}^{1,9} = 700$), $g_{xy,\infty}^{1,10}$: (FIR : $M_{g_{xy}}^{1,10} = 700$), $g_{ey,\infty}^{1,1}$: (FIR : $M_{g_{ey}}^{1,1} = 120$), $g_{py,\infty}^{1,1}$: (FIR : $M_{g_{py}}^{1,1} = 200$), $g_{py,\infty}^{1,2}$: (FIR : $M_{g_{py}}^{1,2} = 200$)); **Signals:** *System Identification:* Random White Noise ($\mathcal{N}(0, 0.2)$), Output: 5 V, $f_s = 65.536$ kHz; Time: $0 - 0.8$ s; **Scenario:** `SystemIdentification(65536Hz)/20080322T003613`.

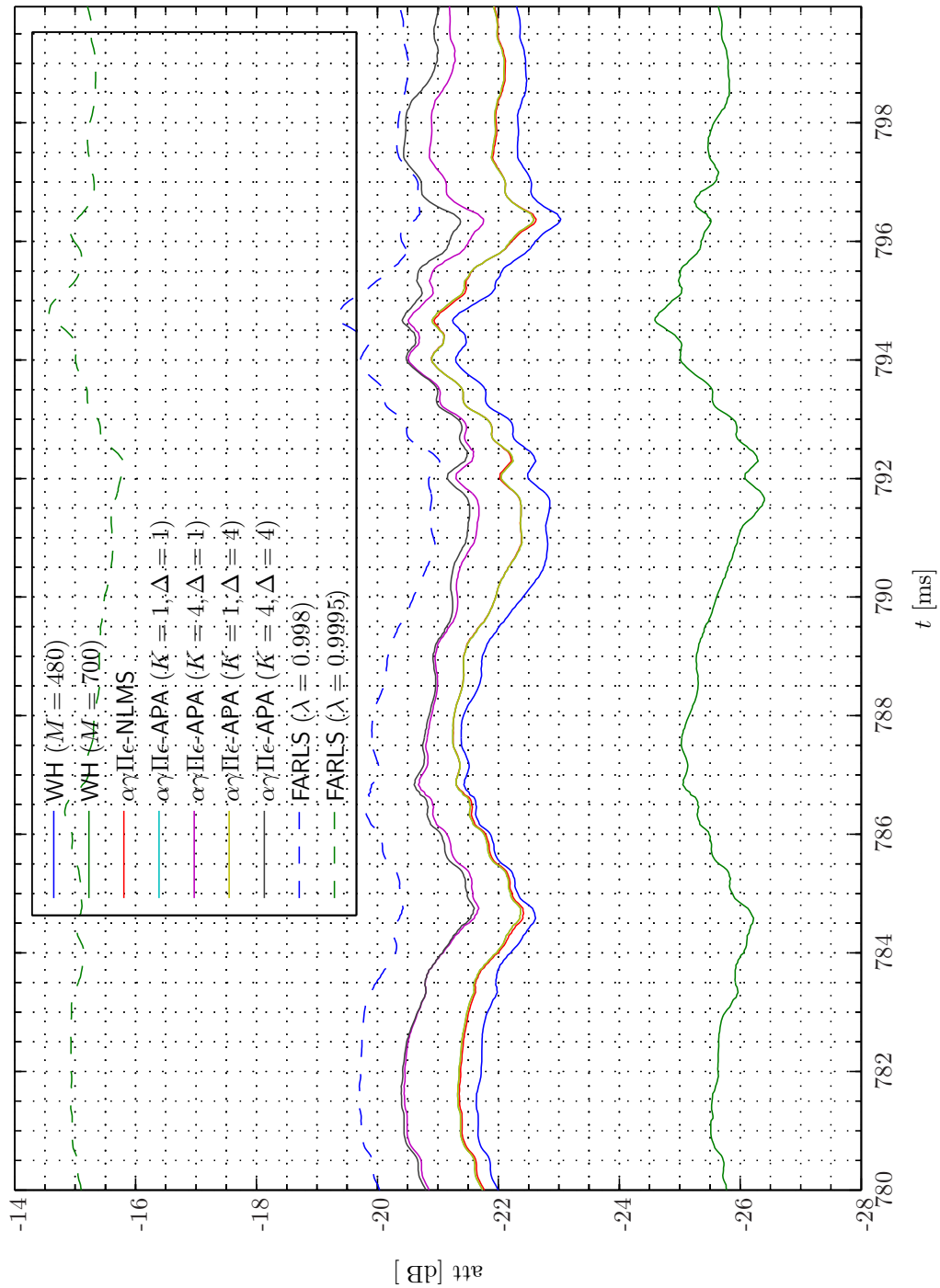

Sim 7.7.26: *Time-Domain: Attenuation Final.* **Adaptive Filter** $\hat{g}_{xy}$: $\hat{g}_{xy}^{1,5}$: WH ($\alpha = 1e-005, T_{WSS} = 0$,**t**-domain);$\alpha\gamma\Pi\epsilon$-NLMS ($M = 480, L_B = 1, \mu = 0.15, \epsilon = 1e-006, T_{Eu} = 20$);$\alpha\gamma\Pi\epsilon$-APA ($M = 480, L_B = 1, \mu = 0.15, \alpha = 1e-005, \gamma = 1e-005, \Pi = 0, \epsilon = 1e-006, \bar{w} = 0, W_e = 1$);FARLS ($M = 480, L_B = 1, \eta = 0.125, \alpha = 1e-005, T_{SW} = 0, Calc = 1$); **Main:** $f_s^0 = 192$ kHz, $f_s^1 = 24$ kHz, $R_\downarrow^1 = \frac{1}{8} = 0.125$, Elliptic LPF ($f_s = 192$ kHz, $f_{pass} = 11$ kHz, $f_{stop} = 12$ kHz, $A_{pass} = 2$ dB, $A_{stop} = 40$ dB), $f_s^2 = 24$ kHz, $R_\downarrow^2 = \frac{1}{1} = 1$, Dummy; **Topology:** BK 4949 surface microphones flush-mounted on Gentex HGU-55/P helmet mounted on a BK 4128 C HATS, Terma Earcup Audio System (Feedforward, mFx, $N_x = 10, N_e = 1, N_y = 1, N_p = 2, N_v = 0$); **Plants:** SysID/20080321T134130 ($g_{xy,\infty}^{1,1}$: (FIR : $M_{gxy}^{1,1} = 700$), $g_{xy,\infty}^{1,2}$: (FIR : $M_{gxy}^{1,2} = 700$), $g_{xy,\infty}^{1,3}$: (FIR : $M_{gxy}^{1,3} = 700$), $g_{xy,\infty}^{1,4}$: (FIR : $M_{gxy}^{1,4} = 700$), $g_{xy,\infty}^{1,5}$: (FIR : $M_{gxy}^{1,5} = 700$), $g_{xy,\infty}^{1,6}$: (FIR : $M_{gxy}^{1,6} = 700$), $g_{xy,\infty}^{1,7}$: (FIR : $M_{gxy}^{1,7} = 700$), $g_{xy,\infty}^{1,8}$: (FIR : $M_{gxy}^{1,8} = 700$), $g_{xy,\infty}^{1,9}$: (FIR : $M_{gxy}^{1,9} = 700$), $g_{xy,\infty}^{1,10}$: (FIR : $M_{gxy}^{1,10} = 700$), $g_{ey,\infty}^{1,1}$: (FIR : $M_{gey}^{1,1} = 120$), $g_{py,\infty}^{1,1}$: (FIR : $M_{gpy}^{1,1} = 200$), $g_{py,\infty}^{1,2}$: (FIR : $M_{gpy}^{1,2} = 200$)); **Signals:** *System Identification:* Random White Noise ($\mathcal{N}(0, 0.2)$), Output: 5 V, $f_s = 65.536$ kHz; Time: $0 - 0.8$ s; **Scenario:** SystemIdentification(65536Hz)/20080322T003613.

[7] Bernard Widrow and Samuel D. Stearns. *Adaptive Signal Processing.* Prentice-Hall, New Jersey, 1985.

7.A Array Description of Feedforward Feedback System

The FFFBS adaptive tap-weight cell matrix at multirate level 2 denoted by $\underset{\oplus}{w}_{t_B^2} \in \mathbb{K}^{(N_e+N_x)\times N_y}$ [6] is defined as the *vertical* catenation of the FBS adaptive tap-weight cell matrix $\underset{\bigcirc}{w}_{t_B^2} \in \mathbb{K}^{N_e\times N_y}$ and the FFS adaptive tap-weight cell matrix $\underset{\frown}{w}_{t_B^2} \in \mathbb{K}^{N_x\times N_y}$, that is,

$$\underset{\oplus}{w}_{t_B^2} \triangleq \operatorname{col}\{\underset{\bigcirc}{w}_{t_B^2}, \underset{\frown}{w}_{t_B^2}\}, \tag{7.A.1}$$

where $\underset{\bigcirc}{w}_{t_B^2}$ and $\underset{\frown}{w}_{t_B^2}$ in turn are defined by

$$\underset{\bigcirc}{w}_{t_B^2} \triangleq \begin{bmatrix} \underset{\bigcirc}{w}^{1,1}_{t_B^2} & \underset{\bigcirc}{w}^{1,2}_{t_B^2} & \cdots & \underset{\bigcirc}{w}^{1,N_y}_{t_B^2} \\ \underset{\bigcirc}{w}^{2,1}_{t_B^2} & \underset{\bigcirc}{w}^{2,2}_{t_B^2} & \cdots & \underset{\bigcirc}{w}^{2,N_y}_{t_B^2} \\ \vdots & \vdots & \ddots & \vdots \\ \underset{\bigcirc}{w}^{N_e,1}_{t_B^2} & \underset{\bigcirc}{w}^{N_e,2}_{t_B^2} & \cdots & \underset{\bigcirc}{w}^{N_e,N_y}_{t_B^2} \end{bmatrix} \tag{7.A.2a}$$

and

$$\underset{\frown}{w}_{t_B^2} \triangleq \begin{bmatrix} \underset{\frown}{w}^{1,1}_{t_B^2} & \underset{\frown}{w}^{1,2}_{t_B^2} & \cdots & \underset{\frown}{w}^{1,N_y}_{t_B^2} \\ \underset{\frown}{w}^{2,1}_{t_B^2} & \underset{\frown}{w}^{2,2}_{t_B^2} & \cdots & \underset{\frown}{w}^{2,N_y}_{t_B^2} \\ \vdots & \vdots & \ddots & \vdots \\ \underset{\frown}{w}^{N_x,1}_{t_B^2} & \underset{\frown}{w}^{N_x,2}_{t_B^2} & \cdots & \underset{\frown}{w}^{N_x,N_y}_{t_B^2} \end{bmatrix} \tag{7.A.2b}$$

respectively. Each element of $\underset{\bigcirc}{w}_{t_B^2}$ and $\underset{\frown}{w}_{t_B^2}$, that is, $\underset{\bigcirc}{w}^{m',l}_{t_B^2}$ and $\underset{\frown}{w}^{j,l}_{t_B^2}$ is a *column* vector of $\underset{\bigcirc}{M}_u^{m',l}$ and $\underset{\frown}{M}_u^{j,l}$ elements respectively, where $m' \in \underline{N}_e, j \in \underline{N}_x, l \in \underline{N}_y$.

The FFFBS regressor block cell matrix at multirate level 2 represented by $\mathring{\underset{\oplus}{u}}_{t_l^2} \in \mathbb{K}^{N_e\times N_y\times(N_e+N_x)}$ is defined as the *horizontal* catenation of the FBS regressor block cell matrix $\mathring{\underset{\bigcirc}{u}}_{t_l^2} \in \mathbb{K}^{N_e\times N_y\times N_e}$ and the FFS regressor block cell matrix $\mathring{\underset{\frown}{u}}_{t_l^2} \in \mathbb{K}^{N_e\times N_y\times N_x}$, that is,

$$\mathring{\underset{\oplus}{u}}_{t_l^2} \triangleq \operatorname{row}\{\mathring{\underset{\bigcirc}{u}}_{t_l^2}, \mathring{\underset{\frown}{u}}_{t_l^2}\}, \tag{7.A.3}$$

where $\mathring{\underset{\bigcirc}{u}}_{t_l^2}$ and $\mathring{\underset{\frown}{u}}_{t_l^2}$ in turn are defined by

[6] We use the (MATLAB®) term *cell matrix* to emphasize that each element of the matrix may be constituted from a different number of components.

$$\mathring{\underset{\circ}{u}}_{t_l^2} \triangleq \begin{bmatrix} \mathring{\underset{\circ}{u}}^{1,1,1}_{t_l^2} & \mathring{\underset{\circ}{u}}^{1,1,2}_{t_l^2} & \cdots & \mathring{\underset{\circ}{u}}^{1,1,N_e}_{t_l^2} \\ \mathring{\underset{\circ}{u}}^{1,2,1}_{t_l^2} & \mathring{\underset{\circ}{u}}^{1,2,2}_{t_l^2} & \cdots & \mathring{\underset{\circ}{u}}^{1,2,N_e}_{t_l^2} \\ \vdots & \vdots & \ddots & \vdots \\ \mathring{\underset{\circ}{u}}^{1,N_y,1}_{t_l^2} & \mathring{\underset{\circ}{u}}^{1,N_y,2}_{t_l^2} & \cdots & \mathring{\underset{\circ}{u}}^{1,N_y,N_e}_{t_l^2} \\ \mathring{\underset{\circ}{u}}^{2,1,1}_{t_l^2} & \mathring{\underset{\circ}{u}}^{2,1,2}_{t_l^2} & \cdots & \mathring{\underset{\circ}{u}}^{2,1,N_e}_{t_l^2} \\ \mathring{\underset{\circ}{u}}^{2,2,1}_{t_l^2} & \mathring{\underset{\circ}{u}}^{2,2,2}_{t_l^2} & \cdots & \mathring{\underset{\circ}{u}}^{2,2,N_e}_{t_l^2} \\ \vdots & \vdots & \ddots & \vdots \\ \mathring{\underset{\circ}{u}}^{2,N_y,1}_{t_l^2} & \mathring{\underset{\circ}{u}}^{2,N_y,2}_{t_l^2} & \cdots & \mathring{\underset{\circ}{u}}^{2,N_y,N_e}_{t_l^2} \\ \vdots & \vdots & \vdots & \vdots \\ \mathring{\underset{\circ}{u}}^{N_e,1,1}_{t_l^2} & \mathring{\underset{\circ}{u}}^{N_e,1,2}_{t_l^2} & \cdots & \mathring{\underset{\circ}{u}}^{N_e,1,N_e}_{t_l^2} \\ \mathring{\underset{\circ}{u}}^{N_e,2,1}_{t_l^2} & \mathring{\underset{\circ}{u}}^{N_e,2,2}_{t_l^2} & \cdots & \mathring{\underset{\circ}{u}}^{N_e,2,N_e}_{t_l^2} \\ \vdots & \vdots & \ddots & \vdots \\ \mathring{\underset{\circ}{u}}^{N_e,N_y,1}_{t_l^2} & \mathring{\underset{\circ}{u}}^{N_e,N_y,2}_{t_l^2} & \cdots & \mathring{\underset{\circ}{u}}^{N_e,N_y,N_e}_{t_l^2} \end{bmatrix} \tag{7.A.4a}$$

and

$$\mathring{\underset{\sim}{u}}_{t_l^2} \triangleq \begin{bmatrix} \mathring{\underset{\sim}{u}}^{1,1,1}_{t_l^2} & \mathring{\underset{\sim}{u}}^{1,1,2}_{t_l^2} & \cdots & \mathring{\underset{\sim}{u}}^{1,1,N_x}_{t_l^2} \\ \mathring{\underset{\sim}{u}}^{1,2,1}_{t_l^2} & \mathring{\underset{\sim}{u}}^{1,2,2}_{t_l^2} & \cdots & \mathring{\underset{\sim}{u}}^{1,2,N_x}_{t_l^2} \\ \vdots & \vdots & \ddots & \vdots \\ \mathring{\underset{\sim}{u}}^{1,N_y,1}_{t_l^2} & \mathring{\underset{\sim}{u}}^{1,N_y,2}_{t_l^2} & \cdots & \mathring{\underset{\sim}{u}}^{1,N_y,N_x}_{t_l^2} \\ \mathring{\underset{\sim}{u}}^{2,1,1}_{t_l^2} & \mathring{\underset{\sim}{u}}^{2,1,2}_{t_l^2} & \cdots & \mathring{\underset{\sim}{u}}^{2,1,N_x}_{t_l^2} \\ \mathring{\underset{\sim}{u}}^{2,2,1}_{t_l^2} & \mathring{\underset{\sim}{u}}^{2,2,2}_{t_l^2} & \cdots & \mathring{\underset{\sim}{u}}^{2,2,N_x}_{t_l^2} \\ \vdots & \vdots & \ddots & \vdots \\ \mathring{\underset{\sim}{u}}^{2,N_y,1}_{t_l^2} & \mathring{\underset{\sim}{u}}^{2,N_y,2}_{t_l^2} & \cdots & \mathring{\underset{\sim}{u}}^{2,N_y,N_x}_{t_l^2} \\ \vdots & \vdots & \vdots & \vdots \\ \mathring{\underset{\sim}{u}}^{N_e,1,1}_{t_l^2} & \mathring{\underset{\sim}{u}}^{N_e,1,2}_{t_l^2} & \cdots & \mathring{\underset{\sim}{u}}^{N_e,1,N_x}_{t_l^2} \\ \mathring{\underset{\sim}{u}}^{N_e,2,1}_{t_l^2} & \mathring{\underset{\sim}{u}}^{N_e,2,2}_{t_l^2} & \cdots & \mathring{\underset{\sim}{u}}^{N_e,2,N_x}_{t_l^2} \\ \vdots & \vdots & \ddots & \vdots \\ \mathring{\underset{\sim}{u}}^{N_e,N_y,1}_{t_l^2} & \mathring{\underset{\sim}{u}}^{N_e,N_y,2}_{t_l^2} & \cdots & \mathring{\underset{\sim}{u}}^{N_e,N_y,N_x}_{t_l^2} \end{bmatrix} \tag{7.A.4b}$$

respectively. Hence, $\mathring{\underset{\oplus}{u}}_{t_l^2}$ may be atomized as follows

$$\mathring{\underset{\oplus}{u}}_{t_l^2} \triangleq \begin{bmatrix} \mathring{u}^{1,1,1}_{\circ t_l^2} & \mathring{u}^{1,1,2}_{\circ t_l^2} & \cdots & \mathring{u}^{1,1,N_e}_{\circ t_l^2} & \mathring{u}^{1,1,1}_{\sim t_l^2} & \mathring{u}^{1,1,2}_{\sim t_l^2} & \cdots & \mathring{u}^{1,1,N_x}_{\sim t_l^2} \\ \mathring{u}^{1,2,1}_{\circ t_l^2} & \mathring{u}^{1,2,2}_{\circ t_l^2} & \cdots & \mathring{u}^{1,2,N_e}_{\circ t_l^2} & \mathring{u}^{1,2,1}_{\sim t_l^2} & \mathring{u}^{1,2,2}_{\sim t_l^2} & \cdots & \mathring{u}^{1,2,N_x}_{\sim t_l^2} \\ \vdots & \vdots & \ddots & \vdots & \vdots & \vdots & \ddots & \vdots \\ \mathring{u}^{1,N_y,1}_{\circ t_l^2} & \mathring{u}^{1,N_y,2}_{\circ t_l^2} & \cdots & \mathring{u}^{1,N_y,N_e}_{\circ t_l^2} & \mathring{u}^{1,N_y,1}_{\sim t_l^2} & \mathring{u}^{1,N_y,2}_{\sim t_l^2} & \cdots & \mathring{u}^{1,N_y,N_x}_{\sim t_l^2} \\ \mathring{u}^{2,1,1}_{\circ t_l^2} & \mathring{u}^{2,1,2}_{\circ t_l^2} & \cdots & \mathring{u}^{2,1,N_e}_{\circ t_l^2} & \mathring{u}^{2,1,1}_{\sim t_l^2} & \mathring{u}^{2,1,2}_{\sim t_l^2} & \cdots & \mathring{u}^{2,1,N_x}_{\sim t_l^2} \\ \mathring{u}^{2,2,1}_{\circ t_l^2} & \mathring{u}^{2,2,2}_{\circ t_l^2} & \cdots & \mathring{u}^{2,2,N_e}_{\circ t_l^2} & \mathring{u}^{2,2,1}_{\sim t_l^2} & \mathring{u}^{2,2,2}_{\sim t_l^2} & \cdots & \mathring{u}^{2,2,N_x}_{\sim t_l^2} \\ \vdots & \vdots & \ddots & \vdots & \vdots & \vdots & \ddots & \vdots \\ \mathring{u}^{2,N_y,1}_{\circ t_l^2} & \mathring{u}^{2,N_y,2}_{\circ t_l^2} & \cdots & \mathring{u}^{2,N_y,N_e}_{\circ t_l^2} & \mathring{u}^{2,N_y,1}_{\sim t_l^2} & \mathring{u}^{2,N_y,2}_{\sim t_l^2} & \cdots & \mathring{u}^{2,N_y,N_x}_{\sim t_l^2} \\ \vdots & \vdots & \vdots & \vdots & \vdots & \vdots & \vdots & \vdots \\ \mathring{u}^{N_e,1,1}_{\circ t_l^2} & \mathring{u}^{N_e,1,2}_{\circ t_l^2} & \cdots & \mathring{u}^{N_e,1,N_e}_{\circ t_l^2} & \mathring{u}^{N_e,1,1}_{\sim t_l^2} & \mathring{u}^{N_e,1,2}_{\sim t_l^2} & \cdots & \mathring{u}^{N_e,1,N_x}_{\sim t_l^2} \\ \mathring{u}^{N_e,2,1}_{\circ t_l^2} & \mathring{u}^{N_e,2,2}_{\circ t_l^2} & \cdots & \mathring{u}^{N_e,2,N_e}_{\circ t_l^2} & \mathring{u}^{N_e,2,1}_{\sim t_l^2} & \mathring{u}^{N_e,2,2}_{\sim t_l^2} & \cdots & \mathring{u}^{N_e,2,N_x}_{\sim t_l^2} \\ \vdots & \vdots & \ddots & \vdots & \vdots & \vdots & \ddots & \vdots \\ \mathring{u}^{N_e,N_y,1}_{\circ t_l^2} & \mathring{u}^{N_e,N_y,2}_{\circ t_l^2} & \cdots & \mathring{u}^{N_e,N_y,N_e}_{\circ t_l^2} & \mathring{u}^{N_e,N_y,1}_{\sim t_l^2} & \mathring{u}^{N_e,N_y,2}_{\sim t_l^2} & \cdots & \mathring{u}^{N_e,N_y,N_x}_{\sim t_l^2} \end{bmatrix}. \quad (7.A.5)$$

Each element of $\mathring{\underset{\circ}{u}}_{t_l^2}$ and $\mathring{\underset{\sim}{u}}_{t_l^2}$, that is, $\mathring{u}^{m,l,m'}_{\circ t_l^2}$ and $\mathring{u}^{m,l,j}_{\sim t_l^2}$ is a *row* vector of $\underset{\circ}{M}_u^{m',l}$ and $\underset{\sim}{M}_u^{j,l}$ elements respectively.

The FFFBS reference signal cell matrix at multirate level 1 denoted by $\underset{\oplus}{x}_{t_l^1} \in \mathbb{K}^{N_y \times (N_e+N_x)}$ is defined as the *horizontal* catenation of the FBS reference signal cell matrix $\mathring{\underset{\circ}{x}}_{t_l^1} \in \mathbb{K}^{N_y \times N_e}$ and the FFS reference signal cell matrix $\mathring{\underset{\sim}{x}}_{t_l^1} \in \mathbb{K}^{N_y \times N_x}$, that is,

$$\underset{\oplus}{x}_{t_l^1} \triangleq \text{row}\left\{\mathring{\underset{\circ}{x}}_{t_l^1}, \mathring{\underset{\sim}{x}}_{t_l^1}\right\}, \quad (7.A.6)$$

where $\mathring{\underset{\circ}{x}}_{t_l^1}$ and $\mathring{\underset{\sim}{x}}_{t_l^1}$ in turn are defined by

$$\mathring{\underset{\circ}{x}}_{t_l^1} \triangleq \begin{bmatrix} \mathring{x}_{\circ 1,t_l^1} & \mathring{x}_{\circ 2,t_l^1} & \cdots & \mathring{x}_{\circ N_e,t_l^1} \end{bmatrix} \quad (7.A.7)$$

and

$$\mathring{\underset{\sim}{x}}_{t_l^1} \triangleq \begin{bmatrix} \mathring{x}_{\sim 1,t_l^1} & \mathring{x}_{\sim 2,t_l^1} & \cdots & \mathring{x}_{\sim N_x,t_l^1} \end{bmatrix} \quad (7.A.8)$$

respectively. Each element of $\mathring{\underset{\circ}{x}}_{t_l^1}$ and $\mathring{\underset{\sim}{x}}_{t_l^1}$, that is, $\mathring{x}^{m'}_{\circ t_l^1}$ and $\mathring{x}^{j}_{\sim t_l^1}$ is a *row* vector of $\underset{\circ}{M}_w^{m',l}$ and $\underset{\sim}{M}_w^{j,l}$ elements respectively.

In order to use the adaptive filter algorithms the adaptive tap-weight vector shall be a column vector and the first dimension of the regressor matrix and reference signal matrix shall equal N_e and N_y respectively. In order to accomplish this we will next rearrange $\underset{\oplus}{w}_{t_B^2}$, $\mathring{\underset{\oplus}{u}}_{t_l^2}$ and $\underset{\oplus}{x}_{t_l^2}$. Then

the entries of the adaptive tap-weight vector at multirate level 2 denoted by $w_{t_B^2} \in \mathbb{K}^{M\times 1}$ are obtained from stacking the successive *columns* of $\underset{\oplus}{w}_{t_B^2}$ on top of each other, that is,

$$w_{t_B^2} \triangleq \operatorname{col}\{\underset{\oplus}{w}_{t_B^2}\}. \tag{7.A.9}$$

The total number of adaptive tap-weights M is the sum of the number of feedback adaptive tap-weights $\underset{\circlearrowleft}{M}_w$ and the number of feedforward adaptive tap-weights $\underset{\frown}{M}_w$, that is,

$$M \triangleq \underset{\oplus}{M}_w = \underset{\circlearrowleft}{M}_w + \underset{\frown}{M}_w, \tag{7.A.10}$$

where $\underset{\circlearrowleft}{M}_w$ and $\underset{\circlearrowleft}{M}_w$ in turn are obtained from

$$\underset{\circlearrowleft}{M}_w = \sum_{m'=1}^{N_e}\sum_{l=1}^{N_y} \underset{\circlearrowleft}{M}_w^{m',l} \tag{7.A.11a}$$

$$\underset{\frown}{M}_w = \sum_{j=1}^{N_x}\sum_{l=1}^{N_y} \underset{\frown}{M}_w^{j,l}. \tag{7.A.11b}$$

Similarly, the total regressor length for adaptive tap-weights M_u is the sum of the total regressor length for feedback adaptive tap-weights $\underset{\circlearrowleft}{M}_u$ and the total regressor length for feedforward adaptive tap-weights $\underset{\frown}{M}_u$, that is,

$$M_u \triangleq \underset{\oplus}{M}_u = \underset{\circlearrowleft}{M}_u + \underset{\frown}{M}_u, \tag{7.A.12}$$

where $\underset{\circlearrowleft}{M}_u$ and $\underset{\circlearrowleft}{M}_u$ in turn are obtained from

$$\underset{\circlearrowleft}{M} = \sum_{m'=1}^{N_e}\sum_{l=1}^{N_y} \underset{\circlearrowleft}{M}_u^{m',l} \tag{7.A.13a}$$

$$\underset{\frown}{M} = \sum_{j=1}^{N_x}\sum_{l=1}^{N_y} \underset{\frown}{M}_u^{j,l}. \tag{7.A.13b}$$

Similarly, by stacking the successive *rows* of the submatrices in $\underset{\oplus}{\mathring{u}}_{t_l^2}$ beside each other we obtain the regressor matrix at multirate level 2 $u_{t_l^2} \in \mathbb{K}^{N_e\times M}$

$$u_{t_l^2} \triangleq \operatorname{row}\{\underset{\oplus}{\mathring{u}}_{t_l^2}\} \tag{7.A.14}$$

$$u_{t_l^2} \triangleq \begin{bmatrix} \mathring{u}_{\circlearrowleft t_l^2}^{1,1,1} & \cdots & \mathring{u}_{\circlearrowleft t_l^2}^{1,1,N_e} & \mathring{u}_{\curvearrowright t_l^2}^{1,1,1} & \cdots & \mathring{u}_{\curvearrowright t_l^2}^{1,1,N_x} & \cdots & \mathring{u}_{\circlearrowleft t_l^2}^{1,N_y,1} & \cdots & \mathring{u}_{\circlearrowleft t_l^2}^{1,N_y,N_e} & \mathring{u}_{\curvearrowright t_l^2}^{1,N_y,1} & \cdots & \mathring{u}_{\curvearrowright t_l^2}^{1,N_y,N_x} \\ \mathring{u}_{\circlearrowleft t_l^2}^{2,1,1} & \cdots & \mathring{u}_{\circlearrowleft t_l^2}^{2,1,N_e} & \mathring{u}_{\curvearrowright t_l^2}^{2,1,1} & \cdots & \mathring{u}_{\curvearrowright t_l^2}^{2,1,N_x} & \cdots & \mathring{u}_{\circlearrowleft t_l^2}^{2,N_y,1} & \cdots & \mathring{u}_{\circlearrowleft t_l^2}^{2,N_y,N_e} & \mathring{u}_{\curvearrowright t_l^2}^{2,N_y,1} & \cdots & \mathring{u}_{\curvearrowright t_l^2}^{2,N_y,N_x} \\ \vdots & \ddots & \vdots & \vdots & \ddots & \vdots & \ddots & \vdots & \ddots & \vdots & \vdots & \ddots & \vdots \\ \mathring{u}_{\circlearrowleft t_l^2}^{N_e,1,1} & \cdots & \mathring{u}_{\circlearrowleft t_l^2}^{N_e,1,N_e} & \mathring{u}_{\curvearrowright t_l^2}^{N_e,1,1} & \cdots & \mathring{u}_{\curvearrowright t_l^2}^{N_e,1,N_x} & \cdots & \mathring{u}_{\circlearrowleft t_l^2}^{N_e,N_y,1} & \cdots & \mathring{u}_{\circlearrowleft t_l^2}^{N_e,N_y,N_e} & \mathring{u}_{\curvearrowright t_l^2}^{N_e,N_y,1} & \cdots & \mathring{u}_{\curvearrowright t_l^2}^{N_e,N_y,N_x} \end{bmatrix} \tag{7.A.15}$$

$$U_i \triangleq \begin{bmatrix} \mathring{u}_{\circlearrowleft i}^{1,1,1} & \cdots & \mathring{u}_{\circlearrowleft i}^{1,1,N_e} & \mathring{u}_{\curvearrowright i}^{1,1,1} & \cdots & \mathring{u}_{\curvearrowright i}^{1,1,N_x} & \cdots & \mathring{u}_{\circlearrowleft i}^{1,N_y,1} & \cdots & \mathring{u}_{\circlearrowleft i}^{1,N_y,N_e} & \mathring{u}_{\curvearrowright i}^{1,N_y,1} & \cdots & \mathring{u}_{\curvearrowright i}^{1,N_y,N_x} \\ \mathring{u}_{\circlearrowleft i}^{2,1,1} & \cdots & \mathring{u}_{\circlearrowleft i}^{2,1,N_e} & \mathring{u}_{\curvearrowright i}^{2,1,1} & \cdots & \mathring{u}_{\curvearrowright i}^{2,1,N_x} & \cdots & \mathring{u}_{\circlearrowleft i}^{2,N_y,1} & \cdots & \mathring{u}_{\circlearrowleft i}^{2,N_y,N_e} & \mathring{u}_{\curvearrowright i}^{2,N_y,1} & \cdots & \mathring{u}_{\curvearrowright i}^{2,N_y,N_x} \\ \vdots & \ddots & \vdots & \vdots & \ddots & \vdots & \ddots & \vdots & \ddots & \vdots & \vdots & \ddots & \vdots \\ \mathring{u}_{\circlearrowleft i}^{N_e,1,1} & \cdots & \mathring{u}_{\circlearrowleft i}^{N_e,1,N_e} & \mathring{u}_{\curvearrowright i}^{N_e,1,1} & \cdots & \mathring{u}_{\curvearrowright i}^{N_e,1,N_x} & \cdots & \mathring{u}_{\circlearrowleft i}^{N_e,N_y,1} & \cdots & \mathring{u}_{\circlearrowleft i}^{N_e,N_y,N_e} & \mathring{u}_{\curvearrowright i}^{N_e,N_y,1} & \cdots & \mathring{u}_{\curvearrowright i}^{N_e,N_y,N_x} \\ \mathring{u}_{\circlearrowleft i-\Delta_u}^{1,1,1} & \cdots & \mathring{u}_{\circlearrowleft i-\Delta_u}^{1,1,N_e} & \mathring{u}_{\curvearrowright i-\Delta_u}^{1,1,1} & \cdots & \mathring{u}_{\curvearrowright i-\Delta_u}^{1,1,N_x} & \cdots & \mathring{u}_{\circlearrowleft i-\Delta_u}^{1,N_y,1} & \cdots & \mathring{u}_{\circlearrowleft i-\Delta_u}^{1,N_y,N_e} & \mathring{u}_{\curvearrowright i-\Delta_u}^{1,N_y,1} & \cdots & \mathring{u}_{\curvearrowright i-\Delta_u}^{1,N_y,N_x} \\ \mathring{u}_{\circlearrowleft i-\Delta_u}^{2,1,1} & \cdots & \mathring{u}_{\circlearrowleft i-\Delta_u}^{2,1,N_e} & \mathring{u}_{\curvearrowright i-\Delta_u}^{2,1,1} & \cdots & \mathring{u}_{\curvearrowright i-\Delta_u}^{2,1,N_x} & \cdots & \mathring{u}_{\circlearrowleft i-\Delta_u}^{2,N_y,1} & \cdots & \mathring{u}_{\circlearrowleft i-\Delta_u}^{2,N_y,N_e} & \mathring{u}_{\curvearrowright i-\Delta_u}^{2,N_y,1} & \cdots & \mathring{u}_{\curvearrowright i-\Delta_u}^{2,N_y,N_x} \\ \vdots & \ddots & \vdots & \vdots & \ddots & \vdots & \ddots & \vdots & \ddots & \vdots & \vdots & \ddots & \vdots \\ \mathring{u}_{\circlearrowleft i-\Delta_u}^{N_e,1,1} & \cdots & \mathring{u}_{\circlearrowleft i-\Delta_u}^{N_e,1,N_e} & \mathring{u}_{\curvearrowright i-\Delta_u}^{N_e,1,1} & \cdots & \mathring{u}_{\curvearrowright i-\Delta_u}^{N_e,1,N_x} & \cdots & \mathring{u}_{\circlearrowleft i-\Delta_u}^{N_e,N_y,1} & \cdots & \mathring{u}_{\circlearrowleft i-\Delta_u}^{N_e,N_y,N_e} & \mathring{u}_{\curvearrowright i-\Delta_u}^{N_e,N_y,1} & \cdots & \mathring{u}_{\curvearrowright i-\Delta_u}^{N_e,N_y,N_x} \\ \vdots & \ddots & \vdots & \vdots & \ddots & \vdots & \ddots & \vdots & \ddots & \vdots & \vdots & \ddots & \vdots \\ \mathring{u}_{\circlearrowleft i-(K-1)\Delta_u}^{1,1,1} & \cdots & \mathring{u}_{\circlearrowleft i-(K-1)\Delta_u}^{1,1,N_e} & \mathring{u}_{\curvearrowright i-(K-1)\Delta_u}^{1,1,1} & \cdots & \mathring{u}_{\curvearrowright i-(K-1)\Delta_u}^{1,1,N_x} & \cdots & \mathring{u}_{\circlearrowleft i-(K-1)\Delta_u}^{1,N_y,1} & \cdots & \mathring{u}_{\circlearrowleft i-(K-1)\Delta_u}^{1,N_y,N_e} & \mathring{u}_{\curvearrowright i-(K-1)\Delta_u}^{1,N_y,1} & \cdots & \mathring{u}_{\curvearrowright i-(K-1)\Delta_u}^{1,N_y,N_x} \\ \mathring{u}_{\circlearrowleft i-(K-1)\Delta_u}^{2,1,1} & \cdots & \mathring{u}_{\circlearrowleft i-(K-1)\Delta_u}^{2,1,N_e} & \mathring{u}_{\curvearrowright i-(K-1)\Delta_u}^{2,1,1} & \cdots & \mathring{u}_{\curvearrowright i-(K-1)\Delta_u}^{2,1,N_x} & \cdots & \mathring{u}_{\circlearrowleft i-(K-1)\Delta_u}^{2,N_y,1} & \cdots & \mathring{u}_{\circlearrowleft i-(K-1)\Delta_u}^{2,N_y,N_e} & \mathring{u}_{\curvearrowright i-(K-1)\Delta_u}^{2,N_y,1} & \cdots & \mathring{u}_{\curvearrowright i-(K-1)\Delta_u}^{2,N_y,N_x} \\ \vdots & \ddots & \vdots & \vdots & \ddots & \vdots & \ddots & \vdots & \ddots & \vdots & \vdots & \ddots & \vdots \\ \mathring{u}_{\circlearrowleft i-(K-1)\Delta_u}^{N_e,1,1} & \cdots & \mathring{u}_{\circlearrowleft i-(K-1)\Delta_u}^{N_e,1,N_e} & \mathring{u}_{\curvearrowright i-(K-1)\Delta_u}^{N_e,1,1} & \cdots & \mathring{u}_{\curvearrowright i-(K-1)\Delta_u}^{N_e,1,N_x} & \cdots & \mathring{u}_{\circlearrowleft i-(K-1)\Delta_u}^{N_e,N_y,1} & \cdots & \mathring{u}_{\circlearrowleft i-(K-1)\Delta_u}^{N_e,N_y,N_e} & \mathring{u}_{\curvearrowright i-(K-1)\Delta_u}^{N_e,N_y,1} & \cdots & \mathring{u}_{\curvearrowright i-(K-1)\Delta_u}^{N_e,N_y,N_x} \end{bmatrix} \tag{7.A.16}$$

Finally, the reference signal vector denoted by $x_{t_l^1} \in \mathbb{K}^{N_y \times N_y(N_e+N_x)}$

$$x_{t_l^1} \triangleq \begin{bmatrix} x_{\oplus 1,t_l^1} & x_{\oplus 2,t_l^1} & \cdots & x_{\oplus N_e,t_l^1} \end{bmatrix} \otimes I_{N_y}, \tag{7.A.17}$$

where I_{N_y} is a $N_y \times N_y$ identity matrix and the Kronecker product $\otimes I_{N_y}$ therefore means that $\begin{bmatrix} x_{\oplus 1,t_l^1} & x_{\oplus 2,t_l^1} & \cdots & x_{\oplus N_e+N_x,t_l^1} \end{bmatrix}$ is repeatedly used N_y times to form the following diagonal matrix

$$x_{t_l^1} \triangleq \begin{bmatrix} \begin{bmatrix} x_{\oplus 1,t_l^1} & x_{\oplus 2,t_l^1} & \cdots & x_{\oplus N_e+N_x,t_l^1} \end{bmatrix} & & 0 & \cdots & & 0 & \\ & 0 & \begin{bmatrix} x_{\oplus 1,t_l^1} & x_{\oplus 2,t_l^1} & \cdots & x_{\oplus N_e+N_x,t_l^1} \end{bmatrix} & \cdots & & 0 & \\ & \vdots & \vdots & \ddots & & \vdots & \\ & 0 & 0 & \cdots & \begin{bmatrix} x_{\oplus 1,t_l^1} & x_{\oplus 2,t_l^1} & \cdots & x_{\oplus N_e+N_x,t_l^1} \end{bmatrix} \end{bmatrix}. \tag{7.A.18}$$

8. ADAPTIVE FILTERING ALGORITHMS FOR LINEAR TIME-VARIANT SYSTEMS

8.1 Introduction

In this chapter we will augment the suite of adaptive filters by new variants of the family of affine projection algorithms (APAs) with extended *leakage* functionality and provision for *weight regularization*. The full-blown adaptive filter will be designated by $\alpha\gamma\Pi\epsilon$-affine projection algorithm. The APA is a generalization to the normalized LMS (NLMS) algorithm in which the data is reused in order to improve the convergence speed albeit at the expense of computational complexity. The basic form of the APA was developed by Ozeki and Omeda [47] using an orthogonal projection to an affine subspace to address the problem of a slow convergence rate of least-mean-squares (LMS)-type filters with colored input. The APA has been used in field of acoustic echo cancelation applications [24]. Demands on computational efficiency has led to development of so-called fast affine projection (FAP) [24, 25] and the frequency-domain block exact fast affine projection (BEFAP) [55, 62]. The FAP has been used for single channel active noise control (ANC) [17] and for multiple-channel (MC)-ANC in [5, 6][1]. Moreover, in [8, 9, 60] different affine projection (AP) algorithms for MC-ANC have been considered. In our development we will consider both *weight-driven leakage* and *control-effort-driven leakage*. Although these two types of leakage functionality are related they also provide the designer with complementary functionality that will be optimal in different contexts. Tap-weight regularization is a well known principle from regularized least-squares problems where it is used to incorporate some *a priori* information regarding the optimal solution is available and the regressor provides insufficient excitation of the pertinent parameters. The regularization parameter can then control to which extend the parameters will be locked in the vicinity of some fixed point vector.

To the author's best knowledge no attempts in the open literature has been made to accommodate control-effort-driven leakage to the APA family of adaptive filtering algorithms. Similarly, although weight regularization often is applied in *deterministic* based adaptive schemes no such attempts were found in the literature for adaptive filtering algorithms with origin in *stochastics*. It is therefore believed that such algorithms should be of general interest within the signal processing community and of particular interest within the active control (AC) community where practical design constraints to a large extent can be addressed by introducing adaptive leakage control.

In order to proceed we will review parts of *adaptive filtering theory* pertinent to signal processing, adaptive control and in particular in an active control context. Readers unfamiliar with adaptive filter theory or who need to refresh their memory should refer to the many excellent books available in the field of signal processing [29, 68, 69] and control theory [61, 74]. Recently, a

[1] An active control of sound (ACS) where either the number of reference sensors, the number of error sensors or the number of actuators exceeds one is referred to as a MC system else it is considered as a single-channel (SC) system.

new and very comprehensive textbook by Sayed [56] has become available. The notation and terminology in this report will largely follow the choice in that textbook.

While the treatment of different adaptive filters tends to be bottom-up, that is, it starts with the most simple version and gradually increase the complexity of the algorithm, the framework adapted here will opposedly be top-down. Hence, we will present the adaptive filtering algorithms in their most general form and describe the simpler models as specific instantiations of the general form. Accordingly, our treatment will from the outset embrace the hybrid MIMO feedforward-feedback system (HMIMOFFFBS) described in chapter 7 on page 291. The accommodation from a single-input and single-output (SISO) to a multiple-input and single-output (MISO) system[2] can be carried out with relative little effort by recasting the formulation by collecting all regressors and weight vectors into a single extended regressor and a single extended weight vector. However, the extension to a SIMO or to a multiple-input and multiple-output (MIMO) system poses somewhat more challenges to the designer as now not only a single error but multiple errors have to be considered. In this chapter we will address the multiple-output cases by using a cost function formulation that incorporates a *weighted sum* of the individual errors. In ACS applications frequency-domain-based adaptive filters are often preferred to time-domain-based adaptive filters. Therefore, the time-domain adaptive filter algorithms will be accompanied with their frequency-domain versions. Finally, the general case of a *time-varying* environment will be addressed from the outset.

As mentioned in chapter 6 the main body of the literature in the field of adaptive digital filtering exclusively consider purely electrical problems that are characterized by the absence of a *physical plant*. The methods to incorporate a plant in an adaptive filtering context were described in chapter 6 and included in this presentation. Then the plant-less application is considered as a specialization of this framework. Finally, but not less importantly this treatment lends itself towards efficient implementation in a simulation environment, e.g., MATLAB®, but also a *real-time* implementation.

8.1.1 Chapter Outline

This chapter has been organized as follows. Following this introduction section 8.2 presents four different modes of adaptive filtering. Next in section 8.3 the concepts of *cost functions*, *leakage* and *regularization* are discussed. Wiener filters are subsequently introduced in section 8.4. Both the unconstrained case, that is, the non causal and the causally constrained case are considered. Subsequently we introduce the method of steepest descent in section 8.5 that represents an intermediate stage of conception between the theoretical oriented Wiener Filter and the stochastic gradient algorithms that are used for many practical purposes. The family of stochastic gradient (SG) algorithms will be presented in section 8.6. New and more general variants of the APA adaptive filtering algorithm that combines a set of different functionalities are derived. This adaptive filter algorithm denoted by $\alpha\gamma\Pi\epsilon$-affine projection algorithm includes parameters for *leakage* control and *adaptive tap-weight regularization* as well as *numerical regularization*. A simplification of this algorithm leads to the $\alpha\gamma\Pi\epsilon$-NLMS algorithm. It is demonstrated how the ordinary ϵ-affine projection algorithm (ϵ-APA) and ϵ-NLMS (ϵ-NLMS) algorithms can be obtained from successive simplifications of the new $\alpha\gamma\Pi\epsilon$-affine projection algorithm ($\alpha\gamma\Pi\epsilon$-APA) and $\alpha\gamma\Pi\epsilon$-NLMS ($\alpha\gamma\Pi\epsilon$-NLMS) algorithms respectively. The theme of section 8.7 is the accom-

[2] An adaptive filter basically takes two types of inputs namely the reference signals and the error signals. However, when we discriminate between single-input and multiple-input it is the number of error signals that counts.

modation necessary for the use of time-domain adaptive filters in the frequency-domain. Of particular concern is to ensure the adaptive filters are causally constrained.

Finally, in section 8.8 the main findings of this chapter will be summarized.

The theme of the appendix section 8.A is in general $\mathcal{H}_2/\mathcal{H}_\infty$ adaptive control and in particular adaptive filtering subjects to inequality constraints. This appendix also serves as a motivation of considering the two dynamic leakage schemes of this chapter.

A comprehensive performance analysis of the multiple-channel-$\alpha\gamma\Pi\epsilon$-affine projection algorithm (MC-$\alpha\gamma\Pi\epsilon$-APA) algorithm is conducted in chapter 9 on page 417.

8.2 Modes of Adaptive Filtering Operation

By the adjective *adaptive* (as opposed to *fixed*) preceding the word filter we understand a self-designing filter that relies on a *recursive algorithm*, which makes it possible for the filter to perform satisfactorily in an environment where complete knowledge of the relevant signal characteristics is not available. Hence, even for stationary data the filter adapts itself in this manner. Moreover, for non-stationary data the adaptive filter supposedly will track the environmental changes. Adaptive filters are therefore a powerful device for signal-processing and control applications.

Adaptive filtering is pertinent to the digital controller involved in the hybrid controller in Figure 4.1 on page 241 in four different aspects:

Adaptive Filter Mode 1. *Interference cancelation.* One set of adaptive filters is used for to determine the cancelation signal.

Adaptive Filter Mode 2. *System identification.* A second set of adaptive filters is used for *system identification* in which the plants are determined.

Adaptive Filter Mode 3. *Inverse modeling.* A third filter is used to correct the plant response towards some prescribed response.

Adaptive Filter Mode 4. *Prediction.* Finally, a linear prediction notch filter is used to suppress influence of the high amount of low-frequency content in the adaptation process.

In the application of active noise reduction headsets the four types of filters are all required to be adaptive. The filter responsible for the interference cancelation is required to be adaptive because as will be discussed in this chapter the optimum controller depends on the spectral properties of the disturbance, as well as the plant response. However, in practice the characteristic of the disturbance is usually not known exactly, or even statistically. [3] Similarly, the plant response will be inter-subject dependent, exhibit variation with the actual fit of the hearing protection device (HPD) on the subject, possible wear and many other parameters [46]. Hence, the plant response should also be considered unknown or at least partially unknown. Finally, adaptation capabilities are also required for the system identification and inverse modeling as explained in section 4.7 on page 245.

Owing to the significant importance the plant poses to the adaptive filtering process in active noise control applications, we devoted the previous chapter 6 on page 273 to describe how the

[3] The statistical properties of the disturbances in two practical military airborne applications are discussed in Appendix D.

family so-called *filtered-X* methods accompanied by repetitive system identifications can be used to address the problems associated with a possible unknown and in general time-varying plants.

In conclusion, the purpose of adaptive filtering is to ensure satisfactory operation and preferably optimal performance in a time-variant but unknown or at least partial unknown environment. Interesting, however, is that the functionality required for this four-fold operation can be provided by basically the same adaptive filtering technique.

The filters discussed in this chapter can basically be considered *linear*. However, during adaptation the filters will inherently exhibit non-linearity, which is a consequence of the process of *adaptation* where the filters do not obey the principle of superposition but are data dependent. Normally, the weights are assumed constant compared on a time frame much smaller that the convergence time. However, this fact should be considered if some otherwise unexplainable convergence problems are experienced.

8.3 Cost Functions

In the design and analysis of adaptive filters one has to establish a framework for evaluating the performance. This is basically the argument for the introducing *cost functions* [4]. Cost functions also referred to as *criterion functions* or *objective functions* themselves are seldom calculated in a real-time implementation. But the underlying adaptation of the filter is based on the principle of minimizing a cost function. Moreover, the optimization might be *constrained* or *unconstrained*, depending on whether the variables are also required to satisfy side equations or not.

As described in section A.2 on page 529 the probably most established figure of merit within the AC community is the steady-state integrated noise attenuation provided by the system over a volume in space. This figure of merit is usually obtained by averaging the attenuation over some discrete positions in space. We will ideally measure or estimate the performance locally at each of the N_p locations of the performance sensors depicted in Figure 1.1. Usually, however, in an *operational* ANC-system no performance sensor exists and the performance is assessed directly from the N_e error sensors. Accordingly, our cost functions should closely resemble the design objectives formulated in section A.2.

In this presentation of the various adaptive filtering algorithms we will establish a complex cost function formulation that honors requirements emerging from practical applications. This top-down presentation should hopefully provide some complementary insight into the operation of these algorithms. In this context we exclusively focus on *linear optimum discrete-time filters*.

8.3.1 Time-Domain Cost Functions

The by far most preferred choice of cost function within the signal processing communities is based on a linear-least-mean-squares estimate (l.l.m.s.e.) criterion in the time-domain. By applying the pertinent premises for a particular algorithm the equations leading to the expression for the weight update can normally be derived without much sophistication. The main disadvantage, however, is that from a practical point of view that some simplifications made are too unrealistic and the implementation is deemed to fail at some time. Accordingly, modifications, some of which are based on pure heuristics are then made to refine the algorithms.

[4] Another approach is to demand the output estimation error to be independent of past data [39].

The choice of linear-least-mean-squares estimation (l.l.m.s.e.) is somewhat arbitrary and is historically related to the assumption of Gaussian distributed data that in turn has been based on the central limit theorem (CLT) from statistics. In [49] and [73] it is also argued that for Gaussian distributed random variables the linear least-mean-square estimator is considered practical optimal. Sherman [58] and Brown [7] investigated a non-mean-square-error criterion in the study of Gaussian processes. We will also consider a more general class of linear minimum mean-even-norm estimation. In recent years attention has been made to the class of so-called SαS processes [45]. The family of SαS distributions which will be the theme of Appendix L on page 773 has efficiently been used to model impulsive signals.

Preferably, the optimal cost function formulation could adaptively be derived from the statistical properties of the signals [39, Ch. 15].

As described in detail in Appendix A on page 529 in the *time-domain* we will usually apply the mean-squared-error reduction criterion and define $\mathcal{A}_m(t)$ attenuation at the m'th error sensor by

$$\mathcal{A}_m(t) \triangleq 10\log_{10}\left(\frac{\mathrm{E}\,|\mathbf{e}_m(t)|^2}{\mathrm{E}\,|\mathbf{d}_m(t)|^2}\right) \quad [\mathrm{dB}], \tag{8.3.1}$$

where $\mathbf{e}_m$ and $\mathbf{d}_m$ designate the error signal and the disturbance signal at the m'th error sensor respectively both considered as RVs. For MISO and MIMO systems the *global* attenuation capability measure is obtained as, e.g., a linear-weighted sum of the local attenuation quantities above (in dB), that is,

$$\mathcal{A}(f,t) \triangleq \sum_{m=1}^{N_e} W_{e,m}^{\mathrm{dB}} \mathcal{A}_m(f,t) \quad [\mathrm{dB}]. \tag{8.3.2}$$

The quantity $W_m^{e,\mathrm{dB}}$ denotes the attenuation weight factor of m'th error sensor. Often a normalization constraint $\sum_{m=1}^{N_e} W_{e,m}^{\mathrm{dB}} = 1$ will be used.

The choice of a cost function formulation depends on whether the particular adaptive filtering algorithm takes origin in *stochastics* or if it is *deterministic* in approach. To the former class belong Wiener Filters, the Method of steepest descent (SD) and the LMS algorithms. They have in common that some statistical information is available in advance or at least is estimated during the process. To the latter class we find among others the least-squares (LS) algorithm and the recursive least-squares (RLS) algorithm. Both of these algorithms are *model-dependent* procedures.

In order to reduce the computational load we will from the outset use a separate time frame for the weight update. The corresponding weight block update iteration number is represented by i_B, where we by i refer to the *iteration* number. The two time indices i and i_B are subject to $i_B = \lfloor (i/B)$ where we by $\lfloor(\,\cdot\,)$ designates the *floor operator*, where we by the integer $B \in \mathbb{N}$ will denote the weight update block size.

Stochastic Approach

For the algorithms with origin in stochastics the estimation problem will make extensive use of the *expectation operator* denoted by $\mathrm{E}(\,\cdot\,)$.

Most often the time-domain cost function $J(w_{i_B}) : \mathbb{K}^{M\times 1} \to \mathbb{R}_+(\mathbb{K}^{M\times M} \succ 0)$ that takes as

argument the adaptive tap-weight vector $w_{i_B} \in \mathbb{K}^{M\times 1}$ and returns a scalar-valued quantity (greater than zero) or a positive definite error-covariance matrix $E_{e_i e_i *} \succ 0$.

For ordinary SISO systems and MISO systems we will let $J(w_{i_B})$ be scalar-valued as only a single error signal is involved. For single-input and multiple-output (SIMO) systems and MIMO systems, however, the cost function will be based on the error-covariance matrix $E_{e_i e_i *}$. The optimization procedure then seeks to minimize the trace of the error covariance matrix and is therefore referred to as a *minimum variance* estimator.

We will most often consider the mean-square error (m.s.e.) criterion where the cost function is defined by $J^{e^2}(w_{i_B})$

$$J^{e^2}(w_{i_B}) \triangleq \begin{cases} \mathrm{E}|\mathbf{e}(i)|^2, & \text{SISO, SIMO,} \\ \mathrm{E}\|\mathbf{e}_i\|^2_{W_e}, & \text{MISO, MIMO.} \end{cases} \tag{8.3.3}$$

The quantity $W_e \in \mathbb{R}^{N_e\times N_e}$ denotes the error sensor weighting diagonal matrix where the individual elements W^e_m denote the weight factor attributed to the m'th error sensor. Often a normalization constraint $\|W_e\| = \sum_{m=1}^{N_e} W^e_m = 1$ will be preferred. The expected error sensor-weighted error $\mathrm{E}\|\mathbf{e}_i\|^2_{W_e}$ can alternatively also be expressed by

$$\mathrm{E}\|\mathbf{e}_i\|^2_{W_e} = \mathrm{E}\, e_i^* W_e e_i = \mathrm{Tr}\,\{W_e\, \mathrm{E}\, e_i e_i^*\}. \tag{8.3.4}$$

We then seek a weight vector that minimizes (8.3.3) in a least-mean-squares estimate (l.m.s.e.) sense, that is,

$$\min_w \big\{ J^{e^2}(w_{i_B}) \big\}. \tag{8.3.5}$$

The minimum value of $J^{e^2}(w_{i_B})$ is referred to as the minimum mean-square error (m.m.s.e.). The m.s.e. criterion (8.3.3) is very general without any assumptions regarding the data and the system. Now we will confine ourselves to linear time-variant (LTV) systems and invoke a linear estimation model (LEM) for the *regression vector (matrix)* $\mathbf{u}_i \in \mathbb{K}^{1\times M}(\mathbf{u}_i \in \mathbb{K}^{N_e\times M})$ and the disturbance signal $\mathbf{d}(i) \in \mathbb{K}(\mathbf{d}_i \in \mathbb{K}^{N_e\times 1})$ both considered as *data sequences*. The details of the LEM can be found in section 9.2 on page 422. Then the general cost function (8.3.3) is formulated as

$$J^{e^2}(w_{i_B}) \triangleq \begin{cases} \mathrm{E}|\mathbf{d}(i) - \mathbf{u}_i w_{i_B}|^2, & \text{SISO, SIMO,} \\ \mathrm{E}\|\mathbf{d}_i - \mathbf{u}_i w_{i_B}\|^2_{W_e}, & \text{MISO, MIMO.} \end{cases} \tag{8.3.6}$$

Then the l.l.m.s.e. of (8.3.5) (8.3.6) is the weight vector $w^o_{i_B}$ that leads to the m.m.s.e..

The quadratic function on elements of the weight vector is a nice property since then the *multi-dimensional error-performance surface* takes form of a bowl-shaped surface with a unique global minima. In practice, however, an ensemble of data is rarely available. Instead an assumption of wide-sense ergodicity (WSE) of the signals is implicitly made. Recalling that WSE implies wide-sense stationary (WSS) (but not the converse!), the data therefore satisfy a criterion on WSS. Consequently, ensemble averages will be replaced by time-averages.

8.3.2 Frequency-Domain Cost Functions

For ACS applications a better choice is usually to apply a frequency-domain cost function based on loudness curves. Similar considerations apply to active control of vibration (ACV) applications although with frequency-domain weighting functions that will be application specific. The l.l.m.s.e. approach has computational advantages and is convenient for theoretical analysis attributed to its tractable mathematics. Accordingly we will also define cost functions in the frequency-domain. In section A.2 on page 529 we formulated different attenuation quantities as measure of the active noise reduction (ANR) performance.

The *local* attenuation at, e.g., the m'th error sensor $\mathcal{A}_m(f)$ will be a function of frequency and generally exhibit time-dependence. The computation of $\mathcal{A}_m(f)$ will primarily be based on signal analysis which is treated in more details in Appendix C. We will define the frequency-domain attenuation by

$$\mathcal{A}_m(f) \triangleq 10\log_{10}\left(W_{e,m}(f)\frac{S_{e_m e_m}(f)}{S_{d_m d_m}(f)}\right) \quad [\text{dB}]. \tag{8.3.7}$$

Here $S_{e_m e_m}(f)$ and $S_{d_m d_m}(f)$ denote the auto spectral density function of the m'th error signal and m'th disturbance signal respectively. The quantity $W_{e,m}(f)$ represents a frequency-dependent weighting function that will be subject to the normalization constrain $\int_{-\infty}^{\infty} W_{e,m}(f)\,\mathrm{d}f = 1$. For example $W_{e,m}(f)$ may be a A-, B-, C- or D-weighting filter. An unweighted attenuation expression is obtained by assigning unity to $W_{e,m}(f)$.

In the discrete Fourier transform (DFT) domain we chose a block size B and uses a $2B$-point fast Fourier transform (FFT) and the *overlap-save method* in order to prevent *circular correlation effects* [56, Ch. 10] [51]. The entire frequency range $[-\frac{f_s}{2}, \frac{f_s}{2}]$ is then subdivided into $2B$ equally sized frequency bins. Usually both M and B are chosen as powers of 2 and such that B/M is an integer, e.g., $M = 1024, B = 32$. The l.l.m.s.e. is similarly the weight vector w^o_{k,i_B} that leads to the m.m.s.e. in (8.3.8)

$$J^{e^2}(\tilde{w}_{k,i_B}) \triangleq \begin{cases} \mathrm{E}\left|\tilde{\mathbf{d}}_k(i) - \tilde{\mathbf{u}}_{k,i}\tilde{w}_{k,i_B}\right|^2 & = \mathrm{E}|\tilde{\mathbf{e}}_k(i)|^2, \quad \text{SISO, SIMO,} \\ \mathrm{E}\|\tilde{\mathbf{d}}_{k,i} - \tilde{\mathbf{u}}_{k,i}\tilde{w}_{k,i_B}\|^2_{W_e} & = \mathrm{E}\|\tilde{\mathbf{e}}_{k,i}\|^2_{W_e(k)}, \quad \text{MISO, MIMO,} \end{cases} \quad k = 0, 1, \ldots, 2B-1 \tag{8.3.8}$$

using the m.s.e. criterion (8.3.9)

$$\min_{w_k}\left\{J^{e^2}(w_{k,i_B})\right\}. \tag{8.3.9}$$

Hence, l.l.m.s.e. is carried out for each of the $2B$ frequency bins in parallel. It should, however, be recalled that the size of the adaptive tap-weight vector is reduced by a factor of B in each of these subfilters [56, Ch. 10].

8.3.3 Weight-Driven Leakage

Motivation

The objective of introducing leakage is at least elevenfold:[5]

Leakage Objective 1. Prevention of the occurrence of overflow in a *finite-precision environment*. The lack of sufficient excitation in the regression data may result in weight estimates growing unbounded and overflowing. The m.s.e. might not be effected by finite precision effects, but the mean-square deviation (m.s.d.) will accumulate with time.

Leakage Objective 2. Alleviation of d.c. drift. In a physical system a d.c. component might be present in the error signal due to offsets in the A/D converters. The adaptive filter will try to suppress this d.c. component by gradually increasing all weights numerically. However, the physical system is not capable of responding to d.c. Eventually, the system (D/A converters) saturate and the system is rendered useless [27, Ch. 7].

Leakage Objective 3. Reduction of eigenvalue spread. It is well known that a white noise signal by definition has an autocovariance matrix equal to its variance $\sigma_v^2(i)$ times the identity matrix, that is, $R_v(i) = \sigma_v^2(i)\mathrm{I}$. Since all eigenvalues equal unity then by addition such a *dither signal* the resulting eigenvalue spread $\mathcal{X}(R_{u+v})$ will be reduced from the eigenvalue spread $\mathcal{X}(R_u)$ of the reference signal [68], that is,

$$\mathcal{X}(R_{u+v}) < \mathcal{X}(R_u). \tag{8.3.10}$$

Accordingly, by applying a dither signal then adaptive filtering algorithms sensitive to eigenvalue spread, e.g., LMS will experience a faster convergence. This may be of particular concern in signal processing in acoustics where the signals often exhibit highly non-stationarity and at times are absent.

Leakage Objective 4. Counteracting *parameter drift*. In the stability analysis of an adaptive filtering algorithm it is useful to partitioning the space spanned by the information vector (regressor) into four mutually non-overlapping subspaces referred to as *unexcited subspace*, *persistently excited subspace*, *decreasing subspace* and *otherwise excited subspace*. If the information vector belong to the *decreasing subspace* or *otherwise excited subspace* the weights can then attain arbitrarily large values despite bounded input bounded output disturbances, and bounded estimation errors [29, Ch. 17] and [57]. The parameter drift is considered a *hidden form of instability* associated with inadequacy of excitation in the input sequence and is characterized by a slow (as opposed to exponential) growth of the weights. This drift mechanism is inherent in the algorithm and is not due to numerical implementation problems or violation of small step-size conditions. In particular, for some types of non-stationary signals parameter drift might be of concern. Moreover, it should be mentioned that stability analysis usually resort to the assumption of the regressor belonging to either the *unexcited subspace* or the *persistently excited subspace*. This phenomena has a separate spectral domain interpretation: An input power spectrum devoid energy over a nontrivial portion of the frequency band and therefore is not complying with a persistent excitation (PE) condition might similarly cause parameter drift [63, Ch. 7]. The signal absent case mentioned above is different as the *unexcited subspace* coincides with $\mathbb{C}^M$.

[5] The list is probably not exhaustive and some of the objectives are to some extent overlapping.

Leakage Objective 5. Preventing the poles from moving outside the unit circle during convergence in an adaptive infinite-duration impulse response (IIR) filter configuration [36]. Therefore, potential instability problems can be avoided by adding an amount of leakage.

Leakage Objective 6. Avoidance of non-linear distortion. By introducing a term in the cost function that penalizes the squared norm (energy) of the vector w the system will then avoid seeking to a solution with potentially large norms. In active noise control this is of specific importance since the secondary sources might be driven into non-linear operation in the presence of high low-frequency resonances [34, Ch. 2] and [44, Ch. 12].

Leakage Objective 7. Reduction of sensitivity to imperfect plant models. Avoiding the risk of a potential negative real-part of the eigenvalues of the mixed autocorrelation matrix of filtered- and estimated- reference signals used in ANC configurations employing a plant filtering scheme. If the plants response is different from that of the plant model the real part of the eigenvalues of the aforementioned mixed autocorrelation matrix can take negative values leading to instability [66]. In active noise control this is of specific importance since small changes in the system might lead to disastrous results for unbounded weights [22, Ch. 3,5].

Leakage Objective 8. Insurance of a *diagonal dominant* response matrix in a multi-channel decoupled ANC-system [21]. By adding a positive term proportional to the modulus of the squared control effort to the cost function, this effectively also increases the diagonal elements of the effective response matrix entering in a stability criterion. This can be proved to have a stabilizing effect on a decoupled multi-channel ANC-system [21].

Leakage Objective 9. Provision of solution to *underdetermined* systems. In AC systems where the number of secondary sourcees exceeds the number of error sensors the optimal solution is nonunique. By also penalizing the control effort in the cost function, however, the solution becomes unique [22, Ch. 4].

Leakage Objective 10. Ignoring modes in MIMO ANC system which contribute only weakly to the error signal, but which require a considerably amount of the available control power. Then the error performance can be maintained with significantly lower control effort [22, Ch. 4].

Leakage Objective 11. Compliance with $\mathcal{H}_\infty$ control design constraints. $\mathcal{H}_\infty$ control can be emulated by means of leakage that in turn is regularized by penalty functions or barrier functions as will be presented in subsection 8.A.1 on page 404.

Leakage objective 1-1 are related to the use of the adaptive delay filter (ADF) in a *quantized* digital environment. Leakage objective 3-4 consider the signal contents of the input data. Leakage objective 5 is specific to the use of IIR filters. Finally, leakage objectives 6 and 11 are concerned with the long-term stable operation of the adaptive filter for ANC applications.

The problems addressed might not necessarily be disastrous but might lead to performance degradation in general if not taking into account.

Besides ANC applications [22, 34] leakage has also successfully been employed in applications such as adaptive control [32] [1, Ch. 6] to avoid estimator windup, antenna systems to prevent self deletion of strong signals [72], fractionally spaced adaptive equalizer (FSAE) for channel equalization [26], adaptive differential pulse code modulation (ADPCM) coders for telephone transmission [15].

In conclusion there are many good reasons for employing some leakage functionality in the adaptive filter schemes used in ANC applications.

Weight-Driven Leakage in the Time Domain

The linear least-mean-squares estimation problem (8.3.5) can be augmented to include a cost function weight norm penalty term that will be represented by $J^{\alpha}(w_{i_B})$ and that is defined as

$$J^{\alpha}(w_{i_B}) \triangleq \|w_{i_B}\|^2_{\alpha_{i_\alpha}(w_{i_B^\alpha})} = w^*_{i_B}\alpha_{i_\alpha}(w_{i_B^\alpha})w_{i_B}, \tag{8.3.11}$$

where the quantity $\alpha_{i_\alpha}(w_{i_B^\alpha}) \in \mathbb{R}^{M\times M}(\alpha_{i_\alpha}(w_{i_B^\alpha}) \in \mathbb{R})$ refers to the *weight-driven leakage control* matrix (parameter) and where i_α denotes the weight leakage control matrix update iteration number and i_B^α is the weight block update iteration number corresponding to i_α. The weight leakage control matrix may be updated at each block-update time or if computational prohibitive then less frequently. Hence, $i_\alpha \leq i_B$ and $i_B^\alpha \leq i_B$. Hence, in the general case the leakage control will be matrix-valued and time-variant. The dependence on the weight has been made explicit in (8.3.11). In section 8.3.4 and subsection 8.A.1 examples of methods dynamically to schedule the weight-driven leakage control matrix are provided. The associated optimization problem is then expressed by the cost function $J^{e^2\alpha}(w_{i_B})$

$$\min_{w}\big\{J^{e^2\alpha}(w_{i_B}) \triangleq J^{e^2}(w_{i_B}) + J^{\alpha}(w_{i_B})\big\}. \tag{8.3.12}$$

The optimal choice of the leakage control parameter will indeed be application dependent. It should be remarked that the introduction of leakage will usually take place at the expense of biased weight estimates as will be addressed in chapter 9 on page 417. This can also be explained in terms of the noise added to the system (8.3.10). By choosing the associated *leakage factor* $\nu(i_{i_\nu}) \triangleq 1-\mu(i_\mu)\alpha(i_\alpha)$ close to unity, that is $(\alpha \gtrapprox 0)$, we can effectively limit this bias error. The integer i_μ refers the step-size parameter update iteration number that in turn will be defined in (8.5.1) on page 389. The weight leakage factor update iteration number i_ν is incremented each time either i_μ or i_α is incremented, that is, $i_\nu = i_\mu + i_\alpha$.

Weight-Driven Leakage in the Frequency Domain

In the frequency-domain adaptive filters leakage can also be used. For example, if the input energy falls below some prescribed input threshold in a certain frequency bin, then the update of that frequency should be omitted since there is not information present to do so intelligently. In the DFT domain the cost function weight norm penalty term is

$$J^{\alpha}(w_{k,i_B}) \triangleq \|w_{k,i_B}\|^2_{\alpha_{i_\alpha,k}(w_{k,i_B^\alpha})}, \quad k = 0,1,2,\ldots,2B-1. \tag{8.3.13}$$

Bibliographic Notes on Weight-Driven Leakage[6]

In [50] three different schemes for enforcing control output constraint in an ANC were considered. It was concluded that the so-called *re-scaling* algorithm that is based on *active set method* somewhat outperforms the FxL-LMS. In practice the re-scaling algorithm is based on monitoring the control output signal and if necessary to re-scale both the weights and the control output

[6]This subsection provides supplementary bibliographic information on weight-driven leakage control that, however, can be skipped on a first reading.

signal in proportion to the magnitude of constrain violation. However, in this study only a fixed as opposed to time-variant leakage control parameter was examined. Another but very straight forward method of just clipping the output signal if a constraint is encountered was deemed to have potential problems with convergence speed and stability.

A more advanced leakage scheme providing stable operation without bias and at the same computational expense as ordinary LMS has been proposed by Nascimento and Sayed [43]. In contrast to ordinary leaky LMS (L-LMS) leakage is here applied to a single adaptive tap-weight at each iteration

$$\alpha(w_{\langle i\rangle_M}) = \begin{cases} \alpha_0, & \text{if } |w_{\langle i\rangle_M}| \geq C_2 \\ \alpha_0 - \frac{\alpha_0}{2}\left(\frac{C_2 - |w_{\langle i\rangle_M}|}{D}\right)^2, & \text{if } C_1 + D \leq |w_{\langle i\rangle_M}| < C_2 \\ \frac{\alpha_0}{2}\left(\frac{|w_{\langle i\rangle_M}| - C_1}{D}\right)^2, & \text{if } C_1 < |w_{\langle i\rangle_M}| < C_1 + D \\ 0, & \text{otherwise} \end{cases}, \tag{8.3.14}$$

where α_0 denotes the *circular leakage control upper value parameter* ($\alpha_0 \gtrapprox 0$) and C_1, C_2, D are the circular leakage control lower-, upper- and medium threshold parameters. By the notion $\langle i\rangle_M$ is understood i modulus M. The author's theoretically development is relying on *averaging theory* and *Lyapunov stability theory*.

Douglas [18] made a performance comparison of the hardware and software approach to obtain a leakage effect. In the software approach the leakage is directly used in the weight update. In the hardware approach the dither noise that is added to the input signal could for example be generated using a maximum-length shift register in very-large-scale integration (VLSI) technology. The author found however, that from a performance standpoint, the direct approach to leaky LMS adaptive filter is to be preferred in terms of lower excess-mean-square error (EMSE) and larger range of useable step-sizes. This performance difference is most pronounced for large signal-to-noise ratios and moderate values of the leakage parameter.

In [41] a m.s.e. analysis of the leaky LMS algorithm with the assumption that the input and the desired signals are jointly Gaussian and zero-mean processes is provided. Rigling and Schniter [54] propose a method referred to as subspace leaky LMS (SL-LMS) where the leakage is selectively applied to above mentioned *unexcited subspace*, but not to the *persistently excited subspace* in order to mitigate the problem of unbounded adaptive tap-weight growth in a finite precision environment. This approach, however, requires a NLMS alike procedure for tracking of the *unexcited subspace* which roughly doubles the computational load. In a highly non-stationary a *unexcited subspace* exceeding 50% a lower drift and less bias compared with L-LMS and circular leaky LMS (CL-LMS) was observed.

In [35] the effect of delay on the performance of the L-LMS adaptive algorithm is investigated.

In his Ph.D. thesis Cartes [10] proposes tuning methods based on *Lyapunov stability* methods for determining time-variant step-size and time-variant leakage control parameters adaptively for feedforward ANC. The essence of this work and the work by the same authors with an low-frequency acoustic test cell can be found in [11–13]. The authors claim that one of the candidate is superior to the traditionally designed fixed leakage NLMS when exposed to highly non-stationary situations provided that the input signal-to-noise ratio (SNR) is known. Hence, the system is *locally* stable but not *globally* stable as also demonstrated in some of their tests.

Apparently, in all of the three candidate algorithms considered the leakage control parameter is normalized with input power. This approach seems somewhat counter-intuitive as the "dither"

then is dosed in a magnitude that is inversely proportional to the SNR.

8.3.4 Control Output-Driven Leakage

Motivation

A more direct approach to the leakage objectives 6 and 11 raised in subsection 8.3.3 is to let the amount of leakage be explicitly dependent on the power of the control output signal. From a practical point the injected power to the secondary sources are directly related to the control output signals and only indirectly through the weights. Despite the many objectives of employing control-effort-driven leakage functionality in the adaptive filters used for AC, however, to the author's best knowledge no attempts have been made to accommodate this type of leakage control to the APA family of adaptive filtering.

In order to preserve generality and the possibility of more directly constricting the control output signals, we will therefore include control output signal-driven leakage in our development. The main point is that weight and control-effort-driven leakage are considered algorithm extensions that can be selected or not.

Control Output-Driven Leakage in the Time Domain

Hence, we will further augment the l.l.m.s.e. problem (8.3.5) to include a cost function control output signal mean-square penalty term represented by $J^{\gamma}(\,\cdot\,)$ and defined as

$$J^{\gamma}(\,\cdot\,) \triangleq \begin{cases} J^{\gamma}\big(\mathbf{y}(i^{\gamma})\big) & = \gamma\big(i_{\gamma}, \mathbf{y}(i^{\gamma})\big)\,\mathrm{E}|\mathbf{y}(i)|^2, \quad \text{SISO, MISO,} \\ J^{\gamma}\big(\mathbf{y}_{i^{\gamma}}\big) & = E\|\mathbf{y}_i\|^2_{\gamma_{i_{\gamma}}(\mathbf{y}_{i^{\gamma}})}, \qquad \text{SIMO, MIMO,} \end{cases} \tag{8.3.15}$$

where $\mathbf{y}(i) \in \mathbb{K}(\mathbf{y}_i \in \mathbb{K}^{N_y \times 1})$ denotes the control output signal, the quantity $\gamma_{i_{\gamma}}(\mathbf{y}_{i^{\gamma}}) \in \mathbb{R}^{N_y \times N_y}(\gamma(i_{\gamma}, \mathbf{y}(i^{\gamma})) \in \mathbb{R})$ refers to the *control-effort-driven leakage* or actuator weighting diagonal matrix (parameter) where the individual elements $\gamma^l_{i_{\gamma}}$ denote the weight factor attributed to the l'th actuator. The integer i_{γ} denotes the control-effort-driven matrix update iteration number and i^{γ} is the iteration number corresponding to i_{γ}, where the individual elements V^y_l denote the weight factor attributed to the l'th actuator.

The control-effort-driven matrix may be updated at each block-update time or if computational prohibitive then less frequently that is, $i_{\gamma} \leq i_B$ and $i^{\gamma} \leq i$. Hence, in the general case the control-effort-driven leakage will be matrix-valued and time-variant. The dependence on the control output signal has been made explicit in (8.3.15). In subsection 8.A.1 an example of a method dynamically to schedule the control-effort-driven leakage matrix is provided. It should also be observed that in order to facilitate further analysis we have deliberately chosen to use a separate iteration number control-effort-driven matrix update such that expectation operator should **not** be applied to the normalization leakage matrix, that is, $\gamma_{i_{\gamma}}(\mathbf{y}_{i^{\gamma}})y$ in (8.3.15).

The associated optimization problem is then expressed by the cost function $J^{e^2\gamma}(w_{i_B})$

$$\min_{w}\big\{J^{e^2\gamma}(w_{i_B}) \triangleq J^{e^2}(w_{i_B}) + J^{\gamma}(w_{i_B})\big\}. \tag{8.3.16}$$

The optimization problem (8.3.16) is over the space of feasible weight vectors w_{i_B} and we

have accordingly made use of the implicit dependence of J^{γ} on w_{i_B} ($\mathbf{y}_i = \mathbf{x}_i w_{i_B}$), where $\mathbf{x}_i \in \mathbb{K}^{1\times M}(\mathbf{x}_i \in \mathbb{K}^{N_y\times M})$ denotes the reference signal. Accordingly, we may reformulate (8.3.15)

$$J^{\gamma}(w_{i_B}) \triangleq \begin{cases} w_{i_B}^* R_{x,i}^{\gamma(i_\gamma,\mathbf{y}(i^\gamma))} w_{i_B} & = \|w_{i_B}\|^2_{R_{x,i}^{\gamma(i_\gamma,\mathbf{y}(i^\gamma))}}, \quad \text{SISO, MISO,} \\ w_{i_B}^* R_{x,i}^{\gamma_{i_\gamma}(\mathbf{y}_{i^\gamma})} w_{i_B} & = \|w_{i_B}\|^2_{R_{x,i}^{\gamma_{i_\gamma}(\mathbf{y}_{i^\gamma})}}, \quad \text{SIMO, MIMO.} \end{cases} \tag{8.3.17}$$

Here $R_{x,i}^{\gamma_{i_\gamma}(\mathbf{y}_{i^\gamma})} \triangleq \mathrm{E}\,\mathbf{x}_i^* \gamma_{i_\gamma}(\mathbf{y}_{i^\gamma})\mathbf{x}_i \in \mathbb{C}^{M\times M}$ is the auto correlation matrix of the actuator-weighted reference signal $\mathbf{x}_i$.

Then by including both weight-driven leakage and control-effort-driven leakage the cost function $J^{e^2\alpha\gamma}(w_{i_B})$ is determined by

$$\min_{w}\big\{J^{e^2\alpha\gamma}(w_{i_B}) \triangleq J^{e^2}(w_{i_B}) + J^{\alpha}(w_{i_B}) + J^{\gamma}(w_{i_B})\big\}. \tag{8.3.18}$$

The term *leakage* used for both methods considered in this section stems from the numerical reduction in weight update. This subject should be more clear in section 8.6 on page 396 where expressions for the adaptive tap-weight update are derived.

Control Output-Driven Leakage in the Frequency Domain

In the frequency-domain the corresponding cost function control output signal mean-square penalty term is

$$J^{\gamma}\big(\tilde{w}_{k,i_B}\big) \triangleq \begin{cases} \mathrm{E}\,\gamma_k(i_\gamma,\tilde{\mathbf{y}}_k(i^\gamma)) & |\tilde{\mathbf{y}}_k(i)|^2, \quad \text{SISO, MISO,} \\ \mathrm{E} & \|\tilde{\mathbf{y}}_{k,i}\|^2_{\gamma_{k,i_\gamma}(\tilde{\mathbf{y}}_{k,i^\gamma})}, \quad \text{SIMO, MIMO} \end{cases}, k = 0,1,2,\ldots,2B-1 \tag{8.3.19}$$

and the cost function including both weight-driven leakage and control-effort-driven leakage is expressed by

$$\min_{\tilde{w}_k}\big\{J^{e^2\alpha\gamma}(\tilde{w}_{k,i_B}) \triangleq J^{e^2}(\tilde{w}_{k,i_B}) + J^{\alpha}(\tilde{w}_{k,i_B}) + J^{\gamma}(\tilde{w}_{k,i_B})\big\}. \tag{8.3.20}$$

From a design point of view some way to schedule the control-output-driven leakage matrix γ_{i_γ} or parameter $\gamma(i_\gamma)$ must be sought for. The l.l.m.s.e. problem considered hitherto in this chapter is within the control community considered as a $\mathcal{H}_2$ performance criterion[7]. However, in order to realize a physical control system additional design criterions emerge. Some of these design criterions are governed by constraints that lend themselves to a $\mathcal{H}_\infty$ control approach.

In subsection 8.A.1 we will see that both weight-driven leakage and control-effort-driven leakage can be used to emulate $\mathcal{H}_\infty$ control.

[7]For a definition of Hardy spaces refer to, e.g., [74, Ch. 4].

Bibliographic Notes on Control-Effort Leakage[8]

The two types of minimum effort estimators, that is, the weight-driven leakage and the control-output-driven leakage schemes (scalar-valued time-invariant parameters) were investigated in a context of feedforward control and for by Darlington [16]. He found that the benefit of superposing a white-noise dither signal on the regressor signal (filtered-reference signal) in terms of an reduction in the eigenvalue spread (see leakage objective 3 in subsection 8.3.3) obtained with weight-driven leakage is no longer present with control effort-driven leakage. In fact as mentioned in [22, Ch. 3] the control output signal-driven leakage corresponds to superposing a dither signal to the filtered-reference signal that is uncorrelated with reference signal and whose value is proportional to γ and whose power spectral factorization is equal to that of reference signal (not the filtered-reference signal). This means that for an adaptive filter operating in interference cancelation mode (refer to section 8.2 on page 373), such dither signal is not white-noise as the reference signal and filtered-reference signal do not coincide. In terms of computational complexity the usual weight-driven leakage approach is somewhat more efficient.

8.3.5 Tap-Weight Regularization

Regularization is a method often applied in control system design, system identification [39] and linear estimation [33]. Regularization techniques dates back to the work by Levenberg [37] and Marquardt [40]. The objective of *regularization* is twofold

Regularization Objective 1. *Numerical regularization.* Preservation of numerical stability.

Regularization Objective 2. *Tap-weight regularization.* Pulling the solution towards some possible dynamic point of attraction $\bar{w}_{i_{\bar{w}}}$. This property can be very useful if some prior information regarding the optimal solution is available and the regressor provides insufficient excitation of the pertinent parameters. The regularization parameter can then control to which extend the parameters will be locked in the vicinity of $\bar{w}_{i_{\bar{w}}}$

The name *regularization* is normally associated with objective 1. However, we will postpone the discussion of numerical regularization to

Tap-Weight Regularization in Time Domain

Hence, we will augment (8.3.12) to include a cost function term $J^{\Pi}(w_{i_B})$ defined as

$$J^{\Pi}(w_{i_B}) \triangleq (w_{i_B} - \bar{w}_{i_{\bar{w}}})^{*}\Pi_{i_\Pi}(w_{i_B} - \bar{w}_{i_{\bar{w}}}) \tag{8.3.21}$$

that penalizes the squared Euclidean norm for the deviation of the weight vector from the point of attraction $\bar{w}_{i_{\bar{w}}} \in \mathbb{K}^{M\times 1}$. The quantity $\Pi_{i_\Pi} \in \mathbb{K}^{M\times M}$ is the weight regularization matrix that is assumed to be positive semi-definite ($\Pi_{i_\Pi} \succ 0$), usually a multiple of the identity. The integer i_Π denotes the weight regularization matrix update iteration number, $i_{\bar{w}}$ denotes the point of attraction update iteration number and i_B^{Π} is the weight block update iteration number corresponding to i_Π. The weight regularization matrix may be updated at each block-update

[8] This subsection provides supplementary historical information on control-effort leakage control that, however, can be skipped on a first reading.

time or if computational prohibitive then less frequently. Hence, $i_\Pi \leq i_B$ and $i_B^\Pi \leq i_B$. Usually, however, Π and $\bar{w}$ are time-invariant[9].

The cost function $J^{e^2\alpha\gamma\Pi}(w_{i_B})$ that takes leakage and regularization into account may now be expressed as

$$\min_{w}\{J^{e^2\alpha\gamma\Pi}(w_{i_B}) \triangleq J^{e^2\alpha\gamma}(w_{i_B}) + J^{\Pi}(w_{i_B})\}. \tag{8.3.22}$$

By assigning $\Pi_{i_\Pi} = 0$ we suppress the weight regularization.

In the literature regularization and leakage are often considered synonyms. By our cost function definitions (8.3.11) and (8.3.21) we could obtain the leakage effect in (8.3.22) by absorbing α in Π by $\Pi \leftarrow \alpha I + \Pi$ for $\bar{w}_{i_{\bar{w}}} = 0$. However, we prefer to preserve both quantities representing different objectives as described previously. In section 8.5 we will introduce yet another parameter ϵ that explicitly will be used to ensure numerical stability during actual operation of the adaptive filter.

Tap-Weight Regularization in the Frequency Domain

In the frequency-domain the weight regularization cost function term is defined by

$$J^{\Pi}(w_{k,i_B}) \triangleq (w_{k,i_B} - \bar{w}_k)^* \Pi_{i_\Pi}(w_{k,i_B} - \bar{w}_k) \tag{8.3.23}$$

Similarly, the l.l.m.s.e. cost function with weight-driven leakage control-effort-driven leakage and weight regularization is expressed as

$$\min_{\bar{w}_k}\{J^{e^2\alpha\gamma\Pi}(w_{k,i_B}) \triangleq J^{e^2\alpha\gamma}(w_{k,i_B}) + J^{\Pi}(w_{k,i_B})\}. \tag{8.3.24}$$

8.4 Wiener Optimal Filter

In textbooks on linear estimation theory and linear adaptive filters extensive reference is made to *Wiener-filters* in honor of the innovative wartime (1942) report on continuous signals and systems by Wiener that, however, was first declassified and published in 1949 [70]. This work took benefit from earlier work by Wiener and Hopf on the solution of singular integral equations referred to as the *Wiener-Hopf equation* [71]. It can be argued that this work is one of the most important developments in linear estimation theory. Later the theory of optimal filtering was adapted to discrete-time signals and systems [38] on which every modern implementation is based. Another important contribution to the literature was the work by Bode and Shannon [4] who augmented the theory of Wiener filtering to include *causality*. By causality is meant that the filter responses are constrained to zero for negative time.

Wiener filters are confined to jointly wide-sense ergodic processes and is derived from ensemble averages. Wiener filters are *linear* and optimum in a probabilistic mean-squared-error sense. Wiener filters are theoretically very useful for prediction, estimation, interpolation, signal and noise filtering, and so on. From a practical implementation point of view the Wiener filter approach is of limited use as it requires a considerably amount of data to accurately calculate

[9] For example the regularization matrix may follow an exponential transition phase, e.g., $\Pi_{i_\Pi} = c_\Pi(1-\mathrm{e}^{-\gamma_\Pi i})\mathrm{I}$ for some constants $c_\Pi, \gamma_\Pi \in \mathbb{R}_+$.

the autocorrelation matrix $R_{u,i}$. However, the optimal Wiener-Hopf solution in subsection 8.4.1 (viz. (8.4.1)) will be used as a frame of reference in MATLAB® simulations. Here no real-time requirements exist and we can post process the data causally as well as noncausally.

The performance of an adaptive filter can therefore conveniently be assessed with reference to the optimal Wiener filter assuming wide-sense stationarity. This pertains in particular to the asymptotic behavior of the adaptive filter. The Wiener Filter (WF) was originally developed for SC systems employing the $J^{e^2}(w_{i_B})$ cost function defined in (8.3.3).

In this section we will exclusively consider SC-WFs that are both constrained to be causal and constrained to be of finite order and optimal in $J^{e^2}(w_{i_B})$ cost function sense. Two variants of the Wiener filter will be considered, namely the time-domain Wiener filter and the somewhat more involved **z**-domain Wiener filter that is also referred to as transform-domain Wiener filter. Later in section 8.5 on page 388 we will derive expressions for the optimal weight vector for MC systems using the more general cost function $J^{\alpha\gamma\Pi}(w_{i_B})$ defined in (8.3.18) viz. (8.5.19) to (8.5.20) on pages 393–394.

8.4.1 Time-Domain Causality-Finite-Order-Constrained Wiener Filter

The time-domain Wiener filter solution requires knowledge concerning auto correlation matrix for the reference signal, $R_{u,i} \triangleq \mathrm{E}\,\mathbf{u}_i^*\mathbf{u}_i$, and cross-correlation between the reference signal and the desired response, $R_{ud,i} \triangleq \mathrm{E}\,\mathbf{u}_i^*\mathbf{d}_i$. The *optimal* weight vector $w_{i_B}^o \in \mathbb{K}^{M\times 1}$ in a finite-duration impulse response (FIR) filter (see Figure I.1 on page 731) implementation is obtained from

$$w_{i_B}^o = R_{u,i}^{-1} R_{ud,i}. \tag{8.4.1}$$

The requirements on causality and finite order are satisfied from restricting the auto correlation matrix $R_{u,i}$ and the cross-correlation matrix $R_{ud,i}$ to be of finite order and by using only entities of $R_{ud,i}$ with non-positive time lags up to 1 less than the FIR filter order. Usually, the weight vector is assumed constant for the Wiener-Hopf (WH) filter. However, in order to provide some tracking capability we will allow a block-update of the weights provided that the reference signals and disturbance signals are locally (in time) wide-sense stationary such that it makes sense to invoke the expectation operator on a finite time window.

Although the Wiener filter is referred to as *optimal* this optimality only applies under the assumption of random white noise signal. For random colored noise signals, however, the weight estimate (8.4.1) will only be suboptimal. For such colored signals the **z**-domain Wiener Filter introduced in subsection 8.4.2 will ensure optimality. Moreover, the process is not *perfect* as the output estimation error will attain some finite value, $e^o(i)$, even when the filter operates in its optimum condition. The cost function, $J_{\min}(w_{i_B}^o)$, attained when the weights are optimal is

$$\begin{aligned} J_{\min}(w_{i_B}^o) &= \mathrm{E}|\mathbf{e}^o(i)|^2 \\ &= \sigma_d^2(i) - R_{ud,i} w_{i_B}^o R_{ud,i}, \end{aligned} \tag{8.4.2}$$

where $\sigma_d^2(i)$ designates the variance of the desired signal $\mathbf{d}(i)$

$$\sigma_d^2(i) = \mathrm{E}\,\mathbf{d}^2(i). \tag{8.4.3}$$

As readily seen from (8.4.1) the optimal Wiener-Hopf solution requires estimation of both auto- and cross-correlation functions, which in practise only can be done from time histories of the reference signal and desired signal. Moreover, the Wiener-Hopf filter requires matrix inversion of the $M \times M$ autocorrelation matrix subject to possible ill-conditioning problems. Even if the symmetric and Toeplitz properties of $R_{u,i}$ is exploited, such matrix inversion requires of the order of M^2 arithmetic operations.

Two very important properties of Wiener filters should be recalled here. The first important property is that when the filter weights attain there optimal values (8.4.1) then there will be no correlation between the error and the input to any of the weights at the same time, that is,

$$E\mathbf{u}(i-k)\mathbf{e}^{o*}(i) = 0, \quad k = 0, 1, 2, \ldots, M-1. \tag{8.4.4}$$

This applies both to time-domain Wiener filters and **z**-domain Wiener filters described in subsection 8.4.2 and is known as the *principle of orthogonality*. Similarly, when the filter operates in its optimum condition then there will be no correlation between the filter output and the error, that is,

$$E\mathbf{y}^{o}(i)\mathbf{e}^{o*}(i) = 0. \tag{8.4.5}$$

Expressed in other words the Wiener Filter makes exhaustive use of the information provided in the covariance matrix and cross-covariance vector.

8.4.2 z-Domain Causality-Finite-Order-Constrained Wiener Filter

The **z**-domain Wiener filter is based on a *spectral factorization* (refer to chapter 3 on page 105) and the optimal weights are accordingly found in the **z**-domain from [3, 4]

$$w^{o}_{i_B}(z) = L^{-1}_{u,i,+}(z)\left\{ L^{-1}_{u,i,+}(z^{-*})S_{ud,i}(z^{-*}) \right\}_{+}. \tag{8.4.6}$$

As for the time-domain Wiener filter we allow block update of the weight in order to provide the filter with some tracking capability assuming that the reference signals and disturbance signals are locally (in time) wide-sense stationary such that **z**-transform operator $\tilde{(\,\cdot\,)} = (\mathcal{Z}(\,\cdot\,))(z)$ makes sense. The *plus operator* $\{\}_+$ determines the *causal part* of the sequence inside the curlets and $L_{u,i,+}$ and $L_{u,i,-}$ refer to the following basic spectral factorization of the z-autospectrum matrix

$$S_{u,i}(z) = L_{u,i,+}(z)L^{*}_{u,i,-}(z^{-*}), \tag{8.4.7}$$

where $L_{u,i,+}(z)$ is *a* spectral factor (minimum phase, modeling filter) and $L_{u,i,-}(z)$ is the para-Hermitian conjugate of $L_{u,i,+}$. The factorization quantity, $L_{u,i,+}$, contains exclusively poles and zeroes **inside** the unit circle in the z-plane whereas all poles and zeroes of $L_{u,i,-}$ are found **outside** the unit circle of the z-plane.

From (8.4.6) and (8.4.7) we appreciate that for the calculation of the optimal **z**-domain WF, mainly two operations are necessary: the nonlinear spectral factorization and the in general unbounded plus-operation. Moreover, in practice the determination of the optimal weights involves the auto- and cross-spectral density functions $S_{uu}(\mathrm{e}^{\imath\omega})$ and $S_{ud}(\mathrm{e}^{\imath\omega})$ with certain smoothness properties. Boche and Pohl [3] who made a system theoretical analysis of the **z**-domain WF

showed that for SC systems that for Hölder continuous[10] spectra, the **z**-domain WF always exists, it is stable and it can be approximated with by a FIR filter. However, for spectra which are continuous, but not Hölder continuous, the WF is not always stable or it cannot be approximated by a FIR filter.

The optimal two-sided solution (8.4.1) will differ from the single sided solution (8.4.6) only if $R_{ud,i}$ contains z-terms to a higher order than $R_{u,i}$. In such cases more time-advanced information is required by the cross-correlation matrix than provided by the correlation matrix. Accordingly, the minimum cost function achievable in the **z**-domain filtering case $J_{\min}^{\{\}+}(w_{i_B}^o)$ is generally smaller than the corresponding cost function in the time-domain filtering case, that is, $J_{\min}^{\{\}+}(w_{i_B}^o) \leq J_{\min}(w_{i_B}^o)$.

8.5 Method of Steepest Descent

8.5.1 Introduction

The purpose of including a description of the method of steepest descent is twofold. Firstly, although the steepest descent is a *stochastic gradient estimation* method it is also descriptive for a so-called *deterministic feedback system* that finds the minimum point of the ensemble-averaged error-performance surface without knowledge of the surface itself [29]. Secondly, the steepest descent serves as an intermediate stage of conception between the theoretical oriented Wiener filter approach discussed in the previous section and the topic of the next section namely the family of least-mean square algorithms that are used for many practical purposes.

In the method of steepest descent knowledge about the local gradient of the ensemble-averaged error-performance surface is assumed available. At each iteration the weights are adjusted so that the trajectory follows a path on the ensemble-averaged error-performance surface leading to the global minimum.

8.5.2 Method of Steepest Descent in the Time Domain

A *step-size* parameter (positive-definite learning matrix) $\mu(i_\mu) \in \mathbb{R}(\mu_{i_\mu} \in \mathbb{R}^{M\times M} \succ 0)$ and a *weight-update direction vector* $\tilde{w}_{i_B} \in \mathbb{K}^{M\times 1}$ both of which in the general case are iteration-dependent, control the amount of weight adjustment along each coordinate. The integer i_μ refers the step-size parameter update iteration number. The step-size parameter may be updated at each block-update time or less frequently. Hence, $i_\mu \leq i_B$. By allowing the step-size parameter μ_{i_μ} to be matrix-valued and time-variant our presentation will then cover a fairly large share of adaptive filter algorithms with roots in *stochastics*[11]. Variable step-size algorithms are used to

[10] Refer to 35 on page 675. In a practical noise environment the auto- and cross-spectral density functions will normally be Hölder continuous. Moreover, applying statistical data analysis (SDA) algorithms using a finite amount of samples results in smearing of the spectraAppendix C on page 539. In a simulation environment, however, abrupt changes in the auto- and cross-spectral density functions are possible resulting in non Hölder continuous spectra.

[11] For example, the relative new class of *proportionate* adaption schemes make use of a time-variant learning matrix. The proportionate NLMS (PNLMS) algorithm was initially developed by the Bell Laboratories for echo canceler adaptation that exploits the sparseness of network impulse responses to achieve significantly faster adaptation than the conventional NLMS algorithm [20]. The general idea of the PNLMS algorithm is to assign different step sizes to different coefficients based on their current estimated magnitudes. If the current magnitude of a coefficient is large, large step size will be assigned, and vice versa. It redistributes the adaptation gains among all the coefficients and emphasizes the large ones in order to speed up their convergence, which explains the

provide a better trade-off between fast convergence and low misadjustment [59].

The adaptive filtering process can generally - without making any assumptions on the cost function involved - be described by the following recursion for the weights update

$$w_{i_B} = w_{i_B-1} + \mu_{i_\mu} \check{w}_{i_B}, \quad i_B \geq 0, \quad i_{i_\mu} \geq 0, \quad w_{-1} = w^{\mathrm{ig}}. \tag{8.5.1}$$

In (8.5.1) the initial (guessed) weight vector $w^{\mathrm{ig}} \in \mathbb{K}^{M\times 1}$ has been introduced. In subsection 8.5.8 the weight initialization procedure will be addressed. As already discussed the shape and therefore also the local gradient of the error-performance surface is indeed dependent on the formulation of the cost function. Most contributions in the literature on the method of steepest descent are based on l.l.m.s.e..

8.5.3 Method of Steepest Descent in the Frequency Domain

In the DFT domain the weights update recursion is

$$w_{k,i_B} = w_{k,i_B-1} + \mu_{k,i_\mu} \check{w}_{k,i_B}, \quad i_B \geq 0, \quad i_{i_\mu} \geq 0, \quad w_{k,-1} = w_k^{\mathrm{ig}}. \tag{8.5.2}$$

8.5.4 Linear-Least-Mean-Squares Estimation

Linear-Least-Mean-Squares Estimation in the Time Domain

As described in [56] even in the simple l.l.m.s.e. case many different choices of the vector quantity $\check{w}_{i_B}$ in (8.5.1) will ensure convergence provided $\mu(i_\mu)$ is sufficiently small. The requirement on the value of the cost function at successive iterations to be monotonically decreasing is satisfied in the l.l.m.s.e. case for [56, Ch. 4]

$$\Re[\nabla_w J(w_{i_B-1})\check{w}_{i_B}] < 0. \tag{8.5.3}$$

A class of vectors $\check{w}_{i_B}$ for which (8.5.3) holds and that has been devoted particular attention is governed by the expression

$$\check{w}_{i_B} = -B(i_B)[\nabla_w J(w_{i_B-1})]^*, \tag{8.5.4}$$

where $B(i_B)$ denotes a possible time-variant positive definite matrix ($B(i_B) \succ 0, \quad i_B \geq 0$). The complex gradient of a scalar-valued function, say, $J(z)$ with vector arguments (∇_z) with respect to a complex-valued *column* vector $z \in \mathbb{C}^{1\times N}$, say[12],

$$z = \mathrm{col}\{\begin{bmatrix} z_1, & z_2, & \dots & , z_N \end{bmatrix}\}, \quad z_i = x_i + \imath y_i \tag{8.5.5}$$

fast initial convergence. This faster convergence is attained at only a modest increase in computational complexity and without sacrifying the estimation quality. In recent years other members have been added to the family *proportionate* adaption schemes among others including proportionate adaptation NLMS (PANLMS), μ-law PNLMS (MPNLMS) and proportionate APA (PAPA) [2]. In many other adaptive filtering schemes the step-size is a simple time-variant scalar or constant scalar.

[12] Subscripts used here to designate elements of a vector.

is defined as the *row* vector

$$\nabla_z[J(z)] = \nabla_z J \triangleq \begin{bmatrix} \partial J/\partial z_1 & \partial J/\partial z_2 & \dots & \partial J/\partial z_N \end{bmatrix}. \tag{8.5.6}$$

The complex gradient of a multi-dimensional-valued function array, say, $\Psi \in \mathbb{C}^{N_\Psi^1 \times N_\Psi^2 \times N_\Psi^3}(z)$ if with vector arguments (∇_z) with respect to a complex-valued *column* vector z is obtained from applying (8.5.6) element-wise. Hence, $\nabla_z(\,\cdot\,) : \Psi \in \mathbb{C}^{N_\Psi^1 \times N_\Psi^2 \times N_\Psi^3}(z) \to \mathbb{C}^{N_\Psi^1 \times N_\Psi^2 \times N_\psi^3 \times N}$ for $z \in \mathbb{C}^{1\times N}$. For later use we will also introduce the corresponding conjugate complex gradient of a scalar-valued function with respect to a complex-valued vector (∇_{z^*}) which is a *column* vector

$$\nabla_{z^*}[J(z)] = \nabla_{z^*} J \triangleq \begin{bmatrix} \partial J/\partial z_1^* \\ \partial J/\partial z_2^* \\ \vdots \\ \partial J/\partial z_n^* \end{bmatrix}. \tag{8.5.7}$$

By insertion of (8.5.4) in (8.5.1) and applying the cost function defined in (8.3.22) we can express the recursion for the weight update as

$$w_{i_B} = w_{i_B-1} - \mu_{i_\mu} B(i_B)[\nabla_w J^{e^2\alpha\gamma\Pi}(w_{i_B-1})]^*, \quad i_B \geq 0, \quad i_{i_\mu} \geq 0, \quad w_{-1} = w^{\mathrm{ig}}. \tag{8.5.8}$$

For reasons that will explained later we will use a more elaborate expression for the class of vectors $\check{w}_{i_B}$ (8.5.1) on the previous page, namely

$$\check{w}_{i_B} = -B^{e^2}(i_B)[\nabla_w J^{e^2}(w_{i_B-1})]^* - B^{\alpha\gamma\Pi}(i_B)[\nabla_w J^{\alpha\gamma\Pi}(w_{i_B-1})]^*, \tag{8.5.9}$$

where both $B^{e^2}(i_B)$ and $B^{\alpha\gamma\Pi}(i_B)$ denote possible time-dependent positive definite matrices (at all time) $(B^{e^2}(i_B) \succ 0, B^{\alpha\gamma\Pi}(i_B) \succ 0)$. In (8.5.9) the quantity $J^{\alpha\gamma\Pi}(w_{i_B})$ denotes the cost function term related to the combined leakage effects and regularization that is defined as

$$J^{\alpha\gamma\Pi}(w_{i_B}) \triangleq J^\alpha(w_{i_B}) + J^\gamma(w_{i_B}) + J^\Pi(w_{i_B}). \tag{8.5.10}$$

From the definition of the cost function (8.3.3), (8.3.11), (8.3.17) and (8.3.21) and by the positive definite properties of $B^{e^2}(i_B)$ and $B^{\alpha\gamma\Pi}(i_B)$ it is then readily seen that (8.5.3) still holds.

8.5.5 Numerical Regularization

A useful choice of the matrix $B^{e^2}(i_B)$ in (8.5.9) is the Hessian matrix $\nabla_w^2 J^{e^2}(w_{i_B-1})$. Now as discussed in subsection 8.3.5 the meaning of regularization is twofold. We will now address the numerical motivation.

Regularization Objective 1. Avoidance of an ill-conditioned Hessian matrix $\nabla_w^2 J^{e^2}(w_{i_B-1})$. In practice the Hessian matrix will often be determined from time-averaging a realization of the regressor data. However, if the system is over parameterized i.e. to many weights are involved or the data is not informative enough the Hessian matrix may become singular or close to singular.

Regularization is a commonly applied method to alleviate problems with rank deficiency in the Hessian matrix by adding a weight regularization term that is positive definite. Now taking numerical regularization into account we may instead define $B^{e^2}(i_B)$ as

$$B^{e^2}(i_B) = [\epsilon_{i_\epsilon} + \nabla_w^2 J^{e^2}(w_{i_B-1})]^{-1}, \tag{8.5.11}$$

where $\epsilon_{i_\epsilon} \in \mathbb{R}^{M\times M}$ represents a likewise possible iteration-dependent *regularization term* at regularization update iteration number i_ϵ. The regularization term may be updated at each block-update time or less frequently. Hence, $i_\epsilon \leq i_B$. Moreover, in (8.5.11) the denoted by *Hessian matrix of J with respect to w* of the cost function $J(w)$ $\nabla_w^2 J$ was introduced. It is determined from the general expression of a Hessian matrix

$$\nabla_z^2 J \triangleq \nabla_{z^*}[\nabla_z J] = \begin{bmatrix} \dfrac{\partial^2 J}{\partial z_1^* \partial z_1} & \dfrac{\partial^2 J}{\partial z_1^* \partial z_1} & \cdots & \dfrac{\partial^2 J}{\partial z_1^* \partial z_N} \\ \dfrac{\partial^2 J}{\partial z_2^* \partial z_1} & \dfrac{\partial^2 J}{\partial z_2^* \partial z_1} & \cdots & \dfrac{\partial^2 J}{\partial z_2^* \partial z_N} \\ \vdots & \vdots & \ddots & \vdots \\ \dfrac{\partial^2 J}{\partial z_N^* \partial z_1} & \dfrac{\partial^2 J}{\partial z_N^* \partial z_1} & \cdots & \dfrac{\partial^2 J}{\partial z_N^* \partial z_n} \end{bmatrix} \tag{8.5.12}$$

from substituting z by w.

The term ϵ_{i_ϵ} in the expression (8.5.11) for $B^{e^2}(i_B)$ is used for *numerical regularization* [13]. By regularization the matrix $B^{e^2}(i_B)$ can then be guarantied to be positive definite at all time ($B^{e^2}(i_B) \succ 0, i_B \geq 0$). Regularization then ensures existence of the inverse in (8.5.11). As argued in [39, Ch. 16] the singular values of the Hessian matrix are often widely spread. By addition of the regularization term an improved convergence can be obtained.

For that part of the cost function that accounts for leakage and weight regularization $J^{\alpha\gamma\Pi}(w_{i_B-1})$ we simply use the identity matrix for $B^{\alpha\gamma\Pi}$, that is,

$$B^{\alpha\gamma\Pi}(i_B) = I. \tag{8.5.13}$$

Now instead of (8.5.8) by insertion of (8.5.11) and (8.5.13) in (8.5.9) and subsequently in (8.5.1) we obtain the following expression for the SD weight update

$$\boxed{\begin{aligned} w_{i_B} = w_{i_B-1} - \mu_{i_\mu}\Big[[\nabla_w J^{\alpha\gamma\Pi}(w_{i_B-1})]^* + [\epsilon_{i_\epsilon} + \nabla_w^2 J^{e^2}(w_{i_B-1})]^{-1}[\nabla_w J^{e^2}(w_{i_B-1})]^*\Big], \\ i_B \geq 0, \quad i_{i_\mu} \geq 0, \quad i_\epsilon \geq 0, \quad w_{-1} = w^{\mathrm{ig}}. \end{aligned}} \tag{8.5.14}$$

[13] The numerical regularization above is usually applied in algorithms with matrix normalization, e.g., RLS and APA for numerically stabilizing the solution. However, the regularization parameter is sometimes used more actively in the filter design. For example, in the field of acoustic echo control abrupt changes in the system response and highly nonstationary speech activities put opposite demands on the time-invariant step-size or regularization parameters. Instead the step-size and regularization parameter constitute a time-variant *pseudo-optimal* control pair [28]. In this application the step-size is a function of the reference signal signal and the error signal while the regularization term is a function of the disturbance signal, that is, $\mu_{i_\mu} \to \mu(e(i), u_i)$ and $\epsilon_{i_\epsilon} \to \epsilon(d(i))$. The term pseudo is used in order to emphasize that several assumptions and approximation are necessary in order to derive simple formulas, which can easily be implemented in a real system.

Invoking the cost functions (8.3.6) (8.3.11) (8.3.17) (8.3.21) and (8.5.12) the local gradients and Hessian matrix are readily obtainable[14]

$$\nabla_w J^{e^2}(w_{i_B-1}) = \begin{cases} -R^*_{ud,i} + w^*_{i_B-1} R_{u,i}, & \text{SISO, SIMO,} \\ -(R^{W_e}_{ud,i})^* + w^*_{i_B-1} R^{W_e}_{u,i}, & \text{MISO, MIMO,} \end{cases} \tag{8.5.15a}$$

$$\nabla_w J^{\alpha}(w_{i_B-1}) = w^*_{i_B-1} \alpha_{i_\alpha}(w_{i^\alpha_B}), \tag{8.5.15b}$$

$$\nabla_w J^{\gamma}(w_{i_B-1}) = \begin{cases} w^*_{i_B-1} R^{\gamma(i_\gamma, \mathbf{y}(i^\gamma))}_{x,i}, & \text{SISO, MISO,} \\ w^*_{i_B-1} R^{\gamma_{i_\gamma}(\mathbf{y}_{i^\gamma})}_{x,i}, & \text{SIMO, MIMO,} \end{cases} \tag{8.5.15c}$$

$$\nabla_w J^{\Pi}(w_{i_B-1}) = (w_{i_B-1} - \bar{w}_{i_{\bar{w}}})^* \Pi_{i_\Pi}, \tag{8.5.15d}$$

$$\nabla^2_w J^{e^2}(w_{i_B-1}) = \begin{cases} R_{u,i}, & \text{SISO, SIMO,} \\ R^{W_e}_{u,i}, & \text{MISO, MIMO.} \end{cases} \tag{8.5.15e}$$

Here $R_{ud} \triangleq \mathrm{E}\,\mathbf{u}_i^* \mathbf{d}_i \in \mathbb{C}^{M\times 1}$ is the cross-correlation vector between the regressor $\mathbf{u}_i$ and disturbance signal $\mathbf{d}_i$, $R_u \triangleq \mathrm{E}\,\mathbf{u}_i^* \mathbf{u}_i \in \mathbb{C}^{M\times M}$ is the auto correlation matrix of the regressor $\mathbf{u}_i$ and $R^{W_e}_u \triangleq \mathrm{E}\,\mathbf{u}_i^* W_e \mathbf{u}_i \in \mathbb{C}^{M\times M}$ is the error sensor-weighted auto correlation matrix of the regressor $\mathbf{u}_i$, $R^{W_e}_{ud} \triangleq \mathrm{E}\,\mathbf{u}_i^* W_e \mathbf{d}_i \in \mathbb{C}^{M\times 1}$ is the error sensor-weighted cross-correlation vector between the regressor $\mathbf{u}_i$ and disturbance signal $\mathbf{d}_i$.

Moreover, it is important to note that in derivation we did not have to apply the chain-rule of differentiation for the complex gradient of a multi-dimensional-valued function array in order to obtain, e.g., $\nabla_w \alpha_{i_\alpha}(w_{i^\alpha_B})$ as the weight-driven leakage matrix is frozen at the value it attained at time i^α_B and is first subsequently updated. Similar considerations apply to $\nabla_w R^{\gamma_{i_\gamma}(\mathbf{y}_{i^\gamma})}_{x,i}$. By substituting (8.5.15) in (8.5.14) we obtain the following recursion algorithm for the MIMO case

$$\boxed{\begin{aligned} w_{i_B} = &\Big(\mathrm{I} - \mu_{i_\mu}\Big(\alpha_{i_\alpha}(w_{i^\alpha_B}) + R^{\gamma_{i_\gamma}(\mathbf{y}_{i^\gamma}) + \Pi_{i_\Pi}}_{x,i}\Big)\Big) w_{i_B-1} \\ &+ \mu_{i_\mu}\big(\epsilon_{i_\epsilon} + R^{W_e}_{u,i}\big)^{-1}\big(R^{W_e}_{ud,i} - R^{W_e}_{u,i} w_{i_B-1}\big) + \mu_{i_\mu} \Pi_{i_\Pi} \bar{w}_{i_{\bar{w}}}, \\ &\text{MIMO}, \quad i \geq 0, \quad i_B \geq 0, \quad i_\alpha \geq 0, \quad i_\gamma \geq 0, \quad i_\mu \geq 0, \quad i_\epsilon \geq 0, \quad w_{-1} = w^{\mathrm{ig}}. \end{aligned}} \tag{8.5.16}$$

In (8.5.16) we recognize the regularization factor ϵ_{i_ϵ} in the denominator of the second term. As seen, by the definition of $B^{e^2}(i_B)$ in (8.5.11) and $B^{\alpha\gamma\Pi_{i_\Pi}}(i_B)$ in (8.5.13) possible numerical regularization effects from the leakage control parameter and weight regularization parameter are suppressed. This explains why we chose to split the cost function in two parts. One part represented by $J^{e^2}(w_{i_B-1})$ is used for l.l.m.s.e. while the other part represented by $J^{\alpha\gamma\Pi}(w_{i_B-1})$ accounts for leakage and weight regularization.

[14] Notice there is subtle difference between the expression for the gradient of the cost function with respect to the weights (8.5.15a) as compared with similar expressions in [29, Ch. 8], where a factor 2 is present. The absence of a factor 2 in (8.5.6) stems from different definitions of a complex gradient with vector arguments (∇_w) (8.5.6) made in [29, App. B.3] and [56, App. 2A]. Moreover, in [56] a complex transposition is present which as proved in subsection 8.B.1 on page 409 can be attributed to the different definition of the observation vector $\mathbf{u}$ and different usage of the tap weight vector w in the two cases (refer to the Notations on page xli). It should, however, be emphasized as also verified in subsection 8.B.1 on page 409 that the present formulation and the textbooks by Haykin [29] and Sayed [56] end up with compatible expressions for the basic SD algorithm (8.5.25) on page 394.

Equation (8.5.14) (8.5.16) constitute several extensions to the *Levenberg-Marquardt method* [37, 40] for quadratic cost functions. The extensions in (8.5.14) comprise

① A time-variant step-size matrix μ_{i_μ}.

② A time-variant weight-driven leakage matrix $\alpha_{i_\alpha}(w_{i_B^\alpha})$.

③ A time-variant control-effort-driven leakage matrix $\gamma_{i_\gamma}(\mathbf{y}_{i^\gamma})$.

④ A time-variant numerical regularization matrix ϵ_{i_ϵ}.

⑤ A time-variant weight regularization matrix Π_{i_Π}.

⑥ A time-variant point of attraction weight $\bar{w}_{i_{\bar{w}}}$.

⑦ Applies to SISO, MISO, SIMO and MIMO systems.

⑧ Weighting among error sensors.

Most often $R_{u,i}, R_{ud,i}$ are estimated from the realizations $\{u_i, d_i\}$ of $\{\mathbf{u}_i, \mathbf{d}_i\}$ by employing some kind of time-average. However, due to finite correlation of the regressor u_i condition number of the estimate $R_{u,i}$ of $R_{u,i}$ in (8.5.16) grows and the inverse of $\widehat{R}_u$ become more and more dubious. Increasing ϵ_{i_ϵ} means that the effective step-size, that is, $\mu_{i_\mu}(\epsilon_{i_\epsilon} + R_{u,i})^{-1}$ is decreased and the search direction is tuned towards the gradient.

We will proceed with the MIMO system as the result for the SISO, MISO and SIMO systems are readily obtained by applying the following substitutions

$$R_{u,i} \leftarrow R_{u,i}^{W_e}, \quad R_{ud,i} \leftarrow R_{ud,i}^{W_e}, \qquad \text{SISO, SIMO,} \tag{8.5.17a}$$

$$R_{x,i}^{\gamma(i_\gamma, \mathbf{y}(i^\gamma))} \leftarrow R_{x,i}^{\gamma_{i_\gamma}(\mathbf{y}_{i^\gamma})}, \qquad \text{SISO, MISO.} \tag{8.5.17b}$$

Moreover, we will for notational convenience suppress the explicit dependence of the leakage control matrix on the weights and the explicit dependence of the control-effort-driven leakage matrix on the control output signal, that is, $\alpha_{i_\alpha} \leftarrow \alpha_{i_\alpha}(w_{i_B^\alpha})$ and $R_{x,i}^{\gamma} \leftarrow R_{x,i}^{\gamma_{i_\gamma}(\mathbf{y}_{i^\gamma})}$.

From (8.5.15) we may deduce the optimal weight vector sought for in section 8.4 on page 385. Hence,

$$\nabla_w J^{e^2}(w_{i_B-1}) = -(R_{ud,i}^{W_e})^* + w_{i_B-1}^* \big[R_{u,i}^{W_e} + \alpha_{i_\alpha} + R_{x,i}^{\gamma} + \Pi_{i_\Pi}\big] - \bar{w}_{i_{\bar{w}}}^* \Pi_{i_\Pi} \tag{8.5.18}$$

and by equating to zero we obtain

$$\boxed{w_{i_B}^o = \big[R_{u,i}^{W_e} + \alpha_{i_\alpha} + R_{x,i}^{\gamma} + \Pi_{i_\Pi}\big]^{-1}\big(R_{ud,i}^{W_e} + \Pi_{i_\Pi}\bar{w}_{i_{\bar{w}}}\big).} \tag{8.5.19}$$

Now in order to obtain the MC-WH solution for the cost function $J^{\alpha\gamma\Pi}(w_{i_B})$ we proceed in a way similar that led from expression (8.4.1) for the time-domain WH filter to expression (8.4.6) for

the **z**-domain WH filter in [22, Ch. 3]. Hence, for the **z**-domain Wiener filter the optimal weights are found from

$$\boxed{w_{i_B}^o(z) = \left\{ \left(L_{u,i,+}^{\alpha\gamma W_e} \right)^{-1} (z^{-*}) S_{ud,i}(z^{-*}) \right\}_+ \left(L_{u,i,+}^{\alpha\gamma W_e} \right)^{-1} (z).} \tag{8.5.20}$$

where the mixed filtered-reference signal z-auto-cross-spectrum $S_{uuxx}^{\alpha\gamma W_e}(z) \in \mathbb{C}^{M\times M}$ is defined by

$$S_{uuxx}^{\alpha\gamma W_e}(z) = S_{uu}^{W_e}(z) + \alpha_{i_\alpha} + S_{xx}^{\gamma}(z) + \Pi_{i_\Pi}. \tag{8.5.21}$$

The basic spectral factorization of the mixed filtered-reference signal z-auto-cross-spectrum $S_{uuxx}^{\alpha\gamma W_e}(z)$ used in (8.5.20) can be obtained from

$$S_{uuxx}^{\alpha\gamma W_e}(z) = L_+^{\alpha\gamma W_e}(z) \big(L_-^{\alpha\gamma W_e} \big)^*(z^{-*}), \tag{8.5.22}$$

and where $L_{ux,i,+}^{\alpha\gamma W_e}(z)$ is *a* spectral factor (minimum phase, modeling filter) and $L_{ux,i,-}^{\alpha\gamma W_e}(z)$ is the para-Hermitian conjugate of $L_{u,i,+}^{\alpha\gamma W_e}(z)$.

8.5.6 Variant of the Method of Steepest Descent

For small values of ϵ_{i_ϵ}, and by omitting leakage and weight regularization, that is, ($\alpha_{i_\alpha} = \gamma_{i_\gamma} = 0, \Pi_{i_\Pi} = 0$) our *extended Levenberg-Marquardt method* (8.5.14) (8.5.16) approaches the *Newton algorithm*

$$w_{i_B} = w_{i_B-1} - \mu [\nabla_w^2 J^{e^2}(w_{i_B-1})]^{-1} [\nabla_w J^{e^2}(w_{i_B-1})]^*, i_B \geq 0, \quad w_{-1} = w^{\text{ig}}, \tag{8.5.23}$$

where a time-independent step-size also is assumed. The Newton algorithm is designed to give one-step convergence for quadratic functions, but is prone to an ill-conditioned Hessian matrix. A more simple but also less effective version of the SD method is obtained by also using an identity matrix for $B^{e^2}(i_B)$ as we did for $B^{\alpha\gamma\Pi}(i_B)$ in (8.5.13). By inspection of (8.5.14) it is readily observed that the corresponding weight recursion update reduces to

$$w_{i_B} = w_{i_B-1} - \mu_{i_\mu} \left[\nabla_w J^{e^2}(w_{i_B-1}) + \nabla_w J^{\alpha\gamma\Pi}(w_{i_B-1}) \right]^*, \quad i \geq 0, \quad i_B \geq 0, \quad w_{-1} = w^{\text{ig}}. \tag{8.5.24}$$

By substituting (8.5.15a) (8.5.15b) (8.5.15c) and (8.5.15d) in (8.5.24) we obtain for $\Pi_{i_\Pi} = 0$

$$w_{i_B} = (\mathrm{I} - \mu_{i_\mu} \alpha_{i_\alpha}) w_{i_B-1} + \mu [R_{ud,i} - R_{u,i} w_{i_B-1}], \quad i \geq 0, \quad i_B \geq 0, \quad w_{-1} = w^{\text{ig}}. \tag{8.5.25}$$

Recall from section 8.3.3 on page 380 that the leakage factor $\nu(i_{i_\nu})$ is defined by $\nu(i_{i_\nu}) = 1 - \mu(i_\mu)\alpha(i_\alpha) \lessapprox 1$. The name *(coefficient) leakage* stems from the leakage introduced in the weight update in (8.5.25).

8.5.7 Linear Least-Mean-Mixed-Even-Order Estimation

Hitherto, we have exclusively been considering the l.l.m.s.e. problem. However, it should be emphasized that the method of steepest descent is not restricted to l.l.m.s.e. problems and the associated m.m.s.e. criterion. The method of SD (8.5.1) is general and can work with other performance criterions as well. In [56] an unregularized least-mean-fourth (LMF) norm and a mixed unregularized linear-least-mean-mixed-even-norm estimation (l.l.m.m.e.n.) SD are considered. The LMF algorithm was originally proposed in [65] as an algorithm that under certain circumstance, will have a substantially lower weight noise than the least-mean-squares.

By applying the procedure from the previous sections of cost function separation to our *extended Levenberg-Marquardt method* SD algorithm (8.5.14) can rather easily be extended to a general combination of least-mean-mixed-even-norms (LMMENs) while still including weight-driven leakage control-effort-driven leakage and weight regularization. The advantage of exclusively using even-order norms is that this ensures that the ensemble-averaged error performance surface is convex and hence that a unique optimum for the weight exists.

Hence, we will also propose the l.l.m.m.e.n. cost function with weight-driven leakage control-effort-driven leakage and weight regularization represented by $J^{e^{2p}\alpha\gamma\Pi}(w_{i_B})$ by

$$\min_{w}\{ J^{e^{2p}\alpha\gamma\Pi}(w_{i_B}) \triangleq J^{e^{2p}}(w_{i_B}) + J^{\alpha\gamma\Pi}(w_{i_B})\}, \tag{8.5.26}$$

where $J^{\alpha\gamma\Pi}(w_{i_B})$ was defined in (8.5.10) and where represents the cost function that is defined by $J^{e^{2p}}(w_{i_B})$

$$\min_{w}\Big\{ J^{e^{2p},\alpha\gamma\Pi}(w_{i_B}) \triangleq \sum_{p=1} \beta_p \,\mathrm{E}\|\mathbf{d}_i - \mathbf{u}_i w_{i_B}\|_{W_e}^{2p}\Big\}, \quad \sum_{p=1}\beta_p = 1. \tag{8.5.27}$$

In the cost function formulation (8.5.26) weight-driven leakage and control-effort-driven leakage penalty terms of mixed-even-norm could also be considered. However, instead similar effects may be obtained by considering the use of appropriate penalty/barrier functions as discussed in section 8.A.1 on page 407.

Unfortunately, the use of higher order estimation criterion requires knowledge about the statical moments of the same order. Higher-order estimation, however, can rather easily be adopted into the framework of the instantaneous gradient estimation methods described in section 8.6.

When we considering general l.l.m.m.e.n. it should be remembered that we then have to adopt the requirement on the weight update direction vector $\breve{w}_{i_B}$ in (8.5.3) to the more complex estimation criterion.

Finally, it should be remarked that, as also discussed in Appendix B for jointly gaussian distributed data the mean and variance quantities fully describe the signal statistics. For such signals neither the LMF nor the LMMN would provide any advantage over the LMS.

8.5.8 Initial Tap-weights

Normally, in the lack of any information it is customary to initialize the weights by 0 ($w^{\mathrm{ig}} = 0$). However, we will try to reuse as much possible information obtained during previous operations of the system. Hence, if the weight vector $w^{ls} \in \mathbb{K}^{M\times 1}$ was successfully saved at the previous

shut-down of the system it will be reused. Alternatively, a weight vector obtained from some averaging procedure denoted by $w^{av} \in \mathbb{K}^{M\times 1}$ could be used. Finally, if no valid weight vector is considered valid we resort to initialize the weights by 0. Hence,

$$w^{\mathrm{ig}} = \begin{cases} 0 & \text{default, } w^{ls} \text{ and } w^{av} \text{ obsolete,} \\ w^{av} & \text{averaged,} \\ w^{ls} & \text{last saved.} \end{cases} \tag{8.5.28}$$

The weight initialization procedure (8.5.28) will be applied in all four modes of adaptive filtering 1- 4 listed on page 373.

8.6 Stochastic Gradient Algorithms

8.6.1 Introduction

In the family of *stochastic gradient algorithms* we find the LMS and APA algorithms. The least-mean-squares has extensively been used as a basis algorithm for adaptive filtering in many sort of signal processing applications. The LMS algorithm was originally proposed by Widrow and Hoff in 1960 [67]. The active noise control community has also widely adopted the least-mean-squares because it is elegant in its simplicity and efficiency.

The fundamental concept behind the stochastic gradient algorithms will first be outlined. We will apply the concept of stochastic gradient method to the most elaborate formulation of the steepest descent method described in section 8.5 pertinent to I.I.m.s.e., viz., our *extended Levenberg Marguardt* method (8.5.14)-(8.5.16) which employ dynamic weight-driven leakage, dynamic control-output-driven leakage, weight regularization and numerical regularization, and a time-dependent step-size parameter. From this we obtain a general expression for the weight update likewise pertinent to the I.I.m.s.e. case. Moreover, our basis for discussion of stochastic gradient algorithm will have origin in the recent advances in the field, viz., the so-called *affine protection algorithm* (APA) [24]. Finally, we will then derive ϵ-NLMS, NLMS and the ordinary LMS algorithm by successive simplification of the more elaborate weight recursion expression.

For supplementary information on the LMS algorithm the reader is referred to the vast body of literature on this subject, e.g., [29, 56, 68, 69]. The family of least-mean-squares algorithm is still very popular and is still subject to refinements more than forty years after it was proposed for the first time. Accordingly, a textbook exclusively devoted the least-mean-squares has recently been published [30].

8.6.2 Fundamentals of Stochastic Gradient Algorithms

The family of stochastic gradient algorithms are based on the heuristics argument of replacing the true gradient provided by the method of steepest descent by an instantaneous gradient estimate, albeit noisy, obtained from a single data sample, without having to resort to perturbation of the weight vector and averaging. This is achieved by replacing the ensemble-averaged covariance matrices $R_{u,i}, R^{W_e}_{u,i}$ and ensemble-averaged cross-covariance vectors $R_{ud,i}, R^{W_e}_{ud,i}$ by their

instantaneous values

$$\hat{R}_{u,i} \approx u_i^* u_i, \quad \hat{R}_{ud,i} \approx u_i^* d_i, \quad \hat{R}_{u,i}^{W_e} \approx u_i^* W_e u_i, \quad \hat{R}_{ud,i}^{W_e} \approx u_i^* W_e d_i. \tag{8.6.1}$$

The same applies to the auto correlation matrixs of the reference signals $R_{x,i}, R_{x,i}^{\gamma}$

$$\hat{R}_x(i) \approx x_i^* x_i, \quad \hat{R}_{x,i}^{\gamma} \approx x_i^* \gamma_{i_\gamma}(\mathbf{y}_{i^\gamma}) x_i. \tag{8.6.2}$$

The noisy estimates, however, are averaged and attenuated by the adaptation process itself [29], [68] which can be expressed by,

$$\mathrm{E}\left[\widehat{\nabla_w J^{\alpha\gamma\Pi}}(w_{i_B-1})\right] \approx \nabla_w J^{\alpha\gamma\Pi}(w_{i_B-1}), \quad \mathrm{E}\left[\widehat{\nabla_w^2 J^{\alpha\gamma\Pi}}(w_{i_B-1})\right] \approx \nabla_w^2 J^{\alpha\gamma\Pi}(w_{i_B-1}). \tag{8.6.3}$$

Hence, both variance quantities will be time-variant. A more accurate but also more involved estimate of the ensemble-averaged covariance matrices $R_{u,i}, R_{u,i}^{W_e}$ and ensemble-averaged cross-covariance vectors $R_{ud,i}, R_{ud,i}^{W_e}$ are obtained by averaging over a number of samples used t in APA , say, K. Usually $K \ll M$. Then the expressions for the estimates of $R_{u,i}, R_{u,i}^{W_e}, R_{ud,i}$ and $R_{ud,i}^{W_e}$ become

$$\widehat{R}_{u,i} \approx K^{-1} U_i^* U_i, \quad \widehat{R}_{ud,i} \approx K^{-1} U_i^* D_i, \quad \widehat{R}_{u,i}^{W_e} \approx U_i^* W_{e\otimes K} U_i, \quad \widehat{R}_{ud,i}^{W_e} \approx U_i^* W_{e\otimes K} D_i, \tag{8.6.4}$$

where $U_i \in \mathbb{K}^{K\times M} (U_i \in \mathbb{K}^{KN_e\times M})$ denotes the regressor time-block matrix that in turn is defined by

$$U_i \triangleq \begin{bmatrix} u_i & u_{i-\Delta_u} & \dots & u_{i-(K-1)\Delta_u} \end{bmatrix}^\top, \tag{8.6.5}$$

and where $D_i \in \mathbb{K}^{KN_e\times 1} (D_i \in \mathbb{K}^{K\times 1})$ is the disturbance signal time-block matrix

$$D_i \triangleq \begin{cases} \begin{bmatrix} d(i) & d(i-\Delta_u) & \dots d(i-(K-1)\Delta_u) \end{bmatrix}^\top & \text{SISO, SIMO} \\ \begin{bmatrix} d_i & d_{i-\Delta_u} & \dots d_{i-(K-1)\Delta_u} \end{bmatrix}^\top & \text{MISO, MIMO.} \end{cases} \tag{8.6.6}$$

The quantity Δ_u denotes the number of samples used for inter-block decorrelation in APA. Moreover, in (8.6.4) the error sensor weighting block diagonal matrix denoted by $W_{e\otimes K} \in \mathbb{R}^{(KN_e)\times(N_eK)}$ was introduced. It is defined by

$$W_{e\otimes K} = K^{-1} W_e \otimes I_K, \tag{8.6.7}$$

where I_K is a $K \times K$ identity matrix and the Kronecker product $W_e \otimes I_K$ therefore means that W_e is repeated K times to form a block matrix that is compatible with the dimensions of U_i.

Hence, in a MC-active noise control system (ANCS) the auto- and cross-correlation functions $R_{u,i}^{W_e}, R_{ud,i}^{W_e}$ are obtained from a combination of *temporal* averaging determined by K, Δ_u and *spatial* averaging determined by N_e. We may similarly obtain improved estimates of the ensemble-averaged covariance matrices $R_{x,i}^{\gamma}, R_{x,i}^{\gamma_{i_\gamma}(\mathbf{y}_{i^\gamma})}$ from

$$\widehat{R}_{x,i} \approx K^{-1} X_i^* X_i, \quad \widehat{R}_{x,i}^{\gamma} \approx X_i^* \gamma_{i_\gamma \otimes K}(\mathbf{y}_{i^\gamma}) X_i, \tag{8.6.8}$$

where $X_i \in \mathbb{K}^{K \times M} (X_i \in \mathbb{K}^{KN_y \times M})$ denotes the reference signal time-block matrix that is defined by,

$$X_i \triangleq \begin{bmatrix} x_i & x_{i-\Delta_u} & \dots & x_{i-(K-1)\Delta_u} \end{bmatrix}^\top. \tag{8.6.9}$$

Similarly, the actuator weighting block diagonal matrix denoted by $\gamma_{i_\gamma \otimes K}(\mathbf{y}_{i^\gamma}) \in \mathbb{R}^{(KN_y)\times(N_y K)}$ was introduced. It is defined by

$$\gamma_{i_\gamma \otimes K}(\mathbf{y}_{i^\gamma}) = K^{-1} \gamma_{i_\gamma}(\mathbf{y}_{i^\gamma}) \otimes I_K. \tag{8.6.10}$$

This block principle expressed by (8.6.4)-(8.6.10) constitutes the fundamentals of affine projection algorithm.

If we expand U_i as in (8.6.11) it is readily observed that the regressor u_i is reused

$$U_i \triangleq \begin{bmatrix} u_i & u_{i-\Delta_u} & \dots & u_{i-(K-1)\Delta_u} \\ u_{i-1} & u_{i-\Delta_u-1} & \dots & u_{i-(K-1)\Delta_u-1} \\ \vdots & \vdots & \ddots & \vdots \\ u_{i-\Delta_u+1} & u_{i-2\Delta_u+1} & \dots & u_{i-K\Delta_u+1} \\ u_{i-\Delta_u} & u_{i-2\Delta_u} & \dots & u_{i-K\Delta_u} \\ u_{i-\Delta_u-1} & u_{i-2\Delta_u-1} & \dots & u_{i-K\Delta_u-1} \\ \vdots & \vdots & \ddots & \vdots \\ u_{i-2\Delta_u+1} & u_{i-3\Delta_u+1} & \dots & u_{i-(K+1)\Delta_u+1} \\ u_{i-2\Delta_u} & u_{i-3\Delta_u} & \dots & u_{i-(K+1)\Delta_u} \\ \vdots & \vdots & \ddots & \vdots \\ u_{i-M+1} & u_{i-\Delta_u-M+1} & \dots & u_{i-(K-1)\Delta_u-M+1} \end{bmatrix}^\top. \tag{8.6.11}$$

The affine projection algorithm is therefore also known as a *data-reusing algorithm*.

8.6.3 $\alpha\gamma\Pi\epsilon$-Affine Projection Algorithm

$\alpha\gamma\Pi\epsilon$-Affine Projection Algorithm in the Time Domain

By insertion of (8.6.4) and (8.6.8) in (8.5.16) we obtain

$$w_{i_B} = \big(\mathrm{I} - \mu_{i_\mu}(\alpha_{i_\alpha} + X_i^* \gamma_{i_\gamma \otimes K}(\mathbf{y}_{i^\gamma}) X_i + \Pi_{i_\Pi})\big) w_{i_B-1} + \mu_{i_\mu}\big(\epsilon_{i_\epsilon} + U_i^* W_{e\otimes K} U_i\big)^{-1} \big(U_i^* W_{e\otimes K} D_i - U_i^* W_{e\otimes K} U_i w_{i_B-1}\big) + \mu_{i_\mu} \Pi_{i_\Pi} \bar{w}_{i_{\bar{w}}},$$
$$\text{MIMO}, \quad i \geq 0, \quad i_B \geq 0, \quad i_\alpha \geq 0, \quad i_\gamma \geq 0, \quad i_\mu \geq 0, \quad i_\epsilon \geq 0, \quad i_\Pi \geq 0, \quad w_{-1} = w^{\mathrm{ig}}. \tag{8.6.12}$$

By defining the *transformed* leakage-weight regularization matrix $\Upsilon_{i_\Upsilon} \in \mathbb{K}^{M\times M}$ by

$$\boxed{\Upsilon_{i_\Upsilon} = \mathrm{I} - \mu_{i_\mu}\big(\alpha_{i_\alpha} + \|X_i\|^2_{\gamma_{i_\gamma}\otimes K} + \Pi_{i_\Pi}\big),} \tag{8.6.13}$$

where i_Υ denotes the transformed weight leakage factor update iteration number which is incremented each time either of $i_\mu, i_\alpha, i_\gamma$ and i_Π is incremented, that is, $i_\Upsilon = i_\mu + i_\alpha + i_\gamma + i_\Pi$ and where the *transformed weight vector* $\breve{w}_{i_{\breve{w}}} \in \mathbb{K}^{M\times 1}$ [15] in turn is defined by

$$\breve{w}_{i_{\breve{w}}} = \Pi_{i_\Pi} \bar{w}_{i_{\bar{w}}}, \tag{8.6.14}$$

where $i_{\breve{w}}$ denotes the transformed point of attraction update iteration number, we can then rewrite (8.6.12) in a more compact form

$$w_{i_B} = \Upsilon_{i_\Upsilon} w_{i_B-1} + \mu_{i_\mu}\big(\epsilon_{i_\epsilon} + U_i^* W_{e\otimes K} U_i\big)^{-1}\big(U_i^* W_{e\otimes K} D_i - U_i^* W_{e\otimes K} U_i w_{i_B-1}\big) + \mu_{i_\mu} \breve{w}_{i_{\breve{w}}},$$
$$\text{MIMO}, \quad i \geq 0, \quad i_B \geq 0, \quad i_\Upsilon \geq 0, \quad i_\mu \geq 0, \quad i_\epsilon \geq 0, \quad w_{-1} = w^{\mathrm{ig}}. \tag{8.6.15}$$

From (8.6.13) it is readily observed that the transformed leakage-weight regularization matrix depends explicitly on the data through X_i and implicitly on the data through α_{i_α} and γ_{i_γ} that themselves in general are data dependent.

The recursion in the form (8.6.15) involves the inverse of a matrix of order $M \times M$. However, by applying the *matrix inversion lemma*[16] we can reformulate the expression (8.6.15) by

$$\boxed{\begin{aligned} w_{i_B} &= \Upsilon_{i_\Upsilon} w_{i_B-1} + \mu_{i_\mu} \epsilon_{i_\epsilon}^{-1} U_i^* (W_{e\otimes K}^{-1} + U_i \epsilon_{i_\epsilon}^{-1} U_i^*)^{-1}(D_i - U_i w_{i_B-1}) + \mu_{i_\mu} \breve{w}_{i_{\breve{w}}}, \\ &\text{MIMO}, \quad i \geq 0, \quad i_B \geq 0, \quad i_\Upsilon \geq 0, \quad i_\mu \geq 0, \quad i_\epsilon \geq 0, \quad w_{-1} = w^{\mathrm{ig}}. \end{aligned}} \tag{8.6.16}$$

The detailed derivation can be found in subsection 8.B.2. In (8.6.16) only a matrix inverse of the order $KN_e \times KN_e$ is required which is an advantage as normally $KN_e \ll M$. We have now derived the novel I.I.m.s.e.-based adaptive filter encompassing leakage functionality and numerical regularization as well as weight regularization. The weight update recursion algorithm governed by (8.6.13) and (8.6.16) will be designated as multiple-channel-$\alpha\gamma\Pi\epsilon$-affine projection algorithm and abbreviated MC-$\alpha\gamma\Pi\epsilon$-APA.

By omitting control-effort-driven leakage, weight regularization and weighting among the error sensors, by assuming a time-invariant and scalar-valued weight-leakage control parameter, numerical regularization parameter and step-size parameter and without the block-update, that is,

[15] Note the subtle difference in $\breve{w}$ (accent *check*) in (8.5.4) on page 389 and $\breve{w}_{i_{\breve{w}}}$ (accent *breve*) in (8.6.14).
[16] Refer for example to [29, Ch. 13] or [56, Ch. 2].

we make the assignments $W_e \leftarrow \mathrm{I}$ and $\alpha_{i_\alpha} \leftarrow \alpha, \gamma \leftarrow 0$ and $\Pi_{i_\Pi} \leftarrow 0, \epsilon_{i_\epsilon} \leftarrow \epsilon, \mu_{i_\mu} \leftarrow \mu, i \leftarrow i_B$, then the general MC-$\alpha\gamma\Pi\epsilon$-APA algorithm (8.6.16) simplifies to the ordinary MC-$\alpha\epsilon$-affine projection algorithm in [5, 6, 60]

$$\begin{aligned} w_i &= (\mathrm{I} - \mu\alpha)w_{i-1} + \mu U_i^*(\epsilon + U_i U_i^*)^{-1}(D_i - U_i w_{i-1}), \\ &\quad \text{MIMO}, \quad i \geq 0, \quad w_{-1} = w^{\mathrm{ig}}. \end{aligned} \tag{8.6.17}$$

This algorithm is also referred to as the *exact-$\alpha\epsilon$*-affine projection algorithm. In order to reduce the computational effort in MC systems different *approximate* $\alpha\epsilon$-affine projection algorithms ($\alpha\epsilon$-APAs) that only require a matrix inversion of order K were considered in [8, 9, 60].

$\alpha\gamma\Pi\epsilon$-Affine Projection Algorithm in the Frequency Domain

8.6.4 Affine Projection Algorithm

By omitting weight-driven leakage, control-effort-driven leakage, weight regularization, by assuming time-invariant and scalar-valued numerical regularization and step-size parameters, that is, we make the assignments $\alpha \leftarrow 0, \gamma \leftarrow 0$ and $\Pi_{i_\Pi} \leftarrow 0, \epsilon_{i_\epsilon} \leftarrow \epsilon, \mu_{i_\mu} \leftarrow \mu$ and $W_e \leftarrow 1$ the $\alpha\gamma\Pi\epsilon$-APA algorithm in (8.6.16) simplifies to the ordinary ϵ-affine projection algorithm for SISO and SIMO systems

$$\boxed{w_{i_B} = w_{i_B-1} + \mu U_i^*(\epsilon I + U_i U_i^*)^{-1}(D_i - U_i w_{i_B-1}), \quad i_B \geq 0, i \geq 0, \quad w_{-1} = w^{\mathrm{ig}}.} \tag{8.6.18}$$

$\alpha\gamma\Pi\epsilon$-Normalized Least-Mean-Squares Algorithm in the Time Domain

If we only use the current data values x_i,u_i and d_i which corresponds to using (8.6.1) and (8.6.2) instead of (8.6.4) and (8.6.8) the MC-$\alpha\gamma\Pi\epsilon$-APA algorithm in (8.6.16) simplifies to

$$\boxed{\begin{aligned} w_{i_B} &= \Upsilon_{i_\Upsilon} w_{i_B-1} + \mu_{i_\mu}\epsilon_{i_\epsilon}^{-1} u_i^*(W_e^{-1} + u_i\epsilon_{i_\epsilon}^{-1}u_i^*)^{-1} W_e(d_i - u_i w_{i_B-1}) + \mu_{i_\mu}\breve{w}_{i_{\breve{w}}}, \\ &\quad \text{MIMO}, \quad i \geq 0, \quad i_B \geq 0, \quad i_\Upsilon \geq 0, \quad i_\mu \geq 0, \quad i_\epsilon \geq 0, \quad w_{-1} = w^{\mathrm{ig}}, \end{aligned}} \tag{8.6.19}$$

where the transformed leakage-weight regularization matrix Υ_{i_Υ} now is obtained from

$$\Upsilon_{i_\Upsilon} = \mathrm{I} - \mu_{i_\mu}(\alpha_{i_\alpha} + x_i^*\gamma_{i_\gamma}x_i + \Pi_{i_\Pi}). \tag{8.6.20}$$

The weight update recursion (8.6.19)-(8.6.20) will be called the $\alpha\gamma\Pi\epsilon$-NLMS ($\alpha\gamma\Pi\epsilon$-NLMS) algorithm and abbreviated by $\alpha\gamma\Pi\epsilon$-NLMS. The ordinary ϵ-NLMS algorithm for SISO and SIMO systems is obtained by omitting weight-driven leakage, control-effort-driven leakage, weight regularization, by assuming time-invariant and scalar-valued numerical regularization and step-size parameters in the MC-$\alpha\gamma\Pi\epsilon$-NLMS algorithm (8.6.19)

$$w_{i_B} = w_{i_B-1} + \frac{\mu}{\epsilon + u_i u_i^*}u_i^*(d(i) - u_i w_{i_B-1}) \quad i \geq 0, \quad i_B \geq 0, \quad w_{-1} = w^{\mathrm{ig}}. \tag{8.6.21}$$

If the regressor u_i possess *shift-structure*, that is,

$$u_i = \begin{bmatrix} u_i^1 \\ u_i^2 \\ \vdots \\ u_i^{N_e} \end{bmatrix} = \begin{bmatrix} u^1(i) & u^1(i-1) & \dots & u^1(i-M+1) \\ u^2(i) & u^2(i-1) & \dots & u^2(i-M+1) \\ \vdots & \vdots & \ddots & \vdots \\ u^{N_e}(i) & u^{N_e}(i-1) & \dots & u^{N_e}(i-M+1) \end{bmatrix} \tag{8.6.22}$$

then computational savings are possible. Considering the SC case and recognizing that $u_i u_i^* = \|u_i\|^2$ is the Euclidean norm squared, that is, the "energy" in the "pulse" spanned by the regressor $\{u(i), u(i-1), \dots, u(i-M+1)\}$ it is then readily observed that this norm can be determined sequentially as devised in [34, Ch. 2] and also in [56, Ch. 5]

$$w_{i_B} = w_{i_B-1} + \frac{\mu}{\epsilon + \widehat{E_{u_w}}(i)} \hat{R}_{ue}(i_B), \quad i \geq 0, \quad i_B \geq 0, \quad w_{-1} = w^{\text{ig}} \tag{8.6.23}$$

where $\widehat{E}_{u_w}(i) \triangleq \widehat{\|u_i\|^2}$ designates the estimate of the pulse energy (used for weight update)

$$\widehat{E_{u_w}}(i) = \frac{M}{N_{E_u}} \widehat{E_{u_E}}(i), \tag{8.6.24}$$

where N_{E_u} denotes the number of samples used for the estimate of the pulse energy and the quantity $\widehat{E_{u_E}}$ represents an estimate of the pulse energy in the pulse $\{u(i-1), u(i-1-1), \dots, u(i-N_{E_u}+1)\}$ and is determined by

$$\widehat{E_{u_E}}(i) = \begin{cases} \widehat{E_{u_E}}(i-1) + |u(i)|^2 - |u(i-N_{E_u})|^2; & i \geq N_{E_u}, \\ \frac{i\widehat{E_{u_E}}(i-1) + N_{E_u}|u(i)|^2}{i+1}; & 0 \leq i < N_{E_u}, \\ 0; & i = -1. \end{cases} \tag{8.6.25}$$

In practice it is probably more convenient to specify a pulse energy estimation time that we will denote by T_{E_u}. Then N_{E_u} is readily obtainable from the sampling frequency f_s

$$N_{E_u} = \lceil (f_s T_{E_u}). \tag{8.6.26}$$

The operator $\lceil(\,\cdot\,)$ designates taking the ceil of the term inside the parentheses.

Instead of obtaining an estimate of the cross-correlation between the regressor and the error signal R_{ue} from instantaneous values of the regressor u_i and error $e(i)$ the following block-wise estimate procedure can be used

$$\begin{aligned} \hat{R}_{ue}(i_B) &= \frac{1}{L} \sum_{j=Li_B}^{(L+1)i_B-1} u_j^*(d(i) - u_i w_{i_B}) \\ &= \frac{1}{L} \sum_{j=Li_B}^{(L+1)i_B-1} u_j^* e(i). \end{aligned} \tag{8.6.27}$$

Then the corresponding block-wise based weighting update is conducted at the end of each block

$$w_{i_B} = w_{i_B-1} + \frac{\mu}{\epsilon + u_i u_i^*}\hat{R}_{ue} \quad i \geq 0, \quad i_B = \lfloor (i/L), \quad w_{-1} = w^{\text{ig}}. \tag{8.6.28}$$

It should be recalled that the term $\widehat{\|u_i\|^2}$ in the denominator of (8.6.28) represents an estimate of an estimate of the Hessian matrix $\nabla_w^2 J(w_{i_B-1})$. Hence, a variety of estimators of more or less equal quality are at our disposition. Instead of a fixed window length of N_{E_u} samples we could use a memory based recursion scheme [56, Ch. 5]

$$\widehat{\|u_i\|^2} = \beta\widehat{\|u_{i-1}\|^2} + (1-\beta)|u_i|^2, \quad \widehat{\|u_{-1}\|^2} = 0, \tag{8.6.29}$$

where β controls the effective memory of the recursion expression for the pulse energy estimate. In [56, Ch. 5] the effective algorithm constituted by (8.6.23) and (8.6.29) is referred to as ϵ-NLMS *with power normalization*. In a finite-precision environment the ϵ-NLMS algorithm with power normalization is more robust than (8.6.23) - (8.6.28).

$\alpha\gamma\Pi\epsilon$-*Normalized Least-Mean-Squares Algorithm in the Frequency Domain*

8.6.5 Least-Mean-Square Algorithm

For the sake of completeness we will provide the expression for the weight recursion for the ordinary least-mean-squares. Following a procedure similar to the ϵ-NLMS in section 8.6.4 but now with the denominator term $B^{e^2}(i_B)$ from (8.5.11) replaced by a unity matrix ($B^{e^2} = I$) we readily obtain

$$w_{i_B} = w_{i_B-1} + \mu u_i^*(d(i) - u_i w_{i_B-1}), \quad i \geq 0, \quad w_{-1} = w^{\text{ig}}. \tag{8.6.30}$$

Although the ϵ-NLMS requires a few more instructions than the ordinary least-mean-squares the former is in favor on two important points. Firstly, the steady-state performance is less sensitive to the statistics of the regression data than for the LMS. Secondly, the stability of the ϵ-NLMS can be (almost) guaranteed provided that the step-size is sufficiently small. For the least-mean-squares information regarding the eigenvalue spread is required in order to determine the step-size [56, Ch. 6-9].

8.6.6 The Family of Least Mean Mixed-Even-Order Adaptive Algorithms

The least-mean-squares is fundamentally optimized for random distributed processes that can be characterized by *second order statistics*. Owing to the CLT many processes are Gaussian distributed and the underlying statistics is therefore fully described from second-order statistics, that is, mean and variance. Although many practical applications are governed by second order statistics, however, in another large set of applications the assumption on Gaussianity cannot be made. Therefore, for such applications algorithms that are specifically optimized for the underlying statistics are needed.

Hence, for noise distributions with a large higher order moment contents in the LMF or the LMMEN algorithms may prove the best choice. In subsection 8.5.7 the cost functions pertinent to the LMF

and the family of LMMEN adaptive algorithms was introduced. The LMF algorithm was originally proposed in [65] as an algorithm that under certain circumstances, will have a substantially lower weight noise than the LMS. By using, e.g., least-mean-fourth a fourth order moments identical to zero is implicitly sought for. However, if the LMF is applied to Gaussian distributions an increase in weight noise and consequently an increased misadjustment is expected.

The reason why even-order as opposed to *odd-order* adaptive algorithms are considered is that the pertinent $\mathbf{u}_i$ and $\mathbf{d}(i)$ will be assumed distributed symmetrically around zero. As a consequence all the odd moments of $\mathbf{u}_i$ and $\mathbf{x}(i)$ are equal to zero.

It was found in [65] that the least-mean-fourth and in general the least-mean-mixed-norm when minimizing the pertinent order of the error will have time constants in the weight relaxation process that are proportional to the least-mean-squares when minimizing the mean square error.

8.6.7 Finite Precision Environment

In the digital implementation of an adaptive filter, both the inputs and the internal variables are quantized to a certain precision. However, upon moving from an infinite precision environment to a finite precision environment *quantization noise* is added to the system leading to a degradation in performance of the adaptive filter that depends on the amount of quantization levels used to represent the variables. Owing to a potential continuously accumulation of quantization errors with time the performance of the adaptive filter might eventually become unacceptable. However, it is usually first until *overflow* occurs that the problem manifests itself in sudden large increase in the mean square error. The susceptibility to the accumulation of quantization errors increases in proportion to the degree of ill-conditioning of the underlying data covariance matrix. The bias error in the m.s.d. is inversely proportional to the step-size. However, this step-size cannot be made arbitrarily large as it is upper-bounded from demands on stability of the algorithm which is of particular importance for the LMS family of adaptive filters. In the analysis it is assumed that a scaling of the variables has been made to prevent any overflow to happened.

From a performance point of view an infinite-precision implementation of the adaptive filter is therefore indeed preferable over a finite-precision implementation. Market demands, however, often prove a floating-point digital signal processor (DSP) implementation to be prohibitive expensive. Moreover, whenever power consumption and associated heat dissipation is of concern a fix-point DSP implementation is often preferred to a floating-point implementation. Therefore, the designer should be able to address the effects of limited-precision in adaptive filtering. What make such attempts difficult is that the problems related to accumulation of quantization effects are often experienced as hidden processes. Hence, a system that apparently is working properly might after some minutes (millions of iterations) of operation experience a performance degradation which ultimately might lead to a need for a reintialization of the system.

An excellent account on limited-precision effects in adaptive filtering can be found in [14].

8.7 Transform Domain Adaptive Filtering

There many cases where the adaptive filtering can be carried out more efficiently in a transform-domain [29, Ch. 10] [56, Ch. 10]. Both the discrete cosine transform (DCT) and discrete sine transform (DST) are useful in spectral analysis of *real* sequences, in solution to boundary value problems, and in transform-domain processing of digital signals. Many data compression tech-

niques employ, in one way or another, the discrete cosine transform (DCT), which has been found to be asymptotically equivalent to the optimal Karhunen Lòeve transform (KLT) for signal decorrelation. For each of the DCT and DST four different types can be defined [53]. Computational efficient FFT and DFT methods were developed by [64].

Narayan, Peterson, and Narasimha [42] demonstrate that for a properly chosen orthogonal transform, some reduction in the eigenvalue spread can be *expected*. As a consequence of this, the transform-domain adaptive algorithm can be expected to have better convergence properties than the corresponding time domain algorithm in particular for the LMS family.

Hitherto the LMS algorithm has been considered for transform-domain processing. This can probably be attributed to the inherent simplicity of this algorithm and also to the alleviation by transformation of a particular weak point of the LMS algorithm namely the high dependence on the eigenvalue spread of the regressor data

8.8 Conclusions

In this chapter we have extended the suite of adaptive filters by new extensions of the family of affine projection algorithms and least-mean-squares that we designated by MC-$\alpha\gamma\Pi\epsilon$-APA and MC-$\alpha\gamma\Pi\epsilon$-NLMS respectively. As an intermediate result several extensions to the famous *Levenberg-Marquardt method* for quadratic cost functions were obtained viz. (8.5.14) (8.5.16) comprising a matrix-valued step-size parameter, a weight-driven leakage matrix, a control-effort-driven leakage matrix, a numerical regularization matrix all of which were formulated as time-variant (as opposed to time-invariant) parameters. In addition a weight regularization matrix, that usually only is considered in *deterministic*-based adaptive filters was adapted to the stochastic domain of adaptive filtering considered in this chapter. Finally, it should be emphasized that the results not only apply to SISO systems but also to MISO, SIMO and MIMO systems. The objectives of including weight-driven leakage and control-effort-driven leakage are numerous in particular for ANC applications with $\mathcal{H}_2/\mathcal{H}_\infty$ adaptive control. Through successive simplifications of the more elaborate MC-$\alpha\gamma\Pi\epsilon$-APA weight recursion expression we then derived both MC and SC versions of the ordinary ϵ-APA, ϵ-NLMS, NLMS and LMS algorithms. A comprehensive performance analysis of the MC-$\alpha\gamma\Pi\epsilon$-APA algorithm is conducted in chapter 9 on page 417.

8.A $\mathcal{H}_2/\mathcal{H}_\infty$ Adaptive Control

8.A.1 Constraints

Equality Constraints

In practical control design constraints are often imposed in the optimization problem for various purposes. For example constraints might be enforced on the weights used in adaptive beamforming applications where the constraints manifest themselves in the form

$$s_j w = g_j, \quad j = 1, 2, \ldots, N_{ec}, \tag{8.A.1}$$

where N_{ec} denotes the number of equality constraints ($N_{ec} < M$), the s_j are prescribed (complex-valued) row vectors and the g_j are (complex) constants. The purpose of the constraints in this

case is to ensure distortionless reception in the desired steering direction in a noiseless case. In other words when our adaptive filter is presented with one of the prescribed vectors s_j it shall return the corresponding constant g_j. Unfortunately, however, constraints typically complicate the solution of the problem. The method of *Lagrange multiplier* [29, App. C] is often invoked in order to convert the constrained problem into an unconstrained problem.

Inequality Constraints

The constraints above are in terms of N_{ec} *equalities*. We will, however, not pursue such equality constraint further in this report. In control applications constraints governed by *inequalities* are often encountered.

Power Handling

In subsection 8.3.3 we already mentioned leakage as a remedy to prevent nonlinear distortion. However, such leakage does not guarantee that the hardware in a secondary source will not be pushed beyond its power handling capabilities. Then in order to protect the secondary source hardware we may restrict the mean-square control output signal such that a predefined upper bound on the control output signal power level C_{y^2} is not exceeded, that is,

$$\mathrm{E}|\mathbf{y}(i)|^2 < C_{y^2}, \quad \forall i \geq -1. \tag{8.A.2}$$

The Wiener-Khinchin Theorem [48, Ch. 9] relates the variance a WSS random variable (RV), say the output $\mathbf{y}(t)$, to the its power spectral density (PSD) according to

$$\mathrm{E}|\mathbf{y}(t)|^2 = R_y(0) = \frac{1}{2\pi}\int_{-\infty}^{\infty} S_y(\omega)\,\mathrm{d}\omega = \|\tilde{y}(\imath\omega)\|_2^2 \geq 0. \tag{8.A.3}$$

and the $\mathcal{H}_2$ cost function can alternatively be expressed by

$$\mathrm{E}|\mathbf{e}(t)|^2 = R_e(0) = \frac{1}{2\pi}\int_{-\infty}^{\infty} S_e(\omega)\,\mathrm{d}\omega = \|\tilde{\mathbf{e}}(\imath\omega)\|_2^2 = \|\tilde{S}(\imath\omega)\sqrt{S_d(\omega)}\|_2^2 \geq 0. \tag{8.A.4}$$

Strictly, the last equality in (8.A.4) applies to a perfect plant model.

For discrete-time sequences and DFT the equivalent relation is referred to as Parseval's relation for the DFT

$$\sum_{n=0}^{2B-1} |x(n)|^2 = \frac{1}{2B}\sum_{k=0}^{2B-1} |\tilde{x}(k)|^2 \tag{8.A.5}$$

$$\mathrm{E}|\mathbf{y}(i)| \approx \sum_{k=0}^{2B-1} |\tilde{x}(k)\tilde{w}_{\circlearrowleft k,i}|^2 \tag{8.A.6}$$

A method to determine a common control-effort-driven leakage parameter $\gamma(i_\gamma)$ based on the total control effort and a method to determine a leakage matrix γ_{i_γ} whose values are determined from the individual control efforts in a MC feedforward system (FFS) are presented in [23].

Moreover, some of the hardware components in the secondary sources might exhibit frequency-dependent power handling capabilities. This pertains in particular to electrostrictive polymer film, PVDF elements and loudspeakers[17]. A power amplifier, however, is usually rather insensitive to the frequency spectrum of the input signal. Hence, we enforce the following constraint on the output power

$$\sup_{\omega}|\sqrt{S_x(\omega)}\underset{\sim}{\tilde{w}}_{i_B}(\imath\omega)W_{y^2}(\omega)| = \|\sqrt{S_x(\omega)}\underset{\sim}{\tilde{w}}_{i_B}(\imath\omega)W_{y^2}(\omega)\|_\infty < C_{y^2}, \quad \text{FFS}, \tag{8.A.7a}$$

$$\sup_{\omega}|\sqrt{S_d(\omega)}\underset{\circ}{\tilde{w}}_{i_B}(\imath\omega)W_{y^2}(\omega)| = \|\sqrt{S_d(\omega)}\underset{\circ}{\tilde{w}}_{i_B}(\imath\omega)W_{y^2}(\omega)\|_\infty < C_{y^2}, \quad \text{FBS}, \tag{8.A.7b}$$

where $W_{y^2}(\omega)$ represents a frequency-dependent weighting function and the concept of a p-norm $\|\cdot\|_p$ of a *Lebesgue measurable function* is defined in subsection M.1.2 on page 788.

In the DFT domain the cost functions (8.A.7) take the form

$$|\sqrt{S_x(k)}\underset{\sim}{\tilde{w}}_{k,i_B}W_{y^2}(k)| < C_{y^2}, \quad \text{FFS}, \tag{8.A.8a}$$

$$|\sqrt{S_d(k)}\underset{\circ}{\tilde{w}}_{k,i_B}W_{y^2}(k)| < C_{y^2}, \quad \text{FBS}, \quad k = 0, 1, \ldots, 2B-1. \tag{8.A.8b}$$

Robust Stability

In feedback system (FBS) design the problems related to *robust stability* and *disturbance enhancement* must also be taking into account. An excellent introduction to these subjects can be found in [22, Ch. 6]. Robust stability is concerned about maintaining bounded errors despite variations in the underlying plant models. Formally, the condition for robust stability as a function of the *complementary sensitivity function* for the nominal plant $\tilde{T}_0(\imath\omega)$ and the magnitude of unstructured multiplicative plant uncertainty $B(\omega)$ is governed by the following inequality[18]

$$\sup_{\omega}|\tilde{T}_0(\imath\omega)B(\omega)| = \|T_0(\imath\omega)B(\omega)\|_\infty < 1 \triangleq C_{\text{RS}}, \tag{8.A.9}$$

where $C_{\text{RS}} \triangleq 1$ is the upper bound on robust stability and where the frequency response of the *complementary sensitivity function* $\tilde{T}(\imath\omega)$ under the assumption of an internal model control (IMC) model for the FBS in turn is a function of $\tilde{g}_{ey}(\imath\omega), \tilde{\hat{g}}_{ey}(\imath\omega)$ and $\underset{\circ}{\tilde{w}}(\imath\omega)$ and equal to

$$\tilde{T}(\imath\omega) = \frac{-\tilde{g}_{ey}(\imath\omega)\underset{\circ}{\tilde{w}}(\imath\omega)}{1 - \big(\tilde{g}_{ey}(\imath\omega) - \tilde{\hat{g}}_{ey}(\imath\omega)\big)\underset{\circ}{\tilde{w}}(\imath\omega)}. \tag{8.A.10}$$

Hence, $\tilde{T}_0(\imath\omega) = -\tilde{g}_{ey}(\imath\omega)\underset{\circ}{\tilde{w}}(\imath\omega)$ and by substituting into (8.A.9) we get

$$\|\tilde{g}_{ey}(\imath\omega)\underset{\circ}{\tilde{w}}(\imath\omega)B(\omega)\|_\infty < 1. \tag{8.A.11}$$

[17] In loudspeakers a *woofer*, *squawker* and *tweeter* are responsible for sound production in the low, middle and high frequency range respectively. A *cross-over network* is required to limit the range of signals fed to each unit. But also within the individual units working frequency range the power handling capabilities will vary.

[18] We will only consider *unstructured* plant uncertainties.

In the DFT domain the constraints are similarly

$$|\tilde{g}_{ey}(k)\underset{\circ}{\tilde{w}}(k)B(k)| < 1, \quad k = 0, 1, \ldots, 2B-1. \tag{8.A.12}$$

Disturbance Enhancement

From control theory it is well known that for a non-minimum plant attenuation can be maintained only for a finite range of frequencies [19, Ch. 6]. Hence, if our FBS provide attenuation in some frequency ranges it will inevitably imply amplification of the disturbance at other frequency ranges. This phenomenon is commonly referred to as the *waterbed effect*. This waterbed effect might be of particular concern if the frequency regions that are subject to amplification are audible. Defining by C_{RD} the upper bound on disturbance enhancement we may express this constraint by

$$\sup_{\omega}|\tilde{S}_0(\imath\omega)W_{\mathrm{RD}}(\omega)| = \|\tilde{S}_0(\imath\omega)W_{\mathrm{RD}}(\omega)\|_\infty < C_{\mathrm{RD}}, \tag{8.A.13}$$

where $\tilde{S}_0(\imath\omega)$ is the *sensitivity function* for the nominal plant, $W_{\mathrm{RD}}(\omega)$ represents a frequency-dependent weighting function and where the frequency response of the *sensitivity function* $\tilde{S}(\imath\omega)$ under the assumption of an IMC model for the FBS in turn is equal to

$$\tilde{S}(\imath\omega) \triangleq \frac{\tilde{\mathbf{e}}(\imath\omega)}{\tilde{\mathbf{d}}(\imath\omega)} = \frac{1+\tilde{\hat{g}}_{ey}(\imath\omega)\big)\underset{\circ}{\tilde{w}}(\imath\omega)}{1-\big(\tilde{g}_{ey}(\imath\omega)-\tilde{\hat{g}}_{ey}(\imath\omega)\big)\underset{\circ}{\tilde{w}}(\imath\omega)}. \tag{8.A.14}$$

Hence, $\tilde{S}_0(\imath\omega) = 1+\tilde{\hat{g}}_{ey}(\imath\omega)\underset{\circ}{\tilde{w}}(\imath\omega)$ and by substituting into (8.A.13) we get

$$\|\big(1+\tilde{\hat{g}}_{ey}(\imath\omega)\underset{\circ}{\tilde{w}}(\imath\omega)\big)W_{\mathrm{RD}}(\omega)\|_\infty < C_{\mathrm{RD}}. \tag{8.A.15}$$

In the DFT domain the constraints are similarly

$$|\big(1+\tilde{\hat{g}}_{ey}(k)\underset{\circ}{\tilde{w}}(k)\big)W_{\mathrm{RD}}(k)| < C_{\mathrm{RD}}, \quad k = 0, 1, \ldots, 2B-1. \tag{8.A.16}$$

It should be recalled that the $\mathcal{H}_2$ performance weighting function $W_e(\omega)$ introduced in (8.3.7) that control the l.l.m.s.e. behavior is not necessarily identical to $W_{\mathrm{RD}}(\omega)$.

In control terminology we consider the limiting constraints (8.A.8) (8.A.12) and (8.A.16) as $\mathcal{H}_\infty$ constraints. A design that on one side seeks a $\mathcal{H}_2$ performance criterion while at the same time complies with $\mathcal{H}_\infty$ constraints is referred to as a $\mathcal{H}_2/\mathcal{H}_\infty$ controller.

Penalty and Barrier Functions

Optimal problems with inequality constraints are often solved by the introduction of *penalty functions* or *barrier functions* to schedule leakage as a function of closeness to violation of the constraints. Penalty functions or barrier functions can be used as an engineering approach to emulate $\mathcal{H}_\infty$ control, and it turns out that the solution so obtained will converge to the solution of the original constrained $\mathcal{H}_\infty$ problem.

Consider for now a value, say, ψ that is subject to an upper constraint, say, $\psi \leq C_\psi$, where C_ψ denotes the *constraint constant* pertaining to variable ψ. For a control parameter that is bounded from below similar considerations but with opposite inequality pertain. Basically, a penalty or a barrier function $\mathcal{P}(\,\cdot\,) : \mathbb{R} \times \mathbb{R} \to \mathbb{R}_+$ is a function that takes as input a variable, say ψ, subject to constraint and the corresponding constrained value C_ψ and return a nonnegative value that depends on the difference $C_\psi - \psi$. For a constrained value less than a certain threshold value both the penalty and barrier functions usually return a zero indicating that no leakage is required. When the constrained value *exceeds* the threshold a penalty function will return a value that increases in relation to how much the threshold is exceeded and dependent on the specific choice of penalty function. For the barrier functions the return value goes to infinity already in the limit $\psi \to C_\psi$, that is, when the constrained value *approaches* the threshold.

Among typically penalty functions we find the family $\big(\max(\psi - C_\psi, 0)\big)^p$ for p even. As barrier functions $(C_\psi - \psi)^{-1}$ and $-\log(C_\psi - \psi)$ are often considered. For more details refer to [31, 52] and the reference herein.

Collectively, we may include the inequalities (8.A.8) (8.A.12) and (8.A.16) in a frequency dependent weight-driven leakage matrix

$$\alpha_{i_\alpha,k} = \sigma_j^\alpha(k) \sum_{j=1}^{N_{iec}^\alpha} \mathcal{P}_j^\alpha(\psi_j^\alpha(i_\alpha), C_{\psi_j}^\alpha), \quad k = 0, 1, \ldots, 2B-1, \tag{8.A.17}$$

where N_{iec}^α denotes the number of inequality constraints related to weight-driven leakage, and $\sigma_j^\alpha(k)$ is the weight for j'th inequality constraints related to weight-driven leakage in frequency bin k. The penalty/barrier functions $\mathcal{P}_j^\alpha(\,\cdot\,)$ are assumed time-invariant. Similarly, the effort-driven leakage matrix may be scheduled according to

$$\gamma_{i_\gamma,k} = \sigma_j^\gamma(k) \sum_{j=1}^{N_{iec}^\gamma} \mathcal{P}_j^\gamma(\psi_j^\gamma(i_\gamma), C_{\psi_j}^\gamma), \quad k = 0, 1, \ldots, 2B-1, \tag{8.A.18}$$

where N_{iec}^γ denotes the number of inequality constraints related to effort-driven leakage and $\sigma_j^\gamma(k)$ is the weight for j'th inequality constraints related to effort-driven leakage in frequency bin k. The penalty/barrier functions $\mathcal{P}_j^\gamma(\,\cdot\,)$ are again assumed time-invariant. The index j is used to select each constraint in turn and has for example the following interpretation

$$\begin{cases} \alpha, j = 1, & \text{Control Output(8.A.8a)} \\ \alpha, j = 2, & \text{Control Output(8.A.8b)} \\ \gamma, j = 1, & \text{Robust Stability(8.A.12)} \\ \gamma, j = 2, & \text{Disturbance Enhancement(8.A.16)} \end{cases} . \tag{8.A.19}$$

Important to note is that by the use of a penalty function the leakage control matrices/parameters $\alpha_{i_\alpha}, \gamma_{i_\gamma}$ become functions of the weights and control output signal respectively.

The specific choice of penalty or barrier function is usually a compromise between requirement how strictly the constraint should be enforced and computational efficiency. Therefore, some practical experimentation has to be conducted for the specific control problem. This stage of the design procedure involves determination of the individual penalty/barrier functions $\mathcal{P}_j$ and

weighting numbers σ_j (see [52, Ch. 11-14] for example). In all cases it is the transform domain adaptive tap-weight $\underset{\circ}{\tilde{w}}$ and $\underset{\sim}{\tilde{w}}$ that are subject to optimization.

In conclusion, we have found that requirements emerging from practical design constraints might be taking into account by means of specialized functions that initiate weight or control effort leakage whenever a control parameter subject to constrain approaches the boundary defined by a constraint parameter.

An advantage of reformulating the $\mathcal{H}_2/\mathcal{H}_\infty$-constrained convex optimization problem by the introduction of the penalty functions as an *unconstrained* convex optimization problem which we can solved by the methods developed in this chapter.

Following this rather long diversion from our cost function discussion we now proceed by introducing weight regularization.

8.B Miscellaneous

8.B.1 Sayed Notation versus Classic Notation

In this section we will establish a link between the notation made by Sayed in the new textbook [56, Notation] that is also adopted in this report and the notation made in classical textbooks on adaptive filters, e.g., [29, 68, 69]. In the subsequent text we will by indices $_S$ and $_L$ refer to the notation by Sayed and the notation used in classical textbooks respectively. In [56, Notation] the observation vector $\mathbf{u}$ is defined as a row vector while it has been customary to use a column vector. The standard approach is to form an inner product with the *complex conjugate* of the tap-weight vector w. Sayed, however, in this context makes no use of conjugation. Both formulations apply the same definition of the desired signal $\mathbf{d}$. Hence,

$$\mathbf{u}_S = \mathbf{u}_L^T \tag{8.B.1a}$$
$$\mathbf{d}_S = \mathbf{d}_L \tag{8.B.1b}$$
$$w_S = w_L^C. \tag{8.B.1c}$$

The superscript ^{C} denotes complex conjugation *without* transposition. Hence,

$$\mathbf{u}_S w_S = \mathbf{u}_L^T w_L^C = \left(w_L^C\right)^T \mathbf{u}_L = w_L^* \mathbf{u}_L. \tag{8.B.2}$$

Moreover, in [56] the autocovariance matrix R_{uu} is adopted to the row vector definition as

$$R_{u_S u_S} = R_{u_S} \triangleq E\mathbf{u}_S^* \mathbf{u}_S. \tag{8.B.3}$$

Classical textbooks apply the column vector based definition of the autocovariance matrix

$$R_{u_L u_L} = R_{u_L} \triangleq E\mathbf{u}_L \mathbf{u}_L^*. \tag{8.B.4}$$

Then by insertion of (8.B.4) in the definition (8.B.3) and using (8.B.1a) we readily obtain we

obtain the following link between the autovariance definitions

$$R_{u_S} \triangleq E\mathbf{u}_S^*\mathbf{u}_S = E\left(\mathbf{u}_L^T\right)^* \mathbf{u}_L^T = E\mathbf{u}_L^C\mathbf{u}_L^{C*} = E^C\mathbf{u}_L\mathbf{u}_L^* \tag{8.B.5}$$

$$\triangleq R_{u_L u_L}^C = R_{u_L}^C. \tag{8.B.6}$$

Moreover, [56] makes use the cross covariance matrix between the desired signal and the input data R_{du}

$$R_{d_S u_S} \triangleq E\mathbf{d}_S\mathbf{u}_S^*. \tag{8.B.7}$$

Classical textbooks makes instead use of the cross covariance matrix between the input data and the desired signal R_{ud}

$$R_{u_L d_L} \triangleq E\mathbf{u}_L\mathbf{d}_L^* = E^*\mathbf{d}_L\mathbf{u}_L^*. \tag{8.B.8}$$

Complex conjugating of (8.B.8) yields

$$R_{u_L d_L}^C = E^T\mathbf{d}_L\mathbf{u}_L^* = E\mathbf{d_L}\mathbf{u}_L^C. \tag{8.B.9}$$

Then, by insertion of (8.B.9) in (8.B.7) and using (8.B.1a) and (8.B.1b) we obtain the following link between the cross variance definitions

$$R_{d_S u_S} \triangleq E\mathbf{d}_S\mathbf{u}_S^* = E\mathbf{d}_L\left(\mathbf{u}_L^T\right)^* = E^C\mathbf{u}_L\mathbf{d}_L^* \triangleq R_{u_L d_L}^C. \tag{8.B.10}$$

We are now in a position where we formally can check some of the important expressions in the textbooks. First consider the expression for the optimal tap-weights w^o. By using (8.B.5) and (8.B.10) we get

$$\begin{aligned} w_S^{o\,C} &= \left(R_{u_s}^{-1}R_{d_S u_S}\right)^C \\ &= R_{u_s}^{-C}R_{d_S u_S}^C \\ &= R_{u_L}^{-1}R_{u_L d_L} \\ &= w_L^o. \end{aligned} \tag{8.B.11}$$

By inspection of (8.B.1c) it is verified that expressions for the optimal tap-weight vector agree.

A check of the expressions for cost function with respect to the tap-weights $\nabla_w J$

$$\begin{aligned} J_S &= \sigma_{d_S}^2 - R_{d_S u_S}^* w_S - w_S^* R_{d_S u_S} + w_S^* R_{u_S} w_S \\ &= \sigma_{d_L}^2 - R_{u_L d_L}^T w_L^C - w_L^T R_{u_L d_L}^C + w_L^T R_{u_L}^C w_L^C \\ &= \sigma_{d_L}^2 - (R_{u_L d_L}^* w_L + w_L^* R_{u_L d_L} - w_L^* R_{u_L} w_L)^C \\ &= \sigma_{d_L}^2 - R_{u_L d_L}^* w_L - w_L^* R_{u_L d_L} + w_L^* R_{u_L} w_L \\ &= J_L. \end{aligned} \tag{8.B.12}$$

Similarly a check of the estimate of the gradient of the cost function with respect to the tap-

weights $\nabla_w J$

$$\begin{aligned}(\nabla_{w_S} J)^* &= (-R^*_{d_S u_S} + w^*_S R_{u_S})^* \\ &= (-R_{d_S u_S} + R^*_{u_S} w_S) \\ &= (-R^C_{u_L d_L} + R^T_{u_L} w^C_L) \\ &= (-R^C_{u_L d_L} + R^C_{u_L} w^C_L) \\ &= (-R_{u_L d_L} + R_{u_L} w_L)^C \\ &= \nabla_{w^C_L} J, \end{aligned} \tag{8.B.13}$$

which corresponds with the difference in usage of the tap-weight vector (8.B.1c). In (8.B.13) the last expression were obtained by taking the different definitions of a complex gradient with vector arguments (∇_w) made in [29, App. B.3] and, e.g., [56, App. 2A] respectively in into account.

For the minimum mean-square error we obtain

$$\begin{aligned} m.m.s.e._S &= \sigma^2_{d_S} - R_{u_S d_S} R^{-1}_{u_S} R_{d_S u_S} \\ &= \sigma^2_{d_L} - R^C_{u_L d_L} R^{-C}_{u_L} R^C_{d_L u_L} \\ &= \sigma^2_{d_L} - (R^{u_L d_L} R^{-1}_{u_L} R_{d_L u_L})^C \\ &= \sigma^2_{d_L} - R^{u_L d_L} R^{-1}_{u_L} R_{d_L u_L} \\ &= m.m.s.e._L. \end{aligned} \tag{8.B.14}$$

Finally, we can verify the agreement in the expression for the ϵNLMS algorithm

$$\begin{aligned}(\Delta w_{i_S})^C &= \frac{\mu}{\epsilon + \|u_{i_S}\|^2} (u^*_{i_S} [d_S(i) - u_{i_S} w_{i-1_S}])^C \\ &= \frac{\mu}{\epsilon + \|u_{i_L}\|^2} (u^C_{i_L} [d_L(i) - u^T_{i_L} w^C_{i-1_L}])^C \\ &= \frac{\mu}{\epsilon + \|u_{i_L}\|^2} u_{i_L} [d_L(i) - w_{i-1_L} u_{i_L}]^C \\ &= \frac{\mu}{\epsilon + \|u_{i_L}\|^2} u_{i_L} e^*(i) \\ &= \Delta w_{i_L}. \end{aligned} \tag{8.B.15}$$

This agrees with (8.B.1a)- (8.B.1c).

Summary

In the box (8.B.16) the main results have been summarized

$$\boxed{\begin{aligned} \mathbf{u}_S &= \mathbf{u}^T_L && \text{(8.B.16a)} \\ \mathbf{d}_S &= \mathbf{d}_L && \text{(8.B.16b)} \\ w_S &= w^C_L && \text{(8.B.16c)} \\ R_{u_S} &= R^C_{u_L} && \text{(8.B.16d)} \\ R_{d_S u_S} &= R^C_{u_L d_L}. && \text{(8.B.16e)} \end{aligned}}$$

8.B.2 APA Derivation

Proof. The matrix lemma is defined by [29, Ch. 13], [56, Ch. 2]

$$(A+BCD)^{-1} = A^{-1} - A^{-1}B(C^{-1}+DA^{-1}B)^{-1}DA^{-1}. \tag{8.B.17}$$

Now by substituting

$$A \longleftarrow \epsilon_{i_\epsilon}, \quad B \longleftarrow U_i^*, \quad C \longleftarrow W_{e\otimes K}, \quad D \longleftarrow U_i \tag{8.B.18}$$

we obtain

$$\begin{aligned}(\epsilon_{i_\epsilon} + U_i^* W_{e\otimes K} U_i)^{-1} U_i^* &= \big(\epsilon_{i_\epsilon}^{-1} - \epsilon_{i_\epsilon}^{-1} U_i^* (W_{e\otimes K}^{-1} + U_i \epsilon_{i_\epsilon}^{-1} U_i^*)^{-1} U_i \epsilon_{i_\epsilon}^{-1}\big) U_i^* \\ &= \epsilon_{i_\epsilon}^{-1} U_i^* - \epsilon_{i_\epsilon}^{-1} U_i^* (W_{e\otimes K}^{-1} + U_i \epsilon_{i_\epsilon}^{-1} U_i^*)^{-1} \big(W_{e\otimes K}^{-1} + U_i \epsilon_{i_\epsilon}^{-1} U_i^* - W_{e\otimes K}^{-1}\big) \\ &= \epsilon_{i_\epsilon}^{-1} U_i^* (W_{e\otimes K}^{-1} + U_i \epsilon_{i_\epsilon}^{-1} U_i^*)^{-1} W_{e\otimes K}^{-1}. \end{aligned} \tag{8.B.19}$$

Moreover, if ϵ is scalar-valued, we may further simplify (8.B.19) by

$$\big(\epsilon(i_\epsilon) + U_i^* W_{e\otimes K} U_i\big)^{-1} U_i^* = U_i^* \big(\epsilon(i_\epsilon) W_{e\otimes K}^{-1} + U_i U_i^*\big)^{-1} W_{e\otimes K}^{-1}. \tag{8.B.20}$$

□

8.B.3 Complex Gradient Differentiation Rules

The complex gradient of a multi-dimensional-valued function array, say, $\Psi \in \mathbb{C}^{N_\Psi^1 \times N_\Psi^2 \times N_\Psi^3}(z)$ with vector arguments (∇_z) with respect to a complex-valued *column* vector z is obtained from applying (8.5.6) element-wise. Hence, the ijk element of $\nabla_z \Psi(z)$, that is, $\{\nabla_z \Psi(z)\}_{ijk}$ is a *row* vector of elements

$$\{\nabla_z \Psi(z)\}_{ijk} \triangleq \begin{bmatrix} \partial\Psi_{ijk}/\partial z_1 & \partial\Psi_{ijk}/\partial z_2 & \dots & \partial\Psi_{ijk}/\partial z_N \end{bmatrix}. \tag{8.B.21}$$

Bibliography

[1] Karl J. Åström and Björn Wittenmark. *Adaptive Control*. Addison-Wesley Longmann, 2nd edition, 1995.

[2] J. Benesty, T. Gänsler, D.R. Morgan, M.M. Sondhi, and S.L. Gay. *Advances in Network and Acoustic Echo Cancellation*. Digital Signal Processing. Springer-Verlag, Berlin, 2000.

[3] Holger Boche and Volker Pohl. Structural properties of the wiener filter - stability, smoothness properties, and fir approximation behavior. *IEEE Transactions on Information Theory*, 52(9):4272–4282, 2006.

[4] H. W. Bode and C. E. Shannon. A simplified derivation of linear least square smoothing and prediction theory. *Proc. IRE*, 38:417–425, 1950.

[5] Martin Bouchard. Multichannel affine and fast affine projection algorithms for active noise control and acoustic equalization systems. *IEEE Transactions on Speech and Audio Processing*, 11(1):54–60, 2003.

[6] Martin Bouchard and Felix Albu. The gauss-seidel fast affine projection algorithm for multichannel active noise control and sound reproduction systems. *International Journal of Adaptive Control and Signal Processing*, 19(2-3):107–123, 2004.

[7] J. L. Brown. Asymmetric non-mean-square error criteria. *IEEE Transactions on Automatic Control*, 7(1):64–66, 1962.

[8] Alberto Carini and Giovanni L. Sicuranza. Steady-state and transient analysis of multichannel filtered-x affine projection algorithms. In *IEEE ICASSP*, Philadelphia, PA, March, 2005.

[9] Alberto Carini and Giovanni L. Sicuranza. Transient and steady-state analysis of filtered-x affine projection algorithms. *IEEE Transactions on Signal Processing*, 54(2):665–678, 2006.

[10] David A. Cartes. *Lyapunov tuning and optimization of feedforward noise reduction for single-point, single-source cancellation.* PhD thesis, Thayer School of Engineering, Dartmouth College, 2001.

[11] David A. Cartes, Laura R. Ray, and Rober D. Collier. Lyapunov tuning and optimization of the leaky LMS algorithm for single-source, single-point noise cancellation. In *American Control Conference*, pages 3600–3605. Thayer School of Engineering, Dartmouth College, 2001.

[12] David A. Cartes, Laura R. Ray, and Rober D. Collier. Experimental evaluation of leaky least-meam-square algorithms. *JASA*, 111(4):1758–1771, 2002.

[13] David A. Cartes, Laura R. Ray, and Rober D. Collier. Lyapunov tuning of the leaky LMS algorithm for single-source, single-point noise cancellation. *Mechanical Systems and Signal Processing*, 17(5):925–944, 2003.

[14] John Cioffi. Limited precision effects in adaptive filtering. *IEEE Transactions on Circuits and Systems*, 34:821–833, 1987.

[15] D. L. Cohn and J. L. Melson. The residual encoder: An improved ADPCM system for speech digitization. *IEEE Transactions on Communications*, 23:935–941, 1975.

[16] Paul Darlington. Performance surfaces of minimum effort estimators and controllers. *IEEE Transactions on Signal Processing*, 43(2):536–539, 1995.

[17] Scott C. Douglas. The fast affine projection algorithm for active noise control. In *29th Asilomar Conference on Signals, Systems, and Computers*, pages 1245–1249, 1996.

[18] Scott C. Douglas. Performance comparison of two implementations of the leaky LMS adaptive filter. *IEEE Transactions on Signal Processing*, 45(8):2125–2129, 1997.

[19] J. C. Doyle, B. A. Francis, and A. R. Tannebaum. *Feedback Control Theory.* Maxwell MacMilan International, 1992.

[20] Donald L. Duttweiler. Proportionate normalized least-mean-squares adaptation in echo cancelers. *IEEE Transactions on Acoustics, Speech, and Signal Processing*, 8(5):508–518, 2000.

[21] Stephen J. Elliott. Interaction between multiple feedforward active control systems. *IEEE Transactions on Speech and Audio Processing*, 2(4):521–530, 1994.

[22] Stephen J. Elliott. *Signal Processing for Active Control*. London: Academic Press, 2001.

[23] Stephen J. Elliott and K. H. Baek. Effort constraints in adaptive feedforward control. *IEEE Signal Processing Magazine*, 3(1):7–9, 1996.

[24] Steven L. Gay. Affine projection algorithms. In Simon Haykin and Widrow Bernard, editors, *Least-Mean-Square Adaptive Filters*. John Wiley & Sons, Inc., 2003.

[25] Steven L. Gay and S. Tavathia. The fast affine projection algorithms. In *International Conference Acoustics, Speech, Signal Processing*, pages 3023–3026, 1995.

[26] R. D. Gitlin, H. C. Meadors Jr., and S. B. Weinstein. The tap-leakage algorithm: An algorithm for the stable operation of a digitally implemented, fractionally spaced adaptive equalizer. *The Bell System Technical Journal*, 61(27):1817–1839, 1982.

[27] Colin H. Hansen and Scott D. Snyder. *Active Control of Noise and Vibration*. E & FN SPON, 1st edition, 1997.

[28] Eberhard Hänsler and Gerhard Uwe Schimidt. Control of LMS-type adaptive filters. In Simon Haykin and Bernard Widrow, editors, *Least-Mean-Square Adaptive Filters*. John Wiley & Sons, Inc., 2003.

[29] Simon Haykin. *Adaptive Filter Theory*. Prentice-Hall Inc. Upper Saddle River New Jersey 07458, 3rd edition, 1996.

[30] Simon Haykin and Widrow Bernard. *Least-Mean-Square Adaptive Filters*. John Wiley & Sons, Inc., 2003.

[31] S Ilanko and S.M Dickinson. Asymptotic modelling of rigid boundaries and connections in the Rayleigh-Ritz method. *Journal of Sound and Vibration*, 219:370–378, 1999.

[32] P. A. Ioannou and V. Kokotović. Instability analysis and improvement of robustness of adaptive control. *Automatica*, 20(5):583–594, 1984.

[33] Thomas Kailath, Ali H. Sayed, and Babak Hassabi. *Linear Estimation*. Printice Hall, Upper Saddle River, New Jersey, 2000.

[34] Sen M. Kuo and Dennis R. Morgan. *Active Noise Control Systems Algorithms and DSP Implementations*. John Wiley & Sons, Inc., 1996.

[35] F. Laichi, T. Aboulnasr, and W. Steenaart. Effect of delay on the performance of the leaky LMS adaptive algorithm. *IEEE Transactions on Signal Processing*, 45(3):811–813, 1997.

[36] Søren Laugesen. *Active Control of Acoustic Noise Using Adaptive Signal Processing*. Ph.D., DTU, 1992.

[37] K. Levenberg. A method for the solution of certain nonlinear problems in least squares. *Quart. Appl. Math.*, 2:164–168, 1943.

[38] N. Levinson. The Wiener rms (root mean square) error criterion in filter design and prediction. *Journal of Mathematical Physics*, 25:261–278, 1947.

[39] Lennart Ljung. *System Identification Theory for the User*. Prentice Hall, Upper Saddle River, NJ, 2nd edition, 1999.

[40] D. W. Marquardt. An algorithm for least squares estimation of nonlinear parameters. *J. SIAM*, 11(431-441), 1963.

[41] K. Mayyas and Tyseer Aboulnasr. The leaky LMS algorithm: MSE analysis for gaussian data. *IEEE Transactions on Signal Processing*, 45(4):927–934, 1997.

[42] S. Shankar Narayan, Allen M. Peterson, and Madihally J. Narasimha. Transform domain LMS algorithm. *IEEE Transactions on Acoustics, Speech, and Signal Processing*, ASSP-31 (3):609–615, 1983.

[43] V. H. Nascimento and A. H. Sayed. Unbiased and stable leakage-based adaptive filters. *IEEE Transactions on Signal Processing*, 47(12):3261–3276, 1999.

[44] Philip A. Nelson and Stephen J. Elliott. *Active Control of Sound*. Academic Press, 1992.

[45] Chrysostomos L. Nikias and Min Shao. *Signal Processing with Alpha-Stable Distributions and Applications*. John Wiley & Sons, Inc., New York, 1995.

[46] C. W. Nixon. *Hearing Protector Devices Ear Protectors in Handbook of Noise Control*. McGraw Hill New York, 1979.

[47] K. Ozeki and T. Omeda. An adaptive filtering algorithm using an orthogonal projection to an affine subspace and its properties. *Electronics and Communication in Japan*, 67-A(5), 1984.

[48] Athanasios Papoulis and S. Unnikrishna Pillai. *Probability, Random Variables and Stochastic Processes*. McGraw-Hill, New York, 4th edition, 2002.

[49] V. S. Pugachev. The determination of an optimal system by some arbitrary criterion. *Automation and Remote Control*, 19:513–532, 1958.

[50] X. Qiu and C. H. Hansen. A study of time-domain FXLMS algorithms with control output constraint. *JASA*, 109(6):2815–2823, 2001.

[51] L. R. Rabiner and B. Gold. *Theory and Application of Digital Signal Processing*. Englewood Cliffs,NJ: Prentice-Hall, 1975.

[52] Boaz Rafaely. *Feedback Control of Sound*. Ph.d thesis, University of Southampton, 1997.

[53] K. Rao and P. Yip. *Discrete Cosine Transform*. Academic Press, Boston, 1990.

[54] Brian D. Rigling and Philip Schniter. Subspace leaky LMS. *IEEE Signal Processing Letters*, 11(2):136–139, 2004.

[55] Geert Rombouts and Marc Moonen. A sparse block exact affine projection algorithm. *IEEE Transactions on Speech and Audio Processing*, 10(2):100–108, 2002.

[56] Ali H. Sayed. *Fundamentals of Adaptive Filtering*. John Wiley & Sons, Inc., New York, NY, USA, 2003.

[57] W. A. Sethares, D. A. Lawrence, Jr. C. R. Johnson, and R. R. Bitmead. Parameter drift in LMS adaptive filters. *IEEE Transactions on Acoustics, Speech, and Signal Processing*, ASSP-34:868–879, 1986.

[58] S. Sherman. Non-mean-square error criteria. *IEEE Transactions on Information Theory*, 4 (3):125–126, 1958.

[59] Hyun-Chool Shin, Ali H. Sayed, and Woo-Jin Song. Variable step-size NLMS and affine projection algorithms. *IEEE Signal Processing Letters*, 11(2), 2004.

[60] Giovanni L. Sicuranza and Alberto Carini. Filtered-x affine projection algorithm for multichannel active noise control using second-order volterra filters. *IEEE Signal Processing Letters*, 11(11):853–857, 2004.

[61] Sigurd Skogestad and Ian Postlethwaite. *Multivariable Feedback Control Analysis and Design*. John Wiley & Sons, Inc., 1996.

[62] Masashi Tanaka, Shoji Makino, and Junji Kojima. A block exact fast affine projection algorithm. *IEEE Transactions on Speech and Audio Processing*, 7(1):79–86, 1995.

[63] J. R. Treichler, JR. C. R. Johnson, and M. G. Larimore. *Theory and Design of Adaptive Filters*. Prentice Hall, 1 edition, 2001.

[64] Martin Vetterli and Henri J. Nussbaumer. Simple FFT and DCT algorithms with reduced number of operations. *Signal Processing*, 6:267–278, 1984.

[65] Eugene Walach and Bernard Widrow. The Least Mean Fourth (LMF) adaptive algorithm and its family. *IEEE Transactions on Information Theory*, IT-30(2):275–283, 1984.

[66] A. K. Wang and W. Ren. Convergence analysis of the multi-variable filtered-u algorithm for active noise control. *Signal Processing*, 73:255–266, 1999.

[67] Bernard Widrow and M. E. Hoff. Adaptive switching circuits. *IRE Conv. Rec. , pt. 4*, pages 96–104, 1960.

[68] Bernard Widrow and Samuel D. Stearns. *Adaptive Signal Processing*. Prentice-Hall, New Jersey, 1985.

[69] Bernard Widrow and Eugene Walach. *Adaptive Inverse Control*. Prentice Hall, 1996.

[70] Norbert Wiener. *Extrapolation, interpolation, and smoothing of stationary time series with engineering applications*. John-Wiley, New York, 1949.

[71] Norbert Wiener and E. Hopf. On a class of singular integral equations. *Proc. Prussian Acad. Math-Phys. Ser.*, page 696, 1931.

[72] C. L. Zahm. Application of adaptive arrays to suppres strong jammers in the prescence of weak signals. *IEEE Transactions on Aerospace and Electronic Systems*, 9(2):260–271, 1973.

[73] Moshe Zakai. General error criteria. *IEEE Transactions on Information Theory*, 10:94–95, 1964.

[74] K. Zhou, J. C. Doyle, and K. Glove. *Robust and Optimal Control*. Prentice Hall, 1996.

9. $\alpha\gamma\Pi\epsilon$-APA PERFORMANCE ANALYSIS

9.1 Introduction

The performance of adaptive filters has been subject to numerous studies in the literature. One objective is to obtain general proofs that require as few as possible assumptions on the data and system models etc. Hence, the linear estimation model (LEM) presented in section 9.2 will make use of the fewest possible assumptions today. Another objective is to expand the performance analysis to new adaptive filters or variants hereof. The present text falls into this later class.

The performance of an adaptive filter is usually characterized in terms of the filters *mean-quare performance*, *tracking performance* and *transient performance*. Many textbooks consider the performance of stochastic gradient methods and in particular the least-mean-squares with respect to *stability*, *rate of convergence*, *misadjustment* etc. [3, 12, 13]. The transient performance is concerned with the *stability* and *convergence rate* of the filter. For stable adaptive schemes the mean-square error (m.s.e.) can then be considered in steady-state, that is, following the transient phase whether subjected to a stationary or subjected to a non-stationary environment.

Basically in the literature three different approaches to the analysis of adaptive filters and in particular the simple least-mean-squares (LMS) filter have more or less successfully been considered. Ljung [6, 7] suggested the use of *Lyapunov stability methods*, that are well-established within the control community for stability analysis, by reducing the adaptive filter difference equation to an equivalent ordinary-differential-equation (ODE). The second class of approaches rely on *averaging analysis* where the performance of an *averaged filter* is studied without requiring the independence condition [11, Ch. 4]. Both the ODE method and the averaging analysis method, however, are limited to small step-sizes, that is, $\mu \approx 0$. In the third class of analysis approaches the so-called *independence assumptions* on the regressor and desired signal are invoked. Although the independence assumption on the regressor data do not hold for tapped-delay-line implementations, practical evidence proves that provided that the step-size is sufficiently small this method will give good results. We will pursue this later class of analysis approaches in this report. Moreover, for the analysis of more complex adaptive filters such as the proposed multiple-channel-$\alpha\gamma\Pi\epsilon$-affine projection algorithm (MC-$\alpha\gamma\Pi\epsilon$-APA) additional assumptions are required. Hence, during our development we will invoke some additional *independence assumptions*, but only at a stage where there are absolutely needed for further progress. Moreover, we will comment on the applicability and make some justification of each of the assumptions made.

Usually the transient analysis is much more challenging than the study of mean-square performance. The literature is rich with approaches to the transient analysis. In the analysis of the performance and stability of the adaptive filters many assumptions are historically made in order to facilitate the analysis [3, Ch. 9]. Moreover, most of this work is characterized by the lack of general applicability and is often restricted to a specific class of input data such as Gaussian distribution or relying on the *independence assumption* on the regressor data or specific assump-

tions on the error data, or limited to an individual adaptive scheme. First with the work by Al-Naffouri and Sayed [1, 2] a unified framework based on *energy-conservation* arguments was established. In those two papers transient analysis of adaptive filters with data-non-linearities and error non-linearities respectively were considered. Among the data-normalized adaptive filters we find the ϵ-NLMS family including a matrix-valued step-size. The adaptive filters with error non-linearities include among others the LMS, least-mean-fourth (LMF) and least-mean-mixed-norm (LMMN) algorithms. Transient analysis has previously been published for the family of non-leaking affine projection algorithm (APA) algorithms [1, 10, 14, 15]. For a more exhaustive bibliographic information on performance analysis of adaptive filters refer to [1, 2] and [9, Ch. 6-9] and the references therein.

The approach devised by Al-Naffouri and Sayed [2] is to introduce weighted estimation errors as well as weighted energy norms and relate these quantities to obtain a *weighted variance relation*. From this weighted variance relation the conditions for stability and closed-form expressions for the m.s.e. and mean-square deviation (m.s.d.) can be derived. Another approach is directly to relate unweighted estimation error and then include tracking performance by introducing a random walk model. In this chapter we will proceed more directly and first establish weighted-energy conservation relations that also pertain to the non-stationary case. Then the mean-error performance and m.s.e. performance can readily be obtained by replacing the weighting matrix by an identity matrix. Moreover, the stationary case is obtained as a specialization of the non-stationary case.

The novelty of the present work is the performance analysis of the linear-least-mean-squares estimate (l.l.m.s.e.)-based MC-$\alpha\gamma\Pi\epsilon$-APA adaptive filter encompassing both dynamic *weight-driven leakage* and dynamic *control-effort-driven leakage* and numerical regularization as well as weight regularization. Moreover, in our presentation we also allow the step-size μ, the leakage control parameters α, γ and the numerical regularization parameter ϵ to attain matrix-values and to be time-variant. Furthermore the analysis conducted in this report uses an advanced random-walk model and also allows a non-vanishing initial weight vector.

9.1.1 Chapter Outline

Following these introductory remarks this section concludes by including various definitions, propositions and rules from matrix theory, algebra of weighted norms and algebra of Kronecker products that will be used in this chapter. The generic stochastic adaptive filtering linear estimation model is introduced in section 9.2 along with a definition of various error quantities and convergence quantities used in stochastic gradient methods.

The topic of section 9.3 is a transient analysis of the proposed MC-$\alpha\gamma\Pi\epsilon$-APA adaptive filter. Next the theme of section 9.4 is the corresponding stability analysis of the MC-$\alpha\gamma\Pi\epsilon$-APA algorithm. The main result of this chapter namely Theorem 1 terminates this section. Finally, in section 9.5 we conclude on the performance analysis of the MC-$\alpha\gamma\Pi\epsilon$-APA adaptive filter. The appendix section 9.A contains miscellaneous derivations used in the course of development.

9.1.2 Matrix Theory

In our development we will use some basic results from matrix theory to be presented for convenience in the subsequent text.

Definition 9.1. For a matrix $A = (a_{ij}) \in \mathbb{K}^{m\times n}$ we associate the vector $\operatorname{vec}(A) \in \mathbb{K}^{mn}$ defined by

$$\operatorname{vec}(A) \triangleq [a_{11}, a_{21}, \ldots, a_{n1}, a_{12}, a_{22}, \ldots, a_{n2}, \ldots, a_{1m}, a_{2m}, \ldots, a_{nm}]^\top. \tag{9.1.1}$$

Hence, by the $\operatorname{vec}\{\,\cdot\,\}$ operation the columns of a matrix are stacked vertically to form a *column* vector.

Proposition 9.1 (Matrix Theory)**.** We will use the following properties from elementary matrix theory.

The trace of the product of $A \in \mathbb{K}^{m\times n}$ and $B \in \mathbb{K}^{n\times m}$ commute, that is,

$$\operatorname{Tr}\{AB\} = \operatorname{Tr}\{BA\}. \tag{9.1.2}$$

Therefore, AB and BA have the same nonzero eigenvalues, counting multiplicity.

The trace of the product of matrices $P \in \mathbb{K}^{n\times m}, \Sigma \in \mathbb{K}^{m\times n}$ and P^* can be found as the inner-product of the associated vectors

$$\operatorname{Tr}\{P^*\Sigma P\} = \operatorname{vec}\{PP^*\}^\top \operatorname{vec}\{\Sigma\}. \tag{9.1.3}$$

For a pair of (square) Hermitian matrices $A \in \mathcal{H}_n(\mathbb{K})$ and $B \in \mathcal{H}_n(\mathbb{K})$ we will use the following property.

① The eigenvalues of the sum (difference) of A and B are related through a double inequality to those of the individual matrices by [16, Ch. 7]

$$j \in \underline{n} : \lambda_j(A) + \lambda_{\min}(B) \le \lambda_j(A+B) \le \lambda_j(A) + \lambda_{\max}(B), \quad A, B \in \mathcal{H}_n(\mathbb{K}) \tag{9.1.4a}$$
$$j \in \underline{n} : \lambda_j(A) - \lambda_{\max}(B) \le \lambda_j(A-B) \le \lambda_j(A) - \lambda_{\min}(B), \quad A, B \in \mathcal{H}_n(\mathbb{K}). \tag{9.1.4b}$$

Enforcing the more restrictive requirement that $A \in \mathbb{K}^{n\times n} \succeq 0$ and $B \in \mathbb{K}^{n\times n} \succeq 0$, that is, the matrices A and B are positive-semidefinite (p.s.d.) provides us with some additional rules.

② The eigenvalues of the product of A and B is related through a double inequality to those of the individual matrices by [16, Ch. 7]

$$j \in \underline{n} : \lambda_i(A)\lambda_{\min}(B) \le \lambda_j(AB) \le \lambda_j(A)\lambda_{\max}(B), \quad A, B \in \mathbb{K}^{n\times n} \succeq 0. \tag{9.1.5}$$

③ The sum of A and B is also p.s.d. [16, Ch. 6], that is,

$$A + B \succeq B \succeq 0, \quad A, B \in \mathbb{K}^{n\times n} \succeq 0. \tag{9.1.6}$$

④ For some matrix $C \in \mathbb{K}^{n\times n}$

$$A = C^*C, \quad A \in \mathbb{K}^{n\times n} \succeq 0. \tag{9.1.7}$$

Proposition 9.2 (Partitioned Matrix Theory)**.** In the development we will use the following proposition regarding the determinant of a partitioned matrix [16, Ch. 2].

① Let M be a square matrix partitioned as

$$M = \begin{bmatrix} A & B \\ C & D \end{bmatrix}, \tag{9.1.8}$$

where $A \in \mathbb{K}^{n\times n}, B \in \mathbb{K}^{n\times q}, C \in \mathbb{K}^{q\times n}$ and $D \in \mathbb{K}^{q\times q}$. Then

$$\det(M) = \det(A)\det(D - CA^{-1}B), \tag{9.1.9a}$$

if A is invertible and

$$\det(M) = \det(D)\det(A - BD^{-1}C), \tag{9.1.9b}$$

if D is invertible and

$$\det(M) = \det(AD - CB) \tag{9.1.9c}$$

if $AC = CA$.

9.1.3 Algebra of Weighted Norms

In the derivations we will use some algebraic properties from [2] presented here for convenience. In addition we will also introduce *weighted inner-products.*

Definition 9.2 (Weighted Norm)**.** For a *row* vector $x \in \mathbb{K}^{1\times M}$, a *column* vector $y \in \mathbb{K}^{M\times 1}$ and a Hermitian matrix $\Sigma \in \mathbb{C}^{M\times M}$ we define the weighted norm by

$$\|x\|_\Sigma^2 \triangleq x\Sigma x^* = \mathrm{Tr}\{x^*x\Sigma\} = \mathrm{vec}\{x^*x\}^\top \mathrm{vec}\{\Sigma\} \tag{9.1.10a}$$
$$\|y\|_\Sigma^2 \triangleq y^*\Sigma y = \mathrm{Tr}\{yy^*\Sigma\}. \tag{9.1.10b}$$

Definition 9.3 (Weighted Inner Product)**.** For *row* vectors $x_1, x_2 \in \mathbb{K}^{1\times M}$, *column* vectors $y_1, y_2 \in \mathbb{K}^{M\times 1}$ and a Hermitian matrix $\Sigma \in \mathbb{C}^{M\times M}$ we define the weighted inner-product by

$$\langle x_1, x_2\rangle_\Sigma \triangleq x_1\Sigma x_2^* \tag{9.1.11a}$$
$$\langle y_1, y_2\rangle_\Sigma \triangleq y_1^*\Sigma y_2. \tag{9.1.11b}$$

Proposition 9.3 (Algebra Weighted Norms)**.** Consider the scalar constants $a_1, a_2 \in \mathbb{C}$, the Hermitian matrices $\Sigma, \Sigma_1, \Sigma_2 \in \mathbb{C}^{M\times M}$ and the matrix $A \in \mathbb{C}^{N\times M}$ then the following algebraic properties holds:

① Superposition.

$$a_1\|\tilde{\mathbf{w}}_{i_B}\|_{\Sigma_1}^2 + a_2\|\tilde{\mathbf{w}}_{i_B}\|_{\Sigma_2}^2 = \|\tilde{\mathbf{w}}_{i_B}\|_{a_1\Sigma_1+a_2\Sigma_2}^2. \tag{9.1.12a}$$

② Polarization.

$$(\mathbf{u}_i\Sigma_1\tilde{\mathbf{w}}_{i_B})(\mathbf{u}_i\Sigma_2\tilde{\mathbf{w}}_{i_B}) = \|\tilde{\mathbf{w}}_{i_B}\|^2_{\Sigma_1\mathbf{u}_i^*\mathbf{u}_i\Sigma_2} \tag{9.1.12b}$$

$$= \|\tilde{\mathbf{w}}_{i_B}\|^2_{\Sigma_2\mathbf{u}_i^*\mathbf{u}_i\Sigma_1}. \tag{9.1.12c}$$

③ Independence. Under the assumption that $\tilde{\mathbf{w}}_{i_B}$ and $\mathbf{u}_i$ are *independent* then it holds that

$$\mathrm{E}(\mathbf{u}_i\Sigma_1\tilde{\mathbf{w}}_{i_B})(\mathbf{u}_i\Sigma_2\tilde{\mathbf{w}}_{i_B}) = \mathrm{E}\|\tilde{\mathbf{w}}_{i_B}\|^2_{\Sigma_1\mathbf{u}_i^*\mathbf{u}_i\Sigma_2} \tag{9.1.12d}$$

$$= \mathrm{E}\|\tilde{\mathbf{w}}_{i_B}\|^2_{\Sigma_{12}} \tag{9.1.12e}$$

$$= \mathrm{E}\|\tilde{\mathbf{w}}_{i_B}\|^2_{\Sigma_{21}}, \tag{9.1.12f}$$

where $\Sigma_{12} = \Sigma_1\,\mathrm{E}\,\mathbf{u}_i^*\mathbf{u}_i\Sigma_2$ and $\Sigma_{21} = \Sigma_2\,\mathrm{E}\,\mathbf{u}_i^*\mathbf{u}_i\Sigma_1$.

④ Linear transformation.

$$\|A\tilde{\mathbf{w}}_{i_B}\|^2_{\Sigma} = \|\tilde{\mathbf{w}}_{i_B}\|^2_{A^*\Sigma A}. \tag{9.1.12g}$$

⑤ Orthonormal Transformation. If Q is orthonormal then

$$\|Q^*\tilde{\mathbf{w}}_{i_B}\|^2 = \|\tilde{\mathbf{w}}_{i_B}\|^2. \tag{9.1.12h}$$

⑥ Notational convention. For notational convenience the $\mathrm{vec}\,(\,\cdot\,)$ operator is often suppressed in the weighting norm, e.g.,

$$\|\tilde{\mathbf{w}}_{i_B}\|^2_{\mathrm{vec}\,(\Sigma_1)} \triangleq \|\tilde{\mathbf{w}}_{i_B}\|^2_{\Sigma_1} \tag{9.1.12i}$$

and

$$\langle\tilde{\mathbf{w}}_{i_B}, w^o\rangle_{\mathrm{vec}\,(\Sigma_1)} \triangleq \langle\tilde{\mathbf{w}}_{i_B}, w^o\rangle_{\Sigma_1}. \tag{9.1.12j}$$

9.1.4 Algebra of Kronecker Products

In the derivations we will use some algebraic properties of Kronecker Products, also known as *tensor products* or *direct products* [4, App. A.1] presented here for convenience.

Proposition 9.4. Consider the arbitrary matrices A, B, the scalar constant $a \in \mathbb{K}$, then the following algebraic properties for the Kronecker products hold:

① Superposition.

$$(aA)\otimes B = a(A\otimes B) = A\otimes(aB), \quad A\in\mathbb{K}^{m\times n}, B\in\mathbb{K}^{p\times q}. \tag{9.1.13a}$$

② Transposition.

$$(A\otimes B)^\top = A^\top\otimes B^\top, \quad A\in\mathbb{K}^{m\times n}, B\in\mathbb{K}^{p\times q}. \tag{9.1.13b}$$

③ Hermitian Transposition.

$$(A\otimes B)^* = A^*\otimes B^*, \quad A\in\mathbb{C}^{m\times n}, B\in\mathbb{C}^{p\times q}. \tag{9.1.13c}$$

④ Product.

$$(A\otimes B)(C\otimes D) = AC\otimes BD, \quad A\in\mathbb{K}^{m\times n}, B\in\mathbb{K}^{p\times q}, C\in\mathbb{K}^{n\times s}, D\in\mathbb{K}^{q\times r}. \tag{9.1.13d}$$

⑤ Inversion.

$$\text{If } A \in \mathbb{K}^{n\times n}, B \in \mathbb{K}^{q\times q} \text{ are nonsingular, then } (A\otimes B)^{-1} = A^{-1}\otimes B^{-1}. \tag{9.1.13e}$$

The following proposition is useful for converting a *linear matrix equation* for X into a *vector equation* for $\operatorname{vec}\{X\}$.

Proposition 9.5. Suppose $A \in \mathbb{K}^{m\times n}, X \in \mathbb{K}^{n\times q}$ and $C \in \mathbb{K}^{q\times r}$, it then holds that

$$\operatorname{vec}(AXC) = (C^{\top}\otimes A)\operatorname{vec}(X). \tag{9.1.14}$$

The eigenvalues of the Kronecker product of two square matrices are determined as follows.

Proposition 9.6. Suppose $A \in \mathbb{K}^{n\times n}$ and $B \in \mathbb{K}^{q\times q}$. If $\lambda \in \sigma(A)$ and $x \in \mathbb{C}^n$ is a corresponding eigenvector, and if $\mu \in \sigma(B)$ and $y \in \mathbb{C}^q$ is a corresponding eigenvector, then $\lambda\mu \in \sigma(A\otimes B)$ with corresponding eigenvector $x\otimes y$. Every eigenvalue of $A\otimes B$ arises as such product for eigenvalues of A and B. If $\sigma(A) = \{\lambda_1,\ldots,\lambda_n\}, \sigma(B) = \{\mu_1,\ldots,\mu_q\}$ then $\sigma(A\otimes B) = \{\lambda_i\mu_j;\quad i = 1,\ldots,n, j = 1,\ldots q\}$ (taking into account multiplicities). In particular, $\sigma(A\otimes B) = \sigma(B\otimes A)$ and $\operatorname{Tr}(A\otimes B) = \operatorname{Tr}(B\otimes A) = \operatorname{Tr}(A)\operatorname{Tr}(B)$. Moreover, the eigenvalues of $A\otimes \mathrm{I}_n + \mathrm{I}_q\otimes B$ are $\{\lambda_i + \mu_j;\quad i = 1,\ldots,n, j = 1,\ldots q\}$.

9.2 Linear Estimation Model

The generic stochastic adaptive filtering model is depicted in Equation 9.2. The model governing the *data sequences* $\{\mathbf{d}_i, \mathbf{x}_i, \mathbf{u}_i\}$ will be presented next. This model covers the four different modes of adaptive filtering presented in section 8.2 on page 373, that is, *interference cancelation*, *system identification*, *inverse modeling* and *prediction*. The underlying assumptions will first be listed using compact notation and subsequently expressed in plain terms.

Assumption 1 (Linear Estimation Model)**.** The following generic multiple-input and multiple-output (MIMO) linear estimation model (LEM) for the *data sequences* $\{\mathbf{d}_i, \mathbf{x}_i, \mathbf{u}_i\}$ that describe a possible nonstationary environment that may be subject to finite-precision arithmetic will used:

$$\forall i_B \geq -1 : \exists \mathbf{w}^o_{i_B} \in \mathbb{K}^{M\times 1} : \quad \mathbf{d}_i = \mathbf{u}_i\mathbf{w}^o_{i_B} + \mathbf{v}_i. \tag{9.2.1a}$$

$$\begin{aligned} \forall i_B, j_B \geq -1 : \quad & \mathbf{w}^o_{i_B} = w^o + \boldsymbol{\theta}_{i_B},\quad \boldsymbol{\theta}_{i_B} = \chi\boldsymbol{\theta}_{i_B-1} + \mathbf{q}_{i_B},\quad w^o \triangleq \mathrm{E}\,\mathbf{w}^o_{i_B}, \\ & f_{q_{i_B}}(q_{i_B}|q_{j_B}) = f_{q_{i_B}}(q_{i_B}) = f_{q_{j_B}}(q_{j_B}) = f_{q_{j_B}}(q_{j_B}|q_{i_B}), \\ & \lim_{i_B\to\infty} \mathrm{E}(\mathbf{w}^o_{i_B} - w^o)(\mathbf{w}^o_{i_B} - w^o)^* = \tfrac{Q}{1-|\chi|^2},\quad 0 \leq |\chi| < 1. \end{aligned} \tag{9.2.1b}$$

$$\forall i, i_B \geq -1 : \quad f_q(q_{i_B}|u_i, v_i) = f_q(q_{i_B}). \tag{9.2.1c}$$

$$\forall i, i_B \geq -1 : \quad \mathrm{E}\,\mathbf{d}_i = \mathrm{E}\,\mathbf{u}_i = \mathrm{E}\,\mathbf{x}_i = \mathrm{E}\,\mathbf{v}_i = \mathrm{E}\,\mathbf{q}_{i_B} = 0. \tag{9.2.1d}$$

$$\forall i, j \geq -1 : \quad f_{v_i}(v_i|v_j) = f_{v_i}(v_i) = f_{v_j}(v_j) = f_{v_j}(v_j|v_i),\quad \mathrm{E}\,\mathbf{v}_i\mathbf{v}_i^* = \sigma_v^2. \tag{9.2.1e}$$

$$\begin{aligned} \forall i, i_B \geq -1 : \quad & f_{w_{-1}}(w_{-1}|d_i, u_i, v_i, q_{i_B}) = f_{w_{-1}}(w_{-1}) \\ \wedge \quad & f_{\theta_{-1}}(\theta_{-1}|d_i, u_i, v_i, q_{i_B}) = f_{\theta_{-1}}(\theta_{-1}). \end{aligned} \tag{9.2.1f}$$

$$\forall i, j \geq -1: \quad f_v(v_i|u_j) = f_v(v_i). \tag{9.2.1g}$$

$$\forall i \geq -1: \quad R_{u,i} = \mathrm{E}\,\mathbf{u}_i^* \mathbf{u}_i \succ 0. \tag{9.2.1h}$$

$$\mathrm{DN} \ll 1. \tag{9.2.1i}$$

Hence, assumption (9.2.1a) proclaims the existence of an *optimal adaptive tap-weight vector* that we denote by $\mathbf{w}_{i_B}^o \in \mathbb{K}^{M\times 1}$. This linear relationship links the *regression vector* $\mathbf{u}_i \in \mathbb{K}^{N_e\times M}$ to the disturbance signal $\mathbf{d}_i \in \mathbb{K}^{N_e\times 1}$. It is customary to absorb any such deviation from a perfect linear model into the quantity $\mathbf{v}_i \in \mathbb{K}^{N_e\times 1}$ that represents the noise signal (estimation error). As such the noise term $\mathbf{v}_i$ should account for input noise corrupting the regressor signal, system non-linearities, component saturation, quantization effects, overflow, insufficient order of filter model, noise corrupting the disturbance signal. This is done for mathematically traceability. In subsection 9.2.3 some remarks will be made regarding the validity of such data model when applying it in an active noise control (ANC) context. It suffices to say here by the adjective *optimal* we are explicitly referring to the cost function J^{e^2} defined in (8.3.5) on page 376 and therefore **not** to the cost function $J^{e^2\alpha\gamma\Pi}$ introduced in (8.3.22) on page 385, that the MC-$\alpha\gamma\Pi\epsilon$-APA adaptive filter actually is designed to minimize. There are two main reasons for this choice. Firstly, as argued at length in subsection 8.3.3 on page 378, weight-driven leakage and control-effort-driven leakage types are introduced as a remedy to various system imperfections. However, as is well-known such leakage functionalities are only included at a cost namely an increased m.s.e.. Hence, we would therefore prefer a "perfect" system and apply the minimum mean-square error (m.m.s.e.) criteria and accordingly the J^{e^2} cost function. Secondly, in order to let the assumptions on zero-mean and independent and identical distributed (i.i.d.) noise in (9.2.1d) and (9.2.1e) make sense we have to subtract the influence of the attraction points constituted by 0 (control-effort-driven leakage) and $\bar{w}_{i_{\bar{w}}}$ (weight regularization) from the system "optimality".

The non-stationarity of the LEM is expressed by a random-walk model in assumption (9.2.1b) where the optimal adaptive tap-weight vector $\mathbf{w}_{i_B}^o$ undergoes random variations around its mean $w^o \in \mathbb{K}^{M\times 1}$, with perturbations random-walk vector $\boldsymbol{\theta}_{i_B} \in \mathbb{K}^{M\times 1}$, being generated by a first-order auto-regressive model with pole position at $\chi \in \mathbb{C}$ that regularizes the randomness in the model and with a random initial condition $\boldsymbol{\theta}_{-1} \in \mathbb{K}^{M\times 1}$. Finally, $\mathbf{q}_{i_B} \in \mathbb{K}^{M\times 1}$ denotes the i.i.d. random-walk vector, and $Q \triangleq \mathrm{E}\,\mathbf{q}_i\mathbf{q}_i^* \in \mathbb{K}^{M\times M}$ is a constant matrix related to the covariance of $\tilde{\mathbf{w}}_{i_B}^o$. It is customary to set $\chi \equiv 1$ in order to simplify the analysis. However, as a result the covariance matrix of $\tilde{\mathbf{w}}_{i_B}^o$ then becomes unbounded as time progresses.

Assumption (9.2.1c) states that the sequence $\{\mathbf{q}_{i_B}\}$ is independent of both $\mathbf{v}_i$ and $\mathbf{u}_i$. The random sequences (RSs) $\{\mathbf{d}_i, \mathbf{u}_i, \mathbf{v}_i, \mathbf{q}_{i_B}\}$ are in assumption (9.2.1d) all assumed to have zero means. Assumption (9.2.1e) expresses that the noise sequence is i.i.d. with constant variance $\sigma_v^2 \in \mathbb{K}^{N_e\times N_e}$.

The *initial weight vector* $\mathbf{w}_{-1} \in \mathbb{K}^{M\times 1}$ and *initial optimal weight vector* $\mathbf{w}_{-1}^o \in \mathbb{K}^{M\times 1}$ are both independent of $\{\mathbf{d}_i, \mathbf{u}_i, \mathbf{x}_i, \mathbf{v}_i, \mathbf{q}_{i_B}\}$ by assumption (9.2.1f).

Then a more controversial assumption is made in (9.2.1g) where it is assumed that the noise sequence $\{\mathbf{v}_i\}$ is independent of $\mathbf{u}_j$. It should be recalled that *independence* implies *uncorrelatedness* but **not** the converse. Hence, assumption (9.2.1g) implies that $\mathrm{E}\,\mathbf{v}_i\mathbf{u}_j^* = 0, \forall i, j \geq -1$, that is, the regressor and the estimation error are *uncorrelated*. From the definition in (9.2.1a) such correlatedness is only guaranteed to hold for $i = j$. Similarly, assumption (9.2.1c) imply

that $\mathrm{E}\,\mathbf{q}_{i_B}\mathbf{v}_i^* = 0$ respectively $\mathrm{E}\,\mathbf{q}_{i_B}\mathbf{u}_i^* = 0, \forall i, i_B \geq -1$, that is, the random-walk vector $\mathbf{q}_{i_B}$ is *uncorrelated* with both the regressor $\mathbf{u}_i$ and the system noise $\mathbf{v}_i$. From assumptions (9.2.1g) (9.2.1e) (9.2.1f) and (9.2.1c) we appreciate that all of $\{\mathbf{u}_j, \mathbf{v}_j, \mathbf{w}_{-1}^o$ and $\mathbf{q}_{j_B}\}$ are *independent* of $\mathbf{v}_i, \forall i > j \geq j_B$. The reason why the stronger assumptions on *independence* is enforced is that then at any particular time instant i, the estimation noise $\mathbf{v}_i$ is independent of all previous weight estimators $\mathbf{w}_j, j < i$ as discussed above. This fact is quite essential for the mathematical tractability of the performance analysis of the adaptive schemes. Moreover, as a consequence it also holds that

$$\forall j < i : \; f_v(v_i | w_j, \tilde{w}_j, e_{a,i}) = f_v(v_i), \tag{9.2.2}$$

that is, the noise term is independent of the *a priori* error and previous weight vectors and weight-error vectors [9, Lemma 7.2.1]. The assumptions on *identical distributions* in (9.2.1b) and (9.2.1e) are not fundamental to the analysis, but led to a constant "maneuver" covariance matrix Q and a constant noise covariance matrix σ_v^2 respectively.

Moreover, recalling the definition of the regressor time-block matrix $\mathbf{U}_i$ (8.6.9) and defining similarly the system noise signal time-block matrix $V_i \in \mathbb{K}^{KN_e \times 1} (V_i \in \mathbb{K}^{K \times 1})$ by

$$\mathbf{V}_i \triangleq \begin{cases} \begin{bmatrix} \mathbf{v}(i) & \mathbf{v}(i-\Delta_u) & \dots & \mathbf{v}(i-(K-1)\Delta_u) \end{bmatrix}^\top & \text{SISO, SIMO} \\ \begin{bmatrix} \mathbf{v}_i & \mathbf{v}_{i-\Delta_u} & \dots & \mathbf{v}_{i-(K-1)\Delta_u} \end{bmatrix}^\top & \text{MISO, MIMO,} \end{cases} \tag{9.2.3}$$

we appreciate that assumption (9.2.1g) also implies that $\forall i, j \geq -1 : f_V(V_i | U_j) = f_V(V_i)$, that is, the noise sequence $\{\mathbf{V}_i\}$ is independent of $\mathbf{U}_j$. Moreover, by virtue of (9.2.1e) the variance of the block-time noise in the LEM denoted by $\sigma_V^2 \in \mathbb{K}^{KN_e \times KN_e}$ is constant and obtained from

$$\mathrm{E}\,\mathbf{V}_i\mathbf{V}_i^* = \sigma_V^2 = \sigma_{v\otimes K}^2. \tag{9.2.4}$$

The auto correlation matrix of the regressor $\mathbf{u}_i \quad R_{u,i} \triangleq \mathrm{E}\,\mathbf{u}_i^*\mathbf{u}_i \in \mathbb{C}^{M \times M}$ is positive definite (assumption 9.2.1h). Finally, assumption (9.2.1i) regards the degree of nonstationarity (DN) that is defined by

$$\mathrm{DN} \triangleq \sqrt{\frac{\mathrm{Tr}\, R_u Q}{\sigma_v^2}}. \tag{9.2.5}$$

Hence, by enforcing $\mathrm{DN} \ll 1$ then the adaptive filter will have time to track the variations in the weight vector w_i^o.

Although apparently very primitive the single-input version of the data model Equation 9.2 finds wide spread applicability in the signal processing community.

Fig. 9.1: Data Model in Adaptive Filtering.

Historically, the derivations involved are based on the following *independence assumption* [3, Ch. 9].

Assumption 2 (Independence of $\mathbf{u}_i, \mathbf{U}_i$)**.** The regressor $\mathbf{u}_i$ is i.i.d., that is,

$$\forall i, j \geq -1: \quad f_{u_i}(u_i|u_j) = f_{u_j}(u_j|u_i) = f_{u_i}(u_i) = f_{u_j}(u_j) \tag{9.2.6a}$$

respectively the time-block matrix $\mathbf{U}_i$ is i.i.d., that is,

$$\forall i, j \geq -1: \quad f_{U_i}(U_i|U_j) = f_{U_j}(U_j|U_i) = f_{U_i}(U_i) = f_{U_j}(U_j). \tag{9.2.6b}$$

Here (9.2.6a) is the "usual" independence assumption used, e.g., in [3, Ch. 9] while (9.2.6b) is the corresponding independence assumption used in APA analysis, e.g., in [10]. It should be noticed that (9.2.6b) is a stronger assumption and therefore often more dubious assumption than (9.2.6a) as the affine projection (AP) algorithm fundamentally is based on reusing the regressor data (see subsection 8.6.2). When the independence assumption (9.2.6a) respectively (9.2.6b) hold it is guaranteed that the weight-error vector $\tilde{\mathbf{w}}_{i_B-1}$ is independent of the regressor data $\mathbf{u}_i$, that is,

$$\forall i_B > 0, j \geq -1: \quad f_{\tilde{w}}(\tilde{w}_{i_B-1}|u_j) = f_{\tilde{w}}(\tilde{w}_{i_B-1}) \tag{9.2.7a}$$

respectively $\tilde{\mathbf{w}}_{i_B-1}$ is independent of the time-block matrix $\mathbf{U}_i$, that is,

$$\forall i_B > 0, j \geq -1: \quad f_{\tilde{w}}(\tilde{w}_{i_B-1}|U_j) = f_{\tilde{w}}(\tilde{w}_{i_B-1}). \tag{9.2.7b}$$

By invoking the *independence theory*, however, the adaptive process is no longer precisely quantified but reliable design guidelines for the stability and mean-squared ensemble-averaged error performance surface of the least-mean-squares are obtained.

9.2.1 Error Quantities in Stochastic Gradient Methods

Next various error quantities that will be used in our analysis will be introduced. The *a priori* error vector $\mathbf{e}_{a,i} \in \mathbb{K}^{KN_e \times 1}$ and the *posteriori* error vector $\mathbf{e}_{p,i} \in \mathbb{K}^{KN_e \times 1}$ are defined by

$$\mathbf{e}_{a,i} = \mathbf{u}_i(\mathbf{w}_{i_B}^o - \mathbf{w}_{i_B-1}) \tag{9.2.8a}$$
$$\mathbf{e}_{p,i} = \mathbf{u}_i(\mathbf{w}_{i_B}^o - \mathbf{w}_{i_B}) = \mathbf{u}_i\tilde{\mathbf{w}}_{i_B}. \tag{9.2.8b}$$

The *a priori* block-time error vector $\mathbf{E}_{a,i} \in \mathbb{K}^{KN_e \times 1}$ and the *posteriori* block-time error vector $\mathbf{E}_{p,i} \in \mathbb{K}^{KN_e \times 1}$ are similarly defined by

$$\mathbf{E}_{a,i} = \mathbf{U}_i(\mathbf{w}_{i_B}^o - \mathbf{w}_{i_B-1}) \tag{9.2.9a}$$
$$\mathbf{E}_{p,i} = \mathbf{U}_i(\mathbf{w}_{i_B}^o - \mathbf{w}_{i_B}) = \mathbf{U}_i\tilde{\mathbf{w}}_{i_B}. \tag{9.2.9b}$$

The block-time error vector $\mathbf{E}_i$ and the *a priori* block-time error vector $\mathbf{E}_{a,i}$ are related as

$$\mathbf{E}_i = \mathbf{E}_{a,i} + \mathbf{V}_i, \tag{9.2.10}$$

where the system noise signal time-block matrix $\mathbf{V}_i$ was defined in (9.2.3).

9.2.2 Convergence of Stochastic Gradient Methods

A convergence criteria in the mean square is invoked due to mathematical simplicity. The adaptive filter is considered to converge if the cost function, $J^{e^2}(i)$, approaches some constant value, $J^{e^2}_{\infty}$, as the iteration number goes to infinity

$$J^{e^2}_{\infty} \triangleq \lim_{i\to\infty} J^{e^2}(i) = \lim_{i\to\infty} \mathrm{E}\|\mathbf{e}_i\|^2_{W_e}. \tag{9.2.11}$$

As demonstrated in [3, Ch. 6] the satisfaction of (9.2.11) is equivalent to ensuring convergence in the mean-squared Euclidian norm of the weight-error vector, that is, the m.s.d. of the adaptive filter denoted by $\mathrm{MSD} \in \mathbb{R}_+$ that is defined as the limiting value of $\|\tilde{\mathbf{w}}_{i_B}\|^2$

$$\mathrm{MSD} \triangleq \lim_{i\to\infty} \mathrm{E}\|\tilde{\mathbf{w}}_{i_B}\|^2. \tag{9.2.12}$$

The limiting error value of $\|\mathbf{e}_i\|^2$ is called the *m.s.e.* of the adaptive filter denoted by $\mathrm{MSE} \in \mathbb{R}_+$

$$\mathrm{MSE} \triangleq \lim_{i\to\infty} \mathrm{E}\|\mathbf{e}(i)\|^2. \tag{9.2.13}$$

Similarly, the steady-state value of $\|\mathbf{e}_i\|^2_{W_e}$ is called the *w.m.s.e.* of the adaptive filter $\mathrm{WMSE} \in \mathbb{R}_+$

$$\mathrm{WMSE} \triangleq \lim_{i\to\infty} \mathrm{E}\|\mathbf{e}_i\|^2_{W_e}. \tag{9.2.14}$$

The limiting *a priori* error $\|\mathbf{e}_{a,i}\|^2$ $\mathrm{EMSE} \in \mathbb{R}_+$ is designated by EMSE of the adaptive filter

$$\mathrm{EMSE} \triangleq \lim_{i\to\infty} \mathrm{E}\|e_{a,i}\|^2 \triangleq \mathrm{MSE} - J^{e^2}_{\min}. \tag{9.2.15}$$

Similarly, the steady-state weighted *a priori* error $\|\mathbf{e}_{a,i}\|^2_{W_e}$ $\mathrm{WEMSE} \in \mathbb{R}_+$ is designated by WEMSE of the adaptive filter

$$\mathrm{WEMSE} \triangleq \lim_{i\to\infty} \mathrm{E}\|e_{a,i}\|^2_{W_e} \triangleq \mathrm{WMSE} - J^{e^2}_{\min}. \tag{9.2.16}$$

9.2.3 Remarks on Linear Estimation Model

Although the linear estimation model in principle should cover the four different modes of adaptive filtering above we will only consider the *Interference cancelation* and *System identification* modes here. It seems reasonable to consider the quality of the LEM above and in particular Assumption 1 by considering the same sources that may lead to imperfect coherence in subsection 2.2.1 on page 18 as potential sources to inadequacies in the LEM[1].

LEM Prob. 1. *Partially Coherent Fields.* Such of lack of perfect coherence is very application dependent and may or may not be modeled according to the LEM.

[1] The list is most likely not exhaustive and many other causes to problems with the LEM may exist.

LEM Prob. 2. Insufficient model order. It seems reasonable to use our model also to let $\mathbf{v}_i$ include spatial aliasing noise related to spatial undersampling of the signals.

LEM Prob. 3. Doppler effects. Doppler effects are of concern in, e.g., wireless communication systems and can be taking into account by replacing (9.2.1a) for the optimal weight by the more elaborate expression

$$\forall i_B \geq -1 : \exists \mathbf{w}_{i_B}^o \in \mathbb{K}^{M\times 1} : \quad \mathbf{d}_i = \mathbf{u}_i \mathbf{w}_{i_B}^o \mathrm{e}\imath(\Omega i + \phi_i) + \mathbf{v}_i \tag{9.2.17}$$

for some frequency offset Ω and phase offset ϕ. The nonstationarity model used in the present analysis viz. (9.2.1b)-(9.2.1d) suffice, but upon replacing (9.2.1a) by (9.2.17) more involved expressions would be obtained.

LEM Prob. 4. Nonlinear system. A nonlinear system will usually generate a model estimation error $\mathbf{v}_i$ that will be directly dependent on the regressor signal $\mathbf{u}_i$. Hence, nonlinearities completely violate assumption (9.2.1g).

LEM Prob. 5. The system is not a constant-parameter system. Such time-variant behavior may or may not comply with our assumptions.

LEM Prob. 6. Finite signal-to-noise ratio (SNR). The presence of extraneous noise at the output is compliant within our framework as long as assumption (9.2.1d)-(9.2.1e) are satisfied. In contrary, extraneous noise that contaminates the inputs will according to the LEM in Equation 9.2 also contaminates $\mathbf{v}_i$ and thereby violating assumption (9.2.1g).

LEM Prob. 7. Aliased signal components in discrete-time systems. Again the LEM holds for aliased components in the outputs, but not for aliasing effects in the inputs. More details pertaining to aliasing effects can be found in Appendix N on page 791.

LEM Prob. 8. Adaptive filter finite-precision errors (refer to subsection 8.6.7 on page 403). Although finite-precision effects are omitted from the present analysis, such effects can rather straightforwardly be included in the model as they manifest themselves in a manner similar to system nonstationarity [9, Ch. 8].

LEM Prob. 9. The underlying random processs (RPs) are not mean and variance stationary or ergodic. Lack of stationarity may or may not comply with our model (9.2.1b)-(9.2.1d).

LEM Prob. 10. Periodicities in the acquired data set. The random-walk model introduced in 3 is more appropriate, whenever such periodicities are encountered.

LEM Prob. 11. A nonzero mean in the acquired data set. If the assumption on zero mean values in (9.2.1d) is violated, then many of our expressions would be somewhat more involved, but the main results would not be fundamentally changed.

Finally, it should be recalled that if the LEM model does not hold entirely, this does not necessarily imply that the adaptive filter is not working. However, most likely the performance of the adaptive filter will be somewhat poorer than predicted from the model. Of particular concern are low SNRs at the input and highly nonstationary signals (DN > 1).

9.3 Transient Analysis of MC-$\alpha\gamma\Pi\epsilon$-APA

In subsection 8.6.3 on page 398 a novel l.l.m.s.e.-based adaptive filter encompassing both dynamic *weight-driven leakage* and dynamic *control-effort-driven leakage* and numerical regularization as

well as weight regularization was derived. This algorithm which for convenience is repeated in (9.3.1) is referred to as multiple-channel-$\alpha\gamma\Pi\epsilon$-affine projection algorithm. The detailed derivation can be found in subsection 8.6.1.

$$\boxed{\begin{array}{c} w_{i_B} = \Upsilon_{i_\Upsilon} w_{i_B-1} + \mu_{i_\mu}\epsilon_{i_\epsilon}^{-1} U_i^*(W_{e\otimes K}^{-1} + U_i\epsilon_{i_\epsilon}^{-1}U_i^*)^{-1}(D_i - U_i w_{i_B-1}) + \mu_{i_\mu}\breve{w}, \\ \text{MIMO}, \quad i \geq 0, \quad i_B \geq 0, \quad i_\Upsilon \geq 0, \quad i_\mu \geq 0, \quad i_\epsilon \geq 0, \quad w_{-1} = w^0. \end{array}} \tag{9.3.1}$$

In the weight update recursion (9.3.1) the quantity Υ_{i_Υ} denotes the transformed leakage-weight regularization matrix defined in (8.6.13) on page 399 and repeated here for convenience

$$\boxed{\Upsilon_{i_\Upsilon} = \mathrm{I} - \mu_{i_\mu}\big(\alpha_{i_\alpha} + X_i^*\gamma_{i_\gamma\otimes K}(\mathbf{y}_{i^\gamma})X_i + \Pi_{i_\Pi}\big),} \tag{9.3.2}$$

where i_Υ denotes the transformed weight leakage factor update iteration number $i_\Upsilon = \max\{i_\mu, i_\alpha, i_\gamma, i_\Pi\}$ introduced in (8.6.15) on page 399 and where $\breve{w} = \Pi_{i_\Pi}\bar{w}$ is the transformed weight vector for weight regularization defined in (8.6.14) on page 399

In the study of the performance of an adaptive filter it is customary to replace a *deterministic* difference equation such as (9.3.1) with an equivalent *stochastic* difference equation (viz. (9.3.8) on the facing page). This replacement is carried out as the weights are data-dependent and therefore consequently are considered as RSs in the analysis. Similarly, in a non-stationary environment the optimal weights will exhibit variation with time typically governed by some random-walk model. As a consequence the optimal weight vector $\mathbf{w}_{i_B}^o$ is also considered as vector-valued RS. Moreover, in our presentation we also allow the step-size μ, the leakage control parameters α, γ and the numerical regularization parameter ϵ to attain matrix-values and to be time-variant. We will therefore equip these quantities with the subscripts $\mu_{i_\mu}, \alpha_{i_\alpha}, \gamma_{i_\gamma}, \epsilon_{i_\epsilon}$ and Π_{i_Π} respectively to indicate this time-dependence. It should also be emphasized that the parameters only need to be updated on a block-update time frame or less frequently. Furthermore, as these parameters in general will attain values that are data-dependent they will also be considered as RSs. We will therefore use bold script for these quantities in order to emphasize their randomness (refer to the Notations on page xli).

Hence, using bold script for random quantities the recursion (9.3.1) becomes

$$\boxed{\mathbf{w}_{i_B} = \boldsymbol{\Upsilon}_{i_\Upsilon}\mathbf{w}_{i_B-1} + \boldsymbol{\mu}_{i_\mu}\boldsymbol{\epsilon}_{i_\epsilon}^{-1}\mathbf{U}_i^*(W_{e\otimes K}^{-1} + \mathbf{U}_i\boldsymbol{\epsilon}_{i_\epsilon}^{-1}\mathbf{U}_i^*)^{-1}\mathbf{E}_i + \boldsymbol{\mu}_{i_\mu}\breve{w}} \tag{9.3.3}$$

where the error signal time-block matrix by $\mathbf{E}_i \in \mathbb{K}^{KN_e}(\mathbf{E}_i \in \mathbb{K}^{K\times 1})$

$$\mathbf{E}_i = \mathbf{D}_i - \mathbf{U}_i\mathbf{w}_{i_B-1} \tag{9.3.4}$$

is constituted by the error signals $\mathbf{e}_i$ according to

$$\mathbf{E}_i \triangleq \begin{cases} \begin{bmatrix} \mathbf{e}(i) & \mathbf{e}(i-\Delta_u) & \dots & \mathbf{e}(i-(K-1)\Delta_u) \end{bmatrix}^\top & \text{SISO, SIMO} \\ \begin{bmatrix} \mathbf{e}_i & \mathbf{e}_{i-\Delta_u} & \dots & \mathbf{e}_{i-(K-1)\Delta_u} \end{bmatrix}^\top & \text{MISO, MIMO.} \end{cases} \tag{9.3.5}$$

Notice, in the general time-variant case the transformed leakage-weight regularization matrix $\boldsymbol{\Upsilon}_{i_\Upsilon}$ that is obtained from

$$\boxed{\boldsymbol{\Upsilon}_{i_\Upsilon} = \mathrm{I} - \boldsymbol{\mu}_{i_\mu}\big(\boldsymbol{\alpha}_{i_\alpha} + \boldsymbol{X}_i^* \boldsymbol{\gamma}_{i_\gamma \otimes K} \boldsymbol{X}_i + \boldsymbol{\Pi}_{i_\Pi}\big),} \tag{9.3.6}$$

is also RS as the step-size $\boldsymbol{\mu}_{i_\mu}$ and the leakage control parameters $\boldsymbol{\alpha}_{i_\alpha}$ and $\boldsymbol{\gamma}_{i_\gamma}$ are all considered as RSs.

We are mostly interested in the propagation of the weight-error vector $\tilde{\mathbf{w}}_{i_B} \in \mathbb{K}^{M\times 1}$ that is defined by

$$\tilde{\mathbf{w}}_{i_B} = \mathbf{w}_{i_B}^o - \mathbf{w}_{i_B}. \tag{9.3.7}$$

Hence, by insertion of (9.3.7) in (9.3.3) the following *stochastic* difference equation is obtained

$$\boxed{\tilde{\mathbf{w}}_{i_B} = \mathbf{w}_{i_B}^o - \boldsymbol{\Upsilon}_{i_\Upsilon}\mathbf{w}_{i_B-1} - \boldsymbol{\mu}_{i_\mu}\boldsymbol{\epsilon}_{i_\epsilon}^{-1}\mathbf{U}_i^*(W_{e\otimes K}^{-1} + \mathbf{U}_i\boldsymbol{\epsilon}_{i_\epsilon}^{-1}\mathbf{U}_i^*)^{-1}\mathbf{E}_i - \boldsymbol{\mu}_{i_\mu}\breve{w}.} \tag{9.3.8}$$

For the ease of the development we will make use of some auxiliary quantities to be introduced in the subsequent text.

The leakage-transformed modified weight-error vector $\tilde{\mathbf{w}}_{i_B-1}^{'\Upsilon} \in \mathbb{K}^{M\times 1}$ defined by

$$\tilde{\mathbf{w}}_{i_B-1}^{'\Upsilon} = \mathbf{w}_{i_B}^o - \boldsymbol{\Upsilon}_{i_\Upsilon}\mathbf{w}_{i_B-1} \tag{9.3.9}$$

is used to represent the first two terms of the right-hand side (RHS) of (9.3.8). By the term *modified* is understood that the optimal weight vector is evaluated at block-time i_B, while the weight vector itself is taking at block-time $i_B - 1$. Moreover, by the notion *leakage-transformed* we explicitly refer to the presence of the transformed leakage-weight regularization matrix $\boldsymbol{\Upsilon}_{i_\Upsilon}$.

Next we will define the auxiliary matrices $\mathbf{P}'_i, \mathbf{P}_i \in \mathbb{K}^{M\times KN_e}$ by

$$\begin{aligned}
\mathbf{P}'_{i_B} &\triangleq \boldsymbol{\mu}_{i_\mu}\boldsymbol{\epsilon}_{i_\epsilon}^{-1}\mathbf{U}_i^*(W_{e\otimes K}^{-1} + \mathbf{U}_i\boldsymbol{\epsilon}_{i_\epsilon}^{-1}\mathbf{U}_i^*)^{-1} && \text{(9.3.10a)}\\
&= \boldsymbol{\mu}_{i_\mu}(\boldsymbol{\epsilon}_{i_\epsilon} + \mathbf{U}_i^* W_{e\otimes K}\mathbf{U}_i)^{-1}\mathbf{U}_i^* W_{e\otimes K}\mathbf{U}_i, && \text{(9.3.10b)}\\
\mathbf{P}_{i_B} &\triangleq \mathbf{P}'_{i_B}\mathbf{U}_i. && \text{(9.3.10c)}
\end{aligned}$$

where the translation from (9.3.10a) to (9.3.10b) stems from subsection 8.B.2 where the derivation actually was in the opposite direction and aimed at reducing the order of the matrix inverse. Moreover, by using the relation between the block-time error vector $\mathbf{E}_i$ and the *a priori* error $\mathbf{E}_{a,i}$ and system noise signal time-block matrix $\mathbf{V}_i$ (9.2.10) and using (9.3.9) we may reexpress the recursion (9.3.8) on this page as

$$\boxed{\tilde{\mathbf{w}}_{i_B} = \tilde{\mathbf{w}}_{i_B-1}^{'\Upsilon} - \mathbf{P}'_{i_B}\mathbf{E}_{a,i} - \mathbf{P}'_{i_B}\mathbf{V}_i - \boldsymbol{\mu}_{i_\mu}\breve{w}.} \tag{9.3.11}$$

On the RHS of (9.3.11) we find both the *a priori* error $\mathbf{E}_{a,i}$ and the leakage-transformed modified weight-error vector $\tilde{\mathbf{w}}_{i_B-1}^{'\Upsilon}$. However, both of these quantities can directly be related to weight-

error vector $\tilde{\mathbf{w}}_{i_B-1}$. By applying the random walk model from the LEM on page 422 to the expression for the *a priori* block-time error vector (9.2.9a) on page 425 we obtain

$$\begin{aligned}\mathbf{E}_{a,i} &= \mathbf{U}_i(\mathbf{w}^o_{i_B} - \mathbf{w}_{i_B-1}) \\ &= \mathbf{U}_i(\mathbf{w}^o_{i_B-1} + \boldsymbol{\theta}_{i_B} - \boldsymbol{\theta}_{i_B-1} - \mathbf{w}_{i_B-1}) \\ &= \mathbf{U}_i(\chi\mathbf{w}^o_{i_B-1} + \mathbf{q}_{i_B} - \mathbf{w}_{i_B-1} + (1-\chi)w^o) \\ &= \mathbf{U}_i\big(\tilde{\mathbf{w}}_{i_B-1} + \mathbf{q}_{i_B} - (1-\chi)(\mathbf{w}^o_{i_B-1} - w^o)\big) \\ &= \mathbf{U}_i\big(\tilde{\mathbf{w}}_{i_B-1} + \bar{\mathbf{q}}_{i_B} - (1-\chi)\mathbf{w}^o_{i_B-1}\big),\end{aligned} \tag{9.3.12}$$

where the quantity $\bar{\mathbf{q}}_{i_B} \in \mathbb{K}^{M\times 1}$ denotes the modified random-walk vector that is defined by

$$\bar{\mathbf{q}}_{i_B} = \mathbf{q}_{i_B} + (1-\chi)w^o. \tag{9.3.13}$$

Similarly, from straightforward manipulation of (9.3.9) and using the random walk model (9.2.1b) on page 422 we can relate the leakage-transformed modified weight-error vector to the optimal weight vector and the weight-error vector both evaluated at block-update time $i_B - 1$

$$\begin{aligned}\tilde{\mathbf{w}}'^{\Upsilon}_{i_B-1} &= \mathbf{w}^o_{i_B} - \boldsymbol{\Upsilon}_{i_\Upsilon}\mathbf{w}_{i_B-1} \\ &= \chi\mathbf{w}^o_{i_B-1} + \mathbf{q}_{i_B} - \boldsymbol{\Upsilon}_{i_\Upsilon}(\mathbf{w}^o_{i_B-1} - \tilde{\mathbf{w}}_{i_B-1}) + (1-\chi)w^o \\ &= (\chi\mathrm{I} - \boldsymbol{\Upsilon}_{i_\Upsilon})\mathbf{w}^o_{i_B-1} + \mathbf{q}_{i_B} + \boldsymbol{\Upsilon}_{i_\Upsilon}\tilde{\mathbf{w}}_{i_B-1} + (1-\chi)w^o \\ &= \boldsymbol{\Upsilon}^{\chi}_{i_\Upsilon}\mathbf{w}^o_{i_B-1} + \bar{\mathbf{q}}_{i_B} + \boldsymbol{\Upsilon}_{i_\Upsilon}\tilde{\mathbf{w}}_{i_B-1},\end{aligned} \tag{9.3.14}$$

where

random-walk-modified leakage-weight regularization matrix $\boldsymbol{\Upsilon}^{\chi}_{i_\Upsilon} \in \mathbb{K}^{M\times M}$ is defined by

$$\boldsymbol{\Upsilon}^{\chi}_{i_\Upsilon} \triangleq \chi\mathrm{I} - \boldsymbol{\Upsilon}_{i_\Upsilon} = -(1-\chi)\mathrm{I} + \boldsymbol{\mu}_{i_\mu}\big(\boldsymbol{\alpha}_{i_\alpha} + \boldsymbol{X}^*_i\boldsymbol{\gamma}_{i_\gamma\otimes K}\boldsymbol{X}_i + \boldsymbol{\Pi}_{i_\Pi}\big). \tag{9.3.15}$$

Finally, by insertion of (9.3.12) and (9.3.14) in (9.3.11) and using (9.3.10) the recursion expression becomes

$$\boxed{\begin{aligned}\tilde{\mathbf{w}}_{i_B} &= \boldsymbol{\Upsilon}^{\chi}_{i_\Upsilon}\mathbf{w}^o_{i_B-1} + \bar{\mathbf{q}}_{i_B} + \boldsymbol{\Upsilon}_{i_\Upsilon}\tilde{\mathbf{w}}_{i_B-1} \\ &\quad - \mathbf{P}_{i_B}\big(\tilde{\mathbf{w}}_{i_B-1} + \bar{\mathbf{q}}_{i_B} - (1-\chi)\mathbf{w}^o_{i_B-1}\big) - \mathbf{P}'_{i_B}\mathbf{V}_i - \boldsymbol{\mu}_{i_\mu}\breve{w}.\end{aligned}} \tag{9.3.16}$$

The recursions (9.3.16) and (9.3.11) will serve as starting points in transient analysis of the mean weight-error vector in subsection 9.A.1 on page 453 and the variance of the weight-error vector in subsection 9.A.2 - 9.A.3 on pages 458–460 respectively. It should be emphasized that (9.3.16) and (9.3.11) are general and have been obtained exclusively under the linear estimation model in Assumption 1.

9.3.1 Transient Analysis of MC-$\alpha\gamma\Pi\epsilon$-APA, Mean Relation

In order to obtain an expression for the time-evolution of the mean weight-error vector, that is, $\mathrm{E}\,\tilde{\mathbf{w}}_{i_B}$ we take the expectation on both sides of the recursion expression (9.3.16) on the

preceding page. The details can be found in subsection 9.A.1 on page 453 and the main result is the following expression

$$\boxed{\mathrm{E}\,\tilde{\mathbf{w}}_{i_B} = \mathrm{E}\,\mathbf{M}_{i_B}\,\mathrm{E}\,\tilde{\mathbf{w}}_{i_B-1} + \mathrm{E}\,\boldsymbol{\Upsilon}'_{i_\Upsilon} w^o - \mathrm{E}\,\boldsymbol{\mu}_{i_\mu}\breve{w},} \tag{9.3.17}$$

where the state-space mean transition matrix $\mathbf{M}_{i_B} \in \mathbb{K}^{M\times M}$ is defined by

$$\begin{aligned}\mathbf{M}_{i_B} &= \boldsymbol{\Upsilon}_{i_\Upsilon} - \mathbf{P}_{i_B}\\ &= \mathrm{I} - \boldsymbol{\mu}_{i_\mu}\big(\boldsymbol{\alpha}_{i_\alpha} + \boldsymbol{X}_i^*\boldsymbol{\gamma}_{i_\gamma\otimes K}\boldsymbol{X}_i + \boldsymbol{\Pi}_{i_\Pi} + \boldsymbol{\epsilon}_{i_\epsilon}^{-1}\mathbf{U}_i^*(W_{e\otimes K}^{-1} + \mathbf{U}_i\boldsymbol{\epsilon}_{i_\epsilon}^{-1}\mathbf{U}_i^*)^{-1}\mathbf{U}_i\big)\end{aligned} \tag{9.3.18}$$

and where the leakage-weight regularization matrix $\Upsilon'_{i_\Upsilon} \in \mathbb{K}^{M\times M}$ is determined from

$$\boldsymbol{\Upsilon}'_{i_\Upsilon} \triangleq \mathrm{I} - \boldsymbol{\Upsilon}_{i_\Upsilon} = \boldsymbol{\mu}_{i_\mu}\big(\boldsymbol{\alpha}_{i_\alpha} + \boldsymbol{X}_i^*\boldsymbol{\gamma}_{i_\gamma\otimes K}\boldsymbol{X}_i + \boldsymbol{\Pi}_{i_\Pi}\big). \tag{9.3.19}$$

For the derivation of (9.3.17) we have only made use of the linear estimation model in Assumption 1, independence Assumptions 5 on page 454 and independence Assumption 6 on page 455. The last two terms on the RHS of (9.3.17) that are identical to $\mathrm{E}\,\boldsymbol{\mu}_{i_\mu}\big(\boldsymbol{\alpha}_{i_\alpha} + \boldsymbol{X}_i^*\boldsymbol{\gamma}_{i_\gamma\otimes K}\boldsymbol{X}_i\big)w^o + \mathrm{E}\,\boldsymbol{\mu}_{i_\mu}\boldsymbol{\Pi}_{i_\Pi}(w^o - \bar{w})$ represent the joint bias error from leakage and weight vector regularization.

9.3.2 Transient Analysis of MC-$\alpha\gamma\Pi\epsilon$-APA, Weighted Energy Relation

By equating the weighted norm of both sides of the weight-error recursion (9.3.16), for some arbitrary weighting matrix $\Sigma \in \mathbb{K}^{M\times M}$ positive-definite (p.d.) (and therefore also Hermitian) we

obtain the following result

$$
\begin{aligned}
\|\tilde{\mathbf{w}}_{i_B}\|_{\Sigma}^2 = \|\tilde{\mathbf{w}}_{i_B-1}\|_{\mathbf{\Sigma}_{i_B}^{\Upsilon}}^2 &+ \|\bar{\mathbf{q}}_{i_B}\|_{\mathbf{\Sigma}_{i_B}^{q}}^2 + \|\mathbf{w}_{i_B-1}^{o}\|_{\mathbf{\Sigma}_{i_B}^{o}}^2 + \|\boldsymbol{\mu}_{i_\mu}\breve{w}\|_{\Sigma}^2 \\
&+ 2\Re\big\{\mathbf{w}_{i_B-1}^{o*}\mathbf{\Upsilon}_{i_\Upsilon}^{\chi *}\Sigma\mathbf{\Upsilon}_{i_\Upsilon}\tilde{\mathbf{w}}_{i_B-1}\big\} \\
&+ 2\Re\big\{\mathbf{w}_{i_B-1}^{o*}\mathbf{\Upsilon}_{i_\Upsilon}^{\chi *}\Sigma\bar{\mathbf{q}}_{i_B}\big\} \\
&+ 2\Re\big\{\bar{\mathbf{q}}_{i_B}^{*}\Sigma\mathbf{\Upsilon}_{i_\Upsilon}\tilde{\mathbf{w}}_{i_B-1}\big\} \\
&- 2\Re\Big\{\mathbf{w}_{i_B-1}^{o*}\mathbf{\Upsilon}_{i_\Upsilon}^{\chi *}\Sigma\mathbf{P}_{i_B}\big(\tilde{\mathbf{w}}_{i_B-1}+\bar{\mathbf{q}}_{i_B}\big)\Big\} \\
&- 2\Re\Big\{\bar{\mathbf{q}}_{i_B}^{*}\Sigma\mathbf{P}_{i_B}\big(\tilde{\mathbf{w}}_{i_B-1}-(1-\chi)\mathbf{w}_{i_B-1}^{o}\big)\Big\} \\
&- 2\Re\Big\{\tilde{\mathbf{w}}_{i_B-1}^{*}\mathbf{\Upsilon}_{i_\Upsilon}^{*}\Sigma\mathbf{P}_{i_B}\big(\bar{\mathbf{q}}_{i_B}-(1-\chi)\mathbf{w}_{i_B-1}^{o}\big)\Big\} \\
&- 2\Re\Big\{\big(\mathbf{w}_{i_B-1}^{o*}\mathbf{\Upsilon}_{i_\Upsilon}^{\chi *}+\bar{\mathbf{q}}_{i_B}^{*}+\tilde{\mathbf{w}}_{i_B-1}^{*}\mathbf{\Upsilon}_{i_\Upsilon}^{*}\big)\Sigma\boldsymbol{\mu}_{i_\mu}\breve{w}\Big\} \\
&+ 2\Re\Big\{(\tilde{\mathbf{w}}_{i_B-1}^{*}+\bar{\mathbf{q}}_{i_B}^{*}-(1-\chi^{*})\mathbf{w}_{i_B-1}^{o*})\mathbf{P}_{i_B}^{*}\Sigma\boldsymbol{\mu}_{i_\mu}\breve{w}\Big\} \\
&+ \tilde{\mathbf{w}}_{i_B-1}^{*}\mathbf{P}_{i_B}^{*}\Sigma\mathbf{P}_{i_B}\big(\bar{\mathbf{q}}_{i_B}-(1-\chi)\mathbf{w}_{i_B-1}^{o}\big) \\
&+ \bar{\mathbf{q}}_{i_B}^{*}\mathbf{P}_{i_B}^{*}\Sigma\mathbf{P}_{i_B}\big(\tilde{\mathbf{w}}_{i_B-1}-(1-\chi)\mathbf{w}_{i_B-1}^{o}\big) \\
&- (1-\chi^{*})\mathbf{w}_{i_B-1}^{o*}\mathbf{P}_{i_B}^{*}\Sigma\mathbf{P}_{i_B}\big(\tilde{\mathbf{w}}_{i_B-1}+\bar{\mathbf{q}}_{i_B}\big) \\
&+ \mathbf{V}_i^{*}\mathbf{A}_{i_B}^{\Sigma}\mathbf{V}_i \\
&- 2\Re\Big\{\mathbf{V}_i^{*}\mathbf{P}_{i_B}^{\prime *}\Sigma\Big(\mathbf{\Upsilon}_{i_\Upsilon}^{\chi}\mathbf{w}_{i_B-1}^{o}+\bar{\mathbf{q}}_{i_B}+\mathbf{\Upsilon}_{i_\Upsilon}\tilde{\mathbf{w}}_{i_B-1} \\
&\qquad -\mathbf{P}_{i_B}\big(\tilde{\mathbf{w}}_{i_B-1}+\bar{\mathbf{q}}_{i_B}-(1-\chi)\mathbf{w}_{i_B-1}^{o}\big)-\boldsymbol{\mu}_{i_\mu}\breve{w}\Big)\Big\},
\end{aligned}
\tag{9.3.20}
$$

where the *stochastic* weighting matrices $\mathbf{\Sigma}_{i_B}^{\Upsilon}, \mathbf{\Sigma}_{i_B}^{o}$ and $\mathbf{\Sigma}_{i_B}^{\bar{q}}$ are defined by

$$
\mathbf{\Sigma}_{i_B}^{\Upsilon} \triangleq \mathbf{\Upsilon}_{i_\Upsilon}^{*}\Sigma\mathbf{\Upsilon}_{i_\Upsilon} - \mathbf{\Upsilon}_{i_\Upsilon}^{*}\Sigma\mathbf{P}_{i_B} - \mathbf{P}_{i_B}^{*}\Sigma\mathbf{\Upsilon}_{i_\Upsilon} + \mathbf{P}_{i_B}^{*}\Sigma\mathbf{P}_{i_B} \tag{9.3.21a}
$$

$$
\begin{aligned}
\mathbf{\Sigma}_{i_B}^{o} \triangleq\ & (\chi\mathrm{I}-\mathbf{\Upsilon}_{i_\Upsilon}^{*})\Sigma\mathbf{\Upsilon}_{i_\Upsilon}^{\chi} + (1-\chi)(\chi\mathrm{I}-\mathbf{\Upsilon}_{i_\Upsilon}^{*})\Sigma\mathbf{P}_{i_B} + (1-\chi^{*})\mathbf{P}_{i_B}^{*}\Sigma\mathbf{\Upsilon}_{i_\Upsilon}^{\chi} \\
& + |1-\chi|^2\mathbf{P}_{i_B}^{*}\Sigma\mathbf{P}_{i_B}
\end{aligned}
\tag{9.3.21b}
$$

$$
\mathbf{\Sigma}_{i_B}^{\bar{q}} \triangleq \Sigma - \Sigma\mathbf{P}_{i_B} - \mathbf{P}_{i_B}^{*}\Sigma + \mathbf{P}_{i_B}^{*}\Sigma\mathbf{P}_{i_B}. \tag{9.3.21c}
$$

The detailed derivation can be found in subsection 9.A.2 on page 458. Comparing the recursion expression for the weighted norm of the weight-error vector $\|\tilde{\mathbf{w}}_{i_B}\|_{\Sigma}^2$ with similar results in [10] for the ϵ-APA we appreciate that many additional terms enter in Equation (9.3.20). Several factors contribute to this increase in complexity. Usually, the random-walk model is omitted from the transient analysis. In the presence analysis, however, we allowed a general random-walk model to model the non-stationarity of the system viz. (9.2.1b). If we instead had used the more simple random-walk where $\chi \equiv 1$ this would reduce the number of terms in the recursion expression (9.3.20) considerably.

Three of the terms that include a $\breve{w}$ factor are explicitly related to inclusion of the weight regularization in (9.3.1). Hence, by making the following assignments $\chi \leftarrow 1$ in (9.3.20) and

(9.3.13) and $\breve{w} \leftarrow 0$ in (9.3.20) we readily obtain

$$\begin{aligned}\|\tilde{\mathbf{w}}_{i_B}\|^2_{\Sigma} = \|\tilde{\mathbf{w}}_{i_B-1}\|^2_{\mathbf{\Sigma}^{\Upsilon}_{i_B}} + \|\mathbf{q}_{i_B}\|^2_{\mathbf{\Sigma}^{q}_{i_B}} + \|\mathbf{w}^{o}_{i_B-1}\|^2_{\mathbf{\Sigma}^{o}_{i_B}} \\ + 2\Re\Big\{\mathbf{w}^{o*}_{i_B-1}(\mathrm{I}-\mathbf{\Upsilon}^{*}_{i_\Upsilon})\Sigma\mathbf{M}_{i_B}\big(\tilde{\mathbf{w}}_{i_B-1}+\mathbf{q}_{i_B}\big)\Big\} \\ + 2\Re\big\{\mathbf{q}^{*}_{i_B}(\mathrm{I}-\mathbf{P}^{*}_{i_B})\Sigma\mathbf{M}_{i_B}\tilde{\mathbf{w}}_{i_B-1}\big\} \\ + \mathbf{V}^{*}_{i}\mathbf{A}^{\Sigma}_{i_B}\mathbf{V}_i \\ - 2\Re\Big\{\mathbf{V}^{*}_{i}\mathbf{P}^{'*}_{i_B}\Sigma\Big((\mathrm{I}-\mathbf{\Upsilon}_{i_\Upsilon})\mathbf{w}^{o}_{i_B-1}+(\mathrm{I}-\mathbf{P}_{i_B})\mathbf{q}_{i_B}+\mathbf{M}_{i_B}\tilde{\mathbf{w}}_{i_B-1}\Big)\Big\},\end{aligned} \tag{9.3.22}$$

where $\mathbf{\Sigma}^{o}_{i_B}$ now reduces to $(\mathrm{I}-\mathbf{\Upsilon}^{*}_{i_\Upsilon})\Sigma(\mathrm{I}-\mathbf{\Upsilon}_{i_\Upsilon})$.

By completely omitting the non-stationarity from the model, that is, $\boldsymbol{q}_{i_B} \leftarrow 0$ and $\mathbf{w}^{o}_{i_B-1} \leftarrow w^{o}$ will lead to further reduction of the complexity

$$\begin{aligned}\|\tilde{\mathbf{w}}_{i_B}\|^2_{\Sigma} = \|\tilde{\mathbf{w}}_{i_B-1}\|^2_{\mathbf{\Sigma}^{\Upsilon}_{i_B}} + \|w^{o}\|^2_{\mathbf{\Sigma}^{o}_{i_B}} + \mathbf{V}^{*}_{i}\mathbf{A}^{\Sigma}_{i_B}\mathbf{V}_i \\ + 2\Re\Big\{\mathbf{w}^{o*}_{i_B-1}(\mathrm{I}-\mathbf{\Upsilon}^{*}_{i_\Upsilon})\Sigma\mathbf{M}_{i_B}\tilde{\mathbf{w}}_{i_B-1}\Big\} \\ - 2\Re\Big\{\mathbf{V}^{*}_{i}\mathbf{P}^{'*}_{i_B}\Sigma\Big((\mathrm{I}-\mathbf{\Upsilon}_{i_\Upsilon})\mathbf{w}^{o}_{i_B-1}+\mathbf{M}_{i_B}\tilde{\mathbf{w}}_{i_B-1}\Big)\Big\}.\end{aligned} \tag{9.3.23}$$

Finally, by also omitting all leakage, that is, $\mathbf{\Upsilon}_{i_\Upsilon} \leftarrow \mathrm{I}$ then (9.3.23) simplifies to

$$\|\tilde{\mathbf{w}}_{i_B}\|^2_{\Sigma} = \|\tilde{\mathbf{w}}_{i_B-1}\|^2_{\mathbf{\Sigma}'_{i_B}} + \mathbf{V}^{*}_{i}\mathbf{A}^{\Sigma}_{i_B}\mathbf{V}_i - 2\Re\Big\{\mathbf{V}^{*}_{i}\mathbf{P}^{'*}_{i_B}\Sigma(\mathrm{I}-\mathbf{P}_{i_B})\tilde{\mathbf{w}}_{i_B-1}\Big\}, \tag{9.3.24}$$

where $\mathbf{\Sigma}'_{i_B} = \Sigma - \Sigma\mathbf{P}_{i_B} - \mathbf{P}^{*}_{i_B}\Sigma + \mathbf{P}^{*}_{i_B}\Sigma\mathbf{P}_{i_B}$. This expression coincides with a similar result in [10].

9.3.3 Transient Analysis of MC-$\alpha\gamma\Pi\epsilon$-APA, Weighted Variance Relation

In order to obtain an expression for the time-evolution of the expected weighted energy norm of the weight-error vector, that is, $\mathrm{E}\|\tilde{\mathbf{w}}_{i_B}\|^2_{\Sigma}$ for some choice of Σ we proceed by taking the expectation on both sides of (9.3.20). Following somewhat lengthy derivations found in subsection 9.A.3 on page 460 we obtain

$$\boxed{\begin{aligned}\mathrm{E}\|\tilde{\mathbf{w}}_{i_B}\|^2_{\Sigma} = \mathrm{E}\|\tilde{\mathbf{w}}_{i_B-1}\|^2_{\Sigma^{\Upsilon}_{i_B}} + \mathrm{Tr}\,\{Q\Sigma^{q}_{i_B}\} + \|w^{o}\|^2_{\Sigma^{w'^{o}}_{i_B}} + \|\breve{w}\|^2_{\Sigma^{\breve{w}}} \\ + 2\Re\langle w^{o*},\breve{w}\rangle_{\Sigma^{w^{o}\breve{w}}_{i_B}} - 2\Re\langle w^{o*},w^{0}\rangle_{\Sigma^{w^{o}w^{0}}_{i_B}} - 2\Re\langle\breve{w}^{*},w^{0}\rangle_{\Sigma^{\breve{w}w^{0}}_{i_B}} \\ + K\sigma^2_v\,\mathrm{Tr}\,\{\mathrm{E}\,\mathbf{P}^{'*}_{i_B}\Sigma\mathbf{P}'_{i_B}\}.\end{aligned}} \tag{9.3.25}$$

where the *deterministic* weighting matrices $\Sigma^{\Upsilon}_{i_B}, \Sigma^{w'^{o}}_{i_B}, \Sigma^{q}_{i_B}$ and $\Sigma^{\breve{w}}_{i_B}$ are defined by

$$\Sigma_{i_B}^{\Upsilon} \triangleq \mathrm{E}\,\boldsymbol{\Upsilon}_{i_\Upsilon}^{*}\Sigma\boldsymbol{\Upsilon}_{i_\Upsilon} - \mathrm{E}(\boldsymbol{\Upsilon}_{i_\Upsilon}^{*})\Sigma\,\mathrm{E}(\mathbf{P}_{i_B}) - \mathrm{E}(\mathbf{P}_{i_B}^{*})\Sigma\,\mathrm{E}(\boldsymbol{\Upsilon}_{i_\Upsilon}) + \mathrm{E}\,\mathbf{P}_{i_B}^{*}\Sigma\mathbf{P}_{i_B} \tag{9.3.26a}$$

$$\begin{aligned}\Sigma_{i_B}^{w'^{o}} &= \mathrm{E}\,\boldsymbol{\Upsilon}_{i_\Upsilon}^{\chi^*}\Sigma\boldsymbol{\Upsilon}_{i_\Upsilon}^{\chi} + (1-\chi)\,\mathrm{E}(\boldsymbol{\Upsilon}_{i_\Upsilon}^{\chi^*})\Sigma + (1-\chi^*)\Sigma\,\mathrm{E}(\boldsymbol{\Upsilon}_{i_\Upsilon}^{\chi}) + |1-\chi|^2(\Sigma + 2\,\mathrm{E}\,\mathbf{P}_{i_B}^{*}\Sigma\mathbf{P}_{i_B}) \\ &\quad + J_{i_B}C_{i_B-1}^{w^o} + C_{i_B-1}^{w^o*}J_{i_B}^{*}\end{aligned} \tag{9.3.26b}$$

and

$$\begin{aligned}\Sigma_{i_B}^{q} &= \Sigma - \Sigma\,\mathrm{E}\,\mathbf{P}_{i_B} - \mathrm{E}\,\mathbf{P}_{i_B}^{*}\Sigma + \mathrm{E}\,\mathbf{P}_{i_B}^{*}\Sigma\mathbf{P}_{i_B} \\ &\quad + \Theta_{i_B-1}\Big(\mathrm{E}\,\boldsymbol{\Upsilon}_{i_\Upsilon}^{\chi^*}\Sigma\boldsymbol{\Upsilon}_{i_\Upsilon}^{\chi} + (1-\chi)\,\mathrm{E}(\boldsymbol{\Upsilon}_{i_\Upsilon}^{\chi^*})\Sigma\,\mathrm{E}(\mathbf{P}_{i_B}) \\ &\qquad + (1-\chi^*)\,\mathrm{E}(\mathbf{P}_{i_B}^{*})\Sigma\,\mathrm{E}(\boldsymbol{\Upsilon}_{i_\Upsilon}^{\chi}) + |1-\chi|^2\,\mathrm{E}\,\mathbf{P}_{i_B}^{*}\Sigma\mathbf{P}_{i_B}\Big)\end{aligned} \tag{9.3.26c}$$

and

$$\Sigma_{i_B}^{\breve{w}} = \mathrm{E}(\boldsymbol{\mu}_{i_\mu}^{*}\Sigma\boldsymbol{\mu}_{i_\mu}) - K_{i_B}C_{i_B-1}^{\breve{w}} - C_{i_B-1}^{\breve{w}*}K_{i_B}^{*}. \tag{9.3.26d}$$

The cross-weighting matrix associated with the coupling between the mean optimal weight vector and the regularized weight vector $\Sigma_{i_B}^{w^o\breve{w}} \in \mathbb{K}^{M\times M}$, the mean optimal weight vector to initial weight vector coupling cross-weighting matrix $\Sigma_{i_B}^{w^o w^0} \in \mathbb{K}^{M\times M}$ and the cross-weighting matrix related to the coupling between the regularized weight vector and the initial weight vector $\Sigma_{i_B}^{\breve{w}w^0} \in \mathbb{K}^{M\times M}$ are defined by

$$\Sigma_{i_B}^{w^o\breve{w}} \triangleq -J_{i_B}C_{i_B-1}^{\breve{w}} + C_{i_B-1}^{w^o*}K_{i_B}^{*} + \mathrm{E}(\boldsymbol{\Upsilon}_{i_\Upsilon}^{*}\Sigma\boldsymbol{\mu}_{i_\mu}) - \Sigma\,\mathrm{E}(\boldsymbol{\mu}_{i_\mu}) \tag{9.3.27a}$$

$$\Sigma_{i_B}^{w^o w^0} \triangleq J_{i_B}C_{i_B}^{w^o,1} \tag{9.3.27b}$$

$$\Sigma_{i_B}^{\breve{w}w^0} \triangleq K_{i_B}C_{i_B-1}^{w^o,1} \tag{9.3.27c}$$

respectively and the auxiliary matrices J_{i_B} and K_{i_B} that enter (9.3.26b) (9.3.26d) and (9.3.27) are in turn defined by

$$J_{i_B} \triangleq \mathrm{E}\big(\boldsymbol{\Upsilon}_{i_\Upsilon}^{\chi^*}\Sigma\boldsymbol{\Upsilon}_{i_\Upsilon}\big) - \mathrm{E}(\boldsymbol{\Upsilon}_{i_\Upsilon}^{\chi^*})\Sigma\,\mathrm{E}(\mathbf{P}_{i_B}) + (1-\chi^*)\Sigma\,\mathrm{E}(\mathbf{M}_{i_B}) \tag{9.3.28a}$$

$$K_{i_B}^{*} \triangleq \mathrm{E}(\mathbf{P}_{i_B}^{*})\Sigma\,\mathrm{E}(\boldsymbol{\mu}_{i_\mu}) - \mathrm{E}(\boldsymbol{\Upsilon}_{i_\Upsilon}^{*}\Sigma\boldsymbol{\mu}_{i_\mu}). \tag{9.3.28b}$$

Finally, we let $C_{i_B}^{w^o}$ and $C_{i_B}^{\breve{w}}$ represent the time evolution matrix for the mean optimal weight vector w^o and time evolution matrix for the regularized weight vector $\breve{w}$ respectively. These quantities are determined by

$$C_{i_B}^{w^o} \triangleq \prod_{j=0}^{i_B} \mathrm{E}\,\mathbf{M}_j + \sum_{j=1}^{i_B} \left(\left[\prod_{j'=j}^{i_B} \mathrm{E}\,\mathbf{M}_{j'} \right] \mathrm{E}\,\boldsymbol{\Upsilon}'_{i_\Upsilon^{j-1}} \right) + \mathrm{E}\,\boldsymbol{\Upsilon}'_{i_\Upsilon^{i_B}} \tag{9.3.29a}$$

$$= C_{i_B}^{w^o,1} + C_{i_B}^{w^o,2} + C_{i_B}^{w^o,3} \tag{9.3.29b}$$

$$C_{i_B}^{\breve{w}} \triangleq \sum_{j=1}^{i_B} \left(\left[\prod_{j'=j}^{i_B} \mathrm{E}\,\mathbf{M}_{j'} \right] \mathrm{E}\,\boldsymbol{\mu}_{i_\mu^{j-1}} \right) + \mathrm{E}\,\boldsymbol{\mu}_{i_\mu^{i_B}} \tag{9.3.29c}$$

$$= C_{i_B}^{\breve{w},2} + C_{i_B}^{\breve{w},3}. \tag{9.3.29d}$$

For the derivation of (9.3.25) we have only made use of the linear estimation model in Assumption 1 and the four independence Assumption 5 - 8 on pages 454–461. Comparing the expression for the time-evolution of the expected weighted energy norm for the MC-$\alpha\gamma\Pi\epsilon$-APA with time-variant parameters in (9.3.25) with similar results in [10] for the ordinary ϵ-affine projection algorithm (ϵ-APA) we observe a considerable increase in complexity for the present analysis. Two reasons for this increase in complexity are due to the inclusion of leakage and weight regularization in the adaptive filter. Another reason is that the analysis conducted in this report uses a more advanced random-walk model and also allows a non-vanishing initial weight vector. Finally, the presence of time-variant parameters as opposed to constant parameters further increases the complexity.

The weighting matrix $\Sigma_{i_B}^{\Upsilon}$ is important for the stability analysis. Owing to the presence of $\boldsymbol{\Upsilon}_{i_\Upsilon}$ we appreciate that leakage and weight regularization do influence the stability of the filter.

It is well known that the covariance of $\mathbf{w}_{i_B}^o - w^o$ grows unbounded for the random-walk model in (9.2.1b) whenever the forgetting factor equals unity, that is, $\chi = 1$. But (9.3.25) and (9.3.26c) actually claim that the weight-error vector increases without bound from one iteration to the next. By examination of (9.3.26c) we appreciate that the term responsible for this divergence is $\Theta\,\mathrm{E}\,\boldsymbol{\Upsilon}_{i_\Upsilon}^{\chi^*}\Sigma\boldsymbol{\Upsilon}_{i_\Upsilon}^{\chi}$ as $\lim_{i_B\to\infty}\Theta = \frac{1}{1-|\chi|^2}$ and therefore $\lim_{i_B\to\infty}\lim_{|\chi|\to 1}\frac{1}{1-|\chi|^2}\,\mathrm{E}\,\boldsymbol{\Upsilon}_{i_\Upsilon}^{\chi^*}\Sigma\boldsymbol{\Upsilon}_{i_\Upsilon}^{\chi} = \infty$, that is, in "steady-state" the mean-square weight-error vector grows unbounded for such simple random walk model. This also explains why we explicitly enforced the requirement $0 \leq |\chi| < 1$ in (9.2.1b). From (9.3.15), however, we see that when leakage and weight regularization are omitted then $\boldsymbol{\Upsilon}_{i_\Upsilon}^{\chi^*} = 0$ and $\Sigma_{i_B}^{q}$ remains bounded. This phenomena might therefore be explained as follows. Although the adaptive filter (in principle) is capable of tracking such unlimited system variations then even small fractions of infinite large weights caused by leakage are themselves infinite large and will therefore lead to unboundedness if $\chi = 1$.

The propagation of the $\Sigma_{i_B}^{q}$ deviates substantially from other works where $\Sigma_{i_B}^{q} \equiv \Sigma$. Extensive analysis of the derivation carried out in subsection 9.A.3 reveals that two factors are responsible for this difference. In other works the presence of the random walk vector $\mathbf{q}$ is not included in $\mathbf{E}_{a,i}$ as it arguably should viz. (9.3.12). As a consequence the terms $-\Sigma\,\mathrm{E}\,\mathbf{P}_{i_B} - \mathrm{E}\,\mathbf{P}_{i_B}^*\Sigma + \mathrm{E}\,\mathbf{P}_{i_B}^*\Sigma\mathbf{P}_{i_B}$ that enter $\Sigma_{i_B}^{q}$ are omitted. From (9.3.10c), however, we see that the first two terms vary linearly with the step-size and the third term varies quadratically with the step-size. Hence, except for large values of $\boldsymbol{\mu}$ the effect of erroneously omitting $\mathbf{q}_{i_B}$ in this place will usually be small. Secondly, by using the more advanced random-walk model with $\chi < 1$ lead to the presence of the term starting with $\Theta_{i_B-1}(\,\cdot\,)$ and this term is related to the propagation of $\mathrm{E}\|\mathbf{w}_{i_B-1}^o\|_{\Sigma_{i_B}^o}^2$ itself.

The inclusion of weight regularization in (9.3.1) leads to the presence of the terms $\|\breve{w}\|_{\Sigma^{\breve{w}}}^2$, $2\Re\langle w^{o*}, \breve{w}\rangle_{\Sigma_{i_B}^{w^o\breve{w}}}$ and $2\Re\langle \breve{w}^*, w^0\rangle_{K_{i_B}C_{i_B-1}^{w^o,1}}$ in (9.3.25).

The terms $2\Re\langle w^{o*}, w^0\rangle_{J_{i_B} C_{i_B}^{w^o,1}}$ and $2\Re\langle \breve{w}*, w^0\rangle_{K_{i_B} C_{i_B-1}^{w^o,1}}$ in (9.3.25) are related to the use of a non-vanishing initial weight vector, that is, $\mathbf{w}_{-1} = w^0 \neq 0$. In many performance analysis $\mathbf{w}_{-1} = w^0$ which means that $\tilde{\mathbf{w}}_{-1} = w^o$ and those two aforementioned terms will be absent.

Now, by assuming a stationary model, a vanishing initial weight vector and by omitting weight regularization, that is, by making the following assignments $Q \leftarrow 0$, $\chi \leftarrow 1$, $\mathbf{w}_{-1} = w^0 = 0$ and $\breve{w} \leftarrow 0$ in (9.3.25) we readily obtain

$$\boxed{\mathrm{E}\|\tilde{\mathbf{w}}_{i_B}\|_{\Sigma}^2 = \mathrm{E}\|\tilde{\mathbf{w}}_{i_B-1}\|_{\Sigma_{i_B}^{\Upsilon}}^2 + \|w^o\|_{\Sigma_{i_B}^{w'^o}}^2 + K\sigma_v^2 \operatorname{Tr}\{\mathrm{E}\,\mathbf{P}_{i_B}^{'*}\Sigma\mathbf{P}_{i_B}'\},} \tag{9.3.30}$$

where $\Sigma_{i_B}^{w'^o} = \mathrm{E}\,\boldsymbol{\Upsilon}_{i_\Upsilon}^{'*}\Sigma\boldsymbol{\Upsilon}_{i_\Upsilon}' + J_{i_B}C_{i_B-1}^{w^o} + C_{i_B-1}^{w^o*}J_{i_B}^*$ and $J_{i_B} = \mathrm{E}\big(\boldsymbol{\Upsilon}_{i_\Upsilon}^{'*}\Sigma\boldsymbol{\Upsilon}_{i_\Upsilon}\big) - \mathrm{E}(\boldsymbol{\Upsilon}_{i_\Upsilon}^{'*})\Sigma\,\mathrm{E}(\mathbf{P}_{i_B})$. Finally, by also omitting all leakage, that is, $\boldsymbol{\Upsilon}_{i_\Upsilon} \leftarrow \mathrm{I}$ then the second term on the RHS of (9.3.30) disappears, that is,

$$\boxed{\mathrm{E}\|\tilde{\mathbf{w}}_{i_B}\|_{\Sigma}^2 = \mathrm{E}\|\tilde{\mathbf{w}}_{i_B-1}\|_{\Sigma_{i_B}^{\Upsilon}}^2 + K\sigma_v^2 \operatorname{Tr}\{\mathrm{E}\,\mathbf{P}_{i_B}^{'*}\Sigma\mathbf{P}_{i_B}'\},} \tag{9.3.31}$$

where $\Sigma_{i_B}^{\Upsilon} = \Sigma - \Sigma\,\mathrm{E}(\mathbf{P}_{i_B}) - \mathrm{E}(\mathbf{P}_{i_B}^*)\Sigma + \mathrm{E}\,\mathbf{P}_{i_B}^*\Sigma\mathbf{P}_{i_B}$.

This expression coincides with a similar result in [10].

9.4 Stability Analysis of MC-$\alpha\gamma\Pi\epsilon$-APA

We are now in a position to use the results from the transient analysis of the MC-$\alpha\gamma\Pi\epsilon$-APA adaptive filter conducted in the previous section and establish stability criterions for the filter.

9.4.1 Stability Analysis of MC-$\alpha\gamma\Pi\epsilon$-APA Time-Variant State Transition Matrix

The presence of a time-variant mean weight-error vector state transition matrix $\mathbf{M}_{i_B}$ complicates the analysis considerably. In general owing to the dynamics of the state transition matrix a system may be unstable even though every time-invariant system $\mathrm{E}\,\tilde{\mathbf{w}}_{i_B} = \mathrm{E}\,\mathbf{M}_\tau\tilde{\mathbf{w}}_{i_B-1} + \mathrm{E}\,\boldsymbol{\Upsilon}_\tau' w^o - \mathrm{E}\,\boldsymbol{\mu}_\tau\breve{w}$ frozen at time τ is asymptotically stable. It is also possible that every frozen system is unstable yet (9.3.17) is stable. It suffice here to say that *exponential stability* for time-variant state-space systems can be assessed by considering the mean weight-error vector state-space evolution matrix $\Phi_M(t, t_0) : \mathbb{K}^{M\times M} \to \mathbb{K}^{M\times M}$, that in the stochastic case is defined by

$$\Phi_M(t, t_0) \triangleq \mathrm{E}\,\mathbf{M}_t\mathbf{M}_{t-1}\ldots\mathbf{M}_{t_0}, \quad t > t_0 \tag{9.4.1}$$

and the associated upper Lyapunov exponent $\bar{\alpha}(\Phi_M) \in \mathbb{R}_+$, defined by

$$\bar{\alpha}(\Phi_M) = \inf\big\{\omega \in \mathbb{R}; \exists M_\omega > 0 \forall t \geq t_0 : \|\Phi(t, t_0)\| \leq M_\omega \mathrm{e}^{\omega(t-t_0)}\big\}. \tag{9.4.2}$$

Then stability is guaranteed if and only if the upper Lyapunov exponent is strictly negative, that

is,

$$\bar{\alpha}(\Phi) < 0. \tag{9.4.3}$$

In practice, the stability criteria (9.4.3), however, is of limited use as the step-size matrix enters the evolution matrix $\Phi_M(t, t_0)$ in factorized form. It therefore exceedingly difficult to establish criterions for the time-evolution of $\boldsymbol{\mu}_{i_\mu}$ that guarantee stability. The stability analysis will therefore in the subsequent stability analysis be very dependent on the specific mechanisms that is used to regularize the step-size parameter. We will therefore in the subsequent stability analysis exclusively consider the MC-$\alpha\gamma\Pi\epsilon$-APA with constant parameters or at least with slowly varying parameters in accordance with Assumption 5 - 8.

9.4.2 Stability Analysis of MC-$\alpha\gamma\Pi\epsilon$-APA, Slowly Varying State Transition Matrix

We will next make the dependence on the step-size matrix $\boldsymbol{\mu}_{i_\mu}$ explicit by reexpressing (9.3.18) as

$$\mathbf{M}_{i_B} \triangleq \mathrm{I} - \boldsymbol{\mu}_{i_\mu} \mathbf{L}_{i_B}, \tag{9.4.4}$$

where the auxiliary matrix $\mathbf{L}_{i_B} \in \mathbb{K}^{M\times M}$, in turn is defined by

$$\mathbf{L}_{i_B} \triangleq \boldsymbol{\alpha}_{i_\alpha} + \boldsymbol{X}_i^* \boldsymbol{\gamma}_{i_\gamma \otimes K} \boldsymbol{X}_i + \boldsymbol{\Pi}_{i_\Pi} + \boldsymbol{\epsilon}_{i_\epsilon}^{-1} \mathbf{U}_i^* (W_{e\otimes K}^{-1} + \mathbf{U}_i \boldsymbol{\epsilon}_{i_\epsilon}^{-1} \mathbf{U}_i^*)^{-1} \mathbf{U}_i. \tag{9.4.5}$$

We may then express the requirement on stability in the mean of the MC-$\alpha\gamma\Pi\epsilon$-APA filter as [4, Ch. 3]

$$\forall i_B, i_\mu \geq -1: \quad \sigma(\mathrm{E}\, \boldsymbol{\mu}_{i_\mu} \mathbf{L}_{i_B}) \subset \mathbb{D}_{(1,0)}, \tag{9.4.6}$$

where $\sigma(A) \in \mathbb{C}^{n\times n}$ denotes the spectrum of A, that is, the set of eigenvalues of A that in turn are the roots of the characteristic polynomial $\chi_A(s)$ defined by

$$\chi_A(s) = \det(sI_n - A) \quad \text{and} \quad \sigma(A) = \{\lambda \in \mathbb{C}; \chi_A(\lambda) = 0\}. \tag{9.4.7}$$

By the notion $\mathbb{D}_{(1,0)}$ we refer to the *unit disc* with origo in $(1, 0)$ in the complex z-plane.

As discussed above, the requirement for mean-square stability may or may not be *sufficient* in the general time-variant case in the sense that we may actually "sometime" violate (9.4.6) by, e.g., allowing larger step-sizes than predicted by (9.4.6) without the MC-$\alpha\gamma\Pi\epsilon$-APA filter becoming unstable. However, such analysis is outside the scope of this presentation. It suffice to remark that in practical use of a time-variant step-size matrix the matrix entities attain their largest values when the error is numerically large and their values decrease numerically during an initial transient phase where also the magnitude of the error decreases. This approach is used to ensure a trade-off between tracking capability and the excess-mean-square error (EMSE). Moreover, the step-size entities are usually bounded from below by zero. Therefore, for practical purposes (9.4.6) is considered a *sufficient* condition for time-variant parameters, but also a *necessary* condition, that is, the MC-$\alpha\gamma\Pi\epsilon$-APA filter is stable in the mean-square *if and only if* at all time

$\sigma(\mathrm{E}\,\boldsymbol{\mu}_{i_\mu}\mathbf{L}_{i_B}) \subset \mathbb{D}_{(1,0)}$ for time-invariant parameters. A formal proof of this claim, however, remains to be made.

Unfortunately, (9.4.6) provides no direct way to obtain a usable step-size matrix as $\boldsymbol{\mu}_{i_\mu}$ only enters implicitly in the inequality. It should be remarked that in the derivation of the mean-square stability criteria (9.4.6) no assumption on the parameters matrices $\boldsymbol{\alpha}_{i_\alpha}, \boldsymbol{\gamma}_{i_\gamma}, \boldsymbol{\epsilon}_{i_\epsilon}$ and $\boldsymbol{\Pi}_{i_\Pi}$ as regards if they are real-valued or complex-valued, Hermitian matrices and positive-semidefinite matrices etc. have been made. However, in order to proceed we will make the following assumption on both $\boldsymbol{\mu}_{i_\mu}$ and $\mathbf{L}_{i_B}$.

Assumption 3 (Positive-definite matrices $\boldsymbol{\mu}_{i_\mu}, \mathbf{L}_{i_B}$)**.** Both the step-size matrix $\boldsymbol{\mu}_{i_\mu}$ and the auxiliary matrix $\mathbf{L}_{i_B}$ are at all time positive-definite matrices, that is,

$$\forall i_B, i_\mu \geq -1: \quad \boldsymbol{\mu}_{i_\mu} \succ 0 \quad \text{and} \quad \mathbf{L}_{i_B} \succ 0. \tag{9.4.8}$$

Now from Proposition 9.1 (9.1.6) and (9.4.5) we find that a *sufficient* conditions for L_{i_B} to be p.s.d. is that one term in (9.4.5) is p.d. while the other three terms are p.s.d. The second term on the RHS of (9.4.5), that is, $\boldsymbol{X}_i^* \boldsymbol{\gamma}_{i_\gamma \otimes K} \boldsymbol{X}_i$ can provided that $\boldsymbol{\gamma}_{i_\gamma \otimes K} \succeq 0$ according to (9.1.7) for some matrix $D \in \mathbb{K}^{M\times M}$ be expressed as $\boldsymbol{X}_i^* D^* D \boldsymbol{X}_i = (D\boldsymbol{X}_i)^*(D\boldsymbol{X}_i)$, which is always p.s.d.. Considering the last term in (9.4.5), that is, $\boldsymbol{\epsilon}_{i_\epsilon}^{-1}\mathbf{U}_i^*(W_{e\otimes K}^{-1} + \mathbf{U}_i\boldsymbol{\epsilon}_{i_\epsilon}^{-1}\mathbf{U}_i^*)^{-1}\mathbf{U}_i$ it should that recalled that this term is identical to $(\boldsymbol{\epsilon}_{i_\epsilon} + \mathbf{U}_i^* W_{e\otimes K}\mathbf{U}_i)^{-1}\mathbf{U}_i^* W_{e\otimes K}\mathbf{U}_i$ (refer to subsection 8.B.2). The product of two p.s.d. matrices, e.g., A and B is itself p.s.d. *if and only if* A and B commute. Obviously, $(\boldsymbol{\epsilon}_{i_\epsilon} + \mathbf{U}_i^* W_{e\otimes K}\mathbf{U}_i)^{-1}$ and $\mathbf{U}_i^* W_{e\otimes K}\mathbf{U}_i$ do not commute. However, as the entries in $\boldsymbol{\epsilon}_{i_\epsilon}$ usually are small the following approximation will hold $(\boldsymbol{\epsilon}_{i_\epsilon} + \mathbf{U}_i^* W_{e\otimes K}\mathbf{U}_i)^{-1}\mathbf{U}_i^* W_{e\otimes K}\mathbf{U}_i = \mathrm{I} - (\boldsymbol{\epsilon}_{i_\epsilon} + \mathbf{U}_i^* W_{e\otimes K}\mathbf{U}_i)^{-1}\boldsymbol{\epsilon}_{i_\epsilon} \approx \mathrm{I} \succ 0$.

Assumption 3 then holds *if* the following conditions are satisfied.

① At all time the MC-$\alpha\gamma\Pi\epsilon$-APA matrix parameters are p.s.d. and the numerical regularization matrix is "small", that is,

$$\forall i_\alpha, i_\gamma, i_\Pi \geq -1: \quad \boldsymbol{\alpha}_{i_\alpha} \succeq 0, \quad \boldsymbol{\gamma}_{i_\gamma} \succeq 0, \quad \text{and} \quad \boldsymbol{\Pi}_{i_\Pi} \succeq 0 \tag{9.4.9a}$$

and

$$\forall i_\epsilon \geq -1: 0 \precapprox \boldsymbol{\epsilon}_{i_\epsilon} \prec \mathbf{U}_i^* W_{e\otimes K}\mathbf{U}_i. \tag{9.4.9b}$$

We may then use Proposition 9.1 (9.1.5) and establish the following *sufficient* constraints on the step-size matrix

$$\forall i_B, i_\mu \geq -1, j \in \underline{M}: 0 < \lambda_j(\mathrm{E}\,\boldsymbol{\mu}_{i_\mu}) < \frac{2}{\lambda_{\max}(\mathrm{E}\,\mathbf{L}_{i_B})}. \tag{9.4.10}$$

The requirement on positive-definiteness (as opposed to positive-semidefiniteness) for matrices $\mathrm{E}\,\boldsymbol{\mu}_{i_\mu}$ and $\mathrm{E}\,\mathbf{L}_{i_B}$ ensures that $0 < \lambda_j(\mathrm{E}\,\boldsymbol{\mu}_{i_\mu})$ and that $0 < \lambda_j(\mathrm{E}\,\mathbf{L}_{i_B}), j \in \underline{M}$. In subsection 9.4.3 we will also make explicit use of the existence of the matrix inverse for $\mathrm{E}\,\boldsymbol{\mu}_{i_\mu}$ and $\mathrm{E}\,\mathbf{L}_{i_B}$.

Furthermore, we may enforce the following mild assumption.

Assumption 4 (Diagonal matrix $\boldsymbol{\mu}_{i_\mu}$)**.** The step-size matrix $\boldsymbol{\mu}_{i_\mu}$ is at all time a diagonal matrix, that is,

$$\boldsymbol{\mu}_{i_\mu} = \mathrm{diag}\,\{\boldsymbol{\mu}_{11,i_\mu}, \boldsymbol{\mu}_{22,i_\mu}, \ldots, \boldsymbol{\mu}_{MM,i_\mu}\} = \mathrm{diag}\,\{\boldsymbol{\mu}_{1,i_\mu}, \boldsymbol{\mu}_{2,i_\mu}, \ldots, \boldsymbol{\mu}_{M,i_\mu}\}. \tag{9.4.11}$$

Then the eigenvalues and the diagonal elements coincide and the requirement on mean-square stability reduces to the following explicit double inequality for $\boldsymbol{\mu}_{j,i_\mu}$

$$\forall i_B, i_\mu \geq -1, j \in \underline{M} : 0 < \mathrm{E}\,\boldsymbol{\mu}_{j,i_\mu} < \frac{2}{\lambda_{\max}(\mathrm{E}\,\mathbf{L}_{i_B})}. \tag{9.4.12}$$

Finally, a scalar-valued step-size parameter $\boldsymbol{\mu}(i_\mu)$ is bounded according to

$$\forall i_B, i_\mu \geq -1 : \quad 0 < \mathrm{E}\,\boldsymbol{\mu}(i_\mu) < \frac{2}{\lambda_{\max}(\mathrm{E}\,\mathbf{L}_{i_B})}. \tag{9.4.13}$$

It should be emphasized that while (9.4.13) establishes *necessary* and *sufficient* conditions for stability both (9.4.10) and (9.4.73b) establish only *sufficient* constraints. That is, for a matrix-valued step-size parameter we may actually increase some of the entries without causing instability.

9.4.3 Stability Analysis of MC-$\alpha\gamma\Pi\epsilon$-APA, State Space Description

Unlike the recursion (9.3.17) for the mean weight-error vector the similar recursion for the propagation of the mean-square weight-error vector is not on state-space form. The next step is therefore to derive a state-space model that characterizes the transient behavior of the MC-$\alpha\gamma\Pi\epsilon$-APA adaptive filter. We do this by following the approach in [1] and appeal to the $\mathrm{vec}\{\cdot\}$ notation defined in Definition 9.1 (9.1.1) and where, e.g., $\sigma = \mathrm{vec}\{\Sigma\} \Leftrightarrow \mathrm{vec}^{-1}\{\sigma\} = \Sigma$ and $\sigma_{i_B}^{\Upsilon} = \mathrm{vec}\{\Sigma_{i_B}^{\Upsilon}\} \Leftrightarrow \mathrm{vec}^{-1}\{\sigma_{i_B}^{\Upsilon}\} = \Sigma_{i_B}^{\Upsilon}$. The aim is to cast the recursive expression (9.3.20) into an equivalent linear state-space formulation for which stability criterias are well established. Then by applying the $\mathrm{vec}\{\cdot\}$ operation the weighting matrix $\Sigma_{i_B}^{\Upsilon}$ will be linked to the mean-square weight-error vector state transition matrix $F_{i_B} \in \mathbb{K}^{M^2\times M^2}$ [5] as $\sigma_{i_B}^{\Upsilon} = \mathrm{vec}\{\Sigma_{i_B}^{\Upsilon}\} = F_{i_B}\sigma$.

In the study of mean-square stability of adaptive filters with a scalar-valued step-size parameter the state transition matrix F is often expressed in the form $F = \mathrm{I}_M - \mu A + \mu^2 B$ with $A \succ 0, B \succeq 0, \mu > 0$. The purpose of this section is to extent the results of [1] and establish conditions for matrix-valued step-size matrices in terms of $\{A, B\}$ that ensure mean-square stability. In such case we express F instead by $F = \mathrm{I}_M - A + B$ where the matrices A and B implicitly contain the step-size matrix in first order and second order respectively with $A \succ 0, B \succeq 0$. Stability is guaranteed *if and only if* $\sigma(F) \subset \mathbb{D}$. Now as A and B are p.d. and p.s.d. respectively the eigenvalues of F will necessarily be real and the stability requirement is then $-1 < \lambda(F) < 1$. We will address the second equality first, that is, $\lambda(F) < 1$. Following a procedure similar to [9, Ch. 9] we readily establish the following requirement

$$\lambda_{\max}(A_{i_B}^{-1} B_{i_B}) < 1. \tag{9.4.14}$$

Hence, in the study of mean-square stability of the adaptive filter we want to establish conditions for the step-size matrix $\boldsymbol{\mu}_{i_\mu}$ that guarantee that the spectrum at all time is strictly inside the unit circle, that is, $\sigma(F_{i_B}) \subset \mathbb{D}, i_B \geq -1$. The approach in [1] where F_{i_B} is time-invariant and where μ attains a fixed scalar value is to establish an expression for F in the form $F = \mathrm{I} - \mu A + \mu^2 B$. The presence of time-variant and matrix-valued parameters in the MC-$\alpha\gamma\Pi\epsilon$-APA scheme complicates the analysis somewhat.

In order to bring $\Sigma_{i_B}^{\Upsilon}$ on appropriate form, we first express the weight-error vector weighting matrix $\Sigma_{i_B}^{\Upsilon}$ in terms of Υ'_{i_Υ} instead of Υ_{i_Υ} using (9.3.19).

$$\begin{aligned}
\Sigma_{i_B}^{\Upsilon} &= \mathrm{E}\,\boldsymbol{\Upsilon}_{i_\Upsilon}^{*}\Sigma\boldsymbol{\Upsilon}_{i_\Upsilon} - \mathrm{E}(\boldsymbol{\Upsilon}_{i_\Upsilon}^{*})\Sigma\,\mathrm{E}(\mathbf{P}_{i_B}) - \mathrm{E}(\mathbf{P}_{i_B}^{*})\Sigma\,\mathrm{E}(\boldsymbol{\Upsilon}_{i_\Upsilon}) + \mathrm{E}\,\mathbf{P}_{i_B}^{*}\Sigma\mathbf{P}_{i_B} \\
&= \mathrm{E}\big((\mathrm{I}_M - \boldsymbol{\Upsilon}_{i_\Upsilon}^{'*})\Sigma(\mathrm{I}_M - \boldsymbol{\Upsilon}'_{i_\Upsilon})\big) - \mathrm{E}(\mathrm{I}_M - \boldsymbol{\Upsilon}_{i_\Upsilon}^{'*})\Sigma\,\mathrm{E}(\mathbf{P}_{i_B}) - \mathrm{E}(\mathbf{P}_{i_B}^{*})\Sigma\,\mathrm{E}(\mathrm{I}_M - \boldsymbol{\Upsilon}'_{i_\Upsilon}) + \mathrm{E}\,\mathbf{P}_{i_B}^{*}\Sigma\mathbf{P}_{i_B} \\
&= \Sigma - \mathrm{E}\,\boldsymbol{\Upsilon}_{i_\Upsilon}^{'*}\Sigma - \Sigma\,\mathrm{E}\,\boldsymbol{\Upsilon}'_{i_\Upsilon} + \mathrm{E}\,\boldsymbol{\Upsilon}_{i_\Upsilon}^{'*}\Sigma\boldsymbol{\Upsilon}'_{i_\Upsilon} \\
&\quad - \Sigma\,\mathrm{E}(\mathbf{P}_{i_B}) + \mathrm{E}(\boldsymbol{\Upsilon}_{i_\Upsilon}^{'*})\Sigma\,\mathrm{E}(\mathbf{P}_{i_B}) - \mathrm{E}(\mathbf{P}_{i_B}^{*})\Sigma + \mathrm{E}(\mathbf{P}_{i_B}^{*})\Sigma\,\mathrm{E}(\boldsymbol{\Upsilon}'_{i_\Upsilon}) + \mathrm{E}\,\mathbf{P}_{i_B}^{*}\Sigma\mathbf{P}_{i_B}.
\end{aligned} \tag{9.4.15}$$

Therefore, by applying Proposition 9.5 (9.1.14) to (9.4.15) we obtain

$$\begin{aligned}
\sigma_{i_B}^{\Upsilon} &= \Big[\mathrm{I}_{M^2} - \mathrm{I}_M \otimes \mathrm{E}\,\boldsymbol{\Upsilon}_{i_\Upsilon}^{'*} - \mathrm{E}\,\boldsymbol{\Upsilon}_{i_\Upsilon}^{'\top} \otimes \mathrm{I}_M + \mathrm{E}\,\boldsymbol{\Upsilon}_{i_\Upsilon}^{'\top} \otimes \boldsymbol{\Upsilon}_{i_\Upsilon}^{'*} - \mathrm{E}\,\mathbf{P}_{i_B}^{\top} \otimes \mathrm{I}_M \\
&\quad + E(\mathbf{P}_{i_B}^{\top}) \otimes \mathrm{E}(\boldsymbol{\Upsilon}_{i_\Upsilon}^{'*}) - \mathrm{I}_M \otimes \mathrm{E}\,\mathbf{P}_{i_B}^{*} + \mathrm{E}(\boldsymbol{\Upsilon}_{i_\Upsilon}^{'\top}) \otimes \mathrm{E}(\mathbf{P}_{i_B}^{*}) + \mathrm{E}\,\mathbf{P}_{i_B}^{\top} \otimes \mathbf{P}_{i_B}^{*}\Big]\sigma \\
&= F_{i_B}\sigma.
\end{aligned} \tag{9.4.16}$$

Accordingly, we may bring F_{i_B} on the desired form

$$F_{i_B} = \mathrm{I}_M - A_{i_B} + B_{i_B}, \tag{9.4.17}$$

where $A_{i_B}, B_{i_B} \in \mathbb{K}^{M^2\times M^2}$ represent two auxiliary matrices that by collecting terms of first-order and second-order in the step-size matrix $\boldsymbol{\mu}_{i_\mu}$ can identified as

$$\begin{aligned}
A_{i_B} &= \mathrm{I}_M \otimes \mathrm{E}\,\boldsymbol{\Upsilon}_{i_\Upsilon}^{'*} + \mathrm{E}\,\boldsymbol{\Upsilon}_{i_\Upsilon}^{'\top} \otimes \mathrm{I}_M + \mathrm{E}\,\mathbf{P}_{i_B}^{\top} \otimes \mathrm{I}_M + \mathrm{I}_M \otimes \mathrm{E}\,\mathbf{P}_{i_B}^{*} \\
&= \mathrm{I}_M \otimes (\mathrm{E}\,\boldsymbol{\mu}_{i_\mu}\mathbf{L}_{i_B})^{*} + (\mathrm{E}\,\boldsymbol{\mu}_{i_\mu}\mathbf{L}_{i_B})^{\top} \otimes \mathrm{I}_M
\end{aligned} \tag{9.4.18a}$$

$$\begin{aligned}
B_{i_B} &= \mathrm{E}\,\boldsymbol{\Upsilon}_{i_\Upsilon}^{'\top} \otimes \boldsymbol{\Upsilon}_{i_\Upsilon}^{'*} + \mathrm{E}(\mathbf{P}_{i_B}^{\top}) \otimes \mathrm{E}(\boldsymbol{\Upsilon}_{i_\Upsilon}^{'*}) + \mathrm{E}(\boldsymbol{\Upsilon}_{i_\Upsilon}^{'\top}) \otimes \mathrm{E}(\mathbf{P}_{i_B}^{*}) + \mathrm{E}\,\mathbf{P}_{i_B}^{\top} \otimes \mathbf{P}_{i_B}^{*} \\
&= \mathrm{E}\big[(\boldsymbol{\Upsilon}'_{i_\Upsilon} + \mathbf{P}_{i_B})^{\top} \otimes (\boldsymbol{\Upsilon}'_{i_\Upsilon} + \mathbf{P}_{i_B})^{*}\big] \\
&= \mathrm{E}\big[(\boldsymbol{\mu}_{i_\mu}\mathbf{L}_{i_B})^{\top} \otimes (\boldsymbol{\mu}_{i_\mu}\mathbf{L}_{i_B})^{*}\big] \\
&= \mathrm{E}\big[(\mathbf{L}_{i_B}^{\top}\boldsymbol{\mu}_{i_\mu}^{\top}) \otimes (\mathbf{L}_{i_B}^{*}\boldsymbol{\mu}_{i_\mu}^{*})\big]
\end{aligned} \tag{9.4.18b}$$

respectively, where we have used Proposition 9.4 (9.1.12a) and where $\mathbf{L}_{i_B}$ was introduced in (9.4.5).

Then assuming independence of $\mathbf{L}$ and $\boldsymbol{\mu}$ in accordance with Assumption 5 - 8 in the subsequent stability analysis and by using (9.1.13d) we obtain

$$A_{i_B} = \mathrm{I}_M \otimes \big(\mathrm{E}(\mathbf{L}_{i_B}^{*})\,\mathrm{E}(\boldsymbol{\mu}_{i_\mu}^{*})\big) + \big(\mathrm{E}(\mathbf{L}_{i_B}^{\top})\,\mathrm{E}(\boldsymbol{\mu}_{i_\mu}^{\top})\big) \otimes \mathrm{I}_M \tag{9.4.19a}$$

$$B_{i_B} = \mathrm{E}(\mathbf{L}_{i_B}^{\top} \otimes \mathbf{L}_{i_B}^{*})\,\mathrm{E}(\boldsymbol{\mu}_{i_\mu}^{\top} \otimes \boldsymbol{\mu}_{i_\mu}^{*}). \tag{9.4.19b}$$

Applying Assumption 3 to (9.4.19) gives

$$A_{i_B} = \mathrm{I}_M \otimes \big(\mathrm{E}(\mathbf{L}_{i_B})\,\mathrm{E}(\boldsymbol{\mu}_{i_\mu})\big) + \big(\mathrm{E}(\bar{\mathbf{L}}_{i_B})\,\mathrm{E}(\bar{\boldsymbol{\mu}}_{i_\mu})\big) \otimes \mathrm{I}_M \tag{9.4.20a}$$

$$B_{i_B} = \mathrm{E}(\bar{\mathbf{L}}_{i_B} \otimes \mathbf{L}_{i_B})\,\mathrm{E}(\bar{\boldsymbol{\mu}}_{i_\mu} \otimes \boldsymbol{\mu}_{i_\mu}). \tag{9.4.20b}$$

Assumption 3 ensures existence of the matrix inverse for $\mathrm{E}\,\boldsymbol{\mu}_{i_\mu}$ and $\mathrm{E}\,\mathbf{L}_{i_B}$ and by Proposition 9.4 (9.1.13e) the existence of the inverse of A_{i_B}

$$A_{i_B}^{-1} = \big[\mathrm{I}_M \otimes \big(\mathrm{E}(\mathbf{L}_{i_B})\,\mathrm{E}(\boldsymbol{\mu}_{i_\mu})\big) + \big(\mathrm{E}(\bar{\mathbf{L}}_{i_B})\,\mathrm{E}(\bar{\boldsymbol{\mu}}_{i_\mu})\big) \otimes \mathrm{I}_M\big]^{-1}. \tag{9.4.21}$$

Then by combining (9.4.20b) and (9.4.21) gives

$$A_{i_B}^{-1}B_{i_B} = \big[\mathrm{I}_M \otimes \big(\mathrm{E}(\mathbf{L}_{i_B})\,\mathrm{E}(\boldsymbol{\mu}_{i_\mu})\big) + \big(\mathrm{E}(\bar{\mathbf{L}}_{i_B})\,\mathrm{E}(\bar{\boldsymbol{\mu}}_{i_\mu})\big) \otimes \mathrm{I}_M\big]^{-1}\,\mathrm{E}(\bar{\mathbf{L}}_{i_B} \otimes \mathbf{L}_{i_B})\,\mathrm{E}(\bar{\boldsymbol{\mu}}_{i_\mu} \otimes \boldsymbol{\mu}_{i_\mu}). \tag{9.4.22}$$

Accordingly, by multiple use of Proposition 9.1 (9.1.5) gives

$$\begin{aligned}
\lambda_{\max}(A_{i_B}^{-1}B_{i_B}) &= \lambda_{\max}\Big(\big[\mathrm{I}_M \otimes \big(\mathrm{E}(\mathbf{L}_{i_B})\,\mathrm{E}(\boldsymbol{\mu}_{i_\mu})\big) + \big(\mathrm{E}(\bar{\mathbf{L}}_{i_B})\,\mathrm{E}(\bar{\boldsymbol{\mu}}_{i_\mu})\big) \otimes \mathrm{I}_M\big]^{-1}\,\mathrm{E}(\bar{\mathbf{L}}_{i_B} \otimes \mathbf{L}_{i_B})\,\mathrm{E}(\bar{\boldsymbol{\mu}}_{i_\mu} \otimes \boldsymbol{\mu}_{i_\mu})\Big) \\
&<= \lambda_{\max}\Big(\big[\mathrm{I}_M \otimes \big(\mathrm{E}(\mathbf{L}_{i_B})\,\mathrm{E}(\boldsymbol{\mu}_{i_\mu})\big) + \big(\mathrm{E}(\bar{\mathbf{L}}_{i_B})\,\mathrm{E}(\bar{\boldsymbol{\mu}}_{i_\mu})\big) \otimes \mathrm{I}_M\big]^{-1}\Big) \\
&\quad \times \lambda_{\max}(\mathrm{E}\,\bar{\mathbf{L}}_{i_B} \otimes \mathbf{L}_{i_B})\lambda_{\max}(\mathrm{E}\,\bar{\boldsymbol{\mu}}_{i_\mu} \otimes \boldsymbol{\mu}_{i_\mu}) \\
&= \lambda_{\min}^{-1}\big[\mathrm{I}_M \otimes \big(\mathrm{E}(\mathbf{L}_{i_B})\,\mathrm{E}(\boldsymbol{\mu}_{i_\mu})\big) + \big(\mathrm{E}(\bar{\mathbf{L}}_{i_B})\,\mathrm{E}(\bar{\boldsymbol{\mu}}_{i_\mu})\big) \otimes \mathrm{I}_M\big] \\
&\quad \times \lambda_{\max}(\mathrm{E}\,\bar{\mathbf{L}}_{i_B} \otimes \mathbf{L}_{i_B})\lambda_{\max}(\mathrm{E}\,\bar{\boldsymbol{\mu}}_{i_\mu} \otimes \boldsymbol{\mu}_{i_\mu})
\end{aligned}$$

using Proposition 9.6 to obtain[2]

$$\begin{aligned}
\lambda_{\max}(A_{i_B}^{-1}B_{i_B}) <= &\; 1/2\lambda_{\min}^{-1}\big(\mathrm{E}(\bar{\mathbf{L}}_{i_B})\,\mathrm{E}(\bar{\boldsymbol{\mu}}_{i_\mu})\big) \\
&\times \lambda_{\max}(\mathrm{E}\,\bar{\mathbf{L}}_{i_B} \otimes \mathbf{L}_{i_B})\lambda_{\max}(\mathrm{E}\,\bar{\boldsymbol{\mu}}_{i_\mu} \otimes \boldsymbol{\mu}_{i_\mu}).
\end{aligned} \tag{9.4.23}$$

Therefore, the stability requirement $\lambda_{\max}(F_{i_B}) < 1$ leads to the following *sufficient* constraints

$$\boxed{\forall i_B, i_\mu \geq -1 : \frac{\lambda_{\max}(\mathrm{E}\,\bar{\mathbf{L}}_{i_B} \otimes \mathbf{L}_{i_B})\lambda_{\max}(\mathrm{E}\,\bar{\boldsymbol{\mu}}_{i_\mu} \otimes \boldsymbol{\mu}_{i_\mu})}{\lambda_{\min}\big(\mathrm{E}(\bar{\mathbf{L}}_{i_B})\,\mathrm{E}(\bar{\boldsymbol{\mu}}_{i_\mu})\big)} < 2.} \tag{9.4.24}$$

Hence, by allowing individual weight step-sizes both the *minimum* and *maximum* step-sizes are of concern.

Unfortunately, in the general case of a matrix-valued step-size parameter it is difficult to obtain permissable values for the matrix entities from expression (9.4.24) that lead to $\lambda_{\max}(A_{i_B}^{-1}B_{i_B}) < 1$ even if the step-size matrix is assumed diagonal and real.

For a deterministic step-size matrix we may use Proposition 9.6 to obtain

$$\forall i_B, i_\mu \geq -1 : \frac{\lambda^2_{\max}(\mu_{i_\mu})}{\lambda_{\min}(\mu_{i_\mu})} < \frac{2\lambda_{\min}(\mathrm{E}\,\mathbf{L}_{i_B})}{\lambda_{\max}(\mathrm{E}\,\bar{\mathbf{L}}_{i_B} \otimes \mathbf{L}_{i_B})}. \tag{9.4.25}$$

If $\boldsymbol{\mu}_{i_\mu}$ is a diagonal matrix as in Assumption 4 then a *sufficient* requirement is obtained from (9.4.23)

$$\forall i_B, i_\mu \geq -1 : \frac{\max^2_{j\in\underline{M}}(\mathrm{E}\,\boldsymbol{\mu}_{j,i_\mu})}{\min_{j\in\underline{M}}(\mathrm{E}\,\boldsymbol{\mu}_{j,i_\mu})} < \frac{2\lambda_{\min}(\mathrm{E}\,\mathbf{L}_{i_B})}{\lambda_{\max}(\mathrm{E}\,\bar{\mathbf{L}}_{i_B} \otimes \mathbf{L}_{i_B})} \tag{9.4.26}$$

and for a deterministic diagonal step-size matrix

$$\forall i_B, i_\mu \geq -1 : \frac{\max^2_{j\in\underline{M}}(\mu_{i_\mu})}{\min_{j\in\underline{M}}(\mu_{i_\mu})} < \frac{2\lambda_{\min}(\mathrm{E}\,\mathbf{L}_{i_B})}{\lambda_{\max}(\mathrm{E}\,\bar{\mathbf{L}}_{i_B} \otimes \mathbf{L}_{i_B})}. \tag{9.4.27}$$

Moreover, if $\boldsymbol{\mu}(i_\mu)$ is real and scalar-valued then by insertion in (9.4.22) and (9.4.23) we can obtain the following explicit expression for the upper bound on the step-size[3].

$$\begin{aligned} \forall i_B, i_\mu \geq -1 : 0 < \frac{\mathrm{E}\,\boldsymbol{\mu}^2_{i_\mu}}{\mathrm{E}\,\boldsymbol{\mu}_{i_\mu}} < & \quad \lambda^{-1}_{\max}\Big(\big[(\mathrm{E}\,\mathbf{L}_{i_B} \otimes \mathrm{I}_M) + (\mathrm{I}_M \otimes \mathrm{E}\,\mathbf{L}_{i_B})\big]^{-1}(\mathrm{E}\,\bar{\mathbf{L}}_{i_B} \otimes \mathbf{L}_{i_B})\Big) \\ < & \quad \frac{2\lambda_{\min}(\mathrm{E}\,\mathbf{L}_{i_B})}{\lambda_{\max}(\mathrm{E}\,\bar{\mathbf{L}}_{i_B} \otimes \mathbf{L}_{i_B})} \end{aligned} \tag{9.4.28}$$

and for the deterministic case

$$\begin{aligned} \forall i_B, i_\mu \geq -1 : \mu_{i_\mu} < & \quad \lambda^{-1}_{\max}\Big(\big[(\mathrm{E}\,\mathbf{L}_{i_B} \otimes \mathrm{I}_M) + (\mathrm{I}_M \otimes \mathrm{E}\,\mathbf{L}_{i_B})\big]^{-1}(\mathrm{E}\,\bar{\mathbf{L}}_{i_B} \otimes \mathbf{L}_{i_B})\Big) \\ < & \quad \frac{\lambda_{\min}(\mathrm{E}\,\mathbf{L}_{i_B}))}{\lambda_{\max}(\mathrm{E}\,\bar{\mathbf{L}}_{i_B} \otimes \mathbf{L}_{i_B})} \end{aligned} \tag{9.4.29}$$

respectively. Actually, the requirements in the first line of (9.4.28) and (9.4.29) are both *necessary* and *sufficient* for the $\lambda(F) < 1$ case. The more simple double inequality in the second line of (9.4.28) and (9.4.29) are *sufficient* conditions that was determined under the use of Proposition 9.1 (9.1.5).

We will next address the first equality on F, that is, $-1 < \lambda(F)$. Following a procedure similar to [9, Ch. 9] we readily establish the following requirement

$$\det(\mathrm{I} - H_{i_B}) = 0, \tag{9.4.30}$$

[3]It should be recalled that in general $\frac{\mathrm{E}\,\boldsymbol{\mu}^2(i_\mu)}{\mathrm{E}\,\boldsymbol{\mu}(i_\mu)} \neq \mathrm{E}\,\boldsymbol{\mu}_{i_\mu}$. For example, consider $\boldsymbol{\mu}(i_\mu)$ to be uniformly distributed in the interval $[0; \mu_{\max}]$, then $\frac{\mathrm{E}\,\boldsymbol{\mu}^2(i_\mu)}{\mathrm{E}\,\boldsymbol{\mu}(i_\mu)} = \frac{2}{3}\mu_{\max} \neq \mathrm{E}\,\boldsymbol{\mu}(i_\mu) = \frac{1}{2}\mu_{\max}$. That is, if the step-size parameter is stochastic in nature then we have to reduce the maximum allowable step-size by one sixth from this "intuitive guess" in order to ensure stability. Also by the presence of the expectation operator we cannot use Proposition 9.6 and conclude that $\lambda_{\max}(\mathrm{E}\,\bar{\mathbf{L}}_{i_B} \otimes \mathbf{L}_{i_B}) = \lambda^2_{\max}(\mathrm{E}\,\mathbf{L}_{i_B})$.

where H_{i_B} is defined by

$$H_{i_B} = \begin{bmatrix} A_{i_B}/2 & -B_{i_B}/2 \\ \mathrm{I}_M & 0 \end{bmatrix}. \tag{9.4.31}$$

By insertion of (9.4.20) that relies on Assumption 3 in (9.4.31) under we may express (9.4.61) as

$$\mathrm{I}_{2M} - H_{i_B} = \begin{bmatrix} \mathrm{I}_M - \Big(\mathrm{I}_M \otimes \big(\mathrm{E}(\mathbf{L}_{i_B})\,\mathrm{E}(\boldsymbol{\mu}_{i_\mu})\big) + \big(\mathrm{E}(\bar{\mathbf{L}}_{i_B})\,\mathrm{E}(\bar{\boldsymbol{\mu}}_{i_\mu})\big) \otimes \mathrm{I}_M\Big)/2 & \mathrm{E}(\bar{\mathbf{L}}_{i_B} \otimes \mathbf{L}_{i_B})\,\mathrm{E}(\bar{\boldsymbol{\mu}}_{i_\mu} \otimes \boldsymbol{\mu}_{i_\mu})/2 \\ -\mathrm{I}_M & \mathrm{I}_M \end{bmatrix} \tag{9.4.32}$$

and by using Proposition 9.2 (9.1.9b) then (9.4.30) becomes[4]

$$\det(\mathrm{I}_{2M} - H_{i_B}) = \det(\mathrm{I}_M - \tfrac{1}{2}E_{i_B}), \tag{9.4.33}$$

where

$$E_{i_B} = \mathrm{I}_M \otimes \big(\mathrm{E}(\mathbf{L}_{i_B})\,\mathrm{E}(\boldsymbol{\mu}_{i_\mu})\big) + \big(\mathrm{E}(\bar{\mathbf{L}}_{i_B})\,\mathrm{E}(\bar{\boldsymbol{\mu}}_{i_\mu})\big) \otimes \mathrm{I}_M - \mathrm{E}(\bar{\mathbf{L}}_{i_B} \otimes \mathbf{L}_{i_B})\,\mathrm{E}(\bar{\boldsymbol{\mu}}_{i_\mu} \otimes \boldsymbol{\mu}_{i_\mu}). \tag{9.4.34}$$

Hence, we wish to establish conditions on the step-size matrix $\boldsymbol{\mu}_{i_\mu}$ that ensure $\lambda_{\max}(E_{i_B}) < 2$. Using Proposition 9.1 (9.1.4b) and (9.1.5) we obtain

$$\begin{aligned}
\lambda_{\max}(E_{i_B}) &= \lambda_{\max}\big[\mathrm{I}_M \otimes \big(\mathrm{E}(\mathbf{L}_{i_B})\,\mathrm{E}(\boldsymbol{\mu}_{i_\mu})\big) + \big(\mathrm{E}(\bar{\mathbf{L}}_{i_B})\,\mathrm{E}(\bar{\boldsymbol{\mu}}_{i_\mu})\big) \otimes \mathrm{I}_M - \mathrm{E}(\bar{\mathbf{L}}_{i_B} \otimes \mathbf{L}_{i_B})\,\mathrm{E}(\bar{\boldsymbol{\mu}}_{i_\mu} \otimes \boldsymbol{\mu}_{i_\mu})\big] \\
&\leq \lambda_{\max}\big[\mathrm{I}_M \otimes \big(\mathrm{E}(\mathbf{L}_{i_B})\,\mathrm{E}(\boldsymbol{\mu}_{i_\mu})\big) + \big(\mathrm{E}(\bar{\mathbf{L}}_{i_B})\,\mathrm{E}(\bar{\boldsymbol{\mu}}_{i_\mu})\big) \otimes \mathrm{I}_M\big] - \lambda_{\min}\big[\mathrm{E}(\bar{\mathbf{L}}_{i_B} \otimes \mathbf{L}_{i_B})\,\mathrm{E}(\bar{\boldsymbol{\mu}}_{i_\mu} \otimes \boldsymbol{\mu}_{i_\mu})\big] \\
&= 2\lambda_{\max}\big(\mathrm{E}(\bar{\mathbf{L}}_{i_B})\,\mathrm{E}(\bar{\boldsymbol{\mu}}_{i_\mu})\big) - \lambda_{\min}\big[\mathrm{E}(\bar{\mathbf{L}}_{i_B} \otimes \mathbf{L}_{i_B})\,\mathrm{E}(\bar{\boldsymbol{\mu}}_{i_\mu} \otimes \boldsymbol{\mu}_{i_\mu})\big] \\
&\leq 2\lambda_{\max}(\mathrm{E}\,\bar{\mathbf{L}}_{i_B})\lambda_{\max}(\mathrm{E}\,\bar{\boldsymbol{\mu}}_{i_\mu}) - \lambda_{\min}(\mathrm{E}\,\bar{\mathbf{L}}_{i_B} \otimes \mathbf{L}_{i_B})\lambda_{\min}(\mathrm{E}\,\bar{\boldsymbol{\mu}}_{i_\mu} \otimes \boldsymbol{\mu}_{i_\mu}).
\end{aligned} \tag{9.4.35}$$

Therefore, the stability requirement $\lambda_{\max}(F_{i_B}) > -1$ leads to the following *sufficient* constraint

$$\boxed{\forall i_B, i_\mu \geq -1 : \frac{\lambda_{\max}(\mathrm{E}\,\bar{\mathbf{L}}_{i_B})\lambda_{\max}(\mathrm{E}\,\bar{\boldsymbol{\mu}}_{i_\mu})}{1 + \frac{1}{2}\lambda_{\min}(\mathrm{E}\,\bar{\mathbf{L}}_{i_B} \otimes \mathbf{L}_{i_B})\lambda_{\min}(\mathrm{E}\,\bar{\boldsymbol{\mu}}_{i_\mu} \otimes \boldsymbol{\mu}_{i_\mu})} < 1.} \tag{9.4.36}$$

Likewise, for the $\lambda(F) < 1$ problem viz. (9.4.23) by allowing individual weight step-sizes both the *minimum* and *maximum* step-sizes are of concern. Unfortunately, (9.4.36) provides no direct way to obtain a usable step-size matrix as $\boldsymbol{\mu}_{i_\mu}$ only enters implicitly in the inequality.

For a deterministic step-size matrix we may use Proposition 9.6 to obtain

$$\forall i_B, i_\mu \geq -1 : \frac{\lambda_{\max}(\mathrm{E}\,\bar{\mathbf{L}}_{i_B})\lambda_{\max}(\mu_{i_\mu})}{1 + \frac{1}{2}\lambda_{\min}(\mathrm{E}\,\bar{\mathbf{L}}_{i_B} \otimes \mathbf{L}_{i_B})\lambda^2_{\min}(\mu_{i_\mu})} < 1. \tag{9.4.37}$$

[4]The same result can obtained by appreciating that the two matrices that enter in the left column of $\mathrm{I} - H$ do commute, that is, $(\mathrm{I} - A_{i_B})(-\mathrm{I}) = (-\mathrm{I})(\mathrm{I} - A_{i_B})$ and by applying Proposition 9.2 (9.1.9c).

If $\boldsymbol{\mu}_{i_\mu}$ is a diagonal matrix as in Assumption 4 then a *sufficient* requirement is obtained from (9.4.38)

$$\forall i_B, i_\mu \geq -1 : \frac{\lambda_{\max}(\mathrm{E}\,\bar{\mathbf{L}}_{i_B})\max_{j\in\underline{M}}(\mathrm{E}\,\boldsymbol{\mu}_{j,i_\mu})}{1+\frac{1}{2}\lambda_{\min}(\mathrm{E}\,\bar{\mathbf{L}}_{i_B}\otimes\mathbf{L}_{i_B})\min^2_{j\in\underline{M}}(\mathrm{E}\,\boldsymbol{\mu}_{j,i_\mu})} < 1. \tag{9.4.38}$$

and for a deterministic diagonal step-size matrix

$$\forall i_B, i_\mu \geq -1 : \frac{\lambda_{\max}(\mathrm{E}\,\bar{\mathbf{L}}_{i_B})\max_{j\in\underline{M}}(\mu_{j,i_\mu})}{1+\frac{1}{2}\lambda_{\min}(\mathrm{E}\,\bar{\mathbf{L}}_{i_B}\otimes\mathbf{L}_{i_B})\min^2_{j\in\underline{M}}(\mu_{j,i_\mu})} < 1. \tag{9.4.39}$$

Moreover, if $\boldsymbol{\mu}(i_\mu)$ is real and scalar-valued then following a procedure similar to [9, Ch. 9] we can obtain the following explicit expression for the upper bound on the step-size.

$$0 < \boldsymbol{\mu}(i_\mu) < \frac{1}{\max\lambda(H'_{i_B})\in\mathbb{R}^+} \tag{9.4.40}$$

and for the deterministic case

$$0 < \mu(i_\mu) < \frac{1}{\max\lambda(H'_{i_B})\in\mathbb{R}^+}, \tag{9.4.41}$$

respectively, where

$$H'_{i_B} = \begin{bmatrix} \big(\mathrm{I}_M\otimes\mathrm{E}\,\mathbf{L}_{i_B}+\mathrm{E}\,\bar{\mathbf{L}}_{i_B}\big)/2 & \mathrm{E}(\bar{\mathbf{L}}_{i_B}\otimes\mathbf{L}_{i_B})/2 \\ \mathrm{I}_M & 0 \end{bmatrix}. \tag{9.4.42}$$

The partitioned matrix H'_{i_B} is not necessarily Hermitian and the eigenvalues therefore not necessarily real. If no real eigenvalues exist then the constraints (9.4.40) and (9.4.41) disappear. Actually, the requirements in the first line of (9.4.40) and (9.4.41) are both *necessary* and *sufficient* for the $\lambda(F) < 1$ case.

9.4.4 Transient Analysis of MC-$\alpha\gamma\Pi\epsilon$-APA, State Space Description

We next consider the control input terms involved in the weighted variance recursion (9.3.25). Proceeding as above with the weighting matrices $\Sigma^{w'^o}_{i_B}, \Sigma^q_{i_B}$ and $\Sigma^{\breve{w}}_{i_B}$ gives

$$\sigma^{w'^o}_{i_B} = G^{w'^o}_{i_B}\sigma \tag{9.4.43a}$$
$$\sigma^{q}_{i_B} = G^{q}_{i_B}\sigma \tag{9.4.43b}$$
$$\sigma^{\breve{w}}_{i_B} = G^{\breve{w}}_{i_B}\sigma, \tag{9.4.43c}$$

where $G^{w'^o}_{i_B} \in \mathbb{K}^{M^2\times M^2}$ denotes the control input matrix associated with the mean optimal weight vector, $G^{q}_{i_B} \in \mathbb{K}^{M^2\times M^2}$ is the random-walk control input matrix and $G^{\breve{w}}_{i_B} \in \mathbb{K}^{M^2\times M^2}$ represents the control input matrix related to the regularized weight vector that in turn are defined by

$$
\begin{aligned}
G_{i_B}^{w'^o} &= \mathrm{E}\,\boldsymbol{\Upsilon}_{i_\Upsilon}^{\chi\top} \otimes \boldsymbol{\Upsilon}_{i_\Upsilon}^{\chi*} + (1-\chi)\mathrm{I}_M \otimes \mathrm{E}\,\boldsymbol{\Upsilon}_{i_\Upsilon}^{\chi*} + (1-\chi^*)\,\mathrm{E}(\boldsymbol{\Upsilon}_{i_\Upsilon}^{\chi\top}) \otimes \mathrm{I}_M + |1-\chi|^2(\mathrm{I}_{M^2} + 2\,\mathrm{E}\,\mathbf{P}_{i_B}^\top \otimes \mathbf{P}_{i_B}^*) \\
&\quad + C_{i_B-1}^{w^o\top}\big(\mathrm{E}\,\boldsymbol{\Upsilon}_{i_\Upsilon}^\top \otimes \boldsymbol{\Upsilon}_{i_\Upsilon}^{\chi*} - \mathrm{E}(\mathbf{P}_{i_B}^\top) \otimes \mathrm{E}(\boldsymbol{\Upsilon}_{i_\Upsilon}^{\chi*}) + (1-\chi^*)\,\mathrm{E}(\mathbf{M}_{i_B}^\top) \otimes \mathrm{I}_M\big) \\
&\quad + \big(\mathrm{E}\,\boldsymbol{\Upsilon}_{i_\Upsilon}^{\chi\top} \otimes \boldsymbol{\Upsilon}_{i_\Upsilon}^* - \mathrm{E}(\boldsymbol{\Upsilon}_{i_\Upsilon}^{\chi\top}) \otimes \mathrm{E}(\mathbf{P}_{i_B}^*) + (1-\chi)\mathrm{I}_M \otimes \mathrm{E}(\mathbf{M}_{i_B}^*)\big)C_{i_B-1}^{w^o*} \qquad (9.4.44a) \\
G_{i_B}^{q} &= \mathrm{I}_{M^2} - \mathrm{E}\,\mathbf{P}_{i_B}^\top \otimes \mathrm{I}_M - \mathrm{I}_M \otimes \mathrm{E}\,\mathbf{P}_{i_B}^* + \mathrm{E}\,\mathbf{P}_{i_B}^\top \otimes \mathbf{P}_{i_B}^* \\
&\quad + \Theta_{i_B-1}\Big(\mathrm{E}\,\boldsymbol{\Upsilon}_{i_\Upsilon}^{\chi\top} \otimes \boldsymbol{\Upsilon}_{i_\Upsilon}^{\chi*} + (1-\chi)\,\mathrm{E}(\mathbf{P}_{i_B}^\top) \otimes \mathrm{E}(\boldsymbol{\Upsilon}_{i_\Upsilon}^{\chi*}) \\
&\qquad\qquad + (1-\chi^*)\,\mathrm{E}(\boldsymbol{\Upsilon}_{i_\Upsilon}^{\chi\top}) \otimes \mathrm{E}(\mathbf{P}_{i_B}^*) + |1-\chi|^2\,\mathrm{E}\,\mathbf{P}_{i_B}^\top \otimes \mathbf{P}_{i_B}^*\Big) \qquad (9.4.44b) \\
G_{i_B}^{\breve{w}} &= \mathrm{E}(\boldsymbol{\mu}_{i_\mu}^\top \otimes \boldsymbol{\mu}_{i_\mu}^*) - C_{i_B-1}^{\breve{w}\top}\big(\mathrm{E}(\mathbf{P}_{i_B}^\top) \otimes \mathrm{E}(\boldsymbol{\mu}_{i_\mu}^*) - \mathrm{E}(\boldsymbol{\Upsilon}_{i_\Upsilon}^\top \otimes \boldsymbol{\mu}_{i_\mu}^*)\big) \\
&\quad - \big(\mathrm{E}(\boldsymbol{\mu}_{i_\mu}^\top) \otimes \mathrm{E}(\mathbf{P}_{i_B}^*) - \mathrm{E}(\boldsymbol{\mu}_{i_\mu}^\top) \otimes \boldsymbol{\Upsilon}_{i_\Upsilon}^*\big)C_{i_B-1}^{\breve{w}*} \qquad (9.4.44c)
\end{aligned}
$$

respectively. Similarly, vectorization of the cross-weighting matrices $\Sigma_{i_B}^{w^o\breve{w}}$, $\Sigma_{i_B}^{w^ow^0}$ and $\Sigma_{i_B}^{\breve{w}w^0}$ gives

$$
\begin{aligned}
\sigma_{i_B}^{w^o\breve{w}} &= G_{i_B}^{w^o\breve{w}}\sigma \qquad (9.4.45a) \\
\sigma_{i_B}^{w^ow^0} &= G_{i_B}^{w^ow^0}\sigma \qquad (9.4.45b) \\
\sigma_{i_B}^{\breve{w}w^0} &= G_{i_B}^{\breve{w}w^0}\sigma, \qquad (9.4.45c)
\end{aligned}
$$

where $G_{i_B}^{w^o\breve{w}} \in \mathbb{K}^{M^2\times M^2}$ denotes the control input matrix associated with the coupling between the mean optimal weight vector and the regularized weight vector, $G_{i_B}^{w^ow^0} \in \mathbb{K}^{M^2\times M^2}$ is the mean optimal weight vector to initial weight vector coupling control input matrix and where $G_{i_B}^{\breve{w}w^0} \in \mathbb{K}^{M^2\times M^2}$ represents the control input matrix related to the coupling between the regularized weight vector and the initial weight vector. They are in turn defined by

$$
\begin{aligned}
G_{i_B}^{w^o\breve{w}} &= C_{i_B-1}^{\breve{w}\top}\big(\mathrm{E}\,\boldsymbol{\Upsilon}_{i_\Upsilon}^\top \otimes \boldsymbol{\Upsilon}_{i_\Upsilon}^{\chi*} - \mathrm{E}(\mathbf{P}_{i_B}^\top) \otimes \mathrm{E}(\boldsymbol{\Upsilon}_{i_\Upsilon}^{\chi*}) + (1-\chi^*)\,\mathrm{E}(\mathbf{M}_{i_B}^\top) \otimes \mathrm{I}_M\big) \\
&\quad + \big(\mathrm{E}(\boldsymbol{\mu}_{i_\mu}^\top) \otimes \mathrm{E}(\mathbf{P}_{i_B}^*) - \mathrm{E}(\boldsymbol{\mu}_{i_\mu}^\top \otimes \boldsymbol{\Upsilon}_{i_\Upsilon}^*)\big)C_{i_B-1}^{w^o*} + \mathrm{E}(\boldsymbol{\mu}_{i_\mu}^\top \otimes \boldsymbol{\Upsilon}_{i_\Upsilon}^*) - E(\boldsymbol{\mu}_{i_\mu}^\top) \otimes \mathrm{I}_M \qquad (9.4.46a) \\
G_{i_B}^{w^ow^0} &= C_{i_B}^{w^o,1\top}\big(\mathrm{E}\,\boldsymbol{\Upsilon}_{i_\Upsilon}^\top \otimes \boldsymbol{\Upsilon}_{i_\Upsilon}^{\chi*} - \mathrm{E}(\mathbf{P}_{i_B}^\top) \otimes \mathrm{E}(\boldsymbol{\Upsilon}_{i_\Upsilon}^{\chi*}) + (1-\chi^*)\,\mathrm{E}(\mathbf{M}_{i_B}^\top) \otimes \mathrm{I}_M\big) \qquad (9.4.46b) \\
G_{i_B}^{\breve{w}w^0} &= C_{i_B}^{w^o,1\top}\big(\mathrm{E}(\mathbf{P}_{i_B}^\top) \otimes \mathrm{E}(\boldsymbol{\mu}_{i_\mu}^*) - \mathrm{E}(\boldsymbol{\Upsilon}_{i_\Upsilon}^\top \otimes \boldsymbol{\mu}_{i_\mu}^*)\big) \qquad (9.4.46c)
\end{aligned}
$$

respectively. Moreover, using Proposition 9.1 (9.1.3) the system noise term in (9.3.25) may be expressed

$$
\mathrm{vec}\left\{K\sigma_v^2\,\mathrm{Tr}\left\{\mathrm{E}\,\mathbf{P}_{i_B}^{'*}\Sigma\mathbf{P}_{i_B}^{'}\right\}\right\} = K\sigma_v^2 r_{P',i_B}^\top\sigma, \qquad (9.4.47)
$$

where $r_{P',i_B} \in \mathbb{K}^{M^2\times M^2}$ denotes the vectorized data auto correlation matrix,

$$
r_{P',i_B} = \mathrm{vec}\left\{\mathrm{E}\,\mathbf{P}_{i_B}^{'}\mathbf{P}_{i_B}^{'*}\right\}. \qquad (9.4.48)
$$

Similarly, we may express the maneuver term in (9.3.25) by

$$\mathrm{Tr}\left\{Q\Sigma_{i_B}^{q}\right\} = q^{\top}\sigma_{i_B}^{q}, \tag{9.4.49}$$

where $q \equiv \mathrm{vec}\left\{Q\right\} \in \mathbb{K}^{M^2\times 1}$ denotes the vectorized random-walk covariance matrix,

By insertion of (9.4.16), (9.4.43)-(9.4.46) and (9.4.47)-(9.4.49) in (9.3.25) and using the notational convention in Proposition 9.4 (9.1.12i) we obtain

$$\boxed{\begin{aligned}\mathrm{E}\|\tilde{\mathbf{w}}_{i_B}\|_{\sigma}^2 = \mathrm{E}\|\tilde{\mathbf{w}}_{i_B-1}\|_{F_{i_B}\sigma}^2 + q^{\top}G_{i_B}^{q}\sigma + \|w^{o}\|_{G_{i_B}^{w'^{o}}\sigma}^2 + \|\breve{w}\|_{G_{i_B}^{\breve{w}}\sigma}^2 + K\sigma_v^2 r_{P',i_B}^{\top}\sigma \\ + 2\Re\langle w^{o*},\breve{w}\rangle_{G_{i_B}^{w^{o}\breve{w}}\sigma} - 2\Re\langle w^{o*},w^{0}\rangle_{G_{i_B}^{w^{o}w^{0}}\sigma} - 2\Re\langle \breve{w}^{*},w^{0}\rangle_{G_{i_B}^{\breve{w}w^{0}}\sigma}.\end{aligned}} \tag{9.4.50}$$

We see from (9.4.50) that in order to evaluate $\|\tilde{\mathbf{w}}_{i_B}\|^2 \equiv \|\tilde{\mathbf{w}}_{i_B}\|_{\mathrm{I}_M}^2 \equiv \|\tilde{\mathbf{w}}_{i_B}\|_{\mathrm{vec}^{-1}\{\mathrm{i}_{M^2}\}}^2$ we need to evaluate $\|\tilde{\mathbf{w}}_{i_B-1}\|_{F_{i_B}\sigma}^2$, with a weighting matrix $\Sigma_{i_B}^{\Upsilon} = \mathrm{vec}^{-1}\left\{F_{i_B}\sigma\right\}$ and to evaluate $\|w^{o}\|_{G_{i_B}^{w'^{o}}\sigma}^2$ with a weighting matrix $\mathrm{vec}^{-1}\left\{G_{i_B}^{w'^{o}}\sigma\right\}$ and so on. We are now in a position to take advantage of the arbitrariness in the choice of weighting matrix Σ introduced in (9.3.20)[5]. Then from successive use of the arbitrary weighting matrix σ as $\sigma \leftarrow \sigma, \sigma \leftarrow F_{i_B}\sigma, \ldots, \sigma \leftarrow F^{M^2-1}\sigma$ and following a procedure similar to [1] leads us to the following state-space model that characterizes the transient behavior of the MC-$\alpha\gamma\Pi\epsilon$-APA adaptive filter:

$$\boxed{\mathcal{W}_{i_B} = \mathcal{F}_{i_B}\mathcal{W}_{i_B-1} + \mathcal{G}_{i_B},} \tag{9.4.51}$$

where $\mathcal{W}_{i_B} \in \mathbb{K}^{M^2\times 1}$ denotes the state vector of weighted mean-square weight-error vector [5]

$$\mathcal{W}_{i_B} \triangleq \begin{bmatrix} \mathrm{E}\|\tilde{\mathbf{w}}_{i_B}\|_{\sigma}^2 \\ \mathrm{E}\|\tilde{\mathbf{w}}_{i_B}\|_{F\sigma}^2 \\ \mathrm{E}\|\tilde{\mathbf{w}}_{i_B}\|_{F^2\sigma}^2 \\ \vdots \\ \mathrm{E}\|\tilde{\mathbf{w}}_{i_B}\|_{F^{(M^2-1)}\sigma}^2 \end{bmatrix} \tag{9.4.52}$$

and where the companion state transition matrix of mean-square weight-error vector $\mathcal{F}_{i_B} \in \mathbb{K}^{M^2\times M^2}$ [9, Ch. 9] is defined by

$$\mathcal{F}_{i_B} = \begin{bmatrix} 0 & 1 & 0 & 0 & \ldots & \ldots & 0 \\ 0 & 0 & 1 & 0 & \ldots & \ldots & 0 \\ 0 & 0 & 0 & 1 & 0 & \ldots & 0 \\ \vdots & \vdots & \vdots & \vdots & \ddots & \ldots & 0 \\ 0 & 0 & 0 & 0 & 0 & \ddots & 0 \\ 0 & 0 & 0 & 0 & 0 & 0 & 0 \\ 0 & 0 & 0 & 0 & 0 & 0 & 1 \\ -\chi_0 & -\chi_1 & -\chi_2 & -\chi_3 & \ldots & -\chi_{M^2-2} & -\chi_{M^2-1} \end{bmatrix} \tag{9.4.53}$$

[5] Σ, however, is assumed p.s.d. and therefore also Hermitian ($\Sigma^* = \Sigma$) which has been used throughout the development leading to (9.3.20).

and where the elements in the last row are the coefficients of the characteristic polynomial $\chi_F(s)$, that is,

$$\chi_F(s) = \det(sI_n - F) = s^{M^2} + \sum_{k=0}^{M^2-1} \chi_k s^k, \quad \text{and} \quad \sigma(F) = \{\lambda \in \mathbb{C}; \chi_F(\lambda) = 0\} \tag{9.4.54}$$

for which the roots are the set of eigenvalues of F_{i_B}.

According to the Cayley-Hamilton theorem [16, Ch. 3] every square matrix satisfies its characteristic equation, that is, $\chi_F(F) \equiv 0$. This explains why we only need the weights $F^k\sigma$ for $k = 0, 1, \ldots, M^2 - 1$. The state-space vector is therefore also of order M^2 corresponding to the number of different weighted norms used.

In the state-space regime the total control input matrix $\mathcal{G}_{i_B} \in \mathbb{K}^{M^2\times 1}$ [5] is obtained by

$$\mathcal{G}_{i_B} \triangleq \mathcal{G}^q_{i_B} + \mathcal{G}^{w'^o}_{i_B} + \mathcal{G}^{\breve{w}}_{i_B} + \mathcal{G}^v_{i_B} + \mathcal{G}^{w^o\breve{w}}_{i_B} + \mathcal{G}^{w^o w^0}_{i_B} + \mathcal{G}^{\breve{w}w^0}_{i_B}, \tag{9.4.55}$$

where $\mathcal{G}^q_{i_B} \in \mathbb{K}^{M^2\times 1}$ is the random-walk control input and $\mathcal{G}^v_{i_B} \in \mathbb{K}^{M^2\times 1}$ is the system noise control input that are defined by

$$\mathcal{G}^q_{i_B} \triangleq q^\top G^q_{i_B} \begin{bmatrix} \sigma \\ F_{i_B}\sigma \\ F^2_{i_B}\sigma \\ \vdots \\ F^{(M^2-1)}_{i_B}\sigma \end{bmatrix} \tag{9.4.56a}$$

$$\mathcal{G}^v_{i_B} \triangleq K\sigma_v^2 r^\top_{P',i_B} \begin{bmatrix} \sigma \\ F_{i_B}\sigma \\ F^2_{i_B}\sigma \\ \vdots \\ F^{(M^2-1)}_{i_B}\sigma \end{bmatrix} \tag{9.4.56b}$$

and where $\mathcal{G}^{w'^o}_{i_B} \in \mathbb{K}^{M^2\times 1}$ denotes the control input associated with the mean optimal weight vector and $\mathcal{G}^{\breve{w}}_{i_B} \in \mathbb{K}^{M^2\times 1}$ represents the control input related to the regularized weight vector that in turn are defined by

$$\mathcal{G}_{i_B}^{w'^o} \triangleq \begin{bmatrix} \|w^o\|^2_{G_{i_B}^{w'^o}\sigma} \\ \|w^o\|^2_{G_{i_B}^{w'^o}F_{i_B}\sigma} \\ \|w^o\|^2_{G_{i_B}^{w'^o}F_{i_B}^2\sigma} \\ \vdots \\ \|w^o\|^2_{G_{i_B}^{w'^o}F_{i_B}^{(M^2-1)}\sigma} \end{bmatrix} \tag{9.4.57a}$$

$$\mathcal{G}_{i_B}^{\breve{w}} \triangleq \begin{bmatrix} \|\breve{w}\|^2_{G_{i_B}^{\breve{w}}\sigma} \\ \|\breve{w}\|^2_{G_{i_B}^{\breve{w}}F_{i_B}\sigma} \\ \|\breve{w}\|^2_{G_{i_B}^{\breve{w}}F_{i_B}^2\sigma} \\ \|\breve{w}\|^2_{G_{i_B}^{\breve{w}}F_{i_B}^{(M^2-1)}\sigma} \end{bmatrix} \tag{9.4.57b}$$

and finally where $\mathcal{G}_{i_B}^{w^o\breve{w}} \in \mathbb{K}^{M^2\times 1}$ denotes the control input associated with the coupling between the mean optimal weight vector and the regularized weight vectors, $\mathcal{G}_{i_B}^{w^o w^0} \in \mathbb{K}^{M^2\times 1}$ is the mean optimal weight vector to initial weight vector coupling control input and where $\mathcal{G}_{i_B}^{\breve{w}w^0} \in \mathbb{K}^{M^2\times 1}$ represents the control input related to the coupling between the regularized weight vector and the initial weight vectors that in turn are defined by

$$\mathcal{G}_{i_B}^{w^o\breve{w}} \triangleq 2\Re\begin{bmatrix} \langle w^{o*}, \breve{w}\rangle_{G_{i_B}^{w^o\breve{w}}\sigma} \\ \langle w^{o*}, \breve{w}\rangle_{G_{i_B}^{w^o\breve{w}}F_{i_B}\sigma} \\ \langle w^{o*}, \breve{w}\rangle_{G_{i_B}^{w^o\breve{w}}F_{i_B}^2\sigma} \\ \vdots \\ \langle w^{o*}, \breve{w}\rangle_{G_{i_B}^{w^o\breve{w}}F_{i_B}^{(M^2-1)}\sigma} \end{bmatrix} \tag{9.4.58a}$$

$$\mathcal{G}_{i_B}^{w^o w^0} \triangleq 2\Re\begin{bmatrix} \langle w^{o*}, w^0\rangle_{G_{i_B}^{w^o w^0}\sigma} \\ \langle w^{o*}, w^0\rangle_{G_{i_B}^{w^o w^0}F_{i_B}\sigma} \\ \langle w^{o*}, w^0\rangle_{G_{i_B}^{w^o w^0}F_{i_B}^2\sigma} \\ \vdots \\ \langle w^{o*}, w^0\rangle_{G_{i_B}^{w^o w^0}F_{i_B}^{(M^2-1)}\sigma} \end{bmatrix} \tag{9.4.58b}$$

$$\mathcal{G}_{i_B}^{\breve{w}w^0} \triangleq 2\Re\begin{bmatrix} \langle \breve{w}^*, w^0\rangle_{G_{i_B}^{\breve{w}w^0}\sigma} \\ \langle \breve{w}^*, w^0\rangle_{G_{i_B}^{\breve{w}w^0}F_{i_B}\sigma} \\ \langle \breve{w}^*, w^0\rangle_{G_{i_B}^{\breve{w}w^0}F_{i_B}^2\sigma} \\ \vdots \\ \langle \breve{w}^*, w^0\rangle_{G_{i_B}^{\breve{w}w^0}F_{i_B}^{(M^2-1)}\sigma} \end{bmatrix} \tag{9.4.58c}$$

respectively. Hence, we have replaced the original M-dimensional matrix recursion expression for the propagation of the weighted mean-square weight-error vector in (9.3.25) with a *linear*

vector relation of order M^2 [6].

For the stability analysis we use the well known results from matrix theory that F_{i_B} and the companion matrix $\mathcal{F}_{i_B}$ have identical spectra, that is, $\sigma(F_{i_B}) \equiv \sigma(\mathcal{F}_{i_B})$.

$$0 < \mu < \min\Big\{\frac{1}{\lambda_{max}(A_{i_B}^{-1}B_{i_B})}, \frac{1}{\max\lambda(H_{i_B}) \in \mathbb{R}^+}\Big\}, \tag{9.4.60}$$

where A_{i_B} and B_{i_B} are defined in (9.4.18) and the auxiliary matrix $H_{i_B} \in \mathbb{K}^{2M\times 2M}$, in turn is defined by

$$H_{i_B} = \begin{bmatrix} A_{i_B}/2 & -B_{i_B}/2 \\ \mathrm{I}_{M^2} & 0 \end{bmatrix}. \tag{9.4.61}$$

The first term in (9.4.60) guarantees that $\lambda(F_{i_B}) < 1$ while the second term guarantees $\lambda(F_{i_B}) > -1$.

Comparing the state-space recursion expression for the mean-square weight-error vector $\|\tilde{\mathbf{w}}_{i_B}\|_\Sigma^2$ in (9.4.51) with similar results in [10] for the ϵ-APA we appreciate that the expressions and associated stability criterias are similar, but that at the same time owing to the inclusion of weight-driven and control-effort driven leakage, a non-vanishing initial weight vector $\mathbf{w}_{-1}$ and the inclusion of weight regularization that many additional control input terms enter in Equation (9.4.51)-(9.4.58). Moreover, the underlying weighting matrices are considerable more complicated as discussed in subsection 9.3.3.

By omitting weight regularization that enter (9.3.1) and the random-walk model and by using a vanishing initial weight vector in the transient analysis, that is, by making the following assignments $\chi \leftarrow 1$, $\breve{w} \leftarrow 0$ and $\mathbf{w}_{-1} = w^0 = 0$ in (9.4.44) (9.4.46) and (9.4.49) we readily obtain the following reductions of (9.4.50) and (9.4.55)

$$\boxed{\mathrm{E}\|\tilde{\mathbf{w}}_{i_B}\|_\sigma^2 = \mathrm{E}\|\tilde{\mathbf{w}}_{i_B-1}\|_{F_{i_B}\sigma}^2 + \|w^o\|_{G_{i_B}^{w'o}\sigma}^2 + K\sigma_v^2 r_{P',i_B}^\top \sigma} \tag{9.4.62}$$

[6] By inspection of (9.3.18) and we see that we may express the weight-error vector-weighting matrix $\Sigma_{i_B}^\Upsilon$ in (9.3.26a) in terms of the state-space mean transition matrix $\mathbf{M}_{i_B}$ that enters the recursion (9.3.17) for the mean weight-error vector as $\Sigma_{i_B}^\Upsilon = \mathrm{E}\,\mathbf{M}_{i_B}^* \Sigma \mathbf{M}_{i_B}$. Accordingly, upon vectorization $\sigma_{i_B}^\Upsilon = \mathrm{E}\,\mathbf{M}_{i_B}^\top \otimes \mathbf{M}_{i_B}^* \sigma$ or $F_{i_B} = \mathrm{E}\,\mathbf{M}_{i_B}^\top \otimes \mathbf{M}_{i_B}^*$. Then, by exploiting the algebraic properties from Proposition 9.4 we may pursue a much more straightforward approach and instead of considering the eigenvalues of F_{i_B} instead consider the eigenvalues of $F_{i_B}^\top$ as $\sigma(F_{i_B}) = \sigma(F_{i_B}^\top)$. Then from (9.4.17) and Proposition 9.4 we get

$$F_{i_B}^\top = \mathrm{E}\,\mathbf{M}_{i_B} \otimes \bar{\mathbf{M}}_{i_B}, \tag{9.4.59}$$

where $\bar{\mathbf{M}}_{i_B}$ denotes the complex conjugate of $\mathbf{M}_{i_B}$. Moreover, from matrix theory it is well known that the spectra of the complex conjugate of a matrix, say, A is the complex conjugate of the spectra of the original matrix, that is, $\sigma(A) = \bar{\sigma}(\bar{A})$ [16]. Hence, we may erroneously conclude that the condition $\sigma(F) \subset \mathbb{D}$ holds *if and only if* $\sigma(\mathrm{E}\,\mathbf{M}) \subset \mathbb{D}$. The evaluation of the condition $\sigma(\mathrm{E}\,\mathbf{M}) \subset \mathbb{D}$ would represent a considerably advantage over the condition $\sigma(F) \subset \mathbb{D}$ as $\mathbf{M}_{i_B}$ is a $M \times M$ matrix whereas the matrices A, B, H used in steady-state analysis in subsection 9.4.3 are of order $M^2 \times M^2, M^2 \times M^2, 2M^2 \times 2M^2$ respectively. The error in the argumentations above is that although according to Proposition 9.6 the eigenvalues of $\mathrm{E}\,\mathbf{M}_{i_B} \otimes \mathrm{E}\,\bar{\mathbf{M}}_{i_B}$ are determined from the set of product of all eigenvalues of $\mathrm{E}\,\mathbf{M}_{i_B}$ and $\mathrm{E}\,\bar{\mathbf{M}}_{i_B}$ this **does not** pertain to $F_{i_B}^\top$ owing to the presence of the expectation operator to the outside of the Kronecker product as in general $\mathrm{E}\,\boldsymbol{\psi}_a^2 \neq (\mathrm{E}\,\boldsymbol{\psi}_a)^2$.

and

$$\mathcal{G}_{i_B} \triangleq \mathcal{G}_{i_B}^{w'^o} + \mathcal{G}_{i_B}^{v}, \tag{9.4.63}$$

where

$$\begin{aligned} G_{i_B}^{w'^o} = \mathrm{E}\,\boldsymbol{\Upsilon}_{i_\Upsilon}^{'\top} \otimes \boldsymbol{\Upsilon}_{i_\Upsilon}^{'*} + C_{i_B-1}^{w^{o\top}}\big(\mathrm{E}\,\boldsymbol{\Upsilon}_{i_\Upsilon}^{\top} \otimes \boldsymbol{\Upsilon}_{i_\Upsilon}^{'*} - \mathrm{E}(\mathbf{P}_{i_B}^{\top}) \otimes \mathrm{E}(\boldsymbol{\Upsilon}_{i_\Upsilon}^{'*})\big) \\ + \big(\mathrm{E}\,\boldsymbol{\Upsilon}_{i_\Upsilon}^{'\top} \otimes \boldsymbol{\Upsilon}_{i_\Upsilon}^{*} - \mathrm{E}(\boldsymbol{\Upsilon}_{i_\Upsilon}^{'\top}) \otimes \mathrm{E}(\mathbf{P}_{i_B}^{*})\big) C_{i_B-1}^{w^{o}*}. \end{aligned}$$

Considering the leaky LMS (L-LMS) case where $K \equiv 1$ and for a time-invariant leakage parameter ($\boldsymbol{\Upsilon}_{i_\Upsilon} \leftarrow \mathrm{I} - \boldsymbol{\mu}_{i_\mu}\alpha$) then (9.4.62) and (9.4.63) are similar to the expressions in [8]. Finally, by also omitting all leakage, that is, $\boldsymbol{\Upsilon}_{i_\Upsilon} \leftarrow \mathrm{I}$ in (9.4.64) we see that $G_{i_B}^{w'^o}$ vanishes and (9.4.62) and (9.4.63) then correspond to the results in [10] for the ϵ-APA.

9.4.5 Mean and Mean-Square Performance of MC-$\alpha\gamma\Pi\epsilon$-APA

In steady-state by definition $\lim_{i_B\to\infty} \mathrm{E}\,\tilde{\mathbf{w}}_{i_B} = \lim_{i_B\to\infty} \mathrm{E}\,\tilde{\mathbf{w}}_{i_B-1}$ and $\lim_{i_B\to\infty}\|\mathrm{E}\,\tilde{\mathbf{w}}_{i_B}\|_\Sigma^2 = \lim_{i_B\to\infty}\|\mathrm{E}\,\tilde{\mathbf{w}}_{i_B-1}\|_\Sigma^2$. However, in the presence case of the MC-$\alpha\gamma\Pi\epsilon$-APA with time-variant step-size matrix and parameters we have to questioning ourselves about the existence of such steady-state quantities. Now by Assumptions 5-6 the weight-error vector is independent of both $\mathbf{P}_{i_B}$ and $\boldsymbol{\Upsilon}_{i_\Upsilon}$ and therefore also independent of $\mathbf{M}_{i_B}$.

By insertion in (9.3.17) and (9.4.50) we readily obtain the following expressions for the error quantities defined in subsection 9.2.2 on page 426

$$\begin{aligned} \lim_{i_B\to\infty} \mathrm{E}\,\tilde{\mathbf{w}}_{i_B} &= (\mathrm{I} - \mathrm{E}\,\mathbf{M}_\infty)^{-1}(\mathrm{E}\,\boldsymbol{\Upsilon}'_\infty w^o - \mathrm{E}\,\boldsymbol{\mu}_\infty \breve{w}) \\ &= (\mathrm{E}\,\boldsymbol{\Upsilon}'_\infty - \mathrm{E}\,\mathbf{P}_\infty)^{-1}(\mathrm{E}\,\boldsymbol{\Upsilon}'_\infty w^o - \mathrm{E}\,\boldsymbol{\mu}_\infty \breve{w}), \end{aligned} \tag{9.4.64}$$

and

$$\begin{aligned} \lim_{i_B\to\infty} \mathrm{E}\|\tilde{\mathbf{w}}_{i_B}\|_{\mathrm{I}-F_{i_B}}^2 = q^\top G_\infty^q \sigma + \|w^o\|_{G_\infty^{w'^o}\sigma}^2 + \|\breve{w}\|_{G_\infty^{\breve{w}}\sigma}^2 + K\sigma_v^2 r_{P',\infty}^\top \sigma \\ + 2\Re\langle w^{o*}, \breve{w}\rangle_{G_\infty^{w^o\breve{w}}\sigma} - 2\Re\langle w^{o*}, w^0\rangle_{G_\infty^{w^o w^0}\sigma} - 2\Re\langle \breve{w}^*, w^0\rangle_{G_\infty^{\breve{w}w^0}\sigma}. \end{aligned} \tag{9.4.65}$$

Now we may use the arbitrariness in the choice of weighting matrix Σ and therefore also in σ. Hence by the choice $\sigma = (\mathrm{I} - F_\infty)^{-1}\mathrm{i}_{M^2}$ where $\mathrm{i}_{M^2} \equiv \mathrm{vec}\,\{\mathrm{I}_M\} \in \mathbb{R}^{M^2\times 1}$ denotes the vectorized identity matrix the m.s.d. can then be obtained from (9.4.65)

$$\begin{aligned} \mathrm{MSD} &\triangleq \lim_{i_B\to\infty} \mathrm{E}\|\tilde{\mathbf{w}}_{i_B}\|^2 \\ &= q^\top G_\infty^q (\mathrm{I} - F_\infty)^{-1}\mathrm{i}_{M^2} + \|w^o\|_{G_\infty^{w'^o}(\mathrm{I}-F_\infty)^{-1}\mathrm{i}_{M^2}}^2 + \|\breve{w}\|_{G_\infty^{\breve{w}}(\mathrm{I}-F_\infty)^{-1}\mathrm{i}_{M^2}}^2 \\ &\quad + K\sigma_v^2 r_{P',\infty}^\top (\mathrm{I} - F_\infty)^{-1}\mathrm{i}_{M^2} + 2\Re\langle w^{o*}, \breve{w}\rangle_{G_\infty^{w^o\breve{w}}(\mathrm{I}-F_\infty)^{-1}\mathrm{i}_{M^2}} \\ &\quad - 2\Re\langle w^{o*}, w^0\rangle_{G_\infty^{w^o w^0}(\mathrm{I}-F_\infty)^{-1}\mathrm{i}_{M^2}} - 2\Re\langle \breve{w}^*, w^0\rangle_{G_\infty^{\breve{w}w^0}(\mathrm{I}-F_\infty)^{-1}\mathrm{i}_{M^2}}. \end{aligned} \tag{9.4.66}$$

By selecting $\sigma = r_{u,\infty}$ where $r_{u,i} \triangleq \mathrm{vec}\{R_{u,i}\} \in \mathbb{K}^{M^2\times 1}$ denotes the vectorized data auto correlation matrix and using that by (9.2.8a) $\mathrm{E}\|e_{a,i}\|^2 = \mathrm{E}\|\tilde{\mathbf{w}}_{i_B}\|^2_{R_{u,i}}$ we can obtain the following expression for the EMSE

$$\begin{aligned}\mathrm{EMSE} &\triangleq \lim_{i\to\infty} \mathrm{E}\|e_{a,i}\|^2 \\ &= q^{\top} G^q_{\infty}(\mathrm{I}-F_{\infty})^{-1} r_{u,\infty} + \|w^o\|^2_{G^{w'^o}_{\infty}(\mathrm{I}-F_{\infty})^{-1}r_{u,\infty}} + \|\breve{w}\|^2_{G^{\breve{w}}_{\infty}(\mathrm{I}-F_{\infty})^{-1}r_{u,\infty}} \\ &\quad + K\sigma_v^2 r^{\top}_{P',\infty}(\mathrm{I}-F_{\infty})^{-1} r_{u,\infty} + 2\Re\langle w^{o*}, \breve{w}\rangle_{G^{w^o\breve{w}}_{\infty}(\mathrm{I}-F_{\infty})^{-1}r_{u,\infty}} \\ &\quad - 2\Re\langle w^{o*}, w^0\rangle_{G^{w^o w^0}_{\infty}(\mathrm{I}-F_{\infty})^{-1}r_{u,\infty}} - 2\Re\langle \breve{w}^*, w^0\rangle_{G^{\breve{w}w^0}_{\infty}(\mathrm{I}-F_{\infty})^{-1}r_{u,\infty}}.\end{aligned} \tag{9.4.67}$$

The weighted excess-mean-square error (WEMSE) is similarly by (9.2.8a) and (9.2.16), obtained by insertion of $\sigma = r^{W_e}_{u,\infty}$ in (9.4.65), where $r^{W_e}_{u,i} \triangleq \mathrm{vec}\{R^{W_e}_{u,i}\} \in \mathbb{K}^{M^2\times 1}$ denotes the vectorized data weighted auto correlation matrix

$$\begin{aligned}\mathrm{WEMSE} &\triangleq \lim_{i\to\infty} \mathrm{E}\|e_{a,i}\|^2_{W_e} \\ &= q^{\top} G^q_{\infty}(\mathrm{I}-F_{\infty})^{-1} r^{W_e}_{u,\infty} + \|w^o\|^2_{G^{w'^o}_{\infty}(\mathrm{I}-F_{\infty})^{-1}r^{W_e}_{u,\infty}} + \|\breve{w}\|^2_{G^{\breve{w}}_{\infty}(\mathrm{I}-F_{\infty})^{-1}r^{W_e}_{u,\infty}} \\ &\quad + K\sigma_v^2 r^{\top}_{P',\infty}(\mathrm{I}-F_{\infty})^{-1} r^{W_e}_{u,\infty} + 2\Re\langle w^{o*}, \breve{w}\rangle_{G^{w^o\breve{w}}_{\infty}(\mathrm{I}-F_{\infty})^{-1}r^{W_e}_{u,\infty}} \\ &\quad - 2\Re\langle w^{o*}, w^0\rangle_{G^{w^o w^0}_{\infty}(\mathrm{I}-F_{\infty})^{-1}r^{W_e}_{u,\infty}} - 2\Re\langle \breve{w}^*, w^0\rangle_{G^{\breve{w}w^0}_{\infty}(\mathrm{I}-F_{\infty})^{-1}r^{W_e}_{u,\infty}}.\end{aligned} \tag{9.4.68}$$

$$\mathrm{MSE} \triangleq \lim_{i\to\infty} \mathrm{E}\|\mathbf{e}(i)\|^2 = \mathrm{EMSE} + J^{e^2}_{\min}. \tag{9.4.69}$$

where $J^{e^2}_{\min}$ is defined in (8.3.5) on page 376

$$\mathrm{WMSE} \triangleq \lim_{i\to\infty} \mathrm{E}\|\mathbf{e}_i\|^2_{W_e} = \mathrm{WEMSE} + J^{e^2}_{\min}. \tag{9.4.70}$$

Comparing with a similar result in [10] we see that the leakage, weight-regularization and the time-variant of the step-size μ, the leakage control parameter α and numerical regularization parameter ϵ leads to a rather involved expression here.

Finally, we will summarize our main results in the following theorem.

Theorem 1 (Stability of multiple-channel-$\alpha\gamma\Pi\epsilon$-affine projection algorithm)**.** *Consider the* MC-$\alpha\gamma\Pi\epsilon$-APA *update recursion* (9.3.3)-(9.3.4) *and* (9.3.6) *and assume that the data* $\{\mathbf{d}_i, \mathbf{x}_i, \mathbf{u}_i\}$ *satisfy the linear estimation model in Assumption 1 and the Independence Assumption 5,* (9.A.6) *and Assumption 6,* (9.A.7)*. Then the filter is convergent in the mean and is mean-square stable for step-sizes satisfying* $\forall i_B, i_\mu \geq -1, j \in \underline{M}$

$$0 < \lambda_{\max}(\mathrm{E}\,\boldsymbol{\mu}_{i_\mu}) < \frac{2}{\lambda_{\max}(\mathrm{E}\,\mathbf{L}_{i_B})} \tag{9.4.71a}$$

$$\frac{\lambda_{\max}(\mathrm{E}\,\bar{\mathbf{L}}_{i_B}\otimes\mathbf{L}_{i_B})\lambda_{\max}(\mathrm{E}\,\bar{\boldsymbol{\mu}}_{i_\mu}\otimes\boldsymbol{\mu}_{i_\mu})}{\lambda_{\min}\big(\mathrm{E}(\bar{\mathbf{L}}_{i_B})\,\mathrm{E}(\bar{\boldsymbol{\mu}}_{i_\mu})\big)} < 2 < \frac{2+\lambda_{\min}(\mathrm{E}\,\bar{\mathbf{L}}_{i_B}\otimes\mathbf{L}_{i_B})\lambda_{\min}(\mathrm{E}\,\bar{\boldsymbol{\mu}}_{i_\mu}\otimes\boldsymbol{\mu}_{i_\mu})}{\lambda_{\max}\big(\mathrm{E}(\bar{\mathbf{L}}_{i_B})\,\mathrm{E}(\bar{\boldsymbol{\mu}}_{i_\mu})\big)}. \tag{9.4.71b}$$

For a deterministic step-size matrix Proposition 9.6 gives

$$0 < \lambda_{\max}(\mu_{i_\mu}) < \frac{2}{\lambda_{\max}(\mathrm{E}\,\mathbf{L}_{i_B})} \tag{9.4.72a}$$

$$\frac{\lambda_{\max}(\mathrm{E}\,\bar{\mathbf{L}}_{i_B}\otimes\mathbf{L}_{i_B})\lambda^2_{\max}(\mu_{i_\mu})}{\lambda_{\min}(\mathrm{E}\,\mathbf{L}_{i_B})\lambda_{\min}(\mu_{i_\mu})} < 2 < \frac{2+\lambda_{\min}(\mathrm{E}\,\bar{\mathbf{L}}_{i_B}\otimes\mathbf{L}_{i_B})\lambda^2_{\min}(\mu_{i_\mu})}{\lambda_{\max}(\mathrm{E}\,\bar{\mathbf{L}}_{i_B})\lambda_{\max}(\mu_{i_\mu})}. \tag{9.4.72b}$$

If $\boldsymbol{\mu}_{i_\mu}$ *is a diagonal matrix as in Assumption 4 then a* sufficient *requirement is*

$$0 < \mathrm{E}\,\boldsymbol{\mu}_{j,i_\mu} < \frac{2}{\lambda_{\max}(\mathrm{E}\,\mathbf{L}_{i_B})} \tag{9.4.73a}$$

$$\frac{\lambda_{\max}(\mathrm{E}\,\bar{\mathbf{L}}_{i_B}\otimes\mathbf{L}_{i_B})\max^2_{j\in\underline{M}}(\mathrm{E}\,\boldsymbol{\mu}_{j,i_\mu})}{\lambda_{\min}(\mathrm{E}\,\mathbf{L}_{i_B})\min_{j\in\underline{M}}(\mathrm{E}\,\boldsymbol{\mu}_{j,i_\mu})} < 2 < \frac{2+\lambda_{\min}(\mathrm{E}\,\bar{\mathbf{L}}_{i_B}\otimes\mathbf{L}_{i_B})\min^2_{j\in\underline{M}}(\mathrm{E}\,\boldsymbol{\mu}_{j,i_\mu})}{\lambda_{\max}(\mathrm{E}\,\bar{\mathbf{L}}_{i_B})\max_{j\in\underline{M}}(\mathrm{E}\,\boldsymbol{\mu}_{j,i_\mu})} \tag{9.4.73b}$$

and for a deterministic diagonal step-size matrix

$$0 < \mu_{j,i_\mu} < \frac{2}{\lambda_{\max}(\mathrm{E}\,\mathbf{L}_{i_B})} \tag{9.4.74a}$$

$$\frac{\lambda_{\max}(\mathrm{E}\,\bar{\mathbf{L}}_{i_B}\otimes\mathbf{L}_{i_B})\max^2_{j\in\underline{M}}(\mu_{i_\mu})}{\lambda_{\min}(\mathrm{E}\,\mathbf{L}_{i_B})\min_{j\in\underline{M}}(\mu_{i_\mu})} < 2 < \frac{2+\lambda_{\min}(\mathrm{E}\,\bar{\mathbf{L}}_{i_B}\otimes\mathbf{L}_{i_B})\min^2_{j\in\underline{M}}(\mu_{j,i_\mu})}{\lambda_{\max}(\mathrm{E}\,\bar{\mathbf{L}}_{i_B})\max_{j\in\underline{M}}(\mu_{j,i_\mu})}. \tag{9.4.74b}$$

Finally, a scalar-valued step-size parameter $\boldsymbol{\mu}(i_\mu)$ *is bounded according to*

$$0 < \mathrm{E}\,\boldsymbol{\mu}(i_\mu) < 2\lambda^{-1}_{max}(\mathrm{E}\,\mathbf{L}_{i_B}) \tag{9.4.75a}$$

$$0 < \frac{\mathrm{E}\,\boldsymbol{\mu}^2(i_\mu)}{\mathrm{E}\,\boldsymbol{\mu}(i_\mu)} < \lambda^{-1}_{\max}\Big(\big[(\mathrm{E}\,\mathbf{L}_{i_B}\otimes\mathrm{I}_M)+(\mathrm{I}_M\otimes\mathrm{E}\,\mathbf{L}_{i_B})\big]^{-1}(\mathrm{E}\,\bar{\mathbf{L}}_{i_B}\otimes\mathbf{L}_{i_B})\Big) \tag{9.4.75b}$$

and for the deterministic case

$$\begin{aligned} 0 < \mu < \min\Big\{ & 2\lambda^{-1}_{max}(\mathrm{E}\,\mathbf{L}_{i_B}), \lambda^{-1}_{\max}\Big(\big[(\mathrm{E}\,\mathbf{L}_{i_B}\otimes\mathrm{I}_M)+(\mathrm{I}_M\otimes\mathrm{E}\,\mathbf{L}_{i_B})\big]^{-1}(\mathrm{E}\,\bar{\mathbf{L}}_{i_B}\otimes\mathbf{L}_{i_B})\Big), \\ & \big(\max(\lambda(H'_{i_B})\in\mathbb{R}^+)\big)^{-1}\Big\}, \end{aligned} \tag{9.4.76}$$

respectively, where A_{i_B} *and* B_{i_B} *are defined in* (9.4.18) *and where the auxiliary matrix* $H'_{i_B}\in\mathbb{K}^{2M\times 2M}$*, in turn is defined by*

$$H'_{i_B} = \begin{bmatrix} \big(\mathrm{I}_M\otimes\mathrm{E}\,\mathbf{L}_{i_B}+\mathrm{E}\,\bar{\mathbf{L}}_{i_B}\otimes\mathrm{I}_M\big)/2 & \mathrm{E}(\bar{\mathbf{L}}_{i_B}\otimes\mathbf{L}_{i_B})/2 \\ \mathrm{I}_M & 0 \end{bmatrix}. \tag{9.4.77}$$

The first term in (9.4.76) *ensures convergence in the mean. The second and third terms in* (9.4.76) *are necessary in order to ensure convergence in the mean-square. The second term guarantees that* $\lambda(F_{i_B})<1$ *while the third term guarantees* $\lambda(F_{i_B})>-1$*.*

If we chose a step-size parameter such that stability is guaranteed we may proceed and derive expressions for the m.s.d. (9.4.66), the EMSE (9.4.67), the WEMSE (9.4.68), the m.s.e. (9.4.69) and the weighted mean-square error (w.m.s.e.) (9.4.70).

9.5 Conclusions

The novelty of the present work is the performance analysis of the l.l.m.s.e.-based MC-$\alpha\gamma\Pi\epsilon$-APA adaptive filter developed in subsection 8.6.3 on page 398 encompassing both dynamic *weight-driven leakage* and dynamic *control-effort-driven leakage* and numerical regularization as well as weight regularization. Moreover, in our presentation we also allow the step-size μ, the leakage control parameters α, γ and the numerical regularization parameter ϵ to attain matrix-values and to be time-variant.

Closed-form expressions for the mean- and mean-square steady-state performance as well as transient response performance of the adaptive filter were obtained.

The main contribution to the performance analysis theory is the inclusion of time-variant parameters that in turn may be either deterministic or stochastic in nature. Furthermore the analysis conducted in this report uses an advanced random-walk model and also allows a non-vanishing initial weight vector. Usually, the random-walk model is omitted from the transient analysis. However, in the presence analysis we allowed a general random-walk model to model the non-stationarity of the system. During the course of analysis many higher-order moments were encountered. By enforcing Assumption 5 - 8 we were able to proceed the theoretical development. Justification of each of the assumptions was made.

The main results are summarized in Theorem 1. The performance expressions for the MC-$\alpha\gamma\Pi\epsilon$-APA adaptive filter in general are considerably more complicated than similar results pertaining to the ordinary ϵ-APA or ϵ-NLMS (ϵ-NLMS) algorithms. Successive simplifications of the MC-$\alpha\gamma\Pi\epsilon$-APA and the LEM in Assumption 1 lead to similar expressions in previously published work for the ordinary ϵ-APA or ϵ-NLMS algorithms.

The MC-$\alpha\gamma\Pi\epsilon$-APA adaptive filter will be subject to extensive future test and evaluation activities.

9.A Miscellaneous Derivations

9.A.1 Transient Analysis of MC-$\alpha\gamma\Pi\epsilon$-APA, Mean Relation

In order to obtain an expression for the time-evolution of the mean weight-error vector, that is, $\mathrm{E}\,\tilde{\mathbf{w}}_{i_B}$ we proceed by taking the expectation on both sides of the recursion expression (9.3.16) on page 430 to obtain

$$\mathrm{E}\,\tilde{\mathbf{w}}_{i_B} = \mathrm{E}\,\boldsymbol{\Upsilon}_{i_\Upsilon}^{\chi}\mathbf{w}_{i_B-1}^{o} + \mathrm{E}\,\bar{\mathbf{q}}_{i_B} + \mathrm{E}\,\boldsymbol{\Upsilon}_{i_\Upsilon}\tilde{\mathbf{w}}_{i_B-1} - \mathrm{E}\,\mathbf{P}_{i_B}\left(\tilde{\mathbf{w}}_{i_B-1} + \bar{\mathbf{q}}_{i_B} - (1-\chi)\mathbf{w}_{i_B-1}^{o}\right) - \mathrm{E}\,\mathbf{P}_{i_B}'\mathbf{V}_i - \mathrm{E}\,\boldsymbol{\mu}_{i_\mu}\breve{w}. \quad (9.A.1)$$

From linear estimation model assumptions on non-stationarity (9.2.1b)-(9.2.1d) and the definition (9.3.10) it can be concluded that $\mathbf{P}_{i_B}$ is independent of $\bar{\mathbf{q}}_{i_B}$. Hence, using (9.3.13) we get

$$\mathrm{E}\,\tilde{\mathbf{w}}_{i_B} = \chi w^o - \mathrm{E}\,\boldsymbol{\Upsilon}_{i_\Upsilon}\mathbf{w}^o_{i_B-1} + (1-\chi)w^o + \mathrm{E}\,\boldsymbol{\Upsilon}_{i_\Upsilon}\tilde{\mathbf{w}}_{i_B-1} - \mathrm{E}\,\mathbf{P}_{i_B}\big(\tilde{\mathbf{w}}_{i_B-1} + (1-\chi)(w^o - \mathbf{w}^o_{i_B-1})\big) - \mathrm{E}\,\mathbf{P}'_{i_B}\mathbf{V}_i - \mathrm{E}\,\boldsymbol{\mu}_{i_\mu}\breve{w}. \quad (9.A.2)$$

Now by using the linear estimation model assumptions on the system noise (9.2.1d) and (9.2.1g) leads to the conclusion that $\mathbf{V}_i$ is independent of $\mathbf{P}'_{i_B}$ and $\mathbf{P}_{i_B}$ and the recursion (9.A.2) therefore becomes

$$\mathrm{E}\,\tilde{\mathbf{w}}_{i_B} = w^o - \mathrm{E}\,\boldsymbol{\Upsilon}_{i_\Upsilon}\mathbf{w}^o_{i_B-1} + \mathrm{E}\,\boldsymbol{\Upsilon}_{i_\Upsilon}\tilde{\mathbf{w}}_{i_B-1} - \mathrm{E}\,\mathbf{P}_{i_B}\tilde{\mathbf{w}}_{i_B-1} + \mathrm{E}\,\mathbf{P}_{i_B}(1-\chi)(w^o - \mathbf{w}^o_{i_B-1}) - \mathrm{E}\,\boldsymbol{\mu}_{i_\mu}\breve{w}. \quad (9.A.3)$$

Hitherto, in the derivation carried out to obtain (9.A.3) we have only made use of Assumption 1 on the LEM. But, from inspection of (9.A.3) we see that in order to describe the transient behavior of the mean weight-error vector for the MC-$\alpha\gamma\Pi\epsilon$-APA adaptive filter with time-variant parameters we need to evaluate the following moments

$$\boxed{\mathrm{E}\,\mathbf{P}_{i_B},\quad \mathrm{E}\,\boldsymbol{\Upsilon}_{i_\Upsilon}\mathbf{w}^o_{i_B-1},\quad \mathrm{E}\,\boldsymbol{\Upsilon}_{i_\Upsilon}\tilde{\mathbf{w}}_{i_B-1},\quad \mathrm{E}\,\mathbf{P}_{i_B}\tilde{\mathbf{w}}_{i_B-1},\quad \mathrm{E}\,\mathbf{P}_{i_B}\mathbf{w}^o_{i_B-1}.} \quad (9.A.4)$$

Moreover, from (9.3.6) we see that $\boldsymbol{\Upsilon}_{i_\Upsilon}$ in turn involves the following moments

$$\boxed{\mathrm{E}\,\boldsymbol{\mu}_{i_\mu}\boldsymbol{\alpha}_{i_\alpha},\quad \mathrm{E}\,\boldsymbol{\mu}_{i_\mu}\boldsymbol{X}^*_i\boldsymbol{\gamma}_{i_\gamma\otimes K}\boldsymbol{X}_i,\quad \mathrm{E}\,\boldsymbol{\mu}_{i_\mu}.} \quad (9.A.5)$$

From (9.A.5) and (9.3.10c) we appreciate that the random sequences $\boldsymbol{\Upsilon}_{i_\Upsilon}$ and $\mathbf{P}_{i_B}$ themselves involve moments of order four and seven respectively. Hence, a term like $\mathrm{E}\,\mathbf{P}_{i_B}\tilde{\mathbf{w}}_{i_B-1}$ is an eight order moment. In conclusion the recursion (9.A.3) is in the general case difficult to propagate. Accordingly we will introduce two other *independence assumptions* in order to proceed. The first assumption concerns the dependence of the weight-error vector $\tilde{\mathbf{w}}_{i_B-1}$ on the regressor data $\mathbf{U}_{i_B}$ through $\mathbf{P}_{i_B}$. The second assumption concerns the dependence of the weight-error vector on the parameters $\boldsymbol{\alpha}_{i_\alpha}, \boldsymbol{\gamma}_{i_\gamma}, \boldsymbol{\epsilon}_{i_\epsilon}, \boldsymbol{\Pi}_{i_\Pi}$ through the transformed leakage-weight regularization matrix $\boldsymbol{\Upsilon}_{i_\Upsilon}$.

Assumption 5 (Independence of $\tilde{\mathbf{w}}_{i_B-1}$, $\mathbf{P}_{i_B}$)**.**

The weight-error vector $\tilde{\mathbf{w}}_{i_B-1}$ is independent of $\mathbf{P}_{i_B}$. Hence,

$$\forall i_B \geq 0: \quad f_{\tilde{w}}(\tilde{w}_{i_B-1}|P_{i_B}) = f_{\tilde{w}}(\tilde{w}_{i_B-1}). \quad (9.A.6)$$

From (9.3.10) we observe that $\mathbf{P}_{i_B}$ is proportional to the step-size matrix $\boldsymbol{\mu}_{i_\mu}$. It can be concluded that in order for Assumption 5 to hold we must impose the following *necessary* constraint on the step-size matrix.

① The step-size matrix $\boldsymbol{\mu}_{i_\mu}$ is constant or varies slowly with time. However, the variation of the numerical regularization parameter $\boldsymbol{\epsilon}_{i_\epsilon}$ is less critical as the two $\boldsymbol{\epsilon}_{i_\epsilon}$ factors in (9.3.10a) tend to cancel each other as $\epsilon_{i_\epsilon} \gtrapprox 0$ as more clearly observed from (9.3.10b).

An example where Assumption 5 generally does not hold is for the family of variable step-size algorithms where usually a scalar-valued step-size $\boldsymbol{\mu}$ is used to provide a better trade-off between fast convergence and low misadjustment. When the error is numerically large a high step-size value is required for fast adaptation. For low misadjustment, however, a small step-size is required. Hence, the error $\mathbf{e}_i$ and therefore also the weight-error vector $\tilde{\mathbf{w}}_{i_B}$ are not independent of the step-size.

Assumption 5, (9.A.6) implies that $\mathrm{E}\,\mathbf{P}_{i_B}\tilde{\mathbf{w}}_{i_B-1} = \mathrm{E}\,\mathbf{P}_{i_B}\,\mathrm{E}\,\tilde{\mathbf{w}}_{i_B-1}$.

It should be noticed that for time-invariant step-sizes Assumption 5, (9.A.6) is generally weaker than Assumption 2, (9.2.6b).

We also need the following somewhat more controversial assumption.

Assumption 6 (Independence of $\tilde{\mathbf{w}}_{i_B-1}, \boldsymbol{\Upsilon}_{i_\Upsilon}$)**.**

The weight-error vector $\tilde{\mathbf{w}}_{i_B-1}$ is independent of the transformed leakage matrix $\boldsymbol{\Upsilon}_{i_\Upsilon}$, that is,

$$\forall i_B \geq 0, i_B \geq i_B^\Upsilon: \quad f_{\tilde{w}}(\tilde{w}_{i_B-1}|\Upsilon_{i_\Upsilon}) = f_w(\tilde{w}_{i_B-1}), \tag{9.A.7}$$

where i_B^Υ is the weight block update iteration number corresponding to i_Υ.

Assumption 6 holds for example under the conditions listed below.

① A *sufficient* condition is when the weight-error vector is independent of each of the step-size matrix $\boldsymbol{\mu}_{i_\mu}$, the leakage control parameters $\boldsymbol{\alpha}_{i_\alpha}, \boldsymbol{\gamma}_{i_\gamma}$ and the weight regularization parameter $\boldsymbol{\Pi}_{i_\Pi}$ that enter expression (9.3.6) for $\boldsymbol{\Upsilon}_{i_\Upsilon}$.

② The transformed leakage matrix $\boldsymbol{\Upsilon}_{i_\Upsilon}$ is constant or varies slowly with time. This will for example be the case if each of $\boldsymbol{\mu}_{i_\mu}, \boldsymbol{\alpha}_{i_\alpha}, \boldsymbol{\gamma}_{i_\gamma}, \boldsymbol{\Pi}_{i_\Pi}$ vary slowly with time.

③ Many block-updates have passed since $\boldsymbol{\Upsilon}_{i_\Upsilon}$ was updated last time, that is, $i_B \gg i_B^\Upsilon = \max\{i_B^\mu, i_B^\alpha, i_B^\gamma, i_B^\Pi\}$. Then the effect from the change in $\boldsymbol{\Upsilon}_{i_\Upsilon}$ will be smoothed out.

④ The combined dynamic effects of $\boldsymbol{\mu}_{i_\mu}, \boldsymbol{\alpha}_{i_\alpha}, \boldsymbol{\gamma}_{i_\gamma}$ and $\boldsymbol{\Pi}_{i_\Pi}$ tends to counter balance each other. This of course implies satisfaction of ②. This will be the case for example if $\boldsymbol{\mu}_{i_\mu}$ decreases inverse-proportionally with $\boldsymbol{\alpha}_{i_\alpha}$.

⑤ The combined leakage effect is small, that is, $\boldsymbol{\alpha}_{i_\alpha} \gtrapprox 0, \boldsymbol{X}_i^* \boldsymbol{\gamma}_{i_\gamma \otimes K} \boldsymbol{X}_i \gtrapprox 0$, that in the absence of weight regularization in turn implies that $\boldsymbol{\Upsilon}_{i_\Upsilon} \succeq \mathrm{I}$. This assumption holds for the more advanced leakage schemes presented in subsection 8.3.3 on page 378, subsection 8.3.4 on page 382 and section 8.A on page 404 except for situations where the weight vector norm or the control output signals are approaching the threshold limit. On the other hand considering the stability of the adaptive schemes it can be argued that one of the arguments for introducing leakage is to ensure robust stability. Although the claimed independence doesn't hold the overall error of invoking this assumption in the performance analysis will be negligible.

Assumption 6, (9.A.7) implies that $\mathrm{E}\,\boldsymbol{\Upsilon}_{i_\Upsilon}\tilde{\mathbf{w}}_{i_B-1} = \mathrm{E}\,\boldsymbol{\Upsilon}_{i_\Upsilon}\,\mathrm{E}\,\tilde{\mathbf{w}}_{i_B-1}$. It should be recalled that Assumption 6 is only required when leakage functionality or weight regularization is applied. The discussion above also reveal the analytic difficulties one faces by allowing data-dependent and therefore also a time-variant step-size μ, time-variant leakage control parameters α, γ, a

time-variant numerical regularization parameter ϵ and a weight vector regularization parameter Π. Assumption 5-6 are based on heuristic arguments.

From (9.2.1b) it can readily be deduced by induction that the optimal weight vector $\mathbf{w}_{i_B}^o$ can determined from the initial random vector $\boldsymbol{\theta}_{-1}$ and the random vectors $\mathbf{q}_0, \mathbf{q}_1, \ldots, \mathbf{q}_{i_B}$ by

$$\mathbf{w}_{i_B}^o - w^o = \boldsymbol{\theta}_{i_B} = \chi^{i_B+1}\boldsymbol{\theta}_{-1} + \sum_{j=0}^{i_B} \chi^{i_B-j}\mathbf{q}_j. \tag{9.A.8}$$

Then according to LEM assumption (9.2.1f) and (9.2.1c) $\boldsymbol{\theta}_{i_B}$ is also independent of $\mathbf{u}_i$ (and therefore also independent of $\mathbf{U}_i$ and in turn by (9.3.10c) independent of $\mathbf{P}_{i_B}$)[7]. The independence of $\boldsymbol{\theta}_{i_B}$ with $\mathbf{P}_{i_B}$ implies that $\mathrm{E}\,\mathbf{P}_{i_B}\mathbf{w}_{i_B-1}^o = \mathrm{E}\,\mathbf{P}_{i_B}(w^o + \boldsymbol{\theta}_{i_B-1}) = \mathrm{E}\,\mathbf{P}_{i_B}\,\mathrm{E}\,\mathbf{w}_{i_B-1}^o$. Moreover, by (9.A.8) and LEM assumption on non-stationarity (9.2.1c) $\mathbf{w}_{i_B-1}^o$ is independent of $\boldsymbol{\Upsilon}_{i_\Upsilon}$. Hence, $\mathrm{E}\,\boldsymbol{\Upsilon}_{i_\Upsilon}\mathbf{w}_{i_B-1}^o = \mathrm{E}\,\boldsymbol{\Upsilon}_{i_\Upsilon}\,\mathrm{E}\,\mathbf{w}_{i_B-1}^o$.

Then by applying Assumption 5 - 6 to (9.A.3) we obtain

$$\mathrm{E}\,\tilde{\mathbf{w}}_{i_B} = w^o - \mathrm{E}\,\boldsymbol{\Upsilon}_{i_\Upsilon}\,\mathrm{E}\,\mathbf{w}_{i_B-1}^o + \mathrm{E}\,\boldsymbol{\Upsilon}_{i_\Upsilon}\,\mathrm{E}\,\tilde{\mathbf{w}}_{i_B-1} - \mathrm{E}\,\mathbf{P}_{i_B}\,\mathrm{E}\,\tilde{\mathbf{w}}_{i_B-1} + \mathrm{E}\,\mathbf{P}_{i_B}\,\mathrm{E}(1-\chi)(w^o - \mathbf{w}_{i_B-1}^o) - \mathrm{E}\,\boldsymbol{\mu}_{i_\mu}\breve{w}. \tag{9.A.9}$$

Finally, applying LEM assumption (9.2.1b) again gives

$$\boxed{\mathrm{E}\,\tilde{\mathbf{w}}_{i_B} = \mathrm{E}\big(\boldsymbol{\Upsilon}_{i_\Upsilon} - \mathbf{P}_{i_B}\big)\,\mathrm{E}\,\tilde{\mathbf{w}}_{i_B-1} + \big(\mathrm{I} - \mathrm{E}(\boldsymbol{\Upsilon}_{i_\Upsilon})\big)w^o - \mathrm{E}\,\boldsymbol{\mu}_{i_\mu}\breve{w}.} \tag{9.A.10}$$

Furthermore, by introducing the state-space mean weight-error vector transition matrix $\mathbf{M}_{i_B} \in \mathbb{K}^{M\times M}$ that we define by

$$\begin{aligned}\mathbf{M}_{i_B} &\triangleq \boldsymbol{\Upsilon}_{i_\Upsilon} - \mathbf{P}_{i_B} \\ &= \mathrm{I} - \boldsymbol{\mu}_{i_\mu}\big(\boldsymbol{\alpha}_{i_\alpha} + \boldsymbol{X}_i^*\boldsymbol{\gamma}_{i_{\gamma\otimes K}}\boldsymbol{X}_i + \boldsymbol{\Pi}_{i_\Pi} + \boldsymbol{\epsilon}_{i_\epsilon}^{-1}\mathbf{U}_i^*(W_{e\otimes K}^{-1} + \mathbf{U}_i\boldsymbol{\epsilon}_{i_\epsilon}^{-1}\mathbf{U}_i^*)^{-1}\big)\mathbf{U}_i\end{aligned} \tag{9.A.11}$$

and by insertion of the leakage-weight regularization matrix (9.3.19) in (9.A.10) gives

$$\boxed{\mathrm{E}\,\tilde{\mathbf{w}}_{i_B} = \mathrm{E}\,\mathbf{M}_{i_B}\,\mathrm{E}\,\tilde{\mathbf{w}}_{i_B-1} + \mathrm{E}\,\boldsymbol{\Upsilon}'_{i_\Upsilon}w^o - \mathrm{E}\,\boldsymbol{\mu}_{i_\mu}\breve{w}.} \tag{9.A.12}$$

For later use we will express the time-evolution of the mean weight-error vector $\mathrm{E}\,\tilde{\mathbf{w}}_{i_B}$ in terms of the mean-value of the optimal weight vector w^o, the transformed weight vector $\breve{w}$ the time-variant state-space mean weight-error vector transition matrix $\mathbf{M}_{i_B}$ and the time-variant step-size matrix $\boldsymbol{\mu}_{i_\mu}$ and the transformed leakage-weight regularization matrix $\boldsymbol{\Upsilon}'_{i_\Upsilon}$.

We will assume that $\mathbf{w}_{-1} = w^0$, where w^0 denotes the initial (guessed) weight vector defined in subsection 8.5.8 on page 395. Therefore by LEM assumption (9.2.1b) and (9.2.1d), $\mathrm{E}\,\tilde{\mathbf{w}}_{-1} =$

[7] An apparent paradox is that for the cost function $J^{e^2}(w_{i_B})$ the Wiener-Hopf (WH) solution is $\mathbf{w}_{i_B}^o = R_{u,i}^{-1}R_{du,i}$. This, however, suggests that $\mathbf{w}_{i_B}^o$ is explicitly dependent on $\mathbf{u}_i$. This might be explained by the *current* regressor $\mathbf{u}_i$ involved in $\mathbf{P}_{i_B}$ being independent of the *previous* perturbation vector $\boldsymbol{\theta}_{i_B-1}$.

$w^o - w^0$. Then by induction of (9.A.12) we obtain

$$
\begin{aligned}
\mathrm{E}\,\tilde{\mathbf{w}}_{-1} &= w^o - w^0 \\
\mathrm{E}\,\tilde{\mathbf{w}}_0 &= \mathrm{E}\,\mathbf{M}_0(w^o - w^0) + \mathrm{E}\,\boldsymbol{\Upsilon}'_{i_\Upsilon^0} w^o - \mathrm{E}\,\boldsymbol{\mu}_{i_\mu^0}\breve{w} \\
\mathrm{E}\,\tilde{\mathbf{w}}_1 &= \mathrm{E}\,\mathbf{M}_1\big(\mathrm{E}\,\mathbf{M}_0(w^o - w^0) + \mathrm{E}\,\boldsymbol{\Upsilon}'_{i_\Upsilon^0} w^o - \mathrm{E}\,\boldsymbol{\mu}_{i_\mu^0}\breve{w}\big) + \mathrm{E}\,\boldsymbol{\Upsilon}'_{i_\Upsilon^1} w^o - \mathrm{E}\,\boldsymbol{\mu}_{i_\mu^1}\breve{w} \\
\mathrm{E}\,\tilde{\mathbf{w}}_2 &= \mathrm{E}\,\mathbf{M}_2\Big(\mathrm{E}\,\mathbf{M}_1\big(\mathrm{E}\,\mathbf{M}_0(w^o - w^0) + \mathrm{E}\,\boldsymbol{\Upsilon}'_{i_\Upsilon^0} w^o - \mathrm{E}\,\boldsymbol{\mu}_{i_\mu^0}\breve{w}\big) + \mathrm{E}\,\boldsymbol{\Upsilon}'_{i_\Upsilon^1} w^o - \mathrm{E}\,\boldsymbol{\mu}_{i_\mu^1}\breve{w}\Big) + \mathrm{E}\,\boldsymbol{\Upsilon}'_{i_\Upsilon^2} w^o - \mathrm{E}\,\boldsymbol{\mu}_{i_\mu^2}\breve{w} \\
&\vdots = \vdots \\
\mathrm{E}\,\tilde{\mathbf{w}}_{i_B} &= \left[\prod_{j=0}^{i_B} \mathrm{E}\,\mathbf{M}_j\right](w^o - w^0) + \left[\sum_{j=1}^{i_B}\left(\left[\prod_{j'=j}^{i_B} \mathrm{E}\,\mathbf{M}_{j'}\right]\mathrm{E}\,\boldsymbol{\Upsilon}'_{i_\Upsilon^{j-1}}\right) + \mathrm{E}\,\boldsymbol{\Upsilon}'_{i_\Upsilon^{i_B}}\right] w^o \\
&\quad - \left[\sum_{j=1}^{i_B}\left(\left[\prod_{j'=j}^{i_B} \mathrm{E}\,\mathbf{M}_{j'}\right]\mathrm{E}\,\boldsymbol{\mu}_{i_\mu^{j-1}}\right) + \mathrm{E}\,\boldsymbol{\mu}_{i_\mu^{i_B}}\right]\breve{w} \\
&= C_{i_B}^{w^o} w^o - C_{i_B}^{w^o,1} w^0 - C_{i_B}^{\breve{w}}\breve{w},
\end{aligned}
\tag{9.A.13}
$$

where we let $C_{i_B}^{w^o} \in \mathbb{K}^{M\times M}$ denote the time evolution matrix for the mean optimal weight vector and similarly let $C_{i_B}^{\breve{w}} \in \mathbb{K}^{M\times M}$ denote the time evolution matrix for the regularized weight vector. The time evolution matrices $C_{i_B}^{w^o}$ and $C_{i_B}^{\breve{w}}$ are in turn are defined by

$$
\begin{aligned}
C_{i_B}^{w^o} &\triangleq \prod_{j=0}^{i_B} \mathrm{E}\,\mathbf{M}_j + \sum_{j=1}^{i_B}\left(\left[\prod_{j'=j}^{i_B} \mathrm{E}\,\mathbf{M}_{j'}\right]\mathrm{E}\,\boldsymbol{\Upsilon}'_{i_\Upsilon^{j-1}}\right) + \mathrm{E}\,\boldsymbol{\Upsilon}'_{i_\Upsilon^{i_B}} && \text{(9.A.14a)} \\
&= C_{i_B}^{w^o,1} + C_{i_B}^{w^o,2} + C_{i_B}^{w^o,3} && \text{(9.A.14b)} \\
C_{i_B}^{\breve{w}} &\triangleq \sum_{j=1}^{i_B}\left(\left[\prod_{j'=j}^{i_B} \mathrm{E}\,\mathbf{M}_{j'}\right]\mathrm{E}\,\boldsymbol{\mu}_{i_\mu^{j-1}}\right) + \mathrm{E}\,\boldsymbol{\mu}_{i_\mu^{i_B}} && \text{(9.A.14c)} \\
&= C_{i_B}^{\breve{w},(2)} + C_{i_B}^{\breve{w},(3)} && \text{(9.A.14d)}
\end{aligned}
$$

and where i_μ^j is the step-size parameter update iteration number at block time j and i_Υ^j similarly is the transformed weight leakage factor update iteration number at block time j. The time evolution matrices $C_{i_B}^{w^o}$ and $C_{i_B}^{\breve{w}}$ can easily be determined recursively $i_B \geq 0$ from

$$C_{i_B}^{w^o,1} \triangleq \prod_{j=0}^{i_B} \mathrm{E}\,\mathbf{M}_j = \mathrm{E}\,\mathbf{M}_{i_B} C_{i_B-1}^{w^o,1}, \quad C_{-1}^{w^o,1} = \mathrm{I}, \tag{9.A.15a}$$

$$C_{i_B}^{w^o,2} \triangleq \sum_{j=1}^{i_B} \left(\left[\prod_{j'=j}^{i_B} \mathrm{E}\,\mathbf{M}_{j'} \right] \mathrm{E}\,\boldsymbol{\Upsilon}'_{i_\Upsilon^{j-1}} \right) = \mathrm{E}\,\mathbf{M}_{i_B} C_{i_B-1}^{w^o,2}, \quad C_{-1}^{w^o,2} = \mathrm{I}, \tag{9.A.15b}$$

$$C_{i_B}^{w^o,3} \triangleq \mathrm{E}\,\boldsymbol{\Upsilon}'_{i_\Upsilon^{i_B}} \tag{9.A.15c}$$

$$C_{i_B}^{\breve{w},2} \triangleq \sum_{j=1}^{i_B} \left(\left[\prod_{j'=j}^{i_B} \mathrm{E}\,\mathbf{M}_{j'} \right] \mathrm{E}\,\boldsymbol{\mu}_{i_\mu^{j-1}} \right) = \mathrm{E}\,\mathbf{M}_{i_B} C_{i_B-1}^{\breve{w},2}, \quad C_{-1}^{\breve{w},2} = \mathrm{I}, \tag{9.A.15d}$$

$$C_{i_B}^{\breve{w},3} \triangleq \mathrm{E}\,\boldsymbol{\mu}_{i_\mu^{i_B}}. \tag{9.A.15e}$$

9.A.2 Transient Analysis of MC-$\alpha\gamma\Pi\epsilon$-APA, Weighted Energy Relation, Derivations

By equating the weighted norm of both sides of the weight-error recursion (9.3.11), for some arbitrary Hermitian positive-definite weighting matrix $\Sigma \in \mathbb{K}^{M\times M}$ gives

$$\|\tilde{\mathbf{w}}_{i_B}\|_\Sigma^2 = \|\tilde{\mathbf{w}}_{i_B-1}^{'\Upsilon} - \mathbf{P}'_{i_B}\mathbf{E}_{a,i} - \mathbf{P}'_{i_B}\mathbf{V}_i - \boldsymbol{\mu}_{i_\mu}\breve{w}\|_\Sigma^2. \tag{9.A.16}$$

Now introducing the auxiliary matrix $\mathbf{A}_{i_B}^\Sigma \in \mathbb{K}^{KN_e\times KN_e}$ defined by

$$\mathbf{A}_{i_B}^\Sigma = \mathbf{P}_{i_B}^{'*}\Sigma\mathbf{P}'_{i_B} \tag{9.A.17}$$

and inserting in (9.A.16) gives

$$\begin{aligned}\|\tilde{\mathbf{w}}_{i_B}\|_\Sigma^2 = {} & \|\tilde{\mathbf{w}}_{i_B-1}^{'\Upsilon}\|_\Sigma^2 + \|\boldsymbol{\mu}_{i_\mu}\breve{w}\|_\Sigma^2 \\ & - 2\Re\Big\{\tilde{\mathbf{w}}_{i_B-1}^{'\Upsilon *}\Sigma\mathbf{P}_{i_B}\mathbf{E}_{a,i}\Big\} - 2\Re\Big\{\tilde{\mathbf{w}}_{i_B-1}^{'\Upsilon *}\Sigma\boldsymbol{\mu}_{i_\mu}\breve{w}\Big\} + 2\Re\Big\{\mathbf{E}_{a,i}^*\mathbf{P}_{i_B}^*\Sigma\boldsymbol{\mu}_{i_\mu}\breve{w}\Big\} \\ & + \mathbf{E}_{a,i}^*\mathbf{A}_{i_B}^\Sigma\mathbf{E}_{a,i} + \mathbf{V}_i^*\mathbf{A}_{i_B}^\Sigma\mathbf{V}_i - 2\Re\Big\{\mathbf{V}_i^*\mathbf{P}_{i_B}^{'*}\Sigma\Big(\tilde{\mathbf{w}}_{i_B-1}^{'\Upsilon} - \mathbf{P}_{i_B}\mathbf{E}_{a,i} - \boldsymbol{\mu}_{i_\mu}\breve{w}\Big)\Big\}.\end{aligned} \tag{9.A.18}$$

On the RHS of (9.A.18) we find both the *a priori* error $\mathbf{E}_{a,i}$ and the leakage-transformed modified weight-error vector $\tilde{\mathbf{w}}_{i_B-1}^{'\Upsilon}$. However, both of these quantities were directly related to weight-error vector $\tilde{\mathbf{w}}_{i_B-1}$ in section 9.3 on page 427. Then by insertion of (9.3.12) and (9.3.14) into

(9.A.18) the expression becomes

$$
\begin{aligned}
\|\tilde{\mathbf{w}}_{i_B}\|_{\Sigma}^2 = {} & \|\boldsymbol{\Upsilon}_{i_\Upsilon}^{\chi}\mathbf{w}_{i_B-1}^{o} + \bar{\mathbf{q}}_{i_B} + \boldsymbol{\Upsilon}_{i_\Upsilon}\tilde{\mathbf{w}}_{i_B-1}\|_{\Sigma}^2 + \|\boldsymbol{\mu}_{i_\mu}\breve{w}\|_{\Sigma}^2 \\
& - 2\Re\Big\{\big(\mathbf{w}_{i_B-1}^{o*}(\chi^*\mathrm{I} - \boldsymbol{\Upsilon}_{i_\Upsilon}^{*}) + \bar{\mathbf{q}}_{i_B}^{*} + \tilde{\mathbf{w}}_{i_B-1}^{*}\boldsymbol{\Upsilon}_{i_\Upsilon}^{*}\big)\Sigma\mathbf{P}_{i_B}\big(\tilde{\mathbf{w}}_{i_B-1} + \bar{\mathbf{q}}_{i_B} - (1-\chi)\mathbf{w}_{i_B-1}^{o}\big)\Big\} \\
& - 2\Re\Big\{\big(\mathbf{w}_{i_B-1}^{o*}(\chi^*\mathrm{I} - \boldsymbol{\Upsilon}_{i_\Upsilon}^{*}) + \bar{\mathbf{q}}_{i_B}^{*} + \tilde{\mathbf{w}}_{i_B-1}^{*}\boldsymbol{\Upsilon}_{i_\Upsilon}^{*}\big)\Sigma\boldsymbol{\mu}_{i_\mu}\breve{w}\Big\} \\
& + 2\Re\Big\{\big(\tilde{\mathbf{w}}_{i_B-1} + \bar{\mathbf{q}}_{i_B} - (1-\chi)\mathbf{w}_{i_B-1}^{o}\big)^{*}\mathbf{P}_{i_B}^{*}\Sigma\boldsymbol{\mu}_{i_\mu}\breve{w}\Big\} \\
& + \big(\tilde{\mathbf{w}}_{i_B-1} + \bar{\mathbf{q}}_{i_B} - (1-\chi)\mathbf{w}_{i_B-1}^{o}\big)^{*}\mathbf{U}_i^{*}\mathbf{A}_{i_B}^{\Sigma}\mathbf{U}_i\big(\tilde{\mathbf{w}}_{i_B-1} + \bar{\mathbf{q}}_{i_B} - (1-\chi)\mathbf{w}_{i_B-1}^{o}\big) + \mathbf{V}_i^{*}\mathbf{A}_{i_B}^{\Sigma}\mathbf{V}_i \\
& - 2\Re\Big\{\mathbf{V}_i^{*}\mathbf{P}_{i_B}^{\prime *}\Sigma\Big(\boldsymbol{\Upsilon}_{i_\Upsilon}^{\chi}\mathbf{w}_{i_B-1}^{o} + \bar{\mathbf{q}}_{i_B} + \boldsymbol{\Upsilon}_{i_\Upsilon}\tilde{\mathbf{w}}_{i_B-1} \\
& \qquad - \mathbf{P}_{i_B}\big(\tilde{\mathbf{w}}_{i_B-1} + \bar{\mathbf{q}}_{i_B} - (1-\chi)\mathbf{w}_{i_B-1}^{o}\big) - \boldsymbol{\mu}_{i_\mu}\breve{w}\Big)\Big\}.
\end{aligned}
\tag{9.A.19}
$$

Finally, by collecting the various weighted norms of $\tilde{\mathbf{w}}_{i_B-1}, \mathbf{w}_{i_B-1}^{o}$ and $\bar{\mathbf{q}}_{i_B}$ into one term each using the *superposition principle* (9.1.12a) and the *linear transformation* property (9.1.12g), we get

$$
\begin{aligned}
\|\tilde{\mathbf{w}}_{i_B}\|_{\Sigma}^2 = {} & \|\tilde{\mathbf{w}}_{i_B-1}\|_{\boldsymbol{\Sigma}_{i_B}^{\Upsilon}}^2 + \|\bar{\mathbf{q}}_{i_B}\|_{\boldsymbol{\Sigma}_{i_B}^{q}}^2 + \|\mathbf{w}_{i_B-1}^{o}\|_{\boldsymbol{\Sigma}_{i_B}^{o}}^2 + \|\boldsymbol{\mu}_{i_\mu}\breve{w}\|_{\Sigma}^2 \\
& + 2\Re\big\{\mathbf{w}_{i_B-1}^{o*}\boldsymbol{\Upsilon}_{i_\Upsilon}^{\chi *}\Sigma\boldsymbol{\Upsilon}_{i_\Upsilon}\tilde{\mathbf{w}}_{i_B-1}\big\} \\
& + 2\Re\big\{\mathbf{w}_{i_B-1}^{o*}\boldsymbol{\Upsilon}_{i_\Upsilon}^{\chi *}\Sigma\bar{\mathbf{q}}_{i_B}\big\} \\
& + 2\Re\big\{\bar{\mathbf{q}}_{i_B}^{*}\Sigma\boldsymbol{\Upsilon}_{i_\Upsilon}\tilde{\mathbf{w}}_{i_B-1}\big\} \\
& - 2\Re\Big\{\mathbf{w}_{i_B-1}^{o*}\boldsymbol{\Upsilon}_{i_\Upsilon}^{\chi *}\Sigma\mathbf{P}_{i_B}\big(\tilde{\mathbf{w}}_{i_B-1} + \bar{\mathbf{q}}_{i_B}\big)\Big\} \\
& - 2\Re\Big\{\bar{\mathbf{q}}_{i_B}^{*}\Sigma\mathbf{P}_{i_B}\big(\tilde{\mathbf{w}}_{i_B-1} - (1-\chi)\mathbf{w}_{i_B-1}^{o}\big)\Big\} \\
& - 2\Re\Big\{\tilde{\mathbf{w}}_{i_B-1}^{*}\boldsymbol{\Upsilon}_{i_\Upsilon}^{*}\Sigma\mathbf{P}_{i_B}\big(\bar{\mathbf{q}}_{i_B} - (1-\chi)\mathbf{w}_{i_B-1}^{o}\big)\Big\} \\
& - 2\Re\Big\{\big(\mathbf{w}_{i_B-1}^{o*}\boldsymbol{\Upsilon}_{i_\Upsilon}^{\chi *} + \bar{\mathbf{q}}_{i_B}^{*} + \tilde{\mathbf{w}}_{i_B-1}^{*}\boldsymbol{\Upsilon}_{i_\Upsilon}^{*}\big)\Sigma\boldsymbol{\mu}_{i_\mu}\breve{w}\Big\} \\
& + 2\Re\Big\{(\tilde{\mathbf{w}}_{i_B-1}^{*} + \bar{\mathbf{q}}_{i_B}^{*} - (1-\chi^*)\mathbf{w}_{i_B-1}^{o*})\mathbf{P}_{i_B}^{*}\Sigma\boldsymbol{\mu}_{i_\mu}\breve{w}\Big\} \\
& + \tilde{\mathbf{w}}_{i_B-1}^{*}\mathbf{P}_{i_B}^{*}\Sigma\mathbf{P}_{i_B}\big(\bar{\mathbf{q}}_{i_B} - (1-\chi)\mathbf{w}_{i_B-1}^{o}\big) \\
& + \bar{\mathbf{q}}_{i_B}^{*}\mathbf{P}_{i_B}^{*}\Sigma\mathbf{P}_{i_B}\big(\tilde{\mathbf{w}}_{i_B-1} - (1-\chi)\mathbf{w}_{i_B-1}^{o}\big) \\
& - (1-\chi^*)\mathbf{w}_{i_B-1}^{o*}\mathbf{P}_{i_B}^{*}\Sigma\mathbf{P}_{i_B}\big(\tilde{\mathbf{w}}_{i_B-1} + \bar{\mathbf{q}}_{i_B}\big) \\
& + \mathbf{V}_i^{*}\mathbf{A}_{i_B}^{\Sigma}\mathbf{V}_i \\
& - 2\Re\Big\{\mathbf{V}_i^{*}\mathbf{P}_{i_B}^{\prime *}\Sigma\Big(\boldsymbol{\Upsilon}_{i_\Upsilon}^{\chi}\mathbf{w}_{i_B-1}^{o} + \bar{\mathbf{q}}_{i_B} + \boldsymbol{\Upsilon}_{i_\Upsilon}\tilde{\mathbf{w}}_{i_B-1} \\
& \qquad - \mathbf{P}_{i_B}\big(\tilde{\mathbf{w}}_{i_B-1} + \bar{\mathbf{q}}_{i_B} - (1-\chi)\mathbf{w}_{i_B-1}^{o}\big) - \boldsymbol{\mu}_{i_\mu}\breve{w}\Big)\Big\},
\end{aligned}
\tag{9.A.20}
$$

where $\boldsymbol{\Sigma}_{i_B}^{\Upsilon} \in \mathbb{K}^{M\times M}$ represents the *stochastic* weight-error vector weighting matrix, $\boldsymbol{\Sigma}_{i_B}^{o} \in$

$\mathbb{K}^{M\times M}$ denotes the *stochastic* optimal weight vector weighting matrix and $\mathbf{\Sigma}^{\bar{q}}_{i_B} \in \mathbb{K}^{M\times M}$ denotes the *stochastic* random walk weight vector weighting matrix. They are defined by

$$\mathbf{\Sigma}^{\Upsilon}_{i_B} \triangleq \mathbf{\Upsilon}^{*}_{i_\Upsilon}\Sigma\mathbf{\Upsilon}_{i_\Upsilon} - \mathbf{\Upsilon}^{*}_{i_\Upsilon}\Sigma\mathbf{P}_{i_B} - \mathbf{P}^{*}_{i_B}\Sigma\mathbf{\Upsilon}_{i_\Upsilon} + \mathbf{P}^{*}_{i_B}\Sigma\mathbf{P}_{i_B} \tag{9.A.21a}$$

$$\mathbf{\Sigma}^{o}_{i_B} \triangleq \mathbf{\Upsilon}^{\chi *}_{i_\Upsilon}\Sigma\mathbf{\Upsilon}^{\chi}_{i_\Upsilon} + (1-\chi)\mathbf{\Upsilon}^{\chi *}_{i_\Upsilon}\Sigma\mathbf{P}_{i_B} + (1-\chi^{*})\mathbf{P}^{*}_{i_B}\Sigma\mathbf{\Upsilon}^{\chi}_{i_\Upsilon} + |1-\chi|^2\mathbf{P}^{*}_{i_B}\Sigma\mathbf{P}_{i_B} \tag{9.A.21b}$$

$$\mathbf{\Sigma}^{\bar{q}}_{i_B} \triangleq \Sigma - \Sigma\mathbf{P}_{i_B} - \mathbf{P}^{*}_{i_B}\Sigma + \mathbf{P}^{*}_{i_B}\Sigma\mathbf{P}_{i_B}. \tag{9.A.21c}$$

9.A.3 Transient Analysis of MC-$\alpha\gamma\Pi\epsilon$-APA, Weighted Variance Relation, Derivations

In order to obtain an expression for the time-evolution of the expected weighted energy norm of the weight-error vector, that is, $\mathrm{E}\|\tilde{\mathbf{w}}_{i_B}\|^2_{\Sigma}$ for some choice of Σ we proceed by taking the expectation on both sides of (9.A.20) to obtain

$$\begin{aligned}
\mathrm{E}\|\tilde{\mathbf{w}}_{i_B}\|^2_{\Sigma} = {} & \mathrm{E}\|\tilde{\mathbf{w}}_{i_B-1}\|^2_{\mathbf{\Sigma}^{\Upsilon}_{i_B}} + \mathrm{E}\|\mathbf{q}_{i_B}\|^2_{\mathrm{E}\,\mathbf{\Sigma}^{\bar{q}}_{i_B}} + |1-\chi|^2\|w^o\|^2_{\mathrm{E}\,\mathbf{\Sigma}^{\bar{q}}_{i_B}} + \mathrm{E}\|\mathbf{w}^{o}_{i_B-1}\|^2_{\mathbf{\Sigma}^{o}_{i_B}} + \mathrm{E}\|\boldsymbol{\mu}_{i_\mu}\breve{w}\|^2_{\Sigma} \\
& + 2\,\mathrm{E}\,\Re\big\{\mathbf{w}^{o*}_{i_B-1}\mathbf{\Upsilon}^{\chi *}_{i_\Upsilon}\Sigma\mathbf{\Upsilon}_{i_\Upsilon}\tilde{\mathbf{w}}_{i_B-1}\big\} \\
& + 2\,\mathrm{E}\,\Re\big\{\mathbf{w}^{o*}_{i_B-1}\mathbf{\Upsilon}^{\chi *}_{i_\Upsilon}\Sigma(1-\chi)w^{o}\big\} \\
& + 2\,\mathrm{E}\,\Re\big\{(1-\chi^{*})w^{o*}\Sigma\mathbf{\Upsilon}_{i_\Upsilon}\tilde{\mathbf{w}}_{i_B-1}\big\} \\
& - 2\,\mathrm{E}\,\Re\Big\{\mathbf{w}^{o*}_{i_B-1}\mathbf{\Upsilon}^{\chi *}_{i_\Upsilon}\Sigma\mathbf{P}_{i_B}\big(\tilde{\mathbf{w}}_{i_B-1} + (1-\chi)w^{o}\big)\Big\} \\
& - 2\,\mathrm{E}\,\Re\Big\{(1-\chi^{*})w^{o*}\Sigma\mathbf{P}_{i_B}\big(\tilde{\mathbf{w}}_{i_B-1} - (1-\chi)\mathbf{w}^{o}_{i_B-1}\big)\Big\} \\
& - 2\,\mathrm{E}\,\Re\Big\{\tilde{\mathbf{w}}^{*}_{i_B-1}\mathbf{\Upsilon}^{*}_{i_\Upsilon}\Sigma\mathbf{P}_{i_B}(1-\chi)(w^{o} - \mathbf{w}^{o}_{i_B-1})\Big\} \\
& - 2\,\mathrm{E}\,\Re\Big\{\big(\mathbf{w}^{o*}_{i_B-1}\mathbf{\Upsilon}^{\chi *}_{i_\Upsilon} + (1-\chi^{*})w^{o*} + \tilde{\mathbf{w}}^{*}_{i_B-1}\mathbf{\Upsilon}^{*}_{i_\Upsilon}\big)\Sigma\boldsymbol{\mu}_{i_\mu}\breve{w}\Big\} \\
& + 2\,\mathrm{E}\,\Re\Big\{(\tilde{\mathbf{w}}^{*}_{i_B-1} + (1-\chi^{*})w^{o*} - (1-\chi^{*})\mathbf{w}^{o*}_{i_B-1})\mathbf{P}^{*}_{i_B}\Sigma\boldsymbol{\mu}_{i_\mu}\breve{w}\Big\} \\
& + \mathrm{E}\,\tilde{\mathbf{w}}^{*}_{i_B-1}\mathbf{P}^{*}_{i_B}\Sigma\mathbf{P}_{i_B}(1-\chi)(w^{o} - \mathbf{w}^{o}_{i_B-1}) \\
& + \mathrm{E}(1-\chi^{*})w^{o*}\mathbf{P}^{*}_{i_B}\Sigma\mathbf{P}_{i_B}\big(\tilde{\mathbf{w}}_{i_B-1} - (1-\chi)\mathbf{w}^{o}_{i_B-1}\big) \\
& - \mathrm{E}(1-\chi^{*})\mathbf{w}^{o*}_{i_B-1}\mathbf{P}^{*}_{i_B}\Sigma\mathbf{P}_{i_B}\big(\tilde{\mathbf{w}}_{i_B-1} + (1-\chi)w^{o}\big) + K\sigma_v^2\,\mathrm{Tr}\,\{\mathrm{E}\,\mathbf{A}^{\Sigma}_{i_B}\}.
\end{aligned} \tag{9.A.22}$$

Here we have used that the last term in (9.A.20) cancels upon expectation by the LEM assumptions on system noise (9.2.1d) and (9.2.1g) and that by applying assumptions (9.2.1e) and (9.2.1g) and using Proposition 9.1 (9.1.2) and (9.2.4) results in $\mathrm{E}\,\mathbf{V}^{*}_{i}\mathbf{A}^{\Sigma}_{i_B}\mathbf{V}_i = \mathrm{Tr}\,\{\sigma_V^2\,\mathrm{E}\,\mathbf{A}^{\Sigma}_{i_B}\} = K\sigma_v^2\,\mathrm{Tr}\,\{\mathrm{E}\,\mathbf{A}^{\Sigma}_{i_B}\}$. Moreover, in (9.A.22) we have used that (9.3.13) and LEM assumptions on non-stationarity (9.2.1b) and (9.2.1d) and the *independence* property of the weighted norm (9.1.12d) lead to $\mathrm{E}\,\bar{q}_{i_B} = (1-\chi)w^{o}$ and $\mathrm{E}\|\bar{\mathbf{q}}_{i_B}\|^2_{\mathbf{\Sigma}^{q}_{i_B}} = \mathrm{E}\|\mathbf{q}_{i_B}\|^2_{\mathrm{E}\,\mathbf{\Sigma}^{\bar{q}}_{i_B}} + |1-\chi|^2\|w^{o}\|^2_{\mathrm{E}\,\mathbf{\Sigma}^{\bar{q}}_{i_B}}$.

From inspection of (9.A.22) we appreciate that in order to describe the transient mean-square behavior of the MC-$\alpha\gamma\Pi\epsilon$-APA adaptive filter we need to evaluate all the moments in Table 9.1.

From the discussion in subsection 9.A.1 on page 453 we saw that the random sequences $\mathbf{\Upsilon}_{i_\Upsilon}$ and $\mathbf{P}_{i_B}$ themselves involve moments of order four and seven respectively. Hence, a term

$\mathrm{E}\,\mathbf{w}_{i_B-1}^{o*}\Sigma\boldsymbol{\Upsilon}_{i_\Upsilon}\tilde{\mathbf{w}}_{i_B-1}$	$\mathrm{E}\,\mathbf{w}_{i_B-1}^{o*}\boldsymbol{\Upsilon}_{i_\Upsilon}^{*}\Sigma\boldsymbol{\Upsilon}_{i_\Upsilon}\tilde{\mathbf{w}}_{i_B-1}$	$\mathrm{E}\,\mathbf{w}_{i_B-1}$	$\mathrm{E}\,\boldsymbol{\Upsilon}_{i_\Upsilon}\mathbf{w}_{i_B-1}^{o}$
$\mathrm{E}\,\boldsymbol{\Upsilon}_{i_\Upsilon}\tilde{\mathbf{w}}_{i_B-1}$	$\mathrm{E}\,\mathbf{w}_{i_B-1}^{o*}\Sigma\mathbf{P}_{i_B}$	$\mathrm{E}\,\mathbf{w}_{i_B-1}^{o*}\boldsymbol{\Upsilon}_{i_\Upsilon}^{*}\Sigma\mathbf{P}_{i_B}$	$\mathrm{E}\,\mathbf{w}_{i_B-1}^{o*}\Sigma\mathbf{P}_{i_B}\tilde{\mathbf{w}}_{i_B-1}$
$\mathrm{E}\,\mathbf{w}_{i_B-1}^{o*}\boldsymbol{\Upsilon}_{i_\Upsilon}^{*}\Sigma\mathbf{P}_{i_B}\tilde{\mathbf{w}}_{i_B-1}$	$\mathrm{E}\,\mathbf{P}_{i_B}\tilde{\mathbf{w}}_{i_B-1}$	$\mathrm{E}\,\mathbf{P}_{i_B}\mathbf{w}_{i_B-1}^{o}$	$\mathrm{E}\,\tilde{\mathbf{w}}_{i_B-1}^{*}\boldsymbol{\Upsilon}_{i_\Upsilon}^{*}\Sigma\mathbf{P}_{i_B}$
$\mathrm{E}\,\tilde{\mathbf{w}}_{i_B-1}^{*}\boldsymbol{\Upsilon}_{i_\Upsilon}^{*}\Sigma\mathbf{P}_{i_B}\mathbf{w}_{i_B-1}^{o}$	$\mathrm{E}\,\boldsymbol{\mu}_{i_\mu}$	$\mathrm{E}\,\mathbf{w}_{i_B-1}^{o*}\boldsymbol{\Upsilon}_{i_\Upsilon}^{*}\Sigma\boldsymbol{\mu}_{i_\mu}$	$\mathrm{E}\,\tilde{\mathbf{w}}_{i_B-1}^{*}\boldsymbol{\Upsilon}_{i_\Upsilon}^{*}\Sigma\boldsymbol{\mu}_{i_\mu}$
$\mathrm{E}\,\mathbf{P}_{i_B}^{*}\Sigma\boldsymbol{\mu}_{i_\mu}$	$\mathrm{E}\,\tilde{\mathbf{w}}_{i_B-1}^{*}\mathbf{P}_{i_B}^{*}\Sigma\boldsymbol{\mu}_{i_\mu}$	$\mathrm{E}\,\mathbf{w}_{i_B-1}^{o*}\mathbf{P}_{i_B}^{*}\Sigma\boldsymbol{\mu}_{i_\mu}$	$\mathrm{E}\,\mathbf{w}_{i_B-1}^{*}\mathbf{P}_{i_B}^{*}\Sigma\mathbf{P}_{i_B}$
$\mathrm{E}\,\tilde{\mathbf{w}}_{i_B-1}^{*}\mathbf{P}_{i_B}^{*}\Sigma\mathbf{P}_{i_B}\mathbf{w}_{i_B-1}^{o}$	$\mathrm{E}\,\mathbf{P}_{i_B}^{*}\Sigma\mathbf{P}_{i_B}\tilde{\mathbf{w}}_{i_B-1}$	$\mathrm{E}\,\mathbf{P}_{i_B}^{*}\Sigma\mathbf{P}_{i_B}\mathbf{w}_{i_B-1}^{o}$	$\mathbf{P}_{i_B}^{\prime *}\Sigma\mathbf{P}_{i_B}^{\prime}$
$\mathrm{E}\,\tilde{\mathbf{w}}_{i_B-1}^{*}\boldsymbol{\Sigma}_{i_B}^{\Upsilon}\tilde{\mathbf{w}}_{i_B-1}$	$\mathrm{E}\,\boldsymbol{\Sigma}_{i_B}^{q}$	$\mathrm{E}\,\mathbf{w}_{i_B-1}^{o*}\boldsymbol{\Sigma}_{i_B}^{o}\mathbf{w}_{i_B-1}^{o}$	$\mathrm{E}\,\boldsymbol{\mu}_{i_\mu}^{*}\Sigma\boldsymbol{\mu}_{i_\mu}$

Tab. 9.1: MC-$\alpha\gamma\Pi\epsilon$-APA mean-square weight-error vector update moments.

like $\mathrm{E}\,\tilde{\mathbf{w}}_{i_B-1}^{*}\mathbf{P}_{i_B}^{*}\Sigma\mathbf{P}_{i_B}\mathbf{w}_{i_B-1}^{o}$ involves a sixteen order moment. In conclusion the recursion for $\mathrm{E}\|\tilde{\mathbf{w}}_{i_B}\|_{\Sigma}^{2}$ in (9.A.22) is in the general case exceedingly difficult to propagate.

Moreover, the propagation of the recursion for $\mathrm{E}\|\tilde{\mathbf{w}}_{i_B}\|_{\Sigma}^{2}$ in (9.A.22) is complicated by the presence of the expectation operator. This expectation is difficult to evaluate as the weighting-function, that is, $\boldsymbol{\Sigma}_{i_B}^{\Upsilon}$ itself is a RS that depends on $\mathbf{U}_i$ viz. (9.3.10) and due to the dependence of $\tilde{\mathbf{w}}_{i_B-1}$ on previous regressors $\mathbf{U}_{i-1}, \mathbf{U}_{i-2}, \ldots$ (9.3.8) which means that $\tilde{\mathbf{w}}_{i_B-1}$ and $\boldsymbol{\Sigma}_{i_B}^{\Upsilon}$ themselves are dependent, but not *if* $\mathbf{U}_i$ is i.i.d.. At this stage we might therefore be tempted to enforce the famous *independence assumption* viz. Assumption 2. However, although this assumption is *sufficient* it is by far not *necessary* here. Hence, by inspection of (9.A.21a) we see that the auxiliary matrix $\mathbf{P}_{i_B}$ defined in (9.3.10c) as well as the transformed leakage matrix $\boldsymbol{\Upsilon}_{i_\Upsilon}$ defined in (9.3.6) enter the expression for $\boldsymbol{\Sigma}_{i_B}^{\Upsilon}$. Accordingly, Assumption 5 - 6 are *sufficient* conditions for the ease of the evaluation of the term $\mathrm{E}\|\tilde{\mathbf{w}}_{i_B-1}\|_{\boldsymbol{\Sigma}_{i_B}^{\Upsilon}}^{2}$ that enters (9.A.22). Hence, by applying Assumption 5 - 6, (9.A.6)-(9.A.7) and by using the *independence* property of the weighted norm (9.1.12d) we get $\mathrm{E}\|\tilde{\mathbf{w}}_{i_B-1}\|_{\boldsymbol{\Sigma}_{i_B}^{\Upsilon}}^{2} = \mathrm{E}\|\tilde{\mathbf{w}}_{i_B-1}\|_{\mathrm{E}\,\boldsymbol{\Sigma}_{i_B}^{\Upsilon}}^{2}$.

Moreover, from the expression for $\boldsymbol{\Sigma}_{i_B}^{o}$ (9.A.21b) we observe that by using the *independence* property of the weighted norm (9.1.12d) and Assumption 5, (9.A.6) then the term $\mathrm{E}\|\mathbf{w}_{i_B-1}^{o}\|_{\boldsymbol{\Sigma}_{i_B}^{o}}^{2}$ in (9.A.22) can be evaluated as $\mathrm{E}\|\mathbf{w}_{i_B-1}^{o}\|_{\boldsymbol{\Sigma}_{i_B}^{o}}^{2} = \|\mathbf{w}_{i_B-1}^{o}\|_{\mathrm{E}\,\boldsymbol{\Sigma}_{i_B}^{o}}^{2}$. Similarly, from the expression for $\boldsymbol{\Sigma}_{i_B}^{q}$ (9.A.21c) we appreciate that by using the *independence* property of the weighted norm (9.1.12d) and LEM assumption on non-stationarity (9.2.1c) that the term $\mathrm{E}\|\bar{\mathbf{q}}_{i_B}\|_{\boldsymbol{\Sigma}_{i_B}^{q}}^{2}$ in (9.A.22) can be expressed as $\|\bar{\mathbf{q}}_{i_B}\|_{\mathrm{E}\,\boldsymbol{\Sigma}_{i_B}^{q}}^{2}$.

Although Assumption 5 - 6 enable us to evaluate $\mathrm{E}\|\tilde{\mathbf{w}}_{i_B-1}\|_{\boldsymbol{\Sigma}_{i_B}^{\Upsilon}}^{2}$, $\mathrm{E}\|\mathbf{q}_{i_B}\|_{\mathrm{E}\,\boldsymbol{\Sigma}_{i_B}^{q}}^{2}$ and $\mathrm{E}\|\mathbf{w}_{i_B-1}^{o}\|_{\boldsymbol{\Sigma}_{i_B}^{o}}^{2}$ that enter (9.A.22), however, we will need the two more assumptions in order to reduce the order of the moments in Table 9.1.

Assumption 7 (Independence of $\mathbf{P}_{i_B}, \boldsymbol{\Upsilon}_{i_\Upsilon}$)**.**

The auxiliary matrix $\mathbf{P}_{i_B}$ defined in (9.3.10c) is independent of the transformed leakage matrix $\boldsymbol{\Upsilon}_{i_\Upsilon}$, that is,

$$\forall i_B \geq 0, i_B \geq i_B^{\Upsilon}: \quad f_P(P_{i_B}|\Upsilon_{i_\Upsilon}) = f_P(P_{i_B}), \tag{9.A.23}$$

Assumption 7 holds for example under the conditions ② ③, ④ and ⑤ listed above under Assumption 6.

Assumption 7, (9.A.23) implies that $\mathrm{E}\,\mathbf{P}_{i_B}\boldsymbol{\Upsilon}_{i_\Upsilon} = \mathrm{E}\,\mathbf{P}_{i_B}\,\mathrm{E}\,\boldsymbol{\Upsilon}_{i_\Upsilon}$.

Finally, the presence of weight regularization necessitates the following assumption.

Assumption 8 (Independence of $\boldsymbol{\mu}_{i_\mu}, \mathbf{w}_{i_B-1}^{o}, \tilde{\mathbf{w}}_{i_B-1}, \mathbf{P}_{i_B}$)**.**

The step-size matrix $\boldsymbol{\mu}_{i_\mu}$ is independent of the optimal weight vector $\mathbf{w}^o_{i_B-1}$, the weight-error vector $\tilde{\mathbf{w}}_{i_B-1}$ and the auxiliary matrix $\mathbf{P}_{i_B}$, that is,

$$\forall i_B \geq 0, i_B \geq i_B^{\Upsilon}: \quad f_\mu(\mu_{i_\mu}|w^o_{i_B-1}, \tilde{w}_{i_B-1}, P_{i_B}) = f_\mu(\mu_{i_\mu}), \tag{9.A.24}$$

Now by Assumptions 6-7 $\boldsymbol{\Upsilon}_{i_\Upsilon}$ is independent of $\mathbf{w}^o_{i_B-1}, \tilde{\mathbf{w}}_{i_B-1}, \mathbf{P}_{i_B}$. Then by (9.3.6) we can conclude that Assumption 9.A.24 (9.A.24) holds for example under the conditions ② ③ and ⑤ listed under Assumption 6. It should be remarked that Assumption 6 point ④ is not a *sufficient* condition as the combined dynamic effects of, e.g., $\boldsymbol{\mu}_{i_\mu}$ and $\boldsymbol{\alpha}_{i_\alpha}$ may tends to counter balance each other. Although this effect makes $\boldsymbol{\Upsilon}_{i_\Upsilon}$ independent of $\mathbf{w}^o_{i_B-1}, \tilde{\mathbf{w}}_{i_B-1}, \mathbf{P}_{i_B}$ this does not necessarily apply to $\boldsymbol{\mu}_{i_\mu}$.

In summary, Assumption 8 holds for example under the conditions listed below.

① The step-size matrix $\boldsymbol{\mu}_{i_\mu}$ is constant or varies slowly with time.

② Many block-updates have passed since $\boldsymbol{\mu}_{i_\mu}$ was updated last time, that is, $i_B \gg i_B^{\mu}$. Then the effect from the change in $\boldsymbol{\mu}_{i_\mu}$ will be smoothed out.

③ In the absence of weight regularization $\boldsymbol{\Pi}_{i_\Pi} = 0$. Then $\breve{w} = 0$ and the pertinent terms in (9.A.22) disappear.

Assumption 8, (9.A.24) implies that $\mathrm{E}\,\mathbf{w}^{o*}_{i_B-1}\boldsymbol{\Upsilon}^*_{i_\Upsilon}\Sigma\boldsymbol{\mu}_{i_\mu} = \mathrm{E}(\mathbf{w}^{o*}_{i_B-1}\boldsymbol{\Upsilon}^*_{i_\Upsilon})\Sigma\,\mathrm{E}(\boldsymbol{\mu}_{i_\mu})$, $\mathrm{E}\,\tilde{\mathbf{w}}^*_{i_B-1}\boldsymbol{\Upsilon}^*_{i_\Upsilon}\Sigma\boldsymbol{\mu}_{i_\mu} = \mathrm{E}(\tilde{\mathbf{w}}^*_{i_B-1}\boldsymbol{\Upsilon}^*_{i_\Upsilon})\Sigma\,\mathrm{E}(\boldsymbol{\mu}_{i_\mu})$, $\mathrm{E}\,\mathbf{P}^*_{i_B}\Sigma\boldsymbol{\mu}_{i_\mu} = \mathrm{E}(\mathbf{P}^*_{i_B})\Sigma\,\mathrm{E}(\boldsymbol{\mu}_{i_\mu})$, $\mathrm{E}\,\tilde{\mathbf{w}}^*_{i_B-1}\mathbf{P}^*_{i_B}\Sigma\boldsymbol{\mu}_{i_\mu} = \mathrm{E}(\tilde{\mathbf{w}}^*_{i_B-1}\mathbf{P}^*_{i_B})\Sigma\,\mathrm{E}(\boldsymbol{\mu}_{i_\mu})$ and $\mathrm{E}\,\mathbf{w}^{o*}_{i_B-1}\mathbf{P}^*_{i_B}\Sigma\boldsymbol{\mu}_{i_\mu} = \mathrm{E}(\mathbf{w}^{o*}_{i_B-1}\mathbf{P}^*_{i_B})\Sigma\,\mathrm{E}(\boldsymbol{\mu}_{i_\mu})$.

Now applying all these remarks and in particular Assumption 5 - 8 to (9.A.22) we therefore obtain

$$\begin{aligned}
\mathrm{E}\|\tilde{\mathbf{w}}_{i_B}\|^2_\Sigma = {} & \mathrm{E}\|\tilde{\mathbf{w}}_{i_B-1}\|^2_{\Sigma^\Upsilon_{i_B}} + \mathrm{E}\|\mathbf{q}_{i_B}\|^2_{\Sigma^{\bar{q}}_{i_B}} + |1-\chi|^2\|w^o\|^2_{\Sigma^{\bar{q}}_{i_B}} + \mathrm{E}\|\mathbf{w}^o_{i_B-1}\|^2_{\Sigma^\circ_{i_B}} + \mathrm{E}\|\boldsymbol{\mu}_{i_\mu}\breve{w}\|^2_\Sigma \\
& + 2\Re\big\{\mathrm{E}(\mathbf{w}^{o*}_{i_B-1})\,\mathrm{E}(\boldsymbol{\Upsilon}^{\chi*}_{i_\Upsilon}\Sigma\boldsymbol{\Upsilon}_{i_\Upsilon})\,\mathrm{E}(\tilde{\mathbf{w}}_{i_B-1})\big\} \\
& + 2\Re\big\{\mathrm{E}(\mathbf{w}^{o*}_{i_B-1})\,\mathrm{E}(\boldsymbol{\Upsilon}^{\chi*}_{i_\Upsilon})\Sigma(1-\chi)w^o\big\} \\
& + 2\Re\big\{(1-\chi^*)w^{o*}\Sigma\,\mathrm{E}(\boldsymbol{\Upsilon}_{i_\Upsilon})\,\mathrm{E}(\tilde{\mathbf{w}}_{i_B-1})\big\} \\
& - 2\Re\Big\{\mathrm{E}(\mathbf{w}^{o*}_{i_B-1})\,\mathrm{E}(\boldsymbol{\Upsilon}^{\chi*}_{i_\Upsilon})\Sigma\,\mathrm{E}(\mathbf{P}_{i_B})\big(\mathrm{E}(\tilde{\mathbf{w}}_{i_B-1}) + (1-\chi)w^o\big)\Big\} \\
& - 2\Re\Big\{(1-\chi^*)w^{o*}\Sigma\,\mathrm{E}(\mathbf{P}_{i_B})\big(\mathrm{E}(\tilde{\mathbf{w}}_{i_B-1}) - (1-\chi)\,\mathrm{E}(\mathbf{w}^o_{i_B-1})\big)\Big\} \\
& - 2\Re\Big\{\mathrm{E}(\tilde{\mathbf{w}}^*_{i_B-1})\,\mathrm{E}(\boldsymbol{\Upsilon}^*_{i_\Upsilon})\Sigma\,\mathrm{E}(\mathbf{P}_{i_B})(1-\chi)\big(w^o - \mathrm{E}(\mathbf{w}^o_{i_B-1})\big)\Big\} \\
& + 2\Re\Big\{\big(\mathrm{E}(\mathbf{w}^{o*}_{i_B-1}) - \mathrm{E}(\tilde{\mathbf{w}}^*_{i_B-1})\big)\,\mathrm{E}(\boldsymbol{\Upsilon}^*_{i_\Upsilon}\Sigma\boldsymbol{\mu}_{i_\mu})\breve{w}\Big\} \\
& - 2\Re\Big\{\big((1-\chi^*)w^{o*} + \chi^*\,\mathrm{E}(\mathbf{w}^{o*}_{i_B-1})\big)\Sigma\,\mathrm{E}(\boldsymbol{\mu}_{i_\mu})\breve{w}\Big\} \\
& + 2\Re\Big\{\big(\mathrm{E}(\tilde{\mathbf{w}}^*_{i_B-1}) + (1-\chi^*)w^{o*} - (1-\chi^*)\,\mathrm{E}(\mathbf{w}^{o*}_{i_B-1})\big)\,\mathrm{E}(\mathbf{P}^*_{i_B})\Sigma\,\mathrm{E}(\boldsymbol{\mu}_{i_\mu})\breve{w}\Big\} \\
& + \mathrm{E}(\tilde{\mathbf{w}}^*_{i_B-1})\,\mathrm{E}(\mathbf{P}^*_{i_B}\Sigma\mathbf{P}_{i_B})(1-\chi)\big(w^o - \mathrm{E}(\mathbf{w}^o_{i_B-1})\big) \\
& + (1-\chi^*)w^{o*}\,\mathrm{E}(\mathbf{P}^*_{i_B}\Sigma\mathbf{P}_{i_B})\big(\mathrm{E}(\tilde{\mathbf{w}}_{i_B-1}) - (1-\chi)\,\mathrm{E}(\mathbf{w}^o_{i_B-1})\big) \\
& - (1-\chi^*)\,\mathrm{E}(\mathbf{w}^{o*}_{i_B-1})\,\mathrm{E}(\mathbf{P}^*_{i_B}\Sigma\mathbf{P}_{i_B})\big(\mathrm{E}(\tilde{\mathbf{w}}_{i_B-1}) + (1-\chi)w^o\big) + K\sigma_v^2\,\mathrm{Tr}\,\{\mathrm{E}\,\mathbf{A}^\Sigma_{i_B}\},
\end{aligned} \tag{9.A.25}$$

and where $\Sigma^{\Upsilon}_{i_B} \in \mathbb{K}^{M\times M}$ represents the *deterministic* weight-error vector weighting matrix, $\Sigma^{o}_{i_B} \in \mathbb{K}^{M\times M}$ denotes the *deterministic* optimal weight vector weighting matrix and $\Sigma^{\bar{q}}_{i_B} \in \mathbb{K}^{M\times M}$ is the *deterministic* random walk weight vector weighting matrix, that is, the *deterministic* weighting matrices corresponding to the *stochastic* weighting matrices in (9.A.21). They are defined by

$$\Sigma^{\Upsilon}_{i_B} \triangleq \mathrm{E}\,\boldsymbol{\Upsilon}^{*}_{i_\Upsilon}\Sigma\boldsymbol{\Upsilon}_{i_\Upsilon} - \mathrm{E}(\boldsymbol{\Upsilon}^{*}_{i_\Upsilon})\Sigma\,\mathrm{E}(\mathbf{P}_{i_B}) - \mathrm{E}(\mathbf{P}^{*}_{i_B})\Sigma\,\mathrm{E}(\boldsymbol{\Upsilon}_{i_\Upsilon}) + \mathrm{E}\,\mathbf{P}^{*}_{i_B}\Sigma\mathbf{P}_{i_B} \tag{9.A.26a}$$

$$\begin{aligned}\Sigma^{o}_{i_B} \triangleq{}& \mathrm{E}\,\boldsymbol{\Upsilon}^{\chi^*}_{i_\Upsilon}\Sigma\boldsymbol{\Upsilon}^{\chi}_{i_\Upsilon} + (1-\chi)\,\mathrm{E}(\boldsymbol{\Upsilon}^{\chi^*}_{i_\Upsilon})\Sigma\,\mathrm{E}(\mathbf{P}_{i_B})\\ &+ (1-\chi^*)\,\mathrm{E}(\mathbf{P}^{*}_{i_B})\Sigma\,\mathrm{E}(\boldsymbol{\Upsilon}^{\chi}_{i_\Upsilon}) + |1-\chi|^2\,\mathrm{E}\,\mathbf{P}^{*}_{i_B}\Sigma\mathbf{P}_{i_B}\end{aligned} \tag{9.A.26b}$$

$$\Sigma^{\bar{q}}_{i_B} \triangleq \Sigma - \Sigma\,\mathrm{E}\,\mathbf{P}_{i_B} - \mathrm{E}\,\mathbf{P}^{*}_{i_B}\Sigma + \mathrm{E}\,\mathbf{P}^{*}_{i_B}\Sigma\mathbf{P}_{i_B} \tag{9.A.26c}$$

respectively. Next by applying LEM assumptions on non-stationarity (9.2.1b) to (9.A.25) and using Definition 9.2 (9.1.10b) we therefore obtain

$$\begin{aligned}\mathrm{E}\|\tilde{\mathbf{w}}_{i_B}\|^2_{\Sigma} = {}& \mathrm{E}\|\tilde{\mathbf{w}}_{i_B-1}\|^2_{\Sigma^{\Upsilon}_{i_B}} + \mathrm{Tr}\,\{Q\Sigma^{\bar{q}}_{i_B}\} + |1-\chi|^2\|w^o\|^2_{\Sigma^{\bar{q}}_{i_B}} + \mathrm{E}\|\mathbf{w}^{o}_{i_B-1}\|^2_{\Sigma^{o}_{i_B}} + \mathrm{E}\|\boldsymbol{\mu}_{i_\mu}\breve{w}\|^2_{\Sigma}\\
&+ 2\Re\Big\{w^{o*}\,\mathrm{E}\big(\boldsymbol{\Upsilon}^{\chi^*}_{i_\Upsilon}\Sigma\boldsymbol{\Upsilon}_{i_\Upsilon}\big)\,\mathrm{E}(\tilde{\mathbf{w}}_{i_B-1})\Big\}\\
&+ 2\Re\Big\{w^{o*}\,\mathrm{E}(\boldsymbol{\Upsilon}^{\chi^*}_{i_\Upsilon})\Sigma(1-\chi)w^{o}\Big\}\\
&+ 2\Re\Big\{(1-\chi^*)w^{o*}\Sigma\,\mathrm{E}(\boldsymbol{\Upsilon}_{i_\Upsilon})\,\mathrm{E}(\tilde{\mathbf{w}}_{i_B-1})\Big\}\\
&- 2\Re\Big\{w^{o*}\,\mathrm{E}(\boldsymbol{\Upsilon}^{\chi^*}_{i_\Upsilon})\Sigma\,\mathrm{E}(\mathbf{P}_{i_B})\big(\mathrm{E}(\tilde{\mathbf{w}}_{i_B-1}) + (1-\chi)w^{o}\big)\Big\}\\
&- 2\Re\Big\{(1-\chi^*)w^{o*}\Sigma\,\mathrm{E}(\mathbf{P}_{i_B})\big(\mathrm{E}(\tilde{\mathbf{w}}_{i_B-1}) - (1-\chi)w^{o}\big)\Big\}\\
&+ 2\Re\Big\{\big(w^{o*} - \mathrm{E}(\tilde{\mathbf{w}}^{*}_{i_B-1})\big)\,\mathrm{E}(\boldsymbol{\Upsilon}^{*}_{i_\Upsilon}\Sigma\boldsymbol{\mu}_{i_\mu})\breve{w}\Big\}\\
&- 2\Re\Big\{w^{o*}\Sigma\,\mathrm{E}(\boldsymbol{\mu}_{i_\mu})\breve{w}\Big\}\\
&+ 2\Re\Big\{\mathrm{E}(\tilde{\mathbf{w}}^{*}_{i_B-1})\,\mathrm{E}(\mathbf{P}^{*}_{i_B})\Sigma\,\mathrm{E}(\boldsymbol{\mu}_{i_\mu})\breve{w}\Big\}\\
&+ K\sigma_v^2\,\mathrm{Tr}\,\{\mathrm{E}\,\mathbf{A}^{\Sigma}_{i_B}\},\end{aligned} \tag{9.A.27}$$

that we may further reduce to

$$\begin{aligned}
\mathrm{E}\|\tilde{\mathbf{w}}_{i_B}\|_{\Sigma}^2 = \mathrm{E}\|\tilde{\mathbf{w}}_{i_B-1}\|_{\Sigma_{i_B}^{\Upsilon}}^2 &+ \mathrm{Tr}\,\{Q\Sigma_{i_B}^{\bar{q}}\} + \|w^o\|_{\Sigma_{i_B}^{q'}}^2 + \mathrm{E}\|\mathbf{w}_{i_B-1}^o\|_{\Sigma_{i_B}^o}^2 + \mathrm{E}\|\boldsymbol{\mu}_{i_\mu}\breve{w}\|_{\Sigma}^2 \\
&+ 2\Re\Big\{w^{o*}\,\mathrm{E}\big(\boldsymbol{\Upsilon}_{i_\Upsilon}^{\chi*}\Sigma\boldsymbol{\Upsilon}_{i_\Upsilon}\big)\,\mathrm{E}(\tilde{\mathbf{w}}_{i_B-1})\Big\} \\
&- 2\Re\Big\{w^{o*}\,\mathrm{E}(\boldsymbol{\Upsilon}_{i_\Upsilon}^{\chi*})\Sigma\,\mathrm{E}(\mathbf{P}_{i_B})\,\mathrm{E}(\tilde{\mathbf{w}}_{i_B-1})\Big\} \\
&+ 2\Re\Big\{(1-\chi^*)w^{o*}\Sigma\big(\mathrm{E}(\boldsymbol{\Upsilon}_{i_\Upsilon}) - \mathrm{E}(\mathbf{P}_{i_B})\big)\,\mathrm{E}(\tilde{\mathbf{w}}_{i_B-1})\Big\} \\
&+ 2\Re\Big\{\big(w^{o*} - \mathrm{E}(\tilde{\mathbf{w}}_{i_B-1}^*)\big)\,\mathrm{E}(\boldsymbol{\Upsilon}_{i_\Upsilon}^{*}\Sigma\boldsymbol{\mu}_{i_\mu})\breve{w}\Big\} \\
&+ 2\Re\Big\{\big(\mathrm{E}(\tilde{\mathbf{w}}_{i_B-1}^*)\,\mathrm{E}(\mathbf{P}_{i_B}^*) - w^{o*}\big)\Sigma\,\mathrm{E}(\boldsymbol{\mu}_{i_\mu})\breve{w}\Big\} \\
&+ K\sigma_v^2\,\mathrm{Tr}\,\{\mathrm{E}\,\mathbf{A}_{i_B}^{\Sigma}\},
\end{aligned} \tag{9.A.28}$$

where the weighting matrix $\Sigma_{i_B}^{q'}$ is defined by

$$\begin{aligned}
\Sigma_{i_B}^{q'} \triangleq\; &|1-\chi|^2(\Sigma_{i_B}^{\bar{q}} + \Sigma\,\mathrm{E}\,\mathbf{P}_{i_B} + \mathrm{E}\,\mathbf{P}_{i_B}^*\Sigma) \\
&+ (1-\chi)\,\mathrm{E}(\boldsymbol{\Upsilon}_{i_\Upsilon}^{\chi*})\Sigma\big(\mathrm{I} - \mathrm{E}(\mathbf{P}_{i_B})\big) + (1-\chi^*)\big(\mathrm{I} - \mathrm{E}(\mathbf{P}_{i_B}^*)\big)\Sigma\,\mathrm{E}(\boldsymbol{\Upsilon}_{i_\Upsilon}^{\chi})
\end{aligned}$$

by insertion of (9.A.21c)

$$= |1-\chi|^2(\Sigma + \mathbf{P}_{i_B}^*\Sigma\mathbf{P}_{i_B}) + (1-\chi)\,\mathrm{E}(\boldsymbol{\Upsilon}_{i_\Upsilon}^{\chi*})\Sigma\big(\mathrm{I} - \mathrm{E}(\mathbf{P}_{i_B})\big) + (1-\chi^*)\big(\mathrm{I} - \mathrm{E}(\mathbf{P}_{i_B}^*)\big)\Sigma\,\mathrm{E}(\boldsymbol{\Upsilon}_{i_\Upsilon}^{\chi}). \tag{9.A.29}$$

Finally, be collecting common factors in (9.A.28) we obtain

$$\begin{aligned}
\mathrm{E}\|\tilde{\mathbf{w}}_{i_B}\|_{\Sigma}^2 = \mathrm{E}\|\tilde{\mathbf{w}}_{i_B-1}\|_{\Sigma_{i_B}^{\Upsilon}}^2 &+ \mathrm{Tr}\,\{Q\Sigma_{i_B}^{\bar{q}}\} + \|w^o\|_{\Sigma_{i_B}^{q'}}^2 + \mathrm{E}\|\mathbf{w}_{i_B-1}^o\|_{\Sigma_{i_B}^o}^2 + \mathrm{E}\|\boldsymbol{\mu}_{i_\mu}\breve{w}\|_{\Sigma}^2 \\
&+ 2\Re\langle w^{o*}, \mathrm{E}(\tilde{\mathbf{w}}_{i_B-1})\rangle_{J_{i_B}} + 2\Re\langle \mathrm{E}(\tilde{\mathbf{w}}_{i_B-1}^*), \breve{w}\rangle_{K_{i_B}^*} \\
&+ 2\Re\{w^{o*}\big(\mathrm{E}(\boldsymbol{\Upsilon}_{i_\Upsilon}^{*}\Sigma\boldsymbol{\mu}_{i_\mu}) - \Sigma\,\mathrm{E}(\boldsymbol{\mu}_{i_\mu})\big)\breve{w}\} + K\sigma_v^2\,\mathrm{Tr}\,\{\mathrm{E}\,\mathbf{A}_{i_B}^{\Sigma}\},
\end{aligned} \tag{9.A.30}$$

where the auxiliary matrix $J_{i_B} \in \mathbb{K}^{M\times M}$ and the auxiliary matrix $K_{i_B} \in \mathbb{K}^{M\times M}$ in turn are defined by

$$J_{i_B} \triangleq \mathrm{E}\big(\boldsymbol{\Upsilon}_{i_\Upsilon}^{\chi*}\Sigma\boldsymbol{\Upsilon}_{i_\Upsilon}\big) - \mathrm{E}(\boldsymbol{\Upsilon}_{i_\Upsilon}^{\chi*})\Sigma\,\mathrm{E}(\mathbf{P}_{i_B}) + (1-\chi^*)\Sigma\,\mathrm{E}(\mathbf{M}_{i_B}) \tag{9.A.31a}$$

$$K_{i_B}^* \triangleq \mathrm{E}(\mathbf{P}_{i_B}^*)\Sigma\,\mathrm{E}(\boldsymbol{\mu}_{i_\mu}) - \mathrm{E}(\boldsymbol{\Upsilon}_{i_\Upsilon}^{*}\Sigma\boldsymbol{\mu}_{i_\mu}). \tag{9.A.31b}$$

The next step is to use the expression (9.A.13) for the time-evolution of the mean weight-error vector $\mathrm{E}\,\tilde{\mathbf{w}}_{i_B-1}$ that enters in the terms $2\Re\langle w^{o*}, \mathrm{E}(\tilde{\mathbf{w}}_{i_B-1})\rangle_{J_{i_B}}$ and $2\Re\langle \mathrm{E}(\tilde{\mathbf{w}}_{i_B-1}^*), \breve{w}\rangle_{K_{i_B}^*}$ in (9.A.30). By inspection of (9.A.13) and (9.A.30) it can be concluded that the term $2\Re\langle w^{o*}, \mathrm{E}(\tilde{\mathbf{w}}_{i_B-1})\rangle_{J_{i_B}}$

can be expressed by

$$2\Re\langle w^{o*},\mathrm{E}(\tilde{\mathbf{w}}_{i_B-1})\rangle_{J_{i_B}}=\|w^o\|^2_{J_{i_B}C^{w^o}_{i_B-1}+C^{w^{o*}}_{i_B-1}J^*_{i_B}}-2\Re\langle w^{o*},\breve{w}\rangle_{J_{i_B}C^{\breve{w}}_{i_B-1}}-2\Re\langle w^{o*},w^0\rangle_{J_{i_B}C^{w^{o,1}}_{i_B}} \tag{9.A.32}$$

and that term $2\Re\langle\mathrm{E}(\tilde{\mathbf{w}}^*_{i_B-1}),\breve{w}\rangle_{K^*_{i_B}}$ can be expressed as

$$2\Re\{\mathrm{E}(\tilde{\mathbf{w}}^*_{i_B-1})K^*_{i_B}\breve{w}\}=-\|\breve{w}\|^2_{K_{i_B}C^{\breve{w}}_{i_B-1}+C^{\breve{w}^*}_{i_B-1}K^*_{i_B}}+2\Re\langle w^{o*},\breve{w}\rangle_{C^{w^{o*}}_{i_B-1}K^*_{i_B}}-2\Re\langle w^{0*},\breve{w}\rangle_{C^{w^{o,1*}}_{i_B-1}K^*_{i_B}}. \tag{9.A.33}$$

Then by insertion of (9.A.32) and (9.A.33) in (9.A.30) gives

$$\begin{aligned}\mathrm{E}\|\tilde{\mathbf{w}}_{i_B}\|^2_{\Sigma}&=\mathrm{E}\|\tilde{\mathbf{w}}_{i_B-1}\|^2_{\Sigma^{\Upsilon}_{i_B}}\\&\quad+\mathrm{Tr}\,\{Q\Sigma^{\bar{q}}_{i_B}\}+\|w^o\|^2_{\Sigma^{q'}_{i_B}}+\mathrm{E}\|\mathbf{w}^o_{i_B-1}\|^2_{\Sigma^o_{i_B}}+\|w^o\|^2_{J_{i_B}C^{w^o}_{i_B-1}+C^{w^{o*}}_{i_B-1}J^*_{i_B}}+\mathrm{E}\|\boldsymbol{\mu}_{i_\mu}\breve{w}\|^2_{\Sigma}\\&\quad-2\Re\{w^{o*}J_{i_B}C^{\breve{w}}_{i_B-1}\breve{w}\}+2\Re\langle w^{o*},\breve{w}\rangle_{C^{w^{o*}}_{i_B-1}K^*_{i_B}}-\|\breve{w}\|^2_{K_{i_B}C^{\breve{w}}_{i_B-1}+C^{\breve{w}^*}_{i_B-1}K^*_{i_B}}\\&\quad+2\Re\{w^{o*}\big(\mathrm{E}(\boldsymbol{\Upsilon}^*_{i_\Upsilon}\Sigma\boldsymbol{\mu}_{i_\mu})-\Sigma\,\mathrm{E}(\boldsymbol{\mu}_{i_\mu})\big)\breve{w}\}\\&\quad-2\Re\langle w^{o*},w^0\rangle_{J_{i_B}C^{w^{o,1}}_{i_B}}-2\Re\langle w^{0*},\breve{w}\rangle_{C^{w^{o,1*}}_{i_B-1}K^*_{i_B}}+K\sigma_v^2\,\mathrm{Tr}\,\{\mathrm{E}\,\mathbf{A}^{\Sigma}_{i_B}\}.\end{aligned} \tag{9.A.34}$$

From LEM assumptions on non-stationarity (9.2.1b) we appreciate that we may express the term $\mathrm{E}\|\mathbf{w}^o_{i_B-1}\|^2_{\Sigma^o_{i_B}}$ in (9.A.34) in terms of the covariance matrix of the random-walk model Q and the mean optimal weight vector w^o

$$\begin{aligned}\mathrm{E}\|\mathbf{w}^o_{i_B-1}\|^2_{\Sigma^o_{i_B}}&=\mathrm{E}\|\mathbf{w}^o_{i_B-1}-w^o\|^2_{\Sigma^o_{i_B}}-\mathrm{E}\|w^o\|^2_{\Sigma^o_{i_B}}+2\Re\langle\mathrm{E}\,\mathbf{w}^{o*}_{i_B-1},w^o\rangle_{\Sigma^o_{i_B}}\\&=\mathrm{Tr}\,\{\mathrm{E}(\mathbf{w}^o_{i_B-1}-w^o)(\mathbf{w}^o_{i_B-1}-w^o)^*\Sigma^o_{i_B}\}-\mathrm{E}\|w^o\|^2_{\Sigma^o_{i_B}}+2\|w^o\|^2_{\Sigma^o_{i_B}}\\&=\frac{1}{1-|\chi|^2}\,\mathrm{Tr}\,\{Q\Sigma^o_{i_B}\}+\|w^o\|^2_{\Sigma^o_{i_B}}.\end{aligned} \tag{9.A.35}$$

where the matrix $\Theta_{i_B-1}\triangleq\mathrm{E}\,\boldsymbol{\theta}_{i_B-1}\boldsymbol{\theta}^*_{i_B-1}\in\mathbb{K}^{M\times M}$ is the covariance matrix of perturbation vector $\boldsymbol{\theta}_{i_B-1}$. Moreover, from LEM Assumption 1 on non-stationarity (9.2.1b) we find that in steady-state we may express $\mathrm{E}\|\mathbf{w}^o_{i_B-1}\|^2_{\Sigma^o_{i_B}}$ by

$$\lim_{i_B\to\infty}\mathrm{E}\|\mathbf{w}^o_{i_B-1}\|^2_{\Sigma^o_{i_B}}=\frac{1}{1-|\chi|^2}\,\mathrm{Tr}\,\{Q\Sigma^o_{i_B}\}+\|w^o\|^2_{\Sigma^o_{i_B}}. \tag{9.A.36}$$

Finally, by using (9.A.35) and by collecting common terms in (9.A.34) we obtain

$$\boxed{\begin{aligned}\mathrm{E}\|\tilde{\mathbf{w}}_{i_B}\|^2_{\Sigma}&=\mathrm{E}\|\tilde{\mathbf{w}}_{i_B-1}\|^2_{\Sigma^{\Upsilon}_{i_B}}+\mathrm{Tr}\,\{Q\Sigma^q_{i_B}\}+\|w^o\|^2_{\Sigma^{w^o}_{i_B}}+\|\breve{w}\|^2_{\Sigma^{\breve{w}}}\\&\quad+\langle w^{o*},\breve{w}\rangle_{\Sigma^{w^o\breve{w}}_{i_B}}-2\Re\langle w^{o*},w^0\rangle_{J_{i_B}C^{w^o,1}_{i_B}}-2\Re\langle w^{0*},\breve{w}\rangle_{C^{w^{o,1*}}_{i_B-1}K^*_{i_B}}+K\sigma_v^2\,\mathrm{Tr}\,\{\mathrm{E}\,\mathbf{A}^{\Sigma}_{i_B}\}.\end{aligned}} \tag{9.A.37}$$

where the mean optimal weight vector weighting matrix $\Sigma_{i_B}^{w'^o} \in \mathbb{K}^{M\times M}$, the random walk weight vector weighting matrix $\Sigma_{i_B}^{q} \in \mathbb{K}^{M\times M}$ and the regularization weight vector weighting matrix $\Sigma_{i_B}^{\breve{w}} \in \mathbb{K}^{M\times M}$ are defined by

$$\begin{aligned}
\Sigma_{i_B}^{w'^o} &\triangleq \Sigma_{i_B}^{q'} + \Sigma_{i_B}^{o} + J_{i_B} C_{i_B-1}^{w^o} + C_{i_B-1}^{w^o *} J_{i_B}^{*} \\
&= |1-\chi|^2(\Sigma + \mathbf{P}_{i_B}^{*}\Sigma\mathbf{P}_{i_B}) + (1-\chi)\,\mathrm{E}(\boldsymbol{\Upsilon}_{i_\Upsilon}^{\chi *})\Sigma\big(\mathrm{I} - \mathrm{E}(\mathbf{P}_{i_B})\big) + (1-\chi^*)\big(\mathrm{I} - \mathrm{E}(\mathbf{P}_{i_B}^{*})\big)\Sigma\,\mathrm{E}(\boldsymbol{\Upsilon}_{i_\Upsilon}^{\chi}) \\
&\quad + \mathrm{E}\,\boldsymbol{\Upsilon}_{i_\Upsilon}^{\chi *}\Sigma\boldsymbol{\Upsilon}_{i_\Upsilon}^{\chi} + (1-\chi)\,\mathrm{E}(\boldsymbol{\Upsilon}_{i_\Upsilon}^{\chi *})\Sigma\,\mathrm{E}(\mathbf{P}_{i_B}) + (1-\chi^*)\,\mathrm{E}(\mathbf{P}_{i_B}^{*})\Sigma\,\mathrm{E}(\boldsymbol{\Upsilon}_{i_\Upsilon}^{\chi}) + |1-\chi|^2\,\mathrm{E}\,\mathbf{P}_{i_B}^{*}\Sigma\mathbf{P}_{i_B} \\
&\quad + J_{i_B} C_{i_B-1}^{w^o} + C_{i_B-1}^{w^o *} J_{i_B}^{*} \\
&= \mathrm{E}\,\boldsymbol{\Upsilon}_{i_\Upsilon}^{\chi *}\Sigma\boldsymbol{\Upsilon}_{i_\Upsilon}^{\chi} + (1-\chi)\,\mathrm{E}(\boldsymbol{\Upsilon}_{i_\Upsilon}^{\chi *})\Sigma + (1-\chi^*)\Sigma\,\mathrm{E}(\boldsymbol{\Upsilon}_{i_\Upsilon}^{\chi}) + |1-\chi|^2(\Sigma + 2\,\mathrm{E}\,\mathbf{P}_{i_B}^{*}\Sigma\mathbf{P}_{i_B}) \\
&\quad + J_{i_B} C_{i_B-1}^{w^o} + C_{i_B-1}^{w^o *} J_{i_B}^{*}
\end{aligned} \tag{9.A.38a}$$

and

$$\begin{aligned}
\Sigma_{i_B}^{q} &\triangleq \Sigma_{i_B}^{\bar{q}} + \frac{1}{1-|\chi|^2}\Sigma_{i_B}^{o} \\
&= \Sigma - \Sigma\,\mathrm{E}\,\mathbf{P}_{i_B} - \mathrm{E}\,\mathbf{P}_{i_B}^{*}\Sigma + \mathrm{E}\,\mathbf{P}_{i_B}^{*}\Sigma\mathbf{P}_{i_B} \\
&\quad + \Theta_{i_B-1}\Big(\mathrm{E}\,\boldsymbol{\Upsilon}_{i_\Upsilon}^{\chi *}\Sigma\boldsymbol{\Upsilon}_{i_\Upsilon}^{\chi} + (1-\chi)\,\mathrm{E}(\boldsymbol{\Upsilon}_{i_\Upsilon}^{\chi *})\Sigma\,\mathrm{E}(\mathbf{P}_{i_B}) \\
&\qquad\qquad + (1-\chi^*)\,\mathrm{E}(\mathbf{P}_{i_B}^{*})\Sigma\,\mathrm{E}(\boldsymbol{\Upsilon}_{i_\Upsilon}^{\chi}) + |1-\chi|^2\,\mathrm{E}\,\mathbf{P}_{i_B}^{*}\Sigma\mathbf{P}_{i_B}\Big)
\end{aligned} \tag{9.A.38b}$$

and

$$\Sigma_{i_B}^{\breve{w}} \triangleq \mathrm{E}(\boldsymbol{\mu}_{i_\mu}^{*}\Sigma\boldsymbol{\mu}_{i_\mu}) - K_{i_B} C_{i_B-1}^{\breve{w}} - C_{i_B-1}^{\breve{w}*} K_{i_B}^{*}. \tag{9.A.38c}$$

The cross-weighting matrix $\Sigma_{i_B}^{w^o\breve{w}} \in \mathbb{K}^{M\times M}$ is finally defined by

$$\Sigma_{i_B}^{w^o\breve{w}} \triangleq -J_{i_B} C_{i_B-1}^{\breve{w}} + C_{i_B-1}^{w^o *} K_{i_B}^{*} + \mathrm{E}(\boldsymbol{\Upsilon}_{i_\Upsilon}^{*}\Sigma\boldsymbol{\mu}_{i_\mu}) - \Sigma\,\mathrm{E}(\boldsymbol{\mu}_{i_\mu}). \tag{9.A.39}$$

Bibliography

[1] Tareq Y. Al-Naffouri and Ali H. Sayed. Transient analysis of adaptive filters with data nonlinearities. *IEEE Transactions on Signal Processing*, 51(3):639–652, 2003.

[2] Tareq Y. Al-Naffouri and Ali H. Sayed. Transient analysis of adaptive filters with error nonlinearities. *IEEE Transactions on Signal Processing*, 51(3):653–663, 2003.

[3] Simon Haykin. *Adaptive Filter Theory*. Prentice-Hall Inc. Upper Saddle River New Jersey 07458, 3rd edition, 1996.

[4] Diederich Hinrichsen and Anthony J. Pritchard. *Mathematical Systems Theory I*. Springer-Verlag, Berlin, 2005.

[5] Thomas Kailath, Ali H. Sayed, and Babak Hassabi. *Linear Estimation*. Printice Hall, Upper Saddle River, New Jersey, 2000.

[6] Lennart Ljung. On positive real transfer functions and the convergence of some recursive schemes. *IEEE Transactions on Automatic Control*, 22(4):539–551, 1977.

[7] Lennart Ljung. Analysis of recursive stochastic algorithms. *IEEE Transactions on Automatic Control*, 22(4):551–575, 1977.

[8] A. H. Sayed and T. Y. Al-Naffouri. Mean-square analysis of normalized leaky adaptive filters. In *ICASSP*, volume 6, pages 3873–3876, Salt Lake City, UT, 2001.

[9] Ali H. Sayed. *Fundamentals of Adaptive Filtering*. John Wiley & Sons, Inc., New York, NY, USA, 2003.

[10] Hyun-Chool Shin and Ali H. Sayed. Mean-square performance of a family of affine projection algorithms. *IEEE Transactions on Signal Processing*, 52(1), 2004.

[11] J. R. Treichler, JR. C. R. Johnson, and M. G. Larimore. *Theory and Design of Adaptive Filters*. Prentice Hall, 1 edition, 2001.

[12] Bernard Widrow and Samuel D. Stearns. *Adaptive Signal Processing*. Prentice-Hall, New Jersey, 1985.

[13] Bernard Widrow and Eugene Walach. *Adaptive Inverse Control*. Prentice Hall, 1996.

[14] Weimin Xiao and Michael L. Honig. Large system transient analysis of adaptive least squares filtering. *IEEE Transactions on Information Theory*, 51(7):2447–2474, 2005.

[15] Nabil R. Yousef and Ali H. Sayed. A unified approach to the steady-state and tracking analyses of adaptive filters. *IEEE Transactions on Signal Processing*, 49(2):314–324, 2001.

[16] Fuzhen Zhang. *Matrix Theory. Basic Results and Techniques*. Springer-Verlag, New York, 1999.

Part IV

ELECTROACOUSTICAL AND VIBROACOUSTICAL ENVIRONMENT

10. HEARING PROTECTOR: PASSIVE ATTENUATION

10.1 Introduction

In this chapter a the brief technical description of the *passive* part of a hearing protection device (HPD) will briefly be reviewed and reference made to some of the pertinent technical literature. In particular an ordinary model for the closed-back headset is developed and results from parameterizations hereof presented. The closed-back headset model is used for example for simulating the disturbance signals resulting when the HPD is subject to a diffuse sound field illumination. One of the objectives pursued in this chapter and the accompanion chapter chapter 11 on page 481 is to establish simple lumped-element models that can be used quantitatively to determine the passive attenuation and to explain the behavior of the group delays pertaining to the primary paths and secondary paths involved in a an active HPD.

10.2 Brief Technical Description

Hearing Protector Devices (HPD) have been used widely for 5-6 decades. A fundamental description of the physical principles was established in the late 1950s by Shaw and Thiessen in their classical papers [6, 7]. The HPD has successfully been modeled as a 2^{nd} order compliance-resistance-mass system. This mechanism is referred to as *passive attenuation* as it involves no active components. In summary, the passive performance of a circumaural HPD is limited by:

1. Hearing Protector Vibration (Non-deformative normal and lateral movements of earcup)
2. Air Leaks (at the interface between the users head and the ear cushion)
3. Material Transmission. (Deformation of earcup, frequency > 1 kHz)
4. Bone and Tissue Conduction

Since then the performance has gradually been improved primarily due to the choice of better material for the ear cushion and the earcups.

In modern HPD design the advantages of active noise control (ANC) have been accommodated in the more expensive range of units. Basically, ANC refers to the technique of:

- Acquisition of a signal with a high coherence with the disturbance, e.g., by a microphone
- Determination of a cancelation response (adaptive filtering, signal processing)
- Activation of the secondary (cancelation) signal, e.g., by a loudspeaker

In his doctorial thesis Schröter [3] developed comprehensive physical models of passive hearing protection devices. Schröter established models for both earplugs and circumaural hearing protectors. This work is summarized in [4, 5].

Recent developments and models for passive as well as active earmuffs can be found in [2].

10.3 Lumped Element Model

In order to establish a reasonable set of primary path functions $g_{e_m x_j}, 1 \leq m \leq N_e, 1 \leq j \leq N_x$ we used the ordinary model of a closed-back headset system in [1, Ch. 7]. However, in order to provide attenuation decay rates that more closely resemble practical field measurements a leakage term was added to the model in accordance with [6, 7]. Hence, following some straightforward derivations our governing equation in the frequency-domain for the insertion loss is

$$\boxed{\frac{\tilde{p}_{e_m}(\mathrm{e}^{\imath\omega})}{\tilde{p}_{x_j}(\mathrm{e}^{\imath\omega})} = \frac{K_a\big(K_c + \imath\omega(R_c + Z_l^A S_h^2) - \omega^2 M_s\big)}{K_a K_c + \imath\omega\big(K_a R_c + (K_a + K_c) Z_l^A S_h^2\big) - \omega^2(K_a M_s + R_c Z_l^A S_h^2) - \imath\omega^3 M_s S_h^2 Z_l},} \tag{10.3.1}$$

where the following parameters enter: stiffness of the air K_a, stiffness of the cushion K_c, *acoustic impedance* related to leakage $Z_l^A = R_l^A + \frac{K_l^A}{\imath\omega}$, resistance of the cushion R_c, mass of the shell M_s and an effective head surface area S_h. The system has a resonance frequency f_0. By the inclusion of the leakage term in (10.3.1) it is ensured that the passive attenuation shift from a decay-rate of $40\,\mathrm{dB}\cdot\mathrm{decade}^{-1}$ to $20\,\mathrm{dB}\cdot\mathrm{decade}^{-1}$ at frequencies above, say, f_l. Then $R_l = a_l \frac{2\pi f_l M_s}{S_h^2}$ for some tuning constant a_l and $K_l = 2\pi f_l R_l$, where low-pass cut-off frequency from leakage f_l.

Provided that the reference sensors and error sensors possess the same sensitivity (10.3.1) also gives the ratio between the m'th error signal and the j'th reference signal.

Moreover, it should be recalled that (10.3.1) pertains to ordinary closed-back headset systems. In the present case of an Gentex HGU 55/P helmet the integral effect of the helmet should also be taking into account. Although a detailed model of such a helmet closed-back headset system would be beneficial for our analysis such model development is left for future research activities.

10.3.1 Parameter Study

The 2nd order compliance-resistance-mass system model for the closed-back headset (10.3.1) was subsequently subject to a parameter study aimed to find those values of K_a, K_c, R_c, Z_l^A and M_s that lead to time-domain and frequency-domain responses that most closely resemble practical evidence. The main results from this study is presented in the subsequent text.

The magnitude and phase of the frequency response function for $K_a = 26\,\mathrm{kN}\cdot\mathrm{m}^{-1}, K_c = 100\,\mathrm{kN}\cdot\mathrm{m}^{-1}, a_l = 1$ corresponding to $R_l^A = 2.51\mathrm{e}7\,\mathrm{N}\cdot\mathrm{s}\cdot\mathrm{m}^{-5}$ for the combination of $R_c = 60, 80, 100, 120, 140, 160\,\mathrm{N}\cdot\mathrm{s}\cdot\mathrm{m}^{-1}$ and $M_s = 0.16$ kg are shown in Simulation 10.3.1 - 10.3.2 on pages 473–474.

We observe how the mechanical resistance of the cushion to a large extent controls the Q-factor and the phase transition at the resonance frequency ($f_0 = 141$ Hz). As we will seen in chapter 11 on page 481 this phase transition also has a great impact on the secondary path function. The low-frequency passive attenuation amounts to 12 dB and is determined by the ratio $\frac{K_a}{K_a + K_c}$.

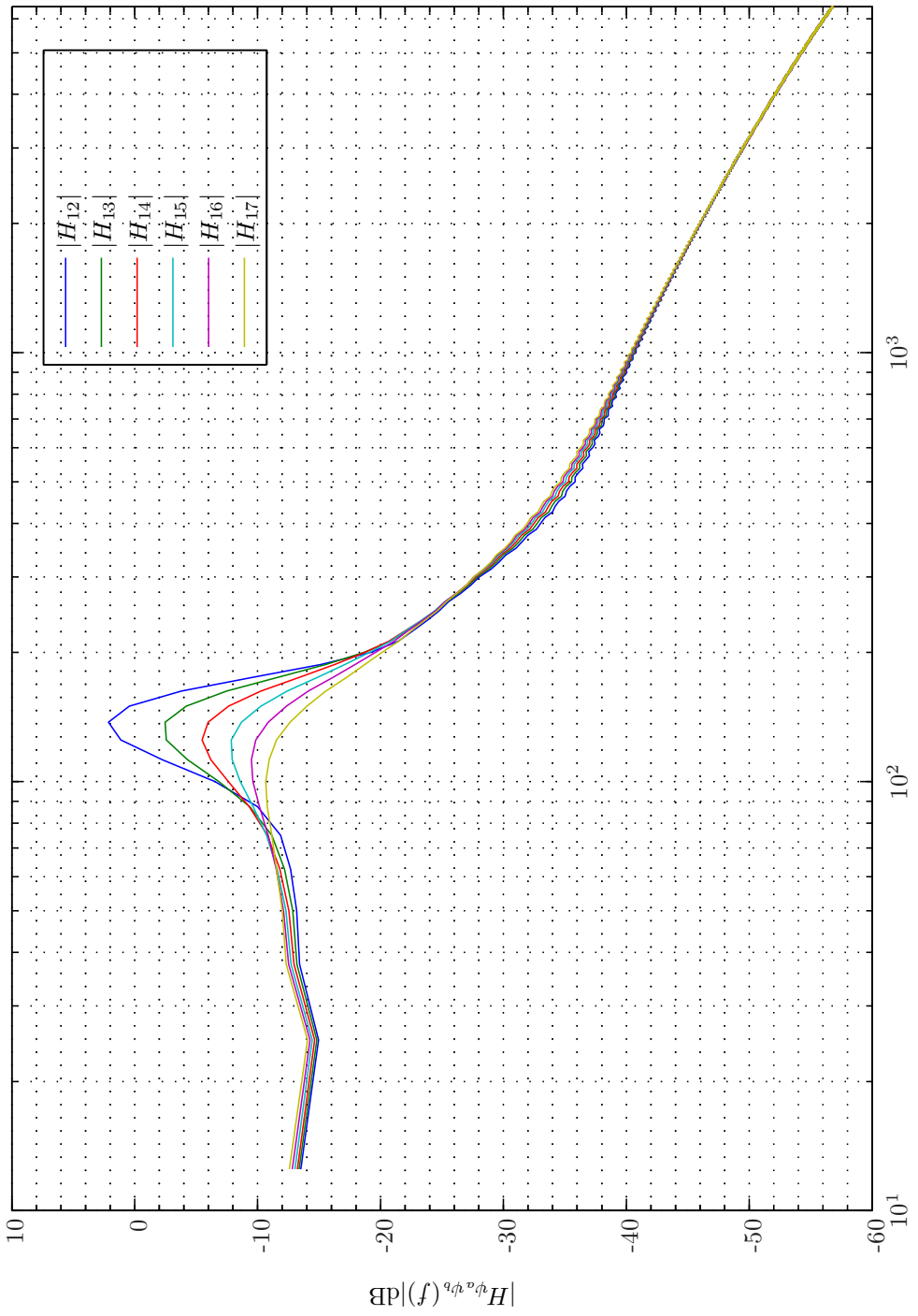

Sim 10.3.1: *Transfer Function, Magnitude:* $|H_{\psi_a\psi_b}(f)|$: **Statistical Data Analysis**: Single-Sided Modified Periodogram, $f_s = 25.6$ kHz, $N_{DFT} = 2048$, $L_{DFT} = 1334$, $R_{DFT} = 667$, Hanning, $\Delta f_m = 76.8192$ Hz, $T_{DFT} = 0.052109$ s, $N_{f,DFT} = 1025$, $\Delta f_{DFT} = 12.5$ Hz, $K_{DFT} = 1$; $g_{ex}^{1,1}$: Closed-Back Headset System: ($f_s = 25.6$ kHz, $K_a = 26$ kN $\cdot$ m^{-1}, $K_c = 100$ kN $\cdot$ m^{-1}, $R_l^A = 2.51\text{e}+007$ N $\cdot$ s $\cdot$ m^{-5}, $f_0 = 141.236$ Hz, $M_s = 0.16$ kg) (FIR : $M_{ex}^{1,1} = 96002$), *Channels:* (#2 $\leftarrow R_c = 60$ N $\cdot$ s $\cdot$ m^{-1}, #3 $\leftarrow R_c = 80$ N $\cdot$ s $\cdot$ m^{-1}, #4 $\leftarrow R_c = 100$ N $\cdot$ s $\cdot$ m^{-1}, #5 $\leftarrow R_c = 120$ N $\cdot$ s $\cdot$ m^{-1}, #6 $\leftarrow R_c = 140$ N $\cdot$ s $\cdot$ m^{-1}, #7 $\leftarrow R_c = 160$ N $\cdot$ s $\cdot$ m^{-1}). **Scenario:** `MultipleSinusoidalsAddiativeNoiseFeedforwardNx2Ne1Ny1Np0/20080305T205250;` .

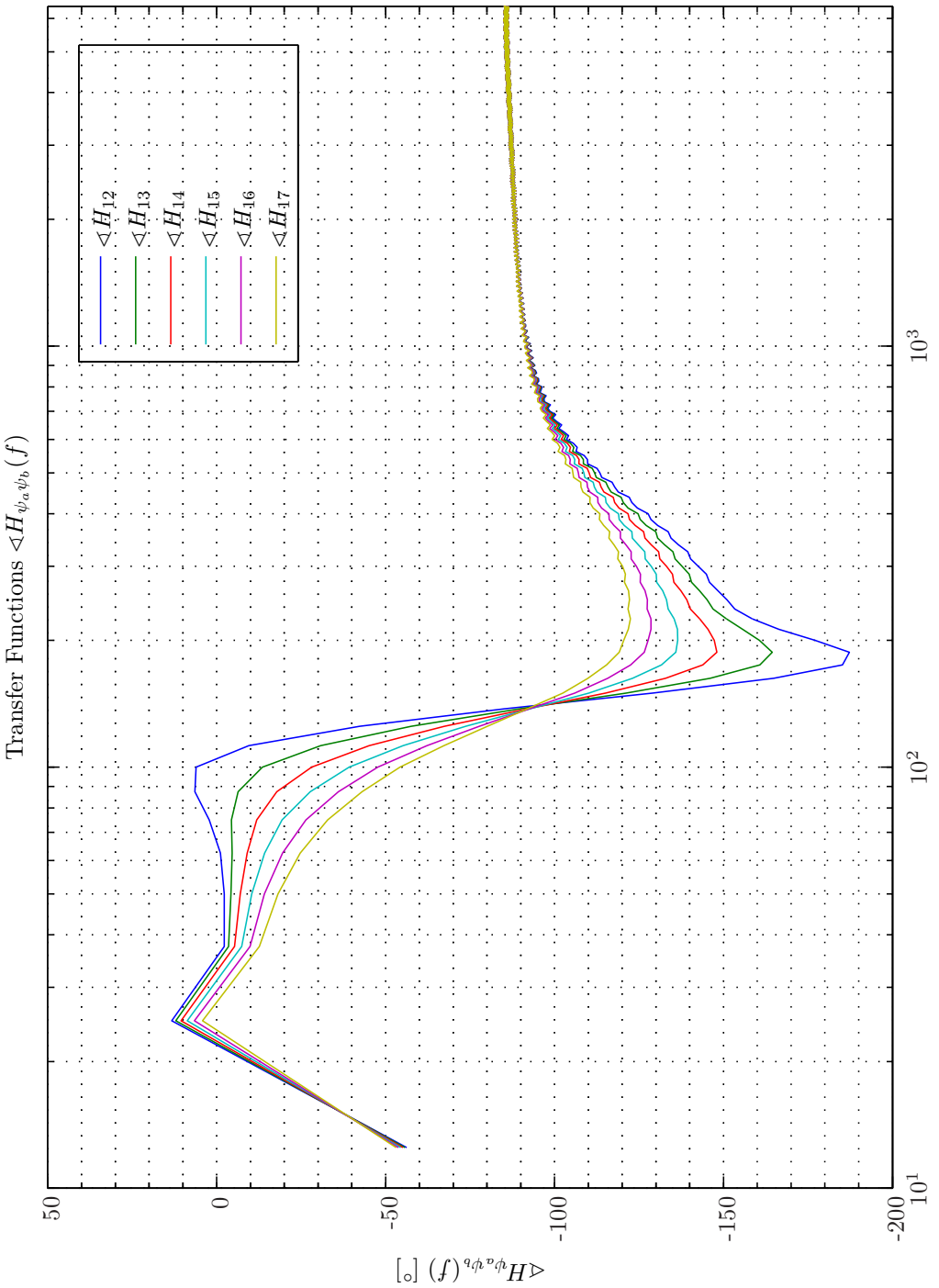

Sim 10.3.2: *Transfer Function, Phase:* $\sphericalangle H_{\psi_a\psi_b}(f)$: **Statistical Data Analysis**: Single-Sided Modified Periodogram, f_s = 25.6 kHz, N_{DFT} = 2048, L_{DFT} = 1334, R_{DFT} = 667, Hanning, Δf_m = 76.8192 Hz, T_{DFT} = 0.052109 s, $N_{f,DFT}$ = 1025, Δf_{DFT} = 12.5 Hz, K_{DFT} = 1; $g_{ex}^{1,1}$: Closed-Back Headset System: (f_s = 25.6 kHz, K_a = 26 kN · m^{-1}, K_c = 100 kN · m^{-1}, R_l^A = 2.51e + 007 N · s · m^{-5}, f_0 = 141.236 Hz, M_s = 0.16 kg) (FIR : $M_{ex}^{1,1}$ = 96002),*Channels:* (#2 ← R_c = 60 N · s · m^{-1}, #3 ← R_c = 80 N · s · m^{-1}, #4 ← R_c = 100 N · s · m^{-1}, #5 ← R_c = 120 N · s · m^{-1}, #6 ← R_c = 140 N · s · m^{-1}, #7 ← R_c = 160 N · s · m^{-1}). **Scenario:** `MultipleSinusoidalsAddiativeNoiseFeedforwardNx2Ne1Ny1Np0/20080305T205250.;` .

Now using the same parameters for the closed-back headset as above but for the acoustical resistance to leakage decreased to $R_l^A = 1.26\text{e}7\,\text{N}\cdot\text{s}\cdot\text{m}^{-5}$ corresponding to $a_l = 0.5$ the magnitude and phase of the transfer function are shown in Simulation 10.3.3 - 10.3.4 on pages 476–477. The associated impulse response function is depicted in Simulation 10.3.5 on page 478.

By comparing Simulation 10.3.3 with Simulation 10.3.1 we appreciate that by decreasing the resistance to leakage the high-frequency decay-rate is lowered and the frequency response fits better to practical measurements. We observe that it takes approximately $0.2 - 20$ ms for the exterior pressure $p_{x_j}(t)$ to manifest itself as the interior pressure $p_{e_m}(t)$. Finally, the group delay associated with the primary path is shown in Simulation 10.3.6 on page 479. We see that the HPD exhibit a very large group delay at the resonance frequency f_0 and that the group delay is actually negative in the frequency region $250 - 550$ Hz where the magnitude of the transfer function decays by $40\,\text{dB}\cdot\text{decade}^{-1}$.

In conclusion, the following model parameter values are selected: $K_a = 26\,\text{kN}\cdot\text{m}^{-1}, K_c = 100\,\text{kN}\cdot\text{m}^{-1}, R_c = 80\,\text{N}\cdot\text{s}\cdot\text{m}^{-1}, M_s = 0.16\,\text{kg}$ and $Z_l^A = (1 + \frac{2\omega_l}{\imath\omega})1.26\text{e}7\,\text{N}\cdot\text{s}\cdot\text{m}^{-5}$, where $\omega_l = 2\pi 500\,\text{rad}\cdot\text{s}^{-1}$.

Bibliography

[1] Stephen J. Elliott. *Signal Processing for Active Control*. London: Academic Press, 2001.

[2] Frederik M. Gren. *Optimization of hearing protector used in jet fighter aircrafts*. M.sc., SDU, 2006.

[3] Jürgen Schröter. *Messung der Schalldämmung von Gehörschützern mit einemphysikalischen Verfahren (Kunstkopfmethode) (In German)*. Doctoral thesis, 1983.

[4] Jürgen Schröter. The use of acoustical test fixtures for the measurement of hearing protector attenuation Part I: Review of previous work;design of an improved test fixture. *JASA*, 79(4): 1065–1081, 1986.

[5] Jürgen Schröter and C. Poesselt. The use of acoustical test fixtures for the measurement of hearing protector attenuation. Part II: Modeling: the external ear simulation bone conduction and comparing test fixture and real ear data. *JASA*, 80(2):505–527, 1986.

[6] E. A. G. Shaw and G. J. Thiessen. Improved cushion for ear defenders. *JASA*, 30(No. 1), 1958.

[7] E. A. G. Shaw and G. J. Thiessen. Acoustics of circumaural ear defenders. *JASA*, 34(No. 9), 1962.

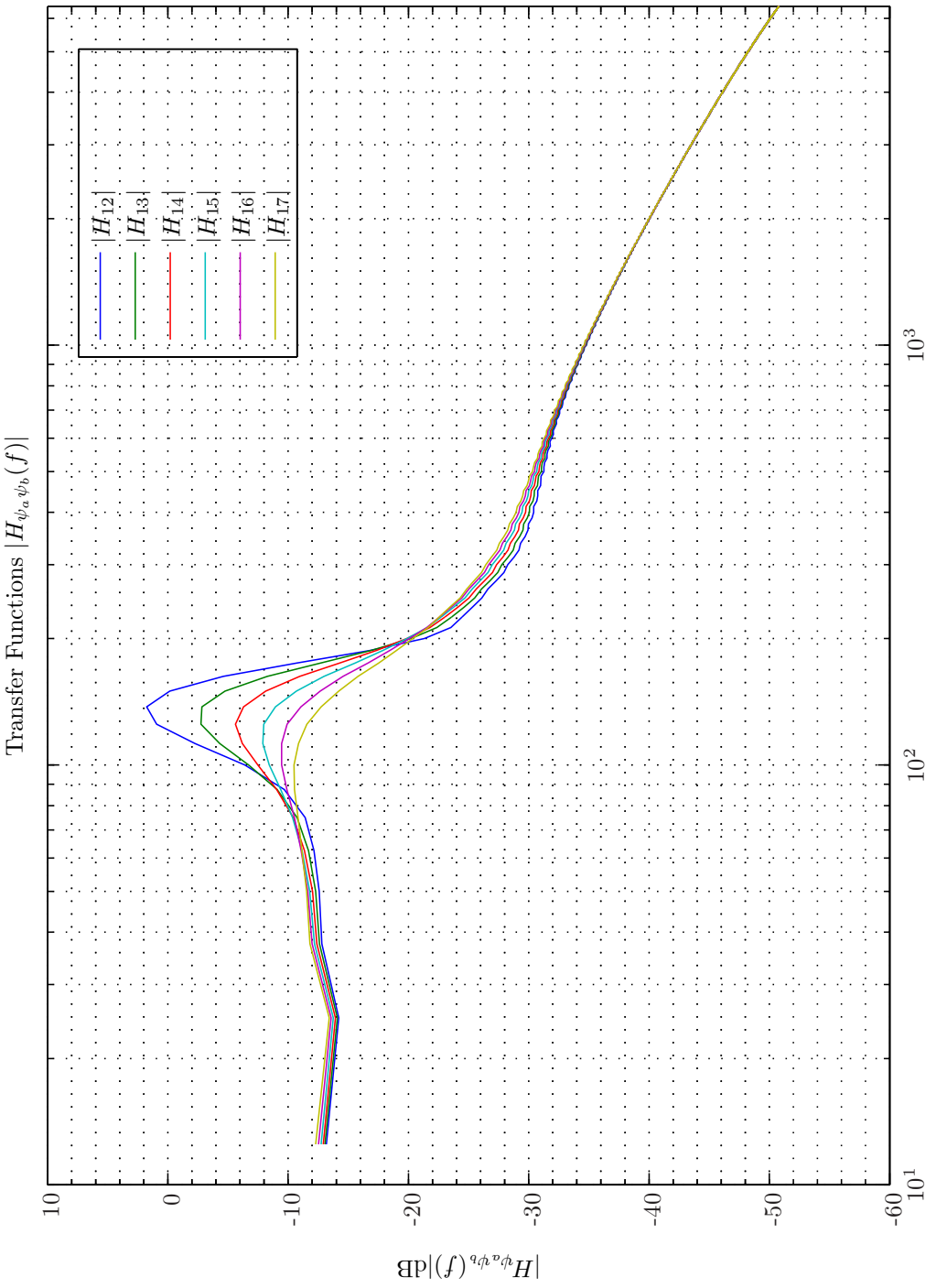

Sim 10.3.3: *Transfer Function, Magnitude*: $|H_{\psi_a\psi_b}(f)|$: **Statistical Data Analysis**: Single-Sided Modified Periodogram, f_s = 25.6 kHz, N_{DFT} = 2048, L_{DFT} = 1334, R_{DFT} = 667, Hanning, Δf_m = 76.8192 Hz, T_{DFT} = 0.052109 s, $N_{f,DFT}$ = 1025, Δf_{DFT} = 12.5 Hz, K_{DFT} = 1; $g_{ex}^{1,1}$: Closed-Back Headset System: (f_s = 25.6 kHz, K_a = 26 kN · m^{-1}, K_c = 100 kN · m^{-1}, R_l^A = 1.26e + 007 N · s · m^{-5}, f_0 = 141.236 Hz, M_s = 0.16 kg) (FIR : $M_{ex}^{1,1}$ = 96002),*Channels:* (#2 ← R_c = 60 N · s · m^{-1}, #3 ← R_c = 80 N · s · m^{-1}, #4 ← R_c = 100 N · s · m^{-1}, #5 ← R_c = 120 N · s · m^{-1}, #6 ← R_c = 140 N · s · m^{-1}, #7 ← R_c = 160 N · s · m^{-1}). **Scenario:** `MultipleSinusoidalsAddiativeNoiseFeedforwardNx2Ne1Ny1Np0/20080305T205250.;` .

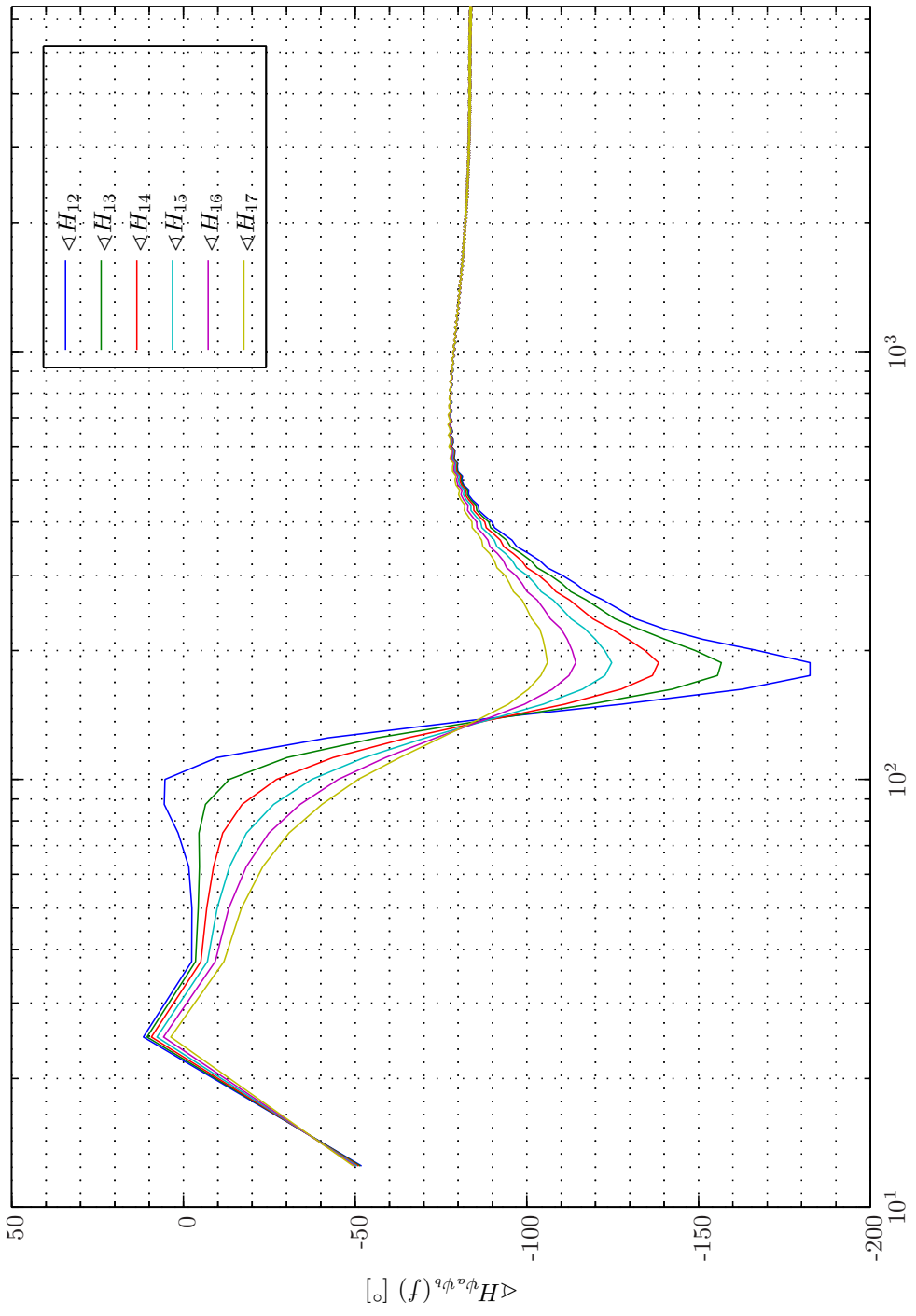

Sim 10.3.4: *Transfer Function, Phase:* $\sphericalangle H_{\psi_a\psi_b}(f)$: **Statistical Data Analysis**: Single-Sided Modified Periodogram, $f_s = 25.6\,\text{kHz}$, $N_{DFT} = 2048$, $L_{DFT} = 1334$, $R_{DFT} = 667$, Hanning, $\Delta f_m = 76.8192\,\text{Hz}$, $T_{DFT} = 0.052109\,\text{s}$, $N_{f,DFT} = 1025$, $\Delta f_{DFT} = 12.5\,\text{Hz}$, $K_{DFT} = 1$; $g_{ex}^{1,1}$: Closed-Back Headset System: ($f_s = 25.6\,\text{kHz}$, $K_a = 26\,\text{kN}\cdot\text{m}^{-1}$, $K_c = 100\,\text{kN}\cdot\text{m}^{-1}$, $R_l^A = 1.26\text{e}+007\,\text{N}\cdot\text{s}\cdot\text{m}^{-5}$, $f_0 = 141.236\,\text{Hz}$, $M_s = 0.16\,\text{kg}$) (FIR : $M_{ex}^{1,1} = 96002$), *Channels:* (#2 $\leftarrow R_c = 60\,\text{N}\cdot\text{s}\cdot\text{m}^{-1}$, #3 $\leftarrow R_c = 80\,\text{N}\cdot\text{s}\cdot\text{m}^{-1}$, #4 $\leftarrow R_c = 100\,\text{N}\cdot\text{s}\cdot\text{m}^{-1}$, #5 $\leftarrow R_c = 120\,\text{N}\cdot\text{s}\cdot\text{m}^{-1}$, #6 $\leftarrow R_c = 140\,\text{N}\cdot\text{s}\cdot\text{m}^{-1}$, #7 $\leftarrow R_c = 160\,\text{N}\cdot\text{s}\cdot\text{m}^{-1}$). **Scenario:** `MultipleSinusoidalsAddiativeNoiseFeedforwardNx2Ne1Ny1Np0/20080305T205250;` .

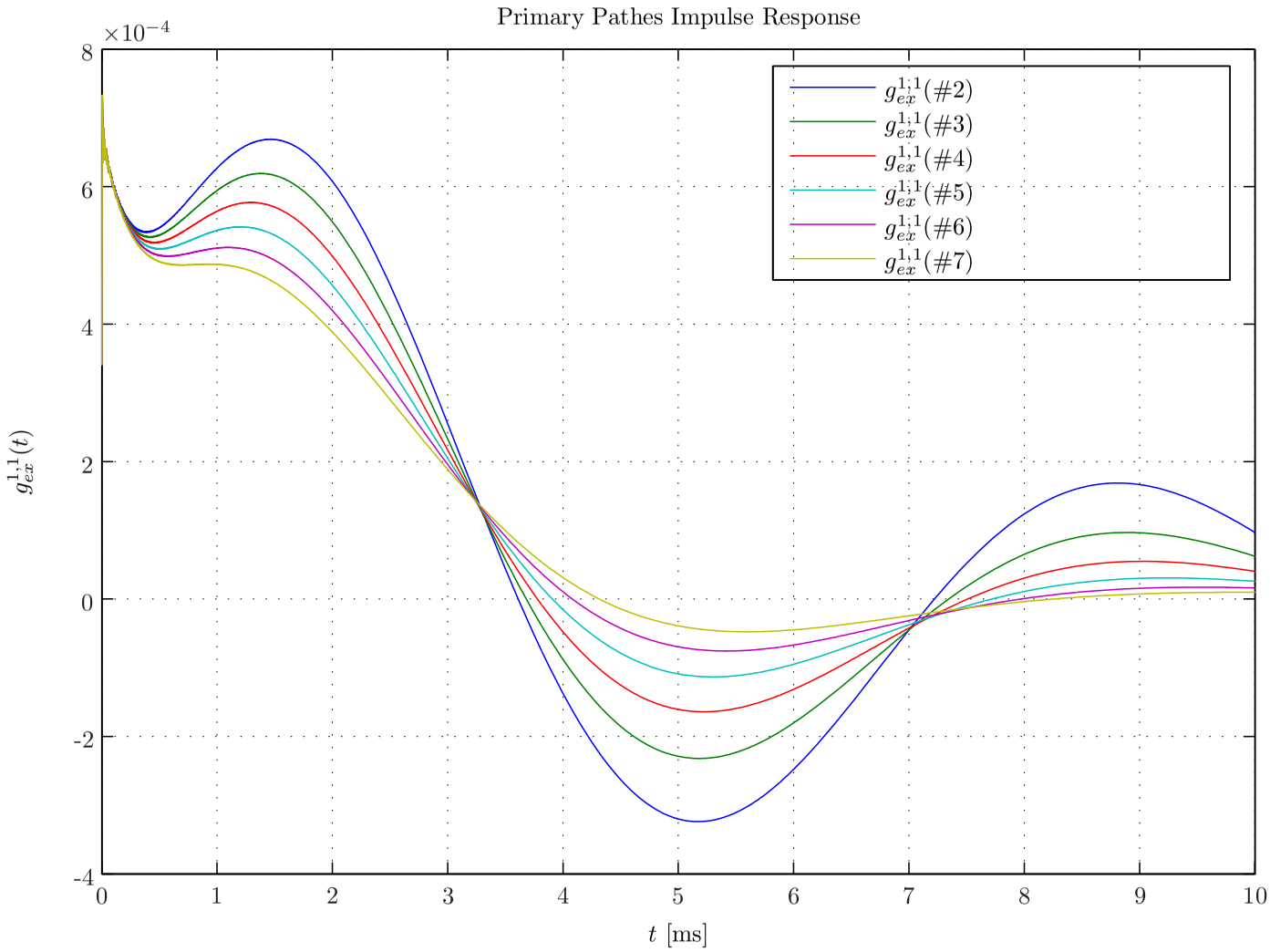

Sim 10.3.5: $g_{ex}^{1,1}$: Closed-Back Headset System: ($f_s = 25.6$ kHz, $K_a = 26\ \mathrm{kN \cdot m^{-1}}$, $K_c = 100\ \mathrm{kN \cdot m^{-1}}$, $R_l^A = 1.26\mathrm{e}+007\ \mathrm{N \cdot s \cdot m^{-5}}$, $f_0 = 141.236$ Hz, $M_s = 0.16$ kg) (FIR : $M_{gex}^{1,1} = 96002$),*Channels:* ($\#2 \leftarrow R_c = 60\ \mathrm{N \cdot s \cdot m^{-1}}$, $\#3 \leftarrow R_c = 80\ \mathrm{N \cdot s \cdot m^{-1}}$, $\#4 \leftarrow R_c = 100\ \mathrm{N \cdot s \cdot m^{-1}}$, $\#5 \leftarrow R_c = 120\ \mathrm{N \cdot s \cdot m^{-1}}$, $\#6 \leftarrow R_c = 140\ \mathrm{N \cdot s \cdot m^{-1}}$, $\#7 \leftarrow R_c = 160\ \mathrm{N \cdot s \cdot m^{-1}}$). **Scenario:** `MultipleSinusoidalsAddiativeNoiseFeedforwardNx2Ne1Ny1Np0/20080305T205250`.

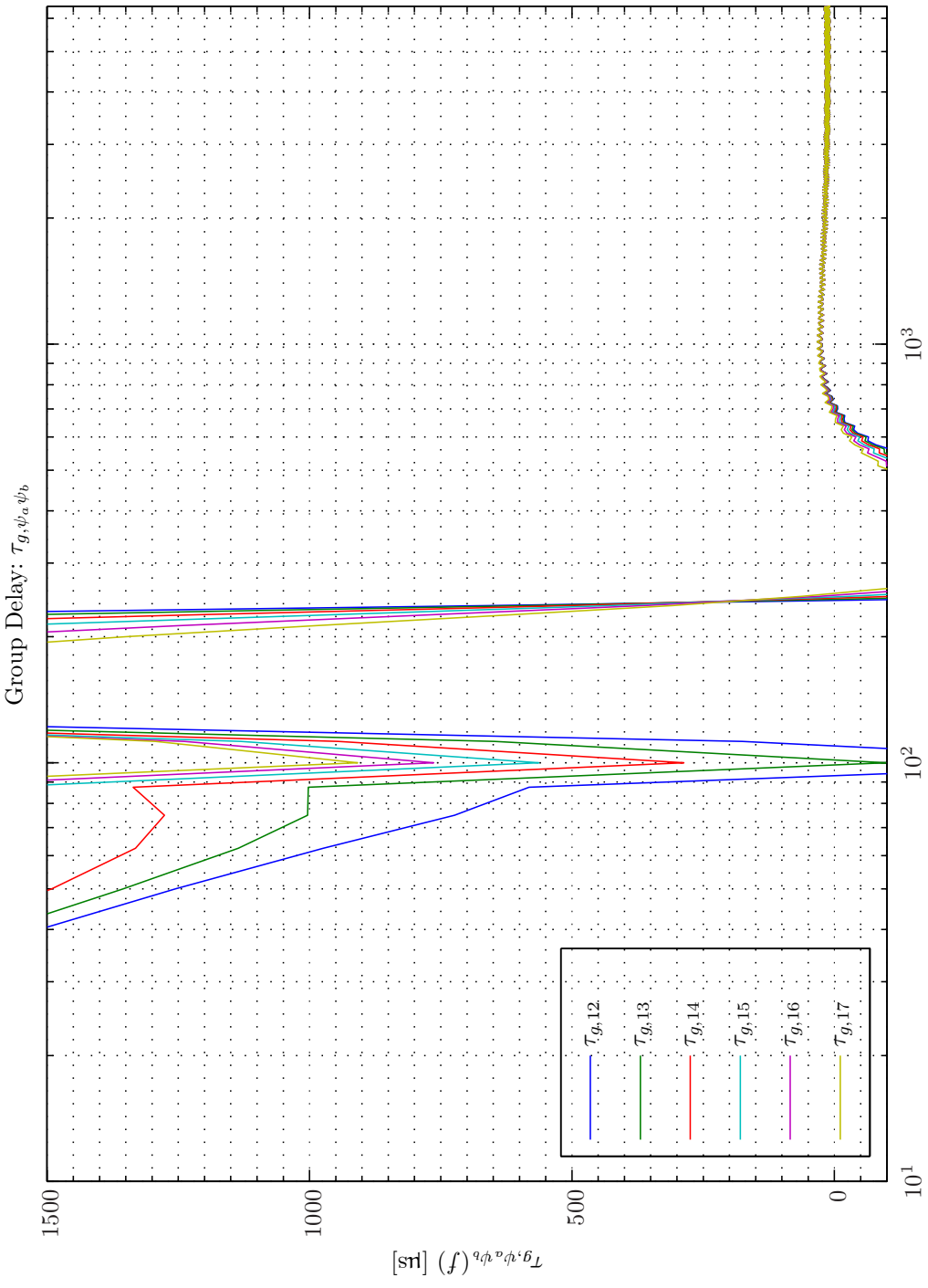

Sim 10.3.6: *Group Delay:* τ_g; f_s^0 = 192 kHz: **Statistical Data Analysis**: Single-Sided Modified Periodogram, f_s = 25.6 kHz, N_{DFT} = 2048, L_{DFT} = 1334, R_{DFT} = 667, Hanning, Δf_m = 76.8192 Hz, T_{DFT} = 0.052109 s, $N_{f,DFT}$ = 1025, Δf_{DFT} = 12.5 Hz, K_{DFT} = 1; $g_{ex}^{1,1}$: Closed-Back Headset System: (f_s = 25.6 kHz, K_a = 26 kN · s · m^{-1}, K_c = 100 kN · m^{-1}, R_l^A = 1.26e + 007 N · s · m^{-5}, f_0 = 141.236 Hz, M_s = 0.16 kg) (FIR : $M_{ex}^{1,1}$ = 96002), *Channels:* (#2 ← R_c = 60 N · s · m^{-1}, #3 ← R_c = 80 N · s · m^{-1}, #4 ← R_c = 100 N · s · m^{-1}, #5 ← R_c = 120 N · s · m^{-1}, #6 ← R_c = 140 N · s · m^{-1}, #7 ← R_c = 160 N · s · m^{-1}). **Scenario:** `MultipleSinusoidalsAddiativeNoiseFeedforwardNx2Ne1Ny1Np0/20080305T205250:` .

11. HEARING PROTECTOR: ACTIVE ATTENUATION

11.1 Introduction

In this chapter a brief technical description of the *active part* of a hearing protection device (HPD) will be carried out and reference made to some of the technical literature in the field. In particular a simple model for the acoustical and electro-acoustical environment interior to closed-back headset is introduced and results from parameterizations hereof presented. Our main objective with this electro-acoustical model is to investigate the influence on the achievable active noise reduction (ANR) performance as determined by group delays. Moreover, the electro-acoustical environment model or secondary path model is used for example in a feedback system (FBS) design employing internal model control (IMC).

In modern HPD design the advantages of active noise control (ANC) have been accommodated in the more expensive range of units. Basically, ANC refers to the technique of:

- Acquisition of a signal with a high coherence with the disturbance, e.g., by a microphone.
- Determination of a cancelation response (adaptive filtering, signal processing).
- Activation of the secondary (cancelation) signal, e.g., by a loudspeaker.

An ideal circumaural earphone would provide maximum attenuation of extraneous noise and optimum coupling between transducer an ear [10]. In his Ph.D. thesis Smeatham [12] provided a detailed but non rigorous assessment of the performance of active noise reduction hearing protectors. From this work it can be concluded that some of the passive attenuation limitations listed in chapter 10 on page 471 also pose problems to the achievable benefits from the introduction of an active noise controller. On the contrary, as the electro-acoustical system is embedded in the mechanical-acoustical system constituted by the earcup the objectives on a high degree of noise reduction and coupling efficiency are at least partially compatible.

Supplementary material on this topic can be found in [11] [5] [7] [3] [8] [1] [13] [2] [9] [4].

11.1.1 Chapter Outline

In section 11.2 a brief discussion of the *electro-acoustical environment* of a closed-back headset will be made. Then in section 11.3 - 11.4 the Terma earcup system and a lumped-element model hereof based on [10] will presented. Finally, in section 11.5 some results from a system identification of the secondary paths partaking in the confined feedforward active control (CFFAC), that is, $g_{ey}^{l,m}$, $g_{xy}^{l,j}$ and $g_{py}^{l,k}$, will be presented.

11.2 Acoustical and Electroacoustical Environment

The total sound field, that is, the residual sound field in the earcup cavities is obtained from *superposition* of a primary and a secondary field.

11.2.1 Primary Sound Pressure Field

In circumaural HPD a hemispheroidal cavity referred to as ear shell encloses the outer ear. Normally, a piston like movement of the ear shells has been assumed. The piston like movement itself will yield some fractional excitation of higher order modes in the cavity. Recent research has revealed that some higher order mode plate excitation will take place with increasing frequency. This higher order mode plate excitation will also add to the fraction of higher order mode contribution to the total primary sound field in the ear cavity.

Moreover, it has been observed that an excitation of the earcups from a direction dependent incident sound field will also increase the level sound pressure variation. Finally, due to a large variation in the mechanical impedance presented by the skin/flesh along the circumference of the ear, the leakage present at the subjective head-ear cushion interface will have circumferential position dependence. In summary, the primary sound field will generally exhibits some deviation from perfect uniformity.

11.2.2 Secondary Sound Pressure Field

In an ANR system a secondary sound field is deliberately introduced in proximity of the ear. Typically a loudspeaker - or more precisely - an earphone, is placed somewhere inside the earcup.

In the literature various problems associated with the earphones have been identified [12]:

- The annular suspension exhibits modes in an irregular manner. In general these resonances are small and confined to a narrow bandwidth. Therefore, this annular mode response of the transducer diaphragm does not affect the passive performance of the ANR system significantly. The annular mode suspension resonances, however, will necessarily lead to non-uniformity in the pressure distribution in the cavity at the particular frequencies.
- Other types of resonance associated with imperfections in the construction of the diaphragm mounting have been reported. As a consequence abrupt changes in magnitude and significant phase shifts has been introduced in the control system making it difficult to maintain stability.

11.2.3 Residual Sound Pressure Field

As neither the primary field nor the secondary field exhibits spatial sound pressure uniformity the residual sound field i.e. the sum of the primary and secondary fields in the cavity **cannot be considered uniform**. In passive HPD the small variation in the primary sound can normally be neglected, since it is the average magnitude of the residual field at the eardrum that is of concern. In contradiction, the ANR system involves at least one so-called error microphone positioned somewhere in the earcup. A deviation from uniformity in the residual field itself might not be a problem when it can be compensated for by adaptive filtering. However, any

deviations from unity in the *coherence function* between the field measured at the position of the error microphone and the field (not measured) at, e.g., the eardrum, will lead to the latter field not being adequately suppressed by the ANR system. Only if it is possible to establish a link between the measured and the sensed sound pressures some additional counter measures can be enforced.

11.2.4 Transducers

Ideally, when designing a critical component as the earcup system is for the helmet based ANR system appropriate models for the suite of embedded transducers, e.g., earphones and microphones should be made.

The choice of earphones and microphones has to some extent been dictated from the environment constraints pertinent to the airborne military applications. The earphones shall have a precise response. The possible benefits from a multi channel control i.e. more than one earphone and/or more than one microphone in each earcup have been pursued. Finally, the location of each transducer have been obtained from a complex optimization procedure, which will involve calculation of the attenuation figures and robustness of the system. The parameters involved should been subject to a Monte Carlo based statistical error analysis.

In particular the design has been focused on environmental constraints pertinent to the airborne military applications and the requirement to produce a sufficient high sound pressure level at low frequencies for the CH-47 helicopter application.

11.3 Terma Earcup Audio System

Under a contract with the Royal Danish Air Force (RDAF) an ANR system has been developed. An exploded view of the Terma earcup system can be found in Figure 11.1. This development includes a solution for the acoustical/electro acoustical system constituted by the circumaural earcups and the loudspeaker and microphone that both have been customized to the application. The earcup system, however, was at the disposition of the present project at a very late stage. It was therefore decided to use a simple lumped element presented next in the simulations. Moreover, as will be evident from the system identification results in section 11.5 on page 489 it turned out that the secondary path exhibit very large group delays in critical frequency region active control (AC). Hence, by using a model we may be able to predict the achievable ANR performance resulting from a second iteration of this design.

11.4 Lumped Element Model

From [10] the so-called[1] *earphone response-ratio* $R(\mathrm{e}^{\imath\omega})$ is defined by

$$R(\mathrm{e}^{\imath\omega}) = \frac{\tilde{p}_{e_m}(\mathrm{e}^{\imath\omega})}{\tilde{Q}(\mathrm{e}^{\imath\omega})}\frac{V}{\rho_0 c^2} = \frac{\tilde{p}_{e_m}(\mathrm{e}^{\imath\omega})}{\tilde{Q}(\mathrm{e}^{\imath\omega})}\frac{S_h^2}{K_a}, \tag{11.4.1}$$

where $\tilde{Q}(\mathrm{e}^{\imath\omega})$ represents the earphone volume displacement of ideal acoustical source with infinite acoustic impedance.

[1] In our context we will preserve the phase information in order to determine the group delays.

Fig. 11.1: Terma Earcup System Exploded View. Error Microphone not included.

In the Terma earcup system a tweeter unit is used as earphone. In order to protect this unit a second-order high-pass filter is inserted as cross-over network. Hence, the actual acoustical source has a earphone volume displacement $\tilde{Q}'(\omega)$, that is obtained from $\tilde{Q}'(\omega) = T_t(\omega)\tilde{Q}(\mathrm{e}^{\imath\omega})$, where $T(\omega)$ denotes the response of the second-order high-pass cross-over filter. This transfer function in turn is govern by

$$T_t(\omega) = \frac{(\imath\omega_r)^2}{(\imath\omega_r)^2 + \imath\omega_r/Q_t + 1}, \tag{11.4.2}$$

where $\omega_r = \omega/\omega_t$ and Q_t denotes the quality factor of the cross-over network. For example, refering to [6, Ch. 9] the quality factor can be realized from a simple cross-over network constituted by a capacitance C_t, and an inductance L_t, according to $L_t = \frac{R_{Et}}{2\pi f_t Q_t}$ and $C_t = \frac{Q_t}{2\pi f_t R_{Et}}$, where R_{Et} is the voice-coil resistance and f_t is the 6 dB cut-off frequency of tweeter.

Introducing now the auxiliary *acoustic* impedance related to mass-spring-resistance of the earcup $Z_m^A(\mathrm{e}^{\imath\omega})$, defined by

$$Z_m^A(\mathrm{e}^{\imath\omega}) = \frac{\imath\omega M_s + R_C + \frac{K_c}{\imath\omega}}{S_h^2}. \tag{11.4.3}$$

Following some trivial derivations the earphone response-ratio defined in (11.4.1) can be expressed as

$$\boxed{R(\mathrm{e}^{\imath\omega}) = \frac{Z_3^A Z_l^A Z_m^A}{Z_3^A(Z_l^A + Z_m^A) + Z_l^A Z_m^A}\frac{S_h^2}{K_a},} \tag{11.4.4}$$

where the auxiliary impedance $Z_3^A(\mathrm{e}^{\imath\omega})$ in turn is obtained as $Z_3^A = \frac{K_a}{\imath\omega S_h^2}$.

Equivalent circuits (*lumped elements*) are only valid for systems where the quantity of an element is not distributed within the space of the element. Therefore, lumped elements cannot be used in connection with modal resonances unless higher order circuits models are introduced. Therefore, the simple model in (11.4.4) will not hold for frequencies above approximately 1200 Hz where the assumption of a uniform field distribution in the interior of the earcup no longer holds.

11.4.1 Simulations

A parameter study was conducted in order to shed light over the secondary path response as a function of the various parameters involved. The following constant parameters were used: $K_a = 26\ \mathrm{kN\cdot m^{-1}}$, $K_c = 100\ \mathrm{kN\cdot m^{-1}}$, $R_l^A = 1.26\mathrm{e}+007\ \mathrm{N\cdot s\cdot m^{-5}}$, $f_0 = 141.236\ \mathrm{Hz}$, $M_s = 0.16\ \mathrm{kg}$. In total six different values of the mechanical resistance of the cushion and two values of Q_t were investigated, namely $R_c = 60, 80, 100, 120, 140, 160\ \mathrm{N\cdot s\cdot m^{-1}}$ and $Q_t = 1.0, 1.6$.

The magnitude and phase of the in total twelve transfer function variants are shown in Simulation 11.4.1 - 11.4.2 on pages 486–487 respectively. The corresponding impulse response can be seen in Simulation 11.4.3 on page 488.

We observe that the mechanical resistance of the cushion that controls the Q-factor and the phase transition at the resonance frequency ($f_0 \approx 141$ Hz) also to a large extent determines the

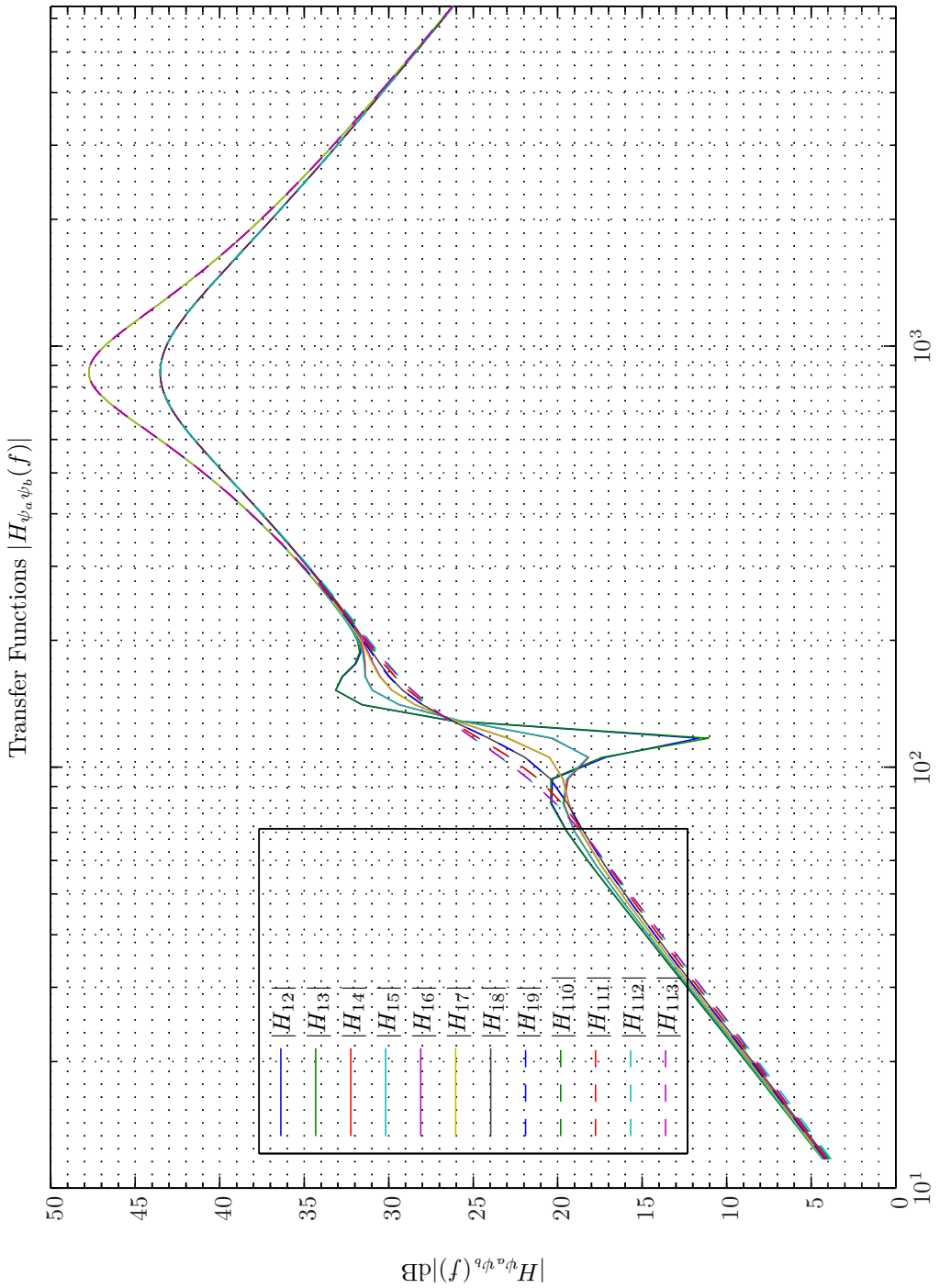

Sim 11.4.1: *Transfer Function, Magnitude:* $|H_{\psi_a\psi_b}(f)|$: **Statistical Data Analysis**: Single-Sided Modified Periodogram, f_s = 192 kHz, N_{DFT} = 16384, L_{DFT} = 10000, R_{DFT} = 5000, Hanning, Δf_m = 76.8077 Hz, T_{DFT} = 0.052083 s, $N_{f,DFT}$ = 8193, Δf_{DFT} = 11.7188 Hz, K_{DFT} = 1; $g_{ey}^{1,1}$: Closed-Back Headset System: (f_s = 192 kHz, K_a = 26 kN · m^{-1}, K_c = 100 kN · m^{-1}, R_l^A = 1.26e + 007 N · s · m^{-5}, f_0 = 141.236 Hz, M_s = 0.16 kg) (FIR : $M_{gey}^{1,1}$ = 96002),*Channels:* (#2 ← R_c = 60 N · s · m^{-1}, Q_t = 1, #3 ← R_c = 60 N · s · m^{-1}, Q_t = 1.6, #4 ← R_c = 80 N · s · m^{-1}, Q_t = 1, #5 ← R_c = 80 N · s · m^{-1}, Q_t = 1.6, #6 ← R_c = 100 N · s · m^{-1}, Q_t = 1, #7 ← R_c = 100 N · s · m^{-1}, Q_t = 1.6, #8 ← R_c = 120 N · s · m^{-1}, Q_t = 1, #9 ← R_c = 120 N · s · m^{-1}, Q_t = 1.6, #10 ← R_c = 140 N · s · m^{-1}, Q_t = 1, #11 ← R_c = 140 N · s · m^{-1}, Q_t = 1.6, #12 ← R_c = 160 N · s · m^{-1}, Q_t = 1, #13 ← R_c = 160 N · s · m^{-1}, Q_t = 1.6). **Scenario:** `MultipleSinusoidalsAddiativeNoiseFeedforwardNx2Nel1Ny1Np0/20080302T203234;` .

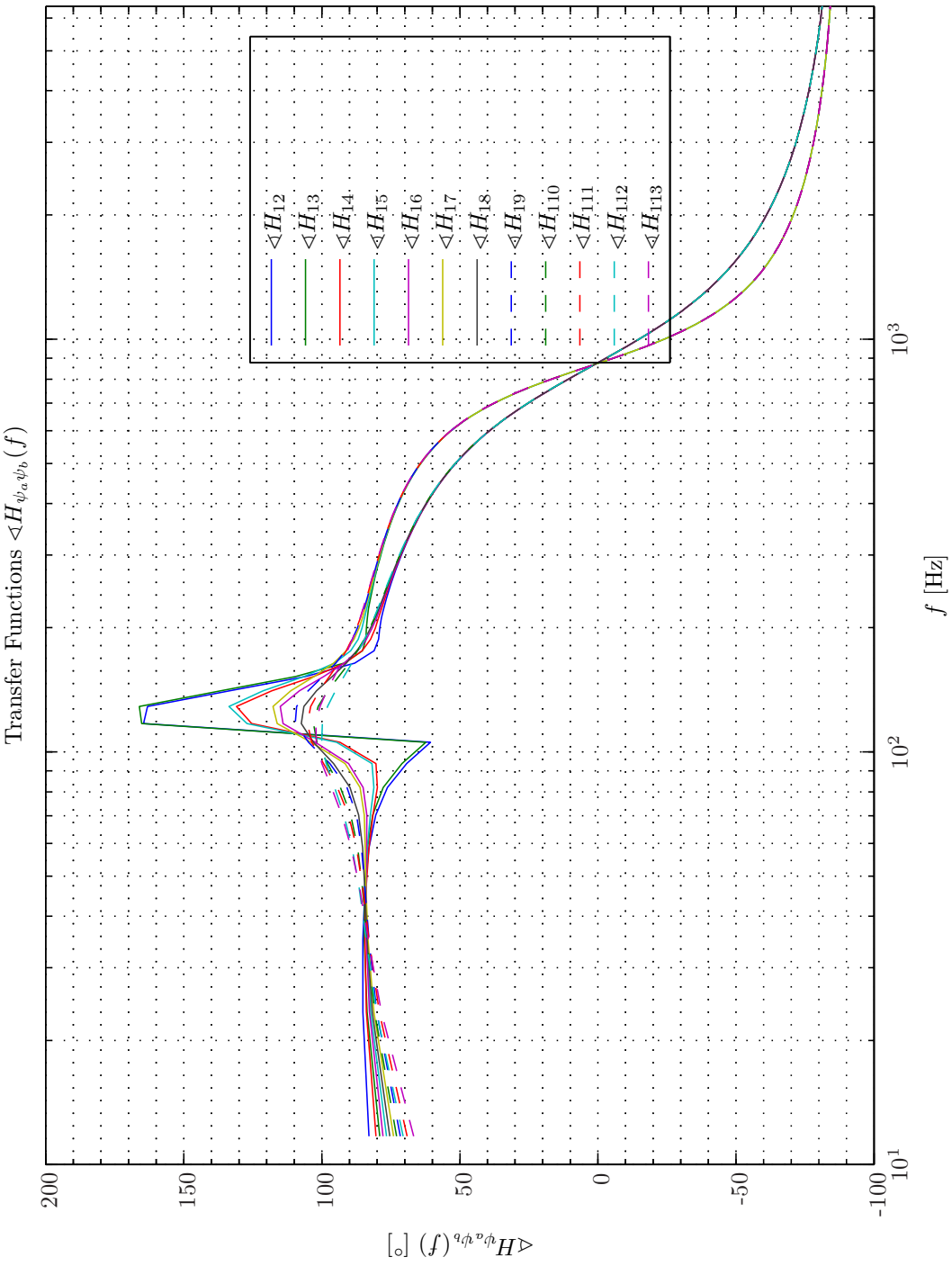

Sim 11.4.2: *Transfer Function, Phase:* $\sphericalangle H_{\psi_a\psi_b}(f)$: **Statistical Data Analysis**: Single-Sided Modified Periodogram, f_s = 192 kHz, N_{DFT} = 16384, L_{DFT} = 10000, R_{DFT} = 5000, Hanning, Δf_m = 76.8077 Hz, T_{DFT} = 0.052083 s, $N_{f,DFT}$ = 8193, Δf_{DFT} = 11.7188 Hz, K_{DFT} = 1; $g_{ey}^{1,1}$: Closed-Back Headset System: (f_s = 192 kHz, K_a = 26 kN · m^{-1}, K_c = 100 kN · m^{-1}, R_l^A = 1.26e + 007 N · s · m^{-5}, f_0 = 141.236 Hz, M_s = 0.16 kg) (FIR : $M_{gey}^{1,1}$ = 96002),*Channels:* (#2 ← R_c = 60 N · s · m^{-1}, Q_t = 1, #3 ← R_c = 60 N · s · m^{-1}, Q_t = 1.6, #4 ← R_c = 80 N · s · m^{-1}, Q_t = 1, #5 ← R_c = 80 N · s · m^{-1}, Q_t = 1.6, #6 ← R_c = 100 N · s · m^{-1}, Q_t = 1, #7 ← R_c = 100 N · s · m^{-1}, Q_t = 1.6, #8 ← R_c = 120 N · s · m^{-1}, Q_t = 1, #9 ← R_c = 120 N · s · m^{-1}, Q_t = 1.6, #10 ← R_c = 140 N · s · m^{-1}, Q_t = 1, #11 ← R_c = 140 N · s · m^{-1}, Q_t = 1.6, #12 ← R_c = 160 N · s · m^{-1}, Q_t = 1, #13 ← R_c = 160 N · s · m^{-1}, Q_t = 1.6). **Scenario:** `MultipleSinusoidalsAddiativeNoiseFeedforwardNx2Ne1Ny1Np0/20080302T203234;`.

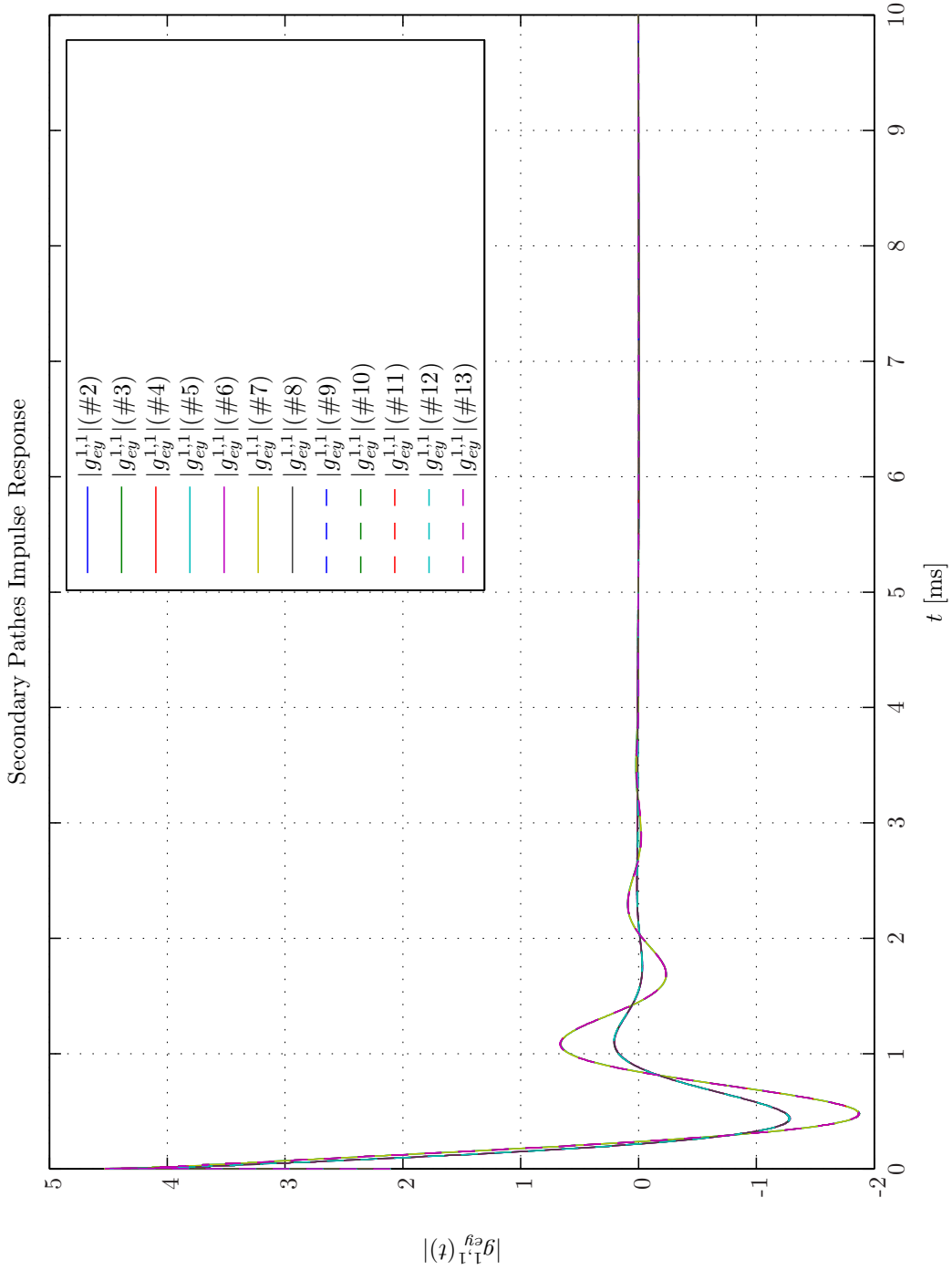

Sim 11.4.3: $g_{ey}^{1,1}$: Closed-Back Headset System: ($f_s = 192$ kHz, $K_a = 26$ kN $\cdot$ m^{-1}, $K_c = 100$ kN $\cdot$ m^{-1}, $R_l^A = 1.26\text{e}+007$ N $\cdot$ s $\cdot$ m^{-5}, $f_0 = 141.236$ Hz, $M_s = 0.16$ kg) (FIR : $M_{geq}^{1,1} = 96002$), *Channels:* ($\#2 \leftarrow R_c = 60$ N $\cdot$ s $\cdot$ m^{-1}, $Q_t = 1$, $\#3 \leftarrow R_c = 60$ N $\cdot$ s $\cdot$ m^{-1}, $Q_t = 1.6$, $\#4 \leftarrow R_c = 80$ N $\cdot$ s $\cdot$ m^{-1}, $Q_t = 1$, $\#5 \leftarrow R_c = 80$ N $\cdot$ s $\cdot$ m^{-1}, $Q_t = 1.6$, $\#6 \leftarrow R_c = 100$ N $\cdot$ s $\cdot$ m^{-1}, $Q_t = 1$, $\#7 \leftarrow R_c = 100$ N $\cdot$ s $\cdot$ m^{-1}, $Q_t = 1.6$, $\#8 \leftarrow R_c = 120$ N $\cdot$ s $\cdot$ m^{-1}, $Q_t = 1$, $\#9 \leftarrow R_c = 120$ N $\cdot$ s $\cdot$ m^{-1}, $Q_t = 1.6$, $\#10 \leftarrow R_c = 140$ N $\cdot$ s $\cdot$ m^{-1}, $Q_t = 1$, $\#11 \leftarrow R_c = 140$ N $\cdot$ s $\cdot$ m^{-1}, $Q_t = 1.6$, $\#12 \leftarrow R_c = 160$ N $\cdot$ s $\cdot$ m^{-1}, $Q_t = 1$, $\#13 \leftarrow R_c = 160$ N $\cdot$ s $\cdot$ m^{-1}, $Q_t = 1.6$). **Scenario:** `MultipleSinusoidalsAddiativeNoiseFeedforwardNx2Ne1Ny1Np0/20080302T203234`.

phase transition of the earphone response ratio. Accordingly, the behavior of *active part* of a HPD and the corresponding *passive part* are interrelated.

In Simulation 11.4.4 - 11.4.5 on pages 490–491 the group delay and estimated achievable ANR attenuation for the single-rate system (SRS) with $f_s^1 = 48$ kHz is depicted. For $Q_t = 1.6$ the group delay is approximately 670 µs at $f_t = 870$ Hz which agrees with the result obtained from a system identification in section 11.5 viz. Simulation 11.5.10 - 11.5.11 on pages 506–507. hence, from group delay considerations we may conclude that the benefit of feedback based AC of random signals above $150 - 200$ Hz dependent on the value of R_c - is rather limited. The advantage of employing the confined feedforward (CFF) topology is clearly exhibited in Simulation 11.4.6 - 11.4.7 on pages 492–493 where a (frequency independent) spatially-weighted-averaged acquisition lead time of 900 µs is included. Except for a small frequency range $200 - 250$ Hz the performance will not be limited from group delays. Moreover, from Simulation 10.3.6 on page 479 we know that the primary path exhibit a very large group delay at resonance frequency of the passive part of the system which means that the effective acquisition lead-time is increased in this frequency range too.

Finally, in Simulation 11.4.8 - 11.4.9 on pages 494–495 the influence of the quality factor Q_t on the group delay for two values of the cushion resistance $R_c = 80, 120\ \mathrm{N \cdot s \cdot m^{-1}}$ for the same SRS with $f_s^1 = 48$ kHz is shown.

We appreciate that for $R_c = 120\ \mathrm{N \cdot s \cdot m^{-1}}$ and $Q_t = 0.5$, the group delay is considerably reduced as compated with actual system for which we have estimated $R_c = 80\ \mathrm{N \cdot s \cdot m^{-1}}$ and $Q_t = 1.6$. However, the fb based AC is still limited to the sub 200 Hz frequency regime from group delay considerations.

11.5 System Identification of Secondary Pathes

The secondary paths all concern sensor signals in response to control output signals. Hence, the secondary paths include the plants that link the control output signals to the error signals, reference signals and performance signals, that is, $g_{ey}^{l,m}$, $g_{xy}^{l,j}$ and $g_{py}^{l,k}$ respectively. The aim of the secondary paths measurements are twofold. Firstly, we want to obtain measurements independent of any adaptive filtering algorithm in order to verify similar - albeit adaptive - system identification measurements within the frame of AC as discussed in chapter 7 on page 291. Secondly, we may use the measurements to assess the quality of the ordinary lumped element model presented in section 11.4.

The system identification measurements were conducted in a sound isolation box in order to prevent interferences from extraneous noise sources. The topology consisted of a total of $N_x = 10$ BK4949 surface microphones flush-mounted on Gentex HGU-55/P helmet mounted on a BK 4128 C head and torso simulator (HATS) that in turn includes the BK 4159 C left ear simulator and the BK 4158 C right ear simulator, that is, $N_p = 2$. The performance signals acquired by the left and right ear simulator are by d_1^p and d_2^p respectively. The Terma Earcup Audio System was used on the left ear only that provide a disturbance signal that will be designated by d_1, that is, $N_e = 1$. Some photos illuminating the measurement setup can be found in Figure 2.1 - 2.2 on pages 33–34.

For all statistical analysis the following power spectral density functions parameters have been chosen: Periodogram, single-sided, $f_s = 65.536$ kHz, $N_{DFT} = 16384, L_{DFT} = 16385, R_{DFT} = 8193$, Hanning, $T_{DFT} = 0.25$ s, $N_{f_{pts}} = 8193, \Delta f_{DFT} = 4$ Hz, $K_{DFT} = 5$.

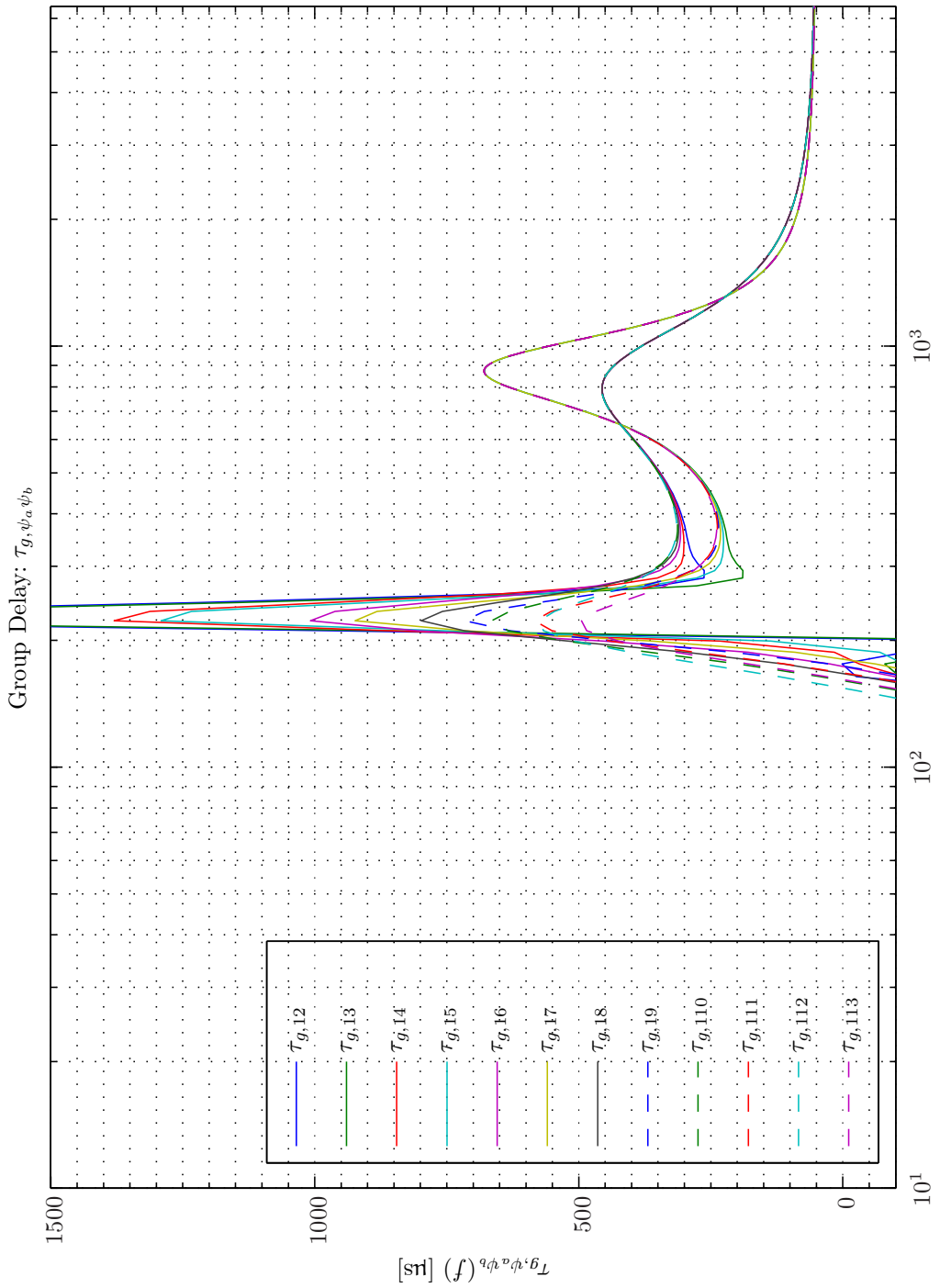

Sim 11.4.4: *Group Delay*: τ_g; f_s^0 = 48 kHz: **Statistical Data Analysis**: Single-Sided Modified Periodogram, f_s = 192 kHz, N_{DFT} = 16384, L_{DFT} = 10000, R_{DFT} = 5000, Hanning, Δf_m = 76.8077 Hz, T_{DFT} = 0.052083 s, $N_{f,DFT}$ = 8193, Δf_{DFT} = 11.7188 Hz, K_{DFT} = 1; $g_{ey}^{1,1}$: Closed-Back Headset System: (f_s = 192 kHz, K_a = 26 kN · m^{-1}, K_c = 100 kN · m^{-1}, R_l^A = 1.26e + 007 N · s · m^{-5}, f_0 = 141.236 Hz, M_s = 0.16 kg) (FIR : $M_{gey}^{1,1}$ = 96002),*Channels:* (#2 ← R_c = 60 N · s · m^{-1}, Q_t = 1, #3 ← R_c = 60 N · s · m^{-1}, Q_t = 1.6, #4 ← R_c = 80 N · s · m^{-1}, Q_t = 1, #5 ← R_c = 80 N · s · m^{-1}, Q_t = 1.6, #6 ← R_c = 100 N · s · m^{-1}, Q_t = 1, #7 ← R_c = 100 N · s · m^{-1}, Q_t = 1.6, #8 ← R_c = 120 N · s · m^{-1}, Q_t = 1, #9 ← R_c = 120 N · s · m^{-1}, Q_t = 1.6, #10 ← R_c = 140 N · s · m^{-1}, Q_t = 1, #11 ← R_c = 140 N · s · m^{-1}, Q_t = 1.6, #12 ← R_c = 160 N · s · m^{-1}, Q_t = 1, #13 ← R_c = 160 N · s · m^{-1}, Q_t = 1.6). **Scenario:** `MultipleSinusoidalsAddiativeNoiseFeedforwardNx2Nel1Ny1Np0/20080302T203234;` .

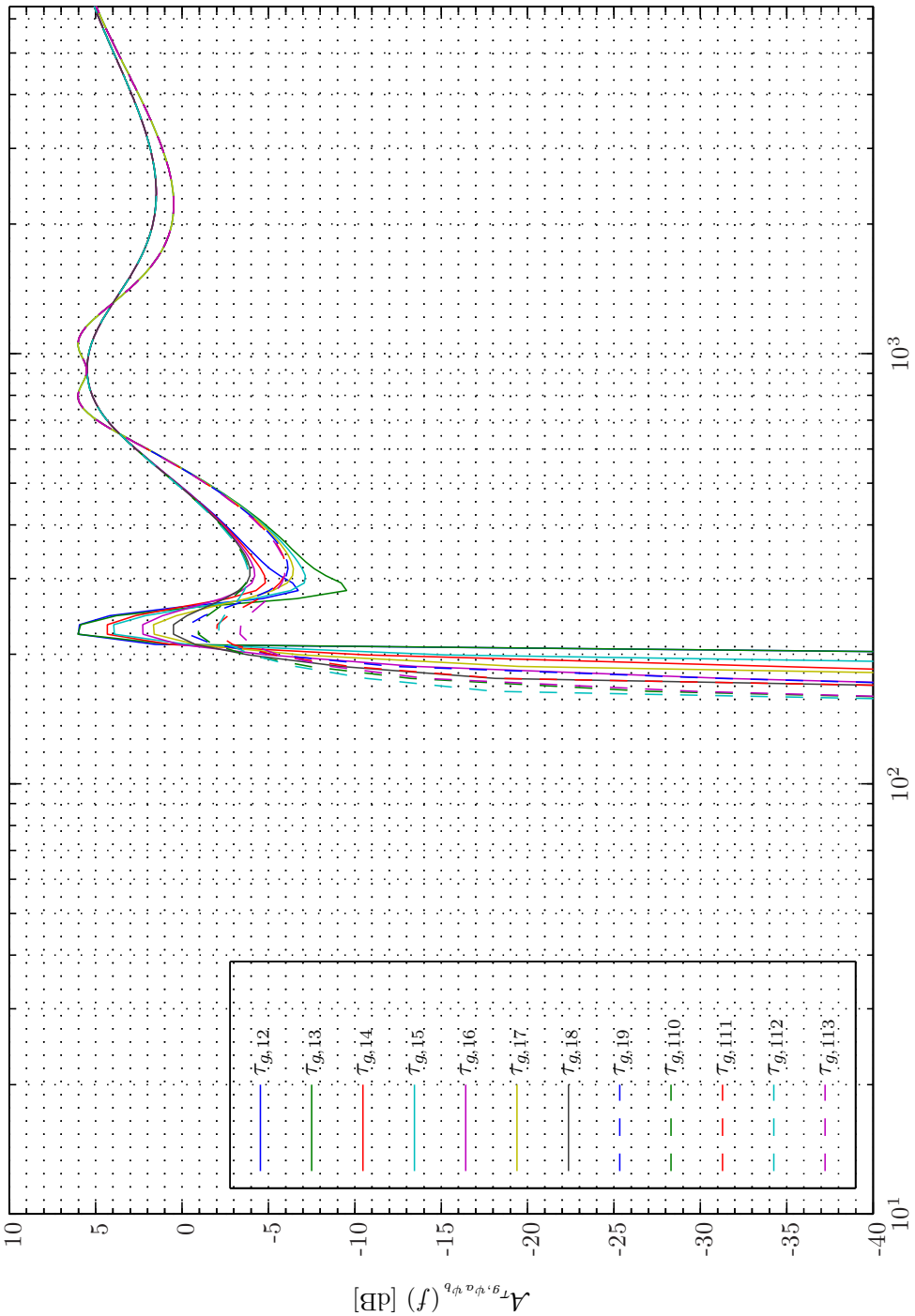

Sim 11.4.5: *Attenuation vs Group Delay:* $20\log_{10}|1-\mathrm{e}^{-\imath 2\pi f \tau_g}|$; $f_s^0 = 48$ kHz: **Statistical Data Analysis**: Single-Sided Modified Periodogram, $f_s = 192$ kHz, $N_{DFT} = 16384$, $L_{DFT} = 10000$, $R_{DFT} = 5000$, Hanning, $\Delta f_m = 76.8077$ Hz, $T_{DFT} = 0.052083$ s, $N_{f,DFT} = 8193$, $\Delta f_{DFT} = 11.7188$ Hz, $K_{DFT} = 1$; $g_{ey}^{1,1}$: Closed-Back Headset System: ($f_s = 192$ kHz, $K_a = 26$ kN $\cdot$ m^{-1}, $K_c = 100$ kN $\cdot$ m^{-1}, $R_l^A = 1.26\mathrm{e}+007$ N $\cdot$ s $\cdot$ m^{-5}, $f_0 = 141.236$ Hz, $M_s = 0.16$ kg) (FIR : $M_{ey}^{1,1} = 96002$),*Channels:* (#2 $\leftarrow R_c = 60$ N $\cdot$ s $\cdot$ m^{-1}, $Q_t = 1$, #3 $\leftarrow R_c = 60$ N $\cdot$ s $\cdot$ m^{-1}, $Q_t = 1.6$, #4 $\leftarrow R_c = 80$ N $\cdot$ s $\cdot$ m^{-1}, $Q_t = 1$, #5 $\leftarrow R_c = 80$ N $\cdot$ s $\cdot$ m^{-1}, $Q_t = 1.6$, #6 $\leftarrow R_c = 100$ N $\cdot$ s $\cdot$ m^{-1}, $Q_t = 1$, #7 $\leftarrow R_c = 100$ N $\cdot$ s $\cdot$ m^{-1}, $Q_t = 1.6$, #8 $\leftarrow R_c = 120$ N $\cdot$ s $\cdot$ m^{-1}, $Q_t = 1$, #9 $\leftarrow R_c = 120$ N $\cdot$ s $\cdot$ m^{-1}, $Q_t = 1.6$, #10 $\leftarrow R_c = 140$ N $\cdot$ s $\cdot$ m^{-1}, $Q_t = 1$, #11 $\leftarrow R_c = 140$ N $\cdot$ s $\cdot$ m^{-1}, $Q_t = 1.6$, #12 $\leftarrow R_c = 160$ N $\cdot$ s $\cdot$ m^{-1}, $Q_t = 1$, #13 $\leftarrow R_c = 160$ N $\cdot$ s $\cdot$ m^{-1}, $Q_t = 1.6$). **Scenario:** `MultipleSinusoidalsAddiativeNoiseFeedforwardNx2Ne1Ny1Np0/20080302T203234;`.

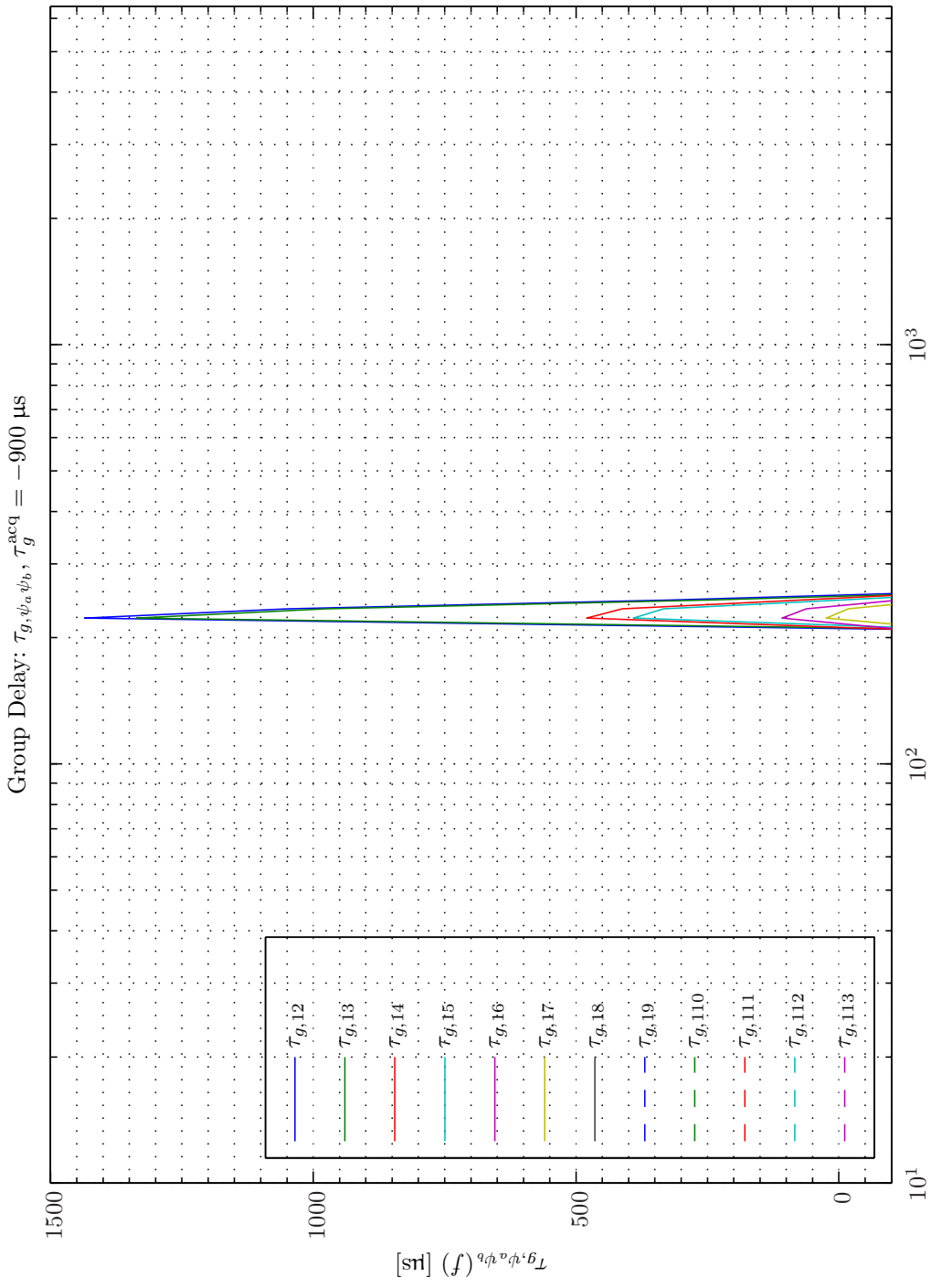

Sim 11.4.6: *Group Delay*: τ_g; $f_s^0 = 48$ kHz: **Statistical Data Analysis**: Single-Sided Modified Periodogram, $f_s = 192$ kHz, $N_{DFT} = 16384$, $L_{DFT} = 10000$, $R_{DFT} = 5000$, Hanning, $\Delta f_m = 76.8077$ Hz, $T_{DFT} = 0.052083$ s, $N_{f,DFT} = 8193$, $\Delta f_{DFT} = 11.7188$ Hz, $K_{DFT} = 1$; $g_{ey}^{1,1}$: Closed-Back Headset System: ($f_s = 192$ kHz, $K_a = 26$ kN $\cdot$ m^{-1}, $K_c = 100$ kN $\cdot$ m^{-1}, $R_l^A = 1.26\text{e}+007$ N $\cdot$ s $\cdot$ m^{-5}, $f_0 = 141.236$ Hz, $M_s = 0.16$ kg) (FIR : $M_{gey}^{1,1} = 96002$),*Channels:* (#2 $\leftarrow R_c = 60$ N $\cdot$ s $\cdot$ m^{-1}, $Q_t = 1$, #3 $\leftarrow R_c = 60$ N $\cdot$ s $\cdot$ m^{-1}, $Q_t = 1.6$, #4 $\leftarrow R_c = 80$ N $\cdot$ s $\cdot$ m^{-1}, $Q_t = 1$, #5 $\leftarrow R_c = 80$ N $\cdot$ s $\cdot$ m^{-1}, $Q_t = 1.6$, #6 $\leftarrow R_c = 100$ N $\cdot$ s $\cdot$ m^{-1}, $Q_t = 1$, #7 $\leftarrow R_c = 100$ N $\cdot$ s $\cdot$ m^{-1}, $Q_t = 1.6$, #8 $\leftarrow R_c = 120$ N $\cdot$ s $\cdot$ m^{-1}, $Q_t = 1$, #9 $\leftarrow R_c = 120$ N $\cdot$ s $\cdot$ m^{-1}, $Q_t = 1.6$, #10 $\leftarrow R_c = 140$ N $\cdot$ s $\cdot$ m^{-1}, $Q_t = 1$, #11 $\leftarrow R_c = 140$ N $\cdot$ s $\cdot$ m^{-1}, $Q_t = 1.6$, #12 $\leftarrow R_c = 160$ N $\cdot$ s $\cdot$ m^{-1}, $Q_t = 1$, #13 $\leftarrow R_c = 160$ N $\cdot$ s $\cdot$ m^{-1}, $Q_t = 1.6$). **Scenario:** `MultipleSinusoidalsAddiativeNoiseFeedforwardNx2Nel1Ny1Np0/20080302T203234;` .

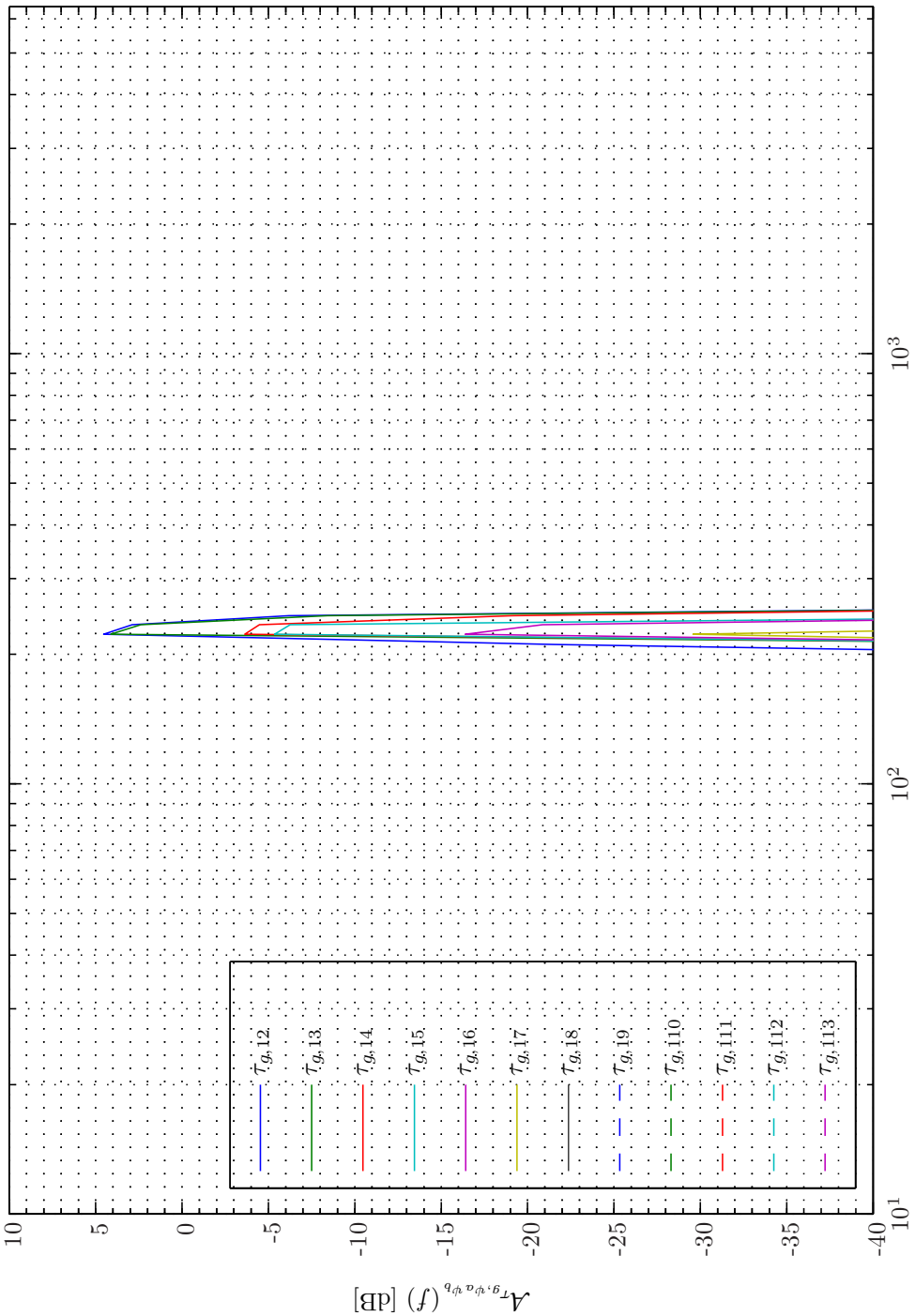

Sim 11.4.7: *Attenuation vs Group Delay:* $20\log_{10}|1-\mathrm{e}^{-\imath 2\pi f \tau_g}|$; $f_s^0 = 48$ kHz: **Statistical Data Analysis**: Single-Sided Modified Periodogram, $f_s = 192$ kHz, $N_{DFT} = 16384$, $L_{DFT} = 10000$, $R_{DFT} = 5000$, Hanning, $\Delta f_m = 76.8077$ Hz, $T_{DFT} = 0.052083$ s, $N_{f,DFT} = 8193$, $\Delta f_{DFT} = 11.7188$ Hz, $K_{DFT} = 1$; $g_{ey}^{1,1}$: Closed-Back Headset System: ($f_s = 192$ kHz, $K_a = 26$ kN $\cdot$ m^{-1}, $K_c = 100$ kN $\cdot$ m^{-1}, $R_l^A = 1.26\mathrm{e}+007$ N $\cdot$ s $\cdot$ m^{-5}, $f_0 = 141.236$ Hz, $M_s = 0.16$ kg) (FIR : $M_{gey}^{1,1} = 96002$),*Channels:* (#2 $\leftarrow R_c = 60$ N $\cdot$ s $\cdot$ m^{-1}, $Q_t = 1$, #3 $\leftarrow R_c = 60$ N $\cdot$ s $\cdot$ m^{-1}, $Q_t = 1.6$, #4 $\leftarrow R_c = 80$ N $\cdot$ s $\cdot$ m^{-1}, $Q_t = 1$, #5 $\leftarrow R_c = 80$ N $\cdot$ s $\cdot$ m^{-1}, $Q_t = 1.6$, #6 $\leftarrow R_c = 100$ N $\cdot$ s $\cdot$ m^{-1}, $Q_t = 1$, #7 $\leftarrow R_c = 100$ N $\cdot$ s $\cdot$ m^{-1}, $Q_t = 1.6$, #8 $\leftarrow R_c = 120$ N $\cdot$ s $\cdot$ m^{-1}, $Q_t = 1$, #9 $\leftarrow R_c = 120$ N $\cdot$ s $\cdot$ m^{-1}, $Q_t = 1.6$, #10 $\leftarrow R_c = 140$ N $\cdot$ s $\cdot$ m^{-1}, $Q_t = 1$, #11 $\leftarrow R_c = 140$ N $\cdot$ s $\cdot$ m^{-1}, $Q_t = 1.6$, #12 $\leftarrow R_c = 160$ N $\cdot$ s $\cdot$ m^{-1}, $Q_t = 1$, #13 $\leftarrow R_c = 160$ N $\cdot$ s $\cdot$ m^{-1}, $Q_t = 1.6$). **Scenario:** `MultipleSinusoidalsAddiativeNoiseFeedforwardNx2Ne1Ny1Np0/20080302T203234;`.

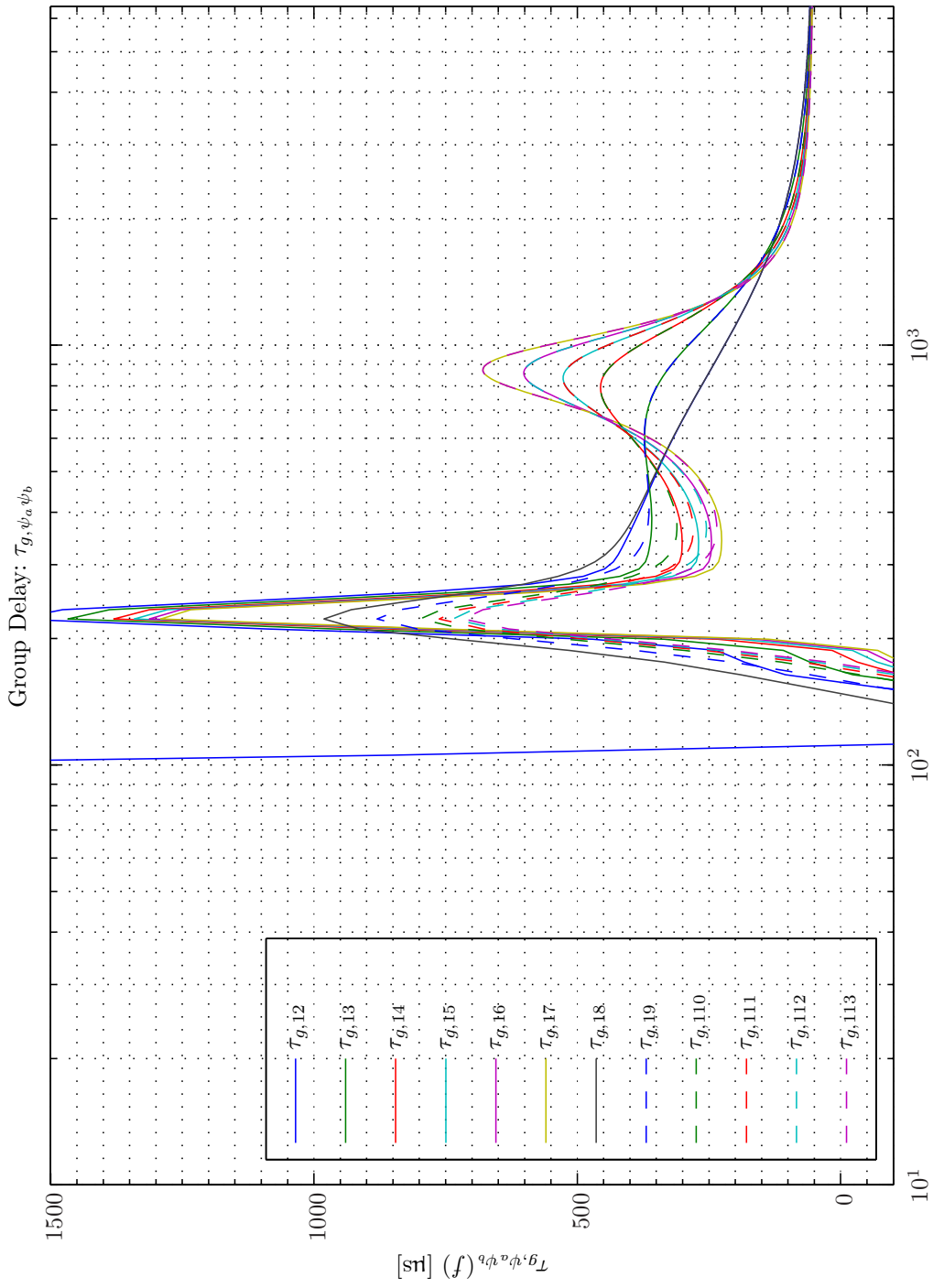

Sim 11.4.8: *Group Delay*: τ_g; f_s^0 = 48 kHz: **Statistical Data Analysis**: Single-Sided Modified Periodogram, f_s = 192 kHz, N_{DFT} = 16384, L_{DFT} = 10000, R_{DFT} = 5000, Hanning, Δf_m = 76.8077 Hz, T_{DFT} = 0.052083 s, $N_{f,DFT}$ = 8193, Δf_{DFT} = 11.7188 Hz, K_{DFT} = 1; $g_{ey}^{1,1}$: Closed-Back Headset System: (f_s = 192 kHz, K_a = 26 kN · m^{-1}, K_c = 100 kN · m^{-1}, R_l^A = 1.26e + 007 N · s · m^{-5}, f_0 = 141.236 Hz, M_s = 0.16 kg) (FIR : $M_{gey}^{1,1}$ = 96002),*Channels:* (#2 ← R_c = 80 N · s · m^{-1}, Q_t = 0.5, #3 ← R_c = 80 N · s · m^{-1}, Q_t = 0.71, #4 ← R_c = 80 N · s · m^{-1}, Q_t = 1, #5 ← R_c = 80 N · s · m^{-1}, Q_t = 1.2, #6 ← R_c = 80 N · s · m^{-1}, Q_t = 1.4, #7 ← R_c = 80 N · s · m^{-1}, Q_t = 1.6, #8 ← R_c = 120 N · s · m^{-1}, Q_t = 0.5, #9 ← R_c = 120 N · s · m^{-1}, Q_t = 0.71, #10 ← R_c = 120 N · s · m^{-1}, Q_t = 1, #11 ← R_c = 120 N · s · m^{-1}, Q_t = 1.2, #12 ← R_c = 120 N · s · m^{-1}, Q_t = 1.4, #13 ← R_c = 120 N · s · m^{-1}, Q_t = 1.6). **Scenario:** `MultipleSinusoidalsAddiativeNoiseFeedforwardNx2Ne1Ny1Np0/20080303T011241:`.

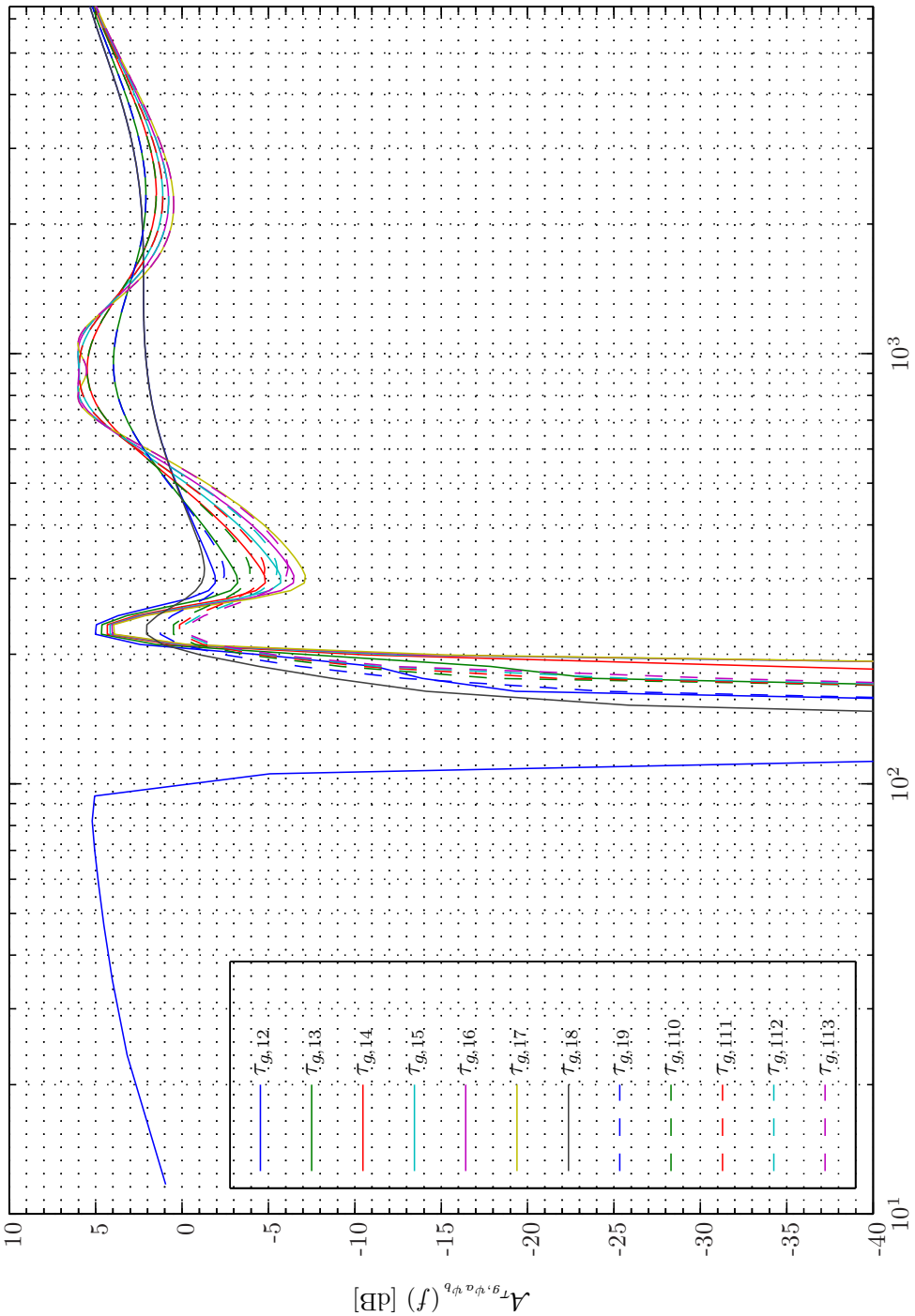

Sim 11.4.9: *Attenuation vs Group Delay:* $20\log_{10}|1-\mathrm{e}^{-\imath 2\pi f \tau_g}|$; $f_s^0 = 48$ kHz: **Statistical Data Analysis**: Single-Sided Modified Periodogram, $f_s = 192$ kHz, $N_{DFT} = 16384$, $L_{DFT} = 10000$, $R_{DFT} = 5000$, Hanning, $\Delta f_m = 76.8077$ Hz, $T_{DFT} = 0.052083$ s, $N_{f,DFT} = 8193$, $\Delta f_{DFT} = 11.7188$ Hz, $K_{DFT} = 1$; $g_{ey}^{1,1}$: Closed-Back Headset System: ($f_s = 192$ kHz, $K_a = 26$ kN$\cdot$m^{-1}, $K_c = 100$ kN$\cdot$m^{-1}, $R_l^A = 1.26\mathrm{e}+007$ N$\cdot$s$\cdot$m^{-5}, $f_0 = 141.236$ Hz, $M_s = 0.16$ kg) (FIR : $M_{gey}^{1,1} = 96002$),*Channels:* (#2 $\leftarrow R_c = 80$ N$\cdot$s$\cdot$m^{-1}, $Q_t = 0.5$, #3 $\leftarrow R_c = 80$ N$\cdot$s$\cdot$m^{-1}, $Q_t = 0.71$, #4 $\leftarrow R_c = 80$ N$\cdot$s$\cdot$m^{-1}, $Q_t = 1$, #5 $\leftarrow R_c = 80$ N$\cdot$s$\cdot$m^{-1}, $Q_t = 1.2$, #6 $\leftarrow R_c = 80$ N$\cdot$s$\cdot$m^{-1}, $Q_t = 1.4$, #7 $\leftarrow R_c = 80$ N$\cdot$s$\cdot$m^{-1}, $Q_t = 1.6$, #8 $\leftarrow R_c = 120$ N$\cdot$s$\cdot$m^{-1}, $Q_t = 0.5$, #9 $\leftarrow R_c = 120$ N$\cdot$s$\cdot$m^{-1}, $Q_t = 0.71$, #10 $\leftarrow R_c = 120$ N$\cdot$s$\cdot$m^{-1}, $Q_t = 1$, #11 $\leftarrow R_c = 120$ N$\cdot$s$\cdot$m^{-1}, $Q_t = 1.2$, #12 $\leftarrow R_c = 120$ N$\cdot$s$\cdot$m^{-1}, $Q_t = 1.4$, #13 $\leftarrow R_c = 120$ N$\cdot$s$\cdot$m^{-1}, $Q_t = 1.6$). **Scenario:** `MultipleSinusoidalsAddiativeNoiseFeedforwardNx2Ne1Ny1Np0/20080303T011241.;`.

The system identification uses a random white noise ($\mathbf{N}(0, 0.2)$) distributed signal described in Appendix E on page 613. Measurements were acquired over a 0.8 s time period.

11.5.1 System Identification of Secondary Pathes $g_{ey}^{l,m}$

System Identification of Secondary Pathes $g_{ey}^{l,m}$ Ordinary Coherence Function

The ordinary coherence function and related attenuation in the SysID is depicted in Simulation 11.5.1 - 11.5.2 on pages 497–498. We appreciate that for frequency above 30 Hz the ordinary coherence function is very close to unity which in turn warrants for validity of the results to be presented in the subsequent text.

System Identification of Secondary Pathes $g_{ey}^{l,m}$ Transfer Function

The secondary path transfer function is shown in Simulation 11.5.3 - 11.5.4 on pages 499–500. It can be observed that the system is resonant with a resonance frequency of approximately $f_t \approx 840$ Hz. The magnitude spans -40 dB from 10 Hz to 840 Hz in accordance with the lumped element model in subsection 11.4.1. The transition from the low frequency region resonance frequency, however, follows two different regimes. For 10 Hz to 100 Hz the magnitude apparently increases by 30 $\mathrm{dB} \cdot \mathrm{decade}^{-1}$ while in the frequency range 100 Hz to 840 Hz the rate is lowered to 10 $\mathrm{dB} \cdot \mathrm{decade}^{-1}$.

For all transfer functions an indication of the calculated ± 3 standard-deviations uncertainty based on subsection C.3.3 on page 543 is made. Although only 5 averages are used ($K_{\mathrm{DFT}} = 5$) owing to the close to unity ordinary coherence function involved in the system identification process except in the very low-frequency range the uncertainty is rather small.

Moreover, we have divided the secondary path transfer function into its minimum-phase components in Simulation 11.5.5 - 11.5.6 on pages 501–502 and its all-pass components in Simulation 11.5.7 - 11.5.8 on pages 503–504.

We appreciate that the magnitude of the minimum phase part $|g_{ey,\mathrm{min}}^{l,m}|$ coincide with $|g_{ey}^{l,m}|$ and that the phase is monotonically non-increasing. It can also be observed that the magnitude of the all-pass component is unity and the phase is monotonically non-decreasing as expected.

System Identification of Secondary Pathes $g_{ey}^{l,m}$ Impulse Response Function

The impulse response function shown in Simulation 11.5.9 exhibit a similar pattern as obtained from an adaptive system identification in Simulation 7.7.1 on page 335.

System Identification of Secondary Pathes $g_{ey}^{l,m}$ Group Delays

The group delay of the secondary path for the multi-rate system (MRS) with $f_s^0 = 192$ kHz, $f_s^1 = 24$ kHz, $f_s^2 = 6$ kHz with the discrete-time group delays listed in Table 5.1 on page 266 are shown in Simulation 11.5.10 - 11.5.11 on pages 506–507. We appreciate that the group delay results from our lumped-element model in section 11.4 viz. (11.4.4) corresponds fairly well with the group delays obtained from system identification. However, in the frequency region $10 - 150$ the

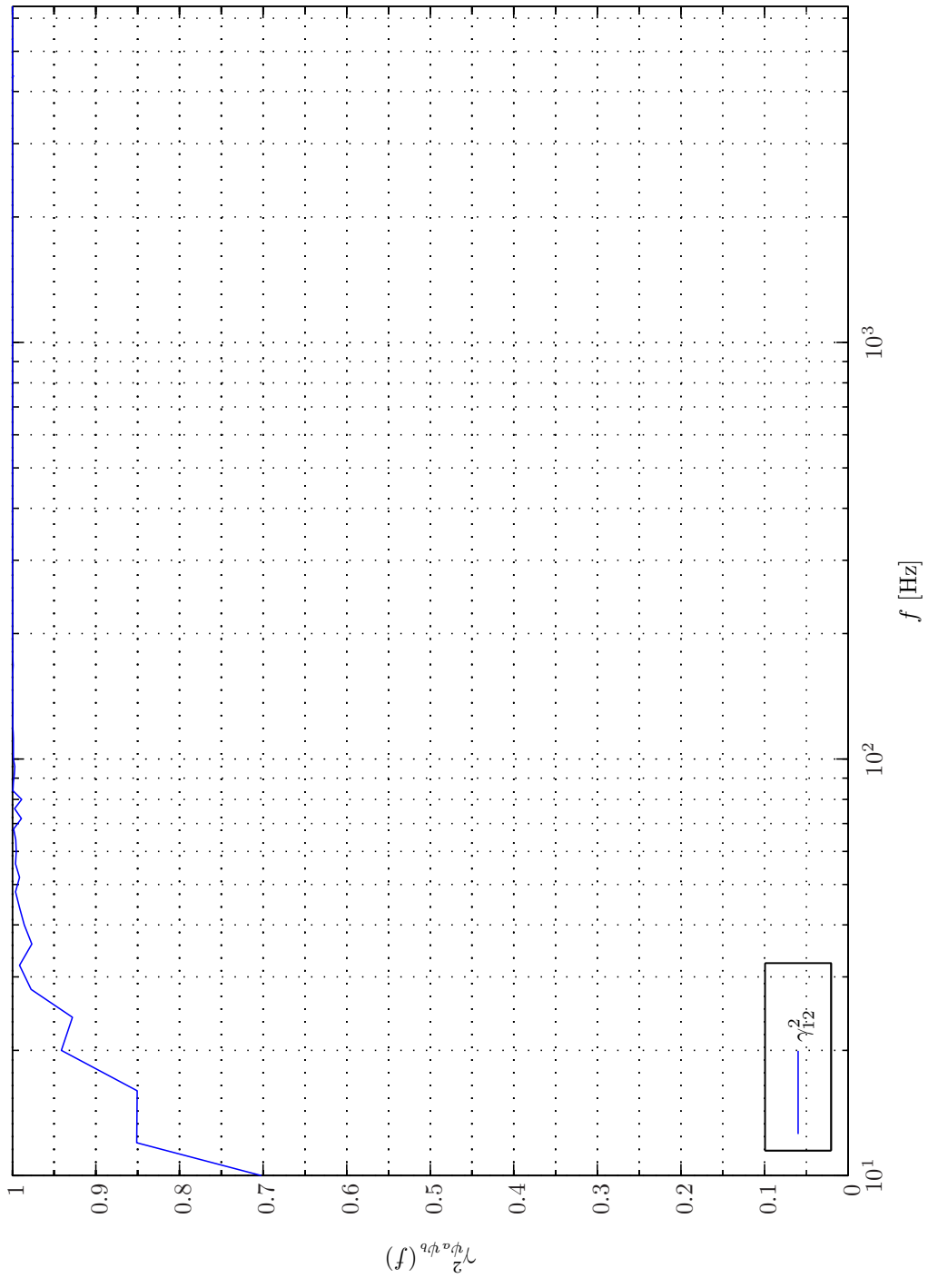

Sim 11.5.1: *Ordinary Coherency-Squared Functions* $\gamma^2_{\psi_a\psi_b}(f)$: **Statistical Data Analysis:** Single-Sided Modified Periodogram, f_s = 65.536 kHz, N_{DFT} = 16384, L_{DFT} = 16385, R_{DFT} = 8193, Hanning, Δf_m = 16 Hz, T_{DFT} = 0.25002 s, $N_{f,DFT}$ = 8193, Δf_{DFT} = 4 Hz, K_{DFT} = 5; *System Identification:* Random White Noise ($\mathcal{N}(0, 0.2)$), Output: 5 V, f_s = 65.536 kHz; Time: $0 - 0.8$ s; *Channels:* #1 $\leftarrow$ $\underset{\mathcal{S}}{y_1}$, #2 $\leftarrow$ $\underset{\mathcal{S}}{d_1}$; **Scenario:** `SystemIdentification(65536Hz)SecondaryPathes/20080223T221518`.

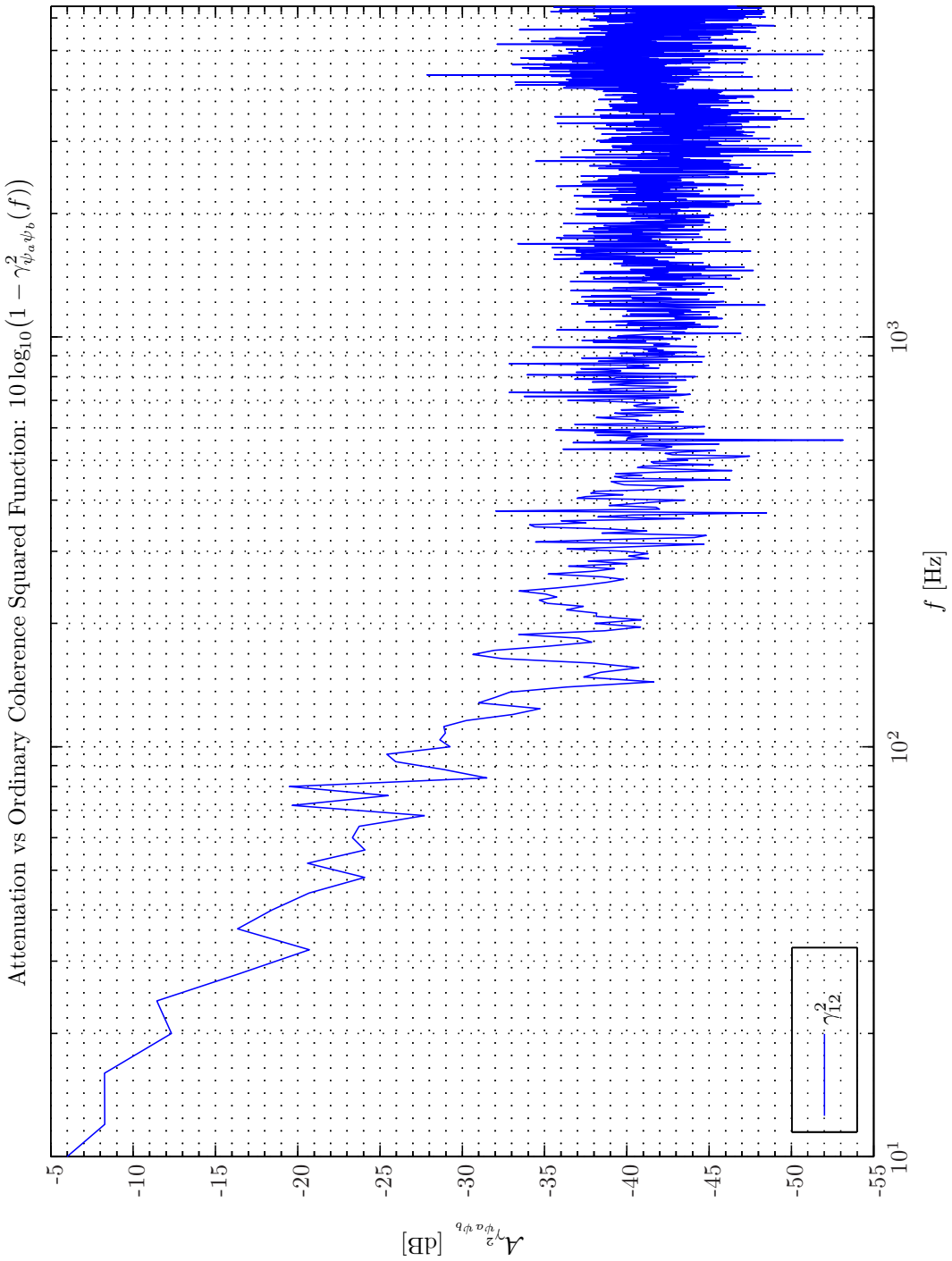

Sim 11.5.2: Attenuation *vs Ordinary Coherency-Squared Functions*: $10\log_{10}(1-\gamma^2_{\psi_a\psi_b}(f))$: **Statistical Data Analysis**: Single-Sided Modified Periodogram, f_s = 65.536 kHz, N_{DFT} = 16384, L_{DFT} = 16385, R_{DFT} = 8193, Hanning, Δf_m = 16 Hz, T_{DFT} = 0.25002 s, $N_{f,DFT}$ = 8193, Δf_{DFT} = 4 Hz, K_{DFT} = 5; *System Identification:* Random White Noise ($\mathcal{N}(0,0.2)$), Output: 5 V, f_s = 65.536 kHz; Time: $0-0.8$ s; *Channels:* #1 $\leftarrow y_1$, #2 $\leftarrow d_1$; **Scenario:** `SystemIdentification(65536Hz)SecondaryPathes/20080223T221518`.

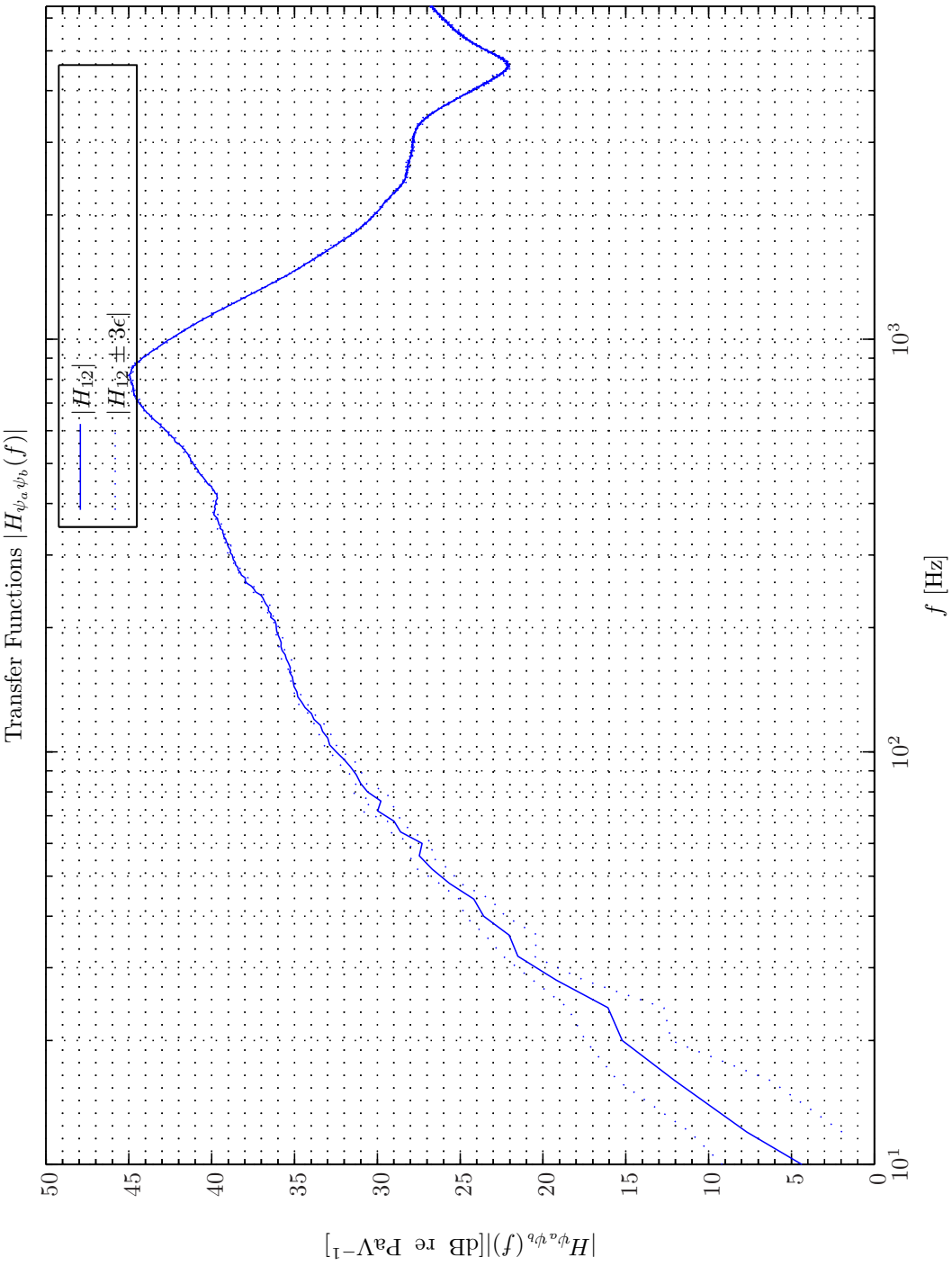

Sim 11.5.3: *Transfer Function, Magnitude:* $|H_{\psi_a\psi_b}(f)|$: **Statistical Data Analysis**: Single-Sided Modified Periodogram, $f_s = 65.536$ kHz, $N_{DFT} = 16384$, $L_{DFT} = 16385$, $R_{DFT} = 8193$, Hanning, $\Delta f_m = 16$ Hz, $T_{DFT} = 0.25002$ s, $N_{f,DFT} = 8193$, $\Delta f_{DFT} = 4$ Hz, $K_{DFT} = 5$; *System Identification:* Random White Noise ($\mathcal{N}(0, 0.2)$), Output: 5 V, $f_s = 65.536$ kHz; Time: $0 - 0.8$ s; *Channels:* #1 $\leftarrow \underset{\circledS}{y_1}$, #2 $\leftarrow \underset{\circledS}{d_1}$; **Scenario:** `SystemIdentification(65536Hz)SecondaryPathes/20080223T221518`.

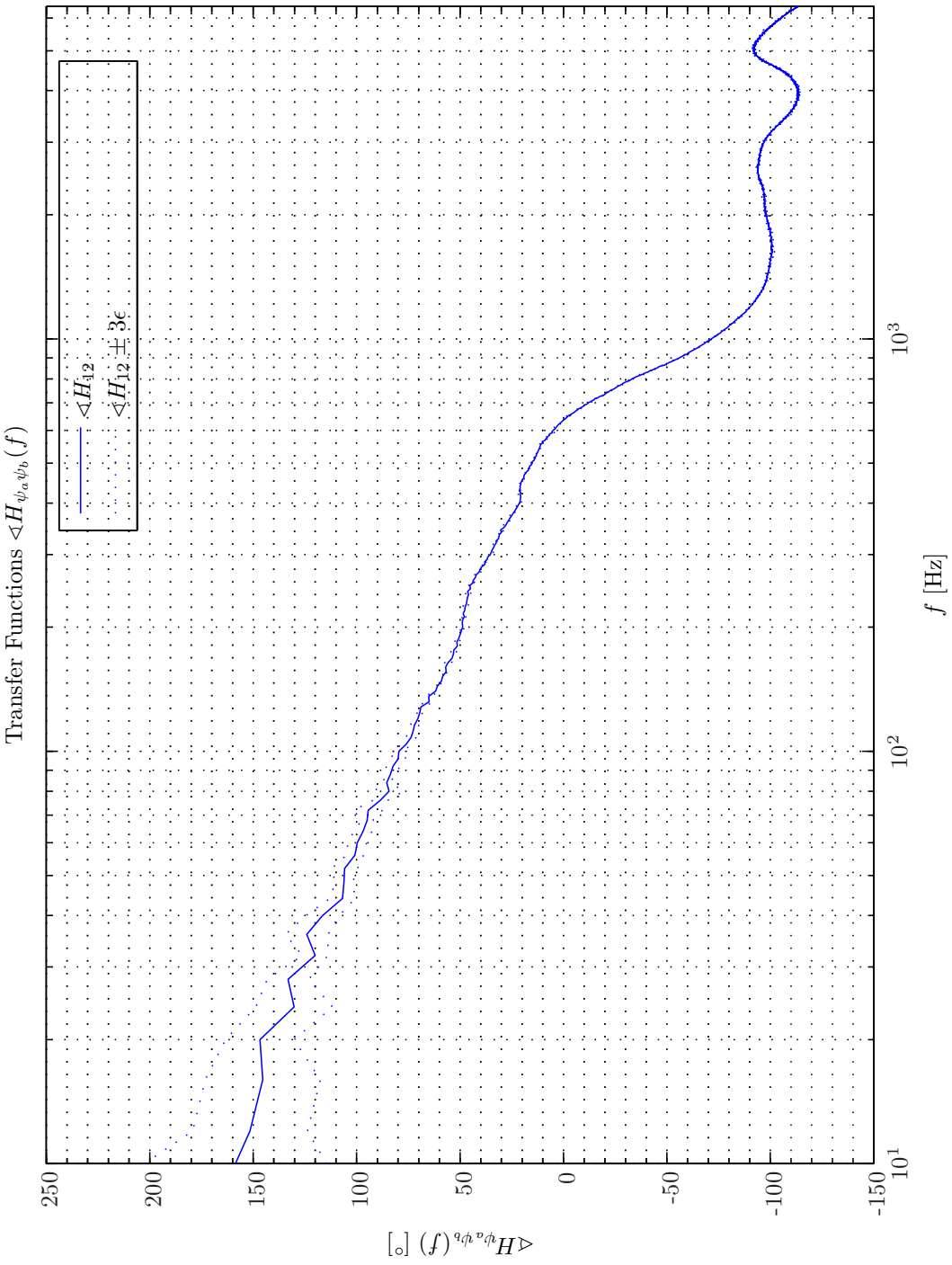

Sim 11.5.4: *Transfer Function, Phase:* $\sphericalangle H_{\psi_a\psi_b}(f)$: **Statistical Data Analysis:** Single-Sided Modified Periodogram, $f_s = 65.536$ kHz, $N_{DFT} = 16384$, $L_{DFT} = 16385$, $R_{DFT} = 8193$, Hanning, $\Delta f_m = 16$ Hz, $T_{DFT} = 0.25002$ s, $N_{f,DFT} = 8193$, $\Delta f_{DFT} = 4$ Hz, $K_{DFT} = 5$; *System Identification:* Random White Noise ($\mathcal{N}(0, 0.2)$), Output: 5 V, $f_s = 65.536$ kHz; Time: $0 - 0.8$ s; *Channels:* $\#1 \leftarrow \underset{\textcircled{s}}{y_1}$, $\#2 \leftarrow \underset{\textcircled{s}}{d_1}$; **Scenario:** `SystemIdentification(65536Hz)SecondaryPathes/20080223T221518`.

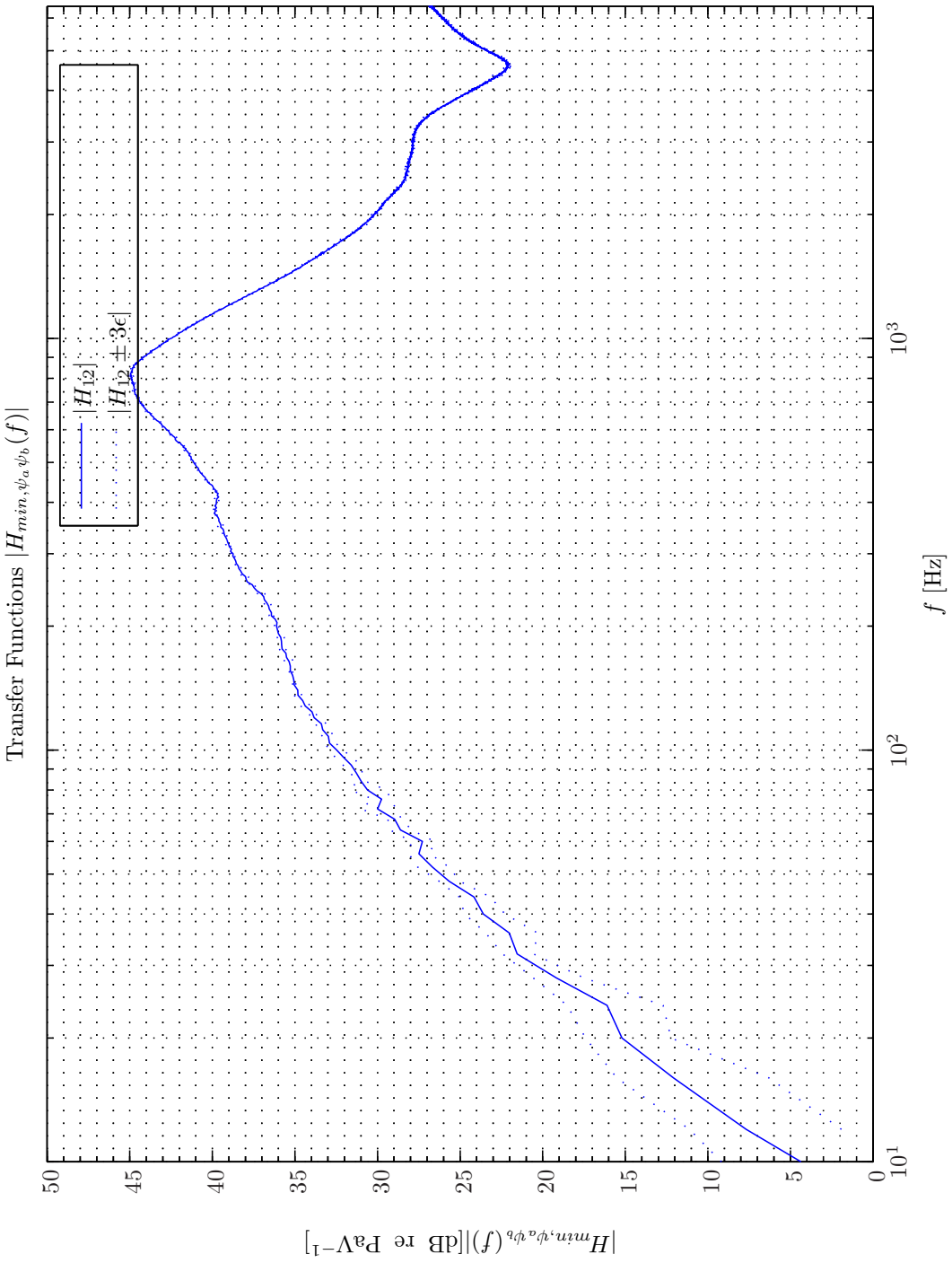

Sim 11.5.5: *Transfer Function, Magnitude*: $|H_{min,\psi_a\psi_b}(f)|$: **Statistical Data Analysis**: Single-Sided Modified Periodogram, f_s = 65.536 kHz, N_{DFT} = 16384, L_{DFT} = 16385, R_{DFT} = 8193, Hanning, Δf_m = 16 Hz, T_{DFT} = 0.25002 s, $N_{f,DFT}$ = 8193, Δf_{DFT} = 4 Hz, K_{DFT} = 5; *System Identification:* Random White Noise ($\mathcal{N}(0, 0.2)$), Output: 5 V, f_s = 65.536 kHz; Time: $0 - 0.8$ s; *Channels:* #1 $\leftarrow$ $\underset{\textcircled{S}}{y_1}$, #2 $\leftarrow$ $\underset{\textcircled{S}}{d_1}$; **Scenario:** `SystemIdentification(65536Hz)SecondaryPathes/20080223T221518`.

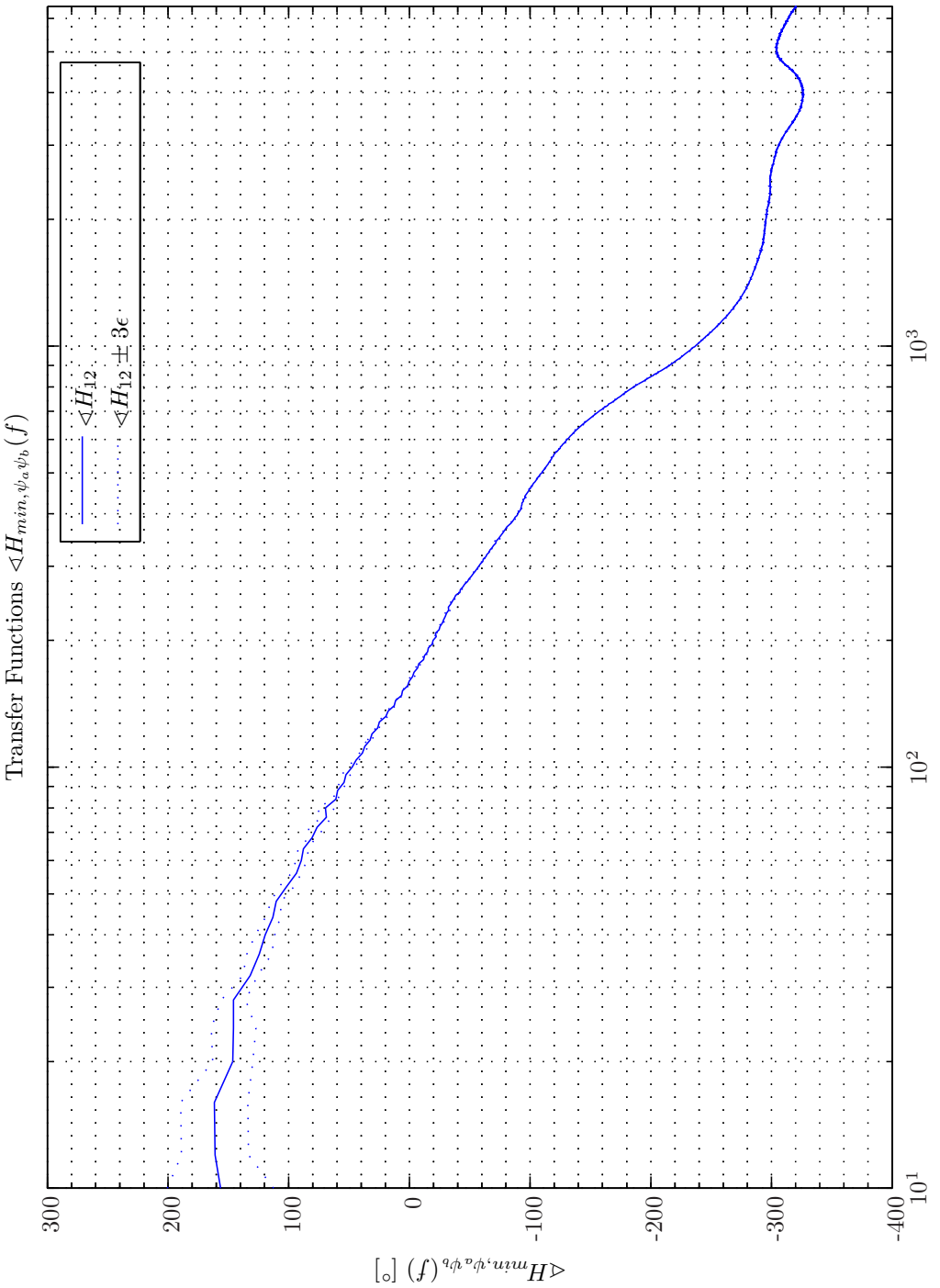

Sim 11.5.6: *Transfer Function, Phase:* $\sphericalangle H_{min,\psi_a\psi_b}(f)$: **Statistical Data Analysis**: Single-Sided Modified Periodogram, $f_s = 65.536$ kHz, $N_{DFT} = 16384$, $L_{DFT} = 16385$, $R_{DFT} = 8193$, Hanning, $\Delta f_m = 16$ Hz, $T_{DFT} = 0.25002$ s, $N_{f,DFT} = 8193$, $\Delta f_{DFT} = 4$ Hz, $K_{DFT} = 5$; *System Identification:* Random White Noise ($\mathcal{N}(0, 0.2)$), Output: 5 V, $f_s = 65.536$ kHz; Time: $0 - 0.8$ s; *Channels:* #1 $\leftarrow y_1$, #2 $\leftarrow d_1$; **Scenario:** `SystemIdentification(65536Hz)SecondaryPathes/20080223T221518`.

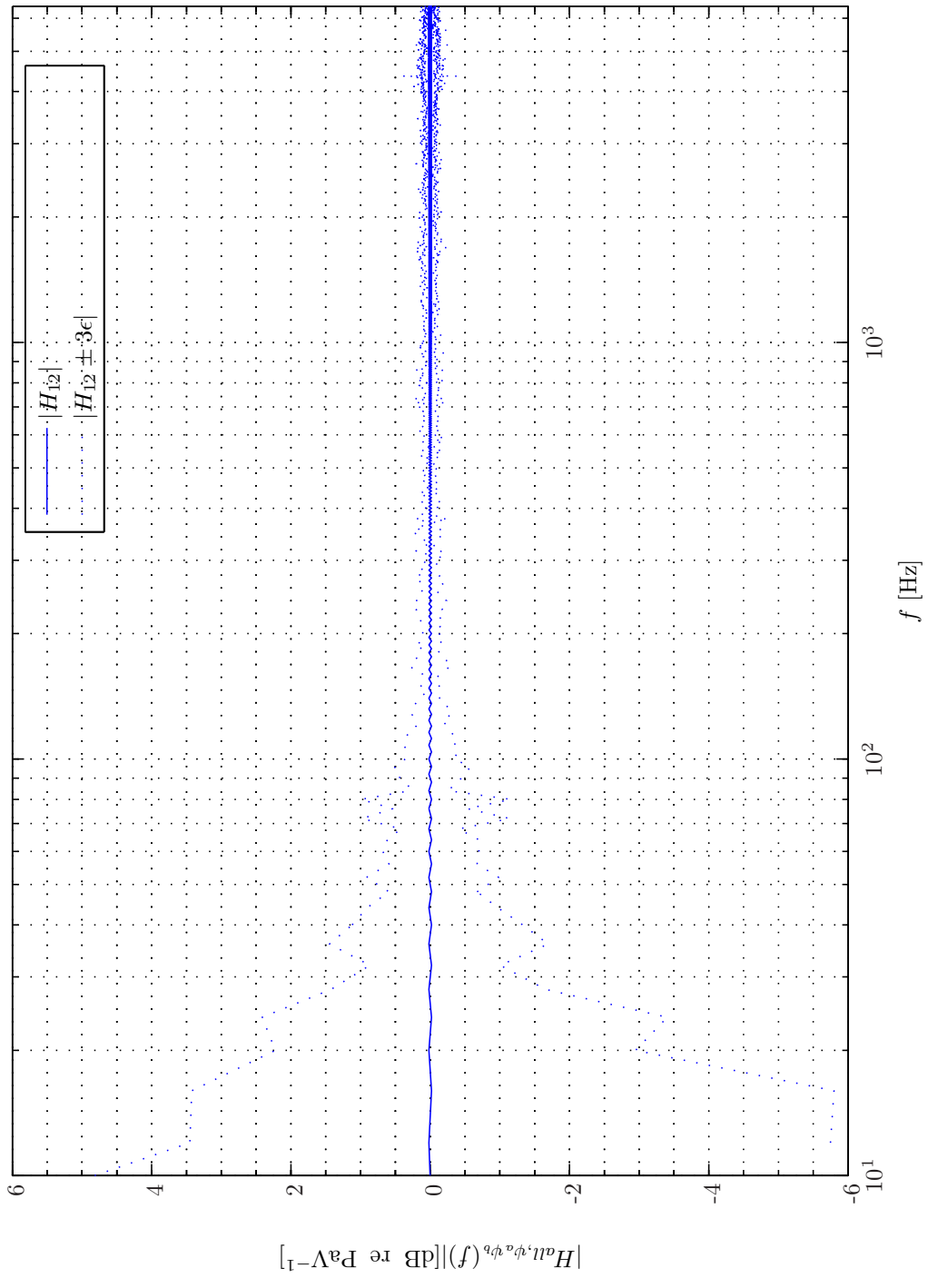

Sim 11.5.7: *Transfer Function, Magnitude*: $|H_{all,\psi_a\psi_b}(f)|$: **Statistical Data Analysis**: Single-Sided Modified Periodogram, f_s = 65.536 kHz, N_{DFT} = 16384, L_{DFT} = 16385, R_{DFT} = 8193, Hanning, Δf_m = 16 Hz, T_{DFT} = 0.25002 s, $N_{f,DFT}$ = 8193, Δf_{DFT} = 4 Hz, K_{DFT} = 5; *System Identification:* Random White Noise ($\mathcal{N}(0, 0.2)$), Output: 5 V, f_s = 65.536 kHz; Time: $0 - 0.8$ s; *Channels:* #1 $\leftarrow$ $\underset{\textcircled{S}}{y_1}$, #2 $\leftarrow$ $\underset{\textcircled{S}}{d_1}$; **Scenario:** `SystemIdentification(65536Hz)SecondaryPathes/20080223T221518`.

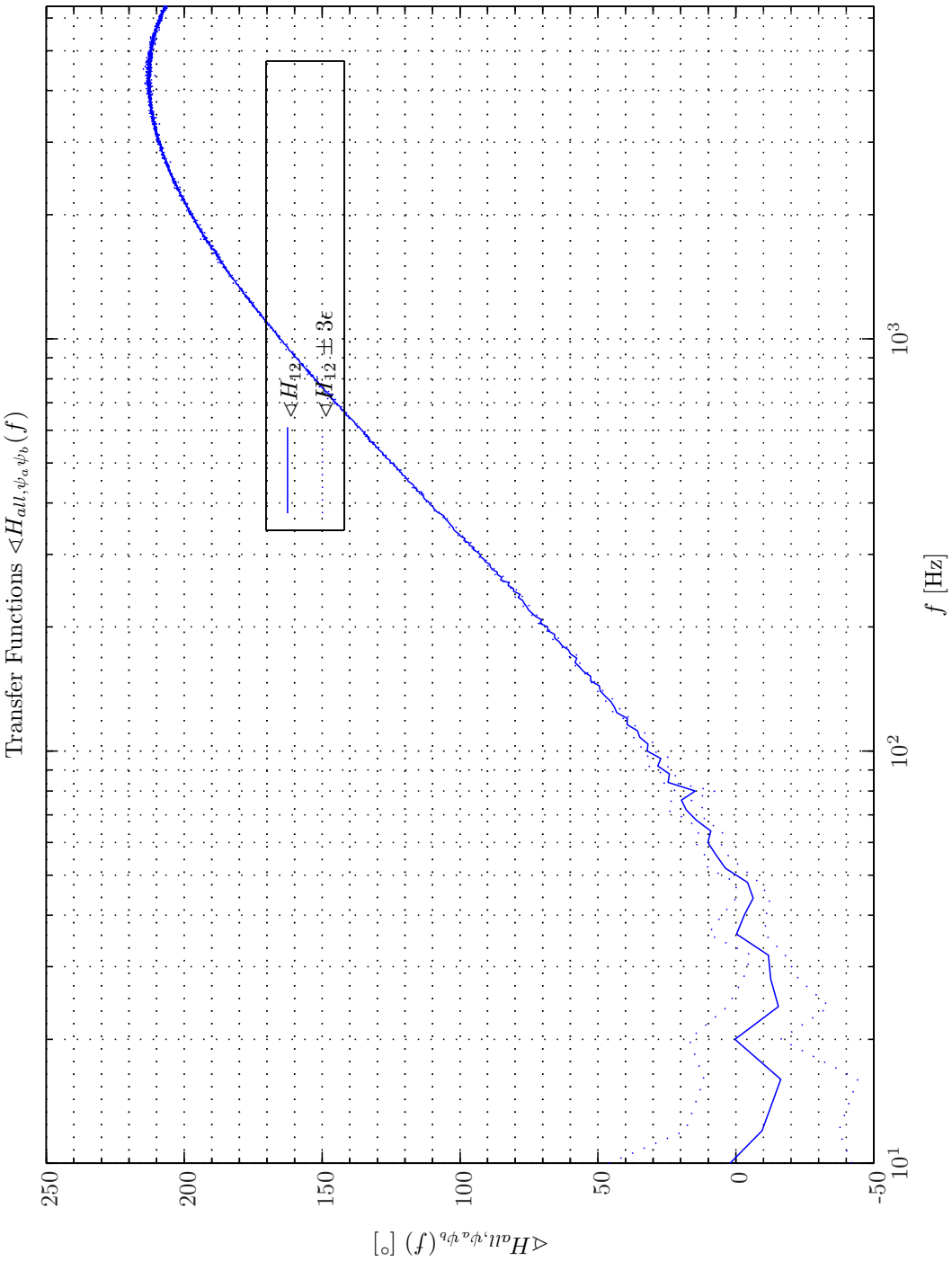

Sim 11.5.8: *Transfer Function, Phase:* $\lhd H_{all,\psi_a\psi_b}(f)$: **Statistical Data Analysis:** Single-Sided Modified Periodogram, $f_s = 65.536$ kHz, $N_{DFT} = 16384$, $L_{DFT} = 16385$, $R_{DFT} = 8193$, Hanning, $\Delta f_m = 16$ Hz, $T_{DFT} = 0.25002$ s, $N_{f,DFT} = 8193$, $\Delta f_{DFT} = 4$ Hz, $K_{DFT} = 5$; *System Identification:* Random White Noise ($\mathcal{N}(0, 0.2)$), Output: 5 V, $f_s = 65.536$ kHz; Time: $0 - 0.8$ s; *Channels:* #1 $\leftarrow y_1$, #2 $\leftarrow \underset{\circledcirc}{d_1}$; **Scenario:** `SystemIdentification(65536Hz)SecondaryPathes/20080223T221518`.

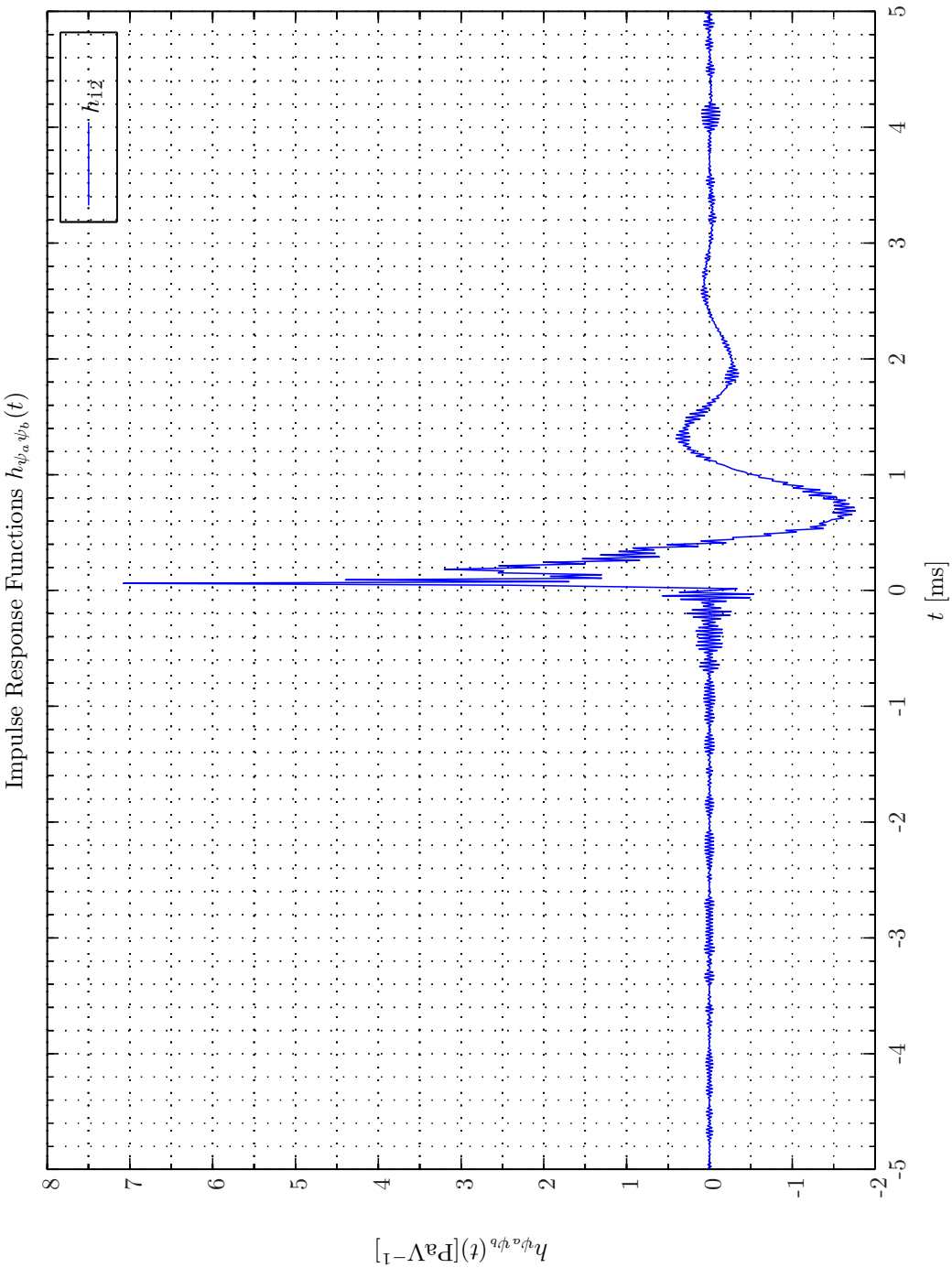

Sim 11.5.9: *Impulse Response Functions*: $h_{\psi_a\psi_b}(t)$: **Statistical Data Analysis**: Single-Sided Modified Periodogram, $f_s = 65.536$ kHz, $N_{DFT} = 16384$, $L_{DFT} = 16385$, $R_{DFT} = 8193$, Hanning, $\Delta f_m = 16$ Hz, $T_{DFT} = 0.25002$ s, $N_{f,DFT} = 8193$, $\Delta f_{DFT} = 4$ Hz, $K_{DFT} = 5$; *System Identification:* Random White Noise ($\mathcal{N}(0, 0.2)$), Output: 5 V, $f_s = 65.536$ kHz; Time: $0 - 0.8$ s; *Channels:* $\#1 \leftarrow \underset{\mathcal{S}}{y_1}$, $\#2 \leftarrow \underset{\mathcal{S}}{d_1}$; **Scenario:** `SystemIdentification(65536Hz)SecondaryPathes/20080223T221518`.

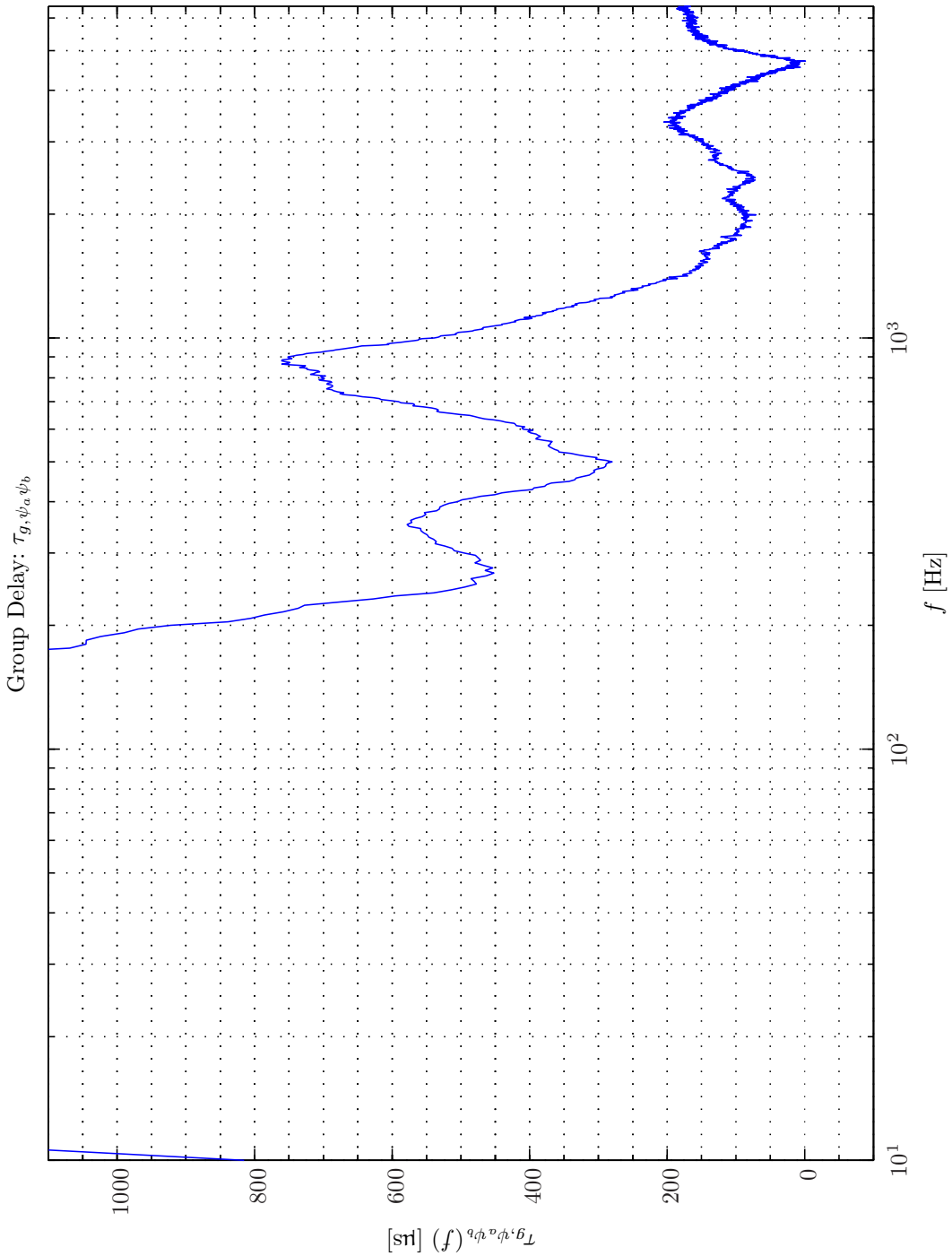

Sim 11.5.10: *Group Delay:* τ_g; $f_s^0 = 192$ kHz, $f_s^1 = 24$ kHz, $f_s^2 = 3$ kHz: **Statistical Data Analysis:** Single-Sided Modified Periodogram, $f_s = 65.536$ kHz, $N_{DFT} = 16384$, $L_{DFT} = 16385$, $R_{DFT} = 8193$, Hanning, $\Delta f_m = 16$ Hz, $T_{DFT} = 0.25002$ s, $N_{f,DFT} = 8193$, $\Delta f_{DFT} = 4$ Hz, $K_{DFT} = 5$; *System Identification:* Random White Noise ($\mathcal{N}(0, 0.2)$), Output: 5 V, $f_s = 65.536$ kHz; Time: $0 - 0.8$ s; *Channels:* #1 $\leftarrow y_1$, #2 $\leftarrow d_1$; **Scenario:** `SystemIdentification(65536Hz)SecondaryPaths/20080223T221518`.

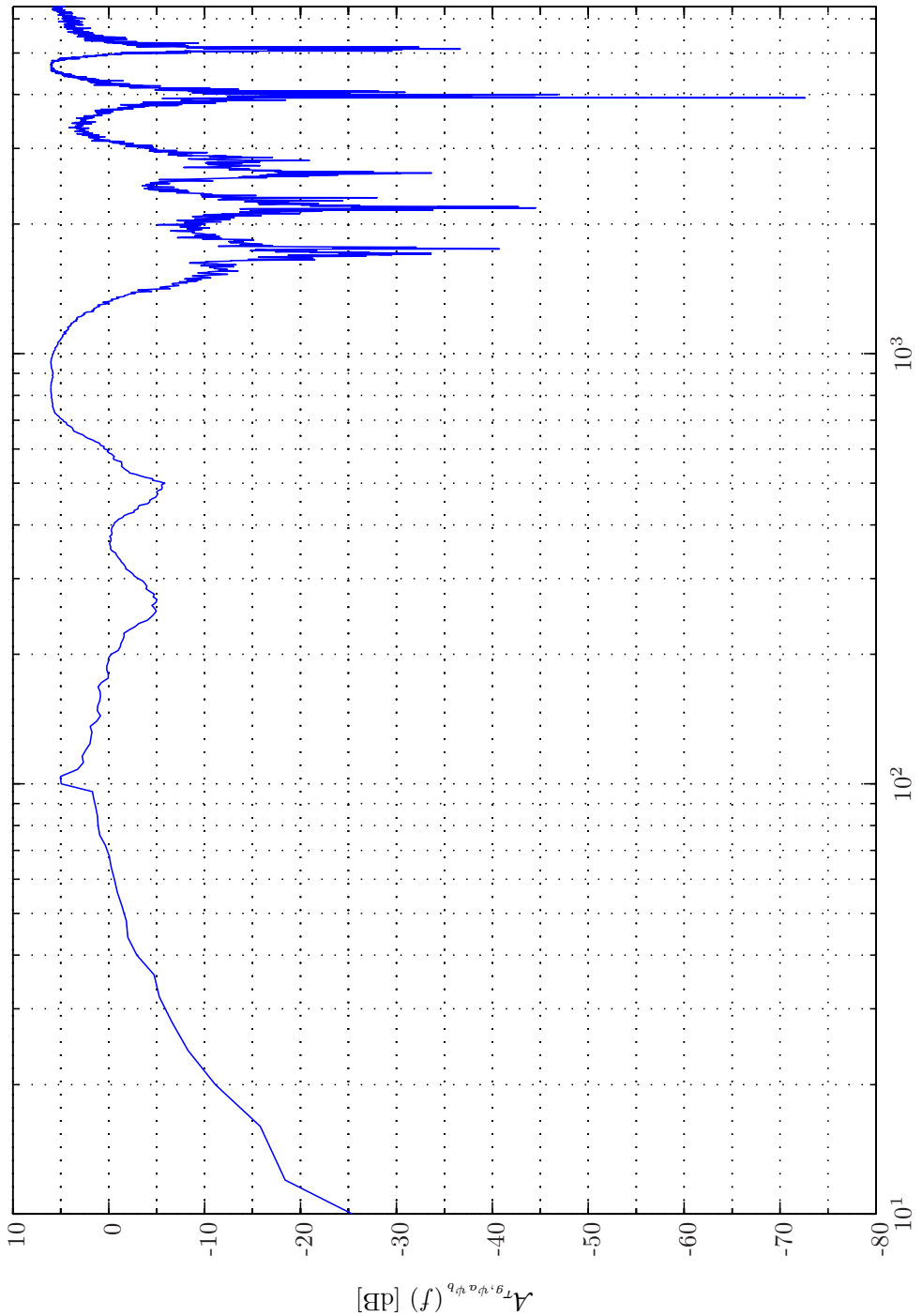

Sim 11.5.11: *Attenuation vs Group Delay*: $20\log_{10}|1-\mathrm{e}^{-\imath 2\pi f \tau_g}|$; $f_s^0 = 192$ kHz, $f_s^1 = 24$ kHz, $f_s^2 = 3$ kHz: **Statistical Data Analysis**: Single-Sided Modified Periodogram, $f_s = 65.536$ kHz, $N_{DFT} = 16384$, $L_{DFT} = 16385$, $R_{DFT} = 8193$, Hanning, $\Delta f_m = 16$ Hz, $T_{DFT} = 0.25002$ s, $N_{f,DFT} = 8193$, $\Delta f_{DFT} = 4$ Hz, $K_{DFT} = 5$; *System Identification:* Random White Noise ($\mathcal{N}(0, 0.2)$), Output: 5 V, $f_s = 65.536$ kHz; Time: $0 - 0.8$ s; *Channels:* #1 $\leftarrow \underset{\circledS}{y}_1$, #2 $\leftarrow \underset{\circledS}{d}_1$; **Scenario:** `SystemIdentification(65536Hz)SecondaryPathes/20080223T221518`.

lumped-element model is inadequate as substantial deviations in the predicted group delays are present.

11.5.2 System Identification of Feedback Pathes $g_{xy}^{l,j}$

In Figure 2.3 on page 35 the positions of the 10 BK 4949 surface microphones flush-mounted on Gentex HGU-55/P helmet are depicted.

System Identification of Secondary Pathes $g_{xy}^{l,j}$ Transfer Function

The feedback path transfer functions are shown in Simulation 11.5.12 - 11.5.13 on pages 509–510.

By comparing with the secondary path transfer function in Simulation 11.5.3 - 11.5.4 on pages 499–500 we conclude that the magnitude of the feedback paths are approximately $35 - 45$ dB below the secondary paths. Hence, the feedback signal cancelation scheme described in subsection 7.3.8 on page 310 is not really necessary for the helmet based hybrid MIMO confined-feedforward-feedback system (HMIMOCFFFBS).

11.5.3 System Identification of Performance Pathes $g_{py}^{l,k}$

System Identification of Secondary Pathes $g_{py}^{l,k}$ Transfer Function

The control-performance path transfer functions are shown in Simulation 11.5.14 - 11.5.15 on pages 511–512.

By comparing with in Simulation 11.5.3 - 11.5.4 on pages 499–500 we see that the control-performance path transfer function and the corresponding secondary path transfer function are very similar up to 1200 Hz, while the earcup to earcup passage leads to a frequency dependent attenuation of the order $30 - 60$ dB.

Bibliography

[1] A. J. Brammer, G. J. Pan, and R. B. Crabtree. Adaptive feedforward active noise reduction headset for low frequency noise. In *ACTIVE97*, pages 365–372, Budapest, 1997.

[2] David A. Cartes, Laura R. Ray, and Rober D. Collier. Experimental evaluation of leaky least-meam-square algorithms. *JASA*, 111(4):1758–1771, 2002.

[3] G. S. Casali, J. G. Robinson. Narrow-band digital active noise reduction in a siren- cancelling headset: Real-ear and acoustical manikin insertion loss. *Noise Contr. Eng.*, 42(3):101–115, 1994.

[4] Frederik M. Gren. *Optimization of hearing protector used in jet fighter aircrafts*. M.sc., SDU, 2006.

[5] Mones E. Hawley. Acoustic interference for noise control. *Noise Control*, 2:61–63, 1956.

[6] W. Marshall Leach. *Introduction to Electroacoustics Audio Amplifier Design*. Kendall/Hunt Publishing Company, 2nd edition, 2001.

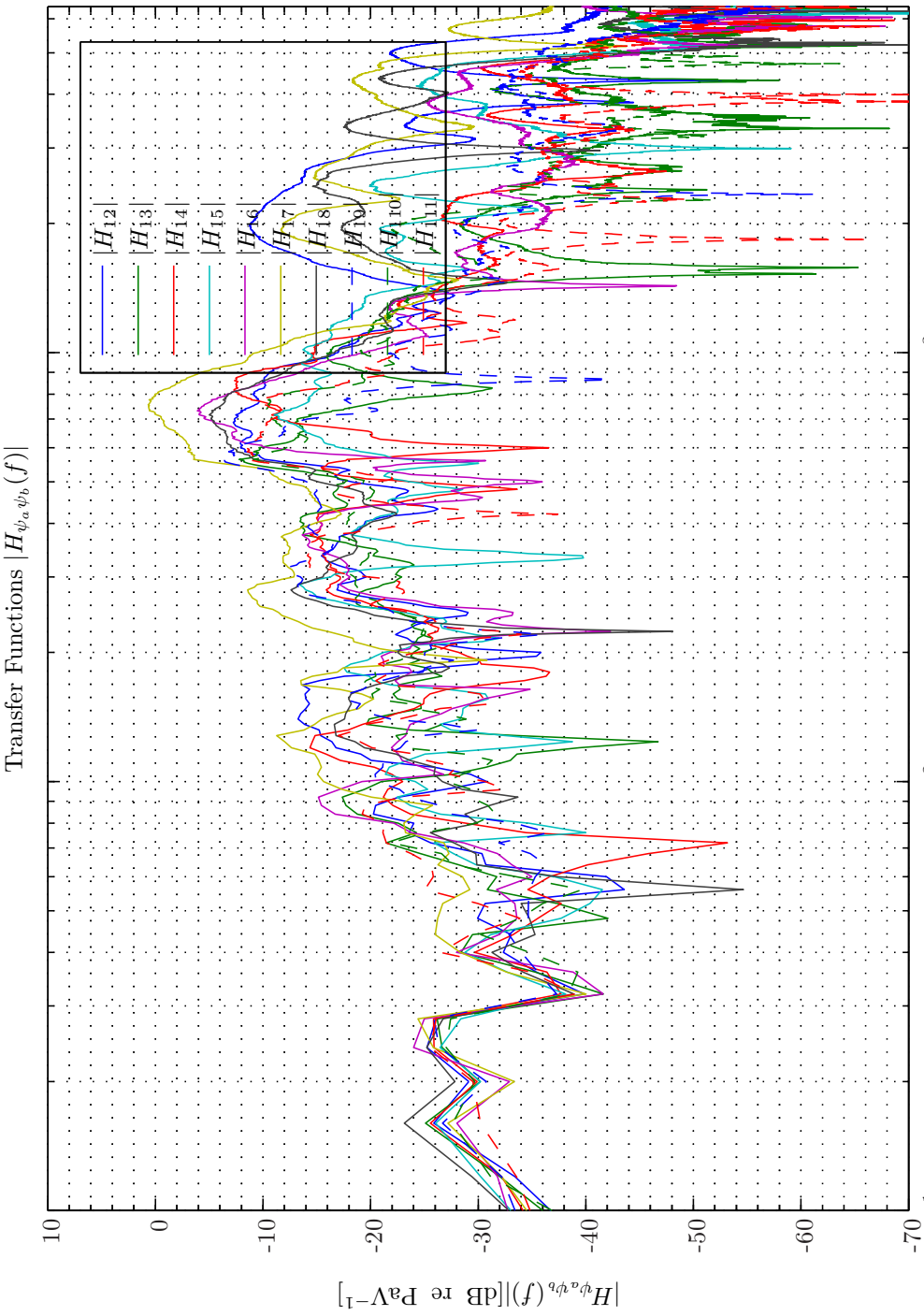

Sim 11.5.12: *Transfer Function, Magnitude:* $|H_{\psi_a\psi_b}(f)|$: **Statistical Data Analysis**: Single-Sided Modified Periodogram, $f_s = 65.536$ kHz, $N_{DFT} = 16384$, $L_{DFT} = 16385$, $R_{DFT} = 8193$, Hanning, $\Delta f_m = 16$ Hz, $T_{DFT} = 0.25002$ s, $N_{f,DFT} = 8193$, $\Delta f_{DFT} = 4$ Hz, $K_{DFT} = 5$; *System Identification:* Random White Noise ($\mathcal{N}(0, 0.2)$), Output: 5 V, $f_s = 65.536$ kHz; Time: $0 - 0.8$ s; *Channels:* $\#1 \leftarrow \underset{\odot}{y}_1$, $\#2 \leftarrow \underset{\odot}{x}_1$, $\#3 \leftarrow \underset{\odot}{x}_2$, $\#4 \leftarrow \underset{\odot}{x}_3$, $\#5 \leftarrow \underset{\odot}{x}_4$, $\#6 \leftarrow \underset{\odot}{x}_5$, $\#7 \leftarrow \underset{\odot}{x}_6$, $\#8 \leftarrow \underset{\odot}{x}_7$, $\#9 \leftarrow \underset{\odot}{x}_8$, $\#10 \leftarrow \underset{\odot}{x}_9$, $\#11 \leftarrow \underset{\odot}{x}_{10}$; **Scenario:** `SystemIdentification(65536Hz)SecondaryPathes/20080223T221518`.

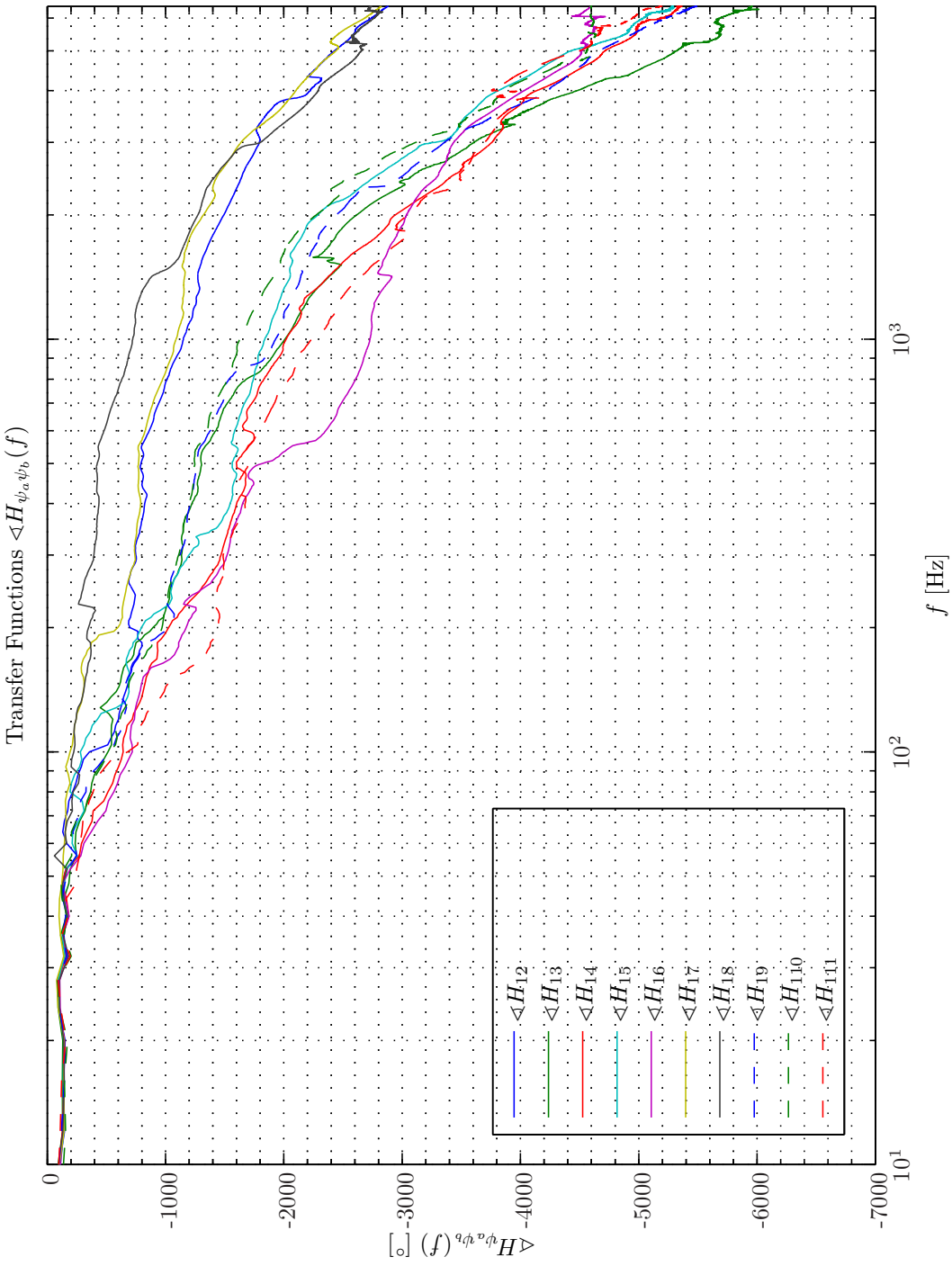

Sim 11.5.13: *Transfer Function, Phase:* $\lhd H_{\psi_a\psi_b}(f)$: **Statistical Data Analysis**: Single-Sided Modified Periodogram, f_s = 65.536 kHz, N_{DFT} = 16384, L_{DFT} = 16385, R_{DFT} = 8193, Hanning, Δf_m = 16 Hz, T_{DFT} = 0.25002 s, $N_{f,DFT}$ = 8193, Δf_{DFT} = 4 Hz, K_{DFT} = 5; *System Identification:* Random White Noise ($\mathcal{N}(0, 0.2)$), Output: 5 V, f_s = 65.536 kHz; Time: 0 − 0.8 s; *Channels:* #1 $\leftarrow \underset{\textcircled{S}}{y_1}$, #2 $\leftarrow \underset{\textcircled{S}}{x_1}$, #3 $\leftarrow \underset{\textcircled{S}}{x_2}$, #4 $\leftarrow \underset{\textcircled{S}}{x_3}$, #5 $\leftarrow \underset{\textcircled{S}}{x_4}$, #6 $\leftarrow \underset{\textcircled{S}}{x_5}$, #7 $\leftarrow \underset{\textcircled{S}}{x_6}$, #8 $\leftarrow \underset{\textcircled{S}}{x_7}$, #9 $\leftarrow \underset{\textcircled{S}}{x_8}$, #10 $\leftarrow \underset{\textcircled{S}}{x_9}$, #11 $\leftarrow \underset{\textcircled{S}}{x_{10}}$; **Scenario:** `SystemIdentification(65536Hz)SecondaryPathes/20080223T221518`.

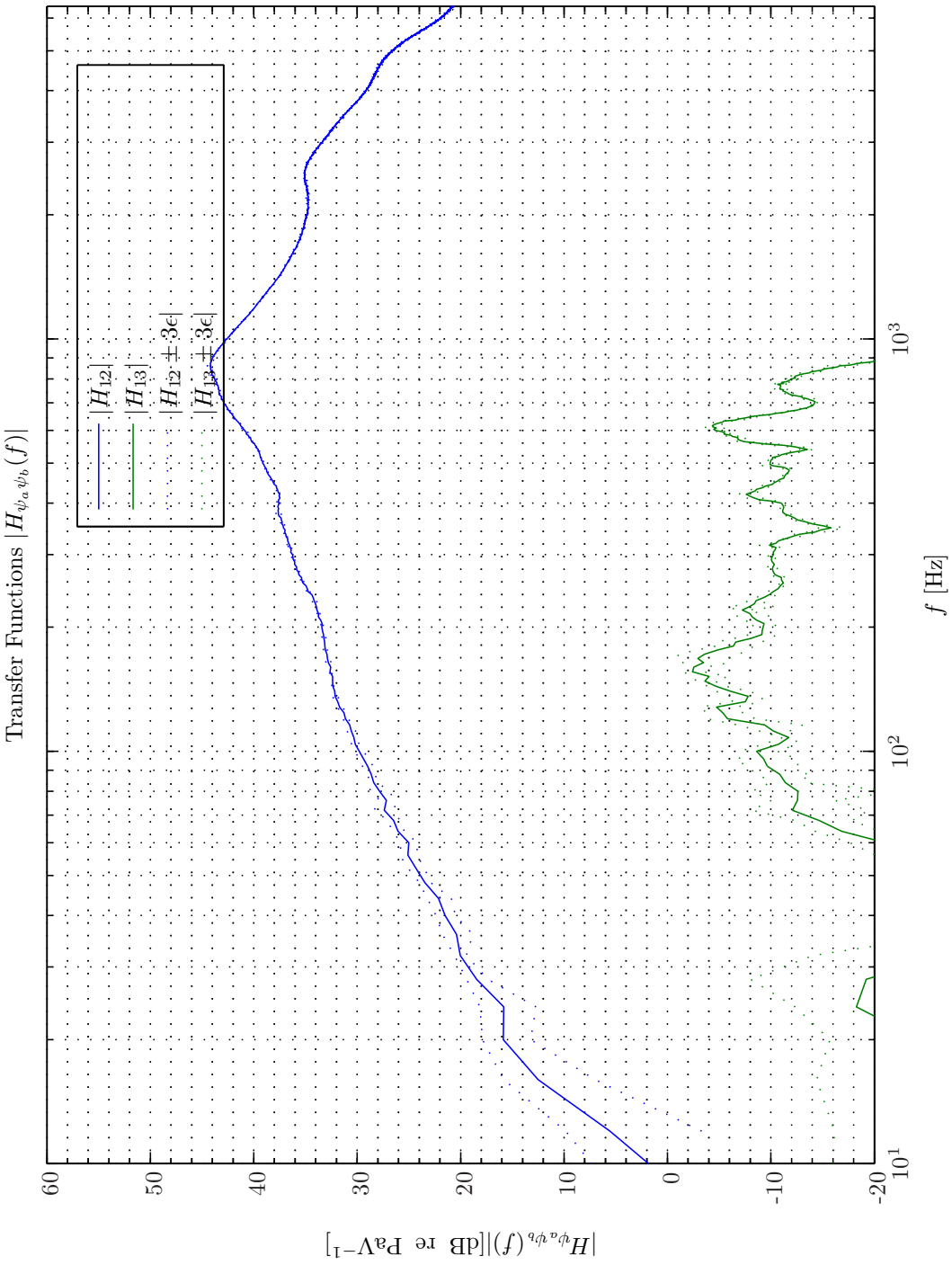

Sim 11.5.14: *Transfer Function, Magnitude:* $|H_{\psi_a\psi_b}(f)|$: **Statistical Data Analysis**: Single-Sided Modified Periodogram, $f_s = 65.536$ kHz, $N_{DFT} = 16384$, $L_{DFT} = 16385$, $R_{DFT} = 8193$, Hanning, $\Delta f_m = 16$ Hz, $T_{DFT} = 0.25002$ s, $N_{f,DFT} = 8193$, $\Delta f_{DFT} = 4$ Hz, $K_{DFT} = 5$; *System Identification:* Random White Noise ($\mathcal{N}(0, 0.2)$), Output: 5 V, f_s =65.536 kHz; Time: $0 - 0.8$ s; *Channels:* $\#1 \leftarrow \underset{\mathcal{S}}{y_1}$, $\#2 \leftarrow \underset{\mathcal{S}}{d_1^p}$, $\#3 \leftarrow \underset{\mathcal{S}}{d_2^p}$; **Scenario:** `SystemIdentification(65536Hz)SecondaryPathes/20080223T221518`.

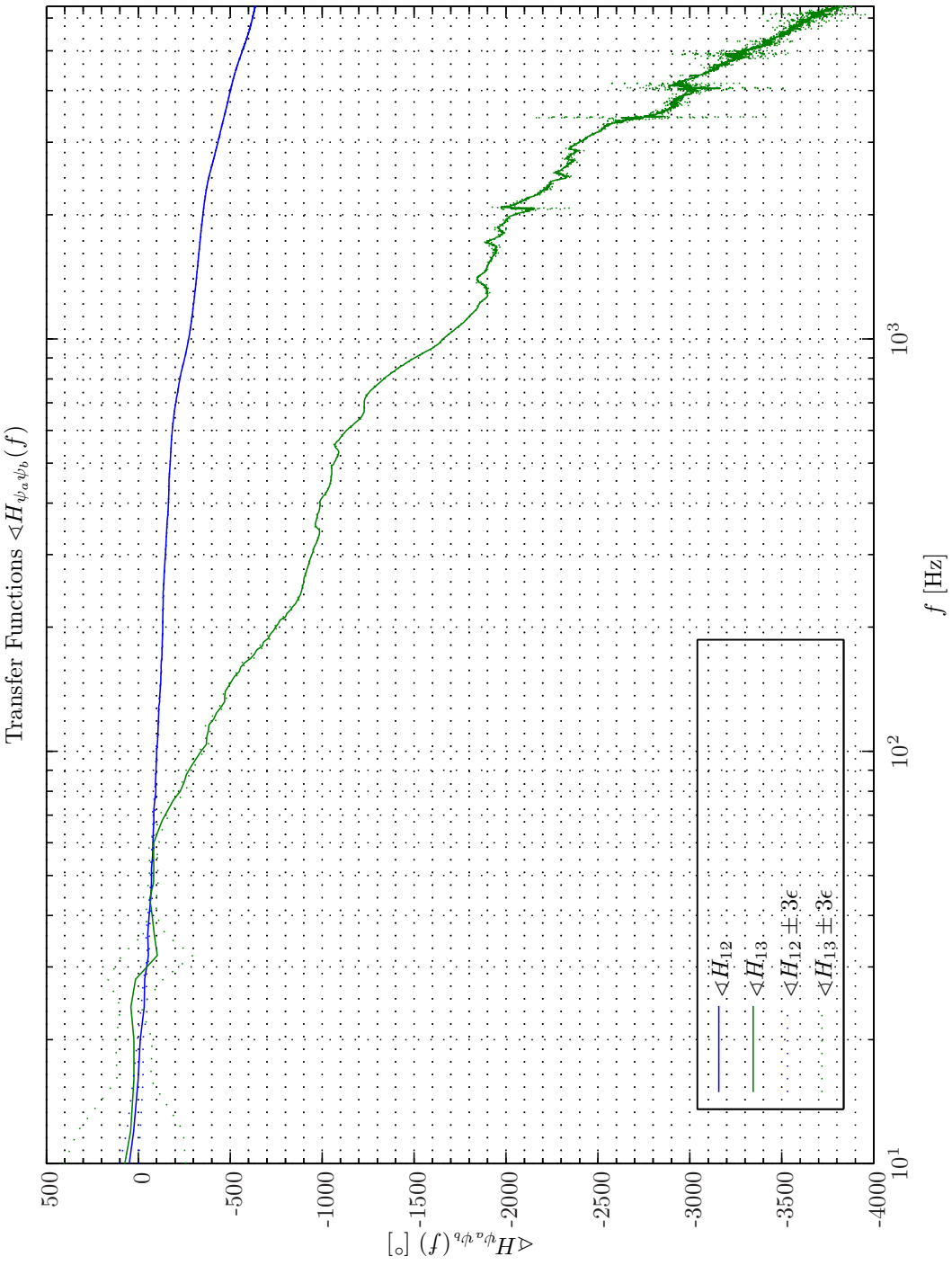

Sim 11.5.15: *Transfer Function, Phase:* $\sphericalangle H_{\psi_a\psi_b}(f)$: **Statistical Data Analysis**: Single-Sided Modified Periodogram, f_s = 65.536 kHz, N_{DFT} = 16384, L_{DFT} = 16385, R_{DFT} = 8193, Hanning, Δf_m = 16 Hz, T_{DFT} = 0.25002 s, $N_{f,DFT}$ = 8193, Δf_{DFT} = 4 Hz, K_{DFT} = 5; *System Identification:* Random White Noise ($\mathcal{N}(0, 0.2)$), Output: 5 V, f_s =65.536 kHz; Time: 0 − 0.8 s; *Channels:* $\#1 \leftarrow \underset{\mathcal{S}}{y_1}$, $\#2 \leftarrow \underset{\mathcal{S}}{d_1^p}$, $\#3 \leftarrow \underset{\mathcal{S}}{d_2^p}$; **Scenario:** `SystemIdentification(65536Hz)SecondaryPathes/20080223T221518`.

[7] Willard F. Meeker. Component characteristics for an active ear defender. *The Journal of the Acoustical Society of America*, 29(11):1252, 1957.

[8] Boaz Rafaely. *Feedback Control of Sound*. Ph.d thesis, University of Southampton, 1997.

[9] Boaz Rafaely and Matthew Jones. Combined feedback-feedforward active noise-reducing headset -the effect of the acoustics on broadband performance. *The Journal of the Acoustical Society of America*, 112(3):981–989, 2002.

[10] E. A. G. Shaw and G. J. Thiessen. Acoustics of circumaural ear defenders. *JASA*, 34(No. 9), 1962.

[11] Elvin D. Simhauser and Mones E. Hawley. The noise-cancelling headset - an active ear defender. *The Journal of the Acoustical Society of America*, 27(1):207, 1955.

[12] David Smeatham. *The performance of Active Noise Reduction Hearing Protectors*. Ph.d thesis, University of Salford, 1998.

[13] W. Winberg, S. Johansson, T. Lago, and I. Claesson. A new passive/active hybrid for a helicopter application. *Int. J. Acoust. Vib.*, 4(2):51–58, 1999.

CONCLUSIONS

12. CONCLUSIONS

In this report the research results obtained during the author's Ph.D. project have been presented.

12.1 Major Achievements

On a conceptual level a to the author's best knowledge new idea to hybrid feedforward feedback control referred to as confined feedforward-feedback active control system (CFFFBACS) has been developed. In this topology a set of reference sensors are positioned on a closed surface completely confining the volumes that should be subject to active control. The principle is based on fundamental field theoretical law's that relate field quantities measured on a closed surface to field quantities exterior or interior to the surface. These fundamental laws have been used extensively for many years in the test of antennas, scatters, acoustical sources etc. In such applications the so-called near-field of the unit under test is scanned on a surface completely confining the unit under test. Accordingly, important quantities describing the far-field radiation pattern of an antenna can be deduced. In the present context of active control the principle is somewhat reversed. Here it is assumed that every noise source is at positions exterior to the scan surface constituted by a set of reference sensors. In addition secondary sound sources are placed within this scan surface. Field quantities can therefore at least theoretically be determined in the interior of the reference sensor surface. In the helmet hearing protection device instantiation of the CFFFBACS such field quantities are not directly estimated. Instead adaptive filters in the CFFFBACS implicitly when subjected to certain cost functions try to minimize the residual fields at the positions of the error sensors.

The main advantage of this topology is twofold. Firstly, complete knowledge of the field in the interior of the scan surface can theoretically be established. Secondly, time-advance information is obtained by this method which is very important in active control applications where causality constraints often put a limit to the achievable performance.

The first part in this report partially paved the road for development of more general framework of sensor data acquisition with application to active control. In the field of acoustical signal processing a new method - at least to the author's best knowledge - that is referred to as joint-channel residual spectral analysis (JCRSA) was developed for the extraction of timing information in spatially distributed multi-channel systems. A problem exists when one attempts to model a naturally spatial distributed system with no obvious input and output channel definition by a finite lumped-elements multi-channel system. By joint-channel-conditioned spectral analysis as opposed to using ordinary spectral analysis individual transfer function information are often discernible from some average transfer function. This proposed method has roots in the multiple coherence function (MCOF) and considers each output channel in turn. A jointly-conditioned power spectral density matrix is constructed by diagonal elements of power spectral density functions that are conditioned on every other input channel and where the off-diagonal elements

are cross-spectral density function jointly-conditioned on all the other input channels. By the term conditioned is meant that only that part of the signal that bears some unique information that could not have been constructed by linear superposition of the signal contents present at the other input channels is used. The ability of the developed method to extract individual channel timing information in a diffuse sound field involving signal information deeply buried in multi-channel interferences was demonstrated. Such timing information could subsequently be used for the determination of a quantity that was referred to as the *acquisition lead time*. The acquisition lead time in turn was used to assess the achievable active noise reduction performance as limited by causality constraints.

The applicability of the method is limited by the spatial sampling frequency, which determines the upper frequency above which spatial aliasing introduces non-linearities preventing correct calculation of the conditioned spectra involved. A remedy for this is to constrain the analysis well below the spatial Nyquist frequency. As is well known, however, low-pass filtering a signal introduces temporal side lobes in the cross-correlation functions thereby blurring the timing information somewhat.

A practical application of this CFFFBACS design is for example for an active noise reduction system for humans wearing a helmet that can be used to support the reference sensors. Such a prototype system has been developed and field measurements subsequently conducted under laboratory conditions, but also conducted onboard airborne military platforms. Parts of these measurements have been reported in this report. In two cases reported data were acquired for an amount of ten respective eleven reference sensors and for two performance sensors that were positioned in order to resemble the noise pressure experienced by humans at a similar position in space. The JCRSA-based analysis was used for "proof of concept". Analysis of the diffuse sound field measurements and field measurements indicated a theoretical active noise reduction (ANR) capability ranging from 35 dB in the very low-frequency region from 20 Hz and gradually decreasing up to 10 dB at $800 - 1000$ Hz. This assessment is based on a linear active control feedforward system using such an amount of reference sensors. It should, however, be recalled that at frequencies under approximately 50Hz the performance would typically be limited by the limited dynamic range of the actuators. Moreover, no apparent saturation in MCOF with increasing number of reference sensors was seen. Hence, by including additional reference sensors the upper frequency limit determined by the MCOF would most likely increase as a consequence of closer spatial sampling. Furthermore, a time-advance of the order of 800-900μs of the reference sensors relative to the performance sensors was deduced. Such time-advance is of great advantage as it basically eliminates causality problems. In comparison ordinary feedback system solutions notoriously suffer from the time-lag that exists between an observation is made by the error sensor and until an appropriately dosed rejection signal is available at the same position.

These observations have been confirmed in MATLAB®-based simulations involving multiple, uncorrelated and spatially distributed noise sources.

Causality constraints pertaining to active control has been examined in depth. Fundamental to the casuality analysis is the so-called plus operator that enters the formula that defines the optimal causally constrained weight vector. Constructed examples, have revealed some of the technicalities associated with the use of the nonlinear plus operator. Accordingly, new insights to the actions of the plus operator $\left\{ \cdot \right\}_+$ was provided.

A practical framework for multiple-channel (MC) spectral factorization using the prediction error filter (PEF) was developed. This technique is referred to as the multiple-channel prediction error filter spectral factorization algorithm. For the purpose of MC spectral factorization a variant of

existing transfer function definitions was proposed. By using this definition more robust estimates of the transfer function of the PEF was obtained. This multiple-channel prediction error filter spectral factorization (MCPEFSF) algorithm has been used in all the presented examples in this chapter. It was demonstrated that by using the MCPEFSF algorithm that the associated **z**-domain Wiener-Hopf (WH) filter when exposed to random white noise signals even outperformed the **t**-domain WH filter that is tailored to such flat spectral excitation. Moreover, for the single-channel (SC) case the MCPEFSF algorithm even outperformed the *cepstral* method.

A suite of examples of increasing complexity was constructed in order to exhibit some of the characteristics related to causality constraints. In a general context it can be concluded that the inverse of the minimum-phase component of the plant is of profound importance for the achievable ANR performance.

Moreover, it can be concluded that although group delays are often considered in an initial design phase, however, in order to assess the ANR capability of a system, such analysis is often deemed to be to primitive and will often leads to an underestimation of the achievable performance. It was, however, confirmed that the discrete-time group delays have a direct impact on the achievable performance while the impact of the continuous-time group delays is less predictable. Hence, the performance analysis should preferably be based on simulations involving one of the expressions presented for the optimal causally constrained and finite-order constrained weight vector for the MC **z**-domain WH filter.

The analysis also revealed that the *current* version of the Terma Earcup System is rather unfortunate being insufficiently damped. However, simulations did reveal that by decreasing the Q-factors associated with the resonance of the passive spring-mass-damper system and the Q-factor associated with the cross-over network of the tweeter unit this would significantly improve the ANR performance of the helmet system. Such improved design is beneficial both for a feedback system and a feedforward system. Hence, from the examples presented, it can be concluded that a considerably amount of ANR performance is available from a well-designed hearing protection device (HPD) in particular the plant that in the present case coincides with the Terma Earcup system. Accordingly, in the design of an active HPD the optimal choice of the secondary path and in particular the resulting inverse of the minimum-phase component is crucial and should receive much attention in the design phase. Such design effort, however, is considered outside the scope of the present Ph.D. project and therefore left for future research activities.

Considering, the proposed confined feedforward system (CFFS)for the actual HPD it was found that owing to the acquisition lead times provided by this topology a higher active control attenuation level is in general obtainable than by a feedback system in particular if we use a finite-duration impulse response (FIR) filter of sufficiently high order and enforce the feedback system to be robustly stable. However, due to the fewer total weights involved the feedback system provides the fastest convergence. The examples also revealed that by optimizing the HPD as discussed above the feedback system will then typically provide the best ANR performance in the low-frequency range while the CFFS is in favour at higher frequencies. Requirement on robust stability, however, may severely limit the upper operational band width of the feedback system.

In a practical design the active control engineer may prefer to use frequency-domain-based adaptive filters in order to tailor the systems to specific costumer preferences and the actual frequency contents of the disturbance signals.

Finally, it should be remarked that the added complexity of the CFFS over the ordinary feedback system (FBS) may render such system prohibitive costly.

Active control systems notoriously suffer from causality constraints which are of particular importance in an ordinary feedback system[s] or the feedback part of a hybrid FFFBS. In order to reduce delays related to the conversion stages a novel and general multirate (triple-rate) system for active control of sound and vibration (ACSV) applications that is based on time-domain adaptive filters (TDAFs) was developed. By using a very fast system (zeroth level) sampling frequency (192 kHz) almost negligible conversion delays are obtained. Active control is conducted at a slower downsampled (first level) speed which, however, is still largely oversampled compared with the operational bandwidth of the system. The one sample control output delay is therefore small while preserving the computational effort required for the generation of the control output signals at an acceptable level. Tap-weight adaptation takes place at even slower downsampled (second level) speed. This sampling frequency is selected as a compromise between the computational burden involved in the adaptive tap-weight updates and the requirement on fast update rates to ensure similar fast convergence and good tracking capabilities to nonstationary signals. Moreover, by limiting the bandwidth subject to adaptive control well below the full frequency span corresponding to the highest sampling frequency potential problems of large eigenvalue spread and poor frequency resolution leading to poor tap-weight convergence rates can be alleviated. Furthermore, instead of operating at the highest sample rates but by restricting the bandwidth of adaptive control the corresponding requirement on very long FIR filters for adaptive tap-weights and plant representation can be avoided. Enforcing some reasonable constraints on the amount of sampling frequencies supported this multi-rate functionality was successfully integrated in the hybrid MIMO feedforward-feedback system (HMIMOFFFBS). Moreover, it should however, be recalled that the multi-rate level 0 is not implemented in the simulator. As a consequence the real benefits are first experienced in the real-time environment (RTE) implementation in terms of a higher operational bandwidth and/or active control involving a higher amount of sensors. The actual computational savings provided by a multirate ANR system will be application dependent. In particular, for computational expensive adaptive filtering algorithms as the fast array recursive least-squares (FARLS) multi-rate adaptive control presents the greatest advantage. For the normalized LMS (NLMS) family the benefit from a slow second level sampling rate is largely lost by the necessity of upsampling of the adaptive tap-weights to the first multi-rate level.

Probably one of the most complicated systems used for active noise control (ANC) in particular for headset applications has been developed. A bottom-up description of the HMIMOFFFBS from basic multiple-input and multiple-output (MIMO) feedback system and MIMO feedforward system to the full blown hybrid MIMO confined-feedforward-feedback system (HMIMOCFFFBS) including provision for system identification and integrated communication (IC) was made. Provision is also made for elimination of feedback systemig[s] that potentially can disturb the reference signals with possible loss of performance as a consequence.

In the active control community the least-mean-squares (LMS) and variants hereof that are most commonly applied both for adaptive control and adaptive plant representation. In a demonstration *off-line* simultaneous system identification capabilities of twenty feedback paths, four secondary paths and four primary paths was made. The superiority of the $\alpha\gamma\Pi\epsilon$-affine projection algorithm ($\alpha\gamma\Pi\epsilon$-APA) over both the FARLS algorithm and in particular over the LMS algorithm in terms of the converging time of the adaptive tap-weights representing the individual plant response was demonstrated. A fast converging times is of practical importance for fast adaptation to changing plant condition and for minimum artificial noise dose, that can be annoying to the user. Moreover, the minimum filter length associated with a FIR filter representation could be determined. Current research addresses the use of α-stable random noise signals for *on-line* system identification.

A new idea for efficient implementation of a multi-channel system in which the adaptive filters involved are allowing to take different lengths was presented. This is accomplished by instead of using matrix-like structures to use cell-like structures allowing much more flexibility. Depending on the specific distribution of the filter length required for the weight representation the number of floating point operations can be reduced by expectably 0-40%. Similarly, considerations apply to the choice of adaptive tap-weight representation of the feedback paths, secondary paths and primary paths. The governing expressions for the control system, however, become a somewhat more involved.

A novel performance analysis of the developed linear-least-mean-squares estimate (l.l.m.s.e.)-based multiple-channel-$\alpha\gamma\Pi\epsilon$-affine projection algorithm (MC-$\alpha\gamma\Pi\epsilon$-APA) adaptive filter encompassing both dynamic *weight-driven leakage* and dynamic *control-effort-driven leakage* and numerical regularization as well as weight regularization was conducted. Moreover, in our presentation we also allowed the step-size μ, the leakage control parameters α, γ and the numerical regularization parameter ϵ to attain matrix-values and to be time-variant. Closed-form expressions for the mean- and mean-square steady-state performance as well as transient response performance of the adaptive filter were obtained. The main contribution to the performance analysis theory is the inclusion of time-variant parameters that in turn may be either deterministic or stochastic in nature. Furthermore the analysis conducted in this report uses an advanced random-walk model and also allows a non-vanishing initial weight vector. Usually, the random-walk model is omitted from the transient analysis. However, in the presence analysis we allowed a general random-walk model to take the non-stationarity of the system into account.

The performance expressions for the MC-$\alpha\gamma\Pi\epsilon$-APA adaptive filter in general are considerably more complicated than similar results pertaining to the ordinary ϵ-affine projection algorithm (ϵ-APA) and ϵ-NLMS (ϵ-NLMS) algorithms.

A suite of adaptive filtering algorithms has been implemented and tested with the use of the ACSV simulation tool.

Owing to the complexity of the system a considerably amount of time has been spent on the development and test of the software underlying the simulator. The RTE implementation is presently being subject to extensive tests.

Although the three branches of physics, acoustics, elasticity and electromagnetics seem quite dissimilar and describe completely different phenomena, however, they are all subjectable to analysis in the mathematical framework of *field theory*. Therefore, by taking the necessary precautions results that have been developed for one type of physical system can in some specific cases be adapted to one of the other two physical systems considered. In particular, thorough examination of the governing equations revealed that results for spherical near-field antenna testing (SNFAT) as used for more than 30 years for example at Ørsted TUD potentially can be generalized to predict field quantities from sensors being responsive to acoustical as well as elastoric waves. Among such sensors we find ordinary pressure microphones, (radial) velocity microphones and accelerometers. For this purpose a so-called probe description of the sensor supposedly used for the acquisition of the sensor information must be made. As implicitly appear from the name SNFAT scanning of the fields takes place on a sphere. However, as discussed in Appendix F the spherical coordinate system is also the only coordinate system in which the vector wave equations separate for all three physical systems considered which in turn greatly simplifies the analysis. The confined array technique is indeed dependent on the availability of a sufficient number of reference sensors in order to avoid spatial aliasing.

The HMIMOCFFFBS is prepared for future replacement of FIR filters by implementation, e.g.,

Kautz/Laguerre filters. An indication of how such replacement should be carried out is made.

12.2 Other Achievements

Besides conducting the research activities that have formed the basis for the production of the present thesis some other work activities have been carried out during the course of the project. Starting from scratch measurement facilities have gradually been established at Terma premises, laboratory equipment as well as equipment for field test have been defined, purchased and implemented. Owing to the long time experience of Terma in the field of military airborne applications three on-site noise recordings F-16/B, CH-47D Chinook and AS-532 Cougar could therefore successfully be conducted. Some indicative examples of noise spectra have been presented. The detailed information, however, is considered Terma property and therefore not included in this thesis.

As part of the project a MATLAB®-based general purpose tool for the analysis and synthesis of ACSV systems and in particular the HMIMOCFFFBS has been developed. This software tool has also largely been used to compensate for the lack of a hardware platform with sufficient channel bandwidth and processing capability to support the HMIMOCFFFBS.

12.3 Present Research and Development Activities

At the time of writing most parts of the active control system has been embedded in a RTE that comprises a digital signal processor (DSP). Unfortunately, this hardware board only supports four microphones. As one channel should always be reserved for the error sensor the number of reference sensors supported accordingly amounts to three. Hence, a new hardware board must be designed and manufactured before the the advantages of the proposed HMIMOCFFFBS can be fully exploited.

The MC-$\alpha\gamma\Pi\epsilon$-APA and MC-$\alpha\gamma\Pi\epsilon$-NLMS adaptive filters will be subject to extensive future test and evaluation activities. Verification of the developed sliding window FARLS adaptive filter algorithm is also planed.

The hybrid continuous-time discrete-time topology (HCTDTT) introduced in chapter 4 and the underlying continuous-time-controller is currently under development outside this project on a contract.

For the development of a reference test unit (RTU) for active control an acoustical transparent sphere and an acoustical semi-transparent-semi-opaque hollow sphere are currently being considered. The aim of the RTU is to provide a highly accurately modeled framework with which reliable and accurate tests and evaluations of developed theories and methods can take place. In contrary, for the specific instantiation of an active control system, namely the helmet based HPDs only very crude models are available. Therefore, when applying a complex active control system including hybrid combination of adaptive feedforward and adaptive feedback elements it may often be exceedingly difficult to predict very accurately the attenuation achievable.

The adaptation of the SNFAT technique discussed in Part V to the domain of acoustics looks as a promising idea in the development of such reference test unit.

12.4 Future Research and Development Activities

Of course not all research work elements involved in the design of a complex active control (AC) system can be carried out within the scope of a single Ph.D. project. Therefore some avenues of future research activities will be suggested in this section.

The JCRSA method developed in chapter 2 should formally be verified including and assessment of the obtainable accuracy. The ACSV RTU described in Appendix G is candidate hardware platform for this purpose.

In the design of an active HPD the optimal choice of the secondary path and in particular the resulting inverse of the minimum-phase component is crucial and should receive much attention in a future design phase.

In the literature it is often seen that the noise attenuation predicted by a HPD measured by the error microphone in the active control loop exceeds the attenuation obtained from either physical ear channel measurements or psychophysical measurements by as much as 10 dB. Measurements made under laboratory conditions as well as field measurements also revealed a loss of coherence between the disturbance signal and the performance signal present at the error sensor and performance sensor respectively. Therefore, the acoustical/electro acoustical environment in modern active HPD determines an upper limit to the achievable attenuation figures, which probably is more problematic than the performance limitations associated with bone conduction. Accordingly improved plant models for the secondary paths and primary paths are required. Such plant model improvement can ultimately lead to better controllability and increased bandwidth of the system. Hence, higher attenuation figures should be obtainable while the requirements on controller robustness are preserved.

In chapter 4 adaptive inverse control (AIC) was proposed as a method to achieve *adaptive control* of unknown and possible time-varying systems by using adaptive filters. The objective of the adaptive inverse controller is to in cascade with the actual plant (secondary path) to obtain a plant that seen from the digital controller equals the transfer function of a chosen reference plant. As the earcup system is still under development, and the plant uncertainties therefore not well known the verification of the AIC is postponed to the completion of this earcup system conducted and experiments exploiting these variations in a practical environment have been conducted.

Upon completion of the ANR hardware tests of the adaptive filter algorithms should recommence. Moreover, the different algorithms and their individual parameterizations will be assessed. Finally, the adaptive filters will be subjected to additional performance analysis and system optimization when the hardware supporting the HMIMOCFFFBS becomes available.

Another avenue of future research is the exploitation of Kautz/Laguerre adaptive filters for more computational efficient representation of the various plants in the system.

In the military domain the trend is to wear complex triple layer hearing protection devices. The first level of protection is provided by the helmet itself. The earcups constitute the second protection layer. The third protection layer is provided by earplugs that are either shallowly or deeply inserted in the ear channels. Both the earcups and the earplugs will be equipped with ANR hardware. The proposed HPD instantiation of the HMIMOCFFFBS involves the first and second protection layer therefore comply with this trend. Future research, however, should therefore also investigate the potential benefit of integrating ANR earplugs into a multi-channel ANR system.

The analysis of stability of MIMO systems with mixed feedback and feedforward topologies is

considerably more complicated than in the single-input and single-output (SISO) feedback case. The requirement on using adaptive filters as opposed to fixed (analogue) filters renders the analysis and synthesis of such filters even more challenging.

The Chinook CH-47D helicopter noise recordings revealed an exceedingly complicated behavior of the signals with large spatial variations and time-dependencies. The behavior is not fully understood and additional measurements are required. An in-depth analysis of acoustical fields experienced in the military aircrafts and in particular helicopters is required in order fully to comprehend how to address this field variation from an AC perspective. Furthermore, previous measurements exclusively were in terms of passive noise recordings. A comprehensive measurement scheme comprising in-situ performance measurements on the developed active control of sound (ACS) should be conducted. In addition the ANR measurements should include microphone in the ear (MIE) techniques.

For passive HPDs a set of physical and subjective based measurements procedures exist. However, at the moment of writing no such standard exists for the test of active HPD. Based on the experiences acquired during future evaluation of realized ANR systems, contribution to such standardization work should be made.

Throughout the report numerous references are made to the literature pertaining the scientific subject being analyzed. Therefore, this present report should among other sources hopefully provide fruitful information for future AC research and development activities.

APPENDICES

APPENDIX

A. ACTIVE NOISE CONTROL PERFORMANCE

A.1 Introduction

The performance of a modern complex active noise control system (ANCS) is determined from numerous system parameters. The objective of this chapter twofold. Firstly, we want to define evaluation criterions for the assessment of the performance of an active noise control (ANC)-system. Secondly, approximate formulas for the frequency-dependent achievable attenuation as a function of delays are provided for feedback system (FBS) and feedforward system (FFS) design.

Our main interest in this chapter is the overall performance of an ANCS. For a more subject specific performance evaluation, e.g., on adaptive filters the reader is referred to relevant chapters, e.g., chapter 9 where the adaptive filter performance is illuminated.

A.1.1 Chapter Outline

This chapter is organized as follows. Following these introductory remarks section A.2 presents various methods to assess the overall performance of an ANC system ranging form single-channel (SC) systems to multiple-channel (MC) systems evaluated over multiple trials and scenarios. Such practical active noise reduction (ANR) performance quantities are also useful when formulating *cost functions* as presented in chapter 8 on page 371. Moreover, the simulations presented in chapter 5 on page 249 and chapter 7 on page 291 make extensive use of the attenuation quantities involved.

In a real system constraints on *causality* apply. Hence, delays in the control loop will often be one of the most important factors that limit the achievable performance. This in particular pertains to FBS design. An expression for the achievable ANC performance as a function of frequency for a FBS when limited exclusively by delays in the secondary path is presented in section A.3. For FFS design time-advanced information may be provided by a set of reference sensors. For the same reason a hybrid MIMO confined-feedforward-feedback system (HMIMOCFFFBS) has been proposed in this report.

A.2 ANC Attenuation

The probably most established figure of merit within the active control (AC) community is the steady-state integrated noise attenuation provided by the system over the volumes in space. This figure of merit is usually obtained by averaging the attenuation over some discrete positions in space. We will generally measure or estimate the performance locally at each of the N_p locations of the performance sensors depicted in Figure 1.1.

A.2.1 ANC Attenuation Time-Frequency Domain

The *local* attenuation at, e.g., the k'th performance sensor $\mathcal{A}_k^p(f,t)$ will be a function of frequency and generally exhibit time-dependence. The computation of $\mathcal{A}$ will primarily be based on signal analysis which is treated in more details in Appendix C. We will define the time-frequency-domain attenuation by

$$\mathcal{A}_k^p(f,t) \triangleq 10\log_{10}\left(W_k^p(f,t)\frac{S_{e_k^p e_k^p}(f,t)}{S_{d_k^p d_k^p}(f,t)}\right) \quad [\text{dB}]. \tag{A.2.1}$$

Here $S_{\psi_a\psi_a}(f,t)$ denotes the *instantaneous* (short term) auto spectral density function (power spectral density (PSD)) of signal $\psi_a(t)$. Similarly, $S_{\psi_a\psi_b}(f,t)$ will be used to denote the *instantaneous* (short term) cross-spectral density function between signal $\psi_a(t)$ and $\psi_b(t)$ [1]. The quantity $W_k^p(f,t)$ is a frequency (time-variant) weighting function, that will be subject to the normalization constrain $\int_{-\infty}^{\infty} W_k^p(f,t)\,\mathrm{d}f = 1, \quad \forall t \in \mathbb{R}$, is applied to the k'th performance sensor. For example $W_k^p(f,t)$ may be a A-, B-, C- or D-weighting filter. An unweighted attenuation expression is obtained by assigning unity to $W_k^p(f,t)$. The overall objective of the ANC-system is to suppress possibly time-variant disturbances. Hence, in order to adapt to changing environmental conditions the cost functions involved in the AF should accommodate this behavior. Tracking capabilities of the adaptive filter algorithms are discussed in detail in chapter 9. Time-variance in the weight functions are therefore sometimes required in order to allow for time-variant ANC-system objectives.

The *global* attenuation capability measure is obtained as a logarithmic-weighted sum of the local attenuation quantities above (in dB), that is,

$$\mathcal{A}^p(f,t) \triangleq \sum_{k=1}^{N_p} W_k^p \mathcal{A}_k^p(f,t) \quad [\text{dB}]. \tag{A.2.2}$$

The quantity $W_k^{p,\text{dB}}$ denotes the attenuation weight factor of k'th performance sensor. Often a normalization constraint $\sum_{k=1}^{N_p} W_k^p = 1$ will be preferred.

In a more advanced analysis we should estimate the performance by considering a number of trials (simulations) N_t . By running multiple *independent and identical distributed (i.i.d.)* trials we can decrease the variance the estimate of $\mathcal{A}^p(f,t)$.

A trial-averaged attenuation estimate $\bar{\mathcal{A}}^p(f,t)$ is then obtained from

$$\bar{\mathcal{A}}^p(f,t) = \frac{1}{N_t}\sum_{n=1}^{N_t} \mathcal{A}^p(f,t,n) \quad [\text{dB}], \tag{A.2.3}$$

where n is the trial index. Finally, as the environmental conditions in which the ANC-system shall operate normally is not known in advance we should examine the robustness of the system to varying conditions by using a number of (different) scenarios N_{sc} [1]. Hence, we will define the

[1] Scenarios will usual not be jointly *i.i.d.*

scenario-averaged attenuation estimate scenario-averaged attenuation estimate $\check{\mathcal{A}}^p(f,t)$ by

$$\check{\mathcal{A}}^p(f,t) = \frac{1}{N_{sc}} \sum_{s=1}^{N_{sc}} \bar{\mathcal{A}}^p(f,t,s) \quad [\text{dB}], \tag{A.2.4}$$

where s is the scenario index.

A.2.2 ANC Attenuation Time Domain

In the *time-domain* will usually apply the mean-squared-error reduction criteria and define the attenuation at the k'th performance sensor $\mathcal{A}_k^p(t)$ by

$$\mathcal{A}_k^p(t) \triangleq 10 \log_{10} \left(\frac{\mathrm{E}\,(\mathbf{e}_k^p(t))^2}{\mathrm{E}\,(\mathbf{d}_k^p(t))^2} \right) \quad [\text{dB}], \tag{A.2.5}$$

where $\mathbf{e}_k^p$ and $\mathbf{d}_k^p$ designate error signal and disturbance signal at the k'th performance sensor respectively both considered as RVs. The expectation operator is designated by $\mathrm{E}\,$.

In practice except for theoretical analysis, however, we will use the discrete-time *realizations* of the error and disturbance signals $e_k^p(i)$ and $d_k^p(i)$ and obtain a filtered *estimate* of $\mathcal{A}_k^p(i)$ $\hat{\mathcal{A}}_k^p(i)$ from

$$\hat{\mathcal{A}}_k^p(i) = 10 \log_{10} \left(\frac{\widehat{(e_k^p(i))^2}}{\widehat{(d_k^p(i))^2}} \right) \quad [\text{dB}]. \tag{A.2.6}$$

The estimated squared-disturbance $\widehat{(d_k^p(i))^2}$ and estimated squared-error $\widehat{(e_k^p(i))^2}$ in turn are obtained from an exponential-time-weighting procedure:

$$\widehat{(d_k^p(i))^2} = \|d_{k,i}^p\|_{\Lambda_{\mathcal{A}}}^2 \tag{A.2.7a}$$

$$\widehat{(e_k^p(i))^2} = \|e_{k,i}^p\|_{\Lambda_{\mathcal{A}}}^2. \tag{A.2.7b}$$

In (A.2.7) the $M_{\mathcal{A}} \times 1$ column vectors $d_{k,i}^p$ and $e_{k,i}^p$ defined by

$$d_{k,i}^p \triangleq \mathrm{col}\,\{d_k^p(i), d_k^p(i-1), \ldots, d_k^p(i-M_{\mathcal{A}}+1)\} \tag{A.2.8a}$$

and

$$e_{k,i}^p \triangleq \mathrm{col}\,\{e_k^p(i), e_k^p(i-1), \ldots, e_k^p(i-M_{\mathcal{A}}+1)\} \tag{A.2.8b}$$

have been introduced. The quantity $M_{\mathcal{A}}$ denotes the number of samples used in the attenuation calculations and the quantity $\Lambda_{\mathcal{A}}$ is a $M_{\mathcal{A}} \times M_{\mathcal{A}}$ positive-definite exponential weight matrix used in time-averaged attenuation calculations

$$\Lambda_{\mathcal{A}} \triangleq \mathrm{diag}\,\lambda_{\mathcal{A}}^0, \lambda_{\mathcal{A}}^1, \ldots, \lambda_{\mathcal{A}}^{M_{\mathcal{A}}-1}, \tag{A.2.9}$$

where the weight scalar (forgetting factor) used in time-averaged attenuation calculations $\lambda_{\mathcal{A}}$ usually is very close to one ($0 \ll \lambda_{\mathcal{A}} \leq 1$).

In practice rather than specifying $M_{\mathcal{A}}$ it is probably more convenient to specify an attenuation estimation time that we will denote by $T_{\mathcal{A}}$. Then $M_{\mathcal{A}}$ is readily obtainable from the sampling frequency f_s

$$M_{\mathcal{A}} = \lceil \{ f_s T_{\mathcal{A}} \}, \tag{A.2.10}$$

where the operator $\lceil (\cdot)$ designates taking the ceil of the term inside the parentheses.

Usually, in an *operational* ANC-system no performance sensor exists and the performance is assessed directly from the error sensors. The attenuation at the m'th error sensor $\mathcal{A}_m^e(f,t)$

$$\mathcal{A}_m^e(f,t) \triangleq 10 \log_{10} \left(\frac{S_{e_m e_m}(f,t)}{S_{d_m d_m}(f,t)} \right) \quad [\text{dB}]. \tag{A.2.11}$$

Similar expressions for *global* attenuation (A.2.2), the trial-averaged attenuation (A.2.3) and for the scenario-averaged attenuation (A.2.4) using the error sensors instead of the performance sensors are readily obtainable. However, it should be remarked that using an error sensor that partakes in the control loop might lead to an **overestimation** of the ANR performance. This problem is for example reported in [2, Ch. 7].

A.2.3 ANC Attenuation Frequency Domain

Under the assumption of wide-sense stationary (WSS) the steady-state frequency-domain attenuation can readily be obtained from (A.2.1) - (A.2.4) by omitting the time-index.

A.3 Delays

A.3.1 Delays in Secondary Signals Generation

In signal processing applications, delays are usually not an important issue as long as the waveform is preserved. However, as will be discussed next delays become crucial in control systems, especially for ANC application owing to the relatively large bandwidth that generally is involved. In pure continuous-time applications delays are contributed by the transducers and the propagation of the rejection signals. In modern discrete-time systems additional delays are encountered. Delays are involved in the analogue to digital converter (ADC) and digital to analogue converter (DAC) conversion stages, the anti-aliasing filter (AAF) and the reconstruction filter (RF) as well as at the computation stage. In multi-rate system (MRS) design delays associated with the decimation interpolation filters (DIFs) should also be taking into account.

From elementary control theory, e.g., [3, Ch. 5], it is well known that delays in the control path will limit the operational bandwidth of a feedback based active control system. In [2, Ch. 6] we can obtain the following expression for the **obtainable** ANR attenuation limited by delays in a random white noise (RWN) $\mathcal{A}_\tau$ as a function of the delay in plant response τ and frequency f

$$\mathcal{A}_\tau(f) = 20 \log_{10} \left| 1 - \mathrm{e}^{-\imath 2\pi f \tau(f)} \right| \quad [\text{dB}], \quad \text{FBS}. \tag{A.3.1}$$

A.3.2 Acquisition Time

In a FFS one of the objective is to obtain time-advanced information concerning the disturbances. However, delays can ultimately limit the compactness of the ANR-system. In section 2.4 on page 32 the acquisition lead-time was defined viz. Definition Definition 2.1. Loosely speaking the acquisition lead-time refers to the time $\tau_{x_j d_m} = t_2 - t_1$ that passes from the acquisition of the j'th reference signal $x_j(\mathbf{r}_j, t_1)$ at time t_1 and at position $\mathbf{r}_j$ in space, until the (coherent) disturbance signal, $d_m(\mathbf{r}_m, t_2)$ is acquired by the m'th error sensor at time t_2. Similarly, the delay $\tau = t_3 - t_1$, where t_3 is the time where the rejection signal, $r_m(\mathbf{r}_m, t_3)$ is acquired by the m'th error sensor. Intuitively in a diffuse sound field the events that $t_2 \leq t_1$ and $t_2 \geq t_1$ both take the probability 0.5. However, as we observed in chapter 2 propagation delays in the primary paths of a confined feedforward system (CFFS) often lead to positive acquisition lead-times. For the FFS (A.3.1) applies but with τ corrected for the acquisition lead-time, that is,

$$\mathcal{A}_\tau(f) = 20\log_{10}\left|1 - \mathrm{e}^{-\imath 2\pi f \max\{0,\tau(f)-\tau_{acq}(f)\}}\right| \quad [\mathrm{dB}], \quad \text{FFS}. \tag{A.3.2}$$

Causality constraint refers to the condition under which $\tau(f) - \tau_{acq}(f) < 0$ (or $t_3 < t_2$). Accordingly, in application with strict space limitation like a helmet ANR system or an active mufflers for motorcycles delays can ultimately limit the achievable performance especially in the upper frequency bandwidth. In the general case of propagation in a dispersive medium τ_{acq} will exhibit dependence on frequency.

Delays caused by the plant in a feedforward active control system (FFACS) has historically been considered as source of instability. As explained in section 6.3 on page 275, by employing the mFx technique synchronization between the reference signal and the error signal is establish and this undesired effect caused by plant delays can largely be compensated for. Of course the secondary source pathes do not in general resemble pure delays. However, as in chapter 2 on page 17 we may determine acquisition lead-times experimentally and use these as a first order delay estimates for more complex systems.

Bibliography

[1] L. Cohen. *Time-Frequency Analysis*. Prentice-Hall, Upper Saddle River, New Jersey, 1995.

[2] Stephen J. Elliott. *Signal Processing for Active Control*. London: Academic Press, 2001.

[3] Sigurd Skogestad and Ian Postlethwaite. *Multivariable Feedback Control Analysis and Design*. John Wiley & Sons, Inc., 1996.

B. RANDOM SIGNALS

In section B.1 we will briefly review the formal definition of random variables (RVs) and random processs (RPs). The formal definition will then be put into perspective using the F-16 application as an example. Subsequently the theme of section 5.3 and section 5.4 is the processing stages involved in the *sensed* signals and *actuated* signals respectively.

B.1 Signals and Stochastic Processes

In the course of active noise cancelation design and analysis extensive use of the term *signal* is made. The term signal is often associated with something that conveys information in contrast to *noise* that tends to deteriorate the perception of the information. In the context of for example active noise control applied to fighter pilot helmets the communication signal and possible 3-D audio constitute *conveying signals*. However, in this report we will use the term *signal* in a more broad sense meaning that it could refer to something that does convey information but also to something that stems from some noise process. It should be recalled that in practice measurement noise will inevitably also be present. Hence, no *exact* knowledge regarding any of the signals is available anyway.

Signals are encountered at the input and output as well as intermediate stages of an ANR controller. A descriptive name will be assigned to each of these signals.

B.1.1 Signal Classification

A signal can generally be classified as being either a *deterministic* or a *nondeterministic* signal [1, 7]. The latter class of signals is also referred to as *stochastic signal*. Further classification of deterministic and random signals can be made [1]. We will address the classification of signals in more details during the discussion of the F-16 noise recordings provided in Appendix D on page 547.

Although estimation historically has been divided in deterministic least-squares estimation and linear least-mean-squares estimation, these estimation problems are equivalent in the sense that solving a problem from on class also solves a problem from the other and vice-versa. We will return to this classification in chapter 8 on page 371.

B.1.2 Stochastic Processes

In the following formal discussion of a RP, time will be chosen as the ordinate axis. However, it should be recalled that the theory of RV is general and therefore also pertains to cases where the RP involved exhibits spatial-dependence instead of time-dependence.

In the mathematical analysis it is convenient to consider all signals as *stochastic* signals. Hence, in the extreme case a deterministic signal can also be viewed as RP with a variance at all time equal to zero ($\sigma^2_{\psi_a} = 0$).

Preceding the definition of a *stochastic process* we need to define a *random variable* [1, 7]. Basically, a RV is a rule, that is, a function for assigning to every outcome ζ of an experiment (measurement) S a *number* $\boldsymbol{\psi}_a(\zeta)$ where we by $\boldsymbol{\psi}_a$ denote an arbitrary random variable, that is, a function of ζ. As is customary boldface type will be used to denote a random variable in order to distinguish RV from dummy variables. By process is understood something that goes on for some period of time (or some range in space). Accordingly a stochastic process or RP is a natural extension to the concept of RV. A RP is a family of time functions depending on the instance parameter ζ. The stochastic process is observed continuously in time or at discrete-time point conducting new but similar experiments. Then an arbitrary stochastic process $\boldsymbol{\psi}_a$ is a rule for assigning to every ζ a function $\boldsymbol{\psi}_a(t, \zeta)$ that generally varies with time. The RVs $\boldsymbol{\psi}_a$ are characterized by a set of probability distribution functions that in general exhibit time-dependence. By $\boldsymbol{\psi}_a(t, \zeta)$ we make explicit reference to a particular sample function of the RP. A collection of such identical experiments is referred to as an *ensemble* in the literature.

Hence, a particular signal can be considered as a sample sequence of a RP. For example in experiment S the objective is to measure the instantaneous sound pressure $p(\mathbf{r}^a, t, \zeta)$ at some fixed but else arbitrarily chosen position $\mathbf{r}^a$ in an F-16 cockpit in the time interval $t_1 \leqslant t \leqslant t_2$ following an event that is repeated in total, e.g., N_E number of times ($1 \leqslant \zeta \leqslant N_E$). An event could be to make some kind of operation invoking the hydraulic system in the F-16. By conducting this experiment repeatedly the stochastic process involved in the activation of the hydraulic system can then be observed and subsequently be subject to a more comprehensive statistical analysis. The main problem in this example is to repeat the experiment while preventing other factors contributing to $p(\mathbf{r}^a, t, \zeta)$ from changing too. Otherwise, the significance of, e.g., invoking the hydraulic system as compared with other variables.

For a more rigorous treatment of the concept of stochastic processes refer to [1, 5, 7].

We will return to the issue of stochastic processes in the analysis of the F-16 noise recording provided in Appendix D.

The concept of RPs is often applied as a model for the various signals involved in the theoretical analysis of adaptive filters. In some contexts, however, only a single measurement and not an ensemble of experiments is available. Instead the statistical information might be derived form time-averages rather than ensemble averages. However, this requires that the signal is *ergodic* in the pertinent parameters. Basically, ergodicity is a topic dealing with relationship between *statistical averages* and *sample averages*. For example. if a signal is ergodic in a *wide sense*, that is, ergodic in the mean and covariance this implies that corresponding ensemble averages and root-mean-square averages can be substituted by similar time-average quantities [7, Ch. 12]. Moreover, it should be remarked that the signal will then necessarily also exhibit stationarity on the same parameter set. However, the converse is not necessarily true. Hence, stationarity does not necessarily imply ergodicity. This means that two particular sample functions of a RP, e.g., $\boldsymbol{\psi}_a(t, \zeta_1)$ and $\boldsymbol{\psi}_a(t, \zeta_2)$, might each be stationary in some statistical sense and though be different in one or more of the statistical variables. In the previous example two consecutive activations of the hydraulic system could possibly lead to a root-mean-square pressure that does not vary with time in the observation interval $[t_1; t_2]$. However, the sound pressure level could be different in the two experiments.

B.1.3 Signal Representation

For the sake of convenience the choice of terminology and symbols used to represent signals will be defined in the subsequent text.

In order to preserve mathematical generality throughout this report complex notation will be used. This choice has been made even though complex-valued baseband signal are not being considered in the active noise reduction system, but made to ensure smooth transition to other applications involving complex-valued signals. The implementations in MATLAB® and real-time environment are at present, however, confined to real-valued data.

The ANR hearing protection device (HPD) of course is a physical system and involves continuous-time signals. The hybrid controller depicted in Figure 4.1 on page 241 encompasses both an analogue filter that operates directly on continuous-time signals and a digital filter that processes digital signals. By definition digital signals are quantized both in amplitude and in time involving a sampling process. We will use the term discrete-time signals for these two-fold quantized signals. In the process of sampling a constant sampling time T will be assumed. In the description of the digital controller, we will mostly be concerned with discrete-time signals.

In $\boldsymbol{\psi}_a(i)$ the integer i in parentheses is used as an abbreviation for $\boldsymbol{\psi}_a(iT)$ that is the quantized value of the corresponding continuous-time function $\boldsymbol{\psi}_a(t)$ at time $t = iT$. Hence, $\boldsymbol{\psi}_a(t) \rightarrow \boldsymbol{\psi}_a(iT) \rightarrow \boldsymbol{\psi}_a(i)$ where the latter abbreviation is chosen for notational convenience.

For a more exhaustive presentation of signal quantities the readers are referred to [1], [4, Ch. 2].

Moreover, we will use the common $\{\mathbf{d}, \mathbf{u}\}$ notation in adaptive filtering, where $\mathbf{d}$ represents the so-called "desired signal" and $\mathbf{u}$ represents the observations (reference signal) respectively. When the adaptive filter operates in interference cancelation mode defined in section 8.2 we consider $\mathbf{d}$ as a *disturbance*. In estimation theory $\mathbf{u}$ is referred to as a *regression vector* [6]. In other contexts $\mathbf{u}$ is called *excitation* [3]. Normally no statistical information regarding random variable $\mathbf{d}$ or the random vector $\mathbf{u}$ is available. Then in practice we have to resort on the *realizations* $\{d(i), u_i\}$ of $\{\mathbf{d}, \mathbf{u}\}$.

We will make extensive use of a finite-length signal vector $\boldsymbol{\psi}_{a,i}$ that is formed from the discrete-time signal sequence, $\boldsymbol{\psi}_a(i)$, according to the first-in-first-out (FIFO) principle

$$\boldsymbol{\psi}_{a,i} = [\boldsymbol{\psi}_a(i) \quad \boldsymbol{\psi}_a(i-1) \quad \dots \quad \boldsymbol{\psi}_a(i-M+1)]. \tag{B.1.1}$$

The number of elements M in the signal vector is typically coincident with the number of tap-weights used for adaptive filtering of the signal.

In the general time-varying case the cross-correlation matrix $R_{\psi_a\psi_b}(t)$ associated with the two arbitrary signal vectors, $\boldsymbol{\psi}_a(i,t)$, $\boldsymbol{\psi}_b(i,t)$, is defined as the expectation of the outer product of the input vector, with itself

$$R_{\psi_a\psi_b}(t) \triangleq R^*_{\psi_b\psi_a}(t) = \mathrm{E}\left[\boldsymbol{\psi}_a(i,t)\boldsymbol{\psi}^{b*}(i,t)\right]. \tag{B.1.2}$$

The asterisk superscript denotes Hermitian transpose and complex conjugation. The quantity $\mathrm{E}[\,\cdot\,]$ denotes the expectation operator. It should be remarked that this convention follows the definition pursued in mathematical textbooks [1, 7] and also in MATLAB®. In other textbooks [2], however, the two signal vectors are interchanged corresponding to a complex conjugation.

Bibliography

[1] Julius S. Bendat and Allan G. Piersol. *Random data Analysis and measurement procedures*. John Wiley & Sons, Inc., 3rd edition, 2000.

[2] Stephen J. Elliott. *Signal Processing for Active Control*. London: Academic Press, 2001.

[3] Steven L. Gay. Affine projection algorithms. In Simon Haykin and Widrow Bernard, editors, *Least-Mean-Square Adaptive Filters*. John Wiley & Sons, Inc., 2003.

[4] Simon Haykin. *Adaptive Filter Theory*. Prentice-Hall Inc. Upper Saddle River New Jersey 07458, 3rd edition, 1996.

[5] Hwei P. Hsu. *Probability, Random Variables, & Random Processes*. Schaum's Outlines. McGraw-Hill Companies, Inc, 1997.

[6] Thomas Kailath, Ali H. Sayed, and Babak Hassabi. *Linear Estimation*. Printice Hall, Upper Saddle River, New Jersey, 2000.

[7] Athanasios Papoulis and S. Unnikrishna Pillai. *Probability, Random Variables and Stochastic Processes*. McGraw-Hill, New York, 4th edition, 2002.

C. STATISTICAL DATA ANALYSIS

C.1 Motivation

The objective of acquiring signal data from field measurements or from laboratory measurements is to obtain information regarding signal characteristics pertinent to each channel involved, but also to obtain information regarding *joint* signal characteristics. Hence, such signal data acquisition has been conducted and reported in this report, e.g., Appendix A on page 529 and Appendix D on page 547. However, some imperfections will inevitably always enter the data acquisition process due to hardware limitations, imperfections in the installation, a finite time slot available for the data acquisition and environmental conditions outside the control of the operator etc. However, by following certain general guidelines, e.g., as recommended in [1, Ch. 10] the level of error introduced during data acquisition especially under laboratory conditions can normally be kept sufficiently low for the purpose. Moreover, *domain specific* considerations like for instance those pertaining to the instrumentation airborne military platforms also have to be taking into account.

The theme of this appendix is an assessment of the errors that result from the *statistical data analysis* during post processing of the acquired data. Unfortunately, in engineering practice such statistical analysis is often neglected. The present appendix does not intend to provide rigorous (if at all possible) expressions for all estimation errors involved, but to provide relative simple expressions that can be used for approximation of such quantities and which holds under fairly reasonable assumptions that can be applied to many practical situations.

As described in Appendix B random signals are described in terms of gross characteristics like for instance the auto- and cross-correlation functions in the time-domain and auto- and cross-spectral density functions in the frequency-domain. The inferences of such quantities constitute another type of error source.

Following this motivational section the *periodogram* based spectra estimation method is presented in section C.2. The specific choice of the discrete Fourier transform (DFT) parameters involved is subject to certain trade-off between different performance measures. Some basic guidelines for the choice of these parameters that have been followed through the course of this project is made. In section C.3 expressions for bias error and random error related to the estimation of various often used quantities in the signal analysis and is provided. These expressions hold under fairly general conditions. Confidence intervals can subsequently be determined from this analysis. However, as the periodogram method operates on a finite amount of data it is prone to such phenomena as *leakage*, *smearing effects*, *unresolved signals* and *side lobes*. The underlying periodogram parameters of a statistical data analysis have therefore to a large extent been included in the figure captions in this report.

C.2 Modified Periodogram Analysis

The statistical analysis often involves estimation of power density spectra. The preferred type of method for this purpose is the *periodogram* method. All periodogram methods are based on the DFT. A *windowing* of the data must therefore take place in order to comply with the requirement on finite-length data. In the ordinary periodogram analysis a rectangular window is multiplied to the signal. In order to reduce spectral bias errors a method referred to as *modified periodogram* which employ a (tapered) data window is used. For an explanation of these techniques the reader should consult [5, Ch. 10] and [6, Ch. 12].

As will be seen in section C.3 the level of *random errors* related to our statistical data analysis can to a large extent be reduced by *averaging* over many records. Hence, the number of full length DFT averages designated by K_{DFT}, that can be obtained is critical to the overall estimation accuracy. This number of averages is largely determined from the amount of samples available denoted by Q_{DFT} and the DFT window length L_{DFT}. Provided that the amount of samples available is large the L_{DFT} should be sufficiently wide to comply with requirements on *resolution* capabilities without compromising K_{DFT}. Hence, in order to resolve two sinusoidal frequency components L_{DFT} and the choice of window type (Kaiser, Chebyshev, Hanning, Hamming, Bartlett etc.) together should result in a sufficiently low *main lobe width* Δf_m. The window type dictates the side lobe level (SLL) while the main lobe width and the extent of the side lobes in the time-domain vary inversely proportional with the window length.

Moreover, is should be remembered that time-variant signals also set an upper limit on Q_{DFT} and therefore also directly on K_{DFT}. However, if the number of samples Q_{DFT} cannot be made arbitrarily large, and we wish to get a near maximum reduction in the variance out of a fixed number of points then a reasonable procedure is overlap the segments. This can be accomplished by moving the DFT window by a number of samples displacement between two consecutive DFT averages denoted here by R_{DFT}. In order not to discard samples the displacement should not exceed the window length, that is $R_{DFT} \leq L_{DFT}$. The assumption on *independent* records of course does not hold for the overlapping windows technique, that is, for $R_{DFT} < L_{DFT}$. Accordingly, we will introduce yet another quantity K'_{DFT} that denotes *effective* number of DFT averages. A common choice is to overlap one half of their length, that is, to let $R_{DFT} = 0.5L_{DFT}$. Then as proved in [7] under the assumption of a Gaussian process the associated variance increase due to overlapping data segments only equals a factor of $\frac{11}{9}$ corresponding to $K'_{DFT} = \left(\frac{9}{11}\right)^2 K_{DFT}$.

Another important parameter for the (modified) periodogram analysis is the the DFT (block) size represented by N_{DFT}. Usually, an oversampling in which $N_{DFT} \gg L_{DFT}$ is applied by zero padding in order increase the number of DFT frequency points $N_{f,DFT}$ and therefore also to improve the DFT frequency resolution Δf_{DFT}. Hereby, fine grain information is provided that can be useful to extract important features. However, the resolution capabilities is solely determined by the window length L_{DFT} and the type of window. Furthermore, some *bias errors* increase squarely with this frequency resolution bandwidth cf. (C.3.3) on page 542, which accordingly should be small as possible.

A computational efficient implementation of the DFT is provided by the fast Fourier transform (FFT). For optimal operation of the FFT a radix 2 number is usually selected for N_{DFT}. Finally, according to the discussion in section 2.2 on page 18 the sizes of the various channel spectral density matrices are proportional to the number of DFT frequency points in use. Hence, for computational reasons $N_{f,DFT}$ cannot be made arbitrary large.

C.3 Estimation Uncertainties

Various factors contribute to statistical errors in the estimates of the various parameters characterizing the signals. In second-order statistics the imperfect estimates manifest themselves as *bias errors*, *random errors* and *rms errors*. For higher order statistics (HOS) corresponding higher-order types of estimation errors exist.

As discussed above spectral estimation procedures involve spectral windows. The bias error is always in a direction that understates the dynamic range of the spectra, that is, the peaks are underestimated and the toughs are underestimated. In practice only a finite amount of data is available for the *statistical data analysis*. Therefore, some variance or (random errors) in the estimated parameters will prevail. However, for *consistent* estimates the variance will in the limiting process of an infinite amount of data vanish. In the subsequent text we will list some relations governing the bias and random error pertaining to both single sample records and to the *joint* sample records statistical data analysis used in this report including the autospectral density functions (ASDFs), ordinary coherence functions (OCOFs), transfer functions and the multiple coherence functions (MCOFs) and partial coherence functions (PCOFs). The results stem primarily from [1, Ch. 8-9], but are adapted here for the use of a modified periodogram. More advanced readings on the statistics of the intervals in ordinary coherence function estimates can be found in [2–4].

Let φ denote an (arbitrary) parameter. The *normalized* errors considered are then the *normalized bias error* in the estimation of (arbitrary) parameter φ designated by $\epsilon_b(\varphi) \triangleq \frac{\mathrm{E}\,\hat{\boldsymbol{\varphi}}}{\varphi} - 1$, the corresponding *normalized random error* denoted by $\epsilon_\sigma(\varphi) \triangleq \frac{\sqrt{\mathrm{E}\,\hat{\boldsymbol{\varphi}}^2 - \mathrm{E}^2\,\hat{\boldsymbol{\varphi}}}}{\varphi}$, and the *normalized root-mean-square (rms) error* represented by $\epsilon(\varphi) \triangleq \frac{\sqrt{\mathrm{E}(\hat{\boldsymbol{\varphi}}^2 - \boldsymbol{\varphi}^2)}}{\varphi}$.

For most *sampling distributions* the central limit theorem (CLT) can be invoked provided that $K'_{DFT} \gtrapprox 5 - 30$ [6, ch. 7]. Hence, as the effective sample size K'_{DFT} becomes large, the *sampling distribution* of the estimated parameter, say, φ approaches a normal distribution regardless of the distribution of the original variable. In Appendix L on page 773 this result is generalized in the discussion of so-called *stable distributions*. A fundamental consequence of this stability property that is possessed by certain phenomena encountered in various aspects (refer to Appendix L on page 773) is the generalized central limit theorem (GCLT) that states that if the sum of i.i.d. random variables has a limiting shaped distribution as the number approaches infinity, the limiting distribution must be a member of the stable distributions.

Henceforth, the CLT assumption is invoked. The implicit assumption on Gaussian distributed sampling distributions is of profound importance. For example the random error in a variance estimate involves the determination of a fourth order moment for which a relative simple expression is obtainable for the normal distribution. Hence, in general the CLT assumption eases the complexity of the expressions involved considerably. In [1, Ch. 8] an assumption of negligible bias error and a small normalized rms error is invoked. However, with an increasing number of samples this will also be the case provided that the estimator is *unbiased* and *consistent*. In this case the normalized rms error and the normalized random error coincide, that is, $\epsilon_\sigma(\varphi) \approx \epsilon(\varphi)$. Now denoting by n_ϵ the number of standard deviations the *confidence interval* can accordingly be expressed by

$$\hat{\varphi}\frac{1}{1 + n_\epsilon \epsilon(\varphi)} \leq \varphi \leq \hat{\varphi}\frac{1}{1 - n_\epsilon \epsilon(\varphi)}. \tag{C.3.1}$$

For small relative normalized rms error, that is, for $\epsilon \lessapprox 0.1$ the following approximation is valid

$$\hat{\varphi}(1 - n_\epsilon \epsilon(\varphi)) \leq \varphi \leq \hat{\varphi}(1 + n_\epsilon \epsilon(\varphi)) \tag{C.3.2}$$

C.3.1 Autospectral Density Estimate

The bias in ASDF estimate of the random signal $\boldsymbol{\psi}_a$ will be designated by $b\big(\hat{S}_{\psi_a\psi_a}\big)$, and is to a first order approximated by

$$b(\hat{S}_{\psi_a\psi_a}(f)) \approx \frac{\Delta f_{DFT}^2}{24} \frac{\partial^2 S_{\psi_a\psi_a}(f)}{\partial f^2}. \tag{C.3.3}$$

Actually, (C.3.3) holds for rectangular DFT windows to first order irrespective of the probability density function of the auto spectral density function. The bias error will be less for tapered windows (modified periodogram analysis) [6, Ch. 12]. It should be observed that, the bias error is inversely proportional to the squared resolution in the spectrum estimation.

In practice the second-order derivative of the auto spectral density function with frequency is rarely known and should therefore be obtained within the estimation process introducing yet another source of uncertainty.

For sinusoidal signals the auto spectral density function is theoretical a Dirac delta function that takes an infinite value at the corresponding frequency. However, due to the finite spectral resolution capabilities and the finite main lobe width of the windowing function the power will be spread over a number of frequency points that approximately counts Δf_m divided by the spectral resolution Δf_{DFT}. This represent another type of bias error in the auto spectral density function estimates. However, as the ASDF estimate is used further in the join sample record estimates, e.g., cross-spectral density function (CSDF) and OCOF and MCOF, these estimates are therefore also effected by the lack of ability correctly to determine spectral peaks.

The normalized rms error in ASDF estimate denoted by $\epsilon\big(\hat{S}_{\psi_a\psi_a}\big)$, is to a first order approximated by

$$\epsilon\big(\hat{S}_{\psi_a \cdot \psi_a}(f)\big) \approx \frac{1}{\sqrt{K'_{DFT}}}, \tag{C.3.4}$$

which generally holds provided that K'_{DFT} is large and $b(\hat{S}_{\psi_a\psi_a}(f)) \approx 0$.

C.3.2 Ordinary Coherence

The key entry to the joint sample record uncertainty calculations is the OCOF that was defined in subsection 2.2.3 on page 23.

The estimate of ordinary coherence squared function (or just coherence function) between the (arbitrary) random signal $\boldsymbol{\psi}_a$ and the (arbitrary) random signal $\boldsymbol{\psi}_b$ denoted by $\hat{\gamma}^2_{\psi_a\psi_b}$, represents the linear dependence (correlation) between the spectral components of $\boldsymbol{\psi}_a$ and those of $\boldsymbol{\psi}_b$. It is defined from the ASDF estimate of the random signal $\boldsymbol{\psi}_a$ designated by $\hat{S}_{\psi_a\psi_a}$, the ASDF estimate

of the random signal $\boldsymbol{\psi}_b$ denoted by $\hat{S}_{\psi_b\psi_b}$ and the CSDF estimate between the random signal $\boldsymbol{\psi}_a$ and $\boldsymbol{\psi}_b$ represented by $\hat{S}_{\psi_a\psi_b}$

$$\boxed{\hat{\gamma}^2_{\psi_a\psi_b}(f) \approx \frac{|\hat{S}_{\psi_a\psi_b}(f)|^2}{\hat{S}_{\psi_a\psi_a}(f)\hat{S}_{\psi_b\psi_b}(f)}.} \tag{C.3.5}$$

A source to bias error is the somewhat erroneous expression (C.3.5) for the mean of a random variable (RV) divided by the product of two RVs. Another source to bias error in joint estimates is propagation time delays τ between the investigated sensor signals. From [1, Ch. 9] we find that cross-spectral density function, transfer function and ordinary coherence function are underestimated according to

$$\hat{S}_{\psi_a\psi_b}(f) = \Big(1 - \frac{\tau}{T_{DFT}}\Big) S_{\psi_a\psi_b}(f) \tag{C.3.6a}$$

$$\hat{H}_{\psi_a\psi_b}(f) = \Big(1 - \frac{\tau}{T_{DFT}}\Big) H_{\psi_a\psi_b}(f) \tag{C.3.6b}$$

$$\hat{\gamma}^2_{\psi_a\psi_b}(f) = \Big(1 - \frac{\tau}{T_{DFT}}\Big)^2 \gamma^2_{\psi_a\psi_b}(f). \tag{C.3.6c}$$

The normalized rms error in the estimate of ordinary coherence squared function between the random signal $\boldsymbol{\psi}_a$ and the (arbitrary) random signal $\boldsymbol{\psi}_b$ denoted by $\epsilon\big(\hat{\gamma}^2_{\psi_a\psi_b}\big)$, is under the assumption of a underlying Gaussian process approximated by

$$\epsilon\big(\hat{\gamma}^2_{\psi_a\psi_b}(f)\big) \approx \frac{\sqrt{2}\big(1 - \gamma^2_{\psi_a\psi_b}(f)\big)}{|\gamma_{\psi_a\psi_b}(f)|\sqrt{K'_{DFT}}}. \tag{C.3.7}$$

Recalling that in the operational bandwidth of active control (AC) we mostly deal with ordinary coherence functions close to unity as otherwise according to section 2.2 on page 18 the attenuation figures obtainable would be limited. With reference to (C.3.7) the parameters with small normalized errors which in turn substantiates the validity of (C.3.2).

C.3.3 Transfer Functions

Similarly, the normalized rms error in the estimate of the magnitude of the transfer function between the random signal $\boldsymbol{\psi}_a$ and the random signal $\boldsymbol{\psi}_b$ denoted by $\epsilon\big(|\hat{H}_{\psi_a\psi_b}|\big)$, is also under the assumption of a underlying Gaussian process approximated by

$$\epsilon\big(|\hat{H}_{\psi_a\psi_b}|(f)\big) \approx \frac{\sqrt{\big(1 - \gamma^2_{\psi_a\psi_b}(f)\big)}}{|\gamma_{\psi_a\psi_b}(f)|\sqrt{2K'_{DFT}}}, \tag{C.3.8}$$

and the standard deviation random error in the estimate of phase of the transfer function between the random signal $\boldsymbol{\psi}_a$ and the random signal $\boldsymbol{\psi}_b$ denoted by $\sigma\big(\sphericalangle\hat{H}_{\psi_a\psi_b}\big)$, is also under the

assumption of a underlying Gaussian process approximated by

$$\sigma\big(\sphericalangle\hat{H}_{\psi_a\psi_b}(f)\big) \approx \frac{\sqrt{\big(1-\gamma^2_{\psi_a\psi_b}(f)\big)}}{|\gamma_{\psi_a\psi_b}(f)|\sqrt{2K'_{DFT}}}. \tag{C.3.9}$$

C.3.4 Multiple Coherence

The uncertainty assessment pertaining to the MCOF that was defined in subsection 2.2.5 on page 25 can be established in a similar way as above. It should, however, be recalled that during the iterative generation of the conditioned transfer functions lead to a successive decrease of the number of independent observations.

Accordingly, the normalized rms error in the estimate of the multiple magnitude-squared coherence function between the random signal $\boldsymbol{\psi}_a$ and the (arbitrary) random signal set $\boldsymbol{\psi}^C$ denoted by $\epsilon\big(\hat{\gamma}^2_{\psi_a\,\cdot\,\psi^C}\big)$, is under the assumption of a underlying Gaussian process approximated by

$$\epsilon\big(\hat{\gamma}^2_{\psi_a\,\cdot\,\psi^C}(f)\big) \approx \frac{\sqrt{2}\big(1-\gamma^2_{\psi_a\,\cdot\,\psi^C}(f)\big)}{|\gamma_{\psi_a\,\cdot\,\psi^C}(f)|\sqrt{K'_{DFT}-N^C_\psi+1}}. \tag{C.3.10}$$

If the effective number of DFT average K'_{DFT} is too small such that $K'_{DFT} < N^C_\psi$ very unpredictable and most likely unreliable results might be experienced. By not properly appreciating (C.3.10) in a statistical data analysis unity multiple coherence function may erroneously be predicted for $\boldsymbol{\psi}_a$ completely uncorrelated with $\boldsymbol{\psi}^C$.

C.3.5 Partial Coherence

The PCOF was defined in subsection 2.2.5 viz. (2.2.28) on page 28. The expression for the normalized rms error in the estimate of the partial coherence function of the random signal $\boldsymbol{\psi}_a$, the random signal $\boldsymbol{\psi}_b$ and the (arbitrary) random signal set $\boldsymbol{\psi}^C$ denoted by $\epsilon\big(\hat{\gamma}^2_{\psi_a\psi_b\perp\psi^C}\big)$, is similarly obtained from

$$\epsilon\big(\hat{\gamma}^2_{\psi_a\psi_b\perp\psi^C}(f)\big) \approx \frac{\sqrt{2}\big(1-\gamma^2_{\psi_a\psi_b\perp\psi^C}(f)\big)}{|\gamma_{\psi_a\psi_b\perp\psi^C}(f)|\sqrt{K'_{DFT}-N^C_\psi+1}}. \tag{C.3.11}$$

The same consideration concerning an insufficient number of independent samples made for the multiple coherence function apply also here.

C.4 Summary

Following the general guidelines for the modified periodogram method in section C.2 it should then be verified that the bias errors really are negligible. If this is not the case, it should be investigated if some remedy to these bias problems exists. For example, negative bias in the ordinary coherence function and transfer function estimate due to propagation delays could potentially be compensated for by appropriate time alignment of the joint sample records involved.

If however, bias errors still prevail then the results in section C.3 are not correct anymore as the underlying assumptions made are not valid. In such cases more advanced analysis methods are required. Otherwise, confidence intervals pertaining to the different parameters investigated in section C.3 can be obtained from applying (C.3.7), (C.3.8), (C.3.9) and (C.3.10) to (C.3.2) for the specified choice of the value of n_ϵ.

Actually these expressions pertain to the use of unknown true values of the desired quantities. However, assuming fairly accurate estimates we may replace the unknown values by estimated values on the RHS of the expressions, that is, $\gamma^2_{\psi_a\psi_b} \leftarrow \hat{\gamma}^2_{\psi_a\psi_b}$, $\gamma^2_{\psi_a \cdot \psi^C} \leftarrow \hat{\gamma}^2_{\psi_a \cdot \psi^C}$ and $\gamma^2_{\psi_a\psi_b \perp \psi^C} \leftarrow \hat{\gamma}^2_{\psi_a\psi_b \perp \psi^C}$.

Bibliography

[1] Julius S. Bendat and Allan G. Piersol. *Random data Analysis and measurement procedures.* John Wiley & Sons, Inc., 3rd edition, 2000.

[2] Vernon A. Benignus. Estimation of the coherence spectrum and its confidence interval using the fast fourier transform. *IEEE Transactions on Audio and Electroacoustics*, 17(2):145–149, 1969.

[3] G. Cliford Carter, Charles H. Knapp, and Albert H. Nuttall. Estimation of the magnitude-squared coherence function via overlapped fast fourier transform processing. *IEEE Transactions on Audio and Electroacoustics*, 21(4):337–344, 1973.

[4] G. Cliford Carter, Charles H. Knapp, and Albert H. Nuttall. Statistics of the estimate of the magnitude-coherence function. *IEEE Transactions on Audio and Electroacoustics*, 21(4): 388–389, 1973.

[5] Alan V. Oppenheim and Ronald W. Schafer. *Discrete-Time Signal Processing.* Prentice Hall International Inc., 2nd edition, 1999.

[6] Athanasios Papoulis and S. Unnikrishna Pillai. *Probability, Random Variables and Stochastic Processes.* McGraw-Hill, New York, 4th edition, 2002.

[7] P. D. Welch. The use of fast fourier transform for the estimation of power spectra: A method based on time averaging over short, modified periodigrams. *IEEE Transactions on Audio and Electroacoustics*, AU-15:70–73, 1967.

D. ANALYSIS OF NOISE RECORDINGS

D.1 Objectives

The Terma active noise reduction (ANR)-system has initially been tailored to military personnel and in particular aircraft pilots. This type of military staff often operates in an environment where high sound pressure levels are experienced. Unfortunately, the availability of noise recordings from the pertinent platforms, however, is rather limited. Moreover, existing measurement only quantitatively describes the operational environment in which the ANR-system should work. In the published literature only a few accounts of ANR related helicopter measurement can be found [4, 5]. Previous measurements conducted by the Danish Rigshospitalet in various Danish military aircrafts and helicopters, however, to a large extent supported the identification of flight scenarios [6]. Accordingly, it has therefore been considered important to identify the noise picture more qualitatively with the overall objective of better facilitating the synthesis of the ANR helmet design leading to an improved performance. Hence, a number of noise recordings in various military platforms was conducted during the course of the project. Some of these noise recordings were supplemented with practical ANR tests.

Before each flight test extensive tests in the laboratory but also in cars were carried out in order to be fully prepared for the on-site measurements in the airborne military platforms involved. During the phases of flight test a lot of experience was gained in the field acoustical measurement in a military environment. This experience largely complemented our experience in avionics engineering (electrical/mechanical) acquired over the past twenty years.

A description of the test suite used to perform recordings and a general description of the test philosophy is provided in [7].

D.1.1 Appendix Outline

Following this introduction a description of the customization of the Gentex HGU-55/P helmets is provided in section D.2. These helmets are used both for the F-16/B and the CH-47D Chinook recordings presented in this Appendix. Next the theme of section D.3 is noise recordings made in an F-16/B Fighting Falcon cockpit. This section contains information regarding the planned flight scenarios, installation of the measurement equipment in the F-16/B Cockpit and the applied strategy for data acquisition and processing. Moreover, the results from a statistical data analysis (SDA) applied to one of the defined noise scenarios are presented. Finally, the results from noise recordings made in a CH-47D Chinook are presented in section D.4.

D.2 Preparation of Helmets

The Gentex HGU-55/P helmet is an advanced lightweight fighter/attack helmet that is used Worldwide by fighter pilots and also by the Danish F-16 pilots. Some description of the helmet and the assembling procedure is considered relevant as the passive noise attenuation is provided by the helmet system. In Part IV the vibro acoustical properties of a helmet fitted to a human is modeled.

The helmet shell is a rigid composite, pressure molded using graphite and aramid fibers (Graphid®). The assembling of the helmets is carried out at the SUN workshop at the airbase Skrydstup shown in Figure D.1 and Figure D.2.

Fig. D.1: SUN Workshop Airbase Skrydstrup, © Leth Data & Foto, 2003

Each helmet is individually customized for the pilot. First a medium, large or X-large shell that suits the pilot's head best is selected. A soft leather edgeroll covers an open cell foam core around the entire periphery of the shell. Visor buffers and bump stops are cemented (from the factory) to the shell to provide for stowing of the visor and protect the shell surface during visor operation. The inner layer is an energy absorbing liner that has nominal thickness of 0.5 inch. This primary impact energy absorbing medium is provided from expanded polystyrene beads, pressure molded to match the dimensions of the shell.

The custom fitting is primary provided by the light weight Thermoplastic Liner (TPL). It incorporates a removable, launderable cover. Gentex delivers the TPL preformed from the factory to a nominal headform in each helmet size. However, in order to obtained optimal fit the SUN workshop at the airbase makes the moulding themselves as illustrated in Figure D.3.

Following the moulding process the headset is assembled. The Gentex HGU-55/P helmet assembly is normally equipped with an H-154A/AIC headset which provides communications of

Fig. D.2: SUN workshop assembling of Helmets, © Leth Data & Foto, 2003

high intelligibility under extreme noise conditions. The headset assembly typically consist of the following components:

- MX-8376/AR earcup assemblies which include noise attenuating ABS plastic shell, earphone holders, and earseals.
- H-143/AIC earphones having frequency response of $100 - 5500$ Hz and 19 Ω impedance.
- CX-4708A/AIC four conductor cord assembly terminated at branched ends with pin type terminals and modified at the other end with a U-179/U connector.

The lightweight Oxygen mask of suitable size is selected and fitted to the pilot by the chin/-nape assemblies. Finally, the integrated chin/nape assemblies and the lightweight Oxygen mask receiver kit is mounted on the helmet. The chin/nape strap provide a comfortable fit ensuring helmet stability and retention.

D.2.1 Background

Noise measurements in an F-16 cockpit are notoriously very expensive and associated with a lot of difficulties and instrumentation efforts. Approximately 1 month was spent on the preparation of the equipment, flight scenarios definition and the practical conduction of the first single F-16/B[1] flight measurement data acquisition.

[1] The B version of the F-16 is twin-seated and the measurement equipment could therefore be installed on the back seat without any annoyance of the pilot.

Fig. D.3: Customization of HGU 55/P Gentex Helmet, © Leth Data & Foto, 2003

The Danish Tactical Air Command (DTAC) is interested in the progress of the Terma ANR programme. DTAC therefore has been willing to assign an F-16/B flight time, a test pilot and other manpower necessary for the instrumentation of the cockpit and the subsequent practical acquisition of the noise recordings.

The objective of the noise recordings is to measure the noise levels inside the cockpit and also the residual noise at the pilot's ear following the passive attenuation provided by the helmet. Hence, a real-time estimate of the attenuation provided by the helmet with embedded ANR is obtained. The flight tests were thoroughly planned jointly by the DTAC pilots and Terma. Preferably, a flight test should cover the majority of the various noise scenarios experienced by the pilots.

Prior to each installation a discussions with the and pertinent military personnel was initiated. The objective of the measurements, the installation of the measurement equipment was identified. An officer responsible for the flight should approved the installation before flight test could commence.

D.2.2 Flight Scenarios

In order to assess the dynamic span of the noise experienced in a F-16/B various flight scenarios were planned. Therefore test pilot (PEL) and former F-16 pilot Ole Kjølberg Træholt (KOL) were interviewed regarding the circumstances that based on their experiences would lead to subjective changes in the perceived noise characteristics. Moreover a previous data recording acquired in 1998 by Rigshospitalet was carefully examined together with KOL. Therefore 13 different flight scenarios could be identified and planned for a test flight of 70 min duration.

When installing equipment in a military platform safety of flight (SOF) will always be an issue. Therefore, the equipment was analyzed with respect to the environmental capabilities.

Altitude test in altitude chamber has been conducted it was decided that the equipment should not be flown at altitudes above 10000 feet. This requirement stems from the decompression considerations.

Moreover, it was decided to minimize the time at which the equipment would be exposed to ambient temperatures outside the operational temperature range, $0 - 40\,^{\circ}\mathrm{C}$. Finally, also for SOF considerations Terma recommended that the flight envelope was kept within 0 to 3 G′s.

D.2.3 Measurement Equipment

The measurement equipment included a BK 4128 C HATS, BK PULSE unit, Sony PC208A DAT, Dell Latitude D 800 laptop and two BK 1/2"4192-C pressure field condenser microphones each positioned in a BK 1/2" UA 1317 microphone holder on each side of the mannequin is illuminated in Figure D.4. The BK PULSE units and the digital audio tape (DAT) recorder were battery powered from rechargeable nickel-metal hybrid batteries[2]. In order to support the measurement gear a frame was customized. The following software (SW) modules were used during the test: BK 7707 Unlimited Analysis Engine, 7701 Harddisc Recorder, 7705 Time Capture.

The noise equipment installed in the F-16/B can be seen in Figure D.4.

The head and torso simulator (HATS) is a mannequin with built-in ear and mouth simulators that provides a realistic reproduction of the acoustic properties of an average adult human. The HATS

[2]The battery capacity is assessed to approximately 1.5 h operation.

Fig. D.4: Noise Recording Equipment, © Leth Data & Foto, 2003

is therefore often used in connection with electroacoustics test on, for example telephone handset, headset, microphones, headphones and hearing aids. However, in test of hearing protection devices (HPDs) some limitations, however, are encountered. In particular the low-frequency attenuation capabilities of a HPD are therefore often largely overestimated. In Part IV the vibro acoustical properties in general is compared with the similar acoustical properties of humans.

The BK 4128 C HATS is equipped with a BK 4158 C right ear simulator and a BK 4159 C left ear simulator. During the test the HATS wore a cotton waistcoat and a pilot torsoharness.

Provision for 6 simultaneous measurement channels was made from a BK PULSE portable data acquisition units. The BK PULSE unit was connected to a Dell Latitude D 800 1.7 GHz laptop equipped with 2048 MB RAM, 1 GB solid-state HDD and a 2 GB flash memory module. The portable PULSE system was configured by BK (Power Supply Type 2827, LAN Interface Type 7533, 6/1 Channel I/O module Type 3032A).

D.3 F-16/B Fighting Falcon Noise Recordings

D.3.1 Installation in F-16/B Cockpit

Figure D.5 - D.10 illustrate the final installation of the measurement equipment.

Fig. D.5: Installation in Hangar Airbase Skrydstrup, © Leth Data & Foto, 2003

Fig. D.6: Flight Captain PEL Informed by Torsten Leth Elmkjær, © Leth Data & Foto, 2003

Fig. D.7: HATS Installed in F-16/B Airbase Skrydstrup, © Leth Data & Foto, 2003

D.3.2 Data Acquisition and Processing

Data Acquisition

Prior to the measurement each of the four BK 1/2" 4192-C pressure field condenser microphones were calibrated with a BK 4231 sound pressure calibrator. This calibration procedure was repeated shortly after the flight test. The deviation between pre flight and post flight measurements were all within fractions of a dB and therefore within the measurement accuracy.

Data Qualification

Most data interpretation methods applies only to data that can be qualified as *stationary Gaussian* random data. In the data qualification phase we therefore first validate if the data have a Gaussian density function by examining if the measurement exhibit nonstationarity characteristics, periodic components, and non-Gaussian properties.

Test for Stationarity

Firstly, as discussed in subsection D.2.2 the test flight should span a set of scenarios that expectably will lead to different noise pictures. During each of the specified test points all parameters should at least in theory be frozen. This goal, however, is hardly achievable as in avionics there are many parameter outside the control of the testpilot and engineers that might influence the properties of noise being recorded. It was anticipated that changes in the aircraft

altitude or airspeed will lead to nonstationarities in the acquired data. Therefore, a inter-scenario stationarity assessment and intra-scenario analysis for each of the scenarios has been conducted.

Data Validation

In a subjective test pilot (PEL) and former F-16 pilot Ole Kjølberg Træholt (KOL) have been listening to reproduction of the recorded data. These experienced pilots found not remarks to the validity of the data. Moreover, the spurious 4.8 kHz signal was confirmed to be related to the environmental control system (ECS).

In order to prevent signal clipping the autorange procedure provided by the PULSE system was invoked. Moreover, a safety margin of additional 10 dB was applied. Therefore the dynamic range of PULSE was set to 10 dB - 16 bit. As a consequence no signal clipping was observed or indicated by PULSE. Moreover, the noise level was also substantially greater than the noise floor of the data acquisition systems.

Fig. D.8: Check of F-16/B setup by Jakob Krogh Sørensen, © Leth Data & Foto, 2003

D.3.3 Measurement Analysis

Approximately 1 GB of data was acquired during the flight. The stored data was then analyzed afterwards. The analysis is based on [1–3].

In Figure D.11 the setup used during on-site analysis phase is shown.

The recordings were subsequently converted to MATLAB®- and Wave-format. The former format was used for in-depth analysis and for synthesis of the Terma ANR headset. The WAVE-format

Fig. D.9: Final inspection of F-16/B setup by Torsten Leth Elmkjær, © Leth Data & Foto, 2003

Fig. D.10: Flight Captain PEL Ready for take-off, © Leth Data & Foto, 2003

Fig. D.11: Noise Recordings Analysis Setup, © Leth Data & Foto, 2003

was used for replay in the Terma noise chamber (TNC) facilities.

Topology

In the topology depicted in Figure D.4 we will consider the two microphones that are positioned outside the left and right ear as reference sensor x_1 and x_2 respectively. The two auxiliary microphones shown in Figure D.5 and Figure D.7 constitute reference sensor x_3 and x_4 respectively. Hence, the number of reference sensors amounts to $N_x = 4$. The left and right ear simulators of the HATS are the performance sensors that henceforth denoted by d_1^p and d_2^p respectively, that is, $N_p = 2$. At the time of measurements the Terma Earcup Audio System was yet developed and no disturbance signal was acquired, that is, $N_e = 0$.

D.3.4 Scenario at 85% Power

In the first scenario presented the aircraft is operated at 85% power. Accordingly, relative medium sound pressure levels are expectable. The parameters governed the periodogram spectra estimate can be found in the figure captions. The results over the period from 0 s to 30 s are presented next.

Statistical Data Analysis

The analysis of the underlying statistical behavior of the data is interesting in it own. Moreover, the specific behavior can have a profound influence on the optimum choice of adaptive filtering

algorithms. In particular it is important to verify if the data complies with an assumption of Gaussianity.

In Simulation D.3.1 - D.3.4 on pages 560–563 the probability density functions (pdfs) of four different signals representing the most extreme characteristics, namely $p_{x_1}(p), p_{x_3}(p), p_{x_4}(p), p_{d_1^p}(p)$ are shown. As readily observed some deviance from zero-mean Gaussian distribution prevails. Moreover, among the sensor signals some variation of the pdfs are experienced. Also some skewness is observed in all the records. In order further to analyze this behavior the software package STABLE from Robust Analysis, Inc. was used for the estimation of the stable parameters $\mathcal{S}(\alpha, \beta, \gamma, \delta)$ defined in Appendix L on page 773 using the maximum likelihood estimation (MLE). The results can be found in Table D.1

Signal	x_1	x_2	x_3	x_4	d_1^p	d_2^p
α	2.00	1.85	1.90	2.00	1.58	1.57
β	0.42	0.86	1.00	0.99	0.30	0.30
γ	0.25	0.20	0.23	0.26	0.09	0.10
δ	-3.37	-2.53	-3.13	-3.84	-0.32	-0.36
$\pm 3\epsilon_\alpha$	0	0.00	0	0	0.01	0.01
$\pm 3\epsilon_\beta$	0	0.03	0	0	0.02	0.02
$\pm 3\epsilon_\gamma$	0	0.00	0	0	0.00	0.00
$\pm 3\epsilon_\delta$	0	0.00	0	0	0.00	0.00

Tab. D.1: F-16/B Scenario where the aircraft is operated at 85% power. Stable parameters γ, δ re. 20 µPa.

As is well known uncertainty values do not make sense when a parameter is at the boundary of the parameter space, e.g., $\alpha \lessapprox 2$ and is therefore set to 0 in such cases. Hence, except for the performance signal the index of stability α is relative close to 2, but the skewness parameter β takes large values that confirms the assumption of non Gaussian distributed signals. However, owing to the lack of contents in the tails of the probability density functions nor do stable distributions fit very well to the data.

The auto spectral density functions are shown in Simulation D.3.5 on page 564.

A pulsating ECS is responsible for the generation of a time-varying and extremely low-frequency 0.8 Hz signal exceeding 140 dB re 20 µPa. From 10 Hz to 800 Hz the exterior spectra exhibit white noise characteristics. Above 800 Hz the pattern is more like brown noise with a decay rate of 20 dB per decade superposed by many periodic signals. The corresponding averaged and maximum sound pressure levels can be found in Simulation D.3.4.

Ch.	# 1	#2	#3	#4	#5	#6
SPL	142.0	141.0	142.9	140.4	139.2	139.3

Tab. D.2: F-16/B Scenario at 85% Power, sound pressure levels re. 20 µPa.

The ordinary coherence functions (OCOFs) $\gamma^2_{d_1^p \cdot x_1}, \gamma^2_{d_1^p \cdot x_2}, \gamma^2_{d_1^p \cdot x_3}, \gamma^2_{d_1^p \cdot x_4}, \gamma^2_{d_2^p \cdot x_1}, \gamma^2_{d_2^p \cdot x_2}, \gamma^2_{d_2^p \cdot x_3}$ and $\gamma^2_{d_2^p \cdot x_4}$ and related achievable attenuation estimated from (2.2.1) on page 18 are depicted in Simulation D.3.6 on page 565 and Simulation D.3.7 on page 566 respectively.

Accordingly, from a feedforward system (FFS) based active control (AC) there is very little perspective in using a single reference sensor at the any of the four exterior positions shown in Figure D.4. Hence, OCOF already becomes a problem at 10 Hz.

The magnitude and phase of the transfer functions from the first reference sensor to the first

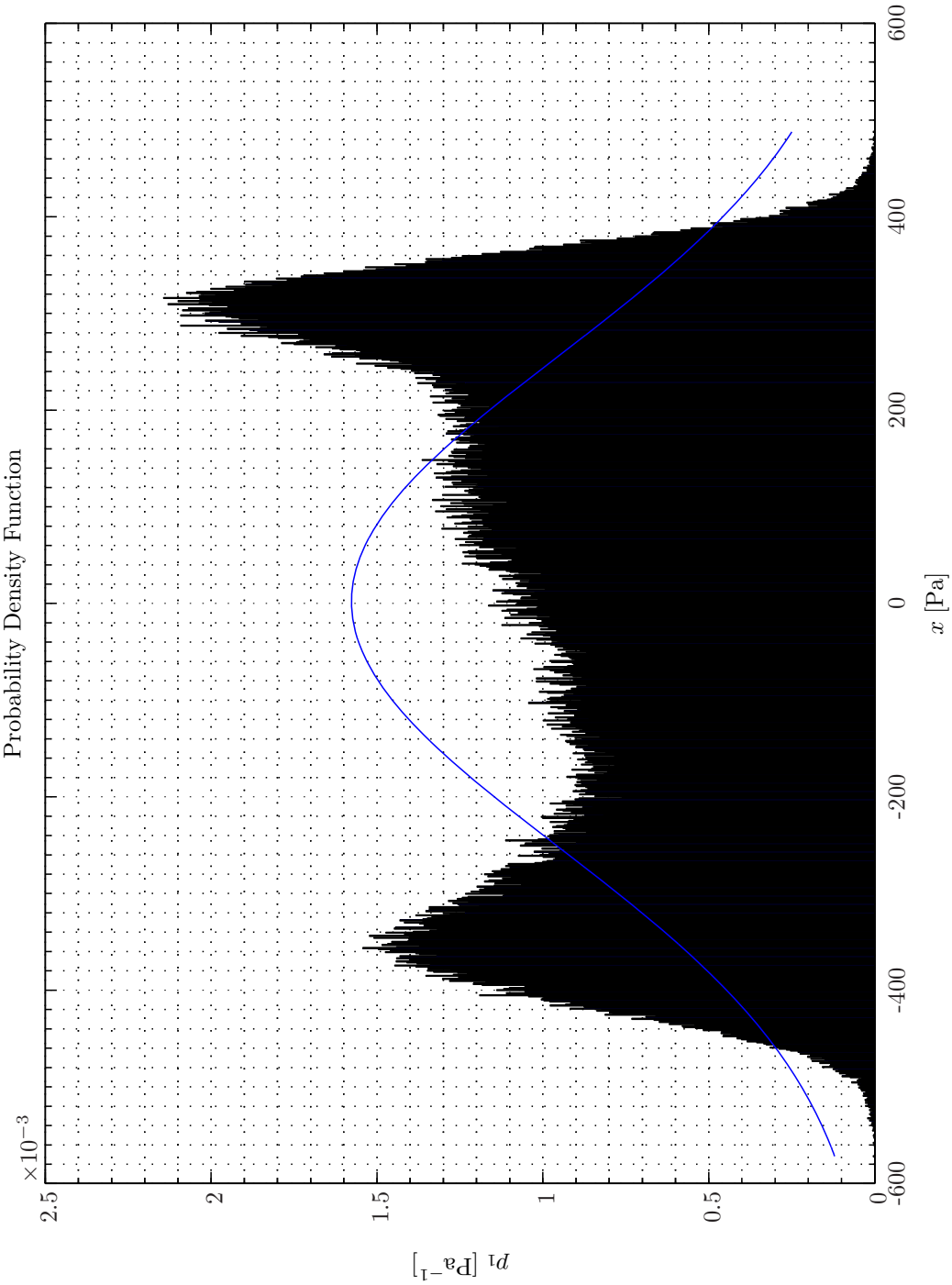

Sim D.3.1: *Probability Density Functions*: **Statistical Data Analysis**: Single-Sided Modified Periodogram, $f_s = 16.384$ kHz, $N_{DFT} = 4096$, $L_{DFT} = 4097$, $R_{DFT} = 2049$, Hanning, $\Delta f_m = 16$ Hz, $T_{DFT} = 0.25006$ s, $N_{f,DFT} = 2049$, $\Delta f_{DFT} = 4$ Hz, $K_{DFT} = 238$; F-16 Recordings Airbase Skrydstrup 20 marts 2003, Channel 1 2 3 4 5 6, Scenario 1, $0 - 30$ s ($f_s = 16.384$ kHz, $N_{A/D} = 16$); **Topology:** Gentex HGU-55/P helmet mounted on a BK 4128 C HATS (Feedforward, mFx, $N_x = 4, N_e = 2, N_y = 2, N_p = 2$); *Channels:* $\#1 \leftarrow x_1$, $\#2 \leftarrow x_2$, $\#3 \leftarrow x_3$, $\#4 \leftarrow x_4$, $\#5 \leftarrow d_1^p$, $\#6 \leftarrow d_2^p$; **Scenario:** F16RecordingSignalAnalysis/20080110T011214.

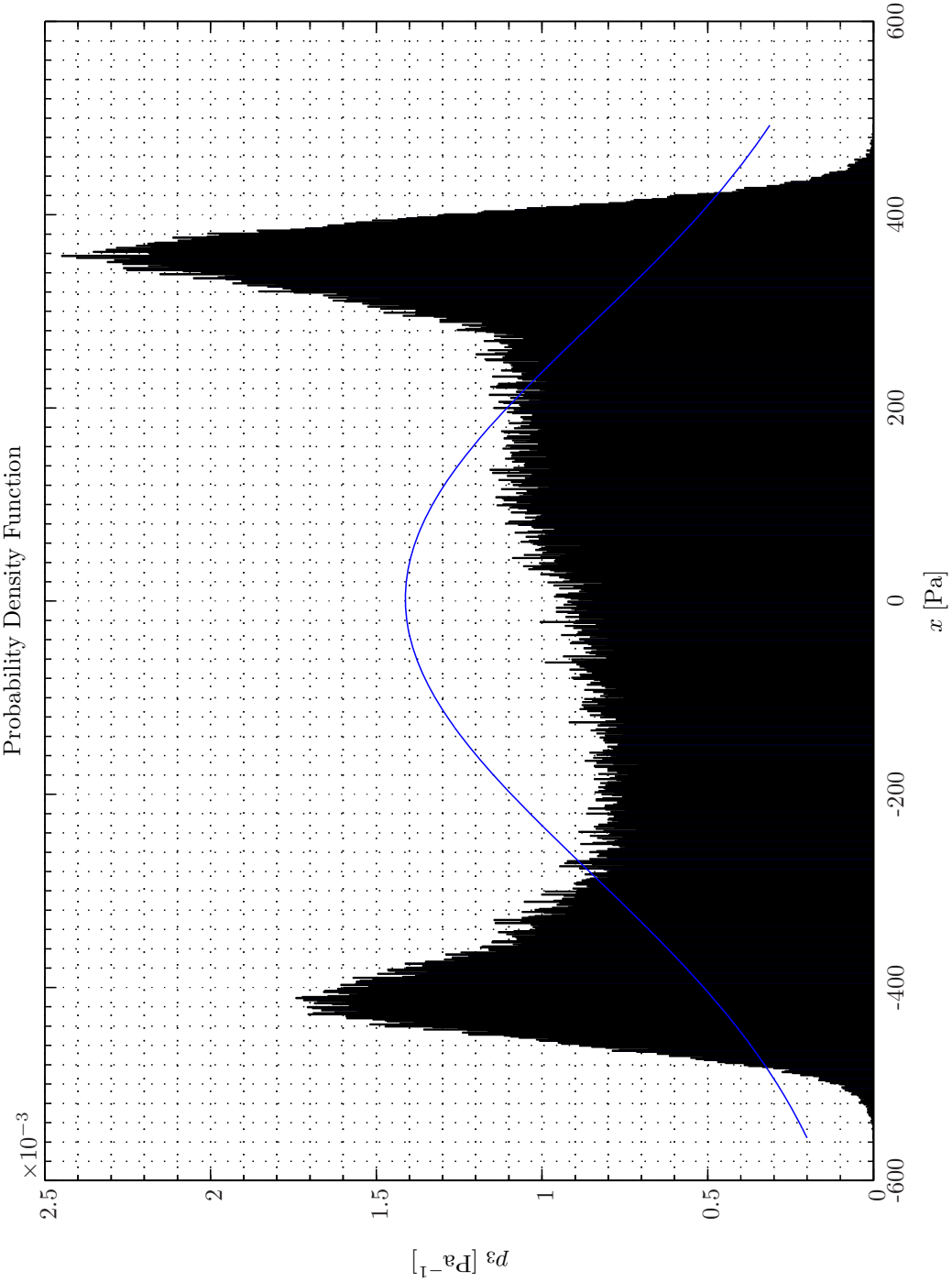

Sim D.3.2: *Probability Density Functions*: **Statistical Data Analysis**: Single-Sided Modified Periodogram, $f_s = 16.384$ kHz, $N_{DFT} = 4096$, $L_{DFT} = 4097$, $R_{DFT} = 2049$, Hanning, $\Delta f_m = 16$ Hz, $T_{DFT} = 0.25006$ s, $N_{f,DFT} = 2049$, $\Delta f_{DFT} = 4$ Hz, $K_{DFT} = 238$; F-16 Recordings Airbase Skrydstrup 20 marts 2003, Channel 1 2 3 4 5 6, Scenario 1, 0 − 30 s ($f_s = 16.384$ kHz, $N_{A/D} = 16$); **Topology:** Gentex HGU-55/P helmet mounted on a BK 4128 C HATS (Feedforward, mFx, $N_x = 4$, $N_e = 2$, $N_y = 2$, $N_p = 2$); *Channels:* #1 $\leftarrow x_1$, #2 $\leftarrow x_2$, #3 $\leftarrow x_3$, #4 $\leftarrow x_4$, #5 $\leftarrow d_1^p$, #6 $\leftarrow d_2^p$; **Scenario:** F16RecordingSignalAnalysis/20080110T011214.

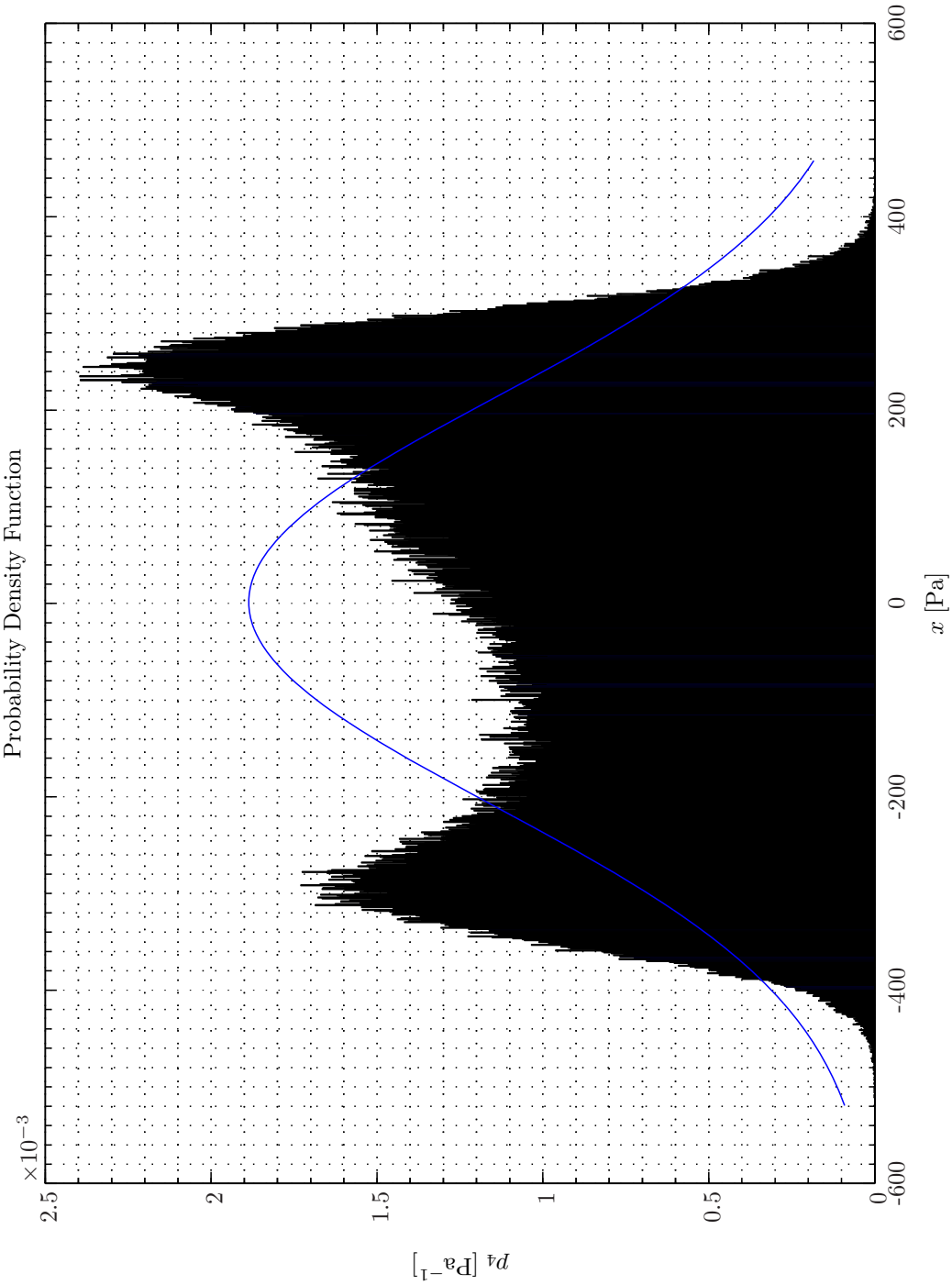

Sim D.3.3: *Probability Density Functions*: **Statistical Data Analysis**: Single-Sided Modified Periodogram, $f_s = 16.384$ kHz, $N_{DFT} = 4096$, $L_{DFT} = 4097$, $R_{DFT} = 2049$, Hanning, $\Delta f_m = 16$ Hz, $T_{DFT} = 0.25006$ s, $N_{f,DFT} = 2049$, $\Delta f_{DFT} = 4$ Hz, $K_{DFT} = 238$; F-16 Recordings Airbase Skrydstrup 20 marts 2003, Channel 1 2 3 4 5 6, Scenario 1, $0 - 30$ s ($f_s = 16.384$ kHz, $N_{A/D} = 16$); **Topology:** Gentex HGU-55/P helmet mounted on a BK 4128 C HATS (Feedforward, mFx, $N_x = 4$, $N_e = 2$, $N_y = 2$, $N_p = 2$); *Channels:* $\#1 \leftarrow x_1$, $\#2 \leftarrow x_2$, $\#3 \leftarrow x_3$, $\#4 \leftarrow x_4$, $\#5 \leftarrow d_1^p$, $\#6 \leftarrow d_2^p$; **Scenario:** F16RecordingSignalAnalysis/20080110T011214.

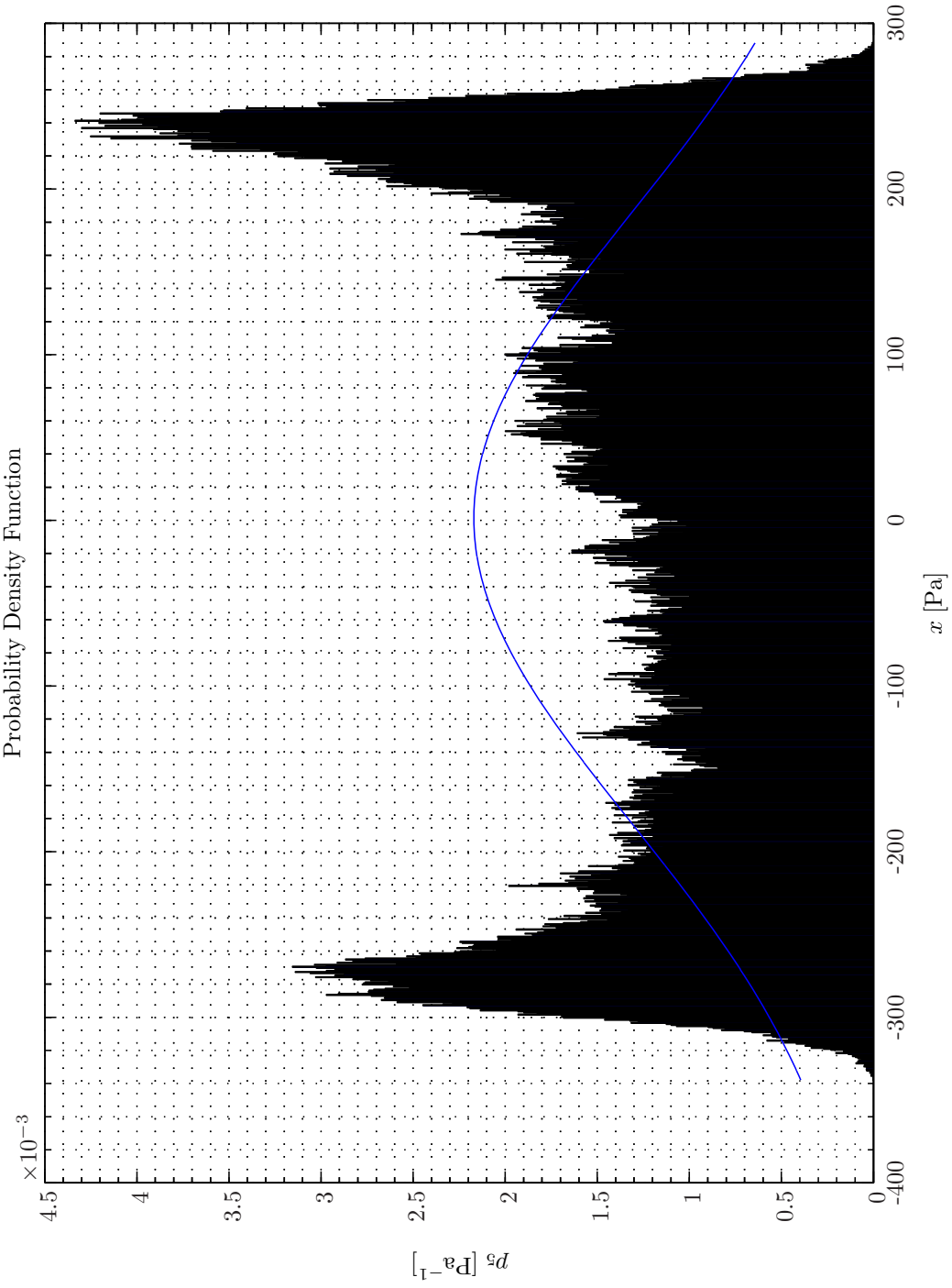

Sim D.3.4: *Probability Density Functions*: **Statistical Data Analysis**: Single-Sided Modified Periodogram, $f_s = 16.384$ kHz, $N_{DFT} = 4096$, $L_{DFT} = 4097$, $R_{DFT} = 2049$, Hanning, $\Delta f_m = 16$ Hz, $T_{DFT} = 0.25006$ s, $N_{f,DFT} = 2049$, $\Delta f_{DFT} = 4$ Hz, $K_{DFT} = 238$; F-16 Recordings Airbase Skrydstrup 20 marts 2003, Channel 1 2 3 4 5 6, Scenario 1, 0 − 30 s ($f_s = 16.384$ kHz, $N_{A/D} = 16$); **Topology:** Gentex HGU-55/P helmet mounted on a BK 4128 C HATS (Feedforward, mFx, $N_x = 4$, $N_e = 2$, $N_y = 2$, $N_p = 2$); *Channels:* $\#1 \leftarrow x_1$, $\#2 \leftarrow x_2$, $\#3 \leftarrow x_3$, $\#4 \leftarrow x_4$, $\#5 \leftarrow d_1^p$, $\#6 \leftarrow d_2^p$; **Scenario:** F16RecordingSignalAnalysis/20080110T011214.

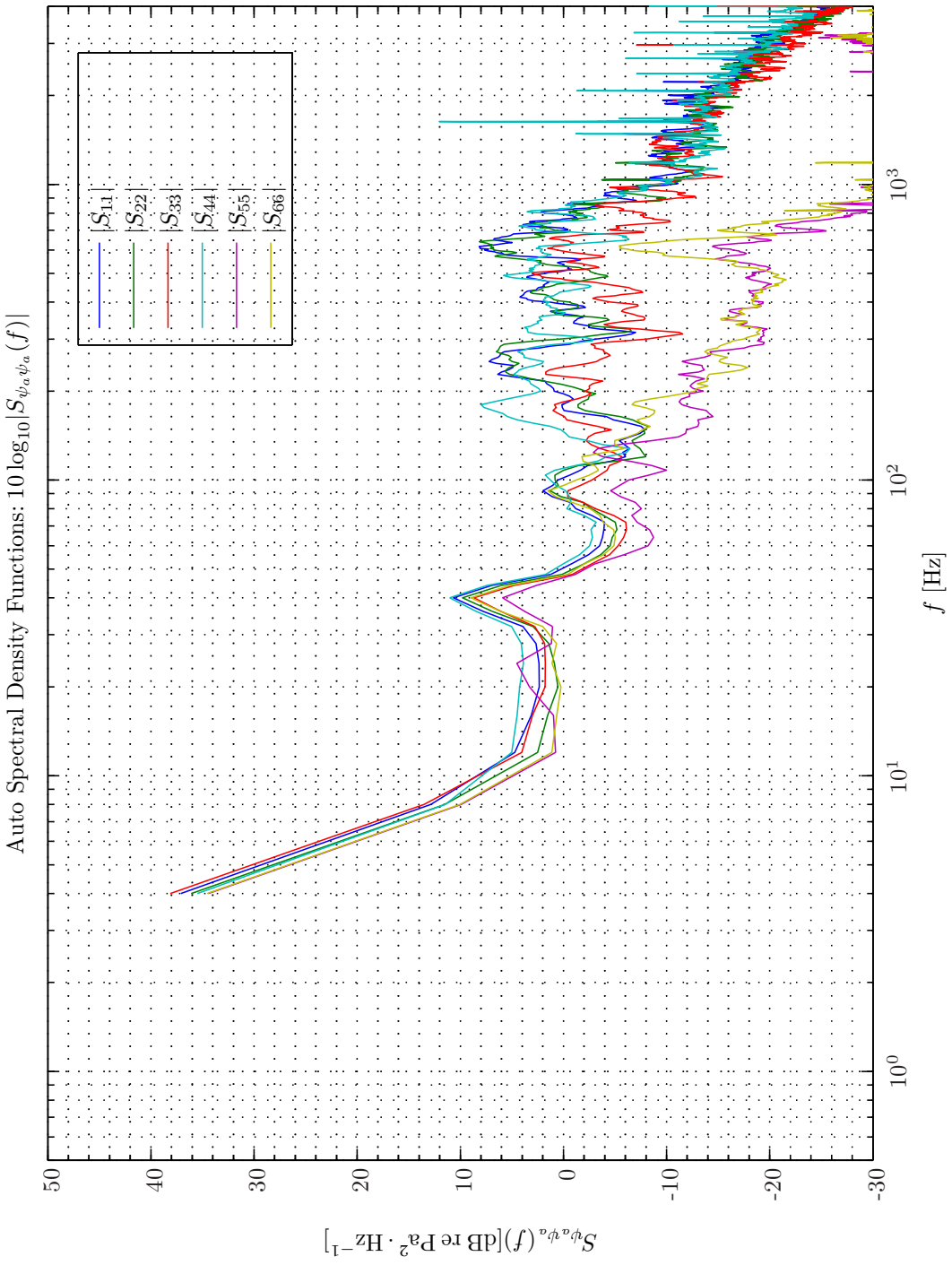

Sim D.3.5: *Autospectral Density Functions:* **Statistical Data Analysis:** Single-Sided Modified Periodogram, $f_s = 16.384$ kHz, $N_{DFT} = 4096$, $L_{DFT} = 4097$, $R_{DFT} = 2049$, Hanning, $\Delta f_m = 16$ Hz, $T_{DFT} = 0.25006$ s, $N_{f,DFT} = 2049$, $\Delta f_{DFT} = 4$ Hz, $K_{DFT} = 238$; F-16 Recordings Airbase Skrydstrup 20 marts 2003, Channel 1 2 3 4 5 6, Scenario 1, $0 - 30$ s ($f_s = 16.384$ kHz, $N_{A/D} = 16$); **Topology:** Gentex HGU-55/P helmet mounted on a BK 4128 C HATS (Feedforward, mFx, $N_x = 4$, $N_e = 2$, $N_y = 2$, $N_p = 2$); *Channels:* #1 $\leftarrow x_1$, #2 $\leftarrow x_2$, #3 $\leftarrow x_3$, #4 $\leftarrow x_4$, #5 $\leftarrow d_1^p$, #6 $\leftarrow d_2^p$; **Scenario:** F16RecordingSignalAnalysis/20080110T011214.

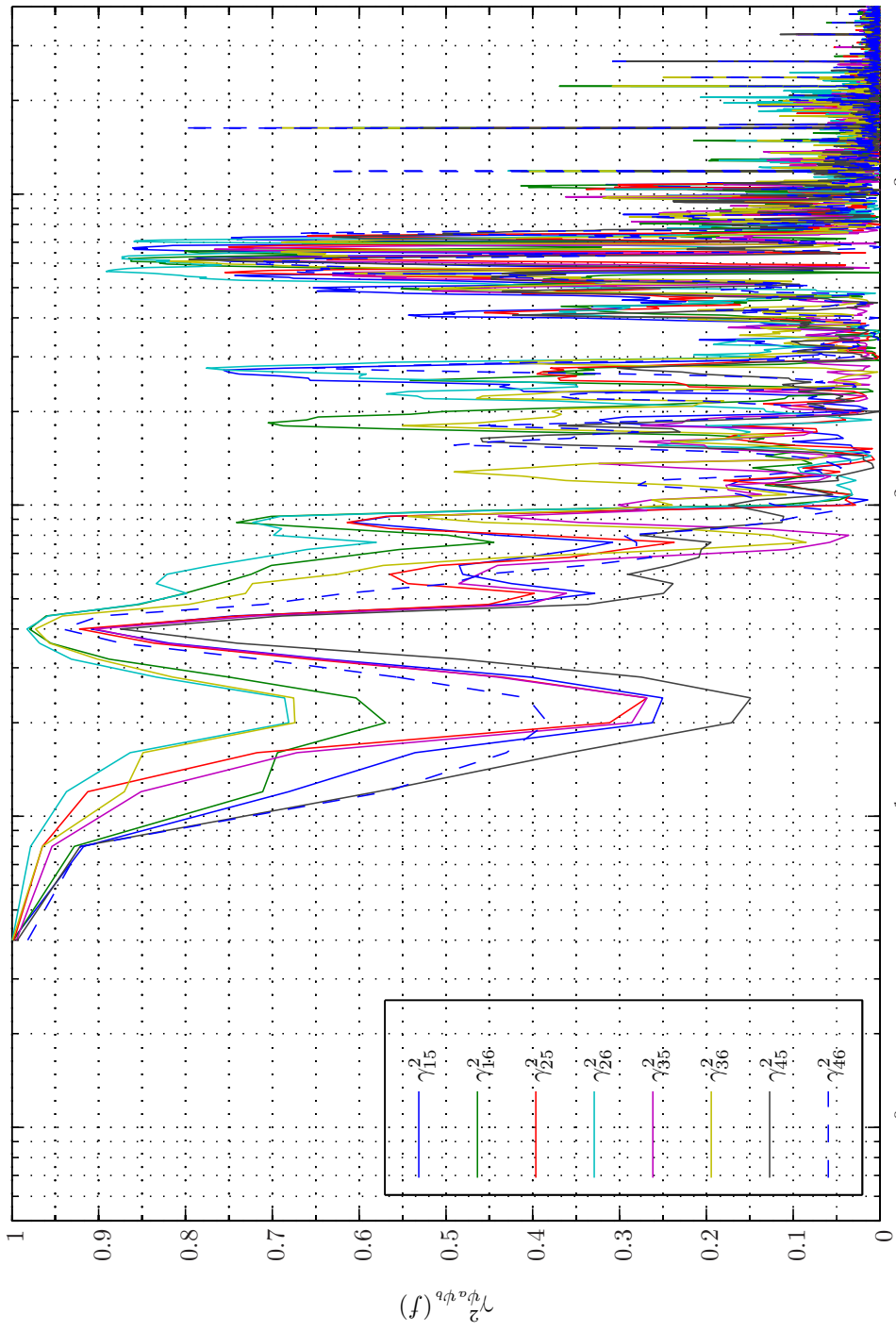

Sim D.3.6: *Ordinary Coherency-Squared Functions* $\gamma^2_{\psi_a\psi_b}(f)$: **Statistical Data Analysis**: Single-Sided Modified Periodogram, $f_s = 16.384$ kHz, $N_{DFT} = 4096$, $L_{DFT} = 4097$, $R_{DFT} = 2049$, Hanning, $\Delta f_m = 16$ Hz, $T_{DFT} = 0.25006$ s, $N_{f,DFT} = 2049$, $\Delta f_{DFT} = 4$ Hz, $K_{DFT} = 238$; F-16 Recordings Airbase Skrydstrup 20 marts 2003, Channel 1 2 3 4 5 6, Scenario 1, $0 - 30$ s ($f_s = 16.384$ kHz, $N_{A/D} = 16$); **Topology:** Gentex HGU-55/P helmet mounted on a BK 4128 C HATS (Feedforward, mFx, $N_x = 4, N_e = 2, N_y = 2, N_p = 2$); *Channels:* #1 $\leftarrow x_1$, #2 $\leftarrow x_2$, #3 $\leftarrow x_3$, #4 $\leftarrow x_4$, #5 $\leftarrow d_1^p$, #6 $\leftarrow d_2^p$; **Scenario:** F16RecordingSignalAnalysis/20080110T011214.

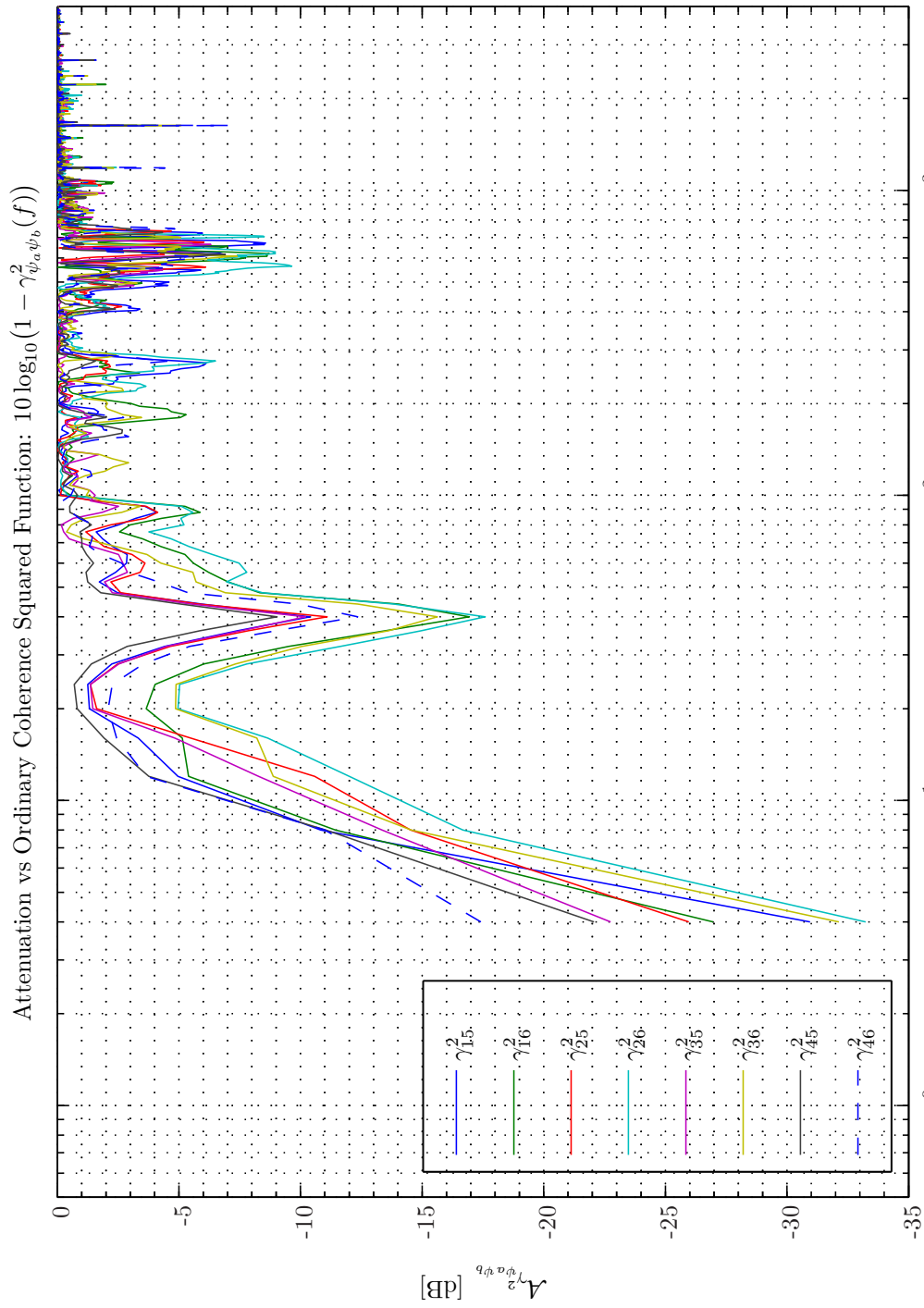

Sim D.3.7: Attenuation *vs Ordinary Coherency-Squared Functions*: $10\log_{10}(1-\gamma^2_{\psi_a\psi_b}(f))$: **Statistical Data Analysis**: Single-Sided Modified Periodogram, f_s = 16.384 kHz, N_{DFT} = 4096, L_{DFT} = 4097, R_{DFT} = 2049, Hanning, Δf_m = 16 Hz, T_{DFT} = 0.25006 s, $N_{f,DFT}$ = 2049, Δf_{DFT} = 4 Hz, K_{DFT} = 238; F-16 Recordings Airbase Skrydstrup 20 marts 2003, Channel 1 2 3 4 5 6, Scenario 1, 0 − 30 s (f_s = 16.384 kHz, $N_{A/D}$ = 16); **Topology:** Gentex HGU-55/P helmet mounted on a BK 4128 C HATS (Feedforward, mFx, N_x = 4, N_e = 2, N_y = 2, N_p = 2); *Channels:* #1 ← x_1, #2 ← x_2, #3 ← x_3, #4 ← x_4, #5 ← d_1^p, #6 ← d_2^p; **Scenario:** `F16RecordingSignalAnalysis/20080110T011214`.

performance sensor, that is, $H_{x_1 d_1^p}$ depicted in Simulation D.3.8 on the following page and Simulation D.3.9 on page 569 respectively. Some variations in all the eight transfer functions from the four reference sensors to the two performance sensor exist especially at higher frequencies as expected considering the topology of the system.

Now, considering the multiple coherence functions (MCOFs) between the four reference sensors and the first performance sensor, that is, $\gamma^2_{d_1^p \cdot x_1 x_2 x_3 x_4}$ displayed in Simulation D.3.10 - D.3.11 on pages 570–571 only a small improvement in coherence is obtained as compared with the OCOF. Unfortunately, at time of noise recordings the confined reference sensors array measurements could be conducted due to lack of the required equipment.

The MCOFs between the four reference sensors and the second performance sensor follow a quite similar pattern.

Finally, the cross-correlation functions from the joint-channel residual spectral analysis (JCRSA) (refer to chapter 2 on page 17) are shown in Simulation D.3.12 on page 572 which also indicates the time-advance information achievable with these positions of the reference sensors. In the CH-47 recordings, however, the reference sensors will all be positioned on the helmet.

D.3.5 Remarks

As the measurement system was rigidly fixed to the backseat in the cockpit no emulations of pilots movement could be made. Therefore, the influence of nonstationary relative noise source positions was not measured. Moreover, no war-time events were simulated. In such situations more impulsive noise signals are expected to be present due to gun blast etc.

D.4 CH-47D Chinook Helicopter Noise Recordings

In this section a brief presentation of the results from helicopter noise recordings conducted in a CH-47D at Airbase Sosterberg will be presented. The measurements follows the test procedure [7].

D.4.1 Measurement Equipment

In Figure D.12 - D.14 the overall instrumentation setup is illustrated. The BK 4128 C HATS described in subsection D.2.3 was also used in this test flight.

Some photos illuminating the BK 4949 surface microphones flush-mounted on the Gentex HGU-55/P helmet tailored to the BK 4128 C HATS were presented in Figure 2.1 - 2.2 on pages 33–34. A total of 10 surface microphones were mounted on the helmet. For this purpose the BK Ø35 mm UA 1668 mounting pads was used and protection grids BK UA 1669 were attached to each surface microphone. In addition the BK 4128 C HATS mouth microphone was used as a reference sensor.

Provision for 17 simultaneous measurement channels was made by the BK PULSE portable data acquisition unit that includes a BK 3560-C-E14 front-end equipped with a BK 3040-B 12 channel (Dyn-X) module and a BK 7540 5 channel (Dyn-X) module integrated LAN module that in turn was connected to a Dell Latitude D 800 1.7 GHz laptop equipped with 2048 MB RAM, 1 GB solid-state HDD and a 2 GB flash memory module.

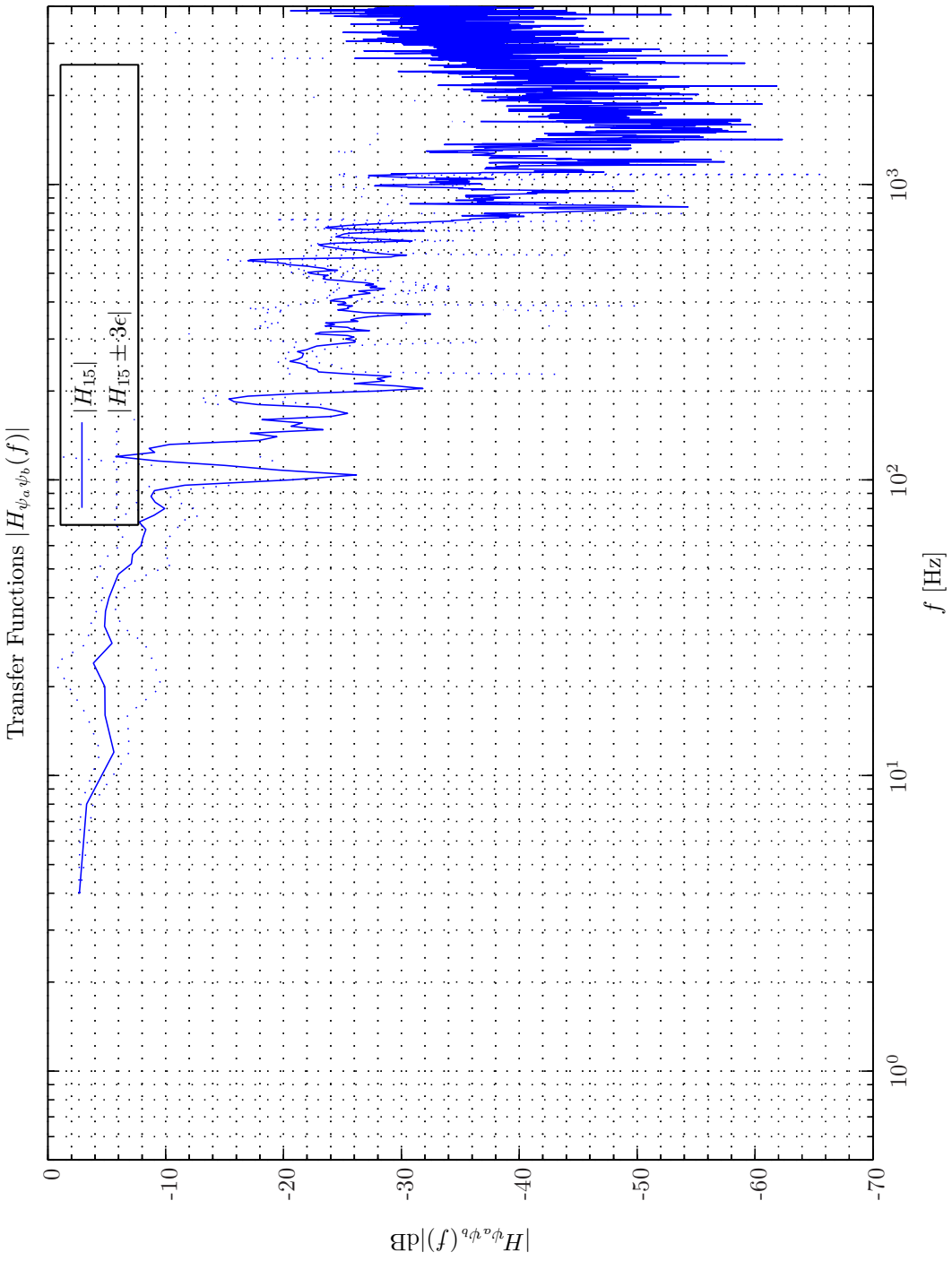

Sim D.3.8: *Transfer Function, Magnitude:* $|H_{\psi_a\psi_b}(f)|$: **Statistical Data Analysis**: Single-Sided Modified Periodogram, f_s = 16.384 kHz, N_{DFT} = 4096, L_{DFT} = 4097, R_{DFT} = 2049, Hanning, Δf_m = 16 Hz, T_{DFT} = 0.25006 s, $N_{f,DFT}$ = 2049, Δf_{DFT} = 4 Hz, K_{DFT} = 238; **F-16** Recordings Airbase Skrydstrup 20 marts 2003, Channel 1 2 3 4 5 6, Scenario 1, 0 − 30 s (f_s = 16.384 kHz, $N_{A/D}$ = 16); **Topology:** Gentex HGU-55/P helmet mounted on a BK 4128 C HATS (Feedforward, mFx, N_x = 4, N_e = 2, N_y = 2, N_p = 2); *Channels:* #1 ← x_1, #2 ← x_2, #3 ← x_3, #4 ← x_4, #5 ← d_1^p, #6 ← d_2^p; **Scenario:** `F16RecordingSignalAnalysis/20080110T011214`.

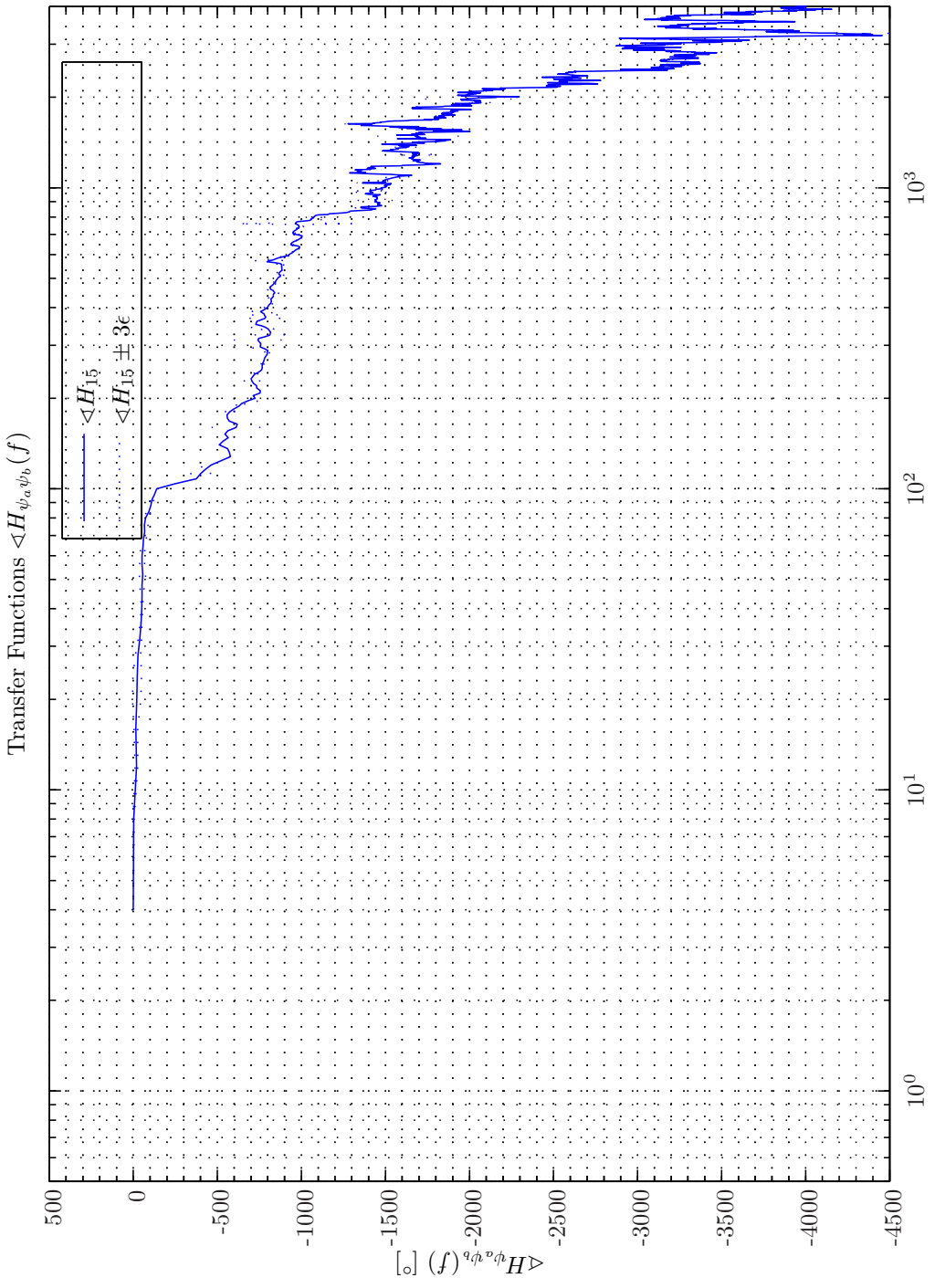

Sim D.3.9: *Transfer Function, Phase:* $\sphericalangle H_{\psi_a \psi_b}(f)$: **Statistical Data Analysis**: Single-Sided Modified Periodogram, $f_s = 16.384$ kHz, $N_{DFT} = 4096$, $L_{DFT} = 4097$, $R_{DFT} = 2049$, Hanning, $\Delta f_m = 16$ Hz, $T_{DFT} = 0.25006$ s, $N_{f,DFT} = 2049$, $\Delta f_{DFT} = 4$ Hz, $K_{DFT} = 238$; F-16 Recordings Airbase Skrydstrup 20 marts 2003, Channel 1 2 3 4 5 6, Scenario 1, $0 - 30$ s ($f_s = 16.384$ kHz, $N_{A/D} = 16$); **Topology:** Gentex HGU-55/P helmet mounted on a BK 4128 C HATS (Feedforward, mFx, $N_x = 4, N_e = 2, N_y = 2, N_p = 2$); *Channels:* #1 $\leftarrow x_1$, #2 $\leftarrow x_2$, #3 $\leftarrow x_3$, #4 $\leftarrow x_4$, #5 $\leftarrow d_1^p$, #6 $\leftarrow d_2^p$; **Scenario:** `F16RecordingSigmalAnalysis/20080110T011214`.

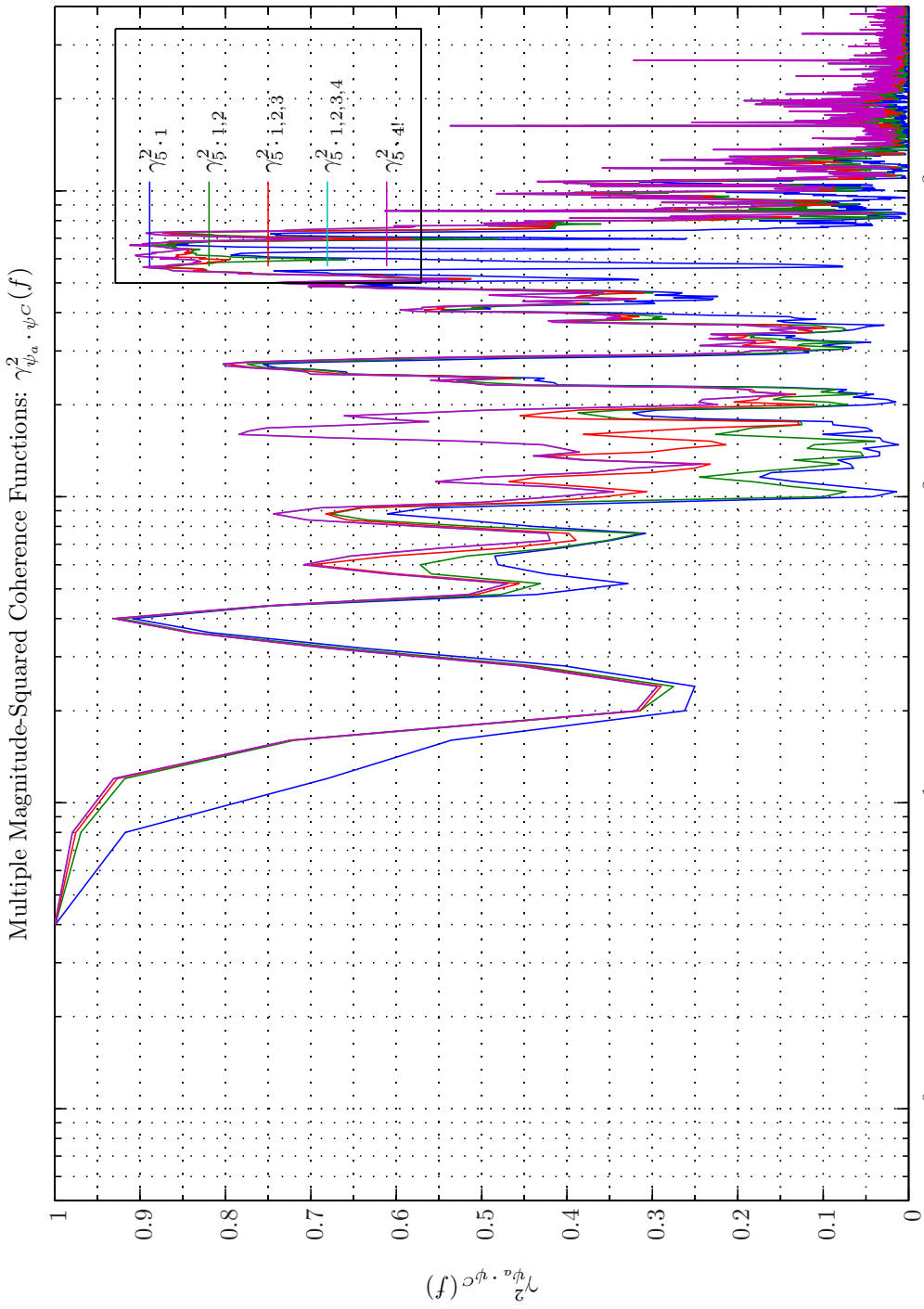

Sim D.3.10: *Multiple Magnitude-Squared Coherence Functions* $\gamma^2_{\psi_a \cdot \psi^C}(f)$: **Statistical Data Analysis**: Single-Sided Modified Periodogram, f_s = 16.384 kHz, N_{DFT} = 4096, L_{DFT} = 4097, R_{DFT} = 2049, Hanning, Δf_m = 16 Hz, T_{DFT} = 0.25006 s, $N_{f,DFT}$ = 2049, Δf_{DFT} = 4 Hz, K_{DFT} = 238; F-16 Recordings Airbase Skrydstrup 20 marts 2003, Channel 1 2 3 4 5 6, Scenario 1, 0 − 30 s (f_s = 16.384 kHz, $N_{A/D}$ = 16); **Topology:** Gentex HGU-55/P helmet mounted on a BK 4128 C HATS (Feedforward, mFx, $N_x = 4, N_e = 2, N_y = 2, N_p = 2$); *Channels:* #1 ← x_1, #2 ← x_2, #3 ← x_3, #4 ← x_4, #5 ← d_1^p, #6 ← d_2^p; **Scenario:** `F16RecordingSignalAnalysis/20080110T011214`.

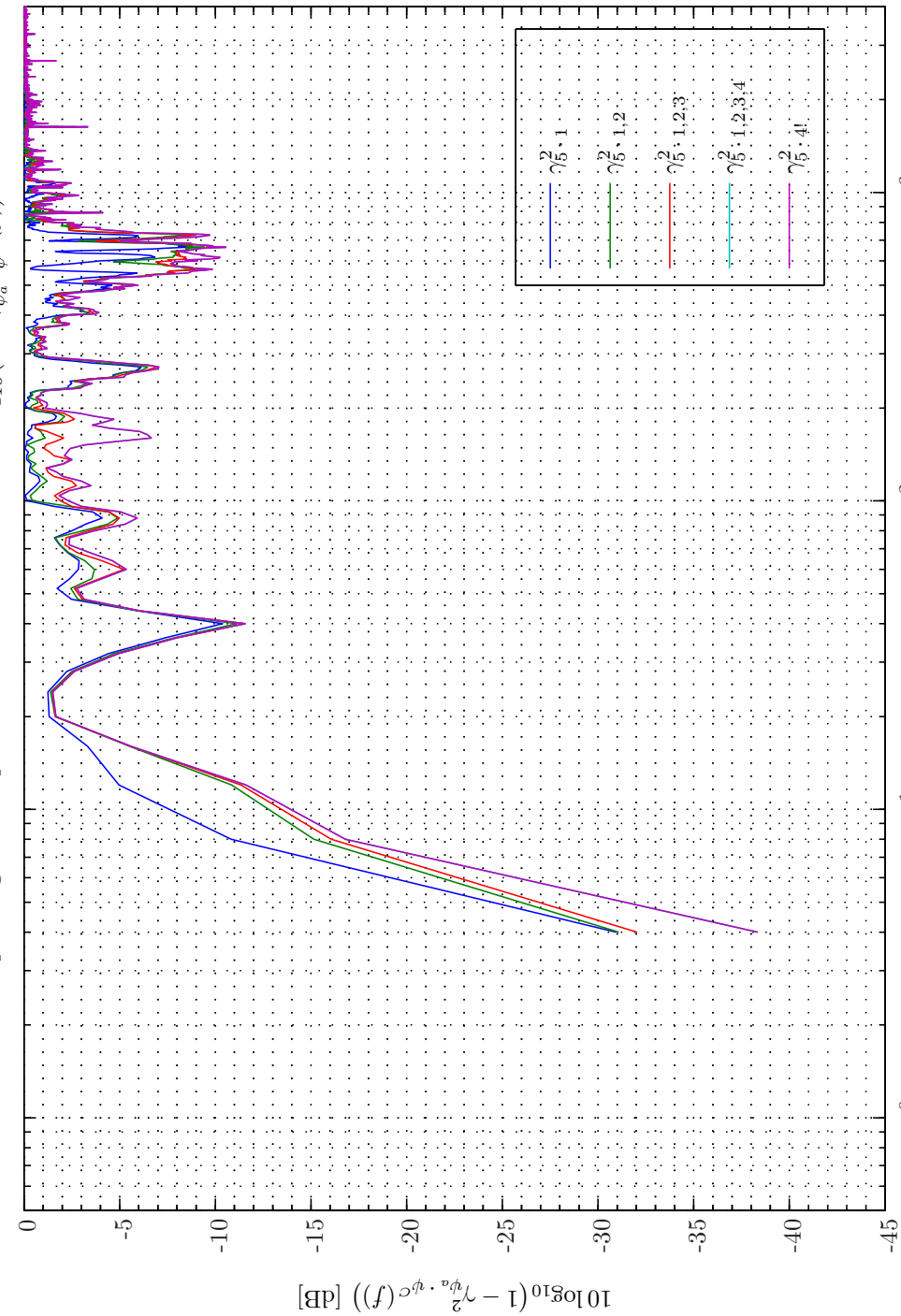

Sim D.3.11: *Attenuation vs Multiple Magnitude-Squared Coherence Functions* $10\log_{10}(1-\gamma^2_{\psi_a\cdot\psi^C}(f))$: **Statistical Data Analysis**: Single-Sided Modified Periodogram, $f_s = 16.384$ kHz, $N_{DFT} = 4096$, $L_{DFT} = 4097$, $R_{DFT} = 2049$, Hanning, $\Delta f_m = 16$ Hz, $T_{DFT} = 0.25006$ s, $N_{f,DFT} = 2049$, $\Delta f_{DFT} = 4$ Hz, $K_{DFT} = 238$; F-16 Recordings Airbase Skrydstrup 20 marts 2003, Channel 1 2 3 4 5 6, Scenario 1, $0-30$ s ($f_s = 16.384$ kHz, $N_{A/D} = 16$); **Topology:** Gentex HGU-55/P helmet mounted on a BK 4128 C HATS (Feedforward, mFx, $N_x = 4, N_e = 2, N_y = 2, N_p = 2$); *Channels:* #1 $\leftarrow x_1$, #2 $\leftarrow x_2$, #3 $\leftarrow x_3$, #4 $\leftarrow x_4$, #5 $\leftarrow d_1^p$, #6 $\leftarrow d_2^p$; **Scenario:** `F16RecordingSignalAnalysis/20080110T011214`.

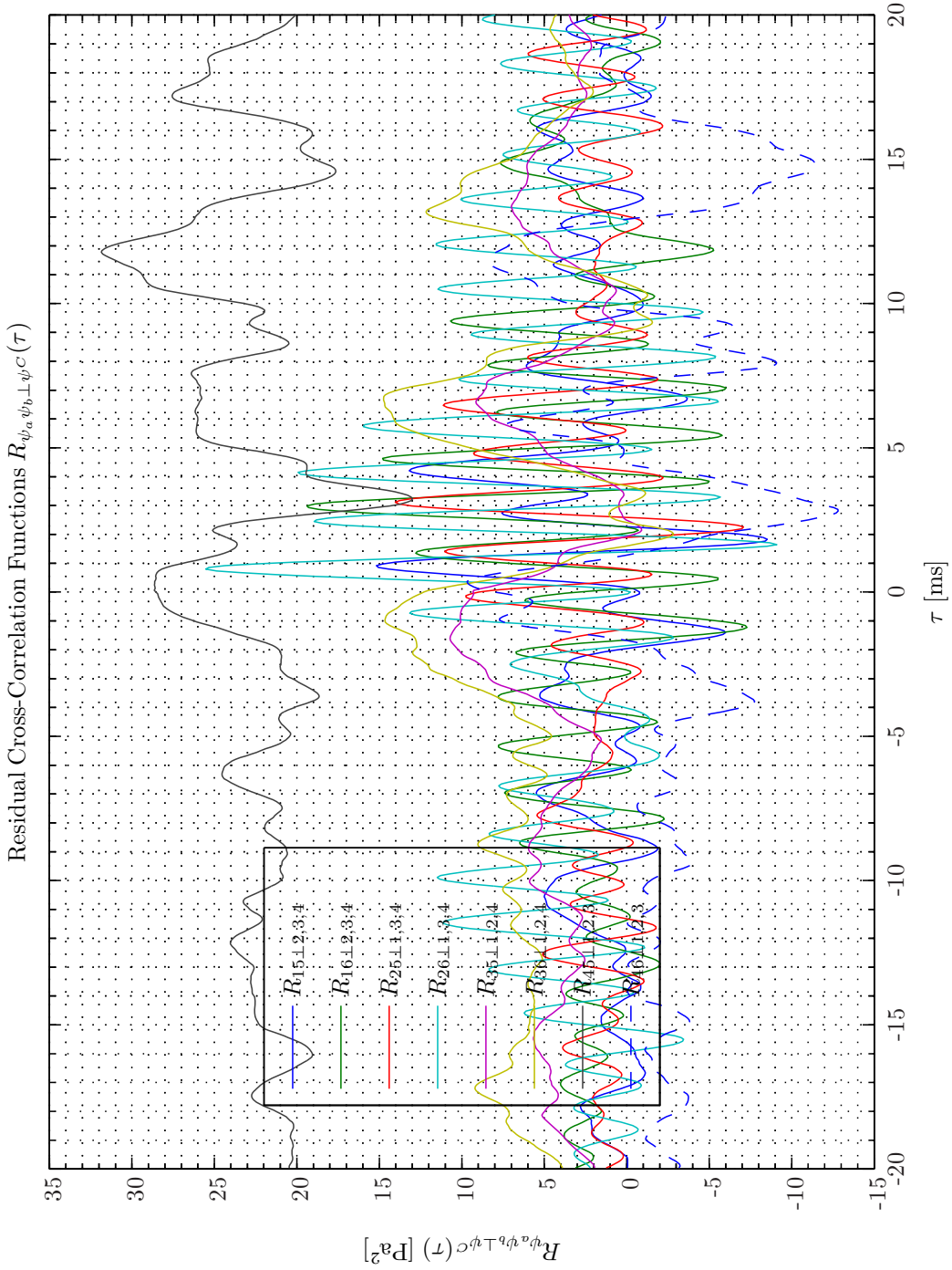

Sim D.3.12: *Residual Cross-Correlation Functions* JCRSA: $R_{\psi_a\psi_b\perp\psi^C}(\tau)$: **Statistical Data Analysis**: Single-Sided Modified Periodogram, $f_s = 16.384$ kHz, $N_{DFT} = 4096$, $L_{DFT} = 4097$, $R_{DFT} = 2049$, Hanning, $\Delta f_m = 16$ Hz, $T_{DFT} = 0.25006$ s, $N_{f,DFT} = 2049$, $\Delta f_{DFT} = 4$ Hz, $K_{DFT} = 238$; F-16 Recordings Airbase Skrydstrup 20 marts 2003, Channel 1 2 3 4 5 6, Scenario 1, $0 - 30$ s ($f_s = 16.384$ kHz, $N_{A/D} = 16$); **Topology:** Gentex HGU-55/P helmet mounted on a BK 4128 C HATS (Feedforward, mFx, $N_x = 4, N_e = 2, N_y = 2, N_p = 2$); *Channels:* #1 $\leftarrow x_1$, #2 $\leftarrow x_2$, #3 $\leftarrow x_3$, #4 $\leftarrow x_4$, #5 $\leftarrow d_1^p$, #6 $\leftarrow d_2^p$; **Scenario:** F16RecordingSignalAnalysis/20080110T011214.

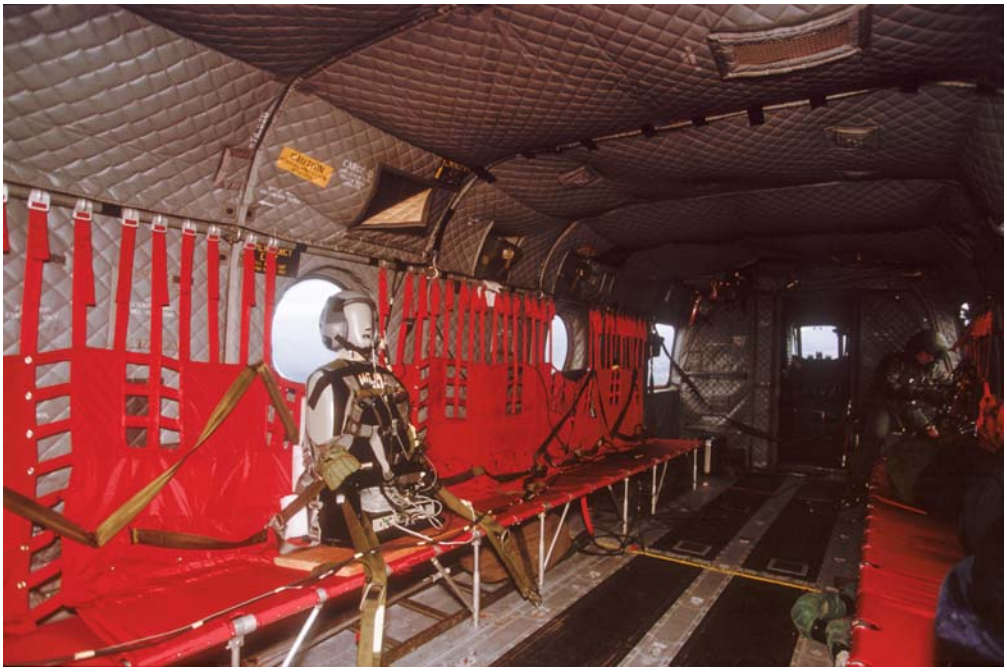

Fig. D.12: Customized frame installed in CH-47D Chinook Helicopter © Leth Data & Foto, 2005.

The customized frame equipped with the BK 4128 C HATS, BK PULSE unit, Dell Latitude D 800 laptop and three BK 1/2" 4192-C pressure field condenser microphones each positioned in a BK 1/2" UA 1317 microphoneholder is illuminated in Figure D.13 on the following page. The two BK PULSE unit was battery powered from rechargeable nickel-metal hybrid batteries[3]. The following SW modules were used during the test: BK 7707 Unlimited Analysis Engine, 7701 Harddisc Recorder, 7705 Time Capture, 7789 PULSE Time, 7769 PULSE Auxiliary Parameter Logging, 7755 Bridge to MATLAB® .

Prior to the measurements each of the ten BK 4949 surface microphone were calibrated with a BK 4231 sound pressure calibrator using the BK DP 0979 adapter. The external BK 4135 and BK 4939 1/4" microphones and the BK 4128 C HATS microphones were calibrated as described in subsection D.2.3 on page 551. This calibration procedure was repeated shortly after the flight test. The deviation between pre flight and post flight measurements were all within fractions of a dB and therefore within the measurement accuracy.

Next the results from a statistical data analysis of the data acquired during the course of two of the prepared scenarios will be presented. The two scenarios represent high and extreme sound pressure levels respectively.

Topology

The set of $N_x = 11$ reference sensors $x_1, \ldots, x_{11}$ was constituted from the ten BK 4949 surface microphones flush-mounted on the Gentex HGU-55/P helmet as shown in Figure D.13 together with the BK 4128 C HATS mouth microphone. The left and right ear simulators of the HATS

[3]The battery capacity is assessed to approximately 1.5 h operation.

Fig. D.13: Customized frame with BK 4128 C HATS, BK PULSE unit, 10 BK 4949 surface microphones and BK 4128 C HATS mouth microphone, Dell Latitude D 800 laptop , © Leth Data & Foto, 2005.

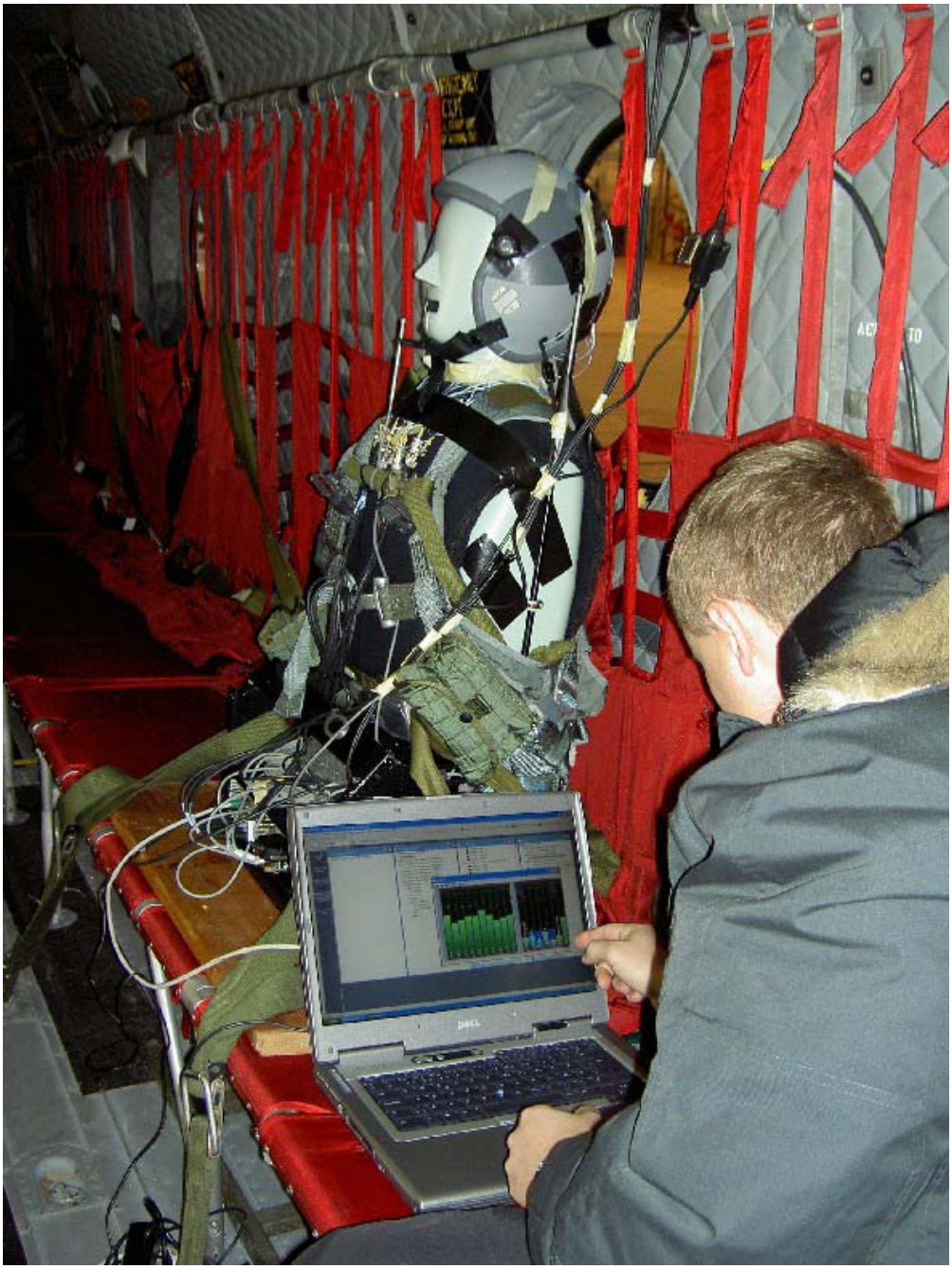

Fig. D.14: Chlinton Møller Nielsen examining the sound pressure levels from the 17 channels.

constitute the $N_p = 2$ performance sensors that will denoted by d_1^p and d_2^p respectively. At the time of measurements the Terma Earcup Audio System was yet developed and no disturbance signal was acquired, that is, $N_e = 0$.

D.4.2 Scenario with Engines and Auxiliary Power Unit (APU) turned off

In the first scenario presented the engines and the APU are turned off. Accordingly, relative low sound pressure levels are expectable. The parameters governed the periodogram spectra estimates can be found in the figure captions. The results from data averaging over the period from 0 s to 30 s are presented next.

In Simulation D.4.1 - D.4.4 on pages 577–580 the pdfs for four different signals representing the most extreme characteristics, namely, $p_{x_1}(p), p_{x_4}(p), p_{x_{10}}(p), p_{d_1^p}(p)$ are shown. As readily observed some deviances from zero-mean Gaussian distributions prevail and some skewness is observed in all the records. Moreover, among the sensor signals some variation of the pdfs are experienced. In particular, the probability density function of the performance signal is indeed narrow without any tail content.

In order further to analyze this behavior the software package STABLE from Robust Analysis, Inc. was used for the estimation of the stable parameters $\mathcal{S}(\alpha, \beta, \gamma, \delta)$ defined in Appendix L on page 773 using the MLE. The results can be found in Table D.3

Signal	x_1	x_2	x_3	x_4	x_5	x_6	x_7	x_8	x_9	x_{10}	x_{11}	d_1^p	d_2^p
α	2.00	1.85	1.90	2.00	2.00	2.00	2.00	1.99	2.00	2.00	1.90	1.58	1.57
β	0.42	0.86	1.00	0.99	0.91	0.43	0.91	1.00	0.97	0.99	0.99	0.30	0.30
γ	0.25	0.20	0.23	0.26	0.28	0.30	0.24	0.23	0.25	0.32	0.26	0.09	0.10
δ	−3.37	−2.53	−3.13	−3.84	−4.10	−4.71	−3.55	−3.38	−3.49	−4.76	−4.28	−0.32	−0.36
$\pm 3\epsilon_\alpha$	0	0.00	0	0	0	0	0	0	0	0	0	0.01	0.01
$\pm 3\epsilon_\beta$	0	0.03	0	0	0	0	0	0	0	0	0	0.02	0.02
$\pm 3\epsilon_\gamma$	0	0.00	0	0	0	0	0	0	0	0	0	0.00	0.00
$\pm 3\epsilon_\delta$	0	0.00	0	0	0	0	0	0	0	0	0	0.00	0.00

Tab. D.3: CH-47D Scenario with Engines and APU turned off, Stable parameters γ, δ re. 20 µPa.

As is well known uncertainty values do not make sense when a stable parameter is at the boundary of the parameter space, e.g., $\alpha \lessapprox 2$ and is therefore set to 0 in such cases. Hence, except for the performance signal the index of stability α is relative close to 2, but the skewness parameter β takes large values that confirms the assumption of non Gaussian distributed signals. However, owing to the lack of contents in the tails of the probability density functions nor do stable distributions fit very well to the data.

The auto spectral density functions are shown in Simulation D.4.5 on page 581. The corresponding averaged sound pressure levels can be found in Table D.4.

Signal	x_1	x_2	x_3	x_4	x_5	x_6	x_7	x_8	x_9	x_{10}	x_{11}	d_1^p	d_2^p
SPL	104.6	102.0	103.9	105.7	106.3	107.5	105.0	104.6	104.9	107.6	106.6	85.1	85.8

Tab. D.4: Scenario with Engines and APU turned off, averaged sound pressure levels re. 20 µPa.

The OCOFs and related achievable ANR from (2.2.1) on page 18 for the first six reference sensors and the two performance sensors are depicted in Simulation D.4.6 on page 582 and Simulation D.4.7 on page 584 respectively. The OCOFs characteristics for the remaining channel combinations are very similar.

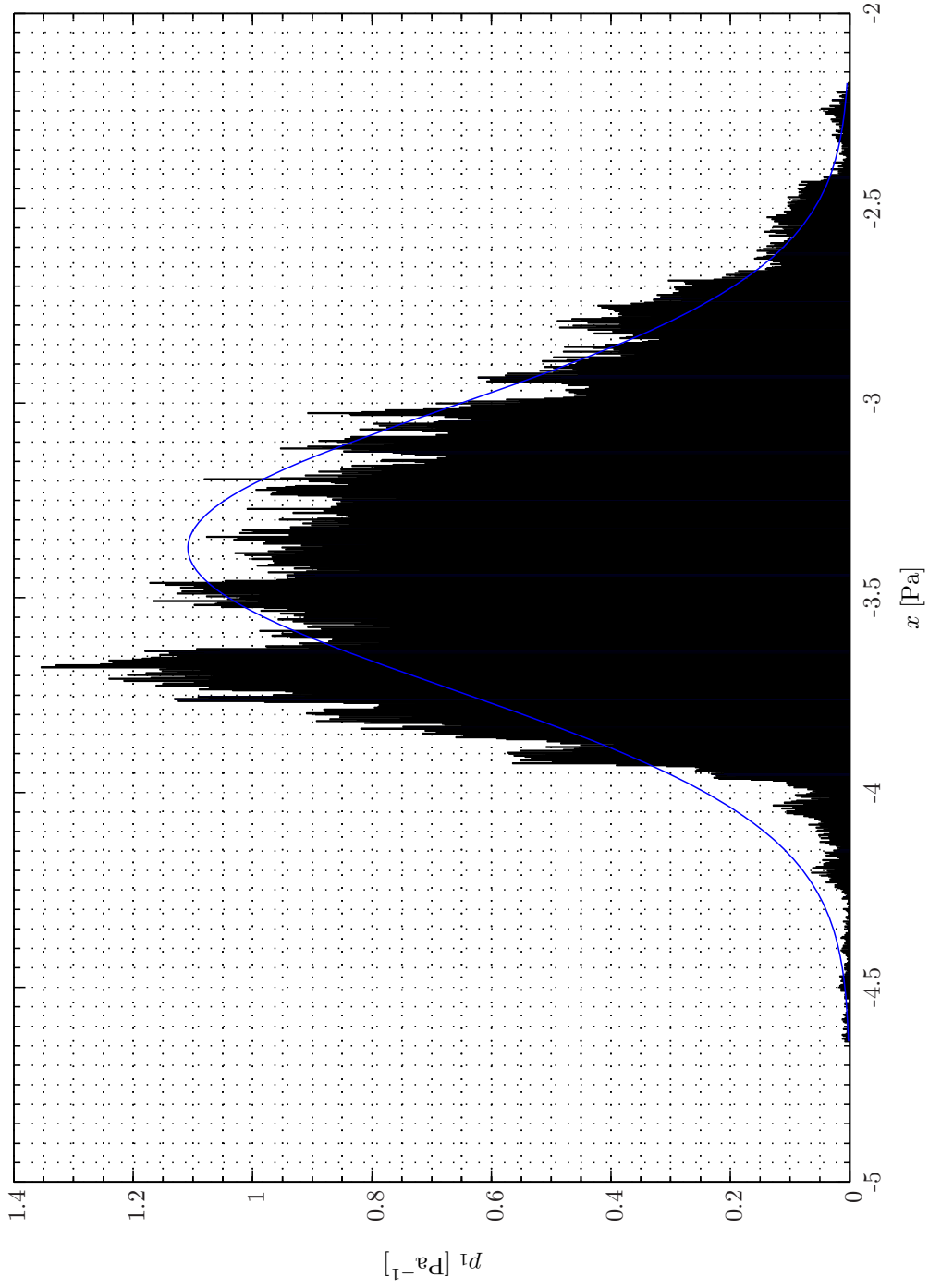

Sim D.4.1: *Probability Density Functions*: **Statistical Data Analysis**: Single-Sided Modified Periodogram, $f_s = 32.768$ kHz, $N_{DFT} = 8192$, $L_{DFT} = 8193$, $R_{DFT} = 4097$, Hanning, $\Delta f_m = 16$ Hz, $T_{DFT} = 0.25003$ s, $N_{f\,DFT} = 4097$, $\Delta f_{DFT} = 4$ Hz, $K_{DFT} = 46$; CH-47 Recordings Airbase Sosterberg 23 November 2005, Channel: 1,2,3,4,5,6,7,8,9,10,11,12,13,14,15,16,17, Scenario(0,1), $0 - 30$ s ($f_s = 32.768$ kHz, $N_{A/D} = 24$); **Topology:** BK 4949 surface microphones flush-mounted on a Gentex HGU-55/P helmet mounted on a BK 4128 C HATS, Terma Earcup Audio System (Feedforward, mFx, $N_x = 11, N_e = 2, N_y = 2, N_p = 2, N_v = 0$); *Channels:* $\#1 \leftarrow x_1$, $\#2 \leftarrow x_2$, $\#3 \leftarrow x_3$, $\#4 \leftarrow x_4$, $\#5 \leftarrow x_5$, $\#6 \leftarrow x_6$, $\#7 \leftarrow x_7$, $\#8 \leftarrow x_8$, $\#9 \leftarrow x_9$, $\#10 \leftarrow x_{10}$, $\#11 \leftarrow x_{11}$, $\#12 \leftarrow d_1^p$, $\#13 \leftarrow d_2^p$; **Scenario:** `CH47RecordingSignalAnalysis/20080220T204528`.

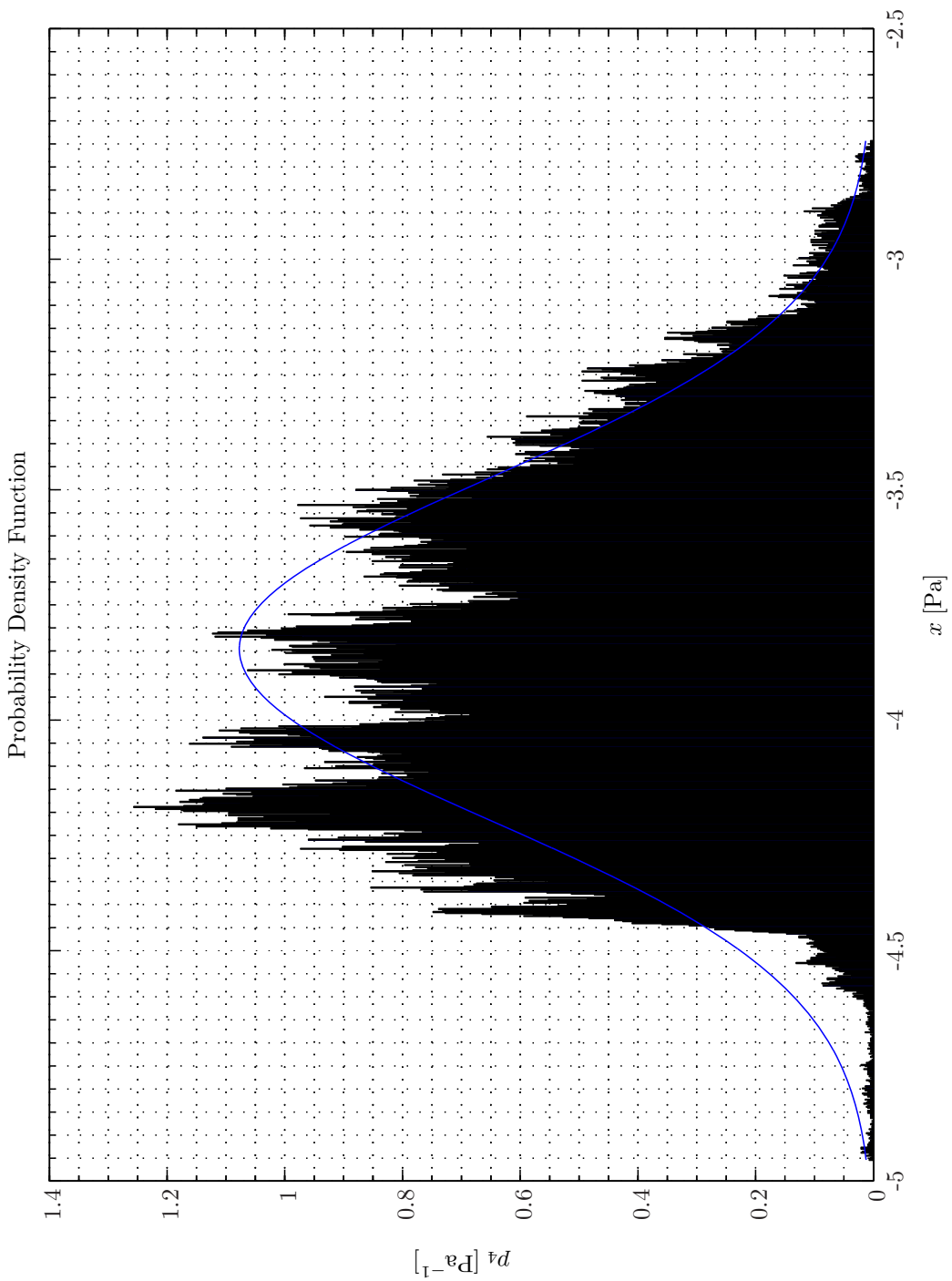

Sim D.4.2: *Probability Density Functions*: **Statistical Data Analysis**: Single-Sided Modified Periodogram, $f_s = 32.768$ kHz, $N_{DFT} = 8192$, $L_{DFT} = 8193$, $R_{DFT} = 4097$, Hanning, $\Delta f_m = 16$ Hz, $T_{DFT} = 0.25003$ s, $N_{f,DFT} = 4097$, $\Delta f_{DFT} = 4$ Hz, $K_{DFT} = 46$; CH-47 Recordings Airbase Sosterberg 23 November 2005, Channel: 1,2,3,4,5,6,7,8,9,10,11,12,13,14,15,16,17, Scenario(0,1), $0 - 30$ s ($f_s = 32.768$ kHz, $N_{A/D} = 24$); **Topology:** BK 4949 surface microphones flush-mounted on a Gentex HGU-55/P helmet mounted on a BK 4128 C HATS, Terma Earcup Audio System (Feedforward, mFx, $N_x = 11, N_e = 2, N_y = 2, N_p = 2, N_v = 0$); *Channels:* #1 $\leftarrow x_1$, #2 $\leftarrow x_2$, #3 $\leftarrow x_3$, #4 $\leftarrow x_4$, #5 $\leftarrow x_5$, #6 $\leftarrow x_6$, #7 $\leftarrow x_7$, #8 $\leftarrow x_8$, #9 $\leftarrow x_9$, #10 $\leftarrow x_{10}$, #11 $\leftarrow x_{11}$, #12 $\leftarrow d_1^p$, #13 $\leftarrow d_2^p$; **Scenario:** `CH47RecordingSignalAnalysis/20080220T204528`.

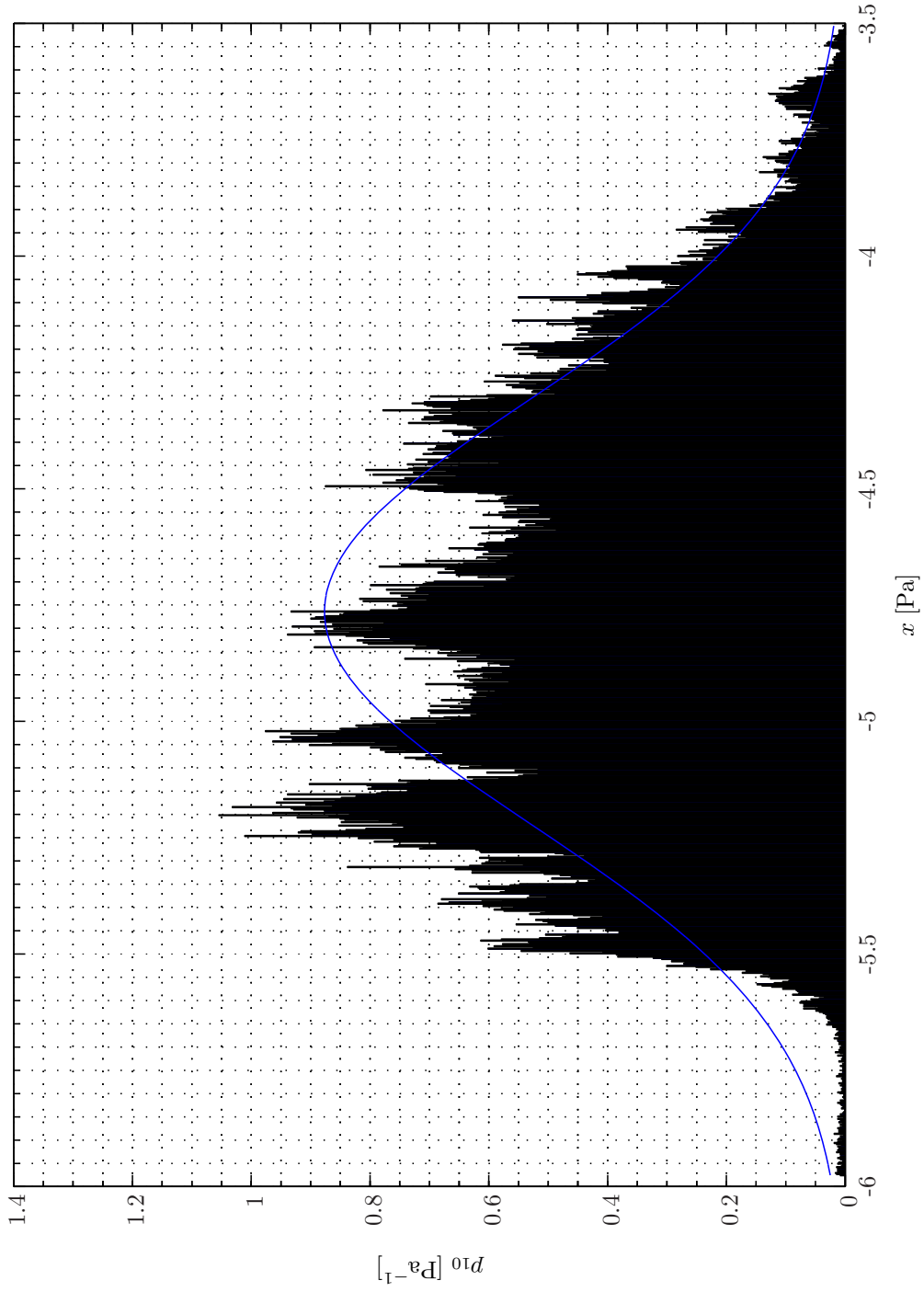

Sim D.4.3: *Probability Density Functions*: **Statistical Data Analysis**: Single-Sided Modified Periodogram, $f_s = 32.768$ kHz, $N_{DFT} = 8192$, $L_{DFT} = 8193$, $R_{DFT} = 4097$, Hanning, $\Delta f_m = 16$ Hz, $T_{DFT} = 0.25003$ s, $N_{f,DFT} = 4097$, $\Delta f_{DFT} = 4$ Hz, $K_{DFT} = 46$; CH-47 Recordings Airbase Sosterberg 23 November 2005, Channel: 1,2,3,4,5,6,7,8,9,10,11,12,13,14,15,16,17, Scenario(0,1), $0 - 30$ s ($f_s = 32.768$ kHz, $N_{A/D} = 24$); **Topology:** BK 4949 surface microphones flush-mounted on a Gentex HGU-55/P helmet mounted on a BK 4128 C HATS, Terma Earcup Audio System (Feedforward, mFx, $N_x = 11, N_e = 2, N_y = 2, N_p = 2, N_v = 0$); *Channels:* $\#1 \leftarrow x_1$, $\#2 \leftarrow x_2$, $\#3 \leftarrow x_3$, $\#4 \leftarrow x_4$, $\#5 \leftarrow x_5$, $\#6 \leftarrow x_6$, $\#7 \leftarrow x_7$, $\#8 \leftarrow x_8$, $\#9 \leftarrow x_9$, $\#10 \leftarrow x_{10}$, $\#11 \leftarrow x_{11}$, $\#12 \leftarrow d_1^p$, $\#13 \leftarrow d_2^p$; **Scenario:** `CH47RecordingSignalAnalysis/20080220T204528`.

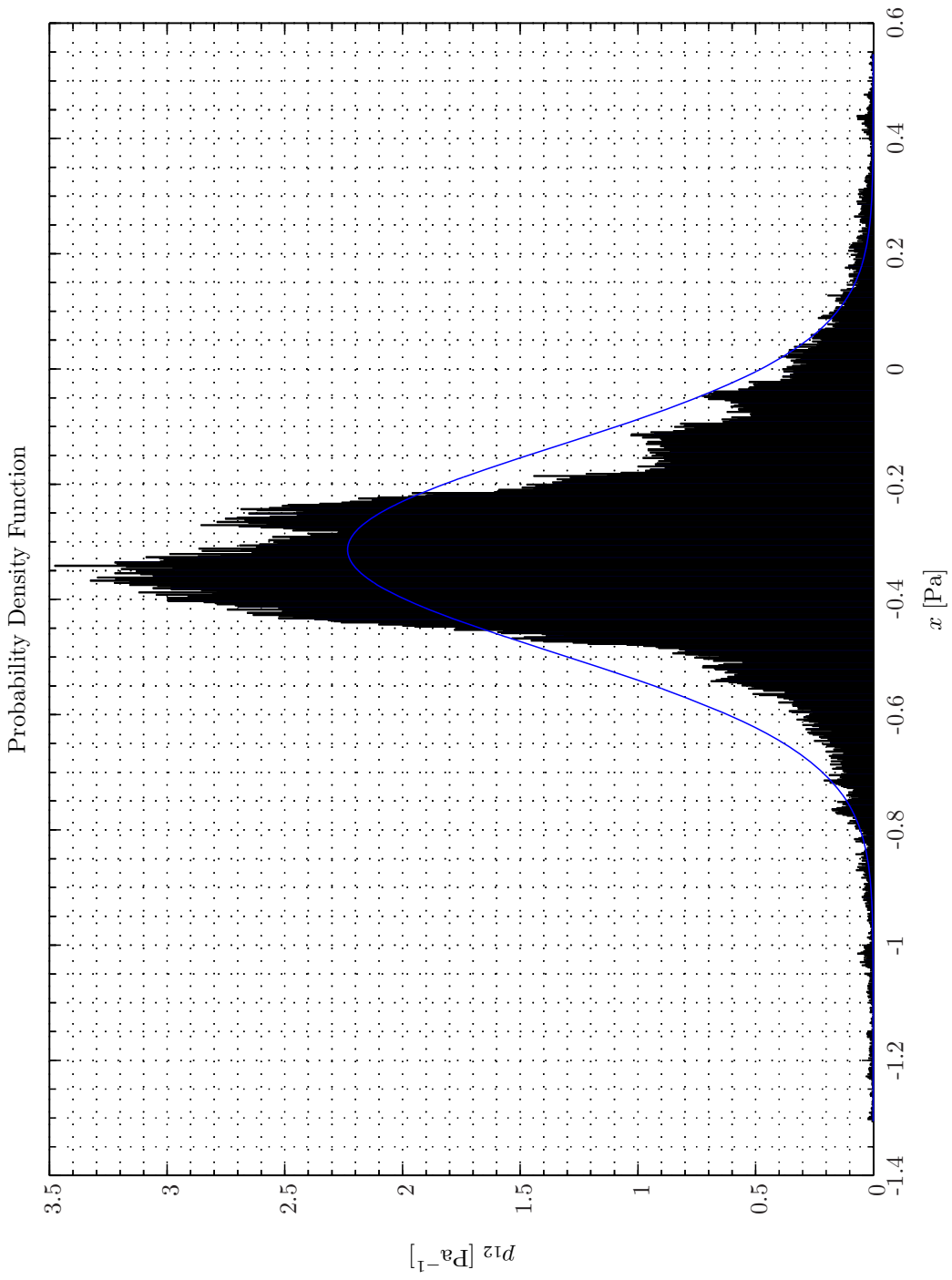

Sim D.4.4: *Probability Density Functions*: **Statistical Data Analysis**: Single-Sided Modified Periodogram, $f_s = 32.768$ kHz, $N_{DFT} = 8192$, $L_{DFT} = 8193$, $R_{DFT} = 4097$, Hanning, $\Delta f_m = 16$ Hz, $T_{DFT} = 0.25003$ s, $N_{f,DFT} = 4097$, $\Delta f_{DFT} = 4$ Hz, $K_{DFT} = 46$; CH-47 Recordings Airbase Sosterberg 23 November 2005, Channel: 1,2,3,4,5,6,7,8,9,10,11,12,13,14,15,16,17, Scenario(0,1), $0 - 30$ s ($f_s = 32.768$ kHz, $N_{A/D} = 24$); **Topology:** BK 4949 surface microphones flush-mounted on a Gentex HGU-55/P helmet mounted on a BK 4128 C HATS, Terma Earcup Audio System (Feedforward, mFx, $N_x = 11, N_e = 2, N_y = 2, N_p = 2, N_v = 0$); *Channels:* #1 $\leftarrow x_1$, #2 $\leftarrow x_2$, #3 $\leftarrow x_3$, #4 $\leftarrow x_4$, #5 $\leftarrow x_5$, #6 $\leftarrow x_6$, #7 $\leftarrow x_7$, #8 $\leftarrow x_8$, #9 $\leftarrow x_9$, #10 $\leftarrow x_{10}$, #11 $\leftarrow x_{11}$, #12 $\leftarrow d_1^p$, #13 $\leftarrow d_2^p$; **Scenario:** `CH47RecordingSignalAnalysis/20080220T204528`.

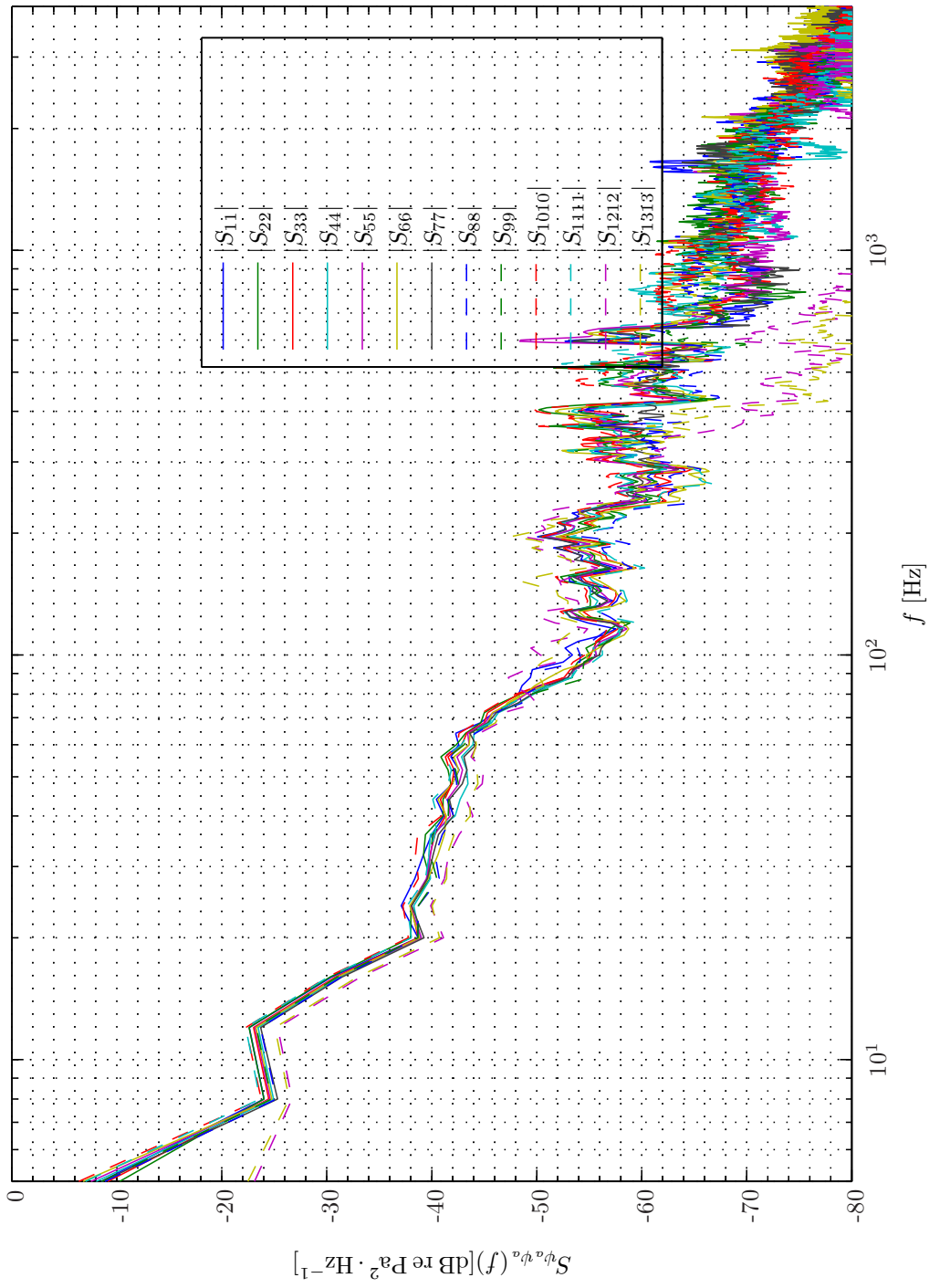

Sim D.4.5: *Autospectral Density Functions:* **Statistical Data Analysis:** Single-Sided Modified Periodogram, $f_s = 32.768$ kHz, $N_{DFT} = 8192$, $L_{DFT} = 8193$, $R_{DFT} = 4097$, Hanning, $\Delta f_m = 16$ Hz, $T_{DFT} = 0.25003$ s, $N_{f,DFT} = 4097$, $\Delta f_{DFT} = 4$ Hz, $K_{DFT} = 46$; CH-47 Recordings Airbase Sosterberg 23 November 2005, Channel: 1,2,3,4,5,6,7,8,9,10,11,12,13,14,15,16,17, Scenario(0,1), $0 - 30$ s ($f_s = 32.768$ kHz, $N_{A/D} = 24$); **Topology:** BK 4949 surface microphones flush-mounted on a Gentex HGU-55/P helmet mounted on a BK 4128 C HATS, Terma Earcup Audio System (Feedforward, mFx, $N_x = 11$, $N_e = 2$, $N_y = 2$, $N_p = 2$, $N_v = 0$); *Channels:* #1 $\leftarrow x_1$, #2 $\leftarrow x_2$, #3 $\leftarrow x_3$, #4 $\leftarrow x_4$, #5 $\leftarrow x_5$, #6 $\leftarrow x_6$, #7 $\leftarrow x_7$, #8 $\leftarrow x_8$, #9 $\leftarrow x_9$, #10 $\leftarrow x_{10}$, #11 $\leftarrow x_{11}$, #12 $\leftarrow d_1^p$, #13 $\leftarrow d_2^p$; **Scenario:** `CH47RecordingSignalAnalysis/20080220T204528`.

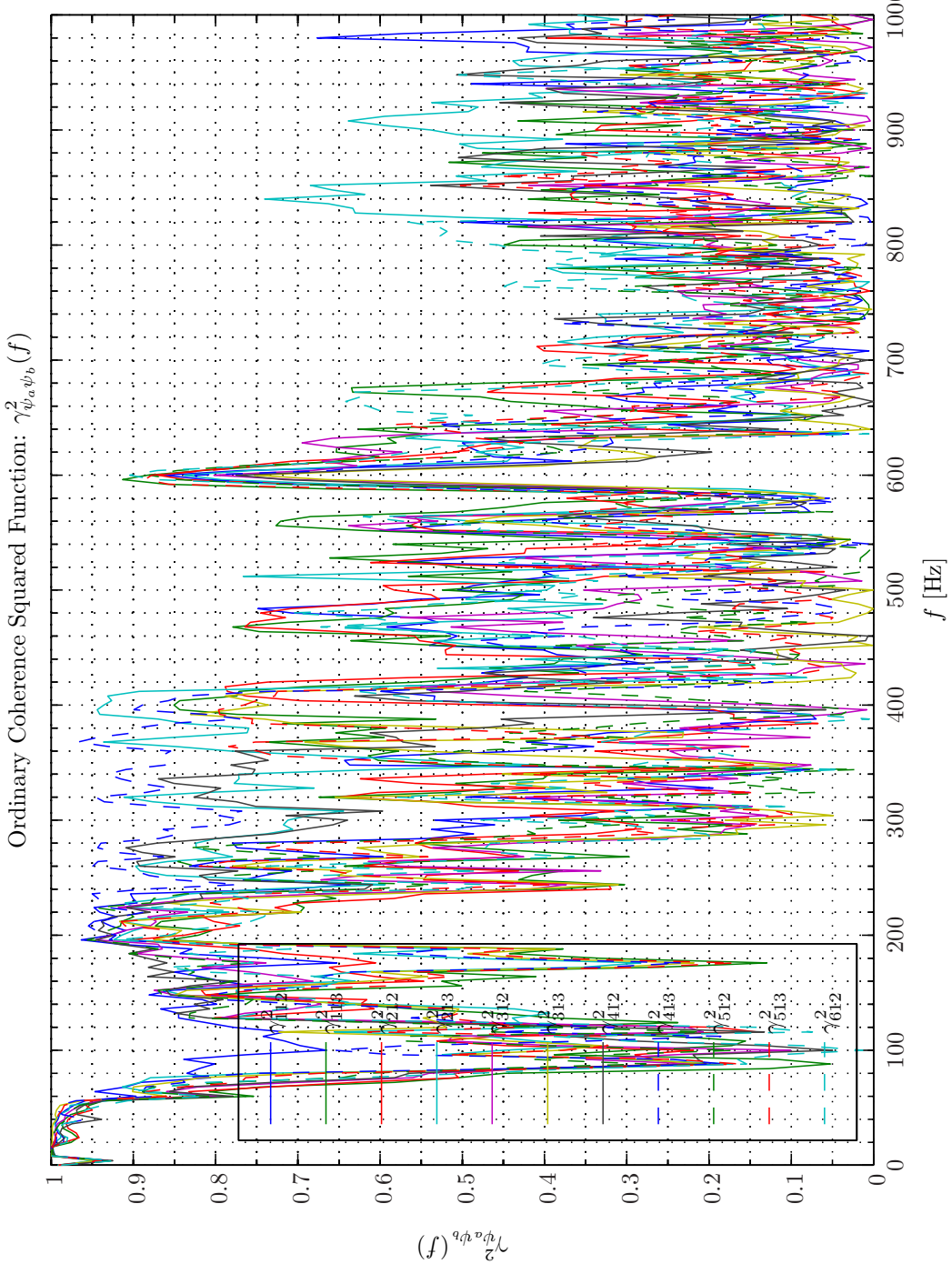

Sim D.4.6: *Ordinary Coherency-Squared Functions* $\gamma^2_{\psi_a\psi_b}(f)$: **Statistical Data Analysis**: Single-Sided Modified Periodogram, $f_s = 32.768$ kHz, $N_{DFT} = 8192$, $L_{DFT} = 8193$, $R_{DFT} = 4097$, Hanning, $\Delta f_m = 16$ Hz, $T_{DFT} = 0.25003$ s, $N_{f,DFT} = 4097$, $\Delta f_{DFT} = 4$ Hz, $K_{DFT} = 46$; CH-47 Recordings Airbase Sosterberg 23 November 2005, Channel: 1,2,3,4,5,6,7,8,9,10,11,12,13,14,15,16,17, Scenario(0,1), $0-30$ s ($f_s = 32.768$ kHz, $N_{A/D} = 24$); **Topology:** BK 4949 surface microphones flush-mounted on a Gentex HGU-55/P helmet mounted on a BK 4128 C HATS, Terma Earcup Audio System (Feedforward, mFx, $N_x = 11, N_e = 2, N_y = 2, N_p = 2, N_v = 0$); *Channels:* $\#1 \leftarrow x_1$, $\#2 \leftarrow x_2$, $\#3 \leftarrow x_3$, $\#4 \leftarrow x_4$, $\#5 \leftarrow x_5$, $\#6 \leftarrow x_6$, $\#7 \leftarrow x_7$, $\#8 \leftarrow x_8$, $\#9 \leftarrow x_9$, $\#10 \leftarrow x_{10}$, $\#11 \leftarrow x_{11}$, $\#12 \leftarrow d_1^p$, $\#13 \leftarrow d_2^p$; **Scenario:** `CH47RecordingSignalAnalysis/20080220T204528`.

Accordingly, from a FFS based AC perspective these result might at first glance look disappointing. Hence, attenuation figures above 10 dB is limited to frequencies less than 60 Hz. A deep trough is observed in the OCOF in the vicinity of 100 Hz except for reference sensor 1.

Considering the magnitude and phase of the transfer functions from the eleven reference sensors to the two performance sensors depicted in Simulation D.4.8 - D.4.9 on pages 585–586 respectively only minor variations are observed except for the phase response at higher frequencies.

The MCOFs obtained from using both the matrix formulation described in section 2.2.5 on page 27 and the iterative procedure presented in section 2.2.5 is displayed in Simulation D.4.10 - D.4.13 on pages 587–590. The MCOF corresponding to the disturbance signal taking every eleven reference signals into account is designated by $\gamma^2_{d_1^p \cdot x_{11!}}(f)$ and $\gamma^2_{d_2^p \cdot x_{11!}}(f)$ using the matrix method and by $\gamma^2_{d_1^p \cdot x_{7,1,4,6,10,9,2,8,5,3,11}}(f)$ and $\gamma^2_{d_2^p \cdot x_{9,2,6,7,4,8,1,10,5,11,3}}(f)$ applying the iterative procedure for performance signals d_1^p and d_2^p respectively. In this simulation the reference signals are sorted in descending order with respect to their ordinary coherence function averaged over the frequency band.

Within the graphical resolution the two methods give identical results as expected. In addition the iterative procedure illuminates the successive increase in MCOF from increasing the number of reference sensors. As seen active noise control (ANC) attenuation figures exceeding 10 dB possible up to approximately 850 Hz is predicted. The deep trough observed in the MCOF at 100 Hz if only reference sensors 6 and 7 are used is largely removed by including reference sensor 1.

In Simulation D.4.10 no apparent saturation in MCOF with increasing number of reference sensors is seen. Hence, by including additional reference sensors the upper frequency limit determined by the MCOF would most likely increase as a consequence of closer spatial sampling. It should be emphasized that we in the iterative multiple coherence function procedure successively enable reference signals that exhibit decreasing coherence with the error sensor. If we instead successively add a reference sensor and reoptimized their positions the increase in multiple coherence function would most likely be higher.

In section 2.4 very similar MCOFs patterns obtained from diffuse sound field measurements in a reverberant chamber were presented.

The particular details including $\pm 3\epsilon$ confidence intervals for the MCOFs (refer to subsection C.3.4 on page 544) using all eleven reference sensors are shown in Simulation D.4.14 - D.4.15 on pages 591–592.

We observe that the random errors correspond to an uncertainty in the attenuation estimation of approximately $+3, -6$ dB. Even though the multiple coherence function is exceeding 0.9 up to 850 Hz this somewhat wide confidence interval stems from the use of a relative small number of averages ($K_{DFT} = 46$). The uncertainty in the attenuation estimation is relative constant over the frequency band. The reasons for this are explained in section C.3 on page 541.

D.4.3 Scenario Flight at Constant Altitude and High Speed

The second scenario presented is from a flight at constant altitude and at high speed of 155 Knots indicated airspeed (KIAS). Accordingly, relative high sound pressure levels are expectable. Also here the results over the period from 0 s to 30 s are presented.

In Simulation D.4.18 - D.4.21 on pages 596–599 the pdfs for the same signals as above are repre-

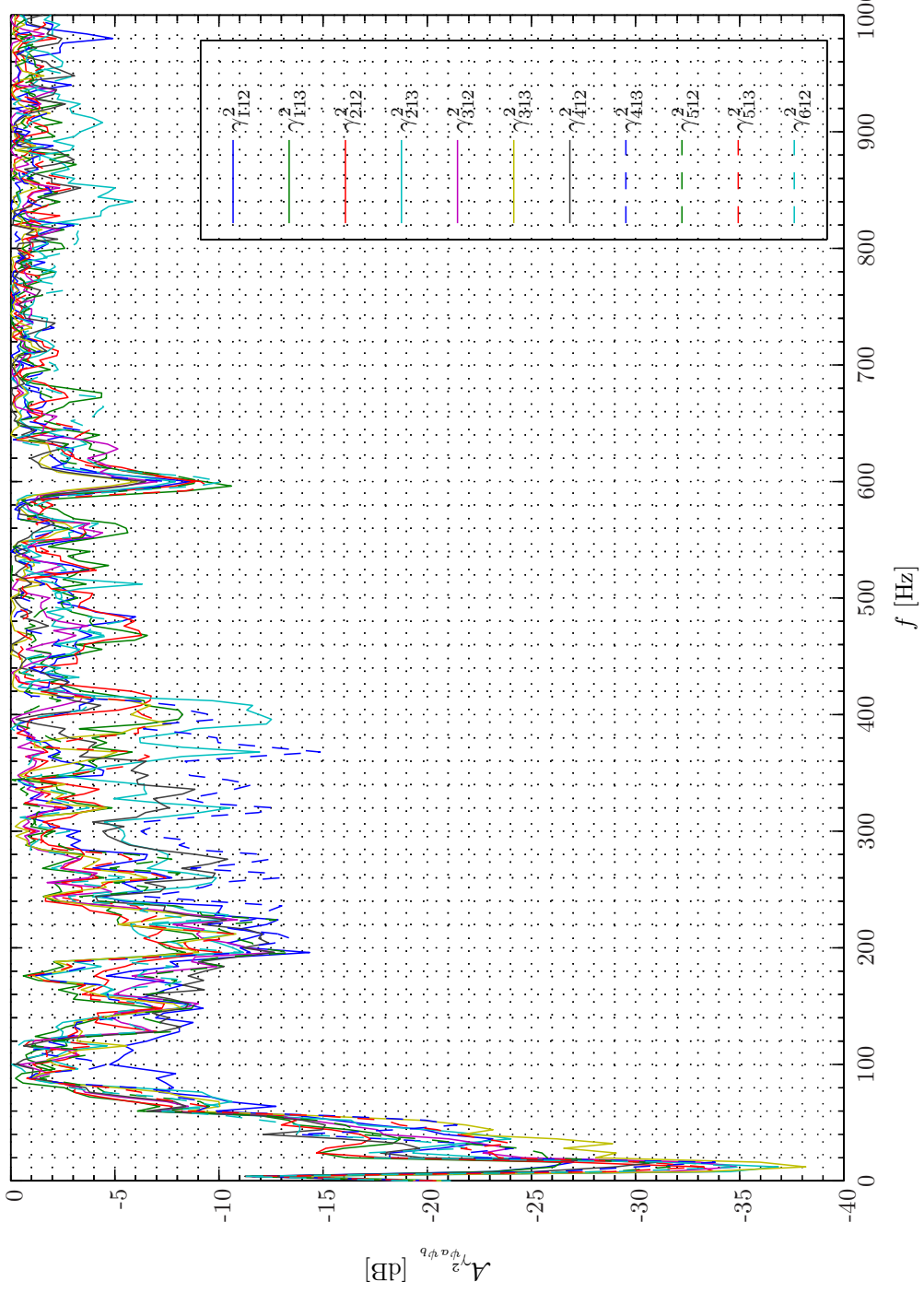

Sim D.4.7: Attenuation *vs Ordinary Coherency-Squared Functions*: $10\log_{10}(1-\gamma^2_{\psi_a\psi_b}(f))$: **Statistical Data Analysis**: Single-Sided Modified Periodogram, f_s = 32.768 kHz, N_{DFT} = 8192, L_{DFT} = 8193, R_{DFT} = 4097, Hanning, Δf_m = 16 Hz, T_{DFT} = 0.25003 s, $N_{f,DFT}$ = 4097, Δf_{DFT} = 4 Hz, K_{DFT} = 46; CH-47 Recordings Airbase Sosterberg 23 November 2005, Channel: 1,2,3,4,5,6,7,8,9,10,11,12,13,14,15,16,17, Scenario(0,1), 0 − 30 s (f_s = 32.768 kHz, $N_{A/D}$ = 24); **Topology:** BK 4949 surface microphones flush-mounted on a Gentex HGU-55/P helmet mounted on a BK 4128 C HATS, Terma Earcup Audio System (Feedforward, mFx, $N_x = 11, N_e = 2, N_y = 2, N_p = 2, N_v = 0$); *Channels:* #1 ← x_1, #2 ← x_2, #3 ← x_3, #4 ← x_4, #5 ← x_5, #6 ← x_6, #7 ← x_7, #8 ← x_8, #9 ← x_9, #10 ← x_{10}, #11 ← x_{11}, #12 ← d_1^p, #13 ← d_2^p; **Scenario:** `CH47RecordingSignalAnalysis/20080220T204528`.

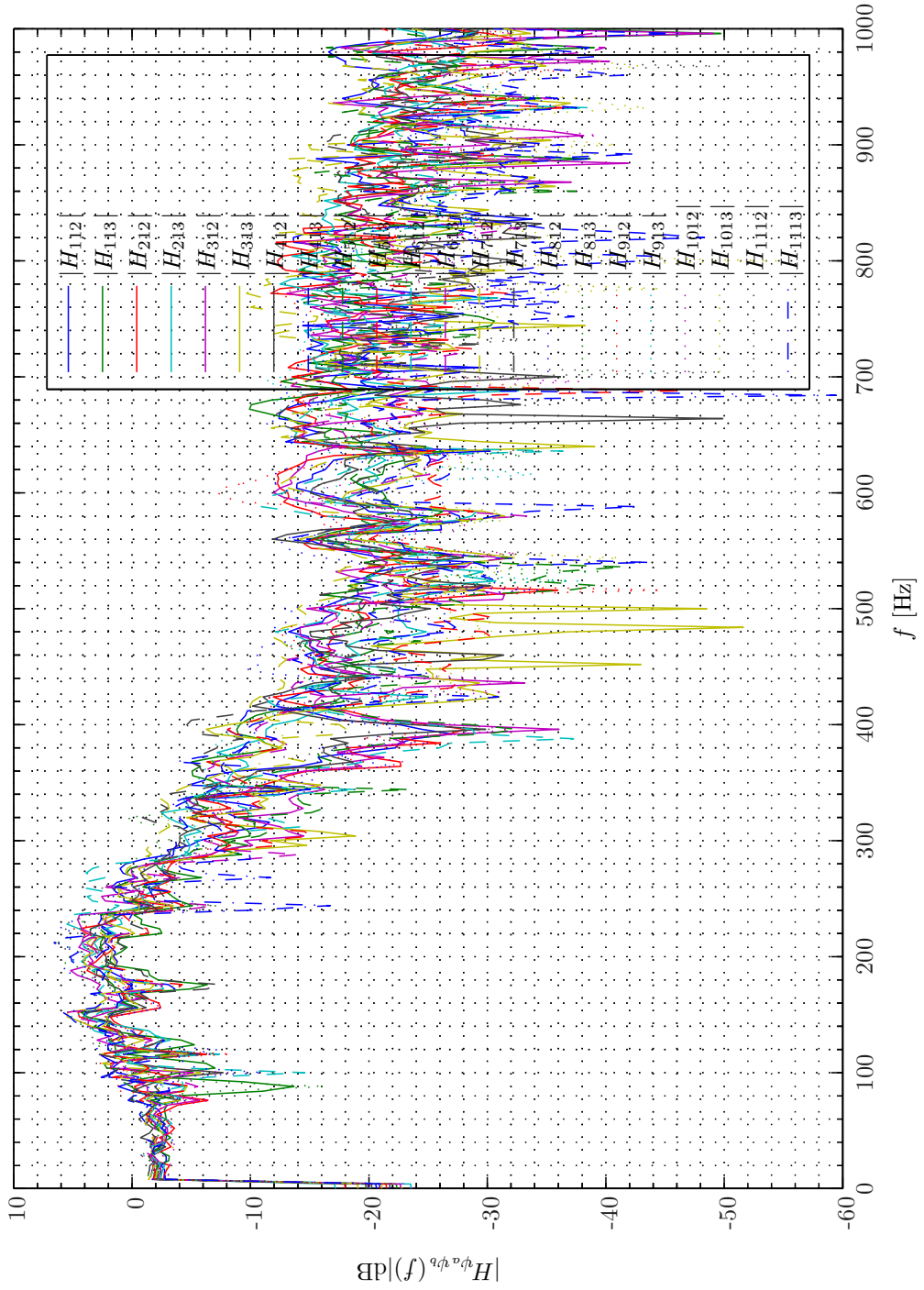

Sim D.4.8: *Transfer Function, Magnitude:* $|H_{\psi_a\psi_b}(f)|$: **Statistical Data Analysis**: Single-Sided Modified Periodogram, $f_s = 32.768$ kHz, $N_{DFT} = 8192$, $L_{DFT} = 8193$, $R_{DFT} = 4097$, Hanning, $\Delta f_m = 16$ Hz, $T_{DFT} = 0.25003$ s, $N_{f\_DFT} = 4097$, $\Delta f_{DFT} = 4$ Hz, $K_{DFT} = 46$; CH-47 Recordings Airbase Sosterberg 23 November 2005, Channel: 1,2,3,4,5,6,7,8,9,10,11,12,13,14,15,16,17, Scenario(0,1), $0 - 30$ s ($f_s = 32.768$ kHz, $N_{A/D} = 24$); **Topology:** BK 4949 surface microphones flush-mounted on a Gentex HGU-55/P helmet mounted on a BK 4128 C HATS, Terma Earcup Audio System (Feedforward, mFx, $N_x = 11, N_e = 2, N_y = 2, N_p = 2, N_v = 0$); *Channels:* $\#1 \leftarrow x_1$, $\#2 \leftarrow x_2$, $\#3 \leftarrow x_3$, $\#4 \leftarrow x_4$, $\#5 \leftarrow x_5$, $\#6 \leftarrow x_6$, $\#7 \leftarrow x_7$, $\#8 \leftarrow x_8$, $\#9 \leftarrow x_9$, $\#10 \leftarrow x_{10}$, $\#11 \leftarrow x_{11}$, $\#12 \leftarrow d_1^p$, $\#13 \leftarrow d_2^p$; **Scenario:** `CH47RecordingSignalAnalysis/20080220T204528`.

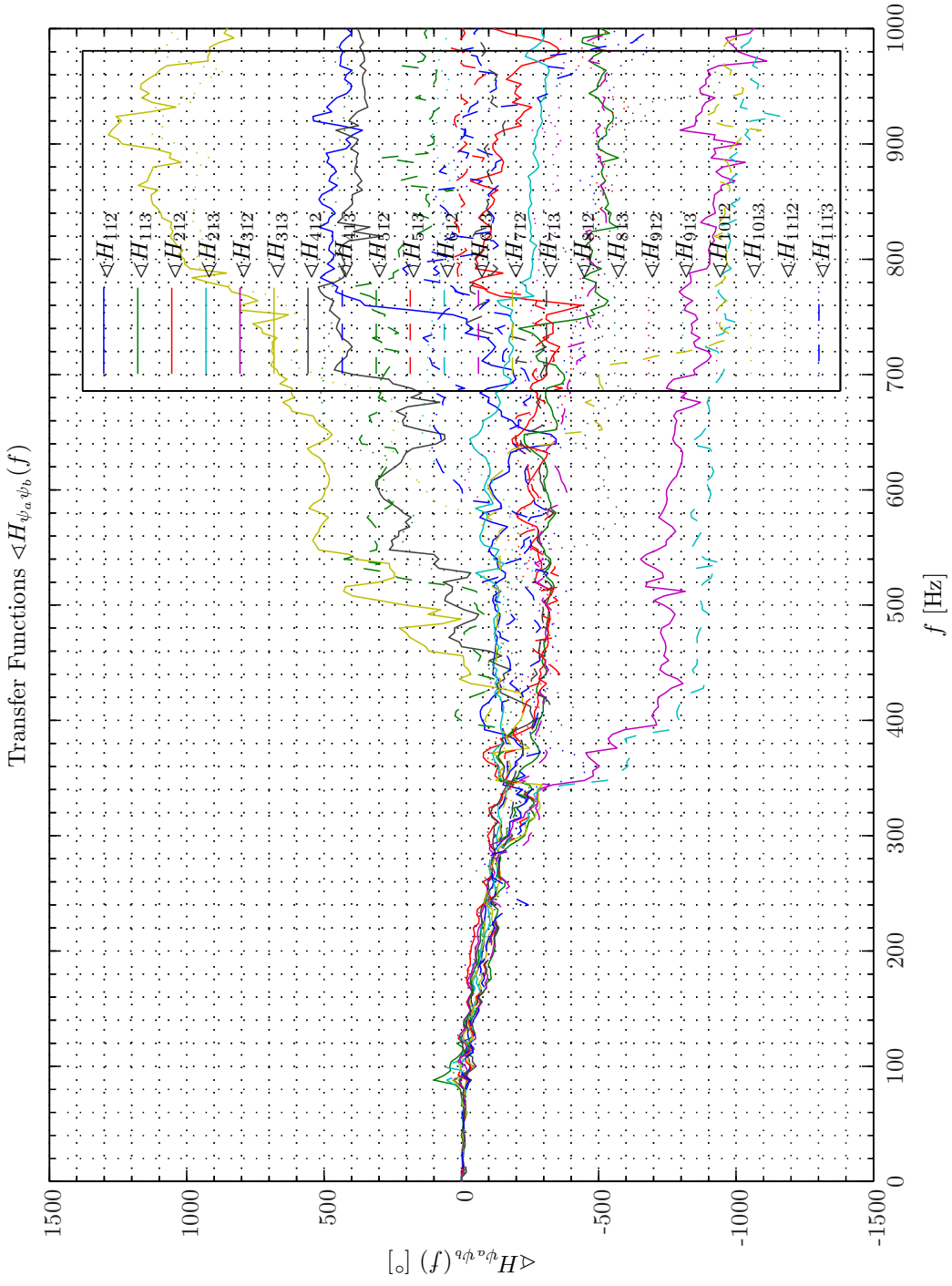

Sim D.4.9: *Transfer Function, Phase:* $\lhd H_{\psi_a\psi_b}(f)$: **Statistical Data Analysis**: Single-Sided Modified Periodogram, f_s = 32.768 kHz, N_{DFT} = 8192, L_{DFT} = 8193, R_{DFT} = 4097, Hanning, Δf_m = 16 Hz, T_{DFT} = 0.25003 s, $N_{f,DFT}$ = 4097, Δf_{DFT} = 4 Hz, K_{DFT} = 46; CH-47 Recordings Airbase Sosterberg 23 November 2005, Channel: 1,2,3,4,5,6,7,8,9,10,11,12,13,14,15,16,17, Scenario(0,1), 0 – 30 s (f_s = 32.768 kHz, $N_{A/D}$ = 24); **Topology:** BK 4949 surface microphones flush-mounted on a Gentex HGU-55/P helmet mounted on a BK 4128 C HATS, Terma Earcup Audio System (Feedforward, mFx, $N_x = 11, N_e = 2, N_y = 2, N_p = 2, N_v = 0$); *Channels:* $\#1 \leftarrow x_1$, $\#2 \leftarrow x_2$, $\#3 \leftarrow x_3$, $\#4 \leftarrow x_4$, $\#5 \leftarrow x_5$, $\#6 \leftarrow x_6$, $\#7 \leftarrow x_7$, $\#8 \leftarrow x_8$, $\#9 \leftarrow x_9$, $\#10 \leftarrow x_{10}$, $\#11 \leftarrow x_{11}$, $\#12 \leftarrow d_1^p$, $\#13 \leftarrow d_2^p$; **Scenario:** CH47RecordingSignalAnalysis/20080220T204528.

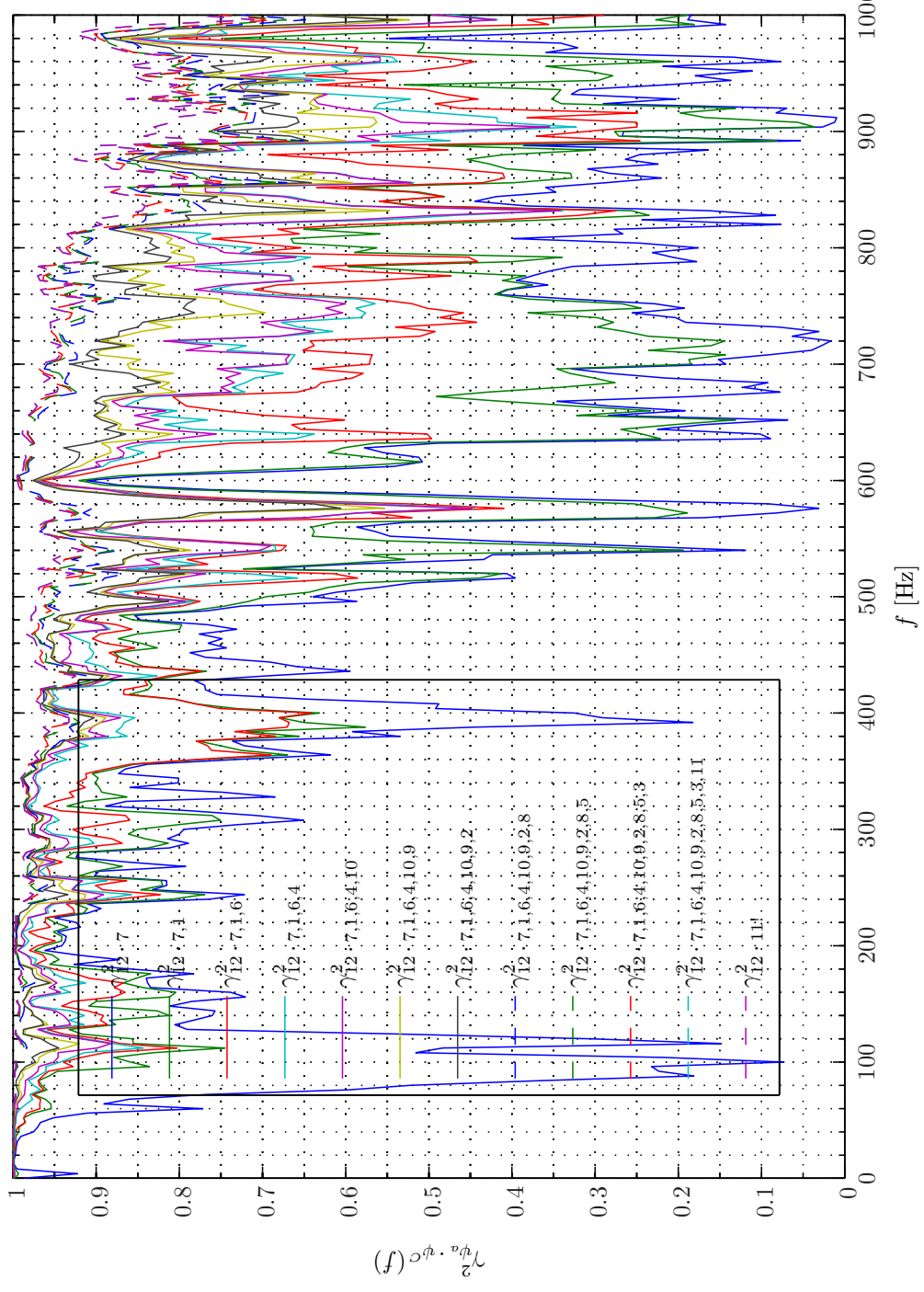

Sim D.4.10: *Multiple Magnitude-Squared Coherence Functions* $\gamma^2_{\psi_a \cdot \psi^C}(f)$: **Statistical Data Analysis**: Single-Sided Modified Periodogram, f_s = 32.768 kHz, N_{DFT} = 8192, L_{DFT} = 8193, R_{DFT} = 4097, Hanning, Δf_m = 16 Hz, T_{DFT} = 0.25003 s, $N_{f,DFT}$ = 4097, Δf_{DFT} = 4 Hz, K_{DFT} = 46; CH-47 Recordings Airbase Sosterberg 23 November 2005, Channel: 1,2,3,4,5,6,7,8,9,10,11,12,13,14,15,16,17, Scenario(0,1), 0 – 30 s (f_s = 32.768 kHz, $N_{A/D}$ = 24); **Topology:** BK 4949 surface microphones flush-mounted on a Gentex HGU-55/P helmet mounted on a BK 4128 C HATS, Terma Earcup Audio System (Feedforward, mFx, $N_x = 11, N_e = 2, N_y = 2, N_p = 2, N_v = 0$); *Channels:* #1 $\leftarrow x_1$, #2 $\leftarrow x_2$, #3 $\leftarrow x_3$, #4 $\leftarrow x_4$, #5 $\leftarrow x_5$, #6 $\leftarrow x_6$, #7 $\leftarrow x_7$, #8 $\leftarrow x_8$, #9 $\leftarrow x_9$, #10 $\leftarrow x_{10}$, #11 $\leftarrow x_{11}$, #12 $\leftarrow d_1^p$, #13 $\leftarrow d_2^p$; **Scenario:** `CH47RecordingSignalAnalysis/20080220T204528`.

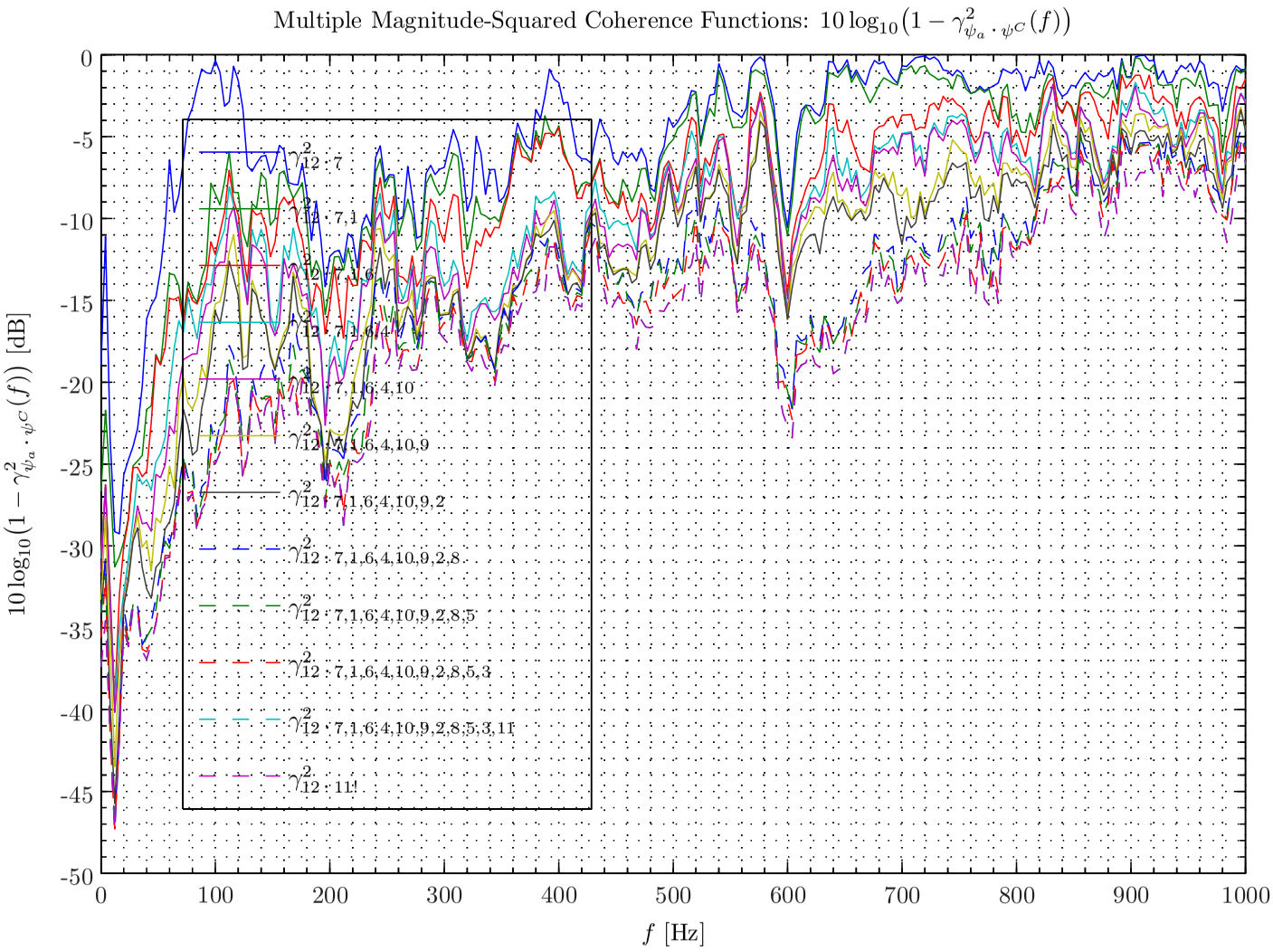

Sim D.4.11: *Attenuation vs Multiple Magnitude-Squared Coherence Functions* $10\log_{10}(1-\gamma^2_{\psi_a\cdot\psi^C}(f))$: **Statistical Data Analysis**: Single-Sided Modified Periodogram, $f_s = 32.768$ kHz, $N_{DFT} = 8192$, $L_{DFT} = 8193$, $R_{DFT} = 4097$, Hanning, $\Delta f_m = 16$ Hz, $T_{DFT} = 0.25003$ s, $N_{f,DFT} = 4097$, $\Delta f_{DFT} = 4$ Hz, $K_{DFT} = 46$; CH-47 Recordings Airbase Sosterberg 23 November 2005, Channel: 1,2,3,4,5,6,7,8,9,10,11,12,13,14,15,16,17, Scenario(0,1), $0-30$ s ($f_s = 32.768$ kHz, $N_{A/D} = 24$); **Topology:** BK 4949 surface microphones flush-mounted on a Gentex HGU-55/P helmet mounted on a BK 4128 C HATS, Terma Earcup Audio System (Feedforward, mFx, $N_x = 11, N_e = 2, N_y = 2, N_p = 2, N_v = 0$); *Channels:* #1 $\leftarrow x_1$, #2 $\leftarrow x_2$, #3 $\leftarrow x_3$, #4 $\leftarrow x_4$, #5 $\leftarrow x_5$, #6 $\leftarrow x_6$, #7 $\leftarrow x_7$, #8 $\leftarrow x_8$, #9 $\leftarrow x_9$, #10 $\leftarrow x_{10}$, #11 $\leftarrow x_{11}$, #12 $\leftarrow d_1^p$, #13 $\leftarrow d_2^p$; **Scenario:** CH47RecordingSignalAnalysis/20080220T204528.

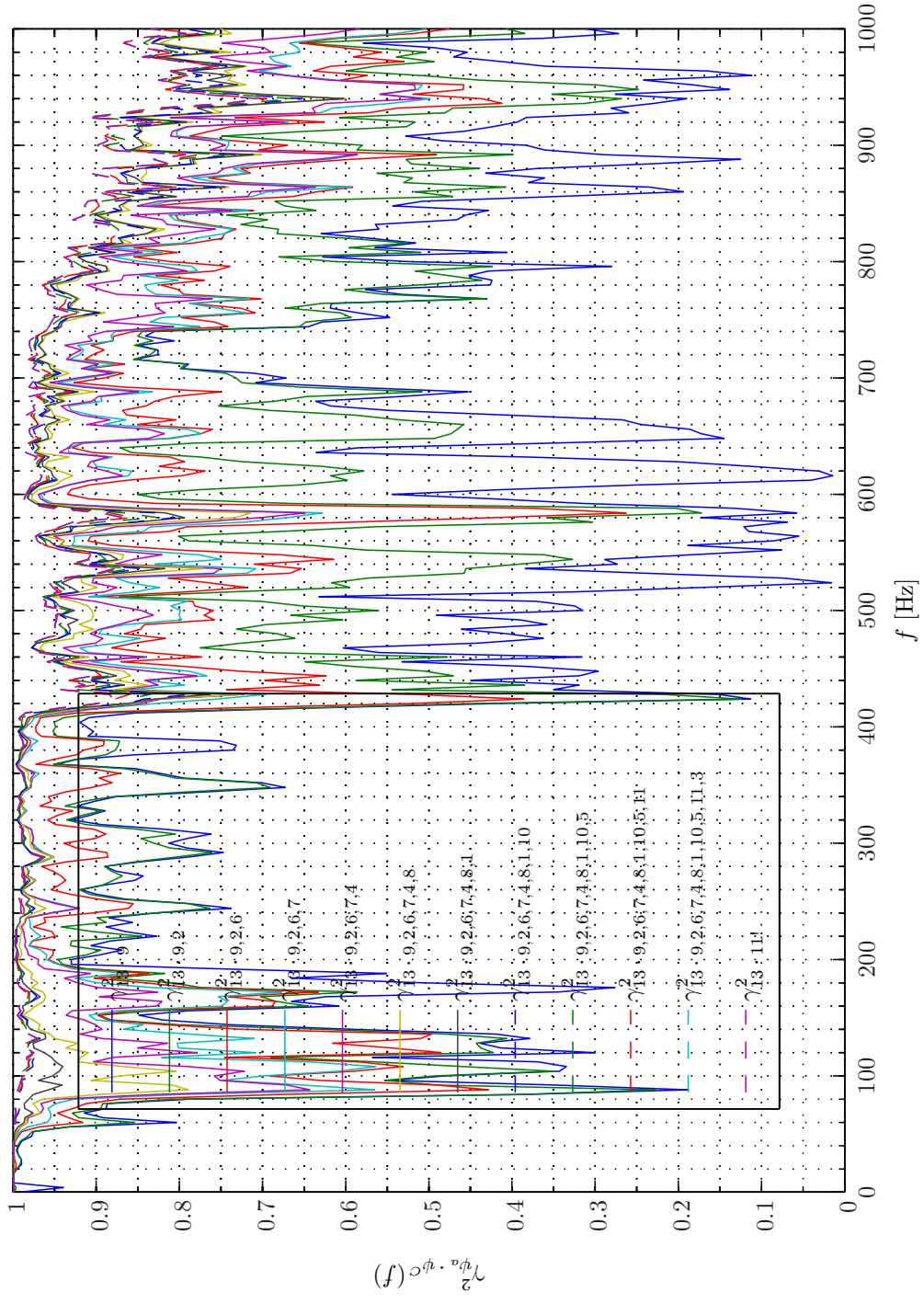

Sim D.4.12: *Multiple Magnitude-Squared Coherence Functions* $\gamma^2_{\psi_a \cdot \psi^C}(f)$: **Statistical Data Analysis**: Single-Sided Modified Periodogram, f_s = 32.768 kHz, N_{DFT} = 8192, L_{DFT} = 8193, R_{DFT} = 4097, Hanning, Δf_m = 16 Hz, T_{DFT} = 0.25003 s, $N_{f,DFT}$ = 4097, Δf_{DFT} = 4 Hz, K_{DFT} = 46; CH-47 Recordings Airbase Sosterberg 23 November 2005, Channel: 1,2,3,4,5,6,7,8,9,10,11,12,13,14,15,16,17, Scenario(0,1), 0 – 30 s (f_s = 32.768 kHz, $N_{A/D}$ = 24); **Topology:** BK 4949 surface microphones flush-mounted on a Gentex HGU-55/P helmet mounted on a BK 4128 C HATS, Terma Earcup Audio System (Feedforward, mFx, $N_x = 11, N_e = 2, N_y = 2, N_p = 2, N_v = 0$); *Channels:* #1 ← x_1, #2 ← x_2, #3 ← x_3, #4 ← x_4, #5 ← x_5, #6 ← x_6, #7 ← x_7, #8 ← x_8, #9 ← x_9, #10 ← x_{10}, #11 ← x_{11}, #12 ← d_1^P, #13 ← d_2^P; **Scenario:** `CH47RecordingSignalAnalysis/20080220T204528`.

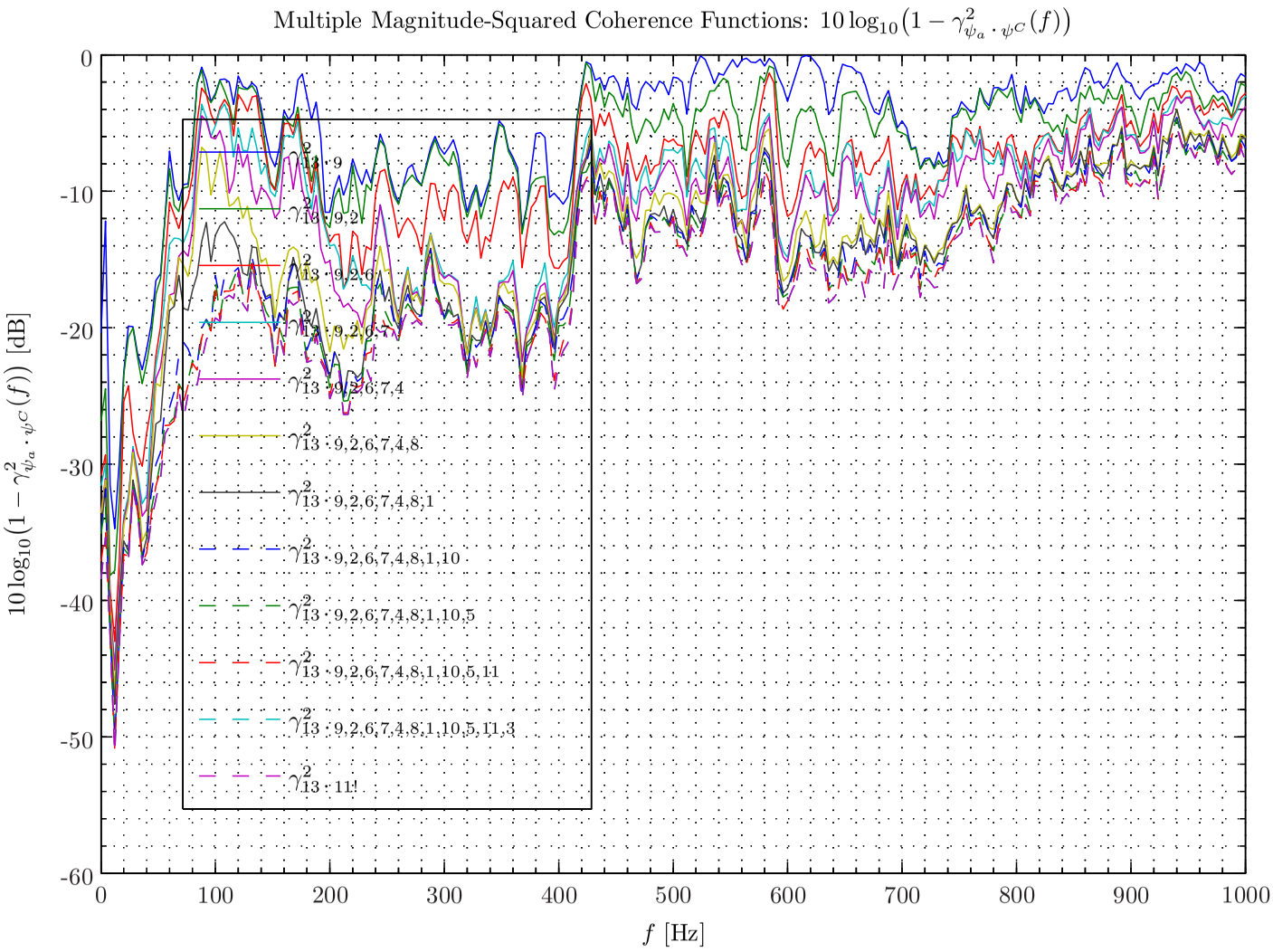

Sim D.4.13: *Attenuation vs Multiple Magnitude-Squared Coherence Functions* $10\log_{10}(1-\gamma^2_{\psi_a\cdot\psi^C}(f))$: **Statistical Data Analysis**: Single-Sided Modified Periodogram, $f_s = 32.768$ kHz, $N_{DFT} = 8192$, $L_{DFT} = 8193$, $R_{DFT} = 4097$, Hanning, $\Delta f_m = 16$ Hz, $T_{DFT} = 0.25003$ s, $N_{f,DFT} = 4097$, $\Delta f_{DFT} = 4$ Hz, $K_{DFT} = 46$; CH-47 Recordings Airbase Sosterberg 23 November 2005, Channel: 1,2,3,4,5,6,7,8,9,10,11,12,13,14,15,16,17, Scenario(0,1), $0-30$ s ($f_s = 32.768$ kHz, $N_{A/D} = 24$); **Topology:** BK 4949 surface microphones flush-mounted on a Gentex HGU-55/P helmet mounted on a BK 4128 C HATS, Terma Earcup Audio System (Feedforward, mFx, $N_x = 11, N_e = 2, N_y = 2, N_p = 2, N_v = 0$); *Channels:* #1 $\leftarrow x_1$, #2 $\leftarrow x_2$, #3 $\leftarrow x_3$, #4 $\leftarrow x_4$, #5 $\leftarrow x_5$, #6 $\leftarrow x_6$, #7 $\leftarrow x_7$, #8 $\leftarrow x_8$, #9 $\leftarrow x_9$, #10 $\leftarrow x_{10}$, #11 $\leftarrow x_{11}$, #12 $\leftarrow d_1^p$, #13 $\leftarrow d_2^p$; **Scenario:** CH47RecordingSignalAnalysis/20080220T204528.

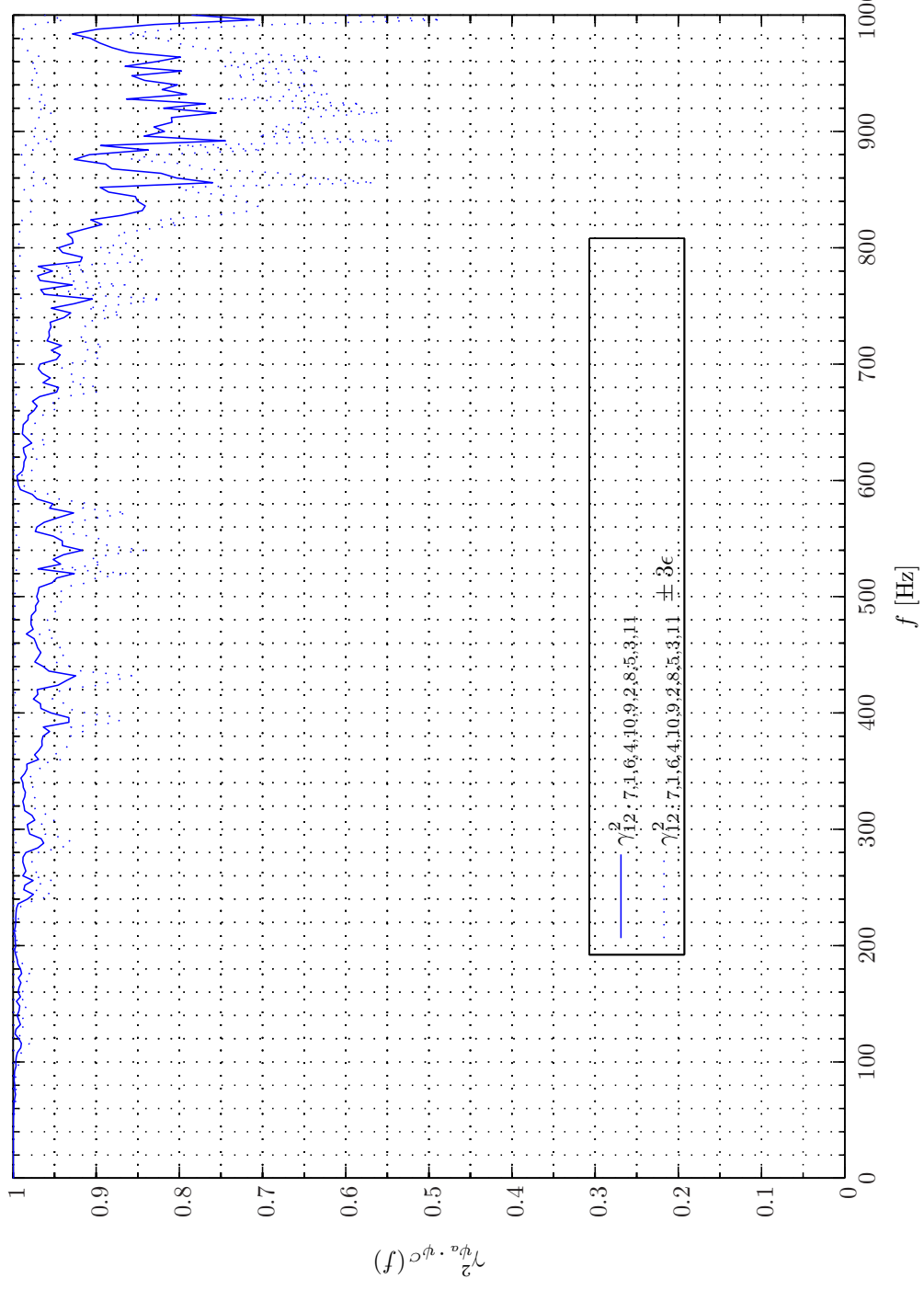

Sim D.4.14: *Multiple Magnitude-Squared Coherence Functions* $\gamma^2_{\psi_a \cdot \psi^C}(f)$: **Statistical Data Analysis**: Single-Sided Modified Periodogram, f_s = 32.768 kHz, N_{DFT} = 8192, L_{DFT} = 8193, R_{DFT} = 4097, Hanning, Δf_m = 16 Hz, T_{DFT} = 0.25003 s, $N_{f,DFT}$ = 4097, Δf_{DFT} = 4 Hz, K_{DFT} = 46; CH-47 Recordings Airbase Sosterberg 23 November 2005, Channel: 1,2,3,4,5,6,7,8,9,10,11,12,13,14,15,16,17, Scenario(0,1), 0 – 30 s (f_s = 32.768 kHz, $N_{A/D}$ = 24); **Topology:** BK 4949 surface microphones flush-mounted on a Gentex HGU-55/P helmet mounted on a BK 4128 C HATS, Terma Earcup Audio System (Feedforward, mFx, $N_x = 11, N_e = 2, N_y = 2, N_p = 2, N_v = 0$); *Channels:* #1 ← x_1, #2 ← x_2, #3 ← x_3, #4 ← x_4, #5 ← x_5, #6 ← x_6, #7 ← x_7, #8 ← x_8, #9 ← x_9, #10 ← x_{10}, #11 ← x_{11}, #12 ← d_1^P, #13 ← d_2^P; **Scenario:** `CH47RecordingSignalAnalysis/20080220T204528`.

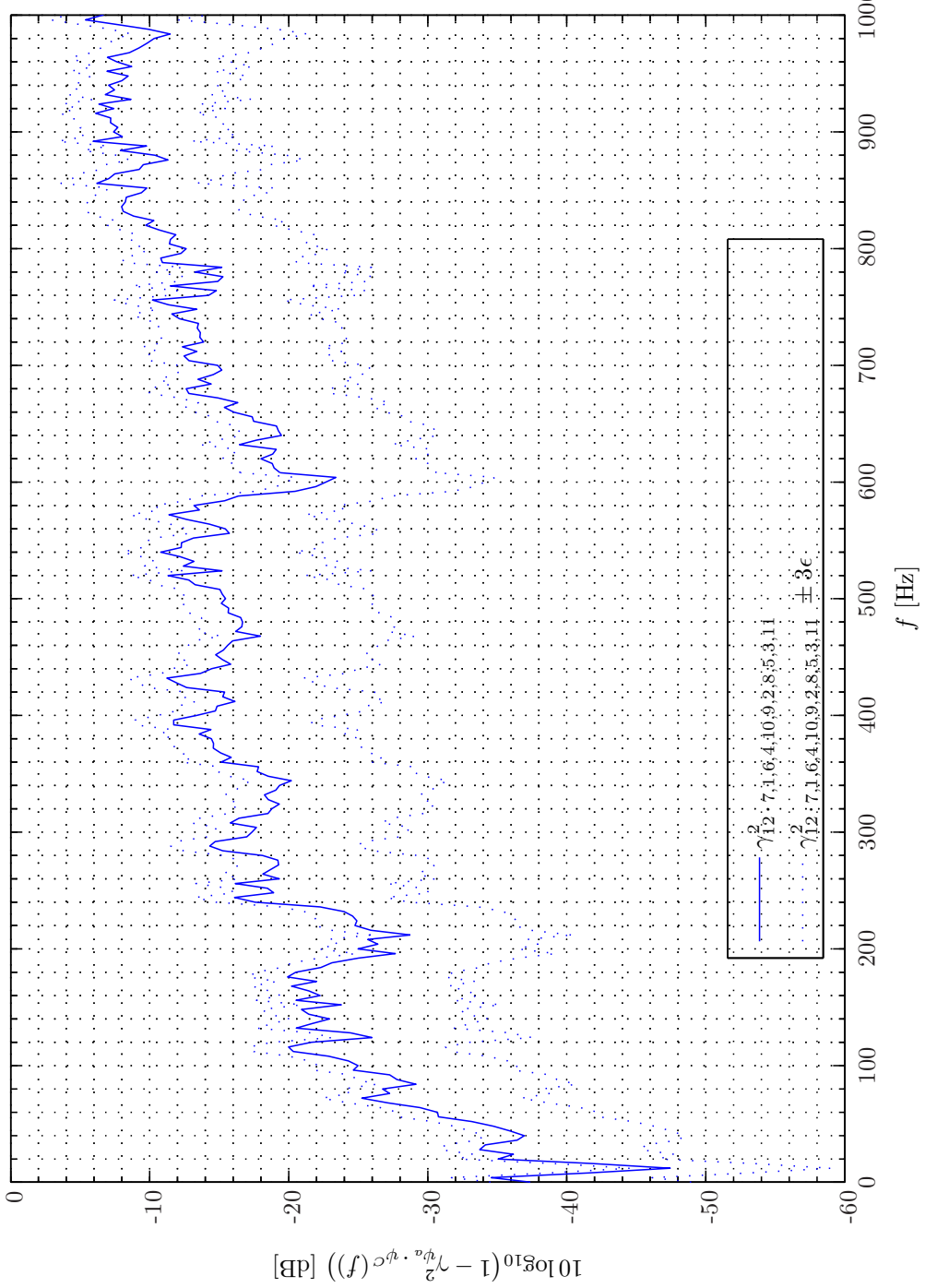

Sim D.4.15: *Attenuation vs Multiple Magnitude-Squared Coherence Functions* $10\log_{10}(1-\gamma^2_{\psi_a\cdot\psi^C}(f))$: **Statistical Data Analysis:** Single-Sided Modified Periodogram, $f_s = 32.768$ kHz, $N_{DFT} = 8192$, $L_{DFT} = 8193$, $R_{DFT} = 4097$, Hanning, $\Delta f_m = 16$ Hz, $T_{DFT} = 0.25003$ s, $N_{f,DFT} = 4097$, $\Delta f_{DFT} = 4$ Hz, $K_{DFT} = 46$; CH-47 Recordings Airbase Sosterberg 23 November 2005, Channel: 1,2,3,4,5,6,7,8,9,10,11,12,13,14,15,16,17, Scenario(0,1), $0-30$ s ($f_s = 32.768$ kHz, $N_{A/D} = 24$); **Topology:** BK 4949 surface microphones flush-mounted on a Gentex HGU-55/P helmet mounted on a BK 4128 C HATS, Terma Earcup Audio System (Feedforward, mFx, $N_x = 11, N_e = 2, N_y = 2, N_p = 2, N_v = 0$); *Channels:* #1 $\leftarrow x_1$, #2 $\leftarrow x_2$, #3 $\leftarrow x_3$, #4 $\leftarrow x_4$, #5 $\leftarrow x_5$, #6 $\leftarrow x_6$, #7 $\leftarrow x_7$, #8 $\leftarrow x_8$, #9 $\leftarrow x_9$, #10 $\leftarrow x_{10}$, #11 $\leftarrow x_{11}$, #12 $\leftarrow d_1^p$, #13 $\leftarrow d_2^p$; **Scenario:** `CH47RecordingSignalAnalysis/20080220T204528`.

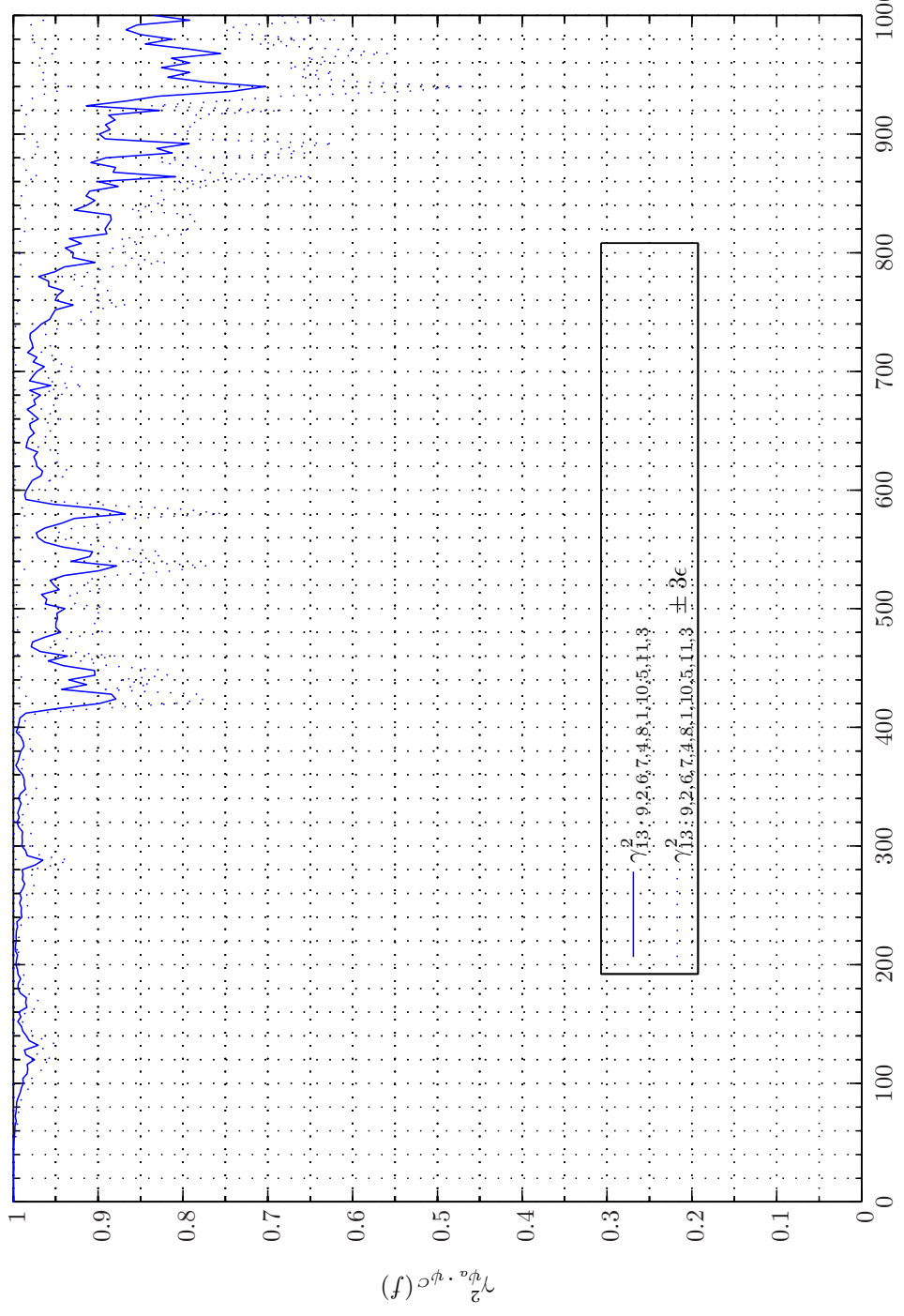

Sim D.4.16: *Multiple Magnitude-Squared Coherence Functions* $\gamma^2_{\psi_a \cdot \psi^C}(f)$: **Statistical Data Analysis**: Single-Sided Modified Periodogram, f_s = 32.768 kHz, N_{DFT} = 8192, L_{DFT} = 8193, R_{DFT} = 4097, Hanning, Δf_m = 16 Hz, T_{DFT} = 0.25003 s, $N_{f,DFT}$ = 4097, Δf_{DFT} = 4 Hz, K_{DFT} = 46; CH-47 Recordings Airbase Sosterberg 23 November 2005, Channel: 1,2,3,4,5,6,7,8,9,10,11,12,13,14,15,16,17, Scenario(0,1), 0 – 30 s (f_s = 32.768 kHz, $N_{A/D}$ = 24); **Topology:** BK 4949 surface microphones flush-mounted on a Gentex HGU-55/P helmet mounted on a BK 4128 C HATS, Terma Earcup Audio System (Feedforward, mFx, $N_x = 11, N_e = 2, N_y = 2, N_p = 2, N_v = 0$); *Channels:* #1 ← x_1, #2 ← x_2, #3 ← x_3, #4 ← x_4, #5 ← x_5, #6 ← x_6, #7 ← x_7, #8 ← x_8, #9 ← x_9, #10 ← x_{10}, #11 ← x_{11}, #12 ← d_1^P, #13 ← d_2^P; **Scenario:** `CH47RecordingSignalAnalysis/20080220T204528`.

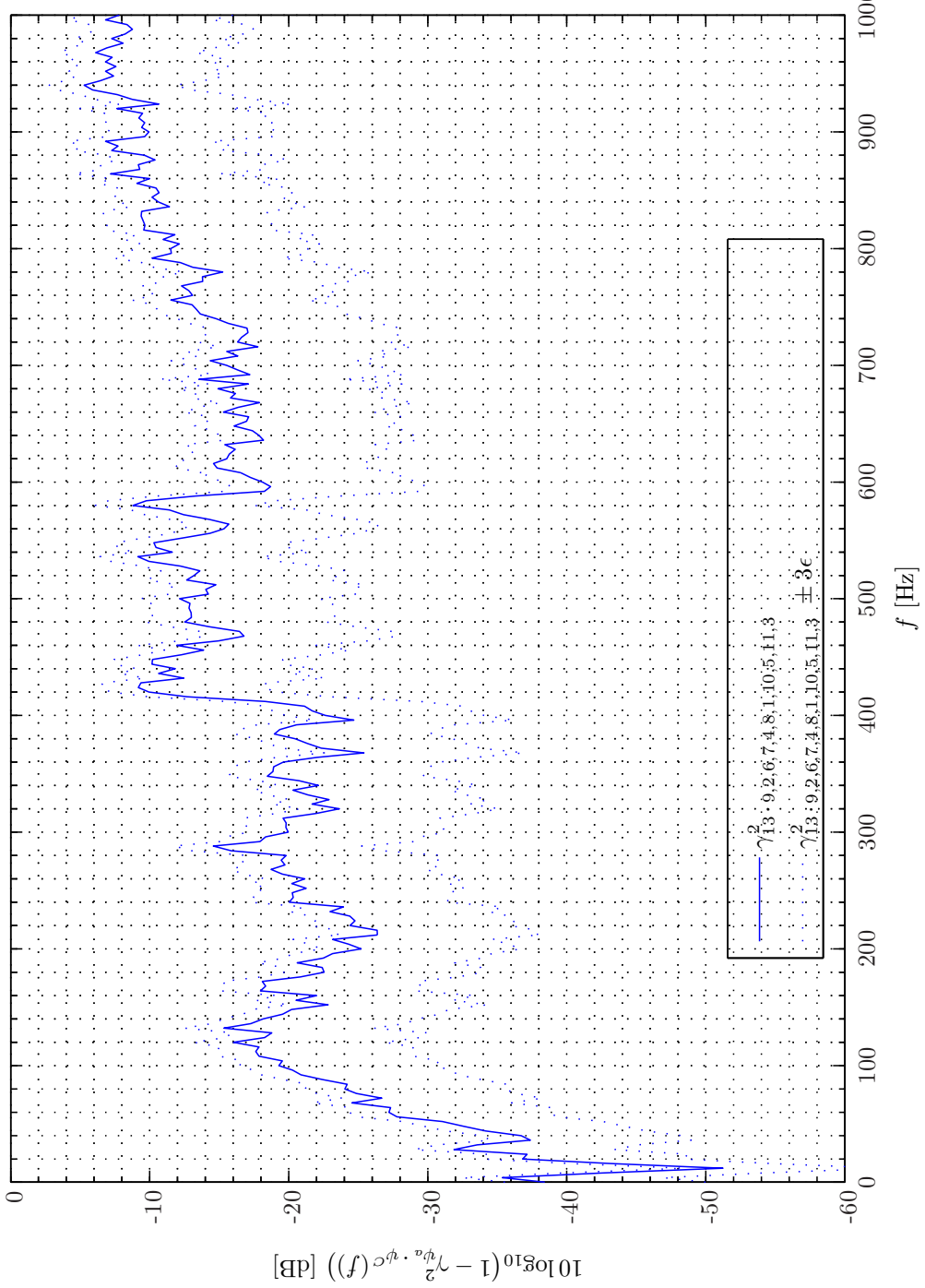

Sim D.4.17: *Attenuation vs Multiple Magnitude-Squared Coherence Functions* $10\log_{10}(1-\gamma^2_{\psi_a\cdot\psi^C}(f))$: **Statistical Data Analysis:** Single-Sided Modified Periodogram, $f_s = 32.768$ kHz, $N_{DFT} = 8192$, $L_{DFT} = 8193$, $R_{DFT} = 4097$, Hanning, $\Delta f_m = 16$ Hz, $T_{DFT} = 0.25003$ s, $N_{f,DFT} = 4097$, $\Delta f_{DFT} = 4$ Hz, $K_{DFT} = 46$; CH-47 Recordings Airbase Sosterberg 23 November 2005, Channel: 1,2,3,4,5,6,7,8,9,10,11,12,13,14,15,16,17, Scenario(0,1), $0-30$ s ($f_s = 32.768$ kHz, $N_{A/D} = 24$); **Topology:** BK 4949 surface microphones flush-mounted on a Gentex HGU-55/P helmet mounted on a BK 4128 C HATS, Terma Earcup Audio System (Feedforward, mFx, $N_x = 11, N_e = 2, N_y = 2, N_p = 2, N_v = 0$); *Channels:* #1 $\leftarrow x_1$, #2 $\leftarrow x_2$, #3 $\leftarrow x_3$, #4 $\leftarrow x_4$, #5 $\leftarrow x_5$, #6 $\leftarrow x_6$, #7 $\leftarrow x_7$, #8 $\leftarrow x_8$, #9 $\leftarrow x_9$, #10 $\leftarrow x_{10}$, #11 $\leftarrow x_{11}$, #12 $\leftarrow d_1^p$, #13 $\leftarrow d_2^p$; **Scenario:** CH47RecordingSignalAnalysis/20080220T204528.

sented. Except for this skewness the distributions most closely resembles a pattern characteristic for a sinusoidal signal in Gaussian noise. This corresponds to the field being largely dominated by the extreme noise field produced under the passage at a constant rotations per minute (rpm) of the rotor blades above the helicopter hull. Now the variation among the sensor signal pdfs is relative small. The pattern is skewed to positive pressures which might explained by the presence of an acoustic flow in the helicopter cabin.

The auto spectral density functions are shown in Simulation D.4.22 on page 600. The corresponding averaged sound pressure levels can be found in Table D.5.

Signal	x_1	x_2	x_3	x_4	x_5	x_6	x_7	x_8	x_9	x_{10}	x_{11}	d_1^p
SPL	132.5	132.2	131.8	131.3	131.7	131.6	131.2	130.6	131.4	132.5	132.5	129.6

Tab. D.5: Scenario Flight at Constant Altitude and High Speed, average sound pressure levels re. 20 µPa.

Compared with the previous scenario viz. Simulation D.4.5 on page 581 a general huge increase in the auto spectral density function can be observed. In particular in the low frequency region the increase is of the order of 50 dB. The OCOFs and related achievable ANR from (2.2.1) on page 18 are depicted in Simulation D.4.23 on page 601 and Simulation D.4.24 on page 602 respectively.

Comparing with the previous example viz. Simulation D.4.6 on page 582 and Simulation D.4.7 on page 584 the trough at 100 Hz is less pronounced here and the OCOF is in general slightly higher in this extreme noise case. A possible explanation for this could be that the direction of sound field propagation is more unidirectional. Still from an FFS based AC perspective using a *single* reference sensor as opposed to the confined array of reference sensors would be very little beneficial as attenuation above 10 dB is limited to the very low-frequency under approximately 60 Hz.

A deep trough observed in the OCOF observed in the vicinity of 100 Hz except for reference sensor x_1.

Now, considering the MCOFs displayed in Simulation D.4.25 - D.4.26 on pages 603–604 we observe a general decrease in coherence. Hence, attenuation figures above 10 dB is now only predicted possible up to 200 Hz.

In the low-frequency region up to 100 Hz the MCOF predicts from 2 dB to 10 dB better ANR performance from using the confined reference sensor array as opposed to a single reference sensor. Unfortunately, the apparent . The reason for this drop in coherence as compared with the results in Simulation D.4.25 - D.4.26 on pages 603–604 is presently not understood. The dynamic range (3% distortion level) of the BK 4158 C right ear simulator and BK 4159 C left ear simulator extends to 161 dB re 20 µPa respectively. For the BK 4949 surface microphones 140 dB re 20 µPa (500 Hz, 3% distortion level) is specified. This corresponds to 200 Pa and referring to Table D.5 we have actually pushed the surface microphones close to their limits for linear operation. The actual behavior of the BK 4949 surface microphones exposed to this very low-frequency contents has to be assessed by some BK experts. It should also be remarked that performance sensor 2 failed during this measurement and therefore not considered here. During the measurement acquisition it was observed that the entire frame depicted in Figure D.14 was heavily vibrating like all of us owing to the extreme noise pressures and relative small vibration isolation provided by bench used by helicopter personnel and passengers under flight. Moreover, in Simulation D.4.25 some saturation MCOF is seen. Hence, by including additional reference sensors would not push the upper frequency limit determined by the MCOF until the reason for the general drop in MCOF has been clarified.

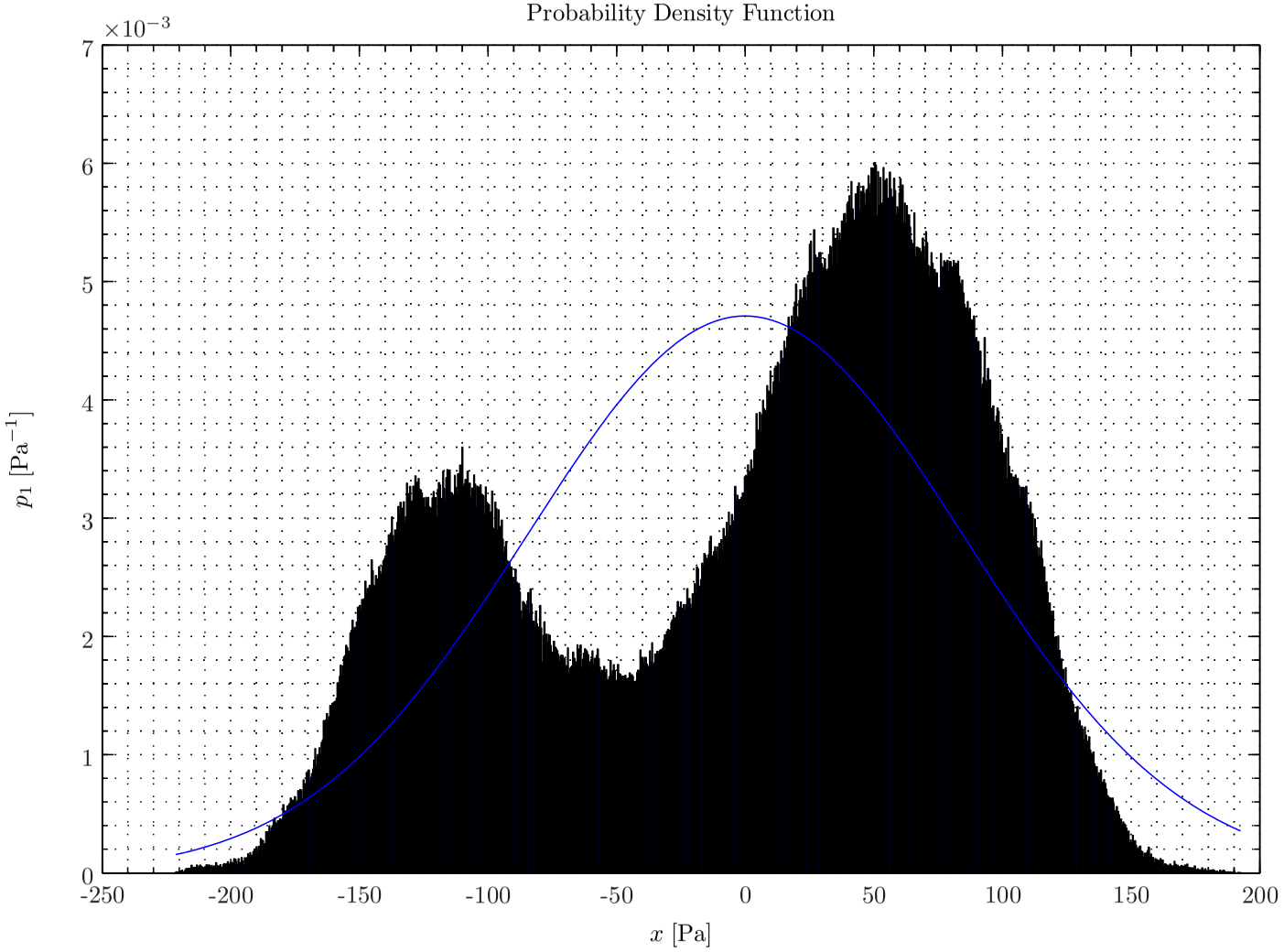

Sim D.4.18: *Probability Density Functions*: **Statistical Data Analysis**: Single-Sided Modified Periodogram, $f_s = 32.768$ kHz, $N_{DFT} = 8192$, $L_{DFT} = 8193$, $R_{DFT} = 4097$, Hanning, $\Delta f_m = 16$ Hz, $T_{DFT} = 0.25003$ s, $N_{f,DFT} = 4097$, $\Delta f_{DFT} = 4$ Hz, $K_{DFT} = 238$; CH-47 Recordings Airbase Sosterberg 23 November 2005, Channel: 1,2,3,4,5,6,7,8,9,10,11,12,13,14,15,16,17, Scenario(2,2), $0 - 30$ s ($f_s = 32.768$ kHz, $N_{A/D} = 24$); **Topology:** BK 4949 surface microphones flush-mounted on a Gentex HGU-55/P helmet mounted on a BK 4128 C HATS, Terma Earcup Audio System (Feedforward, mFx, $N_x = 11, N_e = 2, N_y = 2, N_p = 2, N_v = 0$); *Channels:* $\#1 \leftarrow x_1$, $\#2 \leftarrow x_2$, $\#3 \leftarrow x_3$, $\#4 \leftarrow x_4$, $\#5 \leftarrow x_5$, $\#6 \leftarrow x_6$, $\#7 \leftarrow x_7$, $\#8 \leftarrow x_8$, $\#9 \leftarrow x_9$, $\#10 \leftarrow x_{10}$, $\#11 \leftarrow x_{11}$, $\#12 \leftarrow d_1^p$, $\#13 \leftarrow d_2^p$; **Scenario:** `CH47RecordingSignalAnalysis/20080220T222150`.

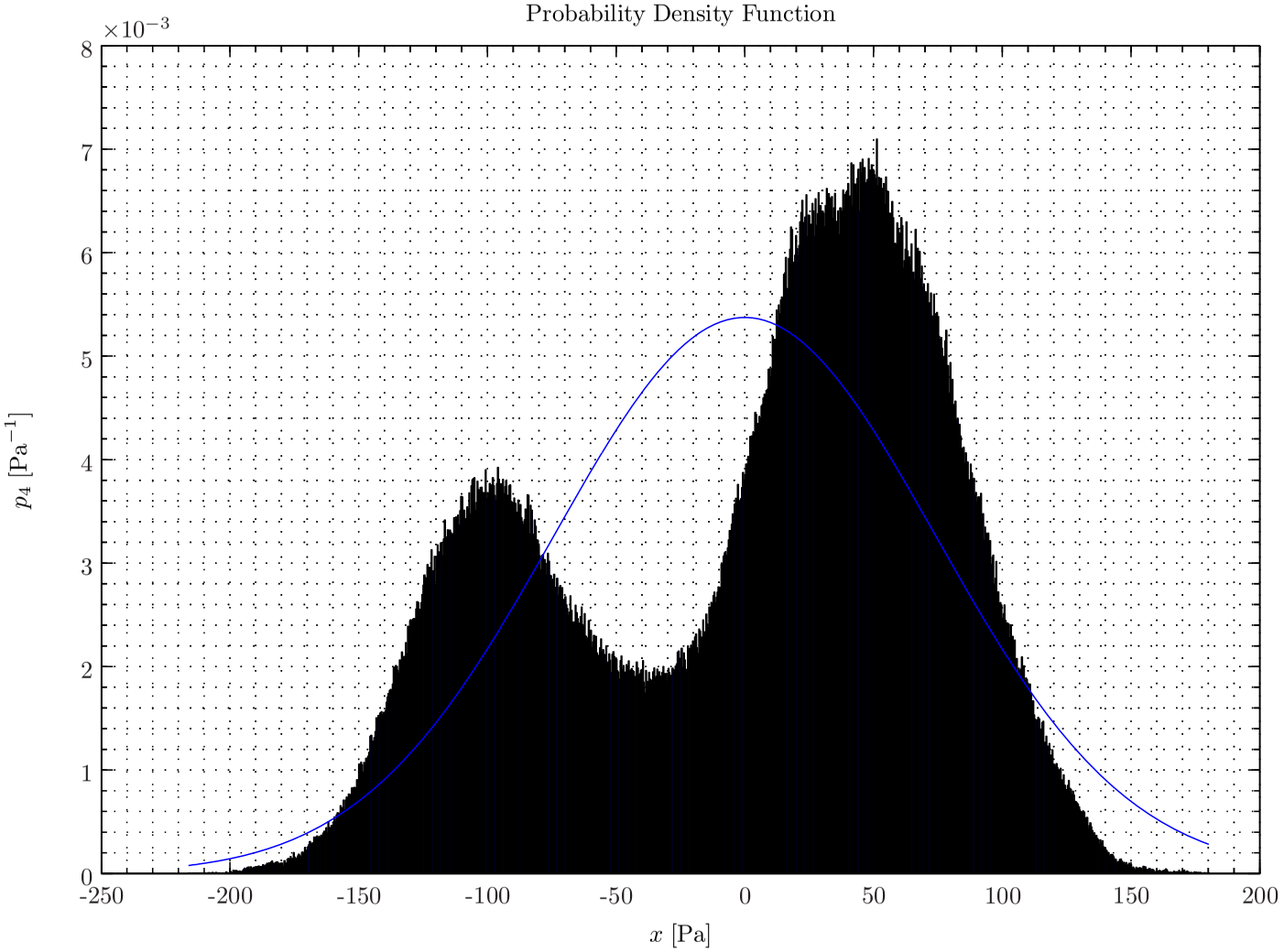

Sim D.4.19: *Probability Density Functions*: **Statistical Data Analysis**: Single-Sided Modified Periodogram, $f_s = 32.768$ kHz, $N_{DFT} = 8192$, $L_{DFT} = 8193$, $R_{DFT} = 4097$, Hanning, $\Delta f_m = 16$ Hz, $T_{DFT} = 0.25003$ s, $N_{f,DFT} = 4097$, $\Delta f_{DFT} = 4$ Hz, $K_{DFT} = 238$; CH-47 Recordings Airbase Sosterberg 23 November 2005, Channel: 1,2,3,4,5,6,7,8,9,10,11,12,13,14,15,16,17, Scenario(2,2), $0 - 30$ s ($f_s = 32.768$ kHz, $N_{A/D} = 24$); **Topology:** BK 4949 surface microphones flush-mounted on a Gentex HGU-55/P helmet mounted on a BK 4128 C HATS, Terma Earcup Audio System (Feedforward, mFx, $N_x = 11, N_e = 2, N_y = 2, N_p = 2, N_v = 0$); *Channels:* $\#1 \leftarrow x_1$, $\#2 \leftarrow x_2$, $\#3 \leftarrow x_3$, $\#4 \leftarrow x_4$, $\#5 \leftarrow x_5$, $\#6 \leftarrow x_6$, $\#7 \leftarrow x_7$, $\#8 \leftarrow x_8$, $\#9 \leftarrow x_9$, $\#10 \leftarrow x_{10}$, $\#11 \leftarrow x_{11}$, $\#12 \leftarrow d_1^p$, $\#13 \leftarrow d_2^p$; **Scenario:** `CH47RecordingSignalAnalysis/20080220T222150`.

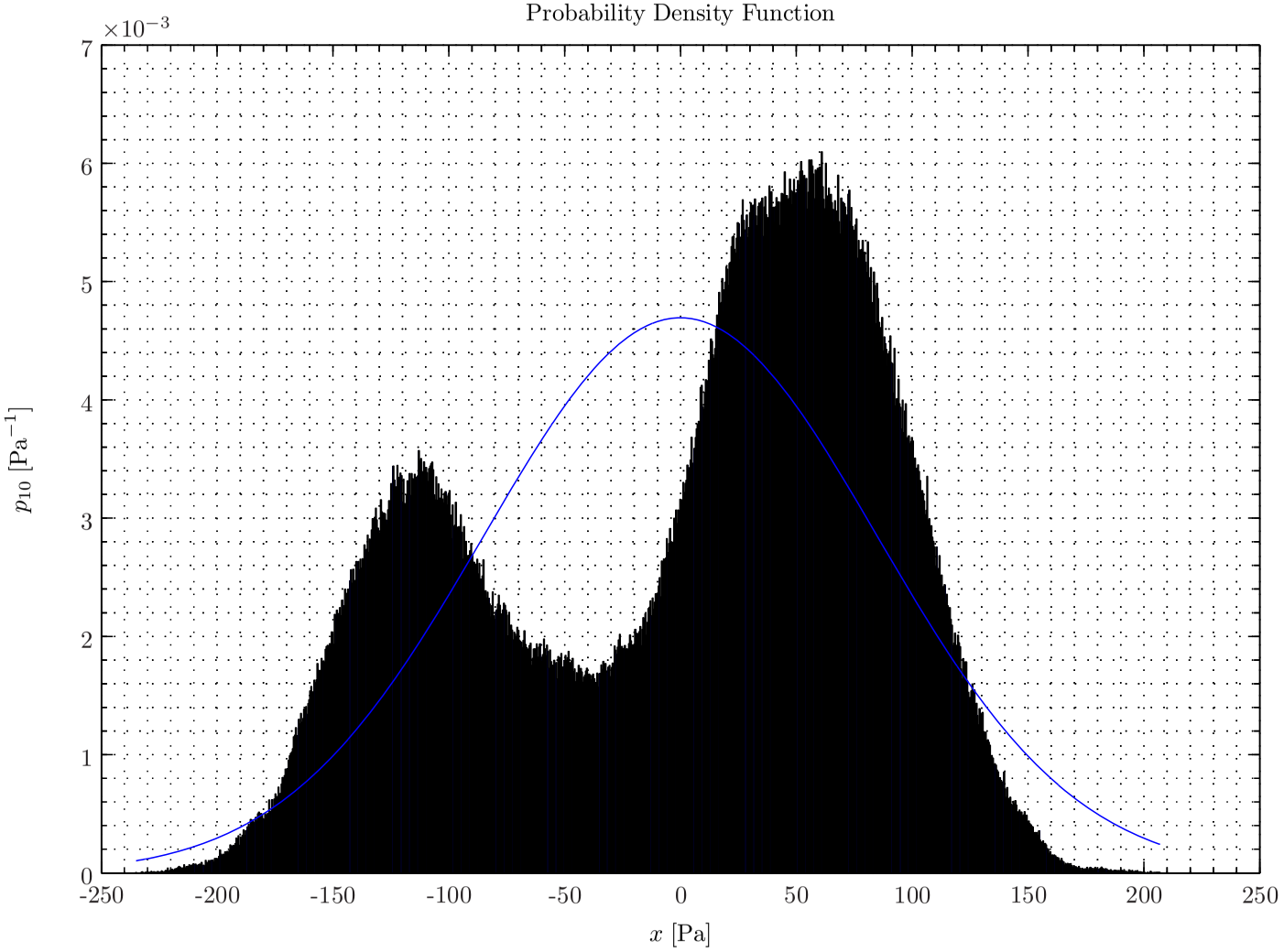

Sim D.4.20: *Probability Density Functions*: **Statistical Data Analysis**: Single-Sided Modified Periodogram, $f_s = 32.768$ kHz, $N_{DFT} = 8192$, $L_{DFT} = 8193$, $R_{DFT} = 4097$, Hanning, $\Delta f_m = 16$ Hz, $T_{DFT} = 0.25003$ s, $N_{f,DFT} = 4097$, $\Delta f_{DFT} = 4$ Hz, $K_{DFT} = 238$; CH-47 Recordings Airbase Sosterberg 23 November 2005, Channel: 1,2,3,4,5,6,7,8,9,10,11,12,13,14,15,16,17, Scenario(2,2), $0 - 30$ s ($f_s = 32.768$ kHz, $N_{A/D} = 24$); **Topology:** BK 4949 surface microphones flush-mounted on a Gentex HGU-55/P helmet mounted on a BK 4128 C HATS, Terma Earcup Audio System (Feedforward, mFx, $N_x = 11, N_e = 2, N_y = 2, N_p = 2, N_v = 0$); *Channels:* $\#1 \leftarrow x_1$, $\#2 \leftarrow x_2$, $\#3 \leftarrow x_3$, $\#4 \leftarrow x_4$, $\#5 \leftarrow x_5$, $\#6 \leftarrow x_6$, $\#7 \leftarrow x_7$, $\#8 \leftarrow x_8$, $\#9 \leftarrow x_9$, $\#10 \leftarrow x_{10}$, $\#11 \leftarrow x_{11}$, $\#12 \leftarrow d_1^p$, $\#13 \leftarrow d_2^p$; **Scenario:** `CH47RecordingSignalAnalysis/20080220T222150`.

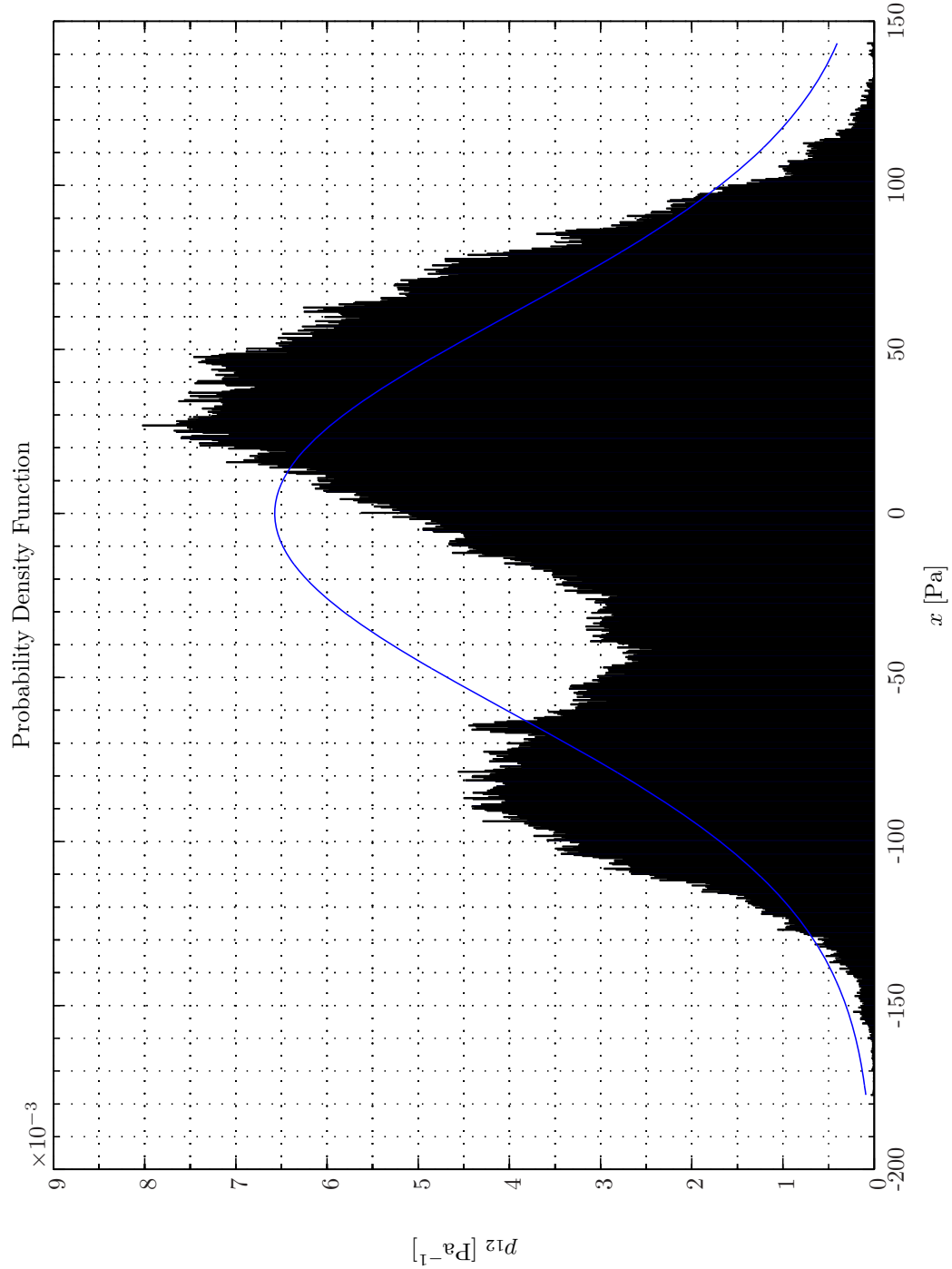

Sim D.4.21: *Probability Density Functions*: **Statistical Data Analysis**: Single-Sided Modified Periodogram, $f_s = 32.768$ kHz, $N_{DFT} = 8192$, $L_{DFT} = 8193$, $R_{DFT} = 4097$, Hanning, $\Delta f_m = 16$ Hz, $T_{DFT} = 0.25003$ s, $N_{f,DFT} = 4097$, $\Delta f_{DFT} = 4$ Hz, $K_{DFT} = 238$; CH-47 Recordings Airbase Sosterberg 23 November 2005, Channel: 1,2,3,4,5,6,7,8,9,10,11,12,13,14,15,16,17, Scenario(2,2), $0 - 30$ s ($f_s = 32.768$ kHz, $N_{A/D} = 24$); **Topology:** BK 4949 surface microphones flush-mounted on a Gentex HGU-55/P helmet mounted on a BK 4128 C HATS, Terma Earcup Audio System (Feedforward, mFx, $N_x = 11, N_e = 2, N_y = 2, N_p = 2, N_v = 0$); *Channels:* $\#1 \leftarrow x_1$, $\#2 \leftarrow x_2$, $\#3 \leftarrow x_3$, $\#4 \leftarrow x_4$, $\#5 \leftarrow x_5$, $\#6 \leftarrow x_6$, $\#7 \leftarrow x_7$, $\#8 \leftarrow x_8$, $\#9 \leftarrow x_9$, $\#10 \leftarrow x_{10}$, $\#11 \leftarrow x_{11}$, $\#12 \leftarrow d_1^p$, $\#13 \leftarrow d_2^p$; **Scenario:** `CH47RecordingSignalAnalysis/20080220T222150`.

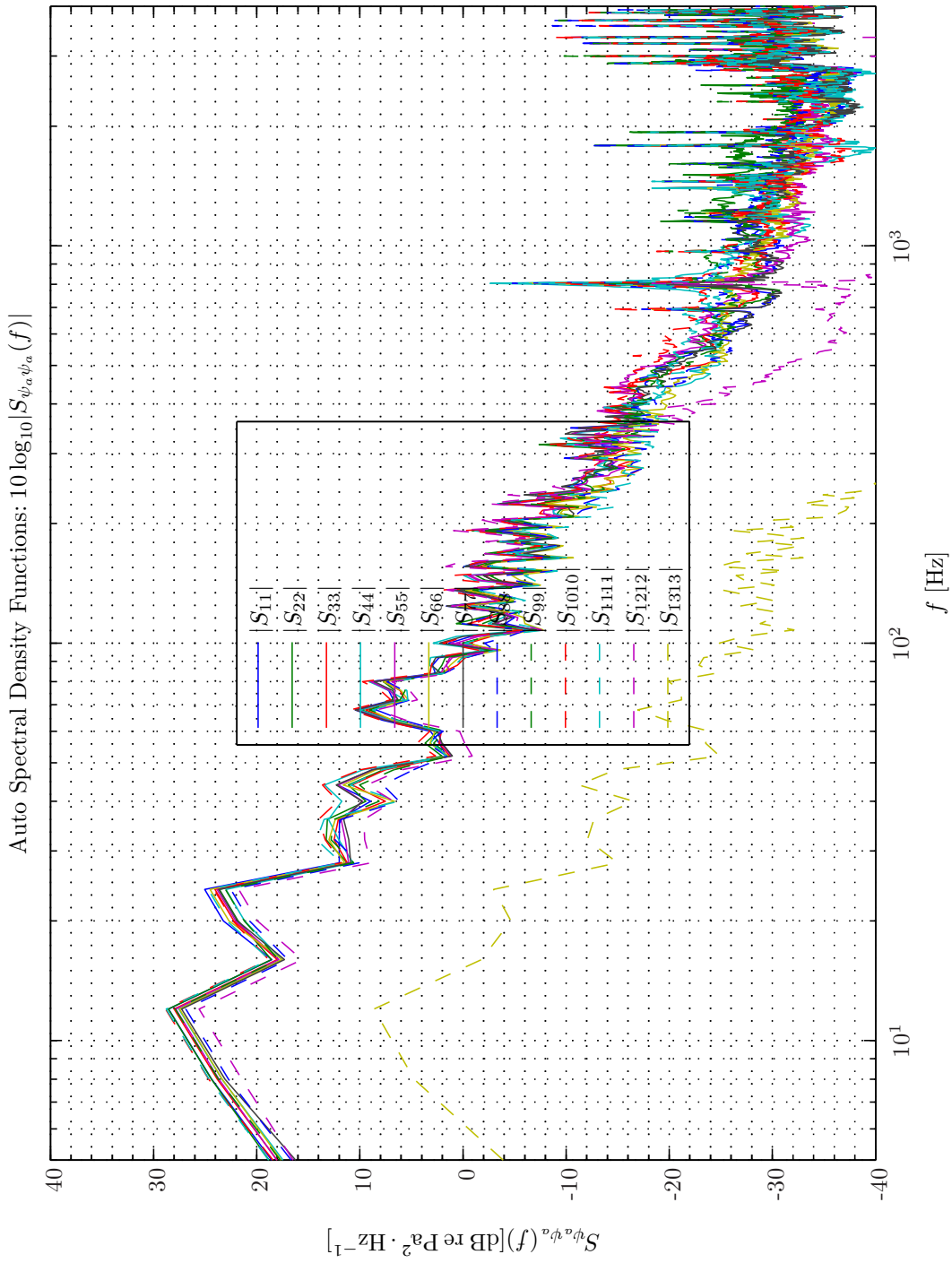

Sim D.4.22: *Autospectral Density Functions*: **Statistical Data Analysis**: Single-Sided Modified Periodogram, f_s = 32.768 kHz, N_{DFT} = 8192, L_{DFT} = 8193, R_{DFT} = 4097, Hanning, Δf_m = 16 Hz, T_{DFT} = 0.25003 s, $N_{f,DFT}$ = 4097, Δf_{DFT} = 4 Hz, K_{DFT} = 238; CH-47 Recordings Airbase Sosterberg 23 November 2005, Channel: 1,2,3,4,5,6,7,8,9,10,11,12,13,14,15,16,17, Scenario(2,2), 0 − 30 s (f_s = 32.768 kHz, $N_{A/D}$ = 24); **Topology:** BK 4949 surface microphones flush-mounted on a Gentex HGU-55/P helmet mounted on a BK 4128 C HATS, Terma Earcup Audio System (Feedforward, mFx, $N_x = 11, N_e = 2, N_y = 2, N_p = 2, N_v = 0$); *Channels:* #1 ← x_1, #2 ← x_2, #3 ← x_3, #4 ← x_4, #5 ← x_5, #6 ← x_6, #7 ← x_7, #8 ← x_8, #9 ← x_9, #10 ← x_{10}, #11 ← x_{11}, #12 ← d_1^p, #13 ← d_2^p; **Scenario:** CH47RecordingSignalAnalysis/20080220T222150.

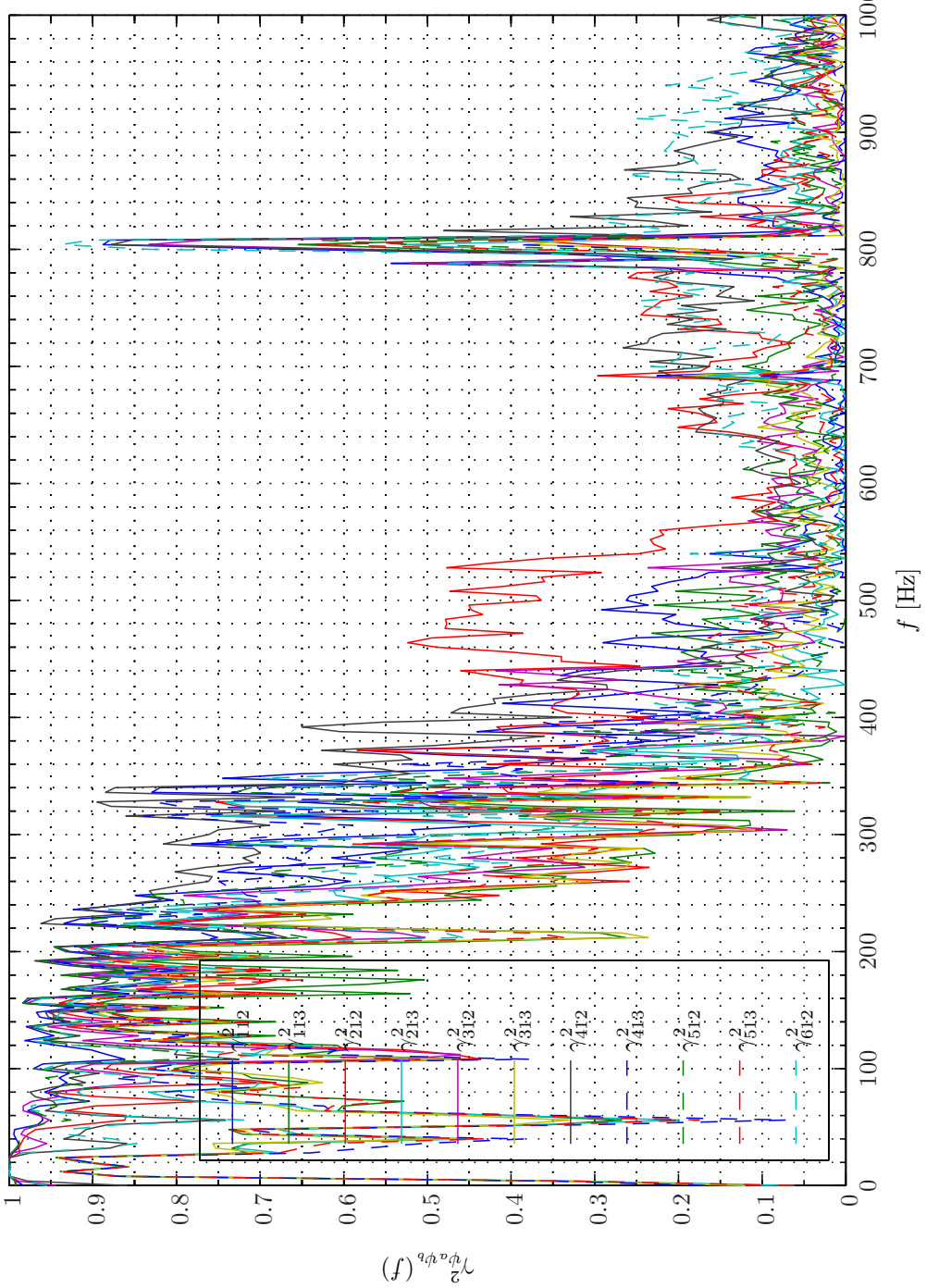

Sim D.4.23: *Ordinary Coherency-Squared Functions* $\gamma^2_{\psi_a\psi_b}(f)$: **Statistical Data Analysis**: Single-Sided Modified Periodogram, $f_s = 32.768$ kHz, $N_{DFT} = 8192$, $L_{DFT} = 8193$, $R_{DFT} = 4097$, Hanning, $\Delta f_m = 16$ Hz, $T_{DFT} = 0.25003$ s, $N_{f,DFT} = 4097$, $\Delta f_{DFT} = 4$ Hz, $K_{DFT} = 238$; CH-47 Recordings Airbase Sosterberg 23 November 2005, Channel: 1,2,3,4,5,6,7,8,9,10,11,12,13,14,15,16,17, Scenario(2,2), $0 - 30$ s ($f_s = 32.768$ kHz, $N_{A/D} = 24$); **Topology:** BK 4949 surface microphones flush-mounted on a Gentex HGU-55/P helmet mounted on a BK 4128 C HATS, Terma Earcup Audio System (Feedforward, mFx, $N_x = 11, N_e = 2, N_y = 2, N_p = 2, N_v = 0$); *Channels:* $\#1 \leftarrow x_1$, $\#2 \leftarrow x_2$, $\#3 \leftarrow x_3$, $\#4 \leftarrow x_4$, $\#5 \leftarrow x_5$, $\#6 \leftarrow x_6$, $\#7 \leftarrow x_7$, $\#8 \leftarrow x_8$, $\#9 \leftarrow x_9$, $\#10 \leftarrow x_{10}$, $\#11 \leftarrow x_{11}$, $\#12 \leftarrow d_1^p$, $\#13 \leftarrow d_2^p$; **Scenario:** `CH47RecordingSignalAnalysis/20080220T222150`.

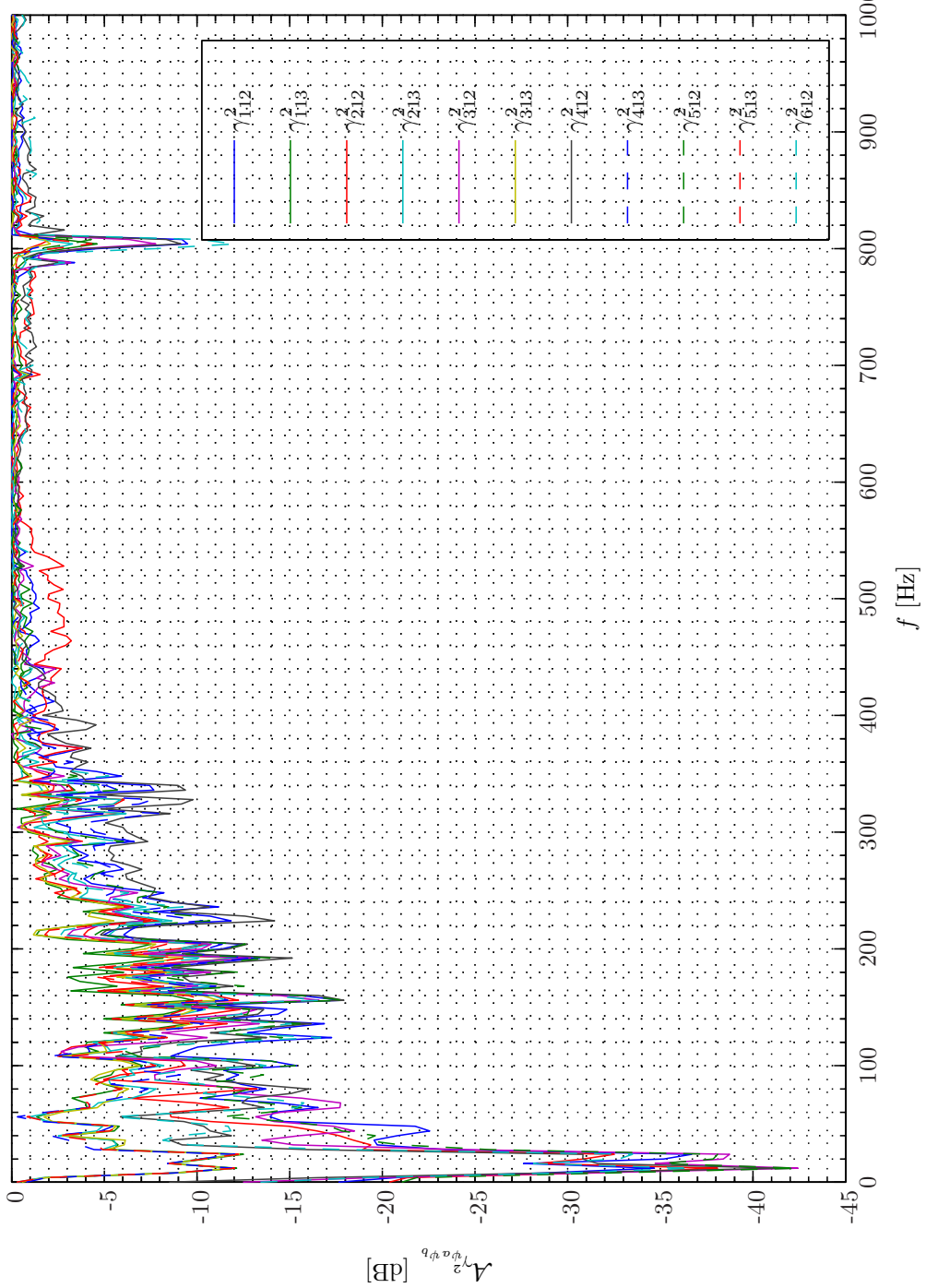

Sim D.4.24: Attenuation *vs Ordinary Coherency-Squared Functions*: $10\log_{10}(1-\gamma^2_{\psi_a\psi_b}(f))$: **Statistical Data Analysis**: Single-Sided Modified Periodogram, $f_s = 32.768$ kHz, $N_{DFT} = 8192$, $L_{DFT} = 8193$, $R_{DFT} = 4097$, Hanning, $\Delta f_m = 16$ Hz, $T_{DFT} = 0.25003$ s, $N_{f,DFT} = 4097$, $\Delta f_{DFT} = 4$ Hz, $K_{DFT} = 238$; CH-47 Recordings Airbase Sosterberg 23 November 2005, Channel: 1,2,3,4,5,6,7,8,9,10,11,12,13,14,15,16,17, Scenario(2,2), $0-30$ s ($f_s = 32.768$ kHz, $N_{A/D} = 24$); **Topology:** BK 4949 surface microphones flush-mounted on a Gentex HGU-55/P helmet mounted on a BK 4128 C HATS, Terma Earcup Audio System (Feedforward, mFx, $N_x = 11, N_e = 2, N_y = 2, N_p = 2, N_v = 0$); *Channels:* $\#1 \leftarrow x_1$, $\#2 \leftarrow x_2$, $\#3 \leftarrow x_3$, $\#4 \leftarrow x_4$, $\#5 \leftarrow x_5$, $\#6 \leftarrow x_6$, $\#7 \leftarrow x_7$, $\#8 \leftarrow x_8$, $\#9 \leftarrow x_9$, $\#10 \leftarrow x_{10}$, $\#11 \leftarrow x_{11}$, $\#12 \leftarrow d_1^p$, $\#13 \leftarrow d_2^p$; **Scenario:** `CH47RecordingSignalAnalysis/20080220T222150`.

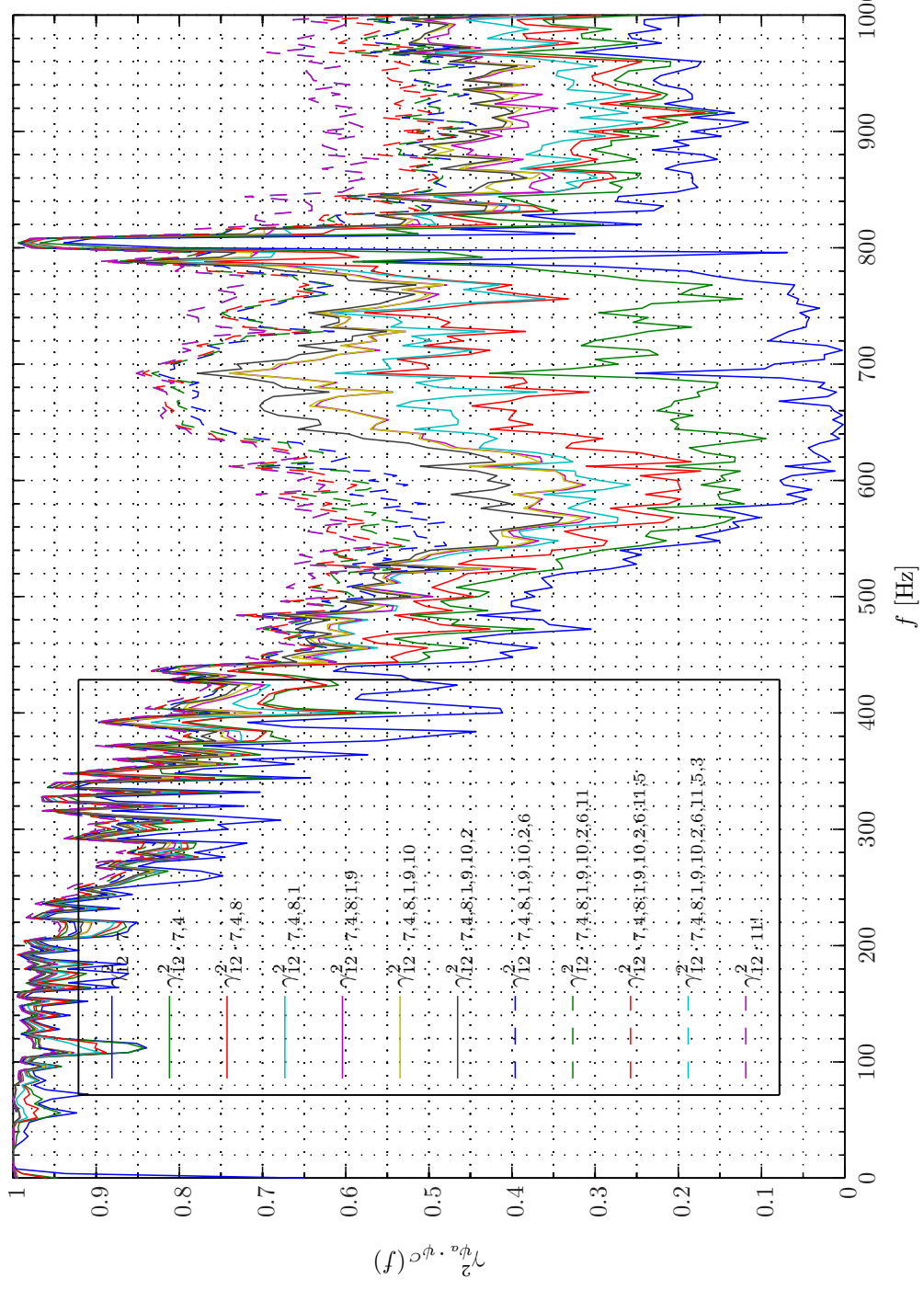

Sim D.4.25: *Multiple Magnitude-Squared Coherence Functions* $\gamma^2_{\psi_a \cdot \psi^C}(f)$: **Statistical Data Analysis**: Single-Sided Modified Periodogram, f_s = 32.768 kHz, N_{DFT} = 8192, L_{DFT} = 8193, R_{DFT} = 4097, Hanning, Δf_m = 16 Hz, T_{DFT} = 0.25003 s, $N_{f,DFT}$ = 4097, Δf_{DFT} = 4 Hz, K_{DFT} = 238; CH-47 Recordings Airbase Sosterberg 23 November 2005, Channel: 1,2,3,4,5,6,7,8,9,10,11,12,13,14,15,16,17, Scenario(2,2), 0 – 30 s (f_s = 32.768 kHz, $N_{A/D}$ = 24); **Topology:** BK 4949 surface microphones flush-mounted on a Gentex HGU-55/P helmet mounted on a BK 4128 C HATS, Terma Earcup Audio System (Feedforward, mFx, $N_x = 11, N_e = 2, N_y = 2, N_p = 2, N_v = 0$); *Channels:* #1 ← x_1, #2 ← x_2, #3 ← x_3, #4 ← x_4, #5 ← x_5, #6 ← x_6, #7 ← x_7, #8 ← x_8, #9 ← x_9, #10 ← x_{10}, #11 ← x_{11}, #12 ← d_1^P, #13 ← d_2^P; **Scenario:** `CH47RecordingSignalAnalysis/20080220T222150`.

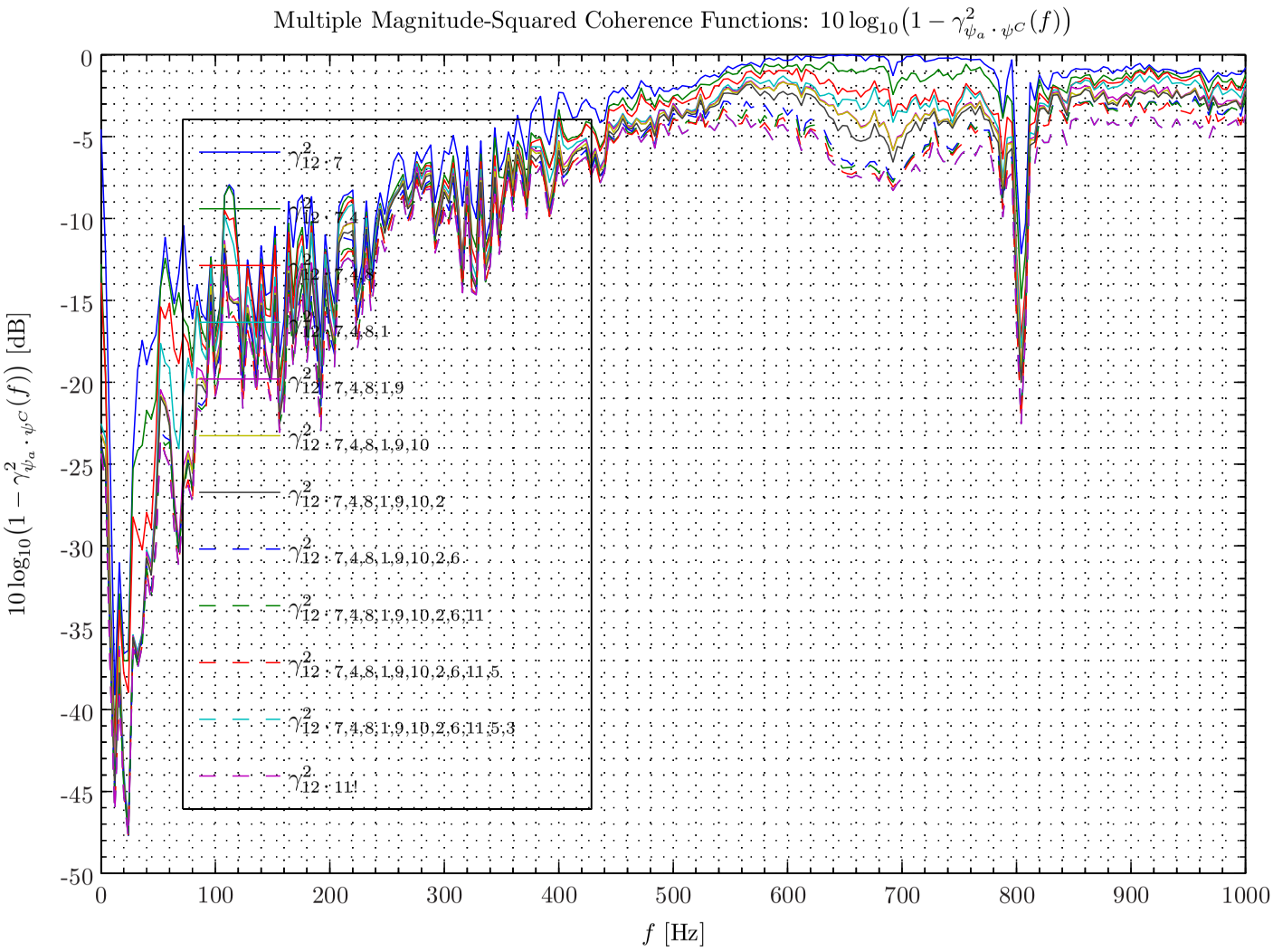

Sim D.4.26: *Attenuation vs Multiple Magnitude-Squared Coherence Functions* $10\log_{10}(1-\gamma^2_{\psi_a\cdot\psi^C}(f))$: **Statistical Data Analysis**: Single-Sided Modified Periodogram, $f_s = 32.768$ kHz, $N_{DFT} = 8192$, $L_{DFT} = 8193$, $R_{DFT} = 4097$, Hanning, $\Delta f_m = 16$ Hz, $T_{DFT} = 0.25003$ s, $N_{f,DFT} = 4097$, $\Delta f_{DFT} = 4$ Hz, $K_{DFT} = 238$; CH-47 Recordings Airbase Sosterberg 23 November 2005, Channel: 1,2,3,4,5,6,7,8,9,10,11,12,13,14,15,16,17, Scenario(2,2), $0-30$ s ($f_s = 32.768$ kHz, $N_{A/D} = 24$); **Topology:** BK 4949 surface microphones flush-mounted on a Gentex HGU-55/P helmet mounted on a BK 4128 C HATS, Terma Earcup Audio System (Feedforward, mFx, $N_x = 11, N_e = 2, N_y = 2, N_p = 2, N_v = 0$); *Channels:* #1 $\leftarrow x_1$, #2 $\leftarrow x_2$, #3 $\leftarrow x_3$, #4 $\leftarrow x_4$, #5 $\leftarrow x_5$, #6 $\leftarrow x_6$, #7 $\leftarrow x_7$, #8 $\leftarrow x_8$, #9 $\leftarrow x_9$, #10 $\leftarrow x_{10}$, #11 $\leftarrow x_{11}$, #12 $\leftarrow d_1^p$, #13 $\leftarrow d_2^p$; **Scenario:** CH47RecordingSignalAnalysis/20080220T222150.

Finally, we give an indication of the spatial variation of the signals acquired from the positions of four of the helicopter personnel (pilot, loadmaster 1 and 2 and gunner), each equipped with a BK 4135 or a BK 4939 1/4" microphones. Hence, the number of reference sensors now amounts to 15 by inclusion of x_{12}, x_{13}, x_{14} and x_{15}.

The pdfs for same scenario as above for $p_{x_{12}}(p), p_{x_{13}}(p), p_{x_{14}}(p), p_{x_{15}}(p)$ are shown in Simulation D.4.27 - D.4.30 on pages 606–609. Owing to different position (a span of 20 m) a large variation of the recorded probability density functions can therefore be observed.

Finally, for the MCOF analysis presented in Simulation D.4.31 - D.4.32 on pages 610–611 in comparison with Simulation D.4.25 - D.4.26 on pages 603–604 that no increase to the MCOF level is made by including the reference signals from the positions of the personnel.

This is also expectable due to the remote distance of these additional reference sensors relative to the performance sensors.

Bibliography

[1] Julius S. Bendat. *Nonlinear System Techniques and Applications*. Wiley-Interscience, New York, 1998.

[2] Julius S. Bendat and Allan G. Piersol. *Engineering Applications of Correlations and Spectral Analysis*. Wiley-Interscience, New York, 2nd edition, 1993.

[3] Julius S. Bendat and Allan G. Piersol. *Random data Analysis and measurement procedures*. John Wiley & Sons, Inc., 3rd edition, 2000.

[4] C. C. Boucher, Stephen J. Elliott, and K-H. Baek. Active control of helicopter rotor tones. In *InterNoise96*, pages 1179–1182, 1996.

[5] Stephen J. Elliott, C. C. Boucher, and T. J. Sutton. Active control of rotorcraft interior noise. In *Conference on Innovations in Rotorcraft Technology, Royal Aeronautical Society, London*, pages 15.1–15.6, 1997.

[6] Arne Nørby Rasmussen, Poul Aabo Osterhammel, Søren Vesterhauge, Julia Sundstrøm-Oldenburg, and Erling S. Jensen. Rapport over støjmålinger foretaget i forsvarets luftfartøjer. Technical report, Rigshospitalet, Audiologisk Laboratorium, 1997.

[7] Terma. Test plan for noise measurements on aircraft, fixed and rotary wing. Technical Report 302522-TB, Terma AS, 2005.

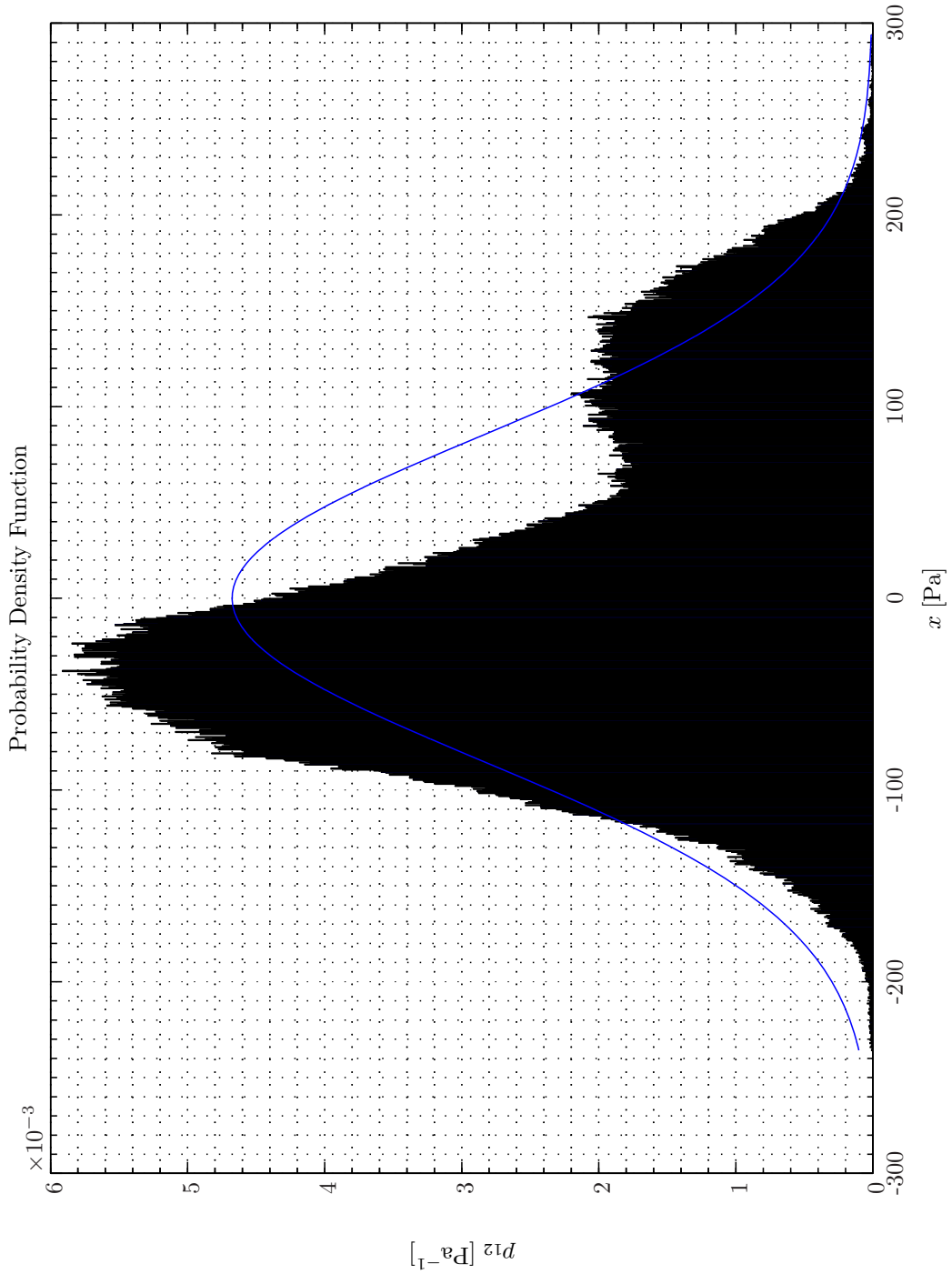

Sim D.4.27: *Probability Density Functions*: **Statistical Data Analysis**: Single-Sided Modified Periodogram, $f_s = 32.768$ kHz, $N_{DFT} = 8192$, $L_{DFT} = 8193$, $R_{DFT} = 4097$, Hanning, $\Delta f_m = 16$ Hz, $T_{DFT} = 0.25003$ s, $N_{f,DFT} = 4097$, $\Delta f_{DFT} = 4$ Hz, $K_{DFT} = 238$; CH-47 Recordings Airbase Sosterberg 23 November 2005, Channel: 1,2,3,4,5,6,7,8,9,10,11,12,13,14,15,16,17, Scenario(2,2), $0 - 30$ s ($f_s = 32.768$ kHz, $N_{A/D} = 24$); **Topology:** BK 4949 surface microphones flush-mounted on Gentex HGU-55/P helmet mounted on a BK 4128 C HATS, Terra Earcup Audio System (Feedforward, mFx, $N_x = 15, N_e = 1, N_y = 2, N_p = 2, N_v = 0$); *Channels:* #1 $\leftarrow x_1$, #2 $\leftarrow x_2$, #3 $\leftarrow x_3$, #4 $\leftarrow x_4$, #5 $\leftarrow x_5$, #6 $\leftarrow x_6$, #7 $\leftarrow x_7$, #8 $\leftarrow x_8$, #9 $\leftarrow x_9$, #10 $\leftarrow x_{10}$, #11 $\leftarrow x_{11}$, #12 $\leftarrow x_{12}$, #13 $\leftarrow x_{13}$, #14 $\leftarrow x_{14}$, #15 $\leftarrow x_{15}$, #16 $\leftarrow d_1^p$, #17 $\leftarrow d_2^p$; **Scenario:** `CH47RecordingSignalAnalysis/20080218T035345`.

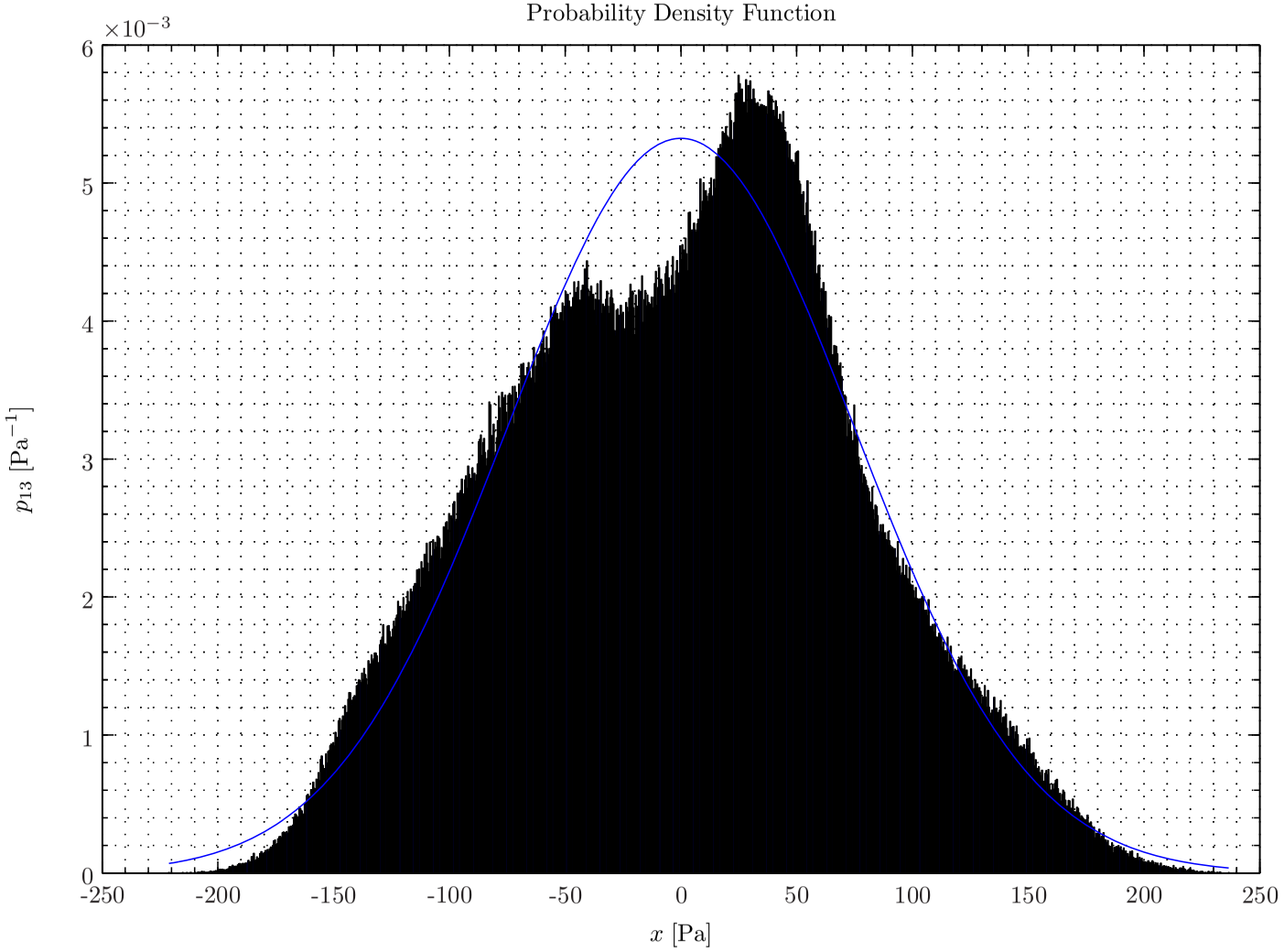

Sim D.4.28: *Probability Density Functions*: **Statistical Data Analysis**: Single-Sided Modified Periodogram, $f_s = 32.768$ kHz, $N_{DFT} = 8192$, $L_{DFT} = 8193$, $R_{DFT} = 4097$, Hanning, $\Delta f_m = 16$ Hz, $T_{DFT} = 0.25003$ s, $N_{f,DFT} = 4097$, $\Delta f_{DFT} = 4$ Hz, $K_{DFT} = 238$; CH-47 Recordings Airbase Sosterberg 23 November 2005, Channel: 1,2,3,4,5,6,7,8,9,10,11,12,13,14,15,16,17, Scenario(2,2), $0 - 30$ s ($f_s = 32.768$ kHz, $N_{A/D} = 24$); **Topology:** BK 4949 surface microphones flush-mounted on Gentex HGU-55/P helmet mounted on a BK 4128 C HATS, Terma Earcup Audio System (Feedforward, mFx, $N_x = 15, N_e = 1, N_y = 2, N_p = 2, N_v = 0$); *Channels:* #1 $\leftarrow x_1$, #2 $\leftarrow x_2$, #3 $\leftarrow x_3$, #4 $\leftarrow x_4$, #5 $\leftarrow x_5$, #6 $\leftarrow x_6$, #7 $\leftarrow x_7$, #8 $\leftarrow x_8$, #9 $\leftarrow x_9$, #10 $\leftarrow x_{10}$, #11 $\leftarrow x_{11}$, #12 $\leftarrow x_{12}$, #13 $\leftarrow x_{13}$, #14 $\leftarrow x_{14}$, #15 $\leftarrow x_{15}$, #16 $\leftarrow d_1^p$, #17 $\leftarrow d_2^p$; **Scenario:** CH47RecordingSignalAnalysis/20080218T035345.

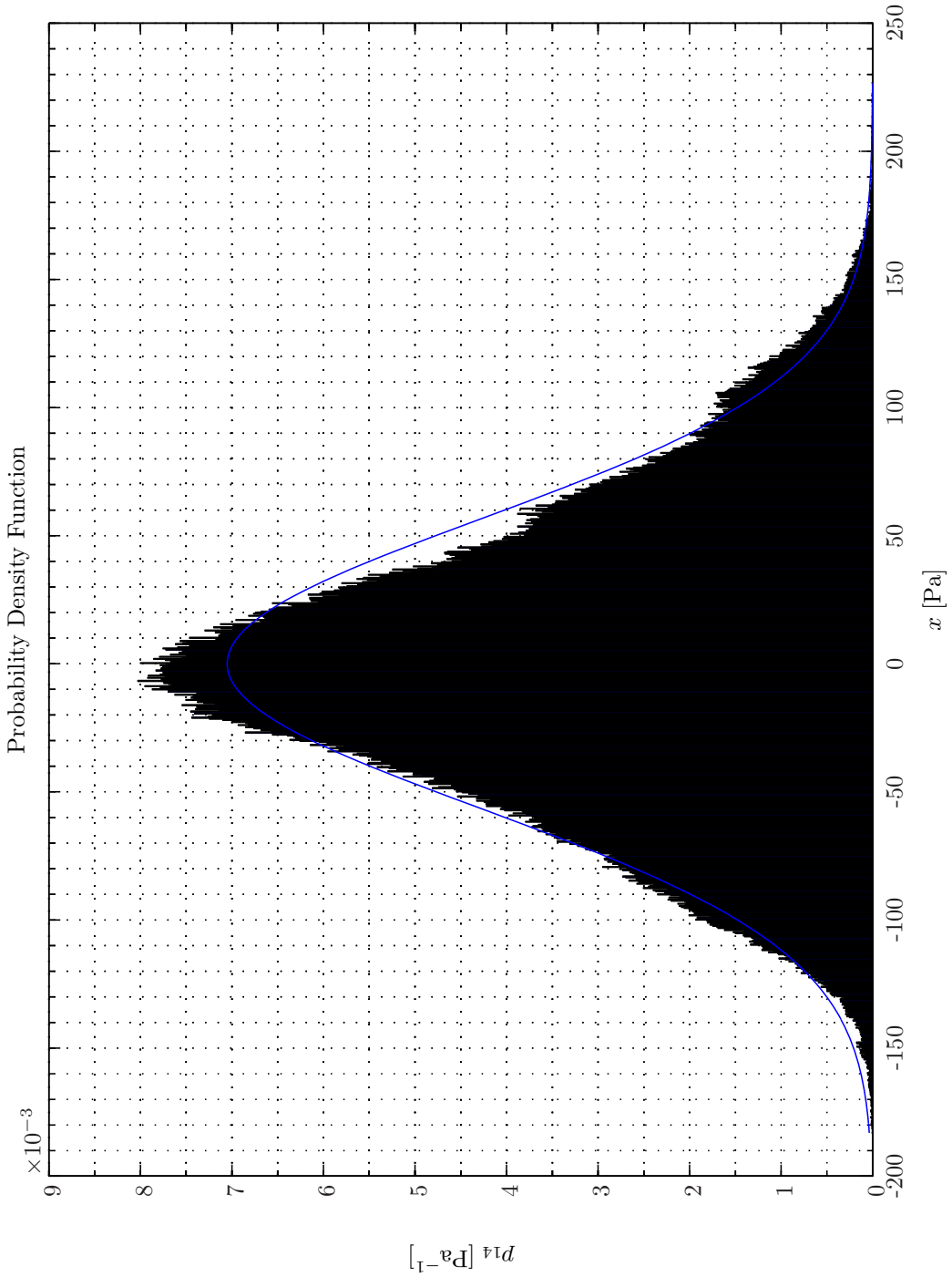

Sim D.4.29: *Probability Density Functions*: **Statistical Data Analysis**: Single-Sided Modified Periodogram, $f_s = 32.768$ kHz, $N_{DFT} = 8192$, $L_{DFT} = 8193$, $R_{DFT} = 4097$, Hanning, $\Delta f_m = 16$ Hz, $T_{DFT} = 0.25003$ s, $N_{f,DFT} = 4097$, $\Delta f_{DFT} = 4$ Hz, $K_{DFT} = 238$; CH-47 Recordings Airbase Sosterberg 23 November 2005, Channel: 1,2,3,4,5,6,7,8,9,10,11,12,13,14,15,16,17, Scenario(2,2), $0 - 30$ s ($f_s = 32.768$ kHz, $N_{A/D} = 24$); **Topology:** BK 4949 surface microphones flush-mounted on Gentex HGU-55/P helmet mounted on a BK 4128 C HATS, Terma Earcup Audio System (Feedforward, mFx, $N_x = 15, N_e = 1, N_y = 2, N_p = 2, N_v = 0$); *Channels:* #1 $\leftarrow x_1$, #2 $\leftarrow x_2$, #3 $\leftarrow x_3$, #4 $\leftarrow x_4$, #5 $\leftarrow x_5$, #6 $\leftarrow x_6$, #7 $\leftarrow x_7$, #8 $\leftarrow x_8$, #9 $\leftarrow x_9$, #10 $\leftarrow x_{10}$, #11 $\leftarrow x_{11}$, #12 $\leftarrow x_{12}$, #13 $\leftarrow x_{13}$, #14 $\leftarrow x_{14}$, #15 $\leftarrow x_{15}$, #16 $\leftarrow d_1^p$, #17 $\leftarrow d_2^p$; **Scenario:** `CH47RecordingSignalAnalysis/20080218T035345`.

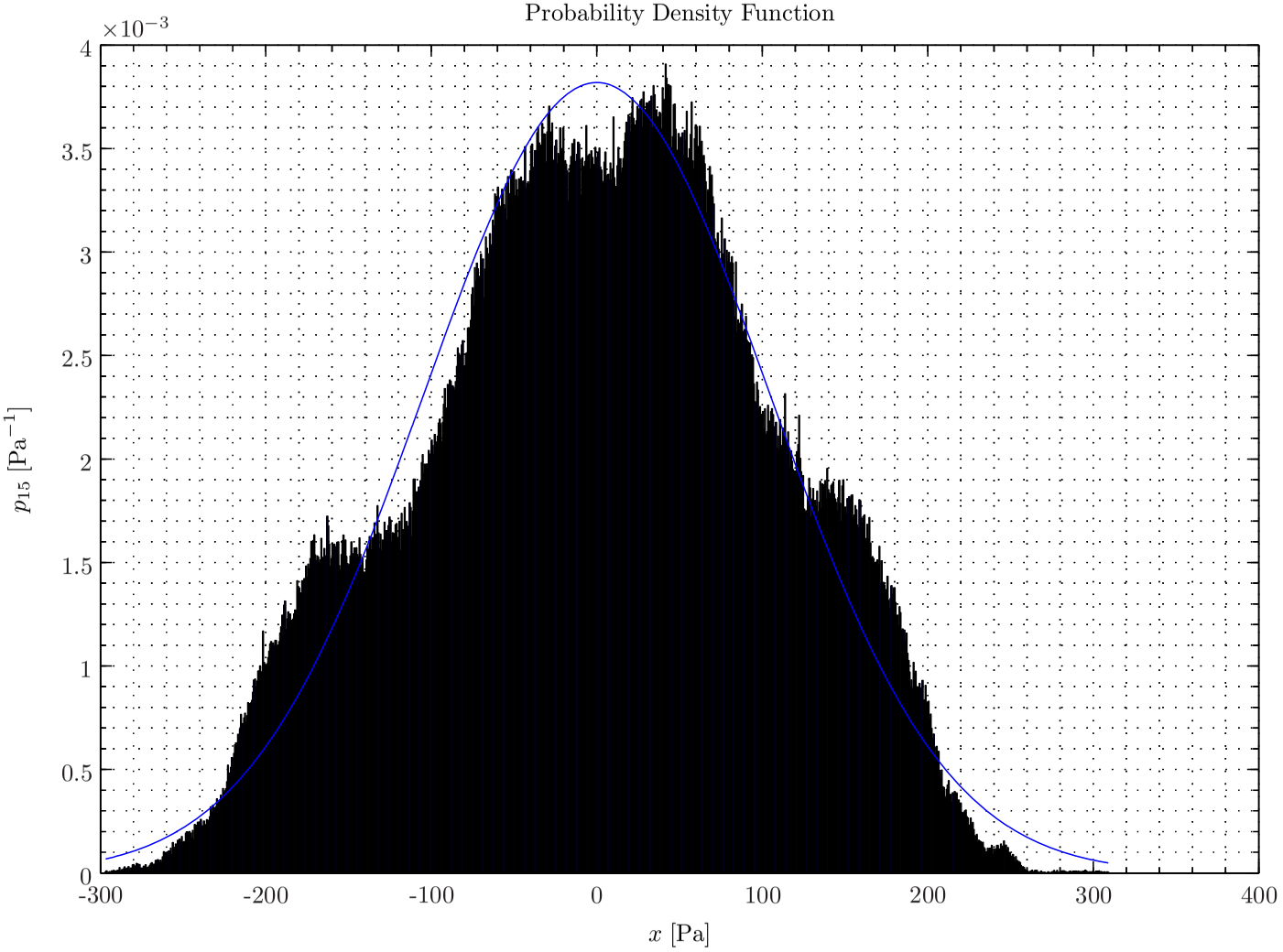

Sim D.4.30: *Probability Density Functions*: **Statistical Data Analysis**: Single-Sided Modified Periodogram, $f_s = 32.768$ kHz, $N_{DFT} = 8192$, $L_{DFT} = 8193$, $R_{DFT} = 4097$, Hanning, $\Delta f_m = 16$ Hz, $T_{DFT} = 0.25003$ s, $N_{f,DFT} = 4097$, $\Delta f_{DFT} = 4$ Hz, $K_{DFT} = 238$; CH-47 Recordings Airbase Sosterberg 23 November 2005, Channel: 1,2,3,4,5,6,7,8,9,10,11,12,13,14,15,16,17, Scenario(2,2), $0 - 30$ s ($f_s = 32.768$ kHz, $N_{A/D} = 24$); **Topology:** BK 4949 surface microphones flush-mounted on Gentex HGU-55/P helmet mounted on a BK 4128 C HATS, Terma Earcup Audio System (Feedforward, mFx, $N_x = 15, N_e = 1, N_y = 2, N_p = 2, N_v = 0$); *Channels:* #1 $\leftarrow x_1$, #2 $\leftarrow x_2$, #3 $\leftarrow x_3$, #4 $\leftarrow x_4$, #5 $\leftarrow x_5$, #6 $\leftarrow x_6$, #7 $\leftarrow x_7$, #8 $\leftarrow x_8$, #9 $\leftarrow x_9$, #10 $\leftarrow x_{10}$, #11 $\leftarrow x_{11}$, #12 $\leftarrow x_{12}$, #13 $\leftarrow x_{13}$, #14 $\leftarrow x_{14}$, #15 $\leftarrow x_{15}$, #16 $\leftarrow d_1^p$, #17 $\leftarrow d_2^p$; **Scenario:** `CH47RecordingSignalAnalysis/20080218T035345`.

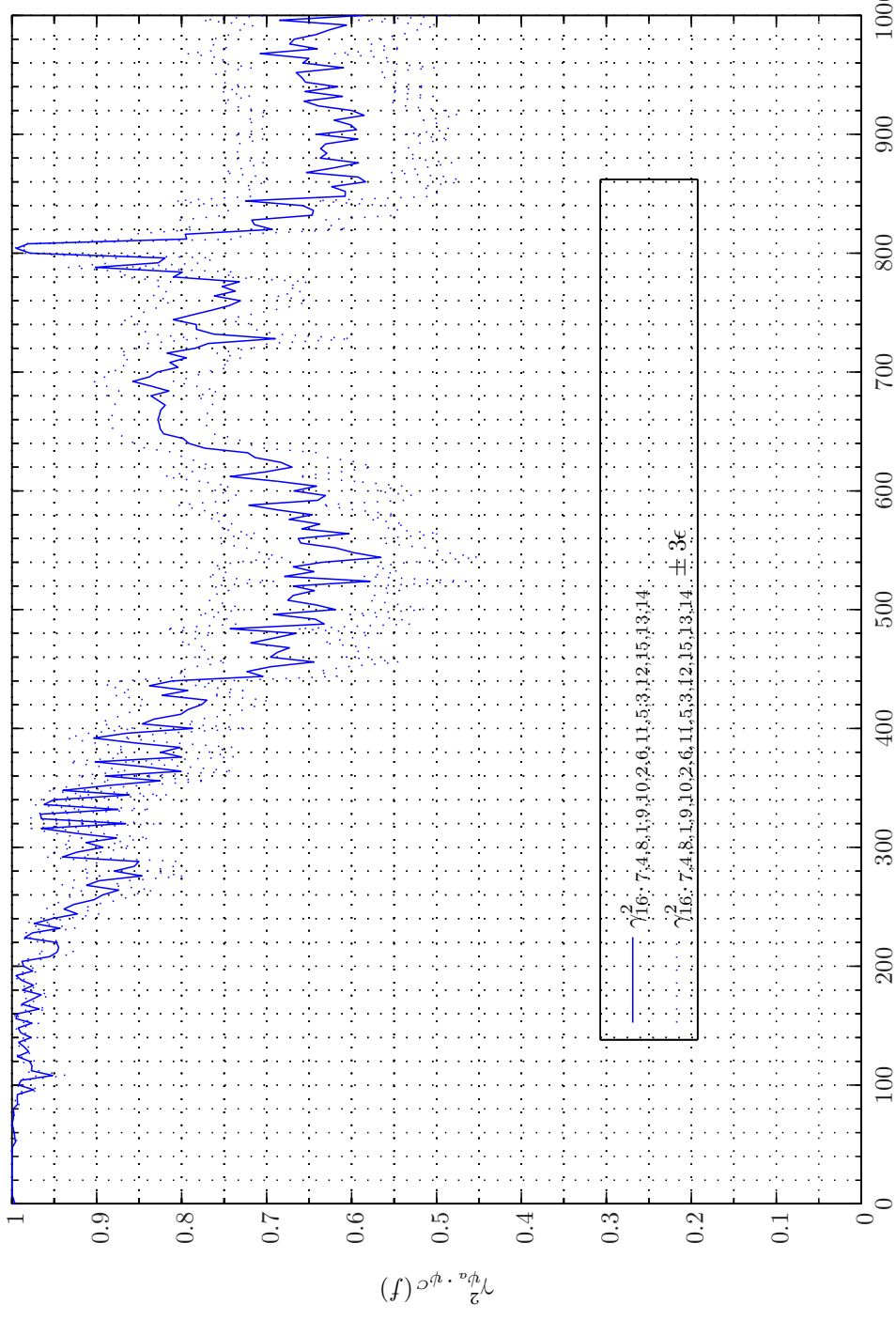

Sim D.4.31: *Multiple Magnitude-Squared Coherence Functions* $\gamma^2_{\psi_a \cdot \psi^C}(f)$: **Statistical Data Analysis**: Single-Sided Modified Periodogram, f_s = 32.768 kHz, N_{DFT} = 8192, L_{DFT} = 8193, R_{DFT} = 4097, Hanning, Δf_m = 16 Hz, T_{DFT} = 0.25003 s, $N_{f,DFT}$ = 4097, Δf_{DFT} = 4 Hz, K_{DFT} = 238; CH-47 Recordings Airbase Sosterberg 23 November 2005, Channel: 1,2,3,4,5,6,7,8,9,10,11,12,13,14,15,16,17, Scenario(2,2), 0 – 30 s (f_s = 32.768 kHz, $N_{A/D}$ = 24); **Topology:** BK 4949 surface microphones flush-mounted on Gentex HGU-55/P helmet mounted on a BK 4128 C HATS, Terma Earcup Audio System (Feedforward, mFx, $N_x = 15, N_e = 1, N_y = 2, N_p = 2, N_v = 0$); *Channels:* #1 $\leftarrow x_1$, #2 $\leftarrow x_2$, #3 $\leftarrow x_3$, #4 $\leftarrow x_4$, #5 $\leftarrow x_5$, #6 $\leftarrow x_6$, #7 $\leftarrow x_7$, #8 $\leftarrow x_8$, #9 $\leftarrow x_9$, #10 $\leftarrow x_{10}$, #11 $\leftarrow x_{11}$, #12 $\leftarrow x_{12}$, #13 $\leftarrow x_{13}$, #14 $\leftarrow x_{14}$, #15 $\leftarrow x_{15}$, #16 $\leftarrow d_1^p$, #17 $\leftarrow d_2^p$; **Scenario:** `CH47RecordingSignalAnalysis/20080218T035345`.

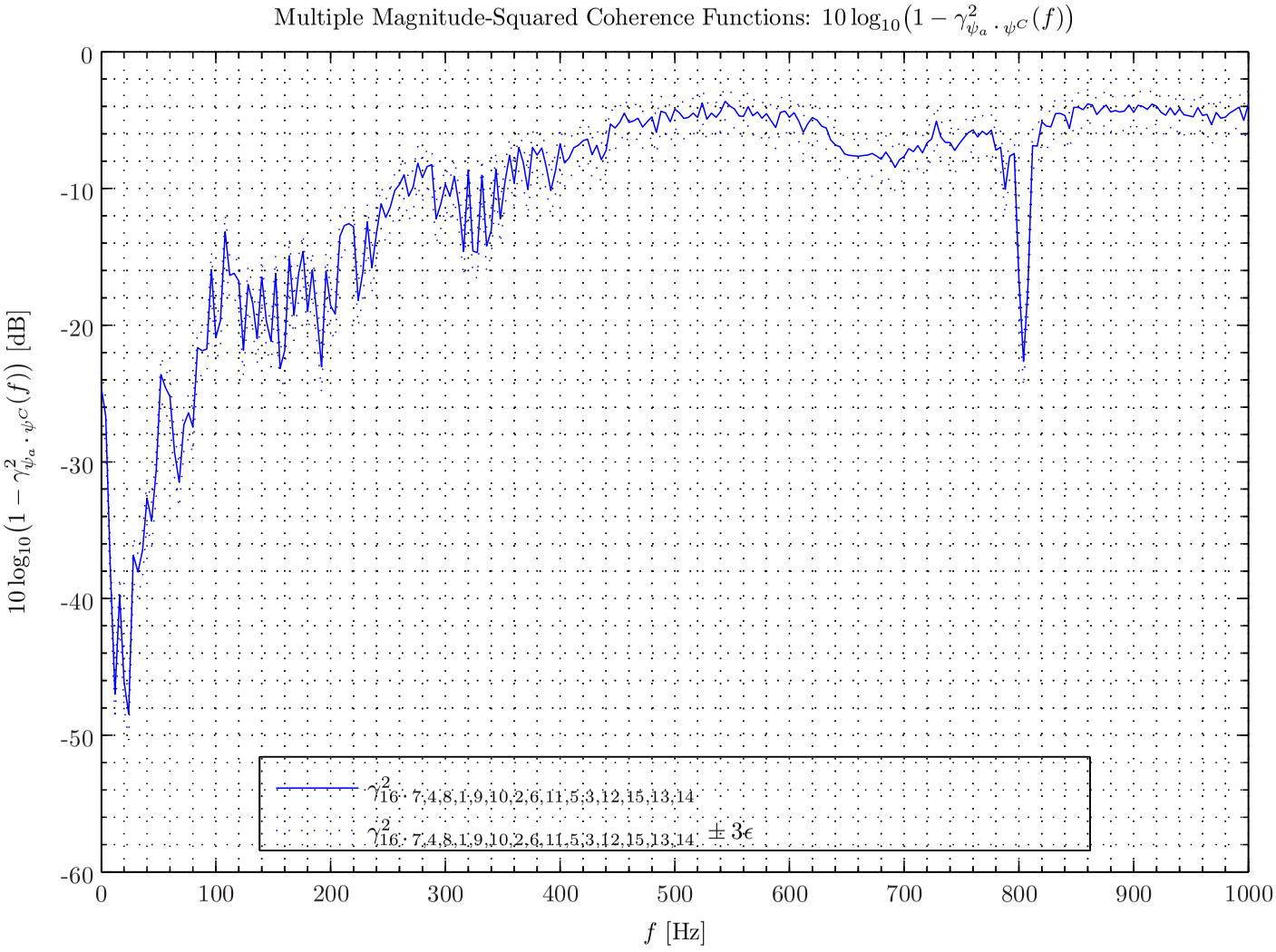

Sim D.4.32: *Attenuation vs Multiple Magnitude-Squared Coherence Functions* $10\log_{10}(1-\gamma^2_{\psi_a\cdot\psi^C}(f))$: **Statistical Data Analysis**: Single-Sided Modified Periodogram, $f_s = 32.768$ kHz, $N_{DFT} = 8192$, $L_{DFT} = 8193$, $R_{DFT} = 4097$, Hanning, $\Delta f_m = 16$ Hz, $T_{DFT} = 0.25003$ s, $N_{f,DFT} = 4097$, $\Delta f_{DFT} = 4$ Hz, $K_{DFT} = 238$; CH-47 Recordings Airbase Sosterberg 23 November 2005, Channel: 1,2,3,4,5,6,7,8,9,10,11,12,13,14,15,16,17, Scenario(2,2), $0-30$ s ($f_s = 32.768$ kHz, $N_{A/D} = 24$); **Topology:** BK 4949 surface microphones flush-mounted on Gentex HGU-55/P helmet mounted on a BK 4128 C HATS, Terma Earcup Audio System (Feedforward, mFx, $N_x = 15, N_e = 1, N_y = 2, N_p = 2, N_v = 0$); *Channels:* #1 $\leftarrow x_1$, #2 $\leftarrow x_2$, #3 $\leftarrow x_3$, #4 $\leftarrow x_4$, #5 $\leftarrow x_5$, #6 $\leftarrow x_6$, #7 $\leftarrow x_7$, #8 $\leftarrow x_8$, #9 $\leftarrow x_9$, #10 $\leftarrow x_{10}$, #11 $\leftarrow x_{11}$, #12 $\leftarrow x_{12}$, #13 $\leftarrow x_{13}$, #14 $\leftarrow x_{14}$, #15 $\leftarrow x_{15}$, #16 $\leftarrow d^p_1$, #17 $\leftarrow d^p_2$; **Scenario:** CH47RecordingSignalAnalysis/20080218T035345.

E. RANDOM NOISE GENERATION

E.1 Algorithm

A versatile portable pseudo-random noise generator has been chosen [2, App. A] and [1, App. C]. The algorithm is also referred to as *linear congruential sequence generator*.

This algorithm ensures that subsequences of reasonable length will be distributed uniformly between zero and one. Moreover, it can be started at any specified point in the sequence.

In the referenced textbooks, integer words up to 32 bits are considered. In the active noise reduction (ANR)-system, a SHARC 21161N Processor that internally facilitates 32 bit words is used. However, the analogue to digital and digital to analogue converters involved in the plant are both limited to 16 bit. Therefore, some adaptation of the algorithm presented in [3, App. A] is necessary.

By I we denote a column vector of M integer elements that is used to contain the random data. The quantity M is the random sequence length. The sequence is initiated by assigning an arbitrary number, say, I_0 to the first element in I

$$I\left[0\right] = I_0. \tag{E.1.1}$$

Then the successive elements of I are determined recursively according to

$$I\left[n+1\right] = \left(JI\left[n\right]+1\right) \bmod M \quad n = 0, 1, \ldots M-1. \tag{E.1.2}$$

By $[n]$ we refer to the n'th number in the sequence. As readily seen in (E.1.2), M also sets an upper limit on the sequence period. In order to ease the theoretical analysis of a linear congruential sequence M must be 2 raised to some integer power, L. Hence,

$$M \triangleq 2^L. \tag{E.1.3}$$

Ideally, the sequence periodicity should coincide with the number of words represented $\left(M = 2^L = 2^{N_b}\right)$. However, in order to restrict $I\left[n\right]$ from overflow and to ensure approximately sample independence the periodicity must attain a (much) lower number ($L < N_b$).

The quantity J is used to ensure sufficient spread between two successive elements in I. In order to guarantee that the buffer length, M, coincide with the periodicity, J shall be set as

$$J = 4K + 1, \tag{E.1.4}$$

where K denote an integer value subject to some constraints discussed next.

The largest value that the terms in the parentheses on the right side of (E.1.2) can attain is $(4K+1)(M-1)+1$.

In a system employing N_b-bit representation, however, it is required that

$$2^L < \frac{2^{N_b-1}-1}{4K+1}+1 = \frac{2^{N_b-1}+4K}{4K+1}. \tag{E.1.5}$$

Now defining a new variable, S, by

$$S \triangleq \log_2(4K) \geqslant 2 \tag{E.1.6}$$

then by inserting (E.1.5) in (E.1.14) we obtain

$$2^L < \frac{2^{N_b-1}+2^S}{2^S+1} = \frac{2^S\left(2^{N_b-1-S}+1\right)}{2^S\left(1+2^{-S}\right)} = 2^{N_b-1-S}\frac{1+2^{-N_b+1+S}}{1+2^{-S}} \tag{E.1.7}$$

which leads to

$$\begin{aligned}
L &< N_b-1-S-\log_2\left(\frac{1+2^{-N_b+1+S}}{1+2^{-S}}\right) && \text{(E.1.8)}\\
&= N_b-1-S-\log_2\left(1+2^{-N_b+1+S}\right)+\log_2\left(1+2^{-S}\right) && \text{(E.1.9)}\\
&= N_b-1-S-\frac{\ln\left(1+2^{-N_b+1+S}\right)-\ln\left(1+2^{-S}\right)}{\ln 2} && \text{(E.1.10)}\\
&\approx N_b-1-S-\frac{2^{-N_b+1+S}-2^{-S}}{\ln 2} && \text{(E.1.11)}\\
&= N_b-1-S+\frac{2^{-S}}{\ln 2}\left(1-2^{-N_b+1}\right) && \text{(E.1.12)}\\
&= N_b-1-S+\varepsilon && \text{(E.1.13)}
\end{aligned}$$

where the small (but strictly positive) quantity, ε, has been introduced

$$\varepsilon = \frac{2^{-S}}{\ln 2}\left(1-2^{-N_b+1}\right) > 0. \tag{E.1.14}$$

As readily seen from (E.1.7) the largest periodicity is obtained when $L < N_b-1-S$.

In a 32 bit system it is customary to set $L=20$ and $K=512 \Rightarrow S=11$ and (E.1.7) is obviously satisfied: $20 < 32-1-11+\varepsilon$. For a 16 bit system, however, we chose to set $K=4 \Rightarrow S=4$ and we get $L=16-1-4=11 \Rightarrow M=2048$ and $J=17$.

E.1.1 Summary

In summary the pseudo-random noise algorithm is

$$I[0]=12357 \wedge I[n]=(17*I[n-1]+1) \bmod 65536, \quad n=1,2,\ldots 65535 \tag{E.1.15}$$

in 16 bit representation and

$$I[0] = 12357 \wedge I[n] = (2045 * I[n-1] + 1) \bmod 1048576, \quad n = 1, 2, \ldots 1048575 \qquad \text{(E.1.16)}$$

in 32 bit representation.

E.2 Test

From incorporating random signal data generated by (E.1.15) into MATLAB® it has been confirmed that the signal exhibit a flat uniform frequency spectrum as expected.

Bibliography

[1] Sen M. Kuo and Dennis R. Morgan. *Active Noise Control Systems Algorithms and DSP Implementations.* John Wiley & Sons, Inc., 1996.

[2] Bernard Widrow and Samuel D. Stearns. *Adaptive Signal Processing.* Prentice-Hall, New Jersey, 1985.

[3] Bernard Widrow and Eugene Walach. *Adaptive Inverse Control.* Prentice Hall, 1996.

Part V

ACTIVE CONTROL OF FIELDS II

F. ACOUSTIC, ELECTROMAGNETIC AND ELASTIC FIELD THEORY

F.1 Motivation

The three branches of physics treated in this context namely *acoustics*, *elasticity theory* and *electromagnetics* are all subjectable to analysis in the mathematical framework of *field theory*. In field theory the underlying often very complicated behavior of a physical system is brought aside and the gross behavior instead described in terms of fairly simple governing equations. For example a system consisting of a cube 10 mm a side and containing a monoatomic gas at atmospheric pressure and temperature. This volume contains approximately 10^{19} atoms. From a *microscopic* point of view we must deal with in the order of 10^{20} equations to describe the first-order kinematics, that is, position and velocity of each atom within the cube. The *macroscopic* framework of field theory concerns the gross or average effects of many molecules, thereby substantially reducing the number of equations required.

Despite the apparent similarities of acoustic and electromagnetic field theory only a few contributions in the literature dealing with both types of fields can be found [12, 16, 26, 27].

Moreover, upon applying results from the electromagnetic domain to the acoustical domain or vice versa careful examination of the underlying assumptions made in the governing equations must be invoked.

The work carried out in the present chapter could generally be fruitful when attempting to project results obtained in one of the physical system to one of the other two physical systems. In particular in Appendix G where spherical near-field antenna testing (SNFAT) techniques used primarily for antenna measurement will be accommodated to measurement of acoustical wave fields as well as elastoric wave fields. In order to accomplish this goal, however, as proclaimed above some care must be exercised when adapting results from one branch of physics to another. Therefore, attention is to make a coherent presentation of the governing equations and the various assumptions made in the particular physical applications. Moreover, in this process different choices in nomenclature, terminology etc. among acousticians, elasticians and antenna theoreticians has to be dealt with.

The following presentation of the field of acoustics, elasticity theory and electromagnetics, however, will mostly be brief and is aimed at exposing the similarities and dissimilarities. Hence, it is assumed that the reader find himself sufficiently confident in these branches of physics. References to excellent textbooks on the specific domains will be made. However, it is the hope that the present review of the fields of acoustic, elasticity and electromagnetics is sufficiently coherent to provide the background necessary to be beneficial for Appendix G on page 707.

In recent years active control of sound and vibration (ACSV) systems have experienced a tendency in growth in size and complexity. In particular ACSV systems with a multiple-input and multiple-output (MIMO) topology have become exceedingly complicated. The increase in complexity,

however, also manifests itself in the design and evaluation phase. Hence, a demand for a active control sound and vibration test unit (ACSVTU) dedicated systematic test of developed systems exist. Preferably, such unit should make provision for test of the acoustical/structural part as well as the control/adaptive filtering part of a system. It is therefore another objective of this report to provide the necessary theoretical background for the development of such ACSVTUs. It suffice here to say that in comparison with ordinary active control (adaptive filtering) of electrical signals confined to electrical wires the problems of active control of fields in general are more numerous and considerably more difficult to be dealt with. The reasons for this increase in complexity is due to fact that active control of fields involves in general vector quantities in 3-D space (as opposed to a scalars in 1-D space), phenomena like polarization and two different and mode-dependent wave propagation velocities have to be taking into account. Moreover, field theory normally concerns the problem of estimating some unknown field variables from source distributions that is assumed known taking various boundary conditions into account. This process we will refer to as *field analysis*. The *inverse problem* or *field synthesis*, that is, to consider the field variables as known and then to deduce the source distributions responsible for this field is considerable more involved and generally no *unique solution* exists. If the field variables are known from measurements, a real source, of course, exists but other sources might lead to the same fields. This has an impact on the active control of fields where one introduces a secondary source distribution so that the resulting field, that is, the sum of the primary field and the secondary field attains the desired distribution (it should normally vanish). However, in this case even the *existence* of such secondary source distribution is by no means guaranteed and some kind of comprise must be made.

F.1.1 Chapter Outline

Following this motivational section general field theory aspects common to the three types of fields considered will be discussed in section F.2. Then the theme of the following three sections, that is, section F.3, section F.4 and section F.5 is the theory of fluid mechanics, elasticity and electromagnetics respectively. The former two have roots in *continuum mechanics* and are to a certain extent much alike. Following the very general discussion of acoustical and electromagnetic field theory the theoretical foundation has then been made and section F.6 will reflect on the similarities and dissimilarities encountered in the three physical domains. Our anticipation on a fair amount of similarities in the domain acoustic, electromagnetic and elasticity field theory is fully confirmed and formalized. A detailed analysis of electromagnetic and *linear* acoustic fields is carried out with roots in integral equations. The theme of section F.7 and section F.8 is the *uniqueness* and the *existence* of the fields respectively. These topics will be examined in parallel for the two domains. In section F.11 we then establish the very close relationship there exists between the two domains when we consider spherical wave decomposition. Spherical time-domain field expansions are considered in section F.12. Whereas the above topics have been the subject of a number of previous studies, the novelty of the present approach is in examining them thoroughly in the time domain as well as the frequency domain. The time-domain formulations are derived in two ways: by Fourier transforming the corresponding frequency-domain expressions, and then directly in the time domain from the properties of Green functions. The identity of the results, sometimes after long and difficult mathematical manipulations, helps the reader gain confidence in the final product even if she or he was unable to follow all the details of the derivation.

The chapter comprises a total of six appendices. In section F.A an expression related to the material derivative is obtained. Next in section F.B a proof of an alternative version of the Reynolds transport theorem that will be used extensively in the development is provided. Then

in section F.C an expression relating the rate of entropy change to the thermodynamic properties and the dilatation rate is derived. Pressure and velocity fields from surface integrals are considered in section F.D. Finally, the theme of section F.E and section F.F is miscellaneous vector identities and time-dependent potential functions encountered in acoustic and electromagnetic field theory.

F.2 General Field Theory

The main ingredients in *field theory* is a set of *sources* responsible for the generation of the fields, a set of *field variables* representing the underlying (complicated) physical behavior of the system and a set *constitutional parameters* that describes the medium supporting the fields. With these quantities being defined a fundamental equation describing the overall behavior of the system is sought for. This process depends on theoretical deduction or experimental evidence, e.g., Maxwell's equations and by invoking a statement on a *continuity relationship* among the source quantities.

F.2.1 Sources

Sources are the cause of fields and in the absence of sources no fields therefore exist. The space spanned by all sources are referred to as the *source region* and denoted by $\mathcal{V}_S$. It is important to note that the governing field equation presented in subsection F.2.5 are *inhomogeneous* inside the source region and *homogeneous* outside the source region. Examples of scalar, vector and tensor sources are the electrical charge density[1] ρ, the volume source of mass flow s and the traction $\mathfrak{T}$ acting on the surface of an elastic medium. The phenomena of acoustical sound generation due to violent fluid motion will be presented in subsection F.3.11 on page 654.

F.2.2 Field Variables

Fields are the consequence of the presence of sources. The field variables are used to describe the state of a physical system. Similar to the sources, scalar, vector and tensor field variables are encountered. For example, the acoustical pressure p in a fluid, the electric intensity $\mathbf{E}$ in a dielectric and the strain $\mathfrak{S}$ inside an elastic medium represent scalar, vector and tensor fields respectively.

Some field variables are considered *primary field variables* while other are *secondary field variables*.

F.2.3 Constitutive Relationships

In the work of formulating the fundamental equations it will, however, turn out that we end up with to few equations in comparison with the number of unknown field variables. A third relationship that involves the media supporting the field is also required. The *constitutive relationships* establish the "missing link" among the field variables themselves or between sources and field variables. Such parameters will be referred to as *constitutive parameters*. A constitutive parameter might be a scalar, vector or a tensor quantity, that varies with position in

[1] Density generally means the amount of a quantity per unit volume.

space and with time. Moreover, a constitutive parameter will to a certain degree vary with the frequency. This dependence on frequency can often be taking into account by defining a complex version of the constitutive parameter where the imaginary part is responsible for the variation with frequency. Furthermore, most of the constitutive parameters may vary with ambient conditions. However, we will usually assume the ambient conditions to be constants. Finally, different sources to nonlinear behavior exist. For example the value of a constitutive parameter might depend on the excitation level. Practical examples hereof will be provided in the subsequent sections.

In case of a *linear*, *homogeneous*[2], *isotropic*[3], time-independent and frequency-independent constitutive (scalar, vector or tensor) parameter, say, υ^a we may write

$$\upsilon^a(\mathbf{r}, t, \omega, A(\psi)) \rightarrow \upsilon^a, \tag{F.2.1}$$

υ^a denotes an *arbitrary* constitutional parameter and where $A(\psi)$ is used to signify the dependence on the excitation level of the field variable ψ.

If L_Υ parameters suffice to describe the system they may be absorbed in the structure $\Upsilon = [\upsilon_1, \upsilon_2, \ldots, \upsilon_{L\Upsilon}]$.

Explicit forms for these constitutive parameters can be found by experimentation, e.g., Hooke's Law or deduced, e.g., from kinematic gas theory.

F.2.4 Taylor Expansion of Field Variables

The constitutive parameters will vary as a function of one or more of the field variables. In many contexts in physics the underlying phenomena is governed by system equations that are inherently nonlinear. Various causes for such imperfections exist and we will in section F.3 explain why acoustical fields always will possess some degree of nonlinearity.

We will next establish a framework to address such situations. The approach in [28, Ch. 14.2] to expand the various acoustical parameters to higher-order.

We can perform a Taylor expansion of an arbitrary field variable, say, $\psi^a(\mathbf{r}, t, s)$, according to, e.g.,

$$\psi^a(\mathbf{r}, t, s) = \sum_{n=0}^{\infty} \psi_n^a(\mathbf{r}, t, s). \tag{F.2.2}$$

In (F.2.2) $\mathbf{r}$ denotes the spatial position, t is the time and s is an amplitude parameter. Index, n, is the order of expansion of the field and no index simply refers to the total field. In general, ψ_n^a denotes the n-order value of the field variable ψ^a that in turn is obtained from

$$\psi_n^a(\mathbf{r}, t, s) = \frac{s^n}{n!} \left(\frac{\partial^n \psi^a(\mathbf{r}, t, s)}{\partial s^n} \right)_0. \tag{F.2.3}$$

[2]The properties of a homogeneous medium are constant from point to point. Some examples of an inhomogeneous medium exist. Gravity is responsible for stratification of the density with the depth in the ocean and with the height in the air. Such regular inhomogeneities can have significant effect on long range propagation in the air or in the sea. In a turbulent air flow the medium will be randomly inhomogeneous.

[3]If the physical properties of a body in the neighborhood of some interior point are the same in all directions, the body is said to be isotropic.

Hence, ψ_0^a refer to the zero-order value of the arbitrary field variable. Other terms are *quiescent (acoustics)*[4], *unperturbed* or *equilibrium* value. Moreover, if the ambient field quantity is time-independent (or at least very slowly varying compared with the time frame of the investigation) it is referred to as a *static value* or *stationary value*. The first order value of the arbitrary field variable is ψ_1^a . Finally, we will by ψ_{-0}^a denote the *dynamic value* of ψ^a, that is, the total value subtracted the equilibrium value

$$\psi_{-0}^a(\mathbf{r},t,s) = \psi^a(\mathbf{r},t,s) - \psi_0^a(\mathbf{r},t,s) \tag{F.2.4a}$$

$$= \sum_{n=1}^{\infty} \psi_n^a(\mathbf{r},t,s). \tag{F.2.4b}$$

It shall be emphasized that the Taylor expansion procedure in (F.2.2) normally only becomes meaningful if the terms are decreasing terms, so that

$$|\psi_0^a(\mathbf{r},t,s)| \gg |\psi_1^a(\mathbf{r},t,s)| \gg |\psi_2^a(\mathbf{r},t,s)| \gg \ldots \gg |\psi_{n-1}^a(\mathbf{r},t,s)| \gg |\psi_n^a(\mathbf{r},t,s)|, \quad \forall n \in \mathbb{N}, \tag{F.2.5}$$

where $\mathbb{N}$ designates the set of natural numbers. In the governing equations terms involving multiplication of two or more field variables or constitutive parameters can be encountered. In such cases some assessment of the actual order of factorization terms must be exercised. For example, if both ψ^a and ψ^b represent field variables or constitutive parameters that comply with (F.2.5), say, $\psi_0^a = 10\psi_1^a = 100\psi_2^a \wedge \psi_0^b = 200\psi_1^b = 40000\psi_2^b$. Then we have the following relations $|\psi_1^a||\psi_0^b|, |\psi_0^a||\psi_1^b| \gg |\psi_2^a||\psi_0^b|, |\psi_1^a||\psi_1^b| \wedge |\psi_0^a||\psi_1^b| \gg |\psi_0^a||\psi_2^b|$, but $|\psi_0^a||\psi_1^b| < |\psi_2^a||\psi_0^b|$.

In most cases the assumption in (F.2.5) holds. Otherwise the analysis often becomes prohibitive complicated. In section F.3 we will in an example make some further assessments on the degree of nonlinearity of acoustical fields. One exception from (F.2.5), however, is made if we let $\psi^a(\mathbf{r},t,s)$ represent the fluid velocity, $\mathbf{u}(\mathbf{r},t,s)$. Then we of course should allow for the normal case of negligible fluid flow, $|\mathbf{u}_0(\mathbf{r},t,s)| \approx 0$. The impact of this deviation from this assumption of elsewhere decreasing terms will be provided in the relevant context.

Finally, it should be emphasized that it takes only a single field variable or constitutive parameter to exhibit nonlinear behavior before second and higher order terms of the (other) field variables enter as artificial source terms in the governing equations in order so to say to "balance" the nonlinearities introduced.

It should, however, also be mentioned that the higher-order terms need not necessarily be undesirable, but may actually be exploited. Some applications involves the *acoustic radiation force* that is solely a non-linear acoustic phenomenon as discussed in [7] and the references herein.

F.2.5 Governing Equations

For later reference we will list some of the partial differential equation encountered in direct somewhat modified form in the three branches of physics studied. They will therefore also appear in the subsequent sections. Different equations will appear for the static and dynamic

[4] A quiescent fluid is also subject to $\mathbf{u}_0 = 0$.

field cases. Both *scalar field* and *vector field* versions of the equations exist. Static fields are often described by the *Laplace equation*

$$\nabla^2\psi = 0 \tag{F.2.6a}$$
$$\nabla \times \nabla \times \boldsymbol{\psi} = 0; \quad \nabla \cdot \boldsymbol{\psi} = 0 \tag{F.2.6b}$$

in the absence of sources or by the *Poisson's equation*

$$\nabla^2\psi = -4\pi\rho \tag{F.2.7a}$$
$$\nabla \times \nabla \times \boldsymbol{\psi} = 4\pi\mathbf{J}; \quad \nabla \cdot \boldsymbol{\psi} = 0 \tag{F.2.7b}$$

in the presence sources. The quantities ψ and $\boldsymbol{\psi}$ are representatives for scalar and vector fields respectively. The description of dynamic fields depends on whether a time-domain or a frequency-domain representation is used. In the time-domain the *wave equation* is encountered

$$\nabla^2\psi - \frac{1}{c^2}\frac{\partial^2\psi}{\partial t^2} = 0 \tag{F.2.8a}$$
$$\nabla \times \nabla \times \boldsymbol{\psi} + \frac{1}{c^2}\frac{\partial^2\boldsymbol{\psi}}{\partial t^2} = 0; \quad \nabla \cdot \boldsymbol{\psi} = 0, \tag{F.2.8b}$$

where c refer to the wave speed. In the frequency-domain the *Helmholtz equation* is considered

$$\nabla^2\psi + k^2\frac{\partial^2\psi}{\partial t^2} = 0 \tag{F.2.9a}$$
$$\nabla \times \nabla \times \boldsymbol{\psi} - k^2\frac{\partial^2\boldsymbol{\psi}}{\partial t^2} = 0; \quad \nabla \cdot \boldsymbol{\psi} = 0, \tag{F.2.9b}$$

where k denotes the wave number. We will return in more details to some of these equations later.

F.2.6 Time-Domain Frequency-Domain

The constant frequency results can be determined with the prescription that the retarded time $t - c/R$ in the argument of a function corresponds to the presence of a factor of $\mathrm{e}^{\imath kR}$ in the complex amplitude and with the replacement of $\partial/\partial t$ by $-\imath\omega$.

This report will use time dependence notion $\mathrm{e}^{-\imath\omega t}$ where ω denotes the angular frequency. Fourier-transform uses the conventions (for each $\mathbf{r}$)

$$p_\omega(\mathbf{r}) = \frac{1}{2\pi}\int_{-\infty}^{\infty} p(\mathbf{r},t)\mathrm{e}^{\imath\omega t}\,\mathrm{d}t \tag{F.2.10a}$$
$$p(\mathbf{r},t) = \int_{-\infty}^{\infty} p_\omega(\mathbf{r})\mathrm{e}^{-\imath\omega t}\,\mathrm{d}\omega, \tag{F.2.10b}$$

thereby producing a time-harmonic function $p_\omega(\mathbf{r})\mathrm{e}^{-\imath\omega t}$, where $p(\mathbf{r},t)$ denote acoustic pressure at position $\mathbf{r}$ at time t and $p_\omega(\mathbf{r})$ is the corresponding frequency-domain acoustic pressure at position $\mathbf{r}$.

The frequency is chosen positive ($\omega > 0$) as we can use the *reality condition* ($f_{-\omega} = f_\omega^*$) to determine fields, sources and equations for negative frequencies.

F.3 Field Theory of Fluid Mechanics

In this section we will present the field theory governing *fluid mechanics* on which theoretic acoustics is founded. The presentation will be based on [26, Ch. 2.3] and [28, Ch. 6.2, 6.4, 14.4].

Definition F.1. A fluid such as water or air, deforms continuously when acted on by shearing stress of any magnitude.

From the very outset it should be remarked that is considered impossible to develop a universal model for *fluid mechanics* that suits all possible circumstances in *fluid-static* or *fluid-dynamic* and for all types of fluids. If such universal fluid dynamical model could be obtained the inherent complexity implies that it would be prohibitively difficult to solve. Instead specialized models are made to suit particular cases. An example of such specialization is made when we are making certain assumptions upon entering the domain of acoustics.

Fluid Mech. Field Theory Assump.# 1. *Macroscopic domain.* Fluid mechanics is characterized by the behavior of average values of the quantities of interest, where the average is evaluated over a small volume (compared with the physical system of interest) yet containing a large number of molecules. The molecular spacing under ordinary conditions is of the order of 1 nm for gases and 0.1 nm for liquids. In practice volume sizes of the order of 100 nm^3 for gases and 10 nm^3 for liquids would let us consider the fluid a continuous distribution. Furthermore, in the high frequency region the shortest wavelength should still be many order of magnitude larger than the size of the infinitesimal volume which serves to define the densities of the field for the wave equation to hold. Accordingly, the upper frequency limit as regards a macroscopic point of view under similar conditions is of the order of 3×10^2 MHz for gases and 1.5 GHz for liquids.

Basically, the theory of fluid motion is founded by five sets of equations that include:

1. A *continuity equation in mass flow density* (F.3.48) on page 642.
2. A *continuity equation in momentum density* (F.3.53) on page 644.
3. An expression of the *conservation of energy* (F.3.66) on page 647.
4. An expression related to *entropy generation* (F.3.68) on page 648.
5. A set *constitutive relations* section F.3.9 on page 648.

However, before entering these fundamental equations it would probably be useful to investigate in some details the mechanism of sound propagation in gases as an example of propagation of a perturbation in a fluid. The mechanism of wave propagation is indeed a characteristic of each physical system. Hence, the mechanism of wave propagation of acoustical waves in fluids and electromagnetic waves in *vacuum* has very little in common. Despite the very different mechanisms involved, as regards the corresponding field theories a large number of similarities between the two physical systems exist.

F.3.1 Thermodynamical Considerations

The motivation for introducing concepts from thermodynamics is twofold. Firstly, as is well known acoustics involve wave propagation of (small) pressure, temperature and density perturbations superposed on the corresponding ambient parameters. Hence, wave propagation is actually supported by a *thermodynamic process* (a contour on $(P-v-T)$ surface plot) in space and in time. Secondly, the losses in a fluid mechanical system in general and therefore also the attenuation of acoustic waves are governed by the first and second law of thermodynamics.

Thermodynamics is the branch of physics that deals with the interior of a system, *work*, *heat* and those properties of substances that bear a relation to heat and work. It is also the science of the abstract concepts of *energy* and *entropy*. Newton's laws of motion concerns mechanical energy of a solid body and works on *mechanical coordinates* such as position and velocity.

Thermodynamic Systems

A (simple) *thermodynamic system* is described by a set *thermodynamic coordinates* that are consistent with the fundamental laws of thermodynamics. Different thermodynamic systems are considered in different branches of physics. Among such simple thermodynamic systems we find a *hydrostatic system*, a stretched wire, a surface film, an electrical cell and a paramagnetic solid [36, Ch. 2]. Compound systems (as opposed to simple systems) are constituted by two or more similar or dissimilar simple systems that may interact thermally or not. For compound systems more than one equation of state (EOS) exist and generally more than two independent thermodynamic properties are required to describe the state of the system. In the present analysis only simple hydrostatic systems will be considered. The stretched wire type of thermodynamic system is useful in the study of thermodynamic effects associated with elastic wave propagation in solid mechanics that will be presented in section F.4 on page 660.

A *hydrostatic system* or *simple compressible system* is a constant mass system that in the absence of surface, gravitational, magnetic and electrical effects exerts on the surroundings a uniform hydrostatic pressure. Hydrostatic systems are divided into the following categories [36, Ch. 2]

1. A *pure substance* is one that has a homogeneous invariable chemical composition in the form of a solid, a liquid, a gas, a mixture of any two, or a mixture of all three.
2. A *homogeneous mixture* of different constituents all of which are in the same phase.
3. A *heterogeneous mixture*, such as a mixture of different gases in contact with a mixture of different liquids.

The pure substance system is simplest to analyse while the heterogeneous mixture system is the most complex. Experimental evidence shows that the state of a hydrostatic system in *ther-*

modynamic equilibrium is uniquely determined from only two *independent* intensive properties (thermodynamic coordinates). [5] This also implies that there exists an EOS which connects the thermodynamic coordinates and which robs of one of them of its independence. Air is not complying with the definition of a pure substance, but air exhibits some of the characteristics of a pure substance as long as there is no change of phase. A mixture of liquid air and gaseous air, however, is not a pure substance because the composition of the liquid phase is different from that of the vapor phase.

In the case of a mixture of ideal gases the overall average properties can under the assumption of Dalton's law of additive pressures be estimated from the corresponding value of the property of the constituting gases on a mass or mole basis [34, Ch. 12]. Functions that are independent of the pressure like internal energy and enthalpy are determined on a mass basis. Pressure is determined on a mole basis and functions like entropy that depends on the pressure accordingly involve the mole basis in the average determination. Once, the mixture properties are found from the composition and the component properties, we can treat the mixture similarly to a pure substance. Unfortunately for solutions of solids or liquids where intermolecular force prevails there is generally no such simple way to determine the overall properties.

Thermodynamic Coordinates

The *state* of a thermodynamic pure substance system is uniquely described by certain independent observable, macroscopic properties. Among these *thermodynamic properties* are pressure, temperature, specific volume, density, mass, internal energy, enthalpy, entropy, constant-pressure and constant-volume specific heats, the Helmholtz function[6] and the Gibb's function (F.3.27) on page 637.

Of these properties only pressure, mass, volume and temperature can measured directly. The other properties should then be deduced from these measurable properties using certain thermodynamic relations. The state of a simple compressible pure substance is as mentioned above uniquely determined from only two *independent* intensive properties. By the adjective simple is understood that body forces and surface forces are absent. Hence, for such simple compressible pure substance the state can be determined from property pairs (P, T) or (v, s) or (m, g) etc. However, as $v = \rho^{-1}$ the specific volume and mass density functions, or course, are not independent. A complication to the analysis arises in two-phase mixtures that occur during *sublimation* (solid to vapor) or the opposite *solidification* (vapor to solid); *melting* (solid to liquid) or the opposite *solidifying* (liquid to vapor); and *vaporization* (liquid to vapor) or the opposite *condensation* (vapor to liquid). In such case the pressure and temperature are not independent properties. Instead pressure and specific volume or pressure and the *quality* that identifies the position on the solid-vapor line or solid-liquid line or liquid-vapor line is required to specify a saturation state of a pure substance [34, Ch. 3]. Hence, for *solidification* and *vaporization* processes the quality is defined as the ratio of the mass of vapor to the total mass. Likewise, for a *fusion* process the quality is defined as the ratio of the mass of liquid to the total mass. Quality, however, has only meaning when the substance is in a *saturated state*, that is, at saturation pressure and

[5] Thermodynamic properties can be divided into two general classes, *extensive properties* that are mass dependent and *intensive properties* that are mass independent. Mass, total volume are examples of extensive field parameters [34]. The intensive field quantities count pressure, temperature, density and all the *specific* (*per unit mass*) field variables.

[6] The specific Helmholtz function f defined as $f \equiv u - Ts$ is a property that is of interest in chemistry and is useful in considering chemical reactions that take place isothermally and isochorically. The Helmholtz function is normally not used in acoustics.

temperature. However, if surface effects, magnetic effects or electrical effects cannot be assumed negligible, then, additional thermodynamic properties like tension in a stretched wire, surface tension on a stretched surface film, electromagnetic force in a reversible cell, magnetic intensity in a paramagnetic solid etc. are required for unique determination of the state [36, Ch. 3]. Work involved by action of such effects should be recognized and treated separately.

Each of the properties of a substance in a given state has only one definite value, and these properties always have the same value for a given state, regardless of how the substance arrived at the state [34, Ch. 2]. In thermodynamics the *control mass* and *control volume* approaches are equivalent to the Lagrangian and Eulerian views respectively.

Ideal Gases

When the density of gas is sufficiently low such that *intermolecular potential energy* associated with forces between molecules can be ignored, an assumption of an *ideal gas law* often is made, where the pressure specific volume and temperature are linked according to

$$PV = n\bar{R}T, \tag{F.3.1}$$

where n denotes the number of moles of the gas and $\bar{R}$ is the universal gas constant. The ideal gas law is particular useful due to the very simple EOS. Another important fact is that the internal energy is a function of temperature only, that is,

$$U = f(T) \tag{F.3.2a}$$

$$\left(\frac{\partial U}{\partial V}\right)_T = \left(\frac{\partial U}{\partial P}\right)_T = 0. \tag{F.3.2b}$$

The ideal property (F.3.2) is particular useful in the analysis of a fluid dynamic system.

Real Gases

In many cases of interest, however, the gas is *real* (as opposed to ideal) and more elaborate methods must be considered. The internal energy of a real gases is a function of pressure as well as temperature. A measure of deviation from ideal gas behavior is provided by the compressibility factor Z

$$Z = \frac{Pv}{RT}. \tag{F.3.3}$$

From (F.3.1) we appreciate that $Z \equiv 1$ for an ideal gas. Many gases exhibit the same compressibility diagram, that is, Z as a function of P for various T in a qualitative sense [34, Ch. 3]. General quantitative compressibility diagrams can be obtained from introducing the reduced pressure P_r and the reduced temperature T_r for a given state as the value of respective property in this state divided by the value of this same property at the *critical point*[7]. Hence,

[7]The critical point of a fluid is the unique state in which saturated liquid and saturated vapor coincide in density.

$$P_r \equiv \frac{P}{P_c} \tag{F.3.4a}$$

$$T_r \equiv \frac{T}{T_c}, \tag{F.3.4b}$$

where P_c is the critical pressure and T_c denotes critical temperature. For simple molecules a *generalized chart*, that is, Z versus (P_r, T_r) can be made [34, App. D]. This generalized chart is particular useful for a substance for which no experimental data is available in the $(P - v - T)$ region of interest. In practice $Z \to 1$ for $P \ll P_c$ irrespective of temperature or if $T \gtrapprox 2T_c, P \lessapprox 4 - 5P_c$.

Equation of State

As already mentioned every thermodynamic system has its own EOS, although in some cases the relation may be so complicated that it cannot be expressed in terms of simple mathematical functions over the entire $(P - v - T)$ domain. In certain cases it desirable to have an EOS that accurately represent the $P-v-T$ behavior for a particular gas beyond the ideal gas region, that is, over the entire superheated region.

Another implication arises as many systems are not pure substances but mixtures of two or more substances. For mixtures of different pure substances the *mass fraction* and the *mole fraction* accordingly enter the system equations. By Gibb's theorem the entropy of a mixture of ideal gases is the sum of the partial entropies [36, Ch. 16.3]. The same applies to the critical pressure and the critical temperature, that is,

$$P_{c_{\text{mix}}} = \sum_{\varkappa=1}^{N_\varkappa} y_\varkappa P_{c_\varkappa} \tag{F.3.5a}$$

$$T_{c_{\text{mix}}} = \sum_{\varkappa=1}^{N_\varkappa} y_\varkappa T_{c_\varkappa}, \tag{F.3.5b}$$

where $y_\varkappa$ is the mole fraction of the $\varkappa$'th constituent defined by

$$y_\varkappa = \frac{n_\varkappa}{\sum_{\varkappa'=1}^{N_\varkappa} n_{\varkappa'}}. \tag{F.3.6}$$

A more elaborate EOS is constituted by the *Lee-Kesler equation* involving 12 constants [19]

$$Z = \frac{P_r \check{v}_r}{T_r} = 1 + \frac{B}{\check{v}_r} + \frac{C}{\check{v}_r^2} + \frac{D}{\check{v}_r^5} + \frac{c_4}{T_r^3 \check{v}_r^2}\left(\beta + \frac{\gamma}{\check{v}_r^2}\right)\exp\left(-\frac{\gamma}{\check{v}_r^2}\right) \tag{F.3.7a}$$

$$B = b_1 - \frac{b_2}{T_r} - \frac{b_3}{T_r^2} - \frac{b_4}{T_r^3} \tag{F.3.7b}$$

$$C = c_1 - \frac{c_2}{T_r} + \frac{c_3}{T_r^2} \tag{F.3.7c}$$

$$D = d_1 + \frac{d_2}{T_r}, \tag{F.3.7d}$$

where $\check{v}_r$ denotes the modified reduced specific volume

$$\check{v}_r = \frac{P_c v}{R T_c} \tag{F.3.8}$$

and b_1, b_2, b_3, b_4, c_1, c_2, c_3, c_4, d_1, d_2 and β, γ are Lee-Kesler EOS constants.

Heat and Work

Work and heat are energy transfer between a control volume (CV)[8] and its surroundings. Work is said to be done if a system undergoes a displacement under the action of a force, the amount of work being equal to the product of the force and the component of the displacement parallel to the force. Accordingly, the character of the work depends on the specific type of thermodynamic system listed in subsection F.3.1 on page 626. Work is done *by* the *system* when the resultant force exerted by the *system* on its *surroundings* is in the *same* direction as the displacement and by convention such work is considered positive. Conversely, when the force exerted by a system on its surroundings is *opposite* to the displacement, work is done *on* the system, and this work is called negative [36, Ch. 3.1].

Heat is energy transferred due to temperature differences and manifest itself as *heat conduction*, *heat convection* or *thermal radiation*. Heat is an universal phenomena and is independent of the type of thermodynamic system introduced in subsection F.3.1 on page 626. By definition heat is positive when it enters a system and negative when it leaves. The oppositive sign convention used for work and heat stems from early applications of thermodynamics in the study of heat engines whose normal operation involves the inflow of heat and the output of work.

Zeroth Law of Thermodynamics

The *zeroth law of thermodynamics* is the basis for temperature measurements and precedes the first and second laws (from which it cannot be deduced). Basically, the zeroth law expresses that two systems in *thermal equilibrium* with a third are in thermal equilibrium with each other. The zeroth law, however, will only be used implicitly in our development as it facilitates the temperature concept.

First Law of Thermodynamics

For a process involving only infinitesimal changes in the thermodynamic coordinates of a system is known as an *infinitesimal process*. For such process we can formulate the first law of thermodynamics on differential form for a CM as

$$\boxed{\mathrm{d}U = \delta Q - \delta W - \mathrm{d}E_{\mathrm{kin}} - \mathrm{d}E_{\mathrm{pot}}.} \tag{F.3.9}$$

The first law predicts the existence of the function known as internal energy function U of the coordinates of a thermodynamic system whose value at the final state of a process minus its value at the initial state is equal to the amount of heat supplied to the CM subtracted the work done by the CM on its surroundings and subtracted the bulk energy transferred to kinetic energy

[8] In this subsection we may consistently replace CV by control mass (CM).

function E_{kin} and potential energy function E_{pot} . The symbol δ denotes an *inexact differential*. The quantity of heat received by the system δQ is denoted δQ rather than $\mathrm{d}Q$ because it is not a perfect differential since it is not necessary that the total heat of a system is supplied as heat; it may come from mechanical energy in compression. Both work and heat involve inexact differentials as both the work and the heat are functions of the integration path as well as the beginning state and end state. There is no function of the thermodynamic coordinates representing the work nor the heat in a body.

Fluid Mech. Field Theory Assump.# 2. In a *quasi-static process* the system passes from an initial equilibrium state to a neighboring equilibrium state[9]. This in turn implies that $\mathrm{d}U$ and δW can be expressed in terms of thermodynamic coordinates only. For a hydrostatic system the first law for a CM becomes

$$\boxed{\mathrm{d}U = \delta Q - P\,\mathrm{d}V - \mathrm{d}E_{\text{kin}} - \mathrm{d}E_{\text{pot}}.} \tag{F.3.10}$$

If the assumption of a quasi-static process fails then there exists a time during the process in which the process is not infinitesimal near a *state of thermodynamic equilibrium*. Then at least one of the requirements on (1) *mechanical equilibrium*, (2) *thermal equilibrium* or (3) *chemical equilibrium* is violated [36, Ch. 3.2]. As a consequence the EOS is not valid for all these states. This in turn complicates the analysis in which the EOS plays a fundamental role viz. subsection F.3.9. The impact of this depends on the degree and nature of the violation and on the particular thermodynamic system considered. For a hydrostatic system violation of the assumption of a quasi-static process could be caused by large and/or rapidly varying perturbations. Processes that not at all times are infinitesimal near thermodynamic equilibrium will most likely be accompanied by losses as will discussed in section F.3.1 on page 634.

Another thermodynamic property that is often used to describe the energy flows across open boundaries of a control surface (CS) fluid dynamics and acoustics is the *enthalpy* H defined by

$$H \equiv U + PV \tag{F.3.11}$$

and the *specific enthalpy* h that is similarly defined by

$$h \equiv u + Pv. \tag{F.3.12}$$

We will make use of the first law in subsection F.3.7 on page 646 dealing with the conservation of energy in a material element.

Second Law of Thermodynamics

While the first law denies the possibility of creating or destroying energy; the second law denies the possibility of utilizing energy in a particular way. The second law of thermodynamics on differential form for a CM may be expressed as

$$\boxed{dS = \frac{\delta Q}{T} + \delta S_{\text{gen}},} \tag{F.3.13}$$

[9] The requirement of a quasi-static process is more restrictive than a requirement of an infinitesimal process.

δS_{gen} represents the amount of entropy generation in the process due to irreversibilities occurring inside the system. This entropy generation in turn is subject to the following constraint:

$$\delta S_{\text{gen}} \begin{cases} = 0; & \text{reversible process} \\ > 0; & \text{irreversible process.} \end{cases} \tag{F.3.14}$$

Hence, according to the second law of thermodynamics the total energy of a CM (or for that sake a closed system) does not increase. Like the internal energy property enabled us to use the first law quantitatively for processes (as opposed to cycles) the *entropy* property enables us to use the second law quantitatively for processes.

The concept of *energy* raises from the first law of thermodynamics and the concept of *entropy* from the second law of thermodynamics. In statistical thermodynamics the entropy represent a likelihood of a the substance to be in a certain state. Accordingly, a change of state from a less probable state to a more probable state occurs in a *irreversible process* associated with an increase of entropy. Entropy increase is experienced in relation to *diffusion processes*.

Hence, the entropy increases as a sound wave attenuates as energy is transferred from a less likely state of organized motion to a more likely state of disorganized motion in terms of heat.

We will make use of the second law in subsection F.3.8 on page 648 addressing the generation of entropy in a material element.

Third Law of Thermodynamics

The absolute value of the entropy of substances is governed by the *third law of thermodynamics* that is of particular importance in low temperature chemistry. Based on *statistical thermodynamics* the third law of thermodynamics states that at the absolute zero of temperature the entropy of a perfect crystal is zero, that is, it attains its maximum degree of order [34, Ch. 14]. The third law provides an absolute base from which to measure the entropy of each substance.

As we are concerned about relative changes to the thermodynamic coordinates including the entropy and do no concern about absolute values of these coordinates we will make no further reference to the third law. It is included here merely for the sake of completeness.

Internal Energy

The *internal energy* is a concept used in *thermodynamics* and generally represents the total energy due to the motion of *molecules*, energy in all *chemical bonds* (*intermolecular energy*), potential energy associated with *intramolecular energy*, rotational energy and vibrational and electric energy of atoms within molecules or crystals, *nuclear energy* and *electron energy* of a result of both orbital angular momentum of the electrons about the nucleus and angular momentum of the electrons spinning on their axis and the energy of a free conducting electrons in metals. It should be remarked that kinetic energy due to bulk (organized) motion, is not part of the internal energy. This energy associated with bulk motion makes up the acoustic energy kinetic density (F.3.108) on page 659. The concept of internal energy plays a central role in the propagation of perturbations in a fluid.

A gas will often be a mixture (as opposed to a *pure substance*) constituted by various species of mono-, di- and polyatomic molecules. Examples of monoatomic molecules are He and Ar. Among

the diatomic molecules of most interest we find N_2 and O_2. In *dry air* the volume content ratios of the constituents (N_2, O_2, Ar) are (78%, 21%, 1%) corresponding to the following *weight ratios* (75%, 23%, 1%) [33, Ch. 1.9]. These ratios are relative constants, but the water H_2O contents is subject to large variations.

The mono-, di- and polyatomic molecules are characterized by different degrees of freedom (dof) in their storage of internal energy. Every molecule, mono-, di- and polyatomic possess a number of dof for translational movements $N_{\rm tr}^{\rm dof}$ identical to 3. In addition, the diatomic and polyatomic molecules possess a number of dof for rotational movements $N_{\rm rot}^{\rm dof}$. This number equals 2 for diatomic and linear polyatomic molecules and equals 3 for nonlinear polyatomic molecules. Finally, the number of dof for vibrational movements $N_{\rm vib}^{\rm dof}$ is $3\mathcal{N}-5$ for diatomic and linear polyatomic molecules and equals $3\mathcal{N}-6$ for nonlinear polyatomic molecules, where $\mathcal{N}$ denotes the number of atoms in molecule.

In the air it normally suffices to consider kinematic energy contribution from translational, rotational and vibrational motion of molecules. However, as discussed in section F.3.1. in gas mixtures like combustion products absorption of sound waves due to chemical reactions, particularly in the high-frequency limit at high temperatures and pressures must be taking into account. Sound waves in sea water can initiate pressure-dependent chemical reactions thereby causing a temporary perturbation from local *chemical equilibrium*. The principal chemicals contributing to such processes in sea water are dissolved magnesium sulfate $MgSO_4$ and dissolved boric acid H_3BO_3.

In the following we will define different forms of *specific* internal energy[10]. In a fluid mixture composed of a total number of gas species $N_\varkappa$ the specific internal energy $u(\mathbf{r},t)$ is constituted by the specific translational kinetic internal energy $u_{\rm tr}(\mathbf{r},t)$, the specific rotational kinetic internal energy $u_{\rm rot}(\mathbf{r},t)$ and the specific vibrational kinetic internal energy $u_{\rm vib}(\mathbf{r},t)$ added the specific chemical bound internal energy $u_{\rm ch}(\mathbf{r},t)$ and the specific electron internal energy $u_{\rm e}(\mathbf{r},t)$, that is,

$$u(\mathbf{r},t) = u_{\rm tr}(\mathbf{r},t) + u_{\rm rot}(\mathbf{r},t) + u_{\rm vib}(\mathbf{r},t) + u_{\rm e}(\mathbf{r},t) + u_{\rm ch}(\mathbf{r},t) \tag{F.3.15a}$$

$$= \sum_{\varkappa=1}^{N_\varkappa} u^{\varkappa}(\mathbf{r},t) \tag{F.3.15b}$$

$$= \sum_{\iota=1}^{N_\iota}\sum_{\varkappa=1}^{N_\varkappa} u_\iota^{\varkappa}(\mathbf{r},t), \tag{F.3.15c}$$

where $\varkappa$ is the species indicator, and where ι is the internal energy index, which takes the following values

$$\iota = \begin{cases} 1; & \text{translation} \\ 2; & \text{rotation} \\ 3; & \text{vibration} \\ 4; & \text{electron} \\ 5; & \text{chemical.} \end{cases} \tag{F.3.16}$$

[10]The terms *specific* and *per unit mass* are synonyms.

By assuming additivity of internal energy modes it is implicitly also assumed that no interaction between the rotational and vibrational modes of energy occurs. Nuclear energy, which, except in the case of nuclear reactions, is constant an omitted from our analysis. The contribution to the internal energy from electrons with the common exceptions of the monoatomic gases O, Cl and F and the diatomic gases O_2, NO and OH is usually very small compared with the translational energies except at very high temperatures. Hence, the number of internal energy modes N_ι considered equals 5. For monoatomic molecules the contribution to rotational and vibrational energy densities is negligible, that is, $u_{\text{rot}} \approx u_{\text{vib}} \gtrapprox 0$.

Relaxation

By definition the *apparent temperature* associated with mode ι for species $\varkappa$ $\breve{T}_\iota^\varkappa(\mathbf{r},t)$ is related to the internal energy density for the same species and energy mode

$$\breve{T}_\iota^\varkappa(\mathbf{r},t) = \frac{2}{N_\iota^{\text{dof},\varkappa}} \frac{u_\iota^\varkappa(\mathbf{r},t)}{R}. \tag{F.3.17}$$

The quantity R denotes the gas constant for a particular gas that is determined from the universal gas constant by division of the molecular weight M , that is,

$$R = \frac{\bar{R}}{M}. \tag{F.3.18}$$

From statistical thermodynamical considerations internal equilibrium is not established until the apparent temperatures corresponding to the translatoric, rotational and vibrational coincide, that is, $T = \breve{T}_{\text{tr}} = \breve{T}_{\text{rot}} = \breve{T}_{\text{vib}}$ and generally in a mixture $T = \breve{T}_\iota^\varkappa; \forall \varkappa \in \underline{N}_\varkappa, \iota \in \underline{N}_\iota$ [33, Ch. 10.7]. Due to finite sluggishness a delay refereed to as the *relaxation time* will occur before internal equilibrium is fully obtained.

Finally, the degree of relative excitation of each internal energy mode term $u_\iota^\varkappa$ is described by a function $F_\iota^\varkappa(T)$

$$F_\iota^\varkappa(T) = 2\frac{M^\varkappa}{R^\varkappa}\left(\frac{\partial u_\iota^\varkappa}{\partial T}\right)_V. \tag{F.3.19}$$

It suffice to say here, that $F_\iota^\varkappa(T) \in [0;1]$ and by definition $F_\iota^\varkappa(T) = 0$ for $T = 0$. For translational and rotational modes $F_\iota^\varkappa(T) \lessapprox 1$ for temperatures of normal interest. The vibrational modes, however, are normally only very weakly excited, that is, $F_\iota^\varkappa(T) \gtrapprox 0$ at ordinary temperatures.

By definition the pressure corresponds to translatoric and no other kinematic terms.

The molecules in the gas are moving randomly and uniformly distributed in space with the root-mean-square of the molecular speed approximately equal to the speed of sound in the fluid. At standard atmospheric pressure and a temperature of 20 °C the density will be such that the mean-free-path of molecules l is of the order of 10^{-5} cm and each molecule will statistically experience a collision approximately each 1 ns.

Imagine a source radiating, say, a compressional pulse of acoustical energy into the surrounding fluid. During compression a fluid element absorbs energy and as a consequence it is somewhat warmer, more denser and will exert higher forces per unit surface area than the ambient fluid,

that is, $(p > 0, \rho > 0, \tau > 0)$. The increase in internal energy of compressed fluid elements is (almost) immediately propagated to the yet undisturbed surrounding region of space in terms of interactions on a molecular scale. Upon each of the aforementioned collisions, energy and momentum transfer with a net transfer from the warmer to the colder fluid will take place. For time-harmonic waves this process will be reverse during rarefaction.

Each mode of internal energy *per unit mass* $u_\iota^\varkappa$ will follow a mode-dependent exponentially-decaying transition curve from one equilibrium point at, say, T_{e_1} towards another equilibrium point at, say, T_{e_2}. This transition is characterized by the time constant in relaxation process $\tau_\iota^\varkappa$

$$\breve{u}_\iota^\varkappa(T) = u_\iota^\varkappa(T_{e_2}) + (u_\iota^\varkappa(T_{e_1}) - u_\iota^\varkappa(T_{e_2})) \exp^{t/\tau_\iota^\varkappa} . \tag{F.3.20}$$

Using the expansions in subsection F.2.4 on page 622 we may express the transition curves in terms of the internal acoustic energy *per unit mass* associated with mode ι for species $\varkappa$ $u_{\iota,-0}^\varkappa$ as

$$\breve{u}_{\iota,-0}^\varkappa(T) = u_{\iota,-0}^\varkappa(T_{e_2}) + (u_{\iota,-0}^\varkappa(T_{e_1}) - u_{\iota,-0}^\varkappa(T_{e_2})) \exp^{t/\tau_\iota^\varkappa} . \tag{F.3.21}$$

The time constants for the three relaxation process are related as follows

$$\tau_{\text{tr}} \approx 0.1 \text{ ns} \lessapprox \tau_{\text{rot}} \approx 1 \text{ ns} \ll \tau_{\text{vib}}^{\text{O}_2} \approx 10 \text{ µs} \ll \tau_{\text{vib}}^{\text{N}_2} \approx 1 \text{ ms}, \tag{F.3.22}$$

where τ_{tr}, τ_{rot}, τ_{vib} are the relaxation time constants for translational-, rotational- and vibrational modes respectively. The indicated time constants pertain to air at meteorological temperatures. Hence, translation respond almost immediately to a change in equilibrium. Rotational modes are also easily excited whereas the vibrational modes are much more difficult to excite. The indicated figures for N_2 and O_2 are very strongly dependent on the humidity. During a collision with a H_2O molecule statistically much more energy is namely set into vibration than when colliding with another O_2 or N_2 molecule.

An example of a chemically reacting fluid is the ocean where the two most important chemical relaxation processes are due to dissolved magnesium sulfate $\tau_{\text{ch}}^{\text{MgSO}_4} \approx 10^{-5}$ s and dissolved boric acid $\tau_{\text{ch}}^{\text{H}_3\text{BO}_3} \approx 10^{-3}$ s.

A consequence of the nonuniform time constants in (F.3.22), the wave propagation will be *dispersive*. In the high-frequency limit, some of the relaxation time-constant might be of the order of several periods of the signal and no appreciably activation of these modes takes place as the sound wave passes. The speed of sound attains it *frozen* value that might be appreciable higher than the low-frequency (equilibrium) value. In between the low- and high-frequency limits where the dispersion is most pronounced the fluid composition oscillates through non-equilibrium states which complicates the analysis.

The relaxation process, however, might be interrupted at three principal stages. At low frequencies ($f \ll \frac{1}{\max \tau_\iota^\varkappa}$) the transition will have sufficient time to complete for all internal energy modes and the process can be assumed to be in constant equilibrium. At medium frequencies ($f \approx \frac{1}{\min \tau_\iota^\varkappa}$), however, the process is interrupted at a non-equilibrium point and as a consequence *hysteresis* and dissipation is introduced. At higher frequencies ($f \gg \frac{1}{\min \tau_\iota^\varkappa}$) the relaxation process is never initiated. Under usual conditions the frequencies can be considered low and the fraction of internal energy contained in vibrational mode is very low. Hence, the dispersive nature can normally be ignored except for propagation of sound waves in moist air.

The level of internal energy excitation will vary inversely proportional to the squared-distance from the source. Depending on the type of source (monopole, dipole, quadropole etc.) different *radiation pattern* is experienced.

This transfer of sound wave energy may be accompanied by dissipative losses due to heat conduction and finite viscosity. It is however important to appreciate that impurities in the air (as opposed to dry air) due to a content of H_2O or CO_2 may lead to an increased level of absorption.

Chemical Relaxation

Among chemical reactions we find *dissociation*, *ionization*, *association*, *precipitation*.

We may write a generic chemical process in a heterogeneous system of a number of constituents $N_\varkappa$ whose chemical symbols are $A_1, A_2, \ldots A_{N_\varkappa}$ as

$$\sum_{i=1}^{N_{\varkappa,l}} \nu_i A_i \rightleftharpoons \sum_{i=N_{\varkappa,l}+1}^{N_\varkappa} \nu_i A_i. \tag{F.3.23}$$

$N_\varkappa$ in turn is obtained as the sum of the number of constituents on the LHS of (F.3.23) $N_{\varkappa,l}$ and number of constituents on the RHS of (F.3.23) $N_{\varkappa,r}$, that is, $N_\varkappa = N_{\varkappa,l} + N_{\varkappa,r}$. The number ν_i is the *stoichiometric coefficient* of the i'th constituent that is proportional to the number of moles of the i'th constituent.

At *chemical equilibrium* the forward chemical reaction rate is exactly equal to the backward chemical reaction rate and there is no change in chemical composition. However, the pressure and temperature variations accompanied with the passage of a sound wave will cause temporary perturbation of the fluid from the equilibrium, and the chemical reaction will, in the net, proceed in a direction to retain chemical equilibrium.

The composition of a *heterogeneous mixture* is described by the set of $n_\varkappa^{(\varphi)}$ changes due chemical activity or by virtue of a transportation of mass across the boundaries between phases, or both. Such kind activities continues until *chemical equilibrium* is attained. However, provided that *thermal equilibrium* and *mechanical equilibrium* is maintained for each of the phases it is assumed that they each be represented with the aid of the coordinates $P, V, T, n_1^{(\varphi)}, n_2^{(\varphi)}, \ldots, n_{N_\varkappa^{(\varphi)}}^{(\varphi)}$ of which only two of (P, V, T) are independent [36, Ch. 16.7].

It should be remarked that from this definition of a phase any extensive property such as V, U, S, H, F or G for a *heterogeneous system* is obtained as the sum of the contribution of each of the phases, that is,

$$X = \sum_{\varphi=1}^{N_\varphi} X^{(\varphi)}, \tag{F.3.24}$$

where X is a surrogate for an arbitrary extensive property, where the phase components $X^{(\varphi)}$ in turn are function of $(P, T, n_1^{(\varphi)}, n_2^{(\varphi)}, \ldots, n_{N_c^{(\varphi)}}^{(\varphi)})$ and where as usual (P, V) or (V, T) may replace (P, T).

The *equations of phase equilibrium* represent an important fact in the development which is that at equilibrium the chemical potential of a constituent in one phase must be equal to the chemical

potential of the same constituent in every other phase, that is,

$$\forall \varphi, \varphi' \in \underline{N}_\varphi, \varkappa \in \underline{N}_\varkappa : \quad \mu_\varkappa^{(\varphi)} = \mu_\varkappa^{(\varphi')}. \tag{F.3.25}$$

The number of components in the thermodynamic system N_c can be obtained from

$$N_c = N_\varkappa - N_r - N_z - N_\varphi + 2, \tag{F.3.26}$$

where N_r is the number of independent reactions, N_z denote the number of independent restricting equations, such as an equation expressing electric neutrality or an equation expression balance of mole fractions. The number 2 appearing in (F.3.26) stems from necessity also in the pure substance case to include two independent thermodynamic properties among (P, v, T). The number of component N_c is the smallest number of constituents whose specification is sufficient to determine the composition of every phase.

The specific Gibb's function g defined as

$$g \equiv h - Ts \tag{F.3.27}$$

is a property that is of interest in chemistry, since chemical reactions can be conceived as to take place isothermally and isobarically. The Gibb's function is normally not used in acoustics, but will be used in the present context to address the general problem of describing propagation of waves in substances that are heterogenous and chemically active. In thermodynamics a *phase* is defined as a system or a portion of a system composed of any number of chemical constituents satisfying the requirement (1) that it is homogeneous and (2) that it has definite boundaries [36, Ch. 16.7]. In the heterogeneous system the total Gibb's function G is the sum of the Gibb's functions of all the phases, that is,

$$G = \sum_{p=1}^{N_\varphi} \sum_{c=1}^{N_\varkappa^{(\varphi)}} \mu_c^{(\varphi)} n_c^{(\varphi)}, \tag{F.3.28}$$

where $n_c^{(\varphi)}$ is the number of moles of the c'th constituent of the p'th phase and where the quantity $\mu_c^{(\varphi)}$ denotes the chemical potential of the c'th constituent of the p'th phase defined by [36, Ch. 18]

$$\mu_c^{(\varphi)} = \frac{\partial G}{\partial n_c^{(\varphi)}}. \tag{F.3.29}$$

The *degree of reaction* ϵ is defined by

$$\epsilon = \frac{n_{\varkappa',\mathrm{l},\ \max} - n_{\varkappa',\mathrm{l}}}{n_{\varkappa',\mathrm{l},\ \max} - n_{\varkappa',\mathrm{l},\ \min}}, \tag{F.3.30}$$

where the index $\varkappa', \mathrm{l}$ refer to (one of) the left-hand side (LHS) substances that if the reaction proceeded to the right would completely disappear. In this case $n_{\varkappa',\mathrm{l}} = n_{\varkappa',\mathrm{l},\ \min} = 0$. Similarly, if the reaction proceed to the left then $n_{\varkappa',\mathrm{l}} = n_{\varkappa',\mathrm{l},\ \max}$. Hence, $\epsilon \in [0, 1]$ and $\epsilon = 0$ when the reaction is completely to the left and $\epsilon = 1$ when the reaction is completely to the right. Moreover,

the partial derivative of the degree of reaction with respect to temperature for constant pressure and the derivative of the degree of reaction with respect to pressure for constant temperature are related to the Gibb's function according to

$$\left(\frac{\partial \epsilon_e}{\partial T}\right)_P = \frac{\left(\frac{\delta Q}{\mathrm{d}\epsilon}\right)_{T,P}}{T\left(\frac{\partial^2 G}{\partial \epsilon^2}\right)_{T,P}} \tag{F.3.31a}$$

$$\left(\frac{\partial \epsilon_e}{\partial P}\right)_T = -\frac{\left(\frac{\partial V}{\mathrm{d}\epsilon}\right)_{T,P}}{\left(\frac{\partial^2 G}{\partial \epsilon^2}\right)_{T,P}}. \tag{F.3.31b}$$

Since G is at a minimum at thermodynamic equilibrium, $\frac{\partial^2 G}{\partial \epsilon^2}$ is positive at $\epsilon = \epsilon_e$. Hence, (F.3.31a) states that an increase of temperature at constant pressure always causes a reaction to proceed in the direction in which heat is absorbed at constant P. From (F.3.31b) we similarly recognize that an increase in pressure at constant temperature causes a reaction to proceed in the direction in which the volume decreases. For low frequencies, the chemical reaction rate is fast enough to essentially instantaneously maintain equilibrium and the fluid can be considered to be in quasi-equilibrium state during the passage of the sound wave.

In the high-frequency limit, the chemical reaction rate is to slow to appreciably change the chemical composition as the sound wave passes and the fluid composition can be treated as a constant. The speed of sound attains it *frozen* value that might be appreciable higher than the low-frequency (equilibrium) value.

In between the low- and high-frequency limits the fluid composition oscillates through non-equilibrium states which complicates the analysis. The manner in which a sound wave propagates within a chemically reacting substance (such as high temperature combustion products [2] or sea water with a contents of boric acid and carbonate [25]) is therefore dependent upon the frequency of the sound wave and the chemical reaction times involved.

In [2] calculations indicated a strong absorption due to $\mathrm{O_2} \rightleftharpoons 2\,\mathrm{O}$ chemical reaction, particularly in the high-frequency limit at high temperatures and pressures. In a series of papers Mellen, Browning, and Simmons proposed a coupled model for the chemical relaxation in sea water supporting experimental data [22–25].

From these studies it was concluded that the chemical relaxation mechanism associated with acid-base exchange between boric acid and carbonate is responsible for low-frequency sound absorption in sea water. These, mechanisms, however, are quite involved and probably not yet fully understood. Experimental evidence suggests that the following coupled processes partake in the low-frequency chemical relaxation [25].

1. The boric acid/borate equilibrium mechanism

$$\mathrm{Na^+ + B(OH)_3 + CO_3^{2-} + H_2O} \overset{1}{\rightleftharpoons} \mathrm{Na^+ + B(OH)_4^- + HCO_3^-} \tag{F.3.32}$$

that as indicated by the $\mathrm{Na^+}$ ion is dependent on the NaCl concentration as the following reaction takes place in parallel [25]

$$\mathrm{NaCO_3^- + B(OH)_3 + H_2O} \overset{2}{\rightleftharpoons} \mathrm{NaB(OH)_4^0 + HCO_3^-}\,\cdot \tag{F.3.33}$$

Accordingly the LHSs of (F.3.32) and (F.3.33) are linked $\uparrow\downarrow$ 3 through a dissociation of $\mathrm{NaCO_3^-}$ and the right-hand sides (RHSs) are linked $\uparrow\downarrow$ 4 through dissociation of $\mathrm{NaB(OH)_4^0}$.

We deduce the following: $N_\varkappa = 8$ (Na^+, $B(OH)_3$, CO_3^2, H_2O, $B(OH)_4^-$, HCO_3^-, $NaCO_3^-$, $NaB(OH)_4^0$), $N_r = 3$ (4 reactions of which only 3 are independent), $N_z = 1$ (electric neutrality $2y_{Na^+} = 2y_{CO_3^{2-}} + y_{NaCO_3^-} + y_{HCO_3^-}$). By insertion in (F.3.26), we obtain $N_c = 8 - 3 - 1 - 2 + 2 = 4$. Hence, in addition to the pressure P and the temperature T we need two mole fractions, such as, $y_{NaB(OH)_4^0}, y_{H_2O}$ in order uniquely to determine the state of the system.

The relaxation frequency is approximately 1 kHz.

2. The magnesium carbonate absorbtion

$$Ca^{2+} + B(OH)_3 + CO_3^{2-} + H_2O \overset{1}{\rightleftharpoons} Ca^{2+} + B(OH)_4^- + HCO_3^- \tag{F.3.34}$$

coupled to

$$CaCO_3^0 + B(OH)_3 + H_2O \overset{2}{\rightleftharpoons} CaB(OH)_4^+ + HCO_3^- \cdot \tag{F.3.35}$$

3. The magnesium carbonate absorbtion

$$Mg^{2+} + B(OH)_3 + CO_3^{2-} + H_2O \overset{1}{\rightleftharpoons} Mg^{2+} + B(OH)_4^- + HCO_3^- \tag{F.3.36}$$

coupled to

$$MgCO_3^0 + B(OH)_3 + H_2O \overset{2}{\rightleftharpoons} MgB(OH)_4^+ + HCO_3^- \cdot \tag{F.3.37}$$

The actual effect of this chemical process, however, is an open question.

There are three principal chemical relaxations processes contributing to low-frequency sound absorption in sea water. The actual absorption coefficient will exhibit large variations with frequency, and the concentrations of NaCl, $MgCl_2$ and $CaCl_2$. The reason for the slow chemical reactions and hence low relaxation frequency is due to structural change between the trigonal planar boric acid molecule and the tetrahedral borate ion.

Summary

In summary, the four laws of thermodynamics, the concepts of *work*, *heat*, *energy* and *entropy* have been presented. The mechanism responsible for propagation of a perturbation in a fluid including the relaxation phenomena was discussed. The dissipative effects of thermal conductivity, viscosity and relaxation hysteresis will be "absorbed" by using a complex wave number k with a finite imaginary part

$$k = k_{re} + \imath k_{im} = \frac{\omega}{c_0}\left\{1 + \frac{\imath\omega}{2\rho c_0^2}\left[\mu_B + \tfrac{4}{3}\mu + (\gamma - 1)\frac{\kappa}{C_P}\right]\right\}, \tag{F.3.38}$$

where

$$c_0 = \sqrt{\frac{1}{K_s\rho}} \tag{F.3.39}$$

(F.3.38) also exhibits the inherent *dispersive* nature of wave propagation in the constitutent dissipative media.

In order to proceed we will invoke the following assumption.

Fluid Mech. Field Theory Assump.# 3. Continuous in time and space. In the development of the Navier-Stokes system of equations for fluids partial derivative with respect to time or space of the field variables will be required. In practice, this excludes, e.g., fluids with contents of voids formed by bubbles of dissolved gases or contents of aggregated particles.

F.3.2 Material Derivative

In fluid dynamics and thermodynamics two interrelated viewpoints are used. In the *Eulerian viewpoint* or *control volume approach* the fluid properties within a CV and the corresponding CS that both are fixed in time as the fluid flows across the CS and through the CV. In this case, the fluid motion is given prescribing the necessary properties such as pressure, fluid velocity, density etc. as functions of space and time. However, as will turn out during the development, all of the laws governing the motion of a fluid are most easily stated in the basic form in terms of the *Lagrangian viewpoint* or *system approach*. The concept of the *material derivative*[11] is very useful in the analysis of field variables in fluids or solids. The material derivative $\frac{\mathrm{D}()}{\mathrm{D}t}$ establishes a link between the Eulerian and Lagrangian perspective and is defined as the rate at which an arbitrary variable changes with time, as measured in a frame of reference moving with the fluid, that is, the *Lagrangian description* [29, Ch. 4]

$$\boxed{\frac{\mathrm{D}()}{\mathrm{D}t} \equiv \frac{\partial()}{\partial t} + (\mathbf{u}(\mathbf{r},t)\cdot\nabla)(),} \tag{F.3.40}$$

where $\mathbf{u}(\mathbf{r},t)$ is the local fluid material velocity at position $\mathbf{r}$ in space and a time t.

In section F.A on page 684 the following general expression for the material derivative applied to the product of a scalar function $\psi(\mathbf{r},t)$ and a vector field quantity $\mathbf{B}(\mathbf{r},t)$, that is, $\frac{\mathrm{D}\left(\psi(\mathbf{r},t)\mathbf{B}(\mathbf{r},t)\right)}{\mathrm{D}t}$ is obtained using tensor notation

$$\frac{\mathrm{D}(\psi(\mathbf{r},t)\mathbf{B}(\mathbf{r},t))}{\mathrm{D}t} = \frac{\partial(\psi(\mathbf{r},t)\mathbf{B}(\mathbf{r},t))}{\partial t} + \nabla\cdot\mathfrak{A}(\mathbf{r},t) - \psi(\mathbf{r},t)\mathbf{B}(\mathbf{r},t)\nabla\cdot\mathbf{u}, \tag{F.3.41}$$

where $\mathfrak{A}(\mathbf{r},t) = \psi(\mathbf{r},t)\mathbf{B}(\mathbf{r},t)\otimes\mathbf{u}(\mathbf{r},t)$ and $\otimes$ denotes the tensor product. We will use (F.3.41) in subsection F.3.6 on page 643 in order to establish a CV interpretation of the expression for continuity in fluid moment density.

F.3.3 Reynolds Transport Theorem

The *Reynolds transport theorem* presented next establishes another link between the Lagrangian and Eulerian[12] perspectives and is widely used in fluid mechanics.

[11] Also referred to as *substantial derivative* or *Lagrange derivative*.

[12] The Eulerian description set up a fixed coordinate system and describes the properties of the fluid what ever happens to be at given point at a given time.

Now lets us by B denote an arbitrary *extensive property* and by b denote the associated *intensive property* that is interrelated with B as $B = mb$, where m is the mass of the material element of interest. The arbitrary extensive property B might be a scalar, vector or tensor. In our context the system should be considered as a material element. In the Eulerian description a CV and corresponding CS that are both fixed in time are being considered. The Reynolds transport theorem is then expressed as [29, Ch. 4]

$$\frac{\mathrm{D}B_{sys}(t)}{\mathrm{D}t} = \frac{\partial}{\partial t}\iiint\limits_{\mathrm{CV}} \rho(\mathbf{r}',t)b(\mathbf{r}',t)\,\mathrm{d}V' + \iint\limits_{\mathrm{CS}} \rho(\mathbf{r}',t)b(\mathbf{r}',t)\mathbf{u}(\mathbf{r}',t)\cdot\,\mathrm{d}\mathbf{S}', \tag{F.3.42}$$

where $B_{sys}(t) = \iiint_{\mathrm{sys}(\mathbf{r},t)} \rho(\mathbf{r}',t)b(\mathbf{r}',t)\,\mathrm{d}V'$ is the amount of the extensive property B that the *system*[13] possess at time t. The surface normal differential vector $\mathrm{d}\mathbf{S}'$ in turn is obtained as $\mathrm{d}\mathbf{S}' = \hat{\mathbf{n}}\,\mathrm{d}S$ where $\hat{\mathbf{n}}(\mathbf{r}')$ denotes the positive (outward drawn) surface normal unit vector at position $\mathbf{r}'$ and $\mathrm{d}S(\mathbf{r}')$ is the surface unit area at position $\mathbf{r}'$.

The first term on the RHS of (F.3.42) represents the rate of change of B within the control volume as the fluid flows through it and therefore represents *unsteady effects* associated with the fact that the values of the parameters within the CV may change with time. The last term in (F.3.42) represents the net flow rate of the parameter B across the entire the control surface and therefore represents *convective effects* associated with the flow of the system across the fixed CS.

By comparing (F.3.40) and (F.3.42) it can be argued that the material derivative is essentially the derivative equivalent of the integral Reynolds transport theorem.

A second expression and for our development more useful expression for the transport theorem is provided without proof in [33, Ch. 1]

$$\boxed{\frac{\mathrm{D}B_{sys}(t)}{\mathrm{D}t} = \frac{\mathrm{D}}{\mathrm{D}t}\iiint\limits_{V(\mathbf{r},t)} \rho(\mathbf{r}',t)b(\mathbf{r}',t)\,\mathrm{d}V' = \iiint\limits_{V(\mathbf{r},t)} \rho(\mathbf{r}',t)\frac{\mathrm{D}b(\mathbf{r}',t)}{\mathrm{D}t}\,\mathrm{d}V'.} \tag{F.3.43}$$

The time-varying extent of the system is described by the time-varying volume integration limits $V(\mathbf{r},t)$. At first glance it might seem that a term involving the partial derivative of the mass density $\rho(\mathbf{r},t)$ with time is missing in (F.3.43). However, in (F.3.43) the time-derivative of a volume integral with *time-varying integration limits* is being considered. It turns out that upon bringing the time-derivative operator under the sign of integration terms that manifest themselves as an expression of mass conservation can be removed.

A formal proof of (F.3.43) is provided in section F.B that utilizes the expression for the continuity of mass flow to be provided in subsection F.3.5.

This second expression for the Reynolds transport theorem will be used repeatedly in the next sections.

F.3.4 Dilatation Rate

Another important quantity encountered in fluid-dynamics is the *dilatation rate* $\dot{\Delta}(\mathbf{r},t)$ that measures the rate of volume strain, that is, the rate of increase in volume of an element of fluid,

[13] System, control mass and material element are all synonyms.

per unit current volume

$$\dot{\Delta}(\mathbf{r},t) \equiv \nabla \cdot \mathbf{u}(\mathbf{r},t). \tag{F.3.44}$$

F.3.5 Conservation of Fluid Mass

The first equation governing the fluid motion is the *equation of continuity for mass flow*, which in a Lagrangian perspective is very simple in that any change in fluid mass equals the amount of specific creation there[14]

$$\frac{\mathrm{D}}{\mathrm{D}t} \iiint\limits_{V(\mathbf{r},t)} \rho(\mathbf{r}',t)\,\mathrm{d}V' = \iiint\limits_{V(\mathbf{r},t)} q(\mathbf{r}',t)\,\mathrm{d}V', \tag{F.3.45}$$

where $q(\mathbf{r},t)$ volume source of mass-flow. Introduction of new mass could for instance be due to an explosion or a combustion process changing a solid or liquid into a gas. The nature of this source term is discussed in more details in subsection F.3.11 on page 654. The dependence of the position of the volume integration limits of the mass element $V(\mathbf{r},t)$ with time has explicit been stated in (F.3.45). We will need the following expression for the time-derivative of a volume integral with time-varying integration limits [17, Ch. 5.15]

$$\frac{\mathrm{D}}{\mathrm{D}t} \iiint\limits_{V(\mathbf{r},t)} F(\mathbf{r}',t)\,\mathrm{d}V' = \iiint\limits_{V(\mathbf{r},t)} \left[\frac{\partial F(\mathbf{r}',t)}{\partial t} + \nabla \cdot (F(\mathbf{r}',t)\mathbf{u}(\mathbf{r},t))\right] \mathrm{d}V', \tag{F.3.46}$$

where $F(\mathbf{r},t)$ is an arbitrary scalar-valued, vector-valued or tensor-valued field quantity. Hence, by insertion of (F.3.46) in (F.3.45) and applying (F.3.40) we obtain

$$\iiint\limits_{V(\mathbf{r},t)} \frac{\mathrm{D}\rho(\mathbf{r}',t)}{\mathrm{D}t}\,\mathrm{d}V' + \iiint\limits_{V(\mathbf{r},t)} \rho(\mathbf{r}',t)\dot{\Delta}(\mathbf{r}',t)\,\mathrm{d}V' = \iiint\limits_{V(\mathbf{r},t)} q(\mathbf{r}',t)\,\mathrm{d}V', \tag{F.3.47}$$

where $\dot{\Delta}(\mathbf{r},t)$ is the dilatation rate defined in (F.3.44) on this page. Appreciating that the mass element was arbitrarily chosen, requires that (F.3.45) must hold for the integrands themselves. We therefore obtain the following differential form of continuity of fluid mass density

$$\boxed{\frac{\mathrm{D}\rho(\mathbf{r},t)}{\mathrm{D}t} + \rho(\mathbf{r},t)\dot{\Delta}(\mathbf{r},t) = q(\mathbf{r},t).} \tag{F.3.48}$$

The differential form of the Lagrangian view states that the rate of change in mass density equals the amount of specific creation there subtracted the spatial rate of density change due to volume expansion of the fluid element.

[14] It is well-known from relativity theory that mass and energy are related by $E = mc^2$. However, the magnitude of change in control mass accompanied with a change in total energy will be beyond the accuracy required in essentially all engineering applications, that is, [34, Sec. 5.9].

From a Eulerian perspective we could similarly argue that any increase in mass density at a specific point in space must have been brought there by the fluid flow or else by specific creation there

$$\frac{\partial \rho(\mathbf{r},t)}{\partial t} + \nabla \cdot (\rho(\mathbf{r},t)\mathbf{u}(\mathbf{r},t)) = q(\mathbf{r},t). \tag{F.3.49}$$

The equivalence of (F.3.48) and (F.3.49) is easily confirmed under usage of (F.3.40) and (F.3.44).

The equation of continuity of mass flow (F.3.48) is a single equation but in 4 unknown variables $(\rho(\mathbf{r},t), \mathbf{u}(\mathbf{r},t))$. We therefore need more information before an expression for the pressure or fluid velocity can be obtained.

F.3.6 Continuity in Fluid Moment Density

The second governing fluid equation expresses the *continuity in fluid linear momentum density*. Based on Lagrangian reasonings it can be deduced that the rate of change in momentum density of a fluid particle equals the combined effects of external forces acting on the fluid body element and stresses acting on the fluid surface elements, that is,

$$\frac{\mathrm{D}}{\mathrm{D}t} \iiint\limits_{V(\mathbf{r},t)} \rho(\mathbf{r}',t)\mathbf{u}(\mathbf{r}',t)\,\mathrm{d}V' = \iiint\limits_{V(\mathbf{r},t)} \rho(\mathbf{r}',t)\mathbf{f}(\mathbf{r}',t)\,\mathrm{d}V' + \iint\limits_{S(\mathbf{r},t)} \mathfrak{P}(\mathbf{r}',t)\cdot \mathrm{d}\mathbf{S}', \tag{F.3.50}$$

where $\mathfrak{P}(\mathbf{r},t)$ is the fluid stress-flux tensor that accounts for the net mechanical actions of contiguous material on the surfaces of a volume element of the fluid. If the traction force is negative, that is, directed inwards the fluid element it is a *pressure*. Similarly, a *tension* is a positive traction force, that is, directed outwards the fluid element[15]. The time-varying extent of the system is described by $V(\mathbf{r},t)$ and the time-varying surface integration limits $S(\mathbf{r},t)$. We will defer a more detailed description of the fluid stress-flux tensor $\mathfrak{P}$ until section F.3.9. It suffice here to say that $\mathfrak{P}$ is a 2-tensor (second-rank) that componentwise is a symmetric 3×3 matrix consisting of stress terms b_{ij} and in order to prevent that the fluid stresses to cause rotation of any part of the medium, but let moment of the source vector $\mathbf{f}(\mathbf{r},t)$ be equal to the rate of change of *angular moment density*, $\mathfrak{P}$ must accordingly be symmetric, that is, $(b_{ij} = b_{ji})$[16]. The dependence of the position of the surface integration limits of the mass element $S(\mathbf{r},t)$ has been made explicit in (F.3.50).

The source vector $\mathbf{f}(\mathbf{r},t)$ is the external body force *per unit mass* due to gravitational, electrical or magnetic fields. Gravitational forces are normally only of interest in the study of *internal waves* which propagation is supported by buoyancy effects due to a - as regards density - horizontally stratified fluid for subsonic frequencies below the so-called *buoyancy frequency*. Another example is *acoustic-gravity wave* that are subsonic waves on a planetary-scale in the Earth's atmosphere. For other applications the effects from gravity can be neglected. Electric and magnetic sources are very important in the domain of *plasma acoustics*[17] [28, Ch. 12]. Plasma acoustics can for

[15] In [28] the opposite sign convention is chosen for $\mathfrak{P}$.

[16] If the fluid possess spinning dof like vortices the symmetry assumption no longer holds.

[17] A plasma is a fourth state of matter in contrast to solids, liquids and gases. It is typically an ionized gas which means that at least one electron has been dissociated from a proportion of the atoms or molecules. The free electric charges make the plasma electrically conductive so that it responds strongly to electromagnetic fields.

example explain the noise mechanism in *electric glow discharge*[18]. For neutral gases (nonionized), however, the coupling to electric fields is very weak, being due to *electrostriction*. The equivalent phenomena of *magnetostriction* due to the presence of a magnetic field is probably not relevant to fluids unless some contents of ferromagnetic material is present in the fluid.

A *sink* can be considered as a source with negative sign.

The external force density in turn is the negative gradient of the *potential energy density* $\Phi(\mathbf{r},t)$

$$\mathbf{f}(\mathbf{r},t) \equiv -\nabla\Phi(\mathbf{r},t). \tag{F.3.51}$$

Now by applying the Reynolds theorem (F.3.43) to (F.3.50) (with $b(\mathbf{r},t) \leftarrow \mathbf{u}(\mathbf{r},t)$) we obtain a simpler integral expression

$$\iiint\limits_{V(\mathbf{r}',t)} \rho(\mathbf{r}',t)\,\mathrm{d}V' \frac{\mathrm{D}\mathbf{u}(\mathbf{r},t)}{\mathrm{D}t} = \iiint\limits_{V(\mathbf{r},t)} \rho(\mathbf{r}',t)\mathbf{f}(\mathbf{r}',t)\,\mathrm{d}V' + \iint\limits_{S(\mathbf{r},t)} \mathfrak{P}(\mathbf{r}',t)\cdot\,\mathrm{d}\mathbf{S}'. \tag{F.3.52}$$

The surface integral in (F.3.52) can be converted to a volume integral by using the divergence theorem using the argument that $V(\mathbf{r}',t)$ in (F.3.52) has been arbitrarily chosen the expression must also hold for the integrands and upon reduction we obtain

$$\boxed{\rho(\mathbf{r},t)\frac{\mathrm{D}\mathbf{u}(\mathbf{r},t)}{\mathrm{D}t} = \rho(\mathbf{r},t)\mathbf{f}(\mathbf{r},t) + \nabla\cdot\mathfrak{P}(\mathbf{r},t).} \tag{F.3.53}$$

Expression (F.3.53) is referred to as *Cauchy's first law of motion*.

Before stating the corresponding CV integral interpretation of the continuity in moment density system we will first introduce two dyads, namely the *stress-momentum-flux tensor* $\mathfrak{T}(\mathbf{r},t)$ and the *fluid momentum-flux tensor* $\mathfrak{J}(\mathbf{r},t)$.

Componentwise the moment flux tensor $\mathfrak{J}$ is a symmetric 3×3 matrix consisting of momentum terms $\rho(\mathbf{r},t)u_i(\mathbf{r},t)$ times a velocity, e.g., $u_j(\mathbf{r},t)$. Hence, each column of $\mathfrak{J}$ represent a momentum flux in a particular direction

$$\mathfrak{J}(\mathbf{r},t) = \begin{pmatrix} \rho(\mathbf{r},t)u_1(\mathbf{r},t)u_1(\mathbf{r},t) & \rho(\mathbf{r},t)u_1(\mathbf{r},t)u_2(\mathbf{r},t) & \rho(\mathbf{r},t)u_1(\mathbf{r},t)u_3(\mathbf{r},t) \\ \rho(\mathbf{r},t)u_2(\mathbf{r},t)u_1(\mathbf{r},t) & \rho(\mathbf{r},t)u_2(\mathbf{r},t)u_2(\mathbf{r},t) & \rho(\mathbf{r},t)u_2(\mathbf{r},t)u_3(\mathbf{r},t) \\ \rho(\mathbf{r},t)u_3(\mathbf{r},t)u_1(\mathbf{r},t) & \rho(\mathbf{r},t)u_3(\mathbf{r},t)u_2(\mathbf{r},t) & \rho(\mathbf{r},t)u_3(\mathbf{r},t)u_3(\mathbf{r},t) \end{pmatrix}. \tag{F.3.54}$$

The stress-momentum-flux tensor $\mathfrak{T}$ is then obtained from subtracting the fluid stress-flux tensor $\mathfrak{P}$ from the fluid momentum-flux tensor $\mathfrak{J}$, that is,

$$\mathfrak{T}(\mathbf{r},t) = \mathfrak{J}(\mathbf{r},t) - \mathfrak{P}(\mathbf{r},t). \tag{F.3.55}$$

In the anticipation that the fluid like a solid will exhibit different behavior to pure *dilatation* and pure *deformation* we split the fluid stress-flux tensor $\mathfrak{P}$ into two viscous stress tensors. Moreover,

[18] Electric glow discharge occurs in lighting (fluorescent lights), television (plasma-screen television), plasma physics, and analytical chemistry.

due to the importance of the hydrostatic pressure P in fluid mechanics it is treated separately. Hence, we may decompose the fluid stress-flux tensor $\mathfrak{P}$ according to

$$p(\mathbf{r},t) \equiv -\tfrac{1}{3}\,\mathrm{Trace}\,\mathfrak{P}(\mathbf{r},t). \tag{F.3.56}$$

In the Eulerian view the momentum density conservation, states that the time-rate of increase in moment density inside a specific CV equals the combined effects of external forces acting on the fluid body element and stresses acting on the fluid surface elements subtracted the amount of moment *efflux* carried through CS by the fluid, that is,

$$\frac{\partial}{\partial t}\iiint\limits_{\mathrm{CV}} \rho(\mathbf{r}',t)\mathbf{u}(\mathbf{r}',t)\,\mathrm{d}V' = \iiint\limits_{\mathrm{CV}} \rho(\mathbf{r}',t)\mathbf{f}(\mathbf{r}',t)\,\mathrm{d}V' + \iint\limits_{\mathrm{CS}} \mathfrak{P}(\mathbf{r}',t)\cdot\,\mathrm{d}\mathbf{S}' - \iint\limits_{\mathrm{CS}} \mathfrak{J}(\mathbf{r}',t)\cdot\,\mathrm{d}\mathbf{S}'. \tag{F.3.57}$$

Upon using the divergence theorem and using the argument that CV has been arbitrarily chosen, then (F.3.57) can be expressed in terms of the integrands

$$\frac{\partial}{\partial t}\big(\rho(\mathbf{r},t)\mathbf{u}(\mathbf{r},t)\big) = \rho(\mathbf{r},t)\mathbf{f}(\mathbf{r},t) + \nabla\cdot\mathfrak{P}(\mathbf{r},t) - \nabla\cdot\mathfrak{J}(\mathbf{r},t). \tag{F.3.58}$$

The CV interpretation (F.3.58) can readily be deduced from the system approach (F.3.53) as follows: First (F.3.53) is expressed as

$$\frac{\mathrm{D}\rho(\mathbf{r},t)\mathbf{u}(\mathbf{r},t)}{\mathrm{D}t} = \rho(\mathbf{r},t)\mathbf{f}(\mathbf{r},t) + \nabla\cdot\mathfrak{P}(\mathbf{r},t) + \mathbf{u}(\mathbf{r},t)\frac{\mathrm{D}\rho(\mathbf{r},t)}{\mathrm{D}t}$$

applying (F.3.41) to obtain

$$\frac{\partial}{\partial t}\big(\rho(\mathbf{r},t)\mathbf{u}(\mathbf{r},t)\big) = \rho(\mathbf{r},t)\mathbf{f}(\mathbf{r},t) + \nabla\cdot\mathfrak{P}(\mathbf{r},t) - \nabla\cdot\mathfrak{J}(\mathbf{r},t) + \mathbf{u}(\mathbf{r},t)\frac{\mathrm{D}\rho(\mathbf{r},t)}{\mathrm{D}t} + \rho(\mathbf{r},t)\mathbf{u}(\mathbf{r},t)\nabla\cdot\mathbf{u}$$

finally, using the conservation of mass density equation (F.3.48) gives

$$\frac{\partial}{\partial t}\big(\rho(\mathbf{r},t)\mathbf{u}(\mathbf{r},t)\big) = \rho(\mathbf{r},t)\mathbf{f}(\mathbf{r},t) - \nabla\cdot\mathfrak{T}(\mathbf{r},t). \tag{F.3.59}$$

The advantage of applying the control system approach in expressing a governing law and the subsequently usage of the second form of the Reynolds transport theorem in (F.3.43) should be clear by now.

Similar results could have been obtained from *angular momentum density* consideration instead of the continuity in moment density approach conducted here.

Together, the equation continuity of mass flow (F.3.48), and continuity of momentum density (F.3.53) constitute 4 equations but now in 10 unknown variables $(\rho(\mathbf{r},t), \mathbf{u}(\mathbf{r},t), \mathfrak{P}(\mathbf{r},t))$. Accordingly, some additional information must become available in order to obtain a solution.

F.3.7 Conservation of Energy

The third equation governing the fluid motion is a consequence of the *first law of thermodynamics* and expresses the continuity in *internal energy*.

In a fluid the specific energy $e(\mathbf{r},t)$ is constituted by the specific kinetic energy $e_{\text{kin}}(\mathbf{r},t)$, the specific potential kinetic energy $e_{\text{pot}}(\mathbf{r},t)$ and the specific internal energy $u(\mathbf{r},t)$ defined in (F.3.15) on page 633, that is,

$$e(\mathbf{r},t) = e_{\text{kin}}(\mathbf{r},t) + e_{\text{pot}}(\mathbf{r},t) + u(\mathbf{r},t). \tag{F.3.60}$$

As discussed in section F.3.1 the internal energy $U(\mathbf{r},t)$ includes compressional energy, thermal energy, and energy associated with thermal bonds, but not kinetic energy due to bulk motion.

The time-derivative of the *kinetic energy density*, that is, $\rho(\mathbf{r},t)e_{\text{kin}}(\mathbf{r},t)$ is

$$\begin{aligned}\frac{\mathrm{D}}{\mathrm{D}t}\iiint\limits_{V(\mathbf{r},t)} \rho(\mathbf{r}',t)e_{\text{kin}}(\mathbf{r}',t)\,\mathrm{d}V' &= \iiint\limits_{V(\mathbf{r},t)} \rho(\mathbf{r}',t)\frac{\mathrm{D}e_{\text{kin}}(\mathbf{r}',t)}{\mathrm{D}t}\,\mathrm{d}V' \\ &= \iiint\limits_{V(\mathbf{r},t)} \rho(\mathbf{r}',t)\mathbf{u}(\mathbf{r}',t)\cdot\frac{\mathrm{D}\mathbf{u}(\mathbf{r}',t)}{\mathrm{D}t}\,\mathrm{d}V',\end{aligned} \tag{F.3.61}$$

where the second equation in (F.3.61) was obtained from the second version of the Reynolds transport theorem (F.3.43). The time-derivative of the *potential energy density*, that is, $\rho(\mathbf{r},t)e_{\text{pot}}(\mathbf{r},t)$ is

$$\begin{aligned}\frac{\mathrm{D}}{\mathrm{D}t}\iiint\limits_{V(\mathbf{r},t)} \rho(\mathbf{r}',t)e_{\text{pot}}(\mathbf{r}',t)\,\mathrm{d}V' &= \iiint\limits_{V(\mathbf{r},t)} \rho(\mathbf{r}',t)\frac{\mathrm{D}e_{\text{pot}}(\mathbf{r}',t)}{\mathrm{D}t}\,\mathrm{d}V' \\ &= -\iiint\limits_{V(\mathbf{r},t)} \rho(\mathbf{r}',t)\frac{\mathrm{D}\big(\mathbf{r}(\mathbf{r}',t)-\mathbf{r}_{\text{pot}}\big)}{\mathrm{D}t}\cdot\mathbf{f}(\mathbf{r}',t)\,\mathrm{d}V' \\ &\quad -\iiint\limits_{V(\mathbf{r},t)} \rho(\mathbf{r}',t)\big(\mathbf{r}(\mathbf{r}',t)-\mathbf{r}_{\text{pot}}\big)\cdot\frac{\mathrm{D}\mathbf{f}(\mathbf{r}',t)}{\mathrm{D}t}\,\mathrm{d}V',\end{aligned} \tag{F.3.62}$$

where $\mathbf{r}_{\text{pot}}(t)$ denotes the reference position in space of zero potential. Normally the material derivative of the body force can be ignored. Considering the static gravity force $\mathbf{f} = \mathbf{f}_g = -g\hat{\mathbf{z}}$ the short-time derivation is identical 0. The other part of the material derivative i.e., the second term on the RHS fo (F.3.62) that is related to transport of the fluid element to another position in the gravity field can normally be ignored owing to the slow variation of gravity with altitude. However, in plasma physics where the electric and magnetic body forces are time-varying quantities the last term of (F.3.62) can no longer be ignored.

Conservation of energy implies that a change in energy of a material element is balanced by work done by external body forces *on the material element* and work done by surface forces *on the*

material element subtracted the amount of heat efflux. By taking the derivative the following integral expression is obtained

$$\begin{aligned}\frac{\mathrm{D}}{\mathrm{D}t}\iiint\limits_{V(\mathbf{r},t)}\big(\rho(\mathbf{r},t)e(\mathbf{r}',t)\big)\,\mathrm{d}V' &= \iiint\limits_{V(\mathbf{r},t)}\rho(\mathbf{r}',t)\mathbf{f}(\mathbf{r}',t)\cdot\mathbf{u}(\mathbf{r}',t)\,\mathrm{d}V' \\ &\quad+\iint\limits_{S(\mathbf{r},t)}\big(\mathfrak{P}(\mathbf{r}',t)\cdot\mathbf{u}(\mathbf{r}',t)\big)\cdot\,\mathrm{d}\mathbf{S}'-\iint\limits_{S(\mathbf{r},t)}\mathbf{q}(\mathbf{r}',t)\cdot\,\mathrm{d}\mathbf{S}',\end{aligned}\tag{F.3.63}$$

where $\mathbf{q}(\mathbf{r},t)$ is the heat flux vector.

Now by applying the Reynolds theorem (F.3.43) to (F.3.63) and by converting surface integrals to volume integrals by using the divergence theorem we obtain the following integral expression

$$\begin{aligned}\iiint\limits_{V(\mathbf{r},t)}\rho(\mathbf{r}',t)\frac{\mathrm{D}e(\mathbf{r}',t)}{\mathrm{D}t}\,\mathrm{d}V' &= \iiint\limits_{V(\mathbf{r},t)}\rho(\mathbf{r}',t)\mathbf{f}(\mathbf{r}',t)\cdot\mathbf{u}(\mathbf{r}',t)\,\mathrm{d}V' \\ &\quad+\iiint\limits_{V(\mathbf{r},t)}\nabla\cdot\big(\mathfrak{P}(\mathbf{r}',t)\cdot\mathbf{u}(\mathbf{r}',t)\big)\,\mathrm{d}V'-\iiint\limits_{V(\mathbf{r},t)}\nabla\cdot\mathbf{q}(\mathbf{r}',t)\,\mathrm{d}V'.\end{aligned}\tag{F.3.64}$$

By using the tensor identity $\nabla\cdot(\mathfrak{A}\cdot\mathbf{B})=(\nabla\cdot\mathfrak{A})\cdot\mathbf{B}+|\mathfrak{A}\cdot(\nabla\mathbf{B})|$ and by applying the argument that the mass element has been arbitrarily chosen, we obtain the following expression in the integrands

$$\begin{aligned}\rho(\mathbf{r},t)\frac{\mathrm{D}e(\mathbf{r},t)}{\mathrm{D}t} &= \rho(\mathbf{r},t)\mathbf{f}(\mathbf{r},t)\cdot\mathbf{u}(\mathbf{r},t)+\big(\nabla\cdot\mathfrak{P}(\mathbf{r},t)\big)\cdot\mathbf{u}(\mathbf{r},t) \\ &\quad+|\mathfrak{P}(\mathbf{r},t)\cdot\big(\nabla\mathbf{u}(\mathbf{r},t)\big)|-\nabla\cdot\mathbf{q}(\mathbf{r},t).\end{aligned}\tag{F.3.65}$$

This conservation law states that the change of *internal energy* $U(\mathbf{r},t)$ equals the amount of heat influx, added the amount of heat internally contributed by viscous friction forces added the work done on the element by changing its volume [28, Ch. 6.4]. Taking the time derivative and dividing by the mass density ρ we obtain

$$\boxed{\frac{\mathrm{D}u(\mathbf{r},t)}{\mathrm{D}t}=\frac{1}{\rho(\mathbf{r},t)}\frac{\mathrm{d}U(\mathbf{r},t)}{\mathrm{d}t}=\frac{1}{\rho}\big[\nabla\cdot\mathbf{q}(\mathbf{r},t)+D(\mathbf{r},t)-P(\mathbf{r},t)\dot{\Delta}(\mathbf{r},t)\big].}\tag{F.3.66}$$

In some presentations, e.g., [3, Ch. 2] and [16, ch. 1] the total energy is considered using the CV approach.

Until now only deduction from simple principles has been made. By inspection of the equation continuity of mass flow (F.3.48), the continuity of momentum density (F.3.53), and the continuity in specific energy (F.3.66) we find 5 equations in 14 unknown variables $(\rho(\mathbf{r},t),\mathbf{u}(\mathbf{r},t),\mathfrak{P}(\mathbf{r},t),\mathbf{q}(\mathbf{r},t),e(\mathbf{r},t))$. Accordingly, some additional information must become available in order to obtain a solution.

F.3.8 Entropy Generation

The fourth equation governing the fluid motion is a consequence of the *second law of thermodynamics* and expresses that the entropy of a closed system never decreases. This implies that a change in entropy of a material element is balanced by irreversible entropy generation within the material element subtracted the amount of heat efflux. By taking the time-derivative the following integral expression is obtained

$$\frac{\mathrm{D}}{\mathrm{D}t}\iiint\limits_{V(\mathbf{r},t)} \rho(\mathbf{r}',t)s(\mathbf{r}',t)\,\mathrm{d}V' = \frac{\mathrm{D}}{\mathrm{D}t}\iiint\limits_{V(\mathbf{r},t)} \rho(\mathbf{r}',t)s_{\mathrm{gen}}(\mathbf{r}',t)\,\mathrm{d}V' - \iint\limits_{S(\mathbf{r},t)} \frac{\mathbf{q}(\mathbf{r}',t)}{T(\mathbf{r}',t)}\cdot \mathrm{d}\mathbf{S}', \tag{F.3.67}$$

where $s(\mathbf{r},t)$ denotes the specific entropy, $s_{\mathrm{gen}}(\mathbf{r},t)$ denotes the specific entropy generated during irreversible processes and is subject to the constraints defined in (F.3.14) on page 632 and $\mathbf{q}(\mathbf{r},t)$ is the heat flux vector.

Now by applying the Reynolds theorem (F.3.43) to (F.3.67) and by converting surface integrals to volume integrals by using the divergence theorem and finally invoking the argument of arbitrariness in the choice of the mass element we obtain the following differential expression

$$\boxed{\rho(\mathbf{r},t)\frac{\mathrm{D}s(\mathbf{r},t)}{\mathrm{D}t} = \rho(\mathbf{r},t)\frac{\mathrm{D}s_{\mathrm{gen}}(\mathbf{r},t)}{\mathrm{D}t} - \nabla\cdot\frac{\mathbf{q}(\mathbf{r},t)}{T(\mathbf{r},t)}.} \tag{F.3.68}$$

F.3.9 Equation of State (Constitutive Relation)

In thermodynamics the *state laws* or *constitutive equations* establish a link between associated *state functions* like pressure, temperature, specific volume, or internal energy and the state of the matter (fluid).

In [3, Ch. 2] and [16, ch. 1] only *polytropic* system are considered. In this section we will augment these results to the more general case of a heterogenous mixture of possible chemically reacting fluids.

Constitutive Parameters

Fluid Mech. Field Theory Assump.# 4. *Local thermodynamic equilibrium.* During the passage of a sound wave a three-fold change in internal energy $U(\mathbf{r},t)$ and an associated perturbation of the fluid from its equilibrium. In practice, however, at medium frequencies well below the reciprocal of the *relaxation time* of the medium and at medium excitation levels an assumption on *quasi-equilibrium* or *thermodynamic reversibility* should hold. This allows us to use the conventional thermodynamic identities. Hence, the equilibrium value of specific entropy $s(\mathbf{r},t)$ can be used.

Fluid Mech. Field Theory Assump.# 5. By assuming that the *state* of the fluid is completely determined from specific internal energy $u(\mathbf{r},t)$ and two other state variables this simplifies the analysis considerably. We will use the specific entropy $s(\mathbf{r},t)$ and specific volume $v(\mathbf{r},t)$ as state variables. This choice of state variables, however, is arbitrary as the thermodynamic properties are mutually interrelated.

In section F.3.1 we found that for a thermodynamic system consisting of $N_\varkappa$ substances each of which may be in one of N_ϕ phases, there is a total of $N_\varkappa N_\varphi + 2$ unknowns. The number 2 stems from necessity also in the pure substance case to include two independent thermodynamic properties among (P, v, T). From the *equations of phase equilibrium* (F.3.25) a total of $N_\varkappa(N_\varphi - 1)$ equations expressing equality of the chemical potential of the constituents is provided. In addition N_φ equations of the form $\sum_{\varkappa=1}^{N_\varkappa} y_\varkappa = 1$ exist. Accordingly, the equation variance N_f , which is the excess of variables over equations can be obtained from

$$N_f = N_\varkappa - N_\varphi + 2. \tag{F.3.69}$$

For chemically reacting gases or liquids or heterogenous mixtures the total molar contents of each specie can no longer be considered as constant. Chemical activities generally imply an increase of the number of different substances and hence a similar increase in N_f. However, from this amount we must subtract the number of independent reactions N_r and the number of independent restricting equations N_z, that is,

$$N_f = N_\varkappa - N_r - N_z - N_\varphi + 2. \tag{F.3.70}$$

In section F.3.1 the following *thermodynamic properties* were introduced: Pressure P, temperature T, specific volume v, density ρ, mass m, specific internal energy u, specific enthalpy h, specific entropy s, constant-pressure and constant-volume specific heats C_V and C_P, specific Helmholtz function f and the specific Gibb's function g. These thermodynamic properties serve different purposes, but generally only two of them are independent. Next we will define some of the constitutive parameters that are often used to establish a link between the thermodynamic properties above. As independent properties an arbitrary choice of P and T is made. The dependence on the parameter set $(\mathbf{r}, t, P, T)$, however, will for notational convenience be suppressed in the defining equations. Referring to the discussion in subsection F.2.4 on page 622 viz. (F.2.3) these constitutive parameters are all of first-order.

The *volume thermal expansivity* α expresses the change in volume as temperature changes while pressure remains constant, is defined by

$$\alpha \equiv \rho\left(\frac{\partial v}{\partial T}\right)_P = -\frac{1}{\rho}\left(\frac{\partial \rho}{\partial T}\right)_P. \tag{F.3.71}$$

The *isothermal compressibility* $K_T(\mathbf{r}, t, P, T)$ is defined by

$$K_T \equiv -\frac{1}{v}\left(\frac{\partial v}{\partial P}\right)_T = \frac{1}{\rho}\left(\frac{\partial \rho}{\partial P}\right)_T \tag{F.3.72}$$

similarly indicates the change in volume as pressure changes while temperature remains constant. For *isentropic* processes we use the isentropic compressibility $K_s(\mathbf{r}, t, P, T)$ defined by

$$K_s \equiv -\frac{1}{v}\left(\frac{\partial v}{\partial P}\right)_s = \frac{1}{\rho}\left(\frac{\partial \rho}{\partial P}\right)_s. \tag{F.3.73}$$

In liquids that have high thermal conductivity K_T should usually by used. Gases are by far the poorest heat conductors and K_s should be used except in regions close to a boundary surface.

The reciprocal of the compressibility is referred to as a *bulk modulus*

$$B = \begin{cases} B_s = -v\big(\frac{\partial P}{\partial V}\big)|_s = \rho\big(\frac{\partial P}{\partial \rho}\big)|_s, & \text{isentropic process,} \\ B_T = -v\big(\frac{\partial P}{\partial V}\big)|_T = \rho\big(\frac{\partial P}{\partial \rho}\big)|_T, & \text{isothermal process,} \end{cases} \tag{F.3.74}$$

where the isentropic bulk modulus $B_s(\mathbf{r}, t, P, T)$ and the isothermal bulk modulus $B_T(\mathbf{r}, t, P, T)$ have been introduced.

The speed of sound is determined from the specific volume and the bulk modulus and therefore also attains slightly different values for isentropic and isothermal processes

$$c^2 = \begin{cases} c_s^2 = -\big(\frac{\partial P}{\partial \rho}\big)|_s = vB_s, & \text{isentropic process,} \\ c_T^2 = -\big(\frac{\partial P}{\partial \rho}\big)|_T = vB_T, & \text{isothermal process,} \end{cases} \tag{F.3.75}$$

where the isentropic speed of sound $c_s(\mathbf{r}, t, P, T)$ and the isothermal speed of sound $c_T(\mathbf{r}, t, P, T)$ have been introduced. The specific heat capacities are constitutive parameters that describe the amount of heat supply needed to increase the temperature by 1 K *per unit mass* of material element.

The specific heat capacity at constant volume $C_v(\mathbf{r}, t, P, T)$ and the specific heat capacity at constant pressure $C_P(\mathbf{r}, t, P, T)$ are defined by

$$C_v \equiv \left(\frac{\partial u}{\partial T}\right)_v \tag{F.3.76a}$$

$$C_P \equiv \left(\frac{\partial h}{\partial T}\right)_P \tag{F.3.76b}$$

respectively. Another useful parameter is the thermal pressure increase at constant volume $\check{\alpha}(\mathbf{r}, t, P, T)$ that expresses the change in pressure as temperature changes at constant volume and is defined by

$$\check{\alpha} \equiv \left(\frac{\partial P}{\partial T}\right)_V = \frac{\alpha}{K_T}. \tag{F.3.77}$$

Maxwell's relations presented next provide relationships between measurable quantities and those which either cannot be measured or are difficult to measure

$$\left(\frac{\partial T}{\partial v}\right)_s = -\left(\frac{\partial P}{\partial s}\right)_v \tag{F.3.78a}$$

$$\left(\frac{\partial T}{\partial P}\right)_s = \left(\frac{\partial v}{\partial s}\right)_P \tag{F.3.78b}$$

$$\left(\frac{\partial P}{\partial T}\right)_v = \left(\frac{\partial s}{\partial v}\right)_T \tag{F.3.78c}$$

$$\left(\frac{\partial v}{\partial T}\right)_P = -\left(\frac{\partial s}{\partial P}\right)_T. \tag{F.3.78d}$$

By using the so-called Tds-equations from thermodynamics [36, Ch. 11], we can express the rate of entropy change in terms of thermodynamic properties and the dilatation rate

$$\rho(\mathbf{r},t)C_v(\mathbf{r},t)\frac{\mathrm{D}T(\mathbf{r},t)}{\mathrm{D}t}+\rho(\mathbf{r},t)C_v(\mathbf{r},t)(\gamma(\mathbf{r},t)-1)\dot{\Delta}(\mathbf{r},t)/\alpha(\mathbf{r},t)+\nabla\cdot\mathbf{q}(\mathbf{r},t)-\phi_\eta(\mathbf{r},t)=0. \tag{F.3.79}$$

The details are provided in section F.C[19].

In [15] different versions of the energy equation (F.3.66) using the different thermodynamic constitutional parameters and field variables, e.g., is provided

$$\rho(\mathbf{r},t)C_v(\mathbf{r},t)\frac{\mathrm{D}T(\mathbf{r},t)}{\mathrm{D}t}+\rho(\mathbf{r},t)C_v(\mathbf{r},t)(\gamma(\mathbf{r},t)-1)\dot{\Delta}(\mathbf{r},t)/\alpha(\mathbf{r},t)+\nabla\cdot\mathbf{q}(\mathbf{r},t)-\phi_\eta(\mathbf{r},t)=0, \tag{F.3.80}$$

Dissipative Parameters

In fluid dynamics dissipate effects are due to viscosity, thermal conduction, relaxation and boundary layer losses. A force times a velocity represents a dissipative term. A *thermoviscous fluid* is a fluid model that includes the effects of heat conduction and viscous stresses, but not other diffusive of relaxation effects.

The thermal dissipation function ϕ_κ is defined by

$$\phi_\kappa(\mathbf{r},t)\equiv -T^{-1}(\mathbf{r},t)\mathbf{q}(\mathbf{r},t)\cdot\nabla T(\mathbf{r},t). \tag{F.3.81}$$

The viscous dissipation function ϕ_η is defined by

$$\phi_\eta(\mathbf{r},t)\equiv -T^{-1}(\mathbf{r},t)\mathbf{q}(\mathbf{r},t)\cdot\nabla T(\mathbf{r},t). \tag{F.3.82}$$

Dissipation due to Heat Transfer

Generally, three mechanisms by which thermal energy is transported exist:

1. *Heat conduction* refers to the transport of energy between two neighboring volume elements by virtue of the temperature difference between them.

   In the general case of a inhomogeneous anisotropic media the *Fourier's law of heat conduction* states that heat energy flow has the following linear dependence on the temperature gradient

   $$\mathbf{q}_{\mathrm{con}}(\mathbf{r},t)=\mathfrak{H}(\mathbf{r},t)\nabla T(\mathbf{r},t), \tag{F.3.83}$$

   where $\mathbf{q}_{\mathrm{con}}(\mathbf{r},t)$ is the heat flux vector due to conduction and $\mathfrak{H}(\mathbf{r},t)$ denotes the thermal conductivity tensor, which in turn componentwise is a symmetric 3×3 matrix consisting of thermal conductivity terms h_{ij} subject to $(h_{ij}=h_{ji})$.

[19] An error enters the similar expression [15, Eq. (22)].

In the usual case of isotropic matter we may replace the thermal conductivity tensor by the scalar, that is, thermal conductivity $\kappa(\mathbf{r},t)$.

$$\mathbf{q}_{\rm con}(\mathbf{r},t) = \kappa(\mathbf{r},t)\nabla T(\mathbf{r},t). \tag{F.3.84}$$

2. *Heat convection* is a heat transfer involving a current of fluid that absorbs heat at one place and then moves to another place, where it mixes with a cooler portion of the fluid and rejects heat. Heat convection is described by Newton's law of cooling

$$\mathbf{q}_{\rm cnv}(\mathbf{r},t) = h(\mathbf{r},t)\big(T(\mathbf{r},t) - T_{\rm amb}(\mathbf{r},t)\big), \tag{F.3.85}$$

where the heat flux vector due to convection $\mathbf{q}_{\rm cnv}(\mathbf{r},t)$ and where the quantity $h(\mathbf{r},t)$ is the thermalconvection coefficient that depends on a number of system factors [36, Ch. 4]. Heat convection is intentionally used in *thermoacoustic refrigeration*. Heat convection can also take place by turbulence.

3. *Thermal radiation* is electromagnetic energy emitted by a hot solid, liquid and gas by virtue of its temperature. Radiation is the only form of heat transfer that can occur in the absence of any form of medium and as such is the only means of heat transfer through a vacuum. Thermal radiation is a direct result of the movements of atoms and molecules in a material. Since these atoms and molecules are composed of charged particles (protons and electrons), their movements result in the emission of electromagnetic radiation, which carries energy away from the surface. At the same time, the surface is constantly bombarded by radiation from the surroundings, resulting in the transfer of energy to the surface. Since the amount of emitted radiation increases with increasing temperature, a net transfer of energy from higher temperatures to lower temperatures results. Thermal heat radiation between a material element at temperature T and some material matter with temperature, say, $T_{\rm amb}$, is governed by *Stefan-Boltzmann Law*

$$\mathbf{q}_{\rm rad}(\mathbf{r},t) = \varepsilon(\mathbf{r},t)\sigma\Big(T^4_{\rm amb}(\mathbf{r},t) - T^4(\mathbf{r},t)\Big), \tag{F.3.86}$$

where $\mathbf{q}_{\rm rad}(\mathbf{r},t)$ denotes the heat flux vector due to radiation, ε is the emissivity and σ denotes the Stefan-Boltzmann constant.

Accordingly we may express the total heat flux vector $\mathbf{q}(\mathbf{r},t)$ by

$$\mathbf{q}(\mathbf{r},t) = \mathbf{q}_{\rm con}(\mathbf{r},t) + \mathbf{q}_{\rm conv}(\mathbf{r},t) + \mathbf{q}_{\rm rad}(\mathbf{r},t). \tag{F.3.87}$$

Dissipation due to Viscosity

Dissipation due to Relaxation Processes

In acoustic the symbol μ_B is often used

$$\breve{P}(\mathbf{r},t) = P(\mathbf{r},t) - \mu_B(\mathbf{r},t)\dot{\Delta}, \tag{F.3.88}$$

where $\breve{P}(\mathbf{r},t)$ is the instantaneous pressure under relaxation (non-equilibrium). The fluid stress-flux tensor $\mathfrak{P}$ is composed of the fluid pressure tensor $P\mathfrak{I}(\mathbf{r},t)$ and the fluid shear-stress-flux (viscous-stress-flux) tensor $\mathfrak{D}(\mathbf{r},t)$

$$\mathfrak{P}(\mathbf{r},t) = -P(\mathbf{r},t)\mathfrak{I} + \mathfrak{D}(\mathbf{r},t). \tag{F.3.89}$$

The pressure tensor P$\mathfrak{I}$ is a diagonal tensor of pressure terms P_{ii} and $\mathfrak{I}$ is the unit dyadic called the *idemfactor* $\mathfrak{I} \equiv \hat{\mathbf{x}}\hat{\mathbf{x}} + \hat{\mathbf{y}}\hat{\mathbf{y}} + \hat{\mathbf{z}}\hat{\mathbf{z}}$.

The viscous-stress tensor $\mathfrak{D}$ is a symmetric tensor

$$D_{ij}(\mathbf{r},t) = \begin{cases} (\eta - \frac{2}{3}\mu)\dot{\Delta}(\mathbf{r},t) + 2\mu\frac{\partial u_i(\mathbf{r},t)}{\partial x_i}, & i = j \\ \mu\frac{\partial u_i(\mathbf{r},t)}{\partial x_j} + \mu\frac{\partial u_j(\mathbf{r},t)}{\partial x_i}, & i \neq j. \end{cases} \tag{F.3.90}$$

The quantity λ is the coefficient of bulk viscosity or *compressional resistance* and μ is the coefficient of viscosity. The coefficient k is defined as $k = \lambda + \frac{2}{3}\mu$ and is referred to as the second coefficient of viscosity[20].

Fluid Mech. Field Theory Assump.# 6. Newtonian Fluids. Most common fluids, both liquids and gases exhibit a linear relationship between shearing stress and the rate of shearing strain and are designated *Newtonian fluids* [29, Ch. 1].

F.3.10 Attenuation of Sound Fields

Attenuation of sound in the air is dominated by relaxation process in the lower frequency range and by viscosity at higher frequencies. For the estimation of attenuation of sound in the air standards from both American National Standards Institute (ANSI) and Système International d'Unités (SI) are available. In [3, App. B] empirical model attenuation curves for propagation in air as a function of frequency, humidity and ambient pressure can be found. For a frequency of 1 kHz the attenuation is approximately $1.5\text{mdB}\cdot\text{m}^{-1}$ for dry air and approximately $15\ \text{mdB}\cdot\text{m}^{-1}$ for an absolute humidity h of 10% (worst case).

Usually the attenuation of sound waves in the audio range for short distance propagation can be ignored outside boundary layers. An exception from this, is found in the field of *metrology* which deals with the realization of the measurement units including the Pa $\cdot$ In such applications a few mdB might be of concern [10].

Dissipation due to Boundaries

In some applications field the viscous and thermal boundary are of pronounced importance. In the vicinity of boundaries the *acoustical modal field* and the *vorticity field* and *entropy modal field* jointly that perfectly matches the boundary condition including thermodynamics.

[20] In [26, Ch. 2.3] λ is defined as the *coefficient of expansion friction* and therefore with opposite sign. However, the sign convention chosen here better lets us recognize the similarities between (F.3.97) on page 656 and (F.4.19) on page 664.

$$\nabla^2\left(P_1(\mathbf{r},t)+\frac{\nu'}{c^2}\frac{\partial P_1(\mathbf{r},t)}{\partial t}\right)-\frac{1}{c^2}\frac{\partial P_1(\mathbf{r},t)}{\partial t^2}=0 \tag{F.3.91a}$$

$$\nabla^2\left(P_2(\mathbf{r},t)+\frac{\nu'}{c^2}\frac{\partial P_2(\mathbf{r},t)}{\partial t}\right)-\frac{1}{c^2}\frac{\partial P_1(\mathbf{r},t)}{\partial t^2}=\nabla\cdot\mathfrak{J}_2\cdot\nabla-\frac{\Gamma}{\rho_0 c_0^4}\frac{\partial}{\partial t}\left(\frac{\partial P_1^2(\mathbf{r},t)}{\partial t}+\nu'\nabla^2 P_1^2(\mathbf{r},t)\right). \tag{F.3.91b}$$

For example in [14] a numerical model for the propagation of sound waves in fluids with viscous and thermal losses was considered. In particular for condenser microphones the viscous and thermal damping in the thin layer of air between the membrane and the back electrode play an important role for the performance. The theory was formulated such that a boundary element method (BEM) could be established under relative mild conditions.

However, for most applications the dissipative effects due to thermal diffusion, viscosity can usually be ignored except in the vicinity of boundaries.

F.3.11 Acoustical Sources

In subsection F.3.5 on page 642 and subsection F.3.6 on page 643 the volume source of mass-flow and the external body force *per unit mass* respectively were introduced. In this subsection another source to acoustical energy namely excitation from violent fluid motion [28, Ch. 7.1] will be briefly presented.

It should, however, be remarked that if one wants to *synthesize* an arbitrary acoustic field by introducing sources one could end up with solutions that although are mathematical correct may be physical realizable. The existence and the uniqueness of a solution also become important.

Violent Fluid Motion

Violent fluid motion might for example be a consequence of *fluid injection*, *heat energy*, a change in *fluid composition*. In such case the full including nonlinear terms must usually be considered. Fluid injection, fluid force and stress-momentum cause respective monopole, dipole, and quadropole wave radiation.

In section F.3.9 on page 648 different constitutive first-order parameters were introduced including the coefficient of volume expansion at constant pressure α, the isothermal compressibility K_T, the isentropic compressibility K_s, and corresponding the specific heat capacities at constant volume C_V respective at constant pressure C_P.

As already discussed these first-order constitutive parameters are mutually interrelated and the following discussion will address the isentropic compressibility K_s as it enters explicitly in the wave equation (F.3.91) on the previous page. The isentropic compressibility K_s is generally a function of the coordinates in space $\mathbf{r}$ and time t, but also viz. (F.3.73) on page 649 a function of pressure P and density ρ, that is, $K_s = K_s(\mathbf{r},t,P,\rho)$. However, as discussed in section F.3.1 on page 627 we may likewise use P and T as independent thermodynamic coordinates, that is, $K_s = K_s(\mathbf{r},t,P,T)$.

Hence, when taking the time-derivative of K_s we have to take the explicit dependence on time because the fluid composition at $\mathbf{r}$ may change with time, in addition to the implicit dependence of K_s on t through the variation of P and T (or ρ) when the composition does not change.

By suppressing the dependence on the $(\mathbf{r}, t, P, T)$ parameters we obtain the following expression for the time-derivative of K_s.

$$\frac{\partial K_s}{\partial t} = \left(\frac{\partial K_s}{\partial t}\right)_{P,T} + \left(\frac{\partial K_s}{\partial P}\right)_{t,T}\frac{\partial P}{\partial t} + \left(\frac{\partial K_s}{\partial T}\right)_{t,P}\frac{\partial T}{\partial t}$$

applying the following mathematical relations [36, Ch. 2.7] (see (F.C.1a))

$$\left(\frac{\partial x}{\partial z}\right)_y = -\left(\frac{\partial x}{\partial y}\right)_z\left(\frac{\partial y}{\partial z}\right)_x$$

in the last term with appropriate substitutions to obtain

$$\begin{aligned}\frac{\partial K_s}{\partial t} &= \left(\frac{\partial K_s}{\partial t}\right)_{P,T} + \left(\frac{\partial K_s}{\partial P}\right)_{t,T}\frac{\partial P}{\partial t} - \left(\frac{\partial K_s}{\partial P}\right)_{t,T}\left(\frac{\partial P}{\partial T}\right)_{t,V}\frac{\partial T}{\partial t}\\ &= \left(\frac{\partial K_s}{\partial t}\right)_{P,T} + \left(\frac{\partial K_s}{\partial P}\right)_{t,T}\left(\frac{\partial P}{\partial t} - \left(\frac{\partial P}{\partial T}\right)_{t,V}\frac{\partial T}{\partial t}\right)\end{aligned}$$

finally by insertion of (F.3.77) to obtain

$$\frac{\partial K_s}{\partial t} = \left(\frac{\partial K_s}{\partial t}\right)_{P,T} + \left(\frac{\partial K_s}{\partial P}\right)_{t,T}\left(\frac{\partial P}{\partial t} - \breve{\alpha}\frac{\partial T}{\partial t}\right). \tag{F.3.92}$$

Now following the procedure of obtaining the wave equation for the pressure from the equation of continuity of mass flow (F.3.48), and continuity of momentum density (F.3.53) in [28, Ch. 7.1] the following expression of the monopole source contribution by fluid injection, heat energy, change in fluid composition and implicit dependence of K_s on P and T can be deduced

$$\begin{aligned}f(\mathbf{r},t) = \underbrace{\frac{\partial}{\partial t}q(\mathbf{r},t)}_{\text{fluid injection}} &+ \underbrace{\frac{\breve{\alpha}(\mathbf{r},t)\gamma(\mathbf{r},t)\rho(\mathbf{r},t)K_s(\mathbf{r},t)}{C_P(\mathbf{r},t)}\frac{\partial h(\mathbf{r},t)}{\partial t}}_{\text{heat energy}}\\ &- \underbrace{\rho(\mathbf{r},t)\left(\frac{\partial K_s}{\partial t}\right)_{PT}\left(\frac{\partial P(\mathbf{r},t)}{\partial t} - \frac{\breve{\alpha}(\mathbf{r},t)\gamma(\mathbf{r},t)h(\mathbf{r},t)}{C_P(\mathbf{r},t)}\right)}_{\text{change of fluid composition}}\\ &- \underbrace{\frac{\rho(\mathbf{r},t)}{\gamma(\mathbf{r},t)}\left[K_s^2(\mathbf{r},t) + \left(\frac{\partial K_s(\mathbf{r},t)}{\partial P(\mathbf{r},t)}\right)_T\right]\left(\frac{\partial P(\mathbf{r},t)}{\partial t} - \frac{\breve{\alpha}(\mathbf{r},t)\gamma(\mathbf{r},t)h(\mathbf{r},t)}{C_P(\mathbf{r},t)}\right)^2}_{K_s(P,T)}.\end{aligned} \tag{F.3.93}$$

In (F.3.93) a description of each term contributing to the monopole source $f(\mathbf{r},t)$ has been made. By $K_s(P,T)$ we make reference to the implicit dependence of K_s on time through the

time-variation of P and T. This later term represent nonlinearities due to amplitude-dependent constitutive parameters as discussed in subsection F.2.4 on page 622. This term will always to some extent be present, but can usually be ignored except for cases were very loud sound pressure levels are involved.

$$\mathfrak{Q}(\mathbf{r},t) = \nabla \cdot \mathfrak{V}(\mathbf{r},t) \cdot \nabla \tag{F.3.94a}$$

$$= \sum_{i=1}^{3} \sum_{j=i}^{3} \tfrac{1}{2}\epsilon_{|j-i|} \frac{\partial^2}{\partial x_i \partial x_j} \big(T_{ij}(\mathbf{r},t) + T_{ji}(\mathbf{r},t)\big) \tag{F.3.94b}$$

$$\approx \sum_{i=1}^{3} \sum_{j=i}^{3} \tfrac{1}{2}\epsilon_{|j-i|} \frac{\partial^2}{\partial x_i \partial x_j} \rho(\mathbf{r},t)\big(u_i(\mathbf{r},t)u_j(\mathbf{r},t) + u_j(\mathbf{r},t)u_i(\mathbf{r},t)\big). \tag{F.3.94c}$$

where stress-momentum-flux tensor $\mathfrak{V}(\mathbf{r},t)$ that is defined as fluid momentum-flux tensor $\mathfrak{J}$ defined in (F.3.54) on page 644 subtracted the viscous-stress tensor $\mathfrak{D}$ defined in (F.3.90) on page 653

$$\mathfrak{V}(\mathbf{r},t) = \mathfrak{J}(\mathbf{r},t) - \mathfrak{D}(\mathbf{r},t). \tag{F.3.95}$$

Nonlinear Acoustics

In the general case of nonlinear acoustics it can be demonstrated that even in the absence of ordinary sources in the solution wave equation for the second- or higher-order pressure involves source terms that are products of first-order terms [28, Ch. 14.4]. If a solution to the first-order wave equation for the pressure has been found those source terms can be regarded as known and then at least in principle we may proceed and determine recursively the second-order and higher-order wave equations by use of Green's function appropriate for the problem at hand.

F.3.12 Acoustics

The primary choice of field variable used to describe acoustical wave motion is the acoustical pressure $p(\mathbf{r},t)$ and the acoustical velocity $\mathbf{u}(\mathbf{r},t)$ and are both field variables to first and higher order. Following the terminology in [28] and using the notation introduced in subsection F.2.4 on page 622 we may write

$$p(\mathbf{r},t) \equiv P_{-0}(\mathbf{r},t) \tag{F.3.96a}$$

$$\delta(\mathbf{r},t) \equiv \rho_{-0}(\mathbf{r},t) \tag{F.3.96b}$$

$$\tau(\mathbf{r},t) \equiv T_{-0}(\mathbf{r},t) \tag{F.3.96c}$$

$$\sigma(\mathbf{r},t) \equiv S_{-0}(\mathbf{r},t) \tag{F.3.96d}$$

$$\mathbf{u}(\mathbf{r},t) \equiv \mathbf{u}_{-0}(\mathbf{r},t). \tag{F.3.96e}$$

By combining the terminology used in [26, Ch. 2.3] and [28, Ch. 6.2, 6.4] we get the following variants for the *Navier-Stokes Equation* that expresses the continuity in moment density of a viscous, compressible fluid possibly subject to external forces from gravity or electricity

$$\big(\rho+\delta(\mathbf{r},t)\big)\frac{\mathrm{D}\mathbf{u}(\mathbf{r},t)}{\mathrm{D}t} \equiv \big(\rho+\delta(\mathbf{r},t)\big)\Big(\frac{\partial\mathbf{u}(\mathbf{r},t)}{\partial t}+\mathbf{u}(\mathbf{r},t)\cdot\nabla\mathbf{u}(\mathbf{r},t)\Big) \tag{F.3.97a}$$

$$= f(\mathbf{r},t)+\nabla\cdot\Big(-p(\mathbf{r},t)\mathfrak{I}+\lambda\nabla\cdot\mathbf{u}(\mathbf{r},t)\mathfrak{I}+\mu\nabla\mathbf{u}(\mathbf{r},t)+\mu\mathbf{u}(\mathbf{r},t)\nabla\Big) \tag{F.3.97b}$$

$$= -\nabla\big(\Phi(\mathbf{r},t)+p(\mathbf{r},t)\big)+(\lambda+\mu)\nabla\nabla\cdot\mathbf{u}(\mathbf{r},t)+\mu\nabla^2\mathbf{u}(\mathbf{r},t) \tag{F.3.97c}$$

$$= -\nabla\big(\Phi(\mathbf{r},t)+p(\mathbf{r},t)\big)+(\lambda+2\mu)\nabla\nabla\cdot\mathbf{u}(\mathbf{r},t)-\mu\nabla\times\nabla\times\mathbf{u}(\mathbf{r},t) \tag{F.3.97d}$$

$$= -\nabla\big(\Phi(\mathbf{r},t)+p(\mathbf{r},t)-(\eta+\tfrac{4}{3}\mu)\nabla\cdot\mathbf{u}(\mathbf{r},t)\big)-\mu\nabla\times\nabla\times\mathbf{u}(\mathbf{r},t). \tag{F.3.97e}$$

The Navier-Stokes equation does not include the effect of thermal conductivity, that is, the thermal conductivity is assumed negligible ($\kappa\approx 0$).

The Navier-Stokes equation (F.3.97) is on the left side first order in the term $\rho\frac{\partial\mathbf{u}}{\partial t}$, second order in $\delta\frac{\partial\mathbf{u}}{\partial t}$ and $\rho\mathbf{u}\cdot\nabla\mathbf{u}$, and third order in $\delta\mathbf{u}\cdot\nabla\mathbf{u}$. On the right the first order terms are ∇p and $(\eta+\frac{4}{3}\mu)\nabla\nabla\cdot\mathbf{u}$ and $\mu\nabla\times\nabla\times\mathbf{u}$. Moreover, it should be noticed that the Navier-Stokes equation does not involve any of the constitutive parameters except for the dissipative parameter μ,λ,γ.

The *equation of continuity of mass density* provides one more equation. From [28, Ch. 6.2] we get

$$\frac{\partial\delta(\mathbf{r},t)}{\partial t} = q(\mathbf{r},t)-\rho_T\nabla\cdot\mathbf{u}-\mathbf{u}\cdot\nabla\rho_T(\mathbf{r},t) \tag{F.3.98a}$$

$$= q(\mathbf{r},t)-(\rho+\delta(\mathbf{r},t))\nabla\cdot\mathbf{u}-\mathbf{u}\cdot\nabla\delta(\mathbf{r},t). \tag{F.3.98b}$$

Hence, in order to obtain an equation for fluid wave motion we need to establish a relation between the pressure and the state of compression of the fluid. The *equation of state* provides such information. In particular the compressibility of the fluid defined in (F.3.72) on page 649 or (F.3.73) on page 649 is useful.

Now in order to proceed we will make the usual assumption of an isentropic compressibility K_s being independent of the pressure

$$\delta(\mathbf{r},t) = \frac{1}{\rho}\Big(\frac{\partial\rho}{\partial P}\Big)\Big|_S p \tag{F.3.99a}$$

$$\approx K_s p. \tag{F.3.99b}$$

First we will make the usual but normally quite reasonable assumptions at ordinary sound pressure levels and within the audible frequency range.

Fluid Mech. Field Theory Assump.# 7. Homogeneous medium. The *ambient* parameters, which are, the ambient (or equilibrium) pressure P, ambient temperature T and the ambient mass density ρ are independent of position in space. The same applies to the constituting parameters.

The analysis becomes considerable simpler by invoking the following assumption on small amplitude signals

Fluid Mech. Field Theory Assump.# 8. Small amplitude i.e., the acoustic quantities p, τ, δ are much smaller than the equivalent quiescent quantities parameters P, T and ρ respectively.

As a consequence of the small amplitude assumption we generally thereby also invoke the following assumption.

Fluid Mech. Field Theory Assump.# 9. Linear medium. This means that the constituting parameters K, γ, K_s, are independent of the acoustic quantities p, τ, δ and σ.

The assumptions 7 - 9 on pages 657–658 imply that we for an arbitrary constitutional parameter, say, υ^a obey (F.2.1) on page 622.

Fluid Mech. Field Theory Assump.# 10. Nonviscous fluid i.e., $\mu = 0$.

Fluid Mech. Field Theory Assump.# 11. Zero heat conductivity in fluid i.e., $K = 0$.

Fluid Mech. Field Theory Assump.# 12. No other diffusive or relaxation processes.

Fluid Mech. Field Theory Assump.# 13. Non-moving medium.

Assumptions 10 - 12 basically state that the fluid is dissipation free.

We will by $\mathcal{V}_f$ refer to the volume (space) of fluid satisfying these criterions. Similarly, T_p will denote the permissable time frame.

We will introduce the linear sound field volume $V_{\tilde{f}}$ according to

$$V_{\tilde{f}} \subset V_f \setminus (\cup_{i \in N_w} V_{b,i} \cup_{j \in N_{src}} V_{src,j}), \tag{F.3.100}$$

where $\cup_{i \in N_w} V_i^w$ is the union of wall boundary regions spanned by the N_b boundary regions and $\cup_{j \in N_{src}} V_j^{src}$ is the union of spherical near-field regions spanned by the N_{src} sources in the system.

In practice (F.3.100) should be considered whenever conducting field measurements. The continuity in fluid mass and moment densities are governed by the differential equations [28, Ch. 6]

$$\rho \nabla \cdot \mathbf{u}(\mathbf{r}, t) + \rho K \frac{\partial}{\partial t} p(\mathbf{r}, t) = q(\mathbf{r}, t) \tag{F.3.101}$$

and

$$\nabla p(\mathbf{r}, t) + \rho \frac{\partial}{\partial t} \mathbf{u}(\mathbf{r}, t) = \mathbf{f}(\mathbf{r}, t), \tag{F.3.102}$$

In order to prove more general uniqueness and existence theorems that can be applied to rapidly varying fields, such as those of *electromagnetic missiles* [12, Ch. 5] we will present the integral forms of (F.3.101) to (F.3.102). We will assume that the time-domain sources are switched off for time $t \leq t_0$ or that the field quantities p and $\mathbf{u}$ are known at time t_0. Then, the continuity

for the fluid mass and moment density equations in integral form are given respectively, by [12, Ch. 2]

$$\rho\nabla\cdot\int_{t_0}^{t}\mathbf{u}(\mathbf{r},t')\,\mathrm{d}t'+\rho K(p(\mathbf{r},t)-p(\mathbf{r},t_0))=\int_{t_0}^{t}s(\mathbf{r},t')\,\mathrm{d}t' \tag{F.3.103}$$

and

$$\nabla\int_{t_0}^{t}p(\mathbf{r},t')\,\mathrm{d}t'+\rho(\mathbf{u}(\mathbf{r},t)-\mathbf{u}(\mathbf{r},t_0))=\int_{t_0}^{t}\mathbf{f}(\mathbf{r},t')\,\mathrm{d}t'. \tag{F.3.104}$$

It may be argued that the integral expressions (F.3.103) to (F.3.104) on this page are slightly more general than the differential equations (F.3.101) to (F.3.102) on the preceding page in that no requirement on the existence of time derivatives are made. This also allows formulation of uniqueness and existence of a larger class of linear acoustic fields.

However, the acoustic velocity $\mathbf{u}$ represents a general vector field which is composed of a *lamellar*[21] field component, $\mathbf{u}_l$, and a *solenoidal*[22] field component $\mathbf{u}_s$ [5], [27, Ch. 13]:

$$\mathbf{u}=\mathbf{u}_l+\mathbf{u}_s, \tag{F.3.105}$$

where $\nabla\times\mathbf{u}_l\equiv 0$, $\nabla\cdot\mathbf{u}_l\neq 0$, $\nabla\cdot\mathbf{u}_s\equiv 0$ and $\nabla\times\mathbf{u}_s\neq 0$.

As the gradient points in the direction of greatest rate of change of the scalar potential while the curl is transverse to this direction $\mathbf{u}_l$ and $\mathbf{u}_s$ are also referred to as *longitudinal* and *transverse* field components respectively. The fundamental problem in the investigation of any irrotational field is the determination of the scalar potential $\phi(\mathbf{r})$.

$$\nabla\times\boldsymbol{\omega}(\mathbf{r},t)=\int_{t_0}^{t}\nabla\times\mathbf{f}(\mathbf{r},t')\,\mathrm{d}t'+\boldsymbol{\omega}(\mathbf{r}). \tag{F.3.106}$$

F.3.13 Acoustic Energy Density

The acoustic energy density $w(\mathbf{r},t)$ is composed of the acoustic potential energy density $w_{\mathrm{pot}}(\mathbf{r},t)$ and the acoustic kinetic energy density $w_{\mathrm{kin}}(\mathbf{r},t)$

$$w(\mathbf{r},t)=w_{\mathrm{pot}}(\mathbf{r},t)+w_{\mathrm{kin}}(\mathbf{r},t), \tag{F.3.107}$$

where

$$w_{\mathrm{pot}}(\mathbf{r},t)=\tfrac{1}{2}K(\mathbf{r},t)p^2(\mathbf{r},t) \tag{F.3.108}$$

and

$$w_{\mathrm{kin}}(\mathbf{r},t)=\tfrac{1}{2}\rho(\mathbf{r},t)|\mathbf{u}(\mathbf{r},t)|^2. \tag{F.3.109}$$

[21] Other names are *irrotational*, *longitudinal* and *curlless* field component.
[22] Other names are *rotational*, *transverse* and *divergenceless* field component.

The time-averaged acoustic energy densities are obtained from (F.3.107) by using time-average values $\langle|\mathbf{u}|\rangle$ and $\langle p\rangle$ instead of $|\mathbf{u}|$ and p.

F.4 Solid Mechanics Field Theory

The subject of *elasticity* is concerned with the determination of the stresses and displacements in a body as a result of applied mechanical or thermal loads, for those cases in which the body reverts to its original state on the removal of the loads [1, Ch. 1]. The theory of elasticity is based on Newton's laws of motion, Euclidean geometry and Hooke's law. In physics and mechanical engineering, the *theory of elasticity* describes how a solid object moves and deforms in response to external stress. When the deformation in response to stress become large the material might not return to its original state, that is, it becomes *plastic*. A change of configuration may, or may not, be accompanied by changes of temperature.

The theory of elasticity represent indeed an interesting scientific discipline itself which can be attributed to the fact that elastic fields (as opposed to electromagnetic and acoustic wave propagation) support both compressional and shear wave propagation types. This in turn, however, generally complicates the analysis considerably.

In active control of sound and in particular in active control of vibration applications the analysis of *structure-borne sound* plays a fundamental role. As is well known vibrational energy generated somewhere in a system (, e.g., some machinery) might be structurally transmitted (generally in a complicated manner) to other part of the system. If the vibrational energy eventually enters a subsystem that posses a small effective radiation impedance sound radiation will take place. The structure-borne sound arguably interconnects the theories of elasticity and acoustics. We will briefly introduce the basics foundations of elasticity theory sufficient for our discussions. For more advanced information refer to [20] and [21].

Solid Mech. Field Theory Assump.# 1. Macroscopic domain. The solid is regarded as a continuous distribution.

A *rigid body* can be subject to translatoric and rotational movements as a whole. *Elastic bodies*, however, can in addition change the relative positions of the *internal parts*. It will, however be preferred to separate out *rigid body* movements such that the only displacements in the *internal parts* is included in the displacement vector $\mathbf{s}(\mathbf{r},t)$ [26, Ch. 1.6] [20] and [6]. Then in the *unstrained state* $\mathbf{s}=0$ while in the *strained state* $\mathbf{s}\neq 0$. In the theory of elasticity the displacement vector plays a role as basis field quantity similarly to the acoustic velocity $\mathbf{u}(\mathbf{r},t)$ in acoustics.

The displacement vector decomposed in ordinary Cartesian coordinates (x_1,x_2,x_3) is written as

$$\mathbf{s}(\mathbf{r},t)=s_{x_1}\hat{\boldsymbol{x}}_1+s_{x_2}\hat{\boldsymbol{x}}_2+s_{x_3}\hat{\boldsymbol{x}}_3. \tag{F.4.1}$$

It is, however, more convenient to work with the relative (differential) displacements. The components of strain $e_{ij}(\mathbf{r},t)$ are defined by

$$e_{ij}(\mathbf{r},t)=\tfrac{1}{2}\epsilon_{|j-i|}\Big(\frac{\partial s_{x_j}}{\partial x_i}+\frac{\partial s_{x_i}}{\partial x_j}\Big), \tag{F.4.2}$$

where $\epsilon_k = \begin{cases} 1; k = 0 \\ 2; k > 0 \end{cases}$; $k \in \mathbb{N}^*$ denotes the Neumann number.

The three independent rotation components $\varpi_{x_i}(\mathbf{r}, t)$ are defined by

$$\varpi_{x_1}(\mathbf{r}, t) = \frac{1}{2}\Big(\frac{\partial s_{x_3}}{\partial x_2} - \frac{\partial s_{x_2}}{\partial x_3}\Big) \tag{F.4.3a}$$

$$\varpi_{x_2}(\mathbf{r}, t) = \frac{1}{2}\Big(\frac{\partial s_{x_1}}{\partial x_3} - \frac{\partial s_{x_3}}{\partial x_1}\Big) \tag{F.4.3b}$$

$$\varpi_{x_3}(\mathbf{r}, t) = \frac{1}{2}\Big(\frac{\partial s_{x_2}}{\partial x_1} - \frac{\partial s_{x_1}}{\partial x_2}\Big). \tag{F.4.3c}$$

We therefore define a dimensionless strain dyadic $\mathfrak{D}(\mathbf{r}, t)$ that componentwise is a 3×3 matrix of strain elements d_{ij} according to

$$\mathfrak{D}(\mathbf{r}, t) = \nabla s(\mathbf{r}, t) \tag{F.4.4a}$$

$$= \mathfrak{S}(\mathbf{r}, t) + \mathfrak{R}(\mathbf{r}, t) \tag{F.4.4b}$$

$$\equiv \sum_{i=1}^{3}\sum_{j=1}^{3} d_{ij}(\mathbf{r}, t)\hat{\mathbf{x}}_i\hat{\mathbf{x}}_j. \tag{F.4.4c}$$

In (F.4.4b) the strain deformation dyadic was divided in a pure strain dyadic $\mathfrak{S}(\mathbf{r}, t)$ and a rotation (deformation) dyadic $\mathfrak{R}(\mathbf{r}, t)$. The symmetric pure strain dyadic $\mathfrak{S}(\mathbf{r}, t)$ in turn is defined by [20, Art. 8], [26, Ch. 1.6]

$$\mathfrak{S}(\mathbf{r}, t) = \tfrac{1}{2}(\nabla\mathbf{s}(\mathbf{r}, t) + \mathbf{s}(\mathbf{r}, t)\nabla) \tag{F.4.5a}$$

$$\equiv \sum_{i=1}^{3}\sum_{j=1}^{3} s_{ij}(\mathbf{r}, t)\hat{\mathbf{x}}_i\hat{\mathbf{x}}_j \tag{F.4.5b}$$

$$= \sum_{i=1}^{3}\sum_{j=i}^{3} s_{ij}(\mathbf{r}, t)(\hat{\mathbf{x}}_i\hat{\mathbf{x}}_j + \hat{\mathbf{x}}_j\hat{\mathbf{x}}_i), \tag{F.4.5c}$$

where each *component of pure strain* s_{ij} of the dyadic is defined by $s_{ij}(\mathbf{r}, t) = \frac{1}{2}\epsilon_{|j-i|}(e_{ij}(\mathbf{r}, t) + e_{ji}(\mathbf{r}, t))$.

The pure rotation antisymmetric dyadic $\mathfrak{R}(\mathbf{r}, t)$ is similarly defined by [20, Art. 8], [26, Ch. 1.6]

$$\mathfrak{R}(\mathbf{r}, t) = -\tfrac{1}{2}\nabla \times \mathbf{s}(\mathbf{r}, t) \times \mathfrak{I} \tag{F.4.6a}$$

$$\equiv \sum_{i=1}^{3}\sum_{j=1}^{3} r_{ij}(\mathbf{r}, t)\hat{\mathbf{x}}_i\hat{\mathbf{x}}_j \tag{F.4.6b}$$

$$= \varpi_{x_1}(\mathbf{r}, t)(\hat{\mathbf{x}}_2\hat{\mathbf{x}}_3 - \hat{\mathbf{x}}_3\hat{\mathbf{x}}_2) + \varpi_{x_2}(\mathbf{r}, t)(\hat{\mathbf{x}}_3\hat{\mathbf{x}}_1 - \hat{\mathbf{x}}_1\hat{\mathbf{x}}_3) + \varpi_{x_3}(\mathbf{r}, t)(\hat{\mathbf{x}}_1\hat{\mathbf{x}}_2 - \hat{\mathbf{x}}_2\hat{\mathbf{x}}_1). \tag{F.4.6c}$$

From Newton's second law of motion it can easily be deduced that by application of forces to a body necessitates the existence of stress within the body [20, Art. 54]. These stresses in turn lead to internal acceleration of the body mass elements provided that the body is not held in equilibrium. A stress dyadic $\mathfrak{T}(\mathbf{r},t)$ that componentwise is a 3×3 matrix of strain element T_{ij} provides a compact method to describe the stresses acting on an infinitesimal volume

$$\mathfrak{T}(\mathbf{r},t)=\sum_{i=1}^{3}\sum_{j=1}^{3}T_{ij}(\mathbf{r},t)\hat{\mathbf{x}}_i\hat{\mathbf{x}}_j \tag{F.4.7a}$$

$$=\sum_{i=1}^{3}\sum_{j=i}^{3}\epsilon_{|j-i|}T_{ij}(\mathbf{r},t)(\hat{\mathbf{x}}_i\hat{\mathbf{x}}_j+\hat{\mathbf{x}}_j\hat{\mathbf{x}}_i). \tag{F.4.7b}$$

In (F.4.7b) the symmetry property of the stress dyadic ($\mathfrak{T}(\mathbf{r},t)=\mathfrak{T}^*(\mathbf{r},t)$) has been utilized. The symmetry in the stress terms is a consequence that any infinitesimally volume must be in static *rotational equilibrium*. The stress dyadic therefore consists of only six *independent* components.

In his experimental work Robert Hooke was the first to confirm existence of a linear relationship between stresses and strains listed in Equation F.4.7. Later work has revealed that this rule applies generally to most hard solids other than cast metals and henceforth referred to as *Hooke's law* [20, Art. 64]. From the ordinary Hooke's law the so-called *Generalized Hooke's Law of proportionality of stress and strain* can be induced [20, Art. 66-69].

Now in the Generalized Hooke's law a *elasticity tensor* (4-tensor) $\mathfrak{C}$ relating the six independent strain components linearly to the six independent stress components is sought for

$$\mathfrak{T}(\mathbf{r},t)=\mathfrak{C}\cdot\mathfrak{S}(\mathbf{r},t). \tag{F.4.8}$$

In principle, this elasticity tensor consist of $3^4=81$ elements. However, due inherent symmetries this number reduces to 36 possibly independent elasticity constants [20, Art. 66] [21, Ch. 4.3]. An intermediate interconnection between stresses and strains is established through the differential $T_{ij}(\mathbf{r},t)=\frac{\partial W(\mathbf{r},t)}{\partial e_{ij}(\mathbf{r},t)}$ where $W(\mathbf{r},t)$ is the *stress energy function* that represents the potential energy per unit volume [20, Art. 62]. This *elastic stored energy function* is defined by

$$W(\mathbf{r},t)\equiv\tfrac{1}{2}\mathfrak{S}(\mathbf{r},t)\cdot\mathfrak{C}\cdot\mathfrak{S}(\mathbf{r},t). \tag{F.4.9}$$

The stress dyadic and elasticity tensors are accordingly obtained from

$$\mathfrak{T}(\mathbf{r},t)=\frac{\partial W(\mathbf{r},t)}{\partial\mathfrak{S}(\mathbf{r},t)} \tag{F.4.10}$$

and

$$\mathfrak{C}(\mathbf{r},t)=\frac{\partial^2 W(\mathbf{r},t)}{\partial\mathfrak{S}(\mathbf{r},t)\partial\mathfrak{S}(\mathbf{r},t)} \tag{F.4.11}$$

respectively. As proved in [20, Art. 62] the stress-energy function exists for *adiabatic* and *isothermal* excitations. From a practical view point small high-frequency vibrations are practically

adiabatic whereas low-frequency excitations that are in continual equilibrium with surrounding bodies will be practical isothermal. Some but small discrepancies in the elasticity constants has been measured in the two cases. From the differential relation between stresses and strains it turns out that the elasticity matrix must be symmetric which reduces the number of potential independent constants from 36 to 21.

In the determination of the elasticity matrix in the general anisotropic case it is also utilized that the strain dyadic components e_{ij} cannot be given arbitrarily as function in space but are subject to some identities among the second-order spatial derivatives [20, Art. 17].

However, if the material is isotropic as regards elasticity the problem reduces considerably. By using the fact that the stress-energy function W now is invariant to the specific choice of orthogonal coordinate system it then turns out that only two elasticity parameters λ and μ, called the Lamé coefficients, suffice to establish the relation sought for

$$W(\mathbf{r},t) = \mu\mathfrak{S}(\mathbf{r},t)\cdot\mathfrak{S}(\mathbf{r},t) + \frac{\lambda}{2}(\mathrm{Trace}\,\mathfrak{S}(\mathbf{r},t))^2. \tag{F.4.12}$$

These parameters describe its resilience; there are two parameters because a solid will resist compressional and shear forces to different degrees.

The governing equation relating stresses to strain in an isotropic media is obtained from insertion of (F.4.12) in (F.4.10)

$$\mathfrak{T}(\mathbf{r},t) = \lambda|\mathfrak{S}(\mathbf{r},t)|\mathfrak{I} + 2\mu\mathfrak{S}(\mathbf{r},t), \tag{F.4.13}$$

where $|\mathfrak{S}| \equiv \mathrm{Trace}\,\mathfrak{S} = \sum_{i=1}^{3} e_{ii}$. A solid isotropic medium is therefore characterized by its density, ρ, and two material parameters λ and μ called the Lamé coefficients, which describe its resilience. Other elastic parameters found in the literature can be defined in terms of these two constants. In Table F.1 the relationships between Young's modulus, longitudinal stiffness and Poisson's ratio and the Lamé coefficients are tabulated in for convenience

Quantity	Definition	Relation
Lamé modulus μ (rigidity)	see (F.4.12)	$\mu = \frac{E\nu}{2(1+\nu)}$
Lamé modulus λ	see (F.4.12)	$\lambda = \frac{E}{2(1+\nu)(1-2\nu)}$
Longitudinal stiffness	$D \equiv \frac{T_{ii}}{e_{ii}}\|_{e_{kl}=0,kl\neq ii}$	$D = \lambda + 2\mu$
Young's modulus	$E \equiv \frac{T_{ii}}{e_{ii}}\|_{T_{kl}=0,kl\neq ii}$	$E = \frac{\mu(3\lambda+2\mu)}{\lambda+\mu}$
Shear modulus (rigidity)	$G \equiv \frac{T_{ij}}{e_{ij}}\|_{T_{kl}=0,kl\neq ij,ji}$	$G = \mu$
Poisson's ratio	$\nu \equiv -\frac{e_{jj}}{e_{ii}}$	$\nu = \frac{\lambda}{2(\lambda+\mu)}$
Modulus of compression	$k \equiv \frac{1}{3}\Delta^{-1}\,\mathrm{Trace}\,\mathfrak{T}$	$k = \lambda + \frac{2}{3}\mu$

Tab. F.1: Miscellaneous Elasticity Parameter Relations.

As already mentioned solids possess an important property which is the support of both compressional (dilatoric) waves involving no rotation and shear (divergence-free) waves that are waves of distortion involving rotation without dilatation. The compressional propagation velocity, c_L, is determined by the longitudinal stiffness, D and the mass density ρ, that is,

$$c_L = \sqrt{\frac{D}{\rho}} \tag{F.4.14}$$

$$= \sqrt{\frac{E(1-\nu)}{\rho(1+\nu)(1-2\nu)}}, \tag{F.4.15}$$

where the quantity, E is Young's modulus of elasticity and ν designate Poisson's ratio, which is the ratio of lateral shrink to longitudinal stretch.

Sometimes c_L is referred to as the *longitudinal, dilatoric* or *irrotational elastic wave velocity.*

The shear wave propagation velocity, c_T, is obtained from the shear modulus, G, which is the ratio between deviatoric shearing stress and corresponding deviatoric shearing strain[23] and the mass density, that is,

$$c_T = \sqrt{\frac{G}{\rho}} \tag{F.4.16}$$

$$= \sqrt{\frac{E}{2\rho(1+\nu)}}. \tag{F.4.17}$$

In some context c_T is referred to as the *transverse* or *equivoluminal elastic wave velocity.*

The net force due to forces acting on all faces of an infinitesimal volume $\mathrm{d}V$ is $\nabla \cdot \mathfrak{T}\,\mathrm{d}V$. Then from (F.4.13) and Newton's second law we obtain the governing wave equation inside an elastic matter supporting compressional as well as shear waves expressed in terms of the Lamé constants [20, Ch. XIII] [24] or [26, Ch. 2]

$$\boxed{\rho\frac{\partial^2 \mathbf{s}(\mathbf{r},t)}{\partial t^2} = \mathbf{f}(\mathbf{r},t) + G\bigg(\nabla^2\mathbf{s}(\mathbf{r},t) + \frac{\nabla\nabla\cdot\mathbf{s}(\mathbf{r},t)}{1-2\nu}\bigg).} \tag{F.4.18}$$

The vector quantity $\mathbf{f}(\mathbf{r},t)$. is the external force intensity

In other part of the literature the following wave equation expressed in terms of Poisson's ratio can be found [6, Ch. 2 Eq. (136d)]

$$\rho\frac{\partial^2 \mathbf{s}(\mathbf{r},t)}{\partial t^2} = \nabla\cdot\Big(\lambda\mathfrak{I}\nabla\cdot\mathbf{s}(\mathbf{r},t) + \mu\nabla\mathbf{s}(\mathbf{r},t) + \mu\mathbf{s}(\mathbf{r},t)\nabla\Big) \tag{F.4.19a}$$

$$= (\lambda+\mu)\nabla\nabla\cdot\mathbf{s}(\mathbf{r},t) + \mu\nabla^2\mathbf{s}(\mathbf{r},t) \tag{F.4.19b}$$

$$= (\lambda+2\mu)\nabla\nabla\cdot\mathbf{s}(\mathbf{r},t) - \mu\nabla\times\nabla\times\mathbf{s}(\mathbf{r},t). \tag{F.4.19c}$$

At first glance the two expressions (F.4.19) and (F.4.18) seem quite dissimilar. However, using the relations between the elasticity constants provided in Table F.1 it can easily be demonstrated that the two wave equations are indeed identical [7].

[23] Sometimes referred to as simple stress and simple shearing.

[24] The expression is in terms of the *dilatation* $\Delta(\mathbf{r},t) = \nabla\cdot s(\mathbf{r},t)$.

F.5 Electromagnetic Field Theory

Electromagnetic field theory, according to the standpoint adapted in this report, is the theory of Maxwell's equations. The sources of an electromagnetic field are a distribution of electric charge density $\rho(\mathbf{r},t)$ and a current density $\mathbf{J}(\mathbf{r},t)$. The time-domain Maxwell equations can be found in every book on electromagnetics and for convenience listed here

$$\nabla \times \mathbf{E}(\mathbf{r},t) + \mu(\mathbf{r})\frac{\partial}{\partial t}\mathbf{E}(\mathbf{r},t) = 0 \tag{F.5.1a}$$

$$\nabla \times \mathbf{H}(\mathbf{r},t) - \epsilon(\mathbf{r})\frac{\partial}{\partial t}\mathbf{H}(\mathbf{r},t) = \mathbf{J}(\mathbf{r},t), \tag{F.5.1b}$$

where $\mathbf{E}(\mathbf{r},t)$ and $\mathbf{H}(\mathbf{r},t)$ denote electric intensity and magnetic intensity respectively. Two constitutive parameters are involved namely the $\epsilon(\mathbf{r})$ the permittivity (capacity) of the medium and $\mu(\mathbf{r})$ permeability (inductivity). In *vacuum* these parameters take the values ϵ_0 and μ_0 respectively. The speed of light in vacuum c_0 is accordingly

$$c_0 = \frac{1}{\sqrt{\epsilon_0\mu_0}} = 2.99790 \times 10^8 \text{ meter} \cdot \text{s}^{-1}. \tag{F.5.2}$$

The Maxwell equation (F.5.1a) finds support in the observations of Faraday on variable fields and the Maxwell equation (F.5.1b) is a generalization of Ampere's circuit law including the displacement current density term $\epsilon\frac{\partial}{\partial t}\mathbf{H}(\mathbf{r},t)$.

From continuity arguments similar to those used in acoustics the conservation of charge[25] leads us to the following equation of continuity between charge density $\rho(\mathbf{r},t)$ and current density $\mathbf{J}(\mathbf{r},t)$

$$\nabla \cdot \mathbf{J}(\mathbf{r},t) + \frac{\partial}{\partial t}\rho(\mathbf{r},t) = 0. \tag{F.5.3}$$

Basically (F.5.3) states that mass or charge cannot be created or destroyed without sources From Maxwell equation (F.5.1) and continuity relation (F.5.3) the following divergence equations can easily be derived

$$\nabla \cdot \mathbf{H}(\mathbf{r},t) = 0 \tag{F.5.4a}$$

$$\nabla \cdot \mathbf{E}(\mathbf{r},t) = \frac{\rho(\mathbf{r},t)}{\epsilon(\mathbf{r})}. \tag{F.5.4b}$$

The divergence theorems (F.5.4a) and (F.5.4b) are frequently included as part of Maxwell's system. However, they are derived from Maxwell equation (F.5.1) and continuity relation (F.5.3) and are therefore not independent relations. With the help of Stoke' theorem (F.5.1a) and (F.5.1b) can be expressed in integral form. Similarly, the Maxwell equation (F.5.4a) and (F.5.4b) can be expressed in an equivalent integral form with the help of the divergence theorem [35, Ch. 1].

[25] There is no experimental evidence to indicate that under ordinary conditions charge may be either created or destroyed in macroscopic amounts.

F.6 Discussion of Field Equations

In the preceding sections we have briefly presented three different branches of physics at a level sufficiently detailed to formulate various types of partial differential equations which govern their fields. These equations are far from being the only field equations encountered in physics, but they actually represents a large fraction of field equations which are important in physics.

By making a few assumptions on the physical systems the underlying complicated behavior could be brought aside and allowed us instead to use the mathematical framework founded in *field theory*. Hence, we will consider a field as some convenient mathematical idealization of a physical system. A *macroscopic* assumption was made for all the three physical systems considered. Accordingly we could treat the physical system as a *continuum*. This meant that we set aside the discontinuous, atomic structure and look into the smoothed-out continuum picture of a fluid and a solid. This has a huge advantage in that we do not have to concern about underlying distribution functions, but merely focus on gross average quantities. We will return to this topic in section F.8 when we discuss *existence theorems* for acoustic and electromagnetic fields. It suffice here to say that a solution of a partial differential equation is more smoothly continuous over most space and time than is the corresponding physical situation. Likewise for convenience in the mathematical framework discontinuities in space and time are normally considered infinitely sharp - a condition that never holds perfectly in reality.

Electromagnetic waves possess the very interesting property of being able to propagate in the absence of any media, that is, in vacuum. In comparison with electromagnetic waves that are not relying on the existence of a medium, propagation of perturbations in fluids, e.g., sound waves are indeed dependent on a medium and therefore also vulnerable to the properties of the supporting media.

The Navier-Stokes equation (F.3.97) on page 656 and the classical equation of motion for an elastic solid under the influence of its own elastic restoring forces (F.4.19) on page 664 was found to be almost identical in form. The main difference is owing to the different choice of field parameter used to describe the system. In the theory of elasticity the displacement $\mathbf{s}(\mathbf{r}, t)$ is used while the velocity $\mathbf{u}(\mathbf{r}, t)$ is used in fluid dynamics. This difference in usage of field parameters is due to the fact that fluids yield to a shearing stress while solids will resist change in shape. As a consequence the governing fluid dynamic equation, that is, the Navier-Stokes equation involves the material time derivative $\frac{D}{\partial t}$ while the equation for elastic wave motion only involves the partial time derivative $\frac{\partial}{\partial t}$. Moreover, another important difference is that a force proportional to a displacement is a conservative force whereas a force proportional to a velocity is a dissipative force.

Concerning the constitutive parameters we recognize that in fluid mechanics the second viscosity coefficient λ and the coefficient of viscosity μ take a similar role to the Lamé moduli λ and shear modulus μ from theory of elasticity viz. (F.4.19) on page 664 except that they operate on the rate of the displacement instead of the displacement itself. For gases many of the constitutive parameters are mutually interrelated and good models are available in particular for ideal gases. Heat conductivity of fluids and in particular heat conductivity of solids are much complicated functions of the media. Experimental evidence confirms that λ and μ are scalars. However, for solids these quantities are usually tensors rendering the analysis much more complicated.

The main results are summarized in Table F.2

Physical System	Sources	Fields I	Fields II	Constitutive Parm.	Dissipative
Acoustics	$q, \mathbf{f}$	$p, \mathbf{u}$	δ, σ, τ	K_s, K_T, K	λ, μ, κ
Elasticity	$\mathbf{f}$	$s, \mathfrak{S}, \mathfrak{T}$		λ, μ	
Electromagnetics	$\rho, \mathbf{J}$	$\mathbf{E}, \mathbf{H}$	$\mathbf{D}, \mathbf{B}$	σ, ϵ, μ	

Tab. F.2: Sources, Fields and Constitutive Parameters in Acoustics, Elasticity and Electromagnetics.

F.6.1 Continuity Equations

The three physical systems considered all involved continuity equations, viz. (F.3.45) on page 642, (F.3.50) on page 643 and (F.5.3) on page 665.

For the two cases of continuum mechanics we saw that the wave speed is inversely proportional to the square root of the compressibility/elasticity (inverse stiffness) times the mass density viz. (F.3.75), (F.4.14) and (F.4.16). The electromagnetic wave speed in vacuum (F.5.2) is of the order of 1 million times faster than the speed of sound under normal conditions. This relationship can be explain from energy considerations. The *total energy density* consist of a *potential energy density* part $E_P = \frac{1}{2}Kp^2$ and a *kinetic energy density* part $E_K = \frac{1}{2}\rho|\mathbf{u}|^2$. The two field energy density constituents are proportional to the elasticity and mass density, which explains the aforementioned proportionality in wave speed.

In our investigations we made at an early stage an assumption of infinite medium corresponding to homogeneous constitutive parameters. The results therefore pertain to the interior of such infinite medium. However, surface waves types included in all three physical branches studied. Therefore, our analysis hitherto do not include flexural wave motion although bending wave indeed are important in the domain of active control of sound and vibration.

F.6.2 Field Equations

In the governing equations both first-order and second-order differential operators are encountered. In the subsequent text an interpretation of these operators will be made. In the equations three first-order differential operators are involved. The gradient ∇ operates on a scalar field $\psi(\mathbf{r})$ and yields a vector. The magnitude of the vector is the value of maximum rate of increase of $\psi(\mathbf{r})$ and the direction of this vector is the corresponding direction of greatest rate of increase of $\psi(\mathbf{r})$. The divergence operator $\nabla\cdot$ and the curl operator $\nabla\times$ both operates on a vector field $\boldsymbol{\psi}(\mathbf{r})$. The divergence operator returns a scalar indicating the rate of increase of lines of flow. The curl operator results in a vector that indicates the rate of twisting of the lines of flow. In the governing differential equations we also recognize three second-order differential operators namely the Laplacian operator ∇^2, the grad div operator $\nabla\nabla\cdot$ and curl curl operator $\nabla\times\nabla\times$. The Laplace operator, operates on both scalar fields $\psi(\mathbf{r})$ and vector fields $\boldsymbol{\psi}(\mathbf{r})$. In the scalar case the Laplacian is a measure of lumpiness of $\psi(\mathbf{r})$. Similarly in the vector case the result is a vector that is a measure of lumpiness in both magnitude and direction of $\boldsymbol{\psi}(\mathbf{r})$. The grad div operator operates on a vector field $\boldsymbol{\psi}(\mathbf{r})$ and is resulting vector is a measure of the change in the divergence of $\boldsymbol{\psi}(\mathbf{r})$. Finally, the curl curl operator is a vector field operator that expresses the difference between the grad div and Laplace operator according to the vector identity $\nabla\times\nabla\times\boldsymbol{\psi} = \nabla\nabla\cdot\boldsymbol{\psi} - \nabla^2\psi$.

The governing time-domain equations (F.5.1) on page 665 can be written in a compact form as

$$\mathcal{L}(\mathbf{r},t)\psi(\mathbf{r},t) = F(\mathbf{r},t) \tag{F.6.1a}$$
$$\mathcal{L}(\mathbf{r},t)\boldsymbol{\psi}(\mathbf{r},t) = \mathbf{F}(\mathbf{r},t), \tag{F.6.1b}$$

where (F.6.1a) and (F.6.1b) pertain to the scalar and vector case respectively. The unknown field quantities $\psi(\mathbf{r},t)$ and $\boldsymbol{\psi}(\mathbf{r},t)$ are scalar and vector functions of space and time respectively. The "source" terms $F(\mathbf{r},t)$ and $\mathbf{F}(\mathbf{r},t)$ will generally also be functions of space and time. Finally, the operators $\mathcal{L}(\mathbf{r},t)$ and $\mathcal{L}(\mathbf{r},t)$ are each a combination of functions (operating on scalar and vector elements respectively) of space and time, of the partial derivative with respect to space and time. We can make the following observations concerning field equations in (F.6.1).

Field Prop.# 1. Linearity in $\psi(\mathbf{r},t)$, that is, no $\psi^k(\mathbf{r},t), k \geq 2$ or $\psi_i(\mathbf{r},t)\psi_j(\mathbf{r},t), i \neq j$ terms are encountered.

Field Prop.# 2. Restricted to second-order in space and time, that is, no $\frac{\partial^k}{\partial x^k}$ or $\frac{\partial^k}{\partial t^k}$ with $k > 2$ terms encountered[26].

Field Prop.# 3. General (as opposed to ordinary) partial differential equation.

Generally, for the solution of field problem governed by partial differential equation and suitable boundary condition we have two methods at our disposal, the integral solution and the separated solution. The integral method involves a (free-space) *Green's function* that for the inhomogeneous part of the equation establish a link between each infinitesimal source element to a corresponding field point. Another Green's function that establish a link between each *equivalent* source element on the boundaries to a specific field point.

A Green's pertains to a specific wave equation and be scalar-valued, vector-valued and tensor-valued. The free space Green's functions are independent of the field equations. The boundary Green's function, however, depends on the particular governing equation.

Numerical evaluation of analytic integral Green's function expression and employing the method of moments (MOM) has successfully been used in various antenna design [8, 9, 31].

A problem with Field Property 3 is that the original equation generally needs to be separated into a set of *ordinary* partial differential equations. An advantage of the integral method is that it is invariant under coordinate transformation and can be generally be used where separation of the original equation cannot be made. We may employ the method of *expansion in eigenfunction* [26, Ch. 6]. Moreover, both methods are only efficient if the boundaries are such that we can find a coordinate system, in which the given partial differential equation will separate.

As we will see the Green's function is a closed function representation of the solution that provides insight into the over-all behavior of the solution.

In our review of the physical system we encountered the scalar Helmholtz equation (F.2.9a) and the vector Helmholtz equation (or variants hereof) in (F.2.9b) on page 624. However, in some cases the solution to the vector Helmholtz equation might not be sufficient as some additional constraints are to be satisfied. For example, the electromagnetics vector potential $A(\mathbf{r})$ where the gauge makes the scalar vector potential $\phi(\mathbf{r}) = 0$, which is applicable to situations where there are no free charge $\rho(\mathbf{r}) = 0$ must also be divergenceless, that is, $\nabla \cdot A(\mathbf{r}) = 0$.

[26] An exception for this rule is found for the wave equation for *bending waves* [6, Ch. II.3].

F.6.3 Curvilinear Coordinates

The choice of coordinate system is usually made (if possible) such that when erected on the boundary such that the boundary surface is one of the coordinate surfaces $\xi_i = C$ constant. Moreover, in order to avoid complicated differential equation with cross differential terms a *separable coordinate system* (ξ_1, ξ_2, ξ_3) is sought for. Then the solutions are separated into factors functions, each dependent on only one of the ξ_i coordinates, that is, $\psi(\xi_1, \xi_2, \xi_3) = F_1(\xi_1)F_2(\xi_2)F_3(\xi_3)$. Such a coordinate system allow families of separated solutions of a given linear partial differential equations from which all solutions of the equation can be built up. The generalized set of curvilinear coordinates ξ_1, ξ_2, ξ_3 constitute a framework to select "natural coordinates". Oblique systems (as opposed to orthogonal systems) have interesting properties but lead to difficulties in the mathematical analysis of the pertinent partial differential equations rigoristic. Hence, an orthogonal curvilinear system defined by the unitary vectors $\hat{\boldsymbol{\xi}}_1, \hat{\boldsymbol{\xi}}_2, \hat{\boldsymbol{\xi}}_3$ that by definition are mutually perpendicular is selected. The orthogonal curvilinear coordinate system is completely characterized by three *metric coefficients* or *scale factors*, h_1, h_2, h_3 that relate the curvilinear coordinate (ξ_1, ξ_2, ξ_3) to the Cartesian coordinates (x_1, x_2, x_3) by

$$h_i^2 = \sum_{i=1}^{3} \Big(\frac{\partial x_i}{\partial \xi_i}\Big)^2 = \Big[\sum_{i=1}^{3} \Big(\frac{\partial \xi_i}{\partial x_i}\Big)^2\Big]^{-1} \tag{F.6.2}$$

having the property that the length of an infinitesimal vector $\mathrm{d}s$ is

$$\mathrm{d}s^2 = \sum_{i=1}^{3} \mathrm{d}x_i^2 = \sum_{1=1}^{3} \mathrm{d}\xi_i^2. \tag{F.6.3}$$

As discussed in subsection F.2.5 the Laplace equation (F.2.6) applies to static fields while the wave equation governs dynamic fields. Independent of the partial differential equation that govern the specific physical problem to find the solution involves the process of determining all possible solutions and then to select those combinations which also satisfy the boundary condition of the case under consideration.

For the wave equation (F.2.8) [26, Ch. 5] eleven separable coordinate systems exist in the three-dimensional case. For the Laplace equation some additional coordinate systems allow separation of the solutions.

In Table F.3 the aforementioned coordinate systems are listed with a √mark indication if the coordinate system allow separation of variable for the Laplace and Helmholtz equations in both scalar and vector case. For more detailed information refer to [26, Ch. 5] [27, Ch. 13].

The systems fall into four classes: Cylindrical coordinates (#1-#4), rotational coordinates (#5-#9), a less symmetric class (#10-#11) and the cyclical coordinates (#12-#13). In all the different physical systems a coordinate system that bear some simple relationship to the boundary surface or to the distribution of singularities is sought for. This also applies to the theoretical study of acoustical, elastics and electromagnetic waves introduced in section F.3, section F.4 and section F.5.

#	Coordinate System	Laplace		Helmholtz			
		ψ	$\boldsymbol{\psi}$	ψ	$\boldsymbol{\psi}$	ξ_1	w
1	**Rectangular**	√	√	√	√	x, y, z	1
2	**Circular Cylinder**	√	√	√	√	z[27]	1
3	**Elliptic Cylinder**	√	√	√	√	z[28]	1
4	**Parabolic Cylinder**	√	√	√	√	z[29]	1
5	**Spherical**	√	√	√	√	r	r
6	**Conical**	√	√	√	√	r	r
7	**Parabolic**	√	√	√	-		
8	**Prolate Spheroidal**	√	√	√	-		
9	**Oblate Spheroidal**	√	√	√	-		
10	**Ellipsoidal**	√	√	√	-		
11	**Paraboloidal**	√	√	√	-		
12	**Bispherical**	√	√	-	-		
13	**Toroidal**	√	√	-	-		

Tab. F.3: 3-D Coordinate Systems Separable to Laplace and Helmholtz Equations.

F.6.4 Boundary Conditions

Any physical problem must state not only the differential equation which is to be solved but also the boundary conditions which the solution must satisfy. The solutions and boundary conditions are somewhat different for each of the three physical systems considered.

F.6.5 Scalar and Vector Fields

From the physical domain governing equations (F.5.1), (F.3.103) to (F.3.101) and (F.4.19) we see that electromagnetic field $\mathbf{E}, \mathbf{H}$, the velocity $\mathbf{u}$ of a fluid and the displacement $\mathbf{s}$ of an elastic solid are all *vector fields*. Likewise there are several other manifestations of vector wave fields in nature.

Although some vector fields, e.g., the acoustic velocity in viscous free fluid might be obtained from the gradient of a scalar quantity (in this case the acoustic pressure). Another similar case of physical interest is the static electric field that can be obtained as the negative gradient of the electric scalar potential $\phi(\mathbf{r})$. Likewise, the *Newtonian potential* $U(\mathbf{r})$ and *Newtonian force* $\mathbf{F}(\mathbf{r})$ is obtained as $\mathbf{F}(\mathbf{r}) = \nabla U(\mathbf{r})$ [18]. We will carry out a detailed analysis of spatial-time-dependent potential functions in section F.F. In general, however, vector fields cannot be derived from a purely scalar function of space and time. As a consequence the analysis of electromagnetic fields and fields in elastic solids are inherently more difficult than a similar analysis of ordinary linear acoustic fields.

Moreover, the vector nature of the field poses additional problems when relating the solutions of the governing differential equations to the prescribed boundary conditions. Intuitive direct approaches to invoking the boundary conditions fail[27, Ch. 13]. Only if can express our solution to the homogeneous governing vector field equation can be that bear a simple relationship to the boundary surface is a simple three-fold uncoupled solution to be expected. For example, the vector Helmholtz equation can be made to separate in three scalar Helmholtz equations where no cross differential enters.

A remedy to this problem is use *Helmholtz's theorem* [26, Ch. 1.5] that states that any vector field $\boldsymbol{\psi}(\mathbf{r})$ is uniquely separable into a divergenceless part, $\boldsymbol{\psi}_s(\mathbf{r}) = \nabla \times \mathbf{A}(\mathbf{r})$, and a curlless part, $\boldsymbol{\psi}_l(\mathbf{r}) = \nabla\phi(\mathbf{r})$, provided that $\boldsymbol{\psi}(\mathbf{r})$ is finite, uniform and continuous and vanishes at infinity. The function $\phi(\mathbf{r})$ is the scalar potential of $\boldsymbol{\psi}(\mathbf{r})$ and $\mathbf{A}(\mathbf{r})$ is its vector potential. Then due to the uniqueness the solution should be obtained indirectly from separating the fields into its lamellar and solenoidal components and through subsequent use of the scalar potential and vector potential instead of working on the field components directly.

Therefore, the coordinate system should also but also to include vector fields and their equations. The solution is obtained from breaking the solution into the field components $\mathbf{L}$, $\mathbf{M}, \mathbf{N}$

The solution of the scalar Helmholtz equation in $\varphi(\mathbf{r})$ i.e., the longitudinal part of the field is obtainable provided that the boundary Now in addition to the requirement on the boundary surface to coincide with one of the coordinate surfaces $\xi_i = C$ constant the coordinate system should also be such that we can chose the two scalar fields from which the two transverse field components are derived, so that part of the field derived from one scalar would be tangential to the surface $\xi_i = C$ and the other would be normal to it. Out of the eleven separable coordinate systems for the scalar Helmholtz equation (and scalar wave equation) only six of these are amendable to the vector Helmholtz equation [27, Ch. 13]. These are the rectangular coordinates in which no preference of ξ_i is made, circular-, elliptical and parabolic cylinder coordinates subject to the requirement that $\xi_i = z$ and finally spherical and conical coordinates subject to $\xi_i = r$.

The peculiar advantages of these coordinate systems are a consequence of the very simple character of their geometrical properties.

Moreover, it should be remarked that for other field equations the situation might be different.

F.6.6 Integral Expressions

The time-domain expression for the vector field $\mathbf{F}(\mathbf{r}, t)$ can be

$$\begin{aligned}
\mathbf{F}(\mathbf{r},t) = &\int_0^{t_+} \Big[\iiint_V \mathfrak{G}(\mathbf{r},t,\mathbf{r}',t') \cdot \mathbf{Q}(\mathbf{r}',t')\,\mathrm{d}V' \Big]\,\mathrm{d}t' \\
&+\frac{1}{4\pi}\int_{t_0}^{t_+} \Bigg[\iint_S \Big[(\nabla' \cdot \mathbf{F}(\mathbf{r}',t'))(\mathfrak{G}(\mathbf{r},t,\mathbf{r}',t') \cdot \hat{\mathbf{n}}) - (\nabla' \cdot \mathfrak{G}(\mathbf{r},t,\mathbf{r}',t'))(\mathbf{F}(\mathbf{r}',t') \cdot \hat{\mathbf{n}}) \\
&\qquad - \mathfrak{G}(\mathbf{r},t,\mathbf{r}',t') \cdot (\hat{\mathbf{n}} \times \nabla' \times \mathbf{F}(\mathbf{r}',t')) - (\nabla' \times \mathfrak{G}(\mathbf{r},t,\mathbf{r}',t')) \cdot (\hat{\mathbf{n}} \times \mathbf{F}(\mathbf{r}',t')) \Big]\,\mathrm{d}S'\,\mathrm{d}t' \Bigg] \\
&-\frac{1}{c^2}\iiint_V \Big[\Big(\frac{\partial}{\partial t'}\mathfrak{G}(\mathbf{r},t,\mathbf{r}',t') \Big) \cdot \mathbf{F}(\mathbf{r}',t') - \mathfrak{G}(\mathbf{r},t,\mathbf{r}',t') \cdot \Big(\frac{\partial}{\partial t'}\mathbf{F}(\mathbf{r}',t') \Big) \Big]_{t'=t_0}\,\mathrm{d}V',
\end{aligned} \tag{F.6.4}$$

where the time-domain Green's dyadic $\mathfrak{G}(\mathbf{r}, t, \mathbf{r}', t')$ is determined from

$$\mathfrak{G}(\mathbf{r},t,\mathbf{r}',t') = \frac{\mathfrak{I}}{R}\delta(t - t' - R/c) \tag{F.6.5}$$

that is a solution to inhomogeneous wave equation

$$\nabla^2 \mathfrak{G}(\mathbf{r}, t, \mathbf{r}', t') - \frac{\partial^2}{\partial t^2} \mathfrak{G}(\mathbf{r}, t, \mathbf{r}', t') = -4\pi\delta(t - t')\delta(\mathbf{r} - \mathbf{r}')\mathfrak{I}. \tag{F.6.6}$$

F.7 Uniqueness

Uniqueness theorems establish conditions for a one-to-one correspondence of a field to its sources. This allows us provided that the underlying assumption warranting uniqueness are satisfied unambigiously to calculate the field from its sources. It should, however, be remarked in general the more unusual reverse procedure to determine the sources from the field. Uniqueness theorems have for many years attracted electromagnetic and acoustic field theorists who attempt to establish uniqueness theorems with as few as possible restrictions as possible. One such contribution has recently be made by Hansen and Yaghjian [12] which also contains derivations, theorems and expressions that are useful but probably yet not widely known especially within the acoustical community. We will make some references to this work here. Thorough analysis of this book reveals that many of the theorems make extensive use of the *divergence theorem* and Leibnitz' rule of differentiation of integrals [17, Ch. 4.9]. This kind of field theory becomes particular important if one attempts to synthesize rather advanced fields like the *electromagnetic missiles* [12, Ch. 5].

In the time-domain uniqueness is proved by hypothetically assuming the existence of two fields that both satisfy the governing equations. The law of conservation of energy or time-integrated energy for the *differential field*, that is the field obtained from subtracting one field solution from another field solution and that in virtue of the linearity of the field equations also is a solution, applied to an entire bounded region of space reveals that the only possible solution is the trivial solution of identical fields. In the frequency-domain uniqueness is similarly proved by invoking the *conservation of complex power* for the differential fields applying to an entire region.

A proof of the reverse problem could most likely be conducted in an equivalent way by hypothetically assuming the existence of two sources that both lead to the same field satisfing the governing equations. However, we do know that we can use *equivalent sources* and thereby producing the original fields, however, in a limitted space determined by the surface spanned by those sources.

In an active control of sound context uniqueness in the sources to field correspondence is of particular importance. For example if the same source contribution, including equivalent sources, due to some other reasons could produce more than one possible field distribution within the control volume it will be needless to state that there will no means to cancel the fields herein. On the other hand if we had more than one secondary source distribution at our disposal that will perfectly match the primary field - at least within a finite control volume, the problem would indeed be more luxurious in that we had to choose the most optimal in some sense.

By invoking the *reciprocity theorem*[30] the uniqueness from fields to sources is proved.

Fundamentally we are interested in determining *equivalent sources* that produce the same field within a certain region of space. This allows us with some flexibility in that the fields in the complementary volume of space can take different values. The analysis becomes considerably

[30]The reciprocity theorem states that the *reaction* of field A on source B equals the reaction of field B on source A [13, Ch. 3].

more simple if the coordinate system in which the scalar wave equation is separable. This also applies to the scan surface.

Fluid Mech. Field Theory Assump.# 14. In the development it is assumed that curves, surface and volumes are *regular* according to the Kellogg definition [18, Ch. 4]. This rather mild assumption does not preclude a more general applicability of the results to be presented in the rest of this chapter, but merely ensures that Riemann's integration of piece-wise continuous can be defined on these topologies.

From [12, Ch. 2] the following uniqueness statement is made:

Theorem 2. *A solution for the acoustic pressure* $p(\mathbf{r},t)$ *and the acoustic velocity* $\mathbf{u}(\mathbf{r},t)$ *that rigorously satisfy the time-domain linear acoustic equations* (F.3.103) *to* (F.3.104) *on page 659, if it exists, is* unique *provided that the fields* $p(\mathbf{r},t)$ *and* $\mathbf{u}(\mathbf{r},t)$ *at all* $(\mathbf{r},t)$ *satisfy the conditions*[31]*:*

1. $s(\mathbf{r},t)$ *and* $\mathbf{f}(\mathbf{r},t)$ *are located within a bounded volume i.e.,* $\mathcal{V}_s \subset \mathcal{V}_\infty$*,*
2. strong causality *which mean that the fields are zero beyond a distance* $c(t-t_0)$ *from a source point that turns on at time* $t=t_0$*. Hence, the speed of propagation must be finite i.e.,* $c<\infty$*,*
3. $p(\mathbf{r},t)$ *and* $\mathbf{u}(\mathbf{r},t)$ *are* continuous *functions of* $\mathbf{r}$ *and* t[32]*.*

By $\mathcal{V}_\infty$ we will denote all space $\mathbb{R}^3$ and by $\mathcal{V}_s$ denote space spanned by all sources. It should be remarked that the conditions listed above are *sufficient* conditions that technically allow the use of the divergence theorem[33] and Leibnitz's rule of differentiation of integrals[34].

The two first conditions above are in principle similar in that they makes it possible to construct a hypothetical surface beyond all sources for which no energy for sure has been radiated at time t. In practice these two requirements will of course always be met.

If the conditions indeed are *necessary* is questionable. For uniqueness of time-domain differential equations (F.3.101) to (F.3.102) on page 658 an additional requirement on the existence of the time derivative of the fields shall be made.

So far no statements on uniqueness for generalized linear acoustic fields that are not everywhere continuous with time and not at all time continuous in space have been made. Some remarks on the finite extension of the source volume should also be made. In some 2-dimensional analysis an assumption of field quantities being independent of the third coordinate. However, this

[31] The solenoidal part of $\mathbf{u}$ i.e., the vorticity is not uniquely determined. Two fields that are identical except for a different time-integrated vorticity variation with range may both be a solution to (F.3.103) to (F.3.104) on page 659 provided that the difference in $\mathbf{u}_s(\mathbf{r},t)$ varies continuously with r for each t.

[32] A function is continuous with $\mathbf{r}$ and t should be understood as it is continuous with all four variables t,x,y and z. This continuity with respect to $(\mathbf{r},t)$ is slightly stronger than continuity with respect to $\mathbf{r}$ for each t.

[33] Suppose V is a subset of V_∞ which is compact and has a piecewise smooth boundary. If $\boldsymbol{\psi}$ is a continuously differentiable vector field defined on a neighborhood of V, then we have $\iiint_V \nabla\cdot\boldsymbol{\psi}\,\mathrm{d}V = \iint_{\partial V}\boldsymbol{\psi}\cdot\mathrm{d}\mathbf{S}$, where ∂V is the boundary of V oriented by outward-pointing normals, and $\mathrm{d}\mathbf{S}$ is shorthand for $\hat{\mathbf{n}}\,\mathrm{d}S$, the outward pointing normal of the boundary ∂V[4].

[34] The Leibnitz's formula can be extended to definite integral for which the boundaries of integration are variable [17, Ch. 4.9]. Let $f(\mathbf{r},t)$ be continuous and have continuous derivative $\partial f/\partial t$. In addition let $\phi_1(t)$ and $\phi_2(t)$ be defined and have continuous derivatives for $t_1\le t\le t_2$. Then for $t_1\le t\le t_2$, $\frac{\mathrm{d}}{\mathrm{d}t}\int_{\phi_1(t)}^{\phi_2(t)} f(\mathbf{r},t)\,\mathrm{d}t = \int_{\phi_1(t)}^{\phi_2(t)}\frac{\partial f(\mathbf{r},t)}{\partial t}\,\mathrm{d}t + f(\mathbf{r},\phi_2)\frac{\mathrm{d}\phi_2}{\mathrm{d}x} - f(\mathbf{r},\phi_1)\frac{\mathrm{d}\phi_1}{\mathrm{d}x}$. The extension to the vector-valued functions is straight forward.

assumption implicitly requires the sources also be of infinite extension along the third dimension and independent of the position along the third axis. Then one has to resort to some limiting consideration of finite yet many wavelength extension along the third dimension.

F.8 Existence

Sometimes one is also concerned as whether a solution exists at all. This become relevant in field synthesis, but is of course not an aspect when dealing with measured quantities.

For the construction of a solution for the linear acoustic problem at hand it is useful to introduce the velocity potential $\Phi(\mathbf{r}, t)$ that is related to the acoustic pressure and acoustic velocity as follows

$$p(\mathbf{r}, t) = \rho \frac{\partial}{\partial t} \Phi(\mathbf{r}, t), \tag{F.8.1}$$

$$\Phi(\mathbf{r}, t) = \frac{1}{\rho} \int_{t_0}^{t} p(\mathbf{r}, t') \, \mathrm{d}t', \tag{F.8.2}$$

$$\mathbf{u}(\mathbf{r}, t) = -\nabla \Phi(\mathbf{r}, t) + \frac{1}{\rho} \int_{t_0}^{t} \mathbf{f}(\mathbf{r}, t') \, \mathrm{d}t'. \tag{F.8.3}$$

In our analysis we are often dealing with expressions involving a scalar source function $\psi(\mathbf{r}', t' - |\mathbf{r} - \mathbf{r}'|/c)$ or vector source function $\boldsymbol{\psi}(\mathbf{r}', t' - |\mathbf{r} - \mathbf{r}'|/c)$ both of which takes two arguments. The first argument is the source position $\mathbf{r}'$ and the second argument is the retarded time $t - |\mathbf{r} - \mathbf{r}'|/c$. In particular, in the time-domain analysis integration over the source region of such a scalar or vector source function that is multiplied by the free-space (infinite domain) Green's function will be carried out. However, the integrand possess a singularity at positions where the field and source point coincide. This results in an improper integral and the study presents some difficulties that must be taking into account. Fortunately, a central theorem on improper volume integrals ensures convergence of the integral in a large class of problems [32, Sec. 55].

Some of the development leading to requirements on the sources and fields for the existence is provided in section F.F that also includes an arguable simpler proof of two central theorems. The classical work by Kellogg [18] on potential functions for time-independent fields in general is used.

From [12, Ch. 2] the following uniqueness statement is made:

Theorem 3. *The acoustic pressure $p(\mathbf{r}, t)$ and acoustic velocity $\mathbf{u}(\mathbf{r}, t)$ defined in* (F.8.1) *and* (F.8.3) *through the velocity potential function $\phi(\mathbf{r}, t)$ are the* unique, causal, continuous *acoustic fields that rigorously satisfy the time-domain linear acoustic equations for the source functions $s(\mathbf{r}, t)$ and $\mathbf{f}(\mathbf{r}, t)$* (F.3.103)-(F.3.104) *provided that $s(\mathbf{r}, t)$ and $\mathbf{f}(\mathbf{r}, t)$ satisfy the conditions:*

1. *$s(\mathbf{r}, t)$ and $\mathbf{f}(\mathbf{r}, t)$ are located within a bounded volume i.e., $\mathcal{V}_s \subset \mathcal{V}_\infty$,*

2. *$s(\mathbf{r}, t), \partial s(\mathbf{r}, t)/\partial t, \mathbf{f}(\mathbf{r}, t)$ and $\nabla \cdot \mathbf{f}(\mathbf{r}, t)$ are continuous functions of $\mathbf{r}$ and t, and*

3. $s(\mathbf{r},t)$ *and* $\nabla\cdot\mathbf{f}(\mathbf{r},t)$ *are Hölder continuous*[35] *functions in* $\mathbf{r}$ *for all* t*.*

Remark. It should again be remarked that the conditions listed above are *sufficient* conditions that technically allow the use of the divergence theorem and Leibnitz's rule of differentiation of integrals. We can therefore the extension of the proof to an even wider class of configuration is left as an open research topic. In addition the theorems underlying the existence condition above involve principal volume integration and source dyadic terms that are ill-defined within the source region without sufficient conditions on the volume source of mass-flow and external force density.

F.9 Pressure and Velocity Fields from Volume Integrals

For sources that first begin at $t=t_0$ it is redundant to include $s(\mathbf{r},t)$ as continuity of $\partial s(\mathbf{r},t)/\partial t$ with respect to $(\mathbf{r},t)$ implies continuity of $s(\mathbf{r},t)$ with respect to $(\mathbf{r},t)$ as well. The following expressions for the acoustical pressure and the acoustical velocity can then be deduced (see subsection F.E.3 on page 696)

$$p(\mathbf{r},t)=\frac{1}{4\pi}\lim_{\delta\to 0}\iiint\limits_{V\setminus V_\delta}\left[\frac{1}{R}\frac{\partial}{\partial t}s(\mathbf{r}',t-R/c)\right.\\ \left.+\left(\frac{1}{c}\frac{\partial}{\partial t}\mathbf{f}(\mathbf{r}',t-R/c)+\frac{\mathbf{f}(\mathbf{r}',t-R/c)}{R}\right)\cdot\frac{\mathbf{R}}{R^2}\right]\mathrm{d}V',\quad \mathbf{r}\in\bar{\mathcal{V}}_x \tag{F.9.1}$$

and

$$\mathbf{u}(\mathbf{r},t)=\frac{1}{4\pi\rho}\lim_{\delta\to 0}\iiint\limits_{V\setminus V_\delta}\left[\left(\frac{1}{c^2}\frac{\partial}{\partial t}\mathbf{f}(\mathbf{r}',t-R/c)\right)\cdot\frac{\mathbf{RR}}{R^3}\right.\\ +\left(\frac{1}{c}\mathbf{f}(\mathbf{r}',t-R/c)+\frac{1}{R}\int_{t_0}^{t}\mathbf{f}(\mathbf{r}',t-R/c)\,\mathrm{d}t'\right)\frac{1}{R^2}\\ \cdot\left(\frac{3\mathbf{RR}}{R^2}-\mathfrak{I}\right)\\ \left.+\left(\frac{1}{c}\frac{\partial}{\partial t}s(\mathbf{r}',t-R/c)+\frac{1}{R}s(\mathbf{r}',t-R/c)\right)\frac{\mathbf{R}}{R^2}\right]\mathrm{d}V'\\ -\frac{1}{\rho}(\mathfrak{L}-\mathfrak{I})\cdot\int_{t_0}^{t}\mathbf{f}(\mathbf{r},t')\,\mathrm{d}t',\quad \mathbf{r}\in\bar{\mathcal{V}}_x, \tag{F.9.2}$$

where $\mathfrak{L}$ is the source or polarization dyadic defined as

$$\mathfrak{L}\equiv\int_{S_\delta}\frac{\hat{\mathbf{n}}\hat{\mathbf{r}}}{r^2}\,\mathrm{d}S \tag{F.9.3}$$

[35] A real-valued function $s(\mathbf{r},t)$ on a metric space (X,d) is Hölder continuous or satisfies a Hölder condition, when there are nonnegative real constants A,α, such that, $\forall\mathbf{r},\mathbf{r}'\in X, |s(\mathbf{r},t)-s(\mathbf{r}',t-R/c)|\le Ad(\mathbf{r},\mathbf{r}')^\alpha$. The Hölder condition is stronger than continuity for all positive α and weaker than differentiability if $\alpha<1$.

and $\mathfrak{I}$ is the unit dyad.

The volume integration takes place over the volume V excluding the *principal volume* V_δ in order to take the singularity at $\mathbf{r} = \mathbf{r}'$ properly into account. In the limit $\delta \to 0$ the contribution from the integral vanishes. Moreover, in [12, Ch. 2] it is proved that the value $\int_{V_\delta} \mathrm{d}V'$ is independent of the shape of V_δ and the position of the singularity within V_δ. However, when it comes to two times spatial differentiation of an integral involving singularity both the shape of V_δ and the position of the singularity within V_δ matters. Hence, the factor $\frac{3\mathbf{RR}}{R^2}$ involving the dyadic $\mathbf{RR}$ stems technically from the use of a spherical principal volume V_δ^s in the integration. For an otherwise shaped principal volume, this factor will change, but will be absorbed elsewhere on the right-hand side of (F.9.2) so as to keep the combined value of terms on the right-hand side of (F.9.2) equal to the unique value of the left-hand side of (F.9.2).

F.10 Pressure and Velocity Fields from Surface Integrals

The time-domain scalar wave equation in the first-order acoustic pressure is in general governed by the following *inhomogeneous first-order* acoustical *second-order* differential wave equation of acoustic motion [28, Ch. 6]:

$$\boxed{\nabla^2 p(\mathbf{r},t) - \frac{1}{c^2}\frac{\partial^2 p(\mathbf{r},t)}{\partial t^2} = -\frac{\partial s(\mathbf{r},t)}{\partial t} + \nabla\cdot\mathbf{f}(\mathbf{r},t),} \tag{F.10.1}$$

where c is the speed of sound ($c = \sqrt{\frac{1}{K\rho}}$). Outside the source region the time-domain scalar wave equation in the acoustic pressure is governed by the following homogeneous *first-order* acoustical *second-order* differential wave equation of acoustic motion [28, Ch. 6]:

$$\nabla^2 p(\mathbf{r},t) = \frac{1}{c^2}\frac{\partial^2 p(\mathbf{r},t)}{\partial t^2}, \quad \mathbf{r} \notin \mathcal{V}^s. \tag{F.10.2}$$

By the notion $\mathbf{r} \notin \mathcal{V}^s$ we refer to field points exterior to the volume spanned by the sources.

It should be recalled at this stage that *second-order* acoustical terms neglected above may modify the equation for simple wave motion (F.10.2), even when viscosity and thermal conductivity are neglected.

Similarly, in the frequency-domain the acoustic field satisfies the inhomogeneous scalar Helmholtz equation outside and within the source region

$$\boxed{\nabla^2 p_\omega(\mathbf{r}) + k^2 p_\omega(\mathbf{r}) = \imath\omega s_\omega(\mathbf{r}) + \nabla\cdot\mathbf{f}_\omega(\mathbf{r}).} \tag{F.10.3}$$

The homogeneous scalar Helmholtz equation outside the source region $\mathcal{V}^s$ is therefore

$$\nabla^2 p_\omega(\mathbf{r}) + k^2 p_\omega(\mathbf{r}) = 0, \quad \mathbf{r} \notin \mathcal{V}^s. \tag{F.10.4}$$

To proceed, we will introduce the free space (FS) (infinite medium) time-domain and frequency-

domain Green's functions $G\big(\mathbf{r},\mathbf{r}',t,t'\big)$ and $G_\omega(\mathbf{r},\mathbf{r}')$ that are defined by

$$G\big(\mathbf{r},\mathbf{r}',t,t'\big)=\frac{1}{4\pi R}\delta\Big(t-t'-\frac{R}{c}\Big) \tag{F.10.5}$$

and

$$G_\omega(\mathbf{r},\mathbf{r}')=\frac{\mathrm{e}^{\imath kR}}{4\pi R}, \tag{F.10.6}$$

respectively, where $\mathbf{R}$ is a vector from source point to field point. The scalar quantity R is the distance from the source point to the field point

$$R=|\mathbf{R}|=|\mathbf{r}-\mathbf{r}'|=\sqrt{(x-x')^2+(y-y')^2+(z-z')^2}. \tag{F.10.7}$$

The Green's function $G\big(\mathbf{r},\mathbf{r}',t,t'\big)$ so defined spatial factor for a wave from a unit point impulsive source at $\mathbf{r}'$. From causality reasons $G\big(\mathbf{r},\mathbf{r}',t,t'\big)$ must be zero for $t<t'$. The Green's function $G_\omega(\mathbf{r},\mathbf{r}')$ so defined is the spatial factor for a wave from a unit, simple-harmonic, point source at $\mathbf{r}'$. The FS Green's functions defined in constitute a Fourier transform pair. The Green's functions posses symmetry properties $G\big(\mathbf{r},\mathbf{r}',t,t'\big)=G(\mathbf{r}',\mathbf{r},-t',-t)$ and $G_\omega(\mathbf{r},\mathbf{r}')=G_\omega(\mathbf{r}',\mathbf{r})$ respectively.

The time-domain Green's function is a solution to an *inhomogeneous* scalar wave equation [28, Ch. 7.1]:

$$\boxed{\nabla^2 G\big(\mathbf{r},\mathbf{r}',t,t'\big)-\frac{1}{c^2}\frac{\partial^2}{\partial t^2}G\big(\mathbf{r},\mathbf{r}',t,t'\big)=-\delta^{(3)}(\mathbf{r}-\mathbf{r}')\delta(t-t'),\quad \mathbf{r}\notin\mathcal{V}^s,} \tag{F.10.8}$$

where $\delta^{(3)}(\mathbf{r}-\mathbf{r}')$ and $\delta(t-t')$ are the delta function in three dimensions and one dimension respectively. Both delta functions are symmetric with their arguments i.e., $\delta^{(3)}(\mathbf{r}-\mathbf{r}')=\delta^{(3)}(\mathbf{r}'-\mathbf{r})$ and $\delta(t-t')=\delta(t'-t)$.

The frequency-domain Green's function is a solution to an *inhomogeneous* scalar Helmholtz equation [28, Ch. 7.1]:

$$\boxed{\nabla^2 G_\omega(\mathbf{r},\mathbf{r}')+k^2 G_\omega(\mathbf{r},\mathbf{r}')=-\delta^{(3)}(\mathbf{r}-\mathbf{r}').} \tag{F.10.9}$$

In section F.D on page 687 Green's second identity[36] is used to derive the following expressions for the time-domain acoustic pressure and acoustic velocity fields

$$\begin{aligned}p(\mathbf{r},t)=\frac{1}{4\pi}\iint_{\partial V}\hat{\mathbf{n}}'\cdot\bigg[\frac{\mathbf{R}}{R^2}\Big(\frac{1}{c}\frac{\partial}{\partial t}p(\mathbf{r}',t-R/c)+\frac{1}{R}p(\mathbf{r}',t-R/c)\Big)\\ +\frac{\rho}{R}\frac{\partial}{\partial t}\mathbf{u}(\mathbf{r}',t-R/c)\bigg]\,\mathrm{d}S',\quad \mathbf{r}\in\bar{\mathcal{V}}_x,\end{aligned} \tag{F.10.10}$$

[36] Let ∂V be a closed surface bounding a region of volume V, $\mathrm{d}\mathbf{S}$ an infinitesimal surface area times a normal vector pointing outwards, then we have $\int_V(\phi\nabla^2\psi-\psi\nabla^2\phi)\,\mathrm{d}V=\int_{\partial V}(\phi\nabla\psi-\psi\nabla\phi)\cdot\mathrm{d}\mathbf{S}$, where ϕ and ψ are scalar functions.

$$\begin{aligned}\mathbf{u}(\mathbf{r},t) = \frac{1}{4\pi}\iint\limits_{\partial V} \hat{\mathbf{n}}'\cdot\Bigg[&\frac{1}{\rho c^2 R}\frac{\partial}{\partial t}p(\mathbf{r}',t-R/c)\frac{\mathbf{R}\mathbf{R}}{R^2}\\ &+\frac{1}{\rho R^2}\left(\frac{1}{c}p(\mathbf{r}',t-R/c)+\frac{1}{R}\int_{t_0}^{t}p(\mathbf{r}',t')\,\mathrm{d}t'\right)\\ &\cdot\left(\frac{3\mathbf{R}\mathbf{R}}{R^2}-\mathfrak{I}\right)\\ &+\left(\frac{1}{c}\frac{\partial}{\partial t}\mathbf{u}(\mathbf{r}',t-R/c)+\frac{1}{R}\mathbf{u}(\mathbf{r}',t-R/c)\right)\frac{\mathbf{R}}{R^2}\Bigg]\,\mathrm{d}S',\quad \mathbf{r}\in\bar{\mathcal{V}}_x.\end{aligned} \tag{F.10.11}$$

Similary, by using Green's second identity the following expressions for the frequency-domain acoustic pressure and acoustic velocity fields can be obtained

$$p_\omega(\mathbf{r}) = -\frac{1}{4\pi}\iint\limits_{\partial V}\hat{\mathbf{n}}'\cdot\left[\frac{\hat{\mathbf{R}}}{R}(\imath kR-1)p_\omega(\mathbf{r}')+\imath\omega\rho\mathbf{u}_\omega(\mathbf{r}')\right]\frac{\mathrm{e}^{\imath kR}}{R}\,\mathrm{d}S',\quad \mathbf{r}\in\bar{\mathcal{V}}_x. \tag{F.10.12}$$

$$\begin{aligned}\mathbf{u}_\omega(\mathbf{r}) = -\frac{1}{4\pi\rho}\iint\limits_{\partial V}\hat{\mathbf{n}}'\cdot\Bigg\{&\left[\hat{\mathbf{R}}\hat{\mathbf{R}}\imath kR-(3\hat{\mathbf{R}}\hat{\mathbf{R}}-\mathfrak{I})\left(1-\frac{1}{\imath kR}\right)\right]\frac{p_\omega(\mathbf{r}')}{c}\\ &+\rho(\imath kR-1)\mathbf{u}_\omega(\mathbf{r}')\hat{\mathbf{R}}\Bigg\}\frac{\mathrm{e}^{\imath kR}}{R^2}\,\mathrm{d}S',\quad \mathbf{r}\in\bar{\mathcal{V}}_x.\end{aligned} \tag{F.10.13}$$

In order to establish a link between the expression for the acoustic pressure and the acoustic velocity in the (F.10.10) and (F.10.11) based on surface integrals with the corresponding volume integral expressions (F.9.1) and (F.9.2) we need *equivalent sources*. Hence, we introduce the mass velocity per unit surface area $s^S(\mathbf{r}',t')$ and the force per unit area acting on the surface $\mathbf{f}^S(\mathbf{r}',t')$

$$s^S(\mathbf{r},t) = \rho\hat{\mathbf{n}}'\cdot\mathbf{u}(\mathbf{r},t) \tag{F.10.14a}$$

$$\mathbf{f}^S(\mathbf{r},t) = \hat{\mathbf{n}}'p(\mathbf{r},t),\quad \mathbf{r}'\in S. \tag{F.10.14b}$$

The surface sources $s^S(\mathbf{r},t)$ and $\mathbf{f}^S(\mathbf{r},t)$ are also commonly referred to as time-domain *Huygens' sources*. Moreover, following the procedure in [30, Ch. 9] we may interpret $s^S(\mathbf{r},t)$ and $\mathbf{f}^S(\mathbf{r},t)$ as surface dipole and surface monopole sources respectively.

Equivalent frequency-domain sources can similarly be used to establish a link between the expression for the acoustic pressure and the acoustic velocity in the (F.10.12) and (F.10.13) based on surface integrals with the corresponding volume integral expressions .

Following a procedure in [30, Ch. 9] we may express the frequency-domain pressure in terms of surface monopole and dipole sources. Hence, we introduce the mass velocity per unit surface area $s^S_\omega(\mathbf{r}')$ and the force per unit area acting on the surface $\mathbf{f}^S_\omega(\mathbf{r}')$

$$s_\omega^S(\mathbf{r}) = \rho \hat{\mathbf{n}}' \cdot \mathbf{u}_\omega(\mathbf{r}) \tag{F.10.15a}$$

$$\mathbf{f}_\omega^S(\mathbf{r}) = \hat{\mathbf{n}}' p_\omega(\mathbf{r}). \tag{F.10.15b}$$

We are interested in canceling the field inside $\mathcal{V}_x$ Although we do no know the actual noise sources, *equivalent sources* on $\mathcal{S}_x$ will serve as well.

If we had perfect knowledge to the acoustic pressure and velocity at $\mathcal{S}_x$ we could in principle set up a perfectly absorbing boundary, a hard boundary or a soft boundary [13].

Recognizing the opposite use of $\mathcal{V}_x$ and the $\mathrm{e}^{\imath\omega t}$ notion herein we can reexpress (F.10.12)

$$p_\omega(\mathbf{r}) = -\frac{1}{4\pi} \iint\limits_{\partial V} \Big[G_\omega(\mathbf{r}, \mathbf{r}') \imath\omega s_\omega^S(\mathbf{r}') - \mathbf{f}_\omega^S(\mathbf{r}') \cdot \nabla' G_\omega(\mathbf{r}, \mathbf{r}') \Big] \, \mathrm{d}S', \quad \mathbf{r} \in \bar{\mathcal{V}}_x. \tag{F.10.16}$$

Description	$s_\omega^{S,s}(\mathbf{r}')$	$\mathbf{f}_\omega^{S,s}(\mathbf{r}')$
Absorption	$-s_\omega^S(\mathbf{r}')$	$-\mathbf{f}_\omega^s(\mathbf{r})$
Soft Boundary	$-s_\omega^S(\mathbf{r}')$	0
Hard Boundary	0	$-\mathbf{f}_\omega^S(\mathbf{r}')$

Tab. F.4: Surface sources.

The Sommerfeld radiation condition [35, Ch. 9.1], [16]

$$\lim_{r\to\infty} \Big[r \big(\frac{\partial p(\mathbf{r}, t)}{\partial r} + \frac{1}{c} \frac{\partial p(\mathbf{r}, t)}{\partial t} \big) \Big] = 0, \quad |r p_\omega(\mathbf{r})| < C, \tag{F.10.17}$$

$$\lim_{r\to\infty} \Big[r \big(\frac{\partial p_\omega(\mathbf{r})}{\partial r} - \imath k p_\omega(\mathbf{r}) \big) \Big] = 0, \quad |r p_\omega(\mathbf{r})| < C, \tag{F.10.18}$$

$$\lim_{r\to\infty} \Big[r \big(\frac{\partial p_\omega(\mathbf{r})}{\partial r} - \imath k p_\omega(\mathbf{r}) \big) \Big] = 0, \quad |r p_\omega(\mathbf{r})| < C, \tag{F.10.19}$$

where C is a positive constant. From (F.D.5) and (F.D.6) we then observed that the surface integrals vanish in the limit of infinite $r \to \infty$.

The outgoing wave condition (F.10.19) is weaker than the Sommerfeld radiation conditions (F.10.18) because $p_o mr$ can satisfy (F.10.19), and yet both $p_\omega(\mathbf{r})$ and $\partial p_\omega(\mathbf{r})/\partial r$ can decay slower than $1/r$ as $r \to \infty$. Hence, we do not intend to integrate over the volume spanned by the primary sources. Instead, the effect from the sources, however, are fully taking into account from the second term in (F.D.7).

F.11 Vector Helmholtz Equation $(\mathbf{L}, \mathbf{M}, \mathbf{N})$ *Vector Eigenfunction Decomposition*

Following the very general discussion of acoustical and electromagnetic field theory in the previous sections we now establish the very close relationship there exist between the two domains when we consider *spherical wave decomposition.*

In acoustics or electromagnetic field theory one needs to construct vector eigenfunctions for the following vector Helmholtz equation and vector wave equation:

$$(\nabla^2 + \lambda_\psi)\boldsymbol{\psi}(\mathbf{r}) = 0 \tag{F.11.1a}$$
$$(\nabla \times \nabla \times -\lambda_\psi)\boldsymbol{\psi}(\mathbf{r}) = 0 \tag{F.11.1b}$$

and the scalar Helmholtz equation

$$(\nabla^2 + \lambda_\psi)\psi(\mathbf{r}) = 0, \tag{F.11.2}$$

where $\boldsymbol{\psi}$ is a vector-valued eigenfunction and λ_ψ is the eigenvalue parameter[37].

In electromagnetic field theory $\boldsymbol{\psi}(\mathbf{r})$ could be a substitute for the electric field $\mathbf{E}_\omega(\mathbf{r})$ or the magnetic field $\mathbf{H}_\omega(\mathbf{r})$.

In acoustic field theory $\psi(\mathbf{r})$ could be a surrogate for the acoustic pressure $p_\omega(\mathbf{r})$ and $\boldsymbol{\psi}(\mathbf{r})$ could be a surrogate for the acoustic velocity in a viscous fluid $\mathbf{u}_\omega(\mathbf{r})$. However, as already discussed in section F.7 for non viscous fluid the acoustic velocity is directly obtainable as the gradient of the acoustic pressure viz. (F.8.3) on page 674. Therefore, for nonviscous fluids it is basically not needed to consider the vector Helmholtz equation. However, as will turn out during our development scalar problems might benefit from the solutions that have been developed for vector problems.

The vector eigenfunctions represented by $\boldsymbol{\psi}(\mathbf{r})$ can be separated into a *lamellar* or *irrotational* field component, $\boldsymbol{\psi}_l(\mathbf{r})$, and a *solenoidal* field component $\boldsymbol{\psi}_s(\mathbf{r})$ [5]:

$$\boldsymbol{\psi}(\mathbf{r}) = \boldsymbol{\psi}_l(\mathbf{r}) + \boldsymbol{\psi}_s(\mathbf{r}), \tag{F.11.3}$$

where $\nabla \times \boldsymbol{\psi}_l(\mathbf{r}) \equiv 0$, $\nabla \cdot \boldsymbol{\psi}_l(\mathbf{r}) \neq 0$, $\nabla \cdot \boldsymbol{\psi}_s(\mathbf{r}) \equiv 0$ and $\nabla \times \boldsymbol{\psi}_s(\mathbf{r}) \neq 0$.

In the literature the irrotational part of the vector eigenfunction is denoted as a $\mathbf{L}$ function. The solenoidal part is in turn composed of two orthogonal functions referred to as $\mathbf{M}$ and $\mathbf{N}$ functions respectively.

In order to proceed we have to chose coordinate system for the specific physical problem. Moreover, as discussed in subsection F.6.3 in the vector Helmholtz equation case the number of coordinate systems amendable to the $(\mathbf{L}, \mathbf{M}, \mathbf{N})$ procedure described above is very limited. In SNFAT the longitudinal component $\mathbf{L}$ is not used [11].

F.11.1 Vector Eigenfunction $(\mathbf{L}, \mathbf{M}, \mathbf{N})$ Separable Coordinates

Three scalar fields ψ_L, ψ_M and ψ_N, all solutions of the scalar Helmholtz equation will constitute the basis for the most general solution vector Helmholtz equation. The vector field solutions, that is, $\mathbf{L}, \mathbf{M}$ and $\mathbf{N}$ are then obtained from [27, Ch. 13]

[37] We prefer to preserve the symbol λ to represent wave-length.

$$\mathbf{L}(\mathbf{r}) = \nabla\psi_L(\mathbf{r}) \tag{F.11.4a}$$

$$\mathbf{M}(\mathbf{r}) = \nabla \times (w\psi_M(\mathbf{r})\hat{\boldsymbol{\xi}}_1) = \nabla(w\psi_M(\mathbf{r})) \times \hat{\boldsymbol{\xi}}_1 \tag{F.11.4b}$$

$$\mathbf{N}(\mathbf{r}) = \frac{1}{k}\nabla \times \nabla \times (w\psi_N(\mathbf{r})\hat{\boldsymbol{\xi}}_1) = kw\psi_N(\mathbf{r})\hat{\boldsymbol{\xi}}_1 + \frac{1}{k}\nabla\left(\frac{\partial(w\psi_N(\mathbf{r}))}{\partial\xi_1}\right). \tag{F.11.4c}$$

In the unrestricted free-space case scalar fields ψ_L, ψ_M and ψ_N, will coincide. Otherwise, these scalar fields must be in a form suitable for the application of boundary conditions. In waveguide and cavity problems where booundary conditions exist the scalar functions ψ_L, ψ_M and ψ_N used to generate the $(\mathbf{L}, \mathbf{M}, \mathbf{N})$ functions will generally be mutually different and also be different from the free-space function.

We may now proceed and use Table F.3 and obtain specific expressions for the vector eigenfunction $(\mathbf{L}, \mathbf{M}, \mathbf{N})$. It should be remarked that the longitudinal part of the vector eigenfunction does not involve ξ_1 or w and will therefore have the same expression irrespective of the coordinate system.

In circular, elliptical, parabolic and rectangular cylindrical coordinates we obtain

$$\mathbf{L}(\mathbf{r}) = \nabla\psi_L(\mathbf{r}) \tag{F.11.5a}$$

$$\mathbf{M}(\mathbf{r}) = \nabla \times \psi_M(\mathbf{r})\hat{\mathbf{z}} = \nabla(\psi_M(\mathbf{r})) \times \hat{\mathbf{z}} \tag{F.11.5b}$$

$$\mathbf{N}(\mathbf{r}) = \frac{1}{k}\nabla \times \nabla \times \psi_l(\mathbf{r})\hat{\mathbf{z}} = k\psi_N(\mathbf{r})\hat{\mathbf{z}} + \frac{1}{k}\nabla\left(\frac{\partial(\psi_N(\mathbf{r}))}{\partial z}\right). \tag{F.11.5c}$$

Slightly different expressions for the $\mathbf{M}$ and $\mathbf{N}$ vector eigenfunctions are obtained in conical and spherical coordinates [5, Ch. 2].

$$\mathbf{L}(\mathbf{r}) = \nabla\psi_L(\mathbf{r}) \tag{F.11.6a}$$

$$\mathbf{M}(\mathbf{r}) = \nabla \times (r\psi_M(\mathbf{r})\hat{\mathbf{r}}) = \nabla(r\psi_M(\mathbf{r})) \times \hat{\mathbf{r}} \tag{F.11.6b}$$

$$\mathbf{N}(\mathbf{r}) = \frac{1}{k}\nabla \times \nabla \times (r\psi_N(\mathbf{r})\hat{\mathbf{r}}) = kr\psi_N(\mathbf{r})\hat{\mathbf{r}} + \frac{1}{k}\nabla\left(\frac{\partial(r\psi_N(\mathbf{r}))}{\partial r}\right), \tag{F.11.6c}$$

where $\hat{\mathbf{z}}$ as usual denotes the unit vector in the along the direction of the cylinder (in the sense used in [26, Ch. 5]. As seen in Table F.3 for rectangular cylindrical coordinates $\hat{\mathbf{z}}$ may be replaced by $\hat{\mathbf{x}}$ or $\hat{\mathbf{y}}$.

In Appendix G use of (F.11.6) will be made in the derivation of the SNFAT expressions for electromagnetic and acoustical waves that is based on spherical coordinates.

F.12 Spherical Time-Domain Expansions

The results obtained so far are very general and may be specialized to any closed reference surface. In particular we will obtain expressions for the time-domain acoustic pressure from

the source distribution and the contribution contained in the surface integral over the reference surface. Now we will specialize to a spherical reference surface.

The normal derivative then coincide with the radial derivative. From (F.10.5) and (F.10.6) we readily obtain

$$\frac{\partial}{\partial r}G\big(\mathbf{r},\mathbf{r}',t,t'\big) = \frac{1}{4\pi R^2}\Big[\frac{\imath k}{R} - \frac{1}{R^2}\Big]\hat{\mathbf{r}}\cdot\mathbf{R} \tag{F.12.1}$$

$$\frac{\partial}{\partial r}G_\omega(\mathbf{r},\mathbf{r}') = \frac{\mathrm{e}^{\imath kR}}{4\pi R}\Big[\frac{\imath k}{R} - \frac{1}{R^2}\Big]\mathbf{e}_R\cdot\mathbf{R}, \tag{F.12.2}$$

where $\mathbf{e}_R$ is a unit vector along $\mathbf{R}$. By applying the inverse Fourier transform (F.2.10b) and using the shift property we obtain

$$\begin{aligned} p(\mathbf{r},t) = \frac{1}{4\pi}\int_{r_o=r^x}\frac{1}{R}\Big[\Big\{ & \frac{1}{cR}\frac{\partial p}{\partial t}(\mathbf{r}',t-\frac{R}{c}) \\ & + \frac{1}{R^2}p(\mathbf{r}',t-\frac{R}{c})\Big\}\mathbf{r}'\cdot\mathbf{R} \\ & - \frac{\partial p}{\partial r_o}(\mathbf{r}',t-\frac{R}{c})\Big]\,\mathrm{d}S', \quad r\in\bar{\mathcal{V}}_x. \end{aligned} \tag{F.12.3}$$

Hence, the field inside the control volume including the boundaries can be expressed in the time-domain in terms of the pressure and its time and normal derivatives *everywhere* on the reference surface. All the quantities taking at the *retarded time* $t-\frac{R}{c}$.

Bibliography

[1] J. R. Barber. *Elasticity (Solid Mechanics and Its Applications)*. Kluwer Academic Publishers, 2nd edition, 2002.

[2] J. P. Barton. Sound propagation within a chemically reacting ideal gas. *Journal of the Acoustical Society of America*, 81(2):233–237, 1987.

[3] David T. Blackstock. *Fundamentals of Physical Acoustics*. John Wiley & Sons, Inc., New York, 2000.

[4] R. Creighton Buck. *Advanced Calculus*. Addison-Wesley Longman, 3rd edition, 2003.

[5] Robert E. Collin. *Field Theory of Guided Waves*. IEEE Press Series on Electromagnetic Waves, 2nd edition, 1991.

[6] L. Cremer, M. Heckl, and E. E. Ungar. *Structure-Borne Sound*. Springer-Verlag, Berlin, 2nd edition, 1988.

[7] Torsten H. Leth Elmkjær. Acoustic radiation pressure, Ph.D. course: Attenuation and damping of structure-borne sound. Technical report, Ørsted TUD, 2003.

[8] Torsten H. Leth Elmkjær, Allan Østergaard, and Axel C. K. Thomsen. A beam-forming network oriented radiation pattern synthesis approach. In *Millennium Conference on Antennas and Propagation, AP 2000*, Davos, Switzerland, 2000.

[9] Torsten H. Leth Elmkjær, Allan Østergaard, and Axel C. K. Thomsen. Full-wave analysis of weak waveguide couplers using higher-order TE- and TM-modes in the coupling slot. In *Antenn00*, Lund, Sweden, 2000.

[10] Salvador Barrera Figueroa. *New Methods for Transducer Calibration: Free-field Reciprocity Calibration of Condenser Microphones*. Ph.d thesis, Technical University of Denmark, 2003.

[11] Jørgen Hald, Jesper E. Hansen, and Flemming Holm Larsen. *Spherical Near-Field Antenna Measurements*. Peragamon Press, 1988.

[12] Thorkild B. Hansen and Arthur D. Yaghjian. *Plane-Wave Theory of Time-Domain Fields Near-Field Scannng Applications*. IEEE Press Series on Electromagnetic Wave Theory, 1999.

[13] Roger F. Harrington. *Time-Harmonic Electromagnetic Fields*. McGraw-Hill Inc., 1961.

[14] Vicente Cutanda Henriquez. *Numerical Transducer Modeling*. Ph.d thesis, Technical University of Denmark, 2002.

[15] Frederick V. Hunt. Notes on the exact equations governing the propagation of sound in fluids. *JASA*, 27(6):1019–1039, 1955.

[16] D. S. Jones. *Acoustic Electromagnetic Waves*. New York: Oxford University Press, 1986.

[17] Wilfred Kaplan. *Advanced Calculus*. Addison-Wesley Longman, 5th edition, 2002.

[18] Oliver Dimon Kellogg. *Foundations of Potential Theory*. Dover Publications, Inc., New York, 1929.

[19] B. I. Lee and M. G. Kesler. A generalized thermodynamic correlation based on three-parameter corresponding states. *AIChE Journal*, 21(3):510–527, 1975.

[20] Augustus E. Love. *Treatise on the Mathematical Theory of Elasticity*. Dover Publications, Inc., New York, 1927.

[21] Jerrold E. Marsden and Thomas J. R. Hughes. *Mathematical Foundations of Elasticity*. Dover Publications, Inc., New York, 1994.

[22] R. H. Mellen, D. G. Browning, and V. P. Simmons. Investigation of chemical sound absorption in sea water by the resonator method. part i. *JASA*, 68(1):248–257, 1980.

[23] R. H. Mellen, D. G. Browning, and V. P. Simmons. Investigation of chemical sound absorption in sea water. part ii. *JASA*, 69(6):1660–1662, 1981.

[24] R. H. Mellen, D. G. Browning, and V. P. Simmons. Investigation of chemical sound absorption in sea water. part iii. *JASA*, 70(1):143–148, 1981.

[25] R. H. Mellen, D. G. Browning, and V. P. Simmons. Investigation of chemical sound absorption in sea water. part iv. *JASA*, 74(3):987–993, 1983.

[26] Philip M. Morse and Herman Feshbach. *Methods of Theoretical Physics*, volume 1. Feshbach Publishing LLC., 1953.

[27] Philip M. Morse and Herman Feshbach. *Methods of Theoretical Physics*, volume 2. Feshbach Publishing LLC., 1953.

[28] Philip M. Morse and K. Uno Ingard. *Theoretical Acoustics*. Princeton University Press Princeton New Jersey, 1968.

[29] Bruce R. Munson, Donald F. Young, and Theodore H. Okiish. *Fundamental of Fluid Mechanics*. John Wiley & Sons, Inc., 4th edition, 2002.

[30] Philip A. Nelson and Stephen J. Elliott. *Active Control of Sound*. Academic Press, 1992.

[31] Allan Østergaard, Torsten H. Leth Elmkjær, and Axel C. K. Thomsen. A novel waveguide to strip-line coupler. In *Millennium Conference on Antennas and Propagation, AP 2000*, Davos, Switzerland, 2000.

[32] H. B. Phillips. *Vector Analysis*. John Wiley & Sons, Inc., New York, 1933.

[33] Allan D. Pierce. *Acoustics An Introduction to Its Physical Principles and Applications*. Acoustical Society of America, 1994.

[34] Richard E. Sonntag, Claus Borgnakke, and Gordon J. Van Wylen. *Fundamentals of Thermodynamics*. John Wiley & Sons, Inc., 6th edition, 2003.

[35] J. A. Stratton. *Electromagnetic Theory*. McGraw Hill New York, 1941.

[36] Mark W. Zemansky. *Heat and Thermodynamics*. McGraw-Hill, 5 edition, 1968.

F.A Material Derivative Utility

In this section we provide an expression for the material derivative $\frac{\mathrm{D}}{\mathrm{D}t}$ applied to the product of a scalar field quantity, say $\psi(\mathbf{r},t)$, and a vector field quantity, say $\mathbf{B}(\mathbf{r},t)$, in terms of tensorial notation. The underlying velocity vector is denoted by $\mathbf{u}(\mathbf{r},t)$. This expression was used to obtain a compact expression for the continuity of the momentum density in the fluid viz. (F.3.59) on page 645.

In the development we will need first need an expression for the gradient of a tensor, say, $\mathfrak{A}(\mathbf{r},t)$ that in turn is obtained as the tensor product $\otimes$ of the vectors $\psi(\mathbf{r},t)\mathbf{B}(\mathbf{r},t)$ and $\mathbf{u}(\mathbf{r},t)$, that is, $\mathfrak{A}(\mathbf{r},t) = (\psi(\mathbf{r},t)\mathbf{B}(\mathbf{r},t)) \otimes \mathbf{u}(\mathbf{r},t)$. For notational convenience the space-time parameters $(\mathbf{r},t)$ will be suppressed in the following derivation.

Proof. From [26, Ch. 1] we obtain

$$\begin{aligned}
\nabla\cdot\mathfrak{A} &\equiv \nabla\cdot((\psi\mathbf{B})\otimes\mathbf{u})\\
&= \frac{\partial((\psi\mathbf{B})\otimes\mathbf{u})_x}{\partial x} + \frac{\partial((\psi\mathbf{B})\otimes\mathbf{u})_y}{\partial y} + \frac{\partial((\psi\mathbf{B})\otimes\mathbf{u})_z}{\partial z}\\
&= \frac{\partial((\psi\mathbf{B})u_x)}{\partial x} + \frac{\partial((\psi\mathbf{B})u_y)}{\partial y} + \frac{\partial((\psi\mathbf{B})u_z)}{\partial z}\\
&= \frac{\partial(\psi\mathbf{B})}{\partial x}u_x + (\psi\mathbf{B})\frac{\partial u_x}{\partial x} + \frac{\partial(\psi\mathbf{B})}{\partial y}u_y + (\psi\mathbf{B})\frac{\partial u_y}{\partial y} + \frac{\partial(\psi\mathbf{B})}{\partial z}u_z + (\psi\mathbf{B})\frac{\partial u_z}{\partial z}\\
&= (\mathbf{u}\cdot\nabla)(\psi\mathbf{B}) + (\psi\mathbf{B})\nabla\cdot\mathbf{u}\\
&= (\mathbf{u}\cdot\nabla)(\psi\mathbf{B}) + (\psi\mathbf{B})\dot{\Delta}.
\end{aligned} \tag{F.A.1}$$

The material derivative is then expressed as

$$\frac{\mathrm{D}(\psi\mathbf{B})}{\mathrm{D}t} \equiv \frac{\partial(\psi\mathbf{B})}{\partial t} + (\mathbf{u}\cdot\nabla)(\psi\mathbf{B})$$

now applying (F.A.1) to obtain

$$\frac{\mathrm{D}(\psi\mathbf{B})}{\mathrm{D}t} = \frac{\partial(\psi\mathbf{B})}{\partial t} + \nabla\cdot\mathfrak{A} - \psi\mathbf{B}\dot{\Delta}, \tag{F.A.2}$$

where $\mathfrak{A}(\mathbf{r},t) = (\psi(\mathbf{r},t)\mathbf{B}(\mathbf{r},t)) \otimes \mathbf{u}(\mathbf{r},t)$. □

F.B Reynolds Transport Theorem Derivation

In this section we provide a proof of the second version of the Reynolds transport theorem (F.3.43) introduced in subsection F.3.3 on page 640. For notational convenience the space-time parameters $(\mathbf{r}',t)$ will be suppressed in the following derivation.

Proof. We will need the following expression for the time-derivative of a volume integral with time-varying integration limits [17, Ch. 5.15]

$$\frac{\mathrm{D}}{\mathrm{D}t}\iiint\limits_{V(\mathbf{r},t)} F(\mathbf{r}',t)\,\mathrm{d}V' = \iiint\limits_{V(\mathbf{r},t)}\left[\frac{\partial F(\mathbf{r}',t)}{\partial t} + \nabla\cdot\big(F(\mathbf{r}',t)\mathbf{u}(\mathbf{r}',t)\big)\right]\mathrm{d}V', \tag{F.B.1}$$

where $\mathbf{u}(\mathbf{r},t)$ is the fluid velocity vector responsible for the time-varying integration limits. Now in the present case $F(\mathbf{r},t)$ is the product of the mass density function $\rho(\mathbf{r},t)$ and an arbitrary *intensive property* $b(\mathbf{r},t)$, that in turn might be a scalar, vector or tensor. The material derivative

of the extensive property $B_{sys}(t)$ introduced in (F.3.42) on page 641 is obtained from

$$\frac{\mathrm{D}B_{\mathrm{sys}}}{\mathrm{D}t} = \frac{\mathrm{D}}{\mathrm{D}t} \iiint\limits_{V(\mathbf{r},t)} \rho b \, \mathrm{d}V'$$

using (F.B.1) to obtain

$$\begin{aligned}
\frac{\mathrm{D}B_{\mathrm{sys}}}{\mathrm{D}t} &= \iiint\limits_{V(\mathbf{r},t)} \left[\frac{\partial \rho b}{\partial t} + \nabla \cdot \big(\rho b \mathbf{u}\big) \right] \mathrm{d}V' \\
&= \iiint\limits_{V(\mathbf{r},t)} \left[b\frac{\partial \rho}{\partial t} + \rho \frac{\partial b}{\partial t} + \rho b \nabla \cdot \mathbf{u} + \mathbf{u} \cdot \nabla(\rho b) \right] \mathrm{d}V' \\
&= \iiint\limits_{V(\mathbf{r},t)} \left[b\frac{\partial \rho}{\partial t} + \rho \frac{\partial b}{\partial t} + \rho b \nabla \cdot \mathbf{u} + b\mathbf{u} \cdot \nabla \rho + \rho \mathbf{u} \cdot \nabla b \right] \mathrm{d}V'
\end{aligned}$$

insertion of the material derivative (F.3.40) yields

$$\frac{\mathrm{D}B_{\mathrm{sys}}}{\mathrm{D}t} = \iiint\limits_{V(\mathbf{r},t)} \left[\rho \frac{\mathrm{D}b}{\mathrm{D}t} + b\bigg(\frac{\mathrm{D}\rho}{\mathrm{D}t} + \rho \nabla \cdot \mathbf{u} \bigg) \right] \mathrm{d}V'$$

finally, applying the conservation of mass expression (F.3.48) we arrive at

$$\frac{\mathrm{D}B_{\mathrm{sys}}}{\mathrm{D}t} = \iiint\limits_{V(\mathbf{r},t)} \rho \frac{\mathrm{D}b}{\mathrm{D}t} + q \, \mathrm{d}V',$$

which is the expression sought augmented by the source term $q(\mathbf{r}', t)$.

(F.B.2)

□

F.C Specific Entropy Rate of Change Derivation

We will use the following thermodynamic relations [36, Ch. 2.7]

$$\left(\frac{\partial P}{\partial T}\right)_V = -\left(\frac{\partial P}{\partial V}\right)_T \left(\frac{\partial V}{\partial T}\right)_P \tag{F.C.1a}$$

$$\mathrm{d}P = \frac{\alpha}{K_T}\,\mathrm{d}T - \frac{1}{K_T V}\,\mathrm{d}V, \tag{F.C.1b}$$

where the volume thermal expansivity $\alpha(\mathbf{r},t)$ and the isothermal compressibility K_T are defined in (F.3.71) on page 649 and (F.3.72) on page 649 respectively.

From [36, Ch. 11] the following Tds-equations can be found

$$Tds = C_v\,\mathrm{d}T + T\left(\frac{\partial P}{\partial T}\right)_V \mathrm{d}v \tag{F.C.2a}$$

$$Tds = C_P\,\mathrm{d}T - T\left(\frac{\partial V}{\partial T}\right)_P \mathrm{d}P. \tag{F.C.2b}$$

For notational convenience the space-time parameters $(\mathbf{r},t)$ will be suppressed in the following derivation

$$\rho(\mathbf{r},t)C_v(\mathbf{r},t)\frac{\mathrm{D}T(\mathbf{r},t)}{\mathrm{D}t} + \rho(\mathbf{r},t)C_v(\mathbf{r},t)(\gamma(\mathbf{r},t)-1)\dot{\Delta}(\mathbf{r},t)/\alpha(\mathbf{r},t) + \nabla\cdot\mathbf{q}(\mathbf{r},t) - \phi_\eta(\mathbf{r},t) = 0, \tag{F.C.3}$$

F.D Pressure and Velocity Fields from Surface Integrals; Derivation

The derivations to be carried out in this section are limitted to field points *exterior* to the source region. It should be recalled that outside the sources the fields are governed by the *homogeneous* wave equation in the time-domain and by the *homogeneous* Helmholtz equation in the frequency-domain.

F.D.1 Pressure Field from Surface Integrals; Derivation

In order to apply the Green's second identity we first multiply the homogeneous wave equations for the acoustic pressure i.e., (F.10.2) and the homogeneous Helmholtz equation (F.10.4) by $G\big(\mathbf{r},\mathbf{r}',t,t'\big)$ and $G_\omega(\mathbf{r},\mathbf{r}')$ respectively. Next we multiply the inhomogeneous wave equation for the time-domain Green's function i.e., (F.10.8) and inhomogeneous Helmholtz equation for the frequency-domain Green's function (F.10.9) by $p(\mathbf{r},t)$ and $p_\omega(\mathbf{r})$ respectively and subtracts these results from the previous results obtaining

$$\begin{aligned} &G\big(\mathbf{r},\mathbf{r}',t,t'\big)\nabla^2 p(\mathbf{r},t) - p(\mathbf{r},t)\nabla^2 G\big(\mathbf{r},\mathbf{r}',t,t'\big) \\ &\qquad = p(\mathbf{r},t)\delta^{(3)}(\mathbf{r}-\mathbf{r}')\delta(t-t') - G\big(\mathbf{r},\mathbf{r}',t,t'\big)\mathbf{f}(\mathbf{r},t), \quad \mathbf{r}\in\mathcal{V}_f, t\in T_p, \end{aligned} \tag{F.D.1}$$

$$\begin{aligned} &G_\omega(\mathbf{r},\mathbf{r}')\nabla^2 p_\omega(\mathbf{r}) - p_\omega(\mathbf{r})\nabla^2 G_\omega(\mathbf{r},\mathbf{r}') \\ &\qquad = p_\omega(\mathbf{r})\delta^{(3)}(\mathbf{r}-\mathbf{r}') - G_\omega(\mathbf{r},\mathbf{r}')\mathbf{f}_\omega(\mathbf{r}), \quad \mathbf{r}\in\mathcal{V}. \end{aligned} \tag{F.D.2}$$

With the objective of obtaining expression where the time-domain source $\mathbf{f}(\mathbf{r},t)$ is a function source coordinates $\mathbf{r}'$ and t' and the frequency-domain source $\mathbf{f}_\omega(\mathbf{r})$ is a function source coordinate $\mathbf{r}'$ we simply interchange $\mathbf{r}$ and $\mathbf{r}'$ in (F.D.1) and (F.D.2) and interchange t and t' in (F.D.1). Next we use the reciprocity property of the Green's function and the symmetry property of the delta functions and integrate over V obtaining

$$\begin{aligned}&\iiint_V \Big[G\big(\mathbf{r},\mathbf{r}',t,t'\big)\nabla^2 p(\mathbf{r}',t') - p(\mathbf{r}',t')\nabla^2 G\big(\mathbf{r},\mathbf{r}',t,t'\big)\Big]\,\mathrm{d}V'\\ &= \iiint_V \Big[p(\mathbf{r}',t')\delta^{(3)}(\mathbf{r}-\mathbf{r}')\delta(t-t') - G\big(\mathbf{r},\mathbf{r}',t,t'\big)\mathbf{f}(\mathbf{r}',t')\Big]\,\mathrm{d}V',\quad \mathbf{r}\in\mathcal{V}_f, t\in T_p,\end{aligned} \tag{F.D.3}$$

and

$$\begin{aligned}&\iiint_V \Big[G_\omega(\mathbf{r},\mathbf{r}')\nabla^2 p_\omega(\mathbf{r}') - p_\omega(\mathbf{r}')\nabla^2 G_\omega(\mathbf{r},\mathbf{r}')\Big]\,\mathrm{d}V'\\ &= \iiint_V \Big[p_\omega(\mathbf{r}')\delta^{(3)}(\mathbf{r}-\mathbf{r}') - G_\omega(\mathbf{r},\mathbf{r}')\mathbf{f}_\omega(\mathbf{r}')\Big]\,\mathrm{d}V',\quad \mathbf{r}\in\mathcal{V}.\end{aligned} \tag{F.D.4}$$

Finally, assuming that the scan surface $\mathcal{S}$ is regular and also continuously curved (smoothed) surface in order to ensure that the normal $\hat{\mathbf{n}}$ to the surface is a continuous function on $\mathcal{S}$ we arrive at the following integral expression relating the pressure at field point $\mathbf{r}$ inside the closed boundary $\bar{\mathcal{V}}_x$ as a summation of the fields from all the elementary sources $f_\omega\,\mathrm{d}V'$ plus the waves reflected by the boundaries within finite distance of the source f_ω:

$$\begin{aligned}p(\mathbf{r},t) &= \iiint_V \mathbf{f}(\mathbf{r}',t')G\big(\mathbf{r},\mathbf{r}',t,t'\big)\,\mathrm{d}V'\\ &+ \iint_{\partial V}\Big[G\big(\mathbf{r},\mathbf{r}',t,t'\big)\frac{\partial}{\partial n'}p(\mathbf{r}',t') - p(\mathbf{r}',t')\frac{\partial}{\partial n'}G\big(\mathbf{r},\mathbf{r}',t,t'\big)\Big]\,\mathrm{d}S',\quad r\in\bar{\mathcal{V}}_x, t\in T_p\end{aligned} \tag{F.D.5}$$

$$\begin{aligned}p_\omega(\mathbf{r}) &= \iiint_V \mathbf{f}_\omega(\mathbf{r}')G_\omega(\mathbf{r},\mathbf{r}')\,\mathrm{d}V'\\ &+ \iint_{\partial V}\Big[G_\omega(\mathbf{r},\mathbf{r}')\frac{\partial}{\partial n'}p_\omega(\mathbf{r}') - p_\omega(\mathbf{r}')\frac{\partial}{\partial n'}G_\omega(\mathbf{r},\mathbf{r}')\Big]\,\mathrm{d}S',\quad r\in\bar{\mathcal{V}}_x.\end{aligned} \tag{F.D.6}$$

The frequency-domain expression (F.D.6) coincides with a similar expression in [1, Ch. 7]. If we further make the assumption that all primary sources f_ω^{ps} are found at positions exterior to $\bar{\mathcal{V}}_x$ i.e.,

$$f_\omega^{ps}(\mathbf{r}) \equiv 0,\quad \forall r\in\bar{\mathcal{V}}_x \tag{F.D.7}$$

then (F.D.7) applies with $f_\omega(\mathbf{r})$ substituted by $f^{ss}_\omega(\mathbf{r})$. It should be recalled that contributions for the primary sources then are implicitly and entirely included in the surface integral as there is no evidence to whether the contributing terms stem form a source or are due to boundary reflections.

F.D.2 Velocity Field from Surface Integrals; Derivation

Bibliography

[1] Philip M. Morse and K. Uno Ingard. *Theoretical Acoustics*. Princeton University Press Princeton New Jersey, 1968.

F.E Miscellaneous Identities

F.E.1 Introduction

In the analysis of vector field certain quantities occur which have the same mathematical form whatever field is considered. In this appendix some commonly used vector identities in acoustic and electromagnetic field theory will be derived. As usual $\mathbf{r}'\mathbf{r} = x'\hat{\mathbf{x}}+y'\hat{\mathbf{y}}+z'\hat{\mathbf{z}}$ and $\mathbf{r} = x\hat{\mathbf{x}}+y\hat{\mathbf{y}}+z\hat{\mathbf{z}}$ denote source and field (observer) position respectively, $\mathbf{R} = \mathbf{r} - \mathbf{r}'$ denotes the source point to field point vector of length $R = |\mathbf{r} - \mathbf{r}'| = \sqrt{(x-x')^2 + (y-y')^2 + (z-z')^2}$. Moreover, we will let x_i be equal to x, y, or z for $i = 1, 2$, or 3, respectively; i.e., $\mathbf{r} = x_1\hat{\mathbf{x}} + x_2\hat{\mathbf{y}} + x_3\hat{\mathbf{z}}$.

In our analysis we are often dealing with expressions involving a scalar function $\psi(\mathbf{r}', t'-|\mathbf{r}-\mathbf{r}'|/c)$ or vector function $\boldsymbol{\psi}(\mathbf{r}', t' - |\mathbf{r} - \mathbf{r}'|/c)$ both of which takes two arguments. The first argument is the source position $\mathbf{r}'$ and the second argument is the retarded time $t - |\mathbf{r} - \mathbf{r}'|/c$. Moreover, in the analysis we have to invoke first-order spatial derivatives $\partial/\partial x_i$, divergence $\nabla\cdot$ and gradient operators ∇. The first order spatial derivatives will be represented by a generalized operator $\square$. However, for functions of two arguments some cautions must be exercised.

Hence, curly brackets on $\{\square'\boldsymbol{\psi}\}^{(1)}$ and $\{\square'\boldsymbol{\psi}\}^{(2)}$ will be used to indicate differentiation with respect to $\mathbf{r}'$ in the first and second argument in $\boldsymbol{\psi}(\mathbf{r}', t - |\mathbf{r} - \mathbf{r}'|/c)$ respectively; that is,

$$\square'\boldsymbol{\psi}(\mathbf{r}', t' - |\mathbf{r} - \mathbf{r}'|/c) = \{\square'\boldsymbol{\psi}\}^{(1)}(\mathbf{r}', t' - |\mathbf{r} - \mathbf{r}'|/c) + \{\square'\boldsymbol{\psi}\}^{(2)}(\mathbf{r}', t' - |\mathbf{r} - \mathbf{r}'|/c), \quad \text{(F.E.1)}$$

where

$$\{\square'\boldsymbol{\psi}\}^{(1)}(\mathbf{r}', t' - |\mathbf{r} - \mathbf{r}'|/c) = \square'\boldsymbol{\psi}(\mathbf{r}', t)|_{(,t=t'-|\mathbf{r}-\mathbf{r}'|/c)} \quad \text{(F.E.2a)}$$
$$= \square\boldsymbol{\psi}(\mathbf{r}, t)|_{(\mathbf{r}=\mathbf{r}', t=t'-|\mathbf{r}-\mathbf{r}'|/c)} \quad \text{(F.E.2b)}$$

and

$$\{\square'\boldsymbol{\psi}\}^{(2)}(\mathbf{r}', t' - |\mathbf{r} - \mathbf{r}'|/c) = \square'\boldsymbol{\psi}(\mathbf{r}, t' - |\mathbf{r} - \mathbf{r}'|/c)|_{(\mathbf{r}=\mathbf{r}',)} \quad \text{(F.E.3a)}$$
$$= -\square\boldsymbol{\psi}(\mathbf{r}', t' - |\mathbf{r} - \mathbf{r}'|/c), \quad \text{(F.E.3b)}$$

where the notion $|_{(,t=t'-|\mathbf{r}-\mathbf{r}'|/c)}$ indicates that the second argument is fixed at time $t = t' - |\mathbf{r} - \mathbf{r}'|/c$ while differentiation takes place on the first argument. Likewise $|_{(\mathbf{r}=\mathbf{r}',)}$ indicates that the first argument is fixed at position $\mathbf{r} = \mathbf{r}'$ while differentiation takes place on the second argument.

Similar convention applies to the gradient operator ∇' applied to ψ and the curl operator $\nabla'\times$ applied to $\boldsymbol{\psi}$.

As the first parameter of ψ and $\boldsymbol{\psi}$ is $\mathbf{r}'$ (as opposed to $\mathbf{r}$) we obtain the following useful expression

$$\begin{aligned}
\Box\boldsymbol{\psi}(\mathbf{r}', t - R/c) = &\quad \{\Box\boldsymbol{\psi}\}^{(1)}(\mathbf{r}', t - R/c) + \{\Box\boldsymbol{\psi}\}^{(2)}(\mathbf{r}', t - R/c) && \text{(F.E.4a)}\\
= &\quad \{\Box\boldsymbol{\psi}\}^{(2)}(\mathbf{r}', t - R/c) && \text{(F.E.4b)}\\
= &-\{\Box'\boldsymbol{\psi}\}^{(2)}(\mathbf{r}', t - R/c) && \text{(F.E.4c)}\\
= &\quad \{\Box'\boldsymbol{\psi}\}^{(1)}(\mathbf{r}', t - R/c) - \Box'\boldsymbol{\psi}(\mathbf{r}, t). && \text{(F.E.4d)}
\end{aligned}$$

where we have replaced $|\mathbf{r} - \mathbf{r}'|$ by R for notational compactness.

For higher order differentiation, e.g., $\partial^2/\partial x_i'\partial x_j'$, grad div $\nabla'\nabla'\cdot$ and curl curl $\nabla'\times\nabla'\times$ applied to $\boldsymbol{\psi}$. We will use the generalized double differential operator $\Box'\Box'$ as a surrogate for such operations. Moreover, curly brackets including a superscript on $\{\Box'\boldsymbol{\psi}\}^{(l,m)}, l, m = 1, 2$ will be used to indicate that the first differentiation is with respect to $\mathbf{r}'$ in the l'th argument in $\boldsymbol{\psi}(\mathbf{r}', t - |\mathbf{r} - \mathbf{r}'|/c)$ and that second differentiation is with respect to the m'th argument in the result hereof; that is,

$$\begin{aligned}
&\Box'\Box'\boldsymbol{\psi}(\mathbf{r}', t' - |\mathbf{r} - \mathbf{r}'|/c) =\\
&\{\Box'\Box'\boldsymbol{\psi}\}^{(1,1)}(\mathbf{r}', t' - |\mathbf{r} - \mathbf{r}'|/c) + \{\Box'\Box'\boldsymbol{\psi}\}^{(2,1)}(\mathbf{r}', t' - |\mathbf{r} - \mathbf{r}'|/c) +\\
&\{\Box'\Box'\boldsymbol{\psi}\}^{(1,2)}(\mathbf{r}', t' - |\mathbf{r} - \mathbf{r}'|/c) + \{\Box'\Box'\boldsymbol{\psi}\}^{(2,2)}(\mathbf{r}', t' - |\mathbf{r} - \mathbf{r}'|/c),
\end{aligned} \qquad \text{(F.E.5)}$$

where

$$\begin{aligned}
\{\Box'\Box'\boldsymbol{\psi}\}^{(1,1)}(\mathbf{r}', t' - |\mathbf{r} - \mathbf{r}'|/c) &= \Box'\Box'\boldsymbol{\psi}(\mathbf{r}', t)|_{(,t=t'-|\mathbf{r}-\mathbf{r}'|/c)} && \text{(F.E.6a)}\\
&= \Box\Box\boldsymbol{\psi}(\mathbf{r}, t)|_{(\mathbf{r}=\mathbf{r}',t=t'-|\mathbf{r}-\mathbf{r}'|/c)}, && \text{(F.E.6b)}
\end{aligned}$$

$$\begin{aligned}
\{\Box'\Box'\boldsymbol{\psi}\}^{(2,1)}(\mathbf{r}', t' - |\mathbf{r} - \mathbf{r}'|/c) &= \nabla'\{\nabla'\cdot\boldsymbol{\psi}(\mathbf{r}', t)|_{(\mathbf{r}=\mathbf{r}',)}\}|_{(,t=t'-|\mathbf{r}-\mathbf{r}'|/c)} && \text{(F.E.7a)}\\
&= -\nabla\{\nabla\cdot\boldsymbol{\psi}(\mathbf{r}, t)|_{(\mathbf{r}=\mathbf{r}',)}\}|_{(,t=t'-|\mathbf{r}-\mathbf{r}'|/c)}, && \text{(F.E.7b)}
\end{aligned}$$

$$\begin{aligned}
\{\Box'\Box'\boldsymbol{\psi}\}^{(1,2)}(\mathbf{r}', t' - |\mathbf{r} - \mathbf{r}'|/c) &= \nabla'\{\nabla'\cdot\boldsymbol{\psi}(\mathbf{r}', t)|_{(,t=t'-|\mathbf{r}-\mathbf{r}'|/c)}\}|_{(\mathbf{r}=\mathbf{r}',)} && \text{(F.E.8a)}\\
&= -\nabla\{\nabla\cdot\boldsymbol{\psi}(\mathbf{r}, t)|_{(,t=t'-|\mathbf{r}-\mathbf{r}'|/c)}\}|_{(\mathbf{r}=\mathbf{r}',)} && \text{(F.E.8b)}
\end{aligned}$$

and

$$\begin{aligned}
\{\Box'\Box'\boldsymbol{\psi}\}^{(2,2)}(\mathbf{r}', t' - |\mathbf{r} - \mathbf{r}'|/c) &= \Box'\Box'\boldsymbol{\psi}(\mathbf{r}, t' - |\mathbf{r} - \mathbf{r}'|/c)|_{(\mathbf{r}=\mathbf{r}',)} && \text{(F.E.9a)}\\
&= \Box\Box\boldsymbol{\psi}(\mathbf{r}', t' - |\mathbf{r} - \mathbf{r}'|/c). && \text{(F.E.9b)}
\end{aligned}$$

Moreover, the order of differentiation is immaterial provided that all derivatives concerned are continuous in the domain considered [2, Sec. 2.15], that is

$$\{\Box'\Box'\boldsymbol{\psi}\}^{(2,1)}(\mathbf{r}', t' - |\mathbf{r} - \mathbf{r}'|/c) = \{\Box'\Box'\boldsymbol{\psi}\}^{(1,2)}(\mathbf{r}', t' - |\mathbf{r} - \mathbf{r}'|/c). \tag{F.E.10}$$

F.E.2 Functions of Retarded Time

It will be useful to introduce two auxiliary functions that take only the retarded time $t-|\mathbf{r}-\mathbf{r}'|/c$ as argument, $\mathbf{F}(t - \frac{|\mathbf{r}-\mathbf{r}'|}{c})$ and $\mathbf{G}(t - \frac{|\mathbf{r}-\mathbf{r}'|}{c}) = \frac{\mathbf{F}(t-\frac{|\mathbf{r}-\mathbf{r}'|}{c})}{|\mathbf{r}-\mathbf{r}'|}$.

Static Green's Function Derivatives

The static Green's function i.e., $frac1R$ enters in many expression. In the subsequent text some useful derivatives related to the Green's function will be provided.

Taking the partial derivative of R, R^{-1}, R^{-2} and R^{-3} with respect to x_i gives

$$\frac{\partial R}{\partial x_i} = \frac{\partial|\mathbf{r} - \mathbf{r}'|}{\partial x_i} = \frac{x_i - x_i'}{R} \tag{F.E.11a}$$

$$\frac{\partial R^{-1}}{\partial x_i} = \frac{\partial|\mathbf{r} - \mathbf{r}'|^{-1}}{\partial x_i} = -\frac{x_i - x_i'}{R^3} \tag{F.E.11b}$$

$$\frac{\partial R^{-2}}{\partial x_i} = \frac{\partial|\mathbf{r} - \mathbf{r}'|^{-2}}{\partial x_i} = -2\frac{x_i - x_i'}{R^4} \tag{F.E.11c}$$

$$\frac{\partial R^{-3}}{\partial x_i} = \frac{\partial|\mathbf{r} - \mathbf{r}'|^{-3}}{\partial x_i} = -3\frac{x_i - x_i'}{R^5} \tag{F.E.11d}$$

and by recurrence

$$\frac{\partial R^{-n}}{\partial x_i} = \frac{\partial|\mathbf{r} - \mathbf{r}'|^{-n}}{\partial x_i} = -n\frac{x_i - x_i'}{R^{n+2}}. \tag{F.E.11e}$$

Accordingly the following gradient relations are readily obtained

$$\nabla R = \nabla|\mathbf{r} - \mathbf{r}'| = \frac{\mathbf{R}}{R} = \hat{\mathbf{R}} \tag{F.E.12a}$$

$$\nabla R^{-1} = \nabla|\mathbf{r} - \mathbf{r}'|^{-1} = -\frac{\mathbf{R}}{R^3} = -\frac{\hat{\mathbf{R}}}{R^2} \tag{F.E.12b}$$

$$\nabla R^{-2} = \nabla|\mathbf{r} - \mathbf{r}'|^{-2} = -2\frac{\mathbf{R}}{R^4} = -2\frac{\hat{\mathbf{R}}}{R^3} \tag{F.E.12c}$$

$$\nabla R^{-3} = \nabla|\mathbf{r} - \mathbf{r}'|^{-3} = -3\frac{\mathbf{R}}{R^5} = -3\frac{\hat{\mathbf{R}}}{R^4} \tag{F.E.12d}$$

and by recurrence or directly from (F.E.11e)

$$\nabla R^{-n} = \nabla|\mathbf{r}-\mathbf{r}'|^{-n} \qquad = -n\frac{\mathbf{R}}{R^{n+2}} \qquad = -n\frac{\hat{\mathbf{R}}}{R^{n+1}}. \tag{F.E.12e}$$

From (F.E.11) the second-order partial derivative of R, R^{-1} and R^{-2} with respect to x_i, x_j are obtained

$$\frac{\partial^2 R}{\partial x_i \partial x_j} = \frac{\partial^2|\mathbf{r}-\mathbf{r}'|}{\partial x_i \partial x_j} \qquad = \quad \frac{1}{R}\delta_{ij} - \frac{(x_i-x_i')(x_j-x_j')}{R^3} \tag{F.E.13a}$$

$$\frac{\partial^2 R^{-1}}{\partial x_i \partial x_j} = \frac{\partial^2|\mathbf{r}-\mathbf{r}'|^{-1}}{\partial x_i \partial x_j} \qquad = -\ \frac{1}{R^3}\delta_{ij} + 3\frac{(x_i-x_i')(x_j-x_j')}{R^5} \tag{F.E.13b}$$

$$\frac{\partial^2 R^{-2}}{\partial x_i \partial x_j} = \frac{\partial^2|\mathbf{r}-\mathbf{r}'|^{-2}}{\partial x_i \partial x_j} \qquad = -2\frac{1}{R^4}\delta_{ij} + 8\frac{(x_i-x_i')(x_j-x_j')}{R^6} \tag{F.E.13c}$$

$$\frac{\partial^2 R^{-3}}{\partial x_i \partial x_j} = \frac{\partial^2|\mathbf{r}-\mathbf{r}'|^{-3}}{\partial x_i \partial x_j} \qquad = -3\frac{1}{R^5}\delta_{ij} + 15\frac{(x_i-x_i')(x_j-x_j')}{R^7} \tag{F.E.13d}$$

and by recurrence or directly from (F.E.11)

$$\frac{\partial^2 R^{-n}}{\partial x_i \partial x_j} = \frac{\partial^2|\mathbf{r}-\mathbf{r}'|^{-n}}{\partial x_i \partial x_j} \qquad = -n\frac{1}{R^{n+2}}\delta_{ij} + n(n+2)\frac{(x_i-x_i')(x_j-x_j')}{R^{n+4}}. \tag{F.E.13e}$$

Moreover, the following divergence relations may be derived from the relation $\nabla\cdot(U\mathbf{A}) = (\nabla U)\cdot\mathbf{A} + U(\nabla\cdot\mathbf{A})$

$$\nabla\cdot\mathbf{R} = \nabla\cdot|\mathbf{r}-\mathbf{r}'|\mathbf{R} \qquad = 3 \tag{F.E.14a}$$

$$\nabla\cdot R^{-1}\mathbf{R} = \nabla\cdot|\mathbf{r}-\mathbf{r}'|^{-1}\mathbf{R} \qquad = \frac{2}{R} \tag{F.E.14b}$$

$$\nabla\cdot R^{-2}\mathbf{R} = \nabla\cdot|\mathbf{r}-\mathbf{r}'|^{-2}\mathbf{R} \qquad = \frac{1}{R^2} \tag{F.E.14c}$$

$$\nabla\cdot R^{-3}\mathbf{R} = \nabla\cdot|\mathbf{r}-\mathbf{r}'|^{-3}\mathbf{R} \qquad = 0. \tag{F.E.14d}$$

Assuming the evaluation of $\mathbf{F}$ and $\mathbf{G}$ to takes place at the retarded time $t = t' - |\mathbf{r}-\mathbf{r}'|/c$ we derive the following identities

$$\begin{aligned}\frac{\partial\mathbf{F}}{\partial x_i} &= \frac{\partial\mathbf{F}}{\partial R}\frac{\partial R}{\partial x_i} \\ &= -\frac{1}{c}\frac{\partial\mathbf{F}}{\partial t}\frac{x_i-x_i'}{R}.\end{aligned} \tag{F.E.15}$$

From (F.E.15) we can easily deduce the following divergence relation

$$\nabla \cdot \mathbf{F} = -\frac{\mathbf{R}}{cR} \cdot \frac{\partial \mathbf{F}}{\partial t}. \tag{F.E.16}$$

Combining (F.E.11b) and (F.E.15) yields

$$\begin{aligned}
\frac{\partial \mathbf{G}}{\partial x_i} &= \frac{\partial \mathbf{F}}{\partial x_i}\frac{1}{R} + \mathbf{F}\frac{\partial R^{-1}}{\partial x_i} \\
&= -\frac{1}{cR}\frac{\partial \mathbf{F}}{\partial t}\frac{x_i - x_i'}{R} - \mathbf{F}\frac{x_i - x_i'}{R^3} \\
&= -\Big(\frac{1}{c}\frac{\partial \mathbf{F}}{\partial t} + \frac{\mathbf{F}}{R}\Big)\frac{x_i - x_i'}{R^2}, \quad \mathbf{r} \neq \mathbf{r}'.
\end{aligned} \tag{F.E.17}$$

From (F.E.17) we can easily deduce the following divergence and curl relations

$$\nabla \cdot \mathbf{G} = -\Big(\frac{1}{c}\frac{\partial \mathbf{F}}{\partial t} + \frac{\mathbf{F}}{R}\Big) \cdot \frac{\mathbf{R}}{R^2}, \quad \mathbf{r} \neq \mathbf{r}' \tag{F.E.18a}$$

$$\nabla \times \mathbf{G} = \Big(\frac{1}{c}\frac{\partial \mathbf{F}}{\partial t} + \frac{\mathbf{F}}{R}\Big) \times \frac{\mathbf{R}}{R^2}, \quad \mathbf{r} \neq \mathbf{r}'. \tag{F.E.18b}$$

$$\frac{\partial^2 \mathbf{G}}{\partial x_i^2} = -\frac{\partial\Big(\frac{1}{c}\frac{\partial \mathbf{F}}{\partial t} + \frac{\mathbf{F}}{R}\Big)}{\partial x_i}\frac{x_i - x_i'}{R^2} - \Big(\frac{1}{c}\frac{\partial \mathbf{F}}{\partial t} + \frac{\mathbf{F}}{R}\Big)\frac{\partial \frac{x_i - x_i'}{R^2}}{\partial x_i}$$

inserting (F.E.15), (F.E.17) and (F.E.11c)

$$\begin{aligned}
&= -\Big(-\frac{1}{c^2}\frac{\partial^2 \mathbf{F}}{\partial t^2}\frac{x_i - x_i'}{R} - \Big(\frac{1}{c}\frac{\partial \mathbf{F}}{\partial t} + \frac{\mathbf{F}}{R}\Big)\frac{x_i - x_i'}{R^2}\Big)\frac{x_i - x_i'}{R^2} - \Big(\frac{1}{c}\frac{\partial \mathbf{F}}{\partial t} + \frac{\mathbf{F}}{R}\Big)\Big(\frac{1}{R^2} - 2(x_i - x_i')\frac{x_i - x_i'}{R^4}\Big) \\
&= \frac{1}{c^2 R}\frac{\partial^2 \mathbf{F}}{\partial t^2}\Big(\frac{x_i - x_i'}{R}\Big)^2 + \Big(\frac{1}{c}\frac{\partial \mathbf{F}}{\partial t} + \frac{\mathbf{F}}{R}\Big)\frac{1}{R^2}\Big(3\Big(\frac{x_i - x_i'}{R}\Big)^2 - 1\Big), \quad \mathbf{r} \neq \mathbf{r}'.
\end{aligned} \tag{F.E.19}$$

The Laplacian of $\mathbf{G}$ is therefore

$$\nabla^2 \mathbf{G} = \frac{1}{c^2 R}\frac{\partial^2 \mathbf{F}}{\partial t^2}, \quad \mathbf{r} \neq \mathbf{r}'. \tag{F.E.20}$$

Combining (F.E.11b), (F.E.11c) and (F.E.18a) yields

$$\begin{aligned}
\frac{\partial \nabla \cdot \mathbf{G}}{\partial x_i} &= -\frac{\partial\Big(\frac{1}{c}\frac{\partial \mathbf{F}}{\partial t} + \frac{\mathbf{F}}{R}\Big)}{\partial x_i}\cdot\frac{\mathbf{R}}{R^2} - \Big(\frac{1}{c}\frac{\partial \mathbf{F}}{\partial t} + \frac{\mathbf{F}}{R}\Big)\cdot\frac{\partial \frac{\mathbf{R}}{R^2}}{\partial x_i} \\
&= -\Big(-\frac{1}{c^2}\frac{\partial^2 \mathbf{F}}{\partial t^2}\frac{x_i - x_i'}{R} - \Big(\frac{1}{c}\frac{\partial \mathbf{F}}{\partial t} + \frac{\mathbf{F}}{R}\Big)\frac{x_i - x_i'}{R^2}\Big)\cdot\frac{\mathbf{R}}{R^2} \\
&\quad - \Big(\frac{1}{c}\frac{\partial \mathbf{F}}{\partial t} + \frac{\mathbf{F}}{R}\Big)\cdot\Big(\frac{\hat{\mathbf{x}}_i}{R^2} - 2\mathbf{R}\frac{x_i - x_i'}{R^4}\Big) \\
&= \frac{1}{c^2}\frac{\partial^2 \mathbf{F}}{\partial t^2}\frac{x_i - x_i'}{R}\cdot\frac{\mathbf{R}}{R^2} + \frac{1}{R^2}\Big(\Big(\frac{1}{c}\frac{\partial \mathbf{F}}{\partial t} + \frac{\mathbf{F}}{R}\Big)(x_i - x_i')\Big)\cdot\frac{3\mathbf{R}}{R^2} - \frac{1}{R^2}\Big(\frac{1}{c}\frac{\partial \mathbf{F}}{\partial t} + \frac{\mathbf{F}}{R}\Big)\cdot\hat{\mathbf{x}}_i, \quad \mathbf{r} \neq \mathbf{r}'.
\end{aligned} \tag{F.E.21}$$

Similarly, by combining (F.E.11b), (F.E.11c) and (F.E.18b) we obtain

$$\begin{aligned}\frac{\partial \nabla \times \mathbf{G}}{\partial x_i} =& \frac{\partial\Big(\frac{1}{c}\frac{\partial \mathbf{F}}{\partial t}+\frac{\mathbf{F}}{R}\Big)}{\partial x_i}\times\frac{\mathbf{R}}{R^2}\Big(\frac{1}{c}\frac{\partial \mathbf{F}}{\partial t}+\frac{\mathbf{F}}{R}\Big)\times\frac{\partial\frac{\mathbf{R}}{R^2}}{\partial x_i}\\ =&\Big(-\frac{1}{c^2}\frac{\partial^2\mathbf{F}}{\partial t^2}\frac{x_i-x_i'}{R}-\Big(\frac{1}{c}\frac{\partial\mathbf{F}}{\partial t}+\frac{\mathbf{F}}{R}\Big)\frac{x_i-x_i'}{R^2}\Big)\times\frac{\mathbf{R}}{R^2}+\Big(\frac{1}{c}\frac{\partial\mathbf{F}}{\partial t}+\frac{\mathbf{F}}{R}\Big)\times\Big(\frac{\hat{\mathbf{x}}_i}{R^2}-2\mathbf{R}\frac{x_i-x_i'}{R^4}\Big)\\ =&-\frac{1}{c^2}\frac{\partial^2\mathbf{F}}{\partial t^2}\frac{x_i-x_i'}{R}\times\frac{\mathbf{R}}{R^2}-\frac{1}{R^2}\Big(\Big(\frac{1}{c}\frac{\partial\mathbf{F}}{\partial t}+\frac{\mathbf{F}}{R}\Big)(x_i-x_i')\Big)\times\frac{3\mathbf{R}}{R^2}+\frac{1}{R^2}\Big(\frac{1}{c}\frac{\partial\mathbf{F}}{\partial t}+\frac{\mathbf{F}}{R}\Big)\times\hat{\mathbf{x}}_i,\quad \mathbf{r}\neq\mathbf{r}'.\end{aligned}\tag{F.E.22}$$

From (F.E.21) we readily obtain the following expression for grad div $\mathbf{G}$

$$\nabla\nabla\cdot\mathbf{G}=\frac{1}{c^2R}\frac{\partial^2\mathbf{F}}{\partial t^2}\cdot\frac{\mathbf{RR}}{R^2}+\frac{1}{R^2}\Big(\frac{1}{c}\frac{\partial\mathbf{F}}{\partial t}+\frac{\mathbf{F}}{R}\Big)\cdot\Big(\frac{3\mathbf{RR}}{R^2}-\bar{\mathbf{I}}\Big),\quad \mathbf{r}\neq\mathbf{r}'.\tag{F.E.23}$$

From (F.E.23) and (F.E.20)

$$\begin{aligned}\nabla\times\nabla\times\mathbf{G}&=\nabla\nabla\cdot\mathbf{G}-\nabla^2\mathbf{G}\\ &=\frac{1}{c^2R}\frac{\partial^2\mathbf{F}}{\partial t^2}\cdot\frac{\mathbf{RR}}{R^2}+\frac{1}{R^2}\Big(\frac{1}{c}\frac{\partial\mathbf{F}}{\partial t}+\frac{\mathbf{F}}{R}\Big)\cdot\Big(\frac{3\mathbf{RR}}{R^2}-\bar{\mathbf{I}}\Big)-\frac{1}{c^2R}\frac{\partial^2\mathbf{F}}{\partial t^2}\\ &=\frac{1}{c^2R}\frac{\partial^2\mathbf{F}}{\partial t^2}\cdot\Big(\frac{\mathbf{RR}}{R^2}-\bar{I}\Big)+\frac{1}{R^2}\Big(\frac{1}{c}\frac{\partial\mathbf{F}}{\partial t}+\frac{\mathbf{F}}{R}\Big)\cdot\Big(\frac{3\mathbf{RR}}{R^2}-\bar{\mathbf{I}}\Big),\quad \mathbf{r}\neq\mathbf{r}'.\end{aligned}\tag{F.E.24}$$

In the subsequent we will applied the identities developed so far and provide a rather simple derivation of the [1, Eq. (2.59)-(2.69) on pp. 21-23] Let $\boldsymbol{\Psi}(\mathbf{r}', t' - |\mathbf{r} - \mathbf{r}'|/c) = \frac{1}{|\mathbf{r}-\mathbf{r}'|}\int_{t_0}^{t} \mathbf{J}(\mathbf{r}', t' - |\mathbf{r} - \mathbf{r}'|/c)\,\mathrm{d}t'$, then by defining $\boldsymbol{\psi}(\mathbf{r}', t' - |\mathbf{r} - \mathbf{r}'|/c) = \int_{t_0}^{t} \mathbf{J}(\mathbf{r}', t' - |\mathbf{r} - \mathbf{r}'|/c)\,\mathrm{d}t'$, we obtain

$$\nabla \cdot \boldsymbol{\Psi}(\mathbf{r}', t' - |\mathbf{r} - \mathbf{r}'|/c) = \Big(\nabla \cdot \frac{1}{|\mathbf{r} - \mathbf{r}'|}\Big)\boldsymbol{\psi}(\mathbf{r}', t' - |\mathbf{r} - \mathbf{r}'|/c) + \frac{1}{|\mathbf{r} - \mathbf{r}'|}\nabla \cdot \boldsymbol{\psi}(\mathbf{r}', t' - |\mathbf{r} - \mathbf{r}'|/c)$$

using the divergence theorem[38] in the first term leads to

$$\nabla \cdot \boldsymbol{\Psi}(\mathbf{r}', t' - |\mathbf{r} - \mathbf{r}'|/c) = \frac{1}{|\mathbf{r} - \mathbf{r}'|}\nabla' \cdot \boldsymbol{\psi}(\mathbf{r}', t' - |\mathbf{r} - \mathbf{r}'|/c) + \frac{1}{|\mathbf{r} - \mathbf{r}'|}\nabla \cdot \boldsymbol{\psi}(\mathbf{r}', t' - |\mathbf{r} - \mathbf{r}'|/c)$$

now applying (F.F.14) and (F.E.4c) gives

$$\begin{aligned}\nabla \cdot \boldsymbol{\Psi}(\mathbf{r}', t' - |\mathbf{r} - \mathbf{r}'|/c) =& \frac{1}{R}\{\nabla' \cdot \boldsymbol{\psi}\}^{(1)}(\mathbf{r}', t' - |\mathbf{r} - \mathbf{r}'|/c) \\ =& \frac{1}{R}\int_{t_0}^{t} \{\nabla' \cdot\}^{(1)}\mathbf{J}(\mathbf{r}', t' - |\mathbf{r} - \mathbf{r}'|/c)\,\mathrm{d}t'.\end{aligned} \tag{F.E.25}$$

Similarly, from (F.E.20) we obtain

$$\begin{aligned}\nabla^2\boldsymbol{\Psi}(\mathbf{r}', t' - |\mathbf{r} - \mathbf{r}'|/c) &= \frac{1}{c^2}\frac{\partial^2\boldsymbol{\Psi}(\mathbf{r}', t' - |\mathbf{r} - \mathbf{r}'|/c)}{\partial t^2} \\ &= \frac{1}{c^2 R}\frac{\partial \mathbf{J}(\mathbf{r}', t' - |\mathbf{r} - \mathbf{r}'|/c)}{\partial t}, \quad \mathbf{r} \neq \mathbf{r}'.\end{aligned} \tag{F.E.26}$$

F.E.3 Pressure and Velocity Fields from Volume Integrals; Derivation

We are now in a position to derive an explicit expression for the acoustic pressure and the acoustic velocity in terms of volume sources.

$$\mathbf{u}(\mathbf{r},t) = -\frac{1}{4\pi}\nabla \lim_{\delta\to 0}\iiint\limits_{V\setminus V_\delta} \frac{j(\mathbf{r}',t-R/c)}{R}\,\mathrm{d}V' + \frac{1}{\rho}\int_{t_0}^{t}\mathbf{f}(\mathbf{r},t')\,\mathrm{d}t'$$

$$= -\frac{1}{4\pi\rho}\nabla \lim_{\delta\to 0}\iiint\limits_{V\setminus V_\delta} \frac{s(\mathbf{r}',t-R/c)}{R} - \frac{\nabla\cdot\int_{t_0}^{t}\mathbf{f}(\mathbf{r}',t-R/c)\,\mathrm{d}t'}{R}\,\mathrm{d}V' + \frac{1}{\rho}\int_{t_0}^{t}\mathbf{f}(\mathbf{r},t')\,\mathrm{d}t'$$

by using [1, Thm. 2-I,II] with an arbitary principal volume V_δ to get

$$= -\frac{1}{4\pi\rho}\lim_{\delta\to 0}\iiint\limits_{V\setminus V_\delta} \frac{\nabla s(\mathbf{r}',t-R/c)}{R} - \frac{\nabla\nabla\cdot\int_{t_0}^{t}\mathbf{f}(\mathbf{r}',t-R/c)\,\mathrm{d}t'}{R}\,\mathrm{d}V' + \frac{2}{3\rho}\int_{t_0}^{t}\mathbf{f}(\mathbf{r},t')\,\mathrm{d}t'$$

from using (F.E.4b) we obtain

$$= -\frac{1}{4\pi\rho}\lim_{\delta\to 0}\iiint\limits_{V\setminus V_\delta} \frac{\{\nabla\}^{(2)}s(\mathbf{r}',t-R/c)}{R} - \frac{\{\nabla\nabla\cdot\}^{(2)}\int_{t_0}^{t}\mathbf{f}(\mathbf{r}',t-R/c)\,\mathrm{d}t'}{R}\,\mathrm{d}V' + \frac{2}{3\rho}\int_{t_0}^{t}\mathbf{f}(\mathbf{r},t')\,\mathrm{d}t'$$

finally, from (F.E.18a) and (F.E.23)

$$= \frac{1}{4\pi\rho}\lim_{\delta\to 0}\iiint\limits_{V\setminus V_\delta}\left[\left(\frac{1}{c^2}\frac{\partial}{\partial t}\mathbf{f}(\mathbf{r}',t-R/c)\right)\cdot\frac{\mathbf{RR}}{R^3} + \left(\frac{1}{c}\mathbf{f}(\mathbf{r}',t-R/c) + \frac{1}{R}\int_{t_0}^{t}\mathbf{f}(\mathbf{r}',t-R/c)\,\mathrm{d}t'\right)\frac{1}{R^2}\cdot\left(\frac{3\mathbf{RR}}{R^2}-\bar{\mathbf{I}}\right)\right.$$
$$\left. + \left(\frac{1}{c}\frac{\partial}{\partial t}s(\mathbf{r}',t-R/c) + \frac{1}{R}s(\mathbf{r}',t-R/c)\right)\frac{\mathbf{R}}{R^2}\right]\mathrm{d}V' - \frac{1}{\rho}\left(\bar{\mathbf{L}}-\bar{\mathbf{I}}\right)\cdot\int_{t_0}^{t}\mathbf{f}(\mathbf{r},t')\,\mathrm{d}t', \quad \mathbf{r}\in V_\infty. \tag{F.E.27}$$

If a spherical principal volume V_δ^S was used instead then the dyadic $\left(\bar{\mathbf{L}} - \bar{\mathbf{I}}\right)$ entering the last term should be replaced by $-\frac{2}{3}$.

Bibliography

[1] Thorkild B. Hansen and Arthur D. Yaghjian. *Plane-Wave Theory of Time-Domain Fields Near-Field Scannng Applications*. IEEE Press Series on Electromagnetic Wave Theory, 1999.

[2] Wilfred Kaplan. *Advanced Calculus*. Addison-Wesley Longman, 5th edition, 2002.

F.F Time-Dependent Potential Functions

F.F.1 Introduction

The problem relates to the determination of the time-independent and time-dependent fields and their first- and second-order spatial derivatives *within* the source region. Thorough analysis of the proofs of [1, Thm. 2-I,II] reveals that the two theorems in turn use theorems on the potentials of volume distributions [3, Ch. VI.3]. The requirement on boundness of $s(\mathbf{r}, t), \mathbf{f}(\mathbf{r}, t)$ is implicitly invoked in [3, Ch. VI.3] and included here for the sake of rigorism.

The development presented will rely on the classical work by Kellogg [3] on the potentials of volume distributions for time-independent fields. Although Kellogg's book primarily considered Newtonian potentials the result are directly applicable to other parts of physics dealing with *static fields*. Hence, first we present the pertinent results on potential function for static fields and potential functions. However, no examination of the second-order cross partial derivatives i.e., $\partial x_i/\partial x_j, i \neq j$ has been made. A remedy for this will therefore be made.

As usual $\mathbf{r}' = x'\hat{\mathbf{x}} + y'\hat{\mathbf{y}} + z'\hat{\mathbf{z}}$ and $\mathbf{r} = x\hat{\mathbf{x}} + y\hat{\mathbf{y}} + z\hat{\mathbf{z}}$ denote source and field (observer) position respectively, $\mathbf{R} = \mathbf{r} - \mathbf{r}'$ denotes the source point to field point vector of length $R = |\mathbf{r} - \mathbf{r}'| = \sqrt{(x-x')^2 + (y-y')^2 + (z-z')^2}$. Moreover, we will let x_i be equal to x, y, or z for $i = 1, 2$, or 3, respectively; i.e., $\mathbf{r} = x_1\hat{\mathbf{x}} + x_2\hat{\mathbf{y}} + x_3\hat{\mathbf{z}}$.

Important for our purpose is to note that upon bringing the grad div operator $\nabla\nabla\cdot$ under the sign of integration the Kronecker delta counts once for each x_i. The curl curl operator $\nabla\times\nabla\times$, however, counts twice for each x_i. Moreover, it should be noticed that it is the unprimed differential operator referring to field coordinates (as opposed to the primed differential operator referring to source coordinates) that is brought inside the sign of integration.

F.F.2 Kellogg's Theorem

We will let the volume mass density $\rho(\mathbf{r}')$ represents a volume distribution. Likewise we will let the *Newtonian potential* $U(\mathbf{r})$ and the *Newtonian force* $\mathbf{F}(\mathbf{r})$ be representatives of general potential functions and forces. From potential theory [3] the following interrelation among these quantities is well known

$$U(\mathbf{r}) = \iiint\limits_V \frac{\rho(\mathbf{r}')}{|\mathbf{r}-\mathbf{r}'|}\,\mathrm{d}V' \tag{F.F.1a}$$

$$\mathbf{F}(\mathbf{r}) = \nabla U(\mathbf{r}). \tag{F.F.1b}$$

Equation (F.F.1a) exposes the problem we are addressing. When the field and source points coincide the integrand becomes unbounded leading to an *improper* integral. Moreover, when we want to determine the Newtonian force $\mathbf{F}(\mathbf{r})$ the question arises to whether differential operation can be brought inside the sign of integration. The usual criterion for the possibility of differentiating under the sign of integration, that is, Leibnitz's rule of integration[39] [2, Ch. 4.9], does not apply to improper integrals. However, in our development the integrand, that is, $f(\mathbf{r}', \mathbf{r}) = \rho(\mathbf{r}')/|\mathbf{r}-\mathbf{r}'|$ is infinitely differentiable outside the singularities. Hence, the use of Leibnitz's rule of integrations is warranted over the principal volume of integration $V \setminus V_\delta$.

In the development we will need the well known result that the attraction of a homogeneous sphere with radius a and constant mass density $\rho(\mathbf{r}') = \rho$ at an interior point ($r < a$) is toward the center, and varies as the distance from the center [3, Ch. 1,p. 19]. When evaluated at the origin this relationship can be expressed by

$$U(\mathbf{r}) = -\frac{2}{3}\pi\rho \begin{cases} r^2, & r < a, \\ -\frac{a^3}{r}, & r \geq a, \end{cases} \tag{F.F.2a}$$

$$\mathbf{F}(\mathbf{r}) = -\frac{4}{3}\pi\rho \begin{cases} r\mathbf{r}, & r < a, \\ \frac{a^3}{r^2}\mathbf{r}, & r \geq a, \end{cases} \tag{F.F.2b}$$

$$\frac{\partial^2}{\partial x_i \partial x_j} U(\mathbf{r}) = -\frac{4}{3}\pi\rho \begin{cases} \delta_{ij}, & r < a, \\ -2\frac{a^3}{r^3}\delta_{ij}, & r \geq a, \end{cases} \tag{F.F.2c}$$

$$\nabla \cdot \mathbf{F}(\mathbf{r}) = -\frac{4}{3}\pi\rho \begin{cases} 1 & r < a, \\ -2\frac{a^3}{r^3}\delta_{ij}, & r \geq a, \end{cases} \tag{F.F.2d}$$

$$\nabla \times \mathbf{F}(\mathbf{r}) = 0. \tag{F.F.2e}$$

These expressions may also readily be deduced from (F.F.1). What is required is knowledge of the variation of $\mathbf{F}(\mathbf{r})$ with $\mathbf{r}$ for an inhomogeneous source (mass) distribution.

The development will use the following central theorem on *improper* volume integrals[40] [4, Sec. 55].

[39] In our extended use of the Leibnitz's formula we consider differentiation of a *proper* definite volume integral where the source coordinates $\mathbf{r}'$ are the integration variables and the field position coordinates $\mathbf{r}$ are *integration parameters* [2, Ch. 4.9]. Let the integrand $f(\mathbf{r}', \mathbf{r})$ be continuous with $\mathbf{r}$ and have continuous partial derivatives $\partial f/\partial x_i$ for $\mathbf{r}' \in V \setminus V_\delta$ and $\mathbf{r} \in V_f$ where $V \setminus V_\delta$ is the *principle volume* of integration excluding every singularity in the integrand. Then for $\mathbf{r} \in V_f$, $\frac{\partial}{\partial x_i}\iiint\limits_{V\setminus V_\delta} f(\mathbf{r}', \mathbf{r})\,\mathrm{d}V' = \iiint\limits_{V\setminus V_\delta} \frac{\partial f(\mathbf{r}', \mathbf{r})}{\partial x_i}\,\mathrm{d}V'$. If in addition the second-order partial derivative $\partial^2 f(\mathbf{r}', \mathbf{r})/\partial x_i \partial x_j$ is continuous with $\mathbf{r}$ then $\frac{\partial}{\partial x_i \partial x_j}\iiint\limits_{V\setminus V_\delta} f(\mathbf{r}', \mathbf{r})\,\mathrm{d}V' = \iiint\limits_{V\setminus V_\delta} \frac{\partial f(\mathbf{r}', \mathbf{r})}{\partial x_i \partial x_j}\,\mathrm{d}V'$. The extension to vector-valued functions is straight forward.

[40] If the Riemann integral[41] fails to exist, one may still be able to obtain a value by treating the integral as an improper integral. In particular we are dealing with a point discontinuity at $\mathbf{r} = \mathbf{r}'$.

Theorem 4. *Let V be a finite region and $R = |\mathbf{r} - \mathbf{r}'|$ the distance between the (source) element of volume $\mathrm{d}V'$ at $\mathbf{r}'$ and a fixed (field) point P at $\mathbf{r}$ inside or on the boundary of V. The integral*

$$\int_V \frac{1}{|\mathbf{r} - \mathbf{r}'|^\beta}\,\mathrm{d}V' \tag{F.F.3}$$

is convergent if β is a positive constant less than 3.

Remark. This theorem ensures convergence of the integral in a large class of problems encountered in physics. If P is outside V the integral is convergent for all $\beta > 0$. Hence, the problem addressed is only of concern when evaluating fields inside the source region. Also recalling that R^{-1}, R^{-2} and R^{-3} enter in the expression for Ψ, $\partial\Psi/\partial x_i$ and $\partial^2\Psi/\partial x_i^2$ respectively explains why special considerations prevails in the second order differentiation case.

From [1, Ch. 2] the following theorems are involved:

Theorem 5. *If $\Psi(\mathbf{r}, t)$ and its time derivative $\partial\Psi(\mathbf{r}, t)/\partial t$ are continuous and bounded functions of $\mathbf{r}$ and t, then*

$$\begin{aligned}\frac{\partial}{\partial x_i}\lim_{\delta\to 0}\int_{V\setminus V_\delta}\frac{\Psi(\mathbf{r}', t - \frac{|\mathbf{r}-\mathbf{r}'|}{c})}{|\mathbf{r} - \mathbf{r}'|}\,\mathrm{d}V' \\ = \lim_{\delta\to 0}\int_{V\setminus V_\delta}\frac{\partial}{\partial x_i}\Big[\frac{\Psi(\mathbf{r}', t - \frac{|\mathbf{r}-\mathbf{r}'|}{c})}{|\mathbf{r} - \mathbf{r}'|}\Big]\,\mathrm{d}V'.\end{aligned} \tag{F.F.4}$$

Theorem 6. *If $\Psi(\mathbf{r}, t)$ and its first and second order time derivative $\partial\Psi(\mathbf{r}, t)/\partial t$, $\partial^2\Psi(\mathbf{r}, t)/\partial t^2$ are continuous and bounded functions of $\mathbf{r}$ and t, and $\Psi(\mathbf{r}, t)$ is Hölder continuous in $\mathbf{r}$ and for all t, then*

$$\begin{aligned}\frac{\partial^2}{\partial x_i\partial x_j}\lim_{\delta\to 0}\int_{V\setminus V_\delta}\frac{\Psi(\mathbf{r}', t - \frac{|\mathbf{r}-\mathbf{r}'|}{c})}{|\mathbf{r} - \mathbf{r}'|}\,\mathrm{d}V' \\ = \lim_{\delta\to 0}\int_{V\setminus V_\delta}\frac{\partial^2}{\partial x_i\partial x_j}\Big[\frac{\Psi(\mathbf{r}', t - \frac{|\mathbf{r}-\mathbf{r}'|}{c})}{|\mathbf{r} - \mathbf{r}'|}\Big]\,\mathrm{d}V' - \frac{4}{3}\pi\Psi(\mathbf{r}, t)\delta_{ij}.\end{aligned} \tag{F.F.5}$$

The results of Theorem 5 - 6 will be used for the calculation of the volume integral expression for the electric and magnetic field and the pressure and velocity fields.

An arguable simpler proof of Theorem 5 - 6 is provided. The classical work by Kellogg [3] The extension to the vector function case is straight forward provided that the assumptions above holds component wise.

F.F.3 First-order Derivatives of Spacial Potential Functions

The source volume is divided into three non overlapping regions $V = V \setminus V_\Sigma^S \cup V_\Sigma^S \cup V_\delta^S$ where V_Σ^S is a sphere about P_0 lying in V and circumscribing the smaller sphere V_δ^S. $V \setminus V_\Sigma^S$ is the remaining part of the V. The superscript ^{S} on V_Σ^S and V_δ^S signifies the spherical structure of these volumes.

From the principle of superposition we have

$$U(\mathbf{r}) = U_{V\setminus V_\Sigma^S}(\mathbf{r}) + U_{V_\Sigma^S}(\mathbf{r}) + U_{V_\delta^S}(\mathbf{r}), \tag{F.F.6}$$

where the subscript signifies the contribution region.

The proof of the theorem will be conducted in the following steps [3, Ch. VI.3], [2, Ch. 6.26]:

① Create the following integral quantities

$$I(\Delta x_i) = I_\Delta(\Delta x_i) - I_\partial(\Delta x_i) \tag{F.F.7a}$$

where

$$I_\Delta(\Delta x_i) = \frac{U(\mathbf{r})|_{\mathbf{r}=\mathbf{r}_0+\Delta x_j \Delta \hat{\mathbf{x}}_\mathbf{j}} - U(\mathbf{r}_0)|_{\mathbf{r}=\mathbf{r}_0}}{\Delta x_j} \tag{F.F.7b}$$

and

$$I_\partial(\Delta x_i) = \iiint\limits_V \left(\frac{\partial}{\partial x_i} \frac{\rho(\mathbf{r}')}{|\mathbf{r}-\mathbf{r}'|} \right)\Bigg|_{\mathbf{r}=\mathbf{r}_0} \mathrm{d}V'. \tag{F.F.7c}$$

Hence, I is the difference between the difference coefficient I_Δ and the differential operator brought inside the sign of integration I_∂ both evaluated at P_0 at position $\mathbf{r}_0$.
Check if the integral $I(\Delta x_i)$ is convergent.

② If convergence is assured proceed in the next step item ③ else construct a new source distribution function $\rho(\mathbf{r}') \curvearrowright \rho(\mathbf{r}') - \rho(\mathbf{r}'_0)$ and go back to Equation ①.

③ Verify for consistency that $I(0) = 0$.

④ Prove that $I(\Delta x_i)$ is a continuous function of Δx_i. This is accomplished by breaking the region of integration i.e., the source region into two, such that in the first region $V \setminus V_\delta$, the integrand is a bounded density times a continuous function of all field coordinates $\mathbf{r}$, and that the integral over the second region V_δ with center in P_0 that also confines P vanishes with the maximum chord of the region. The integral over $V \setminus V_\delta$ is therefore continuous in $\mathbf{r}$, thus restricted. It should then be proved that the integral over the sphere can be made arbitrary small be restricting the radius of the sphere δ, *uniformly* as to $\mathbf{r}$. Then the existence of the partial derivative of the volume integral has been made. Moreover, its value equals I_∂.

The first-order partial derivative of (F.F.7b) with respect to x_i, if it exists, is defined as

$$\begin{aligned} I_\Delta(\Delta x_i) &= \lim_{\Delta x_i \to 0} \frac{U(\mathbf{r})|_{\mathbf{r}=\mathbf{r}_0+\Delta x_i \Delta \hat{\mathbf{x}}_\mathbf{i}} - U(\mathbf{r}_0)|_{\mathbf{r}=\mathbf{r}_0}}{\Delta x_i} \\ &= \lim_{\Delta x_i \to 0} \frac{\left(\iiint\limits_{V_\delta^S} \frac{\rho(\mathbf{r}')}{|\mathbf{r}-\mathbf{r}'|} \, \mathrm{d}V' \right)\Big|_{\mathbf{r}=\mathbf{r}_0+\Delta x_i \Delta \hat{\mathbf{x}}_\mathbf{i}} - \left(\iiint\limits_{V_\delta^S} \frac{\rho(\mathbf{r}')}{|\mathbf{r}-\mathbf{r}'|} \, \mathrm{d}V' \right)\Big|_{\mathbf{r}=\mathbf{r}_0}}{\Delta x_i} \end{aligned}$$

as the integration variables are the source coordinates Δx_i can be brought inside the sign of integration yielding

$$I_\Delta(\Delta x_i) = \lim_{\Delta x_i \to 0} \iiint\limits_{V_\delta^S} \left[\frac{1}{\Delta x_i} \left(\frac{\rho(\mathbf{r}')}{|\mathbf{r}_0 + \Delta x_i \Delta \hat{\mathbf{x}}_\mathbf{i}|} - \frac{\rho(\mathbf{r}')}{|\mathbf{r}_0 - \mathbf{r}'|} \right) \right] \mathrm{d}V'. \tag{F.F.8}$$

Actually, piece-wise continuity in $\rho(\mathbf{r}')$ is sufficient.

F.F.4 Second-order Derivatives of Spacial Potential Functions

The proof of the theorem will be conducted in the following steps [3, Ch. VI.3], [2, Ch. 6.26]:

① Create the following integral quantities

$$I(\Delta x_j) = I_\Delta(\Delta x_j) - I_\partial(\Delta x_j) \tag{F.F.9a}$$

where

$$I_\Delta(\Delta x_j) = \frac{\frac{\partial}{\partial x_i} U(\mathbf{r})|_{\mathbf{r}=\mathbf{r}_0+\Delta x_j \Delta \hat{\mathbf{x}}_\mathbf{j}} - \frac{\partial}{\partial x_i} U(\mathbf{r}_0)|_{\mathbf{r}=\mathbf{r}_0}}{\Delta x_j} \tag{F.F.9b}$$

and

$$I_\partial(\Delta x_j) = \iiint\limits_{V_\Sigma^S} \left(\frac{\partial^2}{\partial x_i \partial x_j} \frac{\rho(\mathbf{r}')}{|\mathbf{r} - \mathbf{r}'|} \right)\Big|_{\mathbf{r}=\mathbf{r}_0} \mathrm{d}V'. \tag{F.F.9c}$$

Hence, I is the difference between the difference coefficient I_Δ and the differential operator brought inside the sign of integration I_∂ both evaluated at P_0 at position $\mathbf{r}_0$.
Check if the integral $I(\Delta x_j)$ is convergent.

② If convergence is assured proceed in the next step item ③ else construct a new source distribution function $\rho(\mathbf{r}') \curvearrowright \rho(\mathbf{r}') - \rho(\mathbf{r}'_0)$ and go back to Equation ①.

③ Verify for consistency that $I(0) = 0$.

④ Prove that $I(\Delta x_j)$ is a continuous function of Δx_j. This is accomplished by breaking the region of integration i.e., the source region into two, such that in the first region $V \setminus V_\delta$, the integrand is a bounded density times a continuous function of all field coordinates $\mathbf{r}$, and that the integral over the second region V_δ with center in P_0 that also confines P vanishes with the maximum chord of the region. The integral over $V \setminus V_\delta$ is therefore continuous in $\mathbf{r}$, thus restricted. It should then be proved that the integral over the sphere can be made arbitrary small be restricting the radius of the sphere δ, *uniformly* as to $\mathbf{r}$. Then the existence of the partial derivative of the volume integral has been made. Moreover, its value equals I_∂.

The second-order partial derivative of (F.F.9b) with respect to x_i and x_j, if it exists, is defined as

$$
\begin{aligned}
I_\Delta(\Delta x_i) &= \lim_{\Delta x_j \to 0} \frac{\frac{\partial}{\partial x_i} U(\mathbf{r})|_{\mathbf{r}=\mathbf{r}_0+\Delta x_j \Delta \hat{\mathbf{x}_j}} - \frac{\partial}{\partial x_i} U(\mathbf{r}_0)|_{\mathbf{r}=\mathbf{r}_0}}{\Delta x_j} \\
&= \lim_{\Delta x_j \to 0} \frac{\frac{\partial}{\partial x_i}\Big(\iiint\limits_{V_\Sigma^S} \frac{\rho_2(\mathbf{r}')}{|\mathbf{r}-\mathbf{r}'|}\,\mathrm{d}V'\Big)\Big|_{\mathbf{r}=\mathbf{r}_0+\Delta x_j \Delta \hat{\mathbf{x}_j}} - \frac{\partial}{\partial x_i}\Big(\iiint\limits_{V_\Sigma^S} \frac{\rho_2(\mathbf{r}')}{|\mathbf{r}-\mathbf{r}'|}\,\mathrm{d}V'\Big)\Big|_{\mathbf{r}=\mathbf{r}_0}}{\Delta x_j}
\end{aligned}
$$

due to Leibnitz's rule of integration the first-order partial differentiation can be brought inside the sign of integration. The same applies to Δx_j as integration variables are the source coordinates yielding

$$
= \lim_{\Delta x_j \to 0} \iiint\limits_{V_\Sigma^S} \left[\Big(\frac{1}{\Delta x_j} \frac{\partial}{\partial x_i} \frac{\rho_2(\mathbf{r}')}{|\mathbf{r}-\mathbf{r}'|} \Big)\Big|_{\mathbf{r}=\mathbf{r}_0+\Delta x_j \Delta \hat{\mathbf{x}_j}} - \frac{\partial}{\partial x_i}\Big(\frac{\rho_2(\mathbf{r}')}{|\mathbf{r}-\mathbf{r}'|} \Big)\Big|_{\mathbf{r}=\mathbf{r}_0} \right] \mathrm{d}V'
$$

insertion of (F.E.11b) yields

$$
= \lim_{\Delta x_j \to 0} \iiint\limits_{V_\Sigma^S} \left[\frac{1}{\Delta x_j} \rho_2(\mathbf{r}') \Big(- \frac{x_i - x_i'}{|\mathbf{r}-\mathbf{r}'|^3}\Big|_{\mathbf{r}=\mathbf{r}_0+\Delta x_j \Delta \hat{\mathbf{x}_j}} + \frac{x_i - x_i'}{|\mathbf{r}-\mathbf{r}'|^3}\Big|_{\mathbf{r}=\mathbf{r}_0} \Big) \right] \mathrm{d}V'
$$

by variable substitution $\mathbf{r}'_\Sigma = \mathbf{r}' - \mathbf{r}_0$ we obtain

$$
= \lim_{\Delta x_j \to 0} \iiint\limits_{V_\Sigma^S} \left[\frac{1}{\Delta x_j} \rho_2(\mathbf{r}'_\Sigma) \Big(\frac{x'_{\Sigma_i} - \Delta x_j \delta_{ij}}{|\mathbf{r}'_\Sigma + \Delta x_j \Delta \hat{\mathbf{x}_j}|^3} - \frac{x'_{\Sigma_i}}{(r'_\Sigma)^3} \Big) \right] \mathrm{d}V'_\Sigma. \tag{F.F.10}
$$

Now $|\mathbf{r}'_\Sigma + \Delta x_j \Delta\hat{\mathbf{x}}_\mathbf{j}|^3 = ((r'_\Sigma)^2 + \Delta x_j^2 - 2r'_\Sigma \Delta x_j \cos\varphi)^{3/2}$ where φ is the direction angle from $\Delta\hat{\mathbf{x}}_\mathbf{j}$ to $\mathbf{r}'_\Sigma$

$$= \lim_{\Delta x_j \to 0} \iiint\limits_{V_\Sigma^S} \left[\frac{1}{\Delta x_j} \rho_2(\mathbf{r}'_\Sigma) \Big(\frac{(x'_{\Sigma_i} - \Delta x_j \delta_{ij}) \big((r'_\Sigma)^2 + \Delta x_j^2 - 2r'_\Sigma \Delta x_j \cos\varphi\big)^{-3/2} - x'_{\Sigma_i}}{(r'_\Sigma)^3} \Big) \right] \mathrm{d}V'_\Sigma$$

from Binomial series expansion we obtain

$$= \lim_{\Delta x_j \to 0} \iiint\limits_{V_\Sigma^S} \left[\frac{1}{\Delta x_j} \rho_2(\mathbf{r}'_\Sigma) \Big(\frac{(x'_{\Sigma_i} - \Delta x_j \delta_{ij}) \Big(1 + 3\frac{\Delta x_j}{r'_\Sigma} \cos\varphi - \frac{3}{2}\big(\frac{\Delta x_j}{r'_\Sigma}\big)^2\Big) - x'_{\Sigma_i}}{(r'_\Sigma)^3} \Big) \right] \mathrm{d}V'_\Sigma$$

$$= \lim_{\Delta x_j \to 0} \iiint\limits_{V_\Sigma^S} \left[\frac{1}{\Delta x_j} \rho_2(\mathbf{r}'_\Sigma) \Big(-\frac{\Delta x_j \delta_{ij}}{(r'_\Sigma)^3} + \frac{3x'_{\Sigma_i} \Delta x_j \cos\varphi}{(r'_\Sigma)^4} - \frac{3\Delta x_j^2 \cos\varphi}{(r'_\Sigma)^4} - \frac{\frac{3}{2} x'_{\Sigma_i} \Delta x_j^2}{(r'_\Sigma)^5} - \frac{\frac{3}{2} x'_{\Sigma_i} \Delta x_j^2}{(r'_\Sigma)^5} \Big) \right] \mathrm{d}V'_\Sigma$$

$$= \lim_{\Delta x_j \to 0} \iiint\limits_{V_\Sigma^S} \left[\rho_2(\mathbf{r}'_\Sigma) \Big(-\frac{\delta_{ij}}{(r'_\Sigma)^3} + \frac{3x'_{\Sigma_i} \cos\varphi}{(r'_\Sigma)^4} - \frac{3\Delta x_j \cos\varphi}{(r'_\Sigma)^4} - \frac{\frac{3}{2} x'_{\Sigma_i} \Delta x_j}{(r'_\Sigma)^5} + \frac{\frac{3}{2} \Delta x_j^2}{(r'_\Sigma)^5} \Big) \right] \mathrm{d}V'_\Sigma$$

finally, from using $x'_{\Sigma_j} = r'_\Sigma \cos\varphi$ we get

$$= \iiint\limits_{V_\Sigma^S} \left[\rho_2(\mathbf{r}'_\Sigma) \Big(-\frac{\delta_{ij}}{(r'_\Sigma)^3} + \frac{3x'_{\Sigma_i} x'_{\Sigma_j}}{(r'_\Sigma)^5} \Big) \right] \mathrm{d}V'_\Sigma \tag{F.F.11}$$

$$I_\partial(\Delta x_i) = \iiint\limits_{V_\Sigma^S} \frac{\partial^2}{\partial x_i \partial x_j} \left(\frac{\rho_2(\mathbf{r}')}{|\mathbf{r} - \mathbf{r}'|} \mathrm{d}V' \right) \Big|_{\mathbf{r}=\mathbf{r}_0}$$

$$= \iiint\limits_{V_\Sigma^S} \left[\rho_2(\mathbf{r}') \Big(-\frac{1}{|\mathbf{r}_0 - \mathbf{r}'|^3} \delta_{ij} + 3\frac{(x_{0_i} - x'_i)(x_{0_j} - x'_j)}{|\mathbf{r}_0 - \mathbf{r}'|^5} \Big) \right] \mathrm{d}V'$$

by variable substitution $\mathbf{r}'_\Sigma = \mathbf{r}' - \mathbf{r}_0$ we obtain

$$= \iiint\limits_{V_\Sigma^S} \left[\rho_2(\mathbf{r}'_\Sigma) \Big(-\frac{1}{(r'_\Sigma)^3} \delta_{ij} + 3\frac{x'_{\Sigma_i} x'_{\Sigma_j}}{(r'_\Sigma)^5} \Big) \right] \mathrm{d}V'_\Sigma$$

Then from (F.F.7a), (F.F.11) and (F.F.12) we see that $I(0) = 0$. Moreover, the integral $I(\Delta x_i)$ is convergent as both the integral $I_\Delta(\Delta x_i)$ and $I_\partial(\Delta x_i)$ are convergent. Hence, $I_\Delta(\Delta x_i)$ tends to $I_\partial(\Delta x_i)$ with Δx_j. It remains to prove that $I(\Delta x_j)$ is continuous in $P(\mathbf{r})$ at $P(\mathbf{r}_0)$.

The is derived in somewhat different ways in [3, Ch. VI.3] and [4, Sec. 55]. Direct application of (F.F.1a) and using (F.E.13a) we obtain

$$\begin{aligned}\frac{\partial^2}{\partial x_i \partial x_j} U(\mathbf{r})|_{\mathbf{r}=\mathbf{r}_0} &= \frac{\partial^2}{\partial x_i \partial x_j} \iiint\limits_V \frac{\rho(\mathbf{r}')}{|\mathbf{r}-\mathbf{r}'|}\,\mathrm{d}V' \\ &= \iiint\limits_V \frac{\partial^2}{\partial x_i \partial x_j}\frac{\rho(\mathbf{r}')}{|\mathbf{r}-\mathbf{r}'|}\,\mathrm{d}V' \\ &= \iiint\limits_V \Big[\rho(\mathbf{r}')\Big(-\frac{1}{|\mathbf{r}-\mathbf{r}'|^3}\delta_{ij} + 3\frac{(x_i - x_i')(x_j - x_j')}{|\mathbf{r}-\mathbf{r}'|^5}\Big)\Big]\,\mathrm{d}V'\end{aligned} \tag{F.F.12}$$

This integral, however, according to Theorem 4 is in general not defined as the nominator in the first term of the integrand is non vanishing while the denominator varies with $|\mathbf{r}-\mathbf{r}'|^{-3}$. The second term in the integrand varies slower with $\mathbf{r}$ in the limit $r \to 0$. The remedy to this is to force the nominator i.e., $\rho(\mathbf{r}')$ to zero. This can be accomplished by separating the mass density into two components and using the principle of superposition. Moreover, it will prove useful to divide the source space V into three parts.

One seeks a value of the integral by a limit process $\lim_{\delta\to 0}\iiint\limits_{V_\delta} \mathrm{d}V' = \lim_{\delta\to 0}\int_\delta^r \int_0^\pi \int_0^{2\pi} \mathrm{d}r'\,\mathrm{d}\theta'\,\mathrm{d}\phi'$. [2, Ch. 4.8] A small inner sphere σ with radius δ is circumscribing the source point $\mathbf{r}_0$. A larger sphere Σ also with center in $\mathbf{r}_0$ is Hence, $\rho(\mathbf{r}') = \rho_d(\mathbf{r}') + \rho_a(\mathbf{r}')$ where $\rho_d(\mathbf{r}') = \rho_d = \rho(\mathbf{r}_0'), \rho_d(\mathbf{r}) = \rho(\mathbf{r}') - \rho(\mathbf{r}_0')$. As ρ_d is homogeneous all over the sphere we readily see from (F.F.2a) that $\frac{\partial^2}{\partial x_i \partial x_j} U_d(\mathbf{r}) = -\frac{4}{3}\pi\rho\delta_{ij}$. Moreover, we see that in order to evaluate the integral with the vanishing mass distribution at position $\mathbf{r}_0$ it is not sufficient. We must also ensure that the source distribution does not increase to rapidly with r in the neighborhood of $\mathbf{r}_0$. This can be accomplished by assuming that the source distribution satisfy the *Hölder condition*.

Definition F.2. A real-valued function $\rho(\mathbf{r}_1)$ in a metric space (Ω^H, d) of coordinates $\mathbf{r}_1$ is said to satisfy a Hölder continuous or satisfies a Hölder condition at points $P_0(\mathbf{r}_0)$ inside Ω^H, when there are positive real constants A, α, r_H, such that, $\forall \mathbf{r}_1, \mathbf{r}_0 \in \Omega^H, |\rho(\mathbf{r}_1) - \rho(\mathbf{r}_0)| \leq Ad(\mathbf{r}_1, \mathbf{r}_0)^\alpha$.

Remark. The usual Euclidean distance measure is used as metric distance, that is, $|\cdot|$ is applied here. The Hölder condition is stronger than continuity for all positive α and weaker than differentiability if $\alpha < 1$. Here r_H denotes the boundary for the Hölder condition, that is, the distance to the closest point on P_0 where the Hölder condition no longer is satisfied.

From Theorem 4 and Definition F.2 we can now formulate the following Lemma that suits our development

Lemma 1. *Let $V, \mathbf{r}, \mathbf{r}'$ and $\mathrm{d}V', P$ be defined as in Theorem 4 and let $f(\mathbf{r}')$ be a function. Then the integral*

$$\int_V \frac{f(\mathbf{r}')}{|\mathbf{r}-\mathbf{r}'|^\beta}\,\mathrm{d}V' \tag{F.F.13}$$

is convergent if $\gamma = \beta - \alpha$ is a positive constant less than 3.

F.F.5 First-order Derivatives of Space-Time Potential Functions

Now invoking the requirement on Hölder continuity we recognize that

$$\frac{\partial}{\partial x_i'}\boldsymbol{\psi}(\mathbf{r}',t'-|\mathbf{r}-\mathbf{r}'|/c)=\big\{\frac{\partial}{\partial x_i'}\boldsymbol{\psi}\big\}^{(1)}(\mathbf{r}',t'-|\mathbf{r}-\mathbf{r}'|/c)+\big\{\frac{\partial}{\partial x_i'}\boldsymbol{\psi}\big\}^{(2)}(\mathbf{r}',t'-|\mathbf{r}-\mathbf{r}'|/c), \quad \text{(F.F.14)}$$

where

$$\big\{\frac{\partial}{\partial x_i'}\boldsymbol{\psi}\big\}^{(1)}(\mathbf{r}',t'-|\mathbf{r}-\mathbf{r}'|/c)=\frac{\partial}{\partial x_i'}\boldsymbol{\psi}(\mathbf{r}',t)|_{(,t=t'-|\mathbf{r}-\mathbf{r}'|/c)} \quad \text{(F.F.15a)}$$

$$=\frac{\partial}{\partial x_i}\boldsymbol{\psi}(\mathbf{r},t)|_{(\mathbf{r}=\mathbf{r}',t=t'-|\mathbf{r}-\mathbf{r}'|/c)} \quad \text{(F.F.15b)}$$

and

$$\big\{\frac{\partial}{\partial x_i'}\boldsymbol{\psi}\big\}^{(2)}(\mathbf{r}',t'-|\mathbf{r}-\mathbf{r}'|/c)= \quad \frac{\partial}{\partial x_i'}\boldsymbol{\psi}(\mathbf{r},t'-|\mathbf{r}-\mathbf{r}'|/c)|_{(\mathbf{r}=\mathbf{r}',)} \quad \text{(F.F.16a)}$$

$$=-\frac{\partial}{\partial x_i}\boldsymbol{\psi}(\mathbf{r}',t'-|\mathbf{r}-\mathbf{r}'|/c), \quad \text{(F.F.16b)}$$

where the notion $|_{(,t=t'-|\mathbf{r}-\mathbf{r}'|/c)}$ indicates that the second argument is fixed at time $t=t'-|\mathbf{r}-\mathbf{r}'|/c$ while differentiation takes place on the first argument. Likewise $|_{(\mathbf{r}=\mathbf{r}',)}$ indicates that the first argument is fixed at position $\mathbf{r}=\mathbf{r}'$ while differentiation takes place on the second argument. Hence, as the time is fixed in (F.F.15a) this effectively corresponds to the static case and is governed by Kellogg' theorems.

The technique employed is to break up the region of integration into two, such that the integral over the first, say $\int_{V_\delta}$, vanishes with the maximum chord of the region uniformly as to P, and that in the second region, say $\int_{V\setminus V_\delta}$, the integrand is a bounded density times a continuous function for all the coordinates of P and Q. The procedure in the proof is as follows. First the difference in second-order differential between a varying field point and a fixed fields point that coincide with the center of the sphere is established merely be assuming that the differentiation actually can be carried out. Next it is demonstrated that this difference vanishes for $\Delta\mathbf{r}=0$. Then it is shown that the difference exhibits continuity for field points P uniformly approaching the origin at P_0.

Bibliography

[1] Thorkild B. Hansen and Arthur D. Yaghjian. *Plane-Wave Theory of Time-Domain Fields Near-Field Scannng Applications*. IEEE Press Series on Electromagnetic Wave Theory, 1999.

[2] Wilfred Kaplan. *Advanced Calculus*. Addison-Wesley Longman, 5th edition, 2002.

[3] Oliver Dimon Kellogg. *Foundations of Potential Theory*. Dover Publications, Inc., New York, 1929.

[4] H. B. Phillips. *Vector Analysis*. John Wiley & Sons, Inc., New York, 1933.

G. SPHERICAL NEAR-FIELD TESTING

G.1 Introduction

In the antenna community near-field scanning techniques have been used extensively over the past 30 years with the aim of accurately determining the radiation characteristic of an antenna or radar cross section pattern of a scatter. In the acoustical community near-field scanning has primarily been exploited to measure noise source and musical instrument characteristics [29].

In both the electrical and the acoustical domain the field that is measured in the near-field[1] of the antenna, noise source or scatter is transformed to field positions *exterior* to the scan surface. In particular far-field radiation pattern has been obtained in spherical near-field testing (SNFT) facilities [7]. Most of the theoretical framework has been established in the frequency domain where one frequency index is analyzed at the time. With the aim of more efficiently to deal with broad band radar system near-field scanning techniques were formulated for planar scanning [10], [11], [12] and for spherical near-field scanning for electromagnetic fields in the time domain [9]. In acoustics SNFT is relevant for measurement of directional patterns of electroacoustic transducers, e.g., loudspeakers and microphones, but also for the determination of the acoustical scattering properties of various objects. In acoustics the signals are notoriously broad band and noise spikes are often encountered. An advantage of time-domain near-field measurements over frequency-domain near-field measurements is a reduction of the measurement time required for pulsed radiators as wide-band and out of band frequency response can be obtained from a single scan in the time-domain near-field. Moreover, as reported in [12, Ch. 8] measurements errors due to finite size of the scan plane can be removed by *time-gating* with time-domain measurements.

In the related scientific field of *acoustic holography* the use of a finite size scan plan in frequency-domain measurements of a broad-beam noise source may lead to large errors at large angle from broadside [14]. The effects of *scan plane truncation* is completely absent with the SNFT as the measurement surface (sphere) is completely confining the source. The SNFT employs the fact that the antenna radiation may always be expressed in terms of a truncated expansion in electromagnetic spherical waves satisfying Maxwell's equations cf. section F.5 on page 665. Similar considerations apply to acoustical noise emission where the spherical wave expansion is governed by fundamental laws of linear acoustics, that is, the continuity in fluid mass and moment densities cf. section F.3 on page 625. Thus, in this respect, time-domain near-field *spherical* scanning is advantageous over time-domain *planar* near-field scanning. However, the time-domain spherical near-field formulas are much more complicated than the corresponding planar formulas and thus much more difficult to implement.

There has therefore within the acoustic community also been interests to extend spherical near-field scanning to the time-domain [8]. The implementation of time-domain near-field measure-

[1] For highly specialized antennas the scan surface is in the near-field of the antenna. However, the techniques apply also to scan surfaces outside the near-field.

ments in the laboratory has been hindered in the past by the need for rigorous probe-corrected formulation in the time-domain. In a particular application which of the frequency-domain and time-domain methods are in favor depends on the bandwidth of the system. Owing to the availability of mathematical models planar-, circular-cylindrical and spherical surfaces have hitherto almost exclusively been used as scan surface near-field measurements.

In this chapter it will be demonstrated that the software developed for electromagnetic measurements with some effort can be adapted to the acoustical domain.

The following references provide supplementary information relevant for this chapter: [22, Ch. 12], [2, 4–6, 15].

G.2 Spherical Scanning

In Figure G.1 three Cartesian coordinate systems, (x_S, y_S, z_S), (x_A, y_A, z_A) and (x_P, y_P, z_P), for space, the unit under test (UUT) and the probe respectively.

The unit (antenna) coordinate system is aligned with the x_A-, y_A- and z_A-axis pointing in upwards-, port- and aft directions respectively

In spherical antenna measurements the E-Plane is defined as the $\phi = 0$ plane and H-Plane is similarly defined as $\phi = \pi/2$ plane. Referring to Figure G.1 the E-Plane scan corresponds to a θ_A cut (great circle cut) with $\phi_A = 0$. Similarly, the H-Plane scan corresponds to a θ_A cut (great circle cut) with $\phi_A = \pi/2$. In Figure G.1 the scan angles, ψ_1 and ψ_2, that refer to E-Plane and H-Plane angles respectively.

$$\psi_1 = \begin{cases} \theta_A, & \phi_A = 0, \\ \theta_A - \pi, & \phi_A = \pi \end{cases}, \tag{G.2.1a}$$

$$\psi_2 = \begin{cases} \theta_A, & \phi_A = \pi/2, \\ \theta_A - \pi, & \phi_A = 3\pi/2. \end{cases} \tag{G.2.1b}$$

The scan angles will be bounded by $\psi_1, \psi_2 \in [-\pi; \pi]$.

G.3 Scalar Homogeneous Helmholtz Equation in Spherical Coordinates

Acoustical and electromagnetic fields may be expanded into spherical waves in source-free regions of space limited by spherical surfaces centered at the origin of a spherical coordinate system (r, ϑ, φ). The series representations are particular attractive when the directional density function may be adequately represented by a relatively small number of harmonics so that the series terminate after a correspondingly small number of terms.

The scalar homogeneous Helmholtz equation (F.10.2) on page 676 in the scalar field $\psi(r, \vartheta, \varphi)$ is written in spherical coordinates (applicable to any of the spherical coordinate systems in Figure G.1) as

$$\frac{1}{r^2}\frac{\partial}{\partial r}\left(r^2\frac{\partial\psi}{\partial r}\right) + \frac{1}{r^2\sin\vartheta}\frac{1}{\partial\vartheta}\left(\sin\vartheta\frac{\partial\psi}{\partial\vartheta}\right) + \frac{1}{r^2\sin^2\vartheta}\frac{\partial^2\psi}{\partial^2\varphi} + k^2\psi = 0, \tag{G.3.1}$$

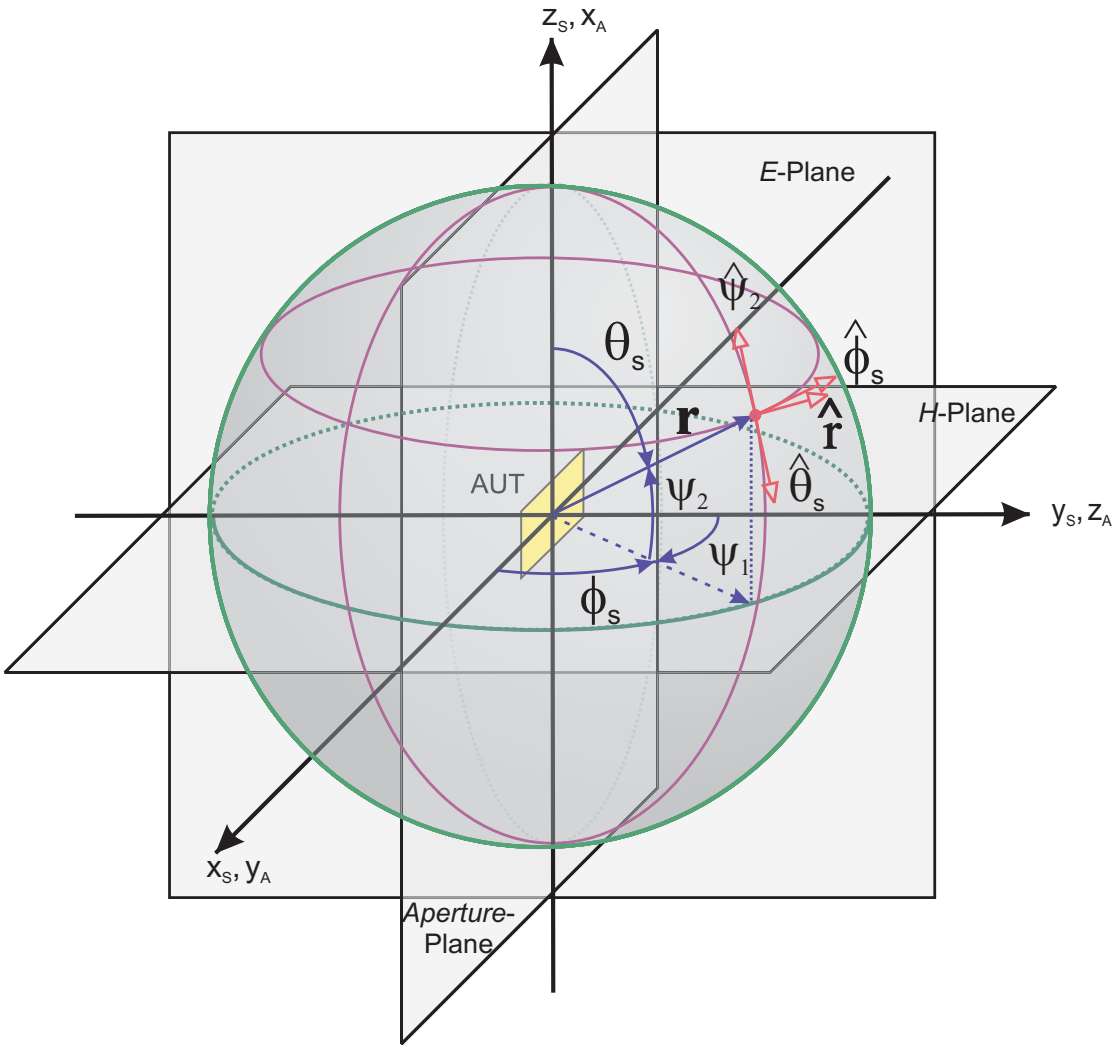

Fig. G.1: Cartesian and Spherical Coordinate Systems, Space and UUT.

where $r = \sqrt{x^2+y^2+z^2}, \vartheta = \tan^{-1}(1/z)\sqrt{x^2+y^2}, \varphi = \tan^{-1}(y/x)$.

The scalar homogeneous Helmholtz equation (G.3.1) separates as follows: $\psi(r,\vartheta,\varphi) = \Xi(r)\Theta(\vartheta)\Phi(\varphi)$,

$$\frac{1}{r^2}\frac{\partial}{\partial r}\left(r^2\frac{\partial \Xi}{\partial r}\right) - \left[k^2 - \frac{n(n+1)}{r^2}\right]\Xi = 0 \tag{G.3.2a}$$

$$\frac{1}{\sin\vartheta}\frac{1}{\partial\vartheta}\left(\sin\vartheta\frac{\partial\Theta}{\partial\vartheta}\right) + \left[n(n+1) - \frac{m^2}{\sin^2\vartheta}\right]\Theta = 0 \tag{G.3.2b}$$

$$\frac{\partial^2\Phi}{\partial^2\varphi} + m^2\Phi = 0, \tag{G.3.2c}$$

where $\Xi(r)$ is the amplitude function of the radius, $\Theta(\vartheta)$ denotes the polar function, $\Phi(\varphi)$ represents the azimthal function respectively.

In the subsequent subsections we will provide more details concerning these separate functions.

G.3.1 Scalar Homogeneous Helmholtz Equation Radial Function

The solution to the radial factor $\Xi(r)$ in (G.3.2a) on the current page is constituted by *spherical Bessel functions* of the first, second, third and fourth kind all of order n [21, Ch. 7.2]. Other names for these functions exist in the literature. The preferred name in this report is found in (G.3.3) on this page.

Following the procedure in [7] we will for the ease of the expressions to come use a common radial function $\Xi_n^{(c)}(r)$ where the upper index (c) specify the kind of the spherical Bessel function. In (G.3.3) the spherical Bessel functions of order n, that is, $j_n(\zeta)$, $n_n(\zeta)$, $h_n^{(1)}(\zeta)$, $h_n^{(2)}(\zeta)$ are listed

$$\Xi_n^{(1)}(\zeta) = j_n^{(}\zeta), \qquad \text{spherical Bessel function,} \tag{G.3.3a}$$

$$\Xi_n^{(2)}(\zeta) = n_n^{(}\zeta), \qquad \text{spherical Neumann function,} \tag{G.3.3b}$$

$$\Xi_n^{(3)}(\zeta) = h_n^{(1)}(\zeta) \quad = j_n(\zeta) + \imath n_n(\zeta), \quad \text{spherical Hankel function of first kind,} \tag{G.3.3c}$$

$$\Xi_n^{(4)}(\zeta) = h_n^{(2)}(\zeta) \quad = j_n(\zeta) - \imath n_n(\zeta), \quad \text{spherical Hankel function of second kind.} \tag{G.3.3d}$$

Hence, the four spherical Bessel functions listed in (G.3.3) are constituted by the spherical Bessel and Neumann functions. Thus, the spherical Hankel functions are constructed from the spherical Bessel and Neumann functions. It is important to note that the upper index (c) for $c = 1$ and $c = 2$ indicates *standing waves*, while $c = 3$ and $c = 4$ represent an *outward traveling wave* and an *inward traveling wave* respectively.

The spherical Bessel function $j_n(\zeta)$ and spherical Neumann function $n_n(\zeta)$ in turn are directly derived from the (ordinary) Bessel function $J_{n+\frac{1}{2}}(\zeta)$ and from the (ordinary) Neumann function $N_{n+\frac{1}{2}}(\zeta)$ both of order $n+\frac{1}{2}$, that is,

$$j_n(\zeta) = \sqrt{\frac{\pi}{2\zeta}} J_{n+\frac{1}{2}}(\zeta), \tag{G.3.4a}$$

$$n_n(\zeta) = \sqrt{\frac{\pi}{2\zeta}} N_{n+\frac{1}{2}}(\zeta). \tag{G.3.4b}$$

G.3.2 Scalar Homogeneous Helmholtz Equation Polar Function

Now turning to the second partial differential equation (G.3.2b) in the polar function $\Theta(\vartheta)$ for which the solutions are the *associated Legendre functions* $P_n^{\breve{m}}(z)$[2] [20, Sec. 10.3]:

$$P_n^{\breve{m}}(\cos\vartheta) = \sin^{\breve{m}}\vartheta T_{n-\breve{m}}^{\breve{m}}(\cos\vartheta), \tag{G.3.5}$$

where $T_\alpha^\beta(z)$ represents *Gegenbauer polynomials* of real parameters α, β. The Legendre functions are finite over the range $0 \leq \vartheta \leq \pi$ only if the order n is an integer that is equal to or greater than $\breve{m}$. Requirements from the solution to the azimuthal function discussed in subsection G.3.3 on the current page necessitates m to take integer values only. Legendre polynomials are closely associated with physical phenomena for which spherical geometry is important. For our purpose, however, both parameters α, β will be zero or take integer values.

The spherical Bessel functions and the associated Legendre functions belong to the class of so-called *special functions* [17] [19, Ch. 6]. Generating functions and recurrence formulas for the Gegenbauer polynomials and the associated Legendre functions can be found, e.g., in [19, Ch. 6]. Generating functions and asymptotic expressions for spherical Bessel functions in the small argument limit ($\zeta \to 0$) or large argument limit ($\zeta \to \infty$) are tabulated in, e.g., [20, Sec. 10.3].

Nowadays, however, C, FORTRAN or MATLAB® based software packages including such special functions are freely available on the World Wide Web (WWW).

$$D(\vartheta,\varphi)Y_n^{\breve{m}}(\vartheta,\varphi) = P_n^{\breve{m}}(\cos\vartheta)\mathrm{e}^{-\imath\breve{m}\varphi}. \tag{G.3.6}$$

The functions $P_n^{\breve{m}}$ are associated Legendre functions and for where $n \in \mathbb{N}$.

G.3.3 Scalar Homogeneous Helmholtz Equation Azimuthal Function

Finally, the solutions of the third partial differential equation (G.3.2c) in the $\Phi(\varphi)$ angle function is readily obtainable as $\cos(\breve{m}\varphi)$ and $\sin(\breve{m}\varphi)$. If no boundaries are along the planes $\varphi =$ constant, requirement of continuity and periodicity of Φ require that $\breve{m} \in \mathbb{N}^*$ where $\mathbb{N}^*$ is the set of 0 and all natural numbers $\mathbb{N}$. In addition as discussed above the Legendre functions $P_n^m(\cos\vartheta)$ are only finite over the range $\varphi \in [0, \pi]$ when $\breve{m} \leq n$. Hence, the upper index $\breve{m}$ takes the values $\breve{m} \in [0, 1, \ldots, n-1, n]$.

The corresponding scalar Laplace's equation is the special case of (G.3.1) where $k = 0$. In this case the radial functions r^n and r^{-n-1} replace the spherical Bessel functions in the solution to $\Xi(r)$ and then no upper limit on $\breve{m}$ exists, that is, $\breve{m} \in \mathbb{N}^*$.

[2] $\breve{m}$ will be used here as m is reserved for a slightly different definition later (G.3.7)

The φ-variation of a mode depends on the azimuthal index $\breve{m}$ which indicates the number of oscillations in the interval $\varphi \in [0, 2\pi)$. For $m \neq 0$ the field of a mode rotates around the z-axis in the positive sense (right-hand) for $m > 0$ and negative sense for $\breve{m} < 0$. The ϑ-variation of a mode depends on both on the polar index n and $\breve{m}$. It has the form of a standing wave with zeros spaced non-equidistantly in the interval $\vartheta \in [0, \pi]$. The zeros are more closely spaced in the neighborhood of the equatorial plane ($\vartheta \approx \pi/2$) than around the poles ($\vartheta \to 0_+, \vartheta \to \pi_-$).

We will also use the exponential form $\mathrm{e}^{\imath m\varphi}$ form instead of the double-index e-mode for $\cos m\varphi$ and o for $\sin m\varphi$ used in [21, Ch. 7]. The exponential form is more convenient in connection with the rotation of spherical waves and the exponential form is more easily adapted to the fast spherical Fourier transform (FSFT). Moreover, expressions using the $\cos, \sin$ formulas are related to the exponential form through the *Euler equation*

$$Y_n^{\breve{m}}(\vartheta, \varphi) = Y_{emn}(\vartheta, \varphi) + \imath Y_{omn}(\vartheta, \varphi) = \mathrm{e}^{\imath m\varphi} P_n^m(\cos\vartheta), \tag{G.3.7}$$

where the upper (azimuthal) index m takes the values $m \in [-n, -n+1, \ldots, 0, \ldots, n-1, n]$.

G.3.4 Scalar Homogeneous Helmholtz Equation Summary

In summary the generating functions (omitting the longitudinal subscript l) can expressed either in $\cos(\,\cdot\,), \sin(\,\cdot\,)$ form or in exponential form as

$$\psi^{(c)}_{\substack{e\\o}\breve{m}n}(r, \vartheta, \varphi) = \Xi_n^{(c)}(kr) P_n^{\breve{m}}(\cos\vartheta) \begin{matrix}\cos\\\sin\end{matrix} \breve{m}\varphi \tag{G.3.8a}$$

$$\psi^{(c)}_{mn}(r, \vartheta, \varphi) = \Xi_n^{(c)}(kr) P_n^{|m|}(\cos\vartheta) \mathrm{e}^{\imath m\varphi}. \tag{G.3.8b}$$

The spherical Hankel functions of the first kind, or any linear combination of them, do not satisfy the homogeneous Helmholtz equation (G.3.1) at $\mathbf{r} = 0$, unless their coefficients are zero and thus $\psi(\mathbf{r}) = 0$. As any field can be decomposed into the sparable spherical-wave solutions that satisfy the Helmholtz equation outside the source region and the outgoing wave condition (F.10.18) have a radial dependence given by spherical Hankel functions of the first kind. This also explains why the uniqueness theorem for the scalar Helmholtz equation.

G.4 Vector Homogeneous Helmholtz Equation in Spherical Coordinates

The eigenfunction solution for the vector Helmholtz equation is obtained from the corresponding scalar equation as discussed in subsection F.11.1. It would prove useful to introduce yet another index s that indicates the $(\mathbf{L}, \mathbf{M}, \mathbf{N})$-type of the vector eigenfunction. We will let s take the value $s = 0, 1$ and 2 in the $\mathbf{L}$, $\mathbf{M}$ and $\mathbf{N}$ cases respectively. Then by insertion in (G.3.8) we get

$$\psi^{(c)}_{\substack{e\\o}\breve{m}n}(r, \vartheta, \varphi) = \Xi_n^{(c)}(kr) P_n^{\breve{m}}(\cos\vartheta) \begin{matrix}\cos\\\sin\end{matrix} \breve{m}\varphi \tag{G.4.1a}$$

$$\psi_{mn^{(c)}}(r, \vartheta, \varphi) = \Xi_n^{(c)}(kr) P_n^{|m|}(\cos\vartheta) \mathrm{e}^{\imath m\varphi}. \tag{G.4.1b}$$

G.4.1 Field Decomposition

The individual components in turn can be found from (G.3.8a) on the facing page for the $\frac{\cos}{\sin} m\varphi$ which is also provided in [27, Sec. 7.11]. However, we will proceed with the $\mathrm{e}^{\imath m\varphi}$ form.

From subsection F.11.1 the scalar fields ψ_L, ψ_M and ψ_N coincide and are identical to the free-space solution $\psi(\mathbf{r})$. We will need the gradient operator expressed in spherical coordinates

$$\nabla\psi(\mathbf{r}) = \hat{\mathbf{r}}\frac{\partial\psi(\mathbf{r})}{\partial r} + \frac{\hat{\boldsymbol{\vartheta}}}{r}\frac{\partial\psi(\mathbf{r})}{\partial\vartheta} + \frac{\hat{\boldsymbol{\vartheta}}}{r\sin\varphi}\frac{\partial\psi(\mathbf{r})}{\partial\varphi}. \tag{G.4.2}$$

Then be applying (F.11.6) on page 681 to (G.3.8b) using (G.4.2) we readily obtain

$$\begin{aligned}\mathbf{l}_{mn}^{(c)}(r,\vartheta,\varphi) &= \nabla\psi(\mathbf{r})\\ &= \frac{\mathrm{d}}{\mathrm{d}r}\Xi_n^{(c)}(kr)P_n^{|m|}(\cos\vartheta)\mathrm{e}^{\imath m\varphi}\hat{\mathbf{r}}\\ &\quad+\frac{1}{r}\Xi_n^{(c)}(kr)\frac{\mathrm{d}}{\mathrm{d}\vartheta}P_n^{|m|}(\cos\vartheta)\mathrm{e}^{\imath m\varphi}\hat{\boldsymbol{\vartheta}}\\ &\quad+\frac{\imath m}{r\sin\vartheta}\Xi_n^{(c)}(kr)P_n^{|m|}(\cos\vartheta)\mathrm{e}^{\imath m\varphi}\hat{\boldsymbol{\varphi}},\end{aligned} \tag{G.4.3}$$

$$\begin{aligned}\mathbf{m}_{mn}^{(c)}(r,\vartheta,\varphi) &= \nabla\times(r\psi_M(\mathbf{r})\hat{\mathbf{r}})\\ &= \nabla(r\psi_M(\mathbf{r}))\times\hat{\mathbf{r}}\\ &= \frac{\imath m}{\sin\vartheta}\Xi_n^{(c)}(kr)P_n^{|m|}(\cos\vartheta)\mathrm{e}^{\imath m\varphi}\hat{\boldsymbol{\vartheta}}\\ &\quad-\Xi_n^{(c)}(kr)\frac{\mathrm{d}}{\mathrm{d}\vartheta}P_n^{|m|}(\cos\vartheta)\mathrm{e}^{\imath m\varphi}\hat{\boldsymbol{\varphi}},\end{aligned} \tag{G.4.4}$$

and

$$\begin{aligned}\mathbf{n}_{mn}^{(c)}(r,\vartheta,\varphi) &= \frac{1}{k}\nabla\times\nabla\times(r\psi_N(\mathbf{r})\hat{\mathbf{r}})\\ &= kr\psi_N(\mathbf{r})\hat{\mathbf{r}} + \frac{1}{k}\nabla\left(\frac{\partial(r\psi_N(\mathbf{r}))}{\partial r}\right)\\ &= \frac{n(n+1)}{kr}\Xi_n^{(c)}(kr)P_n^{|m|}(\cos\vartheta)\mathrm{e}^{\imath m\varphi}\hat{\mathbf{r}}\\ &\quad+\frac{1}{kr}\frac{\mathrm{d}}{\mathrm{d}(kr)}\big(kr\Xi_n^{(c)}(kr)\big)\frac{\mathrm{d}P_n^{|m|}(\cos\vartheta)}{\mathrm{d}\vartheta}\mathrm{e}^{\imath m\varphi}\hat{\boldsymbol{\vartheta}}\\ &\quad+\frac{1}{kr}\frac{\mathrm{d}}{\mathrm{d}(kr)}\big(kr\Xi_n^{(c)}(kr)\big)\frac{\imath mP_n^{|m|}(\cos\vartheta)}{\sin\vartheta}\mathrm{e}^{\imath m\varphi}\hat{\boldsymbol{\varphi}}.\end{aligned} \tag{G.4.5}$$

Then the electrical field is obtained as the sum over the fourfold set of spherical generating functions

$$\mathbf{E}(r,\vartheta,\varphi) = \sum_{c=3}^{4}\sum_{s=1}^{2}\sum_{n=1}^{\infty}\sum_{m=-n}^{n} Q_{smn}^{(c)}\mathbf{F}_{smn}^{(c)}(r,\vartheta,\varphi). \tag{G.4.6}$$

where the fourfold set of excitation coefficients owing to mutual orthogonality can be found by integration over the sphere

$$Y_n^m(\vartheta,\varphi) = \sqrt{\frac{2n+1}{4\pi}\frac{(n-m)!}{(n+m)!}} P_n^m(\cos\vartheta)\mathrm{e}^{-\imath m\varphi} \tag{G.4.7}$$

$$C_{n_\omega}^m = \int_0^{2\pi}\int_0^{\pi} p_\omega(a\hat{r})(Y_n^m)^*(\vartheta,\varphi)\sin\vartheta\,\mathrm{d}\vartheta\,\mathrm{d}\varphi. \tag{G.4.8}$$

Since the series of (G.4.6) has an infinite number of nonzero terms, the spatial harmonic expansion is not a very efficient way of representing a single plane wave.

In [7] the following empirical formula for the number of spherical harmonics required in the expansion is provided.

$$N = \lfloor ka \rfloor + n_1, \tag{G.4.9}$$

where the quantity n_1 depends on the application. However, as both the electromagnetic and acoustical domain shares concepts such as orthogonal modes, cut-off, propagation, evanescent-, Fresnel- and Fraunhofer regions, it then seems not unreasonable to expect the truncation constant N defined in (G.4.9) also to be representative in acoustic SNFT measurements. Moreover, as stated in [7, Ch. 2] the spherical wave expansions of different source distributions show similar behavior. In SNFT measurements a is the radius of the minimum sphere. In the case of the confined feedforward (CFF) topology a represents the radius of the confining sphere. The "floor" operator $\lfloor(\,\cdot\,)\rfloor$ takes the largest integer smaller than or equal to its argument.

G.4.2 Transmission

In SNFT the main problem is to determine receiving and transmitting coefficients for an antenna from measurements in its near-field. In SNFT measurement errors due to various imperfections such as non-perfect polarization of the probes, finite mechanical alignment accuracy, receiver nonlinearity and drift must be assessed. In particular the influence of omitting probe correction should be considered. Another question is then to what extent such error sources will influence the performance of an active control system?

The following *transmission formula* is obtained

$$w(A,\chi,\theta,\phi) = \sum_{\substack{smn\\ \mu=\pm1}} vT_{smn}\mathrm{e}^{\imath m\phi} d_{\mu m}^n(\theta)\mathrm{e}^{\imath\mu\chi} P_{s\mu n}(kA), \tag{G.4.10}$$

where we for notational convenience have replaced $\sum_{c=3}^{4}\sum_{s=1}^{2}\sum_{n=1}^{\infty}\sum_{m=-n}^{n}$ by $\sum_{\substack{smn\\ \mu=\pm1}}$ and where the accumulated index J in turn is defined by

$$J = 2N(N+2) \tag{G.4.11}$$

The quantities $P_{s\mu n}(kA)$ where J_θ where J_ϕ

In the subsequent text we will describe the operation involved in determining the field $\mathbf{F}^{(c_e)}_{s_e m_e n_e}(r_e, \theta_e, \phi_e)$ on a spherical surface that we will refer to as a performance sphere denoted by S^p from the field $\mathbf{F}^{(c_x)}_{s_x m_x n_x}(r_x, \theta_x, \phi_x)$ at the positions of the reference sensors.

Note, that an arbitrary sphere S^a with coordinates (r_a, θ_a, ϕ_a) can be projected into another arbitrary sphere S^b from with coordinates (r_b, θ_b, ϕ_b) by succession of three operations: rotation, translation and expansion/compression. The translation operation in general involve translation along all three axis.

G.4.3 Translation of Spherical Waves

From [7, App. A.3] a spherical wave vector function $F^{(c_1)}_{s_1 m_1 n_1}(r_1, \theta_1, \phi_1)$ upon translation along the z-axis can be expressed in the new rectangular coordinates (r_2, θ_2, ϕ_2) as the sum of a $s_2 = 1$ mode and a $s_2 = 2$ mode

$$\mathbf{F}^{(c_2)}_{s_2 m_2 n_2}(r_2, \theta_2, \phi_2) = \sum_{s_1=1}^{s_1=2} \sum_{\substack{n_1=|m_1| \\ n_1 \neq 0}}^{\infty} C^{s_2 n_2 (c)}_{s_1 m_1 n_1}(kA) \mathbf{F}^{(c_1)}_{s_1 m_1 n_1}(r_1, \theta_1, \phi_1). \tag{G.4.12}$$

From [7, App. A.3] we have find the following expression for the translation coefficients with positive arguments

$$\begin{aligned} C^{s_2 m_2 n_2 (c)}_{s_1 m_1 n_1}(kA) = {} & \sqrt{\frac{(2n_2+1)(2n_1+1)}{n_2(n_2+1)n_1(n_1+1)}} \sqrt{\frac{(n_1+m_1)!(n_2-m_1)!}{(n_1-m_1)!(n_2+m_1)!}} (-1)^{m_1} \tfrac{1}{2} \imath^{n_2-n_1} \\ & \sum_{p=|n_2-n_1|}^{n_2+n_1} \Big[\imath^{-p} \Big(\delta_{s_1 s_2} \big(n_2(n_2+1) + n_1(n_1+1) - p(p+1) \big) + \delta_{3-s_2, s_1} (2\imath m_1 kA) \Big), \\ & \qquad a(m_1, n_2, -m_1, n_1, p) z^{(c)}_p(kA) \Big] \end{aligned} \tag{G.4.13}$$

where the spherical Bessel function orders $\breve{c}_F$ and $\breve{c}_C$ warrant finite solution in the (r_1, θ_1, ϕ_1) and (r_2, θ_2, ϕ_2) rectangular coordinates respectively. These spherical Bessel function orders are in turn defined by

$$\breve{c}_F = \begin{cases} 1, & r_1 < |A| \\ c, & r_1 > |A| \end{cases} \tag{G.4.14}$$

and

$$\breve{c}_C = \begin{cases} c, & r_1 < |A| \\ 1, & r_1 > |A| \end{cases} \tag{G.4.15}$$

respectively. The linearization coefficient $a(m_1, n_2, -m_1, n_1, p)$ in (G.4.13) is determined from

$$a(m_1, n_2, -m_1, n_1, p) = (2p+1) \sqrt{\frac{(n_2+m_1)!(n_1-m_1)!}{(n_2-m_1)!(n_1+m_1)!}} \begin{pmatrix} n_2 & n_1 & p \\ 0 & 0 & 0 \end{pmatrix} \begin{pmatrix} n_2 & n_1 & p \\ m_1 & -m_1 & 0 \end{pmatrix}. \tag{G.4.16}$$

For negative translation ($kA < 0$) we can use the following formula

$$C_{s_1 m_1 n_1}^{s_2 m_2 n_2 (c)}(-kA) = C_{s_2,-m_1,n_2}^{s_2 m_2 n_2 (c)}(kA). \tag{G.4.17}$$

However, it should also remarked that arbitrary translations may be accomplished by successive rotation, axial translation, and inverse rotation.

G.5 Fast Spherical Fourier Transform Techniques

In recent years some mathematical development in field of spherical harmonics and in particular an exploitation of the processing capabilities provided by the FSFT has been made [1, 13, 16, 18, 28]. Practical applications include *spherical microphone arrays* [3, 23–26].

Bibliography

[1] J. R. Driscoll and D.M. Healy. Computing fourier transforms and convolutions on the 2-sphere. *Adv. in Appl. Math*, 15:202–240, 1994.

[2] S. J. Elliott and J. García-Bonito. Active cancellation of pressure and pressure gradient in a diffuse sound field. *Journal of Sound and Vibration*, 186(4):696–704, 1995.

[3] N. Epain and E. Friot. Active control of sound inside a sphere via control of the acoustic pressure at the boundary surface. *Journal of Sound and Vibration*, 299:587–604, 2007.

[4] J. García-Bonito and S. J. Elliott. Local active control of diffracted diffuse sound fields. *JASA*, 98(2):1017–1024, 1995.

[5] J. García-Bonito and S. J. Elliott. Active cancellation of acoustic pressure and particle velocity in the near field of a source. *Journal of Sound and Vibration*, 221(1):85–116, 1999.

[6] J. García-Bonito, S. J. Elliott, and C. C. Boucher. Generation of zones of quiet using a virtual microphone arrangement. *JASA*, 101(6):3498–3516, 1997.

[7] Jørgen Hald, Jesper E. Hansen, and Flemming Holm Larsen. *Spherical Near-Field Antenna Measurements*. Peragamon Press, 1988.

[8] Thorkild B. Hansen. Spherical expansions of time-domain acoustic fields: Application to near-field scanning. *JASA*, 98(2):1204–1215, 1995.

[9] Thorkild B. Hansen. Formulation of spherical near-field scanning for electromagnetic fields in the time domain. *IEEE Transactions on Antennas and Propagation*, 45(4):620–630, 1997.

[10] Thorkild B. Hansen and Arthur D. Yaghjian. Planar near-field scanning in the time domain. part 1: Formulation. *IEEE Transactions on Antennas and Propagation*, 42:1280–1291, 1994.

[11] Thorkild B. Hansen and Arthur D. Yaghjian. Planar near-field scanning in the time domain. part 2: Sampling theorems and computation schemes. *IEEE Transactions on Antennas and Propagation*, 42:1292–1300, 1994.

[12] Thorkild B. Hansen and Arthur D. Yaghjian. *Plane-Wave Theory of Time-Domain Fields Near-Field Scannng Applications*. IEEE Press Series on Electromagnetic Wave Theory, 1999.

[13] R. H. Hardin and N. J. A. Sloane. Mclaren's improved snub cube and other new spherical designs in three dimensions. *Discrete and Computational Geometry*, 15:429–441, 1996.

[14] Finn Jacobsen and Yang Liu. Near field acoustic holography with particle velocity transducers. *The Journal of the Acoustical Society of America*, 118(5):3139–3144, 2005.

[15] M. E. Johnson, S. J. Elliott, K-H. Baek, and J. Garcia-Bonito. An equivalent source technique for calculating the sound field inside an enclosure containing scattering objects. *The Journal of the Acoustical Society of America*, 104(3):1221–1231, 1998.

[16] D.M. Healy Jr., D.N. Rockmore, P.J. Kostelec, and S. Moore. FFTs for the 2-sphere-improvements and variations. *Journal of Fourier Analysis and Application*, 9(4):341–385, 2003.

[17] N. N. Lebedev and Richard R. Silverman. *Special Functions & Their Applications*. Dover Publications, Inc., New York, 1965.

[18] Martin J. Mohlenkamp. A fast transform for spherical harmonics. *Journal of Fourier Analysis and Application*, 5(2-3):159–184, 1999.

[19] Philip M. Morse and Herman Feshbach. *Methods of Theoretical Physics*, volume 1. Feshbach Publishing LLC., 1953.

[20] Philip M. Morse and Herman Feshbach. *Methods of Theoretical Physics*, volume 2. Feshbach Publishing LLC., 1953.

[21] Philip M. Morse and K. Uno Ingard. *Theoretical Acoustics*. Princeton University Press Princeton New Jersey, 1968.

[22] Philip A. Nelson and Stephen J. Elliott. *Active Control of Sound*. Academic Press, 1992.

[23] Munhum Park and Boaz Rafaely. Sound-field analysis by plane-wave decomposition using spherical microphone array. *The Journal of the Acoustical Society of America*, 118(5):3094–3103, 2005.

[24] Boaz Rafaely. Plane-wave decomposition of the sound field on a sphere by spherical convolution. *The Journal of the Acoustical Society of America*, 116(4):2149–2157, 2004.

[25] Boaz Rafaely. Phase-mode versus delay-and-sum spherical microphone array processing. *IEEE Signal Processing Letters*, 12(10):713–716, 2005.

[26] Boaz Rafaely. Analysis and design of spherical microphone arrays. *IEEE Transactions on Speech and Audio Processing*, 13(1):135–143, 2005.

[27] J. A. Stratton. *Electromagnetic Theory*. McGraw Hill New York, 1941.

[28] Benjamin D. Wandelt and Krzysztof M. Górski. Fast convolution on the sphere. *Phys.Rev.*, D63(123002), 2001.

[29] Gabriel Weinreich and Eric B. Arnold. Method for measuring acoustic radiation fields. *JASA*, 68(2):404–411, 1980.

H. APPLIED ACTIVE CONTROL OF FIELDS

H.1 Introduction

The study of the underlying physics of a system subject to active control (AC) is indeed important. Since, no matter the sophistication of the control hardware employed and the amount of control software written pure physical considerations based on *field theory* might reveal that the desired solution will be deemed to be unsuccessful.

In the design of an AC system it is therefore important at an early stage in design cycle to assess the physical environment involved. Hence, the analysis should provide a clear picture of whether we are reasonable in our expectations to the capabilities of the control system or if we are acting to much against the laws of physics.

In AC two sets of sources are considered. The primary sources represent the unwanted disturbances that in general are out of control by the system designer. The primary noise sources are assumed to be entirely confined to positions exterior to the control volume $\mathcal{V}^C$. The secondary sources, however, provides the designer with a "hook" to excite secondary fields. Then by an appropriate choice of distribution and excitation of the secondary sources a superposition of equal amplitude but inverse phase signals a finite zone of quiet is established.

The design of an active noise control system involves several design steps. One of the more important steps is to determine the number of reference sensors required and to find the best location of these with respect to the spatial distribution of the primary sources and their spectra and the position and size of the zones of quite. For example, in AC of sound insufficient spatial sampling will preclude successful operation of the system at higher frequencies [32], which is also evident from chapter 2 - 3. For the actuators the number must not be to costly prohibitive and their excitation within their linear dynamic range.

Moreover, in practical active noise reduction (ANR) systems the control volumes might be subject to translational movements as well as angular rotations, that is, in *roll*, *pitch* and *jaw*. In addition some of the primary sources might change position. Hence, the system should be capable of operating in a space-time-varying environment where the relative positions of primary sources and control volumes vary with time. Moreover, the control volumes may or may not change positions relative to the secondary sources. These considerations of course will be application dependent.

For some time feedforward AC has been applied for the duct case where only two directions of propagation exist. Accordingly, a reference sensor can be positioned upstream and thereby provide time-advance information concerning the direct (as opposed to reflected) field. In the general case, however, the noise sources are uniformly distributed at least in the horizontal plane. As a consequence no open and shut feedforward reference sensor position exists. With the ordinary feedforward multi-channel topology some of the reference sensors will therefore provide

time-advance information for some of the noise sources while providing time-delayed information regarding other noise sources. When applying the confined feedforward (CFF) topology a sufficient amount of reference sensors shall be used and positioned such that time-advance information independently of the spatial distribution of the noise sources is provided. In addition the number of reference sensors required is determined by the level of spatial aliasing that can be tolerated. Or stated in other words the multiple coherence function (MCOF) must exceed a value determined by the requirement on ANR performance cf. chapter 2 and Appendix A.

A practical example where the considerations made above are of profound importance is in ANR *active headrest* applications. A headrest with active noise control (ANC) can supposedly be build into the headrest of passenger seat in an aircraft or train thereby leading to improved convenience. Numerous investigations of the acoustical field properties in *active headrest* applications have been made [13, 20, 21, 36].

An important performance figure is the *zone of quiet* which is the physical volume where the ANR system yields an attenuation of the sound pressure above a certain specified level. It is to a first-order approximation found that the spatial extent of zone of quite in pure-tone diffuse sound field $d^{QZ}_{10\text{ dB}}$ for a single secondary source is approximate of ten'th of a wavelength where the field points are assumed to follow an arc with center at the position of the secondary source. Rafaely [35] by means of simulations found that $d^{QZ}_{10\text{ dB}} \approx 0.088\lambda$.

This chapter addresses the problem of causal prediction of sound fields in a control volume from sampled field point on a surface entirely covering the volume. Expressions in both the time domain and the frequency domain will be provided. In particular, existing spherical near-field techniques from Appendix G are adapted to cases where the sources are positioned outside the spherical scan surface and time-domain field for which the interior field *inside* the sphere can be determined. One of the advantage of spherical expansion is that it can be applied to any primary field.

H.1.1 Chapter Outline

In section H.2 the reference test unit (RTU) that supposedly constitute a framework for the test and evaluation of methods and techniques developed for active control of sound and vibration (ACSV) systems will be developed. Then in section H.3 the problem related to AC of whether either primary, secondary sources or control volumes are subject to dynamic movements is considered.

H.2 Reference Test Unit

The aim of the RTU is to provide a highly accurately modeled framework with which reliable and accurate tests and evaluations of the developed theories and methods can take place. For the development of a RTU for AC purposes an acoustical transparent sphere and an acoustical semi-transparent-semi-opaque hollow sphere are considered. In Figure H.2 a prototype RTU that is an acoustical semi-transparent-semi-opaque hollow sphere is shown.

This RTU will be exposed to high sound pressure levels. Most of the energy incident on the sphere is reflected. A fraction of the incident energy, however, excites the spherical shell into vibrations which in turn leads to excitation of a sound field that is being radiated into the interior of the sphere. A number of reference sensors positioned at the *inner* surface of the shell sense that part

Fig. H.1: RTU in Noise Chamber Facility.

of the primary field that is leaked into the interior of the sphere. To a first order this hollow sphere can be considered as a *spherical waveguide* which was rigorously described in Appendix G.

It is well known in local AC applications that the near-field characteristics of the secondary source are very important in determining the zone of quiet. For mathematical ease a monopole or a piston in an infinite baffle are often used as sound source models. For the RTU design a monopole that can be place arbitrarily within the sphere will be used as secondary source.

Accordingly we have a system where both the primary (leakage) field and the secondary field and therefore also the total field can rigourously be determined.

A few error sensors will be installed thereby making provision for performance feedback for use in an AC system test like for instance the hybrid MIMO confined-feedforward-feedback system (HMIMOCFFFBS). One or two performance sensors positioned within an interior volume that will be considered as a zone of quite act to evaluate and verify the achieved performance.

H.3 Non-stationary Primary, Secondary Source and Control Volume Positions in Space

H.3.1 Moving Primary Noise Sources

This subject has previously been analyzed by Martin [28]. In this work an AC screen composed of groups (masts) of secondary sources is investigated. The purpose of the system is to obtain attenuation of noise originating from airplanes landing or taking off, trains and cars etc. within a control volume in the vicinity of the screen. As is well known ANR performance is sensitive to secondary source position relative to the primary source. This study confirmed that some of the masts yield better attenuation than others depending on the relative position of the noise source. Basically, the mast which viewed from the center of the control area is the most aligned in azimuth with the noise source can provide the highest attenuation. For the individual secondary sources within the group it is more difficult to draw any conclusions as *lobing* effects occur due to the presence of both incident and reflected waves. The adaptive processing scheme involved adaptation of each mast. In each group of secondary sources the adaptive filtered signal is feed to each of the members of the group. Only numerical experiments under rather ideal conditions i.e., no scattering objects constant velocity target moving on a straight line were made. In might be possible to track the primary noise source and choose and appropriate control strategy.

H.3.2 Moving Control Volumes

The control volume might be subject to both translatoric movements as well as time-variant angular coordinates, that is, roll, pitch and yaw movements.

H.3.3 Moving Secondary Noise Sources

The following papers are considered relevant for the completion of this design:

[23] [4] [2] [31] [32] [15] [12] [16] [14] [19] [29] [37] [34] [26] [27] [30] [1] [24] [10] [22] [17] [33] [9] [8] [5] [7] [3] [6] [25] [10] [22] [18] [11] [38].

Fig. H.2: RTU in Noise Chamber Facility. Measurement of transmission loss.

Bibliography

[1] Christer Ahlstrom, Olle Liljefeldt, Peter Hult, and Per Ask. Heart sound cancellation from lung sound recordings using recurrence time statistics and nonlinear prediction. *IEEE Signal Processing Letters*, 12(12):812–815, 2005.

[2] K. H. Baek and S. J. Elliott. The effects of plant and disturbance uncertainties in active control systems on the placement of transducers. *Journal of Sound and Vibration*, 230(2): 261–289, 2000.

[3] Julius S. Bendat. Modern analysis procedures for multiple input/output problems. *JASA*, 68(2):1655–1687, 1980.

[4] K. Brod. On the uniqueness of solution for all wavenumbers in acoustic radiation. *JASA*, 76(4):1238–1243, 1984.

[5] James A. Cadzow and Otis M. Solomon. Linear modeling and the coherence function. *IEEE Transactions on Acoustics, Speech, and Signal Processing*, 35(1):19–28, 1987.

[6] A. C. Callahan. Coherence and maximum likelihood multiple receiver signal detection. *IEEE Transactions on Acoustics, Speech, and Signal Processing*, 29(3):447–448, 1981.

[7] J. Y. Chung, Malcolm J. Crocker, and James F . Hamilton. Measurement of frequency responses and the multiple coherence function of the noise-generation system of a diesel engine. *JASA*, 58(3):635–642, 1975.

[8] Axel Clausen. Asymptotic analysis of the generalized coherence estimate. *IEEE Transactions on Signal Processing*, 49(1):45–53, 2001.

[9] Axel Clausen and Douglas Cochran. An invariance property of the generalized coherence estimate. *IEEE Transactions on Signal Processing*, 45(4):1065–1067, 1997.

[10] Douglas Cochran, Herbert Gish, and Dana Sinno. A geometric approach to multiple-channel signal detection. *IEEE Transactions on Signal Processing*, 43(9):2049–2057, 1995.

[11] M. De Diego and A. Gonzalez. Performance evaluation of multichannel adaptive algorithms for local active noise control. *Journal of Sound and Vibration*, 244(4):615–634, 2001.

[12] S. J. Elliott and J. García-Bonito. Active cancellation of pressure and pressure gradient in a diffuse sound field. *Journal of Sound and Vibration*, 186(4):696–704, 1995.

[13] Stephen J. Elliott, P. Joseph, A. J. Bullmore, and Philip A. Nelson. Active cancellation at a point in a pure tone diffuse sound field. *Journal of Sound and Vibration*, 120(1):183–189, 1988.

[14] J. García-Bonito and S. J. Elliott. Local active control of diffracted diffuse sound fields. *JASA*, 98(2):1017–1024, 1995.

[15] J. García-Bonito and S. J. Elliott. Active cancellation of acoustic pressure and particle velocity in the near field of a source. *Journal of Sound and Vibration*, 221(1):85–116, 1999.

[16] J. García-Bonito, S. J. Elliott, and C. C. Boucher. Generation of zones of quiet using a virtual microphone arrangement. *JASA*, 101(6):3498–3516, 1997.

[17] Herbert Gish and Douglas Cochran. Invariance of the magnitude-squared coherence estimate with respect to second-channel statistics. *IEEE Transactions on Acoustics, Speech, and Signal Processing*, 35(12):1774–1776, 1987.

[18] K. Hiramoto, H. Doki, and G. Obinata. Optimal sensor/actuator placement for active vibration control using explicit solution of algebraic riccati equation. *Journal of Sound and Vibration*, 229(5):1057–1075, 2000.

[19] M. E. Johnson, S. J. Elliott, K-H. Baek, and J. Garcia-Bonito. An equivalent source technique for calculating the sound field inside an enclosure containing scattering objects. *The Journal of the Acoustical Society of America*, 104(3):1221–1231, 1998.

[20] P. Joseph, Stephen J. Elliott, and Philip A. Nelson. Statistical aspects of active control in harmonic enclosed sound fields. *Journal of Sound and Vibration*, 172(5):629–655, 1994.

[21] P. Joseph, Stephen J. Elliott, and Philip A. Nelson. Near field zones of quiet. *Journal of Sound and Vibration*, 172(5):605–627, 1994.

[22] Steven M. Kay, Albert H. Nuttall, and Paul M. Baggenstoss. Multidimensional probability density function approximations for detection, classification, and model order selection. *IEEE Transactions on Signal Processing*, 49(10):2240–2252, 2001.

[23] Gary H. Koopmann, Limin Song, and John B. Fahnlin. A method for computing acoustic fields based on the principle of wave su perposition. *JASA*, 86(6):2433–2438, 1989.

[24] Richard J. Kozick and Brian M. Sadler. Source localization with distributed sensor arrays and partial spatial coherence. *IEEE Transactions on Signal Processing*, 52(3):601–616, 2004.

[25] Geetha Krishnan and Mark E. Chertoff. Insights into linear and nonlinear cochlear transduction: Application of a new system-identification procedure on transient-evoked otoacoustic emissions data. *JASA*, 105(2):770–781, 1999.

[26] T. Martin and A. Roure. Optimization of an active noise control system using spherical harmonics expansion of the primary field. *Journal of Sound and Vibration*, 201:577–593, 1997.

[27] T. Martin and A. Roure. Active noise control of acoustics sources using spherical harmonics expansion and genetic algorithm: Simulation and experiment. *Journal of Sound and Vibration*, 212(3):511–523, 1998.

[28] V. Martin. Active control of moving sound source radiation-numerical modelling in the space-frequency and space-time domains. *Journal of Sound and Vibration*, 228(3):477–509, 1999.

[29] V. Martin and C. Gronier. Sensor configuration efficiency and roubstness against spatial error in the primary field for active sound control. *Journal of Sound and Vibration*, 246(4): 679–704, 2001.

[30] Antonio Mauricio, F. L. Miranda de Sá, Leonardo B. Felix, and Antonio Fernando C. Infantosi. A matrix-based algorithm for estimating multiple coherence of a periodic signal and its application to the multichannel eeg during sensory stimulation. *IEEE Transactions on Biomedical Engineering*, 51(7):1140–1146, 2004.

[31] P.A. Nelson, J.K. Hammond, P. Joseph, and S.J. Elliott. Active control of stationary random sound fields. *JASA*, 87(3):963–975, 1990.

[32] Philip A. Nelson. Active control of aoustic fields and the reproduction of sound. *Journal of Sound and Vibration*, 177(4):447–477, 1994.

[33] A. H. Nutall. Invariance of distribution of coherence estimate to second-channel statistics. *IEEE Transactions on Acoustics, Speech, and Signal Processing*, ASSP-29(1):120–122, 1981.

[34] X. Qiu and C. H. Hansen. Secondary acoustic source types for active noise control in free field: Monopoles or multipoles? *Journal of Sound and Vibration*, 232(5):1005–1009, 2000.

[35] Boaz Rafaely. Zones of quiet in a broadband diffuse sound field. *The Journal of the Acoustical Society of America*, 110(1):296–302, 2001.

[36] Boaz Rafaely, Stephen J. Elliott, and J. Garcia-Bonito. Broadband performance of an active headrest. *The Journal of the Acoustical Society of America*, 106(2):787–793, 1999.

[37] J. E. Ffowcs Williams. Active flow control. *Journal of Sound and Vibration*, 239(4):861–871, 2001.

[38] Lawrence Ziomek. *Fundamentals of Acoustic Field Theory and Space-Time Signal Processing*. CRC Press, 1994.

Part VI

ADAPTIVE FILTERS FOR ACTIVE NOISE CONTROL II

I. ADAPTIVE FILTER TOPOLOGY

I.1 Introduction

In chapter 7 on page 291 a detailed discussion of the topology of multi-channel adaptive control system was conducted. The specific adaptive filtering schemes were introduced in chapter 8. In this chapter we will proceed with a discussion of the topology of the candidate adaptive filters involved. In the signal processing literature numerous *adaptive filter* topologies can be found. The topologies encompass a large range of adaptive filters of varying complexity, performance and varying degree of implementation ease. Some topologies have been developed with a specific application in mind others are more general purpose filters.

In general two different main categories of adaptation schemes referred to as *open-loop* and *closed-loop* adaptation respectively exist [18, Ch. 1]. In this report all adaptive filtering implementation will be based on the close-loop category. This choice has been made because in all of the four applications modes of adaptive filters presented on page 373, performance cannot be deduced analytically exclusive from input data. Therefore, the output is feedback to the adaptation process. This approach is also referred to as *performance feedback*. However, the closed-loop adaptation in general can be an uncertain process related to performance functions that do not have unique optima. Moreover, a close-loop configuration could be associated with instability problems. The uniqueness problem can often be solved by formulating an appropriate performance function associated with the chosen filter topology. By confining poles to the unit disc and by constraining the adaptation rate of the filter potential problems of instability can be avoided.

In the present chapter we exclusively focus on *causal linear discrete-time filters*. The requirement on *causality* stems from requirement on real-time operation.

The choice of linear filters as opposed to non-linear filters is, however, not always optimal. System imperfections imply that some inherent non-linearities will prevail and limit maximum achievable performance from the use of a pure linear adaptive filter. In active control non-linearities are typically experienced for an actuator, e.g., an earphone transducer driven at high control output levels at low frequencies. The field of active non-linear control, however, is considered outside the scope of the report. It suffice here to state the nonlinear adaptive filtering and control lead to severe complication of the theory.

For all four applications modes of adaptive filters listed on page 373 the primary choice of filter topology in the literature has been a finite-duration impulse response (FIR) filter. This choice also pertains to the active control community as regards the controller, but also as regards the model of the secondary paths and feedback paths as discussed in chapter 6. The choice of a FIR filter can be attributed to its simplicity and stability. An other important point is that a linear system can unambiguously be described in terms of its impulse response or equivalently its frequency transfer function [12]. However, we will also investigate other adaptive filter topologies

for active control applications.

The main advantage of a FIR filter as compared with an infinite-duration impulse response (IIR) filter is that the latter suffers from potential instability problems associated with the inherent feedback structure. Moreover, requirements on adaptivity further increases the potential of instability of an IIR filter. From computational considerations, however, the IIR filter is less demanding. In recent years attention has been made to the class of so-called *orthonormal filters* that are a subset of the full-blown IIR filter structure. The orthonormal filters retain most of general modeling capability provided by the full-blown IIR filter structure while preserving stability during filter adaptation. This is achieved by using fixed poles and adapting the zeros.

For each of the adaptive filters different realization methods are available. Among such realizations we find the *direct form* (as opposed to *indirect form*), *parallel*, *cascade* and *lattice* forms The parallel, cascade and lattice forms have been developed aimed at ensuring less sensitivity to finite-precision effects. Moreover, for the IIR filter they offer a simple way of stability monitoring.

Usually, a design is based on a direct form of the filter to be adapted. However, the *indirect form* offer many advantages over the direct form in terms of numerical stability and is much less prone to stability problems during the adaptation phases. In Appendix J we will address such more elaborate filter topologies. Of particular interest is the lattice-like structure used in the implementation of the so-called *fast array recursive least-squares (FARLS)*. The lack of spread of lattice filters can probably be attributed to the mathematical sophistication involved.

The tapped state normalized lattice filter has many desirable properties for fixed coefficient digital filtering [13, Ch. 2].

For each of the adaptive filter topology types the performance can be assessed with respect to *rate of convergence*, *misadjustment*, *robustness*, *tracking capabilities* and *computational efficiency*.

I.1.1 Chapter Outline

Following this introduction section I.2 discusses the adaptive finite-impulse response filter. Next the adaptive infinite-impulse response filter is presented in section I.3. The class of so-called orthonormal filters will be considered separately in Appendix K.

I.2 Adaptive Finite-Duration Impulse Response Filters

The topology of the adaptive finite-duration impulse response filter acting in *interference cancelation* mode is depicted in Figure I.1 on the next page. It comprises a tapped delay line, variable weights, whose input signals are the signals at the delay-line taps, a summer to add the weighted signals. For each of the adaptive filters an adaptation process intentionally seeks an optimal impulse response by adjusting the weights. The filter topology is also referred to as a *tapped-delay-line filter*.

The number of adaptive tap-weights amounts to M. The operator, z^{-1}, designates unit delay. The filter configuration attains its name since there is no feedback (except for the tap-weight adaptation) and the filter therefore exhibits a finite-duration impulse response. Moreover, due to the lack of feedback the filter with frozen tap-weights will also be stable. However, most of the adaptive processing schemes employ a *performance feedback* of the filter weights. Hence, stability is by no means guarantied during adaptation. Therefore, some precautions shall be made in the

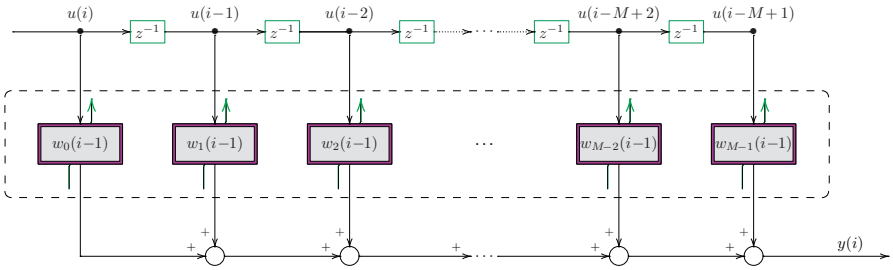

Fig. I.1: Adaptive Finite-Duration Impulse Response Filter.

rate of filter weight adaptation.

The filter weights $w \in \mathbb{C}^{M\times 1}$[2] that are also referred to as *tap-weights* are organized as

$$w = \begin{bmatrix} w(0) \\ w(1) \\ \vdots \\ w(M-1) \end{bmatrix}. \tag{I.2.1}$$

By $\mathbf{u}_i \in \mathbb{C}^{1\times M}$ we will designate the filter input vector, that is, a $1 \times M$ row vector [3]

$$\mathbf{u}_i = [\mathbf{u}(i) \quad \mathbf{u}(i-1) \quad \dots \quad \mathbf{u}(i-M+1)]. \tag{I.2.2}$$

Hence, it is only necessary to store the present and the previous $M-1$ input samples. The integer i denotes the iteration time index. In some context $\mathbf{u}_i$ is also referred to as *observations*, *reference signal* and also as *regressor*. The regressor $\mathbf{u}_i$ coincide with either of the quantities $\mathring{u}_i^w$ or $\mathring{x}_i^w$ used in chapter 6. In the discussion of adaptive filters it is customary to use $\mathbf{u}_i$ to designate the reference signal and it is implicit understood that it is associated with tap weights.

In Figure I.1 we identify the so-called *a priori* output estimation error $e(i)$ as the difference between (or the sum of) the desired signal $d(i)$ and the estimated value $\hat{d}(i\,|\mathcal{U}_{i-1})$ based on the tap-weights w_{i-1} provided the multidimensional space denoted by $\mathcal{U}_{i-1}$ that is spanned by the input samples $\mathbf{u}(i-1), \mathbf{u}(i-2), \dots, \mathbf{u}(i-M)$

[1] Notice that the choice in many textbooks on adaptive filtering, e.g., [8] the complex conjugate of each tap-weight is used. However, we will adopt the notation in [14] and use unconjugated tap-weights.

[2] Formally, the tap-weight vector is an estimate of the optimal tap-weight vector pertinent for a specified cost function. Hence, as in [8] we arguably ought to apply an accent caret to w. However, in order to reduce the notational burden and also be compatible with, e.g., [14] we will suppress the caret and let the estimation process be implicitly understood.

[3] We adopt the notation in [14] and organize $\mathbf{u}_i$ as a *row vector* in contradiction to the choice in, e.g., [8] where $\mathbf{u}_i$ is a *column vector*. The implications of this subtle difference in choice of $\mathbf{u}$ and usage of w is addressed in Appendix 8.B.1.

$$\begin{aligned}\mathbf{e}(i) &\triangleq \mathbf{e}(i|i-1)\\ &= \mathbf{d}(i) \mp \hat{d}(i\,|\mathcal{U}_{i-1}\,)\\ &= \mathbf{d}(i) \mp \mathbf{u}_i w_{i_B-1}. \end{aligned} \tag{I.2.3}$$

The block time index i_B attached to the tap-weight signifies the time where the tap-weight vector was *updated* and **not** when it is actually *used*. This block time index facilitates the use of a block-update scheme (refer to chapter 8).

The signal $d(i)$ is sometimes referred to as a *pilot signal* [18] and commonly as a *disturbance signal* in active noise control applications. It could therefore be argued that $d(i)$ is a *undesired* signal. In the electrical domain it is customary to *subtract* the filter response from the desired signal. However, in the domain of active noise control in sound or vibration applications we actually *superpose* two physical signals that intentionally should be in anti-phase. In order to reuse the mathematical expression and derived software we will preserve the $\mp$ notation where the upper $-$ indicates subtraction of a control output signal from the disturbance signal and the lower $+$ signifies superposition of two physical signals.

It should be noticed that when the filter operates in system identification mode, electrical (as opposed to acoustical) interference cancelation mode and adaptive inverse control, it is the *a priori* output estimation error $e(i)$ that is *observed* or *sensed* cf. section 5.3.

I.3 Adaptive Infinite-Duration Impulse Response Filters

In the active control (AC) community IIR filters have been proposed as a computational efficient substitute to the FIR filters most commonly employed in practical applications owing to the inherent stability [4] [3], [11, Ch. 3.6], [1, Ch. 2.9] and [7, Sec. 6.12].

The recursive method is an especially efficient scheme for either generating sequences of data or for filtering of data. For such purposes adaptive IIR filters can be employed. The topology of the adaptive IIR filter is depicted in Figure I.2 on the facing page. It comprises the same components as the FIR filter in Figure I.1 on the previous page. By M_a we denote the number of adaptive direct (feedforward) coefficients. In addition, the IIR filter contains M_b adaptive recursive (feedback) coefficients. Hence, the IIR filter comprises in total $M = M_a + M_b$ adaptive tap-weights.

An overview of IIR filters is provided in [15]. By comparison of an adaptive IIR filter with an adaptive FIR filter the main following pros and cons can be claimed [6].

IIR filter pros 1. The main benefit of using IIR filter instead of FIR filter is that the same response in many cases can be obtained with a IIR filter using fewer tap-weights.

IIR filter pros 2. As a recursive filter, with poles as well as zeros offer the advantages of resonance, sharp cut-off etc.

IIR filter pros 3. In AC applications it is useful to take feedback into account [2] and to use a IIR filter to model resonant or lightly damped systems [15].

IIR filter cons 1. The performance surfaces are generally nonquadratic and *local minima* may exist which in practice might lead to the tap-weight vector being stuck at a non globally optimal

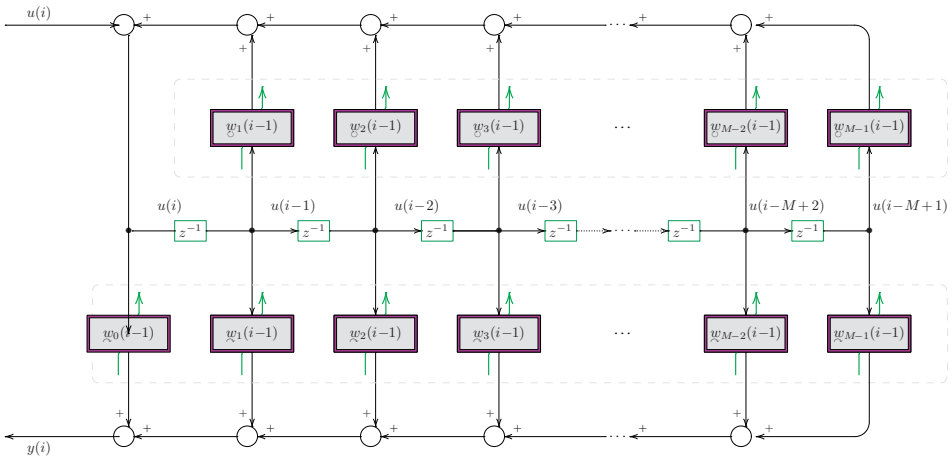

Fig. I.2: Adaptive Infinite-Duration Impulse Response Filter.

position. The remedy against this problem is instead of using the output error method instead to apply the method devised by Steiglitz-McBride [16] and detailed in [13, Ch. 8].

IIR filter cons 2. Susceptible to instability problems even with frozen tap-weights.

IIR filter cons 3. Stability is by no means guarantied during adaptation. Instability can occur if a particular application requires that the poles are close to the unit circle. The adaptation will usually be subject to some *adaptation noise*. Accordingly, an else stable IIR filter might become unstable if one or more of the poles accidently are moved outside the unit circle during filter adaptation. Hence, as compared with FIR filters even more precautions shall be made in the rate of filter weight adaptation.

IIR filter cons 4. Slow initial convergence as compared with a FIR filter for the same number of adaptive tap-weights. However, due to the more efficient modeling capabilities provided by the IIR filter fewer tap-weights might be needed which in turn compensates for this slower adaptation mechanism.

IIR filter cons 5. Reduced tracking capabilities. The same remarks made above applies here.

The IIR filter is normally formulated using either the *equation error* method or the *output error* method [1, 9, 13, 15]. The *equation error* method, however, is a nonlinear regression that can cause convergence of the filter to a local minimum of the error-performance surface. Therefore, IIR filters are more often based on the *output error* method although it leads to a biased estimate. In many cases, however, the bias is at an acceptable level. Moreover, both formulations are subject to potential instability problems.

The *tap-weights* are organized in a $(M_a + M_b) \times 1$ column vector formed by the direct adaptive tap-weight vector $w_a \in \mathbb{C}^{M_a \times 1}$ and the recursive adaptive tap-weight vector $w_b \in \mathbb{C}^{M_b \times 1}$ as

$$w = \begin{bmatrix} w_a^\top & w_b^\top \end{bmatrix}^\top \tag{I.3.1}$$

where

$$w_a = \begin{bmatrix} w_a(0) \\ w_a(1) \\ \vdots \\ w_a(M_a - 1) \end{bmatrix}, \quad w_b = \begin{bmatrix} w_b(0) \\ w_b(1) \\ \vdots \\ w_b(M_b - 1) \end{bmatrix}. \tag{I.3.2}$$

The recursive LMS (RLMS) proposed in [5, 10, 17] is based on the *output error* method and is the direct extension of the ordinary least-mean-squares (LMS) to the use of IIR filter topology [18, Ch. 8]. However, for this algorithm the gradient estimate of the cost function involves derivatives with respect to direct tap weights, but also derivatives with respect to the recursive tap-weights. Accordingly, the gradient with respect to the weights includes terms representing the input as well as derivatives of the past outputs with respect to the weights and derivatives of the direct- and recursive weights with respect to each other.

Bibliography

[1] Stephen J. Elliott. *Signal Processing for Active Control*. London: Academic Press, 2001.

[2] L. J. Eriksson. Development of the filtered-u algorithm for active noise control. *JASA*, 89: 257–265, 1991.

[3] L. J. Eriksson and M. C. Allie. Use of random noise for on-line transducer modeling in an adaptive active attenuation system. *JASA*, 85(2):797–802, 1989.

[4] L. J. Eriksson, M. C. Allie, and R. A. Greiner. The selection and application of an IIR adaptive filter for use in active sound attention. *IEEE Transactions on Acoustics, Speech, and Signal Processing*, 35:433–437, 1987.

[5] P.L. Feintuch. An adaptive recursive LMS filter. *Proceedings of the IEEE*, 64(11):1622–1624, 1976.

[6] Zoran Fejzo and Hanoch Lev-Ari. Adaptive Laguerre-lattice filters. *IEEE Transactions on Signal Processing*, 45(12):3006–3016, 1997.

[7] Colin H. Hansen and Scott D. Snyder. *Active Control of Noise and Vibration*. E & FN SPON, 1st edition, 1997.

[8] Simon Haykin. *Adaptive Filter Theory*. Prentice-Hall Inc. Upper Saddle River New Jersey 07458, 3rd edition, 1996.

[9] Jr. Johnson, C.R. Adaptive IIR filtering: Current results and open issues. *IEEE Transactions on Information Theory*, 30(2):237–250, 1984.

[10] Jr. Johnson, C.R., M.G Larimore, P.L. Feintuch, and N.J. Bershad. Comments on and additions to "an adaptive recursive LMS filter". *Proceedings of the IEEE*, 65(9):1399–1402, 1977.

[11] Sen M. Kuo and Dennis R. Morgan. *Active Noise Control Systems Algorithms and DSP Implementations*. John Wiley & Sons, Inc., 1996.

[12] Lennart Ljung. *System Identification Theory for the User*. Prentice Hall, Upper Saddle River, NJ, 2nd edition, 1999.

[13] P. A. Regalia. *Adaptive IIR Filtering in Signal Processing and Control*. Marcel Dekker, New York, 1995.

[14] Ali H. Sayed. *Fundamentals of Adaptive Filtering*. John Wiley & Sons, Inc., New York, NY, USA, 2003.

[15] J. J. Shynk. Adaptive IIR filtering. *IEEE ASSP Magazine*, 6:4–21, 1989.

[16] K. Steiglitz and L. E. Bride. A technique for identification of linear systems. *IEEE Transactions on Automatic Control*, 10:461–464, 1965.

[17] B. Widrow, J.M McCool, and P.L. Feintuch. Comments on "an adaptive recursive LMS filter". *Proceedings of the IEEE*, 65(9):1402–1404, 1977.

[18] Bernard Widrow and Samuel D. Stearns. *Adaptive Signal Processing*. Prentice-Hall, New Jersey, 1985.

J. ADAPTIVE FILTERING FAST ALGORITHMS LINEAR TIME-VARIANT SYSTEMS

J.1 Motivation

In chapter 8 the advantages of recursive least-squares (RLS) over least-mean-squares (LMS) were explained. However, the computational burden of the order of $\mathcal{O}(M^2)$ of the recursive least-squares precludes practical implementations in a real-time environment. Demands on computational efficient algorithms, i.e., $\mathcal{O}(M)$ have lead to the development of a suite of different fast recursive least-squares (Fast RLS) algorithms.

In order to speed up the calculations at least three possibilities exist.

1. *Orthonormal Filters.* In Appendix I we demonstrate that by substituting a simple pulse function by more elaborate orthonormal models, e.g., Laguerre and Kautz models we can reduce the model order significantly.
2. *Algorithm Efficiency.* By exploiting some underlying structure in the data and by confining the weighting and initial parameters an algorithm of the order $\mathcal{O}(M)$ per update cycle can be obtained.
3. *Sparse Adaptation.* In [1, 3] a brief discussion of sparse adaptation techniques for active control (AC) can be found. However, as the convergence and misadjustment properties of these methods have not yet been established and as the methods are prone to aliasing problems we will not further investigate these sparse adaptation techniques.

The development of the fast recursive least-squares can be attributed to the classical paper by Sayed and Kailath [9] that for the first time established a link between adaptive recursive least-squares and state space models.

The efficient recursive least-squares algorithms broadly fall into three categories. In the first category we find the *array algorithms.* The second class covers the so-called *fixed-order* algorithms including the extended fast transverse filter (eFTF), the extended fast *a priori* error sequential technique (eFAEST) and the extended fast Kalman filter (eFKF). Finally, the third class of fast algorithm is constituted by the so-called *order-recursive* algorithms.

The bottleneck in the recursive least-squares is the calculation of the regularized inverse of the time-averaged correlation matrix P. The key point in the development of the fast algorithm is to exploit the possible *data structure.* Accordingly, two consecutive calculations of the time-averaged correlation matrix will have many terms in common. This can be accomplished if the data possess *shift structure.* The shift structure of the regressor can be expressed by

$$\begin{bmatrix} u_i & u(i-M) \end{bmatrix} = \begin{bmatrix} u(i) & u_{i-1} \end{bmatrix}. \tag{J.1.1}$$

A more general class of *data structure* is governed by

$$\boxed{\begin{bmatrix} u(i,0) & u_{i-1} \end{bmatrix} = \begin{bmatrix} u_i & u(i-1,M-1) \end{bmatrix} \Psi,} \tag{J.1.2}$$

where Ψ is an arbitrary vector.

The route to the development is to some extent a little tricky. However, in recent years this approach has gradually been streamlined [5–8] and basically involves the following steps:

1. *Order-Update*.
2. *Time-Update*. *Inner product* time-update.

In the course of fast recursive least-squares development the following premises are invoked:

① Pre-windowed data. In pre-windowing, the data $\{u(i), d(i)\}$ are assumed to be zero prior to filter operation, i.e., $u(i) = d(i) = 0$ for $i < 0$. The expressions can rather easily be reformulated to the covariance-, autocorrelation- and post-windowing, methods defined in [4, Ch. 11].

② Specific choice of regularization matrix Π. Requirement on efficient calculation of ΔP_{i-1} implies that the regularization matrix Π to be chosen in an appropriate manner

$$\Pi^{-1} = \eta \cdot diag\{\lambda^2, \lambda^3, \ldots, \lambda^{M+1}\}. \tag{J.1.3}$$

As long as the algorithm provide regularization this restriction on the regularization matrix will probably not be of concern.

Actually, there is a freedom in the scaling of Π^{-1}. We could omit the regularization term, but then the we could experience the problems discussed along the objective in on page 384 and follow up on page 390.

When H has full column rank we define the *projection matrix* $\mathcal{P}_H$ by

$$\mathcal{P}_H \triangleq H(H^*H)^{-1}H^*. \tag{J.1.4}$$

By multiplying a vector, say y by the projection matrix amounts to projecting y onto the column span of H. Formally, then the residual part of y, that is, $\tilde{y} \triangleq \mathcal{P}_H^{\perp} y$, where the projection operator $\mathcal{P}_H^{\perp}$ is defined by

$$\mathcal{P}_H^{\perp} \triangleq I - \mathcal{P}_H. \tag{J.1.5}$$

J.2 General Order-Update Relations

Order-update addresses the case where the model order is increased by 1 say from M to $M+1$. Regularized weighted least-squares solutions can be order-updated in a rather elegant fashion by

exploiting certain properties in the data structure. Order-update relations will lead to computational efficient algorithms. Considering the recursive least-squares algorithm an expression for the inverse of the coefficient matrix P is required at each iteration step. However, this requires of the order of $\mathcal{O}(M^2)$ operations. However, as will be derived in this sequel a lot of redundant operations take place in this calculations. Therefore, the aim of the order update is to obtain a fast algorithm $\mathcal{O}(M)$.

The linear weighted regularized least-squares problem is formulated as

$$\min_{w}\big[(w-\bar{w})^*\Pi(w-\bar{w})+(y-Hw)^*W(y-Hw)\big], \tag{J.2.1}$$

where $\bar{w}$ denotes the initial condition (usually zero). Accordingly, the least-squares criterion seek the vector $\hat{y}$ that is closest to a vector y in the column span of the data matrix H in a weighted regularized manner.

The detailed derivation can be found in subsection J.A.1.

$$\underset{\rightarrow}{w}=\underset{\rightarrow}{P}\underset{\rightarrow}{H}^*Wy \tag{J.2.2}$$

$$\underset{\leftarrow}{w}=\underset{\leftarrow}{P}\underset{\leftarrow}{H}^*Wy. \tag{J.2.3}$$

Lattice filters are not concerned with the weight vectors themselves, but rather with the corresponding estimated observation vectors (projections) $\{\hat{y}_{M,i},\hat{y}_{M,i+1}\}$. The name lattice filter stems from the way the propagation of the output estimation errors is carried out. In fact as it will turn out the weight vectors $w_{M,i}$ need neither to be evaluated nor updated. Instead the various versions of the lattice filter relies on the propagation of *a priori* output estimation error and *a priori* estimation error or *posteriori* output estimation error and *posteriori* estimation error. Although the different versions of lattice filters are theoretically equivalent, the performance will differ under finite precision conditions. Moreover, as listed in [10, Table 15.3] the different implementations vary in computational efficiency from $\{\mathcal{O}_{\times}(16M),\mathcal{O}_{+}(8M),\mathcal{O}_{/}(8M)\}$ to $\{\mathcal{O}_{\times}(27M),\mathcal{O}_{+}(8M),\mathcal{O}_{/}(4M),\mathcal{O}_{\sqrt{\cdot}}(2M)\}$.

In [10, Ch. 15] it is demonstrated in an example of channel system identification that the array version is the most robust lattice filter under finite-precision conditions.

In the route of algorithm derivation follow different courses for the array algorithms. The derivation of the fast algorithm ultimately leading to Laguerre filter is rather long and quite involved. Many auxiliary variables are introduced. Moreover, the following mathematical techniques are invoking

Fast RLS Algorithm Components 1. J-unitary transformations. The array algorithms employ the so-called J-unitary transformations, in order to annihilate certain entities in a pre-array of numbers

$$\Theta J\Theta^*=\Theta^*J\Theta=J. \tag{J.2.4}$$

A signature matrix is a diagonal matrix which elements. Due to geometric arguments the J-unitary transformations is also referred to as *hyperbolic transformations*.

However, despite the rather involved derivation the fast recursive least-squares themselves turn out to be quite simple.

J.3 Fast RLS array algorithm

The recursive fast recursive least-squares array introduces the following the signature matrices S and J defined as

$$S = \begin{bmatrix} 1 & 0 \\ 0 & 1 \end{bmatrix}, \quad J = \begin{bmatrix} 1 & \\ & S \end{bmatrix}. \tag{J.3.1}$$

Moreover, key point to the operation is the propagation of the auxiliary quantities $\bar{g}$ and $\bar{\gamma}$ defined by

$$\bar{g}_i = g_i \gamma^{-1/2}(i) \tag{J.3.2a}$$
$$\bar{\gamma}(i) = \gamma^{-1/2}(i) \tag{J.3.2b}$$

respectively. Time-update of $\bar{g}$ and $\bar{\gamma}$ is related to the time-update of the gain vector g and the conversion factor γ.

The algorithm is initialized by

$$w_{-1} = \bar{w}, \tag{J.3.3a}$$
$$\bar{\gamma}_{-1} = 1, \tag{J.3.3b}$$
$$g_{-1} = 0 \tag{J.3.3c}$$

and

$$\bar{L}_{-1} = \sqrt{\eta\lambda} \cdot \begin{bmatrix} 1 & 0 \\ 0 & 0 \\ \vdots & \vdots \\ 0 & 0 \\ 0 & \lambda^{M/2} \end{bmatrix} \tag{J.3.4}$$

and

$$\mathcal{A}\Theta_i = \mathcal{B}, \tag{J.3.5}$$

where the block matrix quantities $\mathcal{A}$ and $\mathcal{B}$ designates pre-array and post-array respectively and defined by

$$\mathcal{A} = \begin{bmatrix} \bar{\gamma}(i-1) & \begin{bmatrix} u_i & u(i-1, M-1) \end{bmatrix} \bar{L}_{i-1} \\ \Psi \begin{bmatrix} 0 \\ \bar{g}_{i-1} \end{bmatrix} & \bar{L}_{i-1} \end{bmatrix} \tag{J.3.6a}$$

$$\mathcal{B} = \begin{bmatrix} \bar{\gamma}(i) & \begin{bmatrix} 0 & 0 \end{bmatrix} \\ \begin{bmatrix} \bar{g}_i \\ 0 \end{bmatrix} & \sqrt{\lambda}\bar{L}_i \end{bmatrix} \tag{J.3.6b}$$

contain the information necessary for the tap-weight update and can be read from the post-array $\mathcal{B}$

$$\boxed{w_i = w_{i-1} + \bar{g}_i \bar{\gamma}^{-1}(i) \left[d(i) - u_i w_{i-1} \right]} \tag{J.3.7}$$

$$\min_{w}\big[\lambda^{N+1}(w-\bar{w})^{*}\Pi(w-\bar{w})+\sum_{j=0}^{N}|d(j)-u_j w|^2\big] \tag{J.3.8}$$

for some time-invariant regularization matrix Π defined by

$$\Pi^{-1}=\eta\cdot diag\{\lambda^2,\lambda^3,\ldots,\lambda^{M+1}\},\quad \eta>0. \tag{J.3.9}$$

It should be remarked that neither the cost function viz. (J.3.8) nor the regularization matrix viz. (J.3.9) are actually determined.

In [2] the superiority of the RLS over LMS, fast transversal filter (FTF) and fast affine projection (FAP) in terms of convergence speed and size of quiet zone is demonstrated for a practical multichannel system ($N_x=1, N_y=2, N_e=2$). However, in some cases the (ordinary) RLS algorithm was exhibiting instablity. This problem, however, might be due to the use of the ordinary filtered-x (Fx) instead of modified-filtered-x (mFx) (refer to chapter 6).

Bibliography

[1] Stephen J. Elliott. *Signal Processing for Active Control*. London: Academic Press, 2001.

[2] Miguel Ferrer, Alberto González, Pedro Zuccarello, and André Camacho. On the practical implementation of multichannel adaptive filters basen on LMS, RLS, FTP and FAP algorithms for active control. In *Tenth International Congress on Sound and Vibration*, pages 361–368, Stockholm, Sweden, 2003.

[3] H. Hamada. Signal processing for active control - adaptive signal processing. In *Int. Symp. on Active Control of Sound and Vibration*, pages 33–44, Tokyo, 1991.

[4] Simon Haykin. *Adaptive Filter Theory*. Prentice-Hall Inc. Upper Saddle River New Jersey 07458, 3rd edition, 1996.

[5] Ricardo Merched. Extended RLS lattice adaptive filters. *IEEE Transactions on Signal Processing*, 51(9):2294–2309, 2003.

[6] Ricardo Merched and Ali H. Sayed. Order-recursive RLS Laguerre adaptive filtering. *IEEE Transactions on Signal Processing*, 48(11):3000–3010, 2000.

[7] Ricardo Merched and Ali H. Sayed. Extended fast fixed-order RLS adaptive filters. *IEEE Transactions on Signal Processing*, 49(12):3015–3031, 2001.

[8] Ricardo Merched and Ali H. Sayed. RLS-Laguerre lattice adaptive filtering: Error-feedback, normalized and array-based algorithms. *IEEE Transactions on Signal Processing*, 49(12): 2565–2576, 2001.

[9] A. H. Sayed and T. Kailath. A state-space approach to adaptive RLS filtering. *ICASSP,MN*, 3:559–562, 1993.

[10] Ali H. Sayed. *Fundamentals of Adaptive Filtering*. John Wiley & Sons, Inc., New York, NY, USA, 2003.

J.A Efficient RLS Algorithm Derivation

In this appendix we will present a streamlined derivation of the various Laguerre based fast recursive least-squares based on the textbook by Sayed [10, Ch. 11-16]. Moreover, in the present derivation is further generalized by allowing a non-vanishing initial condition $\bar{w}$ and a regularization matrix Π that not necessarily is a diagonal matrix.

J.A.1 Order Update

Recalling from (J.A.3) repeated here for convenience that the linear weighted regularized least-squares problem can be formulated as

$$\min_{w}\big[(w-\bar{w})^*\Pi(w-\bar{w})+(y-Hw)^*W(y-Hw)\big], \tag{J.A.1}$$

where $\bar{w}$ denotes the initial condition. Accordingly, the least-squares criterion seek the vector $\hat{y}$ that is closest to a vector y in the column span of the data matrix H in a weighted regularized manner. The data matrix H is modified by adding a column to its left or to its right.

$$\underrightarrow{H}=\begin{bmatrix}H & h\end{bmatrix} \tag{J.A.2a}$$

$$\underleftarrow{H}=\begin{bmatrix}h & H\end{bmatrix} \tag{J.A.2b}$$

$$\underleftrightarrow{H}=\begin{bmatrix}H_L & h & H_R\end{bmatrix}. \tag{J.A.2c}$$

In (J.A.2a) and (J.A.2b) h denotes the $N\times 1$ column vector added. In practice one could consider the case where data from $M+1$ instead of M sensors are used in the estimation of y.

The original least-squares problem (J.A.1) has been transformed into extended least-squares estimation problems

$$\min_{\underrightarrow{w}}[(\underrightarrow{w}-\underrightarrow{\bar{w}})^*\underrightarrow{\Pi}(\underrightarrow{w}-\underrightarrow{\bar{w}})+(y-\underrightarrow{H}\,\underrightarrow{w})^*W(y-\underrightarrow{H}\,\underrightarrow{w})] \tag{J.A.3a}$$

$$\min_{\underleftarrow{w}}[(\underleftarrow{w}-\underleftarrow{\bar{w}})^*\underleftarrow{\Pi}(\underleftarrow{w}-\underleftarrow{\bar{w}})+(y-\underleftarrow{H}\,\underleftarrow{w})^*W(y-\underleftarrow{H}\,\underleftarrow{w})] \tag{J.A.3b}$$

$$\min_{\underleftrightarrow{w}}[(\underleftrightarrow{w}-\underleftrightarrow{\bar{w}})^*\underleftrightarrow{\Pi}(\underleftrightarrow{w}-\underleftrightarrow{\bar{w}})+(y-\underleftrightarrow{H}\,\underleftrightarrow{w})^*W(y-\underleftrightarrow{H}\,\underleftrightarrow{w})], \tag{J.A.3c}$$

where $\underrightarrow{w}$ and $\underleftarrow{w}$ denote the backward- and forward extended tap-weight vector respectively.

The optimal solution to the extended estimation problems (J.A.3a) and (J.A.3b) are

$$\underrightarrow{w}^o=\underrightarrow{\bar{w}}+\underrightarrow{P}\,\underrightarrow{H}^*W(y-\underrightarrow{H}\,\underrightarrow{\bar{w}}) \tag{J.A.4a}$$

$$\underleftarrow{w}^o=\underleftarrow{\bar{w}}+\underleftarrow{P}\,\underleftarrow{H}^*W(y-\underleftarrow{H}\,\underleftarrow{\bar{w}}) \tag{J.A.4b}$$

$$\underleftrightarrow{w}^o=\underleftrightarrow{\bar{w}}+\underleftrightarrow{P}\,\underleftrightarrow{H}^*W(y-\underleftrightarrow{H}\,\underleftrightarrow{\bar{w}}), \tag{J.A.4c}$$

where $\underset{\rightarrow}{w}^o$ and $\underset{\leftarrow}{w}^o$ pertain to the backward- and forward estimation problems respectively.

The quantities $\underset{\leftarrow}{\bar{w}}$ and $\underset{\leftarrow}{\bar{w}}$ refer to the backward and forward order-updated regularization tap-weight vector respectively. The matrix quantities $\underset{\rightarrow}{\Pi}$ and $\underset{\leftarrow}{\Pi}$ refer to the backward and forward order-updated inverse coefficient matrices respectively.

$$\underset{\rightarrow}{P} = (\underset{\rightarrow}{\Pi} + \underset{\rightarrow}{H}^* W \underset{\rightarrow}{H})^{-1} \tag{J.A.5a}$$

$$\underset{\leftarrow}{P} = (\underset{\leftarrow}{\Pi} + \underset{\leftarrow}{H}^* W \underset{\leftarrow}{H})^{-1} \tag{J.A.5b}$$

$$\underset{\leftrightarrow}{P} = (\underset{\leftrightarrow}{\Pi} + \underset{\leftrightarrow}{H}^* W \underset{\leftrightarrow}{H})^{-1}. \tag{J.A.5c}$$

In order to facilitate the order-update (J.A.5a) and (J.A.5b) the regularization matrix Π shall be expanded according to

$$\underset{\rightarrow}{\Pi} = \begin{bmatrix} \Pi & \varrho \\ \varrho^* & \varpi, \end{bmatrix} \tag{J.A.6}$$

$$\underset{\leftarrow}{\Pi} = \begin{bmatrix} \varpi & \varrho \\ \varrho^* & \Pi, \end{bmatrix} \tag{J.A.7}$$

$$\Pi = \begin{bmatrix} \Pi_{UL} & \Pi_{UR} \\ \Pi_{LL} & \Pi_{LR}, \end{bmatrix} \tag{J.A.8}$$

$$\varrho = \begin{bmatrix} \varrho_U \\ \varrho_L \end{bmatrix} \tag{J.A.9}$$

and

$$\underset{\leftrightarrow}{\Pi} = \begin{bmatrix} \Pi_{UL} & \varrho_U & \Pi_{UR} \\ \varrho_U^* & \varpi & \varrho_L^* \\ \Pi_{LL} & \varrho_L & \Pi_{LR}, \end{bmatrix} \tag{J.A.10}$$

where ϱ is a $1 \times M$ column vector and ϖ is a positive scalar. The format of the order-update of the regularization matrix (J.A.6) and (J.A.7) ensures that the order-updated regularization matrices are positive definite i.e. they satisfy $\underset{\rightarrow}{\Pi} > 0 \wedge \underset{\leftarrow}{\Pi} > 0$.

The residual vector $\underset{\rightarrow}{\tilde{y}}$ and $\underset{\leftarrow}{\tilde{y}}$ pertaining to the backward- and forward extended cases respectively are

$$\underset{\rightarrow}{\tilde{y}} = y - \underset{\rightarrow}{H}\,\underset{\rightarrow}{\hat{w}} \tag{J.A.11a}$$

$$\underset{\leftarrow}{\tilde{y}} = y - \underset{\leftarrow}{H}\,\underset{\leftarrow}{\hat{w}} \tag{J.A.11b}$$

$$\underset{\leftrightarrow}{\tilde{y}} = y - \underset{\leftrightarrow}{H}\,\underset{\leftrightarrow}{\hat{w}}. \tag{J.A.11c}$$

The corresponding minimum cost is (ref to recursive least-squares)

$$\xi^b = (y - \underset{\rightarrow}{H}\,\underset{\rightarrow}{\bar{w}})^* W\, \underset{\rightarrow}{\tilde{y}} \tag{J.A.12a}$$

$$\xi^f = (y - \underset{\leftarrow}{H}\,\underset{\leftarrow}{\bar{w}})^* W\, \underset{\leftarrow}{\tilde{y}} \tag{J.A.12b}$$

$$\xi^o = (y - \underset{\leftrightarrow}{H}\,\underset{\leftrightarrow}{\bar{w}})^* W\, \underset{\leftrightarrow}{\tilde{y}}\,. \tag{J.A.12c}$$

The conversion factors are

$$\gamma^b \triangleq 1 - \underset{\rightarrow}{H}_{[\lfloor,:]}\, \underset{\rightarrow}{P}\, \underset{\rightarrow}{H}^*_{[\lfloor,:]} \tag{J.A.13a}$$

$$\gamma^f \triangleq 1 - \underset{\leftarrow}{H}_{[\lfloor,:]}\, \underset{\leftarrow}{P}\, \underset{\leftarrow}{H}^*_{[\lfloor,:]} \tag{J.A.13b}$$

$$\gamma^o \triangleq 1 - \underset{\leftrightarrow}{H}_{[\lfloor,:]}\, \underset{\leftrightarrow}{P}\, \underset{\leftrightarrow}{H}^*_{[\lfloor,:]}, \tag{J.A.13c}$$

where the vector quantities

$$\underset{\rightarrow}{h} \triangleq \underset{\rightarrow}{H}_{[\lfloor,:]} \tag{J.A.14}$$

and

$$\underset{\leftarrow}{h} \triangleq \underset{\leftarrow}{H}_{[\lfloor,:]} \tag{J.A.15}$$

$$\underset{\leftrightarrow}{h} \triangleq \underset{\leftrightarrow}{H}_{[\lfloor,:]} \tag{J.A.16}$$

referring to the last row (i.e. most recent regression vector) of $\underset{\rightarrow}{H}$ and $\underset{\leftarrow}{H}$ respectively have been introduce for notational convenience.

The triple of least-squares estimation problems, viz. (J.A.3), and (J.A.3a) and (J.A.3b) can be used to relating the solution vectors $\{\hat{w}, \underset{\rightarrow}{\hat{w}}, \underset{\leftarrow}{\hat{w}}\}$, $\{P, \underset{\rightarrow}{P}, \underset{\leftarrow}{P}\}$

In this process we will invoke the following two matrix identities

$$\begin{bmatrix} A & B \\ C & D \end{bmatrix}^{-1} = \begin{bmatrix} A^{-1} & 0 \\ 0 & 0 \end{bmatrix} + \begin{bmatrix} -A^{-1}B \\ I \end{bmatrix} (D - CA^{-1}B)^{-1} \begin{bmatrix} -CA^{-1} & I \end{bmatrix} \tag{J.A.17}$$

$$\begin{bmatrix} A & B \\ C & D \end{bmatrix}^{-1} = \begin{bmatrix} 0 & 0 \\ 0 & D^{-1} \end{bmatrix} + \begin{bmatrix} I \\ -D^{-1}C \end{bmatrix} (A - BD^{-1}C)^{-1} \begin{bmatrix} I & -BD^{-1} \end{bmatrix} \tag{J.A.18}$$

The matrix identities (J.A.17) and (J.A.26) relate the inverse of a block matrix to the inverse of its top leftmost and bottom rightmost corner block respectively. By substituting

$$\begin{array}{lcll} A & \leftarrow & P^{-1} = \Pi + H^* W H & \text{(J.A.19a)} \\ B & \leftarrow & \varrho + H^* W\, \underset{\rightarrow}{h} & \text{(J.A.19b)} \\ C & \leftarrow & \varrho^* + \underset{\rightarrow}{h}^* W H & \text{(J.A.19c)} \\ D & \leftarrow & \varpi + \underset{\rightarrow}{h}^* W\, \underset{\rightarrow}{h} & \text{(J.A.19d)} \end{array}$$

in (J.A.17)

$$\begin{aligned}\underset{\rightarrow}{P} &= \begin{bmatrix} P & 0 \\ 0 & 0 \end{bmatrix} + (\varpi + \underset{\rightarrow}{h}^{*} W \underset{\rightarrow}{h} - (\varrho^{*} + \underset{\rightarrow}{h}^{*} WH)P(\varrho + H^{*} W \underset{\rightarrow}{h}))^{-1} \\ &\quad \begin{bmatrix} -P(\varrho + H^{*} W \underset{\rightarrow}{h}) \\ 1 \end{bmatrix} \begin{bmatrix} -(\varrho^{*} + \underset{\rightarrow}{h}^{*} WH)P & 1 \end{bmatrix} \\ &= \begin{bmatrix} P & 0 \\ 0 & 0 \end{bmatrix} + \zeta^{-1} \begin{bmatrix} -\hat{w}^{b} \\ 1 \end{bmatrix} \begin{bmatrix} -\hat{w}^{b*} & 1 \end{bmatrix}, \end{aligned} \tag{J.A.20}$$

where

$$\hat{w}^{b} = P(\varrho + H^{*} W \underset{\rightarrow}{h}) \tag{J.A.21}$$

$$\underset{\rightarrow}{\bar{w}}^{b} = (I - \underset{\rightarrow}{P}\underset{\rightarrow}{H}^{*} W \underset{\rightarrow}{H})^{-1} P\varrho \tag{J.A.22}$$

and

$$\zeta = (\varpi + \underset{\rightarrow}{h}^{*} W \underset{\rightarrow}{h} - (\varrho^{*} + \underset{\rightarrow}{h}^{*} WH)P(\varrho + H^{*} W \underset{\rightarrow}{h})). \tag{J.A.23}$$

Accordingly, the quantity $\hat{w}^{b}$ can interpreted as the weight vector that solves the following weighted regularized problem

$$\min_{\underset{\rightarrow}{w}^{b}} \left[(\underset{\rightarrow}{w}^{b} - \underset{\rightarrow}{\bar{w}}^{b})^{*} \underset{\rightarrow}{\Pi} (\underset{\rightarrow}{w}^{b} - \underset{\rightarrow}{\bar{w}}^{b}) + (\underset{\rightarrow}{h} - \underset{\rightarrow}{H}\underset{\rightarrow}{w}^{b})^{*} W (y - \underset{\rightarrow}{H}\underset{\rightarrow}{w}^{b}) \right] \tag{J.A.24}$$

Similarly by substituting

$$\boxed{\begin{array}{lcll} A & \leftarrow & \varpi + \underset{\leftarrow}{h}^{*} W \underset{\leftarrow}{h} & \text{(J.A.25a)} \\ B & \leftarrow & \varrho + H^{*} W \underset{\leftarrow}{h} & \text{(J.A.25b)} \\ C & \leftarrow & \varrho^{*} + \underset{\leftarrow}{h}^{*} WH & \text{(J.A.25c)} \\ D & \leftarrow & P^{-1} = \Pi + H^{*} WH & \text{(J.A.25d)} \end{array}}$$

in (J.A.26) we readily obtain

$$\begin{bmatrix} A & B \\ C & D \end{bmatrix}^{-1} = \begin{bmatrix} 0 & 0 \\ 0 & D^{-1} \end{bmatrix} + \begin{bmatrix} I \\ -D^{-1}C \end{bmatrix} (A - BD^{-1}C)^{-1} \begin{bmatrix} I & -BD^{-1} \end{bmatrix} \tag{J.A.26}$$

$$\begin{aligned}\underset{\rightarrow}{P} &= \begin{bmatrix} P & 0 \\ 0 & 0 \end{bmatrix} + (\varpi + \underset{\rightarrow}{h}^{*} W \underset{\rightarrow}{h} - (\varrho^{*} + \underset{\rightarrow}{h}^{*} WH)P(\varrho + H^{*} W \underset{\rightarrow}{h}))^{-1} \\ &\quad \begin{bmatrix} -P(\varrho + H^{*} W \underset{\rightarrow}{h}) \\ 1 \end{bmatrix} \begin{bmatrix} -(\varrho^{*} + \underset{\rightarrow}{h}^{*} WH)P & 1 \end{bmatrix} \\ &= \begin{bmatrix} P & 0 \\ 0 & 0 \end{bmatrix} + \zeta^{-1} \begin{bmatrix} -\hat{w}^{b} \\ 1 \end{bmatrix} \begin{bmatrix} -\hat{w}^{b*} & 1 \end{bmatrix}, \end{aligned} \tag{J.A.27}$$

where

$$\hat{w}^b = P(\varrho + H^* W \underset{\rightarrow}{h}) \tag{J.A.28}$$

$$\underset{\rightarrow}{\bar{w}}^b = (I - \underset{\rightarrow}{P}\underset{\rightarrow}{H}^* W \underset{\rightarrow}{H})^{-1} P\varrho \tag{J.A.29}$$

and

$$\zeta = (\varpi + \underset{\rightarrow}{h}^* W \underset{\rightarrow}{h} - (\varrho^* + \underset{\rightarrow}{h}^* W H) P(\varrho + H^* W \underset{\rightarrow}{h})). \tag{J.A.30}$$

Accordingly, the quantity $\hat{w}^b$ can interpreted as the weight vector that solves the following weighted regularized problem

$$\min_{\underset{\rightarrow}{w}^b} [(\underset{\rightarrow}{w}^b - \underset{\rightarrow}{\bar{w}}^b)^* \underset{\rightarrow}{\Pi} (\underset{\rightarrow}{w}^b - \underset{\rightarrow}{\bar{w}}^b) + (\underset{\rightarrow}{h} - \underset{\rightarrow}{H}\underset{\rightarrow}{w}^b)^* W (y - \underset{\rightarrow}{H}\underset{\rightarrow}{w}^b)] \tag{J.A.31}$$

$$\underset{\leftrightarrow}{P}^{-1} = \begin{bmatrix} \Pi_{UL} & \varrho_U & \Pi_{UR} \\ \varrho_U^* & \varpi & \varrho_L^* \\ \Pi_{LL} & \varrho_L & \Pi_{LR} \end{bmatrix} + \begin{bmatrix} H_U^* \\ h^* \\ H_L^* \end{bmatrix} W \begin{bmatrix} H_U & h & H_L \end{bmatrix}. \tag{J.A.32}$$

In summary,

$$\underset{\leftrightarrow}{\hat{y}} = \hat{y} + \kappa \tilde{h} \tag{J.A.33}$$

$$\underset{\leftrightarrow}{\tilde{y}} = \tilde{y} - \kappa \tilde{h} \tag{J.A.34}$$

$$\underset{\leftrightarrow}{\xi} = \xi - \frac{|\rho|^2}{\sigma + \xi_h} \tag{J.A.35}$$

$$\underset{\leftrightarrow}{\gamma} = \gamma - \frac{|\tilde{\alpha}|^2}{\sigma + \xi_h} \tag{J.A.36}$$

$$\underset{\leftrightarrow}{\hat{w}} = \begin{bmatrix} \hat{w}_U \\ 0 \\ \hat{w}_L \end{bmatrix} + \kappa \begin{bmatrix} -\hat{w}_U^s \\ 1 \\ -\hat{w}_L^s \end{bmatrix}, \tag{J.A.37}$$

where

$$\kappa = \frac{\rho^*}{\sigma + \xi_h} \tag{J.A.38}$$

and the corresponding minimum cost $\xi_h = h^* W \tilde{h}$

J.A.2 Time-Update

J.A.3 General Order Update

The filter topology matrix Ψ is defined by

$$\theta_k \triangleq \sqrt{1-|a_k|^2} k = 0, 1, \ldots, M-1 \tag{J.A.39}$$

$$\boxed{\begin{bmatrix} u(i,0) & u_{i-1} \end{bmatrix} = \begin{bmatrix} u_i & u(i-1, M-1) \end{bmatrix} \Psi} \tag{J.A.40}$$

$$\Psi = \begin{bmatrix} 1 & a_0^* & 0 & 0 & \dots & 0 & 0 \\ 0 & \theta_1\theta_0 & a_1^* & 0 & \dots & 0 & 0 \\ & & \dots\dots\dots & & & & \\ 0 & -a_1\theta_2\theta_0 & \theta_2\theta_1 & a_2^* & \dots & 0 & 0 \\ \vdots & \vdots & \vdots & \vdots & \dots & \vdots & \vdots \\ 0 & (-1)^{M-3}\prod_{k=1}^{M-3} a_k\,\theta_{M-2}\theta_0 & (-1)^{M-4}\prod_{k=2}^{M-3} a_k\,\theta_{M-2}\theta_1 & (-1)^{M-5}\prod_{k=3}^{M-3} a_k\,\theta_{M-2}\theta_2 & \dots & a_{M-2}^* & 0 \\ & & \dots\dots\dots & & & & \\ 0 & (-1)^{M-2}\prod_{k=1}^{M-2} a_k\,\theta_0/\theta_{M-1} & (-1)^{M-3}\prod_{k=2}^{M-2} a_k\,\theta_1/\theta_{M-1} & (-1)^{M-4}\prod_{k=3}^{M-2} a_k\,\theta_2/\theta_{M-1} & \dots & \theta_{M-2}/\theta_{M-1} & 0 \\ 0 & (-1)^{M-1}\prod_{k=1}^{M-1} a_k\,\theta_0/\theta_{M-1} & (-1)^{M-2}\prod_{k=2}^{M-1} a_k\,\theta_1/\theta_{M-1} & (-1)^{M-3}\prod_{k=3}^{M-1} a_k\,\theta_2/\theta_{M-1} & \dots & -a_{M-1}\theta_{M-2}/\theta_{M-1} & 1 \end{bmatrix}, \quad \text{(J.A.41)}$$

where S is a 2×2 signature matrix. We then define a 3×3 signature matrix J by

$$J \triangleq (1 \oplus S_{i-1}) \tag{J.A.42}$$

$$\underbrace{\begin{bmatrix} \gamma^{-1/2}(i-1) & \begin{bmatrix} u(i) & u_{i-1} \end{bmatrix} \bar{L}_{i-1} \\ \Psi \begin{bmatrix} 0 \\ g_{i-1}\gamma^{-1/2}(i-1) \end{bmatrix} & \bar{L}_{i-1} \end{bmatrix}}_{\mathcal{A}} \Theta_i = \underbrace{\begin{bmatrix} \mathtt{x} & 0 \\ \mathtt{y} & \mathtt{Z} \end{bmatrix}}_{\mathcal{B}} \tag{J.A.43}$$

we simply compare entries on both sides of the equality:

$$\mathcal{A} \underbrace{\Theta_i J \Theta_i^*}_{J} \mathcal{A}^* = \mathcal{B} J \mathcal{B}^*$$

now

$$\mathcal{A}\underbrace{\Theta_i J \Theta_i^*}_{J}\mathcal{A}^* = \underbrace{\begin{bmatrix} \gamma^{-1/2}(i-1) & \begin{bmatrix} u(i) & u_{i-1}\end{bmatrix}\bar{L}_{i-1} \\ \Psi\begin{bmatrix}0\\ g_{i-1}\gamma^{-1/2}(i-1)\end{bmatrix} & \bar{L}_{i-1}\end{bmatrix}}_{\mathcal{A}} J \underbrace{\begin{bmatrix} \gamma^{-*/2}(i-1) & \begin{bmatrix}0\\ g_{i-1}\gamma^{-1/2}(i-1)\end{bmatrix}^*\Psi^* \\ \bar{L}_{i-1}^*\begin{bmatrix}u(i) & u_{i-1}\end{bmatrix}^* & \bar{L}_{i-1}^*\end{bmatrix}}_{\mathcal{A}^*} \tag{J.A.44}$$

$$= \underbrace{\begin{bmatrix} \gamma^{-1/2}(i-1) & \begin{bmatrix} u(i) & u_{i-1}\end{bmatrix}\bar{L}_{i-1} \\ \Psi\begin{bmatrix}0\\ g_{i-1}\gamma^{-1/2}(i-1)\end{bmatrix} & \bar{L}_{i-1}\end{bmatrix}}_{\mathcal{A}}(1\oplus S_{i-1})\underbrace{\begin{bmatrix} \gamma^{-*/2}(i-1) & \begin{bmatrix}0 & \gamma^{-*/2}(i-1)g_{i-1}^*\end{bmatrix}\Psi^* \\ \bar{L}_{i-1}^*\begin{bmatrix}u^*(i)\\ u_{i-1}^*\end{bmatrix} & \bar{L}_{i-1}^*\end{bmatrix}}_{\mathcal{A}^*} \tag{J.A.45}$$

$$= \underbrace{\begin{bmatrix} \gamma^{-1/2}(i-1) & \begin{bmatrix} u(i) & u_{i-1}\end{bmatrix}\bar{L}_{i-1}S_{i-1} \\ \Psi\begin{bmatrix}0\\ g_{i-1}\gamma^{-1/2}(i-1)\end{bmatrix} & \bar{L}_{i-1}S_{i-1}\end{bmatrix}}_{\mathcal{A}(1\oplus S_{i-1})}\underbrace{\begin{bmatrix} \gamma^{-*/2}(i-1) & \begin{bmatrix}0 & \gamma^{-*/2}(i-1)g_{i-1}^*\end{bmatrix}\Psi^* \\ \bar{L}_{i-1}^*\begin{bmatrix}u^*(i)\\ u_{i-1}^*\end{bmatrix} & \bar{L}_{i-1}^*\end{bmatrix}}_{\mathcal{A}^*} \tag{J.A.46}$$

$$= \begin{bmatrix} \gamma^{-1/2}(i-1)\gamma^{-*/2}(i-1) + \begin{bmatrix} u(i) & u_{i-1}\end{bmatrix}\bar{L}_{i-1}S_{i-1}\bar{L}_{i-1}^*\begin{bmatrix}u^*(i)\\ u_{i-1}^*\end{bmatrix} & \gamma^{-1/2}(i-1)\begin{bmatrix}0 & \gamma^{-*/2}(i-1)g_{i-1}^*\end{bmatrix}\Psi^* + \begin{bmatrix} u(i) & u_{i-1}\end{bmatrix}\bar{L}_{i-1}S_{i-1}\bar{L}_{i-1}^* \\ \Psi\begin{bmatrix}0\\ g_{i-1}\gamma^{-1/2}(i-1)\end{bmatrix}\gamma^{-*/2}(i-1) + \bar{L}_{i-1}S_{i-1}\bar{L}_{i-1}^*\begin{bmatrix}u^*(i)\\ u_{i-1}^*\end{bmatrix} & \Psi\begin{bmatrix}0\\ g_{i-1}\gamma^{-1/2}(i-1)\end{bmatrix}\begin{bmatrix}0 & \gamma^{-*/2}(i-1)g_{i-1}^*\end{bmatrix}\Psi^* + \bar{L}_{i-1}S_{i-1}\bar{L}_{i-1}^*\end{bmatrix} \tag{J.A.47}$$

and

$$\begin{aligned}\mathcal{B}J\mathcal{B}^* &= \underbrace{\begin{bmatrix}\mathtt{x} & 0\\ \mathtt{y} & \mathtt{Z}\end{bmatrix}}_{\mathcal{B}}(1\oplus S_{i-1})\underbrace{\begin{bmatrix}\mathtt{x}^* & \mathtt{y}^*\\ 0 & \mathtt{Z}^*\end{bmatrix}}_{\mathcal{B}^*}\\ &= \underbrace{\begin{bmatrix}\mathtt{x} & 0\\ \mathtt{y} & \mathtt{Z}S_{i-1}\end{bmatrix}}_{\mathcal{B}(1\oplus S_{i-1})}\underbrace{\begin{bmatrix}\mathtt{x}^* & \mathtt{y}^*\\ 0 & \mathtt{Z}^*\end{bmatrix}}_{\mathcal{B}^*}\\ &= \begin{bmatrix}\mathtt{x}\mathtt{x}^* & \mathtt{x}\mathtt{y}^*\\ \mathtt{y}\mathtt{x}^* & \mathtt{y}\mathtt{y}^*+\mathtt{Z}S_{i-1}\mathtt{Z}^*\end{bmatrix}\end{aligned} \tag{J.A.48}$$

to find that

$$\begin{cases}|\mathtt{x}|^2 & = \gamma^{-1}(i-1)+\begin{bmatrix}u(i) & u_{i-1}\end{bmatrix}\bar{L}_{i-1}S_{i-1}\bar{L}_{i-1}^*\begin{bmatrix}u^*(i)\\ u_{i-1}^*\end{bmatrix}\\ \mathtt{y}\mathtt{x}^* & = \Psi\begin{bmatrix}0\\ g_{i-1}\gamma^{-1}(i-1)\end{bmatrix}+\bar{L}_{i-1}S_{i-1}\bar{L}_{i-1}^*\begin{bmatrix}u^*(i)\\ u_{i-1}^*\end{bmatrix}\\ \mathtt{y}\mathtt{y}^*+\mathtt{Z}S_{i-1}\mathtt{Z}^* & = \Psi\begin{bmatrix}0\\ g_{i-1}\gamma^{-1/2}(i)\end{bmatrix}\begin{bmatrix}0\\ g_{i-1}\gamma^{-1/2}(i-1)\end{bmatrix}^*\Psi^*+\bar{L}_{i-1}S_{i-1}\bar{L}_{i-1}^*\end{cases}$$

The Laguerre polynomials are defined by

$$L_k(x)=\sum_{n=0}^{k}\frac{(-1)^n}{n!}\binom{k}{n}x^n,\quad x>0. \tag{J.A.49}$$

By insertion of $f_k(x)=e^{-x/2}L_k(x)$ the corresponding Fourier transform $F_k(\mathrm{j}\Omega)=$ we obtain

$$F_k\left(\tfrac{\mathrm{j}\Omega}{2\alpha}\right)=L_k(x)=\sum_{n=0}^{k}\frac{(-1)^n}{n!}\binom{k}{n}x^n,\quad x>0 \tag{J.A.50}$$

$$\P_N=(\alpha I\lambda^{N+1}\Pi+H_N^*\Lambda_N H_N)^{-1} \tag{J.A.51a}$$

$$\P_{N-1}=(\alpha I\lambda^{N}\Pi+H_{N-1}^*\Lambda_{N-1} H_{N-1})^{-1}. \tag{J.A.51b}$$

J.B Leaky Recursive Least-Squares Algorithm

J.B.1 Introduction

It is well known that so-called fast recursive least-squares array suffers from stability problems. The objective is to introduce *leakage* into the recursive least-squares in order to preserve numerical stability.

A design objective is to formulate a time-variant regularization weight matrix $\bar{W}(M \times M)$ that together with the likewise time-variant data weight matrix $W(N \times N)$ facilitates efficient recursive updates. Recall that the dimension of W increases linearly with time.

$$P_N^{-1} \triangleq \Phi_N = \Upsilon + \bar{W}_N \Pi + H_N^* W_N H_N \tag{J.B.1a}$$
$$P_{N-1}^{-1} \triangleq \Phi_{N-1} = \Upsilon + \bar{W}_{N-1} \Pi + H_{N-1}^* W_{N-1} H_{N-1}, \tag{J.B.1b}$$

where we by $\Pi > 0$ and $\Upsilon > 0$ refer to the regularization matrix and leakage matrix respectively. Both of these matrix quantities are assumed time-invariant.

$$\Upsilon = \upsilon \Delta \upsilon^*. \tag{J.B.2}$$

By $\bar{\Phi}_N$ we denote the correlation matrix excluding the leakage term. Hence,

$$\bar{\Phi}_N \triangleq \Phi_N - \Upsilon. \tag{J.B.3}$$

Similarly, by $\bar{P}_N^{-1}$ we denote the inverse correlation matrix excluding the leakage term. Hence,

$$\bar{P}_N^{-1} \triangleq P_N^{-1} - \Upsilon. \tag{J.B.4}$$

Hence, by invoking the matrix inversion lemma with

$$A \leftarrow \bar{P}_N^{-1}, \quad B \leftarrow \upsilon, \quad C \leftarrow \Delta, \quad D \leftarrow \upsilon^*$$

we can obtain P_N from $\bar{P}_N$ by

$$\begin{aligned} P_N &= \bar{P}_N - \bar{P}_N \upsilon (1 + \upsilon^* \bar{P}_N \upsilon)^{-1} \upsilon^* \bar{P}_N \\ &= \bar{P}_N - \frac{\bar{P}_N \Upsilon \bar{P}_N}{(1 + \upsilon^* \bar{P}_N \upsilon)}. \end{aligned} \tag{J.B.5}$$

Similarly at time $N-1$

$$P_{N-1} = \bar{P}_{N-1} - \frac{\bar{P}_{N-1} \Upsilon \bar{P}_{N-1}}{(1 + \upsilon^* \bar{P}_{N-1} \upsilon)}. \tag{J.B.6}$$

By subtracting (J.B.1b) from (J.B.1a) we obtain

$$\delta \Phi_N \triangleq \delta P_N^{-1} = P_N^{-1} - P_{N-1}^{-1} \tag{J.B.7}$$
$$= \delta \bar{W}_N \Pi + H_{N-1}^* \delta W_N H_{N-1} + u_N^* W_n u_N. \tag{J.B.8}$$

Moreover, it holds that $\delta \Phi \triangleq \delta \bar{P}_N^{-1} = \delta P_N^{-1} \triangleq \bar{\Phi}$

Now by insertion of (J.B.10a) and (J.B.10b) in (J.B.7) we obtain

$$\begin{aligned}\delta P_N &= \bar{P}_N - \frac{\bar{P}_N \Upsilon \bar{P}_N}{1+\upsilon^* \bar{P}_N \upsilon} - \bar{P}_{N-1} + \frac{\bar{P}_{N-1} \Upsilon \bar{P}_{N-1}}{1+\upsilon^* \bar{P}_{N-1} \upsilon} \\ &= \delta \bar{P}_N + \frac{(1+\upsilon^* \bar{P}_N \upsilon)(\bar{P}_{N-1} \Upsilon \bar{P}_{N-1}) - (1+\upsilon^* \bar{P}_{N-1} \upsilon)(\bar{P}_N \Upsilon \bar{P}_N)}{(1+\upsilon^* \bar{P}_N \upsilon)(1+\upsilon^* \bar{P}_{N-1} \upsilon)} \\ &= \delta \bar{P}_N + \frac{(1+\upsilon^* \bar{P}_N \upsilon)(\bar{P}_{N-1} \Upsilon \bar{P}_{N-1}) - (1+\upsilon^* \bar{P}_{N-1} \upsilon)(\bar{P}_N \Upsilon \bar{P}_N)}{(1+\upsilon^* \bar{P}_N \upsilon)(1+\upsilon^* \bar{P}_{N-1} \upsilon)}. \end{aligned} \tag{J.B.9}$$

J.B.2 Leaky Exponentially-Weighted Regularized Recursive Least-Squares Algorithm

In the case of $W_N = \Lambda_N \triangleq diag\{\lambda^N, \lambda^{N-1}, \ldots, \lambda, 1\}$ and $\bar{W}_N = \lambda^{N+1}$ we get a leaky but else ordinary exponentially-weighted regularized recursive least-squares.

$$P_N^{-1} \triangleq \Phi_N = \Upsilon + \lambda^{N+1} \Pi + H_N^* \Lambda_N H_N \tag{J.B.10a}$$

$$P_{N-1}^{-1} \triangleq \Phi_{N-1} = \Upsilon + \lambda^N \Pi + H_{N-1}^* \Lambda_{N-1} H_{N-1} \tag{J.B.10b}$$

The *weighted difference* $\delta_W \bar{\Phi}_N$ between the leakage free coefficient matrices $\bar{\Phi}_N$ and $\bar{\Phi}_{N-1}$ is defined by[1]

$$\delta_W \bar{\Phi}_N \triangleq \bar{\Phi}_N - \lambda \bar{\Phi}_{N-1} \tag{J.B.11}$$

and likewise for the *weighted difference* $\delta_W P_N^{-1}$ pertaining to the inverse coefficient matrix

$$\delta_W \bar{P}_N^{-1} \triangleq \bar{P}_N^{-1} - \lambda \bar{P}_{N-1}^{-1}. \tag{J.B.12}$$

By multiplying (J.B.10b) by λ and subtracting from (J.B.10a) we obtain

$$\begin{aligned}\bar{P}_N^{-1} =& \lambda \bar{P}_{N-1}^{-1} + H_N^* \Lambda_N H_N - \lambda (H_{N-1}^* \Lambda_{N-1} H_{N-1}) \\ =& \lambda \bar{P}_{N-1}^{-1} + u_N^* u_N \end{aligned} \tag{J.B.13}$$

with the identities

$$A \leftarrow \lambda \bar{P}_{N-1}^{-1}, \quad B \leftarrow u_N^*, \quad C \leftarrow 1, \quad D \leftarrow u_N$$

we obtain the following recursion for $\bar{P}_N$:

$$\begin{aligned}\bar{P}_N &= \lambda^{-1} \bar{P}_{N-1} - \lambda^{-1} \bar{P}_{N-1} u_N^* (1 + \lambda^{-1} u_N \bar{P}_{N-1} u_N^*)^{-1} u_N \lambda^{-1} \bar{P}_{N-1} \\ &= \lambda^{-1} \bar{P}_{N-1} - \lambda^{-1} \frac{\bar{P}_{N-1} u_N^* u_N \bar{P}_{N-1}}{\lambda^{-1} + u_N \bar{P}_{N-1} u_N^*}. \end{aligned} \tag{J.B.14}$$

[1] Remark that in general $\delta_W \bar{\Phi}_N \neq \delta_W \Phi_N \triangleq \Phi_N - \lambda \Phi_{N-1}, \quad \lambda < 1.$

Now by insertion of (J.B.9) in (J.B.23)

$$P_N = P_{N-1} - \frac{\bar{P}_N \Upsilon \bar{P}_N}{1 + \upsilon^* \bar{P}_N \upsilon} - \bar{P}_{N-1} + \frac{\bar{P}_{N-1} \Upsilon \bar{P}_{N-1}}{1 + \upsilon^* \bar{P}_{N-1} \upsilon}.$$

J.B.3 Exponentially-Weighted Regularized Recursive Least-Squares Algorithm

If we also set $\Upsilon = 0$ we get the ordinary exponentially-weighted regularized recursive least-squares. The time-update of the inverse of the correlation matrix can then be directly found from (J.B.23) by noting that $\bar{P}_N = P_N$

$$P_N = \lambda^{-1} P_{N-1} - \lambda^{-1} \frac{P_{N-1} u_N^* u_N P_{N-1}}{\lambda + u_N P_{N-1} u_N^*}. \tag{J.B.15}$$

The tap-weight update can then be expressed by

$$\begin{aligned}
w_N &= P_N \left[H_N^* \Lambda_N y_N \right] \\
&= P_N \left[H_{N-1}^* \Lambda_{N-1} y_{N-1} + u_N^* d(N) \right] \\
&= \left(P_{N-1} - \lambda^{-1} \frac{P_{N-1} u_N^* u_N P_{N-1}}{1 + \lambda^{-1} u_N P_{N-1} u_N^*} \right) \left[H_{N-1}^* \Lambda_{N-1} y_{N-1} + u_N^* d(N) \right] \\
&= \underbrace{P_{N-1} H_{N-1}^* \Lambda_{N-1} y_{N-1}}_{=w_{N-1}} - \lambda^{-2} \frac{P_{N-1} u_N^*}{1 + \lambda^{-1} u_N P_{N-1} u_N^*} u_N \underbrace{P_{N-1} H_{N-1}^* \Lambda_{N-1} y_{N-1}}_{=w_{N-1}} \\
&\quad + P_{N-1} u_N^* \left(1 - \lambda^{-1} \frac{u_N P_{N-1} u_N^*}{1 + \lambda^{-1} u_N P_{N-1} u_N^*} \right) d(N).
\end{aligned}$$

Accordingly, the tap-weight update can be expressed by

$$w_N = w_{N-1} - \lambda^{-1} \frac{P_{N-1} u_N^*}{1 + \lambda^{-1} u_N P_{N-1} u_N^*} \left[d(N) - u_N w_{N-1} \right]. \tag{J.B.16}$$

J.B.4 Leaky Exponentially-Weighted Sliding Window Recursive Least-Squares Algorithm

Notation

$$w_{N-1}^u \triangleq w_{[N-L:N-1]} \tag{J.B.17a}$$
$$w_{N-1}^d \triangleq w_{[N-L+1:N-1]} \tag{J.B.17b}$$
$$w_N^u \triangleq w_{[N-L+1:N]} \tag{J.B.17c}$$

and similarly for the inverse coefficient matrix:

$$\bar{P}^u_{N-1} \triangleq P_{[N-L:N-1]} \tag{J.B.18a}$$
$$\bar{P}^d_{N-1} \triangleq P_{[N-L+1:N-1]} \tag{J.B.18b}$$
$$\bar{P}^u_{N} \triangleq P_{[N-L+1:N]} \tag{J.B.18c}$$

and data matrix

$$H^u_{N-1} \triangleq H_{[N-L:N-1]} \tag{J.B.19a}$$
$$H^d_{N-1} \triangleq H_{[N-L+1:N-1]} \tag{J.B.19b}$$
$$H^u_{N} \triangleq H_{[N-L+1:N]}. \tag{J.B.19c}$$

In the case of $W^u_N = W^u_{N-1} = \Lambda_{L-1} \triangleq diag\{\lambda^{L-1}, \lambda^{L-2}, \ldots, \lambda, 1\}$, $W^d_{N-1} = \Lambda_{L-2} \triangleq diag\{\lambda^{L-2}, \lambda^{L-3}, \ldots, \lambda, 1\}$, $\bar{W}^u_N = \lambda^{N+1}$, $\bar{W}^u_{N-1} = \lambda^N$ and $\bar{W}^d_{N-1} = \lambda^N$ we get a leaky exponentially-weighted regularized sliding window recursive least-squares.

$$(\bar{P}^u_{N-1})^{-1} \triangleq \Phi^u_{N-1} \quad = \Upsilon + \lambda^N \Pi + (H^u_{N-1})^* \Lambda_L H^u_{N-1} \tag{J.B.20a}$$
$$(\bar{P}^d_{N-1})^{-1} \triangleq \Phi^d_{N-1} \quad = \Upsilon + \lambda^N \Pi + (H^d_{N-1})^* \Lambda_{L-1} H^d_{N-1} \tag{J.B.20b}$$
$$(\bar{P}^d_{N-1})^{-1} \triangleq \Phi^u_{N} \quad = \Upsilon + \lambda^{N+1} \Pi + (H^u_{N})^* \Lambda_L H^u_{N}. \tag{J.B.20c}$$

Downdating

By *downdating* we understand the process of discarding information acquired earlier in the process. More precisely at time N before using new information we will subtract the influence of the regressor u_{N-L} and the data $d(N-L)$ on the estimate of the tap-weights and inverse coefficient matrix. Hence, $\{w^u_{N-1}, (\bar{P}^u_{N-1})^{-1}\} \xrightarrow{downdating} \{w^d_{N-1}, (\bar{P}^d_{N-1})^{-1}\}$.

The *unweighted difference* $\delta^d_W \bar{\Phi}^d_{N-1}$ between the coefficient matrices $\bar{\Phi}^d_{N-1}$ and Φ^u_{N-L} is defined by [2]

$$\delta\bar{\Phi}^d_{N-1} \triangleq \bar{\Phi}^d_{N-1} - \bar{\Phi}^u_{N-1}$$

and likewise for the inverse coefficient matrix $\delta^d_W \bar{P}^d_{N-1}$

$$\delta(\bar{P}^d_{N-1})^{-1} \triangleq (\bar{P}^d_{N-1})^{-1} - (\bar{P}^u_{N-1})^{-1}. \tag{J.B.21}$$

By insertion of (J.B.20a) and (J.B.20b) in (J.B.21) we readily achieve

$$\begin{aligned}(\bar{P}^d_{N-1})^{-1} =& (\bar{P}^u_{N-1})^{-1} + (H^d_{N-1})^* \Lambda_{L-1} H^d_{N-1} - (H^u_{N-1})^* \Lambda_L H^u_{N-1} \\ =& (\bar{P}^u_{N-1})^{-1} - \lambda^{L-1} u^*_{N-L} u_{N-L}\end{aligned} \tag{J.B.22}$$

[2] The unweighted difference is used here at downdating pertains to the same iteration number.

with the identities

$$A \leftarrow (\bar{P}^u_{N-1})^{-1}, \quad B \leftarrow u^*_{N-L}, \quad C \leftarrow -\lambda^{L-1}, \quad D \leftarrow u_{N-L}$$

we obtain the following recursion for $\bar{P}^u_{N-1}$:

$$\begin{aligned}\bar{P}^d_{N-1} &= \bar{P}^u_{N-1} - \bar{P}^u_{N-1}u^*_{N-L}(-\lambda^{1-L} + u_{N-L}\bar{P}^u_{N-1}u^*_{N-L})^{-1}u_{N-L}\bar{P}^u_{N-1} \\ &= \bar{P}^u_{N-1} + \frac{\bar{P}^u_{N-1}u^*_{N-L}u_{N-L}\bar{P}^u_{N-1}}{\lambda^{1-L} - u_{N-L}\bar{P}^u_{N-1}u^*_{N-L}}. \end{aligned} \tag{J.B.23}$$

The tap-weight update can then be expressed by

$$\begin{aligned} w^d_{N-1} &= P^d_{N-1}\left[(H^d_{N-1})^*\Lambda_{L-1}y^d_{N-1}\right] \\ &= P^d_{N-1}\left[(H^u_{N-1})^*\Lambda_L y^u_{N-1} - \lambda^{L-1}u^*_{N-L}d(N-L)\right] \\ &= \left(P^u_{N-1} + \frac{P^u_{N-1}u^*_{N-L}u_{N-L}P^u_{N-1}}{\lambda^{1-L} - u_{N-L}P^u_{N-1}u^*_{N-L}}\right)\left[(H^u_{N-1})^*\Lambda_L y^u_{N-1} - \lambda^{L-1}u^*_{N-L}d(N-L)\right] \\ &= \underbrace{P^u_{N-1}(H^u_{N-1})^*\Lambda_L y^u_{N-1}}_{=w^u_{N-1}} + \frac{P^u_{N-1}u^*_{N-L}}{\lambda^{1-L} - u_{N-L}\bar{P}^u_{N-1}u^*_{N-L}}u_{N-L}\underbrace{P^u_{N-1}(H^u_{N-1})^*\Lambda_L y^u_{N-1}}_{=w^u_{N-1}} \\ &\quad - \lambda^{L-1}P^u_{N-1}u^*_{N-L}\left(1 + \frac{u_{N-L}P^u_{N-1}u^*_{N-L}}{\lambda^{1-L} - u_{N-L}\bar{P}^u_{N-1}u^*_{N-L}}\right)d(N-L). \end{aligned}$$

Accordingly, the tap-weight update can be expressed by

$$w^d_{N-1} = w^u_{N-1} - \frac{P^u_{N-1}u^*_{N-L}}{\lambda^{1-L} - u_{N-L}P^u_{N-1}u^*_{N-L}}\left[d(N-L) - u_{N-L}w^u_{N-1}\right]. \tag{J.B.24}$$

Updating

Following the downdating we will subsequently use the information in the present regressor u_N and the data $d(N)$. Hence, $\{w^d_{N-1}, (\bar{P}^d_{N-1})^{-1}\} \xrightarrow{updating} \{w^u_N(\bar{P}^u_N)^{-1}\}$. By subtracting (J.B.20a) from (J.B.20c) we obtain

$$\delta\Phi_N \triangleq \delta P_N^{-1} = \lambda^{N+1}\Pi + \lambda H^*_{N-1}H_{N-1} + u^*_N\Lambda_N u_N. \tag{J.B.25}$$

The weighted difference $\delta^u_W\bar{\Phi}^u_N$ between the coefficient matrices $\bar{\Phi}^u_N$ and $\bar{\Phi}^d_{N-1}$ is defined by

$$\begin{aligned}\delta^u_W\bar{\Phi}^u_N &\triangleq \bar{\Phi}^u_N - \lambda\bar{\Phi}^d_{N-1} \\ &= u^*_N\Lambda_N u_N \end{aligned} \tag{J.B.26}$$

and likewise for the inverse coefficient matrix $\delta_W^u \bar{P}_N^u$

$$\delta_W^u (\bar{P}_{N-1}^d)^{-1} \triangleq (\bar{P}_N)^{-1} - \lambda (\bar{P}_{N-1}^d)^{-1}. \tag{J.B.27}$$

By multiplying (J.B.20) by λ and insertion in (J.B.27) it is readily seen

$$\begin{aligned}(\bar{P}_N)^{-1} =& \lambda (\bar{P}_{N-1})^{-1} + H_N^* \Lambda_N H_N - \lambda (H_{N-1}^* \Lambda_{N-1} H_{N-1}) \\ =& \lambda (\bar{P}_{N-1})^{-1} + u_N^* u_N \end{aligned} \tag{J.B.28}$$

with the identities

$$A \leftarrow \lambda \bar{P}_{N-1}^{-1}, \quad B \leftarrow u_N^*, \quad C \leftarrow 1, \quad D \leftarrow u_N$$

$$\begin{aligned}\bar{P}_N &= \lambda^{-1} \bar{P}_{N-1} - \lambda^{-1} \bar{P}_{N-1} u_N^* (1 + \lambda^{-1} u_N \bar{P}_{N-1} u_N^*)^{-1} u_N \lambda^{-1} \bar{P}_{N-1} \\ &= \lambda^{-1} \bar{P}_{N-1} - \lambda^{-2} \frac{\bar{P}_{N-1} u_N^* u_N \bar{P}_{N-1}}{1 + \lambda^{-1} u_N \bar{P}_{N-1} u_N^*}. \end{aligned} \tag{J.B.29}$$

J.B.5 Exponentially-Weighted Sliding Window Recursive Least-Squares Algorithm

Finally, if we also set $\Upsilon = 0$ we get the ordinary exponentially-weighted regularized recursive least-squares.

The time-update of the inverse of the correlation matrix can then be directly found from (J.B.29) by noting that $\bar{P}_N = P_N$

$$P_N = \lambda^{-1} P_{N-1} - \lambda^{-2} \frac{P_{N-1} u_N^* u_N P_{N-1}}{1 + \lambda^{-1} u_N P_{N-1} u_N^*}. \tag{J.B.30}$$

The tap-weight update can then be expressed by

$$\begin{aligned} w_N &= P_N \left[H_N^* \Lambda_N y_N \right] \\ &= P_N \left[\lambda H_{N-1}^* \Lambda_{N-1} y_{N-1} + u_N^* d(N) \right] \\ &= \left(P_{N-1} - \lambda^{-1} \frac{P_{N-1} u_N^* u_N P_{N-1}}{1 + \lambda^{-1} u_N P_{N-1} u_N^*} \right) \left[H_{N-1}^* \Lambda_{N-1} y_{N-1} + u_N^* d(N) \right] \\ &= \underbrace{P_{N-1} H_{N-1}^* \Lambda_{N-1} y_{N-1}}_{=w_{N-1}} - \lambda^{-2} \frac{P_{N-1} u_N^*}{1 + \lambda^{-1} u_N P_{N-1} u_N^*} u_N \underbrace{P_{N-1} H_{N-1}^* \Lambda_{N-1} y_{N-1}}_{=w_{N-1}} \\ &\quad + P_{N-1} u_N^* \left(1 - \lambda^{-1} \frac{u_N^* u_N P_{N-1}}{1 + \lambda^{-1} u_N P_{N-1} u_N^*} \right) d(N). \end{aligned}$$

Accordingly, the tap-weight update can be expressed by

$$w_N = w_{N-1} - \lambda^{-1} \frac{P_{N-1} u_N^*}{1 + \lambda^{-1} u_N P_{N-1} u_N^*} \left[d(N) - u_N w_{N-1} \right]. \tag{J.B.31}$$

K. ORTHONORMAL FILTERS

K.1 Motivation

Pulse functions, *Laguerre functions* and *Kautz functions* belong to a more general class of *orthonormal functions* that among others also including Hermite, Charlie and Meixner functions. Orthonormal functions have received much attention in signal, system and control theory. Due to their inherent modeling capabilities orthonormal functions are extensively used for analysis and synthesis in signal processing and control applications.

Since there is a lot of similarities between the Laguerre and Kautz models [16] a description of these models will be conducted in parallel in this chapter.

For system identification purposes the order M of a finite-duration impulse response (FIR) filter is determined by at least two rules of thumb [46].

1. *Sample interval* T. The sample interval must be smaller than the smallest time constant of interest.

2. *Settling time*. The duration of the finite impulse response provided by the FIR filter, that is, MT must exceed the settling time of the system.

In practice in order to assess model order and sampling frequency one often acquires *a priori* knowledge about the dominating time constants of the system via physical modeling and/or step-response experiments. The main disadvantage of a FIR filter can be attributed to the use of simple delay operator as basis function. The canonical basis of $l^2(\mathbb{N}_0)$ are extremely localized in time or equivalently the memory is too short (only one sample). Accordingly, if the system has poles that are close to the unit circle, then a FIR filter would require a very high order in order accurately to model the system. Therefore, research effort in recent years has given a resurrection to the (complex) Laguerre and Kautz models as replacement to the ordinary FIR filter.

Historically, orthogonal functions have been used for the description of signals and systems by a relatively small number of coefficients. These orthonormal functions have been used for analysis and synthesis of linear networks, the design of cross correlators, computation of the Laplace transform of transients, parametrization in pattern recognition. Due to the ease of practical realization in an analogue computer focussed as been on the general class of *continuous orthonormalized exponential functions*.

The probably most well-known work in this field dates back to the Fourier expansion in cosine and sine functions. Lee [17] and Wiener [48] in a joint effort considered the use of Fourier transforms of Laguerre's functions for electrical network synthesis in particular transient synthesis and provided another application of orthogonal basis functions. The main results from this work can be found summarized in [18]. In the often cited work by Kautz [15] that is detailed in [14]

a fundamental approach to the transient synthesis problem was established. The main achievements of the work by Kautz was to solve the problem of orthogonalizing a set of continuous-time exponential functions by determining the corresponding Laplace transforms, which have very simple structures.

It should be emphasized that the procedure pertains to synthesis of a finite, time-invariant, lumped network. Applying this model for other physical systems must carefully be considered. Nevertheless, from the discussion of Part IV and detailed in the papers by Schröter a hearing protector device can to some extend be modeled by an equivalent time-invariant lumped finite element network.

In latter work Broome [4], Young and Huggins [49] established a solution for the equivalent discrete-time problem. In a manner analogous to Kautz, Broome established a general procedure for the construction of orthonormal sequences. Broome formulated expressions for orthonormal functions in the z-plane. The pertinent coefficients could then be determined by applying Cauchy residue theorem. The Laguerre and Kautz continuous-time functions could be obtained as specialization of this general discrete-time approach in the limit where the sampling interval approaches zero.

The main advantages of decomposing the regression vector in terms of *orthonormal* basis functions is that the approximation can be made with relative few constants. Due to the orthogonality between the individual basis functions it can be stated that the base functions provide no overlapping information. Consequently, the corresponding approximation problem then has a simple and direct solution. Moreover, the orthonormal filter structure allows us to model a larger class of systems normally requiring an infinite-duration impulse response (IIR) filter implementation. The orthogonality ensures that the governing equations have a Toeplitz structure which means a reduced numerical sensitivity. In particular if the filter is driven by white noise the resulting correlation matrix R will be in diagonal form. Furthermore, as the orthogonalized exponentials correspond to all-pass filters their implementation will be numerically robust [47].

In practice the orthonormality condition implies that if the input $s(t)$ is a white noise the tap-weight input are orthogonal. For the pulse function this is well known. Formally, the orthogonality applies to $\mathcal{L}_2(0,\infty)$ and the basis functions form a *complete* set in $\mathcal{L}_2(0,\infty)$ and $\mathcal{L}_1(0,\infty)$. The spaces $\mathcal{L}_1$ and $\mathcal{L}_2$ are defined in, e.g., [11, App. A.1]. Hence, in theory *any* stable system can be represented exactly by an infinite Laguerre/Kautz series. In practice, however, a truncated orthonormal series are used.

Kautz and Laguerre filter structures are based on *orthonormal* discrete-time versions of the Kautz and Laguerre basis functions respectively [15]. In recent years Laguerre and Kautz filters have been proposed as an alternative to FIR filter or IIR filter in different applications including acoustic echo cancelation (AEC) [29] and system identification [46, 47].

Although FIR filter has been the common choice probably due to its simple structure it is demonstrated that both Kautz and Laguerre filter structures can be used instead to describe the pertinent system with fewer parameters or alternatively achieve a better performance for the same number of parameters. The Laguerre model is in fact a particular instance of the more general Kautz model obtained by instead of using pairs of complex conjugated poles to use real poles. System specific *a priori* information can be used to determine if a Laguerre filter structure is sufficient or a the more general Kautz filter structure should be evaluated. From a practical point of view it should be recalled that a real pole corresponds to an exponentially damped system while complex conjugate poles correspond to exponentially damped sinusoids. Therefore, Kautz functions can approximate more efficiently signals with non-negligble oscillatory behav-

ior. Accordingly systems with a dominant first-order dynamics can be modeled by Laguerre functions whereas systems with a dominant second-order resonant dynamics are better modeled with Kautz functions. For the Laguerre filter the real pole α should be determined according to $\alpha = \mathrm{e}^{-T/\tau}$ where τ is the underlying time constant for the system and T is the sampling time.

In signal processing applications as well as control systems filters with relatively long impulse responses are often encountered. The long impulse response could stem from long propagation distances, e.g., acoustic echo cancelation. In active noise control lightly damped structures will normally exhibit long impulse responses [7, Ch. 2].

The filter structure becomes interesting in applications that can be parameterized in terms of a few (1 or 2) time-invariant poles and possibly many time-varying zeros. Such time-variant zero and time-invariant pole configuration has been observed and theoretically justified for room transfer functions. It should be remarked that there is no direct association between the order of poles required by the filter structure and the number of natural resonant frequencies or even the number of distinctive peaks. However, the optimal pole position in the SISO case is related to the system's dominant mode.

K.1.1 Chapter Outline

Following the motivational remarks above the theme of section K.2 is orthonormal basis functions. Then in applicability of orthonormal filters for system identification is discussed in section K.3. In section K.4 - K.6 Kautz and Laguerre filters and a mixture hereof will be addressed. Next procedures to optimize the free parameters involved will be considered in section K.7.

The chapter is concluded by some final remarks in section K.8.

K.2 Orthonormal Basis Functions

The one-sided Laplace-transform is defined by

$$F(s) \triangleq \mathcal{L}\{f(t)\} = \int_0^\infty f(t)e^{-st}\ \mathrm{d}t. \tag{K.2.1}$$

For a lumped element network the transfer function $H(s) \triangleq \mathcal{L}\{h(t)\}$ can be modeled as rational function of nominator polynomial $N(s)$ to a denominator polynomial $D(s)$.

$$\begin{aligned} H(s) = \frac{N(s)}{D(s)} &= A\frac{(s-z_1)(s-z_2)\dots(s-z_{N_z})}{(s-p_1)(s-p_2)\dots(s-p_{N_p})} \\ &= \sum_{k=1}^{N_p^0}\frac{G_k}{s-p_k} + \sum_{k=N_p^0+1}^{N_p^0+N_p^1}\frac{G_k}{s-p_k} + \dots + \sum_{k=\prod_{l=1}^{N_p-1} N_p^{l-1}}^{N_p}\frac{G_k}{s-p_k}, \end{aligned} \tag{K.2.2}$$

where N_p and N_z refer to the number of poles and zeros respectively and A is some real constant. The k'th pole and zero are denoted by p_k and z_k respectively. In the partial fraction expansion $N_p^{(m)}$ designates the number of m-th order poles. Then $N_p^{(1)}$ is the number of *simple poles*.

If the network is to be stable the real parts of all simple poles must be non-positive and the real parts of higher order poles must be strictly negative. Hence,

$$\Re(p_k) \leq 0 \quad k = 1, 2, \dots N_p^1 \tag{K.2.3a}$$

$$\Re(p_k) < 0 \quad k = N_p^1 + 1, N_p^1 + 2, \dots N_p. \tag{K.2.3b}$$

The input output relation is given by

$$y_i = \left(\sum_{n=0}^{p-1} \theta_n \mathcal{B}_m(q, \zeta_n) \right) u_i. \tag{K.2.4}$$

This simple construction preserves orthonormality while at the same time allow *a priori* knowledge about a variety of poles at $\zeta_1, \zeta_2, \dots, \zeta_{N_p}$ to be incorporated. In the network synthesis problem a transfer function $H(s)$ of the form (K.2.2) satisfying the stability criteria (K.2.3) is to be found. The estimated transfer function $\hat{h}(t)$ must approach the desired impulse response $h(t)$ with prescribed tolerances.

In order to preserve compatibility with textbooks on adaptive filtering the linear part of the parameter vector will be denoted by w.

$$\theta \triangleq col\{\zeta, w\}, \tag{K.2.5}$$

where

$$\zeta \triangleq \zeta_1, \zeta_2, \dots, \zeta_{N_\zeta}. \tag{K.2.6}$$

The orthonormality of the basis functions can be formulated in discrete-time for sequences. As proved in [4, App. A] the orthonormality implies

$$\langle \mathcal{B}_l(z), \mathcal{B}_k(z) \rangle = \begin{cases} 1, & l = k \\ 0, & l \neq k \end{cases} \quad 0 \leq l, k \leq M - 1, \tag{K.2.7}$$

where $\mathcal{B}_l$ is a discrete orthonormal function and the index l is an index over the function set and where the inner-product $\langle \mathcal{B}_l(z); \mathcal{B}_k(z) \rangle$ is defined by

$$\langle \mathcal{B}_l(z); \mathcal{B}_k(z) \rangle \triangleq \frac{1}{2\pi \mathrm{j}} \oint_T \mathcal{B}_l(z) \mathcal{B}_k^*(1/z^*) \, \frac{\mathrm{d}z}{z} = \frac{1}{2\pi} \int_{-\pi}^{\pi} \mathcal{B}_l(e^{\mathrm{j}\omega}) \mathcal{B}_k^*(e^{\mathrm{j}\omega}) \, \mathrm{d}\omega. \tag{K.2.8}$$

K.3 System Identification

Wahlberg, Wahlberg [46, 47] has made a detailed analysis of using Laguerre/Kautz models as a linear regression method. In a simple example of a resonant system the advantage of employing a Kautz filter instead of Laguerre and FIR filter was demonstrated. The analysis, however, was restricted to single pole Laguerre and complex conjugate pair poles in Kautz filters.

Therefore, these filters have attracted interest in recent years [12]. Then the objective is to improve the basis functions $\Psi_i(q, \vartheta)$ such that an accurate description of the system can be

achieved by a small order of M. From a system identification point of view the variance of an estimated model is proportional to the number of estimated parameters [19]. Hence, it is advantageous to use as few parameters as possible and still guarantee a useful model. In principle when infinite many terms are included in the parameter vector the choice of the free parameters is somewhat arbitrary. In practice, however, a truncated series is used and an immediate problem is to optimally select the free parameters so as to reduce the truncation error. The free parameters ϑ provides a mean to use *a priori* information concerning dominating time constants or resonant modes of the system into the orthonormal basis functions.

Besides providing low order modeling capability the Lageurre/Kautz filters are also more insensitive to the choice of sampling rate. Another advantage of Laguerre filter is related to the so-called time-delay systems.

In [31] a unifying concept for the construction of orthonormal basis for system identification is provided

$$\boxed{\mathcal{B}_m(q) = \frac{\sqrt{1-|\zeta_m|^2}}{q-\zeta_m}\prod_{l=0}^{m-1}\frac{1-\zeta_l^* q}{q-\zeta_l}}. \tag{K.3.1}$$

It is demonstrated that the pulse function, Laguerre and Kautz filters are restrictive specializations of (K.3.1). The estimation bias error will be decreased. However, the increased flexibility of the generalized orthonormal set has its price. Variance is more susceptible to noise. A more detailed analysis of the convergence properties can be found in [33]. The numerical properties are studied in [32].

K.4 Kautz Filter

Resonant poles (occur in complex conjugated pair) are poorly matched by real poles in Laguerre filter. The governing equations can be found from (K.3.1) by using a complex conjugated pole pairs $\zeta_{2m} = \zeta_{2m+1}^*$

$$\begin{aligned}\Psi_{2m}(z,\zeta_m) &= |1+\zeta_m|\sqrt{\frac{1-\zeta_m\zeta_m^*}{2}}\frac{z^{-1}-1}{(1-\zeta_m z^{-1})(1-\zeta_m^* z^{-1})}\\ &\quad\times\prod_{l=0}^{m-1}\frac{(z^{-1}-\zeta_l)(z^{-1}-\zeta_l^*)}{(1-\zeta_l z^{-1})(1-\zeta_l^* z^{-1})} \qquad \text{(K.4.1a)}\\ \Psi_{2m+1}(z,\zeta_m) &= |1-\zeta_m|\sqrt{\frac{1+\zeta_m\zeta_m^*}{2}}\frac{z^{-1}-1}{(1-\zeta_m z^{-1})(1-\zeta_m^* z^{-1})}\\ &\quad\times\prod_{l=0}^{m-1}\frac{(z^{-1}+\zeta_l)(z^{-1}-\zeta_l^*)}{(1-\zeta_l z^{-1})(1-\zeta_l^* z^{-1})}, \qquad \text{(K.4.1b)}\end{aligned}$$

where $\zeta_m \triangleq \alpha_m + \mathrm{j}\beta_m$ and ζ_m, ζ_m^* are a pair of complex conjugated poles. The number of tap-weights M is even for Kautz basis functions ($k = 0, 1, \ldots, M/2-1$).

The filter structure governed by (K.4.1a) to (K.4.1b) in general provides too many degrees of freedom. A major problem exists in the determination of the optimal pole positions in (K.4.1a)

to (K.4.1b). Moreover, by using a 2-pole configuration a computational more efficient algorithm can be obtained [29]. Therefore, one often resort to use a single pair complex conjugate poles (Kautz filter) or single pole (Laguerre filter). Accordingly, when referring to the discrete-time 2-pole Kautz models the 2-pole designation is normally suppressed.

$$K_{2m}(z,\zeta) = K_{2m}(z,\zeta)A(z,\zeta) \tag{K.4.2a}$$
$$K_{2m+1}(z,\zeta) = K_{2m+1}(z,\zeta)A(z,\zeta), \tag{K.4.2b}$$

where

$$K_0(z,\zeta) = \kappa_0 K_{2m}(z,\zeta)A(z,\zeta) \tag{K.4.3a}$$
$$K_1(z,\zeta) = \kappa_1 K_{2m+1}(z,\zeta)A(z,\zeta) \tag{K.4.3b}$$

and

$$A(z,\zeta) = \frac{(z^{-1}-\zeta)(z^{-1}-\zeta^*)}{(1-\zeta z^{-1})(1-\zeta^* z^{-1})} \tag{K.4.4}$$

and where

$$\kappa_0 = |1+\zeta_m|\sqrt{\frac{1-\zeta\zeta^*}{2}} \tag{K.4.5a}$$
$$\kappa_1 = |1-\zeta_m|\sqrt{\frac{1-\zeta\zeta^*}{2}}. \tag{K.4.5b}$$

The following transformation, which maps the unit disc to the unit disc establishes a link between the simple Laguerre and Kautz filters above and is often used in filter design.

$$\bar{z} = \frac{z(z-b)}{1-bz} \quad -1 < b < 1. \tag{K.4.6}$$

The Kautz topology filter is depicted in Figure K.1 on this page.

Fig. K.1: Adaptive Kautz Filter Topology

K.5 Laguerre Filter

Orthogonal polynomials including Laguerre polynomials were defined in [41]. The free parameter in a Laguerre filter is often referred to as a *time scale*.

The orthonormal filter structure topology is depicted in Figure K.2 on the next page.

The governing equations can be found from (K.3.1) by using a single real pole $\zeta_m = \zeta = \alpha$

$$\mathcal{B}_m(z) = \frac{\sqrt{1-|\alpha_m|^2}}{1-\alpha_m z^{-1}} \prod_{l=0}^{m-1} \frac{z^{-1}-\alpha_l^*}{1-\alpha_l z^{-1}}, \tag{K.5.1}$$

Fig. K.2: Adaptive Orthonormal Filter Topology

where each $\mathcal{B}_m(z)$ links the input signal $s(i)$ to the m'th linear filter tap-weight input. The existence of the continuous-time Laguerre expansion applies under the relative mild condition $g(t) \in \mathcal{L}_2(0,\infty) \cup \mathcal{L}_1(0,\infty)$.

The substitution of the simple time-delay elements with Laguerre filters, however, has a price. The convergence rate is decreased and the tracking capabilities are reduced.

K.6 Mixed Kautz Laguerre Filters

K.7 Optimization of Free Parameters

The parameter vector of the orthonormal model θ contains free parameters viz. (K.2.5). For a given system the truncation error described above will be a function of the number of filters and in particular the values of the free parameters. In the literature numerous references addressing the problem of determining the optimal free parameters for a fixed number of filters can be found. For example for the Laguerre model the free parameter(s) i.e. the pole(s) should be chosen close to the dominating pole(s) of the system. However, if the pole does not match the dominating poles with sufficient accuracy the superiority of Laguerre filters over FIR filter can no longer be warranted. The main problem of determining the free parameter(s) is that the squared error surface of the truncated series involved is highly nonlinear and multi-modal with respect to these parameters [13, 18].

Scientist have investigated two different approaches for the of the optimization of the free parameters. In the first class the optimization is based on minimization of the error energy by invoking a gradient. The second class is based on sub-optimal optimization.

K.7.1 Gradient Based Optimization

The optimum choice of the free parameter in continuous-time Laguerre functions was first analytically investigated by Clowes [6]. It was demonstrated that although analytical expression are readily obtainable the solution involves *root finding* in a polynomial in the free parameter of order at least $M + N_p^{(1)}$, where $N_p^{(1)}$ denotes the number of simple poles of the system. Unfortunately, this approach requires complete specification of the signal to be approximated. Parks [36] developed a procedure for the determination of the free Laguerre parameter in which the signal properties are represented by two "moment" characteristic functions.

In his doctorial thesis Masnadi-Shirazi [21] developed an analytical optimization procedure that has subsequently been refined Masnadi-Shirazi and Ahmed [22, 23]. This method requires finding roots of possible high-order polynomials. In Silva, Silva [38, 39] an analogous method of finding the optimal pole position for nonrational transfer function and for an arbitrary input was described. This work was extended to lattice filter structures in [40].

It is customary to estimate the few time-invariant poles by some off-line optimization process, e.g., Gauss-Newton method. In [20] a Laguerre single-pole optimization approach where the gradient and the Hessian are computed analytically was proposed.

It was demonstrated in an example that this Laguerre pole optimization may contribute to model reduction, since the a model with such an optimized pole may provide a better approximation than a higher order model (in terms of M) with an arbitrary chosen pole. However, their procedure did only provide local convergence in the pole position. By using a first order ARX model an initial pole estimate close to the system pole can be made. If required this estimation process can be repeated in order to accommodate slow variations in the optimal filter pole values.

The methods above are all off-line estimation and require a relatively high computational cost.

To the authors knowledge no general systematic approach for the derivation of multiple Kautz/Laguerre poles has hitherto been presented in the literature. For complex time-invariant *black box* systems with intrinsic multiple pole structure one could therefore consider employing *global optimization* as opposed to local optimization system identification procedures provided by for example a genetic algorithm or neural nets. The coefficients are estimated by suitable linear regression model, e.g., NLMS and RLS [19, 29, 34].

K.7.2 Suboptimal Optimization

Another approach was formulated by Fu and Dumont [8]. Here the linearly weighted sum of the squared Laguerre coefficients is subject to minimization

$$J = \sum_{m=1}^{\infty} m g_m^2. \tag{K.7.1}$$

The objective of (K.7.1) is to linearly increase the weight of each additional orthonormal function coefficient (e.g. Laguerre coefficient). Consequently, by gradually penalizing higher order coefficients the suboptimum will favor a solution requiring relatively few terms to represent the signal (or network).

This suboptimal optimization approach has continuingly being subject to improvements [42–45]. The technique requires only knowledge of few numerical characteristics of the signal. Moreover, the technique applies generally to a broader class of orthonormal functions used in signal processing. The main advantage of this technique is in terms of its simplicity, low computational cost and often according to Tanguy et al. relatively good efficiency. In [42] the work in was generalized by Tanguy et al. to a wider class of orthonormal functions and nonlinear Laguerre weighting was introduced. It was demonstrated that the optimization in [8] is a minimization of a criterion that is equivalent to an upper bound for the quadratic approximation error. Followingly Tanguy et al. [43] established approximation to the Laguerre filter weights. Their method was latter extended by an online method to optimize the Laguerre filter [44]. Finally, Tanguy et al. [45] approved that this approach provided that the number of basis functions to be used is chosen large enough, consists of minimizing an upper bound for the error energy.

By $\varphi_n(i, \theta)$ we refer to an orthonormal function that varies with the time-index i, the index n designates the particular function (*spectral index*) and where θ denotes the free parameter vector to be optimally selected.

The discrete-time inner product for two real-valued functions $\langle \psi^a; \psi^b \rangle$ is defined by

$$\langle \psi^a; \psi^b \rangle = \sum_{k=0}^{\infty} \psi^a(k) \psi^b(k). \tag{K.7.2}$$

Similarly the discrete-time weighted inner product is

$$\langle \psi^a; \psi^b \rangle_{\varpi} = \sum_{k=0}^{\infty} \varpi(k) \psi^a(k) \psi^b(k), \tag{K.7.3}$$

where ϖ designates a weighting function.

$$\langle \varphi_m(\theta); \varphi_n(\theta) \rangle = \delta_{m,n} \tag{K.7.4}$$

and where $\delta_{m,n}$ denotes the Dirac delta function. According to [42] by using weighted Laguerre functions viz. (K.7.3) a better approximation to initial transient response than non-weighted functions viz. (K.7.2). Accordingly we will introduce a time-dependent weight function $\varpi(k)$ and a weighted discrete orthonormal function by $\breve{\varphi}_n(i, \theta)$

$$\breve{\varphi}_n(\theta) = \varpi(k) \varphi_n(\theta) \tag{K.7.5}$$

$$\langle \breve{\varphi}_m(\theta); \breve{\varphi}_n(\theta) \rangle_{\varpi^{-2}} = \delta_{m,n}. \tag{K.7.6}$$

Hence, by using ϖ^{-2} as inner product weighting function it is easily verified that (K.7.7) holds.

$$\varpi(k) = w^2(k). \tag{K.7.7}$$

The two moment functions m_1 and m_2 are defined by

$$m_1 \triangleq \|f\|^{-2} \sum_{k=1}^{\infty} k \left[f(k)/\varpi(k) \right]^2 \tag{K.7.8a}$$

$$m_2 \triangleq \|f\|^{-2} \sum_{k=1}^{\infty} k \left[f(k-1)/\varpi(k-1) \right] \left[f(k)/\varpi(k) \right] \tag{K.7.8b}$$

where the weighted signal energy $\|f\|^2$ is defined by

$$\|f\|^2 \triangleq \sum_{k=1}^{\infty} \left[f(k)/\varpi(k) \right]^2. \tag{K.7.9}$$

Moreover, two quantities $S_1(a)$ and $S_2(a)$ defined by

$$S_1(a) \triangleq \sum_{m=0}^{\infty} (2m+1) w^2(m, a) \tag{K.7.10a}$$

$$S_2(a) \triangleq 2 \sum_{m=1}^{\infty} m w(m, a) w(m-1, a) \tag{K.7.10b}$$

and an auxiliary variable ρ_0

$$\rho_o = \frac{S_2(a) + \rho S_1(a)}{\rho S_2(a) + S_1(a)} \tag{K.7.11}$$

with

$$\rho \triangleq \frac{1 + a^2}{2a} \tag{K.7.12}$$

are used. The procedure first involves an adaptive algorithm for the estimation of the fixed parameters. In principle the suite of adaptive filters described in chapter 8 on page 371 are to our disposition. Then the free parameter is determined $a \leftarrow a_o$. The tap weights are then recalculated from the following exchange relation

$$w(m, a_o) = \sum_{j=0}^{\infty} w(j, a)\varphi_m(j, \frac{a_o - a}{1 - aa_o}), \qquad m = 0 \ldots M-1 \quad a \in]-1, 1[. \tag{K.7.13}$$

In Ngia [28] the nonlinear optimization problem of Laguerre and Kautz filters is solved by a separable nonlinear least-squares method. Hence, the optimization of the parameter vector θ is split into separate optimization of the pole vector ζ and tap-weight vector w.

Both an online algorithm (recursive separable nonlinear least-squares algorithm and here abbreviated by RSNLS) and off-line algorithm based on Gauss-Newton optimization were developed. A key point in this development is use of a theorem [28, Thrm. III.1]. However, this approach does not solve the problem of local minima. Hence, the global optimal choice of the parameter vector will only be found provided some appropriate initial value θ_{-1} is given. Although this is not explicitly stated an example of this paper clearly reveals this lack of global optimization capability.

K.8 Final Remarks

In conclusion Laugerre/Kautz filters can lead to reduced order modeling compared with FIR, AR or ARX modeling and improved numerical accuracy of the corresponding linear regression.

If the system involves several scattered poles a requirement on multi-parameter optimization exists.

In [10] a theory on of generalized orthonormal basis functions for linear time-invariant dynamical system is made. The key point is to make a transformation from time-domain representation to a domain representation more appropriate for the particular system/signal. It is demonstrated that the z-transformation, Laguerre transformation and Kautz transformation are specialized transformation associated with the pulse functions, Laguerre and Kautz polynomials respectively.

$$f(t) \approx \sum_{k=0}^{\infty} c_k L_k(t) \tag{K.8.1}$$

where $f(t)$ is defined for $t > 0$ and where the where the expansion coefficients $c_k(p)$ are also referred to as *Laguerre spectrum* in turn is obtained from

$$c_k(p) = \int_0^\infty e^{-t} L_k(t) f(t)\ \mathrm{d}t. \tag{K.8.2}$$

In the **s**-domain

$$L_k(s,\zeta) = \sqrt{2\zeta}\frac{(s-\zeta)^{k-1}}{(s+\zeta)^k}, \quad k \in \mathbb{N}, \quad \zeta > 0. \tag{K.8.3}$$

Similarly, in the **z**-domain

$$L_k(z,\zeta) = \sqrt{1-\zeta^2}\frac{(z^{-1}-\zeta)^{k-1}}{(1-\zeta z^{-1})^k}, \quad k \in \mathbb{N}, \quad |\zeta| < 1. \tag{K.8.4}$$

Then any square-summable sequence can be composed into its

$$h(i) = \sum_{k=0}^{\infty} c_k(\zeta) L_k(i) \tag{K.8.5}$$

The Laguerre spectral components are in turn obtained from an inner product

$$c_k(\zeta) = \langle h; L_k \rangle. \tag{K.8.6}$$

A major advantage of the continuous-time Laguerre functions and discrete-time Laguerre sequences is that the have transforms that are rational functions with very simple repetitive form viz. (K.8.3) and (K.8.4).

In the case of filter synthesis networks are designed starting from a prescribed *transient response* instead of prescribed *frequency characteristics*.

Laguerre series can be interpreted as Kautz series governed by a single pole.

Supplementary material on this topic is provided in [9] [35] [30] [5] [2, 3] [39] [1] and [24–27]

Bibliography

[1] Ahmed Amghayrir, Noël Tanguy, Pascale Bréhonnet, Pierre Vilbé, and Léon-Claude Calvez. Laguerre -Gram reduced-order modeling. *IEEE Transactions on Automatic Control*, 50(9): 1432–1435, 2005.

[2] A. C. den Brinker. Optimality conditions for a specific class of truncated Kautz series. *IEEE Transactions on Circuits and Systems—Part II: Analog and Digital Signal Processing*, 43 (8):597–600, 1996.

[3] Albertus. C. den Brinker and Harm J. W. Belt. Optimality free parameters in orthonormal approximations. *IEEE Transactions on Signal Processing*, 46(8):2081, 1998.

[4] P. W. Broome. Discrete orthonormal sequences. *Assoc. Computing Machinary*, 12(2):151–168, 1965.

[5] P. R. Clement. Laguerre functions in signal analysis and parameter identification. *J. Franklin Inst.*, 313:82–95, 1982.

[6] G. J. Clowes. Choice of the time-scaling factor for linear system approximations using orthonormal Laguerre functions. *IEEE Transactions on Automatic Control*, 10:487–489, 1965.

[7] Stephen J. Elliott. *Signal Processing for Active Control*. London: Academic Press, 2001.

[8] Y. Fu and G. A. Dumont. An optimum time scale for discrete Laguerre network. *IEEE Transactions on Automatic Control*, 38(6):934–938, 1993.

[9] M. J. Gottlieb. Concerning some polynominals orthogonal on a finite or enumerable set of points. *Amer. J. Mathematics*, 60:453–458, 1938.

[10] Peter S. C. Heuberger, Paul M. J. Van den Hof, and Otto H. Bosgra. A generalized orthornomal basis for linear dynamical systems. *IEEE Transactions on Automatic Control*, 40(3):451–465, 1995.

[11] Diederich Hinrichsen and Anthony J. Pritchard. *Mathematical Systems Theory I*. Springer-Verlag, Berlin, 2005.

[12] P. M. J. Van den Hof, P. S. Heuberger, and J. Bokor. System identification with generalized orthonormal basis functions. *Automatica*, 31(12):1821–1834, 1995.

[13] W. H. Huggins. Signal theory. *IRE Trans. Circuit Theory*, 3:210–216, 1956.

[14] W. H. Kautz. Network synthesis for specified transient responses. Technical Report 209, Mass. Inst. of Tech. Res. Lab. of Elec., 1952.

[15] W. H. Kautz. Transient synthesis in the time-domain. *IRE Trans. Circuit Theory*, 1:29–39, 1954.

[16] Luc Knockaert. On orthonormal müntz-Laguerre filters. *IEEE Transactions on Signal Processing*, 49(4):790–793, 2001.

[17] Y. W. Lee. Synthesis of electrical networks by means of fourier transforms of laguerre's functions. *Math. Phys.*, II:83–113, 1932.

[18] Y. W. Lee. *Statistical Theory of Communication*. John Wiley & Sons, Inc., New York, 1960.

[19] Lennart Ljung. *System Identification Theory for the User*. Prentice Hall, Upper Saddle River, NJ, 2nd edition, 1999.

[20] R. Malti, S. B. Ekongolo, and J. Ragot. Dynamic siso and miso system approximations based on optimal Laguerre models. *IEEE Transactions on Automatic Control*, 43(9):1318–1323, 1998.

[21] M. A. Masnadi-Shirazi. *Optimum Synthesis of Linear Discrete-Time Systems using Orthogonal Laguerre Sequences*. PhD thesis, New Mexico, 1990.

[22] M. A. Masnadi-Shirazi and N. Ahmed. Laguerre approximation of nonrecursive discrete-time systems. In *IEEE Int. Conf. Acoust., Speech, Signal Processing*, pages 1309–1312, Albuquerque, NM, 1990.

[23] M. A. Masnadi-Shirazi and N. Ahmed. Optimum Laguerre networks for a class of discrete-time systems. *IEEE Transactions on Signal Processing*, 39(9):2104–2108, 1991.

[24] Ricardo Merched. Extended RLS lattice adaptive filters. *IEEE Transactions on Signal Processing*, 51(9):2294–2309, 2003.

[25] Ricardo Merched and Ali H. Sayed. Order-recursive RLS Laguerre adaptive filtering. *IEEE Transactions on Signal Processing*, 48(11):3000–3010, 2000.

[26] Ricardo Merched and Ali H. Sayed. Extended fast fixed-order RLS adaptive filters. *IEEE Transactions on Signal Processing*, 49(12):3015–3031, 2001.

[27] Ricardo Merched and Ali H. Sayed. RLS-Laguerre lattice adaptive filtering: Error-feedback, normalized and array-based algorithms. *IEEE Transactions on Signal Processing*, 49(12): 2565–2576, 2001.

[28] Lester S. H. Ngia. Separable nonlinear least-squares methods for efficient off-line and on-line modeling of systems using Kautz and Laguerre filters. *IEEE Transactions on Circuits and Systems—Part II: Analog and Digital Signal Processing*, 48(6):562–579, 2001.

[29] Lester S. H. Ngia. Recursive identification of acoustic echo systems using orthonormal basis functions. *IEEE Transactions on Speech and Audio Processing*, 11(3):278–293, 2003.

[30] Brett Ninness and Juan Carlos Gómez. Frequency domain analysis of tracking and noise performance of adaptive algorithms. *IEEE Transactions on Signal Processing*, 46(5):1314–1332, 1998.

[31] Brett Ninness and Fredrik Gustafsson. A unifying construction of orthonormal bases for system identification. *IEEE Transactions on Automatic Control*, 42(4):515–521, 1997.

[32] Brett Ninness and Håkan Hjalmarsson. Model structure and numerical properties of normal equations. *IEEE Transactions on Circuits and Systems—Part I: Fundamental Theory and Applications*, 48(4):425–438, 2001.

[33] Brett Ninness, Håkan Hjalmarsson, and Fredrik Gustafsson. The fundamental role of general orthonormal bases in system identification. *IEEE Transactions on Automatic Control*, 44 (7):1384–1406, 1999.

[34] Mads Nørgaard, Ole Ravn, Niels Kjølstad Poulsen, and Lars Kai Hansen. *Neural Networks for Modelling and Control of Dynamic Systems*. Advanced Textbooks in Control and Signal Processing. Springer-Verlag, 2000.

[35] Ü. Nurges. Laguerre models in problems of approximation and identification of discrete systems. *Automation and Remote Control*, 48:346–352, 1987.

[36] T. W. Parks. Choice of time scale in Laguerre approximations using signal measurements. *IEEE Transactions on Automatic Control*, 16:511–513, 1971.

[37] Jürgen Schröter. The use of acoustical test fixtures for the measurement of hearing protector attenuation Part I: Review of previous work;design of an improved test fixture. *JASA*, 79 (4):1065–1081, 1986.

[38] Tomás Oliveira e Silva. Optimality condition for truncated Laguerre networks. *IEEE Transactions on Signal Processing*, 42(9):2528–2530, 1994.

[39] Tomás Oliveira e Silva. On the determination of the optimal pole position of Laguerre filters. *IEEE Transactions on Signal Processing*, 43(9):2079–2087, 1995.

[40] Tomás Oliveira e Silva. Optimality conditions for Laguerre lattice filters. *IEEE Signal Processing Letters*, 2(5):97–98, 1995.

[41] Gábor Szegö. *Orthogonal Polynomials*, volume XXIII. American Mathematical Society, Colloquium Publications, 4th edition, 1975.

[42] Noel Tanguy, Pierre Vilbé, and Leon-Claude Calvez. Optimum choice of free parameter in orthonormal approximations. *IEEE Transactions on Automatic Control*, 40(10):1811–1813, 1995.

[43] Noel Tanguy, Riwal Morvan, Pierre Vilbé, and Leon-Claude Calvez. Improved method for optimum choice of free parameter in orthogonal approximations. *IEEE Transactions on Signal Processing*, 47(9):2576–2578, 1999.

[44] Noel Tanguy, Riwal Morvan, Pierre Vilbé, and Leon-Claude Calvez. Online optimization of the time scale in adaptive Laguerre-based filters. *IEEE Transactions on Signal Processing*, 48(4):1184–1187, 2000.

[45] Noel Tanguy, Riwal Morvan, Pierre Vilbé, and Leon-Claude Calvez. Pertinent choice of parameters for discrete Kautz approximation. *IEEE Transactions on Automatic Control*, 47(5):783–786, 2002.

[46] Bo Wahlberg. System identification using Laguerre models. *IEEE Transactions on Automatic Control*, 36(5):551–562, 1991.

[47] Bo Wahlberg. System identification using Kautz models. *IEEE Transactions on Automatic Control*, 39(6):1276–1282, 1994.

[48] Norbert Wiener. *Extrapolation, interpolation, and smoothing of stationary time series with engineering applications*. John-Wiley, New York, 1949.

[49] T. Y. Young and W. H. Huggins. Discrete orthonormal exponentials. In *Nat'l Elec.*, pages 10–18, 1962.

L. ALPHA-STABLE DISTRIBUTIONS

L.1 Motivation

The least-squares criterion has extensively been used for the design of adaptive filtering algorithms. For most of the part this leads to tractable results. However, as already been discussed and detailed in chapter 8 the least-squares criterion is only adequate under Gaussian (normal) assumption. Unfortunately, not all noise is Gaussian. The Gaussian model is not well suited for describing signals with impulsive behavior. Many data set acquired from physical and economic systems exhibit *empirical* evidence for the *stable distributions*[1] to model the heavy tails and skewness encountered. Statistical analysis of observation made in nature, e.g., from atmospheric (thunderstorms) and underwater (ice cracks) environments, low-frequency atmospheric noise, gravitational fields of stars, temperature distributions in nuclear reactors, but also many types of man-made noise have proved to be non-Gaussian. Instead probability density functions for these phenomena are members of a generalization of the Gaussian distribution referred to as the family of *stable distributions*. Other application areas include financial time series, insurance modeling, hydrology data, meteorology data, geophysical signals, stresses in crystalline lattices, annual rainfall, error clustering in telephone circuits. Typical realizations of such random signals contain a large number of *outliers*. For such observations very low or at least moderate signal levels prevail most of the time. However, occasionally very intensive signals are intercepted. In a military context, noise spikes from gunfire or explosions could probably be modeled by a α-stable distribution. Also in the audio signal processing community *stable distributions* have been investigated [7]. In [10] it was observed that speech signals have relative low α-values and in certain intervals approaches the Cauchy distribution. Both speech signals and background noise signals are subject to time-variance. Finally, there is evidence of the heavy-tailed nature of the size distributions of the files sent over the World Wide Web (WWW).

In [36, Ch. 1] some examples of the occurrence of 1-dimensional stable law applications is provided. They all involve the limit theorems for the sums of *independent* and *weakly dependent* random variables (RVs).

Hence, there has been great interest in the last decade in the signal processing community in α-stable distributions. However, the least-squares based adaptive filter algorithms degrade under such impulsive noise conditions as they are not sufficiently robust against outliers in the distribution function.

Two instances of the α-stable have received much attention, namely the symmetric α-stable (SαS) distribution and the positive α-stable (PαS) distribution. The SαS distribution has also been used to model audio noise signals [7], [10] in order to better model the outliers that exists in real signals. In [24] the characteristics and potential applications for the PαS is presented. This distribution is

[1] This name stems from Lévy who together with Khintchine developed the theory of univariate stable distributions in the 1920's and 1930's.

useful for modeling signals related to energy or power where only positive outcomes are possible. For this distribution all negative-order moments exist, and ratios of these moments are used to estimate alpha. Application areas that are examined include: seismic activity, ocean wave variability, and radar sea clutter modulation. In the radar community the α-stable distributions has received attention over the last decade [6, 8, 28, 29, 33].

Finally, it should be remarked that in many other real-time applications data sets have *supergaussian* distributions as opposed to the *subgaussian* distributions above. Moreover, stable distributions are not appropriate for fitting data that exhibit multi-modality or gap in their support. In fact most heavy-tailed distributions do not belong to the class of stable distributions.

The engineering textbook by Nikias and Shao provides more detailed information in particular on the SαS distribution family and corresponding signal processing algorithms.

L.1.1 Chapter Outline

Following these motivational remarks the fundamental theory of α-stable (αS) distributions is presented. Then in the subsequent two sections specializations of the general αS distribution are introduced. Most attention has been paid to the *symmetric α-stable* random variables discussed in section L.3. Another important subclass of the αS distribution is the PαS distribution presented in section L.4. Then the practical problem of *parameter estimation* is addressed in section L.5. Next the related problem of synthesis of stable signals is discussed in section L.6. Then the theme of section L.7 is signal processing applied to signals that belong to the class of αS distributions. Next signal detection of stable signals is discussed in section L.8. Finally, section L.9 concludes the chapter and topics for future research activities are suggested.

L.2 Theory

In addition to agreeing very well with experimental data , α-stable distributions have a strong theoretical justification provided by the generalized central limit theorem (GCLT). Basically, the GCLT states that α-stable distributions are the only class of distributions that can be the limiting distributions for the sum of independent and identical distributed (i.i.d.) RVs.

Historically, the theoretical fundament for the stable distributions can be attributed to the work by Lévy who studied the normalized sums of *i.i.d.* terms from an arbitrary distribution.

Any stable RV can be expressed as an infinite sum which involve the arrival times of a Poisson process [25].

The term *stable* signifies that the distribution satisfy the following *linear stability property* [19, Thrm. 1]: A fundamental consequence of this stability property is the *Generalized Central Limit Theorem* that states that if the sum of i.i.d. random variables has a limiting shaped distribution as the number approaches infinity, the limiting distribution must be a member of the stable distributions. Actually, the objective of finding the limit distributions for sums of i.i.d. random variables lead to the formulation of the stable distributions.

Definition L.1. A random variable $\boldsymbol{\psi}$ (vector $\boldsymbol{\psi} = \boldsymbol{\psi}_1, \boldsymbol{\psi}_2, \ldots, \boldsymbol{\psi}_d$) is said to be a stable variable (vector) in $\mathbb{R}$ ($\mathbb{R}^d$) if and only if $\forall A_1, A_2 \in \mathbb{R}_+ \exists C \in \mathbb{R}_+, D \in \mathbb{R}(\mathbb{R}^d)$

$$A_1\boldsymbol{\psi}_1 + A_2\boldsymbol{\psi}_2 \stackrel{d}{=} C\boldsymbol{\psi} + D, \tag{L.2.1}$$

where $\boldsymbol{\psi}_1$ and $\boldsymbol{\psi}_2$ are independent copies of $\boldsymbol{\psi}$. The symbol $\boldsymbol{\psi}^a \stackrel{d}{=} \boldsymbol{\psi}^b$ denotes equality in distribution. In words, equation (L.2.1) says that the shape of $\boldsymbol{\psi}$ is preserved (up to scale and shift) under addition.

Fundamental to the α-stable distribution is the the *characteristic exponent* or index of stability $\alpha \in (0, 2]$, that links the quantities A_1, A_2 and C in (L.2.1).

Definition L.2. For any random variable $\boldsymbol{\psi}$ (vector $\boldsymbol{\psi} = \boldsymbol{\psi}_1, \boldsymbol{\psi}_2, \ldots, \boldsymbol{\psi}_d$) is said to be a stable variable (vector) in $\mathbb{R}$ ($\mathbb{R}^d$) if $\forall \boldsymbol{\psi} \in \mathbb{R}^d_+, \exists \alpha(0, 2]$

$$C^\alpha = A_1^\alpha + A_2^\alpha. \tag{L.2.2}$$

The characteristic exponent also determines to which abstract space the random variable belongs to

$$\boldsymbol{\Psi}^a \in \begin{cases} \text{Metric space}, & 0 < \alpha < 1 \\ \text{Banach space}, & 1 \leq \alpha < 2 \\ \text{Hardy space}, & 2 \leq \alpha. \end{cases} \tag{L.2.3}$$

The stable distributions are of the form of a four-parameter family of functions, that in addition to the or index of stability α also include the *symmetry parameter* $\beta \in [-1, 1]$, the *scale parameter* $\gamma > 0$ and the *location parameter* $\delta \in (-\infty, \infty)$. These parameters are subject to the following constraints

$$0 < \alpha \leq 2, \quad -1 \leq \beta \leq 1, \quad \gamma > 0, \quad -\infty < \delta < \infty. \tag{L.2.4}$$

The stable distribution is best used to model signals and noise that exhibit impulsive nature. The characteristic exponent ranging between 0 and 2 is a measure of the thickness of the tails of the distribution. Hence, the characteristic exponent sets the degree of impulsiveness.

A few specializations of the parameters in (L.2.4) should be mentioned. When the characteristic exponent equals the upper limit, that is, $\alpha = 2$ and the probability density function (pdf) exhibit no skewness, that is, the symmetry parameter $\beta = 0$, then the stable distribution coincide with a Gaussian distribution $\mathbf{N}(\delta, 2\gamma^2) \stackrel{d}{=} \mathbf{S}(\alpha = 2, \beta = 0, \gamma, \delta)$.

The *Cauchy distribution* is equivalent to $\mathbf{C}(\alpha, \mu) \stackrel{d}{=} \mathbf{S}(\alpha = 1, \beta = 0, \gamma, \delta)$ and the Lévy distribution is obtained from $\mathbf{L}(\alpha, \beta, c, \mu) \stackrel{d}{=} \mathbf{S}(\alpha = 1/2, \beta = 1, \gamma, \delta = 0)$ and the degenerate (constant= μ) distribution is obtained from $\mathbf{S}(\alpha, \beta = 0, \gamma, \delta = \mu)$ [25, p. 10].

In the statistical analysis of α-stable distributions one faces many difficulties as compared with the Gaussian case.

For Gaussian processes the minimum mean-square error (m.m.s.e.) criterion also minimizes the probability of large estimation errors. The m.m.s.e. criterion, however, in no longer appropriate for *stable processes* due to the lack of finite variance.

αS Property § 1. The class of univariate and multivariate stable distributions is very large and cannot be parameterized. Hence, cumulative distribution functions (cdfs) or pdfs are usually not known in closed-form. The stable *univariate* distribution is then instead described by its

characteristic function

$$\psi(t) = \exp\{\imath a t - \gamma|t|^{\alpha}[1 + \imath\beta\,\mathrm{sign}(t)\omega(t,\alpha)]\}, \tag{L.2.5}$$

where

$$\omega(t,\alpha) = \begin{cases} \tan\frac{\alpha\pi}{2}, & \text{if} \quad \alpha \neq 1 \\ \frac{2}{\pi}\log|t|, & \text{if} \quad \alpha = 1 \end{cases} \tag{L.2.6}$$

and where $\mathrm{sign}(\,\cdot\,)$ denotes the signum function.

$$\mathrm{sign}(t) = \begin{cases} -1, & \text{if} \quad t < 0 \\ 0, & \text{if} \quad t = 0 \\ 1, & \text{if} \quad t > 0, \end{cases} \tag{L.2.7}$$

Moreover, the lack of explicit densities causes difficulties or failure of many traditional methods of estimation and simulation etc. Hence, the lack of analytical expressions for the pdf in general makes it difficult building maximum likelihood (ML) estimators for the parameters. Moreover, the presence of the factor $\log|\theta|$ causes difficulties. The characteristic function is not continuous at $\alpha = 1$ except for $\beta = 0$. Generally the case $\alpha = 1$ needs to be treated separately.

More information on the αS distributions can be found in [19, Ch. 2]. It suffice here to list the following other properties of the αS distributions:

αS Property § 2. Non-existence of a closed-form expression for the probability density function except for the cases $\alpha = 1$ (Cauchy distribution) and $\alpha = 2$ (Gaussian distribution).

αS Property § 3. The distribution decays as a power function (algebraic tail) as opposed to an exponential function pertaining to the Gaussian distribution.

αS Property § 4. Only existence of fractional lower-order moments (FLOM). Hence, if the characteristic exponent $\alpha < 2$, then the second- or higher-order moments do not exist.

αS Property § 5. Some degradation of performance of adaptive algorithms derived assuming a SαS distribution compared with least-squares techniques when exposed to Gaussian distributed noise/signals. However, algorithms that are derived assuming a SαS distribution for the noise and/or noise are generally more robust to modeling errors, e.g., in the α-parameter.

αS Property § 6. The estimation of the parameters including the characteristic exponent can be cumbersome, due to the general lack of a closed-form expression for the pdf. Fortunately, we can device an adaptive filter based on stochastic gradient methods that do not require closed-form expressions.

αS Property § 7. Like the Gaussian distribution the family of distributions are smooth, unimodal, symmetric with respect to the median, and bell-shaped.

For multi-variate stable distributions we find some additional properties. Multi-variate also become relevant as a complex RV can be regarded as a two-dimensional random vector whose components are the real and imaginary parts.

αS Property § 8. The *autocovariance* that is powerful tool in the study of Gaussian random elements is not defined when $\alpha < 2$. Instead the *covariation* of $\mathbf{X}_1$ with $\mathbf{X}_2$ $[\mathbf{X}_1, \mathbf{X}_2]_\alpha$ is defined for $1 < \alpha < 2$ by

$$[\mathbf{X}_1, \mathbf{X}_2]_\alpha \triangleq \int_{\text{uc}} x_1 x_2^{\langle \alpha-1 \rangle} \mu(\, \mathrm{d}\mathbf{r}), \quad 1 < \alpha \leq 2, \tag{L.2.8}$$

where $\mu(\,\cdot\,)$ is the *spectral measure* of the SαS random vector $(\mathbf{X}_1, \mathbf{X}_2)$ and where the signed power $a^{\langle p \rangle}$ in turn is defined by

$$a^{\langle p \rangle} = \begin{cases} a^p, & a \geq 0 \\ -|a|^p, & a < 0. \end{cases} \tag{L.2.9}$$

For SαS processes the covariation plays a role similar to covariance for Gaussian processes.

L.3 Symmetric Alpha-Stable Distributions

When positive and negative outcomes are equally likely, then the process posses no skewness and would be SαS; that are defined by $\boldsymbol{\psi}^a \stackrel{d}{=} -\boldsymbol{\psi}^a$. The subset of the general class of αS distributions that is subject to the constraint on the *symmetry parameter* that $\beta = 0$ is very important in practice. The Gaussian and Cauchy distributions belong to this class.

In this report SαS is used to model impulsive interference. Because the field of SαS has received relative little attention in the active control communities, we devote this chapter for a brief review of the basic results of SαS. A more complete presentation of the field and further applications can be found in the textbooks [19, 25].

In [19, Ch. 9] a stable *statistical-physical* (as opposed to *statistical-empirical*) models for impulsive noise is provided. It is shown that under appropriate assumptions on the spatial and temporal distributions of the noise sources and the propagation conditions, the instantaneous amplitude of received noise obeys the SαS distribution. The stable distributions are therefore characterized by a peak in the probability function around a and then a more slowly decreasing tail. The excursion from Gaussianity is governed by the α parameter. The symmetry parameter sets the skewness. The scale parameter sets the dispersion around the mean and is therefore analogous to the variance. The location parameter, or shift parameter sets the shift of the pdf.

The fraction p'th-order moment of a SαS rv is given by

$$E|\boldsymbol{\psi}^a|^p = C(p, \alpha)\gamma p/\alpha, \quad 0 < p < \alpha, \tag{L.3.1}$$

where

$$C(p, \alpha) = \frac{2^{p+1}\Gamma(\frac{p+1}{2})\Gamma(-\frac{p}{\alpha})}{\alpha\pi\Gamma(-\frac{p}{2})} \tag{L.3.2}$$

and $\Gamma(\,\cdot\,)$ denotes the gamma function.

In [27] a *normalized* correlation, moments and cumultants are defined. It is demonstrated that these normalized quantities converge to the true values in probability Recent research fields address the generalized statistical models for mixtures of Gaussian and impulsive noise.

For simulation purposes we will use the *standard* SαS distribution for which $a = 0$ and $\gamma = 1$ with the corresponding probability density function

$$f(\psi;\alpha,\beta) = \frac{1}{\pi}\int_0^\infty \exp(-t^\alpha)\cos[\psi t + \beta t^\alpha \omega(t,\alpha)]\,\mathrm{d}t. \tag{L.3.3}$$

For the class of SαS random variable (RV) the so-called *mixing property* prevails:

Theorem 7. *For* $\mathbf{X}\overset{d}{=}\boldsymbol{N}(0,2\sigma^2)$ *and* $\mathbf{Y}\overset{d}{=}\boldsymbol{S}(\alpha'=\alpha/2,\beta=-1,\delta=0)$ *and independent from* $\mathbf{X}$*, then*

$$\mathbf{Z} = \mathbf{Y}^{1/2}\mathbf{X}, \tag{L.3.4}$$

where $\mathbf{Z}\overset{d}{=}\boldsymbol{S}(\alpha,\beta=0,\sigma,\delta=0)$.

Hence, Theorem 7 basically states that any SαS RV can be represented as the product of a Gaussian RV and a PαS RV. The mixing property Theorem 7 can therefore be exploited for data synthesis [14].

L.3.1 Sub Gaussian Symmetric Alpha-Stable Distributions

An important specialization of the SαS is the so-called Sub Gaussian Symmetric Alpha-Stable Distributions abbreviated SGSαS. This distribution function has successfully been used to model impulsive noise. The characteristic function[2] is defined as

$$\psi(\varpi) = \exp\left[\frac{1}{2}(\varpi^* R\varpi)^{\alpha/2}\right] \tag{L.3.6}$$

and represents *spherical invariant random processes*.

The SGSαS model has also been used to model coherent detection of a signals embedded in heavy-tailed noise with application to radar systems [32]. In such systems a contradicting requirement on a high probability of detection and a low probability of false alarm exists. For a given data intercept two mutually exclusive hypothesis can be made. The first hypothesis states that the data stem from noise only. In the second hypothesis the data is considered as due to a signal embedded in noise. In [32] it is demonstrated that a detector based on a multidimensional Cauchy distribution exhibits resistance to the presence of sub-Gaussian interference and high performance, compared with the performance of the Gaussian detector in Gaussian interference.

It is also argued that the gradient estimate in SαS becomes more and more sensitive to outliers in the distribution as the characteristic exponent α decreases from Gaussian ($\alpha = 2$) and downwards. Therefore, in a block update approach (refer to as *momentum*) the gradient estimates can become less noisy and better convergence achieved. Following the block update procedure both the fractional lower-order statistics (FLOS)-based algorithm and the block normalized LMS. For the studied cases $\alpha = 1.2$ and a 5-th order ARMA process a block length $L = 3$ seems

[2] Recall that the characteristic function and the density function $f(x)$ constitute a Fourier transform pair

$$\Psi_x(\omega) \triangleq \int_{-\infty}^{\infty} f(x)e^{\imath\omega x}\,\mathrm{d}x. \tag{L.3.5}$$

to give a good trade-off between convergence speed and memory consumption. Moreover, by the momentum approaches the performance of the normalized LMS and the proposed fractional lower-order statistics became insignificant. FLOS mitigates the effects of heavy-tailed noise.

L.4 Positive Alpha-Stable Distributions

The PαS is often useful to describe phenomena related to energy or power which are examples of signals where only positive outcomes are possible. In [24] the characteristics and potential applications for the PαS is presented. For this distribution all negative-order moments exist, and ratios of these moments are used to estimate alpha. Application areas that are examined include: seismic activity, ocean wave variability, and radar sea clutter modulation.

L.5 Parameter Estimation

McCulloch [17] extended the quantile-based estimation approach to a more general case $\alpha \in [0.6, 2]$ and $\beta \in [-1, 1]$. Also the estimation problem there exists for $\alpha = 1$ was solved.

The numerical properties of the empirical characteristic function (ECF) and projection method (PROJ) estimators is studied in [22] and some methods for exploratory data analysis (EDA) discussed. Noland [21] demonstrates that it is feasible to fit stable data from different physical and economic systems and to use diagnostics to assess the goodness of fit. Moreover, Noland [21] used [25, Thm. 2.3.1] to parameterizing *multivariable* stable distributions in terms of one dimensional projections.

[23] The software package STABLE from Robust Analysis, Inc. is useful for computation of basic quantities for stable distributions: densities, cumulative distribution functions, quantiles, and simulation. This package has been used in chapter 2 on page 17 and in Appendix D on page 547 for assessing the statistical properties of practical measurements. However, none of these measurements actually exhibited stable distribution characteristics.

L.5.1 Parameter Estimation Symmetric α-Stable Distributions

The lack of closed-form expressions for pdf makes parameter estimation of SαS random variable (RV) challenging. It is well known that important characteristics of a distribution can be deduced from the moments of the distribution. It is therefore customary in statistical analysis to employ first-, second-, and higher (third and fourth) order moments for density estimation. However, the αS distributions do not possess higher order moments. Instead FLOM can be employed.

In [31] a real-time approach for the estimation of the parameters constituting the Alpha-Stable distribution is proposed. The approach is hierarchical in structure and first the location parameter is estimated from sample median of the observations. Secondly, the characteristic exponent is determined from *extreme order statistics*. Thirdly, the dispersion is determined based on *fractional lower order moments*. Monte Carlo simulations revealed, however, that for $\alpha \geq 1.5$ the bias error and an increasing variance in the estimate is observed.

Also most algorithms for blind channel identification of a finite-duration impulse response (FIR) channel with non-Gaussian input are based on second- or higher order statistics (HOS).

They found that the value of p should be small for better estimation performance.

Their experiments also showed that the standard deviation of the parameter estimators increases as the order of the moment of $Y = \log|X|$ increases for a fixed sample size. The estimator is not a ML estimator. Moreover, it has to be proven that the estimators are unbiased and consistent.

However, many signals encountered in real life are impulsive or skewed. Hence a Gaussian autoregressive (AR) processes are not flexible enough. In [11] the general α-stable parametrization problem including nonzero skew was solved analytically. Three types of estimators that have closed-form solutions were proposed. However, the requirement of independent data time series is enforced.

In [2] a target detection algorithm that incorporates SαS distribution for clutter modeling is proposed.

L.6 Signal Synthesis

Various methods for the synthesis of α-stable signals exist [19, 30]. A numerical accurate representation near $\alpha = 1$ requires special treatment.

In [4, 18, 20] methods for simulating random samples for multivariate stable distributions is presented.

L.7 Signal Processing

The non-Gaussianity of impulse noise implies that a noise-suppression filter should be non-linear. In Kuruoğlu, Rayner, and Fitzgerald [12] proposed a nonlinear analogue of the Wiener filtering for removing α-stable distributed noise. The algorithm extension to iteratively reweighted least-squares (IRLS) is obtained by applying a Volterra expansion to the data. They called their algorithm for polynolminal iteratively reweighted least-squares (PIRLS) due to the polynomial entries involved. The superiority of the PIRLS over ordinary IRLS and in particular normalized LMpN (NLMpN) and normalized LMAD (NLMAD) was demonstrated in an example of a synthesized example of an audio signal corrupted with standard $\mathbf{S}(\alpha = 1.5, \beta, \gamma, \delta)$.

For adaptive filtering perspective it is probably better to overestimate the characteristic exponents and chose a relative lower order in an least-mean-p-norm. It can be demonstrated that the performance degradation by using a SαS-optimized adaptive filter algorithm in a Gaussian noise environment is marginal. However, if a least-mean square criteria is used for under impulse interference conditions a pronounced degradation is observed.

In [13] the IRLS method that involves the least l_p-norm (LLpN) is used in the estimation of AR coefficients of SαS processes. The IRLS was proposed by Yarlagadda, Bednar, and Watt [35]. The convergence of the IRLS is analyzed in [3].

In [1] an adaptive filtering approach for non-Gaussian stable processes is proposed.

L.8 Signal Detection

Most of the classical non-Gaussian receiver design techniques cannot be extended to the symmetric α-stable noise case since these techniques require an explicit compact analytical form for the probability density function of the noise distribution. In general α-stable distributions do not

possess such form. A remedy to this lack of an analytical pdf is to represent the noise as a scale mixtures of Gaussians [14]. Any SαS RV can be represented as the product of a Gaussian RV and a positive-stable RV with appropriate parameters [14]. An approximate analytical expression for the pdf is obtained.

In [34] the performance of constant false alarm rate (CFAR) processors subjected to Pearson-distributed clutter is investigated.

In [5] a near-optimal test statistics for the detection of arbitrary non-stationary second-order complex signals, using a bivariate, isotropic α-stable model for the noise is developed. It is demonstrated that this test statistics offers considerably enhanced performance compared with a locally optimal linear receiver in even mildly impulsive noise.

L.9 Future Research Activities

The following list of future activities are foreseen:

- In the active control literature the study of performance under non-Gaussian conditions has received very little attention. Therefore, the influence of the plant and the *filtered-x* methods (cf., chapter 6) used to take the plant response into account will be subject to further analysis.
- It is well-known that the recursive least-squares is superior to the least-mean-squares in most cases. The recursive least-squares is an optimal solution to the least-squares optimization problem, but can also be expressed as a stochastic gradient approximation to the steepest descent method [26, Ch. 5]. It should be investigated if an equivalent recursive *deterministic* algorithm can be formulated for the α-distributed signals.
- To demonstrate general applicability the analysis could optionally include radar clutter data.

Hitherto, the work on α-stable signals has been relative limited. Focus has been on deriving methods that can be use to deduce the statistical properties of a random process (RP). Only a few studies address the design of adaptive filters. Hence, the potential of adaptive filtering of α-stable distributed disturbances has not been full exploited at least in an active control (AC) context. In [16] the convergence properties of the signed-error and sign-sign algorithm for stationary random processes with index $1 < \alpha < 2$ is illuminated. By using system theoretic arguments, e.g., [26, Ch. 6-9] such analysis should be extended to include steady state performance and tracking capabilities. Moreover, the robustness to model parameter errors shall be investigated.

Bibliography

[1] Orhan Arikan, A. Enis Çetin, and Engin Erzin. Adaptive filtering for non-gaussian stable processes. *IEEE Signal Processing Letters*, 1(11):163–165, 1994.

[2] A. Banerjee, P. Burlina, and R. Chellappa. Adaptive target detection in foliage-penetrating SAR images using alpha-stable models. *IEEE Transactions on Image Processing*, 8(12): 1823–1831, 1999.

[3] R.H. Byrd and D.A. Payne. Convergence of the iteratively reweighted least squares algorithm for robust regression. Technical Report Tech. Rep. 313, The Johns Hopkins University, Baltimore, MD, 1979.

[4] J. M. Chambers, C. Mallows, and B. W. Stuck. A method of simulating stable random variables. *Journal of the American Statistical Association*, 71(354):340–344, 1976. Correction in JASA 82 (1987), 704.

[5] M.J. Coates and Ercan E. Kuruoğlu. Time-frequency-based detection in impulsive noise environments using α-stable noise models. *Signal Processing*, 82(12):1917–1925, 2002.

[6] Ernesto Conte, Maurizio Di Bisceglie, Carmela Galdi, and Giuseppe Ricci. A procedure for measuring the coherence length of the sea texture. *IEEE Transactions on Instrumentation and Measurement*, 46(4):836–841, 1997.

[7] Panayiotis G. Georgiou, Panagiotis Tsakalides, and Chris Kyriakakis. Alpha-stable modeling of noise and robust time-delay estimation in the presence of impulsive noise. *IEEE Transactions on Multimedia*, 1(3):291–301, 1999.

[8] Charles-Antoine Guérin. Scattering on rough surfaces with alpha-stable non-gaussian height distributions. *Waves Random Media*, 12:293–306, 2002.

[9] Aleksandr Yakovlevich Khintchine. Predelnye zakony dlya summ nezavisimykh sluchainykh velichin. *GONTI*, 1938.

[10] Preben Kidmose. Alpha-stable distributions in signal processing of audio signals. In Scandinavian Simulation Society, editor, *41st Conference on Simulation and Modelling*, pages 87–94, 2000.

[11] Ercan E. Kuruoğlu. Density parameter estimation of skewed α-stable distributions. *IEEE Transactions on Signal Processing*, 49(10):2192–2201, 2001.

[12] Ercan E. Kuruoğlu, Peter J. W. Rayner, and William J. Fitzgerald. Impulsive noise elimination using polynomial iteratively reweighted least squares. In *Digital Signal Processing Workshop Proceedings, 1996, IEEE*, pages 347–350, 1996.

[13] Ercan E. Kuruoğlu, Peter J. W. Rayner, and William J. Fitzgerald. Nonlinear autoregressive modeling of non-Gaussian signals using lp-norm techniques. In *Acoustics, Speech, and Signal Processing, 1997. ICASSP-97*, volume 5, pages 3533–3536, 1997.

[14] Ercan E. Kuruoğlu, C. Molina, and William J. Fitzgerald. Approximation of α-stable probability densities using finite mixtures of gaussians. In *EUSIPCO'98*, Greece, 1998.

[15] Paul Lévy. Théorie des erreurs la loi de Gauss et les lois exceptionelles. *Bulletin de la société Mathématique de France*, 52:49–85, 1924.

[16] Elias Masry. Alpha-stable signals and adaptive filtering. *IEEE Transactions on Signal Processing*, 48(11):3011–3016, 2000.

[17] J. Houston McCulloch. Simple consistent estimators of stable distribution parameters. *Communications in Statistics. Simulation and Computation*, 15:1109–1136, 1986.

[18] R. Modarres and John P. Noland. A method for simulating stable random vectors. *Computational Statistics*, 9:11–19, 1994.

[19] Chrysostomos L. Nikias and Min Shao. *Signal Processing with Alpha-Stable Distributions and Applications*. John Wiley & Sons, Inc., New York, 1995.

[20] John P. Noland. Numerical computation of stable densities and distribution functions. *Communication in Statistics - Stochastic Models*, 13:759–774, 1997.

[21] John P. Noland. Fitting data and assessing goodness-of-fit with stable distributions. In *Conference of Applications of Heavy Tailed Distributions in Economics, Engineering and Statistics*, American University, Washington, DC, 1999.

[22] John P. Noland and Anna K. Panorska. Data analysis for heavy tailed multivariate samples. *Communication in Statistics - Stochastic Models*, 13:687–702, 1997.

[23] John P. Noland, Anna K. Panorska, and J. Houston McCulloch. Estimation of stable spectral measures. *Mathematical and Computer Modelling*, 34:1113–1122, 2001.

[24] Robert D. Pierce. Application of the positive alpha-stable distribution. In *Higher-Order Statistics, 1997. Proceedings of the IEEE Signal Processing Workshop on*, pages 420–424, 1997.

[25] Gennady Samorodnitsky and Murad S. Taqqu. *Stable Non-Gaussian Random Processes: Stochastic Models with Infinite Variance*. Chapman and Hall, New York, 1994.

[26] Ali H. Sayed. *Fundamentals of Adaptive Filtering*. John Wiley & Sons, Inc., New York, NY, USA, 2003.

[27] Ananthram Swami and Brian Sadler. Parameter estimation for linear alpha-stable processes. *IEEE Signal Processing Letters*, 5(2):48–50, 1998.

[28] W. J. Szajnowski and J. B. Wynne. Simulation of dependent samples of symmetric alpha-stable clutter. *IEEE Signal Processing Letters*, 8(5):151–152, 2001.

[29] Panagiotis Tsakalides, Raffaele Raspanti, and Chrysostomos L. Nikias. Angle/doppler estimation in heavy-tailed clutter backgrounds. *IEEE Transactions on Aerospace and Electronic Systems*, 35(2):419–436, 1999.

[30] George A. Tsihrintzis and Chysostomos L. Nikias. Performance of optimum and suboptimum receivers in the presence of impulsive noise modeled as an alpha-stable process. *IEEE Transactions on Communications*, 43(234):904–914, 1995.

[31] George A. Tsihrintzis and Chysostomos L. Nikias. Fast estimation of parameters of the alpha-stable impulse interference. *IEEE Transactions on Signal Processing*, 44(6):1492–1502, 1996.

[32] George A. Tsihrintzis and Chysostomos L. Nikias. Data-adaptive algorithms for signal detection in sub-gaussian impulse interference. *IEEE Transactions on Signal Processing*, 45 (7):1873–1877, 1997.

[33] George A. Tsihrintzis and Chysostomos L. Nikias. Evaluation of fractional, lower-order statistics-based detection algorithms on real radar sea-clutter data. *Radar, Sonar and Navigation, IEE Proceedings*, 44(1):29–38, 1997.

[34] George A. Tsihrintzis, Flippo Trinci, and Chysostomos L. Nikias. Performance assessment of cfar processors in Pearson-distributed clutter. *IEEE Transactions on Aerospace and Electronic Systems*, 36(4):1377–1385, 2000.

[35] Rao Yarlagadda, J. Bee Bednar, and Terry L. Watt. Fast algorithms l_p deconvolution. *IEEE Transactions on Acoustics, Speech, and Signal Processing*, 33(1):174–182, 1985.

[36] V. M. Zolotarev. *One-Dimesional Stable Distributions*, volume 65 of *Translations of mathematical monographs*. 1986.

APPENDICES II

M. FOURIER TRANSFORMS

In this appendix the continuous-time Fourier transform and the discrete-time Fourier transform will formally be defined.

M.1 Fourier Transforms

Mathematical conditions for the existence of the Fourier transform can be very involved [1, App. A.3].

M.1.1 Continuous-Time Fourier Transforms

Suppose $\psi_a(\,\cdot\,)$ is a function that takes values on the real axis and outputs an m-vector with real or complex entries, that is, $\psi_a(\,\cdot\,) : \mathbb{R} \to \mathbb{K}^m$. Moreover, suppose that $\psi_a(\,\cdot\,)$ is a Lebesgue integrable function[1], that is, $\psi_a(\,\cdot\,) \in L^1(\mathbb{R};\mathbb{K}^m)$, then the bilateral continuous-time Fourier transform of $\psi_a(\,\cdot\,) \in L^1(\mathbb{R};\mathbb{K}^m)$ designated by $\tilde{\psi}_a(\imath\omega)$ is defined by[2]

$$\tilde{\psi}_a(\imath\omega) = (\mathcal{F}_{ct}\psi_a)(\imath\omega) \triangleq \int_{-\infty}^{\infty} \psi_a(t)\mathrm{e}^{-\imath\omega t}\,\mathrm{d}t, \quad \omega \in \mathbb{R}. \tag{M.1.3}$$

The operator $\mathcal{F}_{ct}$ is the bilateral continuous-time Fourier transform operator $\mathcal{F}_{ct} : L^1(\mathbb{R};\mathbb{K}^m) \to L^1(\mathbb{R};\mathbb{C}^m)$. For every $\psi_a(\,\cdot\,) \in L^1(\mathbb{R};\mathbb{K}^m)$ the Fourier transform $\tilde{\psi}_a(\imath\omega)$ is continuous in $\omega \in \mathbb{R}$ and tends to 0 as $\omega \to \mp\infty$. Hence, absolute integrability is a *sufficient* condition for the existence of the Fourier transform (M.1.3) and also guarantees uniform convergence.

Some functions are not absolute-integrable, but are square-integrable (finite-energy), e.g., the $\mathrm{sinc}(\,\cdot\,)$ function. In such cases the Fourier transform of signals $\psi_a(\,\cdot\,) \in L^2(\mathbb{R};\mathbb{K}^m)$ is required. However, as $L^2(\mathbb{R};\mathbb{K}^m) \not\subseteq L^1(\mathbb{R};\mathbb{K}^m)$ [1, (A.3.19)] the integral (M.1.3) is not necessarily con-

[1] In abstract integration theory L^p-spaces are defined by considering an interval $T \subset \mathbb{R}$ and a *Banach space* $(X, \|\cdot\|_X)$. For $p \in [1,\infty]$ the p-norm of a *Lebesgue measurable function* $x(\,\cdot\,) : T \to X$ given by [1, App. A.3]

$$\|x(\,\cdot\,)\|_p = \Big[\int_T \|x(t)\|_X^p\,\mathrm{d}t\Big]^{1/p}, \quad \|x(\,\cdot\,)\|\infty = \inf\{\alpha;\, \|x(t)\|_X \le \alpha, \text{a.e. } t \in T\}. \tag{M.1.1}$$

When using the p *vector norm* for the integrand in (M.1.1), that is, $\|y\|_X = \|y\|_p$ we need the following definition [1, App. A.1]: The vector norm for $y \in \mathbb{C}^m$ and $p \in [1,\infty]$ is defined by

$$\|y\|_p = (|y_1|^p + |y_2|^p + \cdots + |y_m|^p)^{1/p}, \quad 1 \le p < \infty, \quad \|y\|_\infty = \max\{|y_1|, |y_2|, \ldots, |y_m|\}. \tag{M.1.2}$$

[2] The notation $\imath\omega$ for the continuous-time Fourier transform (CTFT) is motivated by considering the substitution of the Laplace transform variable $s \to \imath\omega$. Then, the CTFT; when it exists, is simply $\tilde{\psi}_a(s)$ with $s = \imath\omega$. In other contexts, for instance, among mathematicians the simpler notion $\tilde{\psi}_a(\omega)$ is applied.

vergent. Instead the *Fourier Plancherel transform* of $\psi_a(\,\cdot\,)$ can be obtained from a limiting operation

$$\tilde{\psi}_a(\,\cdot\,) = \lim_{N\to\infty} \tilde{\psi}_{a,N}(\,\cdot\,) \text{ in } L^2(\mathbb{R};\mathbb{C}^m), \quad \tilde{\psi}_{a,N}(\imath\omega) \triangleq \int_{-N}^{N} \psi_a(t)\mathrm{e}^{-\imath\omega t}\,\mathrm{d}t, \quad \omega\in\mathbb{R}, \tag{M.1.4}$$

where $N\in\mathbb{N}$. With the Fourier Plancherel transform convergence takes place a.e. For example $(\mathcal{F}_{ct}\,\mathrm{sinc}(a\,\cdot\,))(\imath\omega) = \frac{\pi}{a}1_{[-a,a]}(\imath\omega)$, a.e. $\omega\in\mathbb{R}$ with the exceptions found at $\omega = \mp a$.

In engineering applications it is useful to have Fourier transform representation for commonly used functions, for instance, constant functions, Euler functions or periodic functions that are neither absolutely-integrable nor square-integrable and therefore strictly speaking, do not have Fourier transforms. Here the theory of *generalized functions* can be invoked and usage of Dirac delta "functions" made[3].

The inverse transform of $\tilde{\psi}_a \in L^1(\mathbb{R},\mathbb{C}^m)$ is defined by[4]

$$\psi_a(t) = (\mathcal{F}_{ct}^{-1}\tilde{\psi}_a)(t) \triangleq \frac{1}{2\pi}\int_{-\infty}^{\infty} \tilde{\psi}_a(\imath\omega)\mathrm{e}^{+\imath\omega t}\,\mathrm{d}\omega, \quad \text{a.e. } t\in\mathbb{R}, \tag{M.1.5}$$

where $\mathcal{F}_{ct}^{-1}$ is the inverse continuous-time Fourier transform (bilateral) operator. If, additionally $\psi_a(\,\cdot\,)$ is continuous then this inversion formula holds for all $t\in\mathbb{R}$.

M.1.2 Discrete-Time Fourier Transforms

Suppose $\psi_a(\,\cdot\,)$ is a function that takes values with indices in $T\subset\mathbb{Z}$ and outputs an m-vector with real or complex entries, that is, $\psi_a(\,\cdot\,) : \mathbb{Z}\to\mathbb{K}^m$. Moreover, suppose that $\psi_a(\,\cdot\,)$ is a Lebesgue summable function[5], that is, $\psi_a(\,\cdot\,)\in l^1(\mathbb{Z};\mathbb{K}^m)$, then the bilateral discrete-time Fourier transform of $\psi_a(\,\cdot\,)\in l^1(\mathbb{Z};\mathbb{K}^m)$ designated by $\tilde{\psi}_a(\mathrm{e}^{\imath\theta})$[6] is defined by

$$\tilde{\psi}_a(\mathrm{e}^{\imath\theta}) = (\mathcal{F}_{dt}\psi_a)(\mathrm{e}^{\imath\theta}) \triangleq \sum_{n=-\infty}^{\infty} \psi_a(n)\mathrm{e}^{-\imath\theta n}; \quad \theta\in[-\pi,\pi]. \tag{M.1.7}$$

The operator $\mathcal{F}_{dt}$ is the DTFT (bilateral) operator. The series converges uniformly in $\theta\in[-\pi,\pi]$ and its limit $\tilde{\psi}_a(\,\cdot\,) : [-\pi,\pi]\to\mathbb{C}^m$ is continuous with $\tilde{\psi}_a(-\pi) = \tilde{\psi}_a(\pi)$.

The corresponding inverse transform are defined by

$$\psi_a(n) = (\mathcal{F}_{dt}^{-1}\tilde{\psi}_a)(n) \triangleq \frac{1}{2\pi}\int_{-\pi}^{\pi} \tilde{\psi}_a(\mathrm{e}^{\imath\theta})\mathrm{e}^{+\imath\theta n}\,\mathrm{d}\theta, \quad n\in\mathbb{Z}, \tag{M.1.8}$$

[3]Formally, Dirac delta functions are not mathematical functions, but considered as distributions.

[4]The definition is not unique. A symmetric definition can also be formulated.

[5]In functional analysis l^p-spaces are defined by considering an interval $T\subset\mathbb{Z}$ and a *Banach space* $(X,\|\,\cdot\,\|_X)$. For $p\in[1,\infty]$ the p-norm of a *Lebesgue measurable function* $x(\,\cdot\,) : T\to X$ given by [1, App. A.3]

$$\|x(\,\cdot\,)\|_p = \Big[\sum_{t\in T}\|x(t)\|_X^p\Big]^{1/p}, \quad 1\le p<\infty, \quad \|x(\,\cdot\,)\|\infty = \sup_{t\in T}\|x(t)\|_X. \tag{M.1.6}$$

[6]The notation $\mathrm{e}^{\imath\theta}$ for the discrete-time Fourier transform (DTFT) is motivated by considering the substitution of the z-domain variable: $z\leftarrow\mathrm{e}^{\imath\theta}$. Then, the DTFT; when it exists, is simply $\tilde{\psi}_a(z)$ with $z=\mathrm{e}^{\imath\theta}$. In other contexts, for instance, among mathematicians the simpler notion $\tilde{\psi}_a(\theta)$ is used.

where $\mathcal{F}_{dt}^{-1}$ denotes the bilateral inverse discrete-time Fourier transform operator.

Bibliography

[1] Diederich Hinrichsen and Anthony J. Pritchard. *Mathematical Systems Theory I.* Springer-Verlag, Berlin, 2005.

N. SIGNAL ALIASING EFFECTS

N.1 Introduction

In this chapter we attempt to establish expressions in general for aliasing effects encountered in active noise control systems (ANCSs). In particular the relation between the continuous-time ordinary coherence squared function and the corresponding discrete-time ordinary coherence squared function will be derived. The conversion from the continuous-time domain to the discrete-time domain and back is related with a risk of introducing *aliasing* and *imaging* problems. In audio system design audible effects from the conversion stages are of concern. In active control system design audible artifacts from conversion is also of concern. In addition aliased or imaging components that are not sufficiently suppressed may also effect the active noise reduction (ANR) performance. Hence, in order to prevent aliasing an anti-aliasing filter (AAF) precedes each of the analogue to digital converters (ADCs). Similarly, in order to prevent imaging problems a reconstruction filter (RF) (or anti-imaging filter) succeeds each of the digital to analogue converters (DACs). In multi-rate systems (MRSs) a design objective is to employ a very fast system (zeroth level) sampling frequency so that almost negligible conversion delays are obtained as discussed in section 5.2 on page 249. However, similar potential *aliasing* and *imaging* problems are related to the use of the decimation interpolation filters (DIFs).

The performance of an ANCS is to a large extent determined by the inherent coherence functions between the reference sensors and the error sensors that in turn are determined from the statistical properties of the signals as explained in detail in chapter 2. The drop in coherence associated with the transition from the continuous-time domain to the discrete-time domain and the reverse transition and as a consequence a drop in ANR performance will be a function of the pertinent auto- and cross-spectral density functions over an extended frequency range beyond the Nyquist frequency and the choice of AAFs or decimation filters (DFs).

In ANCS delays in the control loop are of particular importance in the feedback system (FBS) design as they ultimately will limit the operational bandwidth of the system when exposed to random noise as discussed in Appendix A on page 529. Unfortunately, the requirements on small delays and small aliasing effects are conflicting. Hence, the active control (AC) engineer must make a trade-off between on one side avoiding aliasing/imaging effects and on the other side not introducing delays associated with the AAFs and RFs.

This work has practical applications to the design of AAFs and DIFs used for suppression of aliased components in the ordinary sampled case and the decimated case respectively. The AAFs/DFs may be used both in the error sensors, the reference sensors and possible performance sensors. The requirement imposed by the three sensor types on the AAFs/DFs, however, will be different.

To the author's best knowledge no previous work in this field has yet been published. Some guidelines related to this topic, however, is included in [1, Ch. 10].

N.1.1 Chapter Outline

This chapter is organized as follows. Following these introductory remarks we decompose a signal into an *unaliased* component and an *aliased* component in section N.2. For convenience subsection N.2.1 lists the basic continuous-time and discrete-time ordinary coherence squared functions. Moreover, the well known Fourier transform relations between the auto- and cross-correlation functions and the auto- and cross-spectral density functions are established. Next, in subsection N.2.2 we similarly split the discrete-time auto- and cross-correlation functions into unaliased-, aliased- and cross aliased-unaliased signal components. Using Fourier transform relations between the auto- and cross-correlation functions and the auto- and cross-spectral density functions we establish equivalent partitioning of the discrete-time auto- and cross-spectral density functions into unaliased-, aliased- and cross aliased-unaliased spectral components in subsection N.2.3. The analysis then take a different approach for periodic signals and random signals.

In section N.3 we apply our method to the practical design of AAFs in a single-rate ANR system and DFs in a multirate (MR) ANR system. Finally, we will summarize the main conclusions from this chapter in section N.4.

N.2 Decomposition of Signals into Aliased and Unaliased Components

In our derivation it will be useful to decompose a signal into an *unaliased* component and an *aliased* component. Accents $\overset{\triangleright}{\{\}}$ and $\overset{\triangleleft}{\{\}}$ will be used to designate the unaliased- and aliased signal components respectively. Hence, our arbitrary random sequences (RSs) $\psi_a(i), \psi_b(i)$ may be decomposed according to

$$\psi_a(i) = \overset{\triangleright}{\psi}_a(i) + \overset{\triangleleft}{\psi}_a(i) \tag{N.2.1a}$$

$$\psi_b(i) = \overset{\triangleright}{\psi}_b(i) + \overset{\triangleleft}{\psi}_b(i). \tag{N.2.1b}$$

N.2.1 Coherence

A comprehensive discussion of coherence functions is provided in chapter 2 on page 17. In this section the non-unity ordinary coherence squared function associated with *aliasing effects* will be analyzed in detail. These results will subsequently be used in section N.3 on page 803 to establish some simple design criteria for the filters that partake in the conversion from the continuous-time domain to the discrete-time domain. The continuous-time ordinary coherence squared function between the ψ_a and ψ_b is

$$\gamma^2_{\psi_a\psi_b}(\omega) = \frac{|S_{\psi_a\psi_b}(\omega)|^2}{S_{\psi_a\psi_a}(\omega)S_{\psi_b\psi_b}(\omega)}, \quad \omega \in \mathbb{R}. \tag{N.2.2}$$

The conversion from the continuous-time domain to the discrete-time domain aliasing implies that aliased spectral components and cross aliased-unaliased spectral components enter the discrete-

time ordinary coherence squared function

$$\gamma^2_{\psi_a\psi_b}(\theta) = \frac{|S_{\psi_a\psi_b}(\theta)|^2}{S_{\psi_a\psi_a}(\theta)S_{\psi_b\psi_b}(\theta)}, \quad -\pi \leq \theta \leq \pi. \tag{N.2.3}$$

Expectably, this will lead to a decrease in the ordinary coherence squared function ($\gamma^2_{\psi_a\psi_b}(\theta) \leq \gamma^2_{\psi_a\psi_b}(\omega)|_{\theta=\omega T}$). In the subsequent text we will give a proof of this.

The key to obtain the relation between $\gamma^2_{\psi_a\psi_b}(\theta)$ and $\gamma^2_{\psi_a\psi_b}(\omega)|_{\theta=\omega T}$ is to express relations between the continuous-time auto- and cross-spectral density functions and their discrete-time counterparts. It should be recalled that the auto spectral density function $S_{\psi_a\psi_a}(\omega)$ and auto correlation function $R_{\psi_a\psi_a}(\tau)$ constitute a continuous-time Fourier transform pair and that the same applies to the cross-spectral density function $S_{\psi_a\psi_b}(\omega)$ and cross-correlation function $R_{\psi_a\psi_b}(\tau)$, that is,

$$S_{\psi_a\psi_a}(\omega) \overset{\mathcal{F}_{ct}}{\longleftrightarrow} R_{\psi_a\psi_a}(\tau) \tag{N.2.4a}$$

$$S_{\psi_a\psi_b}(\omega) \overset{\mathcal{F}_{ct}}{\longleftrightarrow} R_{\psi_a\psi_b}(\tau). \tag{N.2.4b}$$

Similarly, the auto spectral density function $S_{\psi_a\psi_a}(\theta)$ and auto correlation function $R_{\psi_a\psi_a}(n)$ constitute a discrete-time Fourier transform pair and that the same applies to the cross-spectral density function $S_{\psi_a\psi_b}(\theta)$ and cross-correlation function $R_{\psi_a\psi_b}(n)$.

$$S_{\psi_a\psi_a}(\theta) \overset{\mathcal{F}_{dt}}{\longleftrightarrow} R_{\psi_a\psi_a}(n) \tag{N.2.5a}$$

$$S_{\psi_a\psi_b}(\theta) \overset{\mathcal{F}_{dt}}{\longleftrightarrow} R_{\psi_a\psi_b}(n). \tag{N.2.5b}$$

For convenience a formal definition of the pertinent Fourier transformations is provided in Appendix M on page 787.

N.2.2 Unaliased, Aliased and Cross Aliased-Unaliased Correlation Functions

In this section we will establish an expression for the discrete-time ordinary coherence squared function in terms of the unaliased-, aliased- and cross aliased-unaliased spectral components. This has applications to the design of AAFs and DIFs used for suppression of aliased components in the ordinary sampled case and decimated case respectively.

From [2, Ch. 4] we find the following link between the continuous-time Fourier transform $\tilde{\psi}_a(\imath\omega)$ of a continuous-time signal $\psi_a(t)$ and the discrete-time Fourier transform $\tilde{\psi}_a(\mathrm{e}^{\imath\theta})$ of the corresponding sampled sequence $\psi_a(nT)$

$$\tilde{\psi}_a(\mathrm{e}^{\imath\theta}) = \frac{1}{T}\sum_{k=-\infty}^{\infty} \tilde{\psi}_a\Big(\imath\Big(\frac{\theta}{T} - \frac{2\pi k}{T}\Big)\Big). \tag{N.2.6}$$

Often it can be assumed that the signal is band limited such that only the first aliasing-bands

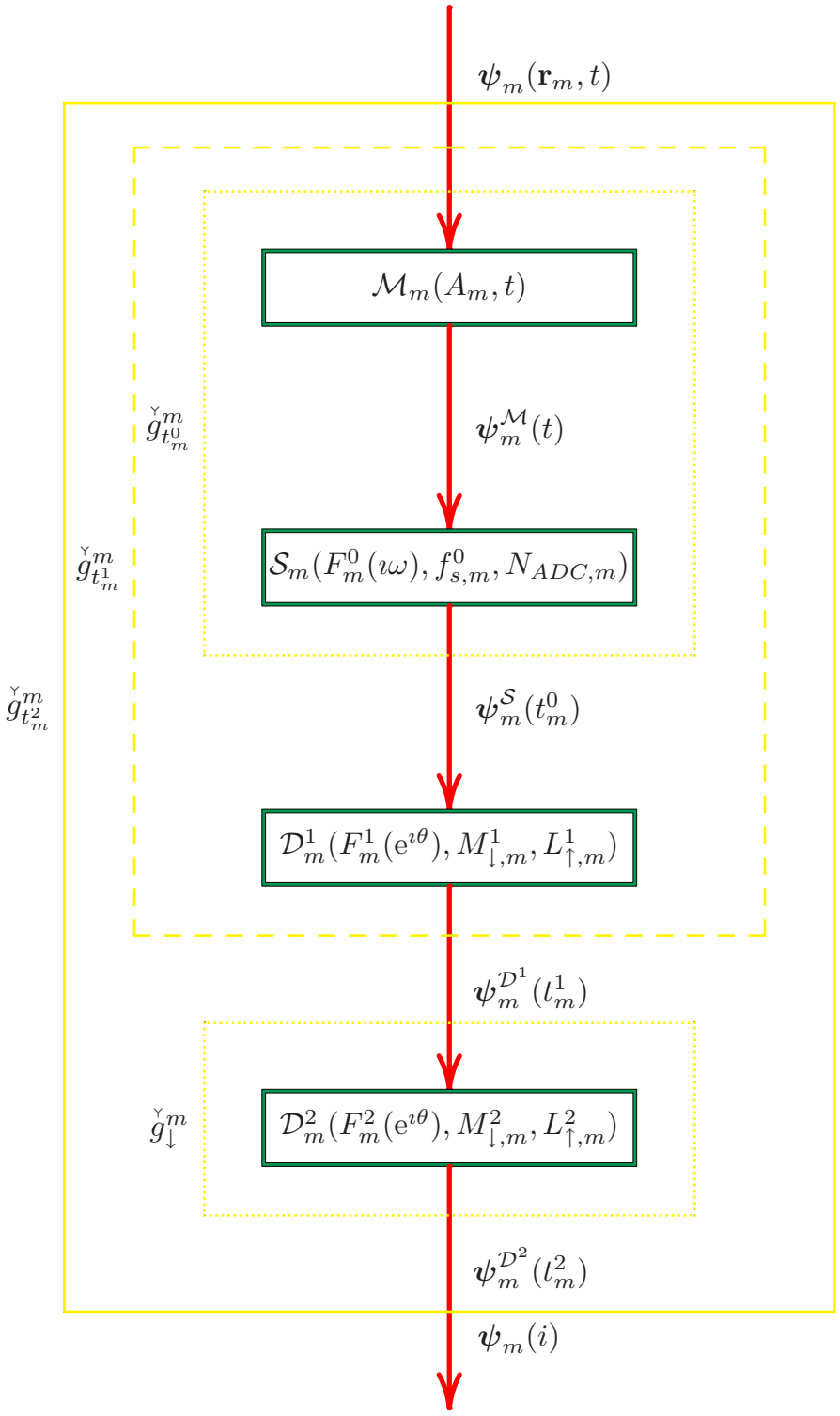

Fig. N.1: Plant Receive Part Sensor Sampling.

are of concern:

$$\tilde{\psi}_a(\mathrm{e}^{\imath\theta}) \approx \frac{1}{T}\sum_{k=-1}^{1} \tilde{\psi}_a\Big(\imath\Big(\frac{\theta}{T} - \frac{2\pi k}{T}\Big)\Big). \tag{N.2.7}$$

Referring to (N.2.1) and (N.2.6) we designate by $\overset{\triangleright}{\tilde{\psi}}_a(\mathrm{e}^{\imath\theta})$ the unaliased signal component of $\tilde{\psi}_a(\mathrm{e}^{\imath\theta})$ that is defined by

$$\overset{\triangleright}{\tilde{\psi}}_a(\mathrm{e}^{\imath\theta}) = \frac{1}{T}\tilde{\psi}_a\Big(\imath\frac{\theta}{T}\Big) \tag{N.2.8}$$

and we designate by $\overset{\triangleleft}{\tilde{\psi}}_a(\mathrm{e}^{\imath\theta})$ the aliased signal component of $\tilde{\psi}_a(\mathrm{e}^{\imath\theta})$ that is defined by

$$\overset{\triangleleft}{\tilde{\psi}}_a(\mathrm{e}^{\imath\theta}) = \frac{1}{T}\sum_{\substack{k=-\infty\\k\neq 0}}^{\infty} \tilde{\psi}_a\Big(\imath\Big(\frac{\theta}{T} - \frac{2\pi k}{T}\Big)\Big), \tag{N.2.9}$$

which sometimes may be approximated by

$$\overset{\triangleleft}{\tilde{\psi}}_a(\mathrm{e}^{\imath\theta}) \approx \frac{1}{T}\tilde{\psi}_a\Big(\imath\Big(\frac{\theta+2\pi}{T}\Big)\Big) + \frac{1}{T}\tilde{\psi}_a\Big(\imath\Big(\frac{\theta-2\pi}{T}\Big)\Big). \tag{N.2.10}$$

In our context $\psi_a(t)$ could represent the signal **succeeding** the AAF. Then, $\psi_a(i)$ would represent the signal following the continuous-time to discrete-time conversion. A design objective is to formulate requirements on the attenuation provided by the AAF as a function of frequency such that the residual aliasing side band content left after the AAF is sufficiently low.

For the continuous-time random signals the Fourier transform (M.1.3) or (M.1.4) do generally not exist as $\psi_a(\,\cdot\,) \notin L^1(\mathbb{R};\mathbb{R}) \cup L^2(\mathbb{R};\mathbb{R})$. Instead the autocovariance and autocorrelation functions that are *aperiodic finite-energy*, that is, $L^2(\mathbb{R};\mathbb{C})$, functions will be used to represent the statistical properties of the signals. Similar considerations lead to the use of the *aperiodic finite-energy* autocovariance and autocorrelation sequences[1] that subsequently will be defined to represent the statistical properties of the discrete-time random signals. For the same reasons, the spectral representation of the random signals plays an important role in describing input-output relations for a linear time-invariant (LTI) system excited by a stochastic signal.

The time-variant auto correlation function of an arbitrary nonstationary continuous-time random signal $\psi_a(t)$ denoted by $R_{\psi_a\psi_a}(t_1,t_2)$ and the time-variant cross-correlation function between two arbitrary nonstationary continuous-time random signals $\psi_a(t), \psi_b(t)$ denoted by $R_{\psi_a\psi_b}(t_1,t_2)$ are defined by

$$R_{\psi_a\psi_a}(t_1,t_2) = \mathrm{E}\,\boldsymbol{\psi}_a(t_1)\boldsymbol{\psi}_a^*(t_2) \tag{N.2.11a}$$
$$R_{\psi_a\psi_b}(t_1,t_2) = \mathrm{E}\,\boldsymbol{\psi}_a(t_1)\boldsymbol{\psi}_b^*(t_2). \tag{N.2.11b}$$

[1] For discrete-time signals we will use the terms function and sequence synonymously.

For discrete-time random signals similar definitions pertain. The time-variant auto correlation function of an arbitrary nonstationary discrete-time random signal $\psi_a(n)$ denoted by $R_{\psi_a\psi_a}(n_1, n_2)$ and the time-variant cross-correlation function between two arbitrary nonstationary discrete-time random signals $\psi_a(n), \psi_b(n)$ denoted by $R_{\psi_a\psi_b}(n_1, n_2)$ are defined by

$$R_{\psi_a\psi_a}(n_1, n_2) = \mathrm{E}\,\boldsymbol{\psi}_a(n_1)\boldsymbol{\psi}_a^*(n_2) \tag{N.2.12a}$$
$$R_{\psi_a\psi_b}(n_1, n_2) = \mathrm{E}\,\boldsymbol{\psi}_a(n_1)\boldsymbol{\psi}_b^*(n_2). \tag{N.2.12b}$$

If $\psi_a(t)$ and $\psi_b(t)$ exhibit *stationarity*[2] then the following *time-independent* definitions for the continuous-time ACF and CCF are obtained

$$R_{\psi_a\psi_a}(\tau) = \mathrm{E}\,\boldsymbol{\psi}_a(t)\boldsymbol{\psi}_a^*(t-\tau) \tag{N.2.13a}$$
$$R_{\psi_a\psi_b}(\tau) = \mathrm{E}\,\boldsymbol{\psi}_a(t)\boldsymbol{\psi}_b^*(t-\tau). \tag{N.2.13b}$$

Similarly if $\psi_a(i)$ and $\psi_b(i)$ exhibit *stationarity*[3] then the following *time-independent* definitions for the continuous-time ACS and CCS are obtained

$$R_{\psi_a\psi_a}(n) = \mathrm{E}\,\boldsymbol{\psi}_a(m)\boldsymbol{\psi}_a^*(m-n) \tag{N.2.14a}$$
$$R_{\psi_a\psi_b}(n) = \mathrm{E}\,\boldsymbol{\psi}_a(m)\boldsymbol{\psi}_b^*(m-n). \tag{N.2.14b}$$

Furthermore, if the underlying process governing $\psi_a(m)$ and $\psi_b(m)$ can be considered as *ergodic processes* then the following *time-averaged* auto correlation function $\langle R_{\psi_a\psi_a}(\tau)\rangle$ and cross-correlation function $\langle R_{\psi_a\psi_b}(\tau)\rangle$ are obtained

$$\langle R_{\psi_a\psi_a}(\tau)\rangle = \lim_{T'\to\infty}\frac{1}{2T'}\int_{-T'}^{T'}\psi_a(t)\psi_a^*(t-\tau)\,\mathrm{d}t \triangleq \{\psi_a(\tau)\}\{\psi_a^*(t-\tau)\} \tag{N.2.15a}$$
$$\langle R_{\psi_a\psi_b}(\tau)\rangle = \lim_{T'\to\infty}\frac{1}{2T'}\int_{-T'}^{T'}\psi_a(t)\psi_b^*(t-\tau)\,\mathrm{d}t \triangleq \{\psi_a(\tau)\}\{\psi_b^*(t-\tau)\} \tag{N.2.15b}$$

for continuous-time signals[4] and

$$\langle R_{\psi_a\psi_a}(n)\rangle = \lim_{L\to\infty}\frac{1}{2L+1}\sum_{m=-L}^{L}\psi_a(m)\psi_a^*(m-n) \triangleq \{\psi_a(m)\}\{\psi_a^*(m-n)\} \tag{N.2.16a}$$
$$\langle R_{\psi_a\psi_b}(n)\rangle = \lim_{L\to\infty}\frac{1}{2L+1}\sum_{m=-L}^{L}\psi_a(m)\psi_b^*(m-n) \triangleq \{\psi_a(m)\}\{\psi_b^*(m-n)\} \tag{N.2.16b}$$

[2]Formally, the transitions from (N.2.11a) to (N.2.13a) and from (N.2.11b) to (N.2.13b) require *stationarity in a autocorrelation function (ACF) sense* and *stationarity in a cross correlation function (CCF) sense* respectively [3].

[3]Formally, the transitions from (N.2.12a) to (N.2.14a) and from (N.2.12b) to (N.2.14b) require *stationarity in a autocorrelation sequence (ACS) sense* and *stationarity in a cross correlation sequence (CCS) sense* respectively [3].

[4]Formally, the transitions from (N.2.13a) to (N.2.15a) and from (N.2.13b) to (N.2.15b) require *ergodicity in an ACF sense* and *ergodicity in a CCF sense* respectively [3].

for discrete-time signals[5].

Next we decompose the auto- and cross-correlation function into unaliased-, aliased- and cross aliased-unaliased components. By insertion of (N.2.1) in (N.2.14a) we obtain

$$R_{\psi_a\psi_a}(n) = \mathrm{E}\,\boldsymbol{\psi}_a(m)\boldsymbol{\psi}_a^*(m-n) \tag{N.2.17a}$$

$$= \mathrm{E}\,\{\overset{\triangleright}{\boldsymbol{\psi}}_a(m)\overset{\triangleright}{\boldsymbol{\psi}}_a^*(m-n) + \overset{\triangleright}{\boldsymbol{\psi}}_a(m)\overset{\triangleleft}{\boldsymbol{\psi}}_a^*(m-n) + \overset{\triangleleft}{\boldsymbol{\psi}}_a(m)\overset{\triangleright}{\boldsymbol{\psi}}_a^*(m-n) + \overset{\triangleleft}{\boldsymbol{\psi}}_a(m)\overset{\triangleleft}{\boldsymbol{\psi}}_a^*(m-n)\} \tag{N.2.17b}$$

$$= R_{\substack{\triangleright\,\triangleright\\ \psi_a\psi_a}}(n) + R_{\substack{\triangleright\,\triangleleft\\ \psi_a\psi_a}}(n) + R_{\substack{\triangleleft\,\triangleright\\ \psi_a\psi_a}}(n) + R_{\substack{\triangleleft\,\triangleleft\\ \psi_a\psi_a}}(n), \tag{N.2.17c}$$

where $R_{\substack{\triangleright\,\triangleright\\ \psi_a\psi_a}}(n)$ represents the ACF of *unaliased* components of ψ_a, $R_{\substack{\triangleright\,\triangleleft\\ \psi_a\psi_a}}(n)$ denotes the CCF between *unaliased* and components of ψ_a and similarly $R_{\substack{\triangleleft\,\triangleright\\ \psi_a\psi_b}}(n)$ is the CCF between *aliased* components of ψ_a and *unaliased* components of ψ_b and finally $R_{\substack{\triangleleft\,\triangleleft\\ \psi_a\psi_a}}(n)$ is the ACF of *aliased* components of ψ_a. The second and third CCFs are related as $R_{\substack{\triangleright\,\triangleleft\\ \psi_a\psi_a}}(n) = R^*_{\substack{\triangleleft\,\triangleright\\ \psi_a\psi_a}}(-n)$.

By insertion of (N.2.1) in (N.2.14b) we obtain

$$R_{\psi_a\psi_b}(n) = \mathrm{E}\,\boldsymbol{\psi}_a(m)\boldsymbol{\psi}_b^*(m-n) \tag{N.2.18a}$$

$$= \mathrm{E}\,\{\overset{\triangleright}{\boldsymbol{\psi}}_a(m)\overset{\triangleright}{\boldsymbol{\psi}}_b^*(m-n) + \overset{\triangleright}{\boldsymbol{\psi}}_a(m)\overset{\triangleleft}{\boldsymbol{\psi}}_b^*(m-n) + \overset{\triangleleft}{\boldsymbol{\psi}}_a(m)\overset{\triangleright}{\boldsymbol{\psi}}_b^*(m-n) + \overset{\triangleleft}{\boldsymbol{\psi}}_a(m)\overset{\triangleleft}{\boldsymbol{\psi}}_b^*(m-n)\} \tag{N.2.18b}$$

$$= R_{\substack{\triangleright\,\triangleright\\ \psi_a\psi_b}}(n) + R_{\substack{\triangleright\,\triangleleft\\ \psi_a\psi_b}}(n) + R_{\substack{\triangleleft\,\triangleright\\ \psi_a\psi_b}}(n) + R_{\substack{\triangleleft\,\triangleleft\\ \psi_a\psi_b}}(n), \tag{N.2.18c}$$

where $R_{\substack{\triangleright\,\triangleright\\ \psi_a\psi_b}}(n)$ represents the CCF between *unaliased* components of ψ_a and ψ_b, $R_{\substack{\triangleright\,\triangleleft\\ \psi_a\psi_b}}(n)$ denotes the CCF between *unaliased* components of ψ_a and *aliased* components of ψ_b and similarly $R_{\substack{\triangleleft\,\triangleright\\ \psi_a\psi_b}}(n)$ is the CCF between *aliased* components of ψ_a and *unaliased* components of ψ_b and finally $R_{\substack{\triangleleft\,\triangleleft\\ \psi_a\psi_b}}(n)$ is the CCF between *aliased* components of ψ_a and ψ_b.

Note that in general $R_{\substack{\triangleright\,\triangleleft\\ \psi_a\psi_b}}(n) \neq R^*_{\substack{\triangleleft\,\triangleright\\ \psi_a\psi_b}}(-n)$.

N.2.3 Unaliased, Aliased and Cross Aliased-Unaliased Power Spectra

Next we want an expression for the time-averaged cross-spectral density functions in terms of the unaliased-, aliased- and cross aliased-unaliased spectral components. The equivalent auto spectral density functions are readily obtained from substituting ψ_b by ψ_a. Using the linearity property of the discrete-time Fourier transform and the relations (N.2.5b) and (N.2.18c) we may similarly decompose the cross-spectral density function by

$$\boxed{S_{\psi_a\psi_b}(\theta) = S_{\substack{\triangleright\,\triangleright\\ \psi_a\psi_b}}(\theta) + S_{\substack{\triangleright\,\triangleleft\\ \psi_a\psi_b}}(\theta) + S_{\substack{\triangleleft\,\triangleright\\ \psi_a\psi_b}}(\theta) + S_{\substack{\triangleleft\,\triangleleft\\ \psi_a\psi_b}}(\theta),} \tag{N.2.19}$$

[5]Formally, the transitions from (N.2.14a) to (N.2.16a) and from (N.2.14b) to (N.2.16b) require *ergodicity in an ACS sense* and *ergodicity in a CCS sense* respectively [3].

where the following discrete-time Fourier transform pairs are involved

$$S_{\substack{\triangleright\,\triangleright\\ \psi_a\psi_b}}(\theta) \overset{\mathcal{F}_{dt}}{\longleftrightarrow} R_{\substack{\triangleright\,\triangleright\\ \psi_a\psi_b}}(\theta) \tag{N.2.20a}$$

$$S_{\substack{\triangleright\,\triangleleft\\ \psi_a\psi_b}}(\theta) \overset{\mathcal{F}_{dt}}{\longleftrightarrow} R_{\substack{\triangleright\,\triangleleft\\ \psi_a\psi_b}}(\theta) \tag{N.2.20b}$$

$$S_{\substack{\triangleleft\,\triangleright\\ \psi_a\psi_b}}(\theta) \overset{\mathcal{F}_{dt}}{\longleftrightarrow} R_{\substack{\triangleleft\,\triangleright\\ \psi_a\psi_b}}(\theta) \tag{N.2.20c}$$

$$S_{\substack{\triangleleft\,\triangleleft\\ \psi_a\psi_b}}(\theta) \overset{\mathcal{F}_{dt}}{\longleftrightarrow} R_{\substack{\triangleleft\,\triangleleft\\ \psi_a\psi_b}}(\theta) \tag{N.2.20d}$$

In (N.2.20) $S_{\substack{\triangleright\,\triangleright\\ \psi_a\psi_b}}(\theta)$ represents the CSDF between *unaliased* components of ψ_a and ψ_b, $S_{\substack{\triangleright\,\triangleleft\\ \psi_a\psi_b}}(\theta)$ is the CSDF between *unaliased* components of ψ_a and *aliased* components of ψ_b, $S_{\substack{\triangleleft\,\triangleright\\ \psi_a\psi_b}}(\theta)$ is the CSDF between *aliased* components of ψ_a and *unaliased* components of ψ_b and finally, $S_{\substack{\triangleleft\,\triangleleft\\ \psi_a\psi_b}}(\theta)$ is the CSDF between *aliased* components of ψ_a and ψ_b.

Once we have obtained expressions for the aliased-unaliased spectra in (N.2.20) we may substitute into expression (N.2.3) on page 793 for the discrete-time ordinary coherence squared function

$$\gamma^2_{\psi_a\psi_b}(\theta) = \frac{\left|S_{\substack{\triangleright\,\triangleright\\ \psi_a\psi_b}}(\theta) + S_{\substack{\triangleright\,\triangleleft\\ \psi_a\psi_b}}(\theta) + S_{\substack{\triangleleft\,\triangleright\\ \psi_a\psi_b}}(\theta) + S_{\substack{\triangleleft\,\triangleleft\\ \psi_a\psi_b}}(\theta)\right|^2}{\left(S_{\substack{\triangleright\,\triangleright\\ \psi_a\psi_a}}(\theta) + S_{\substack{\triangleright\,\triangleleft\\ \psi_a\psi_a}}(\theta) + S_{\substack{\triangleleft\,\triangleright\\ \psi_a\psi_a}}(\theta) + S_{\substack{\triangleleft\,\triangleleft\\ \psi_a\psi_a}}(\theta)\right)\left(S_{\substack{\triangleright\,\triangleright\\ \psi_b\psi_b}}(\theta) + S_{\substack{\triangleright\,\triangleleft\\ \psi_b\psi_b}}(\theta) + S_{\substack{\triangleleft\,\triangleright\\ \psi_b\psi_b}}(\theta) + S_{\substack{\triangleleft\,\triangleleft\\ \psi_b\psi_b}}(\theta)\right)}, \quad -\pi \le \theta \le \pi. \tag{N.2.21}$$

Now the product of the two sequences $\{\overset{\triangleright}{\boldsymbol{\psi}}_a(m-n)\}$ and $\{\overset{\triangleleft}{\boldsymbol{\psi}}{}^*_b(m)\}$ with discrete-time Fourier transform (DTFT) $\mathrm{e}^{-\imath\theta n}\overset{\triangleright}{\tilde{\boldsymbol{\psi}}}_a(\mathrm{e}^{\imath\theta})$ and $\overset{\triangleleft}{\tilde{\boldsymbol{\psi}}}{}^*_b(\mathrm{e}^{\imath\theta})$ respectively can be determined from an inverse discrete-time Fourier transform of the periodic convolution of the corresponding DTFT [2, Ch. 2]. Hence, we may obtain the first term in (N.2.19), that is, the cross-spectral density function (CSDF) between *unaliased* components of ψ_a and ψ_b $S_{\substack{\triangleright\,\triangleright\\ \boldsymbol{\psi}_a\boldsymbol{\psi}_b}}(\theta)$ by

$$S_{\substack{\triangleright\,\triangleright\\ \psi_a\psi_b}}(\theta) \triangleq (\mathcal{F}_{dt} R_{\substack{\triangleright\,\triangleright\\ \psi_a\psi_b}})(\mathrm{e}^{-\imath\theta}) \tag{N.2.22a}$$

$$= \left(\mathcal{F}_{dt}\, \mathrm{E}\, \overset{\triangleright}{\boldsymbol{\psi}}_a(m-n)\overset{\triangleright}{\boldsymbol{\psi}}{}^*_b(m)\right)(\mathrm{e}^{-\imath\theta}) \tag{N.2.22b}$$

using the shift and modulation properties of a discrete-time Fourier transform [2, Ch. 2.9] gives

$$S_{\substack{\triangleright\,\triangleright\\ \psi_a\psi_b}}(\theta) = \frac{1}{2\pi}\int_{-\pi}^{\pi} \mathrm{E}\, \mathrm{e}^{-\imath\theta' n}\overset{\triangleright}{\tilde{\boldsymbol{\psi}}}_a(\mathrm{e}^{\imath\theta'})\overset{\triangleright}{\tilde{\boldsymbol{\psi}}}{}^*_b(\mathrm{e}^{\imath(\theta-\theta')})\,\mathrm{d}\theta' \tag{N.2.22c}$$

insertion of (N.2.8) to obtain

$$S_{\substack{\triangleright\\ \psi_a\end{smallmatrix}\begin{smallmatrix}\triangleright\\ \psi_b}}(\theta) = \frac{1}{2\pi}\int_{-\pi}^{\pi} \mathrm{E}\,\mathrm{e}^{-\imath\theta' n}\frac{1}{T}\tilde{\psi}_a\Big(\imath\Big(\frac{\theta'}{T}\Big)\Big)\frac{1}{T}\tilde{\psi}_b^*\Big(\imath\Big(\frac{\theta-\theta'}{T}\Big)\Big)\,\mathrm{d}\theta' \tag{N.2.22d}$$

$$= \frac{1}{2\pi T}\int_{-\pi/T}^{\pi/T} \mathrm{E}\,\mathrm{e}^{-\imath\omega' \tau}\tilde{\boldsymbol{\psi}}_a(\imath\omega')\tilde{\boldsymbol{\psi}}_b^*\left(\imath(\omega-\omega')\right)\,\mathrm{d}\omega'. \tag{N.2.22e}$$

By considering the expression (N.2.5b) for the continuous-time cross-spectral density function we obtain

$$S_{\psi_a\psi_b}(\omega) \triangleq (\mathcal{F}_{ct}R_{\boldsymbol{\psi}_a\boldsymbol{\psi}_b})(\imath\omega) \tag{N.2.23a}$$

$$= \big(\mathcal{F}_{ct}\,\mathrm{E}\,\boldsymbol{\psi}_a(t-\tau)\boldsymbol{\psi}_b^*(t)\big)(\imath\omega) \tag{N.2.23b}$$

using the product rule and translation property of a continuous-time Fourier transform [4, Ch. 2] gives

$$S_{\psi_a\psi_b}(\omega) = \frac{1}{2\pi}\int_{-\infty}^{\infty} \mathrm{E}\,\mathrm{e}^{-\imath\omega' \tau}\tilde{\boldsymbol{\psi}}_a(\imath\omega')\tilde{\boldsymbol{\psi}}_b^*(\imath(\omega-\omega'))\,\mathrm{d}\omega'. \tag{N.2.23c}$$

From (N.2.22e) and (N.2.23c) we recognize (as expected) that $TS_{\substack{\triangleright\\ \boldsymbol{\psi}_a\end{smallmatrix}\begin{smallmatrix}\triangleright\\ \boldsymbol{\psi}_b}}(\theta) = S_{\boldsymbol{\psi}_a\boldsymbol{\psi}_b}(\omega)|_{\theta=\omega T}$ holds provided that $\boldsymbol{\psi}_a(t), \boldsymbol{\psi}_b(t)$ are bandlimited to $[-\frac{f_s}{2}, \frac{f_s}{2}]$.

The second term in (N.2.19), that is, the unaliased-aliased cross spectra $S_{\substack{\triangleright\\ \boldsymbol{\psi}_a\end{smallmatrix}\begin{smallmatrix}\triangleleft\\ \boldsymbol{\psi}_b}}(\theta)$ is obtained from

$$S_{\substack{\triangleright\\ \psi_a\end{smallmatrix}\begin{smallmatrix}\triangleleft\\ \psi_b}}(\theta) \triangleq \big(\mathcal{F}_{dt}R_{\substack{\triangleright\\ \boldsymbol{\psi}_a\end{smallmatrix}\begin{smallmatrix}\triangleleft\\ \boldsymbol{\psi}_a}}(n)\big)(\mathrm{e}^{-\imath\theta}) \tag{N.2.24a}$$

$$= \big(\mathcal{F}_{dt}\,\mathrm{E}\overset{\triangleright}{\boldsymbol{\psi}}_a(m-n)\overset{\triangleleft}{\boldsymbol{\psi}}_b^*(m)\big)(\mathrm{e}^{-\imath\theta}) \tag{N.2.24b}$$

$$= \frac{1}{2\pi}\int_{-\pi}^{\pi} \mathrm{E}\,\mathrm{e}^{-\imath\theta' n}\overset{\triangleright}{\tilde{\boldsymbol{\psi}}}_a(\mathrm{e}^{\imath\theta'})\overset{\triangleleft}{\tilde{\boldsymbol{\psi}}}_b^*(\mathrm{e}^{\imath(\theta-\theta')})\,\mathrm{d}\theta' \tag{N.2.24c}$$

insertion of (N.2.8) and (N.2.9) to obtain

$$S_{\substack{\triangleright\\ \psi_a\end{smallmatrix}\begin{smallmatrix}\triangleleft\\ \psi_b}}(\theta) = \frac{1}{2\pi}\int_{-\pi}^{\pi} \mathrm{E}\,\mathrm{e}^{-\imath\theta' n}\frac{1}{T}\sum_{\substack{k=-\infty\\ k\neq 0}}^{\infty}\tilde{\boldsymbol{\psi}}_a\Big(\imath\Big(\frac{\theta'}{T}-\frac{2\pi k}{T}\Big)\Big)\sum_{\substack{k=-\infty\\ k=0}}^{\infty}\tilde{\boldsymbol{\psi}}_b^*\Big(\imath\Big(\frac{\theta-\theta'}{T}-\frac{2\pi k}{T}\Big)\Big)\,\mathrm{d}\theta' \tag{N.2.24d}$$

$$= \frac{1}{2\pi T^2}\int_{-\pi}^{\pi} \mathrm{E}\,\mathrm{e}^{-\imath\theta' n}\sum_{\substack{k=-\infty\\ k\neq 0}}^{\infty}\tilde{\boldsymbol{\psi}}_a\Big(\imath\Big(\frac{\theta'}{T}-\frac{2\pi k}{T}\Big)\Big)\tilde{\boldsymbol{\psi}}_b^*\Big(\imath\Big(\frac{\theta-\theta'}{T}\Big)\Big)\,\mathrm{d}\theta' \tag{N.2.24e}$$

$$= \frac{1}{2\pi T}\int_{-\pi/T}^{\pi/T} \mathrm{E}\,\mathrm{e}^{-\imath\omega' \tau}\sum_{\substack{k=-\infty\\ k\neq 0}}^{\infty}\tilde{\boldsymbol{\psi}}_a\big(\imath(\omega'-k\omega)\big)\tilde{\boldsymbol{\psi}}_b^*\big(\imath(\omega-\omega')\big)\,\mathrm{d}\omega'. \tag{N.2.24f}$$

If the approximation in (N.2.7) holds we readily obtain

$$S_{\overset{\triangleright}{\boldsymbol{\psi}}_a\overset{\triangleleft}{\boldsymbol{\psi}}_b}(\theta) \approx \frac{1}{2\pi T}\int_{-\pi/T}^{\pi/T} \mathrm{E}\,\mathrm{e}^{-\imath\omega'\tau}\frac{1}{T}\Big(\tilde{\boldsymbol{\psi}}_a\big(\imath(\omega'+\omega)\big)+\tilde{\boldsymbol{\psi}}_a\big(\imath(\omega'-\omega)\big)\Big)\tilde{\boldsymbol{\psi}}_b^*\big(\imath(\omega-\omega')\big)\,\mathrm{d}\omega'. \quad \text{(N.2.25)}$$

Likewise the third term in (N.2.19), that is, the aliased-unaliased cross spectra $S_{\overset{\triangleleft}{\boldsymbol{\psi}}_a\overset{\triangleright}{\boldsymbol{\psi}}_b}(\theta)$ is obtained from

$$\begin{aligned}
S_{\overset{\triangleleft}{\psi}_a\overset{\triangleright}{\psi}_b}(\theta) &\triangleq \big(\mathcal{F}_{dt}R_{\overset{\triangleright}{\boldsymbol{\psi}}_a\overset{\triangleleft}{\boldsymbol{\psi}}_a}(n)\big)(\mathrm{e}^{-\imath\theta}) && \text{(N.2.26a)}\\
&= \big(\mathcal{F}_{dt}\,\mathrm{E}\,\overset{\triangleright}{\boldsymbol{\psi}}_a(m-n)\overset{\triangleleft}{\boldsymbol{\psi}}_b^*(m)\big)(\mathrm{e}^{-\imath\theta}) && \text{(N.2.26b)}\\
&= \frac{1}{2\pi}\int_{-\pi}^{\pi}\mathrm{E}\,\mathrm{e}^{-\imath\theta' n}\overset{\triangleright}{\tilde{\boldsymbol{\psi}}}_a(\mathrm{e}^{\imath\theta'})\overset{\triangleleft}{\tilde{\boldsymbol{\psi}}}_b^*(\mathrm{e}^{\imath(\theta-\theta')})\,\mathrm{d}\theta' && \text{(N.2.26c)}
\end{aligned}$$

insertion of (N.2.8) and (N.2.9) to obtain

$$\begin{aligned}
S_{\overset{\triangleleft}{\psi}_a\overset{\triangleright}{\psi}_b}(\theta) &= \frac{1}{2\pi}\int_{-\pi}^{\pi}\mathrm{E}\,\mathrm{e}^{-\imath\theta' n}\frac{1}{T}\sum_{\substack{k=-\infty\\k=0}}^{\infty}\tilde{\boldsymbol{\psi}}_a\Big(\imath\Big(\frac{\theta'}{T}-\frac{2\pi k}{T}\Big)\Big)\frac{1}{T}\sum_{\substack{k=-\infty\\k\neq 0}}^{\infty}\tilde{\boldsymbol{\psi}}_b^*\Big(\imath\Big(\frac{\theta-\theta'}{T}-\frac{2\pi k}{T}\Big)\Big)\,\mathrm{d}\theta' && \text{(N.2.26d)}\\
&= \frac{1}{2\pi T^2}\int_{-\pi}^{\pi}\mathrm{E}\,\mathrm{e}^{-\imath\theta' n}\tilde{\boldsymbol{\psi}}_a\Big(\imath\frac{\theta'}{T}\Big)\sum_{\substack{k=-\infty\\k\neq 0}}^{\infty}\tilde{\boldsymbol{\psi}}_b^*\Big(\imath\Big(\frac{\theta-\theta'}{T}-\frac{2\pi k}{T}\Big)\Big)\,\mathrm{d}\theta' && \text{(N.2.26e)}\\
&= \frac{1}{2\pi T}\int_{-\pi/T}^{\pi/T}\mathrm{E}\,\mathrm{e}^{-\imath\omega'\tau}\tilde{\boldsymbol{\psi}}_a(\imath\omega')\sum_{\substack{k=-\infty\\k\neq 0}}^{\infty}\tilde{\boldsymbol{\psi}}_b^*\big(\imath(\omega-\omega'-k\omega)\big)\,\mathrm{d}\omega'. && \text{(N.2.26f)}
\end{aligned}$$

Note that in general $S_{\overset{\triangleleft}{\psi}_a\overset{\triangleright}{\psi}_b}(\theta) \neq S_{\overset{\triangleright}{\psi}_a\overset{\triangleleft}{\psi}_b}(\theta)$.

If the approximation in (N.2.7) holds we readily obtain

$$S_{\overset{\triangleleft}{\boldsymbol{\psi}}_a\overset{\triangleright}{\boldsymbol{\psi}}_b}(\theta) \approx \frac{1}{2\pi T}\int_{-\pi/T}^{\pi/T}\mathrm{E}\,\mathrm{e}^{-\imath\omega'\tau}\tilde{\boldsymbol{\psi}}_a(\imath\omega')\Big(\tilde{\boldsymbol{\psi}}_b^*\Big(\imath(2\omega-\omega')\Big)+\tilde{\boldsymbol{\psi}}_b^*(-\imath\omega')\Big)\,\mathrm{d}\omega'. \quad \text{(N.2.27)}$$

The fourth term in (N.2.19), that is, the spectra of the cross correlation sequence of the aliased signals $S_{\overset{\triangleleft}{\boldsymbol{\psi}}_a\overset{\triangleleft}{\boldsymbol{\psi}}_b}(\theta)$ is obtained by

$$S_{\overset{\triangleleft}{\psi}_a\overset{\triangleleft}{\psi}_b}(\theta) \triangleq \mathcal{F}_{dt}\{R_{\overset{\triangleleft}{\psi}_a\overset{\triangleleft}{\psi}_a}(n)\} \tag{N.2.28a}$$

$$= \frac{1}{2\pi}\int_{-\pi}^{\pi} \mathrm{E}\,\mathrm{e}^{-\imath\theta' n}\tilde{\overset{\triangleleft}{\psi}}_a(\mathrm{e}^{\imath\theta})\tilde{\overset{\triangleleft}{\psi}}^*_b(\mathrm{e}^{\imath(\theta-\theta')})\,\mathrm{d}\theta' \tag{N.2.28b}$$

$$= \frac{1}{2\pi}\int_{-\pi}^{\pi} \mathrm{E}\,\mathrm{e}^{-\imath\theta' n}\frac{1}{T}\sum_{\substack{k=-\infty\\k\neq 0}}^{\infty}\tilde{\psi}_a\Big(\imath\Big(\frac{\theta'}{T}-\frac{2\pi k}{T}\Big)\Big)\frac{1}{T}\sum_{\substack{k=-\infty\\k\neq 0}}^{\infty}\tilde{\psi}^*_b\Big(\imath\Big(\frac{\theta-\theta'}{T}-\frac{2\pi k}{T}\Big)\Big)\,\mathrm{d}\theta' \tag{N.2.28c}$$

$$= \frac{1}{2\pi T}\int_{-\pi/T}^{\pi/T} \mathrm{E}\,\mathrm{e}^{-\imath\omega'\tau}\sum_{\substack{k=-\infty\\k\neq 0}}^{\infty}\tilde{\boldsymbol{\psi}}_a\big(\imath(\omega'-k\omega)\big)\sum_{\substack{k=-\infty\\k\neq 0}}^{\infty}\tilde{\boldsymbol{\psi}}^*_b\big(\imath(\omega-\omega'-k\omega)\big)\,\mathrm{d}\omega'. \tag{N.2.28d}$$

If the approximation (N.2.7) holds we may simplify (N.2.28)

$$S_{\overset{\triangleleft}{\psi}_a\overset{\triangleleft}{\psi}_b}(\theta) \approx \frac{1}{2\pi T}\int_{-\pi/T}^{\pi/T} \mathrm{E}\,\mathrm{e}^{-\imath\omega'\tau}\Big(\tilde{\boldsymbol{\psi}}_a\Big(\imath(\omega'+\omega)\Big)+\tilde{\boldsymbol{\psi}}_a\Big(\imath(\omega'-\omega)\Big)\Big)\Big(\tilde{\boldsymbol{\psi}}^*_b\Big(\imath(2\omega-\omega')\Big)+\tilde{\boldsymbol{\psi}}^*_b(-\imath\omega')\Big)\,\mathrm{d}\omega'. \tag{N.2.29}$$

By inspection of the expressions (N.2.22), (N.2.24), (N.2.26) and (N.2.28) for the cross-spectral density functions we may unfortunately draw the conclusion that some simplifications are necessary in order to obtain practical results.

N.2.4 Anti-Aliasing and Decimation Filters

Referring to the discussion in section 5.3 on page 252 and Figure N.1 on page 794 the frequency response of the AAF will now be taking into account. Moreover, the results obtained can be used for synthesis of AAFs in AC where a compromise between filter delays and aliasing effects prevail.

The discussion now takes different form dependent on the properties of the signals.

N.2.5 Periodic Signals

A signal ψ_a may be constituted by a number of periodic signals , say, $N^{\psi_a}_{\mathrm{ps}}$. Then aliasing might be of concern if the sample frequency ω_s coincide with an integer number of a periodic signal ω_i and therefore will coincide with one of the harmonics of this periodic signal. More precisely, if $\omega_{\mathrm{s}} = n\omega_i; \quad n \in \mathbb{N}^* \setminus \{1\}, i \in \underline{N}^{\psi_a}_{ps}$, then the *aliased frequency* corresponding to periodic signal ω_i which we will denote by $\overset{\triangleleft}{\omega}_i$ and that is obtained as $\overset{\triangleleft}{\omega}_i = \omega_s - \omega_i$ will coincide with the $(n-2)$'th harmonics, that is,

$$\overset{\triangleleft}{\omega}_i = \omega_i^{(n-2)}, \tag{N.2.30}$$

where $\omega_i^{(q)}$ is the q'th harmonics of periodic signal ω_i and the 0'th harmonic is the fundamental frequency, that is, $(\omega_i^{(0)} = \omega_i)$. For example if $\omega_s = 2\pi 1000$ rad/s, $\omega_i = 2\pi 100$ rad/s then $n = 10$ and $\overset{\triangleleft}{\omega}_i = \omega_i^{(3)} = 2\pi 400$ rad/s.

For periodic signals aliased and unaliased signal components may indeed be cross correlated, that is,

$$S_{\substack{\triangleleft\,\triangleright\\ \psi_a\psi_a}}(\theta_i) = S^*_{\substack{\triangleright\,\triangleleft\\ \psi_a\psi_a}}(\theta_i) \neq 0, \quad S_{\substack{\triangleleft\,\triangleright\\ \psi_b\psi_b}}(\theta_i) = S^*_{\substack{\triangleright\,\triangleleft\\ \psi_b\psi_b}}(\theta_i) \neq 0, \quad S_{\substack{\triangleleft\,\triangleright\\ \psi_a\psi_b}}(\theta_i) = S^*_{\substack{\triangleright\,\triangleleft\\ \psi_a\psi_b}}(\theta_i) \neq 0,$$
$$\theta_i = \omega_i T \in [-\pi, \pi], \text{periodic signals.} \tag{N.2.31}$$

N.2.6 Random Signals

For random signals no cross correlation between aliased and unaliased components exists. Hence,

$$S_{\substack{\triangleleft\,\triangleright\\ \psi_a\psi_a}}(\theta) = S_{\substack{\triangleright\,\triangleleft\\ \psi_a\psi_a}}(\theta) = S_{\substack{\triangleleft\,\triangleright\\ \psi_b\psi_b}}(\theta) = S_{\substack{\triangleright\,\triangleleft\\ \psi_b\psi_b}}(\theta) = S_{\substack{\triangleleft\,\triangleright\\ \psi_a\psi_b}}(\theta) = S_{\substack{\triangleright\,\triangleleft\\ \psi_a\psi_b}}(\theta) = 0,$$
$$\theta \in [-\pi, \pi], \quad \text{random signals.} \tag{N.2.32}$$

Hence, expression (N.2.21) on page 798 for the ordinary coherence squared function may be simplified

$$\gamma^2_{\psi_a\psi_b}(\theta) = \frac{\left|S_{\substack{\triangleright\,\triangleright\\ \psi_a\psi_b}}(\theta) + S_{\substack{\triangleleft\,\triangleleft\\ \psi_a\psi_b}}(\theta)\right|^2}{\left(S_{\substack{\triangleright\,\triangleright\\ \psi_a\psi_a}}(\theta) + S_{\substack{\triangleleft\,\triangleleft\\ \psi_a\psi_a}}(\theta)\right)\left(S_{\substack{\triangleright\,\triangleright\\ \psi_b\psi_b}}(\theta) + S_{\substack{\triangleleft\,\triangleleft\\ \psi_b\psi_b}}(\theta)\right)}, \qquad -\pi \leq \theta \leq \pi. \tag{N.2.33}$$

$$S_{ee}(\theta) = S_{\substack{\triangleright\triangleright\\ ee}}(\theta) + S_{\substack{\triangleleft\triangleright\\ ee}}(\theta) + S_{\substack{\triangleright\triangleleft\\ ee}}(\theta) + S_{\substack{\triangleleft\triangleleft\\ ee}}(\theta) \tag{N.2.34a}$$
$$= |F^0(\omega)|^2 S_{ee}(\omega)/T + |F^0(\omega_\mathrm{a})|^2 S_{ee}(\omega_\mathrm{a})/T + 2\Re\{F^0(\omega)(F^0(\omega_\mathrm{a}))^* S_{\substack{\triangleleft\triangleright\\ ee}}(\theta)\}, \tag{N.2.34b}$$

where the aliased frequency ω_a is computed as

$$\omega_\mathrm{a} = \omega_\mathrm{s} - \omega \quad [\mathrm{rad/s}]. \tag{N.2.35}$$

The frequency response of the AAF at the frequencies ω and ω_a is represented by $F^0(\omega)$ and $F^0(\omega_\mathrm{a})$ respectively.

Continuing with the reference sensor and reference sensor-error sensor cross terms yields:

$$S_{xx}(\theta) = S_{xx}(\omega)/T + 2\Re\{S_{\substack{\triangleleft\triangleright\\ xx}}(\theta)\} + S_{\substack{\triangleleft\triangleleft\\ xx}}(\theta) \tag{N.2.36}$$
$$= S_{xx}(\omega)/T + |F^0_j(\omega_\mathrm{a})|^2 S_{xx}(\omega_a)/T + 2\Re\{S_{\substack{\triangleleft\triangleright\\ xx}}(\theta)\} \tag{N.2.37}$$

and

$$S_{xe}(\theta) = S_{\substack{\triangleright\triangleright\\ xe}}(\theta) + S_{\substack{\triangleleft\triangleright\\ xe}}(\theta) + S_{\substack{\triangleright\triangleleft\\ xe}}(\theta) + S_{\substack{\triangleleft\triangleleft\\ xe}}(\theta) \tag{N.2.38}$$
$$= S_{xe}(\omega)/T + S_{\substack{\triangleleft\triangleright\\ xe}}(\theta) + S_{\substack{\triangleright\triangleleft\\ xe}}(\theta) + S_{\substack{\triangleleft\triangleleft\\ xe}}(\theta) \tag{N.2.39}$$
$$= S_{xe}(\omega)/T + |F^0_m(\omega_a)|^2 S_{xe}(\omega_a)/T + S_{\substack{\triangleleft\triangleright\\ xe}}(\theta) + S_{\substack{\triangleright\triangleleft\\ xe}}(\theta). \tag{N.2.40}$$

N.3 Active Control System

We will now use the results from the previous sections in the design of AAFs and DIFs to be employed at the error sensors and reference sensors in an ANCS. The presentation follows [1, Ch. 10] with some extensions. The operation of the error sensors can here be considered passive as no direct secondary source activation takes place, while the reference sensors play an active role in driving the secondary actuators. However, in a FBS using internal model control (IMC) the role of the error sensor is twofold. The error sensors are used both to provide *performance feedback* cf. section I.1, but are also used to deduce the filtered-reference signals. Hence, the AAF in the error sensors must comply with both objectives. Finally, possible aliasing effects at the performance sensors needs separate discussion.

The reference signals, error signals and performance signals can then be decomposed as in (N.2)

$$x(i) = \overset{\triangleright}{x}(i) + \overset{\triangleleft}{x}(i) \tag{N.3.1a}$$

$$e(i) = \overset{\triangleright}{e}(i) + \overset{\triangleleft}{e}(i) \tag{N.3.1b}$$

$$e^p(i) = \overset{\triangleright}{e}{}^p(i) + \overset{\triangleleft}{e}{}^p(i). \tag{N.3.1c}$$

We will consider an active control system with a bandwidth extending from a lower frequency limit f_l to the upper frequency limit f_u [6]. The dynamic range of AC is $A_\mathrm{ac}(f)$.

In [1, Ch. 10] (weighted) uniform spectra are considered. Here we will allow the disturbance signals and reference signals to decay with a rate of $\dot{S}_d(f)$ and $\dot{S}_x(f)$ for $f > f_\mathrm{u}$ respectively both measured in $\mathrm{dB}\cdot\mathrm{octave}^{-1}$ [7].

N.3.1 Aliasing Reference Sensors

The dynamic range of the reference signal $D_x(f)$ is measured in [dB]. First it will be assumed that no aliasing of the error signals occur, that is, $S_{\underset{ee}{\triangleleft\triangleleft}} = S_{\underset{ee}{\triangleright\triangleleft}} = S_{\underset{ee}{\triangleleft\triangleright}} = 0$. The two extreme cases of random signals and periodic signals will be treated separately.

Reference Sensors Random Signals

The requirement on the fall-off rate of the AAF is

$$\dot{F}_j^0(\imath\omega) \geq \frac{D_x + 20}{\log_2(\frac{f_s - f_\mathrm{u}}{f_\mathrm{u}})} - \dot{S}_x. \tag{N.3.2}$$

Reference Sensors Periodic Signals

The reference signal is considered composed by, say, a number of periodic signals N_ps^x . For periodic signals the aliased and unaliased signals will be coherent, that is, $\gamma^2_{\underset{xx}{\triangleright\triangleleft}} = 1$.

[6] In this section we adopt the usual engineering practice and use the frequency f that is obtained from the continuous-time angular frequency as $f = 2\pi\omega = 2\pi\theta/T$.

[7] Recall that pink noise and brown noise decay by 3 $\mathrm{dB}\cdot\mathrm{octave}^{-1}$ and 6 $\mathrm{dB}\cdot\mathrm{octave}^{-1}$ respectively.

Now if we accept that the dynamic range is reduced by $\Delta D(f)$ dB, which is equivalent to a similar increase in the noise floor, then we may allow a level of aliased signal component $L(\overset{\triangleleft}{f_i})$ that is determined from

$$L(\overset{\triangleleft}{f_i}) = -D(f_i) - 20\log_{10}\big(10^{\frac{\Delta D(f_i)}{20}} - 1\big), \quad i \in \underline{N}_{ps}^{x}. \tag{N.3.3}$$

where f_i refers to a periodic signal.

For example, if we only allow the aliased signal components to exceed the noise floor by 0.8 dB, then the aliased signal component must be suppressed to level 20 dB below $D(f)$[8].

For a normalized amplitude of the q'th harmonics of a periodic signal f_i $\bar{A}_i^{(q)}$, that is defined by

$$\bar{A}_i^{(q)} = 20\log_{10}\frac{A_i^{(q)}}{A_i^{(0)}}; \quad i \in \underline{N}_{ps}^{x}, \tag{N.3.4}$$

then the magnitude of the transfer function of the AAF in the error sensors $F_j^0(\imath\omega)$ measured in [dB/octave] must ensure that the aliased component is suppress by

$$|F_j^0(f_i)| = L(f_i) - \bar{A}_i^{(q)}; \quad i \in \underline{N}_{ps}^{x}, \tag{N.3.5}$$

and the requirement on the fall-off rate becomes

$$\dot{F}_j^0(\imath\omega) \geq \max_{i\in\underline{N}_{ps}}\left\{-|F_j^0(f_i)|/\log_2\left(\frac{\overset{\triangleleft}{f_i}}{f_{\mathrm{u}}}\right)\right\}. \tag{N.3.6}$$

N.3.2 Aliasing Error Sensors

The quantity $D_d(f)$ will be used to denote the dynamic range of the disturbance signal. First it will be assumed that no aliasing of the reference signal occur, that is, $S_{\underset{xx}{\triangleleft\triangleleft}} = S_{\underset{xx}{\triangleright\triangleleft}} = S_{\underset{xx}{\triangleleft\triangleright}} = 0$. The two extreme cases of random signals and periodic signals will be again treated separately.

Error Sensors Random Signals

For random error signals we have vanishing aliased unaliased cross spectra, that is, $S_{\underset{ee}{\triangleright\triangleleft}} = S_{\underset{ee}{\triangleleft\triangleright}} = 0$ then the ordinary coherence squared function (N.2.21) reduces to

$$\gamma_{xe}^2(\theta) = \frac{|S_{\underset{xe}{\triangleright\triangleright}}(\theta) + S_{\underset{xe}{\triangleright\triangleleft}}(\theta)|^2}{S_{\underset{xx}{\triangleright\triangleright}}(\theta)(S_{\underset{ee}{\triangleright\triangleright}}(\theta) + S_{\underset{ee}{\triangleleft\triangleleft}}(\theta))}. \tag{N.3.7}$$

which is readily seen to be less than in aliasing-free case, that is, $\gamma_{xe}^2(\theta) \leq \gamma_{xe}^2(\omega)|_{\theta=\omega T}$. However, this should be of less concern as the aliased signal is outside the operational bandwidth of the

[8] In [1, Ch. 10] an aliased signal level equal to the dynamic range is allowed, that is, $L(\overset{\triangleleft}{f_i}) = -D(f_i)$. However, then the noise floor is actually raised by $\Delta D(f_i)$ =6 dB.

controller ($\overset{\triangleleft}{f} > f_{\mathrm{u}}$) and the coherence function $\gamma^2_{\underset{xe}{\triangleright}}(\theta)$ is preserved. Accordingly aliasing effects in the error sensors exposed to random signals would usually not decrease the performance.

In order to ensure that aliasing components are suppressed by more than D_d into the bandwidth of AC $f_{\mathrm{l}} \leq f \leq f_{\mathrm{u}}$ implies that the fall-off rate $\dot{F}^0_m(\imath\omega)$ measured in [dB/octave] must satisfy

Error Sensors Periodic Signals

The error signal as is considered constituted by, say, a number of periodic signals N^e_{ps} . The requirement on the fall-off rate is therefore

$$\dot{F}^0_m(\imath\omega) \geq \max_{i \in N^e_{ps}} \left\{ \frac{D_d + 20}{\log_2(\frac{\overset{\triangleleft}{f}_i}{f_i})} - \dot{S}_d \right\}. \tag{N.3.8}$$

For periodic error signals, that is, $|S_{\underset{ee}{\bowtie}}|^2 = |S_{\underset{ee}{\triangleleft\triangleright}}|^2 = S_{\underset{ee}{\triangleright\triangleright}} S_{\underset{ee}{\triangleleft\triangleleft}}$ then the coherence function becomes

$$\gamma^2_{xe}(\theta) = \frac{|S_{\underset{xe}{\triangleright\triangleright}}(\theta)|^2}{S_{\underset{xx}{\triangleright\triangleright}}(\theta)(S_{\underset{ee}{\triangleright\triangleright}}(\theta) + S_{\underset{ee}{\triangleleft\triangleleft}}(\theta))}. \tag{N.3.9}$$

It should be recalled that the active noise control (ANC) bandwidth normally will be an magnitude of order less than the audible frequency range. As also explained in [1, Ch. 10] for random signal aliasing in the error signal does not pose a real problem to the system performance. The main reason for this is the lack of coherence between the in-band disturbance and the aliased (off-band) disturbance. The off-band disturbance is left unaltered by the system. Some, but normally, full acceptable increase in the excess noise will be expected for the least-mean-squares (LMS) algorithm, but not the recursive least-squares (RLS) algorithm. For tonal disturbances (N.3.8) applies as full coherence between a disturbance and one of its harmonics might exist.

N.3.3 Aliasing Performance Sensors

The performance sensors are only passively monitoring the performance of the active control system. Any aliased component $\overset{\triangleleft}{e}{}^p(i)$ will increase the measured power spectral density (PSD). However, the aliased component $\overset{\triangleleft}{e}{}^p(i)$ is due to measurement imperfections that will not be present if the performance signal is perceived by for example the human ear. The ANR performance is therefore **underestimated** by $\Delta\hat{\mathcal{A}}_{\overset{\triangleleft}{e}{}^p}(f)$ that is obtained from

$$\Delta\hat{\mathcal{A}}_{\overset{\triangleleft}{e}{}^p}(f) = 10\log_{10}\left(\frac{S_{\overset{\triangleright}{e}{}^p\overset{\triangleright}{e}{}^p}(f) + S_{\overset{\triangleright}{e}{}^p\overset{\triangleleft}{e}{}^p}(f) + S_{\overset{\triangleleft}{e}{}^p\overset{\triangleright}{e}{}^p}(f) + S_{\overset{\triangleleft}{e}{}^p\overset{\triangleleft}{e}{}^p}(f)}{S_{e^pe^p}(f)}\right) \quad [\mathrm{dB}]. \tag{N.3.10}$$

N.4 Conclusions

Bibliography

[1] Stephen J. Elliott. *Signal Processing for Active Control*. London: Academic Press, 2001.

[2] Alan V. Oppenheim and Ronald W. Schafer. *Discrete-Time Signal Processing*. Prentice Hall International Inc., 2nd edition, 1999.

[3] Athanasios Papoulis and S. Unnikrishna Pillai. *Probability, Random Variables and Stochastic Processes*. McGraw-Hill, New York, 4th edition, 2002.

[4] Alexander D. Poularikas. *The Transforms and Applications Handbook*. CRC Press, 2nd edition, 2000.

O. MATHEMATICAL MODEL DYNAMICAL SYSTEM

The concept of state-space representation of a dynamical system is widely employed within the control community. The state-space approach involves *external variables* as well as *internal variables*. The external variables include *controlled* and *uncontrolled* inputs, *measured* and *regulated* outputs.

O.0.1 Dynamical System

A dynamical system is characterized by the seven tuple $\Sigma = (T, U, \mathcal{U}, X, Y, \varphi, \eta)$ consisting of the time domain $T \subset \mathbb{R}$, input alphabet U, admissible input functions $\mathcal{U} \subset U^T$, state space X, output value space Y, state transition map $\varphi : \mathcal{D}_\varphi \to X$ and output map $\eta : T \times X \times U \to Y$, where $\mathcal{D}_\varphi \subset T^2 \times X \times \mathcal{U}$ designates the domain of definition of $\varphi(\,\cdot\,)$.

The governing equations for a state-space representation for a linear *continuous-time* but possibly time-varying system is

$$\dot{x}(t) = A(t)x(t) + B(t)u(t), \quad t \in \mathbb{R} \tag{O.0.1a}$$
$$y(t) = C(t)x(t) + D(t)u(t). \tag{O.0.1b}$$

where the state transition matrix $A(t) \in \mathbb{K}^{n\times n}$, the control matrix $B(t) \in \mathbb{K}^{n\times m}$, the observation matrix $C(t) \in \mathbb{K}^{p\times n}$ and the direct input-output coupling matrix $D(t) \in \mathbb{K}^{p\times m}$ have been introduced.

Similarly, the governing equations for a state-space representation for a linear *discrete-time* but possibly time-varying system is

$$x(t+1) = A(t)x(t) + B(t)u(t), \quad t \in T \tag{O.0.2a}$$
$$y(t) = C(t)x(t) + D(t)u(t). \tag{O.0.2b}$$

An advantage of the state-space representation is that it is a *pointwise* approach in which the instantaneous state of the system at time t contains all the necessary information needed to determine the effect of the past inputs upon the present output which is readily seen from (O.0.1b) and (O.0.2b).

For the hybrid MIMO feedforward-feedback system (HMIMOFFFBS) presented in chapter 6 on page 273 the disturbance signals and communication signals can be considered as uncontrolled and controlled inputs respectively. Similarly, the regulated and measured outputs corresponds to the performance signals and error signals respectively. The internal variables describe processes in

the interior of the system. There is no general descriptions for choosing an adequate state vector. In tracking system design kinematic parameters such as position, velocity and acceleration usually constitute the state vector. In a more advanced context of bearings-only tracking system (BOTS) design a state vector consisting of range, bearing, normalized range rate has successfully been implemented [4]. In physical systems state variables are often associated with important energy stores of the system. In active control of sound (ACS) state variables have been associated with acoustical modes in an enclosure. In active control of vibration (ACV) contexts structural modes have been used as state variables [3]. The main problem arises in broad band control where the modal density explodes and renders the dimension of the state-space vector prohibitive large. On the other hand it is difficult to find aggregated internal variables that adequately characterize the system. In active noise control system (ANCS) applications only a limited number of attempts have therefore been made to employ *state space* optimal control.

Additional discussion of the difficulties in employing state-space control is provided in [1, Ch. 6.1] and the references herein.

Instead, the multiple-input and multiple-output (MIMO) system will be considered as *input-output* system where the internal parts in principle are considered as a "black box" [2, Ch. 2.3].

Bibliography

[1] Stephen J. Elliott. *Signal Processing for Active Control*. London: Academic Press, 2001.

[2] Diederich Hinrichsen and Anthony J. Pritchard. *Mathematical Systems Theory I*. Springer-Verlag, Berlin, 2005.

[3] Jakob Mørkholt. *Active Control of Noise Radiation from Vibrating Structures*. Ph.D., DTU, 1996.

[4] Søren Rosenørn and Torsten H. Leth Elmkjær. Sensor fusion and advanced pattern recognition in naval scenarios using ESM and FLIR sensors. In *Symposium on EW Integration for Ships, Aircraft and Land Vehicles*, Ottawa, Canada, 1997.

P. Terma NOISE CHAMBER FACILITY

P.1 Background

As the available time slot for F-16 and CH-47 measurements is scarce and since a considerably time consumption is associated with the preparation and instrumentation of the cockpit, it was decided to build a dedicated noise chamber at Terma premises. The objective of the noise chamber is to establish an acoustical environment that closely resembles the cockpit environment. The following physical quantities are being considered:

- Spatial homogeneity of sound pressure
- Diffuseness of sound
- Reverberation time
- Dynamic range of sound pressure levels
- Instrumentation

The noise chamber has been used during test of the various test units including prototype headset as developed in the project. Basically, the noise chamber is a 6.21 m (width) times 5.77 m (length) times 2.89 m (height) room where the walls, floor and ceiling are made of concrete. The acoustical sources are constituted from 4 loudspeakers positioned on the floor in each of the corners such that the two adjacent walls jointly act as dihedral reflectors. A subwoofer is responsible for the energy contents below 40 Hz. More detailed information regarding the Terma noise chamber facility can be found in [1] and a qualification test is reported in [2].

Bibliography

[1] Terma. Operator's manual for the terma noise chamber measurement facility. Technical Report 301171-HO, Terma AS, 2005.

[2] Terma. Acceptance test of the terma noise chamber measurement facility. Technical Report 302522-TP, Terma AS, 2005.

Acronyms

αS	α-stable distribution
$\alpha\epsilon$-APA	$\alpha\epsilon$-affine projection algorithm
$\alpha\gamma\Pi\epsilon$-APA	$\alpha\gamma\Pi\epsilon$-affine projection algorithm
$\alpha\gamma\Pi\epsilon$-NLMS	$\alpha\gamma\Pi\epsilon$-NLMS (algorithm)
ϵ-NLMS	ϵ-NLMS (algorithm)
ϵ-APA	ϵ-affine projection algorithm
MPNLMS	μ-law PNLMS (algorithm)
AAF	anti-aliasing filter
ABS	acrylonitrile butadiene styrene thermoplastic
AC	active control
ACSV	active control of sound and vibration
ACS	active control of sound
ACS	autocorrelation sequence
ACF	autocorrelation function
ACV	active control of vibration
ACSVTU	active control sound and vibration test unit
ADC	analogue to digital converter
ADF	adaptive delay filter
ALMS	adjoint LMS (algorithm)
AF	adaptive filter
ADPCM	adaptive differential pulse code modulation
AIC	adaptive inverse control
ANC	active noise control
ANCS	active noise control system
ANVC	active noise and vibration control
ANN	artificial neural network
ANR	active noise reduction
ANSI	American National Standards Institute
AP	affine projection

APA	affine projection algorithm
APU	Auxiliary Power Unit
AR	autoregressive model
ASDF	autospectral density function
AUT	antenna under test
BEFAP	block exact fast affine projection (algorithm)
BEM	boundary element method
BK	Brüel & Kjær
BMIO	block multirate input-output
BOTS	bearings-only tracking system
BS	back side
B.Sc.	Bachelor of Science
BWF	Butterworth filter
CCF	cross correlation function
CCS	cross correlation sequence
CFAR	constant false alarm rate
CFF	confined feedforward
CFFAC	confined feedforward active control
CFFS	confined feedforward system
CFFFBACS	confined feedforward-feedback active control system
cdf	cumulative distribution function
CL-LMS	circular leaky LMS (algorithm)
CLT	central limit theorem
CM	control mass
CMAC	Cerebellar Model Articulation Controller
CPSD	cross power spectral density function
CSDF	cross-spectral density function
CoPSD	coincident power spectral density function
CS	control surface
CTFT	continuous-time Fourier transform

CV	control volume
dof	degrees of freedom
DAC	digital to analogue converter
DARE	discrete-time algebraic Riccati equation
DAT	digital audio tape
DF	decimation filter
DIF	decimation interpolation filter
DC	direct current
DCT	discrete cosine transform
DN	degree of nonstationarity
DFT	discrete Fourier transform
DSP	digital signal processor
DST	discrete sine transform
DTAC	Danish Tactical Air Command
DTFT	discrete-time Fourier transform
eFKF	extended fast Kalman filter
eFTF	extended fast transverse filter
eFAEST	extended fast *a priori* error sequential technique
ECA	Engineering College of Aarhus
ECS	environmental control system
ECF	empirical characteristic function
EDA	exploratory data analysis
EMSE	excess-mean-square error
EOS	equation of state
Fast RLS Array	fast recursive least-squares array (algorithm)
FAP	fast affine projection (algorithm)
FDAF	frequency-domain adaptive filter
FARLS	fast array recursive least-squares (algorithm)
Fe	filtered-error (method)
FFFBS	feedforward-feedback system

FFFBICS feedforward-feedback integrated communication system

FFFBICIDS feedforward-feedback integrated communication on-line system identification system

FBS feedback system

FFS feedforward system

FTF fast transversal filter

FFT fast Fourier transform

FFACS feedforward active control system

FIR finite-duration impulse response

FLOM fractional lower-order moments

FLOS fractional lower-order statistics

Fast RLS fast recursive least-squares (algorithm)

FS free space

FSAE fractionally spaced adaptive equalizer

FSFT fast spherical Fourier transform

Fu filtered-u method

FuRLMS filtered-u RLMS (algorithm)

FuRLMS filtered-v RLMS (algorithm)

Fx filtered-x method

FxLMS filtered-x LMS method

mFx modified-filtered-x method

GC generalized coherence

GCLT generalized central limit theorem

GPD group & phase delay

HATS head and torso simulator

HFFFBS hybrid feedforward feedback system (FBS)

HMIMOFFFBS hybrid MIMO feedforward-feedback system

HMIMOCFFFB hybrid MIMO confined-feedforward feedback

HMIMOCFFFBS hybrid MIMO confined-feedforward-feedback system

HCTDTT hybrid continuous-time discrete-time topology

HDD hard disc drive

HFe hybrid Fe (algorithm)

HFeLMS hybrid FeLMS (algorithm)

HGU head gear unit

HOS higher order statistics

HPD hearing protection device

i.i.d. independent and identical distributed

IF interpolation filter

IC integrated communication

IIR infinite-duration impulse response

IMC internal model control

I/O input output

IRF impulse response function

IRLS iteratively reweighted least-squares (algorithm)

IT independence theory

JCRSA joint-channel residual spectral analysis

JHMCS joint helmet mounted cuing systems

KIAS Knots indicated airspeed

KLT Karhunen Lòeve transform

LAN local area network

LEM linear estimation model

l.m.s.e. least-mean-squares estimate

l.l.m.s.e. linear-least-mean-squares estimate

l.l.m.s.e. linear-least-mean-squares estimation

LMMEN least-mean-mixed-even-norm (algorithm)

l.l.m.m.e.n. linear-least-mean-mixed-even-norm estimation

LHS left-hand side

LMAD least-mean-absolute deviation (algorithm)

LMF least-mean-fourth (algorithm)

LMMN least-mean-mixed-norm (algorithm)

MERLLMS multiple error recursive leaky LMS (algorithm)

LMS least-mean-squares (algorithm)

LLpN least l_p-norm (algorithm)

L-LMS leaky LMS (algorithm)

LMpN least-mean-p-norm (algorithm)

LPF low-pass filter

LS least-squares (algorithm)

LTI linear time-invariant

LTV linear time-variant

MC multiple-channel

MCPEFSF multiple-channel prediction error filter spectral factorization (algorithm)

MC-$\alpha\gamma\Pi\epsilon$-APA multiple-channel-$\alpha\gamma\Pi\epsilon$-affine projection algorithm

MC-$\alpha\gamma\Pi\epsilon$-NLMS multiple-channel-$\alpha\gamma\Pi\epsilon$-NLMS (algorithm)

MCOF multiple coherence function

ME maximum entropy

MIMO multiple-input and multiple-output (system)

MISO multiple-input and single-output (system)

MIE microphone in the ear

MIPS million instructions per second

ML maximum likelihood

MLE maximum likelihood estimation

MLP multilayer perceptron

MMSCOF multiple magnitude-squared coherence function

m.m.s.e. minimum mean-square error

MOM method of moments

MR multirate

MRS multi-rate system

m.s.e. mean-square error

MSC magnitude-squared coherence

m.s.d. mean-square deviation

NLMAD normalized LMAD

NLMpN normalized LMpN

NLMS normalized LMS (algorithm)

OCOF ordinary coherence function

OCOSF ordinary coherency squared function

ODE ordinary-differential-equation

p.d. positive-definite

p.s.d. positive-semidefinite

PαS positive α-stable distribution

PC personal computer

PCOF partial coherence function

PE persistent excitation (condition)

PEF prediction error filter

pdf probability density function

PIRLS polynolminal iteratively reweighted least-squares (algorithm)

Ph.D. Doctor of Philosophy

PNLMS proportionate NLMS (algorithm)

PANLMS proportionate adaptation NLMS (algorithm)

PAPA proportionate APA

PROJ projection method

PSD power spectral density function

PVDF Polyvinylidene Difluoride

QPSD quadrature power spectral density function

rms root-mean-square

rpm rotations per minute

RAM random access memory

RDAF Royal Danish Air Force

RF reconstruction filter

RHS right-hand side

RLMS recursive LMS (algorithm)

RLS recursive least-squares (algorithm)

ROC region of convergence

ROC receiver operating characteristic

RP random process

RS random sequence (discrete-time RP)

RTE real-time environment

RTU reference test unit

RV random variable

RWN random white noise

SD steepest descent (algorithm)

SG stochastic gradient (algorithm)

SαS symmetric α-stable distribution

SC single-channel

SDA statistical data analysis

SDCS sampled-data control system

SI Système International d'Unités (mksA)

SID system identification

SIMO single-input and multiple-output (system)

SISO single-input and single-output (system)

SL-LMS subspace leaky LMS (algorithm)

SLL side lobe level

SNFAT spherical near-field antenna testing

SNR signal-to-noise ratio

SNFT spherical near-field testing facility

SOF safety of flight

SPL sound pressure level

SPE secondary path equalization

SRS single-rate system

SS state-space

SW software

TDAF	time-domain adaptive filter
TDOA	time difference of arrival
TF	transfer function
TNC	Terma noise chamber facility
TPL	Thermoplastic Liner
TUD	Technical University of Denmark
uc	unit circle
UUT	unit under test
VLSI	very-large-scale integration
WEMSE	weighted excess-mean-square error
WF	Wiener Filter (algorithm)
WH	Wiener-Hopf
w.m.s.e.	weighted mean-square error
WSE	wide-sense ergodicity
WSS	wide-sense stationary
WWW	World Wide Web
SUN	Sæder, Udrustning og Nødudstyr (in Danish)
AK	aktiv kontrol (in Danish)
ASR	aktiv støjreduktion (in Danish)
IFFAK	indesluttet-feedforward aktiv kontrol (in Danish)
MIMO	mange-input-mange-output (in Danish)
HMIMOIFFFB	hybrid MIMO indesluttet-feedforward feedback (in Danish)
HMIMOIFFFBS	hybrid MIMO indesluttet-feedforward FBS (in Danish)
SKRSA	samlet kanal residual spektral analyse (in Danish)

NOMENCLATURE

$[\mathbf{X}_1, \mathbf{X}_2]_\alpha$	covariation of $\mathbf{X}_1$ with $\mathbf{X}_2$; (L.2.8) on page 777
$\Delta L(z)$	whitening filter error($\Delta L(z) \in \mathbb{C}^{N_x \times N_x}$); (3.5.10) on page 217
ΔS_{vv}	spectral factorization error averaged norm; (3.5.11) on page 217
$\Delta S_{xx}(\mathrm{e}^{\imath\omega})$	spectral factorization error(; (3.5.9) on page 217
$\Delta(\mathbf{r}, t)$	dilatation, $\Delta(\mathbf{r}, t) = \nabla \cdot s(\mathbf{r}, t)$; Equation 24
$\dot{\Delta}(\mathbf{r}, t)$	dilatation rate $[\mathrm{s}^{-1}]$; (F.3.44) on page 642
$\Delta\hat{\mathcal{A}}_{\hat{e}^p}(f)$	deviation in attenuation estimate due to aliasing in the performance sensor, [dB] (N.3.10)
Δf_{DFT}	DFT frequency resolutionin (modified) periodogram in spectrum estimation [Hz]; section C.2 on page 540
Δf_m	main lobe widthof DFT window used in (modified) periodogram in spectrum estimation [Hz]; section C.2 on page 540
Δ_u	number of samples used for inter-block decorrelation in APA; (8.6.9) on page 398
$\Delta s_{xx}(\mathrm{e}^{\imath\omega})$	relative spectral factorization error; (3.5.8) on page 217
$\mathrm{E}(\,\cdot\,)$	expectation operator; section 8.3.1 on page 375
$\Lambda_{\mathcal{A}}$	exponential weight matrix ($M_{\mathcal{A}} \times M_{\mathcal{A}}$) used in time-averaged attenuation calculations (A.2.9)
Λ_e	diagonal matrix of real eigenvalues of $S_{ee}(\mathrm{e}^{\imath\omega})$; (3.5.6) on page 216
Ω	frequency offset; (9.2.17) on page 427
$\Phi_M(t, t_0)$	mean weight-error vector state-space evolution matrix, $\Phi_M(t, t_0) : \mathbb{K}^{M\times M} \rightarrow \mathbb{K}^{M\times M}$; (9.4.1) on page 436
$\Phi(\mathbf{r}, t)$	potential energy density $[\mathrm{J}\cdot\mathrm{m}^{-2}]$; (F.3.97) on page 656
$\Phi(\mathbf{r}, t)$	velocity potential$[\mathrm{m}^2\cdot\mathrm{s}^{-1}]$; (F.8.2) on page 674
$\Phi(\varphi)$	azimthal function(in solution to Laplace or Helmholtz equations); (G.3.2) on page 710
Π_{i_Π}	weight regularization matrix, $\Pi_{i_\Pi} \in \mathbb{K}^{M\times M}$; (8.3.21) on page 384
Ψ	arbitrary vector; (J.A.40) on page 747

Σ Hermitian positive-definite weighting matrix, $\Sigma \in \mathbb{K}^{M\times M}$; (9.3.20) on page 432

$\Sigma_{i_B}^{\Upsilon}$ deterministic weight-error vector weighting matrix, $\Sigma_{i_B}^{\Upsilon} \in \mathbb{K}^{M\times M}$; (9.A.26a) on page 463

$\Sigma_{i_B}^{o}$ deterministic optimal weight vector weighting matrix, $\Sigma_{i_B}^{o} \in \mathbb{K}^{M\times M}$; (9.A.26b) on page 463

$\Sigma_{i_B}^{q}$ random walk weight vector weighting matrix, $\Sigma_{i_B}^{q} \in \mathbb{K}^{M\times M}$; (9.A.38b) on page 466

$\Sigma_{i_B}^{\bar{q}}$ deterministic random walk weight vector weighting matrix, $\Sigma_{i_B}^{\bar{q}} \in \mathbb{K}^{M\times M}$; (9.A.26c) on page 463

$\Sigma_{i_B}^{\breve{w}}$ regularization weight vector weighting matrix, $\Sigma_{i_B}^{\breve{w}} \in \mathbb{K}^{M\times M}$; (9.A.38c) on page 466

$\Sigma_{i_B}^{w'^o}$ mean optimal weight vector weighting matrix, $\Sigma_{i_B}^{w'^o} \in \mathbb{K}^{M\times M}$; (9.A.38a) on page 466

$\Sigma_{i_B}^{w^o w^0}$ mean optimal weight vector to initial weight vector coupling cross-weighting matrix, $\Sigma_{i_B}^{w^o w^0} \in \mathbb{K}^{M\times M}$ (state-space model); (9.3.27a) on page 434

$\Sigma_{i_B}^{w^o \breve{w}}$ cross-weighting matrix, $\Sigma_{i_B}^{w^o \breve{w}} \in \mathbb{K}^{M\times M}$; (9.A.39) on page 466

$\Sigma_{i_B}^{w^o \breve{w}}$ cross-weighting matrix associated with the coupling between the mean optimal weight vector and the regularized weight vector, $\Sigma_{i_B}^{w^o \breve{w}} \in \mathbb{K}^{M\times M}$ (state-space model); (9.3.27a) on page 434

$\Sigma_{i_B}^{\breve{w} w^0}$ cross-weighting matrix related to the coupling between the regularized weight vector and the initial weight vector, $\Sigma_{i_B}^{\breve{w} w^0} \in \mathbb{K}^{M\times M}$ (state-space model); (9.A.39) on page 466

Θ_{i_B-1} covariance matrix of perturbation vector $\boldsymbol{\theta}_{i_B-1}$, $\Theta_{i_B-1} \triangleq \mathrm{E}\,\boldsymbol{\theta}_{i_B-1}\boldsymbol{\theta}_{i_B-1}^{*} \in \mathbb{K}^{M\times M}$(random-walk model) in LEM; section 9.2 on page 422, (9.A.35) on page 465

$\Theta(\vartheta)$ polar function(in solution to Laplace or Helmholtz equations); (G.3.2) on page 710

Υ'_{i_Υ} leakage-weight regularization matrix, $\Upsilon'_{i_\Upsilon} \in \mathbb{K}^{M\times M}$; (9.3.19) on page 431

Υ_{i_Υ} transformed leakage-weight regularization matrix, $\Upsilon_{i_\Upsilon} \in \mathbb{K}^{M\times M}$; (8.6.13) on page 399

$\Upsilon_{i_\Upsilon}^{\chi}$ random-walk-modified leakage-weight regularization matrix, $\Upsilon_{i_\Upsilon}^{\chi} \in \mathbb{K}^{M\times M}$; (9.3.15) on page 430

$\Xi(r)$ amplitude function of the radius(in solution to Laplace or Helmholtz equations); (G.3.2) on page 710

$\bar{\alpha}(\Phi_M)$ upper Lyapunov exponent, $\bar{\alpha}(\Phi_M) \in \mathbb{R}_+$; (9.4.1) on page 436

$\alpha_{i_\alpha}(w_{i_B^\alpha})$ weight-driven leakage control matrix (parameter), $\alpha_{i_\alpha}(w_{i_B^\alpha}) \in \mathbb{R}^{M\times M}(\alpha_{i_\alpha}(w_{i_B^\alpha}) \in \mathbb{R})$, $0 \lessapprox \alpha_{i_\alpha} \prec I(0 \lessapprox \alpha(i_\alpha) \ll 1)$; (8.3.12) on page 380

α	characteristic exponent or index of stability, $\alpha \in (0, 2]$; Appendix L on page 773, Definition L.2 on page 775
α	volume thermal expansivity $[\mathrm{K}^{-1}]$; (F.3.71) on page 649
α_0	circular leakage control upper value parameter ($\alpha_0 \gtrapprox 0$); (8.3.14) on page 381
$\check{\alpha}(\mathbf{r}, t, P, T)$	thermal pressure increase at constant volume $[\mathrm{Pa} \cdot \mathrm{K}^{-1}]$; (F.3.71) on page 649
β, γ	Lee-Kesler equation of state (EOS) constants; (F.3.7) on page 629
β	symmetry parameter, $\beta \in [-1, 1]$; Appendix L on page 773
$\mathbf{\Sigma}^{\Upsilon}_{i_B}$	stochastic weight-error vector weighting matrix, $\mathbf{\Sigma}^{\Upsilon}_{i_B} \in \mathbb{K}^{M \times M}$; (9.A.21a) on page 460
$\mathbf{\Sigma}^{o}_{i_B}$	stochastic optimal weight vector weighting matrix, $\mathbf{\Sigma}^{o}_{i_B} \in \mathbb{K}^{M \times M}$; (9.A.21b) on page 460
$\mathbf{\Sigma}^{\bar{q}}_{i_B}$	stochastic random walk weight vector weighting matrix, $\mathbf{\Sigma}^{\bar{q}}_{i_B} \in \mathbb{K}^{M \times M}$; (9.A.21c) on page 460
$\boldsymbol{\theta}_{i_B}$	random-walk vector, $\boldsymbol{\theta}_{i_B} \in \mathbb{K}^{M \times 1}$ in LEM; section 9.2 on page 422
$\boldsymbol{\theta}_{-1}$	random initial condition, $\boldsymbol{\theta}_{-1} \in \mathbb{K}^{M \times 1}$ of random-walk vector in LEM; section 9.2 on page 422
χ	pole position, $\chi \in \mathbb{C}$ in random-walk model (forgetting factor) in LEM ($0 \leq \lvert\chi\rvert < 1$); section 9.2 on page 422
$\chi_A(s)$	characteristic polynomial of $A \in \mathbb{C}^{n \times n}$; (9.4.7) on page 437
$\chi_F(s)$	characteristic polynomial of $F \in \mathbb{C}^{n \times n}$; (9.4.54) on page 447
$\langle i \rangle_M$	i modulus M; (8.3.14) on page 381
δ	inexact differential
δ	location parameter, $\delta \in (-\infty, \infty)$; Appendix L on page 773
$\delta\mathbb{D}$	$\{z \in \mathbb{C}; \lvert z\rvert = 1\}$
$\delta^{(3)}(\mathbf{r} - \mathbf{r}')$	delta function in three dimensions
$\delta(t - t')$	delta function in one dimension
i^{Π}_B	weight block update iteration number corresponding to i_Π, $i^{\Pi}_B \leq i_B$; (8.3.21) on page 384
i^{Υ}_B	weight block update iteration number corresponding to i_Υ, $i^{\Upsilon}_B \leq i_B$; (9.A.7) on page 455
i^{α}_B	weight block update iteration number corresponding to i_α, $i^{\alpha}_B \leq i_B$; (8.3.11) on page 380
i_B	weight block update iteration number, $i_B = \lfloor (i/B)$; subsection 8.3.1 on page 374

i_Π weight regularization matrix update iteration number, $i_\Pi \leq i_B$; (8.3.21) on page 384

i_Υ^j transformed weight leakage factor update iteration number at block time j where $(i_\Upsilon^{i_B} \equiv i_\Upsilon)$; (9.A.13) on page 457

i_Υ transformed weight leakage factor update iteration number, $i_\Upsilon = i_\mu + i_\alpha + i_\gamma + i_\Pi$; (8.6.15) on page 399

i_α weight leakage control matrix update iteration number, $i_\alpha \leq i_B$; (8.3.11) on page 380

i_ϵ regularization update iteration number, $i_\epsilon \leq i_B$; (8.5.11) on page 391

i_γ control-effort-driven matrix update iteration number, $i_\gamma \leq i_B$; (8.3.15) on page 382

i_μ^j step-size parameter update iteration number at block time j where $(i_\mu^{i_B} \equiv i_\mu)$; (9.A.13) on page 457

i_μ step-size parameter update iteration number, $i_\mu \leq i_B$; (8.5.1) on page 389

i_ν weight leakage factor update iteration number, $i_\nu = \max\{i_\mu, i_\alpha\}$; (8.3.11) on page 380

$\tilde{T}(\imath\omega)$ complementary sensitivity function; (8.A.10) on page 406

$\tilde{T}_0(\imath\omega)$ complementary sensitivity function for the nominal plant; (8.A.9) on page 406

$i_{\bar{w}}$ point of attraction update iteration number, $i_{\bar{w}} \leq i_B$; (8.3.21) on page 384

$\lfloor(\,\cdot\,)$ floor operator; subsection 8.3.1 on page 374

$\epsilon(\varphi)$ normalized root-mean-square (rms) error, $\epsilon(\varphi) \triangleq \frac{\sqrt{\mathrm{E}(\hat{\boldsymbol{\varphi}}^2 - \boldsymbol{\varphi}^2)}}{\varphi}$ in the estimation of (arbitrary) parameter φ; section C.3 on page 541

$\epsilon\big(|\hat{H}_{\psi_a\psi_b}|\big)$ normalized rms error in the estimate of the magnitude of the transfer function between the random signal $\boldsymbol{\psi}_a$ and the random signal $\boldsymbol{\psi}_b$; (C.3.8)

$\sigma\big(\sphericalangle\hat{H}_{\psi_a\psi_b}\big)$ standard deviation random error in the estimate of phase of the transfer function between the random signal $\boldsymbol{\psi}_a$ and the random signal $\boldsymbol{\psi}_b$; (C.3.9)

$\epsilon(\mathbf{r})$ permittivity (capacity) of the medium [$\mathrm{F}\cdot\mathrm{m}^{-1}$]; (F.5.1b) on page 665

ϵ degree of reaction; (F.3.30)

$\epsilon\big(\hat{\gamma}^2_{\psi_a\,\cdot\,\psi^C}\big)$ normalized rms error in the estimate of the multiple magnitude-squared coherence function between the random signal $\boldsymbol{\psi}_a$ and the (arbitrary) random signal set $\boldsymbol{\psi}^C$; (C.3.10)

$\epsilon\big(\hat{\gamma}^2_{\psi_a\psi_b\perp\psi^C}\big)$ normalized rms error in the estimate of the partial coherence function of the random signal $\boldsymbol{\psi}_a$, the random signal $\boldsymbol{\psi}_b$ and the (arbitrary) random signal set $\boldsymbol{\psi}^C$; (C.3.11)

$\epsilon\big(\hat{\gamma}^2_{\psi_a\psi_b}\big)$ normalized rms error in the estimate of ordinary coherence squared function between the random signal $\boldsymbol{\psi}_a$ and the (arbitrary) random signal $\boldsymbol{\psi}_b$; (C.3.7)

ϵ_0 permittivity (capacity) in *vacuum* [8.854 pF $\cdot$ m^{-1}]; (F.5.1b) on page 665

ϵ_{i_ϵ} regularization term, $\epsilon_{i_\epsilon} \in \mathbb{R}^{M\times M}$, $\epsilon_{i_\epsilon} \gtrsim 0$; (8.5.11) on page 391

$\epsilon_\sigma(\varphi)$ normalized random error, $\epsilon_\sigma(\varphi) \triangleq \frac{\sqrt{\mathrm{E}\,\hat{\boldsymbol{\varphi}}^2 - \mathrm{E}^2\,\hat{\boldsymbol{\varphi}}}}{\varphi}$in the estimation of (arbitrary) parameter φ; section C.3 on page 541

$\epsilon_b(\varphi)$ normalized bias error in the estimation of (arbitrary) parameter $\varphi, \epsilon_b(\varphi) \triangleq \frac{\mathrm{E}\,\hat{\boldsymbol{\varphi}}}{\varphi} - 1$; section C.3 on page 541

η output map, $\eta : T \times X \times U \to Y$; subsection O.0.1 on page 807

η_{ψ_a} mean of arbitrary random signal $\boldsymbol{\psi}_a(t)$; (2.2.16) on page 24

γ scale parameter, $\gamma > 0$; Appendix L on page 773

$\gamma^2_{\psi_a\psi_b}(f)$ ordinary coherence squared function (or just coherence function) between (arbitrary) random signal $\boldsymbol{\psi}_a$ and (arbitrary) random signal $\boldsymbol{\psi}_b$; (2.2.10)

$\gamma_{i_\gamma}(\mathbf{y}_{i^\gamma})$ control-effort-driven leakage or actuator weighting diagonal matrix (parameter), $\gamma_{i_\gamma}(\mathbf{y}_{i^\gamma}) \in \mathbb{R}^{N_y\times N_y}(\gamma(i_\gamma, \mathbf{y}(i^\gamma)) \in \mathbb{R})$, $0 \precsim \gamma_{i_\gamma} \prec I (0 \lessapprox \gamma(i_\gamma) \ll 1)$; (8.3.15) on page 382

$\gamma^l_{i_\gamma}$ weight factor attributed to the l'th actuator; (8.3.15) on page 382

$\hat{\gamma}^2(f)$ generalized coherence (GC) estimate; (2.A.3) on page 103

$\gamma^2_{\psi_a\cdot\psi^C}$ multiple magnitude-squared coherence function between the conditioning signal sets $\boldsymbol{\psi}^C$ and random signal $\boldsymbol{\psi}_a$; (2.2.23) on page 27

$\gamma^2_{\psi_a\cdot\psi^C}$ multiple magnitude-squared coherence function between $\boldsymbol{\psi}_a$ and the set of $\boldsymbol{\psi}^C$ signals; subsection 2.2.5 on page 25

$\gamma^2_{\psi_a\psi_b\perp\psi^C}$ partial coherence function between random signals $\boldsymbol{\psi}_a$ and $\boldsymbol{\psi}_b$ conditioned on the random signal set $\boldsymbol{\psi}^C$; subsection 2.2.5 on page 25

$\gamma^2_{th}(p_{fa}, p_d)$ detection threshold; section 2.A on page 102

$\gamma_{\psi_a\psi_b}$ ordinary complex coherence functionbetween (arbitrary) random signal $\boldsymbol{\psi}_a$ and random signal $\boldsymbol{\psi}_b$; (2.2.11) on page 23

$\gamma_{i_\gamma\otimes K}(\mathbf{y}_{i^\gamma})$ actuator weighting block diagonal matrix, $\gamma_{i_\gamma\otimes K}(\mathbf{y}_{i^\gamma}) \in \mathbb{R}^{(KN_y)\times(N_yK)}$; (8.6.10) on page 398

ι internal energy index; (F.3.16) on page 633

$\kappa(\mathbf{r}, t)$ thermal conductivity(isotropic material) [W $\cdot$ K^{-1} $\cdot$ m^{-1}]; (F.3.84) on page 652

λ coefficient of bulk viscosity (compressional resistance) [Pa $\cdot$ s]; (F.3.97) on page 656

$\lambda_{\mathcal{A}}$ weight scalar (forgetting factor) used in time-averaged attenuation calculations; (A.2.9)

λ Lamé constant [Pa]; (F.4.12) on page 663

$\mathbb{D}_+$ $\{z \in \mathbb{C}; |z| \geq 1\}$

$\mathbb{D}_{+}^{*}$ $\{z \in \mathbb{C}; |z| > 1\}$

$\mathbb{D}_{-}^{*}$ $\{z \in \mathbb{C}; |z| < 1\}$

$\mathbb{D}_{(1,0)}$ unit disc with origo in $(1, 0)$ in the complex z-plane; (9.4.6) on page 437

$\mathbf{A}_{i_B}^{\Sigma}$ auxiliary matrix, $\mathbf{A}_{i_B}^{\Sigma} \in \mathbb{K}^{KN_e \times KN_e}$; (9.A.17) on page 458

$\mathbf{E}_i$ error signal time-block matrix, $\mathbf{E}_i \in \mathbb{K}^{KN_e}(\mathbf{E}_i \in \mathbb{K}^{K \times 1})$; (9.3.4) on page 428

$\mathbf{E}_{a,i}$ *a priori* block-time error vector, $\mathbf{E}_{a,i} \in \mathbb{K}^{KN_e \times 1}$; (9.2.9a) on page 425

$\mathbf{E}_{p,i}$ *posteriori* block-time error vector, $\mathbf{E}_{p,i} \in \mathbb{K}^{KN_e \times 1}$; (9.2.9b) on page 425

$\mathbf{L}_{i_B}$ auxiliary matrix, $\mathbf{L}_{i_B} \in \mathbb{K}^{M \times M}$; (9.4.5) on page 437

$\mathbf{M}_{i_B}$ state-space mean weight-error vector transition matrix, $\mathbf{M}_{i_B} \in \mathbb{K}^{M \times M}$; (9.A.11) on page 456 (9.3.18) on page 431

$\mathbf{P}_i', \mathbf{P}_i$ auxiliary matrices, $\mathbf{P}_i', \mathbf{P}_i \in \mathbb{K}^{M \times KN_e}$; (9.3.10a)-(9.3.10c) on page 429

$\mathbf{d}(i)$ disturbance signal, $\mathbf{d}(i) \in \mathbb{K}(\mathbf{d}_i \in \mathbb{K}^{N_e \times 1})$ in SISO, SIMO (SIMO, MIMO); section 8.3.1 on page 375

$\mathbf{d}_i$ disturbance signal, $\mathbf{d}_i \in \mathbb{K}^{N_e \times 1}$ in LEM; section 9.2 on page 422

$\mathbf{e}_{a,i}$ *a priori* error vector, $\mathbf{e}_{a,i} \in \mathbb{K}^{KN_e \times 1}$; (9.2.8a) on page 425

$\mathbf{e}_{p,i}$ *posteriori* error vector, $\mathbf{e}_{p,i} \in \mathbb{K}^{KN_e \times 1}$; (9.2.8b) on page 425

$\bar{\mathbf{q}}_{i_B}$ modified random-walk vector, $\bar{\mathbf{q}}_{i_B} \in \mathbb{K}^{M \times 1}$in LEM; (9.3.13) on page 430

$\mathbf{q}_{i_B}$ random-walk vector, $\mathbf{q}_{i_B} \in \mathbb{K}^{M \times 1}$ in LEM; section 9.2 on page 422

$\mathbf{u}_i$ regression vector (matrix), $\mathbf{u}_i \in \mathbb{K}^{1 \times M}(\mathbf{u}_i \in \mathbb{K}^{N_e \times M})$ in SISO, SIMO (MISO, MIMO); section 8.3.1 on page 375

$\mathbf{u}_i$ regression vector, $\mathbf{u}_i \in \mathbb{K}^{N_e \times M}$ in LEM; section 9.2 on page 422

$\mathbf{v}_i$ noise signal (estimation error), $\mathbf{v}_i \in \mathbb{K}^{N_e \times 1}$ in LEM; section 9.2 on page 422

$\tilde{\mathbf{w}}_{i_B-1}^{'\Upsilon}$ leakage-transformed modified weight-error vector, $\tilde{\mathbf{w}}_{i_B-1}^{'\Upsilon} \in \mathbb{K}^{M \times 1}$; (9.3.9) on page 429

$\tilde{\mathbf{w}}_{i_B}$ weight-error vector, $\tilde{\mathbf{w}}_{i_B} \in \mathbb{K}^{M \times 1}$; (9.3.7) on page 429

$\mathbf{w}_{i_B}^{o}$ optimal adaptive tap-weight vector, $\mathbf{w}_{i_B}^{o} \in \mathbb{K}^{M \times 1}$(time-variant); in LEM section 9.2 on page 422

$\mathbf{w}_{-1}$ initial weight vector, $\mathbf{w}_{-1} \in \mathbb{K}^{M \times 1}$ in LEM; section 9.2 on page 422

$\mathbf{w}_{-1}^{o}$ initial optimal weight vector, $\mathbf{w}_{-1}^{o} \in \mathbb{K}^{M \times 1}$ in LEM; section 9.2 on page 422

$\mathbf{x}_i$ reference signal, $\mathbf{x}_i \in \mathbb{K}^{1 \times M}(\mathbf{x}_i \in \mathbb{K}^{N_y \times M})$ in SISO, MISO (SIMO, MIMO); section 8.3.4 on page 382

$\mathbf{y}(i)$ control output signal, $\mathbf{y}(i) \in \mathbb{K}(\mathbf{y}_i \in \mathbb{K}^{N_y \times 1})$ in SISO, MISO (SIMO, MIMO); section 8.3.4 on page 382

$\mathcal{A}_k^p(t)$ attenuation at the k'th performance sensor; (A.2.5) on page 531

$\mathcal{A}_\tau$ attenuation limited by delays in a random white noise (RWN); (A.3.1)

$\mathcal{D}_\varphi$ domain of definition of $\varphi(\,\cdot\,), \mathcal{D}_\varphi \subset T^2 \times X \times \mathcal{U}$; subsection O.0.1 on page 807

$\mathcal{D}_m^1(\,\cdot\,)$ resampling function (1^{st} level) at m'th error sensor; (5.3.7)

$\mathcal{D}_m^2(\,\cdot\,)$ resampling function (2^{nd} level) at m'th error sensor; (5.3.7)

$\mathcal{F}_{i_B}$ companion state transition matrix of mean-square weight-error vector, $\mathcal{F}_{i_B} \in \mathbb{K}^{M^2 \times M^2}$ (state-space model); (9.4.53) on page 446

$\mathcal{G}_{i_B}$ total control input matrix, $\mathcal{G}_{i_B} \in \mathbb{K}^{M^2 \times 1}$ (state-space model); (9.4.55) on page 447

$\mathcal{G}_{i_B}^q$ random-walk control input, $\mathcal{G}_{i_B}^q \in \mathbb{K}^{M^2 \times 1}$ (state-space model); (9.4.56a) on page 447

$\mathcal{G}_{i_B}^v$ system noise control input, $\mathcal{G}_{i_B}^v \in \mathbb{K}^{M^2 \times 1}$ (state-space model); (9.4.56b) on page 447

$\mathcal{G}_{i_B}^{\breve{w}}$ control input related to the regularized weight vector, $\mathcal{G}_{i_B}^{\breve{w}} \in \mathbb{K}^{M^2 \times 1}$ (state-space model); (9.4.57b) on page 448

$\mathcal{G}_{i_B}^{w'^o}$ control input associated with the mean optimal weight vector, $\mathcal{G}_{i_B}^{w'^o} \in \mathbb{K}^{M^2 \times 1}$ (state-space model); (9.4.57a) on page 448

$\mathcal{G}_{i_B}^{w^o w^0}$ mean optimal weight vector to initial weight vector coupling control input, $\mathcal{G}_{i_B}^{w^o w^0} \in \mathbb{K}^{M^2 \times 1}$ (state-space model); (9.4.58b) on page 448

$\mathcal{G}_{i_B}^{w^o \breve{w}}$ control input associated with the coupling between the mean optimal weight vector and the regularized weight vectors, $\mathcal{G}_{i_B}^{w^o \breve{w}} \in \mathbb{K}^{M^2 \times 1}$ (state-space model); (9.4.58a) on page 448

$\mathcal{G}_{i_B}^{\breve{w} w^0}$ control input related to the coupling between the regularized weight vector and the initial weight vectors, $\mathcal{G}_{i_B}^{\breve{w} w^0} \in \mathbb{K}^{M^2 \times 1}$ (state-space model); (9.4.58c) on page 448

$\mathcal{P}(\,\cdot\,)$ penalty or a barrier function, $\mathcal{P}(\,\cdot\,) : \mathbb{R} \times \mathbb{R} \to \mathbb{R}_+$; subsection 8.A.1 on page 404

$\mathcal{P}_H^\perp$ projection operator; (J.1.5) on page 738

$\mathcal{S}_l(\,\cdot\,)$ sampling function (0^{th} level) at l'th actuator; (5.4.7) on page 259

$\mathcal{S}_m(\,\cdot\,)$ sampling function (0^{th} level) at m'th error sensor; (5.3.3) on page 254

$\mathcal{U}$ admissible input functions, $\mathcal{U} \subset U^T$; subsection O.0.1 on page 807

$\mathcal{U}_l^1(\,\cdot\,)$ resampling function (1^{st} level) at l'th actuator; (5.4.6) on page 259

$\mathcal{U}_l^2(\,\cdot\,)$ resampling function (2^{nd} level)at l'th actuator; (5.4.3) on page 257

$\mathcal{W}_{i_B}$ state vector of weighted mean-square weight-error vector, $\mathcal{W}_{i_B} \in \mathbb{K}^{M^2 \times 1}$ (state-space model); (9.4.52) on page 446

i_{M^2} vectorized identity matrix, $\mathrm{i}_{M^2} \equiv \mathrm{vec}\,\{\mathrm{I}_M\} \in \mathbb{R}^{M^2\times 1}$; subsection 9.4.5 on page 450

$\mu(\mathbf{r})$ permeability (inductivity) of medium $[\mathrm{H}\cdot\mathrm{m}^{-1}]$; (F.5.1a) on page 665

μ coefficient of viscosity $[\mathrm{Pa}\cdot\mathrm{s}]$; (F.3.97) on page 656

μ_0 permeability (inductivity) in *vacuum* $[4\pi\times 10^{-7}\ \mathrm{H}\cdot\mathrm{m}^{-1}]$; (F.5.1a) on page 665

μ_B coefficient of bulk viscosity $[\mathrm{Pa}\cdot\mathrm{s}]$; (F.3.88) on page 652

μ Lamé constant [Pa]; (F.4.12) on page 663

$\mu(i_\mu)$ step-size parameter (positive-definite learning matrix), $\mu(i_\mu)\in\mathbb{R}(\mu_{i_\mu}\in\mathbb{R}^{M\times M}\succ 0)$; (8.5.1) on page 389

$\mu_c^{(\varphi)}$ chemical potential of the c'th constituent of the p'th phase $[\mathrm{J}\cdot\mathrm{mol}^{-1}]$; (F.3.29) on page 637

$\nabla_w^2 J$ Hessian matrix of J with respect to w of the cost function $J(w)$; (8.5.11) on page 391

$\nu(i_{i_\nu})$ leakage factor, $\nu(i_{i_\nu})\triangleq 1-\mu(i_\mu)\alpha(i_\alpha)$, $\nu(i_{i_\nu})\lessapprox 1$; (8.3.12) on page 380

ν Poisson's ratio; (F.4.14) on page 664

ν_i stoichiometric coefficient of the i'th constituent; (F.3.23) on page 636

ω angular frequency $[\mathrm{rad}\cdot\mathrm{s}^{-1}]$

ω continuous-time angular frequency $[\mathrm{rad}\cdot\mathrm{s}^{-1}]$; (5.A.1) on page 268

ω sampling frequency $[\mathrm{rad}\cdot\mathrm{s}^{-1}]$; (5.A.6) on page 269

ω_{a} aliased frequency [rad/s]; (N.2.35)

$\overset{\triangleleft}{\omega}_i$ aliased frequency corresponding to periodic signal ω_i [Hz]; subsection N.2.5 on page 801

$\omega_i^{(q)}$ q'th harmonics of periodic signal ω_i and the 0'th harmonic is the fundamental frequency, that is, $(\omega_i^{(0)}=\omega_i)$ [rad/s]; (N.2.30) on page 801

$\phi(\mathbf{r})$ scalar potential

ϕ phase offset; (9.2.17) on page 427

ϕ_η viscous dissipation function $[\mathrm{W}\cdot\mathrm{m}^{-3}]$; (F.3.82) on page 651

ϕ_κ thermal dissipation function $[\mathrm{W}\cdot\mathrm{m}^{-3}]$; (F.3.81) on page 651

$\boldsymbol{\psi}_a, \boldsymbol{\psi}_b$ arbitrary random signals; section 2.2 on page 18

$\overset{\triangleleft}{\tilde{\psi}}_a(\mathrm{e}^{\imath\theta})$ aliased signal component of $\tilde{\psi}_a(\mathrm{e}^{\imath\theta})$; (N.2.9) on page 795

$S_{\psi^A\psi^A}$ $\boldsymbol{\psi}_a-\boldsymbol{\psi}^C$ channel power spectral density matrix, $S_{\psi^A\psi^A}\in\mathbb{C}^{N_f\times N_\psi^A\times N_\psi^A}$; (2.2.22) on page 26

$\overset{\triangleright}{\tilde{\psi}}_a(\mathrm{e}^{\imath\theta})$ unaliased signal component of $\tilde{\psi}_a(\mathrm{e}^{\imath\theta})$; (N.2.8) on page 795

$\psi_l(j)$ l-th control output signal , $\psi_l(j) \triangleq \boldsymbol{\psi}_l^{\mathcal{U}^2}(t_l^2)$ at sample index j; Figure 5.2 on page 258

$\psi_{\neq j}^I$ subset of input signals obtained from excluding the j'th element , $\psi_{\neq j}^I = \psi^I \setminus \psi_j^I$; subsection 2.2.5 on page 25

$\boldsymbol{\psi}_l^{\mathcal{U}^0}(t_l^0)$ resampled (0^{th} level) l-th control output signal at sample index t_l^0; (5.4.6) on page 259

$\boldsymbol{\psi}_l^{\mathcal{U}^1}(t_l^1)$ resampled (1^{st} level) l-th control output signal at sample index t_l^1; (5.4.3) on page 257

$\psi_m(i)$ m-th error signal at sample index i , $\psi_m(i) \triangleq \boldsymbol{\psi}_m^{\mathcal{D}^2}(t_m^2)$; (5.3.15) on page 256

$\boldsymbol{\psi}_m^{\mathcal{D}^1}(t_m^1)$ resampled (1^{st} level) m-th error signal at sample index t_m^1; (5.3.7) on page 255

$\boldsymbol{\psi}_m^{\mathcal{D}^2}(t_m^2)$ resampled (2^{nd} level) m-th error signal at sample index t_m^2; (5.3.10) on page 256

$\boldsymbol{\psi}_m^{\mathcal{M}}(t)$ transduced m-th error signal at time t; (5.3.1) on page 252

$\boldsymbol{\psi}_m^{\mathcal{S}}(t_m^0)$ sampled m-th error signalat sample index t_m^0; (5.3.3) on page 254

ψ_n^a n-order value of the field variable ψ^a; (F.2.3) on page 622

$n_c^{(\varphi)}$ number of moles of the c'th constituent of the p'th phase; (F.3.28) on page 637

$\boldsymbol{\psi}^A$ set of A signals , $\boldsymbol{\psi}^A = \cup_{j \in \underline{N}_\psi^A} \boldsymbol{\psi}_j^A$; (2.2.8) on page 22

$\boldsymbol{\psi}^B$ set of B signals , $\boldsymbol{\psi}^B = \cup_{k \in \underline{N}_\psi^B} \boldsymbol{\psi}_k^B$; (2.2.8) on page 22

$\boldsymbol{\psi}^C$ set of C (conditioning) signals , $\boldsymbol{\psi}^C = \cup_{l \in \underline{N}_\psi^C} \boldsymbol{\psi}_l^C$; (2.2.4) on page 21

$\boldsymbol{\psi}^I$ set of input signals , $\boldsymbol{\psi}^I = \cup_{j \in \underline{N}_\psi^I} \boldsymbol{\psi}_j^I$; (2.2.4) on page 21

$\boldsymbol{\psi}^O$ set of output signals , $\boldsymbol{\psi}^O = \cup_{k \in \underline{N}_\psi^O} \boldsymbol{\psi}_k^O$; (2.2.4) on page 21

$\boldsymbol{\psi}^S$ set of all signals; (2.2.5) on page 21

ρ ambient mass density [$\text{kg} \cdot \text{m}^{-3}$]; 7 on page 657

$\rho(\mathbf{r}, t)$ volume source of charge density flow [$\text{C} \cdot \text{m}^{-3}$]; (F.5.1) on page 665

$\rho_{\psi_a \psi_b}(\tau)$ correlation coefficient (coherence function in space-time); (2.2.15) on page 23

$\sigma(A)$ spectrum of $A, \sigma(A) \in \mathbb{C}^{n \times n}$; (9.4.7) on page 437

σ Stefan-Boltzmann constant[$56.697\,\text{nW} \cdot \text{m}^{-2} \cdot \text{K}^{-4}$]; (F.3.86) on page 652

σ_V^2 variance of the block-time noise in the LEM, $\sigma_V^2 \in \mathbb{K}^{KN_e \times KN_e}$; Equation 9.2.4 on page 424

$\sigma_d^2(i)$ variance of the desired signal $\mathbf{d}(i)$; (8.4.3) on page 386

$\sigma_j^\alpha(k)$ weight for j'th inequality constraints related to weight-driven leakage; (8.A.17) on page 408

$\sigma_j^{\gamma}(k)$ weight for j'th inequality constraints related to effort-driven leakage; (8.A.18) on page 408

σ_v^2 variance, $\sigma_v^2 \in \mathbb{K}^{N_e \times N_e}$ of the noise in LEM; section 9.2 on page 422

τ delay in plant response; (A.3.1) on page 532

$\tau_g(\omega)$ group delay continuous-time (5.A.1) on page 268

τ_g total group delay [s]; (5.5.1) on page 260

$\tau_g^{\mathcal{L}}$ group delay associated with transduction in the transmitter part of the plant [s]; (5.5.4a) on page 260

$\tau_g^{\mathcal{M}}$ group delay associated with transduction in the receiver part of the plant [s]; (5.5.4b) on page 260

$\tau_g^{\mathcal{S}}, \tau_g^{\mathcal{D}^1}, \tau_g^{\mathcal{D}^2}$ group delays involved in the sampling stage and downsampling stages of the plant [s]; (5.5.5) on page 261, (5.A.8) on page 269

$\tau_g^{\mathcal{U}^2}, \tau_g^{\mathcal{U}^1}, \tau_g^{\mathcal{H}}$ group delays involved in the upsampling stages and the sample and hold stage of the plant [s]; (5.5.5) on page 261, (5.A.10) on page 269

$\overset{\curlyvee}{\tau}_g^{ct}$ group delay from receiver part of the continuous-time part of plant [s]; (5.5.3) on page 260

$\overset{\curlywedge}{\tau}_g^{ct}$ group delay from transmitter part of the continuous-time part of plant [s]; (5.5.3) on page 260

$\widetilde{\tau}_g$ group delay from propagation part of plant [s]; (5.5.1) on page 260

$\overset{\curlyvee}{\tau}_g$ group delay from receiver part of plant [s]; (5.5.1) on page 260

$\overset{\curlyvee}{\tau}_g^{dt,tot}$ total group delay from receiver part of the discrete-time part of plant [s]; (5.5.7) on page 261

$\overset{\curlyvee}{\tau}_g^{dt}$ group delay from receiver part of the discrete-time part of plant [s]; (5.5.5) on page 261

$\overset{\curlywedge}{\tau}_g$ group delay from transmitter part of plant [s]; (5.5.1) on page 260

$\overset{\curlywedge}{\tau}_g^{dt,tot}$ total group delay from transmitter part of the discrete-time part of plant [s]; (5.5.6) on page 261

$\overset{\curlywedge}{\tau}_g^{dt}$ group delay from transmitter part of the discrete-time part of plant [s]; (5.5.5) on page 261

τ_g^{ct} group delay from continuous-time part of plant [s]; (5.5.2) on page 260

$\tau_g(\theta)$ group delay discrete-time (5.A.3) on page 268

τ_g^{dt} group delay from discrete-time part of plant [s]; (5.5.2) on page 260

τ_g^{w} group delay associated with the generation of the control output [s]; (5.5.5) on page 261

$\tau_{\iota}^{\varkappa}$ time constant in relaxation process(F.3.20) on page 635

$\tau_p(\omega)$ phase delay continuous-time (5.A.2) on page 268

$\tau_p(\theta)$ phase delay discrete-time (5.A.4) on page 268

τ_{rot} relaxation time constant for rotational dof [s]; (F.3.22) on page 635

$\hat{\tau}_g^{SI}$ group delay estimate from system identification[s]; (5.A.11) on page 270

τ_{tr} relaxation time constant for translational dof [s]; (F.3.22) on page 635

τ_{vib} relaxation time constant for vibrational dof [s]; (F.3.22) on page 635

$\tau_{\psi_j^I \psi_k^O}$ acquisition lead-time between input signal ψ_j^I and output signal ψ_k^O; Definition 2.1 on page 68

$\tau_{\psi_j^I \psi_k^O}$ spatially-weighted-averaged acquisition lead time between input signal ψ_j^I and output signal ψ_k^O; Definition 2.2 on page 68

θ discrete-time angular frequency [rad $\cdot$ sample^{-1}]; (5.A.4) on page 268

$\theta_{j,s}, \phi_{j,s}$ angles of incidence of the s'th field relative to the j'th reference sensor; (3.2.21) on page 119

$\frac{\mathrm{D}()}{\mathrm{D}t}$ material derivative; (F.3.40) on page 640

υ^a arbitrary constitutional parameter; Equation F.2.1 on page 622

ε emissivity; (F.3.86) on page 652

$\varkappa$ species indicator(F.3.15) on page 633

φ (arbitrary) parameter; section C.3 on page 541

φ state transition map, $\varphi : \mathcal{D}_\varphi \to X$; subsection O.0.1 on page 807

$\varpi_{x_i}(\mathbf{r}, t)$ rotation components; (F.4.3) on page 661

ξ_1, ξ_2, ξ_3 curvilinear coordinates

$\hat{\boldsymbol{\xi}}_{\mathbf{1}}, \hat{\boldsymbol{\xi}}_{\mathbf{2}}, \hat{\boldsymbol{\xi}}_{\mathbf{3}}$ unitary vectors in a curvilinear coordinate system

$\mathbf{A}(\mathbf{r})$ vector potential

A_{i_B}, B_{i_B} auxiliary matrices, $A_{i_B}, B_{i_B} \in \mathbb{K}^{M^2 \times M^2}$ in state-space (SS) representation; (9.4.18) on page 440

$\mathcal{A}_{\gamma^2}$ attenuation limited by (lack of) coherence; (2.2.1) on page 18

$A_{\text{ac}}(f)$ dynamic range of active control (AC) [dB]; section N.3 on page 803

$A_{ALMS}(z)$ adjoint LMS (ALMS) part of error filter in hybrid FeLMS (HFeLMS); (6.4.11) on page 279

$\bar{A}_i^{(q)}$ normalized amplitude of the q'th harmonics of a periodic signal f_i; (N.3.6) on page 804

$\mathcal{A}_m^e(f, t)$ attenuation at the m'th error sensor (A.2.11)

$\bar{\mathcal{A}}^p(f,t)$ trial-averaged attenuation estimate; (A.2.3) on page 530

$\check{\mathcal{A}}^p(f,t)$ scenario-averaged attenuation estimate; (A.2.4)

$\mathcal{A}_m(t)$ attenuation at the m'th error sensor; (8.3.1) on page 375

$\mathcal{A}_k^p(f,t)$ attenuation at the k'th performance sensor; (A.2.1)

$A_{SPE}(z)$ secondary path equalization (SPE) part of error filter in HFeLMS; (6.4.12) on page 279

$A(z)$ error filter; section 6.4 on page 277

b_1, b_2, b_3, b_4 Lee-Kesler EOS constants; (F.3.7) on page 629

B weight update block size, $B \in \mathbb{N}$; subsection 8.3.1 on page 374

B block size in DFT domain adaptive filter; subsection 8.3.2 on page 377

$B(\omega)$ magnitude of unstructured multiplicative plant uncertainty; (8.A.9) on page 406

$B_s(\mathbf{r},t,P,T)$ isentropic bulk modulus [Pa]; (F.3.74) on page 650

$B_T(\mathbf{r},t,P,T)$ isothermal bulk modulus [Pa]; (F.3.74) on page 650

b_{x_j} minimum directivity of the j'th reference sensor ($0 \leq b_{x_j} \leq 1$)(pedestal level); (3.2.21) on page 119

c speed of sound [$\mathrm{m} \cdot \mathrm{s}^{-1}$]

C_1, C_2, D circular leakage control lower-, upper- and medium threshold parameters; (8.3.14) on page 381

c_1, c_2, c_3, c_4 Lee-Kesler EOS constants; (F.3.7) on page 629

c_0 speed of light in vacuum 2.99790×10^8 meter $\cdot\, \mathrm{s}^{-1}$; (F.5.2) on page 665

$C_{i_B}^{\check{w}}$ time evolution matrix for the regularized weight vector, $C_{i_B}^{\check{w}} \in \mathbb{K}^{M\times M}$; (9.A.14c) on page 457

$C_{i_B}^{w^o}$ time evolution matrix for the mean optimal weight vector, $C_{i_B}^{w^o} \in \mathbb{K}^{M\times M}$; (9.A.14a) on page 457

C_ψ constraint constant pertaining to variable ψ; subsection 8.A.1 on page 404

$C_{\psi_a\psi_b}(f)$ CoPSD (co-spectrum)between signal $\boldsymbol{\psi}_a$ and $\boldsymbol{\psi}_b$; (2.2.14) on page 23

C_{RD} upper bound on disturbance enhancement; (8.A.13) on page 407

C_{RS} upper bound on robust stability, $C_{\mathrm{RS}} \triangleq 1$; (8.A.9) on page 406

$\check{c}_C$ spherical Bessel function order; (G.4.15) on page 715

$\check{c}_F$ spherical Bessel function order; (G.4.14) on page 715

$\mathfrak{C}$ elasticity 4-tensor; (F.4.13) on page 663

$\hat{C}(z)$ plant correction transfer function(estimate); (4.7.1) on page 245

c_L compressional propagation velocity $[\mathrm{m}\cdot\mathrm{s}^{-1}]$; (F.4.14) on page 664

$C_P(\mathbf{r},t,P,T)$ specific heat capacity at constant pressure $[\mathrm{J}\cdot\mathrm{K}^{-1}\cdot\mathrm{kg}^{-1}]$; (F.3.76b)

$c_s(\mathbf{r},t,P,T)$ isentropic speed of sound $[\mathrm{m}\cdot\mathrm{s}^{-1}]$; (F.3.75) on page 650

c_T shear wave propagation velocity $[\mathrm{m}\cdot\mathrm{s}^{-1}]$; (F.4.16) on page 664

$c_T(\mathbf{r},t,P,T)$ isothermal speed of sound $[\mathrm{m}\cdot\mathrm{s}^{-1}]$; (F.3.75) on page 650

C_t capacitance in cross-over network tweeter in closed-back headset system; (11.4.2) on page 485

$C_v(\mathbf{r},t,P,T)$ specific heat capacity at constant volume $[\mathrm{J}\cdot\mathrm{K}^{-1}\cdot\mathrm{kg}^{-1}]$; (F.3.76a)

$C_{\psi_a\psi_b}(\tau)$ cross-covariance functionbetween two arbitrary continuous-time random signals $\boldsymbol{\psi}_a(t),\boldsymbol{\psi}_b(t)$; (2.2.16) on page 24

C_{y^2} upper bound on the control output signal power level; (8.A.2) on page 405

$d_m(t_m^1)$ disturbance signal, m'th error sensor at time t_m^1; Figure 7.1 - 7.3 on pages 293–315

D longitudinal stiffness [Pa]; (F.4.14) on page 664

d_1, d_2 Lee-Kesler EOS constants; (F.3.7) on page 629

$d_{10\ \mathrm{dB}}^{QZ}$ spatial extent of zone of quite in pure-tone diffuse sound field [m]

$D_d(f)$ dynamic range of the disturbance signal [dB]; section N.3 on page 803

$\mathfrak{D}(\mathbf{r},t)$ fluid shear-stress-flux (viscous-stress-flux) tensor [Pa]; (F.3.89) on page 653

$\hat{d}(i)$ disturbance estimate at time i; (6.3.3) on page 276

$\hat{d}_m(t_m^1)$ disturbance signal estimate at multirate level 1 , $\hat{d}_m(t_m^1)\in\mathbb{K}$ m'th error sensor FBS at time t_m^1; (7.2.5) on page 296

$\hat{d}_m(t_m^2)$ disturbance signal estimate at multirate level 2 , $\hat{d}_m(t_m^2)\in\mathbb{K}$ m'th error sensor FBS at time t_m^2; (7.2.6) on page 296

$\hat{d}_m(t_m^1)$ disturbance signal estimate at multirate level 1 , $\hat{d}_m(t_m^1)\in\mathbb{K}$ m'th error sensor feedforward system (FFS) at time t_m^1; (7.3.3) on page 305

$\hat{d}_m(t_m^1)$ disturbance signal estimate at multirate level 1 , $\hat{d}_m(t_m^1)\in\mathbb{K}$ m'th error sensor feedforward-feedback system (FFFBS) at time t_m^1; (7.4.4) on page 316

$\hat{d}_m(t_m^1)$ disturbance signal estimate at multirate level 1 , $\hat{d}_m(t_m^1)\in\mathbb{K}$ m'th error sensor feedforward-feedback integrated communication system (FFFBICS) at time t_m^1; (7.5.3) on page 322

$\hat{d}^{\hat{g}_{ey}^{l,m}}(t_G^1)$ desired signal estimate system identification secondary path, FFFBICS at time t_G^1; (7.6.3) on page 329

$\hat{d}^{\hat{g}_{xy}^{l,j}}(t_G^1)$ desired signal estimate system identification feedback path, FFFBICS at time t_G^1; (7.6.4) on page 330

D_i disturbance signal time-block matrix, $D_i \in \mathbb{K}^{KN_e \times 1}(D_i \in \mathbb{K}^{K\times 1})$; (8.6.6) on page 397

$\widehat{(d_k^p(i))^2}$ estimated squared-disturbanceat the k'th performance sensor at the i'th iteration; (A.2.7a) on page 531

$D_x(f)$ dynamic range of the reference signal [dB]; section N.3 on page 803

d_{ij} strain element; (F.4.4) on page 661

$\mathfrak{D}(\mathbf{r},t)$ strain dyadic; (F.4.5) on page 661

$\mathrm{d}S(\mathbf{r}')$ surface unit area at position $\mathbf{r}'$; (F.3.42) on page 641

$\mathrm{d}\mathbf{S}'$ surface normal differential vector; (F.3.42) on page 641

$e(\mathbf{r},t)$ specific energy $[\mathrm{J}\cdot\mathrm{kg}^{-1}]$; (F.3.60) on page 646

$e_{\mathrm{pot}}(\mathbf{r},t)$ specific potential kinetic energy $[\mathrm{J}\cdot\mathrm{kg}^{-1}]$; (F.3.60) on page 646

E Young's modulus of elasticity [Pa]; (F.4.14) on page 664

$\underset{\oplus}{e}(t_m^1)$ error signal, m'th error sensor FFFBS at time t_m^1 (7.4.2) on page 314

$\underset{\circledast}{e}(t_m^1)$ error signal, m'th error sensor FFFBICS at time t_m^1 (7.5.1) on page 322

$e^{\hat{g}_{ey}^{l,m}}(t_G^1)$ error signal system identification secondary path, FFFBICS at time t_G^1 (7.6.7) on page 331

$e^{\hat{g}_{xy}^{l,j}}(t_G^1)$ error signal system identification feedback path, FFFBICS at time t_G^1 (7.6.8) on page 331

$e_{ij}(\mathbf{r},t)$ component of strain; (F.4.2) on page 660

$e_{\mathrm{kin}}(\mathbf{r},t)$ specific kinetic energy $[\mathrm{J}\cdot\mathrm{kg}^{-1}]$; (F.3.60) on page 646

E_{kin} kinetic energy function $[\mathrm{J}\cdot\mathrm{m}^{-3}]$; (F.3.9)

$\underset{\circ}{e}_m(t_m^1)$ error signal, m'th error sensor FBS at time t_m^1; (7.2.2) on page 295

$\underset{\sim}{e}_m(t_m^1)$ error signal, m'th error sensor FFS at time t_m^1 (7.3.1) on page 305

$\widehat{(e_k^p(i))^2}$ estimated squared-errorat the k'th performance sensor at the i'th iteration; (A.2.7a) on page 531

E_{pot} potential energy function $[\mathrm{J}\cdot\mathrm{m}^{-3}]$; (F.3.9)

$\widehat{E_{u_E}}$ estimate of the pulse energy; (8.6.25) on page 401

$\mathbf{E}(\mathbf{r},t)$ electric intensity $[\mathrm{V}\cdot\mathrm{m}^{-1}]$; (F.5.1a) on page 665

$E_{e_ie_i*}$ error-covariance matrix, $E_{e_ie_i*} \succ 0$; subsection 8.3.1 on page 374

$e^{\Delta w}(\,\cdot\,)$ error signal used for tap-weight update; section 6.2 on page 274

$\hat{\underset{\circ}{e}}_m^{\Delta w}(t_m^2)$ error signal estimate (frozen tap-weights), m'th error sensor, FBS at time t_m^2; (7.2.17) on page 298

$\hat{\underset{\sim}{e}}_m^{\Delta w}(t_m^2)$ error signal estimate (frozen tap-weights), m'th error sensor, FFS at time t_m^2; (7.3.18) on page 307

$\hat{\underset{\oplus}{e}}_m^{\Delta w}(t_m^2)$ error signal estimate (frozen tap-weights), m'th error sensor, FFFBS at time t_m^2; (7.4.10) on page 317

EMSE EMSE of the adaptive filter, $\mathrm{EMSE} \in \mathbb{R}_+$; (9.2.15) on page 426

$F_m^0(\imath\omega)$ anti-aliasing filter (AAF) (0^{th} level) at m'th error sensor; (5.3.3)

$F_l^2(\mathrm{e}^{\imath\theta})$ decimation interpolation filter (DIF) (2^{nd} level) at l'th actuator; (5.4.3) on page 257

$F_m^2(\mathrm{e}^{\imath\theta})$ DIF (2^{nd} level) at m'th error sensor; (5.3.7)

f specific Helmholtz function [J · kg]; section 6 on page 627

f_0 resonance frequency of closed-back headset system, ($f_0 = 141$ Hz); (10.3.1) on page 472

F_{i_B} mean-square weight-error vector state transition matrix, $F_{i_B} \in \mathbb{K}^{M^2 \times M^2}$ (state-space model); (9.4.17) on page 440

$\mathcal{F}_{ct}^{-1}$ inverse continuous-time Fourier transform (bilateral) operator; (M.1.5) on page 788

$\mathcal{F}_{ct}$ bilateral continuous-time Fourier transform operator $\mathcal{F}_{ct} : L^1(\mathbb{R};\mathbb{K}^m) \to L^1(\mathbb{R};\mathbb{C}^m)$; (M.1.3) on page 787

$\tilde{\psi}_a(\imath\omega)$ bilateral continuous-time Fourier transform of $\psi_a(\,\cdot\,) \in L^1(\mathbb{R};\mathbb{K}^m)$; (M.1.3) on page 787

$\tilde{\psi}_a(\mathrm{e}^{\imath\theta})$ bilateral discrete-time Fourier transform of $\psi_a(\,\cdot\,) \in l^1(\mathbb{Z};\mathbb{K}^m)$; (M.1.7) on page 788

$\mathcal{F}_{dt}^{-1}$ bilateral inverse discrete-time Fourier transform operator; (M.1.8) on page 788

$\mathcal{F}_{dt}$ bilateral discrete-time Fourier transform operator (M.1.7) on page 788

$\underset{\sim}{f}_j(t_j^1 + 1)$ feedback signal, j'th reference sensor FFS at time $t_j^1 + 1$; (7.3.38) on page 311

$\underset{\oplus}{f}_j(t_j^1 + 1)$ feedback signal, j'th reference sensor FFFBS at time $t_j^1 + 1$; (7.4.16) on page 319

$\underset{\circledast}{f}_j(t_j^1 + 1)$ feedback signal, j'th reference sensor FFFBICS at time $t_j^1 + 1$; (7.5.12) on page 325

$f_{\gamma^2}(\gamma^2)$ pdf of the magnitude-squared coherence function; section 2.A on page 102

$\hat{\underset{\sim}{f}}_j(t_j^1 + 1)$ estimate of $\underset{\sim}{f}_j(t_j^1 + 1)$; (7.3.35) on page 311

$\hat{\underset{\oplus}{f}}_j(t_j^1 + 1)$ estimate of $\underset{\oplus}{f}_j(t_j^1 + 1)$; (7.4.15) on page 318

$\hat{\underset{\circledast}{f}}_j(t_j^1 + 1)$ estimate of $\underset{\circledast}{f}_j(t_j^1 + 1)$; (7.5.11) on page 325

$F_\iota^{\varkappa}(T)$ degree of internal energy function; (F.3.19) on page 634

$F_j^0(\imath\omega)$ transfer function of the AAF in the error sensors [dB/octave]; (N.3.5) on page 804

$\hat{\underset{\circledcirc}{f}}_{j-l}(t_G^1+1)$ estimate of $\underset{\circledcirc}{f}_{j-l}(t_G^1+1)$; (7.6.12) on page 332

f_{l} lower frequency limit in ANC [Hz]; section N.3 on page 803

f_l low-pass cut-off frequency from leakage in closed-back headset system, ($f_l = 500$ Hz); (10.3.1) on page 472

$F_l^0(\imath\omega)$ reconstruction filter (RF) (lowpass filter); (5.4.7) on page 259

$F_l^1(\mathrm{e}^{\imath\theta})$ DIF (1^{st} level) at l'th actuator; (5.4.6) on page 259

$\dot{F}_m^0(\imath\omega)$ fall-off rate of AAF in error sensors for $f > f_{\mathrm{u}}$ [dB/octave]

$F_m^1(\mathrm{e}^{\imath\theta})$ DIF (1^{st} level) at m'th error sensor; (5.3.7)

$f_{s,l}^0$ sampling frequency (0^{th} level) at l'th actuator [Hz]; section 5.4 on page 257

$f_{s,l}^1$ sampling frequency (1^{st} level) at l'th actuator [Hz]; section 5.4 on page 257

$f_{s,l}^2$ sampling frequency (2^{nd} level) at l'th actuator [Hz]; section 5.4 on page 257

$f_{s,m}^0$ sampling frequency (0^{th} level) at m'th error sensor [Hz]; section 5.3 on page 252

$f_{s,m}^1$ sampling frequency (1^{st} level) at m'th error sensor [Hz]; section 5.3 on page 252

$f_{s,m}^2$ sampling frequency (2^{nd} level) at m'th error sensor [Hz]; section 5.3 on page 252

$\mathbf{F}_{s_e m_e n_e}^{(c_e)}(r_e,\theta_e,\phi_e)$ spherical wave vector function at position as defined in reference sphere coordinates (r_e,θ_e,ϕ_e)

$\mathbf{F}_{s_x m_x n_x}^{(c_x)}(r_x,\theta_x,\phi_x)$ spherical wave vector function at position as defined in reference sphere coordinates (r_x,θ_x,ϕ_x)

f_t 6 dB cut-off frequency of tweeter in closed-back headset system, ($f_t = 870$ Hz); (11.4.2) on page 485

f_{u} upper frequency limit in ANC [Hz]; section N.3 on page 803

$\mathbf{f}(\mathbf{r},t)$ external force intensity [$\mathrm{N}\cdot\mathrm{kg}^{-1}$]; (F.4.18) on page 664

$\mathbf{f}(\mathbf{r},t)$ external body force *per unit mass* [$\mathrm{N}\cdot\mathrm{kg}^{-1}$]; (F.3.50) on page 643

$\mathbf{f}_\omega^S(\mathbf{r}')$ force per unit area acting on the surface [Pa]; (F.10.15b) on page 679

$\mathbf{f}^S(\mathbf{r}',t')$ force per unit area acting on the surface [Pa $\cdot\mathrm{s}^{-1}$]; (F.10.15b) on page 679

G shear modulus [Pa]; (F.4.16) on page 664

G total Gibb's function [J];(F.3.28) on page 637

$g(S_{11},\cdots,S_{N_\psi N_\psi})$ Gram determinant of a $N_\psi \times N_\psi$ Gram matrix; (2.A.3) on page 103

g specific Gibb's function [$\mathrm{J}\cdot\mathrm{kg}$]; (F.3.27) on page 637

$G^{q}_{i_B}$ random-walk control input matrix, $G^{q}_{i_B} \in \mathbb{K}^{M^2\times M^2}$ (state-space model); (9.4.44b) on page 445

$G^{\breve{w}}_{i_B}$ control input matrix related to the regularized weight vector, $G^{\breve{w}}_{i_B} \in \mathbb{K}^{M^2\times M^2}$ (state-space model); (9.4.44c) on page 445

$G^{w'^o}_{i_B}$ control input matrix associated with the mean optimal weight vector, $G^{w'^o}_{i_B} \in \mathbb{K}^{M^2\times M^2}$ (state-space model); (9.4.64) on page 450

$G^{w^o w^0}_{i_B}$ mean optimal weight vector to initial weight vector coupling control input matrix, $G^{w^o w^0}_{i_B} \in \mathbb{K}^{M^2\times M^2}$ (state-space model); (9.4.46b) on page 445

$G^{w^o \breve{w}}_{i_B}$ control input matrix associated with the coupling between the mean optimal weight vector and the regularized weight vector, $G^{w^o \breve{w}}_{i_B} \in \mathbb{K}^{M^2\times M^2}$ (state-space model); (9.4.46a) on page 445

$G^{\breve{w} w^0}_{i_B}$ control input matrix related to the coupling between the regularized weight vector and the initial weight vector, $G^{\breve{w} w^0}_{i_B} \in \mathbb{K}^{M^2\times M^2}$ (state-space model); (9.4.46c) on page 445

$\mathfrak{G}(\mathbf{r}, t, \mathbf{r}', t')$ Green's dyadic free space time-domain; (F.6.5) on page 671

$\breve{g}^{l}_{t_l^0}$ transmitter (0^{th} level) part of plantsinvolving the m'th error sensor at sample index t_l^0; section 5.3 on page 252

$\breve{g}^{l}_{t_l^1}$ transmitter (1^{st} level) part of plantsinvolving the m'th error sensor at sample index t_l^1; section 5.3 on page 252

$\breve{g}^{l}_{t_l^2}$ transmitter (2^{nd} level) part of plantsinvolving the l'th actuator at sample index t_l^2; section 5.3 on page 252

$\breve{g}^{l}_{\uparrow}$ transmitter (up conversion) part of plants involving the l'th actuator; section 5.4 on page 257

$\breve{g}^{m}_{\downarrow}$ receiver (down conversion) part of plants involving the m'th error sensor; section 5.3 on page 252

$\breve{g}^{m}_{t_m^0}$ receiver (0^{th} level) part of plantsinvolving the m'th error sensor at sample index t_m^0; section 5.3 on page 252

$\breve{g}^{m}_{t_m^1}$ receiver (1^{st} level) part of plantsinvolving the m'th error sensor at sample index t_m^1; section 5.3 on page 252

$\breve{g}^{m}_{t_m^2}$ receiver (2^{nd} level) part of plantsinvolving the m'th error sensor at sample index t_m^2; section 5.3 on page 252

$G_\omega(\mathbf{r}, \mathbf{r}')$ Green's function in FS frequency-domain (F.10.6) on page 677

$G\big(\mathbf{r}, \mathbf{r}', t, t'\big)$ Green's function in FS time-domain (F.10.5) on page 677

$\breve{g}^{j}_{x,t^1}$ receive part of feedback plants involving the j'th reference sensor; Figure 7.2 - 7.3 on pages 304–315

$\check{g}^{k}_{p,t^1}$ receive partof plants involving the k'th performance sensor; Figure 7.1 - 7.3 on pages 293–315

$\check{g}^{m}_{e,t^1}$ receive part of plants involving the m'th error sensor at time t^1; Figure 7.1 - 7.3 on pages 293–315

$\hat{g}^{l}_{y,t^1}$ transmission partof plants involving the l'th secondary actuator; Figure 7.1 - 7.3 on pages 293–315

$g_{x_j}(\theta_{j,s},\phi_{j,s})$ elementary directivity of the j'th reference sensor; (3.2.21) on page 119

$\hat{\gamma}^2_{\psi_a\psi_b}$ estimate of ordinary coherence squared function (or just coherence function) between the (arbitrary) random signal $\boldsymbol{\psi}_a$ and the (arbitrary) random signal $\boldsymbol{\psi}_b$; (C.3.5)

$g^{l,m}_{ey,t^1}$ physical plant linking the l'th secondary source output to the m'th error sensor input , $g^{l,m}_{ey,t^1} \in \mathbb{K}^{M_{g^{l,m}_{ey}}}$ at time t^1; Figure 7.1 - 7.3 on pages 293–315

$\hat{g}^{\copyright l,m}_{ey,t^1_G}$ estimate of $g^{l,m}_{ey,t^1}$ (copy weights) at multirate level 1 , $\hat{g}^{\copyright l,m}_{ey,t^1_G} \in \mathbb{K}^{M_{g^{l,m}_{ey}}}$ at time t^1_G; Figure 7.1 - 7.3 on pages 293–315

$\hat{g}^{\copyright l,m}_{ey,t^2_G}$ estimate of $g^{l,m}_{ey,t^1}$ (copy weights) at multirate level 2 , $\hat{g}^{\copyright l,m}_{ey,t^2_G} \in \mathbb{K}^{M_{g^{l,m}_{ey}}}$ at time t^2_G; Figure 7.1 - 7.3 on pages 293–315

$\widetilde{g}^{l,m}_{ey,t^1}$ propagation path of secondary path between the l'th secondary source and the m'th error sensor; Figure 7.1 - 7.3 on pages 293–315

$\hat{g}^{l,m}_{ey}(t^1_G)$ secondary path estimate system identification (l'th secondary source to m'th error sensor), FFFBICS at time t^1_G; Figure 7.3 on page 315

$g^{l,k}_{py,t^1_G}$ controller-performance path linking the l'th secondary source output to the p'th performance sensor input at time t^1_G; Figure 7.1 - 7.3 on pages 293–315

$g^{l,k}_{py,t^1}$ physical plant linking the l'th secondary source output to the k'th performance sensor input , $g^{l,k}_{py,t^1} \in \mathbb{K}^{M_{g^{l,k}_{ey}}}$ at time t^1; Figure 7.1 - 7.3 on pages 293–315

$\widetilde{g}^{l,k}_{py,t^1_G}$ propagation pathof control-performance path between the l'th secondary source and the p'th performance sensor; Figure 7.1 - 7.3 on pages 293–315

$g^{l,j}_{xy,t^1}$ physical feedback plant linking the l'th secondary source output to the j'th reference sensor input , $g^{l,j}_{xy,t^1} \in \mathbb{K}^{M_{g^{l,j}_{xy}}}$ at time t^1; Figure 7.3 on page 315

$\hat{g}^{\copyright l,j}_{xy,t^1_G}$ estimate of $g^{l,j}_{xy,t^1}$ (copy weights) at multirate level 1 , $\hat{g}^{\copyright l,j}_{xy,t^1_G} \in \mathbb{K}^{M_{\hat{g}^{l,j}_{ey}}}$ at time t^1_G; Figure 7.3 on page 315

$\widetilde{g}^{l,j}_{xy,t^1_G}$ propagation path of feedback path between the l'th secondary source and the j'th reference sensor; Figure 7.2 - 7.3 on pages 304–315

$\hat{g}^{l,j}_{xy}(t^1_G)$ secondary path estimate system identification (l'th secondary source to j'th reference sensor), FFFBICS at time t^1_G; Figure 7.3 on page 315

h	absolute humidity; subsection F.3.10 on page 653
H'_{i_B}	auxiliary matrix, $H'_{i_B} \in \mathbb{K}^{2M\times 2M}$; (9.4.77) on page 452
h_1, h_2, h_3	metric coefficients in orthogonal curvilinear coordinate system
H	enthalpy [J]; (F.3.11) on page 631
h	specific enthalpy [J · kg]; (F.3.12) on page 631
$h(\mathbf{r}, t)$	thermalconvection coefficient [W · K^{-1} · m^{-2}]; (F.3.85) on page 652
H_{i_B}	auxiliary matrix, $H_{i_B} \in \mathbb{K}^{2M\times 2M}$; (9.4.61) on page 449
$H_C(s)$	continuous-time feedback filter(transfer function); Figure 4.1 on page 241
$\mathfrak{H}(\mathbf{r}, t)$	thermal conductivity tensor [W · K^{-1} · m^{-1}]; (F.3.83) on page 651
$H_l(\imath\omega)$	hold function in DAC (0^{th} order)at l'th actuator; (5.4.7) on page 259
$H_{max}(z)$	maximum-phase lag termof $H(z)$; (6.4.9) on page 279
$H_{min}(z)$	minimum-phase lag termof $H(z)$; (6.4.9) on page 279
$H_{UC}(z)$	delay termof $H(z)$; (6.4.9) on page 279
$\mathbf{H}(\mathbf{r}, t)$	magnetic intensity [A · m^{-1}]; (F.5.1b) on page 665
$H(z^{-1})$	adjoint (time-reversed) transfer function of $H(z)$; (6.4.11) on page 279
i	iteration time index; (I.2.2) on page 731
$i_{\breve{w}}$	transformed point of attraction update iteration number, $i_{\breve{w}} \leq i_B$; (8.6.14) on page 399
i	iteration number; subsection 8.3.1 on page 374
i	iteration number; section 6.2 on page 274
i^γ	iteration number corresponding to i_γ, $i^\gamma \leq i_B$; (8.3.15) on page 382
$\mathfrak{I}$	unit dyadic (idemfactor); F.3.9 on page 653
$i^{\Delta w}(\,\cdot\,)$	tap-weight update time; section 6.2 on page 274
J	accumulated index in spherical harmonics expansion; (G.4.11) on page 714
$J(w_{i_B})$	cost function, $J(w_{i_B}) : \mathbb{K}^{M\times 1} \rightarrow \mathbb{R}_+(\mathbb{K}^{M\times M} \succ 0)$; subsection 8.3.1 on page 374
$J^\alpha(w_{i_B})$	cost function weight norm penalty term (leakage); (8.3.11) on page 380
$J^\gamma(\,\cdot\,)$	cost function control output signal mean-square penalty term (leakage); (8.3.16) on page 382
$J^\Pi(w_{i_B})$	cost function term (weight regularization); (8.3.22) on page 385
$J^{\alpha\gamma\Pi}(w_{i_B})$	cost function term (weight and control-effort-driven leakage and regularization); (8.3.22) on page 385

$J^{e^2\alpha\gamma\Pi}(w_{i_B})$ cost function (l.l.m.s.e. with weight-driven leakage control-effort-driven leakage and weight regularization); (8.3.22) on page 385

$J^{e^2\alpha\gamma}(w_{i_B})$ cost function (l.l.m.s.e. with weight and control-effort-driven leakage); (8.3.18) on page 383

$J^{e^2\alpha}(w_{i_B})$ cost function (l.l.m.s.e. with leakage); (8.3.12) on page 380

$J^{e^2\gamma}(w_{i_B})$ cost function (l.l.m.s.e. with control-effort-driven leakage); (8.3.16) on page 382

$J^{e^2}(w_{i_B})$ cost function (l.l.m.s.e.); (8.3.5) on page 376

$J^{e^{2p}\alpha\gamma\Pi}(w_{i_B})$ l.l.m.m.e.n. cost function with weight-driven leakage control-effort-driven leakage and weight regularization; (8.5.26) on page 395

$J^{e^{2p}}(w_{i_B})$ cost function (l.l.m.m.e.n.; (8.5.27) on page 395

J_{i_B} auxiliary matrix, $J_{i_B} \in \mathbb{K}^{M\times M}$; (9.A.31a) on page 464

J_ϕ number of samples $\varphi \in [0, 2\pi)$; subsection G.4.2*onpage* 714

J_θ number of samples $\vartheta \in [0, 2\pi)$; subsection G.4.2*onpage* 714

$\mathfrak{J}(\mathbf{r}, t)$ fluid momentum-flux tensor [Pa]; (F.3.54) on page 644

$J_{\min}(w^o_{i_B})$ cost function when weights attain their optimal values; (8.4.2) on page 386

$J^{\{\}+}_{\min}(w^o_{i_B})$ minimum cost function $\mathbf{z}$-domain filtering; subsection 8.4.2 on page 387

$j_n(\zeta)$ spherical Bessel function of order n; (G.3.3a) on page 710

$J_{n+\frac{1}{2}}(\zeta)$ Bessel function of order $n + \frac{1}{2}$; (G.3.4a) on page 711

$\mathbf{J}(\mathbf{r}, t)$ current density [A $\cdot$ m^{-2}]; (F.5.1) on page 665

k second viscosity coefficient [Pa $\cdot$ s]; (F.3.97) on page 656

K'_{DFT} effective number of DFT averagesin (modified) periodogram in spectrum estimation; section C.2 on page 540

K used t in APA; (8.6.9) on page 398

k wave number m^{-1} ; (F.3.38) on page 639

K_{i_B} auxiliary matrix, $K_{i_B} \in \mathbb{K}^{M\times M}$; (9.A.31b) on page 464

K_a stiffness of the air in closed-back headset system, ($K_a = 26$ kN $\cdot$ m^{-1}); (10.3.1) on page 472

K_c stiffness of the cushion in closed-back headset system, ($K_c = 100$ kN $\cdot$ m^{-1}); (10.3.1) on page 472

K_{DFT} number of full length DFT averagesin (modified) periodogram in spectrum estimation; section C.2 on page 540

$K_s(\mathbf{r}, t, P, T)$ isentropic compressibility [Pa^{-1}]; (F.3.73) on page 649

$K_T(\mathbf{r},t,P,T)$ isothermal compressibility [Pa^{-1}]; (F.3.72) on page 649

l mean-free-path of molecules [m]

$L(z)$ minimum phase function (modeling filter), $L(z) \in \mathbb{C}^{N_x \times N_x}$; (3.2.3) on page 107

$L^2_{\uparrow,l}$ upsampling factor in resampling (2^{nd} level) at l'th actuator; (5.4.3) on page 257

$L^2_{\uparrow,m}$ upsampling factor in resampling (2^{nd} level) at m'th error sensor; (5.3.7)

$L^*(z^{-*})$ para-Hermitian conjugate of $L(z)$ (whitening filter)($L^*(z^{-*}) \in \mathbb{C}^{N_x \times N_x}$); (3.2.3) on page 107

$\widehat{L^{-1}}(z)$ whitening filter estimate($\widehat{L^{-1}}(z) \in \mathbb{C}^{N_x \times N_x}$); (3.5.10) on page 217

$L_+(z)$ spectral factor (minimum phase, modeling filter); (3.2.5) on page 108

$L_-(z)$ para-Hermitian conjugate of $L_+(z)$; (3.2.5) on page 108

$L(\overset{\triangleleft}{f_i})$ level of aliased signal component; (N.3.3)

$\bar{L}(z)$ minimum phase rational matrix sequence (modeling filter), $\bar{L}(z) \in \mathbb{C}^{N_x \times n_x}$(rank deficient z-autospectrum); (3.2.6) on page 108

L_{DFT} DFT window lengthin (modified) periodogram in spectrum estimation; section C.2 on page 540

$\mathfrak{L}$ source or polarization dyadic; (F.9.3) on page 675

L_t inductance in cross-over network tweeter in closed-back headset system; (11.4.2) on page 485

$L_v(z)$ minimum phase function (modeling filter), $L_v(z) \in \mathbb{C}^{N_v \times N_v}$; (3.3.1) on page 135

$\mathbf{L}$ auxiliary vector component (longitudinal)

$L^1_{\uparrow,l}$ upsampling factor in resampling (1^{st} level) at l'th actuator; (5.4.6) on page 259

$L^1_{\uparrow,m}$ upsampling factor in resampling (1^{st} level) at m'th error sensor; (5.3.7)

$L_{dw}(z)$ minimum phase function (modeling filter), $L_{dw}(z) \in \mathbb{C}^{N_d \times N_v}$; (3.3.3) on page 135

$L_{u,i,+}(z)$ spectral factor (minimum phase, modeling filter); (8.4.7) on page 387

$L_{u,i,-}(z)$ para-Hermitian conjugate of $L_{u,i,+}$; (8.4.7) on page 387

$L^{\alpha\gamma W_e}_{ux,i,+}(z)$ spectral factor (minimum phase, modeling filter); (8.5.22) on page 394

$L^{\alpha\gamma W_e}_{ux,i,-}(z)$ para-Hermitian conjugate of $L^{\alpha\gamma W_e}_{u,i,+}(z)$; (8.5.22) on page 394

$L_{xw}(z)$ minimum phase function (modeling filter), $L_{xw}(z) \in \mathbb{C}^{N_x \times N_v}$; (3.3.2) on page 135

m azimuthal index in spherical harmonic expansion (exponential form); G.3.8 on page 712

$M^2_{\downarrow,l}$ downsampling factor in resampling (2^{nd} level) at l'th actuator; (5.4.3) on page 257

$M^2_{\downarrow,m}$ downsampling factor in resampling (2^{nd} level) at m'th error sensor; (5.3.7)

M number of adaptive tap-weights in FIR filter; section I.2

M total number of adaptive tap-weights, $M \triangleq \underset{\oplus}{M}_w \in\in \mathbb{N}$; (7.A.10) on page 367

M molecular weight $[\mathrm{kg} \cdot \mathrm{mol}]$; (F.3.18)

M_a number of adaptive direct (feedforward) coefficients in infinite-duration impulse response (IIR) filter; section I.3

$M_{\mathcal{A}}$ number of samples used in the attenuation calculations; (A.2.10)

M_b number of adaptive recursive (feedback) coefficients in IIR filter; section I.3

$\breve{m}$ azimuthal index in spherical harmonic expansion ($\cos, \sin$ form); G.3.8 on page 712

$\underset{\circlearrowleft}{M}_u$ total regressor length for feedback adaptive tap-weights, $\underset{\circlearrowleft}{M}_u \in\in \mathbb{N}$; (7.A.13a) on page 367

$\underset{\circlearrowleft}{M}_w$ number of feedback adaptive tap-weights, $\underset{\circlearrowleft}{M}_w \in\in \mathbb{N}$; (7.A.11a) on page 367

$\underset{\frown}{M}_u$ total regressor length for feedforward adaptive tap-weights, $\underset{\frown}{M}_u \in\in \mathbb{N}$; (7.A.13b) on page 367

$\underset{\frown}{M}_w$ number of feedforward adaptive tap-weights, $\underset{\frown}{M}_w \in\in \mathbb{N}$; (7.A.11b) on page 367

$M^{\max}_{\hat{g}^l_{ey}}$ maximum filter order used in the secondary path models involving the l'th secondary source; on page 299

$M^{\max}_{g^l_{py}}$ maximum filter order used in the control-performance path models involving the l'th secondary source; on page 301

$M^{\max}_{\hat{g}^l_{xy}}$ maximum filter order used in the feedback path models involving the l'th secondary source; on page 310

$M_{\hat{g}_{ey}}$ filter order used to represent the secondary path; on page 275

$M^{\max}_{\hat{g}_{ey}}$ maximum filter order used in the secondary path models, $M^{\max}_{\hat{g}_{ey}} \in \mathbb{N}$; (7.2.13) on page 297

$M^{\max}_{\hat{g}^l_y}$ maximum filter order used in path models involving the l'th secondary source; (7.3.41) on page 311

$M_{\hat{C}}$ number of tap-weights in $\hat{C}$; section 4.7 on page 245

$M_{\hat{P}}$ number of tap-weights in $\hat{P}$; section 4.7 on page 245

M_s mass of the shell in closed-back headset system, ($M_s = 0.16$ kg); (10.3.1) on page 472

M_u total regressor length for adaptive tap-weights, $M \triangleq \underset{\oplus}{M}_u \in\in \mathbb{N}$; (7.A.12) on page 367

$\underset{\circlearrowleft}{M}^{m',l,2}_u$ regressor length used for adaptive tap-weights $\underset{\circlearrowleft}{w}^{m',l}_{t^1_B}, \underset{\circlearrowleft}{M}^{m',l,2}_u \in \mathbb{N}$; (7.2.16) on page 298

$\underset{\sim}{M}_u^{j,l}$ regressor length used for the update of the adaptive tap-weights $\underset{\sim}{w}_{t_B^1}^{j,l}, \underset{\sim}{M}_u^{j,l} \in \mathbb{N}$; (7.3.16) on page 307

$\underset{\circ}{M}_u^{\max}$ maximum *regressor* length involved in the adaptive tap-weights update, $\underset{\circ}{M}_u^{\max} \in \mathbb{N}\underset{\circ}{w}_{t_B^2}^{m',l}$; (7.2.15) on page 297

$\underset{\sim}{M}_u^{\max}$ maximum *regressor* length involved in the adaptive tap-weights representation $\underset{\sim}{w}_{t_B^2}^{j,l}, \underset{\sim}{M}_u^{\max} \in \mathbb{N}$; (7.3.16) on page 307

$\underset{\circ}{M}_{w^{m'}}^{\max}$ maximum filter order used for the adaptive tap-weights $\overset{\copyright}{\underset{\circ}{w}}_{t_B^1}^{m',l}, \underset{\circ}{M}_{w^{m'}}^{\max} \in \mathbb{N}^{N_e}$; (7.2.9) on page 296

$\underset{\sim}{M}_{w^j}^{\max}$ maximum filter order used for the adaptive tap-weights $\overset{\copyright}{\underset{\sim}{w}}_{t_B^1}^{j,l}, \underset{\sim}{M}_{w^j}^{\max} \in \mathbb{N}^{N_x}$; (7.3.11) on page 306

$M_{\downarrow,l}^1$ downsampling factor in resampling (1^{st} level) at l'th actuator; (5.4.6) on page 259

$M_{\downarrow,m}^1$ downsampling factor in resampling (1^{st} level) at m'th error sensor; (5.3.7)

MSD m.s.d. of the adaptive filter, $\text{MSD} \in \mathbb{R}_+$; (9.2.12) on page 426

MSE m.s.e. of the adaptive filter, $\text{MSE} \in \mathbb{R}_+$; (9.2.13) on page 426

$\mathbb{N}$ the set of natural numbers, $\mathbb{N} \triangleq \{1, 2, 3, \dots\}$.

$\mathcal{N}$ number of atoms in molecule; section F.3.1 on page 632

n polar index in spherical harmonic expansion

n number of moles of the gas; (F.3.1) on page 628

n_ϵ number of standard deviationsin confidence interval analysis; (C.3.2) on page 542

N_ψ total number of channels; (2.2.5) on page 21

$N_{\text{ps}}^{\psi_a}$ number of periodic signals in ψ_a; subsection N.2.5 on page 801

N_{ADC} number of bits in the ADC; (5.3.3) on page 254

$\mathbb{N}^*$ the set of 0 and all natural numbers, $\mathbb{N}^* \triangleq \{0, 1, 2, 3, \dots\}$.

N_c number of components in the thermodynamic system;(F.3.26) on page 637

$N_\varkappa$ number of constituents(in the thermodynamic system); (F.3.23) on page 636

$N_{\varkappa,l}$ number of constituents on the LHS of (F.3.23)

$N_{\varkappa,r}$ number of constituents on the RHS of (F.3.23)

N_{DFT} DFT (block) sizein (modified) periodogram in spectrum estimation; section C.2 on page 540

N_e number of error sensors; Figure 1.1 on page 7

N_{E_u} number of samples used for the estimate of the pulse energy; (8.6.24) on page 401

N_f equation variance(in the thermodynamic system); (F.3.69) on page 649

$N_{f,DFT}$ number of DFT frequency pointsin (modified) periodogram in spectrum estimation; section C.2 on page 540

$\hat{\mathbf{n}}(\mathbf{r}')$ surface normal unit vector at position $\mathbf{r}'$; (F.3.42) on page 641

$h_n^{(1)}(\zeta)$ spherical Hankel function of first kind and order n; (G.3.3c) on page 710

$h_n^{(2)}(\zeta)$ spherical Hankel function of first kind and order n; (G.3.3d) on page 710

$n_n(\zeta)$ spherical Neumann function of order n; (G.3.3b) on page 710

$N_{n+\frac{1}{2}}(\zeta)$ Neumann function of order $n+\frac{1}{2}$; (G.3.4b) on page 711

N_ι number of internal energy modes;(F.3.15c) on page 633

$N_\varkappa$ number of gas species;(F.3.15b) on page 633

N_p number of filter poles; (5.A.7) on page 269

N_p number of performance sensors; Figure 1.1 on page 7

N_{ps}^e number of periodic signalserror sensors; subsection N.3.2 on page 804

N_{ps}^x number of periodic signals reference sensors; section N.3.1 on page 803

N_ψ^A number of A channels; (2.2.9) on page 22

N_ψ^B number of B channels; (2.2.9) on page 22

N_ψ^C number of C (conditioning) channels; (2.2.5) on page 21

N_ψ^I number of input channels; (2.2.5) on page 21

N_ψ^O number of output channels; (2.2.5) on page 21

N_r number of independent reactions(in the thermodynamic system; (F.3.26) on page 637

$N_{\mathrm{rot}}^{\mathrm{dof}}$ degrees of freedom (dof) for rotational movements; section F.3.1

N_{sc} number of (different) scenarios; (A.2.4) on page 531

N_t number of trials (simulations); (A.2.3) on page 530

$N_{\mathrm{tr}}^{\mathrm{dof}}$ dof for translational movements; section F.3.1

N_v number of random white noise signals; Figure 3.1 on page 112

$N_{\mathrm{vib}}^{\mathrm{dof}}$ dof for vibrational movements; section F.3.1

N_x number of reference sensors; Figure 1.1 on page 7

n_x rank of $S_{xx}(\mathrm{e}^{\imath\omega}), n_x \in \mathbb{N}^*$; (3.2.6) on page 108

N_y number of control output (actuators); Figure 1.1 on page 7

N_z number of filter zeroes; (5.A.7) on page 269

N_z number of independent restricting equations(in the thermodynamic system; (F.3.26) on page 637

N_{ec} number of equality constraints ($N_{ec} < M$); (8.A.1) on page 404

N_{iec}^{α} number of inequality constraints related to weight-driven leakage; (8.A.17) on page 408

N_{iec}^{γ} number of inequality constraints related to effort-driven leakage; (8.A.18) on page 408

$p(\mathbf{r}, t)$ acoustical pressure [Pa]

P ambient (or equilibrium) pressure [Pa]; 7 on page 657

$p_{\omega}(\mathbf{r})$ acoustic pressure at position $\mathbf{r}$ at frequency ω [Pa $\cdot$ s]

$\breve{P}(\mathbf{r}, t)$ instantaneous pressure under relaxation (non-equilibrium) [Pa], (F.3.88) on page 652

P_c critical pressure [Pa]; (F.3.4a) on page 629

p_d probability of detection; section 2.A on page 102

$\mathfrak{P}(\mathbf{r}, t)$ fluid stress-flux tensor [Pa]; (F.3.50) on page 643

p_{fa} probability of false alarm; section 2.A on page 102

$\underset{\circ}{e}{}_k^p(t_k^1)$ performance signal, k'th performance sensor FBS at time i; (7.2.32) on page 301

$\underset{\sim}{e}{}_k^p(t_k^1)$ performance signal, k'th performance sensor FFS at time t_k^1; (7.3.39) on page 311

$\underset{\oplus}{e}{}_k^p(t_k^1)$ performance signal, k'th performance sensor FFFBS at time t_k^1; (7.4.17) on page 319

$\underset{\circledast}{e}{}_k^p(t_k^1)$ performance signal, k'th performance sensor FFFBICS at time t_k^1; (7.5.13) on page 325

$P_n^{\breve{m}}(z)$ associated Legendre functions of integer parameters $\breve{m}, n$; (G.3.5) on page 711

P_r reduced pressure; (F.3.4a) on page 629

$P_{ref}(z)$ reference plant transfer function; Figure 4.1 on page 241, (4.7.1) on page 245

$p(\mathbf{r}, t)$ acoustic pressure; [Pa]

$P_{s\mu n}(kA)$ probe response constants

$P(z)$ plant transfer function; (4.7.1) on page 245

$P_n^{\breve{m}}$ associated Legendre functions, (G.4.9) on page 714

ψ_1 scan angle in E-Plane

ψ_2 scan angle in H-Plane

$\tilde{Q}'(\omega)$ earphone volume displacement of acoustical source in closed-back headset system; (11.4.1) on page 483

$\tilde{Q}(\mathrm{e}^{\imath\omega})$ earphone volume displacement of ideal acoustical source with infinite acoustic impedance in closed-back headset system; (11.4.1) on page 483

Q matrix related to the covariance of $\tilde{\mathbf{w}}^o_{i_B}, Q \triangleq \mathrm{E}\,\mathbf{q}_i\mathbf{q}_i^* \in \mathbb{K}^{M\times M}$(random-walk model) in LEM; section 9.2 on page 422

q vectorized random-walk covariance matrix, $q \equiv \mathrm{vec}\,\{Q\} \in \mathbb{K}^{M^2\times 1}$; (9.4.49) on page 446

$Q_{\psi_a\psi_b}(f)$ QPSD (quad-spectrum)between signal $\boldsymbol{\psi}_a$ and $\boldsymbol{\psi}_b$; (2.2.14) on page 23

δQ quantity of heat received by the system [J]; (F.3.9)

Q_{DFT} amount of samples availablefor a (modified) periodogram based spectrum estimation; section C.2 on page 540

Q_e matrix of real eigenvectors of $S_{ee}(\mathrm{e}^{\imath\omega})$; (3.5.2) on page 207

$q(\mathbf{r},t)$ volume source of mass-flow $[\mathrm{kg}\cdot\mathrm{m}^{-3}\cdot\mathrm{s}^{-1}]$; (F.3.48) on page 642

Q_t quality factor of the cross-over network tweeter in closed-back headset system; (11.4.2) on page 485

$\mathbf{q}(\mathbf{r},t)$ heat flux vector $[\mathrm{W}\cdot\mathrm{m}^{-2}\cdot\mathrm{s}^{-1}]$; (F.3.67) on page 648

$\mathbf{q}(\mathbf{r},t)$ heat flux vector $[\mathrm{W}\cdot\mathrm{m}^{-2}]$; (F.3.63) on page 647

$\mathbf{q}_{\mathrm{cnv}}(\mathbf{r},t)$ heat flux vector due to convection $[\mathrm{W}\cdot\mathrm{m}^{-2}]$; (F.3.85) on page 652

$\mathbf{q}_{\mathrm{con}}(\mathbf{r},t)$ heat flux vector due to conduction $[\mathrm{W}\cdot\mathrm{m}^{-2}]$; (F.3.83) on page 651

$\mathbf{q}_{\mathrm{rad}}(\mathbf{r},t)$ heat flux vector due to radiation $[\mathrm{W}\cdot\mathrm{m}^{-2}]$; (F.3.86) on page 652

R source point - field point distance (F.10.7) on page 677

$R(\mathrm{e}^{\imath\omega})$ earphone response-ratio in closed-back headset system; (11.4.1) on page 483

$R^2_{\uparrow,l}$ resampling factor (2^{nd} level) , $R^2_{\uparrow,l} \triangleq \frac{f^1_{s,l}}{f^2_{s,l}} = \frac{L^2_{\uparrow,l}}{M^2_{\downarrow,l}}$ at l'th actuator; (5.4.3) on page 257

$R^2_{\uparrow,m}$ resampling factor (2^{nd} level) , $R^2_{\uparrow,m} \triangleq \frac{f^2_{s,m}}{f^1_{s,m}} = \frac{L^2_{\uparrow,m}}{M^2_{\downarrow,m}}$ at m'th error sensor; (5.3.7) on page 255

R gas constant $[\mathrm{J}\cdot\mathrm{kg}^{-1}\cdot\mathrm{K}^{-1}]$; (F.3.16) on page 633

$\bar{R}$ universal gas constant $[8.3145\ \mathrm{J}\cdot\mathrm{mol}^{-1}\cdot\mathrm{K}^{-1}]$; (F.3.1) on page 628

R_c resistance of the cushion in closed-back headset system, ($R_c = 80\ \mathrm{N}\cdot\mathrm{s}\cdot\mathrm{m}^{-1}$); (10.3.1) on page 472

R_{DFT} number of samples displacement between two consecutive DFT averagesin (modified) periodogram in spectrum estimation; section C.2 on page 540

R_e normalization matrix (constant), $R_e \in \mathbb{R}^{N_x \times N_x} \succ 0$; (3.2.3) on page 107

$\bar{R}_e$ normalization matrix, $\bar{R}_e \in \mathbb{R}^{n_x \times n_x} \succeq 0$ (rank deficient z-autospectrum); (3.2.6) on page 108

$\underset{\circ}{r}{}^p_k(t^1_k)$ rejection signal, k'th performance sensor FBS at time t^1_k; (7.2.33) on page 301

$\underset{\sim}{r}{}^p_k(t^1_k)$ rejection signal, k'th performance sensor FFS at time t^1_k; (7.3.40) on page 311

$\underset{\oplus}{r}{}^p_k(t^1_k+1)$ rejection signal, k'th performance sensor FFFBS at time t^1_k+1; (7.4.18) on page 319

$\underset{\circledast}{r}{}^p_k(t^1_k+1)$ rejection signal, k'th performance sensor FFFBICS at time t^1_k+1; (7.5.14) on page 325

$\underset{\circ}{r}_m(t^1_m+1)$ rejection signal, m'th error sensor FBS at time t^1_m+1; (7.2.27) on page 300

$\underset{\sim}{r}_m(t^1_m+1)$ rejection signal, m'th error sensor FFS at time t^m_l+1; (7.3.28) on page 309

$\underset{\oplus}{r}_m(t^1_m+1)$ rejection signal, m'th error sensor FFFBS at time t^1_m+1; (7.4.14) on page 318

$\underset{\circledast}{r}_m(t^1_m+1)$ rejection signal, m'th error sensor FFFBICS at time t^1_m+1; (7.5.10) on page 324

$\hat{\underset{\circ}{r}}_m(t^1_m+1)$ estimate of $\underset{\circ}{r}_m(t^1_m+1)$; (7.2.25) on page 299

$\hat{\underset{\sim}{r}}_m(t^1_m+1)$ estimate of $\underset{\sim}{r}_m(t^1_m+1)$; (7.3.27) on page 309

$\hat{\underset{\oplus}{r}}_m(t^1_m+1)$ estimate of $\underset{\oplus}{r}_m(t^1_m+1)$; (7.4.13) on page 318

$\hat{\underset{\circledast}{r}}_m(t^1_m+1)$ estimate of $\underset{\circledast}{r}_m(t^1_m+1)$; (7.5.9) on page 324

$\hat{\underset{\circledcirc}{r}}_{m_{-l}}(t^1_G+1)$ estimate of $\underset{\circledcirc}{r}_{m_{-l}}(t^1_G+1)$; (7.6.10) on page 332

$\mathbf{r}_{\text{pot}}(t)$ reference position in space of zero potentialm ; (F.3.62)

$R_{\psi_a\psi_b}(t)$ cross-covariance matrix/vector (B.1.2) on page 537

$\langle R_{\psi_a\psi_b}(\tau)\rangle$ cross-correlation function between two arbitrary signals ψ_a, ψ_b (time-averaged) (N.2.15b) on page 796

$\langle R_{\psi_a\psi_a}(\tau)\rangle$ auto correlation function of an arbitrary signal ψ_a (time-averaged) (N.2.15a) on page 796

R_u auto correlation matrix of the regressor $\mathbf{u}_i$, $R_u \triangleq \mathrm{E}\,\mathbf{u}^*_i\mathbf{u}_i \in \mathbb{C}^{M\times M}$; (8.5.15a) on page 392

$R^{W_e}_u$ error sensor-weighted auto correlation matrix of the regressor $\mathbf{u}_i$, $R^{W_e}_u \triangleq \mathrm{E}\,\mathbf{u}^*_i W_e \mathbf{u}_i \in \mathbb{C}^{M\times M}$; (8.5.15a) on page 392

$R_{u,i}$ auto correlation matrix of the regressor $\mathbf{u}_i$, $R_{u,i} \triangleq \mathrm{E}\,\mathbf{u}^*_i\mathbf{u}_i \in \mathbb{C}^{M\times M}$ in LEM; section 9.2 on page 422

R_v, R_x radius of the spherical surface virtual sensor and reference sensor surface $\mathcal{S}_v, \mathcal{S}_x$; Figure 1.1 on page 7

$\mathbf{R}$ vector from source point to field point [m], (F.10.7) on page 677

$\mathbf{r}_j$ position in space of the j'th reference sensor; Figure 7.2 on page 304

$\mathbf{r}_l$ position in space of the l'th actuator; Figure 7.1 on page 293

$\mathbf{r}_m$ position in space of the m'th error sensor; Figure 7.1 on page 293

$R^1_{\updownarrow,l}$ resampling factor (1^{st} level) , $R^1_{\updownarrow,l} \triangleq \frac{f^0_{s,l}}{f^1_{s,l}} = \frac{L^1_{\uparrow,l}}{M^1_{\downarrow,l}}$ at l'th actuator; (5.4.6) on page 259

$R^1_{\updownarrow,m}$ resampling factor (1^{st} level) at m'th error sensor; (5.3.7) on page 255

$R_{\substack{\triangleleft \\ \psi_a}\substack{\triangleleft \\ \psi_a}}(n)$ ACF of *aliased* components of ψ_a; (N.2.17) on page 797

$R_{\substack{\triangleleft \\ \psi_a}\substack{\triangleright \\ \psi_b}}(n)$ CCF between *aliased* components of ψ_a and *unaliased* components of ψ_b; (N.2.18) on page 797

$R_{\substack{\triangleright \\ \psi_a}\substack{\triangleleft \\ \psi_a}}(n)$ CCF between *unaliased* and components of ψ_a; (N.2.17) on page 797

$R_{\substack{\triangleright \\ \psi_a}\substack{\triangleright \\ \psi_a}}(n)$ ACF of *unaliased* components of ψ_a; (N.2.17) on page 797

$R_{\psi_a\psi_a}(n_1, n_2)$ time-variant auto correlation function of an arbitrary nonstationary discrete-time random signal $\psi_a(n)$; (N.2.12a) on page 796

$R_{\psi_a\psi_a}(t_1, t_2)$ time-variant auto correlation function of an arbitrary nonstationary continuous-time random signal $\psi_a(t)$; (N.2.11a) on page 795

$R_{\substack{\triangleleft \\ \psi_a}\substack{\triangleleft \\ \psi_b}}(n)$ CCF between *aliased* components of ψ_a and ψ_b; (N.2.18) on page 797

$R_{\substack{\triangleleft \\ \psi_a}\substack{\triangleright \\ \psi_b}}(n)$ CCF between *aliased* components of ψ_a and *unaliased* components of ψ_b; (N.2.18) on page 797

$R_{\substack{\triangleright \\ \psi_a}\substack{\triangleleft \\ \psi_b}}(n)$ CCF between *unaliased* components of ψ_a and *aliased* components of ψ_b; (N.2.18) on page 797

$R_{\substack{\triangleright \\ \psi_a}\substack{\triangleright \\ \psi_b}}(n)$ CCF between *unaliased* components of ψ_a and ψ_b; (N.2.18) on page 797

$R_{\psi_a\psi_b}(n_1, n_2)$ time-variant cross-correlation function between two arbitrary nonstationary discrete-time random signals $\psi_a(n), \psi_b(n)$; (N.2.12b) on page 796

$R_{\psi_a\psi_b}(t_1, t_2)$ time-variant cross-correlation function between two arbitrary nonstationary continuous-time random signals $\psi_a(t), \psi_b(t)$; (N.2.11b) on page 795

$R_{\psi_a\psi_b}(\tau)$ cross-correlation functionbetween two arbitrary continuous-time random signals $\boldsymbol{\psi}_a(t), \boldsymbol{\psi}_b(t)$; (2.2.16) on page 24

R_{Et} voice-coil resistance tweeter in closed-back headset system; (11.4.2) on page 485

r_{P',i_B} vectorized data auto correlation matrix, $r_{P',i_B} \in \mathbb{K}^{M^2\times M^2}$; (9.4.48) on page 445

$R_{u,i}$ auto correlation matrix of reference signal estimate

$r_{u,i}$ vectorized data auto correlation matrix, $r_{u,i} \triangleq \text{vec}\{R_{u,i}\} \in \mathbb{K}^{M^2\times 1}$; subsection 9.4.5 on page 450

$r_{u,i}^{W_e}$ vectorized data weighted auto correlation matrix, $r_{u,i}^{W_e} \triangleq \mathrm{vec}\,\{R_{u,i}^{W_e}\} \in \mathbb{K}^{M^2\times 1}$; subsection 9.4.5 on page 450

R_{ud} cross-correlation vector between the regressor $\mathbf{u}_i$ and disturbance signal $\mathbf{d}_i$, $R_{ud} \triangleq \mathrm{E}\,\mathbf{u}_i^*\mathbf{d}_i \in \mathbb{C}^{M\times 1}$; (8.5.15a) on page 392

$R_{ud}^{W_e}$ error sensor-weighted cross-correlation vector between the regressor $\mathbf{u}_i$ and disturbance signal $\mathbf{d}_i$, $R_{ud}^{W_e} \triangleq \mathrm{E}\,\mathbf{u}_i^* W_e \mathbf{d}_i \in \mathbb{C}^{M\times 1}$; (8.5.15a) on page 392

$R_{x,i}^{\gamma_{i_\gamma}(\mathbf{y}_{i^\gamma})}$ auto correlation matrix of the actuator-weighted reference signal $\mathbf{x}_i$, $R_{x,i}^{\gamma_{i_\gamma}(\mathbf{y}_{i^\gamma})} \triangleq \mathrm{E}\,\mathbf{x}_i^*\gamma_{i_\gamma}(\mathbf{y}_{i^\gamma})\mathbf{x}_i \in \mathbb{C}^{M\times M}$; (8.3.17) on page 383

$\hat{\underset{\circ}{r}}_m^{\Delta w}(t_m^2+1)$ rejection signal estimate (frozen tap-weights), m'th error sensor, FBS at time t_m^1+1; (7.2.31) on page 300

$\hat{\underset{\circ}{r}}_m^{\Delta w}(t_m^2+1)$ rejection signal estimate (frozen tap-weights), m'th error sensor, FBS at time t_m^2+1; (7.2.17) on page 298

$\hat{\underset{\frown}{r}}_m^{\Delta w}(t_m^2+1)$ rejection signal estimate (frozen tap-weights), m'th error sensor, FFS at time t_m^2+1; (7.3.18) on page 307

$\hat{\underset{\frown}{r}}_m^{\Delta w}(t_m^2+1)$ rejection signal estimate (frozen tap-weights), m'th error sensor, FFS at time t_m^2+1; (7.3.31) on page 310

$\hat{\underset{\oplus}{r}}_m^{\Delta w}(t_m^2)$ rejection signal estimate (frozen tap-weights), m'th error sensor, FFFBS at time t_m^2; (7.4.10) on page 317

$\hat{r}^{\Delta w}(i)$ cancelation signal estimate (frozen filter) at time i; (6.3.3) on page 276

$\mathfrak{R}(\mathbf{r},t)$ rotation (deformation) dyadic; (F.4.6) on page 661

s $(\mathbf{L},\mathbf{M},\mathbf{N})$-type indicator; (F.11.4) on page 680

$\tilde{S}(\imath\omega)$ sensitivity function; (8.A.14) on page 407

s amplitude parameter; (F.2.2) on page 622

$\hat{\boldsymbol{s}}_s^C$ propagation direction of the s'th clutter signal; Figure 3.1 on page 112

$\hat{\boldsymbol{s}}_s^S$ propagation direction of the s'th periodic signal; Figure 3.1 on page 112

$\tilde{S}_0(\imath\omega)$ sensitivity function for the nominal plant; (8.A.13) on page 407

$s_{\psi_a\psi_a}(\omega)$ normalized single-sided autospectra; (2.2.19) on page 24

$S_{\psi_a\psi_a\cdot\psi^C}(f)$ coherent auto spectral density functionof random signal $\boldsymbol{\psi}_a$ conditioned on random signal set $\boldsymbol{\psi}^C$; (2.3.1) on page 30

$S_{\psi_a\psi_a\perp\psi^C}(f)$ residual auto spectral density functionof random signal $\boldsymbol{\psi}_a$ conditioned on random signal set $\boldsymbol{\psi}^C$; (2.3.1) on page 30

$S_{\psi_a\psi_b\perp\psi^C}(f)$ residual cross-spectral density functionbetween random signal $\boldsymbol{\psi}_a$ and random signal $\boldsymbol{\psi}_b$ conditioned on random signal set $\boldsymbol{\psi}^C$; (2.3.2) on page 30

$\dot{S}_d(f)$ slope of disturbance signals decay for $f > f_{\mathrm{u}}$

$\mathcal{S}^d$ surface spanned by the error sensors; Figure 1.1 on page 7

$\mathcal{S}^d$ surface spanned by the error sensors; Figure 1.1 on page 7

δS_{gen} entropy generation $[\,\mathrm{J}\cdot\mathrm{K}^{-1}\,]$; (F.3.13)

$P\mathfrak{I}(\mathbf{r},t)$ fluid pressure tensor [Pa]; (F.3.89) on page 653

Ⓢ signal source in a FFFBICS; Figure 7.4 on page 321

$\underset{\text{Ⓢ}}{y_l}(t_l^1+1)$ signal source output, l'th secondary source, FFFBICS at time t_l^1+1; (7.5.7) on page 324

$s_{\text{gen}}(\mathbf{r},t)$ specific entropy generated during irreversible processes $[\,\mathrm{J}\cdot\mathrm{kg}^{-1}\cdot\mathrm{K}^{-1}\,]$; (F.3.67) on page 648

S_h effective head surface area of closed-back headset system, ($S_h = 40\,\mathrm{cm}^2$); (10.3.1) on page 472

s_{ij} component of strain element; (F.4.5) on page 661

S^p Performance surface (sphere)

$S_{\psi^A\psi^A\perp\psi^C}$ residual cross spectral density matrix; (2.3.5) on page 31

$S_{\psi_a\psi_a}(f)$ PSD of signal $\boldsymbol{\psi}_a$

$S_{\psi_a\psi_a}(f,t)$ *instantaneous* (short term) auto spectral density function (power spectral density (PSD)) of signal $\psi_a(t)$; (A.2.1) on page 530

$S_{\psi_a\psi_b}(f)$ CPSD between signal $\boldsymbol{\psi}_a$ and signal $\boldsymbol{\psi}_b$

$S_{\psi_a\psi_b}(f,t)$ *instantaneous* (short term) cross-spectral density function between signal $\psi_a(t)$ and $\psi_b(t)$; (A.2.1) on page 530

$S_{\psi_b\psi_b}(f)$ PSD of signal $\boldsymbol{\psi}_b$

$S(\mathbf{r},t)$ time-varying surface integration limits; (F.3.50) on page 643

$s(\mathbf{r},t)$ specific entropy $[\,\mathrm{J}\cdot\mathrm{kg}^{-1}\cdot\mathrm{K}^{-1}\,]$; (F.3.67) on page 648

$S(\mathbf{r},t)$ surface integration limits of the mass element;(F.3.45)

$s^S_\omega(\mathbf{r}')$ mass velocity per unit surface area $[\,\mathrm{kg}\cdot\mathrm{m}^{-2}\cdot\mathrm{s}^{-1}\,]$; (F.10.15a) on page 679

$s^S(\mathbf{r}',t')$ mass velocity per unit surface area $[\,\mathrm{kg}\cdot\mathrm{m}^{-2}\cdot\mathrm{s}^{-2}\,]$; (F.10.15a) on page 679

$\mathcal{S}^v$ surface spanned by the virtual sensors; Figure 1.1 on page 7

$\mathcal{S}^v$ surfacespanned by the virtual sensors; Figure 3.1 on page 112

$\mathbf{s}(\mathbf{r},t)$ displacement vector [m]; (F.4.1) on page 660

$\dot{S}_x(f)$ slope of reference signals decay for $f > f_{\text{u}}$

$\mathcal{S}^x$ reference surface; Figure 1.1 on page 7

$\mathcal{S}^x$ surface spanned by the reference sensors; Figure 1.1 on page 7

$\mathcal{S}^x$ surface spanned by the reference sensors; Figure 1.1 on page 7

$S_{\psi\psi}$ MIMO channel power spectral density matrix, $S_{\psi\psi} \in \mathbb{C}^{N_f \times N_\psi \times N_\psi}$; (2.2.3) on page 21

$S_{\psi^A\psi^A}$ A channel power spectral density matrix, $S_{\psi^A\psi^A} \in \mathbb{C}^{N_f \times N_\psi^A \times N_\psi^A}$; (2.3.3) on page 30

$S_{\psi^A\psi^C}$ A-C cross channel power spectral density matrix, $S_{\psi^A\psi^C} = S^*_{\psi^C\psi^A} \in \mathbb{C}^{N_f \times N_\psi^C \times N_\psi^A}$; (2.3.3) on page 30

$S_{\psi^C\psi^C}$ C channel power spectral density matrix, $S_{\psi^C\psi^C} \in \mathbb{C}^{N_f \times N_\psi^C \times N_\psi^C}$; (2.3.3) on page 30

$S_{\psi^I\psi^I}$ input channel power spectral density matrix, $S_{\psi^I\psi^I} \in \mathbb{C}^{N_f \times N_\psi^I \times N_\psi^I}$; (2.2.6) on page 21

$S_{\psi^I\psi^O}$ input-output cross channel power spectral density matrix, $S_{\psi^I\psi^O} = S^*_{\psi^O\psi^I} \in \mathbb{C}^{N_f \times N_\psi^O \times N_\psi^I}$; (2.2.6) on page 21

$S_{\psi^O\psi^O}$ output channel power spectral density matrix, $S_{\psi^O\psi^O} \in \mathbb{C}^{N_f \times N_\psi^O \times N_\psi^O}$; (2.2.6) on page 21

$S_{\substack{\triangleleft \\ \psi_a}\,\substack{\triangleleft \\ \psi_b}}(\theta)$ CSDF between *aliased* components of ψ_a and ψ_b; (N.2.20) on page 798

$S_{\substack{\triangleleft \\ \psi_a}\,\substack{\triangleright \\ \psi_b}}(\theta)$ CSDF between *aliased* components of ψ_a and *unaliased* components of ψ_b; (N.2.20) on page 798

$S_{\substack{\triangleright \\ \psi_a}\,\substack{\triangleleft \\ \psi_b}}(\theta)$ CSDF between *unaliased* components of ψ_a and *aliased* components of ψ_b; (N.2.20) on page 798

$S_{\substack{\triangleright \\ \psi_a}\,\substack{\triangleright \\ \psi_b}}(\theta)$ CSDF between *unaliased* components of ψ_a and ψ_b; (N.2.20) on page 798

$S_{\psi_a\psi_b \cdot \psi^C}(f)$ coherent cross-spectral density functionbetween random signal $\boldsymbol{\psi}_a$ and random signal $\boldsymbol{\psi}_b$ conditioned on random signal set $\boldsymbol{\psi}^C$; (2.3.2) on page 30

$S^{\alpha\gamma W_e}_{uuxx}(z)$ mixed filtered-reference signal z-auto-cross-spectrum, $S^{\alpha\gamma W_e}_{uuxx}(z) \in \mathbb{C}^{M \times M}$; (8.5.21) on page 394

$\mathfrak{S}(\mathbf{r}, t)$ pure stain dyadic; (F.4.5) on page 661

$a^{\langle p \rangle}$ signed power, (L.2.9) on page 777

SNR_a SNR at port a; (2.2.2) on page 20

SNR_b SNR at port b; (2.2.2) on page 20

SNR_x signal-to-noise ratio at the reference sensor; (6.5.4) on page 280

$A(t)$ state transition matrix, $A(t) \in \mathbb{K}^{n \times n}$; subsection O.0.1 on page 807

$B(t)$ control matrix, $B(t) \in \mathbb{K}^{n \times m}$; subsection O.0.1 on page 807

$C(t)$ observation matrix, $C(t) \in \mathbb{K}^{p \times n}$; subsection O.0.1 on page 807

$D(t)$ direct input-output coupling matrix, $D(t) \in \mathbb{K}^{p\times m}$; subsection O.0.1 on page 807

T sampling period; [s]

$T(\omega)$ response of the second-order high-pass cross-over filter tweeter in closed-back headset system; (11.4.1) on page 483

T ambient temperature [K]; 7 on page 657

T time domain, $T \subset \mathbb{R}$; subsection O.0.1 on page 807

$T_{\mathcal{A}}$ attenuation estimation time [s]; (A.2.10)

$T_{\alpha}^{\beta}(z)$ Gegenbauer polynomials of real non negative parameters α, β, (G.3.5) on page 711

$\breve{T}_{\iota}^{\varkappa}(\mathbf{r}, t)$ apparent temperature associated with mode ι for species $\varkappa$ (under relaxation) [K], (F.3.88) on page 652

T_c critical temperature [K]; (F.3.4b) on page 629

$\mathfrak{T}(\mathbf{r}, t)$ stress-momentum-flux tensor [Pa]; (F.3.55) on page 644

T_{ij} strain element; (F.4.7) on page 662

T_l^0 sampling period , $T_l^0 \triangleq 1/f_{s,l}^0$ (0^{th} level) at l'th actuator [s]; section 5.4 on page 257

t_l^0 sample index(0^{th} level) at l'th actuator; section 5.4 on page 257

T_l^1 sampling period , $T_l^1 \triangleq 1/f_{s,l}^1$ (1^{st} level) at l'th actuator [s]; section 5.4 on page 257

t_l^1 sample index (1^{st} level) at l'th actuator; section 5.4 on page 257

T_l^2 sampling period , $T_l^2 \triangleq 1/f_{s,l}^2$ (2^{nd} level) at l'th actuator [s]; section 5.4 on page 257

t_l^2 sample index(2^{nd} level) at l'th actuator; section 5.4 on page 257

T_m^0 sampling period(0^{th} level) at m'th error sensor [s]; section 5.3 on page 252

t_m^0 sample index(0^{th} level) at m'th error sensor; section 5.3 on page 252

T_m^1 sampling period , $T_m^1 \triangleq 1/f_{s,m}^1$ (1^{st} level) at m'th error sensor [s]; section 5.3 on page 252

t_m^1 sample index (1^{st} level) at m'th error sensor; section 5.3 on page 252

T_m^2 sampling period , $T_m^2 \triangleq 1/f_{s,m}^2$ (2^{nd} level) at m'th error sensor [s]; section 5.3 on page 252

t_m^2 sample index(2^{nd} level) at m'th error sensor; section 5.3 on page 252

T_p permissable time frame

T_r reduced temperature[ ]; (F.3.4b) on page 629

$T_{AAF}(s)$ anti-aliasing filter(transfer function); Figure 4.1 on page 241

$T_{ADC}(s)$ analogue to digital converter(transfer function); Figure 4.1 on page 241

$T_{DAC}(s)$ digital to analogue converter(transfer function); Figure 4.1 on page 241

$T_{RF}(s)$ reconstruction filter(transfer function); Figure 4.1 on page 241

t_B^2 tap-weight update time (index); on page 274

t_B^1 adaptive tap-weight time index multirate level 1 , $t_B^1 \in \mathbb{N}$; subsection 7.2.5 on page 298 and subsection 7.3.5 on page 307

t_B^2 adaptive tap-weight time index multirate level 2 , $t_B^2 \in \mathbb{N}$; subsection 7.2.5 on page 298 and subsection 7.3.5 on page 307

$\mathfrak{T}(\mathbf{r},t)$ stress dyadic [Nm^{-2}]; (F.4.7) on page 662

t_G^1 plant estimation time index multirate level 1 , $t_G^1 \in \mathbb{N}$; section 7.6 on page 326

t_G^2 plant estimation time index multirate level 2 , $t_G^2 \in \mathbb{N}$; section 7.6 on page 326

$\mathbf{u}_i$ filter input vector, $\mathbf{u}_i \in \mathbb{C}^{1\times M}$; (I.2.2)

$U(\mathbf{r},t)$ internal energy [J]; (F.3.66) on page 647

$u(\mathbf{r},t)$ specific internal energy [$\mathrm{J}\cdot\mathrm{kg}^{-1}$]; (F.3.15) on page 633

U internal energy function [$\mathrm{J}\cdot\mathrm{m}^{-3}$]; (F.3.9)

U input alphabet; subsection O.0.1 on page 807

$\underset{\circ}{u}(t_l^2)$ filtered-reference signalat multirate level 2FBS at time t_l^2; subsection 7.2.4 on page 296

$\underset{\circ}{\mathring{u}}_{t_l^2}$ FBS regressor block cell matrix, $\underset{\circ}{\mathring{u}}_{t_l^2} \in \mathbb{K}^{N_e\times N_y\times N_e}$ at multirate level 2 at time t_l^2; (7.A.4a) on page 365

$\underset{\sim}{u}(t_l^2)$ filtered-reference signal, FFS at time t_l^2; on page 306

$\underset{\sim}{\mathring{u}}_{t_l^2}$ FFS regressor block cell matrix, $\underset{\sim}{\mathring{u}}_{t_l^2} \in \mathbb{K}^{N_e\times N_y\times N_x}$ at multirate level 2 at time t_l^2; (7.A.4b) on page 365

$\underset{\oplus}{\mathring{u}}_{t_l^2}$ FFFBS regressor block cell matrix at multirate level 2, $\underset{\oplus}{\mathring{u}}_{t_l^2} \in \mathbb{K}^{N_e\times N_y\times (N_e+N_x)}$ at time t_l^2; (7.A.3) on page 364

$u_{t_l^2}$ regressor matrix at multirate level 2, $u_{t_l^2} \in \mathbb{K}^{N_e\times M}$ at time t_l^2; (7.A.14) on page 367

U_i regressor time-block matrix, $U_i \in \mathbb{K}^{K\times M}(U_i \in \mathbb{K}^{KN_e\times M})$; (8.6.9) on page 398

$u_{\iota,-0}^{\varkappa}$ internal acoustic energy *per unit mass* associated with mode ι for species $\varkappa$ [$\mathrm{J}\cdot\mathrm{kg}^{-1}$]; (F.3.21) on page 635

$\underset{\circ}{u}_{m,l,m'}(t_l^2)$ filtered-reference signalat multirate level 2, $\underset{\circ}{u}_{m,l,m'}(t_l^2) \in \mathbb{K}$FBS at time t_l^2; (7.2.10) on page 297

$\underset{\sim}{u}_{l,m,j}(t_l^2)$ filtered-reference signal component, FFS at time t_j^2; j refers to reference sensor; l,m refer to the secondary path; (7.3.12) on page 306

$\mathbf{u}(\mathbf{r},t)$ acoustical velocity $[\mathrm{m}\cdot\mathrm{s}^{-1}]$

$u_{\mathrm{ch}}(\mathbf{r},t)$ specific chemical bound internal energy $[\mathrm{J}\cdot\mathrm{kg}^{-1}]$; (F.3.15) on page 633

$u_{\mathrm{e}}(\mathbf{r},t)$ specific electron internal energy $[\mathrm{J}\cdot\mathrm{kg}^{-1}]$; (F.3.15) on page 633

$u_{\mathrm{rot}}(\mathbf{r},t)$ specific rotational kinetic internal energy $[\mathrm{J}\cdot\mathrm{kg}^{-1}]$; (F.3.15) on page 633

$u_{\mathrm{tr}}(\mathbf{r},t)$ specific translational kinetic internal energy $[\mathrm{J}\cdot\mathrm{kg}^{-1}]$; (F.3.15) on page 633

$u_{\mathrm{vib}}(\mathbf{r},t)$ specific vibrational kinetic internal energy $[\mathrm{J}\cdot\mathrm{kg}^{-1}]$; (F.3.15) on page 633

$\mathring{\underset{\circ}{u}}^{w}_{m,l,m',t_l^2}$ filtered-reference signal time-reversed buffer, FBS at time t_l^2; m' refers to reference sensor; l,m refer to the secondary path; (7.2.14) on page 297

$\mathring{\underset{\sim}{u}}^{w}_{l,m,j,t_l^2}$ filtered-reference signal time-reversed buffer, FFS at time t_l^2; j refers to reference sensor; l,m refer to the secondary path; (7.3.15) on page 307

$u^{\Delta w}(\,\cdot\,)$ reference signal used for tap-weight update; section 6.2 on page 274

V_δ principal volume; (F.9.1) on page 675

$\mathcal{V}^C$ control volume; Appendix H on page 719

$\mathfrak{V}(\mathbf{r},t)$ stress-momentum-flux tensor [Pa]; (F.3.95) on page 656

$\mathcal{V}_f$ volume (space) of fluid; subsection F.3.12 on page 656

$V_{\check{f}}$ linear sound field volume; (F.3.100) on page 658

V_i system noise signal time-block matrix, $V_i \in \mathbb{K}^{KN_e\times 1}(V_i \in \mathbb{K}^{K\times 1})$; (9.2.3) on page 424

$\mathcal{V}_\infty$ all space $\mathbb{R}^3$; section F.7 on page 672

V_l^y weight factor attributed to the l'th actuator; (8.3.15) on page 382

$\check{v}_r$ modified reduced specific volume[]; (F.3.8) on page 630

$V(\mathbf{r},t)$ time-varying volume integration limits; (F.3.43) on page 641

$V(\mathbf{r},t)$ volume integration limits of the mass element;(F.3.45)

$\mathcal{V}_s$ space spanned by all sources; section F.7 on page 672

$\mathcal{V}^v,\mathcal{V}^x,\mathcal{V}^d$ interior volumes of $\mathcal{S}^v,\mathcal{S}^x,\mathcal{S}^d$; Figure 1.1 on page 7

$\mathcal{V}^v,\mathcal{V}^x,\mathcal{V}^d$ interior volumes of $\mathcal{S}^v,\mathcal{S}^x,\mathcal{S}^d$; Figure 1.1 on page 7

$W(\mathbf{r},t)$ stress energy function $[\mathrm{J}\cdot\mathrm{m}^{-3}]$; (F.4.9) on page 662

$w(t)$ random colored noise signals, $w(t)\in\mathbb{C}^{N_v\times 1}$; (3.3.1) on page 135

$\check{w}_{i_{\check{w}}}$ transformed weight vector, $\check{w}_{i_{\check{w}}} \in \mathbb{K}^{M\times 1}$(weight regularization); (8.6.14) on page 399

$\check{w}_{i_B}$ weight-update direction vector, $\check{w}_{i_B}\in\mathbb{K}^{M\times 1}$;(8.5.1) on page 389

$w(\mathbf{r},t)$ acoustic energy density $[\mathrm{J}\cdot\mathrm{m}^{-3}]$; (F.3.107) on page 659

w filter weights, $w\in\mathbb{C}^{M\times 1}$(tap-weight vector); (I.2.1) on page 731

w^o mean, $w^o\in\mathbb{K}^{M\times 1}$ optimal weight vector in LEM; section 9.2 on page 422

w^{ig} weight vector, $w^{\mathrm{ig}}\in\mathbb{K}^{M\times 1}$ initial guess; (8.5.28) on page 396

w^{av} weight vector obtained from some averaging procedure, $w^{av}\in\mathbb{K}^{M\times 1}$; (8.5.28) on page 396

w^{ls} weight vector, $w^{ls}\in\mathbb{K}^{M\times 1}$, last saved; (8.5.28) on page 396

w_{i_B} adaptive tap-weight vector, $w_{i_B}\in\mathbb{K}^{M\times 1}$; section 8.3.1 on page 375

$w^o_{i_B}$ optimal weight vector, $w^o_{i_B}\in\mathbb{K}^{M\times 1}$; (8.4.1) on page 386

$W_{\mathrm{RD}}(\omega)$ frequency-dependent weighting function; (8.3.7)

w_a direct adaptive tap-weight vector, $w_a\in\mathbb{C}^{M_a\times 1}$ in IIR filter; (I.3.2) on page 734

w_b recursive adaptive tap-weight vector, $w_b\in\mathbb{C}^{M_b\times 1}$ in IIR filter; (I.3.2) on page 734

$\bar{w}_{i_{\bar{w}}}$ point of attraction, $\bar{w}_{i_{\bar{w}}}\in\mathbb{K}^{M\times 1}$(weight regularization); (8.3.21) on page 384

W_e error sensor weighting diagonal matrix, $W_e\in\mathbb{R}^{N_e\times N_e}$; (8.3.3) on page 376

$W^p_k(f,t)$ frequency and generally time-variant weighting function applied to the k'th performance sensor; (A.2.1)

$\underset{\circ}{w}{}^{m',l}_{t^2_B}$ adaptive tap-weights at multirate level 2 , $\underset{\circ}{w}{}^{m',l}_{t^2_B}\in\mathbb{K}^{M^{m',l}_{\circ}}$ FBS linking the m'th reference signal to the l'th control output signal at time t^2_B; Figure 7.1 on page 293 and Figure 7.3 on page 315

$\underset{\circ}{\overset{\copyright}{w}}{}^{m',l}_{t^1_B}$ adaptive tap-weights copy of $\underset{\circ}{w}{}^{m',l}_{t^2_B}$ at multirate level 1 , $\underset{\circ}{\overset{\copyright}{w}}{}^{m',l}_{t^1_B}\in\mathbb{K}^{M^{m',l}_{\circ}}$ FBS linking the m'th reference signal to the l'th control output signal at time t^1_B; Figure 7.1 on page 293 and Figure 7.3 on page 315

$\underset{\circ}{w}_{t^2_B}$ FBS adaptive tap-weight cell matrix, $\underset{\circ}{w}_{t^2_B}\in\mathbb{K}^{N_e\times N_y}$ at multirate level 2 linking the reference signals to the control output signals at time t^2_B; (7.A.2a) on page 364

$\underset{\circ}{\mathring{x}}_{t^1_l}$ FBS reference signal cell matrix, $\underset{\circ}{\mathring{x}}_{t^1_l}\in\mathbb{K}^{N_y\times N_e}$ at multirate level 1 at time t^1_l; (7.A.7) on page 366

$\underset{\sim}{w}{}^{j,l}_{t^2_B}$ adaptive tap-weights at multirate level 2 , $\underset{\sim}{w}{}^{j,l}_{t^2_B}\in\mathbb{K}^{M^{j,l}_{\sim}}$ FFS linking the j'th reference signal to the l'th control output signal at time t^2_B; Figure 7.1 on page 293 and Figure 7.3 on page 315

$\underset{\sim}{\overset{\copyright}{w}}{}^{j,l}_{t^1_B}$ adaptive tap-weights copy of $\underset{\sim}{w}{}^{j,l}_{t^2_B}$ at multirate level 1 , $\underset{\sim}{\overset{\copyright}{w}}{}^{j,l}_{t^1_B}\in\mathbb{K}^{M^{j,l}_{\sim}}$ FFS linking the m'th reference signal to the l'th control output signal at time t^1_B; Figure 7.1 on page 293 and Figure 7.3 on page 315

$\underset{\sim}{w}_{t_B^2}$ FFS adaptive tap-weight cell matrix, $\underset{\sim}{w}_{t_B^2} \in \mathbb{K}^{N_x \times N_y}$ at multirate level 2 linking the reference signals to the control output signals at time t_B^2; (7.A.2b) on page 364

$\underset{\sim}{\mathring{x}}_{t_l^1}$ FFS reference signal cell matrix, $\underset{\sim}{\mathring{x}}_{t_l^1} \in \mathbb{K}^{N_y \times N_x}$ at multirate level 1 at time t_l^1; (7.A.8) on page 366

$\underset{\oplus}{w}_{t_B^2}$ FFFBS adaptive tap-weight cell matrix at multirate level 2, $\underset{\oplus}{w}_{t_B^2} \in \mathbb{K}^{(N_e+N_x)\times N_y}$ linking the reference signals to the control output signals at time t_B^2; (7.A.1) on page 364

$w_{\mathrm{kin}}(\mathbf{r}, t)$ acoustic kinetic energy density $[\mathrm{J} \cdot \mathrm{m}^{-3}]$; (F.3.109) on page 659

W_m^e weight factor attributed to the m'th error sensor; (8.3.3) on page 376

$W_m^{e,\mathrm{dB}}$ attenuation weight factor of m'th error sensordB-weighting ; (8.3.2) on page 375

$\underset{\sim}{\tilde{w}}^o(z)$ optimal feedforward steady-state tap-weights transfer function; (6.5.3) on page 280

$W_{y^2}(\omega)$ frequency-dependent weighting function; (8.A.7)

$w_{\mathrm{pot}}(\mathbf{r}, t)$ acoustic potential energy density $[\mathrm{J} \cdot \mathrm{m}^{-3}]$; (F.3.108) on page 659

$w_{t_B^2}$ adaptive tap-weight vector at multirate level 2, $w_{t_B^2} \in \mathbb{K}^{M\times 1}$ linking the reference signals to the control output signals at time t_B^2; (7.A.9) on page 367

$\tilde{w}_{\mathrm{PEF}}(z)$ transfer function of the PEF; (3.5.2) on page 207

$W_{e\otimes K}$ error sensor weighting block diagonal matrix, $W_{e\otimes K} \in \mathbb{R}^{(KN_e)\times(N_eK)}$; (8.6.7) on page 397

WEMSE WEMSE of the adaptive filter, WEMSE $\in \mathbb{R}_+$; (9.2.16) on page 426

WMSE w.m.s.e. of the adaptive filter, WMSE $\in \mathbb{R}_+$; (9.2.14) on page 426

X state space; subsection O.0.1 on page 807

$\underset{\circ}{x}_{m'}(t_{m'}^1)$ feedback reference signal at multirate level 1 , $\underset{\circ}{x}_{m'}(t_{m'}^1) \in \mathbb{K}$ m''th reference sensor, FBS at time t_m^1; (7.2.4) on page 295

$\underset{\circ}{x}_{m'}(t_{m'}^2)$ feedback reference signal, m''th reference sensor, FBS at time t_m^2; (7.2.7) on page 296

$\underset{\sim}{x}'_j(t_j^1)$ reference signal (feedback perturbed), FFS at time t_j^1 (7.3.6) on page 306

$\underset{\sim}{x}_j(t_j^1)$ feedforward reference signal, j'th reference sensor, FFS at time t_j^1; (7.3.8) on page 306

$x_j(t_j^1)$ reference signal, j'th reference sensor, FFS at time t_j^1; (7.3.6) on page 306

$\underset{\oplus}{x}_{t_l^1}$ FFFBS reference signal cell matrix at multirate level 1, $\underset{\oplus}{x}_{t_l^1} \in \mathbb{K}^{N_y\times(N_e+N_x)}$; (7.A.6) on page 366

X_i reference signal time-block matrix, $X_i \in \mathbb{K}^{K\times M}(X_i \in \mathbb{K}^{KN_y\times M})$; (8.6.9) on page 398

$x_{t_l^1}$ reference signal vector, $x_{t_l^1} \in \mathbb{K}^{N_y \times N_y(N_e+N_x)}$at multirate level 1 at time t_l^1; (7.A.17) on page 369

$\mathring{\underset{\circ}{x}}^{\hat{g}_{ey}}_{m',t^2_{m'}}$ reference signal time-reversed buffer , $\mathring{\underset{\circ}{x}}^{\hat{g}_{ey}}_{m',t^2_{m'}} \in \mathbb{K}^{M^{\max}_{\hat{g}_{ey}}}$, FBS at time $t^2_{m'}$; (7.2.11) on page 297

$\mathring{\underset{\sim}{x}}^{\hat{g}_{ey}}_{j,t_j^2}$ reference signal time-reversed buffer used in connection with the plant estimate filtering, FFS at time t_j^2; (7.3.13) on page 307

$\underset{\circledS}{x}^{\hat{g}^{l,m}_{ey}}(t_G^1)$ reference signal in connection with secondary path estimation (l'th secondary source to m'th error sensor), FFFBICS at time t_G^1; (7.6.1) on page 328

$\underset{\circledS}{x}^{\hat{g}^{l,j}_{xy}}(t_G^1)$ reference signal in connection with feedback path estimation (l'th secondary source to j'th reference sensor), FFFBICS at time t_G^1; (7.6.1) on page 328

$\mathring{\underset{\circledS}{x}}^{\hat{g}^{l}_{y}}_{t_G^1}$ reference signal time-reversed buffer used in connection with plant estimates involving the l'th secondary source, FFFBICS at time t_G^1; (7.6.2) on page 328

$\Xi_n^{(c)}(r)$ radial function in separated Helmholtz equation in spherical coordinates; (G.3.3) on page 710

$\mathring{\underset{\circ}{x}}^{w}_{m',t^1_{m'}}$ reference signal time-reversed buffer at multirate level 1 , $\mathring{\underset{\circ}{x}}^{w}_{m',t^1_{m'}} \in \mathbb{K}^{M^{\max}_{\circ\, w^{m'}}}$ used in connection with the tap-weights, FBS at time $t^1_{m'}$; (7.2.8) on page 296

$\mathring{\underset{\sim}{x}}^{w}_{j,t^1_j}$ reference signal time-reversed buffer at multirate level 1 , $\mathring{\underset{\sim}{x}}^{w}_{j,t^1_j} \in \mathbb{K}^{M^{\max}_{\sim wj}}$ used in connection with the tap-weights, FFS at time t_j^1; (7.3.10) on page 306

(x_A, y_A, z_A) Cartesian coordinate system for AUT

(x_P, y_P, z_P) Cartesian coordinate probe

(x_S, y_S, z_S) Cartesian coordinate system in space

Y output value space; subsection O.0.1 on page 807

$y_{\varkappa}$ mole fraction of the $\varkappa$'th constituent; (F.3.6) on page 629

$\underset{\circ}{y_l}(t_l^1)$ control output signal, l'th secondary source, FBS at time t_l^1; (7.2.21) on page 299

$\underset{\sim}{y_l}(t_l^1)$ control output signal, l'th secondary source, FFS at time t_l^1; (7.3.22) on page 308

$\underset{\oplus}{y_l}(t_l^1+1)$ control output signal, l'th secondary source, FFFBS at time t_l^1+1; (7.4.11) on page 317

$\underset{\circledS}{y_l}(t_l^1+1)$ control output signal, l'th secondary source, FFFBICS at time t_l^1+1; (7.5.7) on page 324

$\underset{\circledS}{y}^{\hat{g}^{l,m}_{ey}}(t_G^1+1)$ secondary path system identification output signal(l'th secondary source to m'th error sensor), FFFBICS at time t_G^1 +1; (7.6.5) on page 330

$\underset{\circledcirc}{y^{\hat{\vartheta}^{l,j}_{xy}}}(t^1_G+1)$ feedback path system identification output signal(l'th secondary source to j'th reference sensor), FFFBICS at time t^1_G +1; (7.6.6) on page 330

$\underset{\circlearrowleft}{\mathring{y}^{\hat{g}_y}_{l,t^1_l+1}}$ control output signal buffer, l'th secondary source, FBS at time t^1_l+1; (7.2.22) on page 299

$\underset{\sim}{\mathring{y}^{\hat{g}_y}_{l,t^1_l+1}}$ control output signal buffer, l'th secondary source, FFS at time t^1_l+1; (7.3.23) on page 308

Z compressibility factor; (F.3.3) on page 628

z^{-1} reciprocal of z (reflection of z about the uc and reflection of the result hereof about the real axis); (3.2.3) on page 107

z^{-*} conjugate-reciprocal of z (reflection of z about the uc); (3.2.3) on page 107

Z^A_l acoustic impedance related to leakage, $Z^A_l = R^A_l + \frac{K^A_l}{\imath\omega}$ in closed-back headset system, ($Z^A_l = (1+\frac{2\omega_l}{\imath\omega})1.26\text{e}7\ \text{N}\cdot\text{s}\cdot\text{m}^{-5}$); (10.3.1) on page 472

$Z^A_m(\text{e}^{\imath\omega})$ acoustic impedance related to mass-spring-resistance of the earcup in closed-back headset system; (11.4.3) on page 485

INDEX

www.elektro.dtu.dk

Department of Electrical Engineering
Acoustic Technology
Technical University of Denmark
Ørsteds Plads
Building 348
DK-2800 Kgs. Lyngby
Denmark
Tel: (+45) 45 25 38 00
Fax: (+45) 45 93 16 34
Email: info@elektro.dtu.dk

ISBN 978-87-92465-03-0